



NASA TECHNICAL MEMORANDUM

JSC-09166

NASA TM X-58131  
August 1974



APOLLO SCIENTIFIC EXPERIMENTS DATA HANDBOOK



(NASA-TM-X-58131) APOLLO SCIENTIFIC  
EXPERIMENTS DATA HANDBOOK (NASA) 907 p HC  
~~██████~~ 323.75 CSCL 22A

N76-14150

Unclas  
G3/12 J7270

NATIONAL AERONAUTICS AND SPACE ADMINISTRATION

LYNDON B. JOHNSON SPACE CENTER

HOUSTON, TEXAS 77058



LYNDON B. JOHNSON SPACE CENTER MEMORANDUM

REFER TO  
TC3-76-8-2

INITIATOR:  
TC3/WFEichelman:WWLauderdale:pdh:3728

DATE  
AUG 05 1976

TO: Distribution

CC:

ENCL: 1

FROM: TC3/Chief, Payload Requirements and  
Operations Branch

SIGNATURE

*W. F. Eichelman*  
W. F. Eichelman

SUBJ: Update to the Apollo Scientific Experiments Data Handbook

The enclosed is an update to the Apollo Scientific Experiments Data Handbook (TMX-58131). This is not a complete reprint, but the changes are to be made in accordance with the attached changed pages.

Questions about these changes should be directed to Mr. W. W. Lauderdale, TC3, JSC Houston, Texas.

# APOLLO SCIENTIFIC EXPERIMENTS DATA HANDBOOK

## CHANGE PAGES (April 1976)

To update your copy of the Apollo Scientific Experiments Data Handbook (NASA TM X-58131), the attached "change pages" should be substituted in your handbook as indicated. (Please note that page vii of your Apollo Scientific Experiments Data Handbook contains a form to request handbook revisions. If you want to continue receiving the handbook revisions, be sure that this form has been filled out and mailed as indicated in the instructions.)

<u>Change</u>	<u>Replace old page numbers</u>	<u>With new page numbers</u>
Contents	xi	xi
Section 3 -- Experiment Status	3-1 to 3-38	3-1 to 3-54
Divider	Part A, blue sheet following p. 3-38	Part A, pink sheet following p. 3-54
Section 4 -- Passive Seismic Experiment	4-1 to 4-28	4-1 to 4-29
Section 5 -- Active Seismic Experiment	5-1 to 5-22	5-1 to 5-25
Section 6 -- Lunar Surface Magnetometer Experiment	6-1 to 6-11	6-1 to 6-12
Section 7 -- Lunar Portable Magnetometer	7-3 and 7-4 7-7 and 7-8	7-3 and 7-4 7-7 and 7-8
Section 8 -- Solar-Wind Spectrometer Experiment	8-3 to 8-6 8-11 to 8-18	8-3 to 8-6 8-11 to 8-18
Section 9 -- Suprathermal Ion Detector Experiment	9-1 to 9-13	9-1 to 9-23
Section 10 -- Heat Flow Experiment	10-1 and 10-2 10-31 to 10-56	10-1 and 10-2 10-31 to 10-64

<u>Change</u>	<u>Replace old page numbers</u>	<u>With new page numbers</u>
Section 16 -- Tra- verse Gravimeter Experiment	16-1 to 16-29	16-1 to 16-38
Section 18 -- Far UV Camera/Spectrograph	18-1 to 18-10 New input	18-1 to 18-10 18-15 to 18-17
Section 19 -- Lunar Ejecta and Mete- orites Experiment	19-1 to 19-7	19-1 to 19-8
Section 24 -- Lunar Neutron Probe Experiment	24-1 to 24-35	24-1 to 24-61
Section 25 -- Dust Thermal Radiation Engineering Measurement	25-7 to 25-13	25-7 to 25-16
Divider	Part B, blue sheet following p. 25-13	Part B, pink sheet following p. 25-16
Section 31 -- Bistatic-Radar Experiment	31-79 and 31-80	31-79 and 31-80
Section 33 -- Sub- satellite Experiments	33-1 to 33-67	33-1 to 33-73
Section 36 -- Lunar Photographs and Mapping Products	36-1 to 36-25	36-1 to 36-34
Section 37 -- Lunar Sample Research Program	37-3 and 37-4	37-3 and 37-4
Appendix A Apollo Experiment Principal Investigators	A-1 to A-8	A-1 to A-8
Appendix D Solar-Wind- Composition Experiment	(New Input)	Insert pages D-1 to D-20 after appen- dix C

Insert these three pages as pages C-1, C-2, and C-3 immediately following page xi of the table of contents; thus indicating that your handbook contains the revisions of April 1976.

1. Report No NASA TM X-58131	2. Government Accession No.	3. Recipient's Catalog No.	
4. Title and Subtitle APOLLO SCIENTIFIC EXPERIMENTS DATA HANDBOOK		5. Report Date August 1974	
		6. Performing Organization Code	
7. Author(s) W. W. Lauderdale, General Electric Co., and W. F. Eichelman, JSC, Technical Editors		8. Performing Organization Report No. JSC-09166	
		10. Work Unit No. 383-85-00-00-72	
9. Performing Organization Name and Address Lyndon B. Johnson Space Center Houston, Texas 77058		11. Contract or Grant No.	
		13. Type of Report and Period Covered Technical Memorandum	
12. Sponsoring Agency Name and Address National Aeronautics and Space Administration Washington, D.C. 20546		14. Sponsoring Agency Code	
		15. Supplementary Notes	
16. Abstract This publication presents a brief description of each of the Apollo scientific experiments together with the operational history, the data content and formats, and the availability of the data. The lunar surface experiments described are the passive seismic, active seismic, lunar surface magnetometer, solar wind spectrometer, suprathreshold ion detector, heat flow, charged particle, cold cathode gage, lunar geology, laser ranging retroreflector, cosmic ray detector, lunar portable magnetometer, traverse gravimeter, soil mechanics, far UV camera (lunar surface), lunar ejecta and meteorites, surface electrical properties, lunar atmospheric composition, lunar surface gravimeter, lunar seismic profiling, neutron flux, and dust detector. The orbital experiments described are the gamma-ray spectrometer, X-ray fluorescence, alpha-particle spectrometer, S-band transponder, mass spectrometer, far UV spectrometer, bistatic radar, IR scanning radiometer, particle shadows, magnetometer, lunar sounder, and laser altimeter. Also included are a brief listing of the mapping products available and information on the sample program.			
17. Key Words (Suggested by Author(s)) · Moon · Lunar Science · Scientific Satellite · Neutrons · Lunar Landing · Lunar Orbit · Particles · Lunar Exploration · Geophysics · Lunar Environments		18. Distribution Statement	
19. Security Classif. (of this report) Unclassified	20. Security Classif. (of this page) Unclassified	21. No. of Pages 898	22. Price

NASA TM X-58131

**APOLLO SCIENTIFIC EXPERIMENTS DATA HANDBOOK**

Edited by

**W. W. Lauderdale**  
**General Electric Company**  
**Houston, Texas 77058**

and

**W. F. Eichelman**  
**Lyndon B. Johnson Space Center**  
**Houston, Texas 77058**

## FOREWORD

The Apollo Program has provided, and will continue to provide, a wealth of scientific data. Until recently, these data were analyzed primarily by the Principal Investigators and their teams under the proprietary rights recognized by NASA. Following the last Apollo mission, the Lunar Analysis and Synthesis Program was established to encourage the participation of a larger segment of the scientific community in lunar science development (e.g., through the multidiscipline studies, development of comprehensive models of lunar origin and evolution, studies of lunar physical properties and motions, studies of the internal and external processes operating on the Moon, etc.).

One of the first activities of this program was to determine the procedures for disseminating lunar science data as broadly and effectively as possible. This handbook was written to assist in the dissemination of these data to the scientific community and especially to facilitate greater participation in the evaluation of lunar science data.

The NASA Lyndon B. Johnson Space Center acknowledges the efforts of the Geophysical Data Evaluation Working Group in the establishment and implementation of the data archiving procedures. We also appreciate the cooperation of the Principal Investigators and their teams and the Lunar Science Institute in presenting information and written material for this handbook.

INFORMATION ON REVISIONS

This publication will be revised periodically to provide more current information. If you want an updated copy of this document, fill out the attached card and mail to W. F. Eichelman, TN-3, Lyndon B. Johnson Space Center, Houston, Texas 77058.

W. F. Eichelman, TN-3  
Lyndon B. Johnson Space Center

Please place my name on the mailing list for the next revision of the Apollo Scientific Experiments Data Handbook (NASA TM X-58131).

Name: \_\_\_\_\_

Address: \_\_\_\_\_

\_\_\_\_\_

\_\_\_\_\_

Affiliation: \_\_\_\_\_

\_\_\_\_\_

Date \_\_\_\_\_

PRECEDING PAGE BLANK NOT FILMED

CONTENTS

Section	Page
1 INTRODUCTION . . . . .	1-1
2 ALSEP EPHEMERIS DESCRIPTION . . . . .	2-1
3 EXPERIMENT STATUS . . . . .	3-1
PART A: LUNAR SURFACE EXPERIMENTS . . . . .	3-3
PART B: LUNAR ORBITAL EXPERIMENTS . . . . .	3-31
4 PASSIVE SEISMIC EXPERIMENT (NASA EXPERIMENT S-031) . . . . .	4-1
5 ACTIVE SEISMIC EXPERIMENT (NASA EXPERIMENT S-033) . . . . .	5-1
6 LUNAR SURFACE MAGNETOMETER (NASA EXPERIMENT S-034) . . . . .	6-1
7 LUNAR PORTABLE MAGNETOMETER (NASA EXPERIMENT S-198) . . . . .	7-1
8 SOLAR-WIND SPECTROMETER (NASA EXPERIMENT S-035) . . . . .	8-1
9 SUPRATHERMAL ION DETECTOR EXPERIMENT (NASA EXPERIMENT S-036) . . . . .	9-1
10 HEAT FLOW EXPERIMENT (NASA EXPERIMENT S-037) . . . . .	10-1
11 CHARGED-PARTICLE LUNAR ENVIRONMENT EXPERIMENT (NASA EXPERIMENT S-038) . . . . .	11-1
12 COLD CATHODE GAGE EXPERIMENT (NASA EXPERIMENT S-058) . . . . .	12-1
13 LUNAR GEOLOGY (NASA EXPERIMENT S-059) . . . . .	13-1
14 LASER RANGING RETROREFLECTOR (NASA EXPERIMENT S-078) . . . . .	14-1
15 LUNAR SURFACE COSMIC RAY EXPERIMENT (NASA EXPERIMENT S-152) . . . . .	15-1
16 TRAVERSE GRAVIMETER EXPERIMENT (NASA EXPERIMENT S-199) . . . . .	16-1

Section	Page
17 SOIL MECHANICS EXPERIMENT (NASA EXPERIMENT S-200) . . . . .	
18 FAR UV CAMERA/SPECTROGRAPH (NASA EXPERIMENT S-201) . . . . .	
19 LUNAR EJECTA AND METEORITES EXPERIMENT (NASA EXPERIMENT S-202) . . . . .	19-1
20 SURFACE ELECTRICAL PROPERTIES (NASA EXPERIMENT S-204) . . . . .	20-1
21 LUNAR ATMOSPHERIC COMPOSITION EXPERIMENT (NASA EXPERIMENT S-205) . . . . .	21-1
22 LUNAR SURFACE GRAVIMETER (NASA EXPERIMENT S-207) . . . . .	22-1
23 LUNAR SEISMIC PROFILING EXPERIMENT (NASA EXPERIMENT S-203) . . . . .	23-1
24 LUNAR NEUTRON PROBE EXPERIMENT (NASA EXPERIMENT S-229) . . . . .	24-1
25 DUST THERMAL RADIATION ENGINEERING MEASUREMENT (NASA EXPERIMENT M-515) . . . . .	25-1
26 GAMMA-RAY SPECTROMETER (NASA EXPERIMENT S-160) . . . . .	26-1
27 X-RAY FLUORESCENCE SPECTROMETER (NASA EXPERIMENT S-161) . . . . .	27-1
28 ALPHA-PARTICLE SPECTROMETER AND X-RAY FLUOR- ESCENCE SPECTROMETER (TRANSEARTH) (NASA EXPERIMENT S-162) . . . . .	28-1
PART A: ALPHA-PARTICLE SPECTROMETER . . . . .	28-3
PART B: X-RAY FLUORESCENCE SPECTROMETER (TRANSEARTH) . . . . .	28-17
29 LUNAR ORBITAL MASS SPECTROMETER (NASA EXPERIMENT S-165) . . . . .	29-1
30 ULTRAVIOLET SPECTROMETER (NASA EXPERIMENT S-169) . . . . .	30-1

Section	Page
31 BISTATIC-RADAR EXPERIMENT (NASA EXPERIMENT S-170) . . . . .	31-1
32 INFRARED SCANNING RADIOMETER (NASA EXPERIMENT S-171) . . . . .	32-1
33 SUBSATELLITE EXPERIMENTS . . . . .	33-1
PART A: PARTICLES AND FIELDS SUBSATELLITE PARTICLES (NASA EXPERIMENT S-173) . . . . .	33-9
PART B: PARTICLES AND FIELDS SUBSATELLITE MAGNETOMETER (NASA EXPERIMENT S-174) . . . . .	33-35
PART C: S-BAND TRANSPONDER (NASA EXPERIMENT S-164) . . . . .	33-55
34 APOLLO LUNAR SOUNDER EXPERIMENT (NASA EXPERIMENT S-209) . . . . .	34-1
35 LASER ALTIMETER (NASA EXPERIMENT S-175) . . . . .	35-1
36 LUNAR AND PLANETARY MAPPING PRODUCTS . . . . .	36-1
37 LUNAR SAMPLE RESEARCH PROGRAM . . . . .	37-1
APPENDIX A — APOLLO EXPERIMENT PRINCIPAL INVESTIGATORS . . . . .	A-1
APPENDIX B — APOLLO ALSEP DEPLOYMENT CONFIG- URATIONS AND LUNAR GROUNDTRACKS . . . . .	B-1
APPENDIX C — LIST OF ACRONYMS . . . . .	C-1
APPENDIX D — SOLAR-WIND-COMPOSITION EXPERIMENT . . . . .	D-1

1. INTRODUCTION

CONTENTS - SECTION 1

	Page
DATA AVAILABILITY AND ORDERING PROCEDURES . . . . .	1-3
THE NSSDC FACILITIES AND SERVICES . . . . .	1-5

## 1. INTRODUCTION

The purpose of this handbook is to present an overview of the Apollo Program scientific experiments to assist the scientific community in further study and synthesis of the experiment data. The experiment information in this publication is not intended for use in data analysis; it is given only as a guide for the preparation of data analysis plans.

Each experiment is explained and the equipment is described. Limited descriptions are given of the computer programs used in the data processing, together with information about location and availability of the data.

The distribution of data will generally be handled by the National Space Science Data Center (NSSDC). After the user has studied this handbook and decided on the area of investigation or data synthesis, he should request data for specific time periods of specific missions. The procedure for requesting data from NSSDC is described in the following paragraphs.

### DATA AVAILABILITY AND ORDERING PROCEDURES

The purpose of the NSSDC is to provide data and information from space science experiments in support of additional studies beyond those performed by the principal investigators. Therefore, NSSDC will provide data and information, upon request, to any individual or organization in the United States. In addition, the same services are available to scientists outside the United States through the World Data Center A for Rockets and Satellites (WDC-A-R&S). Normally, a charge is made for the requested data to cover the cost of reproduction and the processing of the request. The requester will be notified of the cost, and payment must be received prior to processing the request. The director of NSSDC may waive, as resources permit, the charge for modest amounts of data when they are to be used for scientific studies or for specific educational purposes and when they are requested by an individual affiliated with one of the following:

1. NASA installations, NASA contractors, or NASA grantees

2. Other U.S. Government agencies, their contractors, or their grantees

3. Universities and colleges

4. State and local Governments

5. Nonprofit organizations

A user can obtain data in any of the following ways:

1. Letter request

2. NSSDC Data Request Form (fig. 1-1)

3. Telephone request

4. Onsite request

Anyone who desires to obtain data for a scientific study should specify the NSSDC identification number, the common name and/or number of the satellite and the experiment, the form of data, and the time span (or location, when appropriate) of data requested. (Because some of the Apollo science experiments are still returning useful data and data from others may not have been deposited in the NSSDC, users should consult the most recent NSSDC Data Catalog of Satellite Experiments for specifics on time periods of data coverage and availability.) A requester should also specify why the data are needed, the subject of his work, the name of the organization with which he is affiliated, and any Government contracts he may have for performing his study.

When requesting data on magnetic tape, the user should specify whether he will supply new tapes prior to the processing, return the original NSSDC tapes after the data have been copied, or pay for new tapes.

The NSSDC official address for requests is

National Space Science Data Center  
Code 601.4  
Goddard Space Flight Center  
Greenbelt, Maryland 20771

Phone: 301 982-6695

Users who reside outside the United States should direct requests for data to

World Data Center A for Rockets and Satellites  
Code 601  
Goddard Space Flight Center  
Greenbelt, Maryland 20771 U.S.A.

Phone: 301 982-6695

#### THE NSSDC FACILITIES AND SERVICES

The NSSDC provides facilities for reproduction of data and for onsite data use. Resident and visiting scientists are invited to study the data while at NSSDC. The NSSDC staff will assist users with additional data searches and with the use of equipment. In addition to satellite and space probe data, the NSSDC maintains some correlative data and information on other correlative data that may be related to a specific request. These correlative data are described in the "NSSDC Handbook of Correlative Data" (NSSDC 71-05), which is available from the Data Center.

In addition to its main function of providing selected data and supporting information for further analysis of space science flight experiments, the NSSDC produces a wide spectrum of publications. Among these are documents that announce the availability of spacecraft experiment data, a report on active and planned spacecraft and experiments, and lunar and planetary photographic catalogs and users guides. For additional information on NSSDC and WDC-A-R&S document availability and distribution services, write to the appropriate address as given earlier and ask for document NSSDC/WDC-A-R&S 74-10.

**NSSDC DATA REQUEST FORM\***

Scientists OUTSIDE the United States send order to:		Requesters WITHIN the United States send order to:	
WORLD DATA CENTER A ROCKETS AND SATELLITES CODE 601 GODDARD SPACE FLIGHT CENTER GREENBELT, MARYLAND 20771, USA		NATIONAL SPACE SCIENCE DATA CENTER CODE 601.4 GODDARD SPACE FLIGHT CENTER GREENBELT, MARYLAND 20771	
<b>REQUESTER INFORMATION (Please print)</b>			
NAME		TITLE/POSITION	
DIVISION/BRANCH/DEPARTMENT			MAIL CODE
ORGANIZATION			
ADDRESS			
CITY		STATE	
ZIP CODE OR COUNTRY		TELEPHONE (Area Code) (Number) (Extension)	
DATE OF REQUEST	DATE DATA DESIRED	(Our average processing time for a request is 3 to 4 weeks. Please allow ample time for delivery. We will notify you if we cannot meet the date specified.)	

**INTENDED USE OF DATA (check all that apply)**

<input type="checkbox"/> Support of a NASA effort (project, study, etc.), Contract No. _____	
<input type="checkbox"/> Support of a U.S. Government effort (other than NASA)	
<input type="checkbox"/> Research and analysis project (individual or company sponsored)	
<input type="checkbox"/> Educational purposes (explain below)	<input type="checkbox"/> Exhibit or display
<input type="checkbox"/> Preparation of Master's thesis	<input type="checkbox"/> Reference material
<input type="checkbox"/> Preparation of Doctoral thesis	<input type="checkbox"/> Use in publication
<input type="checkbox"/> Other:	
_____	
_____	
_____	
NSSDC requests the submission of all publications resulting from studies in which data supplied by NSSDC have been used. Please state briefly the research projects in which you are engaged and if you plan to prepare any articles based on this research.	
_____	
_____	
_____	
_____	
_____	
_____	

\*NSSDC has available special forms for ordering photographic data from the Surveyor, Lunar Orbiter, Apollo, and Mariner missions. These forms will be provided on request.

(a) Front.

Figure 1-1.- The NSSDC data request form.

**ORIGINAL PAGE IS  
OF POOR QUALITY**



2. ALSEP EPHEMERIS DESCRIPTION

CONTENTS - SECTION 2

	Page
TECHNICAL DESCRIPTION . . . . .	2-3
USAGE . . . . .	2-3
System 1 . . . . .	2-3
System 2 . . . . .	2-4
System 3 . . . . .	2-5
UNITS . . . . .	2-5
OUTPUT TAPE FORMAT . . . . .	2-6
DATA ARCHIVED AT NSSDC . . . . .	2-8
REFERENCE . . . . .	2-8

## 2. ALSEP EPHEMERIS DESCRIPTION

The Apollo lunar surface experiments package (ALSEP) ephemeris tape is generated by using data obtained from a single precision ephemeris tape containing positions of the Moon and the Sun with respect to the Earth for the period from the year 1950 to the year 2000. This tape was constructed using data provided by the NASA Jet Propulsion Laboratory.

### TECHNICAL DESCRIPTION

The data used to construct the ALSEP ephemeris tape are in the mean equinox of the epoch coordinate system, where the epoch is defined as the nearest beginning of a Besellian year. The positions of the Moon and the Sun are found relative to the position of the Earth at a specified time by applying Newton's fifth-order interpolation to the tabular data. The two resulting vectors are rotated into the true-equinox-of-date system by application of the matrices of precession and nutation. The origin of the coordinate system is then translated to the Moon center, and the transformation into selenographic coordinates is accomplished using the libration matrix (ref. 2-1). The selenographic x-y plane is the true equatorial plane of the Moon, with the x-axis passing through the prime meridian. The z-axis lies along the true axis of the Moon in a northerly direction, and the y-axis completes the right-handed system.

### USAGE

All output coordinate systems are positioned so that their origins are located at the ALSEP. Output is in both the spherical and Cartesian representation of three basic ALSEP-centered coordinate systems.

#### System 1

The primary plane of the first coordinate system is the ALSEP meridian plane. The Cartesian x-axis points radially outward from the ALSEP (toward the zenith), the z-axis lies in the ALSEP meridian plane in a northerly direction, and the y-axis lies in

the equatorial plane completing the right-handed system. The construction of the coordinate system is as follows.

$$\left. \begin{pmatrix} x' \\ y' \\ z' \end{pmatrix} = \begin{bmatrix} \cos \psi \cos \lambda & \cos \phi \sin \lambda & \sin \phi \\ -\sin \lambda & \cos \lambda & 0 \\ -\sin \phi \cos \lambda & -\sin \phi \sin \lambda & \cos \phi \end{bmatrix} \begin{pmatrix} x \\ y \\ z \end{pmatrix} \right\} (2-1)$$

where  $x', y', z'$  denote the ALSEP-centered axes,  $x, y, z$  denote the selenographic axes,  $\lambda$  is the selenographic longitude of the ALSEP, and  $\phi$  is the selenographic latitude of the ALSEP.

The primary plane of the spherical coordinate system is the Cartesian  $x'-z'$  plane; the principal axis is the  $x'$  axis. The in-plane angle  $\theta$  is measured from  $x'$  toward  $z'$  in the range  $-\pi$  to  $\pi$ . The out-of-plane angle  $\psi$  is measured from the primary plane toward the positive  $y'$  axis, in the range  $-\frac{\pi}{2}$  to  $\frac{\pi}{2}$ .

$$\left. \begin{aligned} R &= \sqrt{x'^2 + y'^2 + z'^2} \\ \theta &= \tan^{-1}\left(\frac{z'}{x'}\right) \\ \psi &= \sin^{-1}\left(\frac{y'}{\sqrt{x'^2 + y'^2 + z'^2}}\right) \end{aligned} \right\} (2-2)$$

#### System 2

The Cartesian  $x$ -axis of system 2 is the ALSEP-Earth line, which is positive toward the Earth. The  $y$ -axis lies parallel to the Earth-Moon-line/Moon-velocity plane in the direction opposite the Moon velocity vector. The  $z$ -axis completes the right-handed system as follows.

$$\left. \begin{aligned} \vec{x} &= \hat{R}_{E/A} \\ \vec{z}' &= \vec{R}_{M/E} \times \vec{V}_{M/E} \\ \vec{y} &= \text{unit}(\vec{z}' \times \vec{x}) \\ \vec{z} &= \vec{x} \times \vec{y} \end{aligned} \right\} (2-3)$$

where  $\vec{x}, \vec{y}, \vec{z}$  are the axes of coordinate system 2,  $\hat{R}_{E/A}$  is the unit vector from ALSEP toward Earth,  $\vec{R}_{M/E}$  is the position vector from Earth to Moon,  $\vec{V}_{M/E}$  is the velocity vector of the Moon, and  $\times$  denotes cross product. The primary plane of the spherical system is the x-y plane of coordinate system 2. The principal axis of the spherical system is the Cartesian x-axis. The construction of the spherical vectors of the Earth and the Sun are as follows.

$$\left. \begin{aligned} R &= \sqrt{x^2 + y^2 + z^2} \\ \theta &= \tan^{-1}\left(\frac{y}{x}\right) \\ \psi &= \sin^{-1}\left(\frac{z}{\sqrt{x^2 + y^2 + z^2}}\right) \end{aligned} \right\} (2-4)$$

### System 3

The x-axis of system 3 is the unit vector directed from ALSEP toward the Sun. The z-axis is nearly normal to the ecliptic plane, positive northward. The x-axis is not truly in the ecliptic plane. The y-axis completes the right-handed system.

$$\left. \begin{aligned} \vec{x} &= \hat{R}_{S/A} \\ \vec{z}' &= \hat{H} \\ \vec{y} &= \vec{z}' \times \vec{x} \\ \vec{z} &= \vec{x} \times \vec{y} \end{aligned} \right\} (2-5)$$

where  $\hat{H}$  is the unit vector normal to the ecliptic. The spherical system is directly analogous to system 2.

### UNITS

All output angles are in radians. Distance units are Earth radii (ER). One ER is equal to 20 925 696.3 U.S. ft, 20 925 738.19 international ft, or 6378.165 km.

## OUTPUT TAPE FORMAT

The output tape format is in Univac FORTRAN. The header record consists of a control word; four integers giving ALSEP number, day, month, and year; check sum; and another control word. Data records consist of the control word and 24-hr blocks of ephemeris that will be contained in 468 words per record. The words are as follows.

<u>Word</u>	<u>Description</u>
1	Calendar year
2	G.m.t. elapsed days from January 0
3	00 (two zeros), which corresponds to 00:00 G.m.t.
(Words 4 to 15 will all be relative to system 1.)	
4	x coordinate from the ALSEP to the earth center
5	y coordinate from the ALSEP to the Earth center
6	z coordinate from the ALSEP to the Earth center
7 to 9	Spherical coordinates $\rho, \theta, \psi$ of words 4, 5, and 6, respectively
10 to 12	Cartesian coordinates $x, y, z$ , respectively, measured from the ALSEP to the Sun center for 00:00 G.m.t.
13 to 15	Spherical coordinates $\rho, \theta, \psi$ , of words 10 to 12, respectively
(Words 16 to 27 will be relative to system 2.)	
16 to 18	Cartesian coordinates $x, y, z$ of Earth center at 00:00 G.m.t.
19 to 21	Spherical coordinates $\rho, \theta, \psi$ , of words 16 to 18, respectively
22 to 24	Cartesian coordinates $x, y, z$ of Sun center at 00:00 G.m.t.
25 to 27	Spherical coordinates $\rho, \theta, \psi$ of words 22 to 24, respectively

<u>Word</u>	<u>Description</u>
(Words 28 to 39 will be information using system 3.)	
28 to 30	Cartesian coordinates $x, y, z$ of the Earth center at 00:00 G.m.t.
31 to 33	Spherical coordinates $\rho, \theta, \psi$ of words 28 to 30, respectively
34 to 36	Cartesian coordinates $x, y, z$ Sun center at 00:00 G.m.t.
37 to 39	Spherical coordinates $\rho, \theta, \psi$ of words 34 to 36, respectively
40	Calendar year
41	G.m.t. elapsed days from January 0
42	02 (hours of G.m.t. for word 41)
43 to 78	Repeat of words 4 to 39 except for a new time (word 42)
79	Calendar year
80	G.m.t. elapsed days from January 0
81	04 (hours of G.m.t. for word 80)
82 to 117	Repeat of words 4 to 39 except for a new time (word 81)

This scheme will repeat nine times to complete the day. Words 1, 40, 79, 118, 157, 196, 235, 274, 313, 352, 391, and 430 all will be calendar year. For a given record, each of these words will contain the same constant value. Words 2, 41, 80, 119, 158, 197, 236, 275, 314, 353, 392, and 431 all will contain the number of days elapsed from January 0. For a given record, each of these words will contain the same constant value. Words 3, 42, 81, 120, 159, 198, 237, 276, 315, 354, 392, and 432 all will be hour designators starting at 00 hours and incrementing by 2 for each word. For example, the ephemeris information for 12:00 G.m.t. October 20, 1966, would be the 12 words following word 237 of day 293 of 1966. Within each system, the first three words denote Earth Cartesian coordinates  $x, y, z$ ; the second three words denote Earth spherical coordinates  $\rho, \theta, \psi$ ; the third three words denote Sun Cartesian coordinates  $x, y, z$ ; and the fourth three words denote Sun spherical coordinates  $\rho, \theta, \psi$ .

---

One complete ephemeris 26-bit magnetic tape is sent to each principal investigator (six tapes). Books of ephemeris data from 4020 microfilm are made as the demand requires. The microfilm data are written by the computer just after the output tape is written. The microfilm copy is not, therefore, a copy produced by reading the output data tape.

The Univac can write only 256-word records; therefore, one logical record appears in two physical records on tape. The second of each pair has zeros inserted at the end to fill up the 256-word record. In the control word, bits 11 to 0 give the block number within the logical record and bits 35 to 18 give the number of data words in the physical record.

#### DATA ARCHIVED AT NSSDC

Ephemeris data and appropriate documentation will be available through the National Space Science Data Center (NSSDC).

#### REFERENCE

- 2-1. Kalensher, B. E.: Selenographic Coordinates. NASA CR-53132, 1961.

### 3. EXPERIMENT STATUS

This section gives the current status of lunar surface and lunar orbital experiments conducted during the Apollo Program. Experiment status is divided into two subsections:

Part A: Lunar Surface Experiments

Part B: Lunar Orbital Experiments

Data users should consult this section for the current status of the lunar experiments. The status is updated periodically, and current information can be obtained from the National Space Science Data Center (NSSDC). Sections 4 to 35 of this handbook give background information on each experiment, but the grammatical structure of the sections (e.g., verb tense) is not necessarily an indication of the current operational status of a given experiment.

CONTENTS - SECTION 3

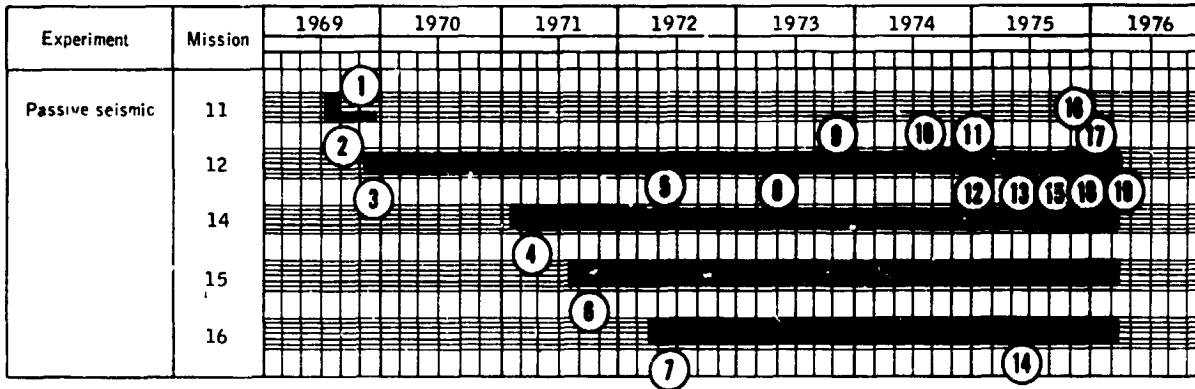
	Page
PART A: LUNAR SURFACE EXPERIMENTS . . . . .	3-3
S-031 PASSIVE SEISMIC EXPERIMENT . . . . .	3-4
S-033 ACTIVE SEISMIC EXPERIMENT . . . . .	3-10
S-034 LUNAR SURFACE MAGNETOMETER . . . . .	3-13
S-035 SOLAR-WIND SPECTROMETER . . . . .	3-18
S-036 SUPRATHERMAL ION DETECTOR . . . . .	3-21
S-037 HEAT FLOW EXPERIMENT . . . . .	3-25
S-038 CHARGED PARTICLE LUNAR ENVIRONMENT EXPERIMENT . . . . .	3-26
S-058 COLD CATHODE ION GAGE . . . . .	3-28
S-078 LASER RANGING RETROREFLECTOR . . . . .	3-30
S-202 LUNAR EJECTA AND METEORITES EXPERIMENT . . . . .	3-31
S-203 LUNAR SEISMIC PROFILING EXPERIMENT . . . . .	3-32
S-205 LUNAR ATMOSPHERIC COMPOSITION EXPERIMENT . . . . .	3-34
S-207 LUNAR SURFACE GRAVIMETER . . . . .	3-39
M-515 DUST DETECTOR EXPERIMENT . . . . .	3-41
CENTRAL STATION ELECTRONICS . . . . .	3-42
PART B: LUNAR ORBITAL EXPERIMENTS . . . . .	3-47

## PART A: LUNAR SURFACE EXPERIMENTS

Scientific data-gathering equipment and related communications equipment were deployed on the lunar surface during each of the six Apollo lunar landing missions from July 20, 1969 (Apollo 11 mission), to December 12, 1972 (Apollo 17 mission). The performance of the deployed equipment, which was designed to provide data after the return of the crewmembers to Earth, is detailed in the following pages. This experiment status is as of April 1, 1976.

S-031 PASSIVE SEISMIC EXPERIMENT

Time history and proportion of full capability of instrument



Legend:  
 Science data output 100%  
 Housekeeping data 0%  
 100%

<u>Item</u>	<u>Apollo mission</u>	<u>Initial date of occurrence</u>	<u>Status</u>
1	11	Aug. 27, 1969	PSE STANDBY mode. Station 11 operated for 20 Earth days before loss of the ALSEP central station command uplink terminated seismometer functions such as leveling, gain adjustments, and calibration.
2	12	Nov. 19, 1969	SPZ component displaying reduced sensitivity at low signal levels. The other three seismometers (J-PX, LPY, LPZ) have operated properly since initial activation.
3	12	Nov. 22, 1969	Thermal control problems. These thermal disturbances are most intense near sunrise and sunset. They are believed to be due to thermal contraction and expansion of the aluminized Mylar shroud that covers the sensor unit or to thermal contraction and expansion of the cable connecting the sensor unit

S-031 PASSIVE SEISMIC EXPERIMENT - Continued

<u>Item</u>	<u>Apollo mission</u>	<u>Initial date of occurrence</u>	<u>Status</u>
			to the central station, or both.
4	14	Feb. 12, 1971	Thermal control problems. The modified thermal shroud used on Apollo 14 provided improved thermal control. It was found that if the heater was commanded OFF for lunar day and AUTO for lunar night, the PSE temperature remained within the expected range for Apollo 14.
5	14	Mar. 20, 1972	LPZ axis inoperative. Analysis of the problem indicated this failure was either component failure or a wire connection problem. It was concluded that the failure was random rather than generic.
6	15	Aug. 13, 1971	Thermal control degradation. Review of lunar surface photographs showed that the periphery of the thermal shroud did not lie flat on the lunar surface. The incomplete deployment of the shroud resulted in excessive thermal leaks and loss of tidal data. For subsequent missions, crew training emphasized the need for the periphery of the shroud to be flat on the surface.
7	16	Apr. 24, 1972	High temperature during lunar day. Photographs of the deployed experiment, television coverage of the lunar module ascent, and comments by the crew indicate the following as possible causes of the problem: (1) some raised portions of the shroud, (2)

S-031 PASSIVE SEISMIC EXPERIMENT - Continued

<u>Item</u>	<u>Apollo mission</u>	<u>Initial date of occurrence</u>	<u>Status</u>
			dirt on the shroud from crew traffic subsequent to the photography, (3) debris from lift-off, and (4) possible contact of the experiment with the lunar surface. Any of the above conditions could cause degraded thermal control, resulting in higher temperatures during lunar day:
8	14	Apr. 14, 1973	Noisy data on long period y-axis were noted originally on Apr. 14, 1973, and intermittently since then by the principal investigator. Noise is caused by one bit not setting. Since July 30, 1974, the noise has appeared more frequently and was noted during real-time support periods from July 30 to Aug. 2, 1974; Aug. 7, 1974; and Aug. 9 to 16, 1974.
9	12	Dec. 28, 1973	Sporadic loss of LPZ axis data during lunar night operation. The anomaly was noted during real-time support periods. It was characterized by a lack of data (quiescent level) on the analog helicorder and by no observed response to calibration commands. The anomaly occurred during three successive lunar night periods (Dec. 28, 1973, to Jan. 2, 1974; Jan. 23 to Feb. 2, 1974; and Feb. 22 to Mar. 3, 1974). All data have been valid since Mar. 3, 1974.
10	12	Sept. 11, 1974	Long period x- and y-axes failed to calibrate on command. The anomaly has been

S-031 PASSIVE SEISMIC EXPERIMENT - Continued

<u>Item</u>	<u>Apollo mission</u>	<u>Initial date of occurrence</u>	<u>Status</u>
			<p>noted during real-time support periods on two separate occasions (Sept. 11 and Nov. 9 and 10, 1974). Long period z-axis was calibrated on command both times. Sensor temperature (DL-07) was 325.82 K (126.81° F) when axes did not calibrate and 325.58 K (126.37° F) when axes again responded to calibration commands. Sun angles during the periods of no response were 187.8° to 200.0° and 187.2° to 199.6°, respectively. A real-time support period at these Sun angles was not conducted in October. Calibration response has been normal at all other times.</p>
11	12	Oct. 16, 1974	<p>The instrument was commanded to operate with the feedback filter IN. The principal investigator requested this operation to obtain data for comparison with data from filter OUT operation. The instrument performed satisfactorily with the feedback filter IN. Test was completed on Apr. 9, 1975, and the instrument was returned to the feedback filter OUT mode.</p>
12	12	Nov. 7 1974	<p>An operational check on Nov. 7, 8, and 9, 1974, indicated that the heater could not be set in the auto OFF or forced OFF modes. Preliminary analysis indicated the cause of the failure to be that the heater ON/OFF relay driver circuit failed "closed" allowing +29 V dc power to be applied at all times.</p>

S-031 PASSIVE SEISMIC EXPERIMENT - Continued

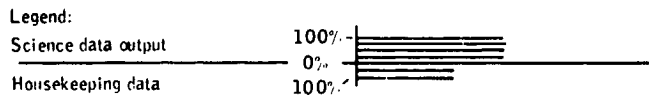
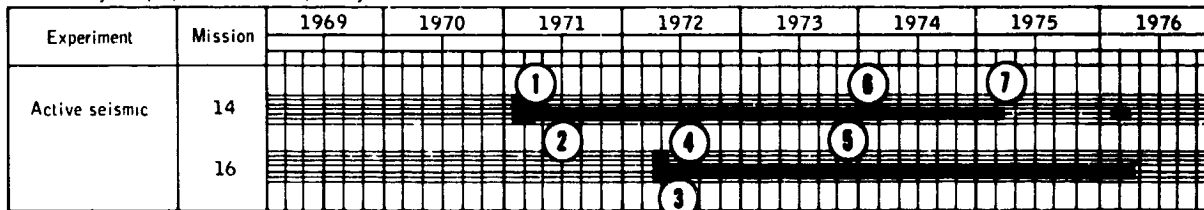
<u>Item</u>	<u>Apollo mission</u>	<u>Initial date of occurrence</u>	<u>Status</u>
13	14	Mar. 5, 1975	Engineering data from the PSE are valid. Science data from the PSE can be used for a period of approximately 9 days when the long period y-axis moves from off scale high to off scale low (Sun angles 55° to 109°) and off scale low to off scale high (Sun angles 185° to 237°). When Apollo 14 central station uplink capability was lost, the PSE heater was in the forced OFF mode for lunar daytime operation. The instrument remains in this configuration.
14	12, 15, and 16	June 28, 1975	From data received during the test conducted with the feedback filter IN of the Apollo 12 PSE, the principal investigator requested that the three experiments be configured to feedback filter IN. The instruments performed satisfactorily in this configuration.
15	14	Aug. 31, 1975 and Sept. 3, 1975	Although no leveling has been accomplished on the PSE since Mar. 1, 1975, because of the loss of command capability, a seismic event on these dates indicated that data were discernible on the long period x- and y-axis on the recorders.
16	12	Nov. 23, 1975	The short period z-axis gain was set at -20 dB. This setting eliminated some of the noise appearing on the long period axes due to crosstalk interference. The operation will continue pending further data analysis by the principal investigator.

S-031 PASSIVE SEISMIC EXPERIMENT - Concluded

<u>Item</u>	<u>Apollo mission</u>	<u>Initial date of occurrence</u>	<u>Status</u>
17	12	Dec. 5, 1975	Noise spike appeared in seismic data as a result of the third bit not setting in the PSE electronics analog-to-digital converter. Increasing the central station heat eliminated the problem.
18	14	Feb. 19, 1976	With return of uplink, subsequent attempts to command the feedback filter IN have shown the loop to be inoperative. The instrument was performing satisfactorily with the filter out. The long period y-axis could not be leveled during the uplink capability period.
19	14	Mar. 17, 1976	When loss of downlink and uplink occurred with the Apollo 14 central station, the PSE was ON and the heater was in the forced OFF mode.

S-033 ACTIVE SEISMIC EXPERIMENT

Time history and proportion of full capability of instrument



<u>Item</u>	<u>Apollo mission</u>	<u>Initial date of occurrence</u>	<u>Status</u>
1	14	Feb. 5, 1971	Thumper misfired 5 of 18 times. The problem was attributed to dirt on the firing switch actuator bearing surface. The situation was subsequently corrected for the Apollo 16 mission.
2	14	Mar. 26, 1971	Geophone 3 data are noisy because of transistor failure in amplifier 3. Data are recoverable to some extent by analysis.
3	16	May 23, 1972	Grenades 2, 4, and 3 were fired. Mortar package pitched down 9° as a result of launching grenade 2. The grenade 2 range wire probably fouled during launch, producing a downward force. Normal real-time event data were not received during flight of grenade 2. Grenade 1 was not fired at this time because of the failure of the pitch sensor of the mortar package after the grenade 4 firing. Internal temperatures of the mortar package vary from off scale low at night to 388.85 K (115.7° C) during lunar day,

S-033 ACTIVE SEISMIC EXPERIMENT - Continued

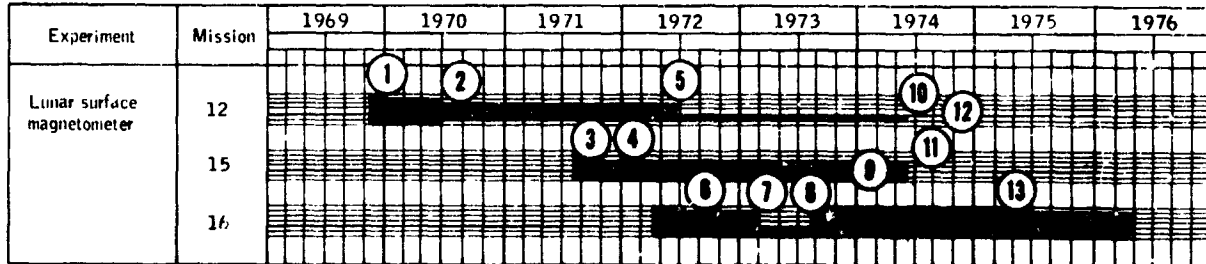
<u>Item</u>	<u>Apollo mission</u>	<u>Initial date of occurrence</u>	<u>Status</u>
			because some thermal protection was removed during the firing of the grenades.
4	16	May 23, 1972	Pitch sensor off scale high after launching of grenade 3. Data imply there was a sensor circuit failure. Detonation of grenade 4 successfully accomplished. Grenade 1 was not fired because of the uncertainty of the mortar pallet position. Launching of grenade 1 may be attempted, as a final experiment, should Apollo 16 ALSEP termination be considered.
5	14 and 16	Dec. 7, 1973	Weekly 30-min passive listening periods terminated in accordance with Apollo 14 ALSEP, SNEAR 86 and Apollo 16 ALSEP, SNEAR 27. The instruments will remain in STANDBY and OFF, respectively, with periodic high-bit-rate checks to verify functional capability.
6	14	Jan. 3, 1974	During the monthly operation check of the experiment, the data from geophone 2 appeared to be invalid. On Jan. 9, 1974, another operational check was conducted to further investigate the problem. Two geophone calibrations were commanded. The data indicated a response to the commanded pulses, but the response was improper. Analysis implies a failure in the amplifier channel 2 circuitry. Operational checks since Jan. 9, 1974, have confirmed that the status is unchanged.

S-033 ACTIVE SEISMIC EXPERIMENT - Concluded

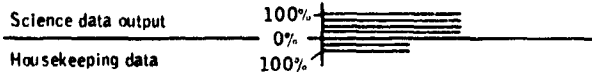
<u>Item</u>	<u>Apollo mission</u>	<u>Initial date of occurrence</u>	<u>Status</u>
7	14	Mar. 5, 1975	Because of the loss of uplink capability with Apollo 14 central station, the ASE can no longer be commanded and the grenades remain unfired.

## S-034 LUNAR SURFACE MAGNETOMETER

Time history and proportion of full capability of instrument



Legend:



<u>Item</u>	<u>Apollo mission</u>	<u>Initial date of occurrence</u>	<u>Status</u>
1	12	Dec. 22, 1969	Y-axis data offset. A bias shift of approximately 75 percent occurs during lunar day when temperatures reach or exceed 333 K (60° C). The data return to normal as the temperature decreases to approximately 308 K (35° C). The failure is suspected to be due to a resistance change in the bias circuitry. It is probably caused by a partially open weld, a sensor connection, or a flexible cable. The bias command has been used for compensating the data in real time.
2	12	June 29, 1970	Science and engineering data are static and invalid. It appears that the static engineering data during the lunar night, the erratic flip calibration data, and no current to the Y-axis flip motor are all caused by open welds in the circuitry. Re-inspection by three independent teams, repairs as required, and the improvements in thermal

S-034 LUNAR SURFACE MAGNETOJET™R - Continued

<u>Item</u>	<u>Apollo mission</u>	<u>Initial date of occurrence</u>	<u>Status</u>
			control were implemented to alleviate the problem for subsequent missions.
3	15	Aug. 30, 1971	Y-axis sensor head failed to flip on command. Normal calibration could not be provided because of the Y-axis flip problem; a modified data processing program was written, using the solar-wind spectrometer data to fulfill the calibration requirements.
4	15	Nov. 2, 1971	Y-axis sensor data loss. To be useful, data from all three axes are required. Data output continues to be recorded and archived; it is hoped that a method to correlate and analyze the data will be developed at some future date.
5	12	June 14, 1972	Suspension of flip calibration sequences. Because of static data output from the instrument, the principal investigator requested that flip calibration sequences be terminated. Flip calibrations would be performed again if science data indicated the need.
6	16	July 24, 1972	Failure of all three axes to flip. Analysis of the data indicated the problem was due to an elevated temperature at lunar-noon conditions.
7	16	Feb. 15, 1973	Intermittent loss of science data. Over a period of several months, the output of the instrument varied from dynamic, valid data to a static condition. Attempts were made to correct the situation by

S-034 LUNAR SURFACE MAGNETOMETER - Continued

<u>Item</u>	<u>Apollo mission</u>	<u>Initial date of occurrence</u>	<u>Status</u>
			ground command with no positive results obtained.
8	16	Aug. 17, 1973	Data processed by the principal investigator since Aug. 17, 1973, indicate that the instrument has returned to a fully operational condition. Return of the science data cannot be fully explained at this time but can be partially attributed to prolonged "cold soak" periods during lunar night.
9	15	Dec. 10, 1973	Loss of all scientific and engineering data. Attempts were made to correct the anomaly by ground command, but all data remain incoherent since initial date of the occurrence. The instrument remains in the power-on condition while investigation of this anomaly continues.
10	12	June 14, 1974	The instrument was permanently commanded OFF. The science and engineering data had been static and invalid since June 14, 1972. Output of the radioisotope thermoelectric generator had been steadily decreasing, and reserve power had become critical during lunar night to the point that a spurious functional change could have caused the loss of the currently functional instruments.
11	15	June 14, 1974	The instrument was permanently commanded OFF. The science and engineering data had been static and invalid since Dec. 10, 1973. Output of the

S-034 LUNAR SURFACE MAGNETOMETER - Continued

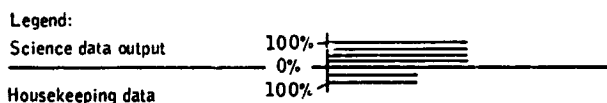
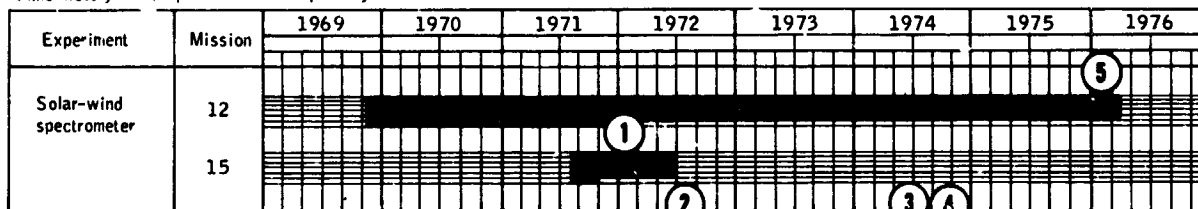
<u>Item</u>	<u>Apollo mission</u>	<u>Initial date of occurrence</u>	<u>Status</u>
			radioisotope thermoelectric generator had been steadily decreasing, and reserve power had become critical during lunar night to the point that a spurious functional change could have caused the loss of the currently functional instruments.
12	12 and 15	July 2, 1974	<p>The Apollo 12 instrument was commanded ON during real-time support on July 2, July 3, and Aug. 5, 1974. The Apollo 15 instrument was commanded ON during real-time support on July 2, 3, 5, and 29, 1974. The instruments did not downlink valid scientific and engineering data but the status bits were functioning properly in the inhibit, flip calibration, and science and calibration modes. This indicated that operation was not degraded after two lunar nights in the OFF mode of operation.</p> <p>On Sept. 3, 1974, both instruments were commanded ON but drew only negligible power and did not return any valid scientific or engineering data.</p> <p>On Jan. 29, 1975, an inadvertent ground command to the Apollo 15 instrument turned it ON, resulting in a 6-W reserve power drain and no science or engineering data in the telemetry downlink. The instrument was commanded OFF, and the reserve power increased 6 W.</p>

S-034 LUNAR SURFACE MAGNETOMETER - Concluded

<u>Item</u>	<u>Apollo mission</u>	<u>Initial date of occurrence</u>	<u>Status</u>
			On Dec. 18, 1975, an inadvertent ground command to the Apollo 15 instrument turned it ON. Later, the instrument was commanded OFF, and a minimal increase of 1 W in reserve power was observed.
13	16	Mar. 3, 1975	The Z-axis-sensor science data had become intermittently static and the temperature had reduced to off scale low during the lunar night. Flip calibrations of the sensor heads have been discontinued, at the principal investigator's request, during the lunar night operation as a result of the low temperatures of the Z-axis sensor.

## S-035 SOLAR-WIND SPECTROMETER

Time history and proportion of full capability of instrument



<u>Item</u>	<u>Apollo mission</u>	<u>Initial date of occurrence</u>	<u>Status</u>
1	12 and 15	Nov. 5, 1971	Intermittent modulation drop in proton energy levels 13 and 14. This thermally induced problem (which occurs each lunation) is attributed to a circuit that was used solely for ground test purposes.
2	15	June 30, 1972	Loss of experiment science and engineering data. Data analysis indicated high-voltage arcing was occurring in the equipment electronics causing excessive power consumption. Because the additional power consumption could not be tolerated by the Apollo 15 ALSEP system, the instrument was left in STANDBY mode indefinitely. The SWS is commanded to OPERATE SELECT periodically to ascertain any change in instrument status.
3	15	June 14, 1974	The instrument was permanently commanded OFF. The science and engineering data had been static and invalid since June 30, 1972. Output of the radioisotope thermoelectric generator had been steadily decreasing, and reserve power had become critical during

S-035 SOLAR-WIND SPECTROMETER - Continued

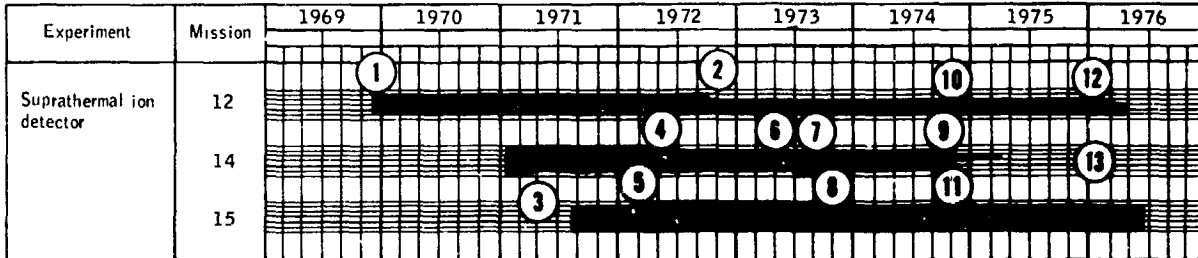
<u>Item</u>	<u>Apollo mission</u>	<u>Initial date of occurrence</u>	<u>Status</u>
			lunar night to the point that a spurious functional change could have caused the loss of the currently functional instruments.
4	15	July 3, 1974	<p>The instrument was commanded ON during real-time support on July 3, July 29, and Sept. 3, 1974. No scientific or engineering data were received in the ALSEP downlink. Reserve power change was 6.00 W on July 29, but was negligible for the other checks.</p> <p>A spurious functional command to ON was received by the instrument on Jan. 25, 1975, resulting in a 3.9-W reserve power drain. The instrument was commanded to STANDBY (no reserve power change) and then to OFF, and the reserve power increased 3.9 W.</p> <p>A spurious functional command to STANDBY POWER ON was received by the instrument on Sept. 15, 1975, resulting in a 4-W reserve power drain. The decrease in reserve power was attributed to the standby heater turning on. The instrument was commanded to OFF and the reserve power increased 4 W.</p> <p>A spurious functional command to ON was received by the instrument on Jan. 31, 1976. The experiment was commanded to OFF by the Guam Tracking Station; an increase or decrease in reserve power was not observed.</p>

S-035 SOLAR-WIND SPECTROMETER -- Concluded

<u>Item</u>	<u>Apollo mission</u>	<u>Initial date of occurrence</u>	<u>Status</u>
5	12	Mar. 3, 1976	The instrument is being turned to STANDBY during the lunar night to provide more heat in the central station PSE electronics to avoid the PSE analog-to-digital converter anomaly.

S-036 SUPRATHERMAL ION DETECTOR

Time history and proportion of full capability of instrument



Legend:  
 Science data output 100%   
 0%   
 Housekeeping data 100%

<u>Item</u>	<u>Apollo mission</u>	<u>Initial date of occurrence</u>	<u>Status</u>
1	12	Nov. 20, 1969	CCIG failure, high-voltage arcing problems. Ground tests verified that a transistor failed in the high-voltage control circuit. A slower response transistor operated satisfactorily in the environment with reasonable margins. Appropriate modifications were made to Apollo 14 SIDE/CCIG.
2	12	Sept. 9, 1972	Intermittent failure of digital electronics to process data. High-voltage arcing occurs at elevated lunar-day temperatures. The instrument is now commanded to OFF when the internal temperature approaches 328 K (55° C).
3	14	Apr. 5, 1971	Loss of the positive-section data of the analog-to-digital converter. The cause appears to be an intermittent connection in one of the modules of the analog-to-digital converter and does not appear to be temperature dependent. Anomaly precludes processing

S-036 SUPRATHERMAL ION DETECTOR - Continued

<u>Item</u>	<u>Apollo mission</u>	<u>Initial date of occurrence</u>	<u>Status</u>
			of any positive-value data inputs to the analog-to-digital converter.
4	14	Mar. 29, 1972	Anomalous STANDBY operation of SIDE. The mode change problem is attributed to arcing or corona in the high-voltage supply at elevated temperatures. The experiment is now commanded to STANDBY when the internal temperature approaches 358 K (85° C) to preclude spurious mode changes.
5	15	May 1, 1972	Full instrument operation instituted. Before Oct. 20, 1972, the Apollo 15 SIDE had been cycled to STANDBY during lunar day because of previous problems with the Apollo 12 SIDE. Based on data accumulated since deployment, it was decided to leave the instrument ON for the complete lunation.
6	14	Apr. 14, 1973	Anomalous STANDBY operation of SIDE. Subsequent to Apr. 1973, the instrument has gone from OPERATE to STANDBY without ground command at (or shortly after) the sunrise terminator crossing. The suspected cause is circuit breaker action in response to a SIDE current in excess of that required to trip the breaker. Data are obtained during lunar night when the instrument is ON. The instrument is permitted to switch itself from ON to STANDBY at sunrise terminator without commanding.
7	14	Aug. 8, 1973	There was no indication of

S-036 SUPRATHERMAL ION DETECTOR - Continued

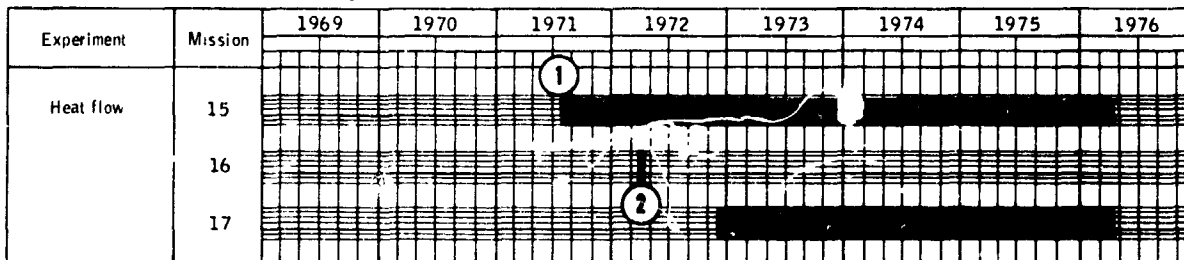
<u>Item</u>	<u>Apollo mission</u>	<u>Initial date of occurrence</u>	<u>Status</u>
			STANDBY power ON or operating power OFF through the console monitor lights or the high-speed printer data. Analysis indicates that the fuse opened in the STANDBY power line; thus, STANDBY operation is now equivalent to OFF.
8	15	Sept. 13, 1973	Cyclic commanding required to preclude spurious mode changes above 358 K (85° C). Internal high-voltage arcing caused -3.5-kV power supply to trip OFF. The instrument is now cycled to STANDBY during lunar day to preclude arcing.
9	12	Sept. 3, 1974	A reduction of high energy calibration and data counts occurred. Normal calibration and energy counts returned on Sept. 4, 1974. A reoccurrence of the anomaly was noted on Nov. 11, 1974. All engineering and science data during lunar night have been normal since Nov. 13, 1974. The suspected cause is a loss of amplifier gain for short periods.
10	12	Nov. 26, 1974	The instrument received a spurious functional command to ON during the lunar day. On Nov. 27, 1974, the experiment was checked; all high voltages were OFF and the electronics temperature (T2) was reading 349.95 K (76.8° C). The instrument was commanded OFF for cooling, below the maximum operating temperature of 328.15 K (55° C). Normal and valid engineering and science data have been obtained in subsequent operations.

S-036 SUPRATHERMAL ION DETECTOR - Concluded

<u>Item</u>	<u>Apollo mission</u>	<u>Initial date of occurrence</u>	<u>Status</u>
11	14	Nov. 29, 1974	The instrument could only be commanded ON briefly because of the lunar eclipse, although 72 commands were executed. Sporadic operation of the instrument was obtained during the next lunar night (Dec. 8 to 22, 1974) and none during the Jan. 6 to 21 and Feb. 5 to 20, 1975, lunar nights. More than 1700 unsuccessful ON commands have been transmitted to the instrument since the Nov. 29 lunar eclipse.
12	12	Jan. 18, 1976	The instrument is being commanded to STANDBY during the lunar night to provide more heat in the central station PSE electronics to avoid the PSE analog-to-digital-converter anomaly.
13	14	Feb. 19, 1976	With the return of uplink to the Apollo 14 central station, the experiment was commanded OFF.

S-037 HEAT FLOW EXPERIMENT

Time history and proportion of full capability of instrument

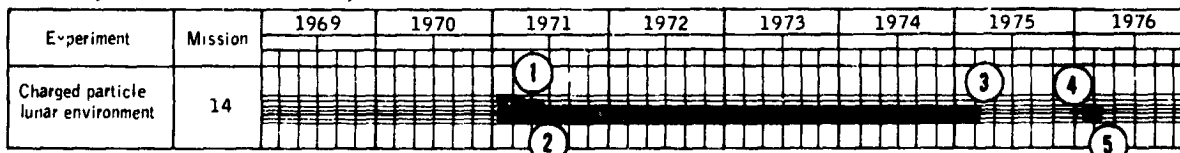


Legend:  
 Science data output 100%  
 Housekeeping data 0%  
 100%

<u>Item</u>	<u>Apollo mission</u>	<u>Initial date of occurrence</u>	<u>Status</u>
1	15	July 31, 1971	Probe 2 was not inserted to full depth because of problems with the Apollo lunar surface drill. Probe 2 still provides useful data to estimate heat flow in the lunar subsurface. Drill bore stems were redesigned for Apollo 16 and 17 missions.
2	16	Apr. 21, 1972	Electrical cable was severed during initial deployment by crew. Contingency repair plan proposed was denied because of higher mission priorities. Cable strain-relief provisions were implemented on all cables for the Apollo 17 mission.
3	17	N/A	Nominal deployment and full experiment operation.

S-038 CHARGED PARTICLE LUNAR ENVIRONMENT EXPERIMENT

Time history and proportion of full capability of instrument



Legend:  
 Science data output 100%   
 0%   
 Housekeeping data 100%

<u>Item</u>	<u>Apollo mission</u>	<u>Initial date of occurrence</u>	<u>Status</u>
1	14	Apr. 8, 1971	Loss of analyzer B data. Analysis indicates that the most probable cause of failure was a short in the high-voltage filter. The instrument continues operation on analyzer A. (Analyzer A provides identical data.)
2	14	June 6, 1971	Analyzer A data decay and undervoltage condition. The problem appears to be caused by the analyzer B anomaly. Further analysis of the anomaly is impossible because the analyzers are not separable by command. Instrument is operated satisfactorily in a locked low-voltage range (-35 V dc) and is commanded to STANDBY when high voltage decays below 2280 V dc. This operational mode results in operation for approximately 50 percent of each lunation.
3	14	Mar. 5, 1975	When the Apollo 14 central-station uplink capability was lost, the experiment was in STANDBY for lunar daytime operation. The instrument remains in this configuration.

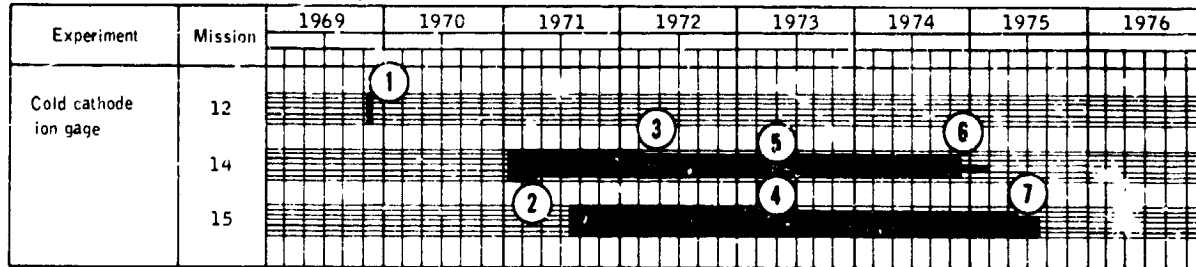
S-038 CHARGED PARTICLE LUNAR ENVIRONMENT

EXPERIMENT - Concluded

<u>Item</u>	<u>Apollo mission</u>	<u>Initial date of occurrence</u>	<u>Status</u>
4	14	Feb. 19, 1976	When the Apollo 14 central-station uplink capability was regained, the experiment was ON. Operation of the instrument will be as specified in item 2.
5	14	Mar. 17, 1976	When the Apollo 14 central-station uplink and downlink capability was lost, the experiment was in STANDBY for lunar daytime operation. The instrument remains in this configuration.

S-058 COLD CATHODE ION GAGE

Time history and proportion of full capability of instrument



Legend  
 Science data output 100% —————  
 0% - - - - -  
 Housekeeping data 100% —————

<u>Item</u>	<u>Apollo mission</u>	<u>Initial date of occurrence</u>	<u>Status</u>
1	12	Nov. 20, 1969	CCIG failure, high-voltage arcing problems. Ground tests verified that a transistor failed in high-voltage control circuit. A slower response transistor operated satisfactorily in the environment with reasonable margins. Appropriate modifications were made to Apollo 14 SIDE/CCIG.
2	14	Apr. 5, 1971	Loss of the positive-section data of the analog-to-digital converter. The cause appears to be an intermittent connection in one of the modules of the analog-to-digital converter and does not appear to be temperature dependent. This anomaly precludes processing of any positive-value data inputs to the analog-to-digital converter.
3	14	Mar. 29, 1972	Anomalous STANDBY operation of SIDE. The mode change problem is attributed to arcing or corona in the high-voltage supply at

S-058 COLD CATHODE ION GAGE - Concluded

<u>Item</u>	<u>Apollo mission</u>	<u>Initial date of occurrence</u>	<u>Status</u>
			elevated temperatures. The experiment is now commanded to STANDBY when the internal temperature approaches 358 K (85° C) to preclude spurious mode changes.
4	15	Feb. 22, 1973	Intermittent science data. Preliminary analysis indicates that the most probable cause is one of the 15 relays. These reed relays perform functions that control the CCIG calibration currents, the ranging and gain change functions, and grounding the instrument during calibration. Currently, no plans exist for continued investigation of this anomaly, because the scientific data are usable when obtained.
5	14	Apr. 8, 1973	See item 6 of the status report on the Suprathermal Ion Detector Experiment.
6	14	Nov. 29, 1974	See item 11 of the status report on the Suprathermal Ion Detector Experiment.
7	15	July 18, 1975	CCIG failure; high voltage was off and could not be commanded ON.

S-078 LASER RANGING RETROREFLECTOR

Time history and proportion of full capability of instrument

Experiment	Mission	Time History (1969-1976)											
		1969	1970	1971	1972	1973	1974	1975	1976				
Laser ranging retroreflector	11	[Shaded area representing data output]											
	14	[Shaded area representing data output]											
	15	[Shaded area representing data output]											

Legend:  
 Science data output 100 [Shaded area]  
 Housekeeping data 0 [Line]  
 Housekeeping data 100 [Shaded area]

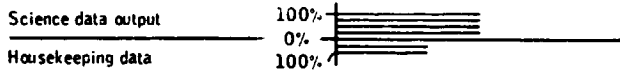
<u>Item</u>	<u>Apollo mission</u>	<u>Initial date of occurrence</u>	<u>Status</u>
1	11 and 14	N/A	Performance of both 100-element arrays (Apollo 11 and 14) has been nominal since their initial deployment.
2	15	July 31, 1971	Resultant data from the 300-element array indicate that its performance is comparable, but not superior, to the 100-element arrays.

S-202 LUNAR EJECTA AND METEORITES EXPERIMENT

Time history and proportion of full capability of instrument

Experiment	Mission	Year											
		1969	1970	1971	1972	1973	1974	1975	1976	1977	1978	1979	1980
Lunar ejecta and meteorites	17												

Legend:



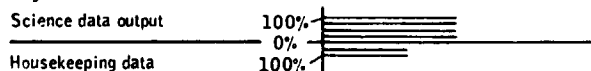
<u>Item</u>	<u>Apollo mission</u>	<u>Initial date of occurrence</u>	<u>Status</u>
1	17	Dec. 17, 1972	Excessive temperature. The experiment is experiencing a higher temperature profile than expected because of an error in calculation of thermal control and a difference in thermal conditions at the Apollo 17 site compared with the design site. The instrument is operated at temperatures below 364 K (196° F). This operational plan results in the monitoring of about 75 percent of each lunation.

## S-203 LUNAR SEISMIC PROFILING EXPERIMENT

Time history and proportion of full capability of instrument

Experiment	Mission	1969												1970												1971												1972												1973												1974												1975												1976																							
Lunar seismic profiling	17																																																	2																																																											

Legend:



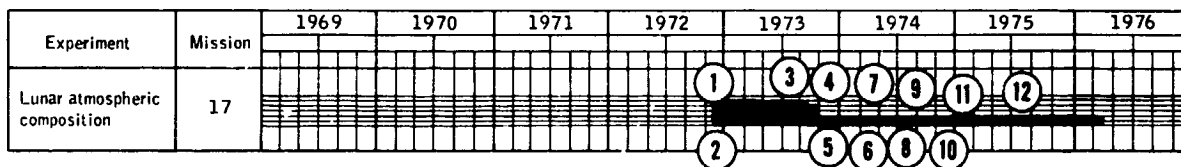
<u>Item</u>	<u>Apollo mission</u>	<u>Initial date of occurrence</u>	<u>Status</u>
1	17	N/A	Initial scientific objective was accomplished with detonation of eight explosive packages. The instrument is currently commanded ON weekly for a 30-min passive listening period. (Note: Operation of the LSPE precludes data from the other four experiments, because of high-bit-rate formatting; therefore, LSPE operation is time limited.)
2	17	July 13, 1973	To pursue a study of meteoroid impacts and thermal moonquakes, passive listening periods have been scheduled to acquire a "listening mode" data record covering one full lunation. The first extended listening period began on July 13, 1973, and was terminated on July 17, 1973 (Sun angles of 100.4° to 147.8°). Subsequent listening periods have been completed on Mar. 3 to 7, 1974 (Sun angles of 59.5° to 102.2°), Aug. 12 to 16, 1974 (Sun angles of 233.7° to 285.6°), Sept. 6 to 10, 1974 (Sun angles of 181.4° to 235.1°), Oct. 22 to 25, 1974 (Sun angles of 22.5° to 60.2°), Nov. 1 to 5, 1974 (Sun angles of 145° to 193.9°), Dec. 12 to

5-203 LUNAR SEISMIC PROFILING EXPERIMENT - Concluded

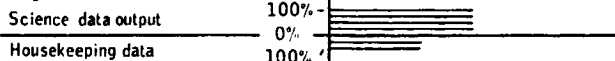
<u>Item</u>	<u>Apollo mission</u>	<u>Initial date of occurrence</u>	<u>Status</u>
			16, 1974 (Sun angles of 283.7° to 333.0°), and Apr. 13 to 18, 1975 (Sun angles of 327.6° to 28.7°), which completed one 360° lunation. Three additional periods, sunrise (Sun angles of 327.6° to 28.7°), and sunset terminators (Sun angles of 126.6° to 140.3°), and eclipse (May 25), were obtained at special request.

## S-205 LUNAR ATMOSPHERIC COMPOSITION EXPERIMENT

Time history and proportion of full capability of instrument



Legend:



<u>Item</u>	<u>Apollo mission</u>	<u>Initial date of occurrence</u>	<u>Status</u>
1	17	Dec. 17, 1972	Excessive temperature with cover on. Both an error in thermal design and temperature-sensitive components limit the experiment operation to temperatures below 325 K (125° F). This situation precluded instrument operation during elevated lunar-day temperatures.
2	17	Dec. 18, 1972	Zero offset in data output of mass channels; cause of this background offset remains undetermined. The data are usable with additional processing during data reduction.
3	17	Sept. 18, 1973	Loss of intermediate-mass-range output caused loss of approximately 12 percent of the experiment data. Subsequent multiple failures of the instrument precluded further analysis of the problem.
4	17	Sept. 23, 1973	Filament 1 failure. The filament accumulated approximately 3000 hr of operation before failure. This was well within the predicted range for operating life. The instrument was reconfigured to the re-

S-205 LUNAR ATMOSPHERIC COMPOSITION EXPERIMENT - Continued

<u>Item</u>	<u>Apollo Mission</u>	<u>Initial date of occurrence</u>	<u>Status</u>
			dundant filament and continued to operate until the loss of all science data occurred on Oct. 17, 1973.
5	17	Oct. 17, 1973	Loss of science data. Preliminary results of troubleshooting and analysis indicate that the multiplier high-voltage power supply apparently failed. The instrument is currently being cycled from ON to OFF to maintain the electronics temperature below the previously established 325 K (125° F) limit, while future troubleshooting or termination of instrument operation is considered.
6	17	Jan. 18, 1974	An operational status check of the LACE was performed. Experiment telemetry data did indicate some change during the 30 min that the multiplier high-voltage power supply was operated, but no significant improvement was noted after initial occurrence of the anomaly on Oct. 17, 1973. Instrument filament 2 was not commanded ON. The instrument was returned to its previous configuration. Periodic checks will be made to determine whether any change in performance has occurred.
7	17	Mar. 20, 1974	A sequence of operational commands was executed by the experiment during real-time support. Telemetry data indicated that the LACE accomplished one complete scientific data sweep before encountering a breakdown of

S-205 LUNAR ATMOSPHERIC COMPOSITION EXPERIMENT - Continued

<u>Item</u>	<u>Apollo mission</u>	<u>Initial date of occurrence</u>	<u>Status</u>
			the high-voltage power supply. (The multiplier high voltage and filament 2 were operated for a 35-min period.) Cycling of the LACE from ON to OFF will be continued to maintain the electronics temperature below the previously established 325 K (125° F) limit.
8	17	May 20, 1974	The instrument was operated for a 6-min period to assess its performance. The high-voltage power supply exhibited the same status as during the previous check on March 20, 1974.
9	17	Aug. 30, 1974	In an attempt to correct the multiplier high-voltage power supply problem, the instrument was commanded to STANDBY with the survival heater ON to increase electronics temperature and outgassing during the lunar day. On Sept. 5, the LACE was commanded ON to assess its performance. The high-voltage power supply status was unchanged from that noted on Mar. 20, 1974. Subsequent "bake-out" operations were accomplished on Sept. 24 and Oct. 23, 1974, with performance checks on Sept. 20, Oct. 14, and Nov. 4 and 13, 1974. No change was noted in the high-voltage power supply.
10	17	Nov. 18, 1974	With the electronics temperature (AM-41) at 254.09 K (-2.3° F), the instrument was commanded OFF at 11:58 G.m.t., Nov. 18, 1974, (Sun angle of 350°) and allowed to "cold soak" for 3 hr 23 min. At 15:21

S-205 LUNAR ATMOSPHERIC COMPOSITION EXPERIMENT - Continued

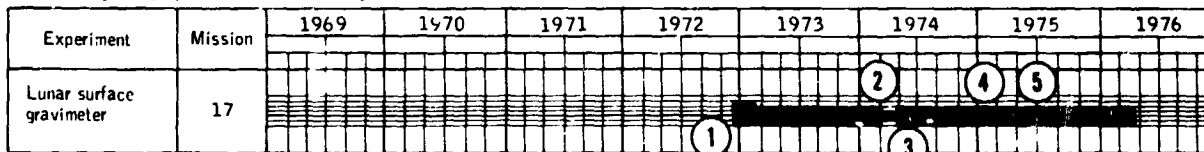
<u>Item</u>	<u>Apollo mission</u>	<u>Initial date of occurrence</u>	<u>Status</u>
			G.m.t., with the electronics temperature at 237.93 K (-31.3° F), the instrument was commanded ON for an operational check. The high-voltage power supply exhibited essentially the same status as noted on Mar. 20, 1974.
11	17	Jan. 13, 1975	Six additional "cold soaks," two normal night operations, and two normal day operations have been conducted. A significant improvement was observed Jan. 13, 1975. The instrument was initially checked with the electron multipliers in LOW, discriminator level LOW, high-voltage power supply ON, filament 2 ON, and in the automatic sweep. The engineering and science data observed gave normal indications the same as the data received before the Oct. 17, 1973, power supply failure. All sweep voltages were at normal values with the electron multipliers in LOW. With the electron multipliers in HIGH, the failure in the high-voltage power supply was indicated again; and, upon the return of the electron multipliers to LOW, the voltages returned to zero as noted on Mar. 20, 1974. Subsequent checks have indicated no improvement in the high-voltage operation.
12	17	Aug. 28, 1975	During a "cold soak" operational check the sweep voltage was at full scale. Further checks on Aug. 29, 30, and 31, and Sept. 2, 1975, have

S-205 LUNAR ATMOSPHERIC COMPOSITION EXPERIMENT - Concluded

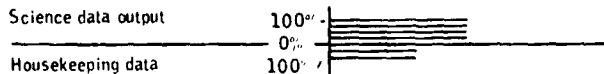
<u>Item</u>	<u>Apollo mission</u>	<u>Initial date of occurrence</u>	<u>Status</u>
			shown the same full-scale operation.
		Sept. 29, 1975	Operational checks performed on Sept. 29 and 30, and Oct. 3, 1975, resulted in the sweep voltage functioning normally. The tests had been conducted following a period of operation with the "bake out" heater ON.
		Feb. 26, 1976	The operational check performed on this date showed the sweep voltage to be at full scale. There was no special preparation of the instrument before the check.

S-207 LUNAR SURFACE GRAVIMETER

Time history and proportion of full capability of instrument



Legend:



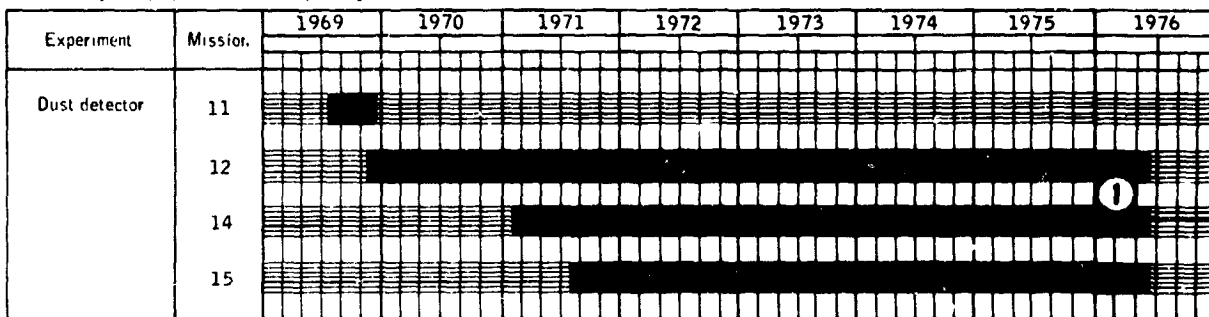
<u>Item</u>	<u>Apollo mission</u>	<u>Initial date of occurrence</u>	<u>Status</u>
1	17	Dec. 12, 1972	Sensor beam could not be stabilized in the null position because 1/6-g mass weights were too light. Weights were light because of an error in calculations converting from 1-g to 1/6-g requirements. Several reconfigurations of the instrument have been made during the past year. The beam has been centered by applying a load on the beam through the mass support springs by partial caging of the mass weight assembly. Signals being received are being processed and analyzed for seismic, free mode, and gravity wave information.
2	17	Mar. 15, 1974	The heater box heater circuit failed full ON during the 16th lunar night. This anomaly caused the sensor temperature (DG-04) to increase above a stabilized temperature of 322.337 K (49.207° C) and eventually drift off scale high. Transducer range is approximately 321.33 to 325.13 K (48.2° to 52.0° C). Useful science data could not be obtained from the instrument unless the sensor assembly

S-207 LUNAR SURFACE GRAVIMETER - Concluded

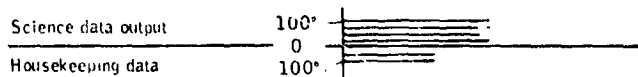
<u>Item</u>	<u>Apollo mission</u>	<u>Initial date of occurrence</u>	<u>Status</u>
			temperature was maintained rigorously at 322.3 K (49.2° C). (The anomaly reoccurred on July 7, 1975, and on Sept. 19, 1975.)
3	17	Apr. 20, 1974	The LSG regained thermal stability. The experiment sensor temperature has remained stabilized at 322.4 K (49.2° C) since Apr. 20, 1974. On Sept. 2, 1975, the thermal stability returned, and the temperature stabilized at 324.65 K (51.5° C). Since Sept. 19, 1975, attempts to regain control have been unsuccessful.
4	17	Jan. 7, 1975	The sensor beam was repositioned to near center (0.0030 V dc) in the "seismic gain low" mode using the north/south and east/west tilt servomotors.
5	17	July 30, 1975	An intermittent operation of the analog-to-digital converter occurred during the periods when the temperature was off scale high. The analog-to-digital converter operated normally when the temperature was reduced, and it operated normally when thermal stabilization was regained. Normal operation is accomplished by manually commanding the heater ON/OFF to maintain the temperature within the transducer range (321.35 to 325.15 K (48.2° to 52.0° C)) as closely as possible.

## M-515 DUST DETECTOR EXPERIMENT

Time history and proportion of full capability of instrument



Legend:

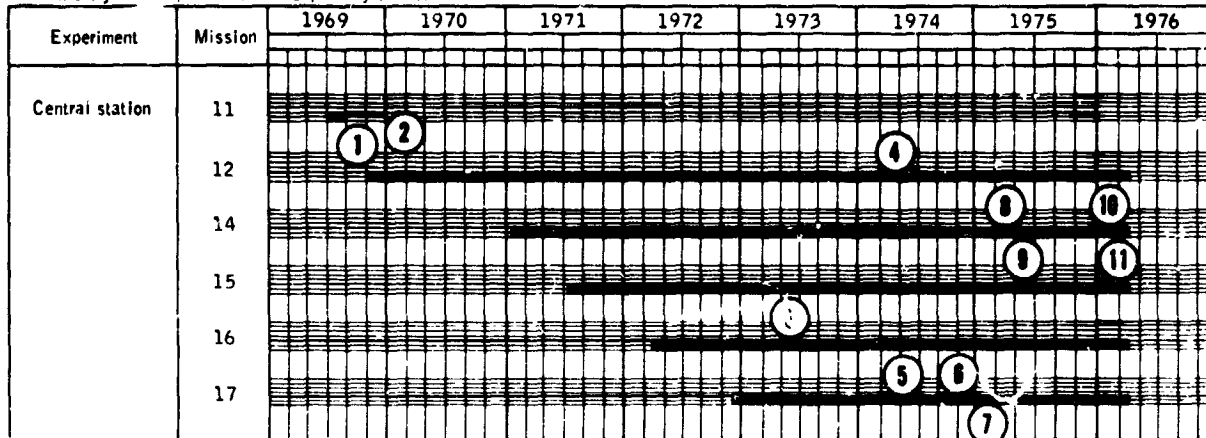


The dust detector experiment functions as a basic engineering measurement to characterize the long-term lunar surface environmental effects (e.g., degradation due to solar radiation effects) on solar cells and dust accretion on the ALSEP central stations. The performance of the equipment has been nominal since initial deployment. The data continue to be processed for long-term analysis.

<u>Item</u>	<u>Apollo mission</u>	<u>Initial date of occurrence</u>	<u>Status</u>
1	14	Mar. 17, 1976	With the loss of downlink and uplink of the Apollo 14 central station, the experiment status at LOS was ON.

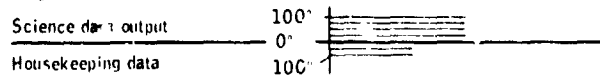
## CENTRAL STATION ELECTRONICS

Time history and proportion of full capability of instrument



Note: All central station data are considered housekeeping, rather than science data.

Legend:



<u>Item</u>	<u>Apollo mission</u>	<u>Initial date of occurrence</u>	<u>Status</u>
1	11	Aug. 25, 1969	Command loss capability. The inability to command the ALSEP central station was attributed to a component failure in the central station command decoder. The failure mode was considered unique to Apollo 11 ALSEP because subsequent ALSEP units maintained a benign thermal environment by comparison. The command system had already exceeded the mission requirements.
2	11	Dec. 14, 1969	Loss of downlink. The Apollo 11 ALSEP apparently responded to a transmitter OFF command or incurred an additional failure. In either case, the system had exceeded its initial mission requirement. NASA subsequently directed

CENTRAL STATION ELECTRONICS - Continued

<u>Item</u>	<u>Apollo mission</u>	<u>Initial date of occurrence</u>	<u>Status</u>
			that no further attempts be made to command the system ON; thus, the frequency could be used for future ALSEP systems.
3	16	Mar. 26, 1973	Transmitter B and processor Y were selected by ground command. The Ascension ground station had been experiencing poor data quality; however, DECOM LOCK could be maintained with transmitter A. Data quality improved and a gain in signal strength of 1 dBm was noted when transmitter B was selected. Analysis did not identify a specific cause, and transmitter A can still be used if necessary.
4	12	May 3, 1974	Loss of downlink signal modulation. Apparent failure of data processor Y. Operation of data processor X, transmitter A, and transmitter B appears normal. Central station currently functioning normally with transmitter B and data processor X selected. Investigation of processor Y anomaly in progress.
5	17	Aug 16, 1974	Intermittent command capability. Frequent attempts to execute certain commands (octals 070, 170, and 174) were unsuccessful using uplink A. Uplink B was selected on Aug. 19. Subsequent to selection of uplink B, system response to commands has been nominal. Investigation of the uplink A anomaly is in progress.
6	17	Oct. 14, 1974	Intermittent DECOM LOCK. While operating with transmit-

CENTRAL STATION ELECTRONICS - Continued

<u>Item</u>	<u>Apollo mission</u>	<u>Initial date of occurrence</u>	<u>Status</u>
			<p>ter A and a received signal strength of -146 dBm, the Bermuda tracking station noted poor quality telemetry data and incurred difficulty in maintaining DECOM LOCK. Transmitter A was commanded OFF at 14:21 G.m.t. and transmitter B commanded ON at 14:22 G.m.t. A gain of 2 dBm was noted in telemetry signal strength. Subsequent operations with transmitter B have been nominal.</p>
7	17	Dec. 6, 1974	<p>Intermittent DECOM LOCK. On Dec. 6, 1974, while operating with transmitter B and a received signal strength of -146.0 to -148.5 dBm, the Ascension and Canary Islands tracking stations reported sporadic data dropouts and poor quality telemetry data. Transmitter B was commanded OFF at 15:31 G.m.t. and transmitter A commanded ON at 15:32 G.m.t., Dec. 9, 1974. A gain of 2 dBm was noted in telemetry signal strength by the Hawaii tracking station. Subsequent operations have been satisfactory with transmitter A.</p>
8	14	Mar. 1, 1975 Mar. 17, 1976	<p>Loss of downlink occurred at 00:08 G.m.t., Mar. 1, 1975. Playback of data before loss of signal showed normal values for all housekeeping parameters. Commands transmitted to the station to turn the transmitters ON were unsuccessful. LOS occurred at 01:46 G.m.t., Mar. 17, 1976.</p>

CENTRAL STATION ELECTRONICS - Concluded

<u>Item</u>	<u>Apollo mission</u>	<u>Initial date of occurrence</u>	<u>Status</u>
9	14	Mar. 5, 1975 Mar. 17, 1976	Acquisition of signal returned at 03:06 G.m.t., Mar. 5, 1976. Real-time engineering data showed that the central station was operating with transmitter A, power control unit 2 (PCU 2), and processor Y. However, both receiver parameters were LOW. Subsequent attempts to uplink commands have been unsuccessful. Loss of uplink occurred at 01:46 G.m.t., Mar. 17, 1976.
10	14	Jan. 18, 1976	Loss of downlink occurred at 19:29 G.m.t. Playback of data prior to the loss of signal again showed normal values for all housekeeping parameters. Commands transmitted to the station to turn the transmitters ON were unsuccessful.
11	14	Feb. 19, 1976	Acquisition of signal returned at 02:32 G.m.t. Real-time engineering data showed the central station was operating with transmitter A, PCU 2, processor Y, and receiver crystal B. Subsequent commands have been successfully uplinked.
12	12 to 17	N/A	Performance of the Apollo 12, 15, 16, and 17 central stations has been essentially nominal since deployment. Although the original design requirement for ALSEP was a 1-yr life, much longer useful lifetimes are being realized.

PART B: LUNAR ORBITAL EXPERIMENTS

Lunar orbital experiments were performed during three of the six lunar landing missions from July 26, 1971 (Apollo 15 mission), to December 12, 1972 (Apollo 17 mission). Experiment information and results are detailed in the following pages. Notes concerning the tabular data are as follows:

1. On some occasions, data were collected both during lunar orbits (revs) and during transearth coast (TEC).
2. Apollo 14 lift-off occurred on Jan. 31, 1971, at 16:03:02 e.s.t.
3. Apollo 15 lift-off occurred on July 26, 1971, at 09:34:00 e.d.t.
4. Apollo 16 lift-off occurred on Apr. 16, 1972, at 12:54:00 e.s.t.
5. Apollo 17 lift-off occurred on Dec. 7, 1972, at 00:33:00 e.s.t.

Experiment	Principal investigator	Apollo mission	Remarks (see note 1)
S-160 Gamma ray	Dr. J. R. Arnold	15	Revs 1 to 44 45 to 48 49 to 74 GET (TEC) 224:10 to 138:30 245:45 to 273:30 273:00 to 288:40
S-161 X-ray fluorescence	Dr. Isidore Adler	15	Revs 1 to 12 15 to 52 53 to 64 GET (TEC) 200:45 to 214:10 220:40 to 261:00
S-162 Alpha particle	Dr. Paul Gorenstein	15	Revs 3 to 9 15 and 16 17 to 35 36 to 44 45 and 46 49 and 50 52 to 73 GET (TEC) 226:25 to 227:50 237:30 to 238:30 245:45 to 249:40 250:50 to 252:10 261:45 to 264:00 267:30 to 271:30 273:00 to 288:40
		16	Revs 3 to 10 17 to 39 40 to 48 54 to 61 GET (TEC) 201:25 to 203:30 220:40 to 227:00 242:00 to 245:45 248:00 to 261:00
		15	Revs 1 to 44 45 to 48 49 to 74 GET (TEC) 224:10 to 238:30 245:45 to 271:30 273:00 to 288:40
		16	Revs 1 to 12 15 to 52 53 to 61 GET (TEC) 200:45 to 214:10 220:40 to 261:00

Experiment	Principal investigator	Apollo mission	Remarks (see note 1)
S-164 S-band transponder (subsatellite, CSM/LM)	W. L. Sjoqren	15	Good CSM/LM and CSM-only data obtained during lunar orbit Subsatellite was launched at 222:39:29 GPT
S-165 Mass spectrometer	Dr. John Hoffman	16	Good CSM/LM data obtained during elliptical orbits and CSM data during lunar portion of mission Subsatellite launched 196:02:09 GPT, crashed May 29, 1972
S-169 Far UV spectrometer	W. G. Pastie	17	Good CSM/LM and CSM-only data obtained during lunar orbit No subsatellite
		15	Revs 3 to 9 16 to 21 27 to 32 52 to 59 60 to 63 63 to 70 GPT (TEC) 228:00 to 238:30 246:40 to 271:30 274:00 to 288:40
		16	Revs 3 to 10 18 to 48 54 to 64 Not applicable
		17	Times: 81:37 to 83:49 (APT) 83:49 to 94:58 110:52 to 112:28 113:20 to 114:48 120:25 to 132:30 154:20 to 160:55 164:40 to 178:06 187:30 to 192:25 193:30 to 208:35 212:10 to 215:40 215:50 to 227:39 229:10 to 229:39 229:59 to 253:00 256:35 to 299:40

Experiment	Principal investigator	Apollo mission	Remarks (see note 1)
S-170 Bistatic radar	H. T. Howard	14	Rev 25 (S-band and VHF)
		15	Revs 17 (S-band and VHF) 28 (S-band and VHF) 53 to 59 (VHF only)
		16	Revs 40 (S-band and VHF) 42 to 46 (VHF only)
S-171 IR scanning radiometer	Dr. Frank Low	17	Times: 81:21 to 81:55 83:49 to 104:10 (APT) 110:51 to 112:26 113:20 to 114:50 120:25 to 132:30 136:35 to 154:04 154:20 to 160:56 164:40 to 178:10 187:30 to 192:25 193:33 to 194:20 195:51 to 208:35 212:10 to 227:40 229:05 to 238:05 249:20 to 252:20 258:51 to 265:20 284:27 to 287:23 297:08 to 299:28
S-173 Particle shadows/ boundary layer (subsatellite)	Dr. K. A. Anderson	15	Launched 222:39:29 GET Limited data from Feb. 3, 1972, to Jan. 29, 1973 Ended data collection Jan. 29, 1973
		16	Subsatellite launched 196:02:09 GET, crashed May 29, 1972

Experiment	Principal investigator	Apollo Mission	Remarks (see note 1)
S-174 Magnetometer (subsatellite)	Dr. Paul J. Coleman, Jr.	15	Launched 222:39:29 GET Lost all magnetometer data Feb. 29, 1972
S-209 Lunar sounder	Dr. R. J. Phillips	16	Subsatellite launched 196:02:09 GET, crashed May 29, 1972
		17	Times: 111:30 to 111:50 (EMI test) (AET) 115:40 to 120:25 131:50 to 136:40 153:40 to 154:18 155:35 to 156:20 160:40 to 164:50 192:30 to 195:51 (includes reception only) 208:05 to 212:16 227:40 to 230:00 (includes reception only) 259:41 to 283:20
Panoramic camera, 24 in.	Photographic team P. J. Doyle	15	Revs 15 and 16 27 61 38 63 50 72 60 73
		16	Revs 3 and 4 16 and 17 18 38 28 39 37 47 59 and 60 63
		17	Revs 14 and 15 27 and 28 49 62 74

Experiment	Principal investigator	Apollo mission	Remarks (see note 1)
Mapping camera, 3 in.	Photographic team F. J. Doyle	15	Revs 15 and 16 34 and 35 60 71 22 and 23 38 62 72 26 and 27 44 63 33 and 34 50 70
		16	Revs 3 and 4 26 and 27 46 to 48 16 to 18 27 to 29 63 25 37 to 39
		17	Times: 88:00 to 89:15 158:50 to 160:05 (AET) 111:15 to 112:30 180:35 to 181:50 113:10 to 114:30 205:25 to 207:35 131:00 to 132:20 212:35 to 213:35 137:00 to 138:15 214:20 to 215:30 139:00 to 140:15 232:10 to 233:15 141:00 to 142:15 234:20 to 235:30 154:56 to 156:05
Laser altimeter	Dr. W. M. Kaula	15	Revs 3 to 9 37 and 38 63 15 and 16 43 and 44 70 21 to 23 60 71 26 and 27 62 72
		16	Revs 3 and 4 46 16 to 18 59 and 60 27 to 29 63 37 to 39
		17	Times: 88:08 to 88:50 158:53 to 160:52 (AET) 111:20 to 112:24 180:36 to 181:45 113:19 to 114:44 206:21 to 207:50 131:06 to 132:13 213:35 to 215:26 137:02 to 138:09 217:19 to 225:02 138:59 to 142:08 229:53 to 231:23 154:45 to 155:59

Experiment	Principal investigator	Apollo mission	Remarks (see note 1)
S-214 Lunar altitude profile determination	Dr. J. Junkins	15	Revs 15 and 16, 21 and 22
		16	Revs 17 and 18 37 to 39 27 to 29 46 to 48 59 and 60
S-215 Laser altitude radii and gravity	Dr. H. Compton	15	Revs 15 and 16, 21 and 22
		16	Revs 17 and 18 37 to 39 27 to 29 46 to 48 59 and 60
S-216 Selenodesy via laser altimeter	W. L. Sjogren	15	Revs 15 and 16, 21 and 22
		16	Revs 17 and 18 37 to 39 28 and 29 46 to 48 59 and 60
S-218 Lunar photo and altimeter analysis	Dr. W. F. Kaula	15	Revs 15 and 16, 21 and 22
		16	Revs 17 and 18 37 to 39 28 and 29 46 to 48 59 and 60
		17	Revs 1 and 2 24 65 and 66 14 27 to 29 49 15 36 62 67 to 70

Experiment	Principal investigator	Apollo mission	Remarks (see note 1)
S-219 and S-223 Corrected altitude and ephemeris, lunar gravity	Dr. Carl Bowin	14 15 16 17	Revs 1 to 17 (SPSN) Revs 1 to 14 (SPSN) 15 and 16, 21 and 22 Revs 1 to 16 (SPSN) 17 and 18 28 and 29 37 to 39 46 to 48 59 and 60 Revs 1 to 13 (SPSN)

## PART A: LUNAR SURFACE EXPERIMENTS

The lunar surface experiments consist of two types: (1) The Apollo lunar surface experiments package (ALSEP) systems, which were left on the lunar surface by the astronauts and which continue sending telemetry data, and (2) those experiments conducted on the lunar surface by the astronaut and returned to Earth in the command module. The ALSEP deployment configuration for each mission is shown in appendix B; the dates and lunar coordinates are given in the following listing. The ALSEP-related experiments are listed on the following page by Apollo mission and experiment number.

**APOLLO 12:** The Apollo 12 ALSEP was deployed on November 19, 1969, at latitude  $3^{\circ}11'$  S, longitude  $23^{\circ}23'$  W in Oceanus Procellarum.

**APOLLO 13:** Because of service module problems, a lunar landing was not accomplished during the Apollo 13 mission.

**APOLLO 14:** The Apollo 14 ALSEP was deployed on February 5, 1971, at latitude  $3^{\circ}40'$  S, longitude  $17^{\circ}27'$  W in the Fra Mauro Formation.

**APOLLO 15:** The Apollo 15 ALSEP was deployed July 31, 1971, at latitude  $26^{\circ}06'$  N, longitude  $3^{\circ}39'$  E in the Hadley-Apennine region.

**APOLLO 16:** The Apollo 16 ALSEP was deployed April 21, 1972, at latitude  $8^{\circ}59'34''$  S, longitude  $15^{\circ}30'47''$  E in the Descartes Highlands.

**APOLLO 17:** The Apollo 17 ALSEP was deployed on December 12, 1972, at latitude  $20^{\circ}09'55''$  N, longitude  $30^{\circ}45'57''$  E in the Taurus-Littrow region.

4. PASSIVE SEISMIC EXPERIMENT (NASA EXPERIMENT S-031)

NSSDC IDENTIFICATION NUMBERS:

APOLLO 11	69-059C-03
APOLLO 12	69-099C-03
APOLLO 14	71-008C-04
APOLLO 15	71-063C-01
APOLLO 16	72-031C-01



CONTENTS - SECTION 4

	Page
EXPERIMENT AND INSTRUMENT CHARACTERISTICS . . . . .	4-3
OPERATIONAL HISTORY . . . . .	4-5
DATA SET DESCRIPTIONS . . . . .	4-6
Compressed-Scale Playouts (Data Set 1) . . . . .	4-6
Event Tapes (Data Set 2) . . . . .	4-6
Event Compressed Scale Playouts (Data Set 3) . . . . .	4-7
Special Event Tapes (Data Set 4) . . . . .	4-7
Expanded Playouts (Data Set 5) . . . . .	4-8
Event Catalog (Data Set 6) . . . . .	4-8
The PSE Tapes (Data Set 7) . . . . .	4-10
TAPE FORMATS AND IRREGULARITIES . . . . .	4-10
Formats . . . . .	4-10
PSE Tape Irregularities . . . . .	4-13
BIBLIOGRAPHY . . . . .	4-15

#### 4. PASSIVE SEISMIC EXPERIMENT

Seismic stations were installed on the lunar surface during Apollo missions 11, 12, 14, 15, and 16. The locations and installation dates are listed in table 4-1. Station 11 operated only 20 Earth days before the loss of the command uplink terminated its operation. The four remaining stations constitute the Apollo seismic network. This network spans the near side of the Moon in an approximate equilateral triangle with 1100-km spacing between stations. (Stations 12 and 14 are 181 km apart at one corner of the triangle as shown in figure 4-1.)

This report contains information necessary to use the lunar seismic data file at the National Space Science Data Center (SSDC). The instruments, the historical background, and the data formats are described; no attempt is made to describe the data results.

#### EXPERIMENT AND INSTRUMENT CHARACTERISTICS

A seismometer consists of a mass that is free to move in one direction and is suspended by means of springs and/or dampers from a framework. The suspended mass is supplied with damping to suppress vibrations at the natural period of the system. The framework rests on and moves with the surface. The suspended mass tends to remain fixed in space, and the resulting relative motion between the mass and the framework can be recorded and used to calculate the original ground motion.

Each Apollo seismic station consists of two main subsystems: the sensor unit and the electronics module. The sensor unit, shown schematically in figures 4-2 and 4-3, contains four seismometers. Three long-period (LP) seismometers form a triaxial set; one of these is sensitive to vertical (Z) motion and two are sensitive to horizontal (X, Y) motion, with sensitivity to ground motion sharply peaked at 0.45 Hz (peaked-response mode). The fourth, a short-period (SP) seismometer, is sensitive to vertical motion with peak sensitivity at 8 Hz. These instruments can detect vibrations of the lunar surface as small as 0.05 nm (0.5 Å) at maximum sensitivity. The sensor unit is constructed principally of beryllium and weighs 11.5 kg, including the electronics module and thermal insulation.

Without insulation, the sensor unit is 23 cm in diameter and 29 cm high. The total power drain varies between 4.3 and 7.4 W. Instrument temperature control is provided by a 6-W heater, a proportional controller, and (except for station 11) an aluminized Mylar insulation. The insulating shroud is spread over the local surface to reduce temperature variations in the surface material.

The seismic response curves are shown in figure 4-4. The LP seismometers have a useful frequency range from 0.004 to 2 Hz. The SP seismometers cover a band from 0.05 to 20 Hz. Two modes of operation, flat and peaked response, are possible for the LP seismometers. In the flat response mode, the LP seismometers have natural periods of 15 sec. In the peaked response mode, the seismometers act like underdamped pendulums with natural periods of 2.2 sec. Maximum sensitivity is increased by a factor of 5.6 in the peaked response mode, but sensitivity to low frequency signals is reduced. Calibration of each sensor is accomplished by applying a step of current to each coil by command from Earth. At tidal frequencies, gravitational acceleration is measured by monitoring the feedback current used to center the seismometer mass. The tidal sensitivity of the instruments is  $8 \times 10^{-8}$  m/sec<sup>2</sup> ( $8 \times 10^{-3}$  mgal) per digital unit.

The LP horizontal seismometers (LPX and LPY) are very sensitive to tilts and must be leveled to high accuracy. This is accomplished by means of a two-axis, motor-driven gimbal. A third motor adjusts the LP vertical seismometer (LPZ). Motor operation is controlled by command.

A caging system was provided to secure all critical elements of the instrument against damage during transport and deployment phases. A pneumatic system was used in which pressurized bellows expanded and clamped fragile parts in place. Uncaging was accomplished by piercing the connecting lines. The seismometer systems are controlled from Earth by a set of 15 commands that govern functions such as leveling, instrument gain (adjustable in 10 dB steps), and calibration.

Time codes recorded on passive seismic experiment (PSE) data tapes are normally those generated from time codes on range tapes, and they are believed to be accurate within a few tens of milliseconds of G.m.t. when signal is received at a range station. However, when it is difficult to extract time information from range tapes, time codes generated from an "internal clock" (a clock internal to a computer at the NASA Lyndon B. Johnson Space Center (JSC)) is substituted. Because this internal clock is not synchronized with tape speed during range tape playback, the

time codes thus generated are only as accurate as the accuracy of the speed of the tape transport. The time codes thus generated may drift as much as several tens of seconds from true G.m.t. if allowed to continue for several hours. Users of the PSE tapes should be aware of possible time code errors in situations where relative time between stations is important. See the section entitled "PSE Tape Irregularities" for further discussion of errors occurring on PSE tapes.

More detailed discussions of instrumentation are given in the bibliography.

#### OPERATIONAL HISTORY

Of the 16 separate seismometers, all but 2 were operating properly at the time of this writing. The SP component at station 12 has failed to operate since initial activation, and one of the LP seismometers at station 14 (the vertical component) became unstable after 1 yr.

Unless otherwise indicated in the operational history listing, table 4-II, the instruments have operated at maximum sensitivity with the LP seismometers in the peaked response mode. This configuration is designated the "standard mode" in table 4-II. The various operating modes are described in the section entitled "Experiment and Instrument Characteristics." Although not noted in table 4-II, all seismometers at a given station were operated at reduced gain while the astronauts remained on the lunar surface.

In addition to signals from natural sources, such as moonquakes and meteoroid impacts, signals were recorded from nine manmade impacts. These were provided by two types of space vehicles: the lunar module (LM) ascent stage and the third, or Saturn IVB (SIVB), stage of the Saturn booster. The lunar modules were guided to impact following the return of the crew to the command service module in lunar orbit. The SIVB stages, after separation from the Apollo spacecraft, were directed by remote control from Earth to planned impact points. Seismic signals from these impacts were recorded at ranges of from 67 to 1750 km. Data pertinent to the impacts are given in the section entitled "Data Set Descriptions."

Seismic disturbances are observed on the LP seismometers of each station throughout the daytime period of each lunar day. These disturbances are most intense near times of sunrise and sunset; they are believed to be due to

thermal contraction and expansion either of the Mylar shroud that covers the seismometers or of the cable connecting the seismometers to the central station (or both).

## DATA SET DESCRIPTIONS

### Compressed Scale Playouts (Data Set 1)

The compressed scale playouts yield a complete time history of the lunar seismic data. Data from each station are read from PSE data tapes supplied by JSC and plotted synchronously in compressed form. To enhance the signal-to-noise ratio for higher frequency events, a difference method is used in the reduction of the data. The absolute value of the difference between consecutive data points is summed over 40 points for LP data (320 points for SP data), and this value is plotted yielding one value for each 6 sec of data. Consecutive points are plotted with opposite polarity to yield a line with the appearance of a seismogram. A horizontal scale of 7.87 min/cm (20 min/in.) and vertical scales of 157 digital units per centimeter (400 digital units per inch) (LP), and 1260 digital units per centimeter (3200 digital units per inch) (SP) are used. Components at each station are arranged LPX, LPY, LPZ, and SPZ with LPX at the top and SPZ at the bottom. Time ticks are displayed every 10 min and each hour (G.m.t.) is labeled. The year and day are displayed every 6 hr. A sample of the compressed data playouts is shown in figure 4-5.

### Event Tapes (Data Set 2)

Seismic events (see data set 6) detected on the LP components by routine manual search of the compressed scale playouts (data set 1) are copied from the original PSE tapes onto event tapes containing only time periods when seismic events are observed. Each event tape contains data from one station only; the same time periods are copied in chronological order onto separate tapes for each station. Thus, intervals that contain no detectable signal at one station may be on event tapes because an event was detected at another station. Separate sets of event tapes are available containing only (1) the largest natural impact signals, (2) selected deep moonquake signals, and (3) all high frequency teleseismic (HFT) signals. See data set 4.

Event tapes are numbered serially and are in chronological order. All tapes are labeled with the event tape number, station number, tape number, and total time interval covered by the tape. Listings of the time

intervals covered on each tape are supplied with the tapes and can also be found using the next data set (data set 3). The format with which event tapes are read is described in the section entitled "Tape Formats and Irregularities."

#### Event Compressed Scale Playouts (Data Set 3)

Each event tape (data sets 2 and 4) has been plotted in compressed scale to provide a visual display of the contents of each event tape. These playouts have the same format as data set 1 with the exceptions that time is not continuous and an amplitude scale twice that of data set 1 is used.

#### Special Event Tapes (Data Set 4)

Currently, four sets of special event tapes are available. These events will be of special interest to many users, and most users' interests will be satisfied by these tapes alone. All tapes are identical in format to those in data set 2. Event compressed playouts, expanded playouts, and listings of the events in this set are available as subgroups of data sets 3, 5, and 6, respectively. The special event groups now available are as follows:

1. Artificial impacts: Impacts of manmade origin were recorded by the Apollo passive seismometers. Table 4-III shows data pertinent to each of the impacts. The location of each impact is shown in figure 4-1. The brief station history in table 4-II gives information concerning the status of each station at times of impacts. There are five tapes in this group; two tapes for station 12 and one tape each for stations 14, 15, and 16.

2. Large meteoroid impacts: Meteoroids hitting the Moon are recorded by the PSE network at a rate of approximately 250 per year (type C events). Meteoroid impacts with compressed scale amplitudes of 10 mm or larger on at least two stations are included on the special event tapes. There are about 40 events in this category per year (approximately two tapes per station per year).

3. Selected moonquakes: Moonquakes with matching signal characteristics (type A events) are observed. Approximately 60 different matching types have been observed to date. The best of these events observed on the most stations are included in this data set. There are seven tapes in this group; two tapes each from stations 12, 14, and 15 and one tape from station 16.

4. High frequency teleseismic events: Distant events, believed to be moonquakes, observed with large amplitudes on the SP components of the PSE are called high frequency teleseismic (HFT) events. These events occur at a rate of approximately five per year (one tape per station).

#### Expanded Playouts (Data Set 5)

Expanded-time-scale (1 min = 10 cm) playouts are available for the following sets of events:

1. All artificial impacts
2. The largest natural impacts
3. Selected deep moonquakes
4. All HFT events

Other relevant facts are as follows:

1. In almost all cases, the data represented by the expanded-time-scale playouts are taken directly from the PSE tapes and are not processed in any way (e.g., no filtering, smoothing, signal averaging, etc.).

2. Notations on the seismograms (such as phase picks (e.g., P, S) and event classification (e.g., A, E, C, M), etc.) are not primary data but interpretations of the data and should be recognized and used as such.

3. Time marks are not corrected for possible clock errors.

A sample of the expanded-scale playouts is shown in figure 4-6.

#### Event Catalog (Data Set 6)

The event catalog has been compiled from the log of LP events observed on the compressed-scale playouts (data set 1). Only events of apparent or probable seismic origin are included. Noise events such as tilts and thermal noise are not included, nor are events observed exclusively on the SP components. The card deck (or tape in card-image format) contains the same set of events as included on the event tapes (data sets 2 and 4), except for events with amplitudes less than 10 observed at station 16. The cards are arranged in chronological order and are divided into volumes. A new volume starts at the onset of data from each station, and

new volumes will be added periodically. Special listings are available for all events in data set 5. The card format is as follows:

<u>Column</u>	<u>Format</u>	<u>Data</u>
3, 4	I2	Year
6, 7, 8	I3	Julian Day
10 to 13	2I2	Start hour-minute
15 to 18	2I2	Stop hour-minute (9999 for overlaps)
20 to 23	F4	Amplitude at station 12 Z-axis
24 to 27	F4	Amplitude at station 14 Y-axis
28 to 31	F4	Amplitude at station 15 Y-axis
32 to 35	F4	Amplitude at station 16 Y-axis
37 to 40	4I1	Playout log = 1, if expanded-scale playout is available at -  Station 12 (col. 37) Station 14 (col. 38) Station 15 (col. 39) Station 16 (col. 40)
42 to 45	4I1	Quality factor <sup>1</sup> as follows:  Blank - normal quality 1 - no data 2 - type 6 time error (See section entitled "PSE Tape Irregularities.") 3 - noisy 4 - masked  For station - 12 (col. 42)

---

<sup>1</sup>Priority given to smallest number.

14 (col. 43)  
15 (col. 44)  
16 (col. 45)

77                    A1                    Event type:<sup>2</sup>  
  
   A - classified moonquake  
   M - suspected moonquake  
   C - suspected impact  
   Z - mostly SP  
   X - special type  
   L - LM impact  
   S - SIVB impact

79, 80                I2                    Moonquake class<sup>2</sup> (only  
   used in conjunction  
   with type "A" events)

#### The PSE Tapes (Data Set 7)

Passive seismic tapes covering continuous operation of the lunar passive seismic system for a period of 1 month (July 7 to Aug. 13, 1973) are archived. These tapes are labeled in sequential order from the day of deployment of the instrument and are also labeled with the Julian day and universal start and stop times. The station number and the date of tape generation also appear on the tapes.

#### TAPE FORMATS AND IRREGULARITIES

##### Formats

Data sets 2 (event tapes), 4 (artificial impact tapes), and 7 (PSE tapes, 1 month of data) formats are described here. All tapes are 7 track, 1.27 cm (0.5 in.), binary, 800 bpi, odd parity, with standard IBM end of file on 731.52-m (2400-ft) reels.

Data are transmitted from the Moon in 64-word frames, 1 frame every 0.60375 sec. The Apollo lunar surface experiments package (ALSEP) words are assigned to meet the requirements of the scientific instruments in the ALSEP.

---

<sup>2</sup>Note that these data are interpretive rather than primary data.

Those ALSEP words assigned to the PSE are given in table 4-IV. Each ALSEP word is 10 bits, or a range from 0 to 1023 digital units. Sensor equilibrium data values are near 500 digital units. Missing ALSEP words in the SP data (2, 46, etc.) should be replaced to obtain equal spacing of data points.

Each frame of data is recorded on tape in a logical record consisting of eighteen 36-bit words for format A and nine 36-bit words for format B. The first three of these words contain timing, synchronization, and error information as described in the following paragraphs. The remaining words containing the data are described in tables 4-V(a) and 4-V(b).

Word 1 contains time at the start of the frame in milliseconds from the beginning of the year starting in bit 1 and ending in bit 35 right-justified in binary. The time on January 01 at 00 hr 00 min 00 sec is reset to  $8.64 \times 10^7$  msec so that the year starts on day 1 rather than day 0.

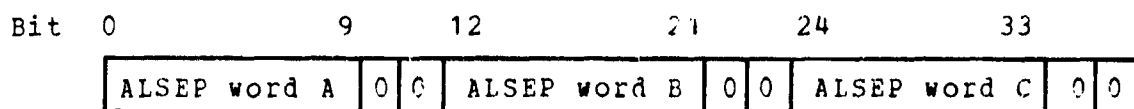
Word 2 contains a range station identification code in bits 0 to 3, a bit error rate in bits 4 to 9, and, starting on day 183 of 1973, a time source indicator in bit 35 (last bit); if this bit is set, then computer clock time rather than G.m.t. was used for updating the time code. Errors of several tens of seconds in time codes have been noted when the computer clock is used.

Word 3 contains synchronization codes and a frame counter. This word should contain the following in bits 0 to 9, 12 to 21, and 24 to 25:

Bit:	0	1	2	3	4	5	6	7	8	9	12	13	14	15	16	17	18	19	20	21	24	25
Value:	1	1	1	0	0	1	0	0	1	1	0	0	0	0	1	1	1	0	1	1	0	1

If this is not the case, then sync has been lost with the data, and errors may be present. Bits 26 to 32 contain a frame counter that steps once per frame and resets to 0 after 89 frames. A break in the sequence may indicate timing errors.

The ALSEP words arranged as shown in table 4-V are packed in the 36-bit words as follows:



Note that in format B (table 4-V(b)) the data are compressed by a factor of 2 because all SP ALSEP words are missing. This was done as a cost-saving procedure because the station 12 SP component is not operating.

Each tape begins with two identical label records written in BCD. These records contain four words each as described below:

<u>Word</u>	<u>Parameter</u>
1	Experiment identification (PSEXP or PSEXPB)
2	ALSEP identification as follows: station 12 = A, station 14 = B, station 15 = C, station 16 = D
3	Mission identification as follows: station 12 = A/S507, station 14 = A/S509, station 15 = A/S510, station 16 = A/S511
4	None or year (BCi blanks or year)

Event tapes, data sets 2 and 4, differ from normal PSE tapes in that time is not continuous because gaps occur between events. All events are recorded in chronological order.

Starting with event tape 125, the label record format is changed to the following:

<u>Word</u>	<u>Bit</u>	<u>Parameter</u>
1	--	(EVENT __) in BCD
2	0 to 17	Event tape number in binary
	18 to 34	Station number (12, 14, 15, 16), binary
3	0 to 17	Year of first event in binary
	35	Data format: A = 0, B = 1
4	--	Time in milliseconds at the beginning of the PSE tape from which the first event on the tape was retrieved

## PSI Tape Irregularities

The following is a list of the types of irregularities, other than tape-reading errors and data problems, found in PSE tapes. The user of PSE tapes should be aware of their existence.

1. Data gap: A normal data gap is represented by a time increment from one logical record to the next by an amount that is an exact multiple of the normal frame rate ( $603.75 \pm 0.05$  msec) and an increment of the frame count corresponding to the time increment. Small data gaps, a few seconds in duration, are quite common; they occur at a rate of several to a few tens of times per day.

2. Data overlap: A normal data overlap is represented by a time decrement from one logical record to the next (by an amount that is an exact multiple of the normal frame rate) and by a decrement of the frame count corresponding to the time decrement. Data overlaps are rare, but they do occur in earlier tapes.

3. Clock offset due to range station switch: When the range station receiving data from the Moon is switched from one station to another, a slight offset in time is observed, which is normally less than 20 msec.

4. Sync error: When data from the Moon are not correctly translated onto PSE tapes because of errors in synchronization, it is reflected on the Barker code that is included in each logical record. A data gap of a few frames normally follows a sync error.

5. Zero record: Some logical records are filled with all zeros. A data gap may or may not occur at the same time.

6. Clock rate error: This occurs when time information based on a computer internal clock is substituted. It can be identified by an abnormal time increment from one frame to the next. The normal time increment per frame is 603 or 604 msec, with the 90-frame average in the range of 603.70 to 603.80 msec. The abnormal clock rate is usually less than 0.5 percent off normal, but larger anomalies are found. The duration of this error is from a few minutes to as much as 6 to 8 hr. An anomalous period usually starts with a small offset in frame count and ends with a large offset in frame count, representing a large clock adjustment. Multiple clock adjustments are found in some cases. The amount of clock adjustment ranges from a fraction of a second to several tens of seconds. The time information on tapes is almost continuous, thus

generating a data gap or a data overlap without clear indication of their existence when the clock is adjusted.

7. Time/frame count error. Simultaneous discontinuities in time and frame count that do not agree with each other occur rather frequently without abnormal clock rate. They occur in pairs or multiples so that the net offset in time and/or frame count is always zero. The offset in time at a discontinuity is often either an exact multiple of the normal frame rate, or it is even seconds. When the offset in time is an exact multiple of the normal frame rate, it is not possible to determine whether the error is in time or in frame count. When an offset in time is not an exact multiple of the normal frame rate or when it is an offset of even seconds, a time error is indicated.

## BIBLIOGRAPHY

- Breseke, D. J.; and Lewko, J., Jr.: The Passive Seismic Experiment. Lunar Surface Exploration, Bendix Tech. J., vol. 4, no. 2, 1971, pp. 28-40.
- Dainty, A. M.; Stein, S.; and Toskoz, M. N.: Variation in the Number of Meteoroid Impacts on the Moon With Lunar Phase. Geophys. Res. Letters, vol. 2, no. 7, July 1975, pp. 273-276.
- Dainty, A. M.; Toskoz, M. N.; Solomon, S. C.; Anderson, K. R.; and Goins, N. R.: Constraints on Lunar Structure. Proceedings of the Fifth Lunar Science Conference, vol. 3, Pergamon Press (New York), 1974, pp. 3091-3114.
- Dainty, Anton M.; Toksoz, M. Nati; Anderson, Kenneth R.; Pines, P. Jacques; et al.: Seismic Scattering and Shallow Structure of the Moon in Oceanus Procellarum. The Moon, vol. 9, no. 1, 1974, pp. 11-29.
- Duenebier, F. K.; Dorman, J.; Lammlein, D.; Latham, G.; and Nakamura, Y.: Meteoroid Flux from Long-Period Lunar Seismic Data. Proceedings of the Sixth Lunar Science Conference, Pergamon Press (New York). (To be published)
- Duenebier, F. K.: Moonquakes and Meteoroids: Results from the Apollo Passive Seismic Experiment Short Period Component. Ph. D. Dissertation, Univ. of Hawaii, 1972.
- Duenebier, Frederick K.; and Sutton, George: Thermal Moonquakes. J. Geophys. Res., vol. 79, no. 29, Oct. 1974, pp. 4351-4363.
- Duenebier, Frederick K.; and Sutton, George: Meteoroid Impacts Recorded by the Short-Period Component of Apollo 14 Passive Seismic Station. J. Geophys. Res., vol. 79, no. 29, Oct. 1974, pp. 4365-4375.
- Ewing, M.; Latham, G.; Press, F.; Sutton, G.; et al.: Seismology of the Moon and Implications of Internal Structure, Origin, and Evolution. Highlights of Astronomy, D. Reidel Co. (Dordrecht, Holland), 1971.
- Lammlein, D. R.; Latham, G. V.; Dorman, J.; Nakamura, Y.; and Ewing, M.: Lunar Seismicity, Structure, and Tectonics. Rev. Geophys. Space Phys., vol. 12, Feb. 1974, pp. 1-21.
- Lammlein, David R.: Lunar Seismicity, Structure, and Tectonics. Ph. D. Dissertation, Columbia Univ., 1973.

Latham, G.; Ewing, M.; Press, F.; and Sutton, G.: The Apollo Passive Seismic Experiment. Science, vol. 165, no. 3890, July 18, 1969, pp. 241-250.

Latham, Gary V.; Ewing, Maurice; Press, Frank; Sutton, George; et al.: Passive Seismic Experiment. Sec. 6 of Apollo 11 Preliminary Science Report, NASA SP-214, 1969.

Latham, Gary V.; Ewing, Maurice; Press, Frank; Sutton, George; et al.: Passive Seismic Experiment. Sec. 3 of Apollo 12 Preliminary Science Report, NASA SP-235, 1969.

Latham, G.; Ewing, M.; Press, F.; Sutton, G.; et al.: Apollo 11 Passive Seismic Experiment. Science, vol. 167, no. 3918, Jan. 30, 1970, pp. 455-467.

Latham, G.; Ewing, M.; Press, F.; Sutton, G.; et al.: Seismic Data from Man-Made Impacts on the Moon. Science, vol. 170, no. 3958, Nov. 6, 1970, pp. 620-626.

Latham, G. V.; Ewing, M.; Press, F.; Sutton, G.; et al.: Apollo 11 Passive Seismic Experiment. Proceedings of the Apollo 11 Lunar Science Conference, vol. 3, Pergamon Press (New York), 1970, pp. 2309-2320.

Latham, Gary V.; Ewing, Maurice; Press, Frank; Sutton, George; et al.: Passive Seismic Experiment. Sec. 6 of Apollo 14 Preliminary Science Report, NASA SP-272, 1971.

Latham, G.; Ewing, M.; Dorman, J.; Lammlein, D.; et al.: Moonquakes. Science, vol. 174, no. 4010, 1971, pp. 687-692.

Latham, Gary; Ewing, Maurice; Dorman, James; Lammlein, David; et al.: Moonquakes and Lunar Tectonism. The Moon, vol. 4, nos. 3/4, June/July 1972, pp. 373-382.

Latham, Gary; Ewing, Maurice; Dorman, James; Lammlein, David; et al.: Moonquakes and Lunar Tectonism, Results from the Apollo Passive Seismic Experiment. Proceedings of the Third Lunar Science Conference, vol. 3, MIT Press (Cambridge, Mass.), 1972, pp. 2519-2526.

Latham, Gary V.; Ewing, Maurice; Press, Frank; Sutton, George; et al.: Passive Seismic Experiment. Sec. 8 of Apollo 15 Preliminary Science Report, NASA SP-289, 1972.

- Latham, Gary V.; Ewing, Maurice; Press, Frank;  
Sutton, George; et al.: Passive Seismic Experiment.  
Sec. 9 of Apollo 16 Preliminary Science Report,  
NASA SP-315, 1972.
- Latham, Gary; Ewing, Maurice; Dorman, James; Nakamura, Yoseo;  
et al.: Lunar Structure and Dynamics - Results from the  
Apollo Passive Seismic Experiment. The Moon, vol. 7,  
nos. 3/4: May/June 1973, pp. 396-420.
- Latham, G.; Dorman, J.; Duennebier, F.; Ewing, M.; et al.:  
Moonquakes, Meteoroids, and the State of the Lunar In-  
terior. Proceedings of the Fourth Lunar Science Confer-  
ence, vol. 3, Pergamon Press (New York), 1973, pp. 2515-  
2528.
- Latham, Gary V.; Ewing, Maurice; Press, Frank; Dorman, James;  
et al.: Passive Seismic Experiment. Sec. 11 of Apollo 17  
Preliminary Science Report, NASA SP-330, 1973.
- Meissner, R.; Sutton, G. H.; and Duennebier, F. K.: Moon-  
beben, Umshau in Wissenschaft und Technik. Heft V., 1971,  
pp. 111-115.
- Nakamura, Y.: Seismic Energy Transmission in the Lunar  
Surface Zone Determined from Signals Generated by Movement  
of Lunar Rovers. Bull. Seismological Soc. of America.  
(To be published)
- Nakamura, Y.; Dorman, J.; Duennebier, F.; Lammlein, D.; and  
Latham, G.: Shallow Lunar Structure Determined from the  
Passive Seismic Experiment. The Moon, vol. 13, nos. 1,  
2, and 3, 1975, pp. 57-66.
- Nakamura, Y.; Lammlein, D.; Latham, G.; Ewing, M.; et al.:  
New Seismic Data on the State of the Lunar Interior.  
Science, vol. 181, no. 4094, July 6, 1973, pp. 49-51.
- Nakamura, Yosio; Dorman, James; Duennebier, Frederick; Ewing,  
Maurice; Lammlein, David; and Latham, Gary: High-Frequency  
Lunar Teleseismic Events. Proceedings of the Fifth Lunar  
Science Conference, vol. 3, Pergamon Press (New York), 1974,  
pp. 2883-2890.
- Nakamura, Yosio; Latham, G. V.; Lammlein, David; Ewing,  
Maurice; Duennebier, Frederick; and Dorman, James: Deep  
Lunar Interior Inferred from Recent Seismic Data.  
Geophys. Res. Letters, vol. 1, no. 3, 1974, pp. 137-140.

- Sutton, George H.; and Latham, Gary V.: Analysis of a Feedback-Controlled Seismometer. *J. Geophys. Res.*, vol. 69, no. 18, Sept. 15, 1964, pp. 3865-3882.
- Toksoz, M. N.; Dainty, A. M.; Solomon, S. C.; and Anderson, K. R.: Velocity, Structure, and Evolution of the Moon. *Proceedings of the Fourth Lunar Science Conference*, vol. 3, Pergamon Press (New York), 1973, pp. 2529-2547.
- Toksoz, M. N.; Press, F.; Dainty, A. M.; and Anderson, K. R.: Lunar Velocity Structure and Compositional and Thermal Inferences. *The Moon*, vol. 9, no. 1, 1974, pp. 31-42.
- Toksoz, M. N.; Press, F.; Dainty, A.; Anderson, K.; et al.: Structure, Composition, and Properties of Lunar Crust. *Proceedings of the Third Lunar Science Conference*, vol. 3, MIT Press (Cambridge, Mass.), 1972, pp. 2527-2544.
- Toksoz, M. N.; Press, Frank; Anderson, Ken; Dainty, A.; et al.: Velocity Structure and Properties of the Lunar Crust. *The Moon*, vol. 4, nos. 3/4, June/July 1972, pp. 490-504.
- Toksoz, M. N.; Press, F.; Anderson, K.; Dainty, A.; et al.: Lunar Crust: Structure and Composition. *Science*, vol. 176, no. 4038, June 2, 1972, pp. 1012-1016.
- Toksoz, M. Nafi: Geophysical Data and the Interior of the Moon. *Annual Rev. Earth Planet. Sci.*, vol. 2, Annual Reviews Inc. (Palo Alto, Calif.), 1974, pp. 151-177.
- Toksoz, M. Nafi; Dainty, Anton M.; Solomon, Sean C.; and Anderson, Kenneth R.: Lunar Structure. *Rev. Geophys. Space Phys.*, vol. 12, no. 4, 1974, pp. 539-567.

TABLE 4-I.- LUNAR PASSIVE SEISMIC STATION STATISTICS

Station	Date of deployment		Coordinates <sup>a</sup>	Distance from lunar module, m	Azimuth <sup>b</sup> of components, deg		Distances and azimuths from other stations			
	Yr	Day			+X	+Y	12	14	15	16
11	1969	202	0.68° N, 23.42° E	16.8	0	90	--	--	--	--
12	1969	323	3.04° S, 23.42° W	130	180	270	--	181 km, 276°	1188 km, 226°	1187 km, 276°
14	1971	036	3.65° S, 17.48° W	178	0	90	181 km, 96°	--	1095 km, 218°	1007 km, 277°
15	1971	212	26.08° N, 3.66° E	110	0	90	1188 km, 40°	1095 km, 33°	--	1119 km, 342°
16	1972	112	8.97° S, 15.51° E	95	334.5	64.5	1187 km, 100°	1007 km, 101°	1119 km, 160°	--

<sup>a</sup>Listed coordinates are derived from the Manned Space Flight Network Apollo tracking data. Locations based on these data are referenced to a mean spherical surface and may differ by several kilometers from coordinates referenced to surface features.

<sup>b</sup>Upward ground motion produces positive-going output signal for the vertical components. The listed azimuths for the horizontal-component seismometers are the directions of ground motion that give positive-going output signal (0° = north, 90° = east, 180° = south, 270° = west).

TABLE 4-II.- OPERATIONAL HISTORY

	Date		Event
Yr	Day	Station	
1969	202	11	Deployment: flat response mode
1969	215	11	Station turned off for lunar night
1969	230	11	Station turned on for second lunar day
1969	237	11	LP components drifted off scale, station overheating and not accepting commands
1969	239	11	Loss of all data
1969	323	12	Deployment: flat response mode, SP component not operating, LPZ operating with abnormal LP response
1969	326	12	Changed LP response to standard mode to bring LPZ back into operation
1970	105	12	Reduced LP gain to -10 dB during Apollo 13 Saturn IVE (SIVB) impact (01 hr 24 min)
1970	105	12	Increased LP gain to 0 dB (02 hr 30 min)
1971	036	14	Deployment: standard mode
1971	210	14	Reduced LP gain to -10 dB during Apollo 15 SIVB impact (21 hr 00 min)
1971	210	14	Increased LP gain to 0 dB (21 hr 47 min)
1971	212	15	Deployment: standard mode
1971 and 1972	330 to 030	14	LPZ axis anomalously noisy, affecting LPX and LPY (After mid-January, LPZ was usually dead but occasionally had periods of normal operation.)

TABLE 4-II.- OPERATIONAL HISTORY - Concluded

Date			Event
Yr	Day	Station	
1972	112	16	Deployment: standard mode
1972	343	16	LPY anomalous noise and reduced gain
1972	345	14	Reduced LP again to -10 dB during Apollo 17 SIVB impact (20 hr 35 min)
1972	345	14	Increased LP gain to 0 dB (20 hr 55 min)
1972	348	16	LPY back to normal
1974	288	12	Changed to flat response
1975	099	12	Changed to standard response
1975	179	12, 15, and 16	Changed to flat response

TABLE 4-III.- ARTIFICIAL IMPACT DATA

Event	Year	Day	Time, hr:min:sec	Coordinates	Distances and azimuths from stations —				Impact angle from horizontal, deg	Impact heading, deg	Impact energy, J
					12	14	15	16			
Apollo 12 LM	1969	324	22:17:17.7	3.94° S, 21.21° W	73 km, 112°	--	--	--	3.7	306	3.36 × 10 <sup>9</sup>
Apollo 13 SIVB	1970	105	01:09:41.0	2.75° S, 27.86° W	135 km, 274°	--	--	--	76	78	4.63 × 10 <sup>10</sup>
Apollo 14 SIVB	1971	035	07:40:55.4	8.09° S, 26.02° W	172 km, 207°	--	--	--	69	103	5.54 × 10 <sup>10</sup>
Apollo 14 LM	1971	038	00:45:25.7	3.42° S, 19.67° W	114 km, 96°	67 km, 276°	--	--	3.6	282	3.25 × 10 <sup>9</sup>
Apollo 15 SIVB	1971	210	20:58:42.9	1.51° S, 11.81° W	355 km, 83°	184 km, 69°	--	--	62	97	4.61 × 10 <sup>10</sup>
Apollo 15 LM	1971	215	03:03:37.0	26.36° N, 0.25° E	1130 km, 36°	1048 km, 29°	93 km, 276°	--	3.2	284	3.43 × 10 <sup>9</sup>
Apollo 16 SIVB	1972	110	*21:02:06 : 4	2.24 : 0.33° N 24.49 : 0.33° W	--	--	--	--	79 (7)	78	4.59 × 10 <sup>10</sup>
Apollo 17 SIVB	1972	345	20:32:42.3	4.21° S, 12.31° W	338 km, 96°	157 km, 96°	1032 km, 209°	850 km, 278°	55	97	4.71 × 10 <sup>10</sup>
Apollo 17 LM	1972	350	06:50:20.8	19.96° N, 30.50° E	1750 km, 64°	1598 km, 61°	770 km, 98°	985 km, 27°	4.9	283	3.14 × 10 <sup>9</sup>

\*Tracking signal lost before impact. The origin time was obtained by interpretation of seismic data, and the location was extrapolated from the early trajectory.

TABLE 4-IV. - THE PSE ALSEP WORDS

Word	Description
Even words (except 2, 124, 46, 56)	SP vertical data
9, 25, 41, 57	LP X component (LPX)
11, 27, 43, 59	LP Y component (LPY)
13, 29, 45, 61	LP Z component (LPZ)
35 (even frames)	X axis tidal
35 (odd frames)	Z axis tidal
37 (even frames)	Y axis tidal
37 (odd frames)	Instrument temperature

<sup>1</sup>Apollo 15 only.

TABLE 4-V.- THE ALSEP WORD LOCATIONS

(a) Format A (for all tapes except station 12 tapes after day 288 of 1971)

36-bit word	ALSEP word	Use
4	4, 6, 8	SP, SP, SP
5	9, 10, 11	LPX, SP, LPY
6	12, 13, 14	SP, LPZ, SP
7	16, 18, 20	SP, SP, SP
8	22, 24, 25	SP, <sup>1</sup> SP, LPX
9	26, 27, 28	SP, LPY, SP
10	29, 30, 32	LPZ, SP, SP
11	33, 34, 35	-, SP, <sup>2</sup> TDLX/Z
12	36, 37, 38	SP, <sup>2</sup> TEMP/TDLY, SP
13	40, 41, 42	SP, LPX, SP
14	43, 44, 45	LPY, SP, LPZ
15	46, 48, 50	-, SP, SP
16	52, 54, 57	SP, SP, LPX
17	58, 59, 60	SP, LPY, SP
18	61, 62, 64	LPZ, SP, SP

(b) Format B (for station 12 starting on day 289 of 1971)

36-bit word	ALSEP word	Use
4	9, 11, 13	LPX, LPY, LPZ
5	25, 27, 29	LPX, LPY, LPZ
6	33, 35, 37	-, TDLX/Z, TEMP/TDLY
7	41, 43, 45	LPX, LPY, LPZ
8	46, 57, 59	-, LPX, LPY
9	61, -, -	LPZ

<sup>1</sup>Not for Apollo 15.

<sup>2</sup>TDL = tidal, TEMP = temperature.

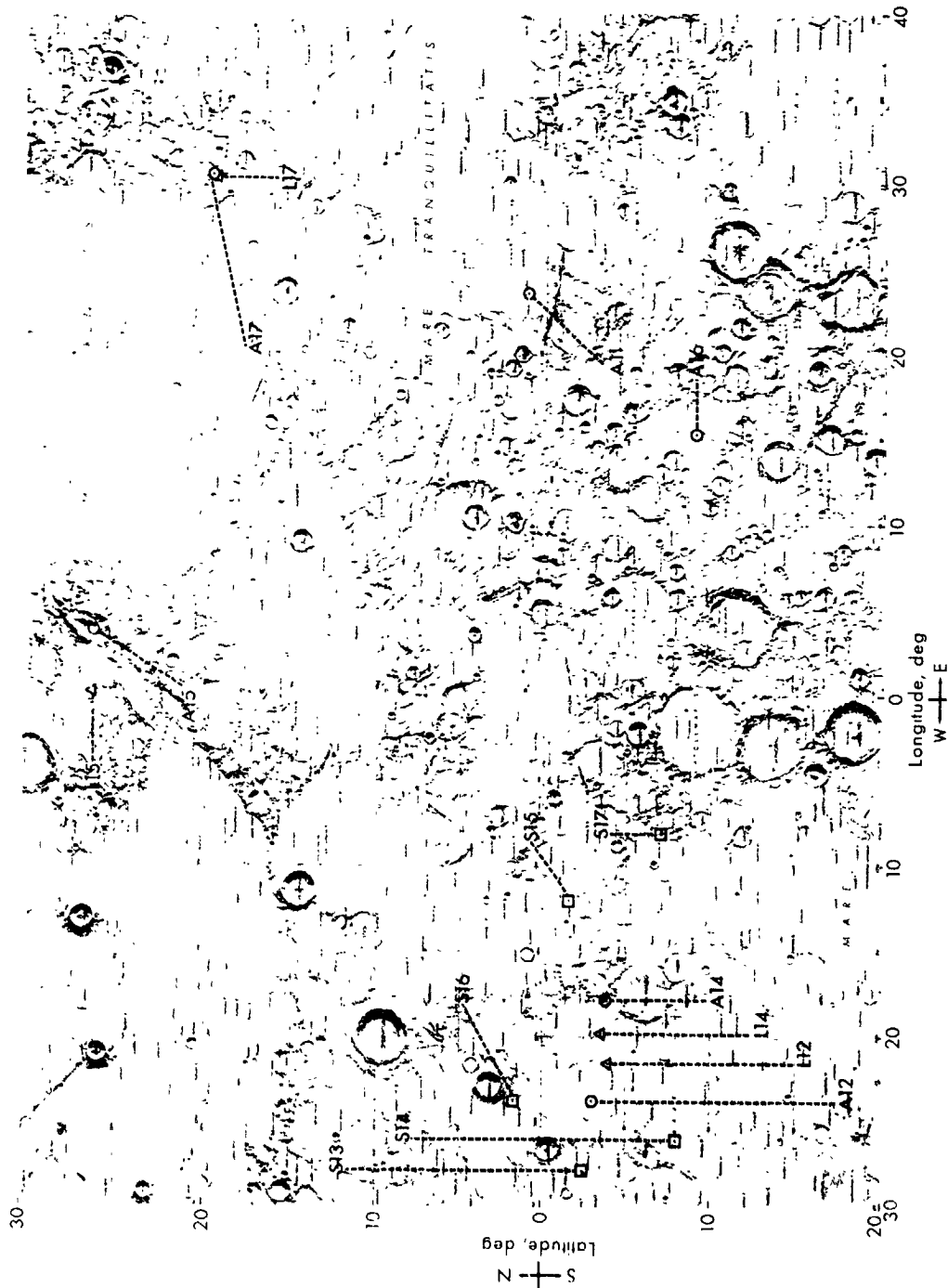


Figure 4-1.- Locations of Apollo lunar surface experiments package (ALSEP) sites (labeled as "A", followed by mission number, and designated with a circle) and Saturn IB (S-IVB) and lunar module (LM) impact locations (labeled as "S" and "L," respectively, and designated with squares and triangles, respectively).

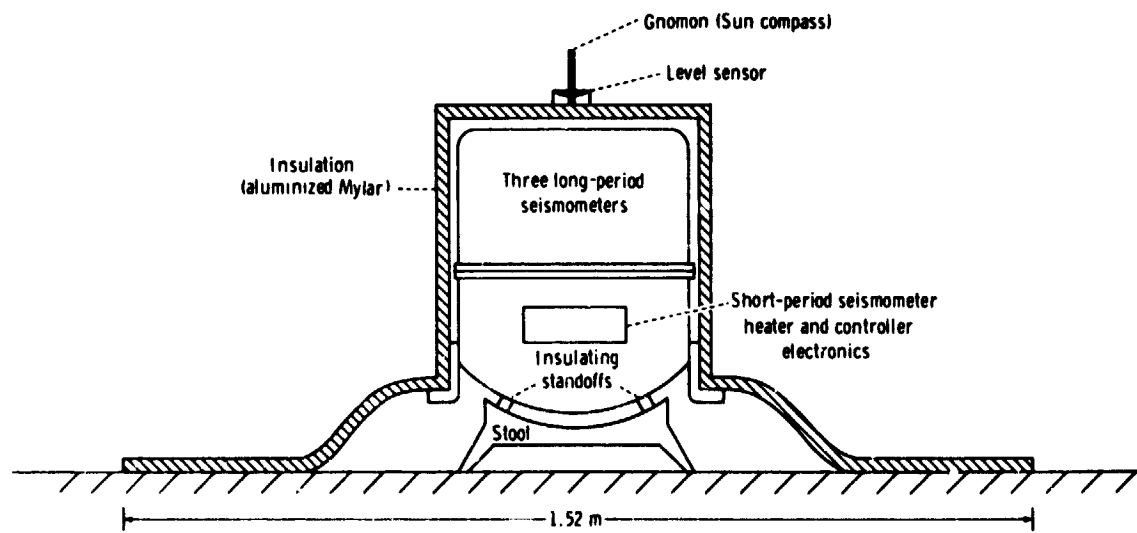


Figure 4-2.- Schematic diagram of the Apollo passive seismic experiment (PSE).

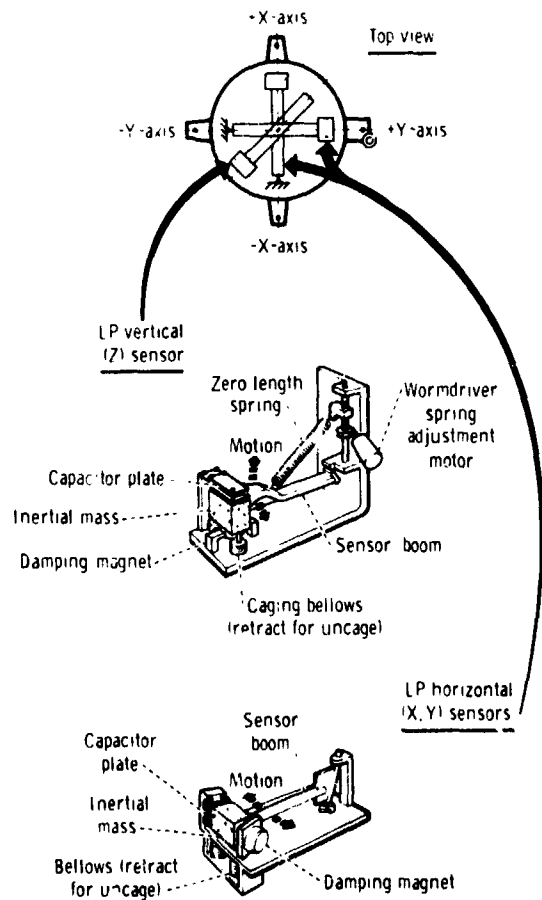


Figure 4-3.- Schematic diagrams of the elements of the LP seismometers.

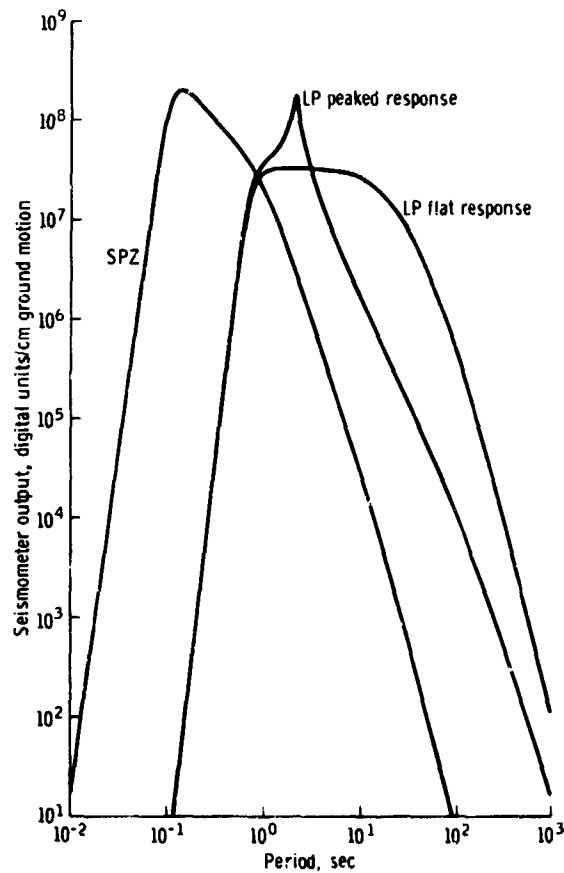
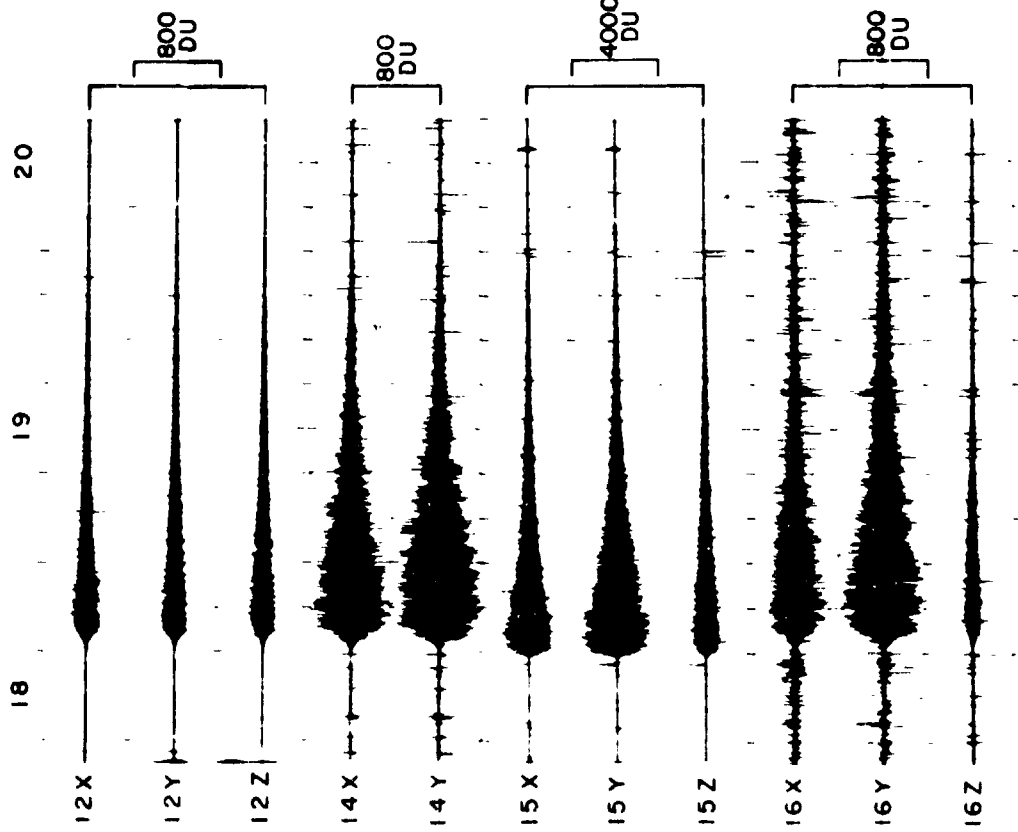


Figure 4-4.- Response curve for the LP and SP vertical-component seismometers. The ordinate scale is in digital units (DU) per centimeter ground motion amplitude. A DU is the signal variation that corresponds to a change in the least significant bit of the 10-bit data word.

CATEGORY C METEOROID IMPACT  
 JULY 31, 1972



CATEGORY A<sub>18</sub> MOONQUAKE  
 JULY 24, 1972

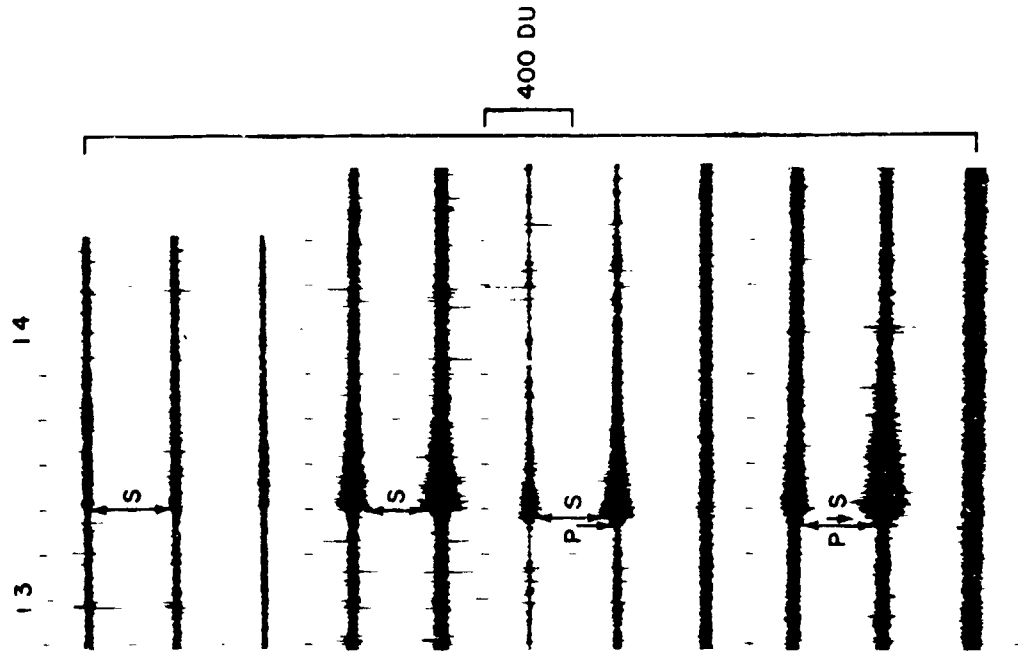


Figure 4-5.- Sample of the compressed data playouts (data set 1).

CATEGORY A20 MOONQUAK

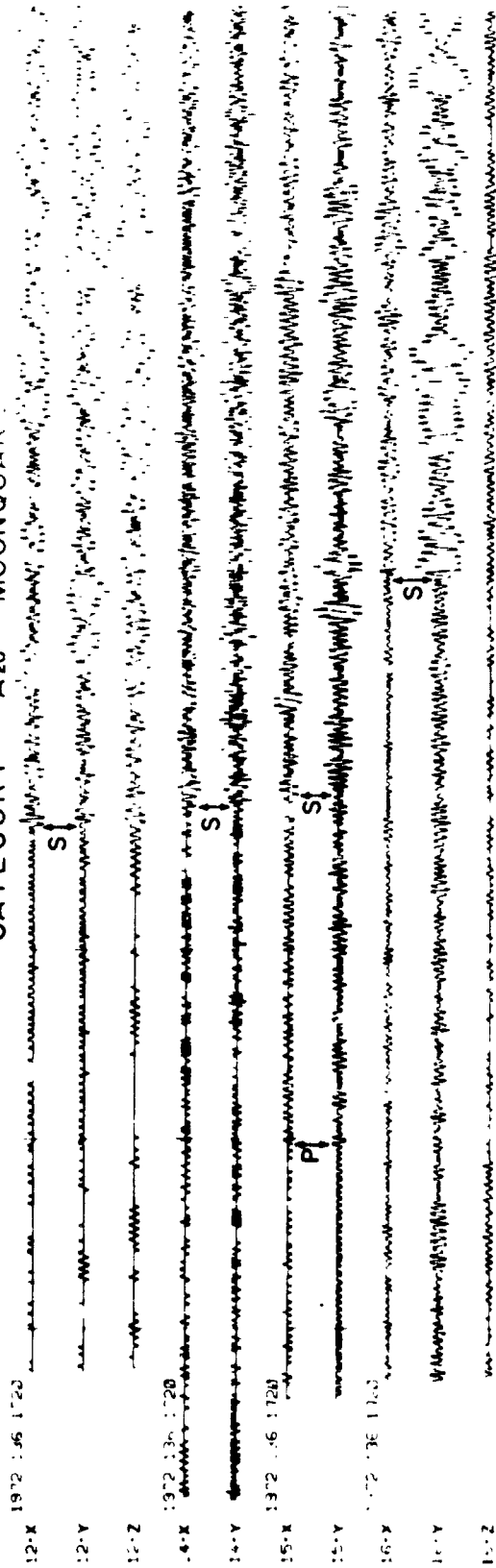
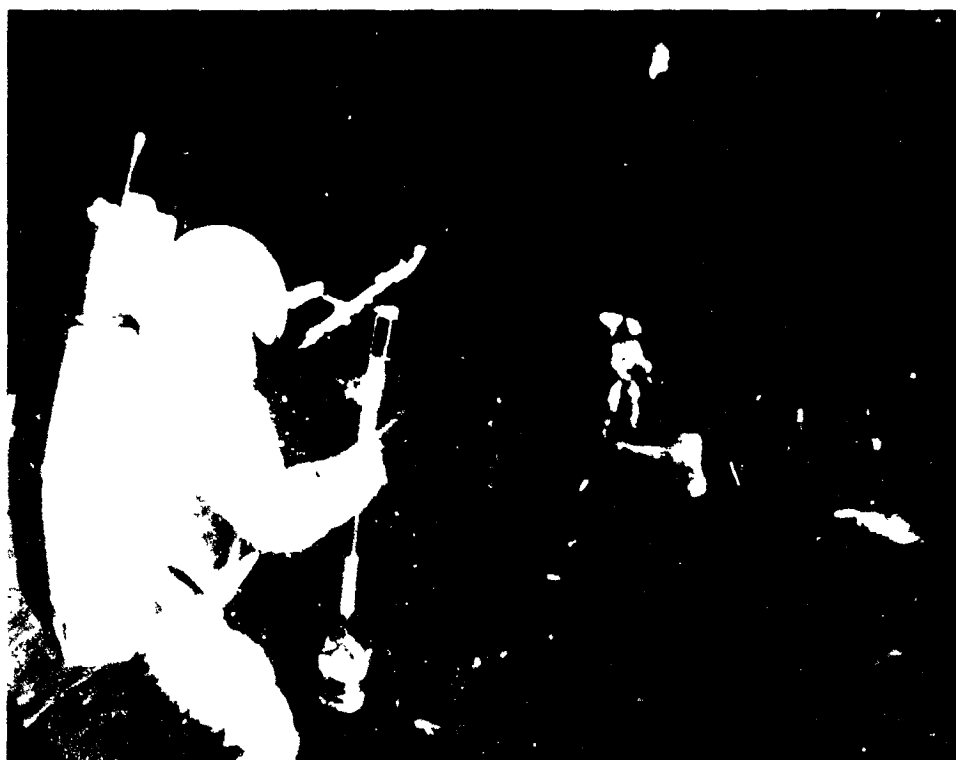


Figure 4-6.- Sample of the expanded-scale data playouts (data set 5).

5. ACTIVE SEISMIC EXPERIMENT (NASA EXPERIMENT S-033)

NSSDC IDENTIFICATION NUMBERS:

APOLLO 14 71-008C-05  
APOLLO 16 72-031C-02



CONTENTS - SECTION 5

	Page
INTRODUCTION . . . . .	5-3
INSTRUMENT DESCRIPTION AND PERFORMANCE . . . . .	5-4
OPERATIONAL HISTORY . . . . .	5-4
Apollo 16 Grenade Firings . . . . .	5-4
Apollo 16 LM Ascent Recorded by ASE . . . . .	5-7
NSSDC DATA DESCRIPTION AND TAPE FORMAT . . . . .	5-8
LOG COMPRESSION . . . . .	5-9
DATA AVAILABLE AT NSSDC . . . . .	5-10
REFERENCES . . . . .	5-10

## 5. ACTIVE SEISMIC EXPERIMENT

The active seismic experiment (ASE) was part of the Apollo lunar surface experiments package (ALSEP) of the Apollo 14 and 16 missions. The purpose of the experiment was to generate and monitor seismic waves in the near lunar surface and to use these data to study the internal structure of the Moon to a depth of several hundred meters.

### INTRODUCTION

The ASE data are obtained from three sources: an astronaut-activated thumper, a mortar package that contains rocket-launched grenades, and the impulse produced by the lunar module (LM) ascent. The Apollo 14 grenades have not been fired at the time of this writing. A study of the deployment photographs and the astronaut's description of the mortar box positioning raised the question of the back-blast effect on other experiments. A post-mission vacuum chamber test was conducted with the ALSEP configuration the same as that deployed on the lunar surface. The results of this test indicated that the back blast might damage the other experiments and the ALSEP central station; therefore, it was decided that the mortars will not be fired until the other experiments fail to return valid scientific data.

Three of the four grenades at the Apollo 16 site have been fired. On May 23, 1972, the Apollo 16 ALSEP was commanded to high bit rate between 05:20:00 and 06:44:00 (hr:min:sec) G.m.t. for the ASE/mortar mode of operation (fig. 5-1). Three of the four high-explosive grenades in the mortar package were successfully launched in the following sequence: Grenade 2 (1024 g) was launched a distance of 900 m; grenade 4 (695 g) was launched a distance of 150 m; and grenade 3 (775 g) was launched a distance of 300 m. Grenade 1, which weighed 1261 g and was to be launched a distance of 1500 m, was not launched because the mortar package pitch angle sensor went off-scale high after grenade 3 was fired. The off-scale indication makes the pitch position of the launch assembly uncertain; therefore, the decision was made to delay launching of the mortar as long as the other Apollo 16 experiments were gathering valid scientific data.

## INSTRUMENT DESCRIPTION AND PERFORMANCE

The ASE consists of a thumper and geophones, a mortar package assembly (MPA), electronics within the ALSEP central station, and interconnecting cabling. The components of the ASE are shown schematically in figure 5-2.

The astronaut-activated thumper is a short staff (fig. 5-3) used to detonate small explosive charges -- single bridgewire Apollo standard initiators. Twenty-one initiators are mounted so that they are perpendicular to the base plate at the lower end of the staff. An arm-fire switch and an initiator-selector switch are located at the upper end of the staff. A pressure switch in the base plate detects the instant of initiation. A cable connects the thumper to the central station to transmit real-time event data. The thumper also stores the three geophones and connecting cables until deployment on the lunar surface.

The three identical geophones are miniature seismometers of the moving coil-magnet type. The coil is the inertial mass suspended by springs in the magnetic field. Above the natural resonant frequency of the geophones (7.5 Hz), the output is proportional to ground velocity. The geophones are deployed at 3-, 49-, and 94-m (10-, 160-, and 310-ft) intervals in a linear array from the central station and are connected to it by cables.

The Apollo 14 and 16 ASE characteristics are given in tables 5-I(a) and 5-I(b). The Apollo 16 nominal ASE grenade parameters are listed in table 5-II.

## OPERATIONAL HISTORY

Geophone distances from the Apollo 14 and 16 thumper shots are given in tables 5-III(a) and 5-III(b). Thumper firing times for the Apollo 14 and 16 seismic experiments are given in tables 5-IV(a) and 5-IV(b). Seismic signals produced by the Apollo 16 LM ascent stage and ASE thumper firings are shown in figures 5-4 and 5-5. The deployed experiment configuration is shown in figure 3 of reference 5-1.

### Apollo 16 Grenade Firings

Grenade number 4.- Firing information for grenade number 4 is in records 527 to 559. The fire command is in record 529, frame 10, at 1972:144:06:32:3.183 (yr:day:hr:min:sec) G.m.t. Detonation is in record 548, frame 7, word count 9, bit count 8 at 1972:144:06:32:14.430 G.m.t.

The launch angle  $\theta$  was  $11.330^\circ$ . Because no valid range line data were obtained for this or for the other two grenades that were fired,  $T_0$  (the time that the fire command was transmitted) was used. The error is no larger than 1 ALSEP data frame or 0.0604 sec.

Range data were calculated as follows. Where time of flight  $T$  of the grenade is computed by

$$T = \frac{2V_I \sin \theta}{g} = 11.247 \text{ sec} \quad (5-1)$$

and where computed initial velocity  $V_I$  is calculated as

$$V_I = \frac{Tg}{2 \sin \theta} = \frac{11.247 \times 5.3245}{2 \sin (45^\circ - 11.33^\circ)} = 54.0085 \text{ ft/sec} \quad (5-2)$$

then the range  $R$  is obtained by the equation

$$R = V_I \cos \theta T = 506 \text{ ft} \quad (5-3)$$

where  $g$  is lunar gravity. Based on these computations, the following distances were derived. (See Kovach and Watkins' deployment geometry of the geophone array relative to the mortar package (fig. 3 in ref. 5-1).)

The Apollo 16 geophone distances from grenade 4 were as follows:

Geophone	Distance		Corrected geophone distance	
	m	ft	m	ft
1	154.23	506	154.23	506
2	108.51	356	107.29	352
3	62.79	206	61.87	203

Grenade number 3.- Firing information for grenade number 3 is in records 1320 to 1360. The fire command is in record 1324, frame 9, at 1972:144:06:40:3.089 G.m.t. Detonation is in record 1358, frame 6, word count 30, bit count 10, at 1972:144:06:40:23.4315 G.m.t.

The launch angle was 7.94° from 45°. The other data are as follows:

$$T = \frac{2V_I \sin \theta}{g} = 20.3425 \text{ sec} \quad (5-4)$$

$$V_I = \frac{Tg}{2 \sin \theta} = 89.86 \text{ ft/sec} \quad (5-5)$$

$$R = V_I \cos \theta T = 1459 \text{ ft} \quad (5-6)$$

The Apollo 16 geophone distances from grenade 3 were as follows:

Geophone	Distance	
	m	ft
1	444.70	1459
2	398.98	1309
3	353.26	1159

Grenade number 2.- Firing information for grenade number 2 is in records 1766 to 1833. The fire command is in record 1771, frame 4, at 1972:144:05:48:3.184 G.m.t. Detonation is in record 1831, frame 7, word count 16, bit count 14, at 1972:144:05:48:39.5015.

The launch angle was 2.07° from 45°. The other data are as follows:

$$T = \frac{2V_I \sin \theta}{g} = 36.3175 \text{ sec} \quad (5-7)$$

$$V_I = \frac{Tg}{2 \sin \theta} = \frac{36.3175 \times 5.3245}{2 \times 0.68115} = 141.9 \text{ ft/sec} \quad (5-8)$$

$$R = V_I \cos \theta T = 3338 \text{ ft} \quad (5-9)$$

The Apollo 16 geophone distances from grenade 2 were as follows:

Geophone	Distance	
	m	ft
1	1017.42	3338
2	971.70	3188
3	925.98	3038

Grenade number 1. - Grenade number 1 was never fired.

#### Apollo 16 LM Ascent Recorded by ASE

The time of LM ascent thrust was computed as 01:25:48.728, based on LM ascent engine startup time plus engine buildup time (01:25:48.588 + 0.140). The time at which the engine achieved approximately 20 percent of peak pressure was used as the engine buildup time.

The geophone distances from the Apollo 16 LM ascent point were as follows:

Geophone	Distance	
	m	ft
1	95.10	312
2	121.31	398
3	156.67	514

NOTE: The LM ascent at the Apollo 14 site was not recorded.

## NSSDC DATA DESCRIPTION AND TAPE FORMAT

The ASE data are available from the National Space Science Data Center (NSSDC) on odd-parity, 7-track, 1.27-cm (0.5 in.), 800-bpi, binary tape with standard end of file. The data are stored as 36-bit words in 228-word logical records (fig. 5-6). As illustrated in figure 5-6, each logical record contains 10 frames of 32 seismic data words each, 10 timing words, and the day, date, and identification information.

The 10 timing words give the time in milliseconds for the start of each of the 10 corresponding data frames. Each 32-word data frame covers 0.060377 sec. The time of a particular data word (e.g., data word  $n$  in frame  $m$ ) is given by

$$t_n = t_m + \frac{0.060377}{32}(n - 1) \quad (5-10)$$

where  $n = 1, 2, \dots, 32$

$t_m$  = the start of frame  $m$

The occurrence of a seismic event (either thumper or mortar) is indicated by the frame mark in word 29 of each frame. (The LM ascent has no frame mark and must be located on the basis of the time given earlier.) If the frame mark in word 29 is 4 (00100) an event has occurred; if it is 0 no event has occurred. The base time for the event is just the start time of the previous frame. The exact time is marked by recording the word count and bit count portions of words 30 and 31, respectively, of the frame in which the event mark is set (fig. 5-7). Thus, the exact firing time  $t_F$  for an event occurring in frame  $m$  is

$$t_F = t_{m-1} + \frac{W_M}{\Delta t_W} + \frac{B_M}{\Delta t_B} \quad (5-11)$$

where  $W_M$  is the word count from word 30,  $B_M$  is the bit count from word 31, and  $\Delta t_W$  and  $\Delta t_B$  are defined as

$$\Delta t_W = \left[ 0.060377 (\text{sec/frame}) \right] \left[ \frac{1}{32 \text{ words/frame}} \right] \quad (5-12)$$

$$\Delta t_W = \left[ 0.060377 (\text{sec/frame}) \right] \left[ \frac{1}{32 \text{ words/frame}} \right] \left[ \frac{1}{20 \text{ bits/word}} \right] \quad (5-13)$$

Note that  $W_M$  is in binary but  $B_M$  is not in binary and must be obtained from table 5-V. Also, note that the engineering word  $E_i$  and the three geophone words  $G_1$ ,  $G_2$ ,  $G_3$  of each data word comprise 20 bits of the word; the last 4 bits are spare.

#### LOG COMPRESSION

To achieve the maximum dynamic range, the seismic data were log compressed into 32 binary levels as shown in table 5-VI. The binary data in the  $G_1$ ,  $G_2$ , and  $G_3$  positions must be decompressed to obtain the actual seismic signal data output from the seismometers.

The appropriate expansion formula to recover true input voltages is

$$V_{IN} = \frac{V_{OUT} - 2.420}{V_3} \quad (5-14)$$

$$\text{if } 2.170 < V_{OUT} < 2.670$$

for decimal 14, 15, and 16; and

$$V_{IN} = \pm \exp \frac{V_{OUT} - V_1}{\pm V_2} \quad (5-15)$$

for decimal 0 to 13 and 17 to 31; the + sign is used for positive input signals.

The values of  $V_3$ ,  $V_1$  (positive and negative), and  $V_2$  (positive and negative) for the Apollo 16 system are as follows:

Geophone	$V_3$	$V_1$		$V_2$	
		Negative, decimal 0 to 13	Positive, decimal 17 to 31	Negative, decimal 0 to 13	Positive, decimal 17 to 31
1	332.0	0.282600	4.557799	-0.268580	0.267730
2	332.0	.301230	4.557980	-.269830	.270650
3	332.0	.261240	4.553029	-.270540	.268130

Geophone calibration data are given in the Apollo 16 Preliminary Science Report (ref. 5-2).

Values of  $V_{OUT}$  for the appropriate binary level are obtained from table 5-VI. For example, if the binary level is 17, then equation (5-15) yields

$$V_{IN} = \exp\left(\frac{2.736220 - 4.557799}{0.267730}\right) = 0.0011 \text{ V} \quad (5-16)$$

#### DATA AVAILABLE AT NSSDC

The following data are available at NSSDC.

1. Tapes and microfilm of log-compressed digital data
2. Supporting documentation

#### REFERENCES

- 5-1. Kovach, R. L.; and Watkins, J. S.: The Velocity Structure of the Lunar Crust. *The Moon*, vol. 7, Apr. 1973, pp. 63-75.
- 5-2. Kovach, Robert L.; Watkins, Joel S.; and Talwani, Pradeep: Active Seismic Experiment. Sec. 10 of Apollo 16 Preliminary Science Report, NASA SP-315, 1972.

TABLE 5-I.- APOLLO 14 AND 16 ASE CHARACTERISTICS

(a) Apollo 14

Component characteristics	Channel no.		
	1	2	3
<b>Geophones:</b>			
Generator constant, V/m/sec . . . . .	250.4	243.3	241.9
Frequency, Hz . . . . .	7.32	7.22	7.58
Resistance, $\Omega$ . . . . .	6065	6157	6182
<b>Amplifiers:</b>			
Noise level, $\mu$ V rms at input . . . . .	0.300	0.325	0.272
Dynamic range, rms signal to rms noise in dB . . . . .	86.8	86.5	87.5
Gain (at 10 Hz and $V_{IN} = 5.0$ mV rms) . . .	666.7	666.7	675.7
<b>Log compressor (compression accuracy for temperature range 288 to 323 K):</b>			
Positive signal error, percent . . . . .	3.79	4.71	2.00
Negative signal error, percent . . . . .	2.07	1.32	3.33
<b>System:</b>			
Signal-to-noise ratio (rms signal to rms noise in dB for a 10-nm peak-to-peak signal at 10 Hz) . . . . .	33.6	33.1	32.9
<b>Calibrator accuracy:</b>			
Generator constant, percent error . . . . .	4.21	9.70	6.40
Natural frequency, percent error . . . . .	3.28	4.99	8.58

TABLE 5-I.- APOLLO 14 AND 16 ASE CHARACTERISTICS - Concluded

(b) Apollo 16

Component characteristics	Channel no.		
	1	2	3
<b>Geophones:</b>			
Generator constant, V/m/sec . . . . .	255	255	257
Frequency, Hz . . . . .	7.42	7.44	7.39
Resistance, $\Omega$ . . . . .	6090	6212	6204
<b>Amplifiers:</b>			
Noise level, mV rms at input . . . . .	.266	.100	.133
Dynamic range, rms signal to rms noise in dB at 10 Hz . . . . .	84.4	92.4	90
Gain (at 10 Hz and $V_{IN} = 2.75$ mV peak to peak). . . . .	698	684	709
<b>Log compressor (compression accuracy for temperature range 288 to 323 K):</b>			
Positive signal error, percent . . . . .	4.04	3.63	4.83
Negative signal error, percent . . . . .	2.46	1.87	1.88
<b>System:</b>			
Signal-to-noise ratio (rms signal to rms noise in dB for a 10-nm peak-to-peak signal at 10 Hz) . . . . .	38.9	37.9	45.0
<b>Minimum discernible signal (based on 0.5-mV zero-to-peak input equal to 1 digital unit at low level)</b>			
Zero to peak at 1 Hz, nm . . . . .	4	4	4
Zero to peak at 4 Hz, nm . . . . .	.3	.3	.3
Zero to peak at 10 Hz, nm . . . . .	.1	.1	.1
Zero to peak at 20 Hz, nm . . . . .	.05	.05	.05

TABLE 5-II.- APOLLO 16 NOMINAL ASE GRENADE PARAMETERS

Parameter	Grenade no.			
	1	2	3	4
Range, m . . . . .	1 500	900	300	150
Mass, g . . . . .	1 261	1 024	775	695
High-explosive-charge mass, g . . . . .	454	272	136	45
Rocket-motor mean peak thrust, N . . . . .	22 224	11 112	7556	5556
Mean velocity, m/sec . . . . .	50	38	22	16
Lunar flight time, sec . . . . .	44	32	19	13
Rocket-motor-propellant mass, g . . . . .	42	27	15	10
Propellant pellets, no. . . . .	2 365	1 520	620	570
Launch angle, deg . . . . .	45	45	45	45
Rocket-motor thrust duration, msec . . . . .	6.0	7.5	10.5	8.5

TABLE 5-III.- GEOPHONE DISTANCES FROM THE  
 APOLLO 14 and 16 THUMPER SHOTS

(a) Apollo 14

Shot	Distance to --					
	Geophone 3		Geophone 2		Geophone 1	
	m	ft	m	ft	m	ft
1	0	0	45.72	150	91.44	300
2	4.57	15	41.14	135	86.87	285
3	9.14	30	36.58	120	82.30	270
4	13.71	45	32.00	105	77.72	255
5	18.29	60	27.43	90	73.15	240
6	22.86	75	22.86	75	68.58	225
7	27.43	90	18.29	60	64.00	210
8	32.00	105	13.71	45	59.44	195
9	36.58	120	9.14	30	54.86	180
10	41.14	135	4.57	15	50.29	165
11	45.72	150	0	0	45.72	150
12	50.29	165	4.57	15	41.14	135
13	54.86	180	9.14	30	36.58	120
14	59.44	195	13.71	45	32.00	105
15	64.05	210	18.29	60	27.43	90
16	68.58	225	22.86	75	22.86	75
17	73.15	240	27.43	90	18.29	60
18	77.72	255	32.00	105	13.71	45
19	82.30	270	36.58	120	9.14	30
20	86.87	285	41.14	135	4.57	15
21	91.44	300	45.72	150	0	0

TABLE 5-III.- GEOPHONE DISTANCES FROM THE APOLLO 14

AND 16 THUMPER SHOTS - Concluded

(b) Apollo 16

Shot	Distance to --					
	Geophone 3		Geophone 2		Geophone 1	
	m	ft	m	ft	m	ft
1	0	0	45.72	150	91.44	300
2	4.57	15	41.14	135	86.87	285
3	9.14	30	36.58	120	82.30	270
4	13.71	45	32.00	105	77.72	255
5	18.29	60	27.43	90	73.15	240
6	22.86	75	22.86	75	68.58	225
7	27.43	90	18.29	60	64.00	210
8	32.00	105	13.71	45	59.44	195
9	36.58	120	9.14	30	54.86	180
10	41.14	135	4.57	15	50.29	165
11	45.72	150	0	0	45.72	150
12	54.86	180	9.14	30	36.58	120
13	59.44	195	13.71	45	32.00	105
14	64.05	210	18.29	60	27.43	90
15	68.58	225	22.86	75	22.86	75
16	73.15	240	27.43	90	18.29	60
17	77.72	255	32.00	105	13.71	45
18	82.30	270	36.58	120	9.14	30
19	91.44	300	45.72	150	0	0

TABLE 5-IV.- THUMPER FIRING TIMES FOR APOLLO 14 AND 16

(a) Apollo 14

Shot	Firing time, hr:min:sec, G.m.t.	Record	Frame <sup>a</sup>	Word count	Bit count
1	18:10:38.781	1067	7	14	11
2	18:12:13.494	1224	6	5	9
3	18:13:33.315	1356	8	11	17
4	18:14:38.890	1465	4	11	10
b <sub>7</sub>	18:20:31.980	2050	2	18	20
11	18:24:12.121	2412	8	23	31
12	18:26:29.733	2640	8	0	1
13	18:27:18.322	2720	2	24	27
17	18:31:16.797	3115	2	18	20
18	18:32:28.716	3234	3	26	12
19	18:33:47.770	3365	3	5	9
20	18:34:42.306	3454	6	14	19
21	18:37:06.960	3694	2	11	14

<sup>a</sup>Frame number is the number of the frame in which the event mode is set.

<sup>b</sup>Shots 5, 6, 8, 9, 10, 14, 15, and 16 misfired.

TABLE 5-IV.- THUMPER FIRING TIMES FOR APOLLO 14 AND 16 - Concluded

(b) Apollo 16

Shot	Firing time, hr:min:sec, G.m.t.	Record	Frame	Word count	Bit count
1	20:01:51.851	717	9	13	19
2	20:02:38.758	795	6	12	13
3	20:03:17.376	859	6	1	13
4	20:03:53.157	918	8	22	16
5	20:04:49.709	1012	5	13	20
6	20:05:27.299	1074	8	2	2
7	20:06:13.675	1151	6	7	11
8	20:06:49.332	1210	6	27	5
9	20:07:30.203	1278	3	26	11
10	20:08:13.808	1350	6	2	9
11	20:09:42.508	1497	5	9	15
12	20:10:29.512	1575	3	27	6
13	20:11:06.603	1636	8	7	8
14	20:12:14.656	1749	5	14	2
15	20:12:45.090	1799	9	17	6
16	20:13:23.572	1863	6	30	5
17	20:14:12.072	1943	10	9	7
18	20:14:52.150	2010	4	4	3
19	20:15:51.232	2108	2	24	5

TABLE 5-V.- BIT COUNT DEFINITIONS FOR WORD 31

Bit	Bit Count	Bit	Bit Count	Bit	Bit Count
0	00001	7	10110	14	11011
1	01100	8	10111	15	11001
2	01110	9	10011	16	00100
3	01111	10	10001	17	00110
4	01011	11	11100	18	00111
5	01001	12	11110	19	00011
6	10100	13	11111		

TABLE 5-VI.- APOLLO 14 AND 16 ASE LOG COMPRESSION

The ASE has 32 binary levels for representing the log-compressed data. Compression is linear if  $V_{OUT}$  is between 2.170 and 2.670 V.

Binary level	Log compressor output, $V_{OUT}$
0	0.059060
1	.216540
2	.374020
3	.531500
4	.688980
5	.846460
6	1.003940
7	1.161420
8	1.318900
9	1.476380
10	1.633860
11	1.791340
12	1.948820
13	2.10630
14	2.263780
15	2.421260
16	2.578740
17	2.736220
18	2.893700
19	3.051180
20	3.208660
21	3.366140
22	3.523620
23	3.681100
24	3.838580
25	3.996060
26	4.153540
27	4.311020
28	4.46850
29	4.625980
30	4.783460
31	4.940940

Linear portion  
of compressor

Negative  
input signals

Linear portion  
of compressor

Positive  
input signals

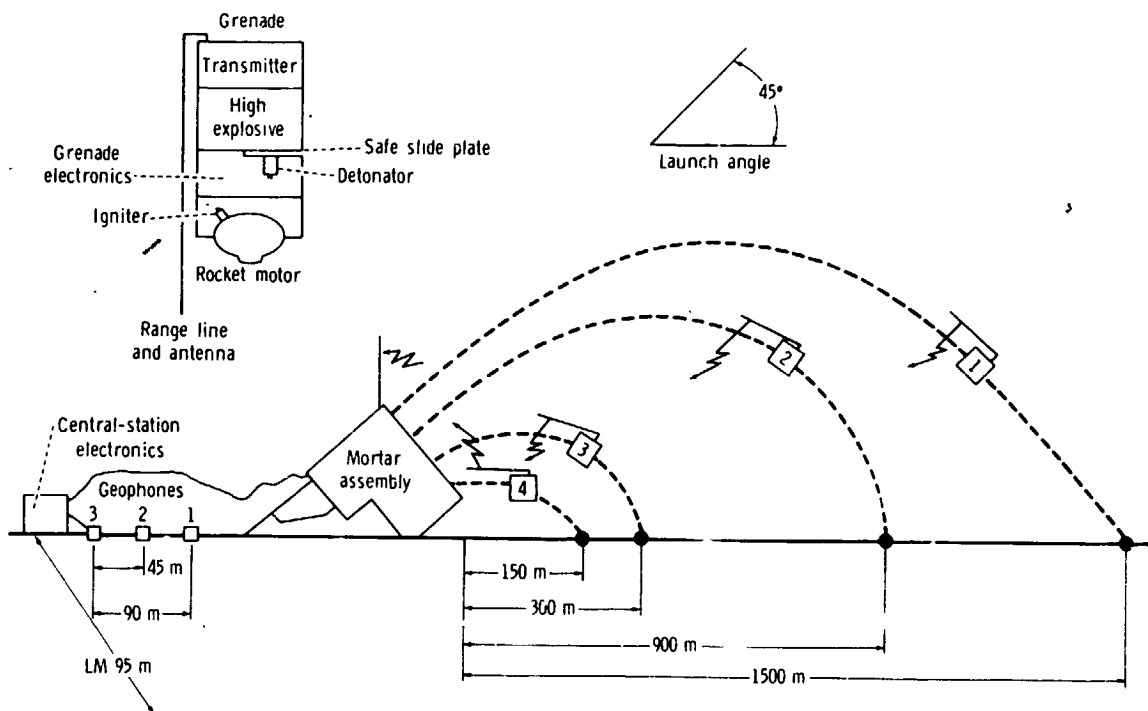


Figure 5-1.- Diagram showing the mortar mode of ASE operation.

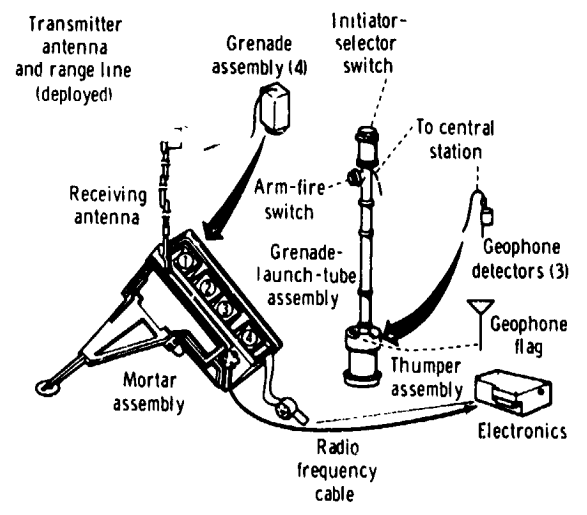


Figure 5-2.- Schematic diagram of the ASE.

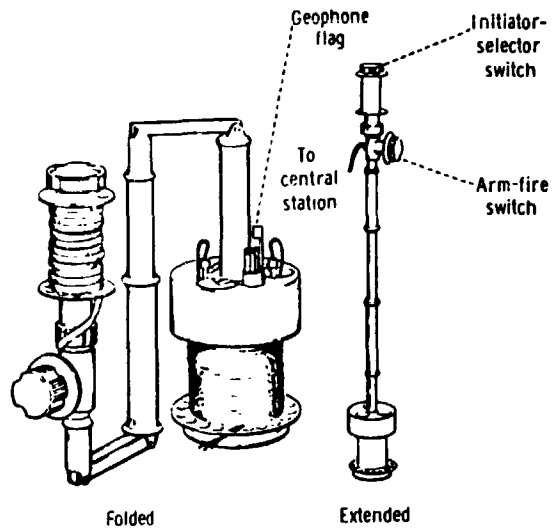


Figure 5-3.- Schematic diagram of the thumper in the folded and extended positions.

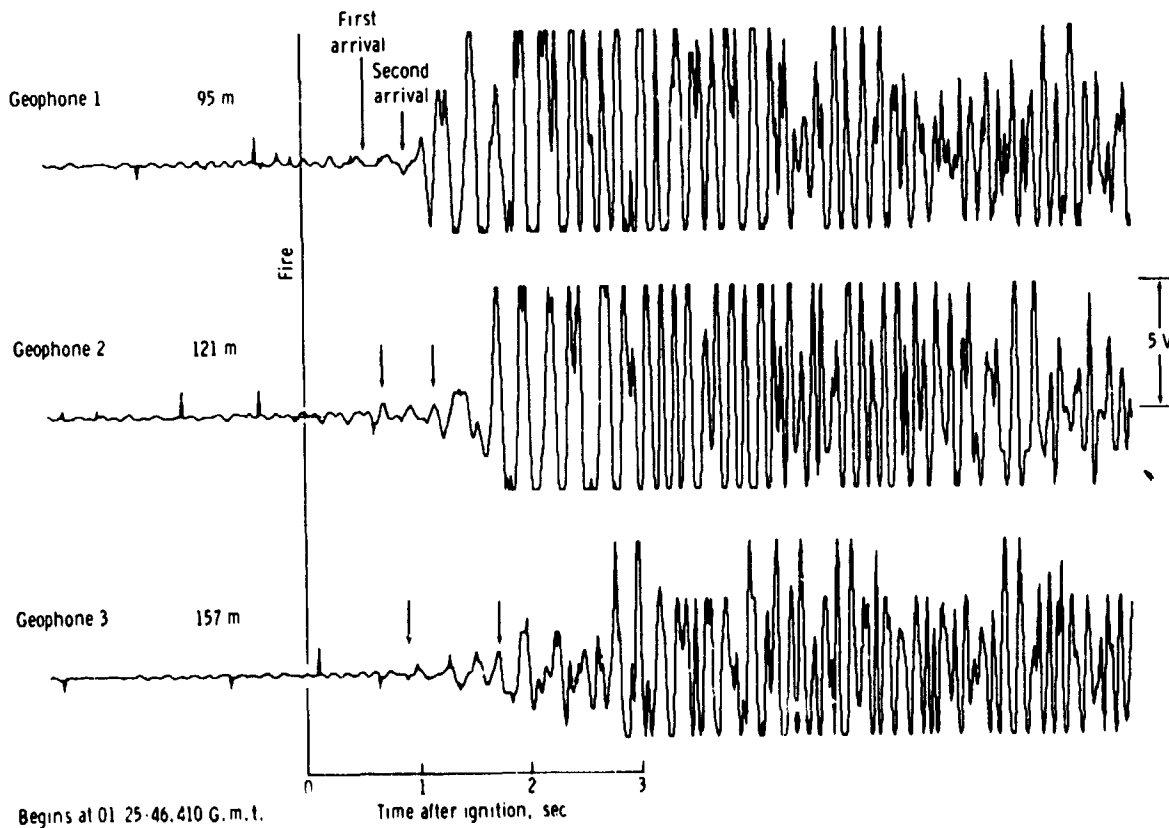


Figure 5-4.- Signals recorded by the ASE geophones from the lift-off of the Apollo 16 LM ascent stage.

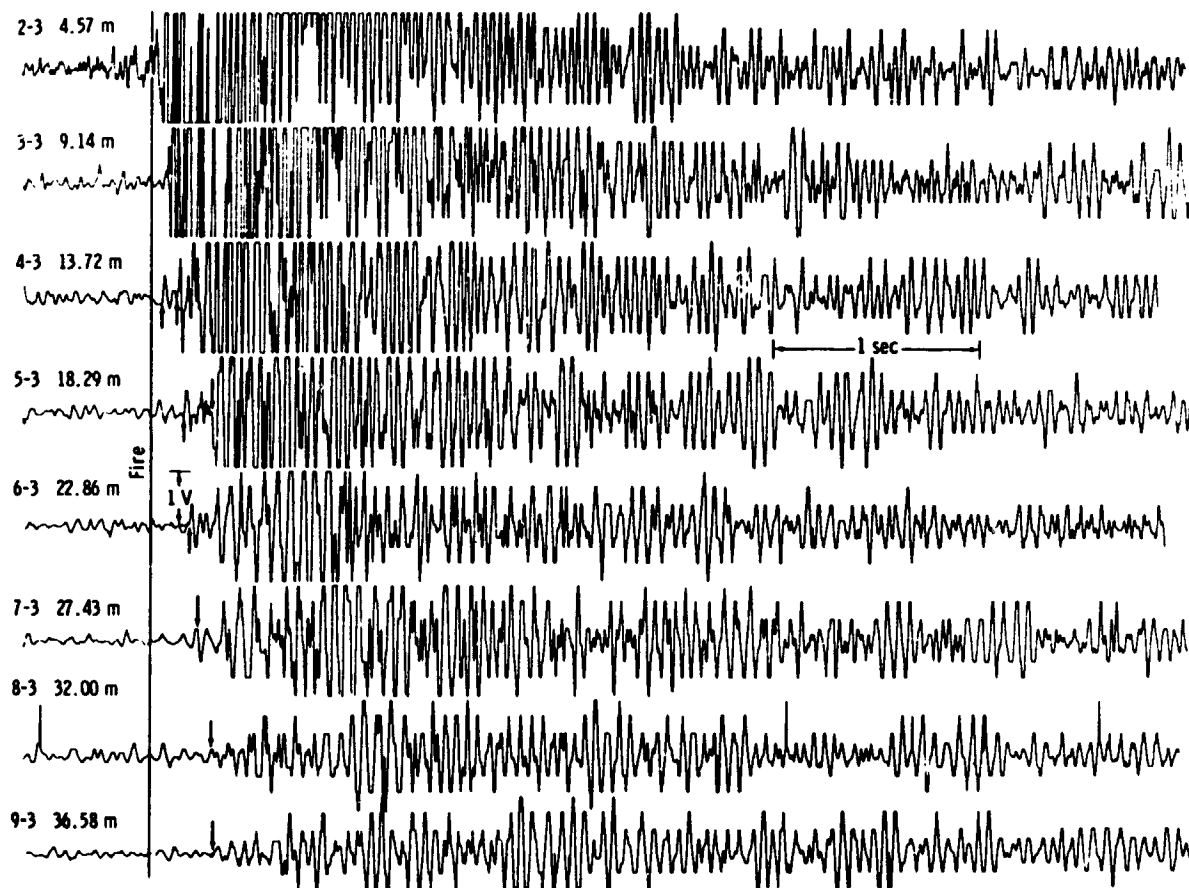


Figure 5-5.- Expanded time playouts of seismic signals produced by Apollo 16 thumper firings 2 to 9 as recorded at geophone 3. The traces are aligned to the same firing instant, and the arrows point to the onset of the seismic signal. (The first number in the data identifier is the thumper firing, and the second number is the geophone on which the data were recorded.)

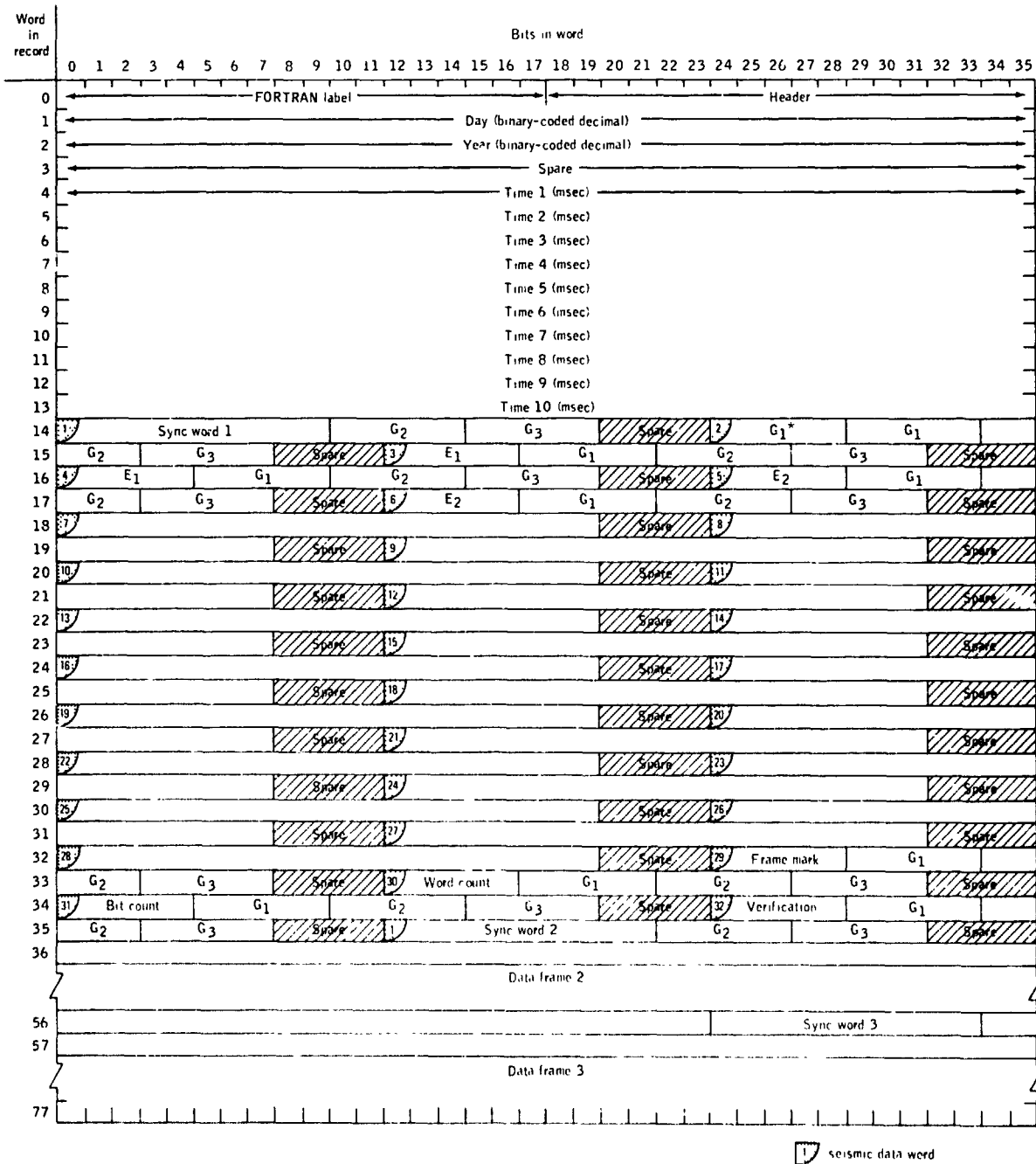


Figure 5-6.- Description of ASE data tape.

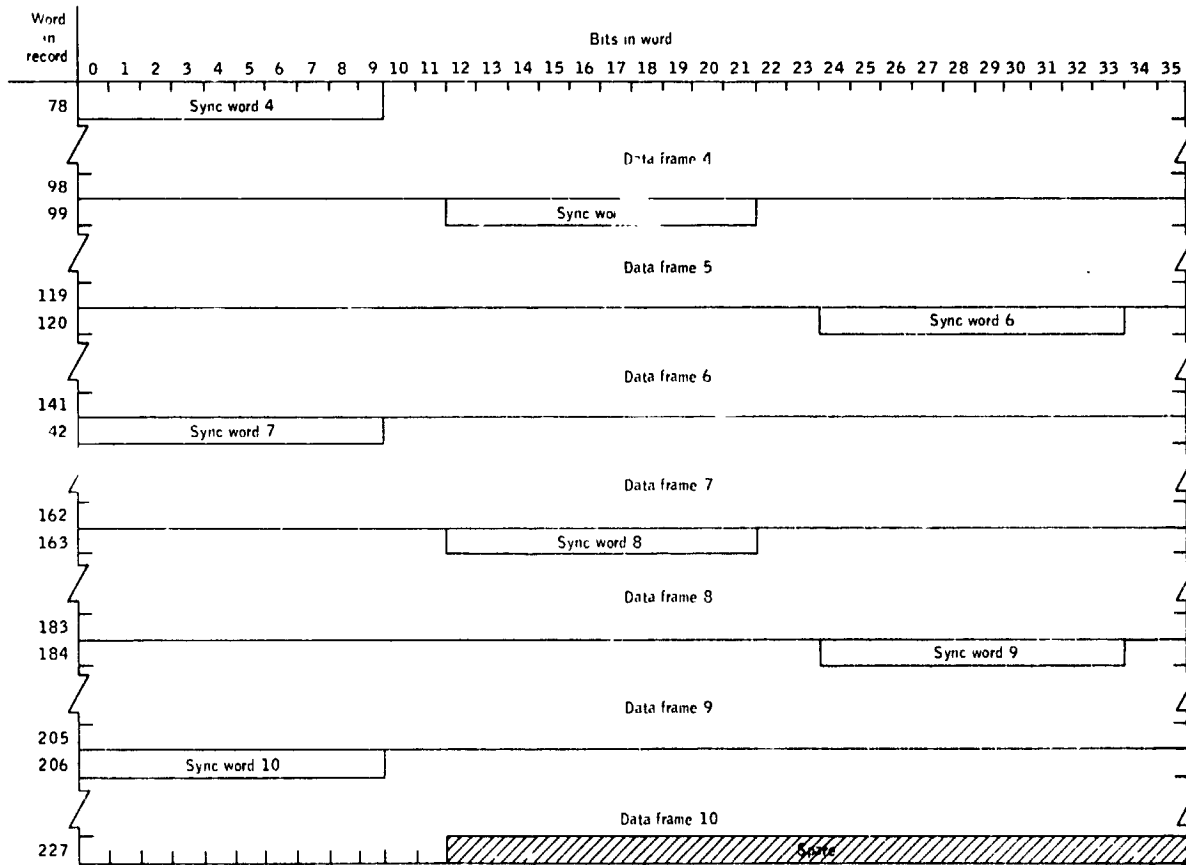
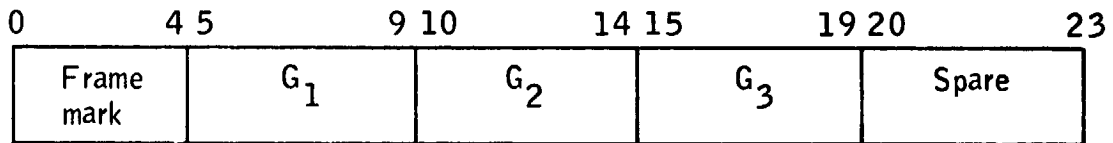
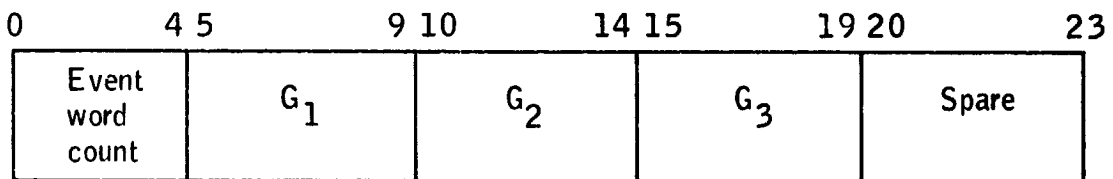


Figure 5-6.- Concluded.

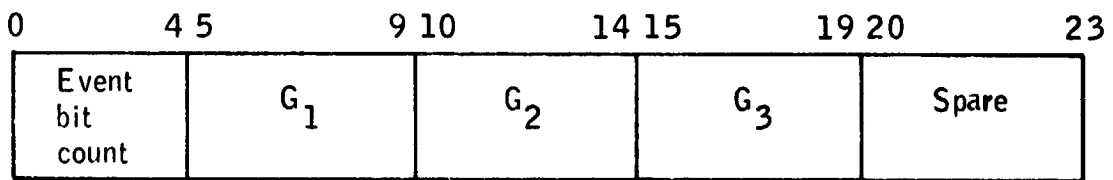
Word 29



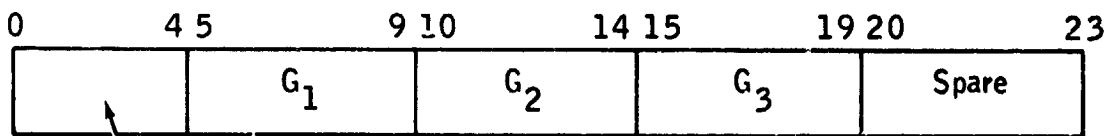
Word 30



Word 31



Word 32



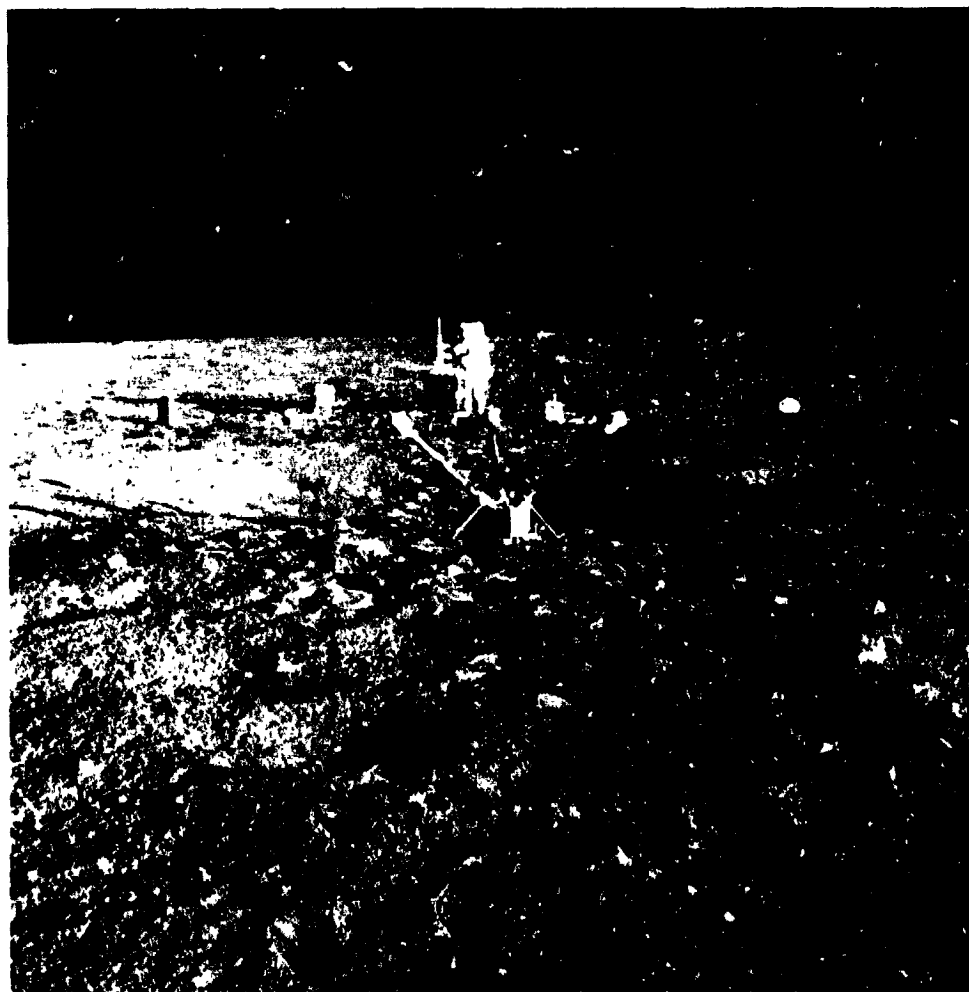
Mode identification and command verification

Figure 5-7.- Format of words 29, 30, 31, and 32.

6. LUNAR SURFACE MAGNETOMETER (NASA EXPERIMENT S-034)

NSSDC IDENTIFICATION NUMBERS:

APOLLO 12	69-099C-04
APOLLO 15	71-063C-03
APOLLO 16	72-031C-03



CONTENTS - SECTION 6

	Page
DESCRIPTION . . . . .	6-3
DATA SETS AND AVAILABILITY THROUGH NSSDC . . . . .	6-4
APOLLO CORRECTION TAPE DESCRIPTION . . . . .	6-4
Output Tape Format . . . . .	6-5
Last Records . . . . .	6-6
Data Plot Formats . . . . .	6-6
SUMMARY OF LSM RESULTS . . . . .	6-6
REFERENCES . . . . .	6-7
BIBLIOGRAPHY . . . . .	6-8

## 6. LUNAR SURFACE MAGNETOMETER

Lunar surface magnetometers were deployed by astronauts on the Apollo 12, 15, and 16 missions. This network of three magnetic observatories on the lunar surface allows simultaneous measurements of the global response of the Moon to large-scale solar and terrestrial magnetic fields. Figure 6-1 shows the Apollo 16 instrument deployed at the Descartes site.

### DESCRIPTION

The three orthogonal vector components of the magnetic field are measured by three fluxgate sensors. Each sensor consists of a toroidal Permalloy core that is driven to saturation by a sinusoidal current having a frequency of 6000 Hz. The three fluxgate sensors are located at the ends of three 100-cm-long orthogonal booms that separate the sensors from each other by 150 cm and position them 75 cm above the lunar surface. Orientation measurements with respect to lunar coordinates are made with two devices. A shadowgraph and bubble level are used by the astronaut to align the lunar surface magnetometer (LSM) and to measure azimuthal orientation with respect to the Moon-to-Sun line to an accuracy of  $0.5^\circ$ . Gravity-level sensors measure instrument tilt angles to an accuracy of  $0.2^\circ$  every 4.8 sec.

The thermal subsystem is designed to allow the LSM to operate over the complete lunar day-night cycle. Thermal control is accomplished by a combination of insulation, control surfaces, and heaters that operates collectively to keep the temperature of the electronics between 267 and 319 K. The electronics and the motor drive assembly are located in a box encased in a thermal blanket. Heat rejection during lunar day and retention during lunar night are controlled by a parabolic reflector array on two sides of the electronics box. The astronaut bubble level and azimuthal shadowgraph, which allow accurate orientation of the magnetometer, are on top of the box.

Power, digital signals, and commands are conveyed through a ribbon cable that connects to the Apollo lunar surface experiments package (ALSEP) central station telemetry receiver and transmitter. The instrument characteristics are listed in table 6-I, and a more detailed description is given in reference 6-1.

## DATA SETS AND AVAILABILITY THROUGH NSSDC

The reduced data are located at Ames Research Center and the National Space Science Data Center (NSSDC). Data have been recorded for the following time periods.

Apollo mission	Period begins		Period ends	
	Year	day:hr:min	Year	day:hr:min
12	1969	323:14:39	1970	093:03:15
15	1971	212:18:00	1972	264:16:36
16	1972	112:20:00	1974	265:00:00

The data are recorded on magnetic tape and are plotted as a function of time.

### APOLLO CORRECTION TAPE DESCRIPTION

The correction tape (FORTRAN binary tape, 36 bits per word) contains lunar magnetic field data in the ALSEP coordinate system. The tape was written by a FORTRAN IV program using a "WRITE (N) LIST" statement. The first word of each record contains time in milliseconds for the first vector (X, Y, Z) within a record. Vectors are at approximately 301.88-msec intervals. Each component has been rounded to the nearest 0.01  $\gamma$  (0.01 nT), multiplied by 100, and stored into 18 bits.



The first bit is "0" for positive field values and "1" for negative field values. For example, a value of -29.376  $\gamma$  (-29.376 nT) will be stored as -2938. Two components are packed into each 36-bit word.



### Last Records

The last record of data is filled with ones (octal ones = 111111111111); the last logical record is filled with all ones followed by end-of-file (EOF). Description: Binary tape, 556 bpi; 7-track, standard IBM EOF.

### Data Plot Formats

Samples of data plot formats are shown in figure 6-2 for Apollo 16 and in figure 6-3 for Apollo 12 and Explorer 35.

### SUMMARY OF LSM RESULTS

The purpose of the LSM experiments was the measuring of remanent and induced lunar magnetic fields to investigate the following properties of the lunar interior and the lunar environment: (1) global electrical conductivity and temperature of the Moon, (2) lunar magnetic permeability and iron abundance, and (3) lunar remanent magnetic fields and their interaction with the solar-wind plasma.

The electrical conductivity of the lunar interior has been determined from measurements of the lunar electromagnetic response to transients in the magnetic field external to the Moon. Initial analyses used simultaneous data from the Apollo 12 LSM and Explorer 35 lunar orbiting magnetometer, measured when the Moon was immersed in the solar-wind plasma with the LSM on the lunar night-side. Recently, a new technique has been applied to conductivity analysis in which simultaneous data are used from a network of three instruments: the Apollo 15 LSM, the Apollo 16 LSM, and the Apollo 16 subsatellite magnetometer, which provide coverage around the entire global circumference. In this analysis, measurements are made when the Moon is located in high-latitude regions of the geomagnetic tail where plasma effects in the lunar environment are minimal. Individual magnetic events are superimposed to obtain a single large transient for analysis. Also, during examination of 5 yr of data, one exceptionally large magnetic transient was recorded when the Moon was in the geomagnetic tail. This single event has allowed substantial improvement in resolution and sounding depth for conductivity analysis.

Although the two types of conductivity analysis are analytically different and use measurements obtained over a 5-yr period from six different magnetometers, results are in surprisingly close agreement. A striking feature is the abrupt transition near 300-km depth where a knee occurs in the conductivity profile. The conductivity increases rapidly from the surface to approximately  $4 \times 10^{-3}$  mhos/m at 300-km depth. At greater depths, the

conductivity increases more slowly to about  $2 \times 10^{-2}$  mhos/m at 800-km depth. This conductivity transition at 300-km depth, the location of which corresponds closely to that of the seismic velocity change reported by Nakamura et al. (ref. 6-2), strongly implies a structural or compositional change at that depth.

The lunar magnetic permeability has been determined using two different analytical techniques, which give consistent results. The first was Apollo 12 or 15 LSM data with simultaneous Explorer 35 data to plot hysteresis curves for the entire Moon. The second method uses simultaneous Apollo 15 and 16 LSM data. The global magnetic permeability is  $\mu = 1.008 \pm 0.005$ . This result implies that the Moon is not composed entirely of paramagnetic material but that ferromagnetic material, such as free iron, exists in sufficient amounts to dominate the bulk lunar susceptibility. The ferromagnetic free-iron abundance can be calculated from the magnetic data. Then, for assumed compositional models of the Moon, the additional paramagnetic iron can be determined, yielding total lunar iron content. The calculated abundances are as follows: ferromagnetic free iron,  $2.5^{+2.3}_{-1.7}$  percentage by weight; total iron in the Moon, 5.0 to 13.5 percentage by weight.

The remanent magnetic fields measured thus far on the Moon are 38  $\gamma$  (38 nT) at the Apollo 12 site in Oceanus Procellarum, 103 and 43  $\gamma$  (103 and 43 nT) at two Apollo 14 Fra Mauro sites separated by 1.1 km, 3  $\gamma$  (3 nT) at the Apollo 15 Hadley-Apennines site, and 112 to 327  $\gamma$  (112 to 327 nT) at the Apollo 16 Descartes highland site.

Measurements show that the remanent field at the Apollo 12 site is compressed by the solar wind. The 38- $\gamma$  (38 nT) remanent field is compressed to 54  $\gamma$  (54 nT) by a solar-wind pressure increase of  $7 \times 10^{-8}$  dyne/cm<sup>2</sup> ( $7 \times 10^{-13}$  N/cm<sup>2</sup>). The ratio of plasma dynamic pressure to total magnetic pressure is 5.9 during the time of maximum field compression. The change in magnetic pressure is directly proportional to the change in plasma dynamic pressure.

#### REFERENCES

- 6-1. Dyal, Palmer; Parkin, Curtis W.; and Sonett, C. P.: Lunar Surface Magnetometer. IEEE Trans. Geosci. Electron., vol. GE-8, no. 4, Oct. 1970, pp. 203-215.
- 6-2. Nakamura, Yosio; Latham, Gary; Lammlein, David; Ewing, Maurice; Duennebier, Frederick; and Dorman, James: Deep Lunar Interior Inferred from Recent Seismic Data. Geophys. Res. Lett., vol. 1, no. 3, July 1974, pp. 137-140.

## BIBLIOGRAPHY

- Dyal, Palmer; and Gordon, Daniel I.: Lunar Surface Magnetometers. IEEE Trans. Magnet., vol. MAG-9, no. 3, Sept. 1973, pp. 226-231.
- Dyal, Palmer; and Parkin, Curtis W.: Global Electromagnetic Induction in the Moon and Planets. Phys. Earth Planet. Inter., vol. 7, no. 3, Sept. 1973, pp. 251-265.
- Dyal, P.; Parkin, C. W.; and Daily, W. D.: Surface Magnetometer Experiments: Internal Lunar Properties. Proceedings of the Fourth Lunar Science Conference, vol. 3, Pergamon Press (New York), 1973, pp. 2925-2946.
- Dyal, Palmer; Parkin, Curtis W.; and Daily, William D.: Lunar Electrical Conductivity and Magnetic Permeability. Proceedings of the Sixth Lunar Science Conference, vol. 3, Pergamon Press (New York), 1975, pp. 2909-2926.
- Parkin, Curtis W.; Daily, William D.; and Dyal, Palmer: Iron Abundance and Magnetic Permeability of the Moon. Proceedings of the Fifth Lunar Science Conference, vol. 3, Pergamon Press (New York), 1974, pp. 2761-2778.
- Schubert, G.; Lichtenstein, B. R.; Russell, C. T.; Coleman, P. J., Jr.; et al.: Lunar Dayside Plasma Sheet Depletion: Inference from Magnetic Observations. Geophys. Res. Lett., vol. 1, no. 3, July 1974, pp. 97-100.
- Schubert, G.; Schwartz, K.; Sonett, C. P.; Smith, B. F.; and Colburn, D. S.: Mare Imbrium: A Regional Site of Anomalous Electrical Conductivity. Lunar Science-V (Abstracts of the Fifth Lunar Science Conference (Houston, Tex.), Mar. 18-22, 1974), Pt. II, pp. 678-680.
- Schubert, G.; Smith, B. F.; Sonett, C. P.; Colburn, D. S.; and Schwartz, K.: Polarized Magnetic Field Fluctuations at the Apollo 15 Site: Possible Regional Influence of Lunar Induction. Science, vol. 183, Mar. 22, 1974, pp. 1194-1197.
- Smith, B. F.; Schubert, G.; Sonett, C. P.; Colburn, D. S.; and Schwartz, K.: Regional Electromagnetic Induction at the Apollo 15 Site. Lunar Science-V (Abstracts of the Fifth Lunar Science Conference (Houston, Tex.), Mar. 18-22, 1974), Pt. II, pp. 715-717.
- Sonett, C. P.; Smith, B. F.; Schubert, G.; Colburn, D. S.; and Schwartz, K.: Polarized Electromagnetic Response of the Moon. Proceedings of the Fifth Lunar Science Conference, vol. 3, Pergamon Press (New York), 1974, pp. 3073-3089.

TABLE 6-I.- APOLLO 16 LUNAR SURFACE  
MAGNETOMETER CHARACTERISTICS

Parameter	Value
Ranges for each sensor, $\gamma$ (nT) . . . . .	0 to $\pm 200$ 0 to $\pm 100$ 0 to $\pm 50$
Resolution, $\gamma$ (nT) . . . . .	$\pm 0.1$
Frequency response, Hz . . . . .	dc to 3
Angular response . . . . .	Cosine of angle between field and sensor
Sensor geometry . . . . .	Three orthogonal sensors at ends of 100-cm booms
Analog zero determination . . . . .	180° flip of sensor
Power, W . . . . .	3.5
Weight, kg . . . . .	8.9
Size, cm . . . . .	63 by 28 by 25
Operating temperature, K . . . . .	223.15 to 358.15
No. of commands	
Ground . . . . .	10
Spacecraft . . . . .	1

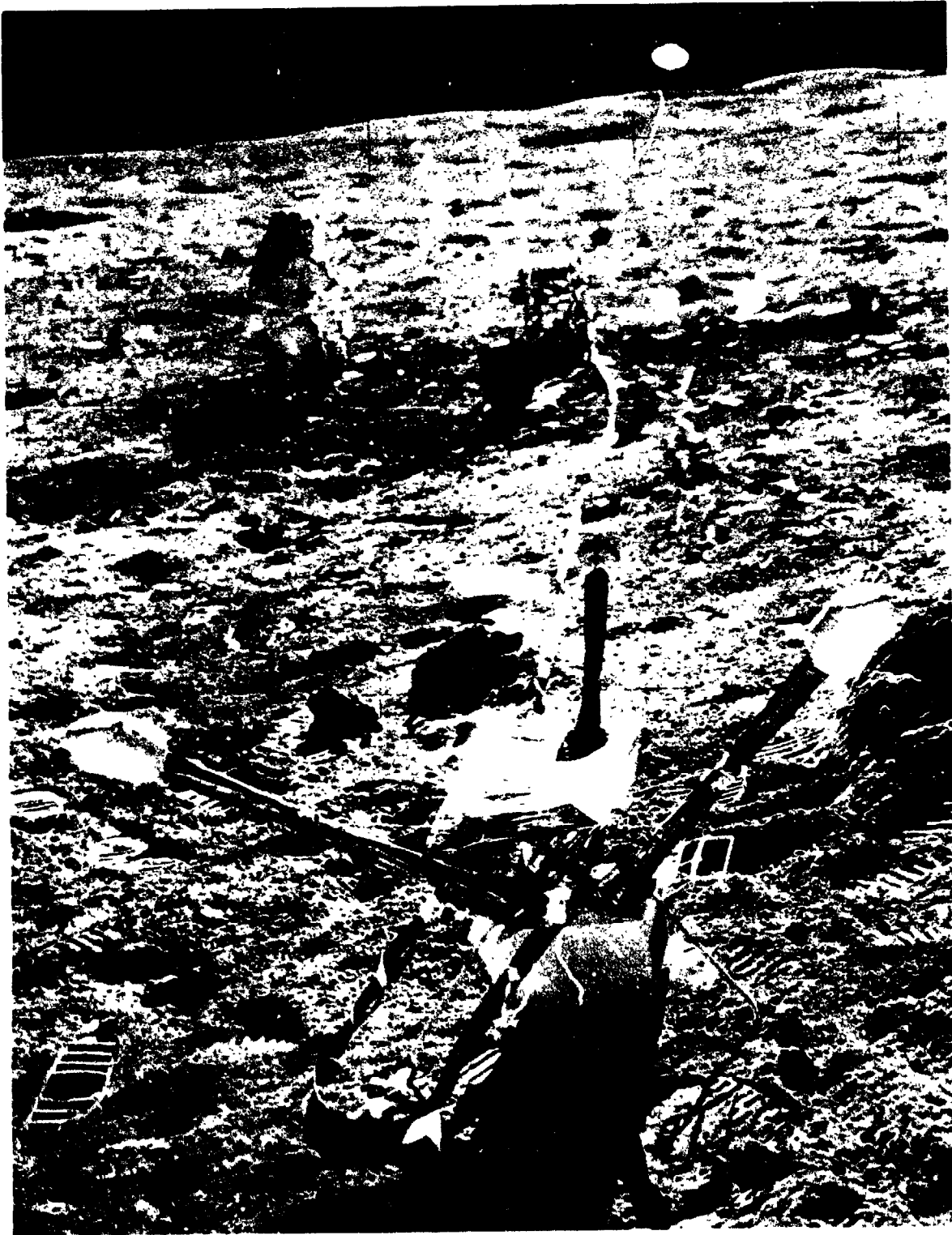


Figure 6-1.- Apollo 16 lunar surface magnetometer deployed at the Descartes site.

6-10

REPRODUCIBILITY OF THE  
ORIGINAL PAGE IS POOR

MAGNETIC FIELD APOLLO 16

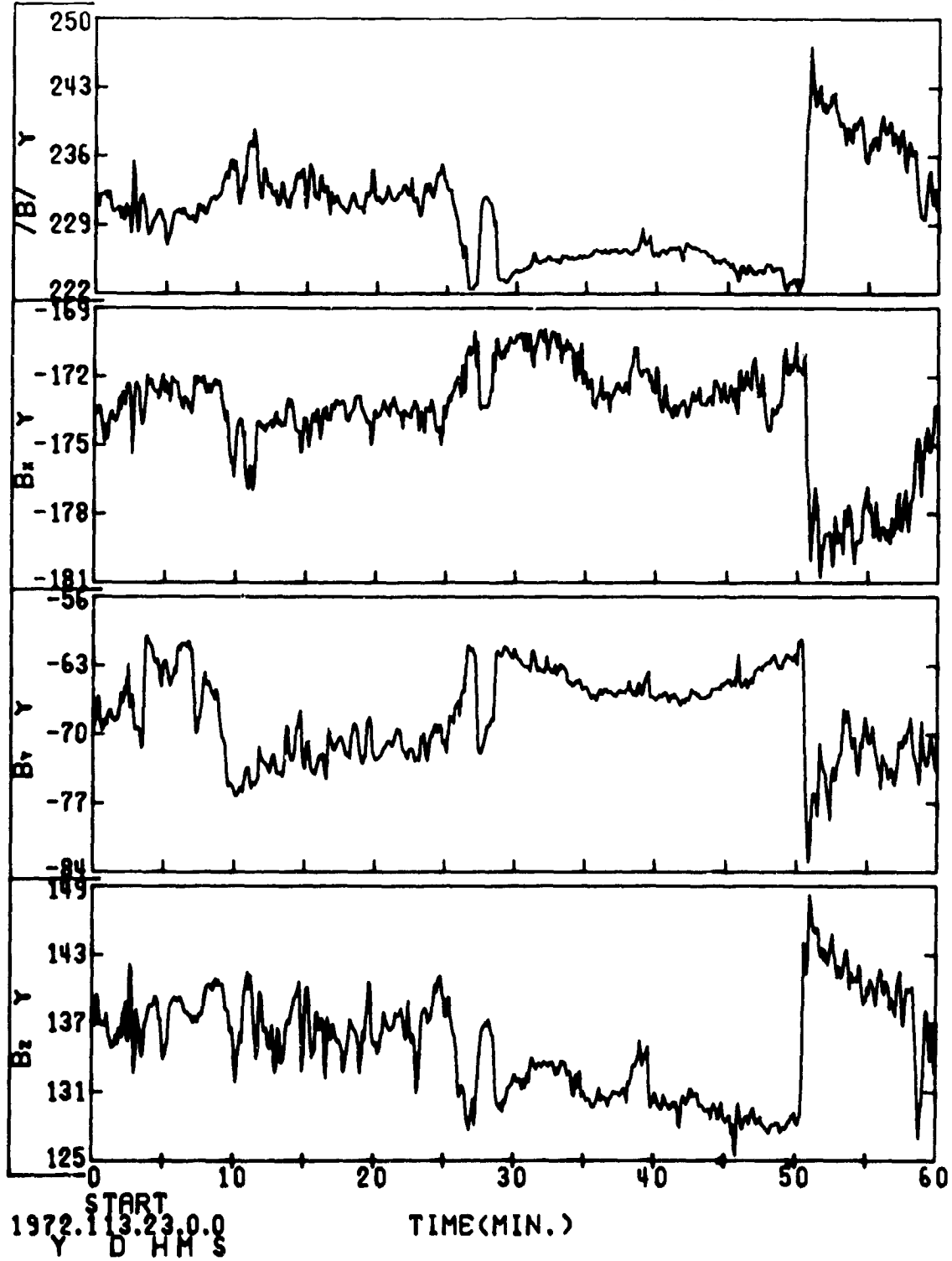


Figure 6-2.- Sample showing LSM data plot format for Apollo 16.

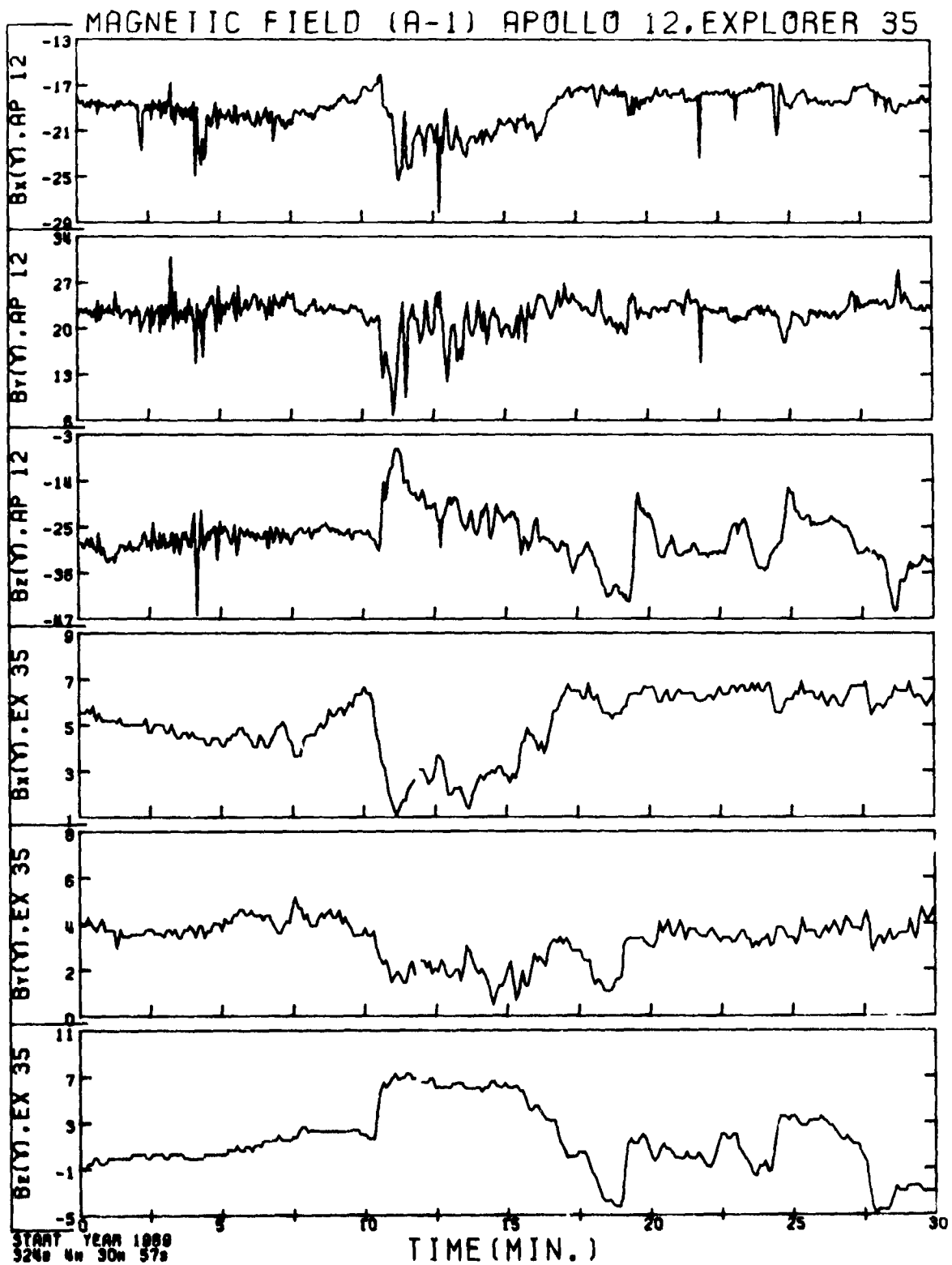
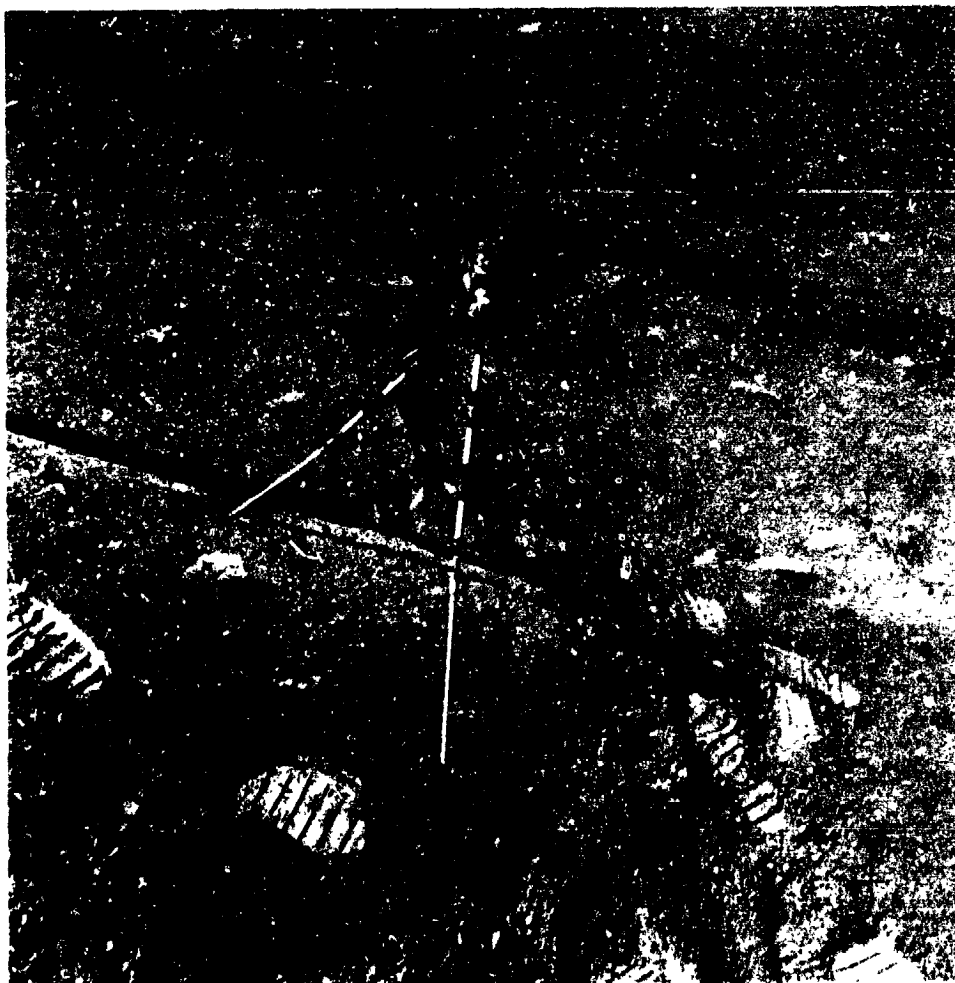


Figure 6-3.- Sample showing LSM data plot format for Apollo 12 (top) and Explorer 35 (bottom).

7. LUNAR PORTABLE MAGNETOMETER (NASA EXPERIMENT S-198)

NSSDC IDENTIFICATION NUMBERS:

APOLLO 14 71-008C-10  
APOLLO 16 72-031C-08



CONTENTS - SECTION 7

	Page
EXPERIMENT AND INSTRUMENT DESCRIPTION . . . . .	7-3
SUMMARY OF LPM DATA . . . . .	7-4
RESJLTS . . . . .	7-4
REFERENCES . . . . .	7-5
BIBLIOGRAPHY . . . . .	7-5

## 7. LUNAR PORTABLE MAGNETOMETER

The purpose of the lunar portable magnetometer (LPM) experiment is to measure the permanent magnetic field at different geological sites on the lunar surface. These measurements can be used to determine the present magnetic and structural properties of the local region and to explain magnetic aspects of the history of the Moon.

### EXPERIMENT AND INSTRUMENT DESCRIPTION

For the experimental technique, the self-contained LPM is used to measure the steady magnetic field at different points along the lunar traverse of the astronauts. The LPM field measurements are a vector sum of the steady remanent field from the lunar crust and of the time-varying ambient fields. The Apollo lunar surface experiments package (ALSEP) lunar surface magnetometer (LSM) simultaneously measures the time-varying components of the field; these components are later subtracted from the LPM measurements to give the desired resultant steady remanent field values due to the magnetized crustal material. The LPM consists of a set of three orthogonal fluxgate sensors mounted on top of a tripod; the sensor-tripod assembly is connected by means of a 15-m ribbon cable to the electronics box, which is mounted on the lunar roving vehicle (LRV) (Apollo 16 LPM) or on the modularized equipment transporter (MET) (Apollo 14 LPM).

The fluxgate sensor is used to measure the vector components of the magnetic field in the magnetometer experiment. Three fluxgate sensors are orthogonally mounted in the sensor block. Each sensor weighs 18 g and uses 15 mW of power during operation.

The sensor block, mounted on the top of a tripod, is positioned 75 cm above the lunar surface (figs. 7-1 and 7-2). The tripod assembly consists of a latching device to hold the sensor block, a bubble level with 1° annular rings, and a shadowgraph with 3° markings used to align the device along the Moon-to-Sun line.

The magnetometer electronics is self-contained with a set of mercury cells for power and three displays for visual readout of the magnetic field components. The instrument characteristics are listed in table 7-1, and detailed

descriptions are reported in the Apollo 14 and 16 Preliminary Science Reports (refs. 7-1 and 7-2).

The astronaut operation is crucial to the execution of this experiment. The following measurement sequence is conducted: Leaving the sensor tripod assembly deployed 15 m away from the LRV (or MET), the astronaut returns to the electronics box on the LRV (or MET); then after waiting 60 sec, he turns the power switch on, reads the digital displays (ammeters for Apollo 14) in sequence, and verbally relays the data back to Earth. At the first site only, two sets of additional readings are taken with the sensor block first rotated 180° about a horizontal axis and then rotated 180° about a vertical axis. These additional readings allow determination of a zero offset for each axis.

#### SUMMARY OF LPM DATA

A summary of all LPM data is given in table 7-II, which also includes the remanent field measurements made by Apollo lunar surface magnetometers.

#### RESULTS

The LPM was used by the Apollo 14 astronauts to measure the steady magnetic field at different sites in the Fra Mauro region. The instrument recorded steady magnetic fields of  $103 \pm 5$  nT and  $43 \pm 6$  nT at two sites separated by 1120 m. These measurements showed that the unexpectedly high 38-nT steady field measured at the Apollo 12 site 180 km away was not unique. Indeed, these measurements and studies of lunar samples and the lunar-orbiting Explorer 35 data indicate that much of the lunar surface material was magnetized at some prior time in lunar history.

The remanent magnetic fields, measured in the Apollo 16 Descartes region, range between 112 to 327 nT. These measurements show that the Descartes highlands have a stronger remanent magnetization than do the mare regions of the previous Apollo landing sites. From the complete set of measurements obtained by the Apollo surface magnetometers, the lunar subsatellite magnetometers, and the orbiting Explorer 35 magnetometer, it is apparent that the Moon is extensively covered with remanent magnetic field sources that show a strong regional variation. One elusive but important finding is the negative evidence of a measurable global dipolar field for the Moon.

From lunar sample measurements, it is generally concluded that the lunar remanent field is primarily of thermoremanent origin; the lunar crustal material probably became magnetized as the material cooled below the Curie temperature in the presence of a strong ambient magnetic field some 3 to 4 billion years ago. Sources of this ancient ambient field, which no longer exists on the Moon, include an extinct lunar dynamo, a stronger solar or terrestrial field, and meteorite-shock-induced fields.

#### REFERENCES

- 7-1. Dyal, P.; Parkin, C. W.; Sonett, C. P.; DuBois, R. L.; and Simmons, G.: Lunar Portable Magnetometer Experiment. Sec. 13 of Apollo 14 Preliminary Science Report, NASA SP-272, 1971.
- 7-2. Dyal, P.; Parkin, C. W.; Sonett, C. P.; DuBois, R. L.; and Simmons, G.: Lunar Portable Magnetometer Experiment. Sec. 12 of Apollo 16 Preliminary Science Report, NASA SP-315, 1972.

#### BIBLIOGRAPHY

Dyal, P.; Parkin, C. W.; and Daily, W. D.: Surface Magnetometer Experiments: Internal Lunar Properties. Proceedings of the Fourth Lunar Science Conference, vol. 3, Pergamon Press (New York), 1973, pp. 2925-2946.

TABLE 7-I.- APOLLO LPM CHARACTERISTICS

Parameter	Apollo 14	Apollo 16
Ranges for each sensor, nT . . . . .	0 to $\pm 100$ 0 to $\pm 50$	0 to $\pm 256$
Resolution, nT . . . . .	$\pm 1.0$ , $\pm 0.5$	1.0
Frequency response, Hz . . . . .	dc to 0.01	dc to 0.05
Angular response . . . . .	Cosine of angle between field and sensor	Cosine of angle between field and sensor
Sensor geometry . . . . .	3 orthogonal sensors in 6-cm cube	3 orthogonal sensors in 6-cm cube
Analog zero determination . . . . .	180° flip of sensor	180° flip of sensor
Battery characteristics		
Power, W . . . . .	1.5	1.5
Weight, kg . . . . .	4.58	4.6
Size, cm . . . . .	56 by 15 by 14	56 by 15 by 14
Operating temperature, K . . . . .	243.15 to 333.15	273.15 to 323.15

REPRODUCIBILITY OF THE ORIGINAL PAGE IS POOR

TABLE 7-II.- SUMMARY OF ALL LPH DATA

Site	Coordinates, deg	Field magnitude, nT	Magnetic field components, nT		
			Up	East	North
Apollo 16					
ALSEP site, LSM	8.9 S, 15.5 E	234 ± 3	-181 ± 3	-57 ± 3	136 ± 2
Site 2, LPH		189 ± 5	-189 ± 4	3 ± 6	10 ± 3
Site 5, LPH		112 ± 5	104 ± 5	-5 ± 4	-40 ± 3
Site 13, LPH		327 ± 7	-159 ± 6	-190 ± 8	-214 ± 6
LRV final site, LPH		113 ± 4	-66 ± 4	-76 ± 4	52 ± 2
Apollo 15					
ALSEP site, LSM	26.1 W, 3.7 E	3.4 ± 2.9	3.3 ± 1.5	0.9 ± 2.0	-0.2 ± 1.5
Apollo 14					
Site A, LPH	3.7 S, 17.5 W	103 ± 5	-93 ± 4	38 ± 5	-24 ± 5
Site C', LPH		43 ± 6	-15 ± 4	-36 ± 5	-19 ± 8
Apollo 12					
ALSEP site, LSM	3.2 S, 23.4 W	38 ± 2	-25.8 ± 1.0	11.9 ± 0.9	-25.8 ± 0.4

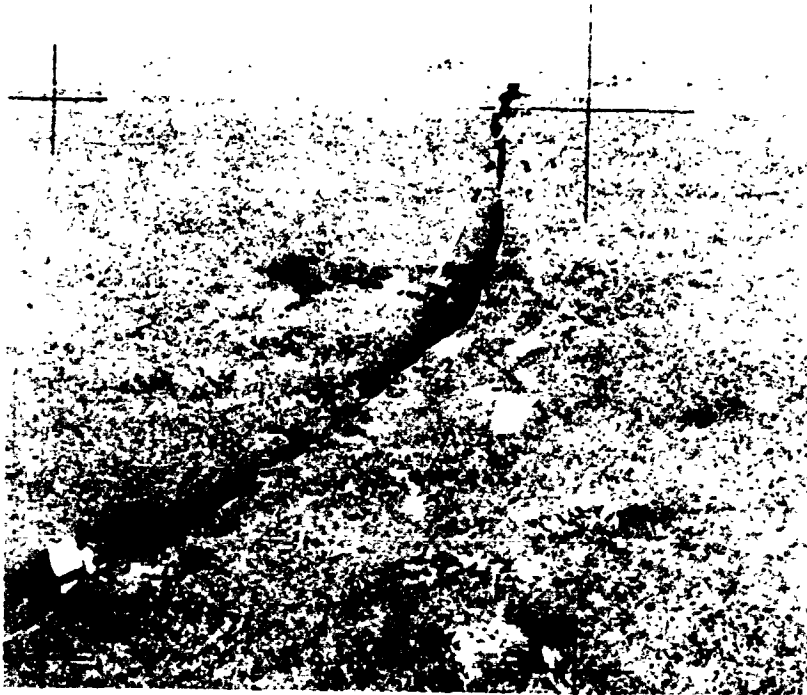


Figure 7-1.- Apollo 14 LPM on the lunar surface.

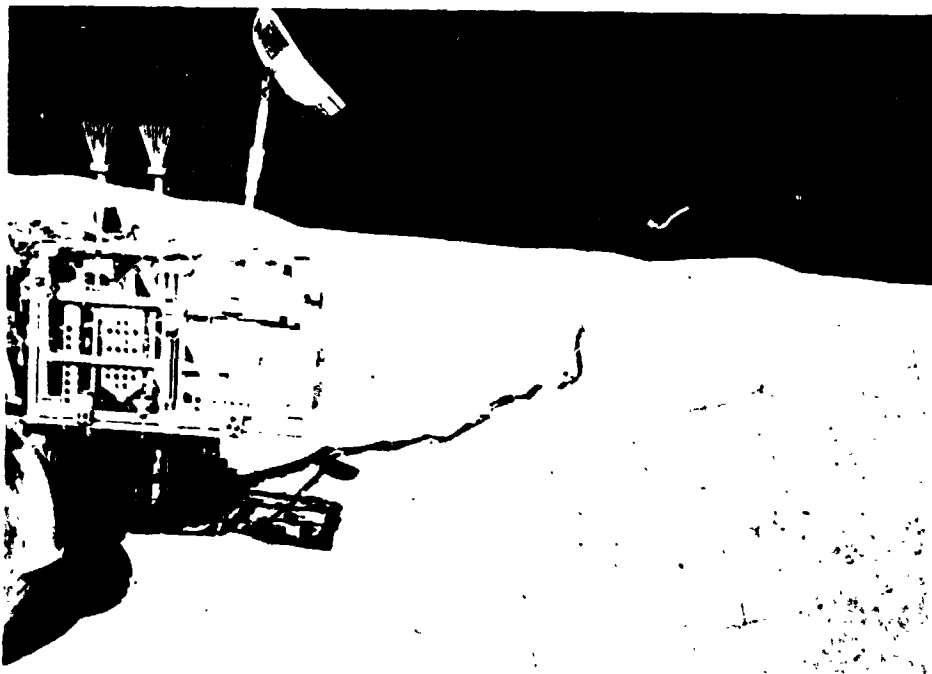


Figure 7-2.- Apollo 16 LPM on the lunar surface.

8. SOLAR-WIND SPECTROMETER (NASA EXPERIMENT S-035)

NSSDC IDENTIFICATION NUMBERS:

APOLLO 12 69-099C-02  
APOLLO 15 71-063C-04



ORIGINAL PAGE IS  
OF POOR QUALITY

CONTENTS - SECTION 8

	Page
INSTRUMENT DESCRIPTION . . . . .	8-3
INSTRUMENT SITE, OPERATION, AND DATA COVERAGE . . . . .	8-4
DATA ACQUISITION SEQUENCE . . . . .	8-4
DATA ANALYSIS . . . . .	8-6
DESCRIPTION OF VARIABLES ON TAPE . . . . .	8-7
FORMAT OF FULL-TIME-RESOLUTION DATA TAPES . . . . .	8-9
FORMAT OF DATA TAPES OF HOURLY AVERAGES . . . . .	8-11
FORMAT OF PLOTS . . . . .	8-13
USE OF DATA . . . . .	8-13
REFERENCES . . . . .	8-15
BIBLIOGRAPHY . . . . .	8-15

## 8. SOLAR-WIND SPECTROMETER

The Jet Propulsion Laboratory (JPL) solar-wind spectrometer (SWS) units are part of the Apollo lunar surface experiments packages operating at the Apollo 12 and 15 landing sites. The data are now available from the National Space Science Data Center (NSSDC) in several forms. Plots are available of hourly average values for solar-wind bulk speed, direction, proton density, thermal speed, and alpha particle to proton ratio. Positive-ion data are available on magnetic tape, both in the form of hourly averages and as unaveraged individual measurements. Plots of unaveraged data and electron data are not available from NSSDC; requests for this information should be directed to the experimenters.

### INSTRUMENT DESCRIPTION

The basic sensor in the SWS is a Faraday cup that measures the charged-particle flux entering the cup. By collecting these ions and using a sensitive current amplifier, the resultant current flow is determined. Energy spectra of positively and negatively charged particles are obtained by applying fixed sequences of square-wave ac retarding potentials to a modulator grid and measuring the resulting changes in current. Similar detectors have been flown on a variety of space probes (ref. 8-1). Further descriptions of the SWS experiments are given in references 8-2 and 8-3.

To be sensitive to solar-wind plasma from any direction (above the horizon of the Moon) and to ascertain the solar-wind angular distribution, the SWS has an array of seven cups. Because the cups are identical, an isotropic particle flux would produce equal currents in each cup. If the flux is not isotropic but appears in more than one cup, analysis of the relative amounts of current in the collectors can provide information on the direction of plasma flow and its anisotropy. The central cup faces vertically, and the remaining six cups symmetrically surround the central cup (fig. 8-1), each facing  $60^\circ$  off vertical. The combined acceptance cones of all cups cover most of the upward hemisphere. Each cup has a circular opening, five circular grids, and a circular collector (fig. 8-2). The functions of the grid structures are to apply an ac modulating field to incoming particles and to screen the modulating field from the inputs to the sensitive preamplifiers. The entrance apertures of the cups were protected from damage or dust by covers that remained in place until after

the departure of the lunar module. The angular sensitivity of the Faraday cup sensor to collimated ion beams has been measured by laboratory plasma calibration. The result, averaged over all seven cups, is shown in figure 8-3 and, for positive ions, agrees quite well with the measured optical transparency.

The electronics package for the SWS is in a temperature-controlled container that hangs below the sensor assembly. The electronics package includes power supplies, a digital programmer that controls the voltages in the sensors as required, current-measuring circuitry, and data-conditioning circuits.

On the Moon, the SWS is hung from a pair of knife edges so that it is free to swing about an east-west horizontal axis and, hence, is self-leveling in one dimension. Rotations about the north-south axis and the vertical axis are determined from shadow patterns on photographs and, for Apollo 12, from the effect of sunlight on a sensor.

#### INSTRUMENT SITE, OPERATION, AND DATA COVERAGE

The Apollo 12 SWS is located at latitude  $3^{\circ}$  S and longitude  $23^{\circ}$  W on the lunar surface; the Apollo 15 SWS, at latitude  $26^{\circ}$  N and longitude  $4^{\circ}$  E. Orientations of the instruments at the local sites are determined from photographs of instrument shadow patterns. The Apollo 12 orientation is known within  $0.5^{\circ}$  and the Apollo 15 orientation within  $1.5^{\circ}$ .

Data coverage for the Apollo 12 SWS began on day 323 of 1969; the instrument is still operational. The Apollo 15 SWS began operations on day 212 of 1971 and failed on day 182 of 1972. Data coverage was essentially complete during these periods, but the data supplied to NSSDC exclude times during lunar night when no currents were measurable.

#### DATA ACQUISITION SEQUENCE

The SWS operates in an invariable sequence in which a complete set of plasma measurements is made every 28.1 sec. The sequence consists of 14 energy steps spaced by a factor of  $\sqrt{2}$  for positive ions and 7 energy steps spaced by a factor of 2 for electrons. Numerous internal calibrations are provided, and every critical voltage is read out at intervals of 7.5 min or less.

In the reduced data records and the analyzed data supplied to the NSSDC, this data acquisition sequence does not appear, because only a small fraction of the readings in the 186-measurement

sequence represents meaningful data at any given time. For most purposes of data analysis, the details of this sequence are irrelevant; however, they do become important when the precise time of a particular measurement is of interest. The following partial description of the sequence will enable the determination of the time of a measurement to a precision of approximately 1 sec.

The sequence begins with the positive-ion measurements, the energy steps proceeding from the lowest to the highest. At each step, eight measurements are made. The first is the sum of the currents in all seven cups; then, the seven cups are sampled in sequence. There are 112 measurements in the positive-ion subsequence, followed by 16 calibration measurements and a 56-measurement electron subsequence. The sequence ends with two data words that provide a sequence counter. In ground data processing, each sequence is tagged with a time corresponding to the Earth receipt time of the end of the last data word in the sequence. Application of a light-transit-time correction provides the time at which the sequence terminated on the Moon. In the reduced data records, the time is rounded off to the nearest whole second.

The time at which the measurement of the plasma properties was actually made can be inferred as follows. Using the calibration data presented in table 8-I and knowing the gain state of the instrument, one can determine the proton bulk velocity, which will indicate the energy step that provided the largest current readings. (If the plasma was incident at a large angle from the cup, a correction by the cosine of the incidence angle will be necessary.) Then, knowing which cup or cups and which energy step or steps were involved in the measurement, one can obtain the measurement time by subtracting from the sequence-end time the time-difference function  $\Delta t$ .

$$\Delta t = 28.13 - 0.15094 \times (\text{STEP} \times 8 + \text{CUP}) \quad (8-1)$$

where

STEP = 1, 2, ... 14, which is obtained from VEL (solar-wind proton velocity) and gain in table 8-I

CUP = all 1, 2, ... 7 cups obtained from KUPA and CUR7/CURA (See definitions in the section entitled "Description of Variables on Tape.")

gain = low or high, depending on bit 30 of FLAG (table 8-II)

## DATA ANALYSIS

For each proton spectrum, the cup with the greatest total current was found. The currents in the individual energy channels were then least-squares fit to the data model. This model assumed a convected Maxwell-Boltzmann proton distribution with unknown parameters — bulk velocity, most probable thermal speed, and density. An alpha-particle distribution with the same velocity and thermal speed as protons was assumed with the alpha-particle density unknown. For these preliminary estimates, the velocity vector was assumed to be perpendicular to the collector plate. Because of the relatively broad energy channels, it was difficult to distinguish between alpha particles and energetic protons when the ratio of most probable thermal speed to proton speed was greater than 0.25. Thus, a jump in alpha-particle/proton ratio across a shock might be estimated. The broad channels also prevented accurate measurement of thermal speeds less than 10 percent of the bulk speed.

The estimates as described in the preceding paragraph are uncorrected for angular direction of the plasma. Angles were estimated from examination of current in other cups as described later in this section. After the angle between the plasma beam and the cup axis was determined, corrections were made to all parameters to account for the angular response of the Faraday cup and for aberration effects.

Several definitions are required as a preliminary to the description of the angular analysis. All cups except cup 7 (the vertical cup) are side cups. The side cup with the greatest current (summed over all channels) is called cup A. The adjacent cup in the counterclockwise direction from cup A (as viewed from above) is cup B; the adjacent clockwise cup is cup C. A noise level based on fluctuations in zero-level currents was chosen. If cup 7, cup A, and cup B or cup C are above noise, the solar-wind direction is determined; otherwise, assumptions are required.

The angle between the plasma and the normal to cup 7 is defined as  $\beta$ . The plasma direction projected downward onto the instrument and measured clockwise from a line between cups 1 and 7 is defined as being the azimuthal angle  $\alpha$  (fig. 8-4). If no current above noise is measured in cup 7, the  $\beta$  angle is assumed to be a radial flow of the solar wind from the Sun. If this assumption, however, implies that current should be measured in cup 7, the assumed angle is limited to increasingly larger angles until the predicted current in cup 7 decreases to the noise level value. Similarly, no current in cup A leads to assuming  $\beta$  or limiting  $\beta$  to smaller values.

The  $\alpha$  angle is similarly predicted, measured, or limited. If current is available only in cup A, then the  $\alpha$  angle for

radial flow from the Sun is assumed. If this condition requires currents above noise in cup B or C, the assumed  $\alpha$  angle is limited closer to the cup A direction. If currents in cup B or C are available, the  $\alpha$  angle is measured directly. After angles were determined, conversion was made to solar ecliptic coordinates taking into account the known orientations of the instruments; that is, the direction of the bulk velocity is given by DELE and DELNE, the angle in the ecliptic and the angle north of the ecliptic, respectively.

#### DESCRIPTION OF VARIABLES ON TAPE

The variables provided on the data tapes are listed here with a brief definition. (Refer also to the discussion of variables in the preceding section.)

<u>Symbol</u>	<u>Description</u>
DP	Proton density, protons/cm <sup>3</sup>
AP	Ratio of alpha-particle density to proton density
VEL	Solar-wind proton velocity, km/sec
THERMV	Most probable thermal velocity, km/sec

Thus, the fitted proton distribution function  $f_p$  is

$$f_p(\vec{v}) = \frac{DP}{THERMV^3 \sqrt{\pi}^3} e^{-\frac{(\vec{v} - VEL\vec{n})^2}{THERMV^2}} \quad (8-2)$$

where  $\vec{n}$  is a unit vector in the solar-wind direction and  $\vec{v}$  is the velocity vector for distribution of protons.

DELE: East-west angle in solar ecliptic coordinates expressed in degrees; no correction has been made for aberration due to orbital velocity. A positive value means a plasma velocity component directed opposite to the orbital motion of the Earth; that is, an average +5° due to aberration is typical.

DELNE: North-south angle in solar ecliptic coordinates expressed in degrees. This number is positive if the plasma velocity has a northward component (i.e., positive values for flow coming from south of the ecliptic).

FLAG: The code FLAG is a 36-bit word, the definition of which is given in table 8-II. Bits are numbered 0 to 35 with bit 0 being the high-order bit. Most of these bits will be of no interest to the users of the data; exceptions to this rule are explained here. Bits 15 and 16 are IA, which has values from 0 to 3; bits 17 and 18 are IB; bit 19 is IDISCP. The code IA is the angle code indicating how the angle  $\alpha$  was derived, as explained in the previous section. If IA is 0,  $\alpha$  is measured. If IA is 1,  $\alpha$  is assumed. If IA is 2,  $\alpha$  is limited. If IA is 3, then IB is also 3 and the cup observing the protons is too far from the Sun direction to be plausible. Similarly, IB is the angle code for the  $\beta$  angle. If IB is 0,  $\beta$  is measured, and so on. An IDISCP of 1 indicates that a side cup not adjacent to cup A had current above noise and greater than the current in cup B or cup C. Bit 30 indicates the instrument gain level that determines the value of the energy steps; 0 is low gain, 1 is high gain.

<u>Symbol</u>	<u>Description</u> <sup>1</sup>
RMS	Percentage error in current-fitting program
KUPA	Cup with the largest current excluding cup 7
CURA	Current in picoamperes in cup A
CURB	Current in picoamperes in cup B
CURC	Current in picoamperes in cup C
CUR7	Current in picoamperes in cup 7

FACTD: Correction factor for Maxwell-Boltzmann least-squares estimates of density to account for decrease in transparency of cup with increasing angle of plasma beam from cup normal; typical values range between 1.2 and 3.5.

PD: The code PD is a product of the preliminary density estimate and the correction factor. The value of VEL is similarly corrected for the cosine of the angle between the plasma beam and the cup normal.

XNOISE: Noise level in picoamperes used in estimating angles.

---

<sup>1</sup>For definitions of cup designations A, B, and C, see the section entitled "Data Analysis."

## FORMAT OF FULL-TIME-RESOLUTION DATA TAPES

The parameters resulting from analysis of each plasma spectrum (each 28 sec) are written onto full-time-resolution data tapes. Several months of data are placed on each digital magnetic tape. These tapes are written in BCD format on seven tracks, at 315 characters/cm (800 characters/in.) and even parity.

All physical records contain 384 words, which are blocked from 32 logical records of 12 words each. There are four types of logical records: plasma data for one spectrum, label information, pseudo end of file (EOF), and fill data.

The plasma data have the following format for each logical record. There are 72 BCD characters in the 12 words.

<u>Character</u>	<u>Parameter</u>
1 to 6	Not significant (used by input/output of specific computer)
7	Blank
8 to 16	TIME, DDDHHMMSS
17 to 20	DP*10
21 and 22	AP*100
23 to 26	VEL
27 to 29	THERMV
30 to 33	DELE*10
34 to 37	DELNE*10
38 to 49	FLAG
50 and 51	RMS
52	KUPA
53 to 56	CURA
57 to 59	CURB
60 to 62	CURC
63 to 66	CUR7

<u>Character</u>	<u>Parameter</u>
67 to 69	FACTD*100
70 to 72	XNOISE*10

The nine characters of TIME have the day:hour:minute:second of the year at the end of spectrum measurement in the form of "DDDHHMSS." The first day of the year is day 1. The 12 characters of FLAG are an octal representation of the 36-bit word.

One can use FORTRAN format controlled READ, and the following example could be successfully used.

```

READ (Unit, 10) ITIM, DP, AP, VEL, THERMV, DELE, DELNE,
*FLAG, RMS, KUPA, CURA, CURB, CURC, CUR7, FACTD, XNOISE
10 FORMAT (6X, 1X, I9, F4.1, F2.2, F4.0, F3.0, 2F4.1, Ø12,
*F2.0, I1, F4.0, 2F3.0, F4.0, F3.2, F3.1)

```

The format-supplied decimal points reduce the appropriate variables by factors of 10 to yield correct values.

The label records are used to identify the information contained on the tape and can be ignored by the general user. The first logical record will always be a label and may be followed by other label records. Each label record has the same format as the plasma data with certain parameters redefined. Label records are identifiable by the illegal time of DDDHHMSS = 000999999. For this record, DP\*10 is the spacecraft number (12 indicates Apollo 12 instrument and 15 indicates Apollo 15), AP\*100 is the year for the first data (e.g., 70 indicates year 1970), VEL is the starting day for processing, THERMV is the starting hour of processing, DELE\*10 is the last day of processing, and DELNE\*10 is the last hour of processing.

The pseudo-EOF record is a logical record with the illegal time of DDDHHMSS = 499000000. All 15 remaining variables contain fill data. This record always follows the last plasma data and precedes the two hardware-produced EOF marks on the tape.

Fill data may be used at any time, but its primary use is to complete the end block. Fill data has the illegal time of +0, -0, or all blanks. All other 15 variables also contain values of +0, -0, or blanks.

## FORMAT OF DATA TAPES OF HOURLY AVERAGES

The averaged values of parameters from analysis of plasma spectra are placed on a digital magnetic tape. This tape is written in BCD format on seven tracks, at 315 characters/cm (800 characters/in.) and even parity. The averaged values are the result of combining individual spectral results into hourly averages.

Four sets of criteria are used to determine which spectra to combine. The first set allows all spectra in which results from analysis give an answer. The average values of six basic parameters (proton density, alpha-particle/proton ratio, plasma velocity, plasma thermal speed, and plasma angle from the direction of the Sun in and out of the ecliptic plane), their six rms deviations, and the number of spectra are included.

The second set of hourly averages is similar to the first except that each spectrum has been screened to pass the requirements of small rms error on curve fitting (rms < 20) and that thermal speed be less than one-half the bulk velocity. This set is a subset of set one.

The third set is a subset of set two and has the further requirement that one, and only one, of the angles be measured (as compared to being merely consistent with assumed solar plasma direction).

The fourth set is also a subset of set two and has the requirement that both angles are measured. This set is quite small for Apollo 12 data and is disjoint with subset three.

The hourly average tape has two logical records of 18 words for each hour of data analyzed and is blocked two logical records per physical record of 36 words. There are two types of records: data and pseudo-EOF. Data records have the following format for the 108 BCD characters of each logical record.

### Logical Record One

<u>Character</u>	<u>Parameter</u>	<u>Comments</u>
1 to 6	Not significant	Input/output control for computer used
7	Blank	--
8 and 9	ISC	Spacecraft number
10 and 11	IYR	Year

<u>Character</u>	<u>Parameter</u>	<u>Comments</u>
12 to 13	TIME	Day:hr:min, DDDHHMM
19 to 21	NS1	Number of spectra in average set one
22 to 25	DP1*10	10 times average proton density, protons/cm <sup>3</sup>
26 and 27	AP1*100	100 times alpha-particle/proton density ratio
28 to 31	VEL1	Velocity of protons, km/sec
32 to 34	THV1	Thermal velocity, km/sec
35 to 38	DE1*10	10 times DELE, deg
39 to 42	DNE1*10	10 times DELNE, deg
43 to 46	DDP1*10	10 times rms deviation of DP1
47 and 48	DAP1	rms deviation of AP1*100
49 to 52	DVEL1	rms deviation of VEL1
53 to 55	DTHV1	rms deviation of THV1
56 to 59	DDE1*10	10 times rms deviation of DE1
60 to 63	DDNE1*10	10 times rms deviation of DNE1
64 to 108	Same 13 variables for average set 2	--

Logical Record Two

<u>Character</u>	<u>Parameter</u>	<u>Comments</u>
1 to 6	Not significant	Used for input/output control
7	Blank	--
8 to 18	Blank	--
19 to 63	Same 13 variables for average set 3	--
64 to 108	Same 13 variables for average set 4	--

If one uses format control for reading each logical record, a FORTRAN READ statement to place data into ISC (spacecraft), IYR (year), ITIM (time = DDDHHMM), NS(4) (number of spectra in each of four averages), and AVE(2,6,4) (average values of parameter, its rms deviation for six variables and for four average sets) is

```
      READ(UNIT,10) ISC, IYR, ITIM, (NS(K), ((AVE(I,J,K),J=1,6),
*   I = 1,2),K = 1,4)
10    FORMAT(6X, 1X, 2I2, I7, 2(I3, 2(F4.1, F2.2, F4.0, F3.0,
*   2F4.1)), 6X, 12X, 2(I3, 2(F4.1, F2.2, F4.0, F3.0, 2F4.1)))
```

The format-supplied decimal point reduces the appropriate variables by factors of 10 to yield correct values.

The last physical record has the same format but is a pseudo-EOF and has the illegal time of DDDHHMM = 4990000. The variables ISC and IYR are the same as for data, but all 52 variables that follow have fill data of blanks. Two hardware EOF marks follow the pseudo-EOF.

#### FORMAT OF PLOTS

Plots provided to NSSDC show hourly averages of selected data (the second set of data described in the section on hourly average data tapes). Proton velocity is expressed in kilometers per second. The most probable thermal speed  $v = \sqrt{2kT/m_p}$  is expressed in kilometers per second (where  $k$  is the Boltzmann constant,  $T$  is temperature Kelvin, and  $m_p$  is the mass of proton). Density is measured in protons per cubic centimeter. The angles DELE and DELNE are discussed in the section entitled "Description of Variables on Tape" and are measured in degrees. The alpha-particle/proton ratio is the ratio of alpha-particle number density to proton number density. January 1 is day 1. Figure 8-5 is a sample plot illustrating the available information.

#### USE OF DATA

Users should reject all fitted parameters for which rms = 99, IA = 3, or DP = 0.0. A somewhat stronger set of criteria for rejecting bad data is rms > 20, IA = 3, IDISCP = 1, THERMV > 1/2 VP, or DP = 0.0.

Changes in assumptions involving angles can cause unrealistic discontinuities in plasma direction, speed, and density. The user is advised to study the section on data analysis. The variables FACTD, CURA, CURB, CURC, CUR7, and XNOISE are provided to allow the user to remove the effects of changes in estimated angle if he so desires.

A final warning is that plasma velocities and densities measured at the Apollo 12 site are often perturbed from solar-wind values. Velocity decreases of 50 km/sec and density increases of 30 percent due to the 38  $\gamma$  (38 nT) field at the Apollo 12 site have been observed. This topic is discussed in reference 8-4. At present, there is no indication that plasma parameters at the Apollo 15 site differ significantly from the values in the unperturbed solar wind.

#### DATA AVAILABILITY

The data described in this section, together with the appropriate documentation, are available from NSSDC.

#### REFERENCES

- 8-1. Hundhausen, A. J.: Direct Observations of Solar Wind Particles. Space Sci. Rev., vol. 8, no. 516, Sept. 24, 1968, pp. 690-749.
- 8-2. Snyder, Conway W.; Clay, Douglas R.; and Neugebauer, Marcia: The Solar-Wind Spectrometer Experiment. Sec. 5 of the Apollo 12 Preliminary Science Report, NASA SP-235, 1970.
- 8-3. Clay, Douglas R.; Goldstein, Bruce E.; Neugebauer, Marcia; and Snyder, Conway W.: Solar-Wind Spectrometer Experiment. Sec. 10 of the Apollo 15 Preliminary Science Report, NASA SP-289, 1972.
- 8-4. Neugebauer, M.; Snyder, C. W.; Clay, D. R.; and Goldstein, B. E.: Solar Wind Observations on the Lunar Surface with the Apollo-12 ALSEP. Planet. Space Sci., vol. 20, no. 2, Oct. 1972, pp. 1577-1591.

#### BIBLIOGRAPHY

- Bratenahl, A.; Goldstein, B. E.; Clay, D. R.; and Neugebauer, M. M.: Magnetopause Boundary Layer Structure at Lunar Distance from Correlated Apollo 12 and 15 ALSEP Data. EOS Trans. Am. Geophys. Union, vol. 54, no. 4, Apr. 1973, p. 428.
- Burke, William J.; Rich, Frederick J.; Reasoner, David L.; Colburn, David S.; and Goldstein, Bruce E.: Effects on the Geomagnetic Tail at  $60 R_e$  of the Geomagnetic Storm of April 9, 1971. J. Geophys. Res., vol. 78, no. 25, Sept. 1, 1973, pp. 5477-5489.
- Burlaga, L. F.; Rahe, J.; Donn, B.; and Neugebauer, M.: Solar Wind Interaction with Comet Bennett (1969i). Solar Phys., vol. 30, no. 1, May 1973, pp. 211-222.
- Clay, D. R.; Goldstein, B. E.; Neugebauer, M.; and Snyder, C. W.: Differences of Solar-Wind Observations at Two Lunar Sites. EOS Trans. Am. Geophys. Union, vol. 53, no. 11, Nov. 1972, SS37.
- Clay, D. R.; Goldstein, B. E.; Neugebauer, M.; and Snyder, C. W.: Lunar Surface Solar Wind Observations at the Apollo 12 and Apollo 15 Sites. J. Geophys. Res., vol. 80, no. 13, May 1, 1975, pp. 1751-1760.

- Dyal, P.; Parkin, C. W.; Snyder, C. W.; and Clay, D. R.: Measurements of Lunar Magnetic Field Interaction with the Solar Wind. *Nature*, vol. 236, no. 5347, Apr. 21, 1972, pp. 381-395.
- Dyal, Palmer; Parkin, Curtis W.; and Cassen, Patrick: Surface Magnetometer Experiments: Internal Lunar Properties and Lunar Field Interactions with the Solar Plasma. *Proceedings of the Third Lunar Science Conference*, vol. 3, MIT Press (Cambridge, Mass.), 1972, pp. 2287-2307.
- Goldstein, B. E.: Observation of Electrons at the Lunar Surface. *EOS Trans. Am. Geophys. Union*, vol. 53, no. 11, Nov. 1972, SM79.
- Goldstein, Bruce E.: Observations of Electrons at the Lunar Surface. *J. Geophys. Res.*, vol. 79, no. 1, Jan. 1, 1974, pp. 23-35.
- Jockers, K.; and Lüs', Rh.: Tail Peculiarities in Comet Bennett Caused by Solar Wind Disturbances. *Astron. and Astrophys.*, vol. 26, 1973, pp. 113-121.
- Lindeman, R. A.; Vondrak, R. R.; Freeman, J. W.; and Snyder, C. W.: The Interaction Between an Impact-Produced Neutral Gas Cloud and the Solar Wind at the Lunar Surface. *J. Geophys. Res.*, vol. 79, no. 16, June 1, 1974, pp. 2287-2296.
- Neugebauer, Marcia: Large-Scale and Solar-Cycle Variations of the Solar Wind. *Space Sci. Rev.*, vol. 17, nos. 2/3/4, Mar./May/June 1975, pp. 221-254.
- Ogilvie, K. W.; and Hirshberg, J.: The Solar Cycle Variation of the Solar Wind Helium Abundance. *J. Geophys. Res.*, vol. 79, no. 31, Nov. 1, 1974, pp. 4595-4602.
- Schubert, Gerald; and Lichtenstein, Bernard R.: Observations of Moon-Plasma Interactions by Orbital and Surface Experiments. *Rev. Geophys. and Space Phys.*, vol. 12, no. 4, Nov. 1974, pp. 592-626.
- Siscoe, G. L.; and Goldstein, B.: Solar Wind Interaction with Lunar Magnetic Fields. *J. Geophys. Res.*, vol. 78, no. 28, Oct. 1, 1973, pp. 6741-6748.

TABLE 8-I.- AMPLITUDE AND WIDTH OF SWS ENERGY STEPS  
 IN TERMS OF PROTON VELOCITY FOR NORMAL INCIDENCE  
 [Velocities expressed in km/sec]

Low gain			High gain		
Step	Mean	Width	Mean	Width	Step
Apollo 12 SWS					
1	62	20	112	21	1
2	91	18	143	25	2
3	120	22	175	30	3
4	156	28	216	37	4
5	191	32	259	43	5
6	235	40	314	53	6
7	285	48	377	62	7
8	337	57	446	74	8
9	400	67	527	87	9
10	480	79	629	104	10
11	569	92	744	122	11
12	682	114	893	149	12
13	807	132	1055	172	13
14	968	157	1266	206	14
Apollo 15 SWS					
1	66	13	105	20	1
2	90	17	135	25	2
3	120	20	169	28	3
4	151	26	208	35	4
5	188	31	252	42	5
6	230	38	305	51	6
7	280	46	370	60	7
8	333	55	439	71	8
9	395	64	519	83	9
10	469	77	616	103	10
11	557	91	730	119	11
12	666	109	874	144	12
13	791	130	1039	170	13
14	946	154	1235	218	14

TABLE 8-II.- SIGNIFICANCE OF FLAG WORD

Bit	Values	Significance
0	0	Unused
1	0	Unused
2	0,1	1 = no current detectable
3	0	Unused
4	0,1	1 = peak current too small to determine spectrum
5	0,1	1 = peak current in cup not near the Sun
6,7	0,1,2,3	Number of cups with measurable current (0 = 4 cups)
8	0,1	1 = no proton analysis (see other bits for reason)
9	0,1	1 = spurious negative currents at low energies
10	0,1	1 = spectrum too broad (hot) for meaningful analysis
11	0,1	1 = current in analyzed cup marginally small (<7 pA)
12	0,1	1 = rms fit worse than 25 percent
13	0,1	1 = peak current in lowest or highest energy level
14	0,1	1 = proton energy levels 13 and 14 unused
15,16	0,1,2,3	Angle code for $\alpha$ (see text)
17,18	0,1,2,3	Angle code for $\beta$ (see text)
19	0,1	1 = discrepancy in cup currents (IDISCP)
20	0,1	1 = rms fit worse than 60 percent
21	0,1	1 = pickup current from modulator higher than normal
22	0,1	1 = value of DELE or DELNE > 30
23	0,1	1 = electrometer zero level shifted by >0.8 pA
24	0,1	1 = no electron data for this time
25	0,1	1 = electron currents marginally small
26	0	Unused
27	0	Unused
28	0	Unused
29	0	Time dubbed (error up to several seconds)
30	0,1	0 = low gain, 1 = high gain
31	0,1	No proton data for this time
32	0,1	No proton data for this time (bit errors)
33	0,1	1 = no electron data for this time
34	0,1	1 = no electron data for this time (bit errors)
35	0	Unused

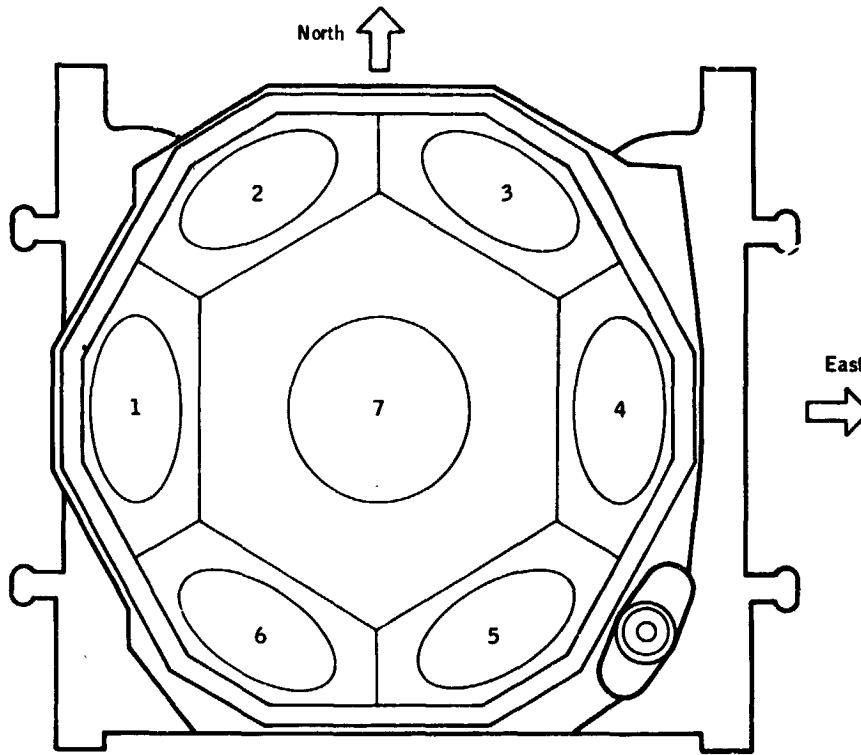


Figure 8-1.- Orientation of Apollo 12 SWS on the lunar surface.  
The Apollo 15 SWS is rotated 180°.

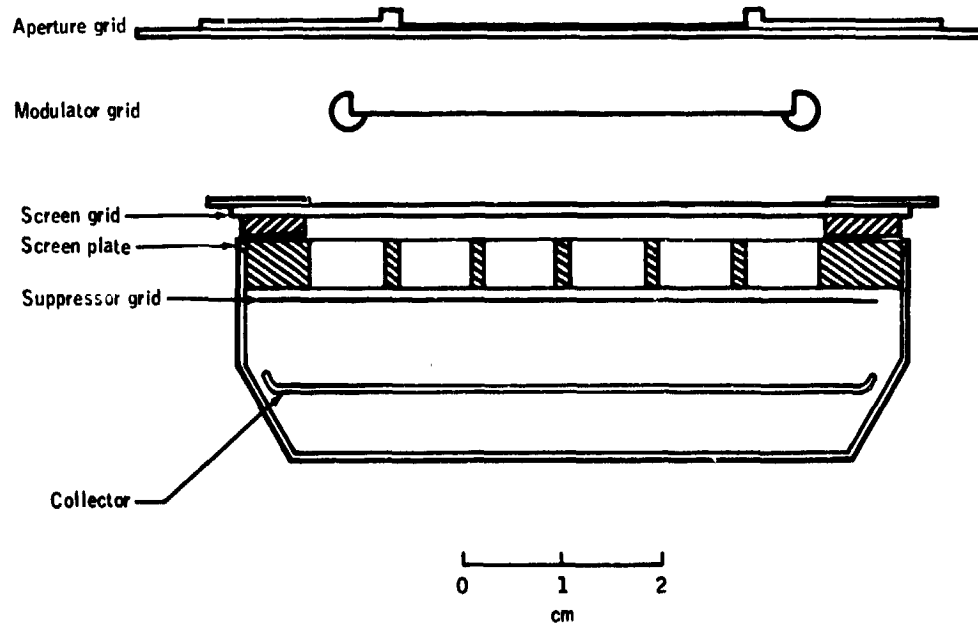


Figure 8-2.- Faraday cup sensor.

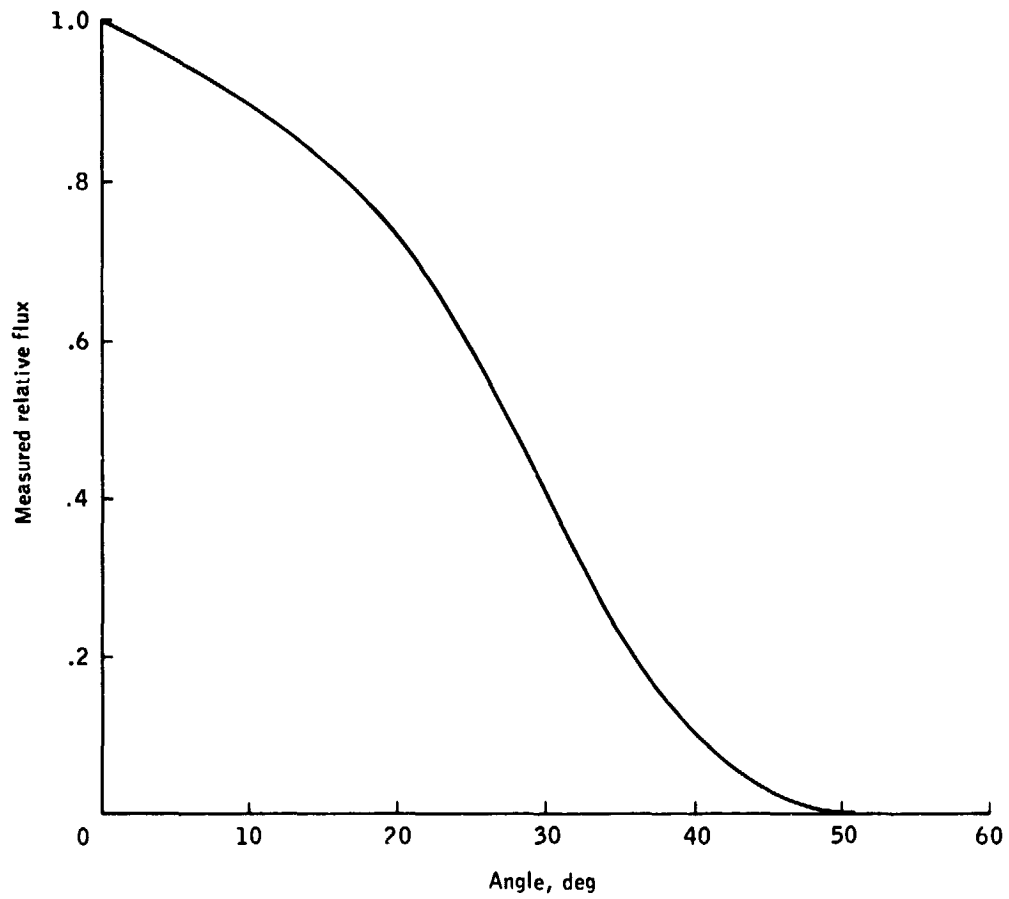


Figure 8-3.- Angular response of the Faraday cup.

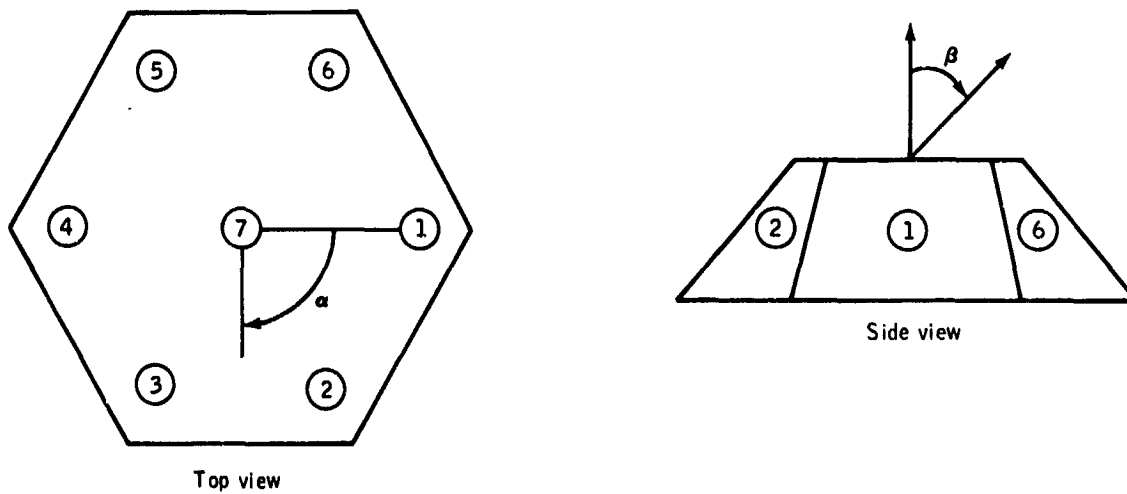


Figure 8-4.- Illustration of the  $\alpha$  and  $\beta$  angles.

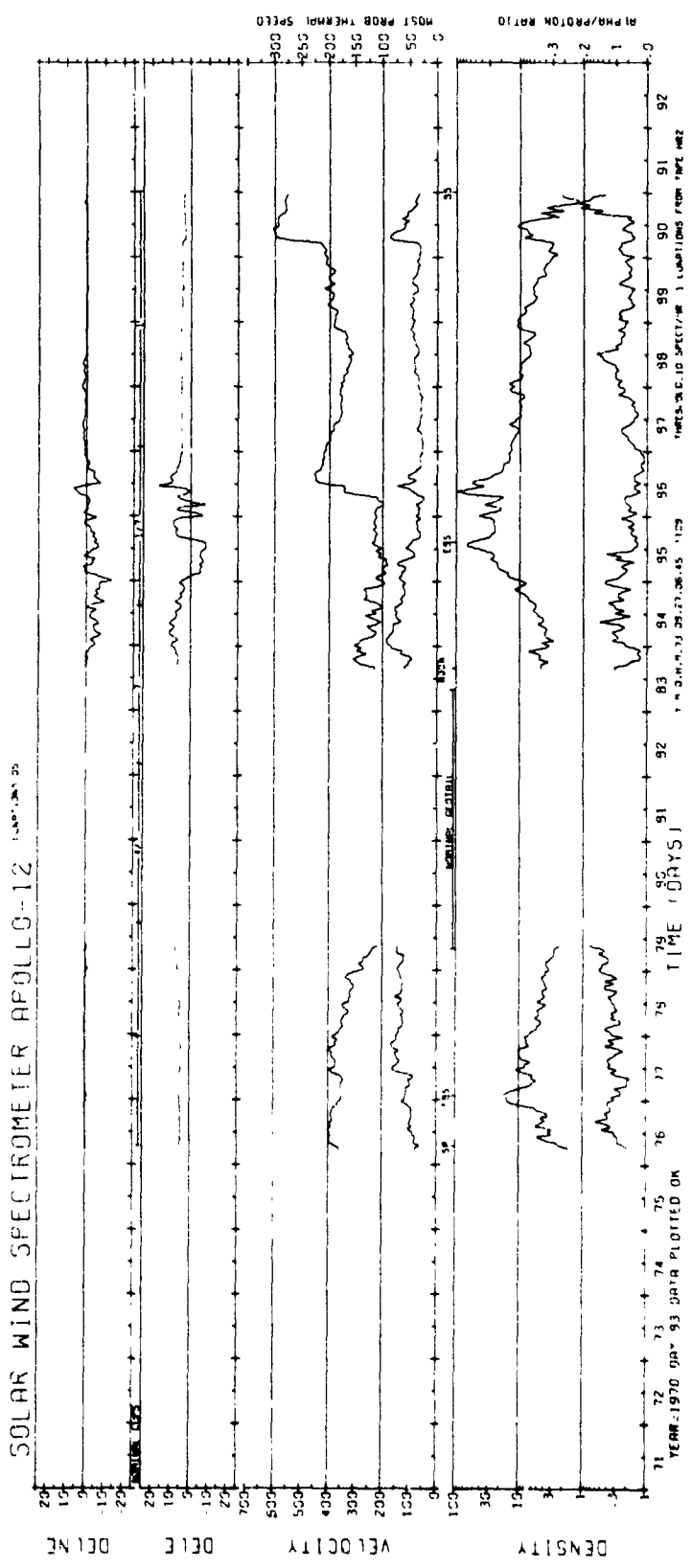
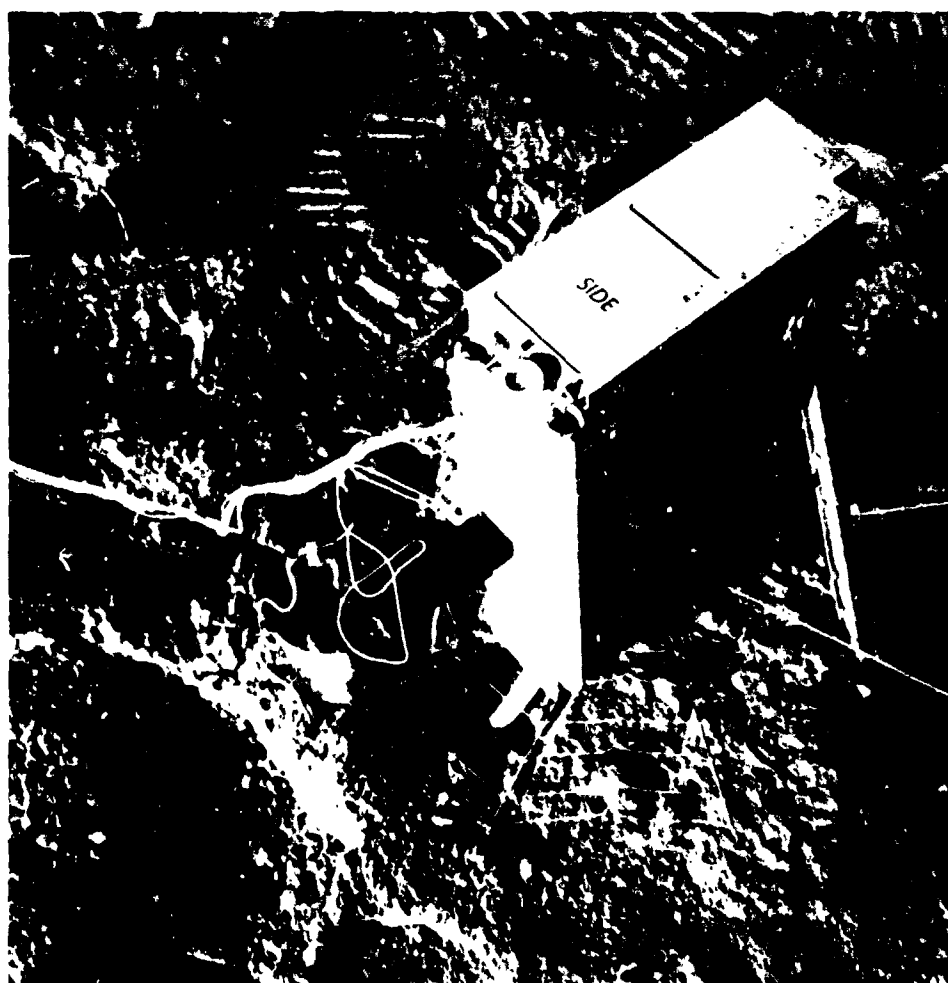


Figure 8-5.- Sample plot of hourly averages. Lunation is the number of lunations after the Apollo 12 SWS was turned on in November 1969. Year and day are the time for local noon at the Apollo 12 site. Thermal speed is located below the bulk velocity in the velocity graphs and alpha-particle/proton density ratio is located below the proton density in the density graph. Data are plotted only for hours that contain 10 or more spectra.

9. SUPRATHERMAL ION DETECTOR EXPERIMENT  
(NASA EXPERIMENT S-036)

NSSDC IDENTIFICATION NUMBERS:

APOLLO 12	69-009C-05
APOLLO 14	71-008C-06
APOLLO 15	71-063C-05



CONTENTS - SECTION 9

	Page
DESCRIPTION . . . . .	9-3
OPERATIONAL HISTORY . . . . .	9-4
Apollo 12 SIDE . . . . .	9-4
Apollo 14 SIDE . . . . .	9-5
Apollo 15 SIDE . . . . .	9-5
DATA SETS AND AVAILABILITY THROUGH NSSDC . . . . .	9-6
DESCRIPTION OF NSSDC DATA TAPES . . . . .	9-8
DISCUSSION . . . . .	9-8
The Lunar Ionosphere . . . . .	9-8
The Electric Potential of the Lunar Surface . . . . .	9-9
The Lunar Nightside . . . . .	9-10
Bow Shock Protons . . . . .	9-11
Magnetosheath . . . . .	9-11
Magnetotail . . . . .	9-11
Solar Wind/Neutral Gas Cloud Interactions . . . . .	9-12
Rocket Exhaust Products . . . . .	9-12
Synoptic and Secular Studies and Transient Events . . . . .	9-13
Penetrating Solar Particles . . . . .	9-13
Future Research . . . . .	9-14
SUMMARY OF PRINCIPAL RESULTS . . . . .	9-15
REFERENCES . . . . .	9-17
BIBLIOGRAPHY . . . . .	9-19

## 9. SUPRATHERMAL ION DETECTOR EXPERIMENT

The suprathermal ion detector experiment (SIDE) was designed to achieve the following objectives: (1) provide information on the energy and mass spectra of the positive ions close to the lunar surface (the lunar exosphere), (2) measure the flux and energy spectra of positive ions in the magnetotail and magnetosheath during the periods when the Moon passes through the magnetic tail of the Earth, (3) provide data on the plasma interaction between the solar wind and the Moon, and (4) determine a preliminary value for the electric potential of the lunar surface.

### DESCRIPTION

Three SIDE instruments were deployed (at the Apollo 12, 14, and 15 sites). The SIDE consists of two positive-ion detectors, the mass analyzer (MA) and the total ion detector (TID). Both use curved plate analyzers for energy per unit charge discrimination. The MA also uses a Wien velocity filter (crossed electric and magnetic fields), because knowledge of the energy per unit charge and the velocity is sufficient to allow determination of the mass per unit charge. The MA measures a 20-channel mass spectrum at each of six energy levels: 48.6, 16.2, 5.4, 1.3, 0.6, and 0.2 eV. The mass ranges covered are approximately 10 to 1000 atomic mass units per charge (amu/Q) for the Apollo 12 unit, 6 to 750 amu/Q for Apollo 14, and 1 to 90 amu/Q for Apollo 15. While each mass spectrum is being observed by the MA, the TID measures a 20-channel differential energy spectrum (including all masses) from 3500 eV/Q down to 10 eV/Q. Each 20-channel spectrum is obtained in 24 sec.

Each detector has a field of view that is roughly a square solid angle,  $6^\circ$  on a side. Numerous commands are possible, some of which allow certain measurements to be omitted to devote more time to other measurements. To establish electrical reference to the lunar surface, a wire screen (the lunar-surface ground plane in figure 9-1) is deployed on the surface beneath the SIDE. This screen is connected to the SIDE ground through a power supply that can cycle through 24 steps from -27.6 to +27.6 V. The effects of stepping this voltage through its cycle can be used in certain circumstances to determine the lunar-surface potential. A schematic diagram of the SIDE instrument is

shown in figure 9-1, a cutaway view of the SIDE in figure 9-2, and the SIDE as deployed at the Apollo 12 and 14 sites in figure 9-3.

The look direction of each instrument was angled 15° east (Apollo 14 and 15) or west (Apollo 12) from the local meridian plane. The Apollo 15 instrument (at latitude 26° N) was deployed tilted 26° from vertical toward the south, so that the sensor look directions of all three instruments included the ecliptic plane (fig. 9-4).

#### OPERATIONAL HISTORY

This section summarizes the time periods when the instruments were in full operation and returning science data. Periods when only housekeeping data were returned are not included. The design goal was full operation continuously after an initial period to allow for outgassing during the lunar daytime. Summaries of SIDE operation for Apollo 12, 14, and 15 are as follows.

##### Apollo 12 SIDE

<u>Period</u>	<u>Description</u>
November 19 and 20, 1969	Deployment and operation during mission activities.
December 1969 to January 1970	Operation during lunar night (and a short time before and after).
February 1970 to August 1972	Operation during lunar night, plus cyclic operation for approximately 10 days centered on local noon. Cyclic operation involves 2 hr on and 10 hr, or more, off. More coverage was obtained during continuous real-time support of Apollo lunar surface experiments package (ALSEP) missions (i.e., the first 45 days of the mission).

September 1972 to January 1976      Operation as for preceding period but with intermittent loss of data during lunar night (for periods of minutes to periods of many days) during the months of September, November, and December 1972, and during January, June, and August 1973, also other periods.

January 1967 to date of this publication      Operation as for preceding period, except not operated from approximately midnight until sunrise, because of low ALSFP reserve power.

Apollo 14 SIDE

<u>Period</u>	<u>Description</u>
February 5 to 7, 1971	Deployment and operation during mission activities.
February 1971 to July 1971	Operation during the night and part of the day but off for approximately 8 days centered on noon.
August 1971 to October 1971	Operation as for preceding period, plus short cycles of operation periodically for approximately 8 days near noon.
November 1971 to March 1973	Continuous operation.
April 1973 to December 14, 1974	Operation during the night from approximately 1 day before sunset until sunrise. No useful data after December 14, 1974.

Apollo 15 SIDE

<u>Period</u>	<u>Description</u>
July 3 <sup>rd</sup> to August 3, 1971	Deployment and operation during mission activities.

August 1971 to September 1971	Operation except during approximately 10 days centered on local noon.
October 1971 to November 1971	Operation as for preceding period, plus short intervals of operation intermittently for approximately 4 to 7 days near noon.
December 1971 to April 1972	Operation except during 3 to 5 days centered on local noon.
May 1972 to September 1973	Continuous operation.
October 1973 to date of this publication	Continuous operation except 3 to 5 days at local noon, when operated for short intervals.

#### DATA SETS AND AVAILABILITY THROUGH NSSDC

The following list gives the SIDE data sets, their form, and their availability through the National Space Science Data Center (NSSDC).

<u>Data set</u>	<u>Form</u>	<u>Availability</u>
1. Machine plots (MA and TID on same plot) of counting rates as a function of frame number	16-mm micro-film	Data for times after about August 1972 to September 1974 are (or soon will be) available at NSSDC. Data for times from about June 1971 to August 1972 will be available at NSSDC after production of copies; otherwise, only available at Rice University. Data not available in this form after September 1974.
2. Listings of counting rates as a function of	16-mm micro-film	Same as preceding set.

- frame number,  
with limited  
amount of house-  
keeping data
3. Machine plots (three-dimensional) of TID average energy spectra as a function of time. One lunation per plot. 76 by 91 cm (30 by 36 in.) paper All data will eventually be available at NSSDC.
  4. Machine plots (three-dimensional) of MA average mass spectra as a function of time. One lunation per plot. 76 by 91 cm (30 by 36 in.) paper Same as preceding set.
  5. TID spectra as a function of time Digital, on magnetic tape Data for times through April 1973 are available at NSSDC.
  6. MA spectra as a function of time Digital, on magnetic tape Same as preceding set.
  7. Engineering parameters Digital, on magnetic tape Data for times from about June 1971 to September 1974 will be available at NSSDC.
  8. TID and MA data, including everything telemetered from SIDE, plus evaluations of data quality and instrument mode of operation. Called "NPAK" by Rice University. Digital, on magnetic tape Data available only at Rice University.

## DESCRIPTION OF NSSDC DATA TAPES

Data tapes are standard 731.5-m (2400 ft), 1.27-cm (0.5 in.), 7-track IBM-compatible tapes, recorded at 800 bpi with odd parity. Words are 24-bit binary integers with negative numbers represented as 2's complement; with 28 such words per logical record (for both MA and TID). Physical records are fixed-length, blocked, with 100 logical records per physical record, and with no record-length descriptors or control words. There is only one file per reel, containing 1850 physical records. A standard tapemark is written after the last physical record. The last reel of a calendar year's data is the only one that will have less than 1850 records and the only one that will have less than 100 logical records in its last physical record. The TID and MA data are written on separate tapes but have almost identical formats; the first word in the logical record allows them to be distinguished from each other. The 28 words in a logical record contain time, 20 channels (mass for MA, energy for TID) of accumulated counts, and housekeeping parameters (including energy for the MA data). Where reliable data are not available, the value -1 is inserted.

## DISCUSSION

### The Lunar Ionosphere

Because the lunar ionosphere is promptly accelerated by the solar-wind electric field, the majority of SIDE data on the ionosphere come from the terminator regions. Here the orientation between the electric field and the detector "look axes" is such that the ions can be accelerated into the SIDE field of view. The observed fluxes of ions in the mass range of approximately 20 amu/Q (probably neon) are highly variable, depending on solar-wind magnetic field conditions and local time. Typical values for the stronger events are approximately  $10^5$  ions/cm<sup>2</sup>/sec in the energy range 10 to 3500 eV. Assuming accepted values for the ultraviolet and charge exchange ionization rates leads to neon neutral number densities of  $5 \times 10^4$  to  $5 \times 10^5$  atoms/cm. Although the investigators have observed events in which ions in the mass 40 amu/Q range were represented, these events are not as clean, and the investigators are not able to quote fluxes and number densities for argon ions and atoms.

A particularly interesting feature of the terminator ion data is the ion energy spectrum itself. This spectrum has proven to be quite tractable and illuminating. Several

examples are given in reference 9-1. The differential energy spectrum is exponential above the main peak because of the exponential nature of the lunar atmosphere and the homogeneous solar-wind electric field. The e-folding energy gives the product of the neutral gas scale height and the solar-wind electric field strength. Because the scale height is determined independently, this provides direct measure of the solar-wind electric field. The peak energy is an approximate measure of the lunar-surface electric potential that is found to be negative near the terminator. The shape of the dip in the spectrum below the peak energy indicates the rate at which the lunar-surface electric field falls off with height. Fits to an exponential function indicate an e-folding height of several kilometers, a much larger distance than the free streaming solar-wind Debye length of several meters. These spectra provide a great deal of information on the electric field environment of the Moon as well as the ion environment.

When the solar-wind electric field is not oriented such as to accelerate ions into the SIDE at the terminator, ion fluxes are sometimes still observed. These fluxes are due to atmospheric ions accelerated toward the lunar surface by the lunar-surface electric field alone. The differential energy spectrum of these ions (fig. 4 of ref. 9-1) is very narrow and in fact rarely seen in more than one SIDE energy channel. Because the spectrum is so narrow, it is not mathematically tractable except to calculate that the peak energy is a direct measure of the local electric potential of the lunar surface, usually between -10 and -100 V in the terminator region.

The SIDE's also detect the lunar ionosphere on the dayside of the Moon. In this case, the accelerating electric field is provided by the SIDE itself. A stepped voltage supply provides a potential difference between the ground plane grid and the ion entrance aperture. When the aperture is negative relative to the lunar surface, ions can be accelerated into the detectors. This mode of operation is used to determine the dayside lunar-surface potential that is due to photoelectrons (ref. 9-2). It also provides a measure of the ion number density at the surface. This number is found to lie between 1 and 7 ions/cm in the solar wind or magnetosheath plasma. As expected, this ion number density does not exceed that of the solar wind.

#### The Electric Potential of the Lunar Surface

As indicated previously, the surface potential in sunlight is determined by the energy spectrum of ions accelerated by the ground plane stepper supply. Because

this electric field extends about 1 Debye length or less from the SIDE, it provides a measure of the lunar potential relative only to the immediate surrounding plasma (i.e., the surface potential that is due chiefly to the photoelectrons). This potential is found to be about +10 V from solar zenith angles of 0° to about 45°. Beyond 45°, the potential falls rapidly to values as low as -100 V near the terminator. The lunar-surface potential is not symmetric with regard to positive and negative zenith angles. At about +50°, the potential rises abruptly to about +18 volts. No equivalent peak is observed at negative angles. As shown by the CPLEE data (ref. 9-3), the potential of the lunar surface on the dayside relative to the solar wind may be considerably higher in regions where there exists a substantial surface magnetic field. Further details of the surface potential is available in reference 9-4.

#### The Lunar Nightside

Ions in the energy range 250 to 1500 eV are observed on the nightside of the Moon. These ions may be observed throughout almost the entire lunar night, but activity increases in the period 1 to 6 days before local sunrise and has a strong peak 2 to 3 days before sunrise as noted with the Apollo 14 and 15 SIDE's. The Apollo 12 SIDE shows an equivalent activity following sunset.

The ion energies are generally less than solar-wind energies. The spectra vary from mono-energetic at 250 to 500 eV to broad. There is an indication that the peak energy changes with lunar local time, reaching a maximum of 750 eV at 3 to 4 days before sunrise.

The ion fluxes are of the order of  $10^6$  ions/cm<sup>2</sup>-sec-sr. They occur in bursts usually less than 1 hr in duration. They show no  $K_p$  dependence.

These ions are not understood. Their energy suggests that they are of solar-wind origin. They are of too high energy to be detected by the SIDE mass analyzer. Possible explanations include

1. Atmospheric ions accelerated by the solar wind into circumlunar trajectories
2. Solar-wind protons escaping from a lunar limbshock as recompression shock
3. The positive ion sheath of the lunar nightside negative surface potential

For further details see reference 9-5.

#### Bow Shock Protons

Protons and other solar-wind ions accelerated in the Earth's bow shock can escape upstream along magnetic field lines. The SIDE's established that these ions can travel at least as far as the lunar orbit. At the Moon, these ions have energies ranging from 250 eV to beyond the upper limit of the SIDE at 3500 eV. Integral fluxes of the order of  $10^5$  ions/cm<sup>2</sup>-sec-sr are typical. Their arrival at the Moon is correlated with the interplanetary magnetic field direction. Further details are available in references 9-6 to 9-8.

#### Magnetosheath

The Moon provides a good platform from which to study the distant magnetotail and magnetosheath. Using SIDE energy spectra, the plasma parameters of bulk velocity, temperature, number density, pressure, and energy density ratio were computed for 10 lunations throughout the magnetosheath. These parameters generally follow the predictions of laminar flow. The presence of nonthermal particles concentrating in a high energy tail of the energy spectrum is observed to increase near the bow shock in the dusk magnetosheath.

An unexpected result is an asymmetry in the correlation between this high energy tail and  $K_p$ . The dusk magnetosheath shows a good correlation, but the dawn magnetosheath shows no such correlation. This result is believed to be related to the presence of oblique shocks at the dawn magnetosheath. Further information can be found in references 9-9 to 9-11.

#### Magnetotail

Perhaps the most important and least expected result from the SIDE data is the discovery of a new plasma regime in the high latitude lobes of the geomagnetic tail. Principally because of the SIDE's high sensitivity to low energy ions, it detects what is referred to as the "lobe plasma."

The lobe plasma consists of protons of energy 50 to 250 eV streaming along the geomagnetic tail field lines away from the Earth. Integral fluxes range from  $10^5$  to  $10^8$  ions/cm<sup>2</sup>-sec-sr, temperatures  $4 \times 10^4$  to  $5 \times 10^5$  K and number densities 0.1/cm<sup>3</sup> to 5/cm<sup>3</sup> (refs. 9-12 and 9-13).

This plasma is observed to be sometimes, but not always, contiguous with the plasma sheet. It is believed to convect toward the plasma sheet from the polar magnetopause and to form the source region for the plasma sheet. Its frequency of occurrence in certain areas of the tail appears to be correlated with the east-west component of the interplanetary magnetic field, thus providing convincing evidence for the highly controversial magnetic merging on the dayside magnetopause.

Detailed investigations of the plasma sheet using the SIDE data are only now getting underway. One feature of interest is the appearance of multiple bulk flow velocities. Also, the correlation of plasma sheet flow with substorm activity remains a promising subject to be investigated.

#### Solar Wind/Neutral Gas Cloud Interactions

An important aspect of cosmic physics is the interaction between neutral and ionized gas streams. An opportunity to investigate such an interaction occurred following the impact of the Apollo 13 Saturn IVB (S-IVB) stage at a location 140 km west of the Apollo 12 ALSEP site. Both the SIDE and the solar wind spectrometer observed a large flux of positive ions (maximum flux of approximately  $3 \times 10^8$  ions/cm<sup>2</sup>-sec-sr). Two separate streams of ions were seen: a horizontal flux that appeared to be deflected solar-wind ions and a smaller vertical flux of predominantly heavy ions (>10 amu/Q) that probably consisted of material vaporized from the S-IVB stage. The important result is that hot electrons (50 eV) were created and were an important ionization mechanism in the impact-produced neutral gas cloud. Thus strong ionization and acceleration were observed under near collisionless conditions. For further information, refer to reference 9-14.

#### Rocket Exhaust Products

Along with ions from the ambient atmosphere, the SIDE's detect ions arising from exhaust gases from the Apollo missions. The Apollo 12 SIDE data were studied briefly with the objective of determining the dissipation rates of these gases. Two mass analyzer spectra were examined: one was examined 14 hr after the Apollo 12 landing; the other 2 months later. Both spectra showed good agreement with the predicted mass spectra for exhaust gases. When fitted to an exponential decay curve, and e-folding time of approximately 30 days was obtained for the majority of the gases (ref. 9-15). This study has not been completed. The lifetimes of individual gases have not been examined in detail, nor have

the data from the Apollo 14 and 15 SIDE's been carefully examined with a study of exhaust gases as the principal objective.

#### Synoptic and Secular Studies and Transient Events

Because of the sporadic nature of the lunar ionosphere measurements, it has been difficult to make secular and synoptic measurements. It has been observed, however, that ion densities computed from data taken approximately 6 months after the deployment of the Apollo 15 instrument are about a factor of 10 higher than those computed from data taken 2 yr after deployment. The numbers quoted earlier in this report are from the later data. These numbers agree with the neutral number densities for neon found by the Lunar Atmospheric Composition Experiment on Apollo 17 (ref. 24-16).

A possible explanation for this apparent change is calibration drifts in the instruments. Several independent tests of the long-term calibration integrity are under way but have not been completed. An alternative explanation is that the early data are in some way still affected by contaminants from the landing or a locally enhanced neon flux that is due to the heating of the lunar surface by the rocket plume. A final possibility is that there has occurred a natural secular variation in the atmospheric neon concentration. One should withhold judgment on this until all possibilities have been thoroughly investigated.

In 1973, the investigators reported a 14-hr period during which water vapor ions dominated the ion mass per unit charge spectrum at the Apollo 14 site (ref. 9-17). By examining all possible sources of contamination and extralunar sources, the investigators concluded that the ions were probably of lunar origin. Since this time, no additional water vapor events have been observed. Consequently, it appears unlikely that the water vapor came from a lunar source, although the details of the ion production are still unclear. Aside from this enigmatic event, no evidence exists in the SIDE data for transient events.

#### Penetrating Solar Particles

The SIDE was designed to measure 10 to 3500 eV ions that enter the detector aperture. However, particles of sufficiently high energy can penetrate the instrument from any direction and be detected. Such was the case during the intense solar flare activity of early August 1972. High

energy solar protons produced by the flares constituted an isotropic flux by the time they reached the vicinity of Earth, and were recorded by the SIDE's although the instruments were on the nightside of the Moon. The penetrating particles produced a high counting rate in all channels of all three SIDE's, and the event was observed for several days. An unusual feature of the event was a sudden sharply increased flux that lasted for about 2 hr and ended as suddenly as it began. This so-called "square wave" was discussed in references 9-18 and 9-19 as well as in earlier conference reports and collected papers on the topic. Other instruments on several other spacecraft have also reported such observations, and multispacecraft intercomparisons may provide information on the nature of the disturbance that produced this event.

#### Future Research

The success of the SIDE experiments is characterized by the variety of phenomena about which the data provide information. This wide range of phenomena has made it difficult to find time to examine all the phenomena in great depth. A great deal of data analysis still remains. The in-depth study so far has been limited to the lunar ionosphere. The lunar surface electric potential, the nightside ions, the magnetotail, and the bow shock data have been skimmed for the gross features; but a number of specific features need investigating further. A partial list of these features is as follows:

1. Investigation of the asymmetry in the lunar-surface potential to determine its cause
2. Correlation between SIDE and CPLEE lunar-surface potential data in the magnetotail
3. Correlation of the nightside energetic ion fluxes with the interplanetary magnetic field to determine the origin of these fluxes
4. Correlation between the lobe plasma and magnetospheric substorm data from ground and satellites
5. Determination of plasma sheet parameters and their correlation with other magnetospheric data
6. Statistical studies on the location of the magnetopause and bow shock front
7. High resolution studies of the plasma parameters at the magnetopause and bow shock front

8. Studies of the decay rates of the individual rocket exhaust product gases

9. Investigation of the interaction between a rocket exhaust neutral gas cloud and the magnetosheath plasma

10. Investigation of the cause of a background enhancement near the terminator possibly as the result of dust movement above the lunar surface

11. Investigation of long-term variations in the intensities of several phenomena observed (Preliminary work indicates definite variations as a result of seasonal and longer-term periodicities in the lunar orbit and directions with respect to the Sun. When these effects can be recognized and removed, the magnitude of secular variations, if any, can be investigated.)

#### SUMMARY OF PRINCIPAL RESULTS

1. Lunar ions accelerated by the solar-wind-induced field ( $E = -\vec{V} \times \vec{B}$ ) were observed (where  $E$  is the electric field and  $-\vec{V} \times \vec{B}$  is the negative cross product of velocity and magnetic field).

2. During lunar night, 1 to 3 keV protons (considered to be protons from the bow shock of the Earth) were observed.

3. Ion mass spectra due to the LM exhaust gas were observed, and the intensity decay rate was determined.

4. Multisite observation was made of the energetic ion characteristics in the Earth magnetosheath and at its boundaries, and correlation with geomagnetic activity was made.

5. The effects of the lunar module (LM) ascent engine exhaust on magnetosheath ion fluxes were observed.

6. Multisite observations of apparent motions of ion "clouds" related to lunar impact events and observations of mass spectra during the events were made.

7. Ion fluxes were monitored during local solar eclipses; no changes were observed.

8. Energetic ions were observed during lunar night when the site was shielded from the solar-wind direction.

9. Observation of ion events near terminators suggests a turbulent region of solar-wind plasma interaction with the solid Moon.

10. Positive ion fluxes were monitored while in the geomagnetic tail and correlated with geomagnetic storm activity.

11. Mass spectra of ions were observed from the ambient atmosphere, including a single observation of water vapor ions, possibly of natural origin.

12. The electric potential of the lunar surface was determined (a) in the magnetosheath or solar wind and (b) near the terminators.

13. Solar wind was observed during interplanetary storms.

14. Penetrating ions from solar flares were observed.

## REFERENCES

- 9-1. Benson, J.; Freeman, J. W.; and Hills, H. K.: The Lunar Terminator Ionosphere. Proceedings of the Sixth Lunar Science Conference, vol. 3, Pergamon Press (New York), 1975, pp. 3013-3021.
- 9-2. Fenner, M. A.; Freeman, J. W., Jr.; and Hills, H. K.: The Electric Potential of the Lunar Surface. Proceedings of the Fourth Lunar Science Conference, vol. 3, Pergamon Press (New York), 1973, pp. 2877-2889.
- 9-3. Burke, William J.; Reiff, Patricia, H.; and Reasoner, David L.: The Effect of Local Magnetic Fields on the Lunar Photoelectron Layer While the Moon Is in the Plasma Sheet. Proceedings of the Sixth Lunar Science Conference, vol. 3, Pergamon Press (New York), 1975, pp. 2985-2997.
- 9-4. Freeman, J. W.; and Ibrahim, M.: Lunar Electric Fields, Surface Potential and Associated Plasma Sheaths. The Moon, vol. 14, no. 1, Sept. 1975, pp. 103-114.
- 9-5. Schneider, Henry Emil: An Observation of Lunar Nighttime Ions. M. S. Thesis, Rice Univ., 1975.
- 9-6. Benson, J.; Freeman, J. W.; Hills, H. K.; and Vondrak, R. R.: Bow Shock Protons in the Lunar Environment. The Moon, vol. 14, no. 1, Sept. 1975, pp. 19-25.
- 9-7. Benson, John L.: Observations of Bow Shock Protons at the Lunar Orbit. M. S. Thesis, Rice Univ., 1974.
- 9-8. Benson, John Louis: The Lunar Exosphere. Ph. D. Dissertation, Rice Univ., 1975.
- 9-9. Fenner, M. A.; and Freeman, J. W., Jr.: Dawn-Dusk Magnetosheath Plasma Asymmetries at  $60 R_E$ . J. Geophys. Res., vol. 80, no. 25, Sept. 1, 1975, pp. 3693-3697.
- 9-10. Fenner, Martha Ann: Magnetosheath Plasma at  $60 R_E$ . M. S. Thesis, Rice Univ., 1971.
- 9-11. Fenner, Martha Ann: Observations of Magnetosheath Plasma at the Lunar Orbit. Ph. D. Dissertation, Rice Univ., 1974.

- 9-12. Hardy, D. A.; Hills, H. K.; and Freeman, J. W.: A New Plasma Regime in the Distant Geomagnetic Tail. *Geophys. Res. Letters*, vol. 2, no. 5, May 1975, pp. 169-172.
- 9-13. Haluy, David A.: Observation of Low Energy Protons in the Geomagnetic Tail at Lunar Distances. M. S. Thesis, Rice Univ., 1974.
- 9-14. Lindeman, R. A.; Vondrak, R. R.; Freeman, J. W.; and Snyder, C. W.: The Interaction Between an Impact-Produced Neutral Gas Cloud and the Solar Wind at the Lunar Surface. *J. Geophys. Res.*, vol. 79, no. 16, June 1, 1974, pp. 2237-2296.
- 9-15. Freeman, J. W., Jr.; Fenner, M. A.; Hills, H. K.; Lindeman, R. A.; et al.: Suprathermal Ions Near the Moon. *Icarus*, vol. 16, no. 2, Apr. 1972, pp. 328-338.
- 9-16. Hoffman, J. H.; Hodges, R. R., Jr.; Johnson, F. S.; and Evans, D. E.: Lunar Atmospheric Composition Results From Apollo 17. *Proceedings of the Fourth Lunar Science Conference*, vol. 3, Pergamon Press (New York), 1973, pp. 2865-2875.
- 9-17. Freeman, J. W., Jr.; Hills, H. K.; Lindeman, R. A.; and Vondrak, R. R.: Observations of Water Vapor Ions at the Lunar Surface. *The Moon*, vol. 8, nos. 1/2, 1973, pp. 115-126.
- 9-18. Medrano, R. A.; Bland, C. J.; Freeman, J. W., Jr.; Hills, H. K.; and Vondrak, R. R.: Solar Cosmic Ray "Square Wave" of August 1972. *J. Geophys. Res.*, vol. 80, no. 13, May 1, 1975, pp. 1735-1743.
- 9-19. Medrano-Balboa, R. A.: Unusual Solar Wind and Solar Proton Events Observed on the Lunar Surface. Ph. D. Dissertation, Rice Univ., 1973.

## BIBLIOGRAPHY

- Freeman, J. W., Jr.: Energetic Ion Bursts on the Night Side of the Moon. *J. Geophys. Res.*, vol. 77, no. 1, Jan. 1, 1972, pp. 239-243.
- Freeman, J. W., Jr.: Suprathermal Ion Detector Results from Apollo Missions. *Space Research XIII, Proceedings of the Fifteenth Plenary Meeting of COSPAR (Committee on Space Research)*, vol. 3, Akademie-Verlag (Berlin), 1973, pp. 821-830.
- Freeman, J. W., Jr.; Balsiger, H.; and Hills, H. K.: Suprathermal Ion Detector Experiment (Lunar Ionosphere Detector). Sec. 6 of Apollo 12 Preliminary Science Report, NASA SP-235, 1970.
- Freeman, J. W., Jr.; Fenner, M. A.; and Hills, H. K.: The Electric Potential of the Moon in the Solar Wind. *Photon and Particle Interactions with Surfaces in Space*, R. J. L. Grand, ed., D. Reidel Publishing Company, 1973, pp. 363-368.
- Freeman, J. W., Jr.; Hills, H. K.; and Fenner, M. A.: Some Results from the Apollo 12 Suprathermal Ion Detector. *Proceedings of the Second Lunar Science Conference*, vol. 3. A. A. Levinson, ed., MIT Press (Cambridge, Mass.), 1971, pp. 2093-2102.
- Freeman, J. W., Jr.; Fenner, M. A.; and Hills, H. K.: The Electric Potential of the Moon in the Solar Wind. *J. Geophys. Res.*, vol. 78, no. 22, Aug. 1, 1973, pp. 4560-4567.
- Freeman, J. W., Jr.; Hills, H. K.; and Vondrak, R. R.: Water Vapor, Whence Comest Thou? *Proceedings of the Third Lunar Science Conference*, vol. 3, David R. Criswell, ed., MIT Press (Cambridge, Mass.), 1972, pp. 2217-2230.
- Garrett, H. B.; Hill, T. W.; and Fenner, M. A.: Plasma-Sheet Ions at Lunar Distance Preceding Substorm Onset. *Planet. Space Sci.*, vol. 19, 1971, pp. 1413-1418.
- Hills, H. K.; and Freeman, J. W., Jr.: Suprathermal Ion Detector Experiment (Lunar Ionosphere Detector). Sec. 8 of Apollo 14 Preliminary Science Report, NASA SP-272, 1971.
- Hills, H. Kent; Meister, Jurg C.; Vondrak, Richard R.; and Freeman, John W., Jr.: Suprathermal Ion Detector Experiment (Lunar Ionosphere Detector). Sec. 12 of Apollo 15 Preliminary Science Report, NASA SP-289, 1972.

- Ibrahim, Mohamed Esam: The Electric Potential of the Lunar Surface. M. S. Thesis, Rice Univ., 1975.
- Lindeman, Robert A.: Recurring Ion Events at the Lunar Surface. M. S. Thesis, Rice Univ., 1971.
- Lindeman, Robert A.: Observation of Ions from the Lunar Atmosphere. Ph. D. Dissertation, Rice Univ., 1973.
- Lindeman, R.; Freeman, J. W., Jr.; and Vondrak, R. R.: Ions from the Lunar Atmosphere. Proceedings of the Fourth Lunar Science Conference, vol. 3, Pergamon Press (New York), 1973, pp. 2889-2896.
- Manka, Robert H.: Plasma and Potential at the Lunar Surface. Photon and Particle Interactions with Surfaces in Space, R. J. L. Gard, ed., D. Reidel Publishing Company, 1973, pp. 347-361.
- Manka, Robert Hall: Lunar Atmosphere and Ionosphere. Ph. D. Dissertation, Rice Univ., 1972.
- Manka, R. H.; and Michel, F. C.: Lunar Atmosphere as a Source of Lunar Surface Elements. Proceedings of the Second Lunar Science Conference, vol. 2, A. A. Levinson, ed., MIT Press (Cambridge, Mass.), 1971, pp. 1717-1728.
- Manka, R. H.; and Michel, F. C.: Lunar Ion Energy Spectra and Surface Potential. Proceedings of the Fourth Lunar Science Conference, vol. 3, Pergamon Press (New York), 1973, pp. 2897-2908.
- Manka, R. H.; and Michel, F. C.: Lunar Ion Flux and Energy. Photon and Particle Interactions with Surfaces in Space, R. J. L. Gard, ed., D. Reidel Publishing Company, 1973, pp. 429-442.
- Medrano-Balboa, Rene A.: Solar Plasma Disturbance Observed by a Suprathermal Ion Detector on the Moon. M. S. Thesis, Rice Univ., 1971.
- Medrano, Rene A.; Freeman, John W., Jr.; Hills, H. Kent; Vondrak, Richard R.: Penetrating Solar Flare Particle and Solar Wind Observations in the Lunar Night, August 1972. Collected Data Reports on August 1972 Solar-Terrestrial Events, Rept. UAG-28, pt. II, H. E. Coffey, ed., World Data Center A for Solar-Terrestrial Physics, Boulder, Colo., 1973.
- Schneider, H. E.; and Freeman, J. W.: Energetic Lunar Nighttime Ion Events. The Moon, vol. 14, no. 1, Sept. 1975, pp. 27-33.

Shane, Robert L.: Design and Calibration of the  
Suprathermal Ion Detector Experiment (SIDE). M. S.  
Thesis, Rice Univ., 1969.

Vondrak, Richard R.: Creation of an Artificial Lunar  
Atmosphere. *Nature*, vol. 248, no. 5450, Apr. 19, 1974,  
pp. 657-659.

Vondrak, Richard R.; Freeman, John W.; and Lindeman, Robert  
A.: Measurements of Lunar Atmospheric Loss Rate.  
*Proceedings of the Fifth Lunar Science Conference*, vol. 3,  
Pergamon Press (New York), 1974, pp. 2945-2954.

Young, David Thad: A Suprathermal Ion Accelerator. M. S.  
Thesis, Rice Univ., 1967.

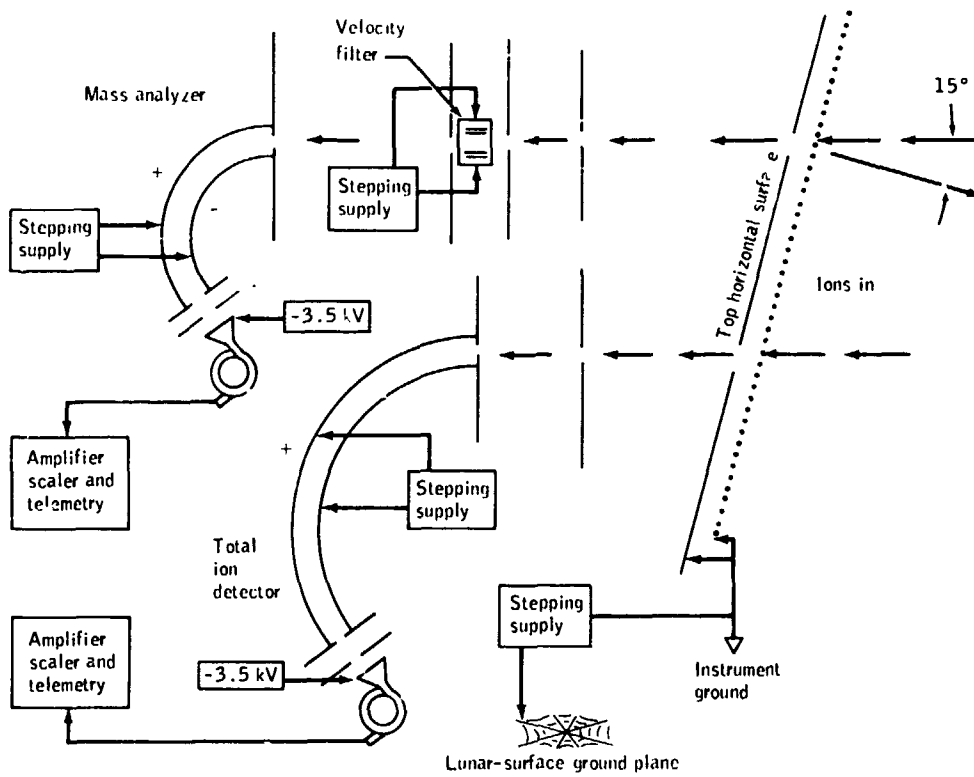


Figure 9-1.- Schematic diagram of SIDE.

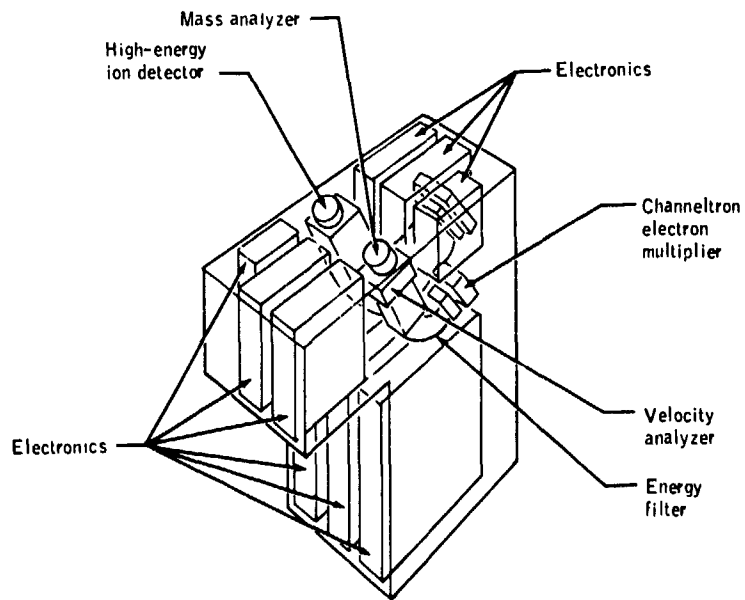


Figure 9-2.- Cutaway view of SIDE.

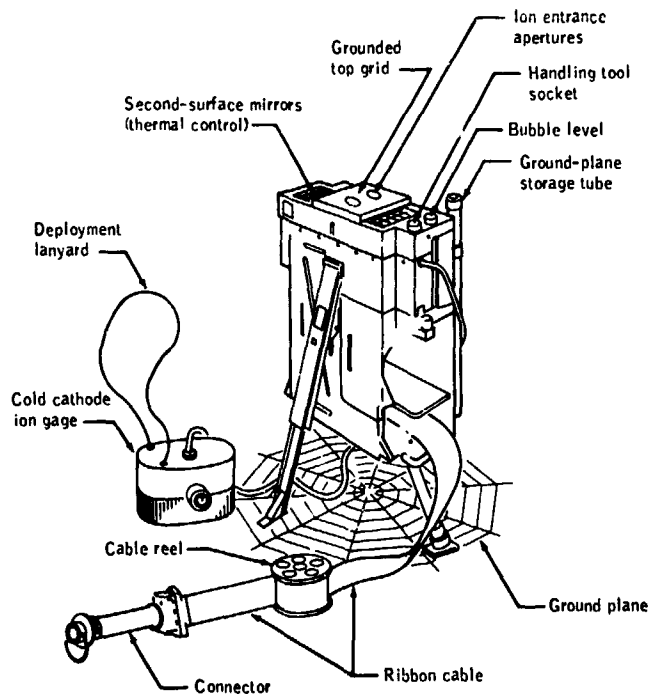


Figure 9-3.- The SIDE configuration as deployed at the Apollo 12 and 14 sites.

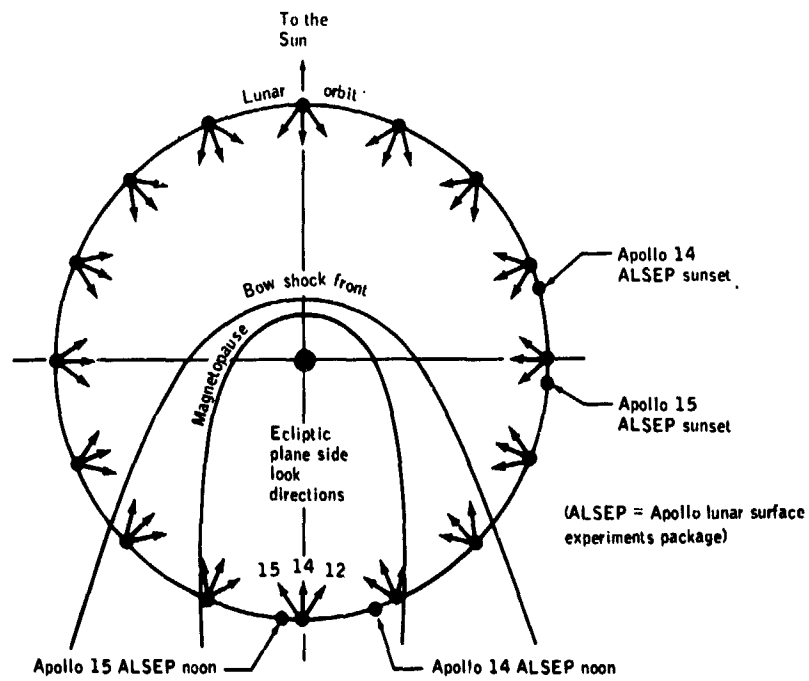


Figure 9-4.- Sensor look directions of SIDE instruments deployed at the Apollo 12, 14, and 15 sites.

10. HEAT FLOW EXPERIMENT (NASA EXPERIMENT S-037)

NSSDC IDENTIFICATION NUMBERS:

APOLLO 15 71-063C-06  
APOLLO 17 72-096C-01



CONTENTS - SECTION 10

	Page
SYMBOLS . . . . .	10-3
EXPERIMENT THEORY . . . . .	10-5
EXPERIMENT DESCRIPTION . . . . .	10-7
EQUIPMENT DESCRIPTION . . . . .	10-8
SENSOR CHARACTERISTICS . . . . .	10-10
ELECTRONIC MEASUREMENT SYSTEM . . . . .	10-12
THERMOCOUPLE MEASUREMENTS . . . . .	10-18
PACKAGE CONSTRUCTION AND THERMAL CONTROL . . . . .	10-20
CALIBRATION AND TESTING . . . . .	10-22
OPERATIONAL HISTORY . . . . .	10-27
INSTRUMENT MALFUNCTIONS . . . . .	10-30
SUMMARY OF RESULTS . . . . .	10-30
LONG-TERM DATA ANALYSIS . . . . .	10-32
FUNCTIONAL FLOW OF DATA REDUCTION . . . . .	10-34
THE L-DGO MASTER DISK ORGANIZATION . . . . .	10-37
THE L-DGO NSSDC TAPES . . . . .	10-38
DATA ARCHIVED AT NSSDC . . . . .	10-39
REFERENCES . . . . .	10-40
BIBLIOGRAPHY . . . . .	10-40

## 10. HEAT FLOW EXPERIMENT

The flow of heat from the lunar surface and the associated subsurface temperature fields have evolved from the conditions that existed when the Moon was formed (under the influence of accumulated thermal and structural developments, including those deep in the interior). A knowledge of the present level of surface heat flow may therefore place some important limits on the range of feasible lunar models. To determine this level, instruments capable of making lunar subsurface measurements (from which local heat flow could be derived) were carried to the Moon on the Apollo 15, 16, and 17 missions.

### SYMBOLS

The following symbols are used in this discussion of the heat flow experiment (HFE). Because the HFE data output is in degrees Celsius and the experiment was designed accordingly, pertinent discussion must be in degrees Celsius (instead of Kelvin) to avoid misinterpretation by the data user. The International System of Units is used for all other measurements.

$A_{1...6}$	platinum bridge constants determined by calibration
$B_{1...6}$	platinum bridge constants determined by calibration
C	constant
$dT/dz$	mean vertical temperature gradient
G	system gain
$I_E$	bridge excitation current
J	heat flow
k	thermal conductivity
$\bar{m}$	mean value
n	point of constant input ratio

$N_{1...4}$	digital numbers
$N'_{1...4}$	N - 4096
$R_0$	resistance at 0° Celsius
$R_{1...4}$	Wheatstone bridge arm resistances
$R_{100}$	resistance at 100° Celsius
$R_B$	total bridge resistance
$R_I$	idealized output ratio
$R_T$	resistance at T
T	temperature in degrees Celsius
$T_R$	reference-bridge temperature
TC	thermocouple
u	digit resolution (2.4412 millivolts)
$V^+$	positive voltage
$V^-$	negative voltage
$v^+$	sensed positive voltage
$v^-$	sensed negative voltage
$v_e$	sensed reference-bridge excitation voltage
$v_o$	sensed reference-bridge output voltage
$v_{off}$	error offset voltage referred to amplifier input
$V_E$	bridge excitation voltage
$V'_E$	sensed bridge excitation voltage

$V_L$	potential difference across 20-ohm resistance for current $I_E$
$V_O$	bridge output voltage
$V_T$	potential difference across 2-ohm resistance for current $I_E$
$V_X$	voltage at connection point X
$V_Y$	voltage at connection point Y
$X_{1...4}$	calibration constants for reference bridge
$z$	vertical distance
$Z$	attenuation ratio $V_E'/V_E$
$\alpha_s$	solar absorptance
$\beta$	Van Dusen calibration constant
$\delta$	Callendar calibration constant
$\Delta T$	temperature difference in degrees Celsius
$\epsilon$	system error offset
$\epsilon_O$	output-sense-line offset
$\epsilon_1$	excitation-sense-line offset
$\epsilon_{IR}$	infrared emittance
$\sigma$	standard deviation

#### EXPERIMENT THEORY

The heat flow instrument performs measurements to determine the mean vertical temperature gradient  $dT/dz$  (where  $T$  is temperature in degrees Celsius and  $z$  is vertical distance) and the effective thermal conductivity  $k$  of the material across

which the measured gradient is developed. Conducted heat flow  $J$  diffuses down a temperature gradient in accord with the relationship between these two quantities in one dimension

$$J = -k(dT/dz) \quad (10-1)$$

Table 10-I gives ranges of predicted density of heat flow ratio and soil thermal conductivities with the corresponding limits of average temperature gradients.

The average absolute temperature at any point in the subsurface (regolith) results from the balance between the solar heat influx and the total heat outflow acting through the regolith. Solar radiation power incident at the lunar surface varies from  $1.45 \text{ kW/m}^2$  at one extreme to 0 at the other extreme. Resultant Moon surface temperatures vary from approximately 400 K at lunar noon to 100 K at lunar night, with an annual modulation of about 8 K caused by the elliptical orbit of the Moon about the Sun. The attenuations and phase shifts of these periodic variations as they propagate into the Moon are determined by the diffusivity of the regolith materials. Nonperiodic variations also occur as a result of changes in the infrared (IR) emittance and solar absorptance of the surface when it is disturbed by the astronauts. Variations were also caused by heat generated during instrument emplacement operations — hole drilling, in particular. To extract meaningful data regarding average gradient from the composite temperatures that may exist at practical lunar measuring depths, the temperature-measuring instrument must have a wider range than the predicted gradients; readings must be recorded frequently for more than a year; and absolute measurement accuracy must equal the relative accuracy requirement for the lowest mean temperature gradient expected.

Two different approaches are used in measuring lunar subsurface thermal conductivity by means of the heat flow instrument. In the first approach, the thermal response of in situ lunar material to known heat sources is tested. In the second, vertical strings of temperature sensors record the characteristics of the periodic propagations into the surface to determine diffusivity; with this diffusivity information and with good estimates of soil mass density and specific heat, thermal conductivity can be calculated.

The first of these approaches takes into account local inhomogeneities, and measurements should sample the volume of material that immediately influences the temperature gradient. Two variations within this approach are required to cover the conductivity range of expected subsurface lunar materials. For soils with low

conductivities (less than  $5 \times 10^{-2}$  W/m-K), a tubular heater wound around one of a pair of temperature sensors vertically separated by 0.5 m is energized with a small amount (2 mW) of power. The rate of rise and the steady-state value of the heated sensor temperature relative to the undisturbed reference level are functions of the thermal coupling from the heater to the lunar material and of the thermal conductivity of the surrounding lunar soil. The temperature rise is inversely proportional to both thermal conductivity and absolute temperature level. Useful range is limited at higher thermal conductivities by reduced sensitivity and by the magnitude of the radiative and conductive thermal resistance of the coupling paths from instrument to soil. For materials such as rock, with conductivities greater than  $5 \times 10^{-2}$  W/m-K, the heater is powered to 0.5 W; the transient and steady-state responses of the lunar medium between the heat source and a remote sensor 0.1 m away are determined by subtracting the characteristic short-time constant response of the intervening sensor support structure from the overall response.

#### EXPERIMENT DESCRIPTION

The optimum site configuration for the HFE is depicted in figure 10-1. Two hollow fiberglass borestems, 2.5 cm in diameter, are drilled into the lunar surface to a depth of 3 m at a distance of 10 m from each other. Four sets of temperature sensors, spaced along a probe consisting of two flexibly joined rigid sections, occupy the bottom meter of each hole. The sensors, which are primarily radiatively coupled to the borestem and lunar soil, are connected electrically by 8-m woven cables to a package of electronics on the surface. Each cable carries four precisely located thermocouple junctions in the borestems above the probes. The electronics unit is connected to the Apollo lunar surface experiments package (ALSEP) by a 9-m-long flat ribbon cable.

The heat flow instrument returns data that give average-temperature information, differential-temperature information, and low- and high-thermal-conductivity information from four locations on each probe; the thermocouples supply readings for temperature determinations in the upper part of the boreholes. Instrument performance requirements for these measurements are summarized in table 10-II.

In the normal operating mode, the heat flow instrument (1) gathers ambient and high- and low-sensitivity differential temperature data from the gradient sensors situated at the ends of each half-probe section and (2) samples the thermocouple outputs during the 7.25-min measurement sequence. Various sub-sequences can be selected (e.g., measurements on one probe only), but most of them are not normally used. Low-conductivity experiments are

performed on command, with each heater activated in turn to 0.002 W for about 40 hr. The normal measurement sequence is unchanged. The high-conductivity mode of operation requires the selection of measurements on the remote sensors in any half-probe section; the type of data returned alternates between high-sensitivity differential and absolute temperature measurements. Either of the adjacent heaters at the ends of the probe half may be activated by command. Each heater should be on for about 6 hr, but this depends on the conductivity experienced.

### EQUIPMENT DESCRIPTION

The platinum resistance sensors used in the HFE probe contribute significantly to the quality of the measurements obtained. Two types of platinum resistance thermometers are used in the heat flow instrument: the so-called gradient sensor and the ring or remote sensor.

#### Gradient Sensor

The gradient sensor detail is shown in figure 10-2. The sensor incorporates a unique method of supporting the resistance wire to reduce instability normally induced by mechanical or thermal stress. Pure annealed 0.04-mm-diameter platinum wire, coiled in a 0.3-mm-diameter helix that is extended to 0.07 mm pitch, is mounted on a glass-insulated platinum mandrel. The base of each loop is arranged so that only 10 percent of the turn is embedded in the substrate. The mandrel and glass have the same expansion coefficients as the coil, and the assembly is annealed at 673 K for 15 hr before sealing. The platinum coil is isolated from contamination by an atmosphere of pure helium contained within a gold-sealed platinum outer case. Platinum-wire coaxial leads extend through ceramic-insulated tubes for silver brazing to Evanohm and Manganin connecting wires. Each sensor assembly houses two separate elements, effectively bifilar wound, with nominal resistances of 500  $\Omega$  at 273.15 K (0° C).

#### Remote Sensor

The construction of the remote sensor is illustrated in figure 10-3. It consists of two 500- $\Omega$ -nominal-resistance platinum wires set in a ceramic glaze around a thin platinum ring. Because the remote sensor is intended for use in the short-term high-conductivity experiments, it has a less stringent stability requirement (0.002 K/6 hr) than the gradient sensor; however, it has demonstrated a long-term stability comparable to that of the gradient sensor.

The sensors are mounted as shown in figure 10-4, which illustrates the configuration common to the ends of all half-probe sections. The gradient assembly is epoxied at the mounting bushing (at the sensor-lead exit end) to the inside of the probe end sheath. The small tube on the opposite end (also shown in figure 10-2) is supported by a snugly fitting fiberglass bushing that permits strain-free differential expansion and good mounting support. Associated with each gradient sensor is a 1000- $\Omega$  Karma wire heater, wound concentrically with the gradient sensor on the thin section of the end sheath. The ring sensor platinum band is partially cemented internally to a filler sheath that is attached to the outer sheath of the probe. A tube joins the two end pieces to form a probe half-section.

The structural components providing the span between the sensors were manufactured from low-conductivity, thin-walled, filament-wound epoxy fiberglass. All cabling is carried through the probe body inside the split inner sheath that is shielded with multilayer insulation to reduce radiative coupling between the wiring and probe wall, particularly during conductivity experiments with a heater on. The areas around the sensors are partially enclosed with guards for protection during handling.

A probe assembly is 1.09 m long when unfolded at the closely coiled extension spring that joins the two half-sections. The complete unit is coated with a matte-black thermal control paint. An assembled probe (with its 8-m, 35-conductor connecting cable) weighs less than 0.5 kg.

Gradient and ring sensors are each interconnected within a probe half with AWG 23 Evanohm wire to form bridges, the opposite arms of which are physically situated in the same sensor assembly at a common temperature. A schematic of this resistance bridge arrangement is shown in figure 10-5, where  $T_1$  is the temperature of one sensor assembly and  $T_2$  the temperature of the other. The gradient sensor assemblies, which form one bridge, are separated by 47 cm; the remote sensor assemblies, which form the other bridge, are located 29 cm apart and 9 cm from the heater windings.

Six wires connect each bridge to the electronics unit. Those from a lower half-probe are conveyed in the upper section through the hollow sensor assemblies. Evanohm wire is used because it has a remarkably small temperature coefficient of resistance (0.00002/K), a closely controllable resistivity, and a thermal conductivity that is low for an electrical conductor.

## SENSOR CHARACTERISTICS

In Callendar's empirical parabolic equation

$$T = 100 \left( \frac{R_T - R_0}{R_{100} - R_0} \right) + \delta \left( \frac{T}{100} - 1 \right) \frac{T}{100} \quad (10-2)$$

the constant  $\delta$  defines the characteristics of an individual platinum resistance thermometer over the temperature range  $0^\circ$  to  $630^\circ$  C, where  $T$  is temperature in degrees Celsius,  $R_T$  is resistance at temperature  $T$ ,  $R_0$  is resistance at  $0^\circ$  C, and  $R_{100}$

is resistance at  $100^\circ$  C. The Callendar constant is determined by calibration at the following three fixed points: the triple point of water ( $0.0100^\circ$  C), the steam point ( $100^\circ$  C), and the boiling point of sulfur ( $444.600^\circ$  C). For use between  $0^\circ$  and  $-183^\circ$  C, a correction term devised by Van Dusen is added to the Callendar equation to give

$$T = 100 \left( \frac{R_T - R_0}{R_{100} - R_0} \right) + \delta \left( \frac{T}{100} - 1 \right) \frac{T}{100} + \beta \left( \frac{T}{100} - 1 \right) \left( \frac{T}{100} \right)^3 \quad (10-3)$$

where the constant  $\beta$  for an individual thermometer is found by calibrating at the boiling point of oxygen ( $-182.97^\circ$  C). The resistance of one platinum element at temperature  $T$  relative to its resistance at  $0^\circ$  C is therefore

$$\frac{R_T}{R_0} = 1 + \frac{1}{100} \left( \frac{R_{100}}{R_0} - 1 \right) \left[ T - \delta \left( \frac{T}{100} - 1 \right) \frac{T}{100} - \beta \left( \frac{T}{100} - 1 \right) \left( \frac{T}{100} \right)^3 \right] \quad (10-4)$$

Referring to figure 10-5, the bridge voltage ratio is defined

$$\frac{V_O}{V_E} = \frac{R_1 R_4 - R_2 R_3}{(R_1 + R_3)(R_2 + R_4)} \quad (10-5)$$

where  $R_1$ ,  $R_2$ ,  $R_3$ , and  $R_4$  are Wheatstone bridge arm resistances;  $V_E$  is the excitation voltage across the bridge; and  $V_O$  is the output voltage. By combining equations (10-4) and (10-5) and eliminating small terms, the following simplified expression is obtained:

$$\begin{aligned} \frac{V_O}{V_E} R_B = & A_1 + A_2 T + A_3 T^2 + A_4 \Delta T + A_5 \Delta T (\Delta T + 2T) \\ & + A_6 [\Delta T (4T^3 - 300T^2) + \Delta T^2 (6T^2 - 300T) \\ & + \Delta T^3 (4T - 100) + \Delta T^4] \end{aligned} \quad (10-6)$$

where  $R_B$  is total bridge resistance;  $T$  is the temperature of one sensor assembly expressed in degrees Celsius;  $\Delta T$  is the temperature differential between sensor assemblies in degrees Celsius; and  $A_1$ ,  $A_2$ ,  $A_3$ ,  $A_4$ ,  $A_5$ , and  $A_6$  are constants. Similarly, bridge resistance  $R_B$  can be related to temperature  $T$  and temperature differential  $\Delta T$  by the simplified expression

$$\begin{aligned} R_B = & B_1 + B_2 T + B_3 T^2 + B_4 (T - 100) T^3 + B_5 \Delta T \\ & + B_6 \Delta T (\Delta T + 2T) \end{aligned} \quad (10-7)$$

where  $B_1$ ,  $B_2$ ,  $B_3$ ,  $B_4$ ,  $B_5$ , and  $B_6$  are constants. Equations (10-6) and (10-7) are transcendental in  $T$  and  $\Delta T$ . To find absolute and differential temperatures, an iterative simultaneous solution of both calibration equations is required.

## ELECTRONIC MEASUREMENT SYSTEM

### System Operation

Equations (10-6) and (10-7) show that the electrical measurements required to solve for  $T$  and  $\Delta T$  are total bridge resistance  $R_B$  (measured as a single element), excitation voltage  $V_E$ , and differential output voltage  $V_O$ . The system by which these measurements are made is represented in the simplified block diagram in figure 10-5, which includes the essential features of the bridge measurement method. The diagram includes only one of the eight probe bridges and omits thermocouple circuits, power supplies, and most of the logic and control circuits.

Each of the bridges is selected through reed relays for excitation by direct current. The bridges produce a differential output-to-input voltage ratio  $V_O/V_E$  of approximately  $+5.8 \times 10^{-3}$  for a dynamic range of  $\pm 2$  K. With 8 V applied to the bridge excitation cables, the data-chain maximum input requirement is set at  $\pm 34$  mV. The gradient bridge low-sensitivity range of  $\pm 20$  K requires 0.8 V excitation for a similar output maximum. Measurements for total bridge resistance are made at the 8-V supply level. Excitation voltage  $V_E$  is reduced to the maximum level of the output voltage by an attenuator in the excitation sense circuit.<sup>1</sup> The output impedance is arranged to be the same as the bridge differential output impedance. At the low-sensitivity excitation level of 0.8 V, the attenuator output  $V_E$  is one-tenth of the maximum bridge unbalance voltage  $V_O$  at  $\pm 20$  K temperature extremes. To effectively normalize these readings and at the same time avoid attenuator switching or gain changes, excitation current  $I_E$  is sensed. This current is combined with the total bridge resistance value determined from readings at 8-V excitation made within a short time of the current measurement) to calculate the low-level-excitation supply voltage. Low-sensitivity current is found from the potential difference  $V_L$  developed across a precision 18- $\Omega$  plus 2- $\Omega$  resistance in the supply line; high-sensitivity current is found from the potential difference  $V_T$  across the 2- $\Omega$  resistor only. The latter value is used with the attenuated bridge-excitation-voltage measurement

---

<sup>1</sup>The series elements of the attenuator include cable resistance that does fluctuate slightly with the large surface-temperature variations, but the proportion of cable resistance in the temperature-matched attenuator is small, and very high attenuation-ratio stability is achieved.

to determine total bridge resistance  $R_B$ . Differential output voltages are read directly.

These various measurements are presented sequentially through a low-level field effect transistor (FET) multiplexer to the input of the common signal amplifier, which has a gain of 288 and a full-scale output of  $\pm 10$  V. The amplified signal is converted to a 13-bit digital number and clocked into a shift register along with a 7-bit mode-identification and binary-measurement code. The resulting 20-bit number is serially shifted into the ALSEP central station for insertion as two 10-bit words into the ALSEP data stream for transmission to Earth. On Earth, the binary numbers are converted back to the sensor temperatures from which they originated by applying the calibration factors for each bridge or thermocouple and each measuring channel. The sources of error to which the reconverted temperature values may be subject are as follows:

1. Platinum bridge error sources
  - a. Initial calibration accuracy
  - b. Element stability with age
  - c. Dissimilar metal electromotive forces at sense-wire connections
2. Measurement system error sources
  - a. Initial calibration of electronics
  - b. System noise
  - c. Spurious electromotive forces in multiplexer
  - d. Excitation voltage
    - (1) Stability
    - (2) Sense-attenuation stability
    - (3) Bridge heating
  - e. Amplifier
    - (1) Common-mode rejection
    - (2) Gain and offset stability

- (3) Linearity
- (4) Settling time
- f. Analog-to-digital converter
  - (1) Linearity
  - (2) Reference voltage stability
  - (3) Quantizing magnitude

3. Data-processing error sources

- a. Truncation errors
- b. Iterative solution accuracy of bridge equations

Ratio Measurement Technique

Errors due to long-term system gain and offset instability are circumvented by a scheme that paradoxically amounts to a calibration of each measuring channel by the unknown signal being measured. A ratio technique is used that eliminates system gain and offset as factors in the reconstitution of the original bridge ratio. The success of the technique depends only on gain and offset stability during the brief measurement period. All measurements are made twice (at two different levels). To utilize the full system range and obtain maximum resolution, it is convenient for each bridge input and output measurement to be made at reversed polarity and with equal bipolar excitation levels. The bridge is pulsed twice in 2.4 sec for 2.6 msec at a maximum duty cycle ( $0.2 \times 10^{-3}$ ) that limits self-heating to an acceptable  $0.1 \mu\text{W}$ ; two measurements are made during each excitation pulse. The sequence outlined in figure 10-6 for a high-sensitivity differential measurement is typical of all measurements. Power is applied to the bridge from the excitation-pulse supply at bipolar 4-V levels, which gives a positive 8-V total excitation. After 1 msec to allow the system to settle, the attenuator output  $V_E^+$  corresponding to excitation level  $V_E^+$  is converted to a digital number  $N_1$ . Output voltage  $V_O^+$  is then selected for measurement; and, after a 2.3-msec positive pulse duration,  $V_O^+$  conversion to  $N_2$  is executed. The entire process is repeated 2.4 sec from the start of the sequence with the pulse-excitation supply output reversed to -8 V; during application of this negative

pulse,  $V_E^-$  and  $V_O^-$  are converted to digital numbers  $N_3$  and  $N_4$ , respectively.

If  $G$  represents amplifier and analog-to-digital-converter gain

$$\begin{aligned} \frac{N_2 - N_4}{N_1 - N_3} &= \frac{G(V_O^+ + \epsilon_0 + \epsilon) - G(V_O^- + \epsilon_0 + \epsilon)}{G(V_E^+ + \epsilon_1 + \epsilon) - G(V_E^- + \epsilon_1 + \epsilon)} \\ &= \frac{V_O^+ - V_O^-}{V_E^+ - V_E^-} \end{aligned} \quad (10-8)$$

$$= \left( \frac{V_O^+}{V_E^+} \right) \left( \frac{1 - \frac{V_O^-}{V_O^+}}{1 - \frac{V_E^-}{V_E^+}} \right)$$

where  $\epsilon$  is the amplifier and analog-to-digital-converter offset,  $\epsilon_0$  is the output-sense-line offset, and  $\epsilon_1$  is the excitation-sense-line offset. Because the temperature of a bridge in the lunar regolith will not change during the 2.4-sec measurement period

$$\frac{V_O^+}{V_E^+} = \frac{V_O^-}{V_E^-} = C \quad (10-9)$$

where  $C$  is a constant regardless of the excitation magnitudes of  $V_E^+$  and  $V_E^-$ . Rearranging equation (10-9) to read

$$\frac{V_O^-}{V_O^+} = \frac{V_E^-}{V_E^+} \quad (10-10)$$

and combining equations (10-8) and (10-9) results in

$$\frac{N_2 - N_4}{N_1 - N_3} = \frac{V_O^+}{V_E^+} \quad (10-11)$$

where  $V_O^+/V_E^+$  is the ratio between measured bridge signals, independent of gain and offset. The required bridge ratio  $V_O/V_E$  is obtained by applying the excitation-sense measurement attenuation factor  $Z$ , the accuracy and stability of which clearly affect the result. Since  $Z = V_E'/V_E$ , then

$$\frac{V_O}{V_E} = \frac{ZV_O}{V_E'} \quad (10-12)$$

#### Other Design Features

The use of excitation-polarity reversal, with one data converter for all measurements, eliminates some major sources of error and obviates the need for separate periodic calibrations on the Moon and for additional circuitry with which to perform them. Nevertheless, numerous sources of error remain. It is therefore pertinent to summarize here the more significant features of the principal components of the data chain, which account for demonstrated measurement accuracies of better than 0.02 percent full-scale probable error over a temperature range of 273.15 to 333.15 K (0° to 60° C).

The pulsed-power supply produces 4000 V  $\pm$  1 mV bipolar pulses that are stable to within 0.002 percent during bridge excitation and output measurements. The supply operates from positive and negative reference levels, which are derived from constant-current-driven, low-temperature-coefficient zener diodes that are switched by the control logic for positive and negative bridge excitation outputs from two series-connected operational amplifiers. Each amplifier has a push/pull output stage to supply the 20-mA bridge current.

The multiplexer for the heat flow instrument is a double-tiered N-channel FET commutator, with 32 differential input pairs. It is divided into four sections, one for each probe set of gradient sensors and one each for the remote sensors and the thermocouples. Each FET section is powered only when necessary to restrict the effects of a single-channel failure. The FET

temperature-dependent offset voltages and mismatched differential impedances, which act with circuit impedances and amplifier bias currents to introduce variable offset voltages for each channel and different offsets between channels, are canceled by the ratio measurement technique previously described.

The most basic design trade-offs in analog-to-digital converter design are speed and accuracy; neither is of great consequence in this application, where extreme linearity, stability, and sensitivity are the only critical requirements. Digital conversion of the amplified sensor signals is achieved by 13-bit successive approximation to the sum of a generated  $+10.000 \text{ V} \pm 1 \text{ mV}$  offset supply and the  $\pm 10\text{-V}$  full-scale output from the data amplifier. The offset binary number produced is linear to within 0.0075 percent full scale, with a resolution of 2.4414 mV per bit. Conversion speed is 20  $\mu\text{sec}$  per bit. The device is a conventional successive-approximation analog-to-digital converter, with the two most significant bits of the ladder network trimmed to remove errors due to voltage drops across the switches.

The signals are amplified by a differential-input single-ended-output two-stage amplifier, with differential and common-mode impedances exceeding 50 and 20  $\text{M}\Omega$ , respectively, at frequencies below 5 kHz. The common-mode rejection ratio is greater than 120 dB over the same frequency range. The characteristics most important to the ratio technique are linearity, which is within 0.005 percent full scale, and short-term stability, which is better than 0.001 percent for 5 sec at a maximum rate of temperature change of 0.01 K/sec (0.01° C/sec). The common-mode rejection ratio becomes important when bridge current is sensed at 8-V excitation levels.

Constant-current sources are supplied to each base of the differential input pair to compensate for the bias current required by the matched semiconductors, but the more usual constant-current-source common-emitter supply is replaced with a variable current source that maintains the constant output of combined collector currents. The differential output from the collectors connects to an operational amplifier, the output of which feeds back to the emitters of the input stage to force the total of the collector currents to divide equally between the two halves of the differential pair. Stable operating points are thus established independently of common-mode inputs over a wide temperature range. The first-stage gain is 100. After filtering, the signal is applied to the input of the second-stage amplifier that normally operates with a gain of 2.88. The total amplifier gain of 288 is used for all bridge measurements.

Thermocouple measurements require an input range of  $\pm 10 \text{ mV}$  rather than  $\pm 34 \text{ mV}$ . During thermocouple sequences, therefore,

the second-stage gain is changed from 2.88 to 10 by switching an FET to introduce a potential divider in the feedback path of the second stage.

#### THERMOCOUPLE MEASUREMENTS

Eight Constantan and two Chromel wires from the thermocouple junctions in the probe cables connect to Kovar leads at an isothermal block inside the electronics package. The Kovar leads convey the thermocouple voltages to the multiplexer. The isothermal block also contains a platinum/Evanohm bridge thermometer with two constant-value resistance arms. A schematic that represents one probe-cable set of thermocouple junctions and the reference-temperature bridge is presented in figure 10-7.

Thermocouple measurements of absolute temperature have an inherent accuracy an order of magnitude lower than platinum resistance measurements in part because of thermocouple instability, but primarily because of difficulties in measuring low-level voltage sources. Because the ratio technique is not applicable to thermocouple measurements, a calibration method is used to establish system gain and offset during the measurement sequence to find the isothermal block temperature with the bridge thermometer.

Measurements on the reference-temperature bridge follow the same pattern as those on the probe bridges, except that the amplitude of excitation is attenuated to give a  $\pm 10$  mV full-scale output, which is the range of the thermocouple voltages. An amplifier nominal gain of 1000 is selected for reference-bridge and thermocouple measurements. To find system gain and error offset values, it is assumed that the attenuated positive and negative bridge excitation voltages  $V_E$  are of known, equal, and opposite magnitudes because they are derived from the precisely controlled pulsed-power supply and are connected to the bridge by short leads within the electronics package.

The sensed excitation signals  $v_e^+$  and  $v_e^-$  are converted by the analog-to-digital converter to binary numbers  $N_1$  and  $N_3$  in accord with the relationships

$$\left. \begin{aligned} N_1 &= \frac{G(v_e^+ + v_{\text{off}})}{u} \\ N_3 &= \frac{G(v_e^- + v_{\text{off}})}{u} \end{aligned} \right\} \quad (10-13)$$

where  $v_{\text{off}}$  is error offset voltage referred to the amplifier input and  $G$  is system gain. The full-scale, 13-bit binary output count is 0 to 8191, which corresponds to an offset amplified signal range of 0 to 20 V and gives a digit resolution  $u$  of 2.4414 mV. Gain is found from

$$G = \frac{u(N_1 - N_3)}{v_e^+ - v_e^-} \quad (10-14)$$

when the offset voltages cancel. To find the error offset voltage  $v_{\text{off}}$ , the offset binary outputs  $N_1$  and  $N_3$  are converted to positive and negative numbers by subtracting offset count 4096. If  $N_1' = (N_1 - 4096)$  and  $N_3' = (N_3 - 4096)$ , then

$$v_{\text{off}} = u \frac{N_1' + N_3'}{2} \quad (10-15)$$

The use of known balanced inputs in the reference bridge measuring sequence thus establishes system gain and offset. The measured outputs are converted through electronics calibration data, and the bridge voltage ratio is then used to solve iteratively a third-order calibration equation for reference-bridge temperature and hence for isothermal-block and reference-thermocouple temperature. Measurements of thermocouple voltages made shortly thereafter (in the sequence  $N_1$ ,  $N_2$ ,  $N_3$ , and  $N_4$  as shown on the fig. 10-7 schematic) are processed by using calculated gain and offset values to arrive at true thermocouple voltage outputs.

The output from the Chromel/Constantan reference junction in the isothermal block is measured relative to only one of the junctions in the cable — the junction inside the hollow of the gradient sensor at the top of the probe. The remaining three junctions in each probe cable are also measured relative to this top junction. The double-referencing arrangement is designed to center the mean of the thermocouple output extremes close to 0 V for maximum measurement resolution. The predicted temperature range for the thermocouple junction at the top of the probe is 200 to 260 K; the full-scale thermocouple range is 90 to 350 K, and the isothermal-block temperature is controlled to between 278 and 328 K.

The voltage/temperature characteristics of the thermocouples are described by calibration correction factors applied to standard tables of the National Bureau of Standards (NBS).

#### PACKAGE CONSTRUCTION AND THERMAL CONTROL

The heat flow instrument operates from a 29-V dc supply and requires data-interlace and mode-control signals from the ALSEP central station. The unit is otherwise self-contained with respect to logic and power management for all the sensor measurements and for probe-heater control.

In the deployed configuration, a ribbon cable consisting of 40 flat copper conductors in a plastic film extends from the instrument package across 9 m of the lunar surface to the ALSEP central station. This cable is connected to an astronaut connector that the astronauts mated with the ALSEP central station outlet for power to and communication with the heat flow instrument.

The two probe cables each consist of 35 unshielded conductors, interwoven for a uniform stress distribution so that the weight of the astronaut can be supported without degradation in cable performance. These cables are very flexible and exhibit little residual torque when extended; they are covered with a woven Teflon sleeve to provide a low coefficient of friction during deployment. Heatleaks from the cables on the lunar surface to the probes and the electronics package are small because the conductors are made from wire that has low thermal conductivity.

#### Electronics Package

The electronics package is made up of five multilayer printed-circuit boards that are joined in a stack by interlocking spacers bonded to each board. The stack is 6 by 19 by 14 cm (2.5 by 7.6 by 5.6 in.); the boards consist of as many as

12 layers, each 0.1 mm (0.004 in.) thick. The layers of circuit tracks are interconnected through plated holes in the composite board, and as many as 210 component subpackages are mounted on one board. The components are in physical contact with a heavy printed-circuit conductor that forms a heat path to the interlocking spacers. Column screws pass through the spacers to a metal plate that serves as a thermal control plate and as a support for the board stack. A dc/dc converter for the instrument power supplies is packaged on a board that is bonded to the thermal control plate. Heating elements are also mounted in good thermal contact with the plate. A short length of Manganin cable provides thermal insulation from the copper conductors in the ribbon cable. Bonded to the thermal control plate at the other side of the unit is a 70-pin isothermal connector to which the two probe cables are soldered. When the unit is assembled, the board stack is enclosed by a metal cover with a compressible, electrically conducting gasket to provide a barrier to electromagnetic interference.

#### Thermal Control Design

A thermal insulation bag, shaped as a container for the metal cover surrounding the board stack, is hooked by Velcro pads to a low-thermal-conductivity mounting ring fitted around the inside edge of the thermal plate. The bag is constructed of 12 layers of closely spaced, high-reflectivity shields that have very low transverse conductivity; bridal-silk netting separates the layers and covers the inside and outside of the bag. The IR emissivity of the 0.00064 cm (0.25 mil) aluminized Mylar used for the shields is approximately 0.02.

The electronics assembly is supported and protected by a thin fiberglass outer case that is connected to the mounting ring by low-conductivity joints. When the unit is standing on the feet of this outer case, the well-insulated electronics compartment is situated beneath the exposed thermal control plate. Internally generated heat is conducted to the plate and radiated from a spectrally selective surface coating having a high IR emittance ( $\epsilon_{IR} = 0.9$ ) and a low absorptance ( $\alpha_s = 0.2$ ) at frequencies where solar power is most intense.

This simple thermal control arrangement could not modify the extreme heat of solar radiation as well as the cold of deep space in the tenuous atmosphere of the Moon to meet the required electronics-temperature operating range (278 to 328 K) without using excessive power during lunar night or permitting the upper limit to be exceeded during lunar day. The thermal plate is therefore protected from direct solar radiation by a sunshield fitted over the assembly. The sunshield is an insulated box with one open side, which is placed to face away from the equator with its edge aligned in the east/west direction. The numbered marks

on the sunshield are used as a shadowgraph; the shadow is cast by the universal handling tool that fits into the center socket. A specular reflector slopes from the top edge of the sunshield at an angle of  $57^\circ$  from vertical and almost touches the thermal plate. The reflector increases the view of the thermal radiator plate to the near-absolute-zero temperature of space and minimizes the lunar-surface-radiation reflections that reach the thermal plate from the exposed inside surfaces of the enclosure. The side curtains adjoining the sloping reflector are also specular surfaces. The reflecting mirrors are produced by a vacuum process in which a thin layer of aluminum is deposited on polished fiberglass. The back of the reflector and the thermal control plate inside the sunshield are heavily blanketed with aluminized Mylar, layered in the same way as in the thermal bag. The concealed interior surfaces of the sunshield are also coated with metal by a vacuum process to reduce radiant interchange of IR energy inside. The exterior surfaces of the entire package are covered with thermal control coating.

A mast of multilayer insulation is attached to the edge of the thermal plate to prevent direct sunlight from reaching it in the event of a moderate misalignment from an east/west line or an instrument-leveling error. To aid in leveling in the stark lighting of the Moon, the bubble level situated at one corner on a recessed platform is illuminated by reflection of sunlight from the vertical wall of the step.

The thermal control design for the heat flow instrument is dictated largely by the power dissipation of the unit at lunar noon. The average dissipation is minimized by gating off as many circuits as possible when they are not required for measurements. During power gating, the average operational power dissipation is 3.9 W. The power-sharing mode is set to switch in when thermal plate temperatures exceed 300 K. During lunar night, when the electronics temperature falls below 290 K, additional power is dissipated by the heaters on the thermal control plate. The thermal control system is designed for instrument deployment between lunar latitudes of  $\pm 45^\circ$ .

#### CALIBRATION AND TESTING

To ensure that the heat flow instrument would meet its performance requirements, the calibration and test program was extensive and thorough. A substantial part of the large array of calibration and test apparatus used was developed specifically for this purpose. The sensors, probes, and electronics were subjected to worst-case mission environments and were calibrated as subunits before assembly as flight instruments. The subassembly calibrations were verified by tests on the complete unit, which then underwent a further series of tests closely simulating all the

conditions anticipated for travel to and operation on the Moon. After exposure to such critical environments as system vibration, the stability of the instrument was carefully checked.

### Sensors

The platinum resistance thermometers were calibrated as a bridge by a comparison method. Each sensor, together with a standard thermometer, was immersed in an isothermal bath of trichloroethylene. The baths had separate temperature controls so that temperatures could be independently set for each thermometer of the differential bridge. The standard thermometers were interchanged for several measurements to determine offset. The unit of measure (Kelvin) was established from standard thermometers calibrated by the NBS. Secondary absolute-value resistance standards of 1000  $\Omega$ , referenced to an NBS standard, were maintained for the electrical measurements.

To check for random errors, each gradient bridge was calibrated at 42 points, which were least-squares fitted to equations (10-6) and (10-7) to yield the 12 constants in these equations. The standard deviation of the least-squares fit to the data points in equation (10-6), did not exceed  $0.48 \times 10^{-3}$  K for any of the sensor assemblies tested, and more than 60 such assemblies have been produced. The gradient bridges were calibrated at differential temperatures of +20, +10, +2, 0, -1, -2, -10, and -20 K; they were calibrated at absolute temperatures of 200, 212.5, 225, 237.5, and 250 K. The equivalent differential-temperature drift of some randomly selected gradient sensors tested periodically at 200 and 270 K over a 3-yr period was approximately  $0.3 \times 10^{-3}$  K. The average absolute-temperature drift for individual sensor elements over the same 3-yr period was  $0.5 \times 10^{-3}$  K. The ring sensors were calibrated at a minimum of 14 points to calculate 12 calibration constants.

Thermal-plate reference-temperature bridges in the electronics package were calibrated at 253, 273, 298, 323, and 363 K (-20°, 0°, +25°, +50°, and +90° C) to yield the constants  $X_1$ ,  $X_2$ ,  $X_3$ , and  $X_4$  in the relationship

$$\frac{V_O}{V_E} = X_1 + X_2(T_R) + X_3(T_R)^2 + X_4(T_R)^3 \quad (10-16)$$

where  $T_R$  is the reference bridge temperature and  $V_O/V_E$  is the bridge voltage ratio. During reference-bridge calibration at 273 K (0° C), all eight cable thermocouple junctions were immersed in an isothermal bath for calibration at 90, 200, 250, and 350 K.

### Electronics

Testing of the electronics data chain involved adjustment by resistance-value selection for zero offset, common-mode rejection, and gain. A calibration factor was found for each measuring channel by calibrating the channel as it would be used; that is, by performing ratio measurements. A set of resistance networks, calibrated to an accuracy of 0.002 percent, was substituted for bridge and line resistances to simulate high-sensitivity and low-sensitivity ratios and bridge resistance. The various types of measurements were made through separate channels. Calibration was performed at 9 different differential-ratio amplitudes and 5 levels of bridge resistance; at least 10 measurements were made for each of the input ratios. The mean  $\bar{m}$  and standard deviation  $\sigma$  of the output ratios for a constant input were calculated, and a linear calibration factor was found from the mean values corresponding to ratios near the limits of channel range ( $n = 1$  and  $n = 9$  in fig. 10-8). The ideal transfer function of the channel was the calibration factor. The error at any point  $n$  was defined as the difference between the ideal output  $R_1(n)$  and the mean output  $\bar{m}(n)$ , summed with the standard deviation  $\sigma(n)$ . To verify system linearity, these measurements were made at temperature intervals throughout the operating range of the heat flow instrument. A maximum error of 0.0375 percent full scale was specified, but the typical maximum for instruments tested to date has been 0.02 percent. Calibration factors were modified for the actual bridge-lead resistances. Thermocouple channel accuracy was also checked by multiple measurements at nine points throughout the  $\pm 10$  mV input range.

### Probes

Assembled probes were characterized over ambient- and differential-temperature operating ranges in a temperature-gradient apparatus (gradient chamber) that had an overall height of 3.4 m (11 ft) and a diameter of 0.6 m (2 ft). The probes were inserted in a gradient tube (2.5 cm internal diameter) in which a positive or negative temperature field could be developed. A liquid-nitrogen bath surrounded the gradient-tube assembly to provide a constant-temperature heat sink for heat introduced in developing average and linear differential temperatures. A double-vacuum shell minimized heatleaks and permitted the probe to be inserted without unduly disturbing the thermal equilibrium. Thermocouples

and thermopiles in the gradient tube, along with associated readout instrumentation, provided accuracies of temperature measurement that approximated those of the heat flow instrument. Probe-measured differential temperature was compared with apparatus-measured differential temperature in the form of a "shorting" ratio, which was approximately a linear function of the absolute temperature along the gradient; the probes were radiatively coupled to the gradient tube. This shorting ratio varied from bridge to bridge because of small differences in probe construction. The probes were tested at mean ambient temperatures of 205, 225, and 245 K, with linear gradients of 0, 2, and 18 K across each probe half-section. At least five tests were performed with each flight-instrument probe, including two tests in which the probe was integrated with electronics. Tests in the gradient chamber at 0 K checked the zero offset of the gradient bridges and determined the offset values for the ring bridges, the cables of which were shortened during probe assembly. Each of the probe heaters was turned on at the 0.002-W level by the electronics to characterize the low-conductivity performance of the probe in an infinitely conducting environment, which the gradient-tube apparatus represented since it was an almost perfect heat sink.

Thermal conductivity testing was also performed in an apparatus that simulated the properties of the lunar regolith. In essence, this thermal conductivity test apparatus was a 3.2- by 0.9-m (10.5- by 3-ft) Dewar flask, with inner-vessel-wall cooling to the temperature range 200 to 250 K. A probe boretube extended into a bed of glass microbeads in the inner container. The outer cavity and the boretube were evacuated, and the thermal conductivity of the glass-bead bed was varied over the anticipated lunar range by controlling the gas-filling pressure. Two thermal conductivity test units were constructed to permit the simultaneous testing of the two probes of a heat flow instrument.

#### Heat Flow Instrument

For functional testing of the probes and the heat flow instrument as a whole, thermal simulators were used to provide a stable temperature environment for the probes in the lunar-temperature operating range. Each simulator was an insulated container 2.5 m (8 ft) deep, filled with solid carbon dioxide and ethanol, in which a heavy metal double boretube was vertically situated. The ethanol fluid stabilized at the temperature of the subliming dry ice that it surrounded. Because the temperature of sublimation is a function of pressure, the fluid temperature increased with depth to impose a gradient along the boretubes. Thermocouples and thermopiles within the metal block measured the temperature profile along the tubes. The laboratory thermal simulator had a compartment for the electronics package so that the whole instrument could be operated in a vacuum. When inserted

into the boretubes, the two probes of the instrument were in a similar, uncontrolled but slowly changing temperature field; and comparisons could be made of processed measurements on the probe bridges at given heights in the bath.

A comparable simulator was built into an adjunct of an 8.3- by 6.2-m (27- by 20-ft) thermal vacuum chamber. During ALSEP system testing, the heat flow electronics package was deployed inside the main chamber, with the probes situated in the stabilized thermal simulator boretubes. The entire ALSEP system, including the heat flow instrument, was exposed to the temperature conditions of lunar dawn, lunar noon, and lunar night in a vacuum of  $6.7 \times 10^{-6}$  N/m<sup>2</sup> ( $5 \times 10^{-8}$  torr). Cold space was simulated in the chamber by pumping liquid nitrogen under pressure through black, optically tight panels. Solar heat was simulated by the use of carbon arc lamps, and dust degradation on instrument surfaces was simulated by subjecting them to additional IR radiation.

Table 10-III presents a comparison of thermal-simulator temperature measurements made in a changing temperature environment by the heat flow instrument probes and electronics package during simulated lunar-night testing of the Apollo 16 ALSEP system. The means of the differences between the temperatures measured by adjacent bridges, which have been corrected for bridge shorting ratio, and the standard deviations from the means are tabulated. The very small differences noted may have been caused by differences in the transient responses of the two probes; by different probe responses to nonlinear gradients; or by slightly different temperature fields, the result either of inherent differences between the apparatus boretubes or of different times of measurement. Aside from these factors, the probe-measurement differences reflect the consistency of total instrument calibration, stability, and signal processing.

The low-sensitivity measurements on the upper gradient bridges illustrate an effect of data averaging that is generally seen in heat flow instrument test results. Although resolution in the  $\pm 20$  K range is 10 times less than in the high-sensitivity range — a fact reflected by the standard deviations — the averages are about the same in the two ranges. The number of measurements that did not follow this pattern decreased as the number of data cycles increased. Thus, system resolution was effectively increased by multiple-measurement averaging in both the low- and high-sensitivity ranges. Use of this technique can result in an effective resolution that is better than analog-to-digital-conversion quantization would allow for a single measurement.

During the simulated lunar-night test in which these results were obtained, the probe cables were lying in an uncontrolled temperature zone. There is little value, therefore, in comparing thermocouple readings 2, 3, and 4. However, the mean of the

measurement differences for the thermocouples situated at the top of the probes (0.073 K) relative to the single-measurement resolution of 0.17 K again demonstrates the data-averaging effect. The readings also provide a good comparative check of the thermocouples.

## OPERATIONAL HISTORY

### Apollo 15

Probe configuration.- The heat flow probes were not buried to the planned depth of the experiment because of difficulties in drilling holes into the regolith. A map of the probe placement relative to other ALSEP experiments is shown in figure 10-9, and the subsurface configuration of the probes is shown in figure 10-10.

Initiation of the experiment.- Times important to the initiation of the Apollo 15 experiment (in 1971) are as follows:

<u>Event</u>	<u>Day</u>	<u>Hr, G.m.t.</u>
Probe 1 insertion	212	18.78
Probe 2 insertion	213	17.28
Instrument turn-on	212	19.47

Ring-bridge surveys.- In mode 1, full sequence, the temperatures at the ring-bridge sensors are not measured. To obtain measurements at these thermometers, the experiment is periodically commanded to mode 3 with heaters off, and all bridge sensors are sampled by sending the appropriate sequence of commands. This procedure is called a ring-bridge survey. Initially, the surveys were taken frequently, every 6 hr; they have been continued to the present time with a longer interval between samples. The routine schedule beyond the real-time postmission support is three ring-bridge surveys weekly.

Conductivity measurements.- During real-time support, conductivity experiments at low power, 0.002 W, were run on the following schedule:

Heater location	Depth, cm	Heater on -		Heater off -	
		Day	Time, hr:min, G.m.t.	Day	Time, hr:min, G.m.t.
1971					
H11	35	242	17:00	243	17:00
H12	83	247	05:04	248	16:55
H13	91	238	04:58	239	16:57
H14	138	245	05:01	246	16:55
H23	49	236	05:00	237	17:01
H24	96	250	05:00	251	17:00
1972					
<sup>a</sup> H11	35	073	15:01	075	15:00
<sup>a</sup> H12	83	045	14:42	047	02:26

<sup>a</sup>These positions were rerun because they were strongly affected by diurnal variations, and more optimal times were selected to decrease transient variations during the observation.

Eclipses.- During total eclipses, the experiments are commanded into the thermocouples-only mode.

Photographs used in analysis.- The following lunar surface photographs were used in the analysis: AS15-87-11849, 87-11860, 92-12407 to 92-12409, 92-12416, and 92-12421. These photographs are available at the National Space Science Data Center (NSSDC).

#### Apollo 16

The cable connecting the heat flow electronics package with the ALSEP central station was inadvertently broken during ALSEP deployment activities, rendering the experiment hardware inoperative.

## Apollo 17

Probe configuration.- The probes were both buried to the desired depth. A map of the probe placement relative to other ALSEP experiments is shown in figure 10-11, and the configuration of the probes in the subsurface is shown in figure 10-12.

Initiation of the experiment.- Times important to the initiation of the Apollo 17 experiment (in 1972) are as follows:

<u>Event</u>	<u>Day</u>	<u>Hr, G.m.t.</u>
Probe 1 insertion	347	02.730
Probe 2 insertion	347	03.133
Instrument turn-on	347	03.033

Ring-bridge surveys.- Ring-bridge surveys are run on approximately the same schedule as that of the Apollo 15 experiment.

Conductivity measurements.- All eight experiments at low power were run during the real-time support period (1973) by the following schedule:

Heater location	Depth, cm	Heater on -		Heater off -	
		Day	Time, hr:min, G.m.t.	Day	Time, hr:min, G.m.t.
H11	130	003	05:58	004	18:00
H12	177	014	00:03	015	11:48
H13	185	021	00:03	022	12:31
H14	233	008	06:21	009	16:02
H21	131	005	05:18	007	06:07
H22	178	016	12:06	018	00:05
H23	186	023	00:31	024	12:30
H24	234	010	05:59	011	17:59

On day 25, 1973, at 18:00 G.m.t., H14 was turned on at high power, 0.5 W. After 3 hr of observation, the ring bridge (DTR12) went off-scale high and the heater was shut off at 20:30 G.m.t.

Photographs used in analysis.- The following lunar surface photographs were used in the analysis: AS17-134-20493 to 20497, 147-22590 to 22600, 147-22602, and 147-22603. These photographs are available at the NSSDC.

#### INSTRUMENT MALFUNCTIONS

Instrument malfunctions as of December 10, 1973, were as follows:

1. Apollo 15: The data channel for the reference thermometer stopped operating August 7, 1971. This channel is redundant, and no data have been lost.
2. Apollo 16: The cable was broken at the ALSEP central station plug. One probe was deployed. The instrument is inoperative.
3. Apollo 17: The only significant problem is the very high noise level of the thermocouples during the lunar day just before noon.

#### SUMMARY OF RESULTS

During the Apollo missions, two heat flow measurement sites were successfully established on the lunar surface. Both measurement sites are in similar regional settings in the northeast quadrant of the Moon. The Taurus-Littrow and Rima Hadley sites are located in embayments in the mountainous rims of the Imbrium and Serenitatis mascon basins that have been flooded by mare-type basalts.

Surface brightness temperatures were calculated from the temperature of the thermocouples suspended several centimeters above the lunar surface. The mean surface temperature at Rima Hadley throughout a lunation cycle is 207 K. The mean temperature increases with depth very rapidly in the upper few centimeters and is approximately 252 K at a depth of 90 cm. The main reason for this increase of 45 K is the predominant role of radiative heat transfer in the loosely packed upper layer. During the lunar night, the surface temperature at Rima Hadley falls to 93 K. From the cooldown history after sunset, it was deduced that the upper 2 cm of the regolith is characterized by a conductivity of  $1.5 \times 10^{-5}$  W/cm-K. Below this depth, the conductivity increases rapidly and probably in a continuous manner until it reaches values of approximately  $1.5 \times 10^{-4}$  W/cm-K at depths where the probes are emplaced.

At Taurus-Littrow, the mean surface temperature is 216 K and, as in the case of Rima Hadley, increases a few tens of degrees in the upper 2 cm so that, at a depth of 67 cm, a mean temperature of 254 K is measured. The minimum temperature just before lunar dawn is 103 K, 10 K higher than that at Rima Hadley. This higher temperature is primarily attributable to the existence of a relatively high conductivity layer at a depth 2 cm below the surface. From the point of view of thermal properties, the regolith at Taurus-Littrow can be described as two layers: (1) an upper 2-cm, loosely packed layer of very low conductivity ( $1.5 \times 10^{-5}$  W/cm-K) in which heat transfer by radiation predominates and (2) a lower layer with much higher conductivity ( $>1.2 \times 10^{-4}$  W/cm-K) and higher density (1.8 to 2.0 g/cm<sup>3</sup>).

Subsurface temperature and conductivity measurements at depths below 90 cm, where the large diurnal variations are negligibly small, indicate a steady-state heat flow through the surface at Rima Hadley of  $3.1 \times 10^{-6}$  W/cm<sup>2</sup> and at Taurus-Littrow of  $2.8 \times 10^{-6}$  W/cm<sup>2</sup> with an estimated error of  $\pm 20$  percent. Temperature and conductivity data are given in tables 10-IV to 10-VIII. These fluxes are deduced from average temperature gradients in the regolith between 1.3 and 1.7 K/m and an average conductivity in the range of  $1.7 \times 10^{-4}$  to  $2.0 \times 10^{-4}$  W/cm-K. Conductivity generally increases with depth in the regolith, although some layering (high conductivity materials overlying lower conductivity materials) is found at both sites. A conductivity value of almost  $3 \times 10^{-4}$  W/cm-K was measured at the bottom of probe 1 at the Apollo 17 site. In some cases, thermal gradients decrease with depth in response to the increase in conductivity. At Taurus-Littrow probe site 2, a large decrease in gradient with depth is possibly attributable to a large subsurface boulder close to the probe.

The heat flows at both sites are affected to some extent by local topography. Preliminary estimates indicate that a correction of -15 to -25 percent may be applicable to the Taurus-Littrow values because of the adjacent massifs. However, a more refined analysis is required.

The heat flow measured at the two sites is approximately one-half of the average heat flow of the Earth ( $6.3 \times 10^{-6}$  W/cm<sup>2</sup>). If these two values are representative of heat flow from the Moon as a whole, then a heat flow of one-half that of the Earth requires a heat production per unit mass for the lunar interior of more than twice that of the Earth. This statement assumes both planetary bodies are near steady state so that total surface heat loss is nearly equal to the present interior heat production.

Because the long-lived radioisotopes of potassium-40, uranium-235, uranium-238, and thorium-232 are the principal source of heat in the Earth and Moon, the heat flow results imply a two-fold to threefold enrichment of uranium in the Moon relative to that in the Earth. Lunar samples show that the abundance of potassium relative to uranium is one-third to one-fourth that of the Earth so that, in the Moon, uranium is the main contributor to internal heating. At present, these isotopes must be concentrated in the outer 100 to 200 km of the Moon to avoid extensive melting at shallow depth.

Reinterpretation of Earth-based measurements of microwave brightness temperatures using the new data on regolith thermal and electrical properties will be important in determining the representativeness of the in situ lunar heat flow measurements. Additional and more refined microwave observations of the Moon, especially narrower beamed measurements over discrete portions of the lunar disk, would be valuable in determining possible variations of heat flow over the lunar surface.

#### LONG-TERM DATA ANALYSIS

Figure 10-13 shows the 3.5-yr absolute temperature histories at representative Apollo 15 and 17 probe sensors. Three distinct temporal components are apparent in the data: (1) A diurnal component (period = 29.53 days) is evident at the sensors closest to the lunar surface. Below approximately 80 cm, the almost 300 K peak-to-peak surface variation is attenuated to a level below the noise of the absolute temperature measurements. (2) Temperature variations of 1-yr period are detectable at all sensors within 120 cm of the surface. Although the annual variation in mean surface temperature due to the eccentricity of the Earth-Moon orbit about the Sun is only approximately 3 K peak-to-peak, the amplitude attenuation is only  $1/\sqrt{12.37}$  that of the diurnal variation. A significant annual component is evident in the more accurate temperature difference data at depths up to 200 cm at the Apollo 17 site. (3) At all sensors, there is an aperiodic temperature rise that is characterized by a decreasing magnitude and increasing time delay before onset at greater depths. These transients were initiated during experiment emplacement when astronaut activity disrupted the thermal and radiative properties of the surface material surrounding each borestem. The subsequent effects of local changes in mean surface temperature are detectable at all subsurface sensors. It is estimated that reequilibration of the deepest sensors to the new steady state regime will require 5 to 7 yr.

## Refinement of Subsurface Temperature Profiles

The identification and removal of diurnal, annual, and transient variations and the corrections for shallow sensor radial fluxes allow reliable temperature profiles to be calculated at the Apollo 15 probe 2 site and the upper section of probe 1. Only the probe 1 lower-section results have been previously reported for Apollo 15. Figure 10-14 shows the steady-state temperature profiles at the Apollo 15 and 17 sites. Corrections at the Apollo 15 probe 1 lower section and at both Apollo 17 stations due to transient and annual effects were quite small (less than 5 percent) and the results are largely unchanged from those reported previously (refs. 10-1 and 10-2).

The temperatures shown at 65 cm at the Apollo 17 stations are thermocouple measurements that are substantially less accurate than the probe sensor results. Except for probe 2 of Apollo 17 (65-cm temperature), all profiles are remarkably linear, suggesting a vertical uniformity of bulk regolith thermal properties at probe depths. The gradients indicated were calculated from a linear least squares fit to the probe sensor results. The anomalously low gradient at the Apollo 17 probe 2 appears to increase significantly at shallower depths and may indicate a local disturbance to the heat flow, because no comparable change in thermal conductivity is indicated by the analysis.

## Revised Regolith Conductivity and Lunar Heat Flow

The determination of regolith conductivity from the revised diffusivity results requires specification of the regolith volumetric heat capacity. The specific heat of a number of lunar particulate samples have been measured (ref. 10-3). Results indicate substantial variation with temperature but almost no variation from sample to sample. A value of 0.67 W-sec/g-K, measured at 250 K, is used for all probe depth conductivity calculations.

The bulk densities of drill core samples have been reported by Carrier (ref. 10-4). The results from the Apollo 15 drill core indicate densities that range from 1.75 to 1.84 g/cm<sup>3</sup> from depths of 40 to 160 cm. Because of disruption of the soil during drilling, these data probably represent minimum estimates of the in situ values. Maximum density measurements on Apollo 15 soils of 1.89 ± 0.03 g/cm<sup>3</sup> were obtained by Carrier (ref. 10-4). Thus, a reasonable range of densities to use for converting the Apollo 15 diffusivity estimates to thermal conductivities is 1.75 to 1.90 g/cm<sup>3</sup>. Similar results for Apollo 17 soils lead to an estimated range of 1.83 to 2.09 g/cm<sup>3</sup>.

Revised results are shown in figure 10-15. On the left, the thermal conductivities deduced from the long-term analysis are compared with the point measurements made by the heater experiment designed into the probe and reported earlier. Notice that these new determinations are significantly lower than the earlier measurements. The fact that the difference between the old and new measurements increases with depth suggests that the difference may be due to increasing compaction of the regolith around the drill stem as the stem penetrated deeper and deeper.

Revised (solid line) and preliminary (dashed lines) heat flow results are shown at the right in figure 10-15. The lowered heat flow values are accounted for almost entirely by the revised conductivity determinations. At the Apollo 15 site, a heat flow value of  $2.1 \mu\text{W}/\text{cm}^2$  is the mean of the two probe measurements; and, at Apollo 17, the probe 1 value of  $1.6 \mu\text{W}/\text{cm}^2$  is considered the more reliable measurement. Errors of the measurements, deriving primarily from the resolution constraints of the annual wave diffusivity deductions, are estimated at  $\pm 15$  percent.

#### FUNCTIONAL FLOW OF DATA REDUCTION

A flow diagram for the reduction of one lunation of data is given in figure 10-16. Descriptions of the computer programs are given in the following paragraphs.

#### PROG6 (Diagnostic Dump of JSC Tape)

The PROG6 program reads the NASA Lyndon B. Johnson Space Center (JSC) tape and prints the header records and the data records on an online printer. The printout includes record number, time, station identification, bit error rate, data rate, frame number, and ALSEP word 33 (that is, word 33 (ordinal) of the 64 10-bit binary words (640 bits) that constitute one frame of the ALSEP bit stream which spans an interval of 54/90 sec). The ALSEP word 33 is given as a decimal equivalent of 10 binary bits. The program recognizes end of tape (EOT) marks and will call exit upon encountering one. The following errors generate error messages:

1. Permanent read error in a record (code = 3)
2. Short record (code = 7)
3. Long record (code = 5)

### PROG8 (Intermediate Reduction) and Intermediate Data File

The PROG8 program reads the JSC tape and prints the header record on an online printer. Further (optional) printout includes record numbers (in and out), time, station identification, bit error rate, data rate, frame number, and ALSEP word 21 (that is, word 21 (ordinal) of the 64 10-bit binary words (640 bits) that constitute one frame of the ALSEP bit stream which spans an interval of 54/90 sec). The ALSEP word 21 is given as a decimal equivalent of 10 binary bits. The program recognizes EOT marks and will call exit and rewind the JSC (input) tape upon encountering an EOT. The following errors generate error messages and stop execution:

1. Permanent read error in a record (code = 3)
2. Short record (code = 7)
3. Long record (code = 5)

The output of this program, which is stored in the "Intermediate data file (disk file 19)," is the same data that appear in the (optional) printout.

The usual sampling sequence for the HFE (mode 1, sub-sequence 1; or full sequence) includes all the data points except those for the ring bridges. A full sequence covers an interval of 7.2 min in the ALSEP bit stream. (Two consecutive ALSEP 21 words are required for one "N-value"; four consecutive N-values constitute one data point; one full sequence consists of 16 consecutive data points; and the HFE has allocated to it frames 0 through 15 of every 90 frames (54 sec).) The routine reduction procedure only stores every eighth usable full sequence of data in file 19. If the full density option is being exercised, or if the sampling sequence is other than usable mode 1 sub-sequence 1, all the available data are stored in file 19. There are also provisions for printing and/or storing and/or dumping bad or unusable data if such is desired.

### PROGP (Complete Reduction) and Reduced Data File

The PROGP program reads the "Intermediate data file (disk file 19)" and reduces the ALSEP 21 words to temperatures and temperature differences. The reduced data for one lunation are stored on tape and in disk file 17. Associated with each complete sequence of data points is the time corresponding to when the sequence began and a code word containing mode, sub-sequence, and heater state. (The disk data contain the mode and sub-sequence information implicitly and do not contain the heater state information.) The routine reduction procedure reduces all the data

that are in disk file 19 unless it is considered necessary to reduce the data density further (e.g., to satisfy storage requirements (2400 records in disk file 17 or one tape per lunation)) in which case any desired density can be obtained for a particular sampling mode and sub-sequence. The online printout for PROGPs consists of mode changes, reduced data sequences (optional), and/or errors that occur therein (optional), and/or bad or unusable data (optional). There are also provisions for storing and/or dumping bad or unusable data if desired.

#### DATAL (Postreduction Processing), Lunation Printout, and Lunation Plots

The DATAL (datalook) program has three independent functions all of which operate on or from disk file 17 (reduced data for one lunation):

1. Reading the reduced data tape for a lunation and storing the data in file 17. This function is rarely used and is intended primarily to cover mistakes in the routine postreduction processing.

2. Printing all the reduced data for one lunation on the online printer from file 17. Two copies of this printout are routinely made; one for the permanent reduced data file at the Lamont-Doherty Geological Observatory (L-DGO) and one for NASA. The printout format consists of two identical title pages that specify lunation, days of the year spanned by the lunation, and the year in which the lunation occurs, followed by the lunation data in the following three sets.

- a. Probe 1 data for modes 1 and 2 with summary statistics.
- b. Probe 2 data for modes 1 and 2 with summary statistics.
- c. Mode 3 data for both probes with summary statistics

3. Plotting all the reduced data for one lunation from disk file 19. The original plot is stored in the L-DGO permanent reduced data file. Three 50-percent (black-and-white) reproductions are made for distribution to the principal investigators and other interested people. The data for each sensor (or pair of sensors in the case of gradients) are plotted separately except for the thermocouples, four of which are superposed on one grid with the reference bridge temperature for that probe. The plots are arranged to facilitate comparison of sensor data for different sensors. Superposed on the time axis of each plot is a Sun angle

grid for relating sensor data with the Sun's position as seen from the experiment.

#### HFA21, HFA22, and the Master Disk Files

The HFA21 and HFA22 programs transfer to master disks OA21 (probe 1) and OA22 (probe 2), respectively, the lunation of data residing in the reduced data file (disk file 17). The data for each pair of sensors are stored in a separate file except in the case of thermocouples, which are all stored in one file with the corresponding reference bridge temperature for that probe. The data in each file are in chronological order. There is also a file of file pointers for bookkeeping purposes. When the data are transferred, two modifications are performed.

1. The correct time for each data point is computed by adding a constant to the time the data point sequence began, where the constant depends on when the data point occurs in the sequence. This correct time is stored with the data on the master disk.

2. The temperatures and temperature differences are converted to integer values, which permits storage of up to 3 yr of data for one probe on one disk.

#### THE L-DGO MASTER DISK ORGANIZATION

For each experiment, all data are stored on two L-DGO master disks, one for each probe. Each disk can hold approximately 3 yr of data, and each disk consists of six files that are described as follows.

<u>File</u>	<u>Description of data</u> <sup>2</sup>	<u>Length of record</u>	<u>Maximum number of records in file</u>
1	T and $\Delta T$ of upper section gradient bridge	4 disk words <sup>3</sup>	30 000
2	T and $\Delta T$ of lower section gradient bridge	4 disk words	30 000
3	Thermocouple temperatures	8 disk words	30 000
4	T and $\Delta T$ of upper section ring bridge <sup>4</sup>	4 disk words	1 200
5	T and $\Delta T$ of lower section ring bridge <sup>4</sup>	4 disk words	1 200
7	Present record count for each file and time of last record on disk	7 disk words	1

#### THE L-DGO NSSDC TAPES

The L-DGO tapes prepared for NSSDC are described here. Machine format specifications: 7 track, 800 bpi, standard IBM interrecord gap, odd parity, data convert "on," translate "off." There is no end of file.

<sup>2</sup>The first two disk words in each record on files 1 to 7 give the time in milliseconds since 00:00 January 1, 1971, for Apollo 15; since 00:00 January 1, 1972, for Apollo 17 as a floating point variable.

<sup>3</sup>To save space, the data are converted from real to integer format by multiplying by an appropriate power of 10 and truncating the meaningless fractional part (which is smaller by an order of magnitude than the precision of the apparatus).

<sup>4</sup>Each data point in this file is the average of about 10 contiguous values measured during a ring-bridge survey.

Data organization: There is one 183-m (600-ft) tape for each probe, and there are five groups of data on each tape. (Size of physical record for each group equals 100 logical records.)

<u>Group</u>	<u>Type of data</u>	<u>Size of logical record</u>
1	Time, T, and $\Delta T$ of upper section gradient bridge	3 real words
2	Time, T, and $\Delta T$ of lower section gradient bridge	3 real words
3	Time, T, and $\Delta T$ of upper section ring bridge	3 real words
4	Time, T, and $\Delta T$ of lower section ring bridge	3 real words
5	Time, blank, reference bridge and thermocouple temperatures	7 real words

Each tape contains data for a period of 1 yr.

#### DATA ARCHIVED AT NSSDC

As a year of reduced L-DGO data become available, the data are transferred to a magnetic tape (one for each probe) from the master disks with no modifications or editing. These tapes with documentation are sent to NSSDC.

#### REFERENCES

- 10-1. Langseth, M. G., Jr.; Clark, S. P., Jr.; Chute, J. L., Jr.; Keihm, S. J.; and Wechsler, A. E.: Heat-Flow Experiment. Sec. 11 of Apollo 15 Preliminary Science Report. NASA SP-289, 1972.
- 10-2. Langseth, Marcus G., Jr.; Keihm, Stephen J.; and Chute, John L., Jr.: Heat Flow Experiment. Sec. 9 of Apollo 17 Preliminary Science Report, NASA SP-330, 1973.
- 10-3. Hemingway, B. S.; Robie, R. A.; and Wilson, W. H.: Specific Heats of Lunar Soils, Basalt, and Breccias from the Apollo 14, 15 and 16 Landing Sites, Between 90 and 350 K. Proceedings of the Fourth Lunar Science Conference, vol. 3, Pergamon Press (New York), 1973, pp. 2481-2487.
- 10-4. Carrier, W. David, III: Apollo Drill Core Depth Relationships. The Moon, vol. 10, no. 2, 1974, pp. 183-194.

#### BIBLIOGRAPHY

- Ade, P. A.; Bastin, J. A.; Marston, A. C.; Pandya, S. J.; and Puplett, E.: Far Infrared Properties of Lunar Rock. Proceedings of the Second Lunar Science Conference, vol. 3, A. A. Levinson, ed., MIT Press (Cambridge, Mass.), 1971, pp. 2203-2211.
- Baldwin, J. E.: Thermal Radiation from the Moon and the Heat Flow Through the Lunar Surface. Monthly Notices, Roy. Astron. Soc., vol. 122, 1961, pp. 513-522.
- Bassett, H. L.; and Shackelford, R. G.: Dielectric Properties of Apollo 14 Lunar Samples at Microwave and Millimeter Wavelengths. Proceedings of the Third Lunar Science Conference, vol. 3, David R. Criswell, ed., MIT Press (Cambridge, Mass.), 1972, pp. 3157-3160.
- Buhl, D.; Welch, W. J.; and Rea, D. G.: Anomalous Cooling of a Cratered Lunar Surface. J. Geophys. Res., vol. 73, no. 24, Dec. 15, 1968, pp. 7593-7608.
- Carslaw, H. S.; and Jaeger, J. C.: Conduction of Heat in Solids. Clarendon Press (Oxford), 1959, pp. 64-69.
- Conel, J. E.; and Morton, J. B.: Interpretation of Lunar Heat Flow Data. The Moon, vol. 14, no. 2, Oct. 1975, pp. 263-289.

- Cooper, M. R.; Kovach, R. L.; and Watkins, J. S.: Lunar Near-Surface Structure. *Rev. Geophys. Space Phys.*, vol. 12, Aug. 1974, pp. 291-308.
- Cremers, C. J.; and Birkebak, R. C.: Thermal Conductivity of Fines from Apollo 12. *Proceedings of the Second Lunar Science Conference*, vol. 3, A. A. Levinson, ed., MIT Press (Cambridge, Mass.), 1971, pp. 2311-2315.
- Cremers, C. J.; and Hsia, H. S.: Thermal Conductivity and Diffusivity of Apollo 15 Fines at Low Density. *Proceedings of the Fourth Lunar Science Conference*, vol. 3, Pergamon Press (New York), 1973, pp. 2459-2464.
- Gast, P. W.: Limitations on the Composition of the Upper Mantle. *J. Geophys. Res.*, vol. 65, no. 4, Apr. 1960, pp. 1287-1297.
- Gold, T.; Bilson, E.; and Baron, R. L.: Electrical Properties of Apollo 17 Rock and Soil Samples and a Summary of the Electrical Properties of Lunar Material at 450 MHz Frequency. *Lunar Science-VII* (Rev. abs. of papers presented at the Seventh Lunar Science Conference (Houston, Tex.), Mar. 15-19, 1976), pp. 298-300.
- Gold, T.; O'Leary, B. T.; and Campbell, M.: Some Physical Properties of Apollo 12 Lunar Samples. *Proceedings of the Second Lunar Science Conference*, A. A. Levinson, ed., vol. 3, MIT Press (Cambridge, Mass.), 1971, pp. 2173-2184.
- Haji-Scheikh, Abdolhossein: Application of Monte Carlo Methods to Thermal Conduction Problems. Ph. D. Dissertation, Univ. of Minnesota, 1965.
- Hanks, T. C.; and Anderson, D. L.: Origin, Evolution, and Present Thermal State of the Moon. *Phys. Earth Planet. Interiors*, vol. 5, no. 5, Oct. 1972, pp. 409-425.
- Hays, J. F.: Radioactive Heat Sources in the Lunar Interior. *Phys. Earth Planet. Interiors*, vol. 5, no. 1, Jan. 1972, pp. 77-84.
- Horai, K.; Simmons, G.; Kanamori, H.; and Wones, D.: Thermal Diffusivity and Conductivity of Lunar Material. *Science*, vol. 167, no. 3918, Jan. 30, 1970, pp. 730-731.
- Horai, K.; and Winkler, J. L., Jr.: Thermal Diffusivity of Four Apollo 17 Rock Samples. *Proceedings of the Seventh Lunar Science Conference*, 1976, (to be published).

- Jaeger, J. C.: Conduction of Heat in an Infinite Region Bounded Internally by a Circular Cylinder of a Perfect Conductor. Australian J. Phys., vol 9, no. 2, June 1956, pp. 167-179.
- Jeffreys, H.: The Disturbance of the Temperature Gradient in the Earth's Crust by Inequalities of Height. Monthly Notices, Roy. Astron. Soc., Geophys. Supp., vol. 4, no. 4, 1937.
- Katsube, T. J.; and Collett, L. S.: Electrical Properties of Apollo 11 and Apollo 12 Lunar Samples. Proceedings of the Second Lunar Science Conference, A. A. Levinson, ed., vol. 3, MIT Press (Cambridge, Mass.), 1971, pp. 2367-2379.
- Kaula, W. M.; Schubert, G.; Lingenfelter, R. E.; Sjogren, W. L.; and Wollenhaupt, W. R.: Apollo Laser Altimetry and Inferences as to Lunar Structure. Proceedings of the Fifth Lunar Science Conference, vol. 3, Pergamon Press (New York), 1974, pp. 3049-3058.
- Keihm, S. J.; Chute, J. L.; Peters, K.; and Langseth, M. G., Jr.: Apollo 15 Measurement of Lunar Surface Brightness Temperatures: Thermal Conductivity of the Upper 1-1/2 Meters of Regolith. Earth Planet. Sci. Letters, vol. 19, no. 3, July 1973, pp. 337-351.
- Keihm, S. J.; and Langseth, M. G., Jr.: Surface Brightness Temperatures at the Apollo 17 Heat Flow Site: Thermal Conductivity of the Upper 15 cm of Regolith. Proceedings of the Fourth Lunar Science Conference, Pergamon Press (New York), vol. 3, 1973, pp. 2503-2513.
- Keihm, Stephen J.; and Langseth, Marcus G.: Lunar Microwave Brightness Temperature Observations Reevaluated in the Light of Apollo Program Findings. Icarus, vol. 24, no. 2, 1975, pp. 211-230.
- Klaven, L.; Lofgren, L.; and Felsenthal, P.: A Rugged, Stable, Differential Platinum Resistance Thermometer. Rev. Sci. Instr., vol. 41, no. 4, 1970, pp. 541-544.
- Krotikov, V. D.; and Troitskii, V. S.: Detecting Heat Flow from the Interior of the Moon. Soviet Astron., vol. 7, no. 6, May/June 1964, pp. 822-826.
- Lachenbruch, A. H.: Rapid Estimation of the Topographic Disturbance to Superficial Thermal Gradients. Rev. Geophys., vol. 6, no. 3, Aug. 1968, pp. 365-400.
- Lachenbruch, Arthur Herold: Three-Dimensional Heat Conduction in Permafrost Beneath Heated Buildings. U.S. Geol. Survey Bull. 1052-B, 1957, pp. 51-69.

- Lachenbruch, Arthur H.: The Effect of Two Dimensional Topography on Superficial Thermal Gradients. U.S. Geol. Survey Bull. 1203-E, 1969, pp. E1-E86.
- Langseth, M. G., Jr.; More, K. A.; and Johnson, W. E.: An Experiment to Measure Heat Flow from the Interior of the Moon. Bendix Technical Journal, vol. 1, no. 1, 1968, pp. 33-43.
- Langseth, M. G., Jr.; Wechsler, A. E.; Drake, E. M.; Simmons, G.; et al.: Apollo 13 Lunar Heat Flow Experiment. Science, vol. 168, no. 3928, Apr. 10, 1970, pp. 211-217.
- Langseth, M. G., Jr.; and Von Herzen, R. P.: Heat Flow Through the Floor of the World Oceans. The Sea, vol. 4, part I, 1971, pp. 299-352.
- Langseth, M. G., Jr.; Clark, S. P., Jr.; Chute, J. L., Jr.; Keihm, S. J.; and Wechsler, A. E.: Heat-Flow Experiment. Sec. 11 of Apollo 15 Preliminary Science Report. NASA SP-289, 1972.
- Langseth, M. G., Jr.; Drake, E. M.; Nathanson, D.; and Fountain, J. A.: Development of an In Situ Thermal Conductivity Measurement for the Lunar Heat Flow Experiment. Thermal Characteristics of the Moon. AIAA Progress in Astronautics and Aeronautics Series, vol. 28, MIT Press (Cambridge, Mass.), 1972, pp. 169-204.
- Langseth, Marcus G., Jr.; Keihm, Stephen J.; and Chute, John L., Jr.: Heat Flow Experiment. Sec. 9 of Apollo 17 Preliminary Science Report, NASA SP-330, 1973.
- Latham, G. V.; Ewing, M.; Press, R.; Sutton, G.; et al.: Passive Seismic Experiment. Sec. 9 of the Apollo 16 Preliminary Science Report. NASA SP-315, 1972.
- Lee, W. H. K.; and Uyeda, S.: Review of Heat Flow Data. Terrestrial Heat Flow, American Geophysical Union (Washington, D.C.), 1965, pp. 68-190.
- Linsky, J. L.: Models of the Lunar Surface Including Temperature-Dependent Thermal Properties. Icarus, vol. 5, no. 6, Nov. 1966, pp. 606-634.
- Linsky, Jeffrey L.: The Moon as a Proposed Radiometric Standard for Microwave and Infrared Observations of Extended Sources. Astrophys. J., Supp. No. 216, vol. 25, 1973, pp. 163-203.

- Metzger, A. E.; Trombka, J. I.; Peterson, L. E.; Reedy, R. C.; and Arnold, J. R.: Lunar Surface Radioactivity: Preliminary Results of the Apollo 15 and Apollo 16 Gamma-Ray Spectrometer Experiments. *Science*, vol. 179, no. 4075, Feb. 23, 1973, pp. 800-803.
- Metzger, A. E.; Trombka, J. I.; Reedy, R. C.; and Arnold, J. R.: Element Concentrations from Lunar Orbital Gamma-Ray Measurements. *Proceedings of the Fifth Lunar Science Conference*, vol. 2, Pergamon Press (New York), 1974, pp. 1067-1078.
- Mizutani, Hitoshi; and Osako, Masahiro: Elastic-Wave Velocities and Thermal Diffusivities of Apollo 17 Rocks and Their Geophysical Implications. *Proceedings of the Fifth Lunar Science Conference*, vol. 3, Pergamon Press (New York), 1974, pp. 2891-2901.
- Robie, R. A.; Hemingway, B. S.; and Wilson, W. H.: Specific Heats of Lunar Surface Materials from 90 to 350 Degrees Kelvin. *Science*, vol. 167, no. 3918, Jan. 30, 1970, pp. 749-750.
- Smith, B. D.: The Lunar Heat Flow Experiment. *Bendix Tech. J.*, vol. 4, no. 2, 1971, pp. 64-79.
- Solomon, Sean C.: Mare Volcanism and Lunar Crustal Structure. *Proceedings of the Sixth Lunar Science Conference*, vol. 1, Pergamon Press (New York), 1975, pp. 1021-1042.
- Strangway, D. W.; Chapman, W. B.; Olhoeft, G. R.; and Carnes, J.: Electrical Properties of Lunar Soil Dependence on Frequency, Temperature, and Moisture. *Earth Planet. Sci. Letters*, vol. 16, no. 2, Oct. 1972, pp. 275-281.
- Talwani, Manik; Thompson, George; Dent, Brian; Kahle, Hans-Gert; and Buck, Sheldon: Traverse Gravimeter Experiment. Sec. 13 of Apollo 17 Preliminary Science Report. NASA SP-330, 1973.
- Taylor, S. R.: Geochemical Constraints on the Composition of the Moon. *Lunar Science-VII* (Rev. abs. of papers presented at the Seventh Lunar Science Conference (Houston, Tex.), Mar. 15-19, 1976), pp. 855-857.
- Taylor, S. R.; and Jakes, P.: The Geochemical Evolution of the Moon. *Proceedings of the Fifth Lunar Science Conference*, vol. 2, Pergamon Press (New York), 1974, pp. 1287-1305.
- Tikhonova, T. V.; and Troitskii, V. S.: Effect of Heat from Within the Moon on Its Radio Emission for the Case of Lunar Properties Which Vary with Depth. *Soviet Astron.*, vol. 13, no. 1, July/Aug. 1969, pp. 120-128.

Turcotte, D. L.; Hsui, A. T.; Torrance, K. E.; and Oxburgh, E. R.:  
Thermal Structure of the Moon. J. Geophys. Res., vol. 77,  
no. 35, Dec. 10, 1972, pp. 6931-6939.

Urey, H. C.: Proc. Natl. Acad. Sci. U.S., vol. 42, 1956, p. 889.

Wasserburg, G. J.; MacDonald, G. J. F.; Hoyle, F.; and Fowler,  
W. A.: Relative Contributions of Uranium, Thorium, and Potas-  
sium to Heat Production in the Earth. Science, vol. 143,  
no. 3605, Jan. 31, 1964, pp. 465-467.

Watson, K. I.: Thermal Conductivity Measurements of Selected  
Silicate Powders in Vacuum from 150-350 K, II. An Interpreta-  
tion of the Moon's Eclipse and Lunation Cooling Curve as  
Observed Through the Earth's Atmosphere from 8-14 Microns.  
Ph. D. Dissertation, California Institute of Technology, 1964.

Weaver, H.: The Interpretation of Thermal Emissivity from the  
Moon. Solar System Radio Astronomy, Plenum Press (New York),  
1965, pp. 295-354.

Williams, David L.; and Von Herzen, Richard P.: Heat Loss from  
the Earth; New Estimate. Geology, vol. 2, no. 7, 1974, pp. 327-  
328.

TABLE 10-I.- PREDICTED EXPERIMENT RANGES

Temperature gradient $dT/dz,$ K/m	Heat flow J, W/m <sup>2</sup>	Thermal conductivity k, W/m-K
0.1	$4.2 \times 10^{-3}$	$42 \times 10^{-3}$
12	25	2.1

TABLE 10-II.- PERFORMANCE REQUIREMENTS OF THE HEAT FLOW INSTRUMENT

Measurement	Requirement			Minimum stability
	Range	Resolution	Accuracy <sup>1</sup>	
Temperature difference across 0.5-m probe section in lowest meter of hole	±2 K (high sensitivity) ±20 K (low sensitivity)	0.0005 K (high sensitivity) 0.005 K (low sensitivity)	±0.003 K	0.003 K/yr
Ambient temperature of probe in lowest meter of hole	200 to 250 K	0.02 to 0.08 K	±0.1 K	0.05 K/yr
Temperature of thermocouples in upper 2 m of hole	90 to 350 K	±0.17 K	±0.5 K	0.5 K/yr
Thermal conductivity of material surrounding probes	0.002 to 0.4 W/m-K	±20 percent	±20 percent	--

<sup>1</sup>Maximum Probable error.

TABLE 10-III.- APOLLO 16 HEAT FLOW INSTRUMENT TEST RESULTS IN LUNAR-NIGHT ENVIRONMENT

[Test performed on July 26, 1971]

(a) Sensor data

Data	Upper gradient bridge, K	Lower gradient bridge, K	Upper remote bridge, K	Lower remote bridge, K
Absolute temperature, mean difference <sup>1</sup>	-0.002	-0.020	-0.028	-0.036
Absolute temperature, standard deviation <sup>2</sup>	.016	.037	.034	.032
High-sensitivity temperature differential, mean difference <sup>1</sup>	.001	-.001	.003	.002
High-sensitivity temperature differential, standard deviation <sup>2</sup>	.0002	.0002	.0021	.0010
Low-sensitivity temperature differential, mean difference <sup>1</sup>	.001	-.003	--	--
Low-sensitivity temperature differential, standard deviation <sup>2</sup>	.002	.002	--	--
Cycles	8	8	10	10

(b) Thermocouple data (9 cycles)

Data	Thermocouple 1, K	Thermocouple 2, K	Thermocouple 3, K	Thermocouple 4, K
Thermocouple temperature, mean difference <sup>1</sup>	-0.073	1.946	-2.928	0.343
Thermocouple temperature, standard deviation <sup>2</sup>	.190	.193	.220	.193

<sup>1</sup>Mean difference in readings of two opposed sensors.

<sup>2</sup>Standard deviation of difference in readings of two opposed sensors about the mean difference.

TABLE 10-IV.- APOLLO 15 HFE SUBSURFACE TEMPERATURE DATA

(a) Temperature difference measurements

Bridge	Interval, cm	Equilibrium temperature difference, K	Corrected temperature difference, K <sup>1</sup>	Annual wave correction, K
Probe 1				
DTG12	91 to 138	0.803	0.833	-0.37
DTR12	100 to 129	.484	.479	-.28

<sup>1</sup>The effect of the annual wave on Sept. 29, 1971, has been removed.

(b) Absolute temperature measurements

Sensor type	Depth, cm	Equilibrium temperature, K	Corrected temperature, K
Probe 1			
Platinum resistance	91	252.20	252.16
Platinum resistance	100	252.33	252.33
Platinum resistance	129	252.81	252.81
Platinum resistance	138	253.00	253.01

TABLE 10-V.- APOLLO 17 HFE SUBSURFACE TEMPERATURE DATA

(a) Temperature difference measurements

Bridge	Interval, cm	Equilibrium temperature difference <sup>1</sup> , K	Corrected temperature difference <sup>2</sup> , K	Annual wave correction, K
Probe 1				
DTG11	130 to 177	0.707	0.755	-0.027
DTR11	139 to 168	.435	.467	-.018
DTG12	185 to 233	.533	.559	-.001
DTR12	194 to 224	.322	.326	<.001
Probe 2				
DTG21	131 to 178	0.370	0.390	-0.027
DTR21	140 to 169	.218	.223	-.018
DTG22	196 to 234	.336	.359	-.001
DTR22	195 to 225	.206	.212	<.001

<sup>1</sup>The error associated with extrapolating to equilibrium temperature differences is  $\pm 0.003$  K.

<sup>2</sup>The uncertainty introduced by these corrections is estimated to be  $\pm 2$  percent.

(b) Absolute temperature measurements

Sensor type	Depth, cm	Equilibrium temperature <sup>1</sup> , K	Corrected temperature <sup>2</sup> , K
Probe 1			
Thermocouple TC4	66	254.20	254.20
Platinum resistance	130	255.06	255.02
Platinum resistance	139	255.19	255.17
Platinum resistance	168	255.62	255.64
Platinum resistance	177	255.76	255.78
Platinum resistance	185	255.91	255.91
Platinum resistance	194	256.03	256.04
Platinum resistance	224	256.36	256.37
Platinum resistance	233	256.44	256.47
Probe 2			
Thermocouple TC4	57	254.70	254.70
Platinum resistance	131	256.07	256.05
Platinum resistance	140	256.09	256.09
Platinum resistance	169	256.31	256.31
Platinum resistance	179	256.44	256.44
Platinum resistance	186	256.48	256.48
Platinum resistance	195	256.52	256.51
Platinum resistance	225	256.73	256.73
Platinum resistance	234	256.82	256.84

<sup>1</sup>The accuracy of extrapolated absolute temperatures is  $\pm 0.05$  K for the platinum resistances.

<sup>2</sup>The correction for the annual wave to be applied to the thermocouple is 0.04 K.

TABLE 10-VI.- CONDUCTIVITIES FROM COOLDCWN HISTORIES

Sensor depth, CM	Heater location	Conductivity with drill heating effects, W X 10 <sup>-4</sup> /CM-K	Conductivity without drill heating effects, W X 10 <sup>-4</sup> /CM-K
Probe 1			
66		1.0	--
130	H11	2.3	1.3
139		1.5	1.1
168		1.9	1.1
177	H12	2.0	1.0
185	H13	1.9	1.1
194		2.1	1.1
224		2.8	1.4
233	H14	2.7	1.6
Probe 2			
67		1.0	--
131	H21	2.0	1.2
140		2.0	1.1
169		2.4	1.3
178	H22	2.7	1.7
186	H23	2.9	1.7
195		2.7	1.5
225		2.8	1.5
234	H24	2.5	1.5

TABLE 10-VII.- RESULTS OF THE CONDUCTIVITY EXPERIMENTS

Heater location	Depth, cm	Conductivity, <sup>1</sup> W X 10 <sup>-4</sup> /cm-K	Contact conductance, <sup>2</sup> W X 10 <sup>-4</sup> /cm <sup>2</sup> -K
Apollo 17 probe 1			
H11	130	2.50	1.4
H12	177	1.72	1.6
H13	185	1.79	1.4
H14	233	2.95	1.2
Apollo 17 probe 2			
H21	131	2.06	1.6
H22	178	2.36	1.1
H23	186	2.64	1.5
H24	234	2.24	2.3
Apollo 15 probe 1			
H11	35	1.41	0.8
H12	83	2.11	.8
H13	91	1.60	.9
H14	138	2.50	1.0
Apollo 15 probe 2			
H23	49	1.46	0.5
H24 <sup>3</sup>	96	2.43	.6

<sup>1</sup>The estimated error of conductivity measurement is ±15 percent.

<sup>2</sup>Estimated error is ±20 percent. In the theoretical model, the thickness of the contact zone is 2 mm.

<sup>3</sup>It is probable that a section of broken borestem lies just outside this location so that the uncertainty of this measurement is very large.

TABLE 10-VIII.- HEAT FLOW DATA

Depth interval, cm	Temperature gradient, K/cm	Average conductivity, $W \times 10^{-6}/cm-K$	Heat flow, $W \times 10^{-6}/cm^2$
Apollo 17 probe 1			
66 to 130	0.0130	1.60	2.10
130 to 177	.0158	1.79	2.83
139 to 168	.0163	1.72	2.80
185 to 233	.0118	2.39	2.81
194 to 224	.0113	2.48	2.81
66 to 233	.0140	1.80	2.50
Apollo 17 probe 2			
67 to 131	0.0210	1.50	3.10
131 to 178	.0082	2.26	1.86
140 to 169	.0078	2.30	1.79
186 to 234	.0076	2.50	1.89
195 to 225	.0074	2.53	1.87
67 to 234	.0130	2.00	2.50
Apollo 15 probe 1			
91 to 138	0.0175	1.78	3.11
100 to 129	.0166	1.68	2.82

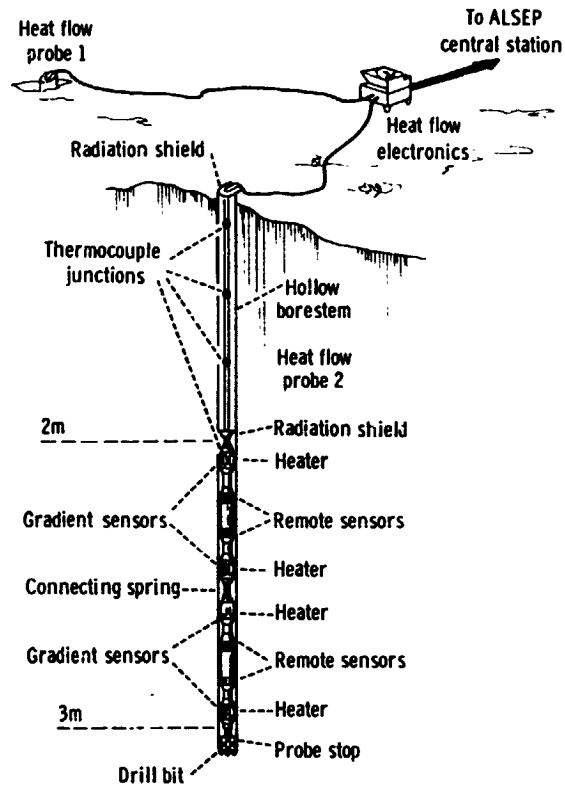


Figure 10-1.- Optimum site configuration for lunar HFE.

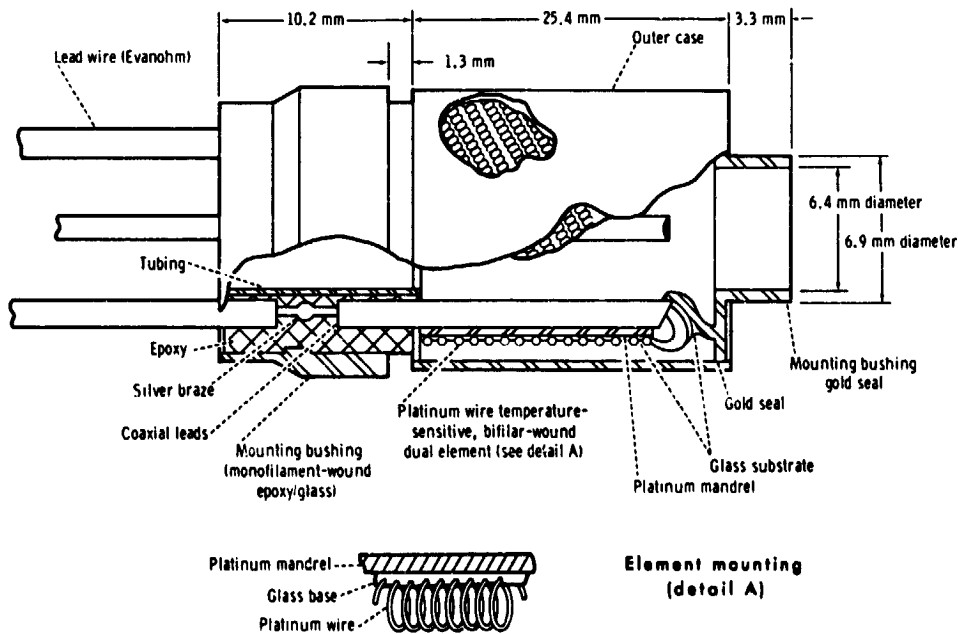


Figure 10-2.- Gradient-sensor construction.

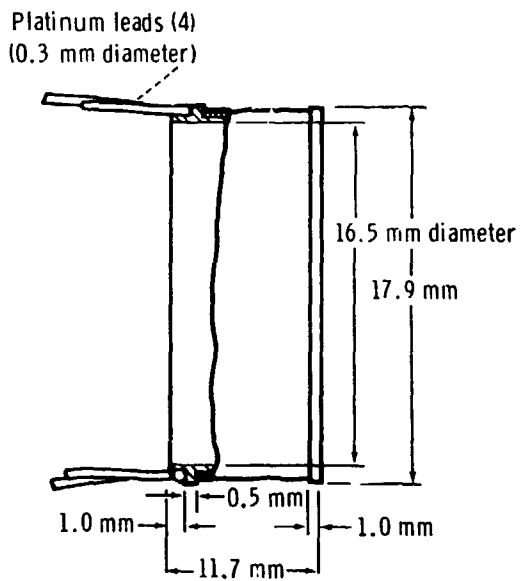


Figure 10-3.- Ring- or remote-sensor construction.

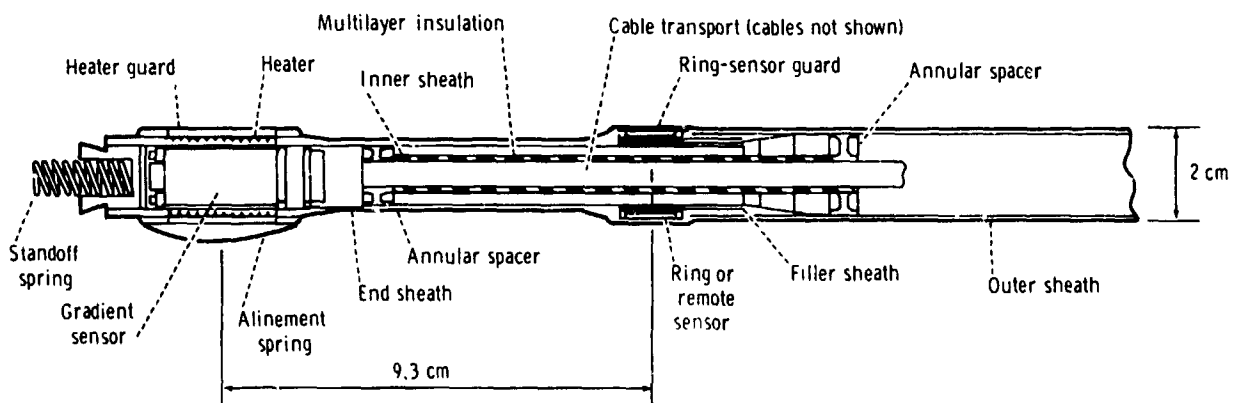


Figure 10-4.- Half-probe end section.

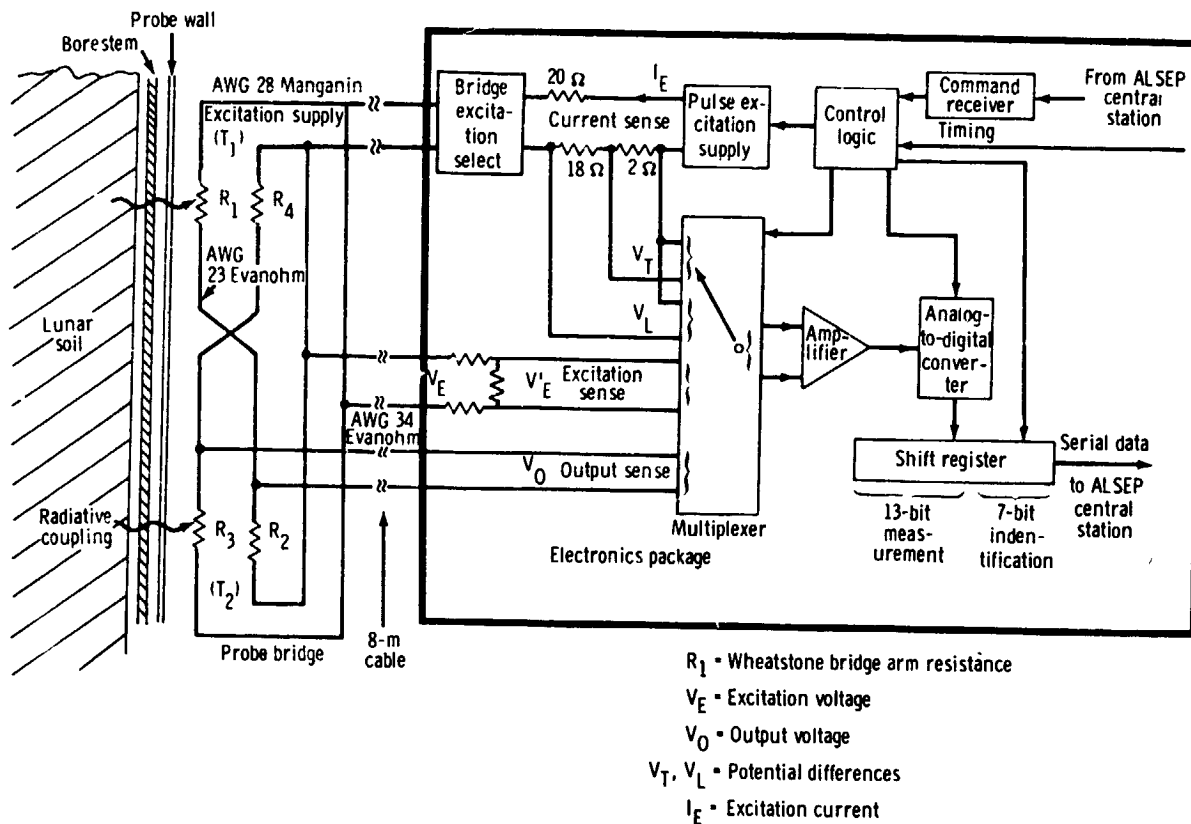


Figure 10-5.- Schematic of electronics measurements on bridge sensors.

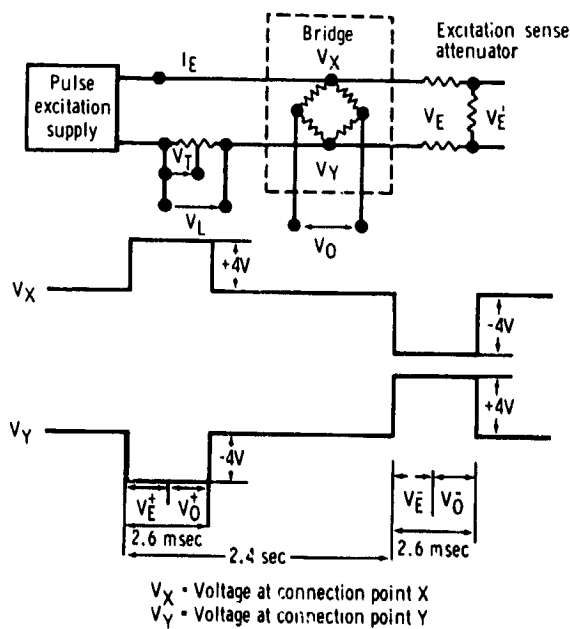


Figure 10-6.- Typical sequence for bridge measurements.

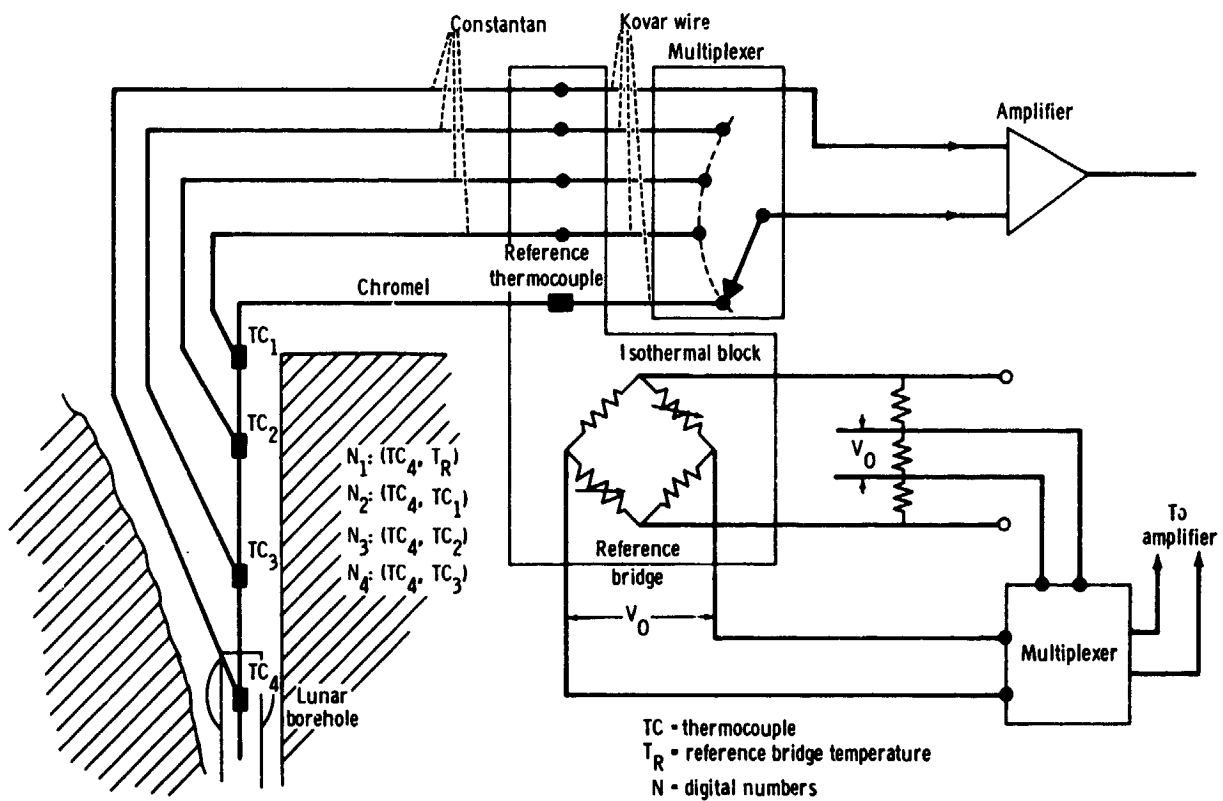


Figure 10-7.- Schematic for thermocouple and reference-temperature bridge measurements.

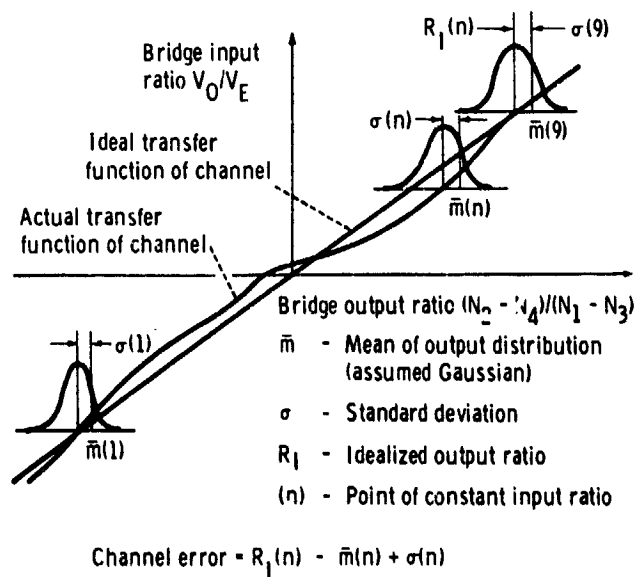
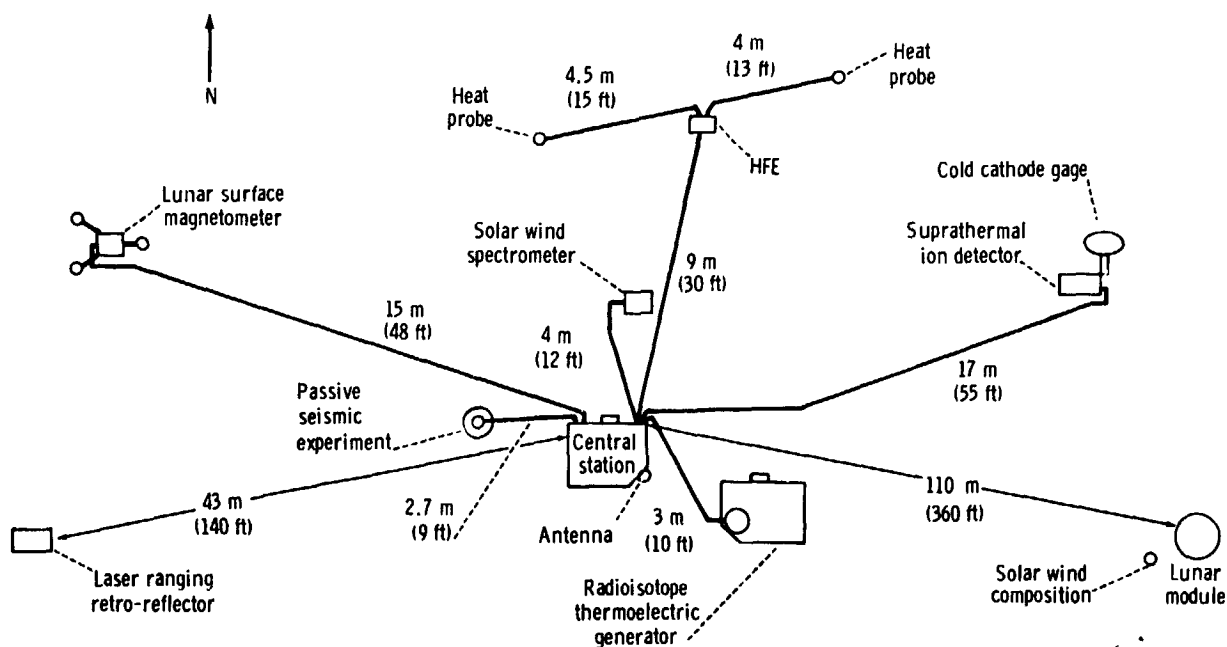


Figure 10-8.- Error definition for instrument measuring channels.



Note: The solar wind composition experiment was located about 15 m (50 ft) from the lunar module

Figure 10-9.- Apollo 15 ALSEP deployment.

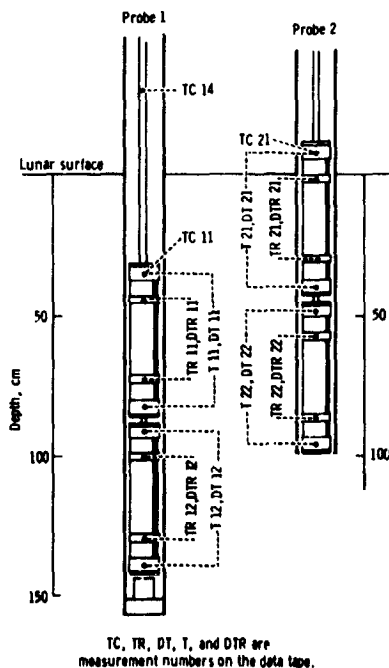


Figure 10-10.- Subsurface configuration of the HFE probes for Apollo 15.

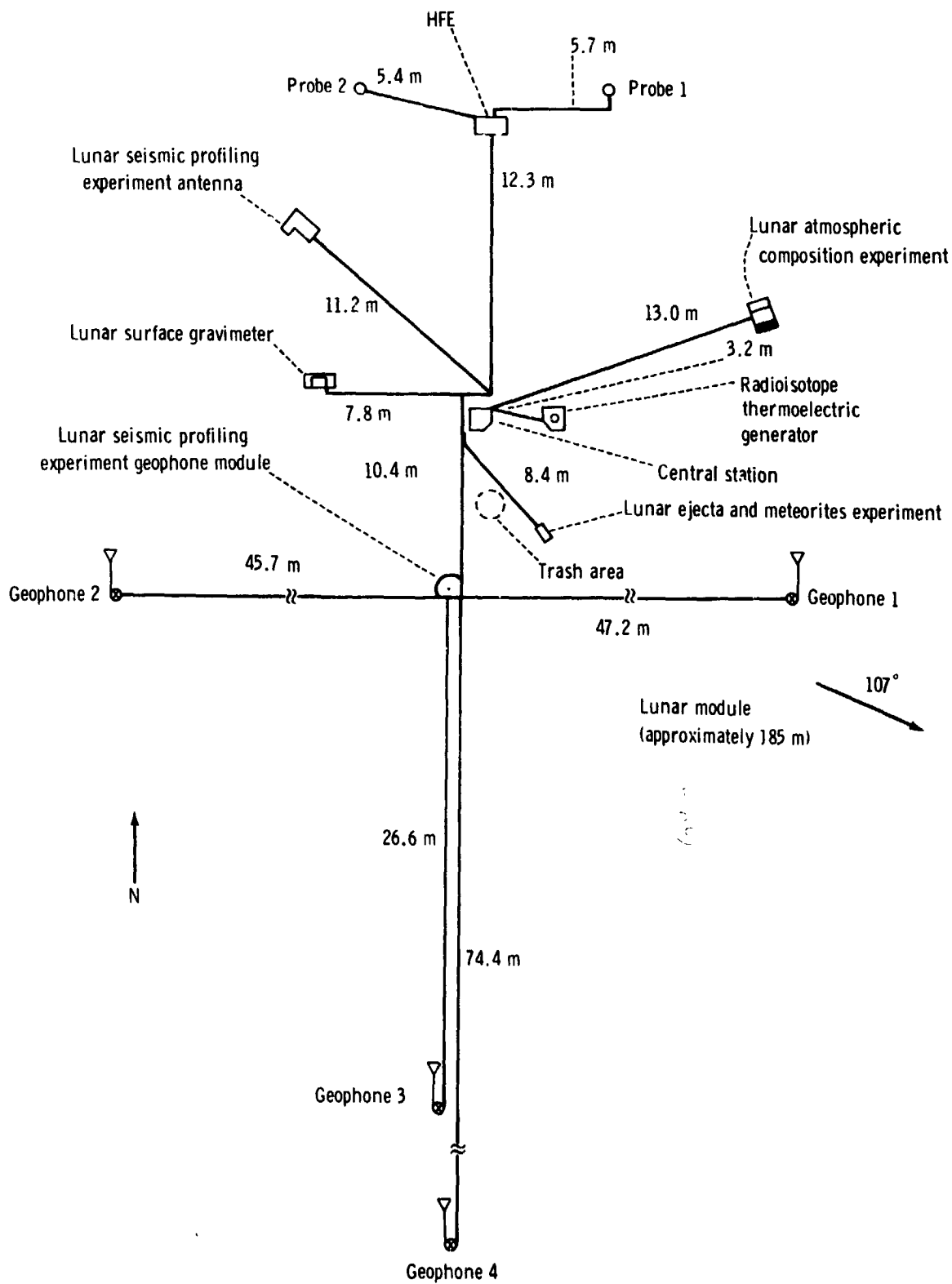


Figure 10-11.- Apollo 17 ALSEP experiment geometry.

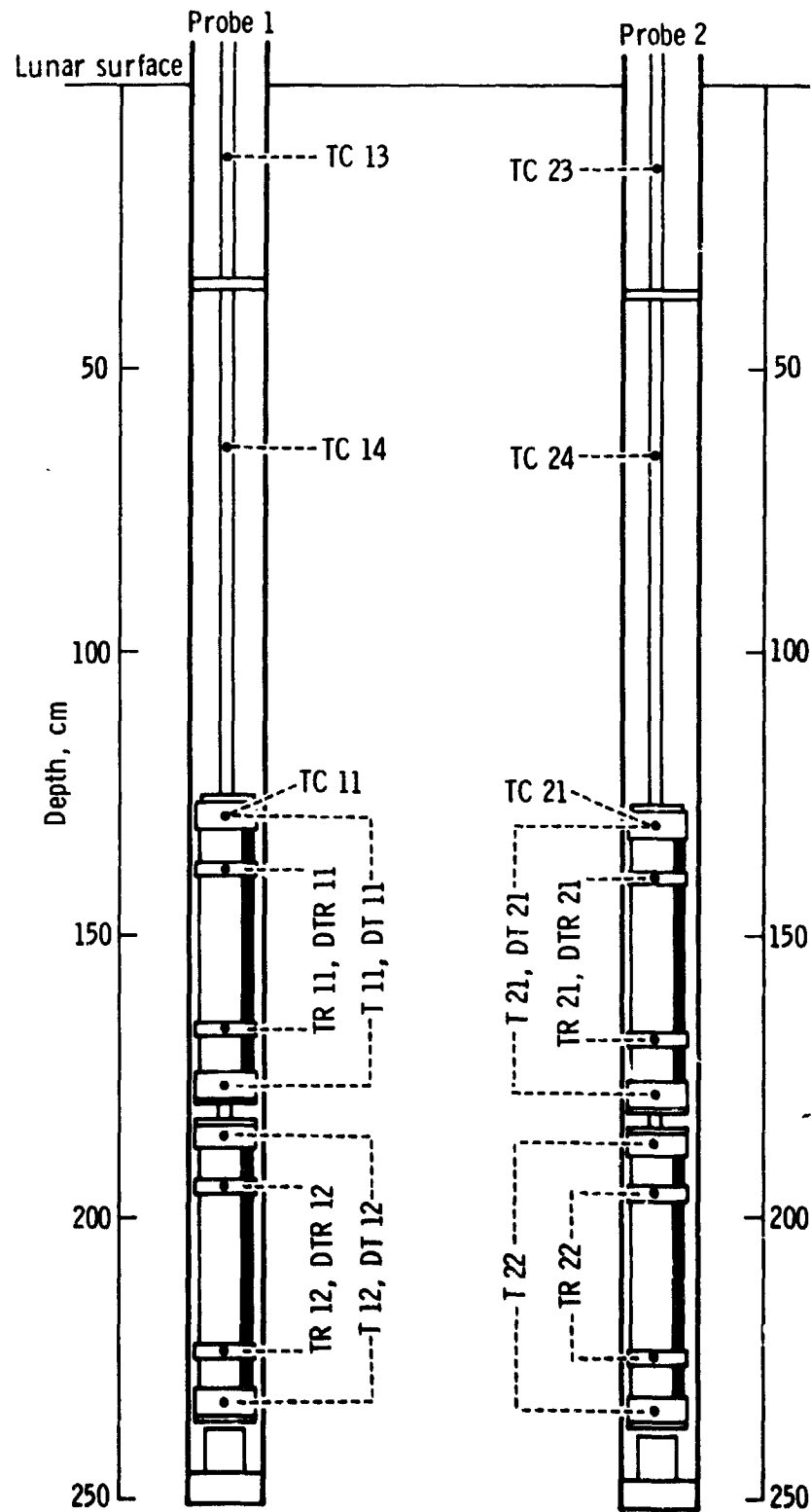


Figure 10-12.- Subsurface geometry of the HFE probes for Apollo 17.

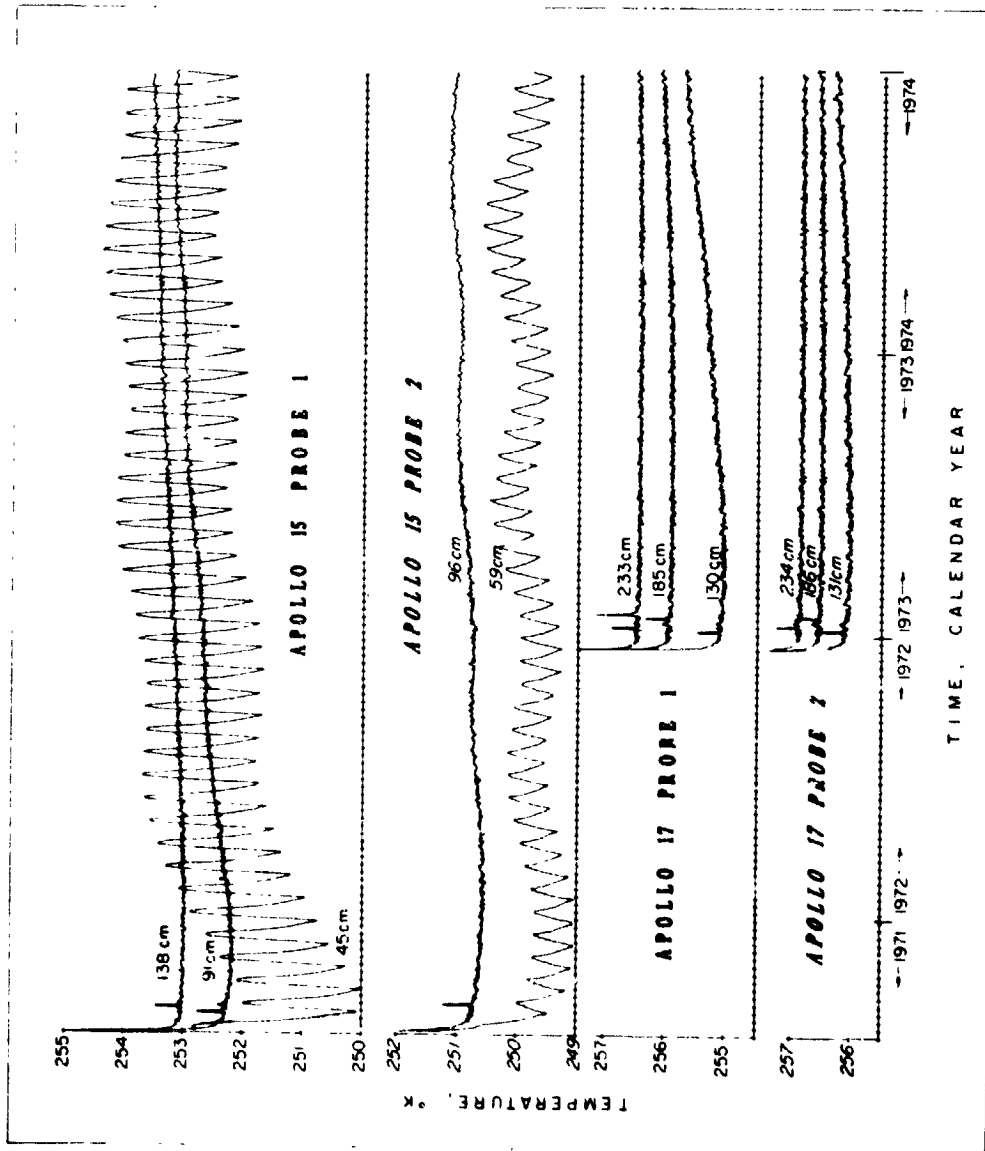


Figure 10-13.- Subsurface temperature histories covering a 3.5-yr period of representative sensors on the four heat flow probes. Initial cooldown of the probes after insertion is indicated at the start of each history. The small spikes in the first 60 days result from the short-term conductivity experiments.

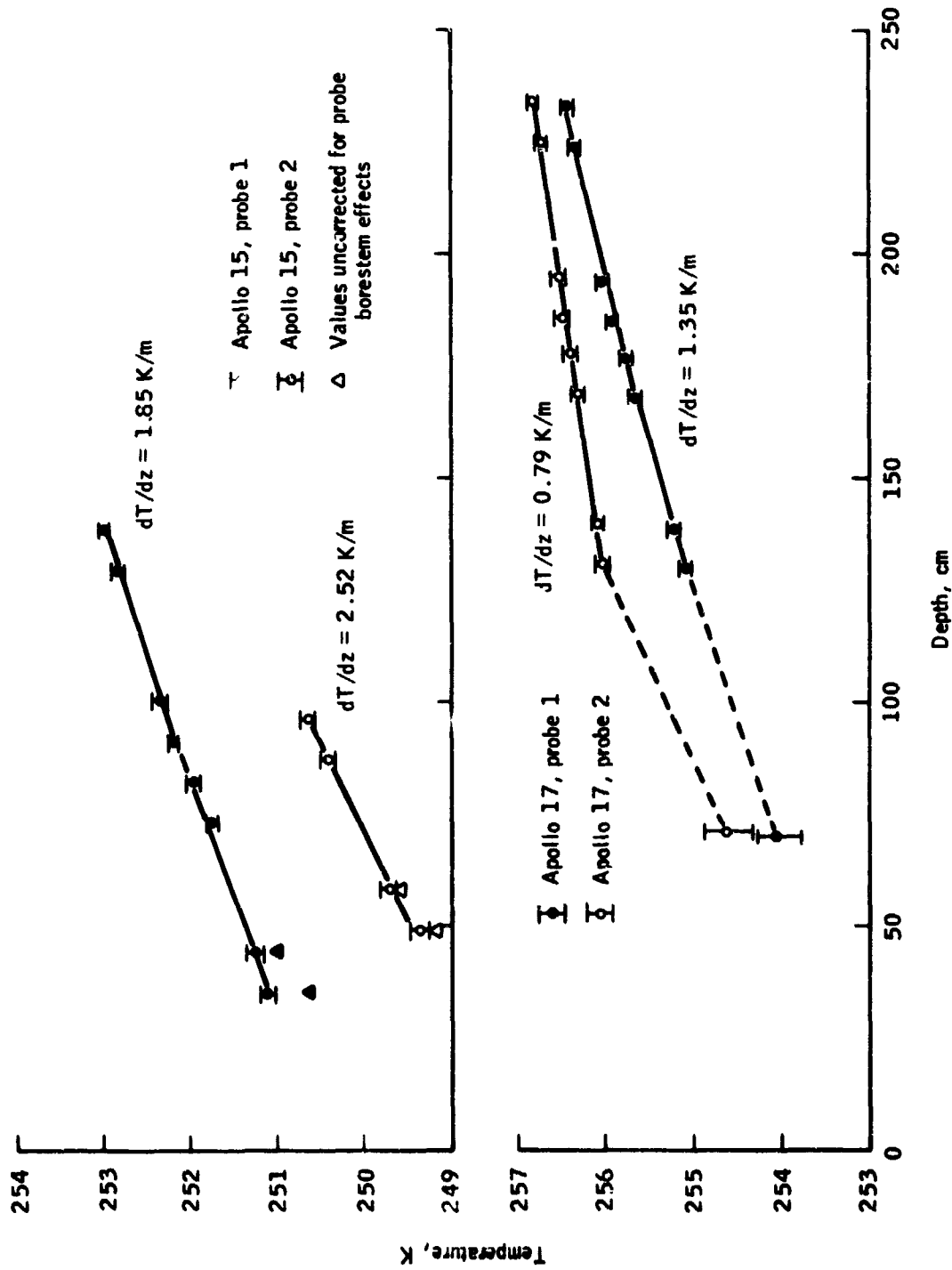


Figure 10-14.- Mean subsurface temperatures at the four probes as a function of depth. Note that temperatures of sensors shallower than 65 cm have been corrected upward to account for a steady radiative heat loss to the surface.

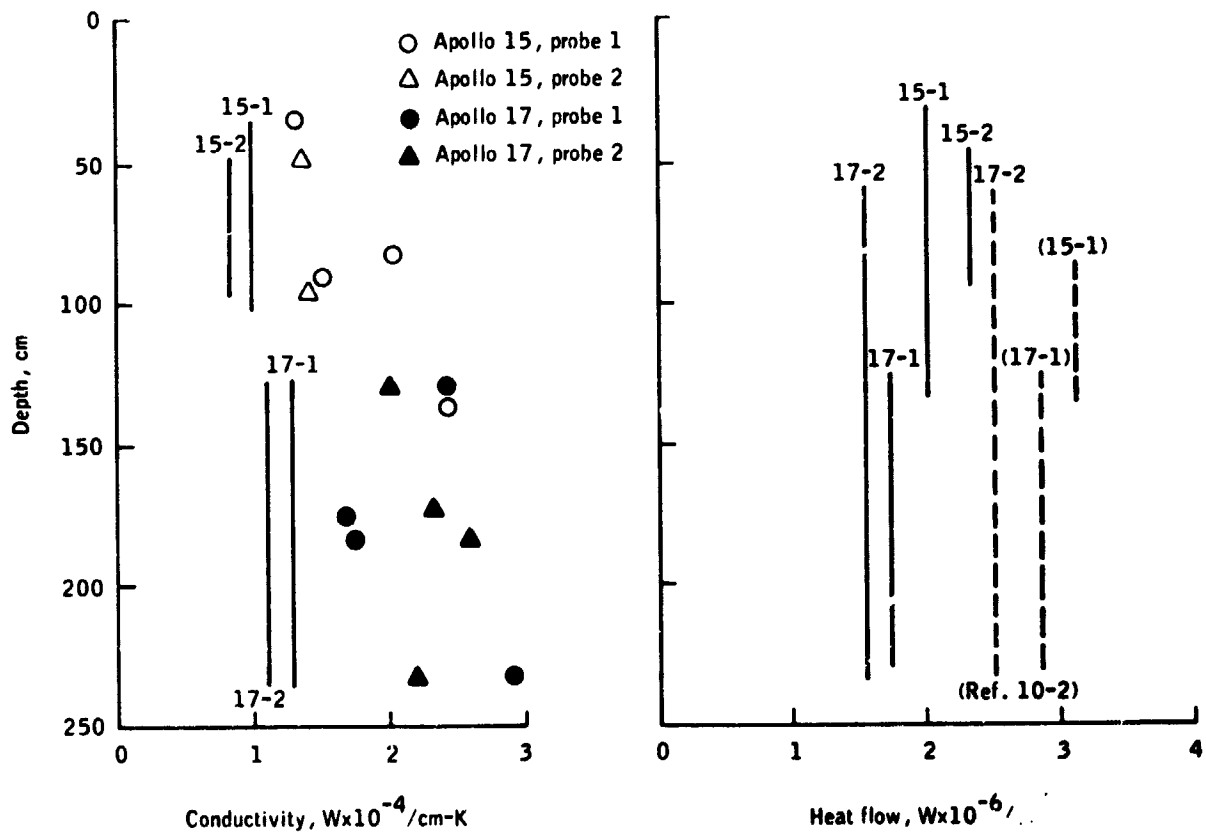
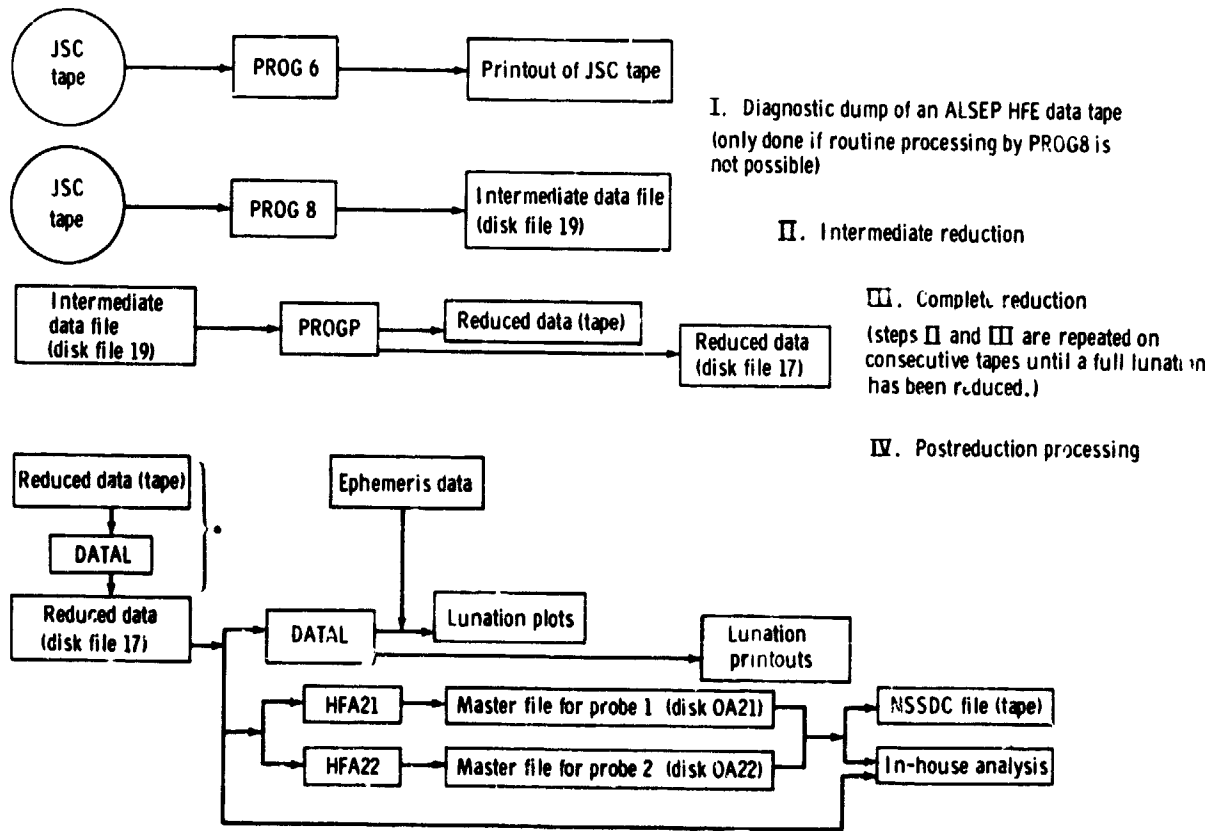


Figure 10-15.- Revised conductivity values are shown on the left as solid lines over the intervals where applicable. The short-term point measurements (ref. 10-2) are shown for comparison. The revised heat flow values (solid lines) are shown on the right together with the preliminary results (dashed lines) that were based on interpolation of the short-term conductivity measurements. (Mission and probe numbers are designated 15-1, 15-2, etc.)



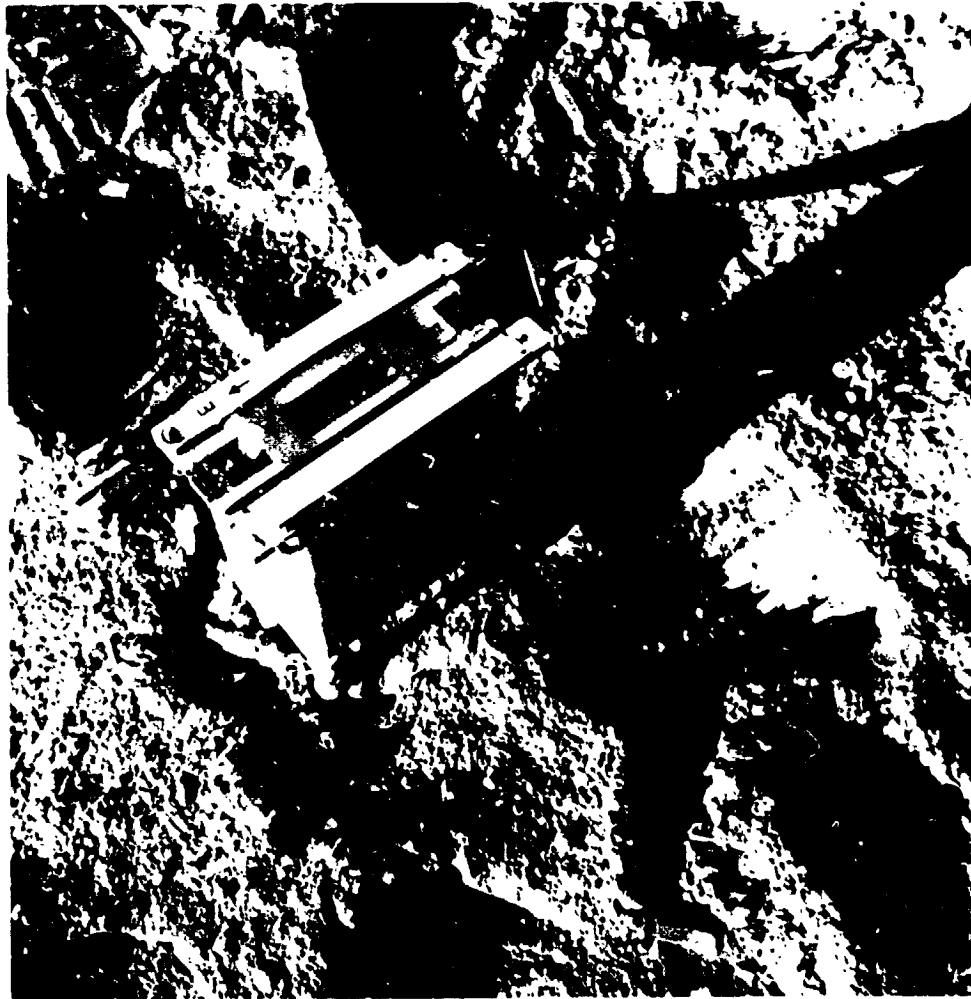
\* Not part of routine processing; only done if necessary.

Figure 10-16.- Flow diagram for reduction of one lunation of data.

11. CHARGED-PARTICLE LUNAR ENVIRONMENT EXPERIMENT  
(NASA EXPERIMENT S-038)

NSSDC IDENTIFICATION NUMBER:

71-008C-08



11-1

REPRODUCIBILITY OF THE  
ORIGINAL PAGE IS POOR

CONTENTS - SECTION 11

	Page
DESCRIPTION . . . . .	11-3
DATA AND OPERATIONAL HISTORY . . . . .	11-4
DATA SETS AND AVAILABILITY THROUGH NSSDC . . . . .	11-4
DATA EXAMPLE . . . . .	11-5
THE CPLEF DATA TAPE FORMAT . . . . .	11-5
Data Array (Words 5 to 100) . . . . .	11-6
Mode and Identification Bits (Word 101) . . . . .	11-7
Last Valid Line (Word 102) . . . . .	11-8
Year (Word 105) . . . . .	11-8
Housekeeping (Words 107 to 111) . . . . .	11-8
Tape Termination . . . . .	11-9
CPLEF EPHEMERIS TAPE DESCRIPTION . . . . .	11-9
SUMMARY OF KEY RESULTS . . . . .	11-13
BIBLIOGRAPHY . . . . .	11-14

## 11. CHARGED-PARTICLE LUNAR ENVIRONMENT EXPERIMENT

The charged-particle lunar environment experiment (CPLEE) instrument is designed to measure the charged-particle fluxes impacting the lunar surface from a variety of sources. The instrument contains two similar physical charged-particle analyzers, two different programable high-voltage supplies, twelve 20-bit accumulators, and appropriate conditioning and shifting circuitry.

### DESCRIPTION

Each physical analyzer contains five C-shaped channel electron multipliers with a nominal aperture of 1 mm each and one helical channel electron multiplier with a nominal aperture of 8 mm. These multipliers are shown schematically in figure 11-1.

As shown in figure 11-1, incident particles enter an analyzer through a series of slits and then pass between two deflection plates across which a voltage can be applied. Thus, at a given deflection voltage, the five small-aperture electron multipliers make a five-point measurement of the energy spectrum of charged particles of a given polarity (e.g., electrons), while, simultaneously, the large-aperture electron multiplier makes a single wide-band measurement of particles with the opposite polarity.

In the CPLEE, the deflection-plate voltage is stepped through a sequence of eight levels (including a background step and a calibration step) resulting in a measurement of ion and electron energies in 15 steps between 40 eV and 20 keV each 19.2 sec. The deflection-plate voltage can be stopped by ground command on any of the eight levels to concentrate on a particular range of particle energy with higher time resolution (2.4 sec).

The instrument contains two particle analyzers, A and B. Analyzer A points toward the lunar vertical and analyzer B points 60° from the vertical toward the lunar west.

The CPLEE was deployed on the lunar surface at lunar coordinates 3°40' S latitude and 17°27' W longitude on February 5, 1971. Leveling and east-west orientation to

within  $\pm 1^\circ$  were accomplished with a bubble level and a Sun compass.

#### DATA AND OPERATIONAL HISTORY

The CPLEE was first commanded on February 5, 1971. The following is a brief chronology of its operational history.

February 5, 1971	The CPLEE was first commanded on.
April 8, 1971	The CPLEE Channeltron power supply for analyzer B failed; operation continued with analyzer A only.
June 6, 1971	The CPLEE Channeltron power supply for analyzer A partially failed, and the CPLEE was commanded off.
January to November 1972	The CPLEE operated during periods of lunar night only. High daytime temperatures caused low voltage condition in analyzer A Channeltron power supply.
December 1972 to March 1973	The CPLEE was restored to continuous operation with analyzer A only.
March 1973 to present	Analyzer A Channeltron power supply fails to operate under lunar-day conditions. Operation is possible only at lunar night.

#### DATA SETS AND AVAILABILITY THROUGH NSSDC

The following data are available from the National Space Science Data Center (NSSDC).

1. Complete instrument and data tape documentation
2. Data tapes for the periods February 5 to June 6, 1971; July 31 to August 12, 1972; and December 4, 1972, to

March 2, 1973. (The periods include the one for the August 1972 solar flare event.)

3. Five-min averaged plots of the count rates of the 200-eV electron channel for the period February 5, 1971, to March 12, 1971 (These plots, available on microfilm, show a typical passage of the instrument through the various regions of space in the course of a lunar orbit.)

4. Ephemeris data tape for the years 1971, 1972, and 1973

#### DATA EXAMPLE

An example of CPLEE data showing passage from the magnetosheath into the magnetotail is shown in figure 11-2. Prior to 02:00, CPLEE was in the magnetosheath as indicated by high, erratic electron fluxes. Between 02:00 and 03:00, multiple boundary crossings are observed (see the 40-eV electron trace); after 03:00, CPLEE was in the magnetotail as indicated by the low, stable 40-eV electron levels that are due to lunar-surface photoelectrons. The top two traces are the longitude ( $\phi$ ) and latitude ( $\theta$ ) of the magnetic field measured by the Explorer 35 magnetometer. The enhancements in the 500-eV electron flux and 2-keV ion flux observed between 04:00 and 24:00 represent encounters with the plasma sheet.

#### THE CPLEE DATA TAPE FORMAT

The data tape records are organized around the CPLEE deflection voltage cycles. The tapes are seven-track, 556 bpi, binary, odd parity with 1110-word physical records. A logical record contains timing and housekeeping information and 96 data words. The 96 data words represent either one CPLEE cycle in the automatic mode (19.2 sec) or eight CPLEE cycles (2.4 sec/cycle) in the manual mode. Words to identify the deflection voltage step and polarity are also included.

Each data tape begins with a 4-word header record written in odd parity and SDS-92 internal code. The label is "CPLEE ALSEP APOLLO 14." All periods when the instrument was off are deleted from the tape, and each tape contains 4 days of data beginning at day  $n$ , 17:44:00, and ending at day  $n + 4$ , 17:43:59.

Each logical record is constructed as follows, with 10 logical records per physical record.

<u>Word number</u>	<u>Function</u>
1	Days (day 1 = Jan. 1)
2	Hours
3	Minutes
4	Milliseconds
5 to 100	Data array
101	Mode and step indicator
102	Last valid line (manual)
103	Not applicable
104	Not applicable
105	Year
106	Not applicable
107	Analyzer B Channeltron power supply voltage
108	Analyzer A Channeltron power supply voltage
109	dc/dc converter voltage
110	Physical analyzer temperature, °C
111	Electronics temperature, °C

Data Array (Words 5 to 100)

1. Automatic mode:

<u>Word number</u>	<u>Function</u>
5 to 10	Analyzer A, +3500, channels 1 to 6
11 to 16	Analyzer B, +3500, channels 1 to 6
17 to 22	Analyzer A, +350, channels 1 to 6

<u>Word number</u>	<u>Function</u>
23 to 28	Analyzer B, +350, channels 1 to 6
29 to 34	Analyzer A, +35, channels 1 to 6
35 to 40	Analyzer B, +35, channels 1 to 6
41 to 46	Analyzer A, +0, channels 1 to 6
47 to 52	Analyzer B, +0, channels 1 to 6
53 to 58	Analyzer A, -3500, channels 1 to 6
59 to 64	Analyzer B, -3500, channels 1 to 6
65 to 70	Analyzer A, -350, channels 1 to 6
71 to 76	Analyzer B, -350, channels 1 to 6
77 to 82	Analyzer A, -35, channels 1 to 6
83 to 88	Analyzer B, -35, channels 1 to 6
89 to 94	Analyzer A, -0, channels 1 to 6
95 to 100	Analyzer B, -0, channels 1 to 6

2. Manual mode:

<u>Word number</u>	<u>Function</u>
5 to 10	Analyzer A, channels 1 to 6
11 to 16	Analyzer B, channels 1 to 6

This sequence is repeated seven times to fill the data array. If the instrument returns to the automatic mode or changes deflection voltage before the eight cycles are completed, the remainder of the array will be filled with zeros.

Mode and Identification Bits (Word 101)

1. Automatic mode: If the instrument is in the automatic mode, the 24th bit ( $2^{23}$ ) will be set to "1" and all other bits to "0."

2. Manual mode: If the instrument is in the manual mode, the 24th bit will be "0" and the lowest-order four bits will indicate the deflection voltage step according to the following:

<u>Octal</u>	<u>Decimal</u>	<u>Binary</u>	<u>Deflection_voltage</u>
16	14	1110	+3500
14	12	1100	+350
12	10	1010	+35
10	8	1000	+0
06	6	0110	-3500
04	4	0100	-350
02	2	0010	-35
00	0	0000	-0

When checking to determine if the instrument is in manual mode or automatic mode, simply check if word 101 is greater than, or less than, 100.

#### Last Valid Line (Word 102)

The last valid line word (word 102) is an integer from 1 to 8, which is the number of the last valid line in the data array. Because all lines are valid in the automatic mode, this value is significant only in the manual mode. Normally, eight manual cycles are packed into a logical unit, but a data gap or a change in mode or deflection voltage will abort the packaging process. Therefore, some logical units will have fewer than eight lines of good, time-consecutive data in them, and this parameter tells how many lines are good.

#### Year (Word 105)

The year word is a binary integer for the data year; that is, 1971.

#### Housekeeping (Words 107 to 111)

The housekeeping data have all been multiplied by 100 to preserve two decimal places in the binary integer form.

## Tape Termination

Tapes are terminated with two IBM end-of-file (EOF) marks.

### CPLEE EPHEMERIS TAPE DESCRIPTION (NSSDC: 71-008C-08B)

The various ephemeris parameters appropriate for CPLEE are written on a seven-track, 556-bpi tape in binary integer 36-bit format. The data are computed for each 2-hr interval, and the results for a 2-hr interval comprise one record. There is no header record, and there are 4380 records per file (12 X 365 = 4380). Data are supplied for the years 1971, 1972, and 1973, but data for December 31, 1972, have been omitted. Ephemeris data for the years 1971, 1972, and 1973 are combined on one tape; the data for each year are set off by EOF marks. Each record contains these 43 words.

- |    |                    |  |
|----|--------------------|--|
| 0. | Control Word       |  |
| 1. | Year               |  |
| 2. | Day                | Day 1 = Jan. 1   |
| 3. | Hour               | 00 to 22 in steps of 2   |
| 4. | OMEGA <sup>1</sup> | The angle between the analyzer A look direction and the Sun  |
| 5. | OMEGA <sup>B</sup> | The angle between the analyzer B look direction and the Sun  |
| 6. | THETA <sup>2</sup> | The angle between the analyzer A look direction and the Sun projected into the Y-Z plane of the instrument |

---

<sup>1</sup>All angles are in degrees. Words 4 to 40 were multiplied by 100 before conversion to integer for writing on tape; for example, 29.73 would appear as 2973 on tape.

<sup>2</sup>In the instrument coordinate system, Z is toward the local vertical, X is toward lunar east, and Y is toward lunar north.

7. PHIA<sup>3</sup> The angle between analyzer A and the Sun projected into the X-Z plane of the instrument
8. THETB<sup>3</sup> The angle between analyzer B and the Sun projected into the X-Z plane of the instrument
9. PHIB The angle between analyzer B and the Sun projected into the Y-Z plane of the instrument (Because the analyzer A and B look directions both lie within the instrument X-Z plane, THETA is identical to PHIB.)
10. DSMA The projection of CMEGA onto the plane of the ecliptic
11. PSMB The projection of CMEGB onto the plane of the ecliptic
12. LAMDA The angle between analyzer A look direction and the Earth
13. LAMDB The angle between analyzer B look direction and the Earth
14. LLT Local lunar time (LLT) (The angle between the lunar meridian of the instrument and the instantaneous lunar midnight meridian. LIT = 0° at local midnight; LLT = 180° at local lunar noon.)
15. HA Hour angle, LLT expressed in units of hours with 360° = 24 hr

---

<sup>3</sup>PHIA and THETB are only computed between lunar sunrise and sunset. During lunar night, PHIA = 720° and THETB = 780°.

- |     |                    |   |
|-----|--------------------|---|
| 16. | RTAM <sup>4</sup>  | Time in hours after local lunar midnight  |
| 17. | TBSR               | Time in hours before local sunrise, based on a smooth Moon (Time is positive before, negative after, sunrise. Actual sunrise at the Apollo 14 site is 5 hr 30 min later than that predicted due to topographic features.) |
| 18. | TBLN               | Time in hours before local lunar noon   |
| 19. | TBSS               | Time in hours before local lunar smooth-Moon sunset (Actual sunset at the Apollo 14 site occurs 2 hr 30 min before prediction.)   |
| 20. | SELDA <sup>5</sup> | Solar ecliptic latitude of the look direction of analyzer A, positive when looking northward out of the plane of the ecliptic   |
| 21. | SELDB              | Solar ecliptic latitude of the look direction of analyzer B   |
| 22. | SELODA             | Solar ecliptic longitude of the look direction of analyzer A  |
| 23. | SELCDB             | Solar ecliptic longitude of the look direction of analyzer B  |
| 24. | SEA                | The angle between the line from the Earth to the Sun and the line from the Earth to ALSFP   |

---

<sup>4</sup>Similar to HA, except  $360^\circ =$  lunar synodic period in hours 708 hr. All times are in hours.

<sup>5</sup>Standard geocentric solar ecliptic (SE) and solar magnetospheric (SM) coordinates are used; X-axis is positive from Earth to Sun in SE and SM; Z-axis is positive north from ecliptic plane in SE, positive north in plane containing X-axis, and tilted geomagnetic dipole axis in SM.

- |     |              |   |
|-----|--------------|---|
| 25. | ELA          | Solar ecliptic latitude of the instrument   |
| 26. | SELCA        | Solar ecliptic longitude of the instrument  |
| 27. | LTA          | Not applicable  |
| 28. | SMLA         | Solar magnetospheric latitude of the instrument   |
| 29. | SMLOA        | Solar magnetospheric longitude of the instrument  |
| 30. | SMLCA        | Solar magnetospheric latitude and longitude, respectively, of the look directions of analyzers A and B, respectively                                    |
| 31. | SMLCB        |   |
| 32. | SMLCDA       |   |
| 33. | SMLCEB       |   |
| 34. | XSM          | Geocentric solar magnetospheric coordinates in units of Earth radii of the instrument position  |
| 35. | YSM          |   |
| 36. | ZSM          |   |
| 37. | XSE          | Geocentric solar-ecliptic coordinates in units of Earth radii of the instrument position  |
| 38. | YSE          |   |
| 39. | ZSE          |   |
| 40. | ZSMRB*       | The distance from the neutral sheet in the Russell-Ercdy model (This is only computed for $XSM < 0$ and $YSM \leq 11 R_e$ . Otherwise, $ZSMRB = ZSM$ .) |
| 41. | Control word |   |
| 42. | Control word |   |

-----  
 \*All distances are in units of Earth radii  $R_e$ .

## SUMMARY OF KEY RESULTS

1. The photoelectron sheath surrounding the sunlit lunar surface was measured.
2. Particle fluxes associated with artificial lunar impact events were measured.
3. The characteristics and distribution of the plasma sheet at the lunar orbit were determined.
4. Penetrating proton and hot electron fluxes associated with the August 1972 solar flare event were measured.
5. The response of the magnetospheric tail to geomagnetic storms was investigated.
6. The characteristics of the magnetosheath and magnetopause electron fluxes were measured.

## BIBLIOGRAPHY

- Burke, William J.; Rich, Frederick J.; Reasoner, David L.; Colburn, David S.; and Goldstein, Bruce E.: Effects on the Geomagnetic Tail at 60  $R_E$  of the Geomagnetic Storm of April 9, 1971. *J. Geophys. Res.*, vol. 78, no. 25, Sept. 1, 1973, pp. 5477-5489.
- Burke, W. J.; and Reasoner, D. L.: Observation of Plasma Flow in the Neutral Sheet at Lunar Distance During Two Magnetic Bays. *J. Geophys. Res.*, vol. 78, no. 28, Oct. 1, 1973, pp. 6790-6792.
- Medrano, R. A.; Freeman, J. W., Jr.; and Hills, H. K.: Penetrating Particles on the Night Side of the Moon Associated with the August, 1972, Solar Flares. *Trans. Am. Geophys. Union*, vol. 53, no. 11, Nov. 1972, p. 1056.
- O'Brien, Brian J.; and Reasoner, David L.: Charged-Particle Lunar Environment Experiment. Sec. 10 of Apollo 14 Preliminary Science Report, NASA SP-272, 1972.
- Reasoner, David L.; and O'Brien, Brian J.: Measurement on the Lunar Surface of Impact-Produced Plasma Clouds. *J. Geophys. Res.*, vol. 77, no. 7, Mar. 1, 1972, pp. 1292-1299.
- Reasoner, David L.; and Burke, William J.: Characteristics of the Lunar Photoelectron Layer in the Geomagnetic Tail. *J. Geophys. Res.*, vol. 77, no. 34, Dec. 1, 1972, pp. 6671-6687.
- Rich, Frederick J.; Reasoner, David L.; and Burke, William J.: Plasma Sheet at Lunar Distance: Characteristics and Interactions with the Lunar Surface. *J. Geophys. Res.*, vol. 78, no. 34, Dec. 1, 1973, pp. 8097-8112.

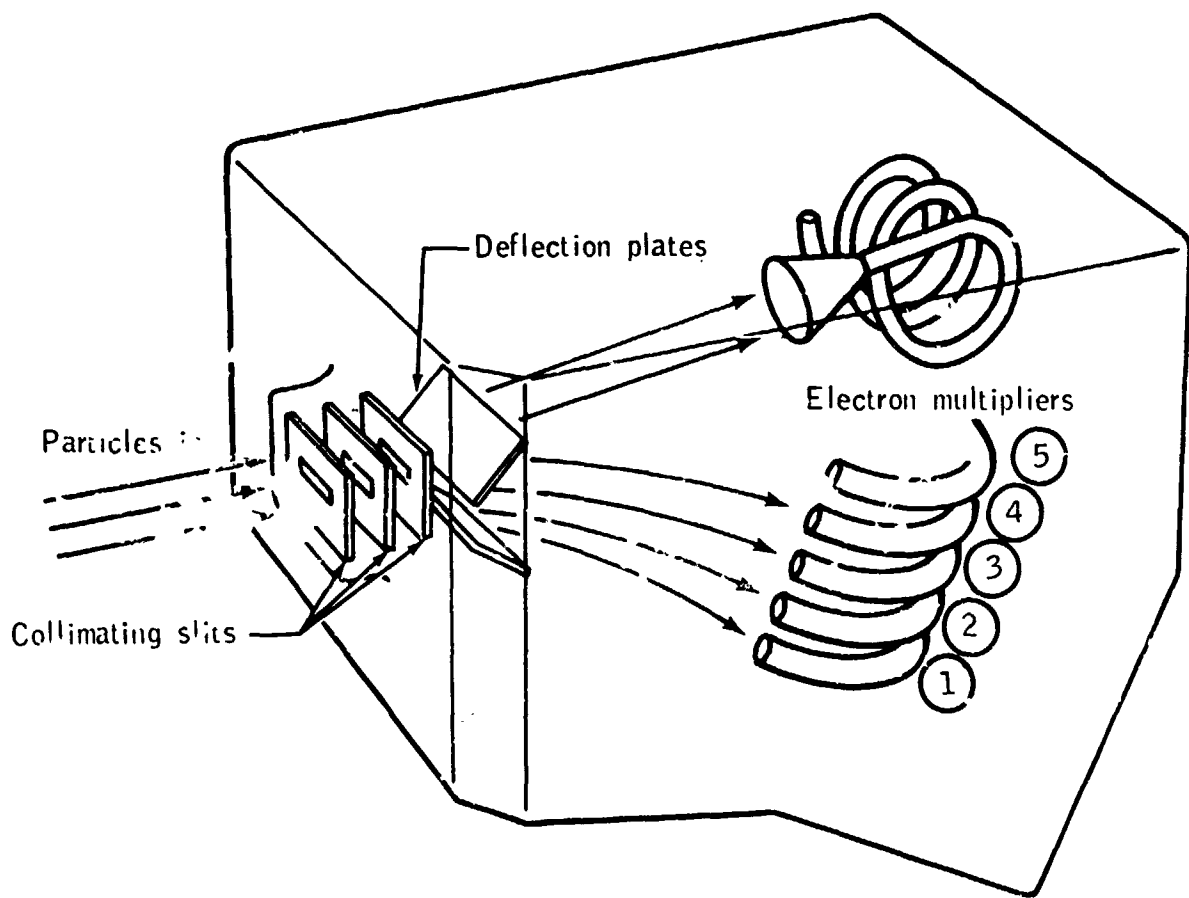


Figure 11-1.- The CPLEE physical analyzer.

February 8, 1971

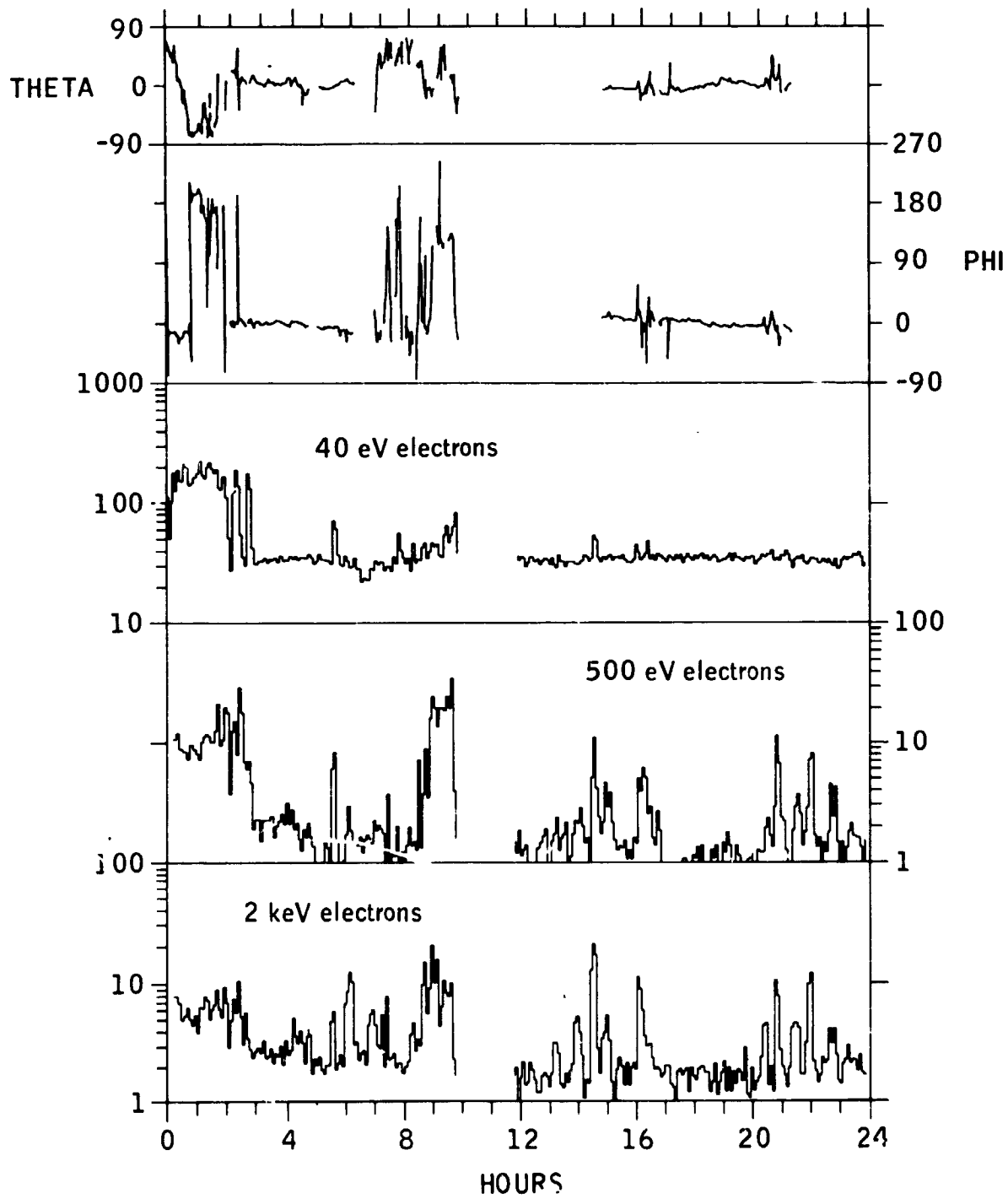
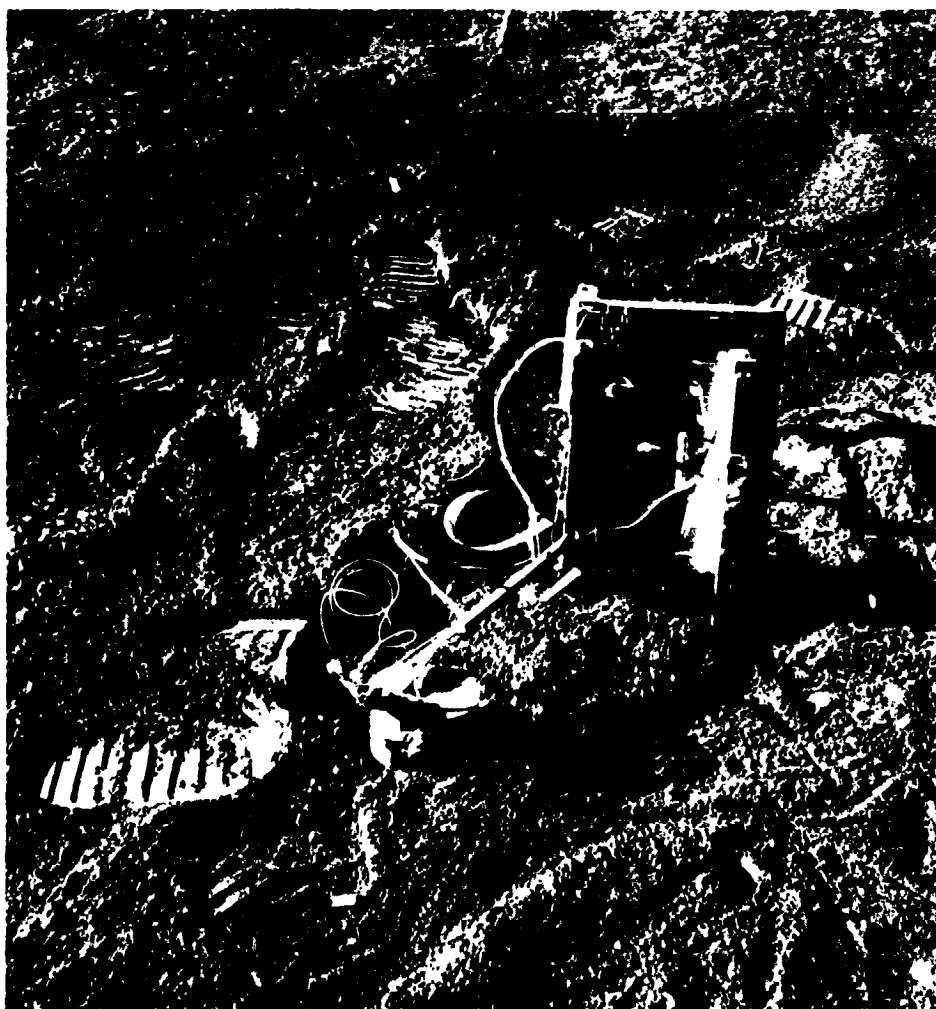


Figure 11-2.- Example of CPLEE data showing passage from the magnetosheath into the magnetotail.

12. COLD CATHODE GAGE EXPERIMENT (NASA EXPERIMENT S-058)

NSSDC IDENTIFICATION NUMBERS:

APOLLO 12 69-099C-06  
APOLLO 14 71-008C-07  
APOLLO 15 71-063C-07



ORIGINAL PAGE IS  
OF POOR QUALITY

CONTENTS - SECTION 12

	Page
OBJECTIVES . . . . .	12-3
INSTRUMENTATION . . . . .	12-4
APOLLO 14 CCGE DATA . . . . .	12-6
APOLLO 15 CCGE DATA . . . . .	12-7
DATA SETS AND AVAILABILITY THROUGH NSSDC . . . . .	12-9
BIBLIOGRAPHY . . . . .	12-9

## 12. COLD CATHODE GAGE EXPERIMENT

The cold cathode gage experiment (CCGE) was included in the Apollo lunar surface experiments package (ALSEP) on the Apollo 12, 13, 14, and 15 missions. The Apollo 12 instrument failed after only a few hours of operation, and the Apollo 13 package was not deployed because of spacecraft problems and the cancellation of the lunar landing.

### OBJECTIVES

Although the lunar atmosphere is known to be tenuous, its existence cannot be doubted because the solar wind striking the lunar surface constitutes one source, and there may be other sources as well. The most significant source of lunar atmosphere, if it were to prove detectable, would be degassing from the interior. Such degassing would constitute useful information on how planetary atmospheres originate.

The gas concentration at the lunar surface must depend on the balance between source and loss mechanisms as well as on properties of diffusion over the lunar surface. The dominant loss mechanisms for lunar gases are thermal escape for particles lighter than neon and escape through interaction with the solar wind after photoionization has occurred for neon and heavier particles. The gas particles lighter than neon have such high thermal velocities that a significant fraction of them can escape from the gravitational field of the Moon owing to their greater-than-escape velocity. The average lifetime on the Moon for helium is approximately  $10^4$  sec. Heavier particles, with lower thermal velocities, have longer lifetimes; the lifetime for neon is approximately  $10^{10}$  sec, and the lifetime for heavier particles is much longer.

Particles exposed to solar ultraviolet radiation become ionized in approximately  $10^7$  sec; once ionized, the particles are accelerated by the electric field associated with the motion of the solar wind. The initial acceleration is at right angles to the direction of both the solar wind and the embedded magnetic field; then, the direction of motion is deviated by the magnetic field so that the ionized particle acquires an average velocity equal to the solar-wind-velocity component perpendicular to the embedded magnetic field. The time required for this acceleration is approximately the ion gyro period in the embedded magnetic

field. The radii of gyration for most ions are comparable to or greater than the lunar radius. As a consequence of this acceleration process, particles in the lunar atmosphere are largely swept away into space within a few hundred seconds (the ion gyro period) after becoming ionized. Thus, the time required for ionization regulates the loss process, which results in lifetimes for particles in the lunar atmosphere on the order of  $10^7$  sec.

The CCGE was included in the ALSEP to evaluate the amount of gas present on the lunar surface. The amount of gas observed can be compared with the expectation associated with the solar-wind source to obtain an indication of whether other sources of gases are present. Contamination from the lunar module (LM) and from the astronaut suits constitutes an additional source, but one that should decrease with time in an identifiable way. In the long run, measurements of the actual composition of the lunar atmosphere should be made with a mass spectrometer to examine constituents of particularly great interest geochemically and to identify and discriminate against contaminants from the vehicle system.

#### INSTRUMENTATION

The vacuum gage included in the ALSEP is a cold cathode ionization gage; the general configuration is shown in figure 12-1. The envelope and electrodes are stainless steel. An axial magnetic field of approximately 0.09 T (900 G) is provided by a permanent magnet. The orifice was closed, but not sealed, with a spring-loaded cover that was released by an electrical impulse to a squib motor. To reduce the possible effects of the magnet on other instruments, a magnetic shield can was mounted around the gage and its magnet.

The response of the gage in terms of cathode current as a function of gas concentration is shown in figure 12-2. The gage response can be expressed as pressure, which also depends on the ambient temperature, but the gage is actually sensitive to gas density rather than pressure. A temperature sensor was attached to the gage envelope to permit making corrections to the gage response based on the wide variations in temperature encountered on the lunar surface, approximately 100 to 400 K. The gage response is also somewhat dependent on gas composition, and the calibration was for nitrogen. Because the composition of lunar atmospheric gases is not known, a fundamental uncertainty is introduced into the interpretation of the data; and the results are presented as if the gas on the lunar surface were nitrogen. The difference between the nitrogen equivalent pressure and the true pressure is probably less than a factor of 2.

The gage anode is connected to a  $+4500 \pm 200$  V power supply, which is shown diagrammatically in figure 12-3. The supply consists basically of a regulator, a converter, a voltage-multiplier network, and a feedback network to the low-voltage supply. The regulator furnishes a 24-V output for conversion to a 5-kHz squarewave that is applied to the converter transformer. The output of the transformer goes to a voltage-multiplier network consisting of stacked standard doublers. The output is filtered and applied to the gage anode and divided down to provide a monitor signal. A high resistance in the connection to the gage anode provides overload protection for the gage and power supply, limiting the maximum current to approximately  $2 \mu\text{A}$ . The output regulation is within 2 percent for load currents as high as  $1 \mu\text{A}$ .

The gage cathode is connected to an autoranging, autozeroing electrometer that measures currents in the range  $10^{-13}$  to  $10^{-6}$  A with an output of  $-15$  mV to  $-15$  V. The output goes to an analog-to-digital (A/D) converter for transmission over the ALSEP data link to Earth. The electrometer consists of a high-gain, low-leakage, differential amplifier with switched high-impedance feedback resistors for range changes. The output voltage and input current are related by  $E = R_f(I_i + I_l)$ , where  $E$  is the electrometer output,  $I_i$  the input current,  $I_l$  the leakage current, and  $R_f$  the feedback resistance. When the input current is zero, the output voltage does not go to zero because of leakage and other factors, and the output voltage can be expressed as  $R_f I_l$ ; this voltage is the zero offset voltage and is canceled by introducing a compensating error voltage from the autozeroing network into a second grid in the electrometer tube, as indicated in figure 12-4. Autozeroing is accomplished by disconnecting the sensor (by opening relay S1) and switching in the autozeroing amplifier in a feedback network to the second grid (by closing S3) for a short interval; capacitor C1 holds the zero-corrected potential until the next autozeroing cycle. Relay S2 connects the sensor to ground during the interval that it is disconnected from the electrometer.

The electrometer operates in three automatically selected overlapping ranges:  $1 \times 10^{-13}$  to  $9 \times 10^{-11}$  A,  $3.3 \times 10^{-12}$  to  $3.2 \times 10^{-9}$  A, and  $1 \times 10^{-9}$  to  $9.3 \times 10^{-7}$  A. The electrometer has strong feedback to maintain the input grid potential at almost zero. Automatic range switching is accomplished by the switching of two feedback resistors, R1 and R2, across permanent feedback resistor R3, as indicated in figure 12-4. To control the range changes, the electrometer output is compared against  $-15$  mV and  $-15$  V references by means of comparators. The outputs of these comparators pass to a logic circuit that drives relays S4 and S5

and generates a range signal for transmission to Earth; a signal is also generated to select the proper current generators for calibration by closing S6, S7, or S8 and S9, S10, or S11.

The normal operating sequence of the electrometer circuit includes a 16-sec calibration function, including autozeroing, at approximately 2.5-min intervals. The first operation is the zero check and correction; S1 is opened and S2 is closed to disconnect the gage. Then, after approximately 9 sec, the output of the electrometer is sampled, followed by closing S3 for approximately 2 sec to accomplish the autozeroing. This is followed by the first step of the calibration cycle, accomplished by closing S13, and then by the second step, accomplished by opening S13 and closing S12. After the calibration cycle, the gage is reconnected to the electrometer. The electrometer output is then sampled five times at 2.4-sec intervals and three times at 40-sec intervals. The cycle of operation can be altered by ground command to provide readings every 2.4 sec without any calibration or zero correction. The zero correction drifts only slightly over a period of an hour, because its time constant is approximately 6 hr.

The method chosen for presentation of the data is a microfilm plot with particle concentration plotted at the bottom of the frame and the gage temperature plotted at the top of the frame, as shown in figure 12-5. The time used on all the frames is Greenwich mean time (G.m.t.). In the normal operating mode of the instrument, an average of four data points is obtained each minute. The data are recorded on 35-mm film with approximately 15 hr of data on each frame. The range of concentration is plotted logarithmically from  $10^5$  ( $10^4$ ) to  $10^{11}$  ( $10^{10}$ ) particles/cm<sup>3</sup>, and the range of temperature is linear from 0 to 400 K. The values shown on the plots have been computed using the calibration curves of the appropriate gage and temperature sensor.

Brief descriptions of the data for the Apollo 14 and 15 experiments are given in the following sections.

#### APOLLO 14 CCGE DATA

The Apollo 14 CCGE instrument was first activated on February 6, 1971, while the astronauts were still on the lunar surface. The unit was operated for short periods of time (approximately 30 min) during LM venting for the second and third extravehicular activity (EVA). The experiment was then turned off until lunar sunset.

In the following months, the instrument was not activated during the lunar daytime except for brief periods to allow the

package to outgas and minimize the possibility of high-voltage arcing. Table 12-I(a) shows the approximate time of operation. The period of operation was increased each month until complete operation was obtained during the daytime in November 1971.

Data are available for all periods of operation except during periods when problems occurred. The first problem occurred in April 1971 when the +A/D converter became erratic. This problem was not serious as far as the CCGE data were concerned because it affected only the temperature and housekeeping data. Other than occasionally noisy data, no additional problems were encountered with the CCGE until the nighttime operation in February 1972. At that point, the CCGE data dropped out for approximately 4 days at the end of the lunar night but came back at sunrise. This problem occurred intermittently until the nighttime operation in late November 1972, at which time all nighttime data were lost. This complete loss of nighttime data lasted for 2 months followed by 1 month of complete data in late March 1973 and then 2 more months of no nighttime data.

The start of the lunar day on April 15, 1973, produced the third and the most serious problem. At that time, the supra-thermal ion detector experiment (SIDE)/CCGE went into the standby condition, and no data were available from either the SIDE or the CCGE. Attempts to restore the experiment to normal operation were unsuccessful until the following lunar night, at which time the CCGE high voltage was restored but the SIDE high voltage had to be left off. In this condition, the CCGE nighttime data were again good and remained good until an unsuccessful attempt was made at approximately sunrise to restore the SIDE high voltage. After sunrise, it was not possible to obtain operation with either of the high voltages on, and the experiment was left in standby until sunset. No daytime operation has been successful since about April 15, 1973. The nighttime operation continued to be normal with both high voltages operating. Tapes for this period show intermittent operation.

#### APOLLO 15 CCGE DATA

The Apollo 15 CCGE was operated only for short time periods after deployment and initial activation on July 30, 1971. The data shown in figure 12-6 represent this mode of operation. The operating times coincided with the depressurization of the LM for the various EVA periods and for the LM lift-off. After lift-off, the unit was turned on at approximately 215:02:53 G.m.t. for another short period. The instrument amplifier was left on to monitor temperature, but the high-voltage supply was off to prevent the possibility of arcing within the package as it heated up and degassed. Table 12-I(b) shows the approximate times of operation of the Apollo 15 CCGE.

The high-voltage supply was turned on at approximately 225:01:30 G.m.t. and remained on until approximately 242:09:52 G.m.t. During this period, several changes in concentration were observed, apparently due to the release of gas from various hardware items left on the lunar surface. The high voltage was turned off during most of the lunar daytime for the first few months to minimize the possibility of arcing. However, when the voltage was turned off at approximately 271:05:00 G.m.t., a low value of leakage current appeared and continued to be present from that point on. This leakage current appears on the plot as a very low concentration.

Several anomalies appearing in the plots generally have been traced to noisy data that appear to originate in the gage or its associated electronics. The noise is worse near sunrise or sunset when the package temperature is changing. One example is shown in figure 12-7 where the scattered points above and below the main plot were caused by range changes in the instrument. The range change is automatic and normally there is no problem except when the noise factor becomes so large that unreported range changes occur. Because the range data are not updated just prior to converting the concentration data, the computer occasionally produces a bad point on the plot because of the use of the incorrect range. The double traces that appear from 271:02:52 to 271:05:52 of 1971 seem to be an instrument problem involving crosstalk in certain words of the SIDE frame.

The abrupt concentration changes that occasionally appear, such as at 333:00:52 (fig. 12-8), are due to the operating characteristics of the cold cathode gage and are identified as mode changes. Oscillation between the upper and lower levels of the mode sometimes occurs if the concentration is changing slowly.

A definite increase in concentration occurred at sunset during the early months of operation. The amount of gas released decreased with each sunset and eventually disappeared, thus indicating that the gas was associated with hardware left on the surface.

The Apollo 15 CCGE operation was good until February 1973, at which time the nighttime data became erratic. During the problem periods, the data are very noisy and the automatic-zero and calibration functions do not appear to be operating. This problem persisted during all subsequent nighttime operations.

## DATA SETS AND AVAILABILITY THROUGH NSSDC

The data listed in table 12-I are available at the National Space Science Data Center (NSSDC) on 35-mm film in the form shown in figure 12-5.

### BIBLIOGRAPHY

- Johnson, F. S.; Evans, D. E.; and Carroll, J. M.: Cold Cathode Gage (Lunar Atmosphere Detector). Sec. 7 of the Apollo 12 Preliminary Science Report, NASA SP-235, 1970.
- Johnson, F. S.; Evans, D. E.; and Carroll, J. M.: Cold-Cathode-Gage Experiment (Lunar Atmosphere Detector). Sec. 9 of the Apollo 14 Preliminary Science Report, NASA SP-272, 1971.
- Johnson, F. S.: Lunar Atmosphere. Rev. Geophys. Space Phys., vol. 9, no. 3, Aug. 1971, pp. 812-823.
- Johnson, F. S.; Evans, D. E.; and Carroll, J. M.: Cold Cathode Gage Experiment (Lunar-Atmosphere Detector). Sec. 13 of the Apollo 15 Preliminary Science Report, NASA SP-289, 1972.
- Johnson, F. S.; Evans, D. E.; and Carroll, J. M.: Observations of Lunar Atmosphere. Vol. I of Space Res. XII, Proceedings of the 14th Plenary Meeting of COSPAR, Akademie-Verlag (Berlin), 1972, pp. 99-105.
- Johnson, Francis S.; Evans, Dallas E.; and Carroll, James M.: Vacuum Measurements on the Lunar Surface. J. Vacuum Sci. Tech., vol. 9, no. 1, Jan.-Feb. 1972, pp. 450-456.
- Johnson, Francis S.; Evans, Dallas E.; and Carroll, James M.: Lunar Atmosphere Measurements. Proceedings of the Third Lunar Science Conference, vol. 3, David R. Criswell, ed., MIT Press (Cambridge, Mass.), 1972, pp. 2231-2242.

TABLE 12-I.- APOLLO 14 AND 15 CCGE DATA AVAILABLE AT THE  
NATIONAL SPACE SCIENCE DATA CENTER (NSSDC)

(a) Apollo 14

(b) Apollo 15

Period of operation, G.m.t., day:hr:min	
From	To
1971	
<sup>a</sup> 37:00:51	37:13:40
50:16:30	66:21:00
77:14:00	97:10:44
107:12:15	128:14:15
135:13:00	157:23:40
159:12:00	159:14:00
165:13:00	187:19:10
194:14:44	217:10:44
<sup>a</sup> 217:21:00	219:09:00
223:21:00	232:17:46
236:17:44	246:05:44
253:22:15	275:20:30
<sup>a</sup> 276:16:30	281:19:55
282:15:45	311:00:44
312:17:44	365:23:59
1972	
000:00:08	009:00:00
009:17:44	068:17:44
069:17:44	177:06:44
179:17:44	205:06:30
207:14:44	271:12:50
275:17:44	307:17:44
311:17:44	346:22:50
351:17:44	365:23:59

<sup>a</sup>Spot operation.

Period of operation, G.m.t., day:hr:min	
From	To
1971	
<sup>a</sup> 212:18:56	215:02:53
225:01:30	242:09:52
253:16:30	271:05:40
<sup>b</sup> 271:05:40	282:15:53
282:15:53	302:23:20
<sup>b</sup> 302:23:20	312:13:02
312:13:02	336:13:10
341:16:52	352:18:52
356:18:52	364:15:30
1972	
004:18:52	030:13:52
034:14:00	057:18:52
<sup>b</sup> 058:12:52	063:14:00
053:14:00	006:18:52
087:18:52	088:16:10
092:14:52	118:01:20
122:21:40	148:04:10
149:05:00	190:02:30
191:18:52	194:03:00
195:18:52	263:23:52
267:18:52	365:23:59

<sup>a</sup>Original turn-on  
and spot operation.

<sup>b</sup>Spot operation.

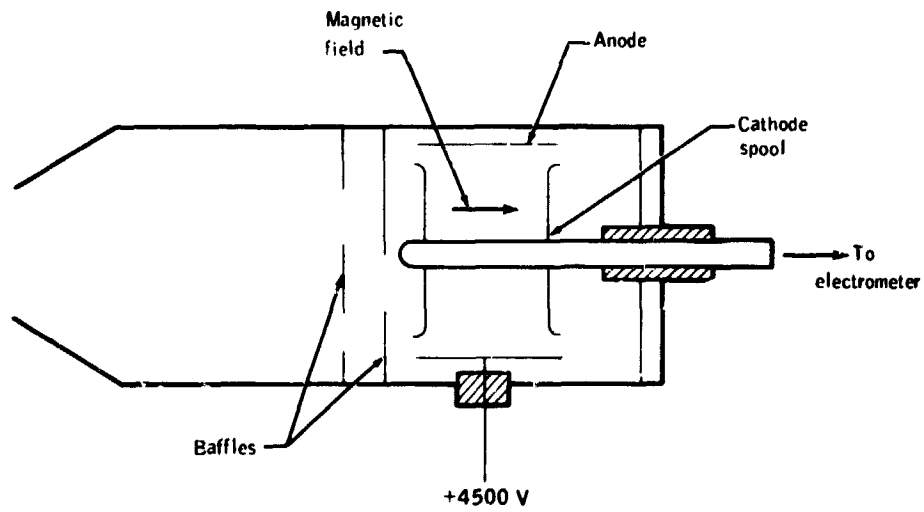


Figure 12-1.- Configuration of the cold cathode ionization gage.

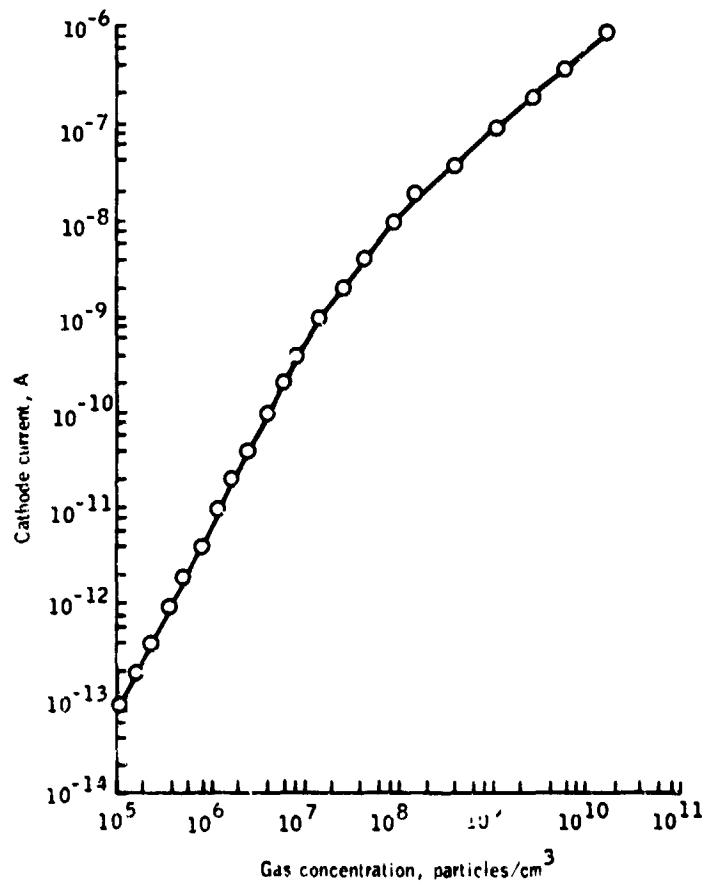


Figure 12-2.- Response curve for the CCGE.



24

APOLLO 15  
1971

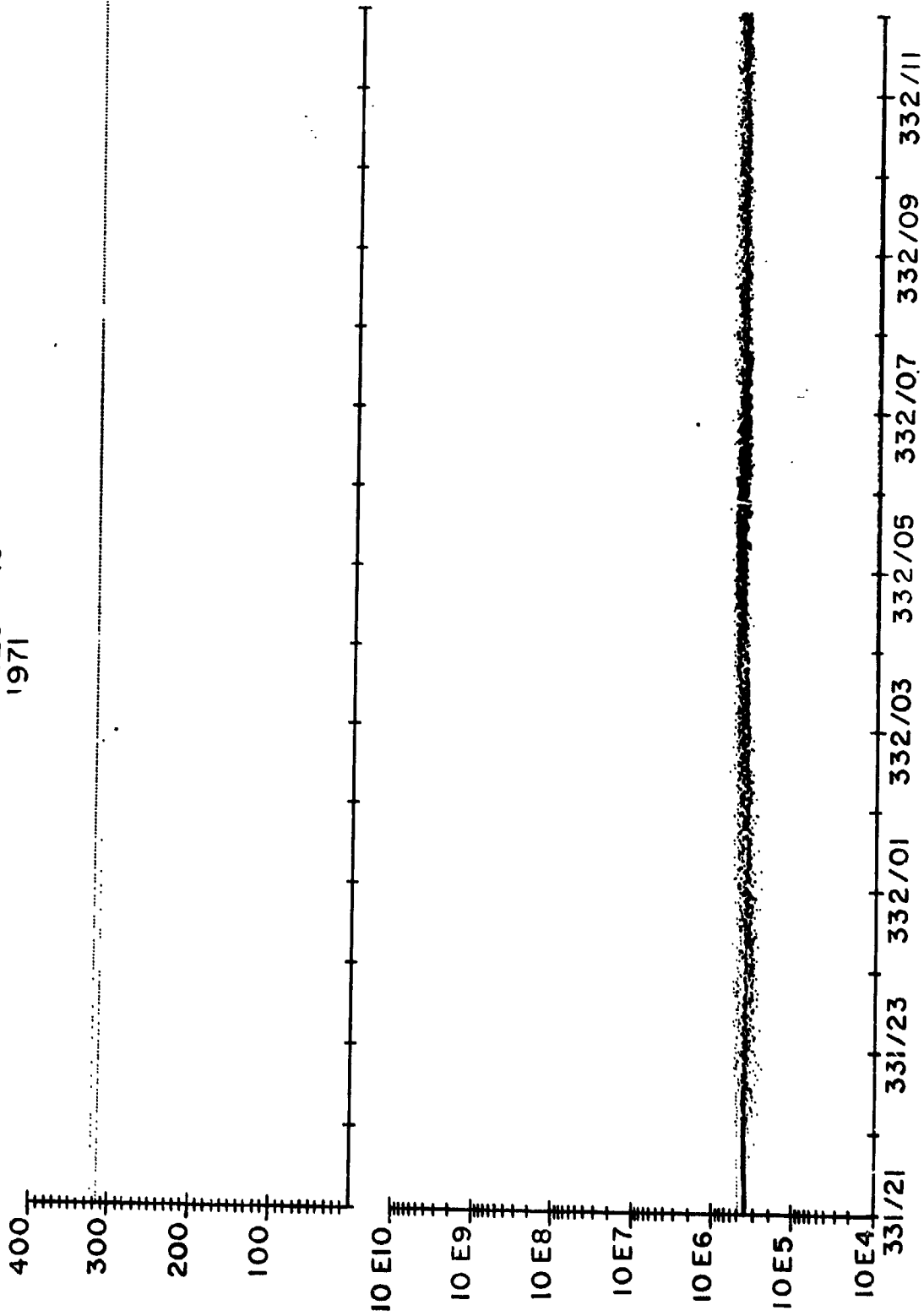


Figure 12-5.- Example of data presentation as microfilm plot.

APOLLO 15  
1971

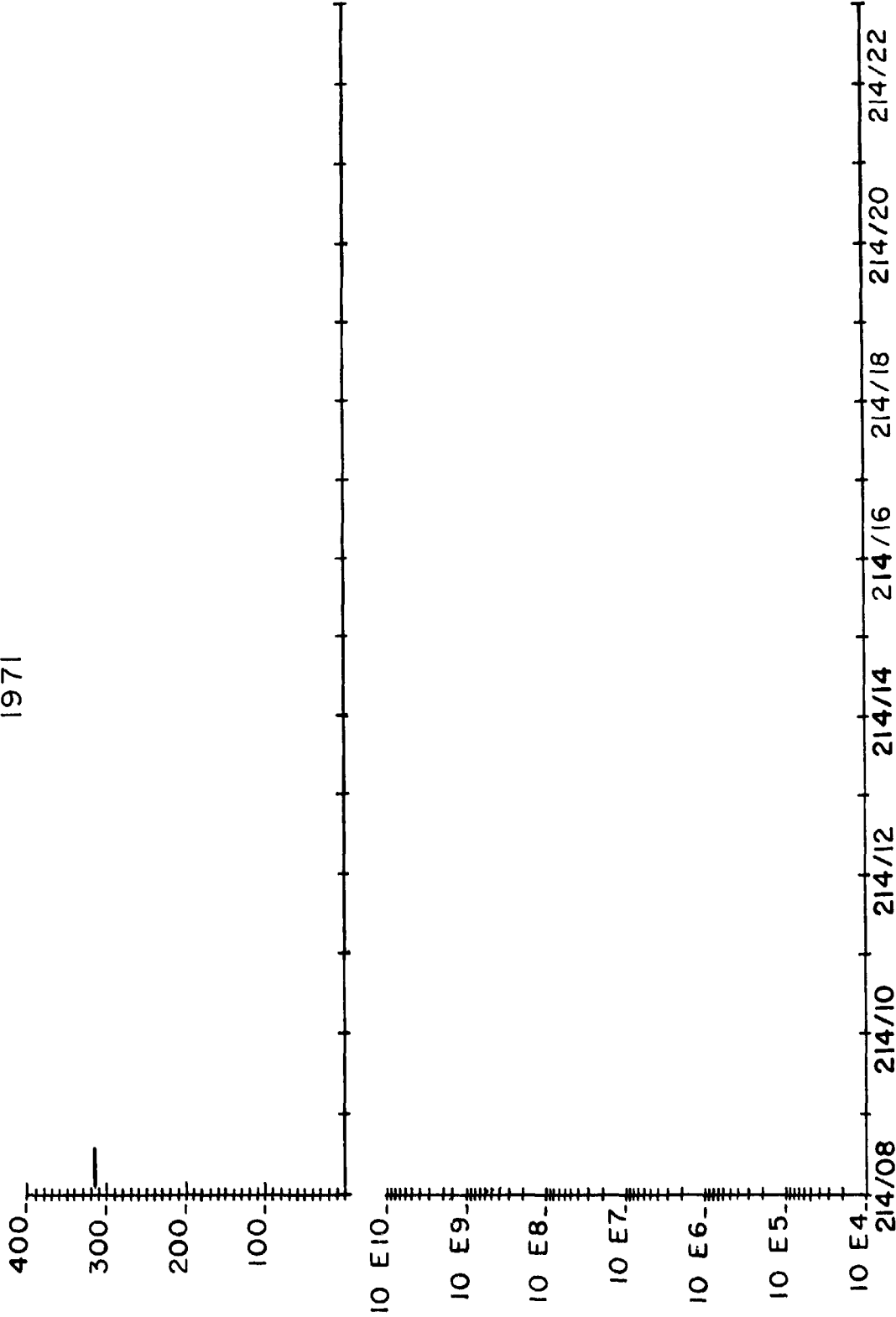


Figure 12-6.- Example of data for Apollo 15 CCGE after deployment and original activation on July 30, 1971.

APOLLO 15  
1971

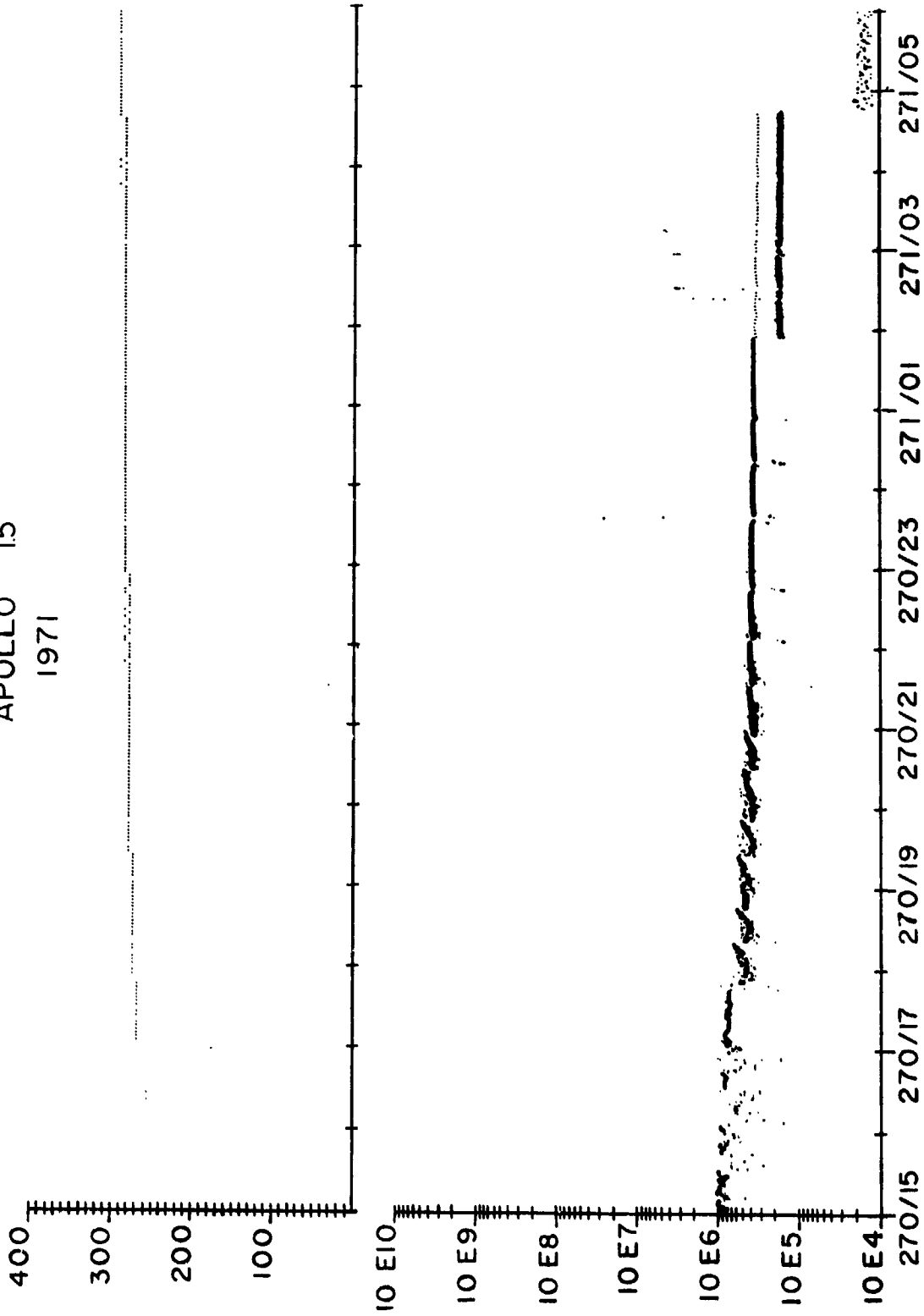


Figure 12-7.- Plot showing example of COGE data anomaly (scattered data points) resulting from noise factor.

APOLLO 15  
1971

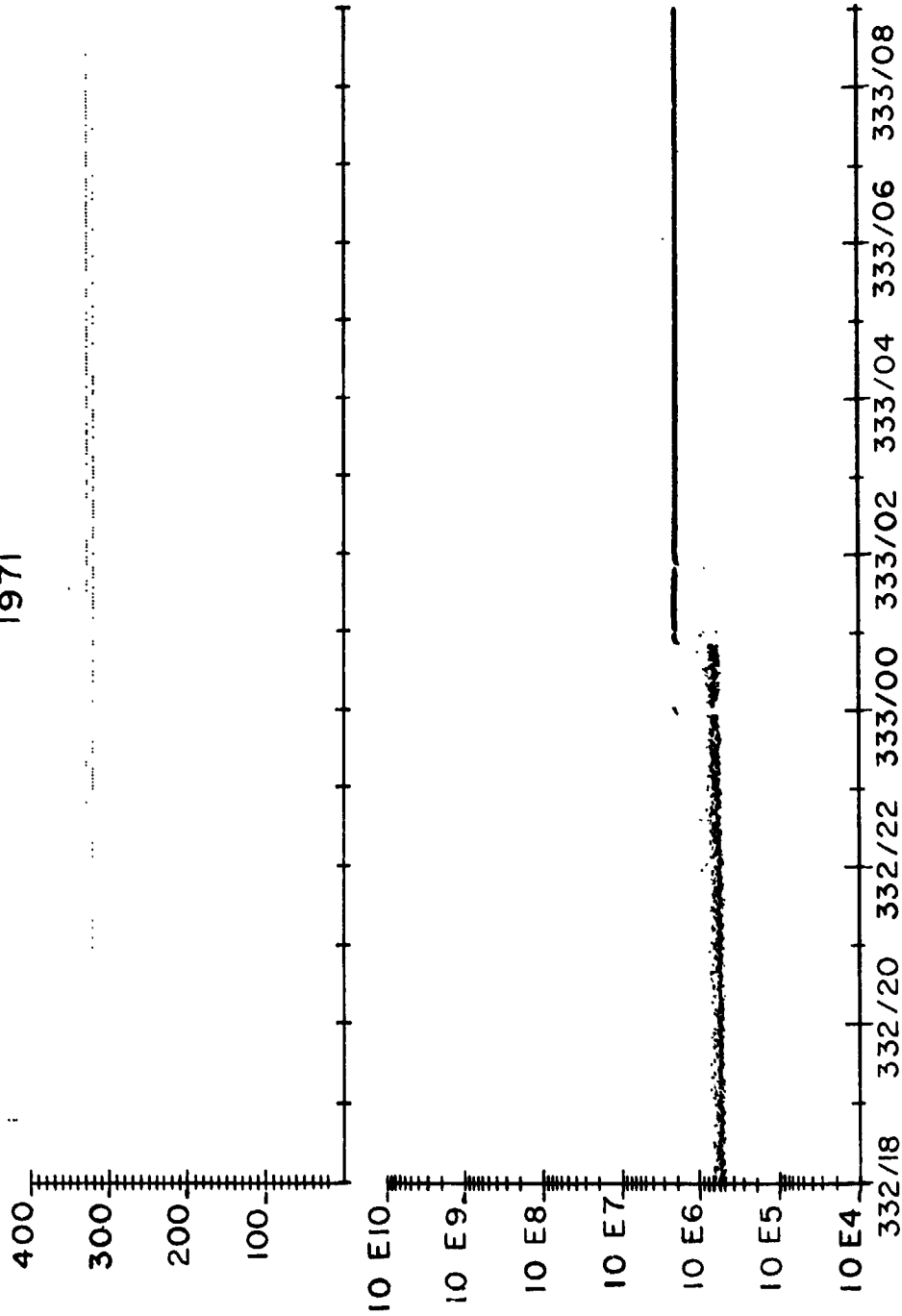
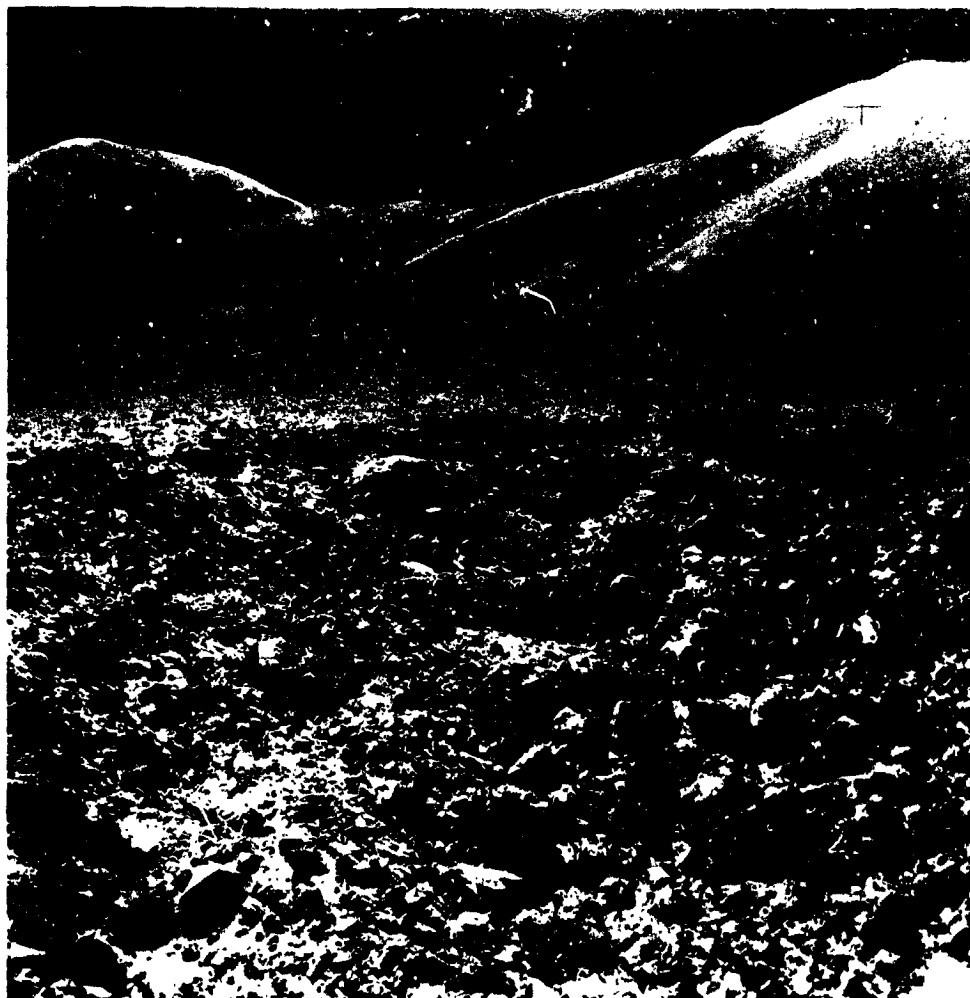


Figure 12-8.- Example of plot showing abrupt concentration changes due to CGGE operating characteristics (mode changes).

13. LUNAR GEOLOGY (NASA EXPERIMENT S-059)

NSSDC IDENTIFICATION NUMBERS:

APOLLO 11	69-059C-01
APOLLO 12	69-C99C-01
APOLLO 14	71-008C-01
APOLLO 15	71-063C-10
APOLLO 16	72-031C-05
APOLLO 17	72-096C-02



ORIGINAL PAGE IS  
OF POOR QUALITY

CONTENTS - SECTION 13

	Page
APOLLO 11 LANDING SITE . . . . .	13-3
APOLLO 12 LANDING SITE . . . . .	13-6
Linear Grooves . . . . .	13-7
Craters . . . . .	13-8
Panoramas . . . . .	13-10
APOLLO 14 LANDING SITE . . . . .	13-11
Lunar Photographs . . . . .	13-12
Geology of Fra Mauro Site . . . . .	13-12
Regional Geologic Setting . . . . .	13-13
Local Geologic Setting . . . . .	13-14
APOLLO 15 LANDING SITE . . . . .	13-15
APOLLO 16 LANDING SITE . . . . .	13-20
APOLLO 17 LANDING SITE . . . . .	13-25
DATA TO BE ARCHIVED AT NSSDC . . . . .	13-32
REFERENCES . . . . .	13-33
BIBLIOGRAPHY . . . . .	13-34

### 13. LUNAR GEOLOGY

This section contains brief descriptions of geological investigations conducted at the lunar landing sites of Apollo missions 11, 12, 14, 15, 16, and 17. Much of the information presented here was taken from the Preliminary Science Reports for the respective missions, which are included in the bibliography together with additional reference material. The six lunar landing sites are discussed in mission sequence.

#### APOLLO 11 LANDING SITE

The lunar module (LM) landed approximately 400 m west of a sharp-rimmed ray crater, approximately 180 m in diameter and 30 m deep (fig. 13-1), which had been informally named West Crater. West Crater is surrounded by a blocky ejecta apron that extends almost symmetrically outward approximately 250 m from the rim crest. Blocks as large as 5 m wide occur on the rim and in the interior of the crater. Rays of blocky ejecta with many fragments from 0.5 to 2 m in width extend beyond the ejecta apron west of the landing point (fig. 13-2). The LM landed in a region between these rays that is relatively free of extremely coarse blocks.

At the landing site, the lunar surface consists of unsorted fragmental debris, which ranges in size from particles that are too fine to be resolved by the naked eye to blocks 0.8 m wide. This fragmental debris forms a layer, the lunar regolith, which is porous and weakly coherent at the surface. The regolith grades downward into similar, but more densely packed, material. The bulk of the regolith consists of fine particles, but many rock fragments were encountered on the surface and in the subsurface.

The surface of the regolith is pockmarked with small craters ranging in diameter from only a few centimeters to several tens of meters. Immediately southwest of the LM landing site is a double crater (15 m long, 8 m wide, and 1 m deep) with a subdued raised rim. Approximately 60 m east of the LM landing site is a steep-walled, but shallow, crater with a raised rim. This crater, which is 33 m in diameter and 4 m deep, was visited by Astronaut Neil A. Armstrong near the end of the EVA.

Many of the small craters have low, but distinct, raised rims; some rims are sharply formed, but most rims are subdued. Other craters are shallow and rimless, or nearly rimless. The small rimless craters are commonly merged together to form irregular shallow depressions. Both the craters and the irregular depressions are distributed without apparent alignment or pattern. Small craters are scattered irregularly on the rims, walls, and floors of larger craters.

All the craters in the immediate vicinity of the LM landing site have rims, walls, and floors composed of fine-grained material. Scattered, coarser fragments occur in about the same abundance in these craters as on the inter-crater areas. These craters are approximately 1 m or less in depth; they have evidently been excavated entirely in the regolith.

In the 33-m-diameter crater east of the LM landing site, the crater walls and rim have the same texture as the regolith elsewhere; however, a pile of blocks occurs on the floor of the crater. The crater floor probably lies close to the base of the regolith. Several craters of about the same size as the 33-m-diameter crater (with steep walls and shallow, flat floors or floors with central humps) occur in the region around the landing site. Judging from the depths of these craters, the thickness of the regolith is estimated to range from 3 to 6 m.

An unexpected discovery made by Astronaut Armstrong was the presence of blebs of material with specular surfaces. These blebs of material partially covered 2- to 10-cm-diameter areas in the bottom of six or eight 1-m-diameter raised-rim craters. Astronaut Armstrong observed these apparently glassy blebs, which resembled drops of solder, only in craters. The form of the blebs suggests they had been formed by the splashing of molten material traveling at low velocity. The distribution of the blebs suggests that they are natural features on the lunar surface; however, the possibility exists that the blebs are artifacts that were produced by the landing of the LM.

In addition to craters, the surface of the regolith is marked by small, shallow troughs. By using photographs taken 19 m southeast and 12 m north of the center of the LM landing site, a preliminary study was made of the troughs. Most of the troughs are a fraction of a centimeter to a centimeter deep, approximately 0.5 to 3 cm wide, and 3 to 50 cm long; three of these troughs that were observed are 2 to 3 m long. The troughs are located 3 to 5 cm apart in areas in which they are prominent. One set of troughs trends northwest; another set (which is comparable to the

northwest-trending troughs in abundance, but are more dispersed in orientation) trends northeast to north-northeast. A few troughs were observed that trend in other directions. Troughs of similar appearance were noted in many other photographs, but the orientations of these other troughs have not yet been determined.

Coarse fragments are scattered in the vicinity of the LM landing site in approximately the same or somewhat greater abundance than is found at the Surveyor I landing site (ref. 13-1). These coarse fragments are distinctly more abundant in these two sites than at other Surveyor landing sites on the maria, including the Surveyor V landing site, which is northwest of the LM landing site. Similar to the Apollo 11 LM, Surveyor I landed near a fresh blocky rim crater but beyond the apron of coarse blocky ejecta. It may be inferred that many rock fragments in the immediate vicinity of the spacecraft, at both the Surveyor I and the Apollo 11 landing sites, were derived from the nearby blocky rim crater. Fragments derived from West Crater may have come from depths as great as 30 m beneath the mare surface.

The fine-grained matrix of the regolith consists chiefly of microscopic particles. The regolith is weak and easily trenched to depths of several centimeters. Surface material was easily dislodged when kicked. When the flagpole for the U.S. flag and the core tubes were pressed into the surface, they penetrated with ease to a depth of 10 to 12 cm. At that depth, the regolith was not sufficiently strong, however, to hold the core tubes upright; a hammer was needed to drive them to depths of 15 to 20 cm. At several places, rocks were encountered in the subsurface by the tubes, rods, and scoop that were pressed into the subsurface.

The astronauts' boots left prints approximately 3 mm to 3 cm deep in the fine-grained regolith material. Smooth molds of the boot treads were preserved in the footprints, and angles of 70° were maintained in the walls of the footprints. The fine-grained surficial material tended to break into slabs, cracking as far as 12 to 15 cm from the edges of the footprints.

The finest fraction of the regolith adhered weakly to boots, gloves, spacesuits, handtools, and rocks on the lunar surface. On repeated contact, the coating on the boots thickened until boot color was completely obscured. When the fine particles of the regolith were brushed off, a stain was left on the spacesuits.

In places where fine-grained material was kicked by the astronauts, the freshly exposed material was conspicuously

darker than the undisturbed surface. As at the Surveyor landing sites, the subsurface material probably lies at depths no greater than a millimeter from the surface. The existence of a thin surface layer of lighter colored material at widely scattered localities indicates that some widespread process of surface-material alteration is taking place on the Moon.

Fillets of fine-grained material are banked against the sides of most rock fragments. The fillets were observed at least as far as 70 m from the LM, and most of the fillets are almost certainly natural features of the surface. On sloping surfaces, Astronaut Armstrong observed that the fillets were larger on the uphill sides of rocks than on the downhill sides of rocks. The sides of rocks are ballistic traps, and the fillets have probably been formed by the trapping of low-velocity secondary particles. Asymmetric development of fillets around rocks on slopes may be partly caused by preferential downhill transport of material by ballistic processes and partly caused by downhill creep or flow of the fine-grained material.

#### APOLLO 12 LANDING SITE

The LM landed on the northwest rim of the 200-m-diameter Surveyor Crater (in which Surveyor III touched down on April 20, 1967) in the eastern part of Oceanus Procellarum (fig. 13-3). The landing site was at 23.4° W and 3.2° S, approximately 120 km southeast of the crater Lansberg and due north of the center of Mare Cognitum.

The landing site is on a broad ray associated with the crater Copernicus, which is located approximately 370 km to the north. The site is characterized by a distinctive cluster of craters ranging in diameter from 50 to 400 m. The lunar surface at the landing site is underlain by fragmental material, the lunar regolith, which ranges in size from particles too fine to be seen with the naked eye to blocks several meters across. Along several parts of the traverse made during the second extravehicular activity (EVA) period, the astronauts found fine-grained material of relatively high albedo that, at some places, was in the shallow subsurface and, at other places, was at the surface. This light-gray material was specifically reported to be at the surface near Sharp Crater and a few centimeters below the surface near Head, Bench, and Block Craters. It is possible that some of this light-gray material may constitute a discontinuous deposit that is observed through telescopes as a ray of Copernicus.

Darker regolith material that generally overlies the light-gray material is only a few centimeters thick in some places, but probably thickens greatly on the rims of some craters. It varies from place to place in the size, shape, and abundance of its constituent particles and in the presence or absence of patterned ground. Most local differences are probably the result of local cratering events.

Many comments of the astronauts concern the large amount of glass that is contained in the regolith. Irregularly shaped, small fragments of glass and glass beads are abundant both on and within the regolith; glass is also splattered upon some of the blocks of rock at the surface and is found within many shallow craters.

#### Linear Grooves

Much of the surface in the area of the geologic traverse made during the second EVA period is patterned by small, linear grooves. These grooves are visible on the returned photographs and were reported from several localities by the astronauts. They are similar in appearance to those visible on some of the Apollo 11 photographs (ref. 13-2).

The astronauts referred to the patterned ground as "trenches," "grooves," "lines," and "streaks." When referred to as "trenches," the grooves were estimated to be approximately 3 mm deep. The linear features were reported to trend generally north (north-northeast or northeast in Surveyor Crater) and were reported to occur in strips of patterned ground perhaps 30 m wide. During postmission debriefings of the crew, the strips of patterned ground were also reported to be north trending.

Examination of returned photographs shows an additional set of grooves that trend roughly west in the areas where the north-trending grooves are present. In addition to the grooves, north- and west-trending chains of small elongate depressions and small scarps are also present. At an azimuth of approximately 325° from the LM is a nearly square crater, 4 or 5 m across, whose sides are parallel to the north- and west-trending grooves.

All of the linear features have a vertical relief generally less than 1 cm, are commonly approximately 2 cm wide, and are approximately 5 cm to 1 m long. A few of these features observed in the photographs are several meters long. The grooves, chains, and scarps cross small

craters and other surface irregularities without apparent change in form or direction.

Similar linear features noted at the Apollo 11 site trend roughly northeast and northwest and have been interpreted as being caused by drainage of fine-grained material into fractures in the underlying bedrock (ref. 13-3). This would imply northeast- and northwest-trending joint sets in the bedrock of the Apollo 11 site and north- and east-trending joint sets in the Apollo 12 site bedrock. The lineated strips of ground reported by the crew probably reflect joint sets within larger fracture zones in the bedrock.

### Craters

The Apollo 12 landing site contains a wide variety of craters; their characteristics can be seen in the panoramas. The general pattern of small craters (from approximately 2 cm to several meters in diameter) is shown in the foreground of most of the panoramas.

The cross-sectional shapes of the craters range from very subdued, rimless depressions to very sharp, well-defined craters. Middle Crescent Crater is a large subdued depression with its blocky areas concentrated inside the rim. Smaller depressions range in size from less than a meter across to the one approximately 25 m across.

Sharp, well-defined craters range from fresh craters less than a meter across and a few centimeters deep to craters approximately 13 m across and 3 m deep, such as Sharp and Block Craters. The small, fresh craters have rubbly rims, apparently comprising aggregates of fine-grained material and small rock fragments derived from the upper few centimeters of the regolith. Both Sharp and Block Craters are fresh, but differ in the distribution of their associated ejecta. Sharp Crater has a rubbly bottom and inner walls, but its rim surface is similar to the general regolith surface in that the rim consists of fine-grained material with some scattered blocks. The freshness of Sharp Crater is suggested by its radiating pattern of high-albedo material described by the astronauts. In contrast to Sharp Crater, Block Crater has a very blocky rim and ejecta blanket; the freshness of this crater is suggested by the large abundance of angular blocks.

Many craters are intermediate in shape - between the subdued depressions and the fresh, sharp craters. These intermediate-type craters range in size from several centimeters across (foreground of most panoramas) up to

---

larger craters like Head, Surveyor, and Bench Craters. These craters are characterized by fairly smooth rims and bottoms. Bench Crater is characterized by a distinct bench high on its northeastern side. The bench may be a resistant layer within or under the regolith. There is a lower bench near the bottom of the crater that may be another resistant layer, or it may be the result of mass wasting of the crater walls.

The larger craters at the Apollo 12 landing site are probably widely different in age. The age sequence from oldest to youngest is interpreted as follows:

1. Middle Crescent Crater
2. Surveyor and Head Craters
3. Bench Crater
4. Sharp, Halo, and Block Craters

Rock fragments collected from the rims of these craters may be expected to have a wide range of exposure ages, which are related, in part, to the ages of the craters.

Northwest of the LM is the largest crater visited, the 400-m-diameter Middle Crescent Crater. On looking down into the crater, the astronauts noticed huge blocks on the crater wall, which were probably derived from the local bedrock. Large rock fragments in this crater probably have been exposed since the crater was formed and probably represent the deepest layers excavated at the Apollo 12 landing site.

Both rounded and angular blocks litter the surface of the rims of Head and Bench Craters. Some rocks appeared to be coarse grained; to the astronauts, the coarse-grained rock crystals were clearly visible. Many rocks on the rim of Bench Crater were reported to be splattered with glass.

Samples were collected from three small, very fresh, blocky-rimmed craters that apparently penetrate through the regolith into underlying materials. These craters are Sharp Crater, approximately 14 m across and 3 m deep; Block Crater, approximately 13 m across and 3 m deep; and an unnamed crater, 4 m across and approximately 1 m deep, that lies on the south rim of Surveyor Crater just north of Halo Crater.

Sharp Crater has a rim 0.66 m high that is composed of material with high albedo. This material has been splashed out radially around the crater and is softer than the normal regolith. A core tube driven into the rim of the crater

penetrated the ejecta without difficulty. Samples collected near the center may show the youngest exposure ages. Sharp Crater appears to have just barely penetrated the regolith. A terrace near the crater floor is probably controlled by the subregolith bedrock at a depth of approximately 3 m.

At Block Crater, high on the north wall of Surveyor Crater, nearly all the ejected blocks are sharply angular, which suggests that the crater is very young. Many of the blocks clearly show lines of vesicles similar in appearance to vesicular lavas on Earth. The blocks are probably derived from the older, coarse blocky ejecta deposit underlying the rim that resulted from the Surveyor Crater event. The regolith at Block Crater may be a meter or less thick.

The 2-m-diameter blocky crater on the southern rim crest of Surveyor Crater may have been excavated in the old rim deposit of Surveyor Crater at a depth of less than 0.5 m. In this blocky crater, the regolith may be very thin. It is also possible that some of the blocks in this small crater were derived from a low-velocity (secondary) impacting projectile.

#### Apollo 12 Panoramas

A total of 23 panoramas were taken during the Apollo 12 lunar stay to document the astronauts' traverses. These include partial panoramas taken from inside the LM through both LM windows, complete 360° panoramas taken from the surface at intervals throughout the traverse, and partial panoramas that were frequently taken in pairs for stereoscopic coverage of large features of particular interest. Panoramas taken from the LM windows are useful because of their high vantage point, even though their azimuthal field of view is less than 180°.

Complete panoramas were taken to record as much lunar surface detail as possible with a surface-based camera. When joined as mosaics, the panoramas provide accurate map control data in the form of horizontal angles. Control can be obtained analytically, with high precision, from measurements of glass-plate reproductions of the photographs or graphically, with moderate precision, by measuring the mosaics. Complete panoramas are more useful than broken or partial panoramas because complete panoramas provide an immediate check of error accumulation in measuring horizontal angles and because lunar directions can be determined accurately and independently of any other data from the location of the image of the Sun and of the image of the astronaut's shadow. This was one of the reasons that

the crew was requested to take photographs looking into the Sun, even though poor photograph quality was anticipated.

Partial panoramas produce some of the same data as complete panoramas at a considerable saving of film. They are useful for photographic documentation of large features of geologic interest. When two partial panoramas are taken of the same feature from slightly different vantage points, pairs of photographs from the adjacent panoramas can be viewed stereoscopically, and precise photogrammetric measurements of the feature can be made.

#### APOLLO 14 LANDING SITE

The LM landed about 1100 m west of Cone Crater, which is located on a ridge of Fra Mauro Formation (fig. 13-4). Cone Crater is a sharp-rimmed, relatively young crater approximately 340 m in diameter that ejected blocks of material up to 15 m across, which were derived from beneath the regolith. Sampling and photographs of these blocks were primary objectives of the mission. Rays of blocky ejecta from Cone Crater extend westward beyond the landing site. The landing took place on a smooth terrain unit recognized in premission Lunar Orbiter and Apollo orbital photographs. Sampling and description of this unit were other main objectives of the mission.

During the first EVA period, the crew traversed westward over the smooth terrain for a round-trip distance of approximately 550 m and deployed the Apollo lunar-surface experiments package (ALSEP). Sixty-nine rock samples for which locations have been determined were collected by the crew: seven in the contingency sample, 29 in the comprehensive sample, 31 in the bulk sample, and two small football-size rocks.

The crew covered a round-trip distance of approximately 2900 m (eastward from the LM during the second EVA). During the traverse, they crossed the smooth terrain, the Fra Mauro ridge unit, and a section through the continuous ejecta blanket of Cone Crater to within 20 m of the crater rim crest. Forty-eight rock samples, the locations of which have been determined, were collected at points along the traverse.

Detailed analysis of surface photographs of boulders ejected from Cone Crater and comparison of these photographs with returned samples indicate that the Fra Mauro Formation is mainly composed of moderately coherent breccias in which dark lithic clasts up to 50 cm or more across and less

abundant light clasts are set in a light matrix. Subordinate rock types that may be part of the Fra Mauro Formation include coherent breccias with about equal amounts of light and dark clasts and breccias with irregular bands of very light clastic rock.

Boulders ejected from Cone Crater record a complex history in which the youngest structures (several sets of intersecting fractures and planar, glass-lined sheeting structures that cross clasts and matrices alike) may have resulted from the cratering event. Earlier events, presumably relating to the origin of the Fra Mauro Formation or older ejecta blankets, include lithologic layering, deformation, and induration of the breccias. Clasts of breccia within the breccias may represent pre-Imbrian cratering in the Imbrium Basin region.

#### Lunar Photographs

Photographic surveys taken during the Apollo 14 lunar stay were designed to accomplish the following tasks:

1. Locate and illustrate topographic features at each major geologic station
2. Record the surface characteristics of each sample area and determine the orientation and location on the lunar surface of the samples at the time of collection
3. Document geologic targets of opportunity

Other photographic surveys were taken to document the deployment of the AISEF and the soil mechanics experiment.

Four hundred and seventeen photographs were taken on the lunar surface with the Hasselblad Electric data camera during the Apollo 14 mission. Fifteen panoramas, consisting of 275 photographs, were taken for major station location and general geologic documentation. Forty-nine pictures were taken for sample documentation, and 27 pictures were taken to document AISEF deployment. The remaining pictures were of miscellaneous targets of opportunity.

#### Geology of Fra Mauro Site

The surface of the Moon is grossly divided into relatively dark, low-lying plains or maria, and the brighter, generally more rugged areas of the terra. The maria, sites of the Apollo 11 and 12 landings, are densely covered with craters from several centimeters to a few

hundred meters in diameter, with a scattering of larger craters up to a few tens of kilometers in diameter. Much of the terra, site of the Apollo 14 landing, is densely covered with craters several tens of kilometers in diameter; before the Apollo 14 mission, Lunar Orbiter and Apollo photographs showed that small craters are also present on the terra in large numbers down to sizes of a few meters.

### Regional Geologic Setting

The Fra Mauro Formation is an extensive blanketlike deposit lying in a broad band around the Imbrium Basin and is interpreted as ejecta from the impact that formed the basin. Stratigraphic relationships around the margin of the Imbrium Basin show that a significant number of geologic events occurred between the formation of the basin and its later filling by mare material. These events included formation of large craters such as Archimedes, emplacement of the relatively light terra plains materials, and, in the western part of the Moon, formation of the Orientale Basin. The Fra Mauro Formation is, therefore, older than the mare materials sampled by the Apollo 11 and 12 crews. The ridges are the most characteristic feature of the Fra Mauro Formation. Locally, somewhat flatter tracts, typically measuring a few kilometers across, have slightly lower albedos than those of the ridges and occur in shallow surface depressions of the Fra Mauro Formation. Some of these are mapped as a smoother Fra Mauro component and others as possible overlying accumulations of volcanic, probably pyroclastic, material. Elsewhere, distinct plains-forming units of the terra that are obviously younger than the Fra Mauro Formation have been mapped, and these are, in turn, overlapped by still younger dark plains of the maria. Some hills in the area appear to be volcanoes superposed on the Fra Mauro Formation, and other similar but more heavily cratered hills may be volcanoes that were formed before the Fra Mauro Formation was deposited.

Ridges of the Fra Mauro Formation in the vicinity of the landing site are mostly 1 to 4 km wide, a few to several tens of meters high, and from 5 to 10 times as long as they are wide. The ridges are slightly sinuous and roughly radial to the Imbrium Basin. Comparison of the Imbrium Basin with the younger and better preserved Orientale Basin suggests that the ridges were formed largely by flowage of material (probably fragmental rock debris) radially along the ground during excavation of the basin. Fracturing of the pre-Fra Mauro Formation rocks in a pattern radial to the Imbrium Basin may also have contributed, at least locally, to the relief of the ridges.

The major geologic objectives of the mission were to describe, photograph, and sample the ejecta blanket of the 340-m-diameter Cone Crater. This crater is situated on one of the ridges that may be Fra Mauro Formation material that flowed radially outward from the Imbrium Basin. Lunar Orbiter photographs indicate that the crater penetrates below the fine-grained lunar regolith into a blocky or bedrock substrate. It was anticipated that this substrate would be Imbrium Basin ejecta more or less in the original form.

#### Local Geologic Setting

Three principal photogeologic map units were traversed during the two Apollo 14 periods of EVA: A smooth terrain unit on which the LM landed, slopes of a cratered ridge of the Fra Mauro Formation, and the blocky rim deposit of Cone Crater. The smooth terrain unit is grossly level over distances of one to several kilometers, but is densely populated with subdued crater forms several tens of meters to several hundred meters across and generally several meters to several tens of meters deep, which cause the surface to be undulating. The Fra Mauro ridge, which extends several kilometers north of Cone Crater, has slopes of  $10^{\circ}$  to  $15^{\circ}$  covered with patterned ground in the vicinity of the second EVA. At least four, old, moderately subdued, 200- to 1000-m-diameter craters, which are older than Cone Crater, are cut into the Fra Mauro ridge north, east, and south of Cone Crater within several hundred meters of the rim crest of Cone Crater. Rim deposits of these older craters are essentially unrecognizable photogeologically, but some unmodified remnants are to be expected at depth under the regolith formed since deposition of these rim materials. The interiors of these craters have slopes of  $10^{\circ}$  to  $15^{\circ}$  as do the slopes of the Fra Mauro ridge. Cone Crater is approximately 340 m in diameter. The rim of Cone Crater is moderately to densely strewn with 2- to 15-m blocks as seen in Lunar Orbiter III high-resolution photography. Spacings between blocks of a few to several meters are common in several dense patches extending as far out as 125 m from the rim crest. In the remainder of the mapped rim deposit, spacings as much as several tens of meters between blocks 2 m across and larger are common.

In addition to these major units, the Apollo 14 landing site is dotted with abundant craters ranging in diameter from several hundred meters down to the limit of resolution of the hand-held cameras and in morphology from relatively fresh to almost completely obliterated. Craters in the size range from 400 m to 1 km are both more numerous and more subdued than craters in the same size range in the lunar maria; this distribution is consistent with the inferred

greater age of the Fra Mauro Formation. The slope of the cumulative crater-size frequency-distribution curve on the Fra Mauro Formation between diameters of 1 km and 400 m is approximately -2 and lies close to the theoretical steady-state curve suggested in references 13-4 and 13-5. In sizes below the 400- category, fewer craters are located on the Fra Mauro Formation than on the mare material, an anomaly probably caused by a combination of thicker regolith and higher slopes at the Fra Mauro site. Small craters in the lunar regolith probably are being destroyed at a faster rate by downslope movement of loose debris on the rolling hills of the Fra Mauro area than on the more level surfaces. The fact that the walls of the trench dug by the Apollo 14 commander (CDR) caved in quickly and his comment that many small craters in the area appeared to be slumped are significant in this regard. From a consideration of the diameters of craters having blocky ejecta blankets, the regolith in the Fra Mauro region is estimated to range from 10 to 20 m in thickness.

Variations in morphology of craters in the site indicate a homologous series of craters of different ages. The age sequence of craters along the traverses from oldest to youngest is interpreted as follows:

1. Highly subdued craters expressed as very gentle depressions at the landing site of the LM, west of the LM in the area of AISEP deployment, and north of station A
2. The crater designated "North Triplet," the moderately subdued 50-m crater east of station F, and the moderately subdued 10-m crater at station A
3. Cone Crater and the sharp 45-m crater at station E
4. The sharp 300-m crater at station C' and the small 10-m crater next to which a football-size rock was collected on the first EVA

#### APOLLO 15 LANDING SITE

The Apollo 15 LM landed at longitude 03°39'20" E, latitude 26°26'00" N on the mare surface of Palus Putredinis on the eastern edge of the Imbrium Basin (fig. 13-5). The site is between the Apennine Mountain front and Hadley Rille. The objectives of the mission, in order of decreasing priority, were description and sampling of three major geologic features (Apennine Front, Hadley Rille, and the mare).

The greater number of EVA periods and the mobility provided by the lunar roving vehicle (LRV) allowed much more geologic information to be obtained from a much larger area than those explored by previous Apollo crews. A total of 5 hr was spent at traverse station stops, and the astronauts transmitted excellent descriptions of the lunar surface while in transit between stations. Approximately 78 kg of rock and soil samples were collected, and 1152 photographs were taken with the 60- and 500-mm focal-length Hasselblad cameras. Much useful information was obtained from the lunar surface television camera at eight of the 12 stations. Some information was gained from the data-acquisition (sequence) camera, and many useful photographs of the site were taken from orbit.

The stations shown on the geologic map (fig. 13-5) are located at the panorama stations although much of the geologic data and many of the samples were taken from areas a significant distance from the panorama stations. All crater sizes refer to the rim-to-rim diameter unless otherwise specified. The sizes of fragments and blocks are generally given as the largest dimension of the field of view.

A topographic base for the geologic map was compiled on an AS11 stereoplotter using Apollo 15 panoramic camera photographs AS15-9809 and AS15-9814. Frame 9809 is somewhat distorted for optimum photogrammetric use but probably did not introduce significant error into this map, because only a very small part of the frame was used in the compilation.

The Apollo 15 crew, like the Apollo 14 crew, investigated features related to the huge multiringed Imbrium Basin. The landing site is on a dark mare plain (part of the Marsh of Decay or Palus Putredinis) near the sinuous Hadley Rille and the frontal scarp of the Apennine Mountains. This scarp is the main boundary of the Imbrium Basin, which is centered approximately 650 km to the northwest. The largest mountains of the Apennines are a chain of discontinuous rectilinear massifs 2 to 5 km high. These mountains are interpreted as large fault blocks uplifted and segmented at the time of the Imbrium impact. Between the massifs and outward beyond them are hilly areas that merge outward with the Fra Mauro Formation, interpreted as a blanket of ejecta from the Imbrium Basin and sampled by the Apollo 14 crew. The hills appear to be jostled blocks subdued by the Fra Mauro blanket. The large massifs, however, are not subdued in this manner and so may be composed mainly of pre-Imbrian rock, perhaps thinly veneered by Imbrium ejecta. The area is near the old Serenitatis basin, which suggests that at least part of the pre-Imbrian material in the massifs is ejecta from Mare Serenitatis.

Mare material of Palus Putredinis fills lowlands at the base of the Apennines, forming a dark plain. Regional relations west of the site show that a number of events occurred between formation of the Imbrium Basin and emplacement of the mare deposits. These include deposition of the Apennine Bench Formation and the cratering event that formed Archimedes (ref. 13-6). Morphologies of craters on the mare surface at the site indicate that the mare age is late Imbrian or early Eratosthenian. It is a "red" mare, one whose spectral reflectance is enhanced in the red (ref. 13-7).

Some of the hills and mountains in the area are dark like the mare, perhaps indicating that they are coated by a thin mantle of dark material. The region contains numerous diffuse light-colored rays and satellitic clusters of secondary impact craters from the large Copernican-age craters (Autolycus and Aristillus) to the north.

Hadley Rille follows a sinuous course through the mare and locally abuts premare massifs. The rille is one of the freshest sinuous rilles on the Moon, and rock outcrops are common along the upper part of the walls.

The landing site is on the mare surface, nearly on the crest of a very gentle ridge that trends northwest between Crescent Crater and North Complex. This part of the mare is slightly higher in albedo than elsewhere, suggesting a broad diffuse ray from Aristillus or Autolycus. Another gentle ridge in the mare is present at Elbow Crater and apparently is truncated by Hadley Rille. The mare surface contains numerous subdued craters 100 to 400 m in diameter, and many smaller ones, some of which are quite fresh. A prominent concentration of the larger craters known as the South Cluster is one of many in Palus Putredinis that form a pattern satellitic to Aristillus or Autolycus. A less distinctive cluster of more subdued craters lies immediately northwest of the landing site. The mare surface is covered with regolith approximately 5 m thick.

Two major Apennine massifs tower over the Hadley plain to heights of 4.5 and 3.5 km. These are Mt. Hadley to the northeast and Hadley Delta just south of the landing site. The face of Mt. Hadley is steep and has very high albedo. The north face of Hadley Delta, called the "Front" during the Apollo 15 mission, rises abruptly above the younger mare surface except near Elbow Crater, where the contact is gradational, apparently as a result of debris that has moved down the slopes. As elsewhere on the Moon, the steep slopes of the massifs are sparsely cratered because of rapid mixing of debris and destruction of craters by downslope movement.

A prominent exception is St. George Crater, 2.5 km wide, which predates the mare and is very subdued.

Hadley Rille is 350 m deep near the landing site. Rimrock outcrops are exposed along the upper part of the walls, and blocky talus deposits cover the lower part. An important objective of the mission, successfully achieved, was stereophotography of the rille walls and sampling of bedrock at the lip.

The North Complex consists of low irregularly shaped hills that lie a few kilometers north of the landing site. The hills appear slightly darker than the adjacent mare. North Complex and similar but slightly less dark low hills to the northwest resemble, except for the low albedo, hilly intramassif Apennine features in other parts of the region. These hills may therefore consist mainly of Imbrium ejecta, mantled by a thin layer of dark material. On the other hand, some peculiar scarps, lobes, and irregular crater chains suggest that North Complex may be a constructional volcanic form.

The combination of Apollo 15 panoramic and surface photography afforded a unique opportunity to study the optical properties of a large area of the Hadley-Apennine landing site. The additional use of a Hasselblad camera with a 500-mm lens further increased the area from which photometric measurements can be made (including the west wall of Hadley Rille and the North Complex). The photometry also benefited from the use of a black-and-white film different from that used on previous missions, reducing the halation effects and increasing the resolution and range of exposure. Preliminary results of more than 1000 measurements from the film densitometry are presented in the following ways: an estimated normal-albedo map, a range of estimated normal albedos of the fine-grain material and documented samples of each station, and the photometric properties of the rocks and fines on the rille wall and at the North Complex.

The source of the photometric data was a black-and-white second-generation master-positive film. Panoramic camera frame AS15-9814 over the Hadley-Apennine site was copied at approximately triple enlargement onto negative stock, and the relative densities of the film were measured with a Joyce-Loebel microdensitometer and recorded on digital magnetic tape. The scanning aperture was  $250 \times 10^{-12} \text{ m}^2$ , which is the equivalent of a  $10 \text{ m}^2$  integrated area of the lunar surface.

Surface photography was controlled in two ways. The first method involved the use of the gnomon and the

photometric chart. The second used the film sensitometry data furnished by the Photographic Technology Laboratory at the NASA Lyndon B. Johnson Space Center. At the early deployment of the gnomon at station 1, the photometric chart data and the sensitometry data agreed within  $\pm 3$  percent. Subsequent comparisons between the two disagreed by an increasing amount. The probable cause for this disagreement is the accumulation of lunar material on the chart as the mission progressed. Thus, for later periods of EVA, more reliance was placed on the film sensitometry, whereas the photometric chart aided in checking the f-stop at which the photograph was taken.

The extrapolated normal-albedo map was prepared by formatting the digital data from microdensitometry of the panoramic camera film into the VICAR image-processing system. The resulting digital numbers are a function of the film density and are thus related to the albedos of the lunar surface. The digital data were calibrated to the normal albedo at each station (except 3 and 9) by extrapolating the photometric data obtained from surface photographs of fine-grained regolith areas close to zero-phase angle. The photographs taken at stations 3 and 9 were not suitable for this type of analysis.

Each station has a variation in extrapolated normal albedos because the astronauts photographed different areas at the station. The averages for each station lie along an approximate line on a log-log plot, indicating that the station information was on the linear portion of the characteristic curve of the panoramic camera film. The processing of the panoramic camera frame was continued by associating a range of digital numbers with the albedo and producing a photomap of each albedo level. Hand corrections were made on the west side of the rille and the Apennine Front by measuring the local slope directions from the stereoscopic photopairs and profiles and by correcting the photometric geometry. For these areas, the photometric function applied was the same as for the mare. Because of the shadows present, photometric data were not obtained on the east wall of the rille or in crater shadows.

The albedo map shows a range of 9 to 19 percent albedo for the mare area, while the Apennine Front has an albedo range of 15 to 23 percent. The zone between the Front and the mare is an area of mixing of debris from both areas. The rille wall is brighter than typical mare material because of the high proportion of the surface that is covered by blocky rock talus.

The mare surface is darker toward the east, which may indicate either areal variations in the underlying mare

volcanic rocks or the presence of ray material in the western areas. The LM may have landed in an area of diffuse ray material. This lighter area can be seen in photographs AS15-84-11324 and 11325, where the lighter material has a measured albedo of 16 to 17 percent and the adjacent darker material has a measured albedo of 13 to 14 percent. Short (80-m-long) rays can be observed radiating outward from the LM on panoramic camera frame AS15-9814, suggesting that the exhaust from the descent engine exposed lighter materials.

#### APOLLO 16 LANDING SITE

The LM landed at the western edge of the Descartes Mountains approximately 50 km west of the Kant Plateau, part of the highest topographic surface on the near side of the Moon (fig. 13-6). The Apollo 16 mission accomplished the first landing in the central lunar highlands, and the crew successfully explored and sampled a kind of terrain never before visited on the lunar surface. The landing site was selected as an area characteristic of both terra plains and rugged hilly and furrowed terra.

The Apollo 16 mission was the only manned landing accomplished or planned in the central lunar highlands. The geologic diversity and significance of the site; the extended traverse capability provided by three EVA periods and by the LRV; the real-time television coverage of the site and of crew activities; and the large suite of returned samples and surface photographs contributed to a successful mission. The Apollo 16 mission was important in understanding the evolution of the terra and in providing data that ultimately may be extrapolated over wide areas of the lunar surface.

The Apollo 16 landing site in the lunar central highlands encompassed terra plains and adjacent mountainous areas of hilly and furrowed terra. These morphologic units, representing important terrain types in the lunar highlands, had been interpreted as volcanic on most premission geologic maps. However, it became apparent during the mission that there are indeed few or no volcanic rocks or landforms at the site but rather that the area is underlain by a wide variety of impact-generated breccias.

During the three EVA traverses of the mission, 95 kg of rocks and soils were collected, 1774 surface photographs were taken, and a traverse length of 20.3 km was covered. These data and the observations and geologic descriptions of the astronauts provide basic data for analysis and synthesis.

Ray materials derived from North Ray and South Ray Craters are the two most apparent sources of surface debris on the Cayley Plains. Ejecta from South Ray Crater also appear to mantle much of the surface of Stone Mountain in the vicinity of stations 4 and 5, so that it is still uncertain whether Descartes materials were, in fact, sampled. Size distribution studies of fragments on the lunar surface suggest that the ejecta units of these two craters differ in character. Rock fragments are much less abundant in the North Ray ejecta blanket, which suggests that the North Ray impact may have excavated more friable material, that the length of time since the cratering event has been sufficient for subsequent impacts to destroy the smaller blocks, or both. South Ray ejecta, as mapped, include bright and dark areas, but the only surface differences observed are that the brightest areas have larger block sizes and a greater abundance of blocks. The mapped interray areas have no lunar surface characteristics that distinguish them from adjacent South Ray ejecta. Both ray and interray areas show a progressive northward decrease in total rock abundance and in relative abundance of the coarser sizes.

The regolith present on the ejecta blanket of North Ray Crater is only a few centimeters thick. Where ejecta blankets or ray deposits are not identifiable, the regolith is 10 to 15 m thick. The surface of the regolith is medium gray, but high-albedo soils are present at depths of 1 to 2 cm in most of the traverse area.

The Cayley Plains in the region of the IM and ALSEP are smooth but broadly undulating with a maximum relief of several meters. Two percent of the surface is covered by 2- to 20-cm fragments. Subdued craters between 150 and 240 m in diameter are present together with many smaller, more youthful craters, including abundant 0.5- to 2.0-m secondaries and some primary craters as large as 30 m in diameter.

Station 1 is near the rim of Plum Crater, a 30-m-diameter crater on the rim of the 300-m-diameter Flag Crater. Flag Crater is approximately 50 m deep and probably penetrates through the regolith into the underlying bedrock. The crater is subdued and no rocky exposures are visible in its walls or floor. The eastern part of the station 1 area appears to be crossed by a very faint ray from South Ray Crater, but rock fragments larger than approximately 10 cm cover less than 1 percent of the surface. A number of slightly buried, angular rocks in the photographs are interpreted to be ejecta from South Ray Crater. Because of the depth of penetration by Flag Crater and the relative scarcity of South Ray ejecta, samples from station 1 have

the highest probability of being material representative of the upper units of the subjacent Cayley Formation.

Station 2 is located just north of Spook Crater (400 m in diameter) on the south rim of Euster Crater (90 m in diameter). The area is crossed by a faint ray that is apparently derived from South Ray Crater. Fragments, most of which are 5 to 10 cm, cover 2 to 3 percent of the surface. Scattered craters as large as 2 m in diameter are generally subdued, but a few small fresh ones have sharp rims and associated ejecta. Spook Crater is symmetrical with a slightly raised rim. No rock exposures occur in the walls and no deposits of ejecta were seen. In contrast, the floor and part of the walls of Buster Crater are covered by blocky debris with angular rocks as large as 5 m across.

Stone Mountain is a westward projection of the Descartes highlands into the southeastern part of the landing area. The mountain rises approximately 540 m above the Cayley Plains and is domical in form. Major though subtle step and bench topography parallels the slope of Stone Mountain. Stations 4 and 5 were located on Stone Mountain; station 6 was on the Cayley Plains near the foot of its lowest bench. Approximately 2 percent of the traverse area is sprinkled with blocks 10 cm and smaller. Blocks range from well rounded to angular but most are of intermediate shape. Local concentrations of blocks are found especially on the east sides and rims of craters facing away from South Ray Crater. It is presumed that these blocks were contributed largely from South Ray Crater and that an appreciable fines fraction accompanied them. The majority of craters on Stone Mountain range from 50 m down to the limit of resolution. The crater density is approximately that seen in the adjacent Cayley Plain, but craters larger than 100 m are more abundant in the Cayley Plain than on Stone Mountain.

The lunar surface in the vicinity of stations 8 and 9 is gently undulating with a northeasterly slope of a few degrees. Between 1 and 3 percent of the surface is covered by fragments 1 cm and larger. The largest blocks (1 to 2 m) are few and scattered. The blocks increase in size and abundance between stations 8 and 9 but decrease again at station 9, where blocks are somewhat less abundant than at station 8. There are many subdued craters as large as 3 m in diameter in this area. Most have slightly raised, rounded rims. Several craters at station 8 have concentrations of blocks on the northeast rims, and a few of these are somewhat elongate in a northeast-southwest direction, suggesting that they are South Ray secondaries.

At stations 11 and 13, a large young crater was investigated along its rim crest, walls, and continuous ejecta blanket and was extensively photographed and sampled. North Ray Crater, 900 to 950 m in diameter, is on a 50-m-high ridge at the western edge of Smoky Mountain near the eastern boundary of the Cayley Formation in this area. The geologic importance of North Ray Crater lies in its youth and in the depth of penetration (160 to 200 m) into materials underlying the Cayley Plains. The distribution of craters superposed on North Ray Crater is apparently random and the density is very low. Few craters larger than 25 m are observed, and very few are recognized in the surface photographs. The random distribution and low density presumably reflect the relative youth of the crater and, for the smaller craters, probably result from a thin regoli over a hard subunit.

The total returned net sample weight is approximately 95.33 kg. Of the total sample weight, almost 75 percent consists of rock fragments larger than 1 cm in diameter, nearly 20 percent consists of soil or residue fines, and the remainder consists of core and drive tube samples. The Apollo 16 rocks may be divided into three broad groups: (1) fine- to coarse-grained, mostly homogeneous crystalline rocks; (2) rocks composed substantially of glass; and (3) fragmental rocks (breccias). The proportion of fragmental rocks in the returned samples exceeds 75 percent. Twenty-five rocks are classified as crystalline rocks. Of these, seven appear to be igneous rocks. Although all the igneous rocks have been shattered and deformed to some extent, the predeformation textures are substantially intact. The two largest samples returned are coarse-grained, nonvesicular rocks composed largely of plagioclase. These rocks resemble Apollo 15 anorthosite sample 15415 but are probably more severely shock deformed. Three are fine-grained, highly feldspathic rocks with crystal-lined vugs. Eighteen crystalline rocks appear to be metaclastic rocks with generally small proportions of lithic debris. These are hard, angular rocks characterized by fine-grained sugary textures. Five samples largely composed of glass were returned. Two of these are glass spheres, one hollow and one solid. The remaining three glass samples are irregular, coarse, vitric agglutinates with numerous small lithic inclusions. The fragmental rocks have been divided into five main groups on the basis of proportions of light and dark clasts and matrix color. All five groups are varieties of impact-generated breccias; none appear to be of volcanic origin. The majority of the rocks are polyictic breccias, but a substantial minority are monomictic. Two types of clasts are clearly dominant: (1) dark, aphanitic to finely crystalline metaclastic rocks and (2) white, partly crushed to powdered feldspathic rocks. Less common clast types

include light-gray or white rocks with granoblastic textures, a variety of gabbroic to anorthositic rocks with medium to coarse grain size, and rare feldspar-poor basaltic rocks. Matrices of the light- and medium-gray-matrix breccias are, for the most part, friable and not visibly altered by subsequent thermal events, whereas those of dark-matrix breccias are coherent and annealed or fused.

The rock distribution suggests that the section underlying the Cayley Plains is stratified, with an upper unit of medium-gray breccia and lower units composed mainly of light- and dark-matrix breccias. The areal extent of the supposed upper unit is not known but presumably extends at least between stations 1 and 6; considering the relative scarcity of the medium-gray breccias, the unit is probably not more than a few meters thick. Evidence derived from the photographs, astronaut descriptions, and samples collected at station 11 suggests that light-matrix breccias overlie dark-matrix breccias, whereas the color of ejecta on the rims of South Ray and Baby Ray Craters suggests that dark-matrix breccias overlie light-matrix breccias in the vicinity of those craters. Such a stratigraphic sequence in the South Ray area is consistent with the dominance of dark-matrix breccias described and photographed in South Ray ejecta between the LM site and station 8.

The Cayley Formation at the Apollo 16 site is a thick (at least 200 and possibly more than 300 m), crudely stratified debris unit, the components of which are derived from plutonic anorthosites and feldspathic gabbros and from metamorphic rocks of similar composition. The Formation has an elemental composition similar to that observed over large regions of the lunar highlands by the orbital X-ray experiments of the Apollo 15 and 16 missions. The observed textures and structures of the breccias resemble those of impact breccias. They do not resemble those of volcanic rocks nor do the plutonic or metamorphic source rocks of the breccias have the textures or compositions of terrestrial or nearly all previously sampled lunar volcanic rocks.

Available sample data indicate that the Descartes highlands differ from the adjacent Cayley Formation more in physiographic expression than in actual lithologic character. Whether it is a stratified unit, as suggested by several subtle topographic benches, has not been established.

The character of the Cayley Formation emerging from the Apollo 16 site studies supports consideration of an impact-related origin. The sources of the debris that might be considered include (1) ejecta from the Imbrium Basin (ref. 13-8), (2) ejecta from the Nectaris Basin, or (3) some

combination of ejecta from various local and more distant sources accumulated over an extended time interval. Each possibility has a very different historical implication. Isotopic age studies on samples of the various breccia types and their included clasts should permit a test of these possibilities.

The incomplete characterization of the Descartes materials on Stone Mountain makes extended geological speculation premature. Materials of the same morphological unit partially fill the crater Descartes to the south. These steep-sloped, relatively uncratered, high-albedo uplands have been interpreted as relatively youthful, volcanic constructional features. If work in progress confirms that the Descartes Mountains are composed of breccias similar in lithology and composition to materials of the Cayley Formation, the postulated volcanic origin will require reassessment. Additional petrologic information, soil analyses, and possibly age studies of the returned samples are necessary to conduct such an evaluation.

#### APOLLO 17 LANDING SITE

The Apollo 17 LM landed at latitude  $20^{\circ}10'$  N, longitude  $30^{\circ}46'$  E (fig. 13-7) on the flat floor of a deep narrow valley that embays the mountainous highlands at the eastern rim of the Serenitatis basin. Serenitatis, the site of a pronounced mascon, is one of the major multi-ringed basins on the near side of the Moon. The Taurus-Littrow valley, which is radial to the Serenitatis basin, is interpreted as a deep graben formed by structural adjustment of lunar crustal material to the Serenitatis impact.

During their stay on the lunar surface, the Apollo 17 crew traversed a total of approximately 30 km, collected nearly 120 kg of rocks and soil, and took more than 2200 photographs. Their traverses, sampling, direct observations, and photographs span the full width of the Taurus-Littrow valley.

The highlands surrounding the valley can be divided on the basis of morphology into (1) high smooth massifs; (2) smaller, closely spaced domical hills referred to as the Sculptured Hills; and (3) materials of low hills adjacent to the massifs and the Sculptured Hills. Boulders that had rolled down the slopes of the massifs north and south of the valley provided samples of that area. These boulders are composed of complex breccias that are generally similar to those returned from the Apollo 15 and 16 missions.

Materials of the valley fill were sampled at many stations. Ejecta around many craters on the valley floor consists of basalt, showing that the graben was partly filled by lava flows. A relatively thick layer (approximately 15 m) of unconsolidated material overlies the subfloor basalt; this debris consists largely of finely comminuted material typical of the lunar regolith.

The surface material over much of the Taurus-Littrow region has a very low albedo and was believed to be a thin young mantle, possibly pyroclastic, that covered the valley floor and parts of the adjacent highlands. No clear evidence of the existence of such a mantle as a discrete layered unit has yet been found, but it may be mixed in with the more typical debris of the lunar regolith. An unusual bright deposit extends across the valley floor from the foot of the South Massif. This deposit consists of breccias similar to those of the massif and is interpreted as an avalanche generated on the massif slopes.

South Massif materials were collected from three breccia boulders that were probably derived from a blocky area near the top of the massif where a blue-gray unit overlying tan-gray material is exposed. Boulder 1, sampled at station 2, is a foliated and layered breccia, the only one of its type seen by the crew. The four samples collected from boulder 1 are breccias composed of dark-gray fine-grained lithic clasts in a light-gray friable matrix.

Boulder 2, sampled at the South Massif, is a fractured rock from which five samples of vuggy, annealed, greenish-gray breccia were collected. A breccia clast and its host were sampled from boulder 3 at the South Massif. The clast is light-greenish-gray breccia with abundant mineral clasts and sparse lithic clasts. The matrix of the clast consists largely of angular fragments of a mafic silicate embedded in a very-fine-grained groundmass. The host material is a blue-gray breccia with scattered vesicles.

Materials of the North Massif were sampled primarily from a 6- by 10- by 18-m fragmented boulder at station 6 and a 3-m boulder at station 7. The station 6 boulder, which broke into five pieces, is at the lower end of a boulder track the apparent beginning of which is in an area of light boulders approximately one-third of the way up the massif. Photographs using the 500-mm lens demonstrate that dark boulders are abundant higher on the mountain, and light boulders occur again in the upper part. Thus, there may be a layer or lenses of darker rock high on the mountain with lighter rocks both above and below. The source of the station 7 boulder on the North Massif is unknown, but the

boulder contains rock types like those of the station 6 boulders.

Four of the five large pieces of the station 6 boulder were sampled. The boulder consists of two major breccia types, greenish-gray and blue-gray. They are in contact in a 0.5-m-wide zone that appears to be an area of mixing between the two rock types. The greenish-gray breccia is tough and annealed, with sparse lithic and mineral clasts set in a vuggy fine-grained matrix.

Samples of blue-gray breccia from the station 6 boulder contain a high proportion (40 to 60 percent) of blue-gray breccia fragments in a vuggy greenish-gray matrix. The matrix is a tough, finely crystalline material. Large friable inclusions ranging from 1 cm to 1 m across are in sharp irregular contact with the blue-gray breccia. Samples of one of these are very-light-gray cataclasites.

The station 6 boulder is intricately sheared. Comparison with the oriented returned samples shows that movement along some of the shear planes has deformed the clasts. Major events recorded in the station 6 boulder are the formation of the light cataclasite, its incorporation in the blue-gray breccia, and subsequent enclosure of the blue-gray breccia in the greenish-gray breccia.

The station 7 boulder is similar to the station 6 boulder in that the two major rock types, greenish-gray breccia and blue-gray breccia, are present. A large white clast (1.5 by 0.5 m), similar to those in the station 6 boulder, is penetrated by narrow blue-gray breccia dikes. The blue-gray breccia is in sharp irregular contact with the younger greenish-gray breccia. Like the station 6 boulder, the station 7 boulder is intricately fractured. At least two fracture sets are confined to the large white cataclasite inclusion and the blue-gray breccia.

Smaller chips collected at stations 6 and 7 include the major rock types of the two large boulders, as well as a few other breccia types, one coarse-grained gabbroic rock, and one light-colored fine-grained hornfels. A few basalt fragments that are probable ejecta from the valley floor were also collected.

The South Massif boulders most probably came from the highest part of the massif (boulder 1, station 2, from the blue-gray unit; boulder 2, station 2, from the underlying tan-gray unit), and the station 6 and 7 boulders probably came from within the lower third of the North Massif. Hence, two different stratigraphic intervals may have been sampled. Conversely, the lithologies of the South Massif

boulders closely resemble those of the North Massif boulders in many respects. The similarity seen in early examination suggests the possibility that only one stratigraphic unit is represented. Whichever the case, the massifs are composed of intensely shocked breccias reasonably interpreted as ejecta from ancient large impact basins.

On the accessible part of the Sculptured Hills, hand-sized samples are essentially absent, and no boulders that clearly represent Sculptured Hills bedrock were found. Small fragments of basalt, probably ejected from the valley floor, and regolith breccia dominate the samples, which consist mainly of chips collected with soils or by raking. Samples of friable feldspathic breccia from the wall of a 15-m crater and of a glass-covered gabbroic boulder that is almost certainly exotic were also collected. The greater dissection, lower slopes, lack of large boulders, and limited sample suite suggest that the Sculptured Hills may be underlain by less coherent breccias than the massifs.

Subsequent to the formation of the Taurus-Littrow graben by the Serenitatis impact, the valley floor was inundated and leveled by basaltic lava flows. Geophysical evidence suggests that the prism of basalt filling the valley is more than a kilometer thick. The uppermost 130 m was sampled in the ejecta of craters on the valley floor.

In general, the subfloor basalt blocks seen at the landing site were not visibly shocked or even intensely fractured. In some rocks, planar partings parallel bands expressed as differing concentrations of vesicles. Almost all returned samples of basalt can be divided into five classes: (1) vesicular, porphyritic, coarse-grained basalts; (2) vesicular coarse-grained basalts; (3) vesicular fine-grained basalts; (4) dense aphanitic basalts; and (5) vesicular aphanitic basalts.

Before final accumulation of the Serenitatis mare fill, broad arching east of the Serenitatis basin tilted the subfloor lavas to the east, forming the present 1° eastward tilt of the valley floor. The subfloor basalt is overlain by fragmental debris approximately 15 m thick. For the most part, this is impact-generated regolith similar to that developed on mare basalts elsewhere on the Moon. The central cluster ejecta, the light mantle, and the ejecta of Shcrty and Van Serg Craters are discrete deposits recognized within the regolith.

The lower part of the regolith is thought to be represented in the abundant dark friable breccias in the ejecta of the 90-m-diameter Van Serg Crater. The breccias contain scattered, light-colored lithic clasts as well as

abundant dark glass, mineral and lithic fragments derived from basalts, and variable percentages of orange glass spheres and fragments. They are interpreted to be regolith breccias indurated and excavated from the deeper, older part of the regolith by the Van Serg impact. Basalt bedrock is not known to have been excavated by Van Serg.

The central cluster ejecta is derived from the cluster of craters south and east of the LM. It is distinguished by the abundance of blocks in the unit, and the unit is too young for the blocks to have been reduced much in size by later impacts. All sampled blocks in the central cluster ejecta are subfloor basalt.

The young pyroclastic dark mantle anticipated before the mission was not recognized in the traverse area as a discrete surface layer. Strong photogeologic evidence for the existence of such a mantle on the valley floor and in parts of the highlands still exists. Albedo measurements show that abnormal surface darkening, consistent with the concept of the introduction of exotic dark material - the "dark mantle" - increases to the east and south in the Taurus-Littrow area. If the dark mantle is younger than the central cluster ejecta, it must be so thin in the landing site that it is thoroughly intermixed with the younger part of the regolith. Such mixed dark mantle may be represented by the dark glass spheres that abound in the soils of the valley floor. An alternative hypothesis is that the dark mantle may have accumulated shortly after the extrusion of the subfloor basalt. In this case, the deposit would be intimately mixed with subsequently formed regolith.

The light mantle is an unusual deposit of high-albedo material with finger-like projections that extend 6 km across dark plains from the South Massif. Rock fragments collected from the light mantle are similar in lithology to the breccias of the South Massif. This similarity supports the hypothesis that the light mantle is an avalanche deposit formed from loose materials on the face of the South Massif. A cluster of secondary craters on the top of the South Massif may record the impact event that initiated the avalanche. Size-frequency distribution and morphologies of craters on the light mantle suggest that its age is comparable to that of Tycho Crater, on the order of 100 million years.

Shorty is a 110-m-diameter impact crater penetrating the light mantle. Unusual orange soil was identified in two places on the rim of Shorty Crater and in the ejecta from a small crater on the inner wall. A trench on the crater rim exposed an 80-cm-wide zone of orange soil, consisting largely of orange glass spheres. A double drive tube sample

showed that the orange soil overlies black fine-grained material (consisting of tiny, opaque, black spheres) at a depth of 25 cm. The old age for the orange glass material implies solidification shortly after the period of subfloor basalt volcanism. The black and orange glass material, whatever its origin, must have been present in the Shorty target area; it was excavated or mobilized by the Shorty impact.

Fine-grained soil, darker than the underlying unconsolidated debris, was recognized at the surface at Shorty Crater, at Van Serg Crater, on the light mantle, and on the massif talus. The soil is thin (e.g., 0.5 cm at Shorty, approximately 7 cm on the flank of Van Serg) and probably represents the regolith that has formed on these young ejecta or talus surfaces. Relatively young structural deformation in the landing area is recorded by the Lee-Lincoln Scarp and by small fresh grabens that trend northwest across the light mantle. The sharp knickpoint at the base of the massifs may indicate that some fairly recent uplift of the massifs has kept the talus slopes active.

Materials of the valley fill were sampled at numerous stations around the LM and en route to and from the massifs. Ejecta around many craters on the valley floor consists of basalt, confirming that volcanic materials underlie the Taurus-Littrow valley floor. A relatively deep layer of unconsolidated material overlies the subfloor basalt; this debris consists of finely comminuted material typical of the lunar regolith. It may also contain the dark mantle mapped in premission studies. No clear evidence for the existence of a dark mantle as a discrete layered unit has yet been found, but it may well be mixed in with the more typical debris of the lunar regolith. The bright deposit extending across the valley floor from the foot of the South Massif consists of breccias similar to those of the massif; the interpreted origin of this deposit as a landslide thus appears to be confirmed.

Returned basalt samples may be divided into five classes of hand specimens:

1. Vesicular, porphyritic, coarse-grained basalts
2. Vesicular coarse-grained basalts
3. Vesicular fine-grained basalts
4. Dense aphanitic basalts
5. Vesicular aphanitic basalts

Individual samples of types (1) and (2) were generally termed "vesicular gabbro" by the Apollo 17 crew. Examples of (3), (4), and (5) were described as "fine-grained basalt," "basalt," and "obsidian," respectively.

Rocks called vesicular, porphyritic, coarse-grained basalts are characterized by 3- to 4-mm, blocky, pyroxene-ilmenite intergrowths that are present in amounts ranging from 5 to 15 percent in the basalts of this class. Olivine is present in trace amounts in some of these rocks; where present, it commonly occurs as partially reacted cores in the pyroxene phenocrysts. The ilmenite content, while high for mare basalts as a whole, is relatively low compared to other Apollo 17 basalts and averages between 15 and 20 percent. The plagioclase content averages 25 to 35 percent. Some layering occurs in larger hand samples: in one case, grain-size variations are noted; in others, feldspar and ilmenite laths are alternately foliated and randomly oriented. Vugs are more common than vesicles, although both may be present in the same rock. Cavity content is variable but averages 10 to 15 percent; vugs are aligned in planes, are clearly elongate, and are layered by abundance. Sample 70035 is a typical example of this class of basalts.

Vesicular coarse-grained basalts are very similar to those of the above class except that they lack the pyroxene-ilmenite phenocrysts, and their average grain size tends to be somewhat finer (approximately 1.0 mm). This class of basalts is typified by sample 75055.

Vesicular fine-grained basalts are characterized by a high proportion of vugs and vesicles with ilmenite-rich linings and by a groundmass grain size ranging from 0.3 to 0.6 mm. Olivine is commonly present in rocks of this class as microphenocrysts in amounts of 1 to 2 percent. These rocks are characterized by vug and vesicle abundances of more than 30 percent; some are frothy. Sample 71055 is a typical example of this class of basalts.

Dense aphanitic basalts are characterized by their very low abundance of cavities and their extremely fine grain size. Olivine microphenocrysts are widely represented but not abundant. The average grain size of these rocks is approximately 0.1 to 0.2 mm. Sample 70215 is typical of this class of basalts.

Vesicular aphanitic basalts are characterized by abundant and exceptionally large cavities and very fine grain size. Small amounts of olivine are present in some samples. Vugs are commonly as large as a centimeter and reach 3 to 4 cm. Sample 74235 typifies this group.

It is possible that the two coarse-grained basalt types are gradationally related by decrease of porphyritic pyroxene-ilmenite aggregates, but the best judgment at present is that they represent separate flow units. It seems more likely that the vesicular fine-grained basalts are gradationally related to the vesicular aphanitic basalts through decrease in grain size and increase in vesicle size. The dense aphanitic basalts seem clearly to be fragments of a separate flow unit.

A few samples cannot at present be fitted into these five categories. Samples 71549, 71557, and 71568 are coarse-grained basalts, but analysts cannot at present say whether or not they are porphyritic. Sample 71597 contains 20 to 25 percent olivine - more than any other basalt in the Apollo 17 collection. Table 13-I relates the field terminology to sampling areas, representative samples, and laboratory terminology.

#### DATA TO BE ARCHIVED AT NSSDC

The following information will be archived at the National Space Science Data Center (NSSDC).

1. Detailed traverse maps of each Apollo lunar site
2. A panoramic photograph taken at each station of the respective Apollo missions
3. Copies of every photograph taken on the lunar surface during the Apollo missions
4. Film of all television transmitted from the lunar surface

#### REFERENCES

- 13-1. Shoemaker, E. M.; Morris, E. C.; Batson, R. M.; Holt, H. E.; et al.: Television Observations from Surveyor. TR 32-1265, Jet Propulsion Laboratory, Calif. Inst. Tech., 1969, pp. 21-136.
- 13-2. Shoemaker, E. M.; Bailey, W. G.; Batson, R. M.; Dahlem, D. H.; et al.: Geologic Setting of the Lunar Samples Returned by the Apollo 11 Mission. Sec. 3 of Apollo 11 Preliminary Science Report. NASA SP-214, 1969.
- 13-3. Shoemaker, E. M.; Hait, M. H.; Swann, G. A.; Schleicher, D. L.; et al.: Lunar Regolith at Tranquility Base. Science, vol. 167, no. 3918, Jan. 30, 1970, pp. 452-455.
- 13-4. Trask, Newell J.: Size and Spatial Distribution of Craters Estimated From Ranger Photographs: Rangers VIII and IX. Part II of Experimenters' Analyses and Interpretations. Preliminary Geologic Map of a Small Area in Mare Tranquillitatis, Tech. Rept. 32-800, Mar. 1966, pp. 252-263.
- 13-5. Shoemaker, E. M.; Hait, M. H.; Swann, G. A.; Schleicher, D. I.; et al.: Origin of the Lunar Regolith at Tranquility Base. Physical Properties. Proceedings of the Apollo 11 Lunar Science Conference, vol. 3, Pergamon Press (New York), 1970, pp. 2399-2412.
- 13-6. Carr, M. H.; and El-Baz, Farouk: Geologic Map of the Apennine-Hadley Region of the Moon - Apollo 15 Pre-Mission Map. U.S. Geol. Survey Misc. Geol. Inv. Map I-723 (sheet 1 of 2), 1971.
- 13-7. Soderblom, I. A.; and Lebofsky, L. A.: Technique for Rapid Determination of Relative Ages of Lunar Areas from Orbital Photography. J. Geophys. Res., vol. 77, no. 2, Jan. 10, 1972, pp. 279-296.
- 13-8. Eggleton, R. E.; and Marshall, C. H.: Notes on the Apenninian Series and Pre-Imbrian Stratigraphy in the Vicinity of Mare Humcrum and Mare Nubium. Astrogeologic Studies Semiannual Progress Report, Feb. 26, 1961, to Aug. 24, 1961, U.S. Geol. Survey, Mar. 1962, pp. 132-137.

## BIBLIOGRAPHY

Apollo Lunar Geology Investigation Team: Preliminary Report on the Geology and Field Petrology at the Apollo 15 Landing Site. U.S. Geol. Survey Interagency Rept., Astrogeol. 32, Aug. 5, 1971.

Apollo Lunar Geology Investigation Team: Geologic Setting of the Apollo 15 Samples. Science, vol. 175, no. 4020, Jan. 28, 1972, pp. 407-415.

Apollo Lunar Geology Investigation Team: Documentation and Environment of the Apollo 16 Samples: A Preliminary Report. U.S. Geol. Survey Interagency Rept., Astrogeol. 51, May 26, 1972.

Apollo Lunar Geology Investigation Team: Progress Report, Apollo 16 Sample Documentation. U.S. Geol. Survey Interagency Rept., Astrogeol. 49, May 1972.

Apollo Lunar Geology Investigation Team: Preliminary Report on the Geology and Field Petrology at the Apollo 16 Landing Site. U.S. Geol. Survey Interagency Rept., Astrogeol. 48, Apr. 1972.

Apollo Field Geology Investigation Team: Apollo 16 Exploration of Descartes: A Geologic Summary. Science, vol. 179, no. 4068, Jan. 5, 1973, pp. 62-69.

Apollo Lunar Geology Investigation Team: Documentation and Environment of the Apollo 17 Samples: A Preliminary Report. U.S. Geol. Survey Interagency Rept., Astrogeol. 71, Jan. 21, 1973.

Apollo Field Geology Investigation Team: Geologic Exploration of Taurus-Littrow: Apollo 17 Landing Site. Science, vol. 182, no. 4113, Nov. 16, 1973, pp. 672-680.

Batson, R. M.; Larson, K. B.; Reed, V. S.; Rennilson, J. J.; et al.: Preliminary Catalog of Pictures Taken on the Lunar Surface During the Apollo 15 Mission. U.S. Geol. Survey Interagency Rept., Astrogeol. 35, Aug. 27, 1971.

Batson, R. M.; Larson, K. B.; and Sutton, R. I.: Preliminary Log of 70 mm Pictures Taken on the Lunar Surface During the Apollo 14 Mission: Magazines II, JJ, KK, LL, MM, with Sample Information by R. L. Sutton. U.S. Geol. Survey Interagency Rept., Astrogeol. 25, Mar. 1971.

Batson, R. M.; Larson, K. B.; Reed, V. S.; and Tyner, R. L.: Preliminary Catalog of Pictures Taken on the Lunar

- Surface During the Apollo 16 Mission. U.S. Geol. Survey Interagency Rept., Astrogeol. 50, May 19, 1972.
- Boudette, E. L.; Schafer, J. P.; and Elston, D. P.: Apollo 16 (Descartes) Landing Site Road Log. U.S. Geol. Survey Interagency Rept., Astrogeol. 46, Apr. 1972.
- Carr, M. H.; and Froudfoot, S. J.: Debris on the Surveyor 3 Mirror. Analysis of Surveyor 3 Material and Photographs Returned by Apollo 12. NASA SP-284, 1972, pp. 47-50.
- Colton, G. W.; Howard, K. A.; and Moore, H. J.: Mare Ridges and Arches in Southern Oceanus Procellarum. Sec. 29 of Apollo 16 Preliminary Science Report. NASA SP-315, 1972.
- Eggleton, R. E.; and Schaber, G. G.: Cayley Formation Interpreted as Basin Ejecta. Sec. 29, Part B, of Apollo 16 Preliminary Science Report. NASA SP-315, 1972.
- Elston, D. P.; Boudette, E. L.; Schafer, J. P.; Muehlberger, W. R.; et al.: Geology of the Region of the Descartes (Apollo 16) Site. Lunar Science-III (Rev. abs. of papers presented at the Third Lunar Science Conference (Houston, Tex.), Jan. 10-13, 1972), pp. 227-229.
- Elston, D. P.; Boudette, E. L.; and Schafer, J. P.: Geologic Map of the Apollo 16 (Descartes) Region. U. S. Geol. Survey Open File Rept., 1972. (Available from Center of Astrogeology, Flagstaff, Ariz.)
- Elston, D. P.; Boudette, E. L.; Schafer, J. P.; Muehlberger, W. R.; et al.: Apollo 16 Field Trips. Geotimes, vol. 17, no. 3, Mar. 1972, pp. 27-30.
- Hait, M. H.: The White Rock Group and Other Eoulders of the Apollo 14 Site: A Partial Record of Fra Mauro History. Lunar Science III (Rev. abs. of papers presented at the Third Lunar Science Conference (Houston, Tex.), Jan. 10-13, 1972), p. 353.
- Hodges, C. A.: Sketch Map of the Candidate Descartes Apollo Landing Site. Sec. 18, Part E, of Apollo 14 Preliminary Science Report. NASA SP-272, 1971, pp. 293-296.
- Hodges, C. A.: Descartes Highlands: Possible Analogs Around the Orientale Basin. Sec. 29, Part D, of Apollo 16 Preliminary Science Report. NASA SP-315, 1972.
- Hodges, C. A.; Eggleton, R. E.; Schaber, G. G.; and Muehlberger, W. R.: Some Geologic Implications of the Apollo 16 Mission. Geol. Soc. Am. Abs., vol. 4, no. 7, 1972, p. 54C.

- Hodges, C. A.; Muehlberger, W. R.; Eggleton, B. E.; and Schaber, G. G.: Geologic Setting of Apollo 16. Lunar Science IV (Abs. of papers presented at the Fourth Lunar Science Conference (Houston, Tex.), Mar. 5-8, 1973), pp. 368-370.
- Hodges, C. A.; Muehlberger, W. R.; and Ulrich, G. E.: Geologic Setting of Apollo 16. Proceedings of the Fourth Lunar Science Conference, vol. 1, Pergamon Press (New York), 1973, pp. 1-25.
- Howard, K. A.: Ejecta Blankets of Large Craters Exemplified by King Crater. Sec. 29, Part N, of Apollo 16 Preliminary Science Report. NASA SF-315, 1972.
- Howard, K. A.: Lunar Rock Avalanches and Apollo 17. Science, vol. 180, June 8, 1973, pp. 1052-1055.
- Howard, K. A.; and Head, J. W.: Regional Geology of Hadley Rille. Sec. 25, Part F, of Apollo 15 Preliminary Science Report. NASA SF-289, 1972.
- Howard, K. A.; Head, J. W.; and Swann, G. A.: Geology of Hadley Rille: Preliminary Report. U. S. Geol. Survey Interagency Rept., Astrogeol. 41, 1971.
- Larson, K. B.; Batson, R. M.; Feed, V. S.; and Wolfe, E. W.: Preliminary Catalog of Pictures Taken on the Lunar Surface During the Apollo 17 Mission. U.S. Geol. Survey Interagency Rept., Astrogeol. 70, Jan. 19, 1973.
- Lucchitta, B. K.: The Apollo 17 Landing Site. Nature, vol. 240, no. 5379, Dec. 1, 1972, pp. 259-260.
- Lucchitta, B. K.: Photogeologic Setting of the Dark Mantling Material in the Taurus-Littrow Region of the Moon. Lunar Science IV (Abs. of papers presented at the Fourth Lunar Science Conference (Houston, Tex.), March 5-8, 1973), p. 483.
- Lucchitta, B. K.: Photogeology of the Dark Material in the Taurus-Littrow Region of the Moon. Proceedings of the Fourth Lunar Science Conference, vol. 1, Pergamon Press (New York), 1973, pp. 149-162.
- Lunar Sample Preliminary Examination Team: A Petrographic and Chemical Description of Samples from the Lunar Highlands. Sec. 7, Part A, of Apollo 16 Preliminary Science Report. NASA SF-315, 1972.

- M'Gonigle, J. W.; Schleicher, David L.; and Lucchitta, Ivo:  
A Proposed Scheme for Lunar Geologic Description U.S.  
Geol. Survey Interagency Rept., Astrogeol. 18, Nov. 1969.
- Moore, H. J.: Large Blocks Around Lunar Craters. Analysis  
of Apollo 10 Photography and Visual Observations. NASA  
SP-232, 1971, pp. 26-27.
- Moore, H. J.: Lunar Impact Craters. Analysis of Apollo 10  
Photography and Visual Observations. NASA SP-232, 1971,  
pp. 24-26.
- Moore, H. J.: Ranger and Other Impact Craters Photographed  
by Apollo 16. Sec. 29, Part J, of the Apollo 16 Prelimi-  
nary Science Report. NASA SP-315, 1972.
- Morrison, D. A.; McKay, D. S.; Heiken, G. H.; Moore, H. J.;  
et al.: Microcraters on Lunar Rocks. Proceedings of the  
Third Lunar Science Conference, vol. 1, David Criswell,  
ed., MIT Press (Cambridge, Mass.), 1972, pp. 2767-2791.
- Muehlberger, W. R.; Batson, R. M.; Boudette, E. L.; Duke,  
C. M.; et al.: Preliminary Geologic Investigation of the  
Apollo 16 Landing Site. Sec. 6 of Apollo 16 Preliminary  
Science Report. NASA SP-315, 1972.
- Muehlberger, W. R.; Batson, R. M.; Cernan, E. A.; Freeman,  
V. L.; et al.: Preliminary Geologic Investigation of the  
Apollo 17 Landing Site. Sec. 6 of the Apollo 17 Prelimi-  
nary Science Rept. NASA SP-320, 1973.
- Muehlberger, W. R.; Boudette, E. L.; Elston, C. P.; Hodges,  
C. A.; and Milton, D. J.: Geologic Setting of Apollo 16  
Landing Site; Descartes. Geol. Soc. Am. Abs., vol. 3, no.  
7, 1971, p. 654.
- Muehlberger, W. R.; and Wolfe, E. W.: The Challenge of  
Apollo 17. Am. Scientist, vol. 61, no. 6, Nov.-Dec. 1973,  
pp. 660-669.
- Pike, R. J.: Crater Morphometry. Sec. 29, Part L, of the  
Apollo 16 Preliminary Science Report. NASA SP-315, 1972.
- Pohn, H. A.; Wildey, R. L.; and Radin, H. W.: Theoretical  
Photometry. Analysis of Apollo 8 Photography and Visual  
Observations, NASA SP-201, 1970, pp. 40-41.
- Rennilson, J. J.; Holt, H. E.; and Moll, K. W.: Changes in  
Optical Properties of the Surveyor 3 Camera. Analysis of  
Surveyor Material and Photographs Returned by Apollo 12.  
NASA SP-284, 1972, pp. 60-76.

- Schaber, G. G.; Scott, D. R.; and Irwin, J. E.: Glass in the Bottom of Small Lunar Craters: An Observation from Apollo 10. Geol. Soc. Am. Bull., vol. 83, June 1972, pp. 1573-1578.
- Schaber, G. G.; and Swann, G. A.: Surface Lineaments at the Apollo 11 and 12 Landing Sites. Proceedings of the Second Lunar Science Conference, vol. 1, A. A. Levinson, ed., MIT Press (Cambridge, Mass.), 1971, pp. 27-38.
- Schleicher, David I., ed.: Geologic Transcript from Apollo 11 Mission. U.S. Geol. Survey Interagency Rept., Astrogeol. 20, Dec. 1969.
- Schleicher, David I., ed.: Paraphrased Geologic Excerpts from Apollo 12 Mission. U.S. Geol. Survey Interagency Rept., Astrogeol. 21, June 1970.
- Schmitt, H. H.; Iofgren, G.; Swann, G. A.; and Simmons, G.: The Apollo 11 Samples: Introduction. Proceedings of the Apollo 11 Lunar Science Conference, vol. 1, Pergamon Press (New York), 1970, pp. 1-54.
- Scott, D. H.: Structural Aspects of Imbrium Sculpture. Sec. 29, Part G, of Apollo 16 Preliminary Science Report. NASA SP-315, 1972.
- Scott, D. H.; West, M. N.; Lucchitta, B. K.; and McCauley, J. F.: Preliminary Geologic Results from Orbital Photography. Sec. 18 of Apollo 14 Preliminary Science Report. NASA SP-272, 1971.
- Shoemaker, E. M.; Batson, R. M.; Bean, A. I.; Conrad, C., Jr.; et al.: Geology of the Apollo 12 Landing Site. Sec. 10, Part A, of Apollo 12 Preliminary Science Report. NASA SP-235, 1970.
- Shoemaker, E. M.; Hait, M. H.; Swann, G. A.; Schleicher, D. L.; et al.: Lunar Regolith at Tranquility Base. Science, vol. 167, no. 3918, Jan. 30, 1970, pp. 452-455.
- Shoemaker, E. M.; Hait, M. H.; Swann, G. A.; Schleicher, D. L.; et al.: Origin of the Lunar Regolith at Tranquility Base. Proceedings of the Apollo 11 Lunar Science Conference, vol. 3, Pergamon Press (New York), 1970, pp. 2399-2412.
- Shoemaker, E. M.; and M'Gonigle, J. W.: Geological Results from the First Landing of American Astronauts on the Moon. Report of the Twenty-Third Session, International Geological Congress (Prague, Czechoslovakia), 1968.

- Soderblom, Laurence A.; and Boyce, J. M.: Relative Ages of Some Near-Side and Far-Side Terra Plains Based on Apollo 16 Metric Photography. Sec. 29, Part A, of Apollo 16 Preliminary Science Report. NASA SP-315, 1972.
- Sutton, R. L.; Batson, R. M.; Larson, K. E.; Schafer, J. P.; et al.: Documentation of the Apollo 14 Samples. U.S. Geol. Survey Interagency Rept., Astrogeol. 28, May 1971.
- Sutton, R. L.; Hait, M. H.; Larson, K. E.; and Swann, G. A.: Documentation of Apollo 15 Samples. U.S. Geol. Survey Interagency Rept., Astrogeol. 47, Apr. 1972.
- Sutton, R. L.; and Schaber, G. G.: Lunar Locations and Orientations of Rock Samples from Apollo Missions 11 and 12. Proceedings of the Second Lunar Science Conference, vol. 1, A. A. Levinson, ed., MIT Press (Cambridge, Mass.), 1971, pp. 17-26.
- Sutton, R. L.; Hait, M. H.; and Swann, G. A.: Geology of the Apollo 14 Landing Site. Proceedings of the Third Lunar Science Conference, vol. 1, MIT Press (Cambridge, Mass.), 1972, pp. 27-38.
- Sutton, R. L.; Hait, M. H.; Wolfe, E. W.; et al.: Preliminary Documentation of the Apollo 15 Samples. U.S. Geol. Survey Interagency Rept., Astrogeol. 34, Aug. 26, 1971.
- Swann, G. A.; Bailey, N. G.; Batson, R. M.; Eggleton, R. E.; et al.: Preliminary Geologic Investigations of the Apollo 14 Landing Site. Sec. 3 of Apollo 14 Preliminary Science Report, NASA SP-272, 1971.
- Swann, G. A.; Bailey, N. G.; Batson, R. M.; Freeman, V. L.; et al.: Preliminary Geologic Investigation of the Apollo 15 Landing Site. Sec. 5 of Apollo 15 Preliminary Science Report. NASA SP-289, 1972.
- Swann, G. A.; Hait, M. H.; Schaber, G. G.; Freeman, V. L.; et al.: Preliminary Description of Apollo 15 Sample Environments. U.S. Geol. Survey Interagency Rept., Astrogeol. 36, Sept. 1971.
- Swann, G. A.; Harbour, Jerry; Moore, H. J.; Watkins, J. S.; and Milton, D. J.: Preliminary Scientific Mission Profiles for the First Seven Apollo Missions. Geol. Survey Tech. Letter, Astrogeol. 3, Nov. 12, 1964.
- Swann, G. A.; Schaber, G. G.; Silver, I. I.; Holt, H. E.; and Freeman, V. L.: Geology of the Apollo 15 Landing Site. Lunar Science III (Rev. abs. of papers presented at the Third Lunar Science Conference (Houston, Tex.), Jan.

- 10-13, 1972), pp. 735-737.
- Swann, G. A., Schaber, G. G.; and Sutton, R. I.: Geology of the Apollo 11 and Apollo 12 Landing Sites. Geol. Soc. Am. Abs., vol. 2, no. 7, 1970, pp. 697-698.
- Swann, G. A.; Schaber, G. G.; and Sutton, R. I.: The Lunar Surface at the Apollo 11 and Apollo 12 Landing Sites. Abstracts of Papers Presented at the 24th Brazilian Geol. Cong., Brazilian Geol. Soc., West Central Section, Spec. Bull. 1, 1970, pp. 34-37.
- Swann, G. A.; Trask, N. J.; Hait, M. H.; and Sutton, R. I.: Geologic Setting of the Apollo 14 Samples. Science, vol. 173, no. 3998, Aug. 20, 1971, pp. 716-719.
- Trask, N. J.: Geologic Maps of Early Apollo Landing Sites of Set C. U.S. Geol. Survey Interagency Rept., Astrogeol. 17, Oct. 1969.
- Trask, N. J.: Photographs of Apollo Landing Site 3. Analysis of Apollo 10 Photography and Visual Observations. NASA SP-232, 1971, pp. 36-37.
- Ulrich, G. E.: Closeup Photography of Rocks and Soils--An Evaluation of the Apollo Lunar Closeup Stereo Camera and the Hasselblad Electric Data Camera. U.S. Geol. Survey Interagency Rept., Astrogeol. 31, 1971.
- Ulrich, G. E.: A Geologic Model for North Ray Crater and Stratigraphic Implications for the Descartes Region. Proceedings of the Fourth Lunar Science Conference, vol. 1, Pergamon Press (New York), 1973, pp. 27-39.
- Warner, Jeffery, compiler: Apollo 12 Lunar-Sample Information. NASA TR R-353, 1970.
- Willey, R. I.: Regional Variations in the Magnitude of Heiligenschein and Causal Connections. Sec. 25, Part O, of Apollo 15 Preliminary Science Report. NASA SP-289, 1972.
- Willey, R. I.: Physical and Geological Aspects of Heiligenschein Measurements. Sec. 29, Part Y, of Apollo 16 Preliminary Science Report. NASA SP-315, 1972.
- Willey, R. L.; and Pohn, H. A.: The Normal Albedo of the Apollo 11 Landing Site and Intrinsic Dispersion in the Lunar Heiligenschein. Analysis of Apollo 10 Photography and Visual Observations. NASA SP-232, 1971, pp. 35-36.
- Wilhelms, D. E.: Reinterpretations of the Northern Nectaris

- Basin. Sec. 29, Part F, of Apollo 16 Preliminary Science Report. NASA SF-315, 1972.
- Wilhelms, D. E.; and McCauley, J. F.: Geologic Setting of the Apollo 14 and Apollo 15 Landing Sites. Geol. Soc. Am. Abs., vol. 3, no. 7, 1971, pp. 751-752.
- Wilhelms, D. E.; and McCauley, J. F.: Geologic Setting of the Apollo 14 and Apollo 15 Landing Sites. Lunar Science III (Rev. abs. of papers presented at the Third Lunar Science Conference (Houston, Tex.), Jan. 10-13, 1972), pp. 800-802.
- Wolfe, E. W.; and Bailey, N. G.: Lineaments of the Apennine Front - Apollo 15 Landing Site. Proceedings of the Third Lunar Science Conference, vol. 1, MIT Press (Cambridge, Mass.), 1972, pp. 15-25.
- Wolfe, E. W.; Bailey, N. G.; and Muehlberger, W. R.: Geology of the Apennine Front--Apollo 15 Landing Site. Lunar Science III (Rev. abs. of papers presented at the Third Lunar Science Conference (Houston, Tex.), Jan. 10-13 1972), pp. 809-810.
- Wolfe, E. W.; Freeman, V. L.; Lucchitta, E. K.; Scott, F. H. et al.: Geologic Setting of the Apollo 17 Landing Site. Geol. Soc. Am. Abs., vol. 4, no. 7, 1972, p. 710.
- Wolfe, E. W.; Freeman, V. L.; Muehlberger, W. R.; Head, J. W.; et al.: Apollo 17 Exploration at Taurus-Littrow. Geotimes, vol. 17, no. 11, Nov. 1972, pp. 14-18.
- Wu, S. S. C.; and Moore, H. J.: Frequency Distributions of Lunar Slopes. Sec. 30, Part C, of Apollo 16 Preliminary Science Report. NASA SF-315, 1972.
- Wu, S. S. C.; Schafer, F. J.; Jordan, Raymond; and Nakata, G. M.: Photogrammetry Using Apollo 16 Orbital Photography. Sec. 30, Part B, of Apollo 16 Preliminary Science Report. NASA SF-315, 1972.
- Zisk, S. H.; Masursky, Harold; Milton, D. J.; Schaber, G. G.; et al.: Apollo 16 Landing Site: Summary of Earth-Based Remote Sensing Data. Sec. 29, Part W, of Apollo 16 Preliminary Science Report, NASA SF-315, 1972.
- Zisk, S. H.; and Moore, H. J.: Calibration of Radar Data from Apollo 16 Results. Sec. 29, Part X, of Apollo 16 Preliminary Science Report. NASA SF-315, 1972.

TABLE 13-1.- FIELD AND LABORATORY CLASSIFICATION OF APOLLO 17 SAMPLES

Geologic entity	Geologic unit	Collection site	Station	Sample number or type	Laboratory designation
Van Serg	Dark surface material Light-gray fragmental material Dark matrix-rich breccia Dark-matrix fragment-rich breccia	Van Serg ejecta Van Serg blanket trench Van Serg ejecta Van Serg floor	9 9 9 9	79220 and 79249 79260 79035 and 79195 Not sampled	Dark-matrix breccia
Shorty	Dark surface material Orange glass material Light-gray fragmental material Black glass material Floor material	Shorty rim core Shorty rim trench Shorty rim trench Shorty rim core Shorty floor	4 4 4 4 4	74002 (top 0.5 cm) 74220 74240 and 74260 74001	
Light mantle	Medium-gray material Light-gray material Marbled material Light component Dark component	Surface of light mantle Below medium-gray surface material of light mantle Below medium- and light-gray material of light mantle on crater rim	2A, 3 2A, 3 2A, 3	73220 and 73120 73240 and 73140 73280 73260	
Dark regolith	Dark floor material	Steno-Camelot area	0, 1, 5		
Subfloor	Aphanitic basalt Vesicular Nonvesicular Fine-grained basalt Coarse-grained basalt Porphyritic Nonporphyritic	General area	0, 1, 5, 6, 8	74235 74215 71055 74035 75055	Same terms as field classification
Massifs	Medium-gray surface material Light-gray talus material Pilliated and layered breccia Tan matrix-rich breccia Blue-gray matrix-rich breccia Blue-gray fragment-rich breccia	South and North Massifs South and North Massifs South Massif South and North Massifs South and North Massifs North Massif	2, 6 2, 6 2 2, 6, 7 2, 6, 7 6, 7	Take samples Take samples 72255 and 72275 76215 and 72395 72435 and 76315 76275	Light-gray breccia Greenish-gray breccia Blue-gray breccia Light-gray breccia and greenish-gray breccia
Sculptured Hills	Slope material	Sculptured Hills	8	78500 and 78530	
Source unknown	Gabbroic rocks Feldspathic breccia	Exotics on Sculptured Hills and North Massif	6, 8 6, 8	78235 and 76535 76335 and 78155	Gabbroic rocks Cataclasite and hornfels

ORIGINAL PAGE IS  
OF POOR QUALITY



0 500  
m

ORIGINAL PAGE IS  
OF POOR QUALITY

Figure 13-1.- Mosaic of Lunar Orbiter V photographs showing location of the Apollo 11 landing site and of West Crater.

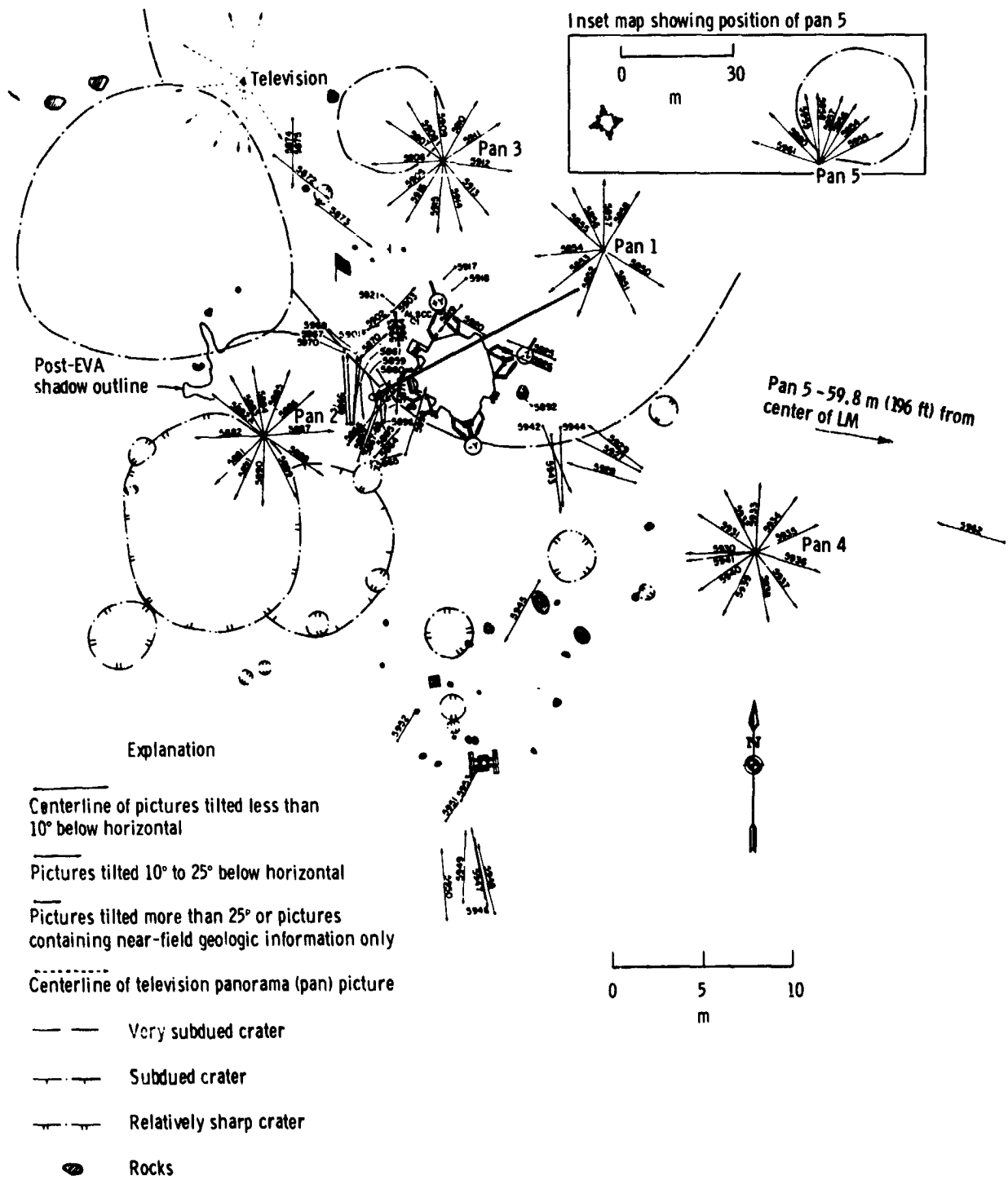
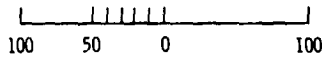
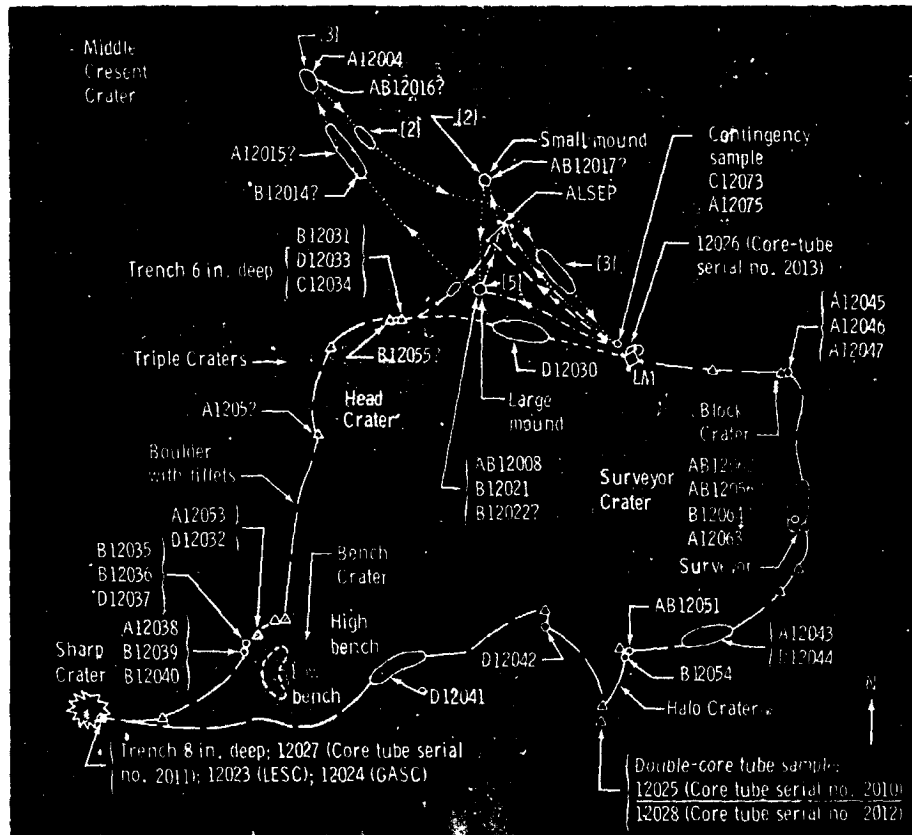


Figure 13-2.- Apollo 11 landing site and preliminary map of extravehicular activity (EVA) photographs and television pictures.

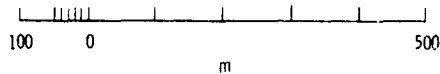
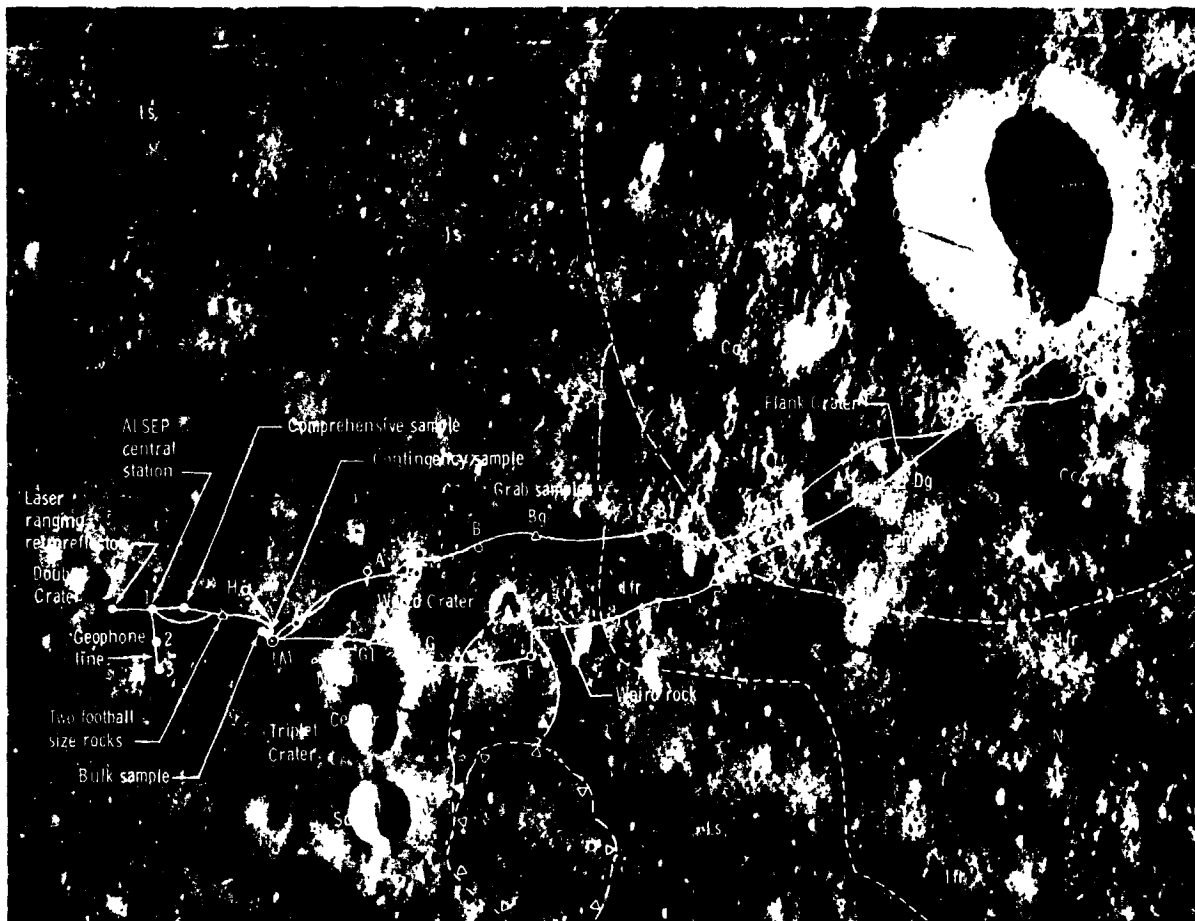


m

- Explanation
- |       |  |       |                     |
|-------|--|-------|---------------------|
| ..... | First EVA traverse   | ..... | Second EVA traverse |
| ..... | Both astronauts  | ..... | Both astronauts     |
| ..... | Commander  | ..... | Commander           |
| ..... | Lunar module pilot   | ..... | Lunar module pilot  |
| △     | Photographic control station   |       |                     |
| ○     | Sample locality. Number refers to sample number assigned in Lunar Receiving Laboratory.                    |       |                     |
| ○     | Letters refer to rock type. Queried where sample identification is uncertain. Rock types are as follows:   |       |                     |
|       | A - fine-grained igneous rock  |       |                     |
|       | B - medium-grained igneous rock  |       |                     |
|       | AB - intermediate, fine-to-medium-grained igneous rock   |       |                     |
|       | C - breccia  |       |                     |
|       | D - fine-grained material  |       |                     |
| ○     | Sample locality. Circle indicates locality not accurately determined. Dot shows best estimate of location. |       |                     |
| {3}   | Number of rocks collected in sample locality   |       |                     |
| ★     | diagrammatic sketch of fresh ray pattern around Sharp Crater   |       |                     |
| ALSEP | Apollo lunar surface experiments package   |       |                     |
| LESC  | Lunar environment sample container   |       |                     |
| CASC  | Gas analysis sample container  |       |                     |

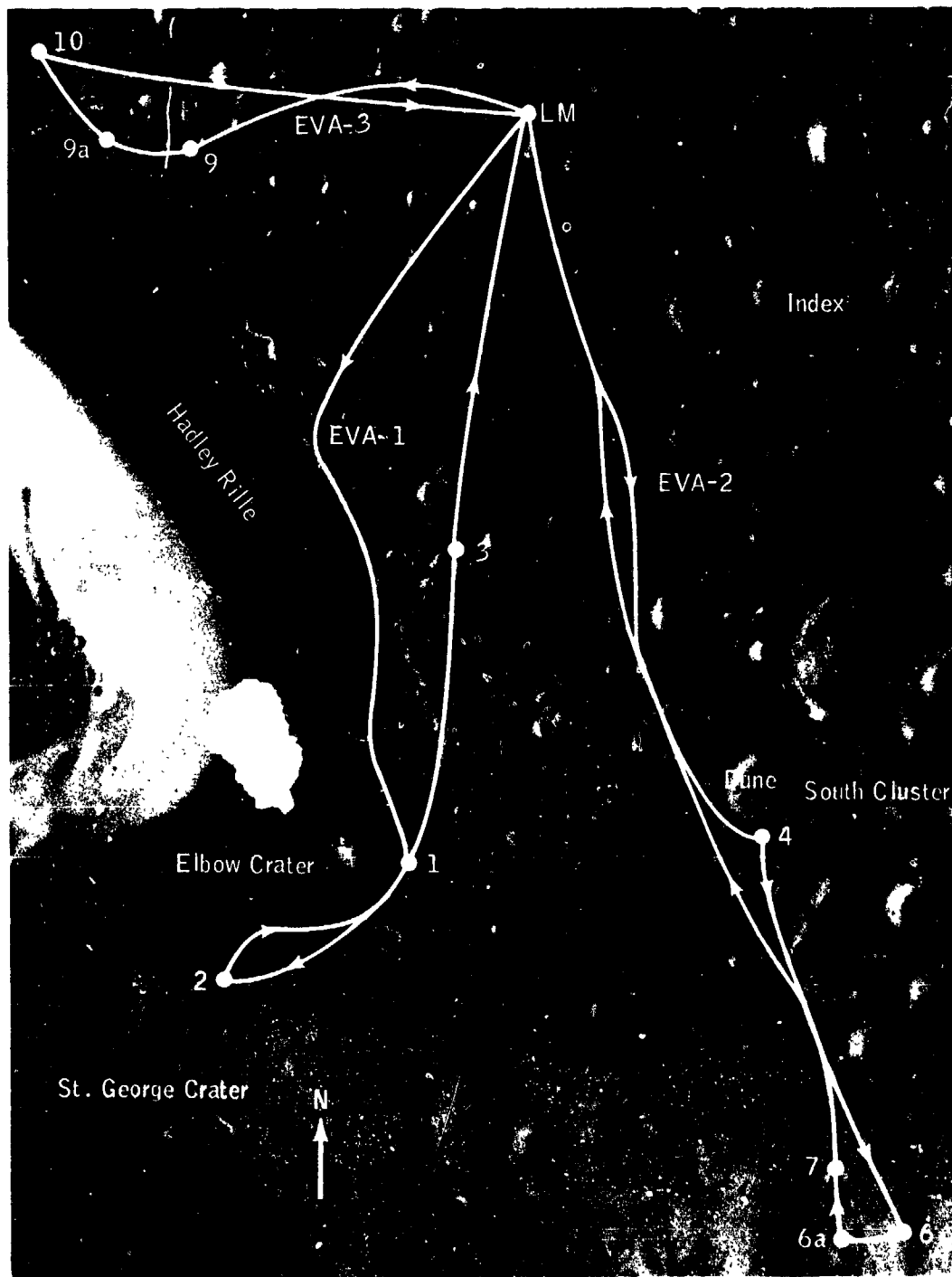
**ORIGINAL PAGE IS  
OF POOR QUALITY**

Figure 13-3.- Traverse map for Apollo 12.



Explanation		Contact	
Cc4	Materials of Cone Crater	---	Long dashed lines indicate approximate locations, and short dashed lines indicate location is inferred without local evidence.
Is	Smooth terrain material of the Fra Mauro Formation	▲-▲-	Foot of scarp The line bounds a small mesa, and the triangles point downslope. The short dashed lines indicate inferred location.
Itr	Ridge material of the Fra Mauro Formation	▽ ▽ ▽	Edge of hill Long dashed lines indicate approximate locations, and short dashed lines indicate inferred location. The triangles point downslope.
○	Panorama station	—	Traverse routes for first and second EVA.
△	Station without panorama		

Figure 13-4.- Map of major geologic features in Apollo 14 traverse area.



ORIGINAL PAGE IS  
OF POOR QUALITY

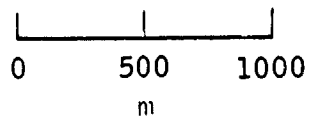
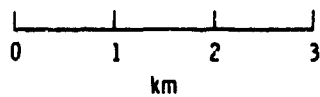


Figure 13-5.- Traverse map for Apollo 15.





**Explanation**

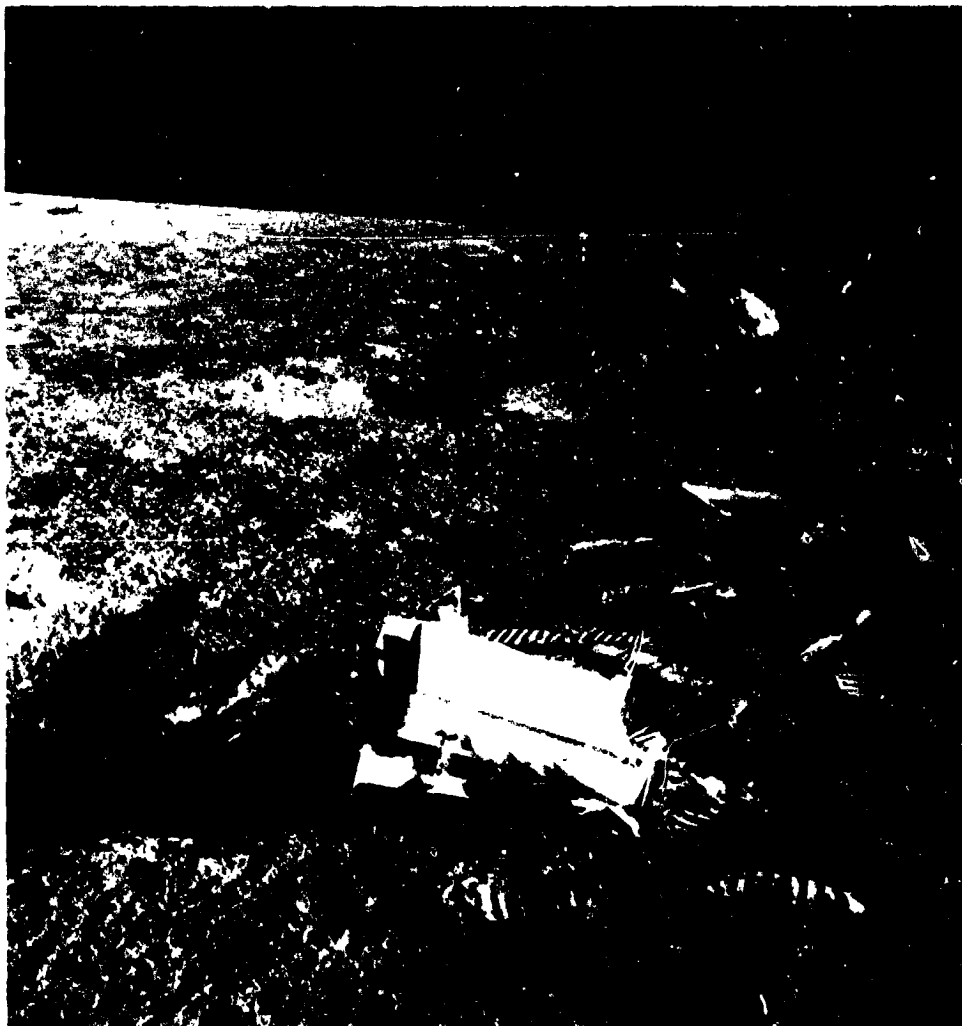
- Locations accurate within 10 m
- ◻ Approximate locations
- Approximate traverse
- Traverse path derived in part from very long base interferometry by I. Salzburg, Goddard Space Flight Center
- EP-7 Lunar seismic profiling experiment (LSPE) explosive package number

**Figure 13-7.- Traverse map for Apollo 17.**

14. LASER RANGING RETROREFLECTOR (NASA EXPERIMENT S-078)

NSSDC IDENTIFICATION NUMBERS:

APOLLO 11	69-059C-04
APOLLO 14	71-008C-09
APOLLO 15	71-063C-08



ORIGINAL PAGE IS  
OF POOR QUALITY

CONTENTS - SECTION 14

	Page
OBSERVATORY AND REFLECTORS . . . . .	14-3
FILTERED DATA . . . . .	14-4
UNFILTERED PHOTON DETECTIONS . . . . .	14-5
DATA DESCRIPTION . . . . .	14-6
REFERNCES . . . . .	14-7

#### 14. LASER RANGING RETROREFLECTOR

One of the most striking new techniques in modern astrometry is that of laser ranging to a reflector fixed on a celestial object. The precision attained by this technique is so high that the data provide as much information about Earth as about the observed object. The Apollo crewmen have now placed three widely separated reflector arrays on the Moon as a part of the Lunar Laser Ranging Experiment (LURE).

Although the development of the experiment began much earlier, the data-taking process did not begin until July 1969, when the Apollo 11 mission was flown. Success in recognizing returns from the reflector was achieved shortly thereafter. A learning period followed during which various improvements in the ranging techniques were made. Since the early part of 1970, the success rate in attaining lunar ranges has been satisfyingly high.

This report is the documentation to be used in conjunction with the deposition in the National Space Science Data Center (NSSDC) of the filtered data obtained during laser ranging operations between the McDonald Observatory; (Fort Davis, Texas) and the Apollo 11, 14, and 15 reflectors for the 6 months ending December 31, 1971, and the unfiltered photon detections for the succeeding 6 months.

#### OBSERVATORY AND REFLECTORS

The laser ranging equipment is mounted on the 272-cm reflector at the McDonald Observatory, Fort Davis, Texas. The physical installation is fully described in reference 14-1. The nominal coordinates presently recommended for this instrument, based on high-order land survey ties to the Smithsonian Astrophysical Observatory (SAO) Organ Pass Tracking Station, New Mexico, are as follows.

<u>Coordinate</u>	<u>Value</u>
Geocentric radius $\rho$ , km	6374.665
East longitude $\lambda$ , deg	255.97779
Geocentric latitude $\psi'$ , deg	30.50320

These coordinates refer to the intersection of the polar and transverse axes of the telescope. The center of the primary mirror, as the telescope tracks across the sky, describes a circle with a radius of 305 cm the plane of which is normal to the polar axis.

The present data refer to the reflectors at Tranquility Base, Fra Mauro, and Hadley, the nominal coordinates of which are noted in the following table and are based on data supplied by the NASA Lyndon B. Johnson Space Center during Apollo missions tracking operations.

<u>Coordinate</u>	<u>Tranquility Base</u>	<u>Fra Mauro</u>	<u>Hadley</u>
Selenocentric radius			
$\rho$ , km	1735.730	1736.680	1735.64
East longitude $\lambda$ ,			
deg	+23.485	-17.4628	+3.673
Latitude $\beta$ , deg	+0.642	-3.6680	+26.094

#### FILTERED DATA

The photon detections have been submitted to a data-filtering procedure developed at the University of Texas. This process is based on the assumption of the linearity of the residuals over a relatively short time interval and relies on Poisson statistics for establishing a level of confidence in a collection identified by the filter. Application of the process resulted in the identification of the observations during the subject interval.

Potential users of the data should be aware that the laser cannot be relied on to produce a simple pulse shape; occasionally, there is a complex and/or biased structure within the pulse. Therefore, residuals derived from signal photons are not necessarily expected to show a Gaussian distribution. The uncertainties assigned are based on the sum of the pulse half-width and the measured uncertainty in calibrating the electronic system. Beginning with the April-May 1972 lunation, a letter code appears in column 32

(formerly unused) of the "Z" card image that provides an estimate of the accuracy of the electronic calibration correction. The code is defined in the following table.

<u>Code</u>	<u>Calibration correction range</u>
A	Less than $\pm 200$ psec
B	$\pm 200$ to $\pm 400$ psec
C	$\pm 400$ to $\pm 600$ psec
D	$\pm 600$ to $\pm 1000$ psec
F	$\pm 1.0$ to $\pm 1.5$ nsec
F	$\pm 1.5$ to $\pm 2.0$ nsec
G	$\pm 2.0$ to $\pm 4.0$ nsec
H	More than $\pm 4.0$ nsec

The calibrations were performed by E. C. Silverberg; otherwise, the data format is as defined in reference 14-2.

#### UNFILTERED PHOTON DETECTIONS

The potential user should note the designation "unfiltered," which means that the raw data are heavily interspersed with noise photons from any of the various sources of stray light. Any attempt to use these data in a simple Gaussian application would probably result in a solution closely adhering to the prediction ephemeris used to control the detector range gating. Some filtering process must be applied to these data before effective use can be made of them. Such filtering is now underway at the University of Texas at Austin, and all filtered data will also be deposited with NSSDC; but the unfiltered data may be of direct use or interest to those potential users who may wish to replace the present filter criteria with their own. These data also conform to the data format standard defined in reference 14-2, except that, for all data before November 1972, the clock epoch error carries the opposite sign, as is the case with all previous NSSDC depositions. Data after November 1972 have the clock epoch error sign as defined in reference 14-2.

## DATA DESCRIPTION

The data are contained on two files of a binary magnetic tape written in card image format, using a CDC 6600 computer. The tape is written with odd parity at 800 bpi. Two types of cards are present, distinguished by an alphabet character in column 1. The letter Z designates a "run" card, giving environmental and operational parameters for a series of shots. Except for clock epoch error, these parameters will not customarily be required for application of the range data but serve to provide information on the observing conditions and the state of the equipment. Most users will find them helpful only as separators between observing sessions. The letter P in column 1 represents a "shot" card, containing the result of a single laser firing.

Users should note that some of the specified data items may not be available. In the card images, a blank field is a "no information" indicator. Actual null values will be represented by zero punches.

---

#### REFERENCES

- 14-1. Silverberg, E. C.; and Currie, D. G.: A Description of the Lunar Ranging Station at McDonald Observatory. Space Research XIV, Akademie-Verlag (Berlin), 1972.
- 14-2. Mulholland, J. D.: Proposed Standards for Distribution and Documentation of Lunar Laser Ranging Data. COSPAR Bulletin, No. 61, Mar. 1971.

15. LUNAR SURFACE COSMIC RAY EXPERIMENT (NASA EXPERIMENT S-152)

NSSDC IDENTIFICATION NUMBER:

APOLLO 16 72-031C-07



ORIGINAL PAGE IS  
OF POOR QUALITY

CONTENTS - SECTION 15

	Page
EXPERIMENT OBJECTIVES . . . . .	15-3
EQUIPMENT DESCRIPTION . . . . .	15-4
OPERATION OF THE EXPERIMENT . . . . .	15-8
INVESTIGATION PROCEDURES . . . . .	15-10
SUMMARY OF SCIENTIFIC RESULTS . . . . .	15-13
UNIVERSITY OF CALIFORNIA FINDINGS . . . . .	15-16
DISPOSITION OF FLIGHT MATERIALS . . . . .	15-16
REFERENCES . . . . .	15-17

## 15. LUNAR SURFACE COSMIC RAY EXPERIMENT

The major objective of the lunar surface cosmic ray experiment was to determine the energy spectra and abundances of low-energy heavy cosmic rays ( $0.03 < E < 150$  MeV/nucleon). The cosmic ray experiment equipment consists of a four-panel array of passive particle track detectors for observing cosmic ray and solar wind nuclei and thermal neutrons. The equipment includes metal foils for trapping light solar wind gases. The materials in the panels were chosen for experiments performed by groups at General Electric (GE), the University of California, and Washington University.

The cosmic rays were detected with plastic and glass particle track detectors. Particles emitted during the April 18, 1972, solar flare dominated the spectra for energies below approximately 70 MeV/nucleon. Two conclusions emerge from the low energy data:

1. The differential energy spectra for solar particles vary rapidly (approximately  $E^{-3}$ ) for energies as low as 0.05 MeV/nucleon for iron-group nuclei.
2. The abundance ratio of heavy elements changes with energy at low energies; heavy elements are increasingly enhanced relative to higher elements as the energy decreases.

Galactic particle fluxes recorded in the spacecraft agree with those predicted, taking into account solar modulation and spacecraft shielding. The composition of the nuclei at energies above 70 MeV/nucleon imply that these particles originate outside the solar system and hence are galactic cosmic rays.

### EXPERIMENT OBJECTIVES

The detector array for the Apollo 16 cosmic ray experiment was designed for multiple purposes; however, the primary objective was to learn as much as possible about the lowest energy nuclei in the cosmic rays, that is, those below 150 MeV/amu. Little was known about this energy range, and the solid nuclear track detectors offered the possibility for analysis. Two mutually exclusive, alternate objectives were to be served. One was to examine the composition and the energy spectra of solar flare particles; the other was to determine whether the lowest energy nuclei were solar or galactic in origin. Because the Sun became

active during the mission, the first objective was best served; however, in the energy range above 70 MeV/nucleon, it has been possible to show that the background particles were galactic. In contrast to these studies, which were based on detectors in three of the four panels of the experiment, the fourth panel was primarily aimed at studying the heavy nuclei in the solar wind. The GE portion of the equipment had the additional purposes of obtaining calibration data on various glass detectors that were included, of establishing from the data the possibility of measuring the space exposure of tektites through recognition of cosmic ray tracks, and of measuring heavy cosmic ray doses to which the astronauts were exposed during the latter half of the Apollo 16 mission.

#### EQUIPMENT DESCRIPTION

A four-panel array was used in the cosmic ray experiment. Panel 1 contained 31 sheets of 250- $\mu$ m Lexan, each 16.5 by 25.4 cm, fastened so that alternate sheets were translated by 2 mm when the astronauts folded the four hinged panels. This feature made possible the rejection of tracks of cosmic rays that passed through the spacecraft on the Apollo 16 mission return trip. The 31 sheets were covered with a sheet of 50- $\mu$ m Teflon, silvered on the back, with holes 2.5 cm apart and 0.5 cm in diameter. The holes allowed a fraction of the stack to have a view of space with no covering material. The Teflon sheet was used to minimize absorption of visible sunlight, maximize emission of infrared, and keep the temperature of the underlying sheets below 343 K.

In panel 2, the entire exposed detector area of 14.7 by 22.6 cm was composed of 31 sheets of 0.25-cm Lexan polycarbonate plastic 9070-112. In panel 3, 39 sheets of 0.02-cm Eastman Kodacel cellulose triacetate TA-401 with no plasticizer made up the major volume fraction. The lower part of panel 3 contained five types of glass detectors: 2.5- by 1.3- by 0.1-cm GE phosphate-uranium glass 1484(ref. 15-1), 2.5- by 2.5- by 0.1-cm GE phosphate glass 1457(ref. 15-2), 2.5- by 2.5- by 0.1-cm Corning alumina-silicate glass 1720, 2.5- by 2.5- by 0.1-cm silicon dioxide (Suprasil 2 silica glass from Amersil, Inc.), and a nearly elliptical tektite slab (Santiago, Philippines, tektite 1, supplied by D. Chapman, NASA Ames Research Center) that fit within a 2.5- by 3.8- by 0.1-cm space.

Panel 4 of the cosmic ray experiment consisted of several detector systems designed to study various aspects of the radiation environment of the Moon. The detectors included mica, feldspar, three varieties of glass, two varieties of plastic, aluminum foil, and aluminum-coated platinum foil. Panel 4, as it was returned from the Moon by the Apollo 16 astronauts, is shown

in figure 15-1. The lower part of the stack, labeled I, consisted of a series of alternating layers of 60- $\mu$ m-thick cellulose triacetate (Triafol TN) and polycarbonate plastic (Makrofol KG). This detector stack was covered with a 50- $\mu$ m-thick coating of metallized Teflon to provide thermal protection and could thus be used only to study particles of  $>2$  MeV/nucleon that were capable of penetrating this thermal shield. The last sheet in the stack was a large TN foil designed to measure alpha particles from thermal neutron capture on an enriched boron-10 target plate found in the rear of part III.

Immediately adjacent to the plastic stack was a mineral assembly plate (part II) containing samples of mica, feldspar, soda-lime glass, tektite glass, and fused quartz. The mica detectors, which were included principally for measuring heavy solar wind ions with  $Z \geq 26$ , were also to be used to study any heavy particles with energy  $\geq 1$  keV/nucleon. The other mineral detectors were included to complement the mica and to provide samples that would be more directly comparable with lunar minerals.

Above the mineral assembly plate is an aluminum-coated platinum foil (part IV) that can be seen in figure 15-1 in a partially retracted position. This foil was flush against part III during the outbound voyage and was retracted by the astronauts during the first extravehicular activity (EVA). The purpose of this foil was to measure the light solar wind in the interplanetary region and to serve as a calibration for the heavy solar wind ions registered as tracks in the mica detector. Particles that entered the array after it was folded were recognized, if they crossed from one sheet to another, by means of a 2-mm relative shift of alternate sheets (fig. 15-2). This shift was produced automatically by the folding of the array at the end of EVA 3 just before the array was stowed in the lunar module (LM). The designed full 2-mm shift occurred in panel 2, and a lesser shift occurred in panel 3.

Detector temperatures are important because thermal effects can be observed in the plastics and in some of the glasses used in panel 3 after the materials were exposed at temperatures above 328 K. Although tracks are retained to much higher temperatures in all the detectors, the quantitative relation between the ionization rate of the particle and the track etching rate is disturbed. Consequently, for particle identification to be possible, all tracks must have identical thermal histories above 328 K (ideally, no exposure above that temperature). To keep temperatures at less than 328 K in full sunlight during both translunar flight and the time spent on the Moon, panels 1, 2, and 3 were covered with a perforated thermal-control material, 0.005-cm Teflon backed with thin silver and Inconel coatings. This composite has a high reflectivity in the visible region of the solar spectrum and a high emissivity at infrared wavelengths.

The space-exposed surfaces of the detectors also were coated with a 210-nm aluminum film to avoid ultraviolet (UV) exposure of the plastics, which is known to affect track etching rates (refs. 15-3 and 15-4). Because of the slowing down of cosmic ray nuclei in the silver-backed Teflon, particles of less than 5 to 6 MeV/nucleon were registered in the plastic detectors only through the perforations in the Teflon. There were 60 0.3-cm-diameter perforations above the Lexan detectors (4.26 cm<sup>2</sup> total area) and 15 above the Kodacel (1.06 cm<sup>2</sup> total area). Similarly for the glasses (fig. 15-3), nuclei of less than 10 to 20 MeV/nucleon were registered only beneath the single 0.5-cm-diameter hole that was positioned over the center of each glass plate.

Consequently, for the low-energy nuclei that are of primary interest, the Teflon constitutes a shield, the quantitative effect of which on the observed track density can be calculated. For an isotropic bombardment with  $\varphi$  nuclei/[(area) X (solid angle)], the track density  $\rho$  is given by  $\int \varphi \cos \theta d\Omega$ , where  $\theta$  is the angle of incidence and the integration is over the solid angle  $\Omega$  permitted by the Teflon shield and the cone angle of the etched tracks. The Teflon is approximated by a straight-edged semi-infinite sheet spaced a distance  $h$  from the detector. For this case, the ratio  $\rho/\varphi$  depends only on the track cone angle  $\theta_c$  and the ratio  $u$  of the distance  $x$  along the detector under the shield to the spacing  $h$ . The result

$$\rho/\varphi = \cos^2 \theta_c \cos^{-1}(u \tan \theta_c) - (1 + u^{-2})^{-1/2} \quad (15-1)$$

$$\times \frac{\tan^{-1} [1 - (u \tan \theta_c)^2]^{1/2}}{\tan \theta_c (1 + u^2)^{1/2}}$$

is plotted in figure 15-4 for various values of  $\theta_c$ . The figure illustrates how increasing the cone angle decreases the observable track density and increases the abruptness of the transition from maximum to zero track density near the edge of the shield. These same results are useful for computing effective solid angle of detection for particles of all energies in the case of a thick shield such as the Moon was while the experiment was located close to the lunar surface.

Under the partially retracted platinum foil (part IV) was another set of foils mounted in part V. Two of these consisted of aluminum-covered platinum, and one was anodized aluminum. The aluminum foil was provided by J. Geiss of the University of Bern. It was the same material used in his more extensive light solar wind experiment. These part V foils were intended to measure differences in light solar wind flux and composition in time and space.

Two strips of mica (M10 and M11) were located on the left side of part V. During the flight to the Moon, the upper piece of mica (M10) was exposed to space through a 1.9-cm hole in the platinum foil. One-half of this hole can be seen at the upper left corner of part IV. If the foil had been fully retracted, the second piece of mica would have been exposed to space starting with the time the astronaut shifted part IV. The purpose of this mica was to assess the importance of radon in producing shallow tracks (through the production of recoil atoms from alpha decay) that could be confused with extremely heavy solar wind ions.

The neutron detector experiment was located in the rear of the panel. A schematic of this experiment is shown in figure 15-5. During the outbound voyage, a metal plate containing target strips of enriched boron-10 was located in the upper half of the panel behind parts III and IV. This target plate was connected to a wire lanyard. Pulling the lanyard (which moved the target plate down into the bottom part of the panel behind the plastic stack (part I)) activated the experiment. The photograph in figure 15-6, taken after removal of the mineral assembly plate, shows one target strip completely covered with plastic and another that has not moved into the plastic region. The target plate in turn was connected to the platinum foil (part IV). Pulling the lanyard also retracted part IV and exposed part V.

The proposed sequence of events was as follows. When the experiment was originally deployed, the minerals on part III, the plastic detectors (part I), and the aluminum-covered platinum foil (part IV) began registering solar and galactic particles. One piece of mica (M10) mounted on part V was also exposed during this time. Early in the first EVA, the astronaut was to pull a lanyard that would retract part IV and expose part V. The mica (M10) on part V that had been irradiated up to that time would then be shut off from low-energy particles by being covered with a tab of platinum foil attached to the lower left edge of part IV. Another piece of mica on part V (M11) would then be uncovered and start to register particle tracks. The lanyard shift would also move a boron-10 target plate into position to measure thermal neutrons. Both the neutron experiment and the plastic stack were deactivated by a final shift in the plastics that occurred automatically when the experiment was folded at the end of the final EVA.

The scheduled sequence of events did not occur entirely as planned. When the commander attempted to pull the lanyard that would have retracted part IV, he achieved only a partial shift of 2.5 cm, then the lanyard broke. The failure to obtain a complete shift seriously degraded the neutron experiment and reduced the collection area for part V, making difficult the detection of differences in the solar wind at various times during the flight. Also, the mica (M11) on part V was never exposed to the space environment. This result was particularly unfortunate because the solar flare was almost over by that time, and the part V mica would not have sustained the enormous solar flare track background seen in the other micas.

The second unscheduled event was a relocation of the entire experiment package at the end of the first EVA because of an increase in temperature as shown by several color indicators. The entire experiment was placed in the shade, further reducing the time of solar wind registration on the foils of part V. A summary of exposure histories of the various samples is given in table 15-I. The temperature rise in panel 4 was monitored by several color indicators. Readings on the backs of parts II and III and on the back of panel 4 indicated that the temperature was  $>344$  K and  $<355$  K.

The effects of temperature on the tracks themselves were monitored in several ways. First, the plastic stack included a set of preirradiated samples of TN and KG that had been exposed to oxygen ions of different energies. This calibration set of plastics was located deep in the plastic stack, next to the T foil used in the neutron experiment. No difference was observed in the etching of the oxygen tracks in control samples kept in the laboratory and in those returned from the Moon.

Although no temperature effects were seen in the preirradiated foils, there are clear indications that temperature affected the registration of the tracks produced during flight. For example, in the neutron experiments, the alpha tracks are smaller and harder to recognize than normal alpha tracks registered in vacuum at room temperature.

#### OPERATION OF THE EXPERIMENT

The experiment was exposed during the mission for nearly 1 week, distributed in time and solid angle as listed in table 15-II. The solid angle restrictions listed are merely the shadowing effects of the Moon. The degree of obstruction caused by the struts, the scientific equipment bay, and the other parts of the spacecraft varies with different positions in the array. For panels 2 and 3, the obstruction was such that the best solid

angle factors for  $\theta_c < 20^\circ$  were probably those calculated for  $\theta_c = 20^\circ$ . The LM orientation distribution during lunar orbit prior to landing has been averaged for the appropriate 30.1-hr period. As noted in table 15-II, the last part of the exposure occurred on the LM minus-Y footpad with the apparatus leaning against the strut with its face in the down-Sun direction and tilted upward at an angle of  $69^\circ$  to the horizontal. This inference was reached through a pair of up-Sun and cross-Sun photographs. Shifting the experiment from the LM was a contingency procedure designed to minimize solar heating by exposing to the direct Sun only the multilayer insulation at the back of the experiment.

Although the clean equipment should not have overheated, a deposit of as much as a 10-percent cover of lunar dust or other deposit with similar optical and infrared properties would have produced excessive heating before the end of EVA 3. At the end of EVA 1, temperature labels on the outboard frame of the panels indicated that the polycarbonate temperature had exceeded 318 K. Temperature labels on recovered panels 2 and 3 indicated that temperatures of at least 344 K had been reached. The time line for exposure of the cosmic ray experiment is as follows:

<u>Event</u>	<u>Significance</u>	<u>Ground elapsed time,<sup>1</sup> hr:min</u>
Undocking	Detectors exposed to space	3:04
Lunar orbit insertion	Detectors faced Moon part of time	94:27
Lunar landing	Dust deposited on detectors, absorbs solar heat	104:31

---

<sup>1</sup> Measured from launch at 17:54 G.m.t. on April 16, 1972.

<u>Event</u>	<u>Significance</u>	<u>Ground elapsed time,<sup>1</sup> hr:min</u>
Red ring pulled		120:50
Experimental package moved to footpad	Experiment faces down-Sun; cools	125:25
Experimental package folded for storage	Most of experiments terminated; dosimetry experiment begun	170:21
Entry to Earth atmosphere	Dosimetry experiment terminated	265:31

#### INVESTIGATION PROCEDURES

Etching and readout have been performed on Lexan sheets from panel 2 and on glass 1457 from panel 3. For glasses, the final steps in the preflight preparation were annealing (for the tektite and glass 1484, removing preexisting tracks), polishing, etching, inspecting, and coating with an evaporated-aluminum reflective coating approximately 210 nm thick. The 210-nm aluminum coating also was present on the top Lexan and Kodacel sheets. After the flight, before the panels were disassembled, the outlines of the 0.5-cm-diameter openings above the glasses and the 0.3-cm-diameter holes above the plastics were scribed into the detector surfaces.

The track etching rates of the detectors can be altered by thermal annealing, the glasses to a lesser extent than the plastics. In figure 15-7, the changes in the track etching rates caused by 1-hr anneals are shown for several glasses. In figure 15-7,  $V_T$  is the average track etching rate for californium-252 fission fragments, and  $V_G$  is the general etching rate for unirradiated regions. The extreme cases, GE phosphate glass 1457 and Corning glass 1720, were two of the glasses flown on this experiment.

---

<sup>1</sup> Measured from launch at 17:54 G.m.t. on April 16, 1972.

After the panels were disassembled, the glass samples were carefully sectioned by sawing from the underside through most of the thickness and then fracturing the remaining near-upper-surface thickness to avoid the loss of valuable surface material. One portion of each glass was then etched in room-temperature sodium hydroxide for 1 to 2 min to remove the aluminum coating. The same part was then etched in 50 percent hydrofluoric acid to remove approximately 0.5  $\mu$ m of glass from each surface and reveal cosmic ray tracks. The etched glasses were scanned at 1000X in an optical microscope, then were replicated (cellulose acetate, gold coated), and then scanned at 5000X in a scanning electron microscope (SEM). Parts of the top sheet of Lexan, after removal of the aluminum by a 296 K sodium hydroxide solution, were etched for 3 or 6 hr in 313 K 6.25N sodium hydroxide solution saturated with etch products (ref. 15-5). In one case, a preirradiation with UV was used to accelerate etching attack along the tracks (refs. 15-3 and 15-4). Results are given for a 6-hr etch of a sheet from the lower left part of panel 2 (hole 2) and a 6-hr etch of a UV-treated sheet from the upper right corner of panel 2 (hole 59). These parts are thought to correspond to the warmest and coolest parts of panel 2, respectively, as judged from the distribution of dust cover and temperature label readings. Sheets 2 to 11 below hole 2 were etched for 40 hr under the etching conditions described previously. Solar flare tracks on the exposed surfaces of the phosphate glass and Lexan are shown in figure 15-8. From the optical scans in the central open regions of the various detectors, the track length distributions given in table 15-III were obtained. The differential energy spectrum is derived from these track lengths using range-energy relations (ref. 15-6) for iron nuclei, allowing for the thicknesses of the aluminum layer and the layer etched away and assuming that the aluminum is crossed at 45° incidence.

The justification for assuming that all particles are iron when computing the energies is derived from the plot given in figure 15-9. For GE phosphate glass 1457, neon ions give tracks having an average cone angle of 30° to 35° over a distance of approximately 15  $\mu$ m. The SEM photographs of cosmic ray tracks give the cone angle distribution for the >1- $\mu$ m tracks shown in figure 15-9. This cone angle distribution indicates that the tracks are predominantly from particles much heavier than neon. Separate experiments using argon-40 and iron-56 beams indicate that the tracks were made by ions heavier than argon and close to iron in atomic number. From known solar abundances (ref. 15-7), it is expected that iron is dominant and that most of the nuclei observed have range-energy relations that are adequately approximated by that of iron. The justification in using iron for the 6-hr etch of hole 2 is that the results there agree with the phosphate glass. For hole 59 (UV treatment before a 6-hr etch), this assumption was shown to be useful but quantitatively wrong.

Particles stopping at greater depths than were observed at the exposed Lexan surface could be counted on the same surface but beneath the silver-backed Teflon, at the back of the top sheet, and in sheets 2 to 11. These data lead to spectral information at  $\approx 10$  MeV/nucleon and above.

One interesting anomaly was the observation beneath the silver-backed Teflon of a high density ( $\approx 3000$  tracks/cm<sup>2</sup> in the non-UV-irradiated Lexan and  $\approx 10\ 000$  tracks/cm<sup>2</sup> in the UV-irradiated Lexan) of short tracks ranging to  $\approx 10^{-3}$  cm long with rapidly decreasing numbers of tracks with increasing length. Such tracks were fewer at the opposite side of the Lexan sheet (depth 0.035 to 0.050 cm rather than 0.010 to 0.014 cm). The falloff with depth is too rapid to be consistent with direct effects in the plastic of the appreciable proton irradiation from trapped particles encountered while leaving the vicinity of the Earth. A proton flux of  $\approx 3 \times 10^9$  protons/cm<sup>2</sup>,  $> 3$  MeV, and  $\approx 8 \times 10^6$  protons/cm<sup>2</sup>,  $> 30$  MeV, is inferred from reference 15-8, extrapolating to greater distances from the Earth on the basis of reference 15-9. The most likely source of the short tracks is the aluminum-Inconel-silver-Teflon composite adjacent to the surface where these short tracks were found. Whether these are reaction products, compound nuclei, or recoil nuclei has not been determined. The cosmic ray flux at 0.010- to 0.014-cm depth was inferred from the abundance of tracks  $> 15 \times 10^{-4}$  cm length, which appear to form a distinctly separate population.

The mineral detectors consisted of mica, feldspar (labradorite), soda-lime glass, tektite glass, and fused quartz. The areas and exposure conditions are listed in table 15-I. The mica was taken from a large sheet of Indian muscovite and was preannealed at 923 K to remove fossil fission and alpha-recoil tracks. As a further step in eliminating stored tracks or potential spurious tracks, the mica was then pre-etched for 4 hr at 298 K in 40 percent hydrogen fluoride (HF). Following this step, it was verified that the surfaces were capable of registering tracks from 1-keV/nucleon heavy ions. The other detectors all consisted of polished surfaces obtained in a sequence of grinding and polishing steps that culminated in the use of 0.05- $\mu$ m aluminum oxide powder. The tektite and feldspar also were annealed, but no pre-etching was done. All samples except the fused quartz had a narrow vapor-deposited strip of aluminum 100 nm thick across the center of the sample.

A summary of the track densities observed in the various materials is given in table 15-IV. The differences in track density arise from differences in the registration characteristics of the materials and do not represent inconsistencies in the track data. After photographic documentation, test pieces were removed from the detectors and etched to reveal particle tracks. The appearance of the tracks in mica and in two glass samples is shown in figure 15-10. The appearance of tracks in the feldspar after brief etching is similar to that in the mica and also to that in lunar feldspars etched for similar periods.

The mica showed the highest track density and has been the most extensively studied to date. A summary of the integral track length distribution measured by a combination of several techniques is given in table 15-V. This table does not include data on very shallow pits (or short tracks), the depth of which is within the range  $\leq 100$  nm. The length distribution for tracks in the range from 0.2 to 2  $\mu$ m was obtained from SEM stereophotographs of a sample that had been etched for 2 hr to produce rather wide pits. A typical example is shown in figure 15-11. The length distribution from 2 to 12  $\mu$ m was obtained to optical microscopy on a sample etched for 10 min. The length distribution for tracks  $\geq 12$   $\mu$ m was obtained on a sample etched for 1 hr. Because the total track density did not vary during the etching times used, the data for different samples are directly comparable.

#### SUMMARY OF SCIENTIFIC RESULTS

The relative abundances and energy spectra of heavy solar flare and cosmic ray nuclei contain a wealth of information about the Sun and other particle sources and about the acceleration and propagation of the particles. At the time of the Apollo 16 experiment, the lowest energy range, from a few MeV/nucleon or MeV/amu to a few keV/nucleon, was largely unexplored. The cosmic ray experiment was designed to examine this energy range using passive, solid, particle track detectors.

At the time of the Apollo 16 mission, April 1972, the solar activity was approaching the 1975 minimum in its 11-yr cycle. There was thus the possibility that the experiment results would resolve the question concerning the source of low energy, heavy cosmic ray particles during a period when the Sun was quiet.

The experiment was designed to measure this low particle flux. If, on the other hand, a solar particle event occurred during the exposure, the experiment would yield valuable information about the energy spectra and composition of low energy, heavy solar particles. Because a solar flare occurred during the translunar

portion of the mission, the low energy results characterize solar flare particles. The experiment results are presented in detail in references 15-10 to 15-12.

The results presented in figure 15-12 are based on the most recent data and analyses. Two main points emerge from these results:

1. The differential energy spectra for solar particles are rapidly varying functions of energy down to very low energies, well into the new energy range made available by the Apollo 16 experiment. Thus, for the iron group cosmic rays (points labeled "heavy cosmic rays" in fig. 15-12), the differential fluence varies approximately as  $E^{-3}$  between 0.05 MeV/nucleon and 30 MeV/nucleon.

2. At low energies, the spectral shape changes. Thus, below 0.05 MeV/nucleon, the iron group spectrum flattens. This break, with its characteristic flattening, also occurs for the spectra of other elements, but it occurs at energies that depend inversely on atomic number. Thus, for carbon-and-heavier cosmic rays (points labeled "Lexan + UV" in fig. 15-12), the break occurs at  $\approx 1$  MeV/nucleon, and for the satellite proton data, the break occurs at  $\approx 10$  MeV/nucleon. This sequence of changes in spectral shape yields the result shown in table 15-VI; the elemental abundance ratios for solar cosmic rays change as the energies decrease. At higher energies, the ratio of iron group to carbon-and-heavier nuclei is essentially equivalent to that of the solar photosphere, 0.04; at lower energies, the heavier elements are enhanced relative to the lighter elements.

The data imply that heavy nuclei in solar cosmic rays are appreciably more abundant than in the solar photosphere. As early as 1958, Korchak and Syrovatskii (ref. 15-13) predicted preferential enhancement (at low energies) of heavier nuclei during the acceleration process. They predicted that this enhancement of heavier nuclei would occur because of their lower effective charge-to-mass ratios. More recent explanations involve not only the acceleration processes but also possible variations in the composition of the solar atmosphere in the vicinity of solar flares (ref. 15-14).

The heavy cosmic rays above about 70 MeV/amu, where the curve in figure 15-1 has again flattened, are galactic, not solar, in origin. These data were obtained from interior Lexan sheets, after UV irradiation, by measuring etching rate as a function of residual range in the manner described by Price and Fleischer (ref. 15-15).

Other galactic cosmic rays, recorded while the experiment was stowed within the command module in its folded or shifted mode (ref. 15-10), make it possible to determine the effects of solar modulation and spacecraft shielding on the flux of heavy galactic cosmic rays (ref. 15-12). The results are important to manned space missions because of the lethal damage to biological cells caused by these highly ionizing particles. This experiment together with earlier experiments using Apollo 8 and Apollo 12 helmets (ref. 15-16) and the results from the Apollo 14 electrophoresis experiment (ref. 15-17) yield two conclusions:

1. Extended space missions (e.g., a 2-yr flight to Mars and back) would be safest during times of peak solar activity, because the solar modulation from an active Sun decreases the flux of highly penetrating galactic heavy cosmic rays. (The much higher flux of solar particles is relatively easy to shield against because of their lower energies.)

2. The shielding from galactic cosmic rays due to the mass of the spacecraft and its contents could be considerably enhanced by judicious planning of the distribution of the mass.

Analysis of the glass detectors from this experiment continues. As an illustration of the differences in sensitivity of these glasses, the track densities observed in the GE 1457 phosphate glass, the GE 1484 uranium phosphate glass, and the tektite glass (ref. 15-10) are in the ratio 50:20:1 for surface removals of 0.5, 0.3, and 3.7  $\mu\text{m}$ , respectively. For the uranium phosphate glass exposed under the Teflon thermal shield, approximately 1 in 10 of the tracks are multipronged, presumably the result of scattering events in which uranium was the target. The elemental abundances of the higher energy cosmic rays have just been determined, using interior Lexan sheets. Analysis of abundances indicates that the elements of atomic numbers 21 to 25 are abundant relative to iron; and, for elements in the energy range 70 to 150 MeV/nucleon, the observed nuclei are dominantly galactic in origin, just as the higher energy nuclei normally are.

#### UNIVERSITY OF CALIFORNIA FINDINGS

The findings of the University of California cosmic ray experiment have had a significant impact on the understanding of galactic cosmic rays and solar particles. The study yielded the following major new results.

1. The composition of heavy ions in interplanetary space at energies between  $\approx 30$  and  $\approx 130$  MeV/nucleon is the same, within experimental errors, as that previously determined by other

experiments concerned with higher energy particles that are identified with galactic cosmic rays. Adiabatic deceleration as these particles enter the solar system could account for the absence of any change of composition that might be expected of low-energy particles due to ionization loss and spallation.

2. The ability of a Lexan stack to determine simultaneously the energy spectra of major elements from helium up to iron in the energy interval 0.2 to 30 MeV/nucleon has revealed systematic changes in the composition of solar flare particles as a function of energy. Compared with the composition of the solar photosphere, the particles emitted during a solar flare are enriched in heavy elements by an amount that increases with atomic number (up to a factor  $\approx 10^2$  for iron compared with helium at 0.2 MeV/nucleon) and decreases with increasing energy.

3. Heavy ions emitted in a solar flare appear to be completely stripped of electrons and thus are not in charge equilibrium at the time of acceleration and release from the Sun.

#### DISPOSITION OF FLIGHT MATERIALS

Research regarding the glass detectors from the experiment will continue. The flight parts of the GE panels were returned to the NASA Lyndon B. Johnson Space Center together with the plastic detector sheets for refrigerated storage. The appropriate reports, publications, and data will be forwarded to the National Space Science Data Center for archiving.

## REFERENCES

- 15-1. Fleischer, R. L.; Price, P. B.; and Walker, R. M.: Ion Explosion Spike Mechanism for Formation of Charged-Particle Tracks in Solids. *J. Appl. Phys.*, vol. 36, no. 11, Nov. 1965, pp. 3645-3652.
- 15-2. Fleischer, R. L.; Price, P. B.; and Woods, R. T.: Nuclear-Particle-Track Identification in Inorganic Solids. *Phys. Rev.*, vol. 188, no. 2, Dec. 10, 1969, pp. 563-567.
- 15-3. Crawford, W. T.; DeSorbo, W.; and Humphrey, J. S., Jr.: Enhancement of Track Etching Rates in Charged Particle-Irradiated Plastics by a Photo-Oxidation Effect. *Nature*, vol. 220, Dec. 28, 1968, pp. 1313-1314.
- 15-4. Price, P. B.; and Fleischer, R. L.: Particle Identification by Dielectric Track Detectors. *Radiation Effects*, vol. 2, 1970, pp. 291-298. Proceedings of the International Topical Conference on Nuclear Track Registration in Insulating Solids and Applications. May 1969, vol. I, D. Isabelle, ed., pp. IV2-34.
- 15-5. Peterson, D. D.: Improvement in Particle Track Etching in Lexan Polycarbonate Film. *Rev. Sci. Instr.*, vol. 41, no. 8, Aug. 1970, pp. 1252-1253.
- 15-6. Northcliffe, L. C.; and Schilling, R. F.: Range and Stopping Power Tables for Heavy Ions, Texas A&M (College Station), 1970; *Nuclear Data Tables*, vol. 7, 1970, p. 233ff.
- 15-7. Allen, L. H.: *Abundance of the Elements*. J. Wiley & Sons (New York), 1961.
- 15-8. Fillius, R. Walker; and McIlwain, Carl E.: Anomalous Energy Spectrum of Protons in the Earth's Radiation Belt. *Phys. Rev. Letters*, vol. 12, no. 22, June 1, 1964, pp. 609-612.
- 15-9. Katz, Ludwig: *Electron and Proton Observations. Radiation Trapped in the Earth's Magnetic Field*, vol. 5, Billy M. McCormac, ed., Gordon & Breach (New York), 1966, pp. 129-153.
- 15-10. Fleischer, R. L.; and Hart, H. R., Jr.: *Cosmic Ray Experiment. Sec. 15 of Apollo 16 Preliminary Science Report, NASA SP-315, 1972.*

- 15-11. Fleischer, R. L.; and Hart, H. R., Jr.: Enrichment of Heavy Nuclei in the 17 April 1972 Solar Flare. Phys. Rev. Letters, vol. 30, no. 1, Jan. 1, 1973, pp. 31-34.
- 15-12. Fleischer, R. L.; Hart, H. R., Jr.; Comstock, G. M.; Carter, M.; et al.: Apollo 14 and 16 Heavy Particle Dosimetry Experiments. Science, vol. 181, no. 4098, Aug. 3, 1973, pp. 436-438.
- 15-13. Korchak, A. A.; and Syrovatskii, S. I.: On the Possibility of a Preferential Acceleration of Heavy Elements in Cosmic-Ray Sources. Soviet Phys. Dokl., vol. 3, no. 5, Sept.-Oct. 1958, pp. 983-985.
- 15-14. Price, P. B.; Chan, J. H.; Hutcheon, I. D.; MacDougall, D.; et al.: Low-Energy Heavy Ions in the Solar System. Proceedings of the Fourth Lunar Science Conference, vol. 3, Pergamon Press (New York), 1973, pp. 2347-2362.
- 15-15. Price, P. B.; and Fleischer, R. L.: Identification of Energetic Heavy Nuclei with Solid Dielectric Track Detectors: Applications to Astrophysical and Planetary Studies. Annual Review of Nuclear Science, vol. 21, 1971, pp. 295-334.
- 15-16. Comstock, G. M.; Fleischer, R. L.; Giard, W. R.; Hart, H. R., Jr.; et al.: Cosmic-Ray Tracks in Plastics - The Apollo Helmet Dosimetry Experiment. Science, vol. 172, no. 3979, April 9, 1971, pp. 154-157.
- 15-17. McKannan, E. C.; Krupnick, A. C.; Griffin, R. N.; and McCreight, L. R.: Electrophoresis Separation in Space: Apollo 14. NASA TM X-64611, 1971.

#### BIBLIOGRAPHY

- O'Sullivan, D.; Thompson, A.; and Price, P. B.: Composition of Galactic Cosmic Rays with  $30 < E < 10$  MeV/Nucleon. Nature (Phys. Sci.), vol. 243, no. 123, May 7, 1973, pp. 8-9.

TABLE 15-I.- EXPOSURE CONDITIONS OF VARIOUS DETECTORS

Detector	Size, cm <sup>2</sup>	Condition and time, hr:min
Mica (M1 to M5) Quartz Tektit Soda-lime glass Feldspar Lower part of platinum foil Plastic stack	7.7 2.2 .5 2.7 .58 112 75	LM deployed at 3:04 Experiment set in shade at 125:25 Experiment folded at 140:15 Total space exposure — 167:11 Exposure on Moon — 20:54 in Sun and 44:50 in shade Estimated total Sun exposure — 71:38
Mica (M10) Upper part of platinum foil	3.6 38	LM deployed at 3:04 Mica covered with platinum foil at 120:50 Total space exposure — 117:46 Exposure on Moon — 16:19 in Sun and 00:00 in shade Estimated total Sun exposure — 67:03
Lowest part of part V Tab on part IV foil	28 10	Exposed at 120:50 Set in shade at 125:25 Folded at 170:15 Total space exposure — 49:25 Total Sun exposure — 4:35
Mica (M11) Upper part of part V foils		Always covered with 50- $\mu$ m platinum foil
Neutron experiment		Activated at 120:50 Deactivated at 170:15 Total exposure — 49:25

TABLE 15-II.- CCSMIC RAY EXPOSURE OF THE COSMIC RAY EXPERIMENT

Mission segment	Time, hr	Relative solid angle	Tracks per unit flux		
			$\theta_c=0^\circ$	$\theta_c=20^\circ$	$\theta_c=70^\circ$
En route to Moon	71.4	1.0	3.14	2.76	0.164
In lunar orbit	30.1	0 to <sup>a</sup> 1.0	.726	.541	.030
On LM on Moon	20.7	.5	1.57	1.38	.082
On LM footpad (69° to horizontal)	44.9	.64	1.95	1.70	≈ 0
Weighted averages	—	.75	2.19	1.87	.085
Total	167.1	—	—	—	—

<sup>a</sup>Variable with time; 0.5-hr averages used.

TABLE 15-III.- TRACK LENGTH DISTRIBUTIONS AT  
DETECTOR SURFACES

(a) Track length

Length, cm	Number	Tracks/cm <sup>2</sup>
Phosphate glass 1457		
(0 to 0.5) × 10 <sup>-4</sup>	82	0.92 × 10 <sup>6</sup>
(.5 to 1.0)	26	.29
(1 to 2)	19	.21
(2 to 3)	10	.11
(3 to 6)	10	.11
Lexan (hole 2, 6-hr etch)		
(0.1 to 0.5) × 10 <sup>-4</sup>	108	1.1 × 10 <sup>6</sup>
(.3 to 1)	127	1.3
(.5 to 1)	65	.65
(1 to 2)	≈50	1.5
(2 to 3)	51	.52
(3 to 4)	34	.35
(. to 6)	25	.064
(6 to 8)	20	.034
(8 to 11)	9	.0066
(11 to 14)	9	.0042
(14 to 17)	6	.0028
(17 to 30)	3	.0014
Lexan (hole 59, UV + 6-hr etch)		
(0.5 to 1.5) × 10 <sup>-4</sup>	22	1.34 × 10 <sup>6</sup>
(.5 to 1.0)	79	2.07
(1.5 to 2.5)	8	.49
(2.4 to 4.5)	10	.61
(4.5 to 6.5)	5	.31
(6.5 to 10.5)	3	.18
(10.5 to 18.5)	3	.18

(b) Track density at exterior surface

Phosphate glass 1457 .....	1.8 (±0.1)
Lexan (hole 2, 6-hr etch) ..	6.10 (±0.35) optical
Lexan (hole 59, UV + 6-hr etch) .....	7.5 (±0.3)

TABLE 15-IV.- SURFACE TRACK DENSITIES ON MINERAL DETECTORS

Sample	Density, tracks/cm <sup>2</sup>	Etching conditions	Mode of observation
Mica (M1 to M5)	$1.8 \pm 0.1 \times 10^6$	10 min to 2 hr, 303 K (30° C) in 40 percent hydrofluoric acid (HF)	Optical (OPT) (transmitted light) and scanning electron microscope (SEM)
Feldspar	$6.0 \pm 0.6 \times 10^5$	13 min to 1 hr, boiling sodium hydroxide (6 g sodium hydroxide, 8 g H <sub>2</sub> O)	OPT
Soda-lime glass	$5.8 \pm 0.4 \times 10^5$	400 sec in dilute HF, 303 K (30° C), maximum pit diameter 3.0 μm	SEM
Tektite	$2.5 \pm 0.3 \times 10^5$	2" min in dilute HF, 303 K (30° C), maximum pit diameter 2.0 μm	SEM

TABLE 15-V.- INTEGRAL TRACK DATA IN MICA

Track length, $\mu\text{m}$ (a)	Track density, tracks/cm <sup>2</sup>
>0.2	$1.8 \pm 0.1 \times 10^6$ (SEM)
>.5	$1.8 \pm 0.1 \times 10^6$ (SEM)
>1	$1.1 \pm 0.15 \times 10^6$ (SEM)
>2	$7.4 \pm 0.7 \times 10^5$ (OPT)
	$4.4 \pm 0.7 \times 10^5$ (SEM)
>4	$2.6 \pm 0.5 \times 10^5$ (OPT)
>6	$5.5 \pm 1.5 \times 10^4$ (OPT)
>8	$2.2 \pm 0.2 \times 10^4$ (OPT)
>12	$6.3 \pm 1 \times 10^3$ (OPT)
>20	$1.4 \pm 0.4 \times 10^3$ (OPT)
>34	$2.8 \pm 0.5 \times 10^2$ (OPT)
>50	$8.5 \pm 3$ (OPT)

<sup>a</sup><sub>≤2</sub> percent of total between 0.2 and 0.5  $\mu\text{m}$ .

TABLE 15-VI.- ABUNDANCE RATIOS

Energy, MeV/nucleon	Iron/(carbon and heavier)	Iron/proton
10	0.04	$2.5 \times 10^{-6}$
3	.03	$1.5 \times 10^{-5}$
1	...	$.8 \times 10^{-4}$
.3	.11	$.8 \times 10^{-3}$
.1	.5	--
.03	1	--
Photospheric	.04	$4 \times 10^{-5}$

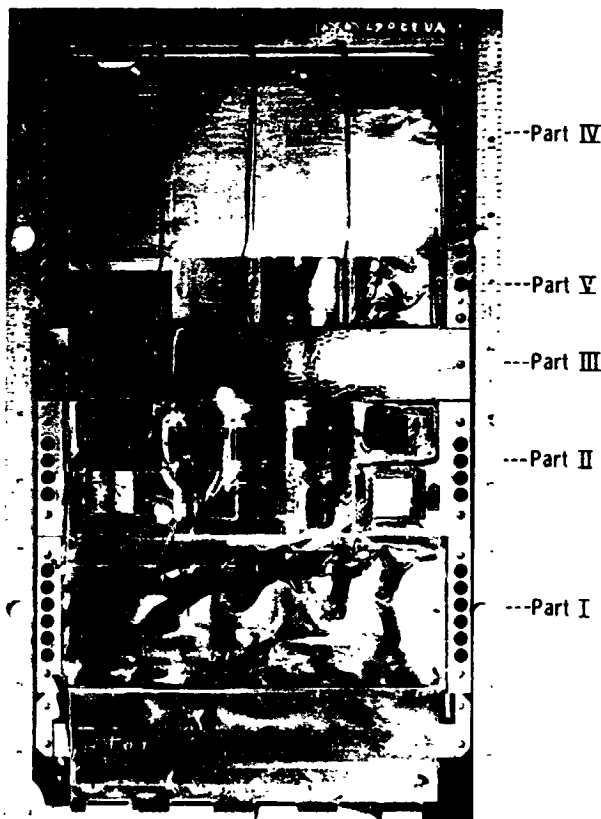


Figure 15-1.- Panel 4 as received on return from the Moon. Part labeled I is a stack of plastic detectors. Part II, the mineral assembly plate, contains mica, feldspar, and glass. Parts IV and V (partially visible) contain foils for trapping light solar wind.

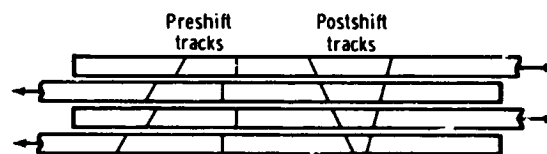


Figure 15-2.- Shifting procedure. A 2-mm relative shift of alternate plastic sheets allowed the preshift and postshift tracks to be distinguished. Postshift tracks are interesting only for personnel dosimetry purposes because the tracks represent particles that penetrated the spacecraft before entering the detectors.

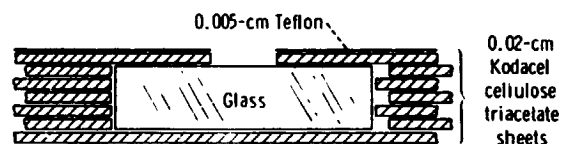
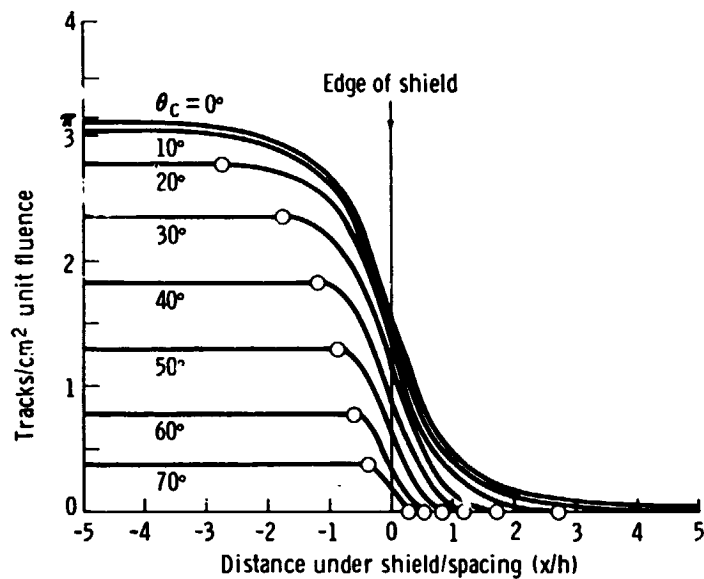
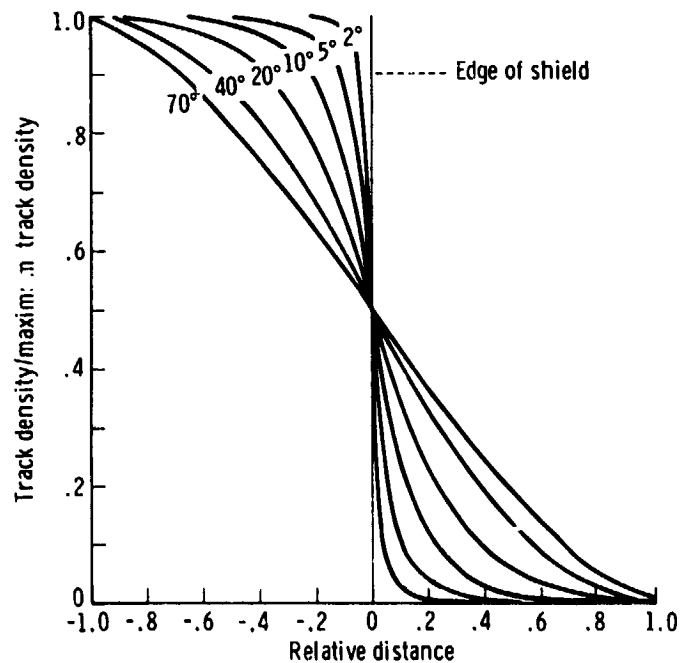


Figure 15-3. Exposure of glass detectors. Glass plates were recessed within the triacetate sheets as sketched. Except for the single 0.5-cm-diameter perforation, the aluminized glass was covered by a 0.005-cm Teflon sheet and a 0.02-cm triacetate sheet. The 0.3-cm-diameter perforations allowed portions of the top Lexan and Kodacel sheets to be directly exposed. The Teflon was backed by a  $165 \pm 15$  nm silver coating covered with an  $85 \pm 15$  nm Inconel layer.

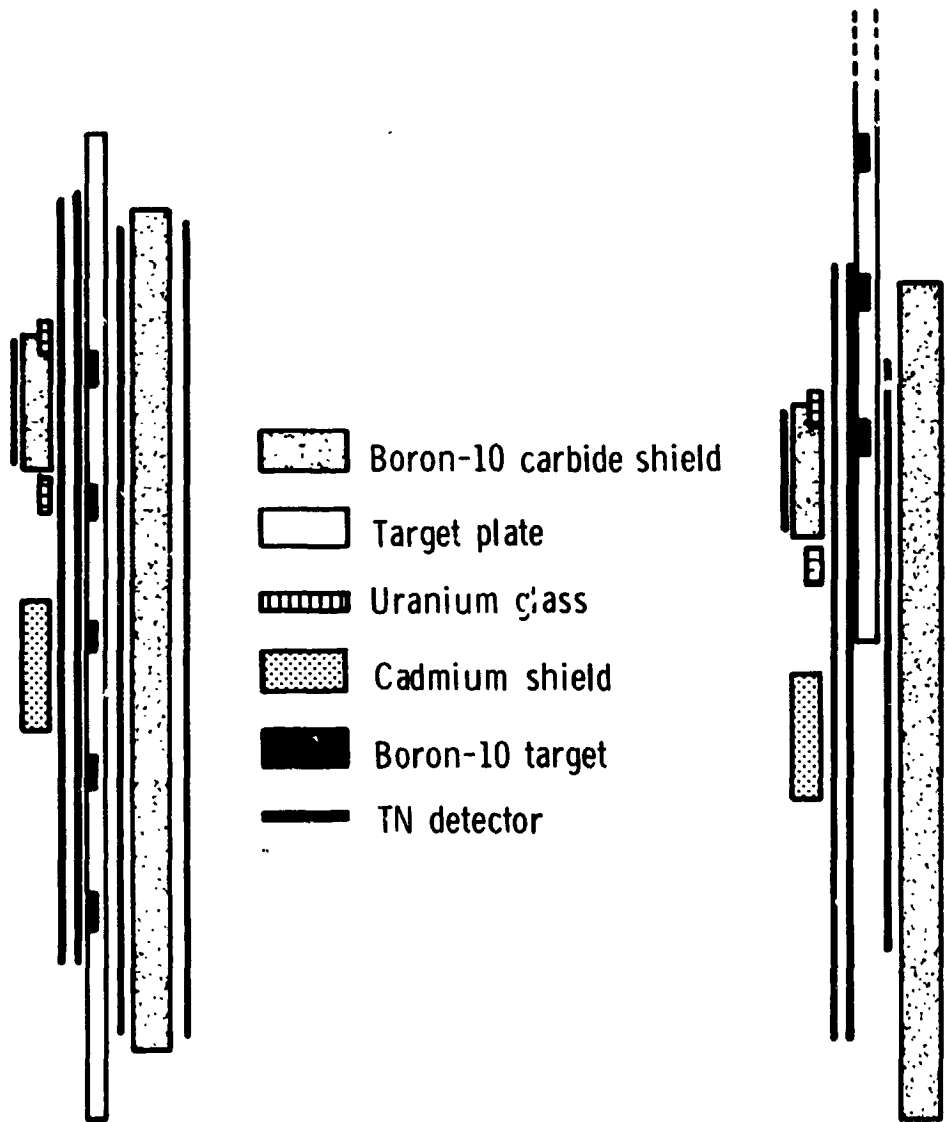


(a) The  $x$  is the distance under a parallel, semi-infinite shield a distance  $h$  from the detector surface.



(b) Normalized data relative to the position where the etched track density goes to zero.

Figure 15-4.- Effect of a shield on the etchable tracks per unit fluence as a function of track cone angle.



(a) The experiment as it was designed.

(b) The experiment as it was actually deployed because of the failure to achieve full activation.

Figure 15-5.- Schematic diagrams of the neutron leakage flux experiment in panel 4. The scale in the horizontal direction has been grossly exaggerated to separate the components for easier viewing.



Figure 15-6.- Boron-10 target strip. The mineral assembly plate has been removed, and one target strip is visible through the covering sheet of Triafol TN detector.

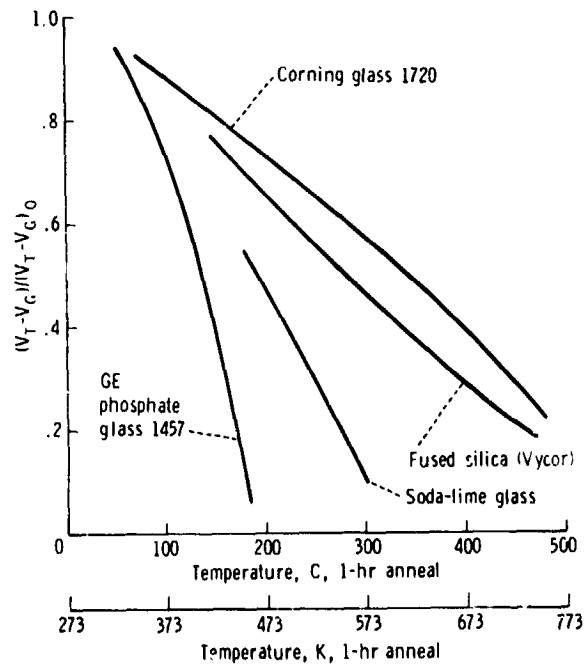


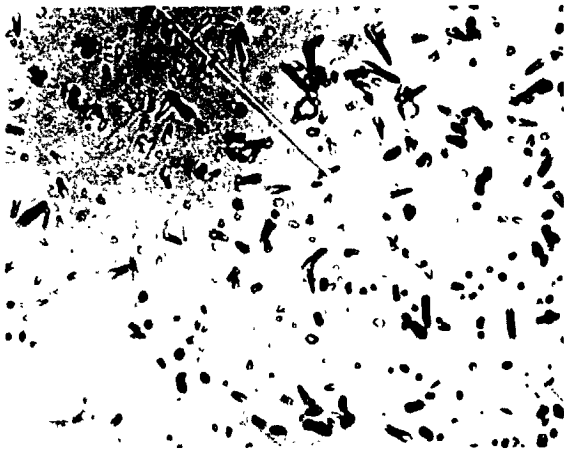
Figure 15-7.- Annealing of the track etching rate for californium-252 fission fragments in several glasses. The  $V_T$  is the average track etching rate, and  $V_G$  is the general etching rate for an unirradiated region. The reference  $V_T$  is that obtained after a long time at room temperature.



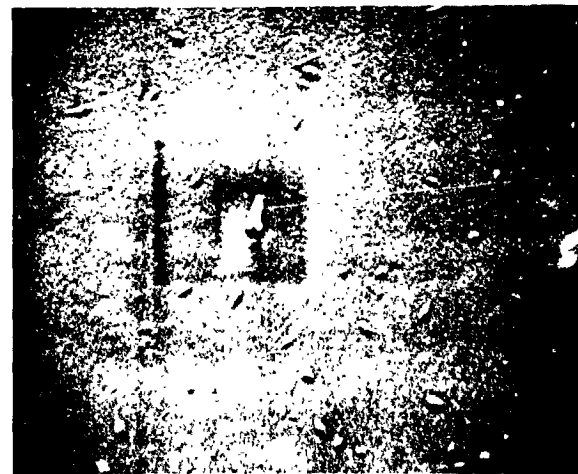
(a) Glass 1457 viewed optically.



(b) Glass 1457 viewed in a scanning electron microscope. The SEM replica is cellulose acetate.



(c) Lexan polycarbonate hole 4 viewed optically.



(d) Lexan polycarbonate viewed in a scanning electron microscope. The SEM replica is silicone rubber.

Figure 15-8.- Heavy solar cosmic ray tracks in plastic and glass detectors. The surface removal is  $5 \times 10^{-5}$  cm for the glass and  $10^{-4}$  cm for the plastic.

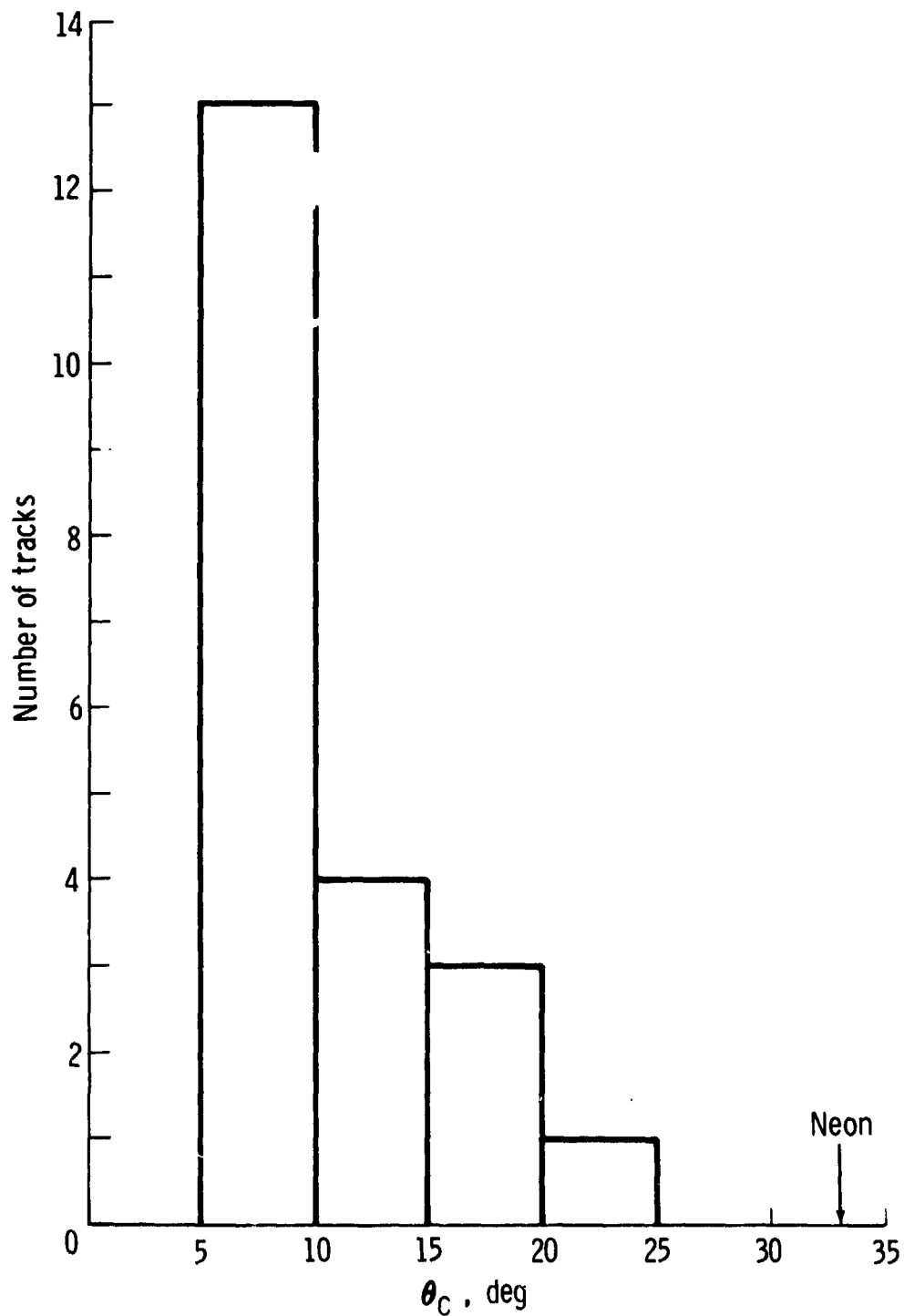


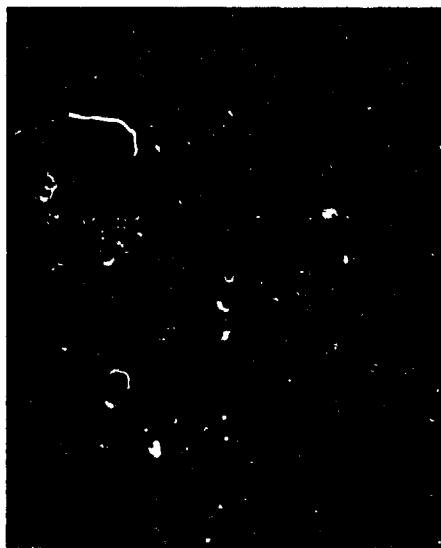
Figure 15-9.- Distribution of projected cone angles measured for solar flare tracks in phosphate glass 1457. The angles are obtained from SEM photographs of a cellulose acetate replica after a 12-min etch of the glass in 50 percent hydrofluoric acid.



(a) Mica,  $1.8 \times 10^6$  tracks/cm<sup>2</sup>.



(b) Soda-lime glass,  $6 \times 10^5$  tracks/cm<sup>2</sup>.



(c) Tektite glass,  $2 \times 10^5$  tracks/cm<sup>2</sup>.

Figure 15-10.- Surface track densities in different detectors.  
Picture (a) was taken in an optical microscope at  $\approx 1000X$ ;  
(b) and (c) were taken in an SEM at  $2000X$ . A feldspar crystal  
(not shown) has a similar appearance to picture (a) but has a  
track density more like picture (b).



Figure 15-11.- An SEM photograph of short tracks in mica. The mica was etched for 2 hr at 303 K (30° C) in concentrated hydrofluoric acid to produce the enlarged pits.

ORIGINAL PAGE IS  
OF POOR QUALITY

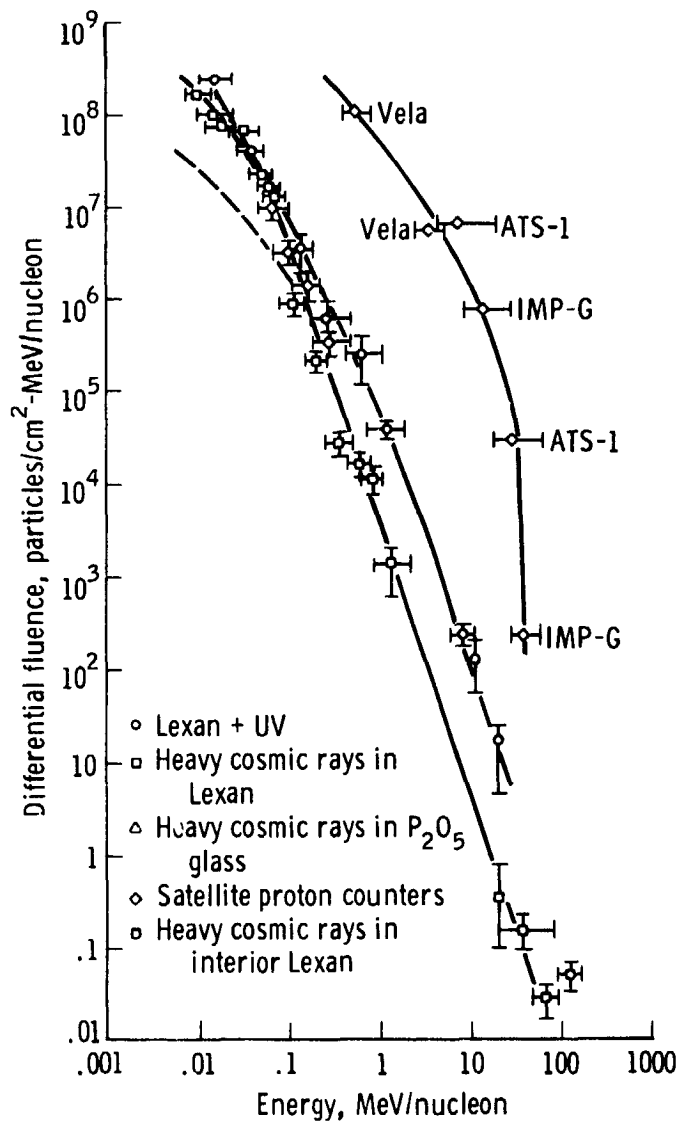


Figure 15-12.- Differential energy spectra for heavy cosmic rays during the period from April 16 to April 23, 1972, compared to the spectrum derived from various satellite proton counters.

Fluence is given in particles/cm<sup>2</sup>-MeV/nucleon integrated over a 2 $\pi$  solid angle. See reference 15-10 for a detailed schedule of exposure solid angle. The dashed line represents P<sub>2</sub>O<sub>5</sub>

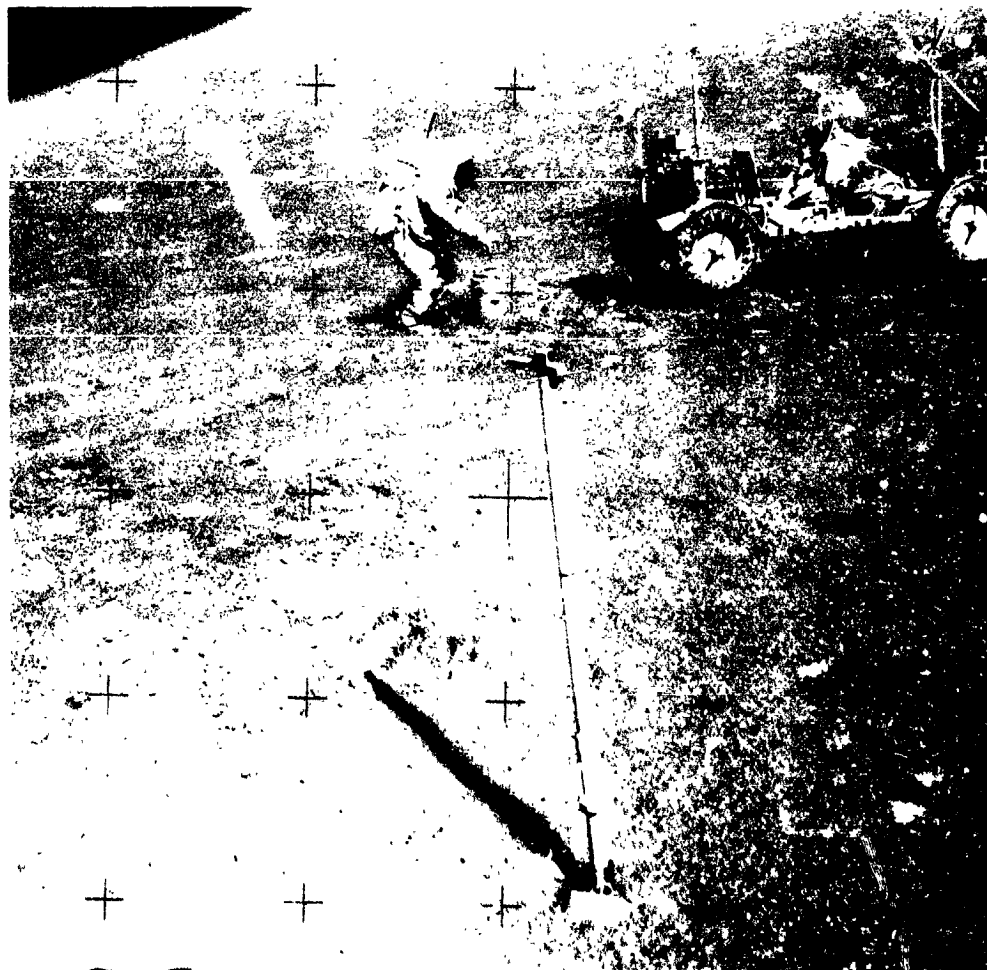
glass data reanalyzed assuming a zero-range deficit instead of the 0.185  $\mu$ m range deficit assumed for the square points.

The interior Lexan points were obtained using the methods described in reference 15-16. The proton results are from preliminary data from satellite proton counters operated by C. Bostrum, Interplanetary Monitoring Platform (IMP), G. Paulikas, Applied Technology Satellite (ATS), and S. Singer, Vela Satellite.

16. TRAVERSE GRAVIMETER EXPERIMENT (NASA EXPERIMENT S-199)

NSSDC IDENTIFICATION NUMBER:

APOLLO 17 72-096C-03



CONTENTS - SECTION 16

	Page
BASIC THEORY . . . . .	16-3
Free-Air and Bouguer Anomalies . . . . .	16-3
Two-Dimensional Calculations . . . . .	16-5
Three-Dimensional Calculations . . . . .	16-5
EQUIPMENT . . . . .	16-6
Sensor . . . . .	16-6
Filtering and Phase Lock Loop . . . . .	16-7
Measurement . . . . .	16-7
Leveling . . . . .	16-8
Temperature Control and Monitoring . . . . .	16-9
Physical Description . . . . .	16-9
Deployment and Operation of Instrument . . . . .	16-10
RESULTS . . . . .	16-11
Number of Readings . . . . .	16-11
Gravimeter Drift . . . . .	16-12
Comparison of On-LRV and Off-LRV Values . . . . .	16-12
Earth-Moon Gravity Tie . . . . .	16-13
DISCUSSION . . . . .	16-14
Computation of Bouguer Anomalies . . . . .	16-14
Densities of Lunar Rocks . . . . .	16-17
INTERPRETATION OF GRAVITY DATA . . . . .	16-19
SUMMARY AND CONCLUSIONS. . . . .	16-22
REFERENCES . . . . .	16-23

## 16. TRAVERSE GRAVIMETER EXPERIMENT

The traverse gravimeter makes relative measurements of gravity. The primary goal of the traverse gravity experiment (TGE) was to make gravity measurements at a number of sites in the Apollo 17 landing area and to use the measurements to obtain information about the geological substructure of the Moon. A secondary goal was to obtain the value of the gravity at the landing site relative to an accurately known value on Earth. Both goals were successfully achieved. A gravity tie has been obtained between the Taurus-Littrow landing site and the Earth with an estimated accuracy of approximately  $5 \times 10^{-5} \text{ m/sec}^2$  (5 mgal). Relative gravity measurements that can be used to infer the substructure of the area have been obtained at stations occupied during the periods of extravehicular activity (EVA). The appropriate corrections were applied to these measurements. The resulting Bouguer anomaly curve reveals a systematic relationship to the geometry of the valley. The values are approximately  $25 \times 10^{-5} \text{ m/sec}^2$  (25 mgal) higher near the center of the valley compared to the values near the edges. The gravity data are interpreted in terms of an infilling of the valley by a layer of basalt approximately 1-km thick.

### BASIC THEORY

#### Free-Air and Bouguer Anomalies

The basic theory for the interpretation of the traverse gravity measurements can be described with the help of the sketch in figure 16-1. As a simplifying approximation, two-dimensionality is assumed; the sketch shows a hypothetical geological cross section. The gravity measurements are made at the lunar module (LM) landing site and at certain stations (stations 1, 2, 3, 4, 5, etc.). The gravity value at the LM site is subtracted from the value at the other stations, and, for this report, only the relative values at the stations will be considered.

The first step in the interpretation of the relative gravity values is to make the free-air correction for elevation; that is, to allow for the differences in the distances of these stations from the center of the Moon. If  $g_m$  denotes the gravity at the surface of the Moon,  $M$  the mass of the Moon,  $r$  its radius, and  $k$  the universal constant of gravitation, then

$$g_m = \frac{kM}{r^2} \quad (16-1)$$

The free-air gradient then is

$$\frac{\partial g_m}{\partial r} = \frac{-2kM}{r^3} = \frac{-2g_m}{r} \quad (16-2)$$

and the free-air correction is  $2g_m/r$ , which yields a value of  $0.19 \times 10^{-5} \text{ m/sec}^2/\text{m}$  (0.19 mgal/m). The elevation in meters is measured from an arbitrary reference level (fig. 16-1). The free-air correction is added to the relative gravity values to obtain the free-air anomalies.

The next step in the interpretation of the free-air anomalies involves the Bouguer correction. The Bouguer correction allows for the gravity effect (i.e., the vertical component of the gravitational attraction) of the material above the elevation datum computed at the gravity stations. This correction involves a knowledge of the density of the material above the elevation datum. In the sketch in figure 16-1, densities of  $\rho_1$  for the material comprising the massifs and  $\rho_2$  for the material of the valley floor have been assumed. That the actual situation can be much more complicated must be considered in the interpretation of the Bouguer anomalies.

In gravity interpretation, the Bouguer correction is usually applied in two steps. The first, the flat-plate Bouguer, assumes that the elevation is the same at all points as it is at the station where the correction is being applied. The second, the terrain correction, allows for the departure of the actual terrain from a plane at the height of the station. For the Taurus-Littrow landing site, the terrain corrections are large and no particular advantage is gained by computing the flat-plate Bouguer corrections and the terrain corrections separately. By computing the gravity effect of all the material above the elevation datum with

a single computation, the combined Bouguer correction is applied; and, by adding it to the free-air anomaly, the Bouguer anomaly is obtained. In these calculations, a flat Moon rather than a spherical Moon is used. The relative error at the different stations is negligible for the present calculations.

The final step is the interpretation of the Bouguer anomalies. The Bouguer anomalies have allowed for the elevation differences between the different stations and for the gravitational effect of the material above the elevation datum. Therefore, the Bouguer anomalies are interpreted in terms of, and therefore provide information about, the density contrasts of rocks lying below the elevation datum. In the simplified model shown in the sketch in figure 16-1, for instance, the density contrast  $\rho_1 - \rho_2$  between the material comprising the massifs and the material lying below the valley floor gives rise to the Bouguer anomalies at the stations. The actual structural situations as well as the density variations are probably much more complicated than those shown in the sketch. The interpretation approach will be to work with simple models consistent with available geological information and to see how these models explain the gravity data. The final structural solution will be constrained by the gravity results, by considerations of geological plausibility, and by the results from the other geological and geophysical data.

#### Two Dimensional Calculations

As a first approximation, two-dimensionality is assumed. The gravity effect of a body is obtained by approximating its cross section by an irregular polygon. The gravity effect of a body with a polygonal cross section has been given by Talwani et al. (ref. 16-1).

#### Three-Dimensional Calculations

For more careful analysis of the gravity data, it is essential to compute and to interpret the Bouguer anomalies without the assumption of two-dimensionality. The basic formula used in this calculation is the gravity effect of a vertical prism (ref. 16-2). For distant areas, prisms of large area can be chosen and an average elevation assumed for them. For closer areas, prisms of smaller area must be chosen. By actual trial and error, prisms of optimum area are chosen at various distances from the landing site for use in the calculations. Such a determination has been made. The results of three-dimensional calculations are presented.

## EQUIPMENT

### Sensor

The gravity sensor in the TGE is a Bosch Arma D4E vibrating string accelerometer (VSA). The accelerometer is schematically shown in figure 16-2. Each of the two strings, when energized, generates continuous vibrations with its own frequency, the value of which depends on the value of  $g$ . The difference between the two frequencies can be obtained. The difference frequency between the two strings  $\Delta f_n$  when the sensor is in its normal vertical position can be written as

$$\Delta f_n = k_0 + k_1 g + k_2 g^2 + k_3 g^3 + \dots \quad (16-3)$$

Terms of order higher than 3 can be neglected. Nominal values for  $k_0$ ,  $k_1$ , et cetera, for the flight vibrating string accelerometers are  $k_0 = 7$  Hz,  $k_1 = 129$  Hz/g,  $k_2 = -0.00034$  Hz/g<sup>2</sup>, and  $k_3 = 0.003$  Hz/g<sup>3</sup>. A principal reason for the use of a double-stringed instrument rather than a single-stringed instrument is the reduction in the values of the higher order terms. Even-order terms of the type  $k_2 g^2$  give rise to nonlinear rectification of inertial accelerations caused by vibrations; therefore, it is very important to keep the terms small.

The constants  $k_0$ ,  $k_1$ ,  $k_2$ , and  $k_3$  are determined for the sensor before the mission. However, experience with sensors of this type had shown that  $k_0$  is subject to drift as well as tares (sudden dc shifts). Any shift of  $k_0$  would degrade the Earth-Moon gravity tie. (Shifts in  $k_1$ ,  $k_2$ , etc., are much less important.) Also, if, at a station during a traverse, a large difference of gravity from the value at the LM site was indicated, it would be necessary to inquire whether this was a real variation in gravity or whether the value of  $k_0$  had shifted. For this reason, provision was made to make independent determinations of

$k_0$  when necessary. Such a determination is called a bias determination and is made by inverting the instrument. In the inverted case

$$\Delta f_i = -k_0 + k_1g - k_2g^2 + k_3g^3 \quad (16-4)$$

Assuming the values of  $k_1$ ,  $k_2$ , and  $k_3$ , the values of  $k_0$  and  $g$  can be determined from the values of  $\Delta f_n$  and  $\Delta f_i$  by combining equations (16-3) and (16-4).

#### Filtering and Phase Lock Loop

The electrically conducting VSA strings are placed in a permanent magnetic field (fig. 16-2). When a voltage is applied across the string, the resulting current causes motion of the string and induces a voltage across the string. The voltage is regenerated through a stable high-gain amplifier and fed back to the string.

The output of each of the VSA strings is a sine wave of a frequency between 9.25 and 9.75 kHz. The signal is fed to a phase lock loop module. The purpose of the phase lock loop module is to determine the difference frequency between the outputs of the two strings and to filter from the resultant signal the effect of undesirable vibrations. Should any vibrations cause the input frequency from the VSA to exceed a previously specified limit, a phase lock loop alarm is generated. This alarm is indicated by the TGE display.

#### Measurement

Since the lunar value of  $g$  is approximately  $163\,000 \times 10^{-5} \text{ m/sec}^2$  (163 000 mgal) and a measurement to the precision of  $0.1 \times 10^{-5} \text{ m/sec}^2$  (0.1 mgal) is desired, the difference frequency of the VSA must be measured to an accuracy of approximately  $1 \times 10^{-6}$ . Because the nominal values of the difference frequencies in the normal and inverted positions are approximately 28 and 14 Hz, respectively, a simple counting of the cycles would take an impossibly long time. Instead, a gate is generated that is inversely proportional to the difference frequency. For the normal case, the gate consists of 1536 cycles of the difference frequency  $\Delta f_n$  (approximately 55 sec at this frequency); for the inverted case, the gate consists of 384 cycles of the difference

frequency  $\Delta f_i$  (approximately 27 sec). The width of the gate is measured by counting the pulses from a precision 125-kHz clock by a counter. If  $D_n$  and  $D_i$  are the counts in the normal and inverted case

$$\Delta f_n = \frac{1536 \times 125 \times 10^3}{D_n} = \frac{1.92 \times 10^8}{D_n} \quad (16-5)$$

$$\Delta f_i = \frac{384 \times 125 \times 10^3}{D_i} = \frac{4.8 \times 10^7}{D_i} \quad (16-6)$$

If  $k_0$ ,  $k_1$ ,  $k_2$ , and  $k_3$  are all known, equation (16-3) can be used to determine the value of  $g$  from  $\Delta f_n$ . If  $k_0$  is not assumed to be known, equations (16-3) and (16-4) together can be used to determine the value of  $g$  as well as  $k_0$  from  $\Delta f_n$  and  $\Delta f_i$ .

#### Leveling

If the VSA axis is not vertical but is inclined at an angle  $\theta$  to the vertical,  $g \cos \theta$  is measured instead of  $g$ . For a small  $\theta$ , the error is  $0.5 g \theta^2$ . The TGE is designed to keep  $\theta$  less than  $00^\circ 03'$  of arc and, consequently, the error caused by leveling is less than  $0.06 \times 10^{-5} \text{ m/sec}^2$  (0.06 mgal).

To provide the leveling, the sensor is mounted on a gimballed frame. Two vertical pendulums mounted on the gimbal frame sense departures from the vertical with comparator circuits. These comparator circuits provide information to stepping motors that drive the gimbals until the pendulums are level. The leveling is accomplished in two modes. When a pendulum is more than  $00^\circ 32'$  of arc from level, the corresponding stepper motor slews faster; at less than  $00^\circ 32'$ , the motor slews at a slower rate to avoid overshoot. When the pendulums are within  $00^\circ 03'$  of arc of being level, the slew commands are disabled.

When the instrument is inverted in the bias mode, a set of bias pendulums is used that gives signals unless the gimbal frame is similarly leveled in an inverted position. The TGE can only be leveled if it is initially placed in a position less than  $15^\circ$  from level. In the normal mode, the time for leveling is between 0 and 20 sec; in the bias mode, the time is between 90 and 130 sec.

## Temperature Control and Monitoring

The VSA sensor is extremely sensitive to temperature; therefore, it is necessary to control its temperature to within 0.01 K (0.01° C). The VSA and its oscillator-amplifiers are cased in a precision oven that is maintained at a temperature near 322 K (49° C) to within 0.01 K (0.01° C) by the temperature control and monitor circuit. The precision oven, in turn, is encased in an outer oven that protects the inner oven from the external thermal disturbance.

The precision oven temperature circuit is a proportional and rate-controlled loop using an electrical heater and a resistance thermometer element for a sensor. The complete temperature sensor is an ac excited bridge, two arms of which are thermistors. The bridge output is demodulated and used to control drivers for the precision heaters. A tap from the demodulator output is converted to digital form and forms a digit of the TGE display. The displayed digit marks the deviations of the precision oven temperature from a preset value. The outer oven thermostat and heater circuit merely react to temperature changes to control the power supplied to the heater.

A thermal blanket provides good thermal insulation for the TGE. A radiator at the top of the instrument provides the primary means of heat expulsion.

The mode of operation of the instrument was such that the radiator was left closed during each EVA. The instrument electronics produced heat, but this heat merely reduced the heating to be done by the ovens. Between EVA periods, the instrument was placed in the shade with the radiator open, and heat was then expelled into space. The information from the temperature monitors is converted to digits (the eighth and ninth digits of the TGE display). The eighth digit gives the thermal condition of the outer oven and the sign for the ninth digit. The ninth digit of the numerical display is a number from 0 to 7 that represents a deviation of the precision oven temperature from a set point of 0.005 K (0.005° C) times the digit displayed. Polarity of the deviation is obtained from the value displayed in the eighth digit.

## Physical Description

The TGE consists of the instrument package, a battery pack assembly, a thermal blanket, and an isoframe assembly. A cutaway view of the TGE is shown in figure 16-3.

The outer structure of the TGE is cylindrical with a flat rear surface. A folding handle at the top of the instrument is

used for hand carrying and for latching the instrument to the isoframe assembly. Three feet at the base of the instrument enable lunar surface operations. A radiator at the top of the instrument provides the primary means of heat expulsion. The radiator and the display panel are protected from the environment by hinged insulating covers.

Inner structure of the TGE consists of a two-axis gimbal system, which contains a VSA housed in a thermally protected and evacuated two-stage oven assembly. The oven assembly is enclosed in an electronic frame (E-frame) assembly of similar structural design. The E-frame assembly is pivoted about its axis and is supported by a middle gimbal assembly. The middle gimbal controls the vertical positioning of the inner gimbal over a 30° range. The middle gimbal assembly is attached through bearings to the base housing and can rotate 210°. Stepper motors and a gear train provide the drive and positioning of the gimbal assemblies. The stepper motors react to signals from pendulums that sense departures from the vertical as explained in the section entitled "Leveling."

#### Deployment and Operation of Instrument

Gravimeter measurements were made both with the TGE mounted on the lunar roving vehicle (LRV) and with the TGE placed on the lunar surface. During a measurement, the TGE must be placed on a surface such that the vertical axis of the TGE is within 15° of vertical. The TGE must not be disturbed for approximately 3 min after a measurement has been initiated.

A normal measurement (one with the sensor in the normal, vertical position) is initiated by depressing the "GRAV" pushbutton on the TGE (fig. 16-3). The measurement cycle starts with leveling of the instrument. During the leveling cycle, the indicator light flashes off and on. When the instrument comes to a rest within 00°03' of arc of the vertical, the light stops flashing and remains illuminated until the difference frequency of the strings has been measured. The number of counts of a precision clock (from which the frequency can be obtained as explained in the section entitled "Measurement") forms the first seven digits of the TGE display. The eighth and ninth digits of the display are thermal monitors, as explained in the section entitled "Temperature Control and Monitoring."

The display stays on for 20 sec. The display can, however, be turned on at any subsequent time by depressing the "READ" pushbutton, and it stays on for 20 sec.

A measurement with the sensor in the inverted position is made by depressing the "BIAS" pushbutton. The bias pendulums are

used for leveling, and the indicator light flashes on and off until the sensor is leveled in an inverted position. The counting and display then proceeds as for the normal measurement.

To conserve power, a toggle switch is provided to select the "STANDBY" or "ON" modes of operation. In the "STANDBY" mode, power is supplied only to the oven temperature controls and to the VSA oscillator-amplifiers. Cycling the switch from "ON" to "STANDBY" to "ON" will erase any stored data. Depressing the "READ" button after such a switching provides valid readings only for the eighth digit, which is the temperature monitor for the outer oven and for the battery.

## RESULTS

### Number of Readings

Of the 26 readings obtained (table 16-I), three (readings 1, 10, and 18) were obtained to learn the thermal state of the instrument before EVA periods. No gravity values were obtained with these readings.

Reading 8 at the LM site showed that the TGE had been accidentally moved during the measurement as indicated by the phase lock loop alarm, which gives zeros in the first three digits of the display in such instances. This reading, therefore, was valueless, and another reading was obtained at the same site.

At the LM site, nine readings were made. Six of these were readings with the TGE in the normal position on the lunar surface (readings 3, 9, 11, 17, 19, and 25); one reading was made at the start of each EVA and one at the end of each EVA. Two readings (4 and 26) were made in the inverted position to determine the value of the bias term  $k_0$  at the beginning and at the end of the measurements. One reading (2) was made on the LRV to compare "on LRV" and "off LRV" measurements.

Besides the readings at the LM site, 11 other discrete measurements were made at different sites (readings 5, 6, 7, 12, 13, 14, 15, 16, 20, 21, and 23). Two extra measurements (readings 22 and 24) were made at stations 8 and 9 on the lunar surface to compare on-LRV and off-LRV measurements at these sites.

In the preliminary evaluation of gravity in table 16-I, the constants  $k_2$  and  $k_3$  of equation (16-3) are ignored and a value of  $k_1 = 13.18 \text{ Hz/m/sec}^2$  ( $k_1 = 0.0001318 \text{ Hz/mgal}$ ) is assumed.

For obtaining the value of gravity  $\Delta g$  at the stations relative to the value at the LM site, it can be shown that, when  $k_2$  and  $k_3$  are ignored, an approximate value is given by

$$\Delta g = (D_n - D_{n \text{ base}}) \times (-0.03245) \quad (16-7)$$

where  $D_n$  is the display (first seven digits) at that station and  $D_{n \text{ base}}$  is the display at the LM site. The first off-LRV reading at the LM site (3) was chosen as the  $D_{n \text{ base}}$ . The values of  $\Delta g$  thus obtained are given in table 16-I.

#### Gravimeter Drift

For the flight instrument, it was determined before the mission that the drift during the EVA period (approximately 7 hr) was essentially zero. It was decided to adopt a zero drift rate unless the off-LRV values at the LM site showed a consistent drift pattern. Table 16-II gives off-LRV values at the LM site. Relative to the first reading, the gravity values range from  $2.1 \times 10^{-5} \text{ m/sec}^2$  (2.1 mgal) to  $-3.2 \times 10^{-5} \text{ m/sec}^2$  (-3.2 mgal). The only positive value,  $2.1 \times 10^{-5} \text{ m/sec}^2$  (2.1 mgal), was at reading 25. Before reading 25, during the traverse from station 9 to the LM site, the pallet on which the traverse gravimeter was mounted swung open and, as noted later in the report, the resultant banging of the pallet may have caused instrument problems resulting in an erroneous reading 25. All the remaining values were negative. Nevertheless, a consistent drift pattern was not detected; hence, a zero drift was adopted. The variation in values is attributed to instrument noise, which has an rms value of  $1.8 \times 10^{-5} \text{ m/sec}^2$  (1.8 mgal).

#### Comparison of On-LRV and Off-LRV Values

Readings 2 and 3 were both obtained at the LM site. Reading 2 was taken with the gravimeter on the LRV, and reading 3 was taken with the gravimeter on the lunar surface. The difference between the two readings was  $4.6 \times 10^{-5} \text{ m/sec}^2$  (4.6 mgal). In an effort to determine whether this difference was random or systematic, on- and off-LRV readings were also taken at stations 8 and 9. Table 16-III shows that lunar surface readings are, in all three cases, lower than the LRV values (the free-air difference is negligible) by amounts ranging from  $4.6 \times 10^{-5}$  to

$6.9 \times 10^{-5}$  m/sec<sup>2</sup> (4.6 to 6.9 mgal). No explanation for this difference has been found, but on the basis of three readings, an empirical correction of  $-6.0 \times 10^{-5}$  m/sec<sup>2</sup> (-6.0 mgal) has been made to all on-LRV measurements (table 16-I). Some support for this correction comes also from postmission tests with the engineering and spare flight models. When the handle of the gravimeter was jarred, temporary shifts in the gravimeter measurements occurred that were always in the same direction (although these shifts were  $<6 \times 10^{-5}$  m/sec<sup>2</sup> (<6 mgal). Applying the  $-6.0 \times 10^{-5}$ -m/sec<sup>2</sup> (-6.0 mgal) correction to the value at the Apollo lunar surface experiments package (ALSEP) site brings the ALSEP measurement into agreement with the measurement at the LM site. The gravity values at the two sites are expected to be close. However, agreement between the LM site value and the nearby surface electrical properties (SEP) experiment site value deteriorates slightly as a result of this correction.

#### Earth-Moon Gravity Tie

On the basis of normal reading 2 and inverted reading 3 (table 16-IV), a value of  $g = 162\,694.6 \times 10^{-5}$  m/sec<sup>2</sup> ( $g = 162\,694.6$  mgal) was measured at the LM site at Taurus-Littrow. The constants  $k_1$ ,  $k_2$ ,  $k_3$  used in this determination were obtained during preflight tests. The value of  $k_0$  obtained as a result of readings 2 and 3 was 7.21592 Hz. A predicted value of  $k_0$  based on laboratory test data was 7.2144 Hz. The total shift during the translunar phase was 0.0015 Hz. This corresponds to a bias shift of approximately  $11 \times 10^{-5}$  m/sec<sup>2</sup> (11 mgal), which is considered reasonable when compared to typical bias shifts experienced during acceptance and vibration testing.

On the basis of normal reading 25 and inverted reading 26, a second value of  $g = 162\,701.5 \times 10^{-5}$  m/sec<sup>2</sup> ( $g = 162\,701.5$  mgal) was determined after EVA-3. The value for the bias constant  $k_0$  differed by approximately 0.00064 Hz from the initial value, which implies a shift of approximately  $5 \times 10^{-5}$  m/sec<sup>2</sup> (5 mgal) in the bias value. However, the normal measurement of gravity obtained for reading 25, if the initial value of  $k_0$  is used, differs by only  $2 \times 10^{-5}$  m/sec<sup>2</sup> (2 mgal) from the initial value.

During the traverse from station 9 to the LM site, the pallet on which the traverse gravimeter was mounted apparently swung loose and banged against the LRV. This was the only time during the entire mission that the gravimeter was shocked in this manner.

Because deterioration in the performance might have resulted from this shock, less emphasis has been placed on readings 25 and 26, and the initial determination of  $162\ 694.6 \times 10^{-5}$  m/sec<sup>2</sup> (162 694.6 mgal) has been adopted. An uncertainty of  $\pm 5 \times 10^{-5}$  m/sec<sup>2</sup> ( $\pm 5$  mgal) is ascribed to this measurement.

## DISCUSSION

### Computation of Bouguer Anomalies

Two-dimensional calculations.- For a preliminary interpretation of the gravity measurement, two-dimensionality is assumed. The problem then is reduced essentially to the determination of the substructure of the linear Taurus-Littrow valley with linear massifs on either side. The stations at which the gravity measurements were made are located in figure 16-4, and the values at these stations were projected to a roughly southwest-to-northeast cross section. The value at station 6 could not be appropriately projected to this cross section and has been ignored in the discussion of the two-dimensional approximation. The great structural relief of the area necessitates three-dimensional calculations, which are discussed in the section entitled "Three-Dimensional Calculations." The topographic profile with the locations of the projected stations is shown in figure 16-5.

The observed anomaly  $\Delta g$ , as obtained in table 16-I, is plotted as a function of distance in figure 16-6. The observed anomaly is approximately  $50 \times 10^{-5}$  m/sec<sup>2</sup> (50 mgal) lower at station 2, closest to the South Massif, and approximately  $30 \times 10^{-5}$  m/sec<sup>2</sup> (30 mgal) lower at station 8, closest to the North Massif, relative to the value of gravity at the IM site. The observed anomaly curve therefore shows a pronounced dip toward the massifs on either side.

The free-air correction is applied by using the correction previously given,  $2g_m/r$ . The free-air anomaly thus obtained (also plotted in fig. 16-6) dips to  $-30 \times 10^{-5}$  m/sec<sup>2</sup> (-30 mgal) near the South Massif and to  $-20 \times 10^{-5}$  m/sec<sup>2</sup> (-20 mgal) near the North Massif relative to the value at the IM site.

The two-dimensional Bouguer correction is applied next. In making the free-air correction, as well as the Bouguer correction, an elevation datum must be chosen (fig. 16-1). The elevation chosen was that of the IM site (fig. 16-5), which was the lowest elevation on the profile.

The two-dimensional Bouguer correction is, in effect, made in three parts to show the effect of (1) the valley floor (i.e., material lying between the elevation of the stations and the elevation datum shown with a density of  $\rho_2$  in fig. 16-1), (2) the North Massif, and (3) the South Massif. The three Bouguer correction curves and the total Bouguer correction are shown in figure 16-7. Note that the effect of the valley floor tends to cancel the effect of the massifs; hence, the total Bouguer correction is quite small (less than  $5 \times 10^{-5}$  m/sec<sup>2</sup> (5 mgal)). The two-dimensional Bouguer correction was calculated with a density of  $2.0 \text{ g/cm}^3$  ( $\rho_1 = \rho_2 = 2.0 \text{ g/cm}^3$ ). This value is lower than the values for breccia densities shown in figure 16-8(a). However, if an average density of  $2.5 \text{ g/cm}^3$  were used instead of  $2.0 \text{ g/cm}^3$ , the difference in the computed total correction would, in all cases, be less than  $1 \times 10^{-5}$  m/sec<sup>2</sup> (1 mgal). That difference can be ignored for the present discussion.

The two-dimensional Bouguer anomaly curve (fig. 16-9) shows minimums of nearly  $-25 \times 10^{-5}$  m/sec<sup>2</sup> (-25 mgal) at the stations closest to the massifs. The variation in the central part of the valley floor is within  $10 \times 10^{-5}$  m/sec<sup>2</sup> (10 mgal) of the value at the LM site.

Three-dimensional calculations.- While the Taurus-Littrow valley itself can be considered a two-dimensional structural feature, the surrounding massifs (especially the South Massif) cannot be considered as two-dimensional features. For this reason, three-dimensional topographic reductions are important. The important reduction is the Bouguer correction. As explained earlier, it is usually made in two steps, which are the flat-plate Bouguer and the terrain correction.

If  $\rho_1$  is the density of the Bouguer plate and  $\Delta H$  is the elevation of the station in meters above a reference level, the flat-plate Bouguer correction in m/sec<sup>2</sup> is  $0.0419 \times \rho_1 \times \Delta H \times 10^{-5} = 0.0838 \times \Delta H \times 10^{-5}$  ( $0.0419 \times \rho_1 \times \Delta H = 0.0838 \times \Delta H$  in mgal). This correction is subtracted from the free-air anomaly to obtain the simple Bouguer anomaly.

To compute the terrain correction, one needs to compute at each station the gravitational effect of the surrounding topography that lies above or below the horizontal plane passing through the station.

When terrain corrections are manually computed, it is customary to consider the topography within a fixed distance from each station. When computations are made with the help of a computer, it is simpler to consider the same fixed area for all the stations. The two methods give equivalent results when the stations lie close together and far from the boundaries of the fixed area. At any rate, any differences in the result vary slowly between stations and are considered unimportant for these calculations.

For the Taurus-Littrow sites, the investigators selected a fixed area (fig. 16-10) lying between  $18^{\circ}30'$  and  $22^{\circ}00'$  in latitude and between  $29^{\circ}00'$  and  $32^{\circ}30'$  in longitude. The total area is approximately 105.84 by 99.96 km. For the present calculations, this area is further divided into 49 subareas, each  $0.5^{\circ}$  by  $0.5^{\circ}$ , or 15.12 by 14.28 km in dimensions. In Figure 16-10, these areas are numbered 1 to 49. All the stations at which gravity measurements were made lie within subarea 25.

In making terrain corrections, the prism formula was used. For this purpose, elevations of distant subareas can be represented by large prisms; however, areas close to the stations must be divided into small prisms or the effect of averaging elevations implicit in using large prisms will give rise to serious errors.

The choice of the size of the prisms was by trial and error. One can of course represent the entire area by small prisms of equal size, but this approach results in a very large increase in computing time.

For the final calculations, prisms were chosen with the following areas (of the top and bottom surface of the prism). The subareas 1 to 16, 20 to 23, 27 to 30, and 34 to 49 were each used to form a single prism. Thus, the area of the top surface of each of these prisms is  $215.91 \text{ km}^2$  ( $14.28 \text{ km} \times 15.12 \text{ km}$ ). The subareas 17, 18, 19, 26, 31, 32, and 33 (with the exclusion of some parts) were each subdivided into 36 smaller areas, each of which had an area of approximately  $6 \text{ km}^2$  ( $2.38 \text{ km} \times 2.52 \text{ km}$ ).

Subarea 25 was in part divided into smaller areas that had dimensions of 476 by 504 m (i.e.,  $1/900$  of the original subarea). Other parts of subareas were divided into yet smaller areas that had the dimensions of 238 by 252 m (i.e.,  $1/3600$  of the original subarea). More complete details are given in table 16-V, which also summarizes the results of the calculations. Instead of adding the flat-plate Bouguer correction to the free-air correction to obtain the simple Bouguer anomaly and then adding the terrain correction to obtain the total Bouguer anomaly, table 16-V shows the total Bouguer effect in the last column as the sum of the total terrain effect and Bouguer flat-plate correction.

In adding the total Bouguer correction at each station to the free-air anomaly to obtain the total three-dimensional Bouguer anomaly (fig. 16-11), the investigators subtracted the constant amount of  $5 \times 10^{-5} \text{ m/sec}^2$  (5 mgal). This procedure made all the values negative, which provided a convenience in making the structural interpretation. This procedure is valid because the absolute level of the anomalies is purely arbitrary. The three-dimensional Bouguer anomaly calculations are shown in figure 16-11.

In comparing the two-dimensional and the three-dimensional total Bouguer anomaly curves (fig. 16-12), note that the difference is not large. However, it is evident that the gradient near the South Massif is steepened by the three-dimensional calculations; whereas, near the North Massif, the gradient is decreased. The principal difference between the two-dimensional and the three-dimensional calculations is that the former underestimate the terrain correction near the North Massif.

Also, it should be pointed out that station 6, which lies close to the North Massif and therefore should probably be considered lying close to station 8 (fig. 16-12), would have a three-dimensional Bouguer anomaly of  $-19 \times 10^{-5} \text{ m/sec}^2$  (-19 mgal). That consideration would somewhat steepen the Bouguer anomaly curve near the North Massif.

The three-dimensional Bouguer anomaly curve must be interpreted in terms of the substructure of the Taurus-Littrow valley. Therefore, the interpretation must consider the available information concerning the densities of the lunar rocks.

#### Densities of Lunar Rocks

Only a few measured bulk density values of the lunar rocks have been reported in the literature; most of these values were obtained in the course of measuring other physical properties of lunar rocks (e.g., seismic velocity, heat conductivity, etc.). These published values (refs. 16-3 to 16-21)<sup>1</sup> are plotted in the histograms in figure 16-8, one for the lunar basalts and the other for the lunar breccias.

---

<sup>1</sup>Also N. Warren, private communication, 1972, and G. D. O'Keiley, personal communication, 1973.

The methods used to obtain these density values were not always indicated in the literature, but when a method was given, it was one of the following:

1. The volumes of aluminum foil models of the whole rocks were measured, and the bulk densities were computed using the weights of the rocks. Because the aluminum foil models were not made to great accuracy, these density values can have 10 percent or larger errors.

2. The volumes of small, precisely shaped samples of the rocks were computed by measuring their linear dimensions. The small samples are generally parallelepipeds,  $1 \times 1 \times 2$  cm. The densities were then computed using the measured weights of the small samples.

3. The densities of some small samples were measured directly using Archimedes' principle.

The density values tended to group on the basis of the method used to compute the density; the first method gave low values, the third method gave high values, and the second method gave values in the middle. This result is reasonable because the samples were generally vuggy, vesicular, porous, and/or highly fractured. Thus, the first method includes the effect of the largest vugs and vesicles, and the third method includes only the effect of the unconnected pores and cracks; the second method will generally eliminate the effect of large vesicles and vugs but not that of small cracks and pores that cannot be avoided in cutting the small samples. Thus, an intrinsic density of approximately  $3.4 \text{ g/cm}^3$  for the lunar basalts is indicated in figure 16-8(b).

The limited number of reported values and the effects of the different methods of measuring the densities make it impossible to determine if a density difference exists between highland and mare basalts or between highland and mare breccias; so far there is no indication of a density difference. For the same reasons, it is impossible to divide the breccias into separate groups characterized by different density and petrology; the majority of the reported values are for unshocked microbreccias.

Porosities have been measured for a few samples by point counts on thin sections or cut surfaces. A plot of density as a function of porosity and the intrinsic densities calculated from the porosities is given in figure 16-13. The intrinsic densities for the three basalts range from  $3.25$  to  $3.49 \text{ g/cm}^3$  and for the four breccias from  $2.99$  to  $3.14 \text{ g/cm}^3$ . All but one of these data are from the Apollo 11 rocks.

Figures 16-8(b) and 16-13 indicate that the bulk densities of mare basalt samples are determined by their porosity and that the samples have an intrinsic density of approximately  $3.4 \text{ g/cm}^3$ . Thus, a thick mare lava flow with a thin vesicular top would have a bulk density somewhat less than  $3.4 \text{ g/cm}^3$ . The data on the breccias are not as conclusive, but there is no evidence that the highly fractured rocks and breccias forming the highlands are more dense, on the average, than the average of the breccia samples reported thus far. Therefore, the density contrast between a thick mare basalt formation and highland breccia material should be at least  $3.2 - 2.8 = 0.4 \text{ g/cm}^3$  and may be as much as  $3.3 - 2.3 = 1.0 \text{ g/cm}^3$ .

#### INTERPRETATION OF GRAVITY DATA

Before the Apollo 17 gravity measurements were made on the Moon, there was no knowledge concerning the variation of lunar gravity on the scale of a few kilometers. At the Taurus-Littrow site, would the variations in gravity from station to station be so small as to be imperceptible? Or, would they be so large (but chaotic) that, while some general statement could be made about gravity variations, no structural interpretations could be made? The best hope was that the gravity variations would be large and would have some systematic relationship to the geometry of the valley. Before the mission, in the case of a systematic relationship, two possibilities were envisaged. One possibility was that in which the values at the center of the valley were low and attained high values as the massifs were approached. This is the usual situation in the case of terrestrial valleys for which gravity minimums in the valley are ascribed to low density sedimentary valley fill. In the lunar case, low gravity values in the valley would have been ascribed to a thick regolith mixed with the "dark mantle" or "plains unit" material. The other possibility was that the valley values would be higher, in which case they would be ascribed to infilling by basaltic material.

From an examination of the Apollo 17 results, the investigators' best hopes regarding the utility of gravity data were realized. A variation of gravity from station to station does exist, and these variations have a systematic relationship to the geometry of the valley. From station 4 (fig. 16-12), moving toward the South Massif, the value of the three-dimensional Bouguer anomaly decreases systematically. Similarly, from the LM station and moving toward the North Massif, the three-dimensional Bouguer values again decrease systematically. At station 6 (fig. 16-4), which is also close to the South Massif, the gravity value is also low. Station 5 appears to be somewhat anomalous in that it has a lower value than at station 4 and lower than at the LM

---

site. When the two-dimensional and the three-dimensional Bouguer curves are compared, the minimum at station 5 is more pronounced in the two-dimensional curve than in the three-dimensional curve. This suggests that the low value at station 5 is not an erroneous value and that a more comprehensive knowledge of topography and a correspondingly better terrain correction might further raise the Bouguer curve at this station. Alternatively, some buried local structure otherwise unnoticed is present near station 5.

Notice in figure 16-12 that the largest gradients in the Bouguer curve are not at the edge of the valley but within it. Thus, on the south side, the largest gradient is present between stations 3 and 2A, and, on the north side, probably between stations 9 and 8.

#### Structural Model

With the results of the previous sections, a very simple model has been used to explain the gravity results. Assuming that the subvalley floor material consists of basalt flows that have a positive density contrast of  $0.8 \text{ g/cm}^3$  with respect to brecciated highland material on either side, a block with a thickness of 1 km is obtained for the basaltic material (fig. 16-12). (This is a two-dimensional model; uncertainties in densities and so forth do not warrant a more complicated three-dimensional model.) As discussed in the section entitled "Densities of Lunar Rocks," the measured densities of the lunar samples indicate that the difference in density between the basalts and the breccias could lie between  $0.4$  and  $1.0 \text{ g/cm}^3$ . Correspondingly, the thickness of the basalt fill in the valley could range from 0.8 to 2 km.

The large Bouguer gradients at the valley edges indicate steep sides for the postulated block of basaltic material. Note that the gradient is steeper near the South Massif than it is near the North Massif, indicating a steeper edge to the basaltic material near the south side. Also note from the model that the basaltic material does not extend to the massifs but lies within the valley. On the south side, the edge of the basaltic material appears to lie between stations 2A and 3. Because the Bouguer anomaly curve is nearly as steep as the model curve, the edge of the high density body must be nearly vertical. Near the North Massif, the Bouguer anomaly curve is less steep than the curve for the model anomaly. This suggests that the edge is not so steep on this side and perhaps lies somewhere between station 8 and 9.

Comparison With Seismic Refraction Results  
and Geological Significance of Traverse  
Gravity Experiment Results

The seismic refraction experiment (ref. 16-22) near the Apollo 17 landing site also reveals subsurface layering, but there is an important difference from the results just described. The gravity results require infilling of the Taurus-Littrow valley with shallow high-density material that therefore overlies material of lower density. On the other hand, the seismic refraction results reveal low velocity material overlying higher velocity material. Velocity at depths less than 400 meters is less than 500 m/sec. Between 400 m and 1.4 km, the velocity is 1 km/sec; and, at 1.4 km, it increases to 4.7 km/sec.

By comparing the seismic and the gravity results, one arrives at the conclusion that the basaltic layer lying just below the regolith has a velocity of approximately 1 km/sec, but a density of  $3.2 \text{ g/cm}^3$ . This result would be considered remarkable for terrestrial basalts. For lunar samples, Cooper et al. (ref. 16-22) cite measured values of seismic velocity that vary from slightly less than 1 km/sec to more than 4 km/sec. Thus, it seems possible, but only barely so, to explain both the gravity and the seismic results by postulating a highly fractured layer of basalt approximately 1-km thick that has a density of approximately  $3 \text{ g/cm}^3$  but the very low seismic velocity of 1 km/sec.

For the lower layer, the opposite problem exists. Measured velocities for the breccias range again from approximately 1 to 5 km/sec (ref. 16-22); therefore, the higher end of this range has to be selected to satisfy the seismic results.

In summary, the gravity and the seismic results can be reconciled by invoking highly fractured basalts, which have a high density but a very low seismic velocity, for the top kilometer or so of the valley floor overlying highland breccia material that has a significantly lower density than the basalts but a much higher seismic velocity.

Because breccia boulders, which have rolled down from the massifs, as well as basalt boulders excavated from deep craters have been examined, the solution suggested here is geologically plausible. Therefore, gravity results indicate the presence of basalt flows about 1 km in total thickness underlying the regolith of the Taurus-Littrow valley.

## SUMMARY AND CONCLUSIONS

The successful performance of the TGE indicated that the value of gravity at the Taurus-Littrow landing site is  $162\,694.6 \pm 5 \times 10^{-5} \text{ m/sec}^2$  ( $162\,694.6 \pm 5 \text{ mgal}$ ). The Bouguer anomaly shows values approximately  $25 \times 10^{-5} \text{ m/sec}^2$  (25 mgal) lower at the edges of the valley than at the LM site. The Bouguer anomaly curve is interpreted in terms of a 1-km-thick block of basaltic material lying below the valley floor with a positive density contrast of  $0.8 \text{ g/cm}^3$  with respect to the material on either side.

Comparison with the seismic refraction experiment, which reveals very low velocity material (approximately 1 km/sec) overlying higher velocity material (4.7 km/sec), suggests that the basaltic material is highly fractured. The underlying lower density breccia, on the other hand, has a velocity that is relatively high when one considers the range of laboratory measurements.

## REFERENCES

- 16-1. Talwani, Manik; Worzel, J. Lamar; and Landisman, Mark: Rapid Gravity Computations for Two-Dimensional Bodies with Application to the Mendocino Submarine Fracture Zone. *J. Geophys. Res.*, vol. 64, no. 1, Jan. 1959, pp. 49-59.
- 16-2. Talwani, Manik: Computer Usage in the Computation of Gravity Anomalies. *Methods in Computational Physics*, vol. 13, Bruce A. Bolt, ed., Academic Press, 1973, pp. 343-389.
- 16-3. O'Kelley, G. Davis; Eldridge, James S.; Schonfeld, E.; and Northcutt, K. J.: Concentrations of Primordial Radioelements and Cosmogenic Radionuclides in Apollo 15 Samples by Nondestructive Gamma-Ray Spectrometry. *Lunar Science-III (Rev. abs. of the Third Lunar Science Conference (Houston, Tex.), Jan. 10-13, 1972)*, pp. 587-589.
- 16-4. O'Kelley, G. D.; Eldridge, J. S.; Schonfeld, E.; and Bell, P. R.: Primordial Radionuclide Abundances, Solar Proton and Cosmic Ray Effects and Ages of Apollo 11 Lunar Samples by Nondestructive Gamma-Ray Spectrometry. *Proceedings of the Apollo 11 Lunar Science Conference*, vol. 2, Pergamon Press (New York), 1970, pp. 1407-1423.
- 16-5. Schmitt, H. H.; Lofgren, G.; Swann, G. A.; and Simmons, G.: The Apollo 11 Samples: Introduction. *Proceedings of the Apollo 11 Lunar Science Conference*, vol. 1, Pergamon Press (New York), 1970, pp. 1-54.
- 16-6. Anderson, O. L.; Scholz, C.; Soga, N.; Warren, N.; and Schreiber, E.: Elastic Properties of a Micro-Breccia, Igneous Rock and Lunar Fines from Apollo 11 Mission. *Proceedings of the Apollo 11 Lunar Science Conference*, vol. 3, Pergamon Press (New York), 1970, pp. 1959-1973.
- 16-7. Horai, K.; Simmons, G.; Kanamori, H.; and Wones, D.: Thermal Diffusivity, Conductivity and Thermal Inertia of Apollo 11 Lunar Material. *Proceedings of the Apollo 11 Lunar Science Conference*, vol. 3, Pergamon Press (New York), 1970, pp. 2243-2249.
- 16-8. Kanamori, H.; Nur, A.; Chung, D. H.; and Simmons, G.: Elastic Wave Velocities of Lunar Samples at High Pressures and Their Geophysical Implications. *Proceedings of the Apollo 11 Lunar Science Conference*, vol. 3, Pergamon Press (New York), 1970, pp. 2289-2293.

- 16-9. Stephens, D. R.; and Lilley, E. M.: Loading-Unloading Pressure-Volume Curves to 40 kbar for Lunar-Crystalline Rock, Micro-Breccia and Fines. Proceedings of the Apollo 11 Lunar Science Conference, vol. 3, Pergamon Press (New York), 1970, pp. 2427-2434.
- 16-10. Stephens, D. R.; and Lilley, E. M.: Pressure-Volume Properties of Two Apollo 12 Basalts. Proceedings of the Second Lunar Science Conference, vol. 3, MIT Press (Cambridge, Mass.), 1971, pp. 2165-2172.
- 16-11. Kanamori, H.; Mizutani, H.; and Hamano, Y.: Elastic Wave Velocities of Apollo 12 Rocks at High Pressures. Proceedings of the Second Lunar Science Conference, vol. 3, MIT Press (Cambridge, Mass.), 1971, pp. 2323-2326.
- 16-12. Wang, H.; Todd, T.; Weidner, D.; and Simmons, G.: Elastic Properties of Apollo 12 Rocks. Proceedings of the Second Lunar Science Conference, vol. 3, MIT Press (Cambridge, Mass.), 1971, pp. 2327-2336.
- 16-13. Warren, N.; Schreiber, E.; Scholz, C.; Morrison, J. A.; et al.: Elastic and Thermal Properties of Apollo 11 and Apollo 12 Rocks. Proceedings of the Second Lunar Science Conference, vol. 3, MIT Press (Cambridge, Mass.), 1971, pp. 2345-2360.
- 16-14. Chao, E. C. T.; Boreman, J. A.; and Desborough, G. A.: The Petrology of Unshocked and Shocked Apollo 11 and Apollo 12 Micro-Breccias. Proceedings of the Second Lunar Science Conference, vol. 1, MIT Press (Cambridge, Mass.), 1971, pp. 797-816.
- 16-15. Katsube, T. J.; and Collett, L. S.: Electrical Properties of Apollo 11 and Apollo 12 Lunar Samples. Proceedings of the Second Lunar Science Conference, vol. 3, MIT Press (Cambridge, Mass.), 1971, pp. 2367-2379.
- 16-16. Chung, D. H.; and Westphal, W. B.: Dielectric Properties of Apollo 14 Lunar Samples. Lunar Science-III (Rev. abs. of the Third Lunar Science Conference (Houston, Tex.), Jan. 10-13, 1972), pp. 139-140.
- 16-17. Mizutani, H.; Fujii, N.; Hamano, Y.; Osako, M.; and Kanamori, H.: Elastic Wave Velocities and Thermal Diffusivities of Apollo 14 Rocks. Lunar Science-III (Rev. abs. of the Third Lunar Science Conference (Houston, Tex.), Jan. 10-13, 1972), pp. 547-549.

- 16-18. Chung, Dae H.: Laboratory Studies on Seismic and Electrical Properties of the Moon. *The Moon*, vol. 4, nos. 3/4, June/July 1972, pp. 356-372.
- 16-19. Horai, Ki-iti; and Fujii, Naoyuki: Thermophysical Properties of Lunar Material Returned by Apollo Missions. *The Moon*, vol. 4, nos. 3/4, June/July 1972, pp. 442-445.
- 16-20. Todd, Terrence; Wang, Herbert; Baldrige, W. Scott; and Simmons, Gene: Elastic Properties of Apollo 14 and 15 Rocks. *Proceedings of the Third Lunar Science Conference*, vol. 3, MIT Press (Cambridge, Mass.), 1972, pp. 2577-2586.
- 16-21. Chung, D. H.; Westphal, W. B.; and Olhoeft, G. R.: Dielectric Properties of Apollo 14 Lunar Samples. *Proceedings of the Third Lunar Science Conference*, vol. 3, MIT Press (Cambridge, Mass.), 1972, pp. 3161-3172.
- 16-22. Cooper, M. R.; Kovach, R. L.; and Watkins, L. S.: Lunar Near-Surface Structure. *Rev. Geophys. Space Phys.*, vol. 12, no. 3, 1974, p. 291.

TABLE 16-1.- TRAVERSE GRAVIMETER READINGS

Point	Location	Elapsed time at which measurement initiated, hr:min:sec	Display	D <sub>n</sub> - D <sub>n</sub> base <sup>a</sup>	g = (D <sub>n</sub> - D <sub>n</sub> base) * (-0.03245)		g after application of empirical correction <sup>b</sup>		Elevation, m	Comments
					m/sec <sup>2</sup>	mgal	m/sec <sup>2</sup>	mgal		
EVA-1										
1	LM site	-	XrX XXXX OX	-	-	-	-	-	-	Thermal monitor reading
2	LM site	01:17:32	670 0031 01	-1.1	-	-	-	4510	4510	On LRV; adopted as base reading D <sub>n</sub> base
3	LM site	01:40:32	670 0172 01	0	4.6	0	-1.4	0	0	Off LRV; inverted position
4	LM site	01:44:29	337 4540 01	-	-	-	-	-	-	Off LRV; inverted position
5	ALSEP site	02:15:16	670 0026 01	-1.6	4.7	-	-1.3	4510	4510	On LRV
6	Station 1	05:08:03	670 0129 01	-4.3	1.4	-	-4.6	4510	4510	On LPV
7	SE <sub>1</sub> site	05:56:03	670 0101 01	-71	2.3	-	-3.7	4510	4510	On LRV; measurement disturbed and disregarded
8	LM site	06:39:44	600 0312 01	-	-	-	-	-	-	Off LRV
9	LM site	06:55:42	670 0215 01	43	-1.4	-	-1.4	4510	4510	Off LRV
EVA-2										
10	LM site	-	XrX XXXX OX	-	-	-	-	-	-	Thermal monitor reading
11	LM site	02:17:46	670 0177 01	5	-0.2	-	-0.2	4510	4625	Off LRV
12	Station 2	02:18:05	670 1552 01	1380	-44.8	-	-50.8	4625	4605	On LRV
13	Station 2A	03:21:09	670 1235 01	1063	-34.5	-	-40.5	4605	4665	On LRV
14	Station 3	04:04:59	670 0497 01	325	-10.5	-	-16.5	4665	4543	On LRV
15	Station 4	04:56:12	670 0725 01	-47	1.5	-	-4.5	4543	4525	On LRV
16	Station 5	06:00:11	670 0314 01	142	-1.2	-	-4.6	4525	4510	On LRV
17	LM site	-	670 0235 01	83	-2.0	-	-2.0	4510	4510	Off LRV
EVA-3										
18	LM site	-	XXX XXXX OY	-	-	-	-	-	-	Thermal monitor reading
19	LM site	00:17:20	670 0270 01	98	-3.2	-	-3.2	4510	4575	Off LRV
20	Station 6	01:23:00	670 1098 01	426	-30.0	-	-36.0	4575	4575	On LRV
21	Station 7	03:23:19	670 0960 01	788	-25.6	-	-31.6	4575	4575	On LRV
22	Station 8	04:13:46	670 1173 01	1001	-32.5	-	-32.5	4515	4515	On LRV
23	Station 9	04:30:46	670 0378 01	206	-6.7	-	-12.7	4515	4515	On LRV
24	Station 9	05:55:58	670 0571 01	393	-12.9	-	-12.9	4510	4510	On LRV
25	LM site	06:03:00	670 0107 01	-65	2.1	-	2.1	4510	4510	Off LRV; inverted position
26	LM site	-	337 4171 01	-	-	-	-	-	-	Off LRV; inverted position

<sup>a</sup>Reference between the display (first seven digits) at a station D<sub>n</sub> and the display at the LM site D<sub>n</sub> base (reading 3).

<sup>b</sup>Empirical correction of  $-6.0 \times 10^{-5}$  m/sec<sup>2</sup> (-6.0 mgal) applied to all on-LRV values; off-LRV values are unchanged.

<sup>c</sup>Apollo lunar surface experiments package

<sup>d</sup>Surface electrical properties experiment.

TABLE 16-II.- OFF-LRV  $\Delta g$  VALUES AT LM  
 SITE RELATIVE TO FIRST VALUE OBTAINED  
 [rms deviation =  $1.8 \times 10^{-5}$  m/sec<sup>2</sup> (1.8 mgal)]

Reading	$\Delta g$	
	m/sec <sup>2</sup>	mgal
3	0	0
9	$-1.4 \times 10^{-5}$	-1.4
11	-.2	-.2
17	-2.0	-2.0
19	-3.2	-3.2
25	2.1	2.1

TABLE 16-III.- COMPARISON OF OFF-LPV AND ON-LRV VALUES AT LM SITE, STATION 8, AND STATION 9  
 (For on-LRV/off-LPV difference without empirical correction,  $6.0 \times 10^{-5}$  m/sec<sup>2</sup> (6.0 mgal);  
 with empirical correction,  $1.0 \times 10^{-5}$  m/sec<sup>2</sup> (1.0 mgal))

Location	On LRV			Off LPV			Difference		Difference after application of empirical correction <sup>a</sup>		
	Reading	:g		Reading	:g		m/sec <sup>2</sup>	mgal	m/sec <sup>2</sup>	mgal	
		m/sec <sup>2</sup>	mgal		m/sec <sup>2</sup>	mgal					
LM site	2	$4.6 \times 10^{-5}$	4.6	3	0	0	0	$4.6 \times 10^{-5}$	4.6	$-1.4 \times 10^{-5}$	-1.4
Station 8	21	-25.6	-25.6	22	$-32.5 \times 10^{-5}$	-32.5	-32.5	6.9	6.9	.9	.9
Station 9	23	-6.7	-6.7	24	-12.9	-12.9	-12.9	6.2	6.2	.2	.2

<sup>a</sup>Empirical correction of  $-6.0 \times 10^{-5}$  m/sec<sup>2</sup> (-6.0 mgal) applied to on-LRV values.

TABLE 16-IV.- DETERMINATION OF  $k_0$  AND  $g$  AT LM SITE FROM READINGS IN NORMAL AND INVERTED POSITIONS

Reading	Position	Display	$\Delta f_n = \frac{192 \times 10^8}{D_n}$ , Hz	$\Delta f_i = \frac{4.8 \times 10^7}{D_i}$ , Hz	$k_0$ , Hz	g	
						m/sec <sup>2</sup>	mgal
EVA-1							
3	Normal	$D_n = 670\ 0172$	28.655981	-	7.215910	162 694.6 $\times 10^{-5}$	162 694.6
4	Inverted	$D_i = 337\ 4540$	-	14.224161			
EVA-3							
25	Normal	$D_n = 670\ 0107$	28.65626	-	7.215272	162 701.5 $\times 10^{-5}$	162 701.5
26	Inverted	$D_i = 337\ 4171$	-	14.225716			



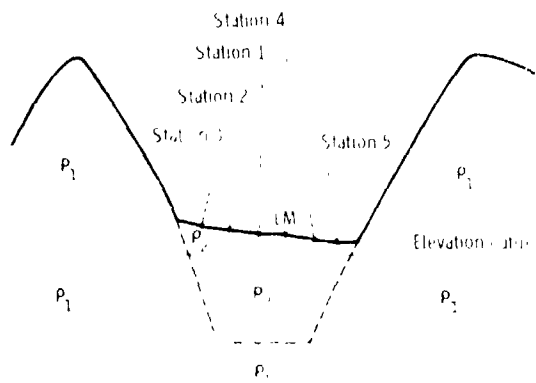


Figure 16-1.- Schematic diagram showing assumed density configurations for a hypothetical geological cross section.

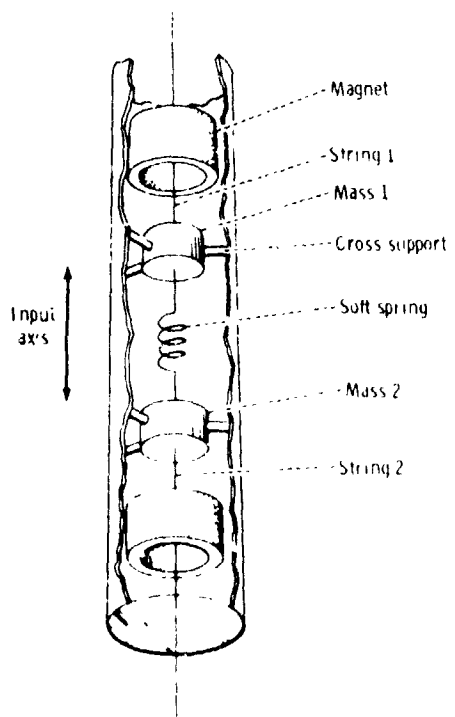


Figure 16-2.- Schematic view of double-stringed VSA.

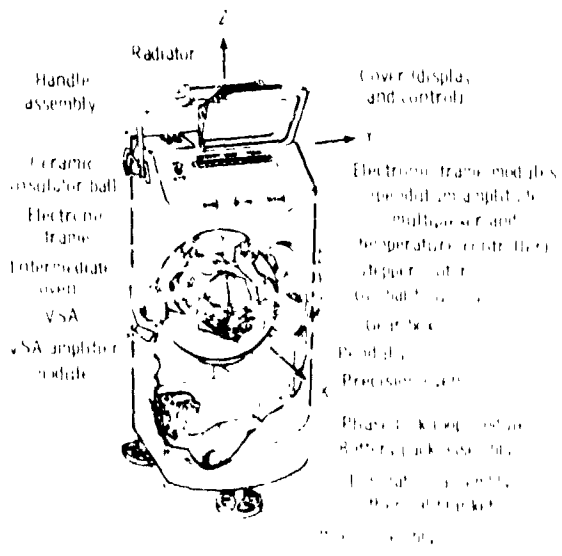


Figure 16-3.- Cutaway view of the TGE.

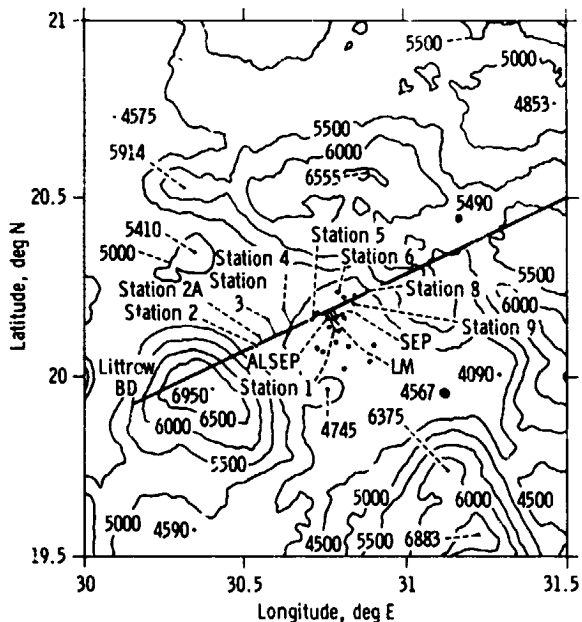


Figure 16-4.- Contour map of Taurus-Littrow landing site, showing the stations at which gravity measurements were made. The straight line starting near Littrow BD Crater (lower left) and trending northeast through the landing site is the cutting plane for the cross section to which the gravity measurements were projected. (Based on operational topographic map prepared by U.S. Army Topographic Command, October 1972. Contour interval, 500 m.)

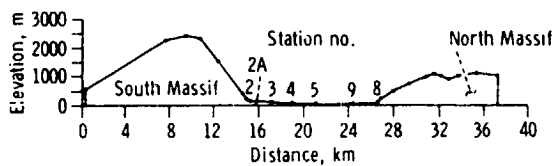


Figure 16-5.- Topographic profile showing locations of projected stations. Station 1 and the ALSEP and SEP sites have been omitted because their elevations are the same as that of the LM site. The elevation datum (abscissa) is the elevation of the LM site.

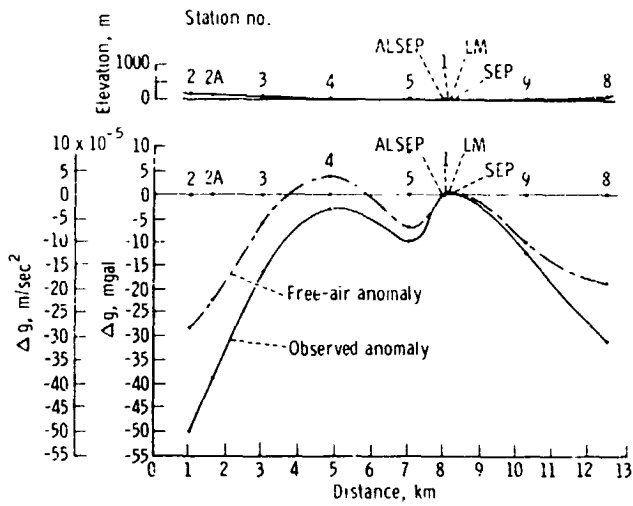


Figure 16-6.- Observed anomaly and free-air anomaly profiles across the Taurus-Littrow valley.

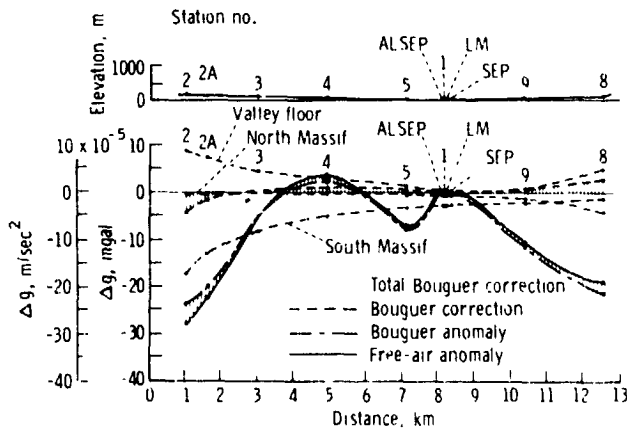
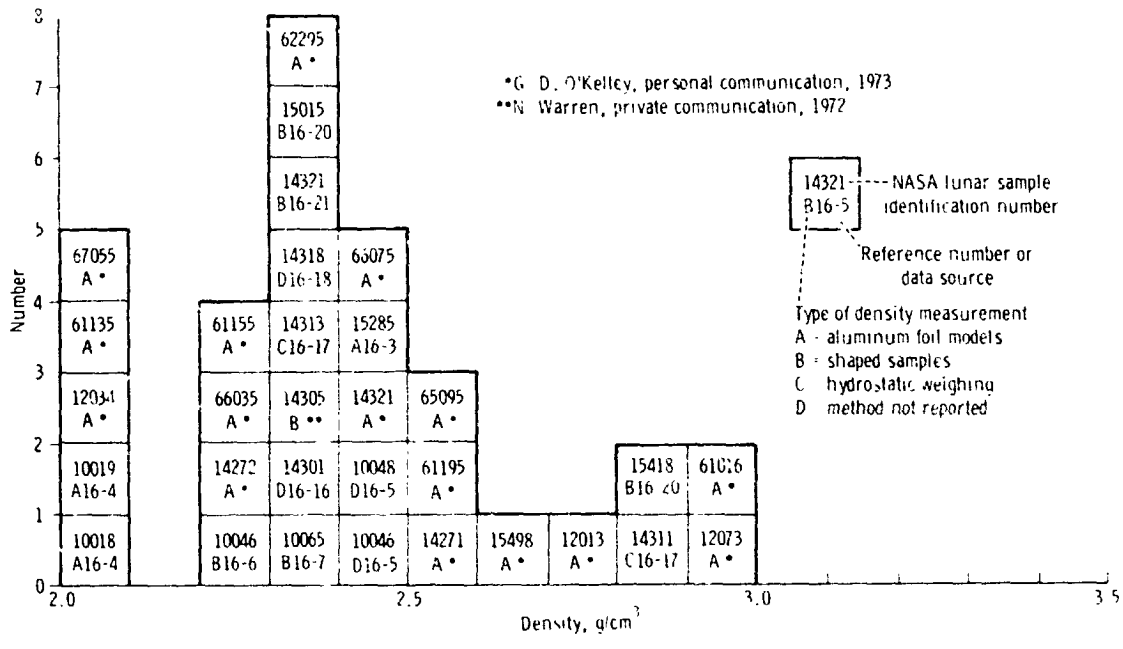
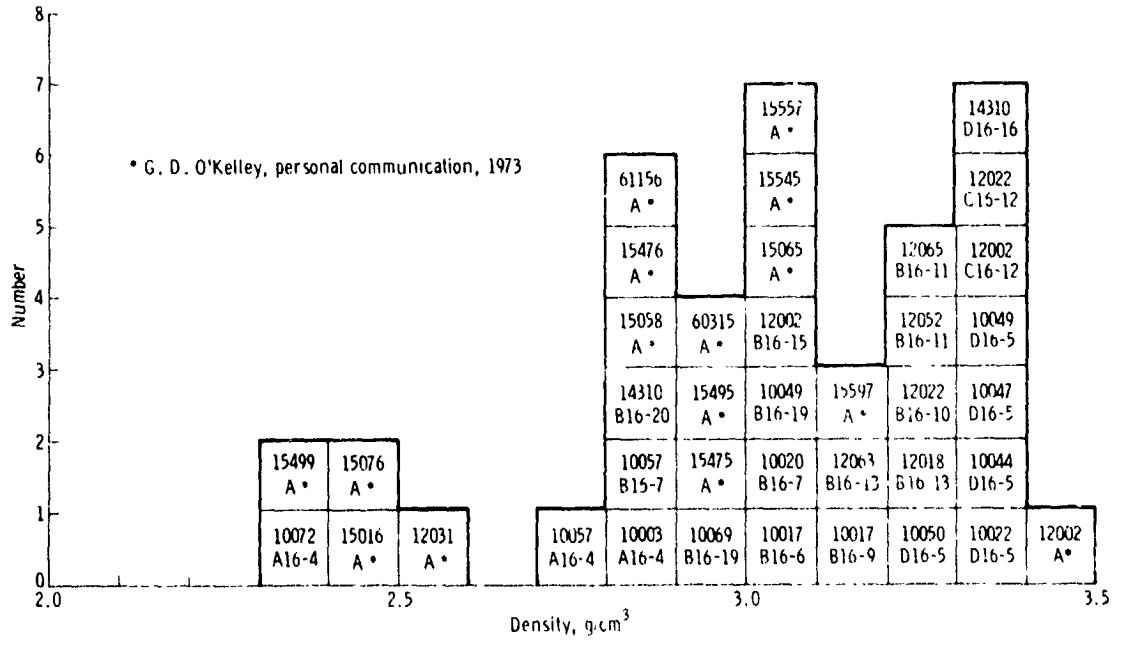


Figure 16-7.- Application of the Bouguer correction to determine the Bouguer anomaly profile across the Taurus-Littrow valley, showing the effect of the valley floor, of the North Massif, and of the South Massif and the total Bouguer correction. The free-air anomaly curve (fig. 16-6) is included for comparison with the Bouguer anomaly curve.



(a) Breccia.



(b) Basalt.

Figure 16-8.- Measured density values for lunar samples.

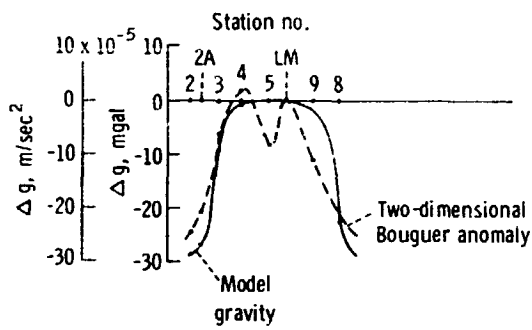


Figure 16-9.- Two-dimensional Bouguer anomaly curve.

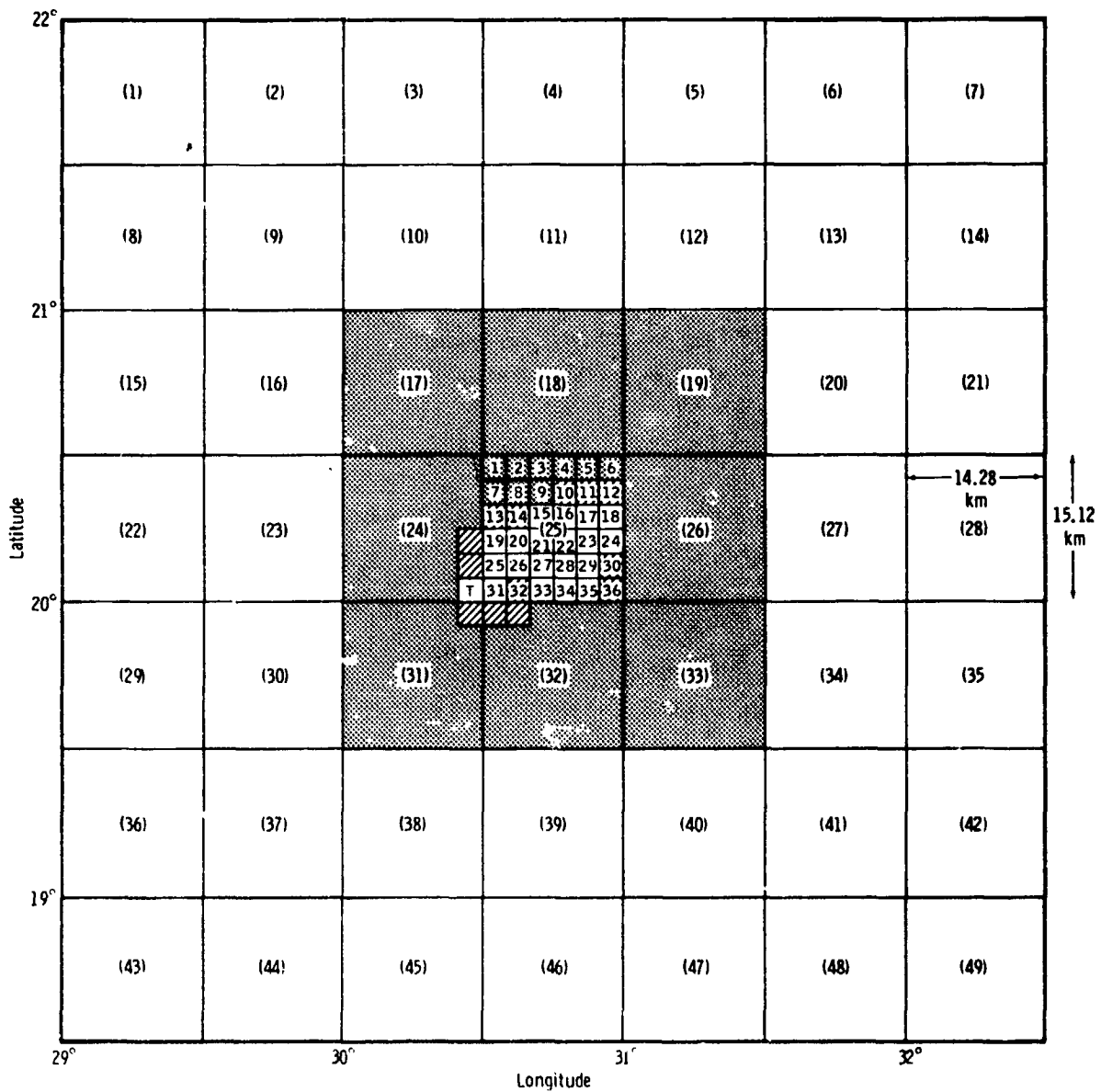


Figure 16-10.- Division of areas around the stations (which all lie within subarea 25) to make three-dimensional topographic corrections.

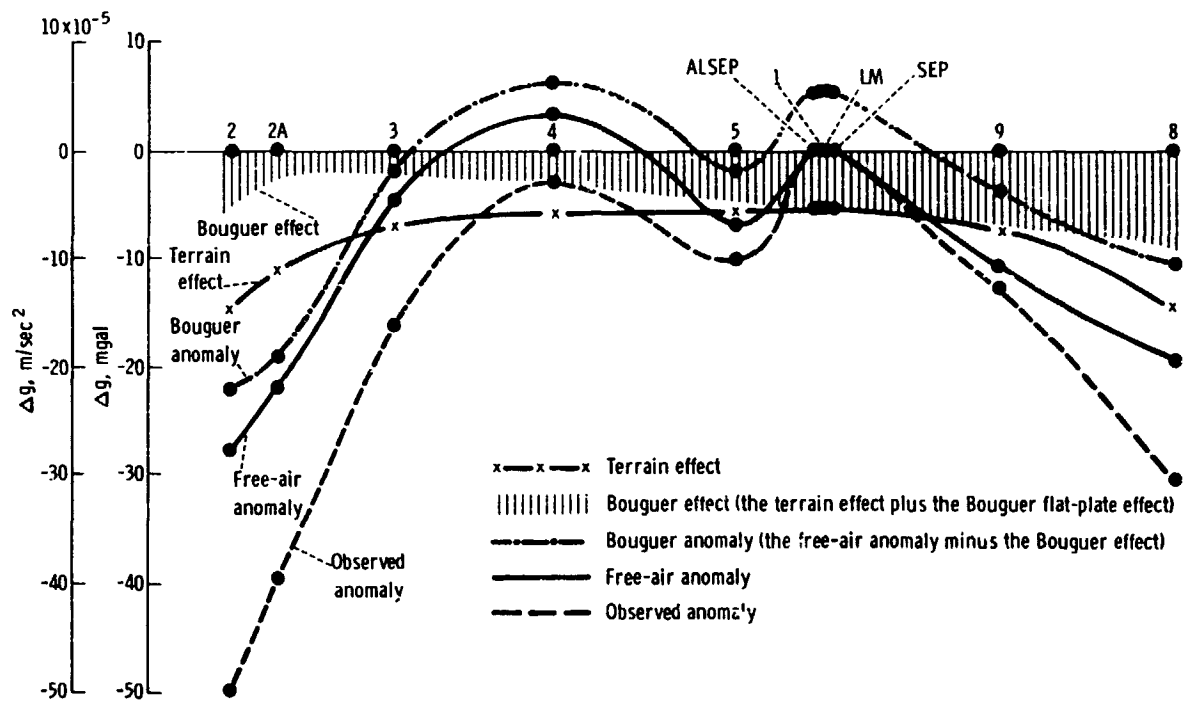


Figure 16-11.- Three-dimensional Bouguer anomaly calculations.

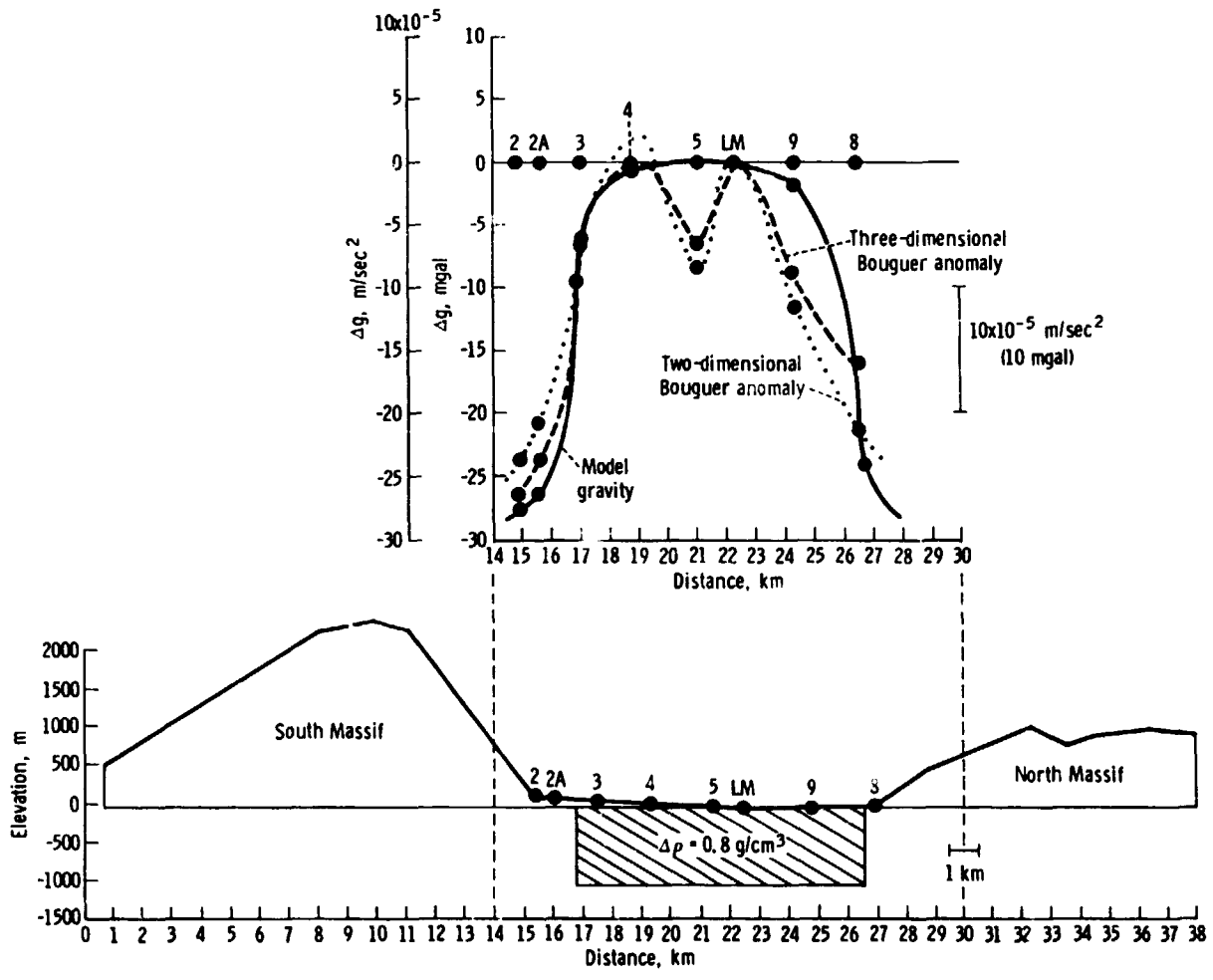


Figure 16-12.- Assumed model for subvalley densities to explain gravity anomalies.

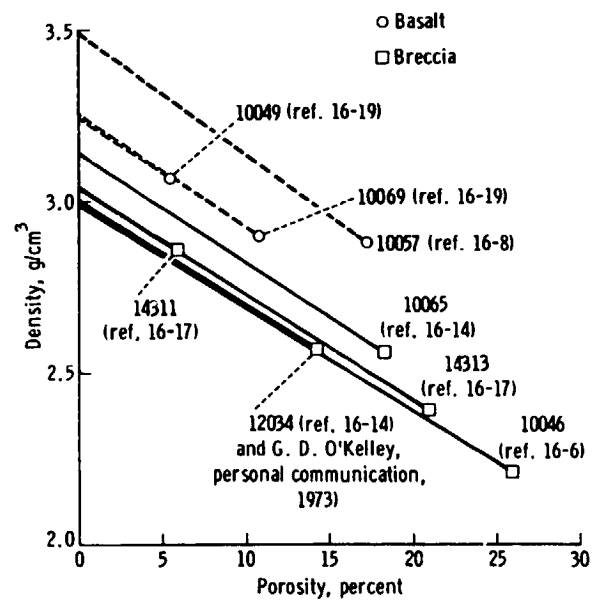
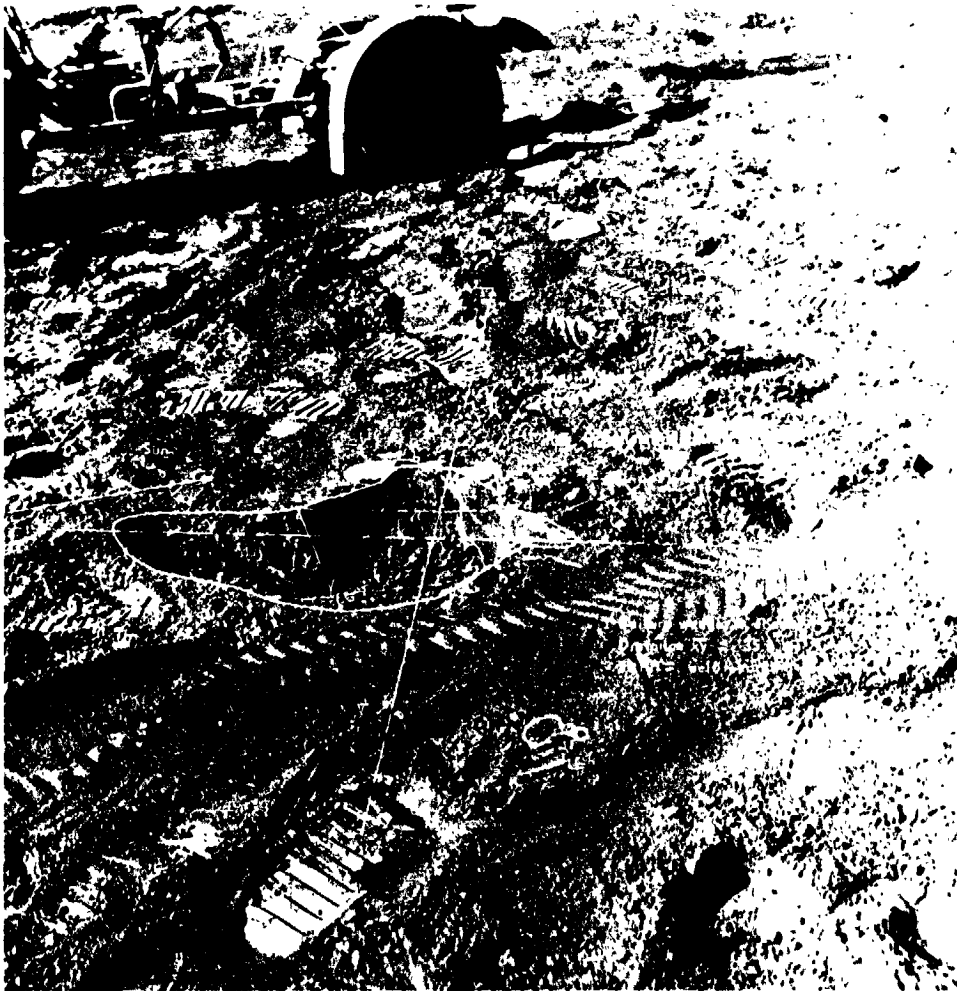


Figure 16-13.- Dependence of density on porosity for breccia and basalt lunar samples.

17. SOIL MECHANICS EXPERIMENT (NASA EXPERIMENT S-200)

NSSDC IDENTIFICATION NUMBERS:

APOLLO 12	69-099C-10
APOLLO 14	71-008C-02
APOLLO 15	71-063C-02
APOLLO 16	72-031C-09
APOLLO 17	72-096C-04



CONTENTS - SECTION 17

	Page
EXPERIMENT DESCRIPTION . . . . .	17-3
DATA SOURCES AND AVAILABILITY . . . . .	17-3
DATA ARCHIVED AT NSSDC . . . . .	17-4
SUMMARY OF KEY RESULTS . . . . .	17-4
REFERENCES . . . . .	17-6
BIBLIOGRAPHY . . . . .	17-6

## 17. SOIL MECHANICS EXPERIMENT

The purpose of the soil mechanics experiment was to determine the physical characteristics and mechanical properties of the lunar soil to depths of several decimeters and their variations in lateral directions, on slopes, and between different regions of the Moon.

### EXPERIMENT DESCRIPTION

Soil mechanics data were derived from television, photography, core-tube and bag samples, measurements that used a self-recording penetrometer, and data from other lunar surface experiments. The self-recording penetrometer (SRP) (fig. 17-1), the main quantitative data source for the soil mechanics experiment, was used to obtain data on soil-penetration resistance as a function of depth below ground surface. Maximum possible penetration depth of the SRP is 76.5 cm, and the maximum recordable penetration force is 215 N. The record of each penetration is inscribed on a recording drum contained in the upper housing assembly. The lunar surface reference plane rests on the lunar surface during a measurement and serves as a datum for measurement of penetration depth. A 2.54- by 12.7-cm bearing plate and two penetrating cones (having base areas of 1.29 and 3.22 cm<sup>2</sup> and an apex angle of 30°) were available for attachment to the penetration shaft.

The core drive tubes for Apollo 15, 16, and 17 are thin-walled tubes that are 37.5 cm in length, with an inside diameter of 4.13 cm and an outside diameter of 4.38 cm. The tubes were used singly and also in combination as double-core tubes.

### DATA SOURCES AND AVAILABILITY

Soil mechanics data were derived from the following sources.

1. Crew commentary (air-to-ground transcript)
2. Crew debriefing sessions following each mission

3. Lunar-surface television
4. Lunar-surface photography
5. Performance data and observations of interactions between lunar soil and the lunar roving vehicle
6. Drive-tube (core tube) samples
7. Deep-drill samples, taken with the Apollo lunar surface drill
8. Lunar sample characteristics, as determined by the Lunar Sample Preliminary Examination Team
9. Measurements taken with the SRP

The only data unique and specific to the soil mechanics experiment were obtained with the SRP during the Apollo 15 and 16 missions.

#### DATA ARCHIVED AT NSSDC

Data packages containing the results of measurements taken with the SRP have been archived at the National Space Science Data Center (NSSDC). Each data package includes:

1. Curves showing penetration resistance as a function of depth
2. Calibration data (preflight and postflight)
3. Tables showing force as a function of depth (data from the recording drum)

#### SUMMARY OF KEY RESULTS

The mechanical properties of lunar soil as deduced to date have been summarized by Mitchell et al. (refs. 17-1 and 17-2) who note that the soil behavior is similar to that of terrestrial soils of comparable gradation, even though the two soil types are compositionally dissimilar. Particle-size distribution, bulk density, and particle shape appear to control physical behavior.

A variety of data sources indicates that the soil porosity, density, and strength vary locally and with depth. Densities may be in the range of 1.0 to 2.0 g/cm<sup>3</sup>, and

values greater than  $1.5 \text{ g/cm}^3$  are probable at depths of 10 to 20 cm. Despite these local variations, however, Houston et al. (ref. 17-3) have found that the mean porosity at each of the Apollo landing sites is the same (43.3 percent) for the upper few centimeters of soil. The soil on crater rims and on crater and rille slopes was found to have a somewhat higher porosity (an average value of 46 to 47 percent). Apollo 15 and 16 results also suggest somewhat lower densities for soil on slopes.

For a given lunar soil, porosity appears to be the most important single variable controlling the strength parameters, with most probable values lying in the range of 0.1 to 1.0 kN/m<sup>2</sup> for cohesion and 30° to 50° for friction angle; the higher values are associated with lower porosities. Available data indicate that, in general, strength (and therefore density) increases with depth.

#### REFERENCES

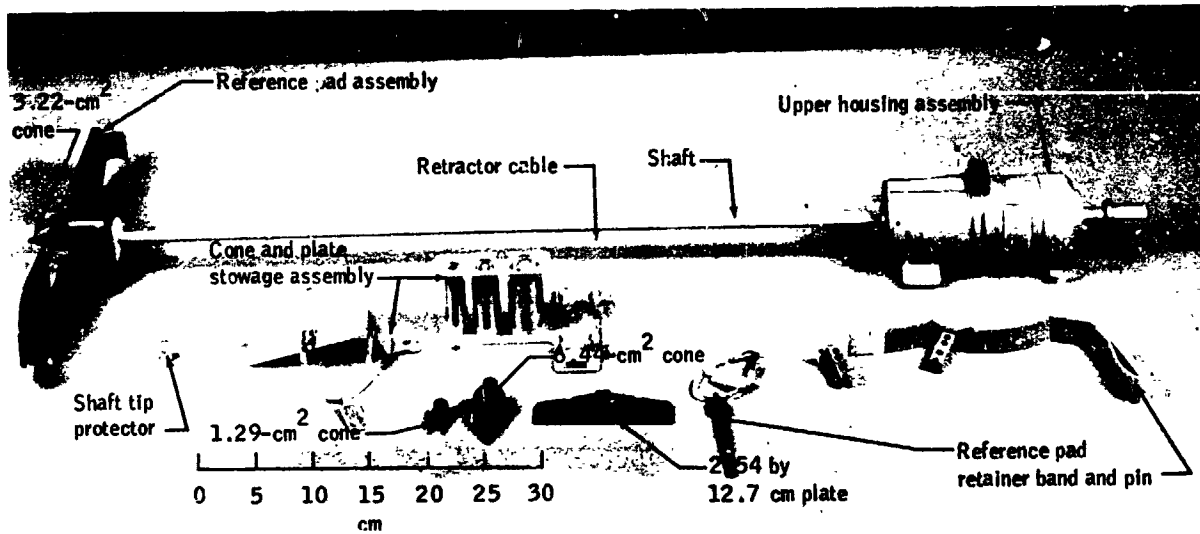
- 17-1. Mitchell, James K.; Carrier, W. David, III; Costes, Nicholas C.; Houston, William N.; et al.: Soil Mechanics. Sec. 8 of Apollo 17 Preliminary Science Report, NASA SP-330, 1973.
- 17-2. Mitchell, J. K.; Houston, W. N.; Carrier, W. D., III; and Costes, N. C.: Apollo Soil Mechanics Experiment S-200, Final Report. Space Science Laboratory Series 15, Issue 7, Univ. of Calif., Berkeley, Jan. 1974.
- 17-3. Houston, W. N.; Hovland, H. J.; and Mitchell, J. K.: Lunar Soil Porosity and Its Variation as Estimated from Footprints and Boulder Tracks. Proceedings of the Third Lunar Science Conference, vol. 3, MIT Press (Cambridge, Mass.), 1972, pp. 3255-3263.

#### BIBLIOGRAPHY

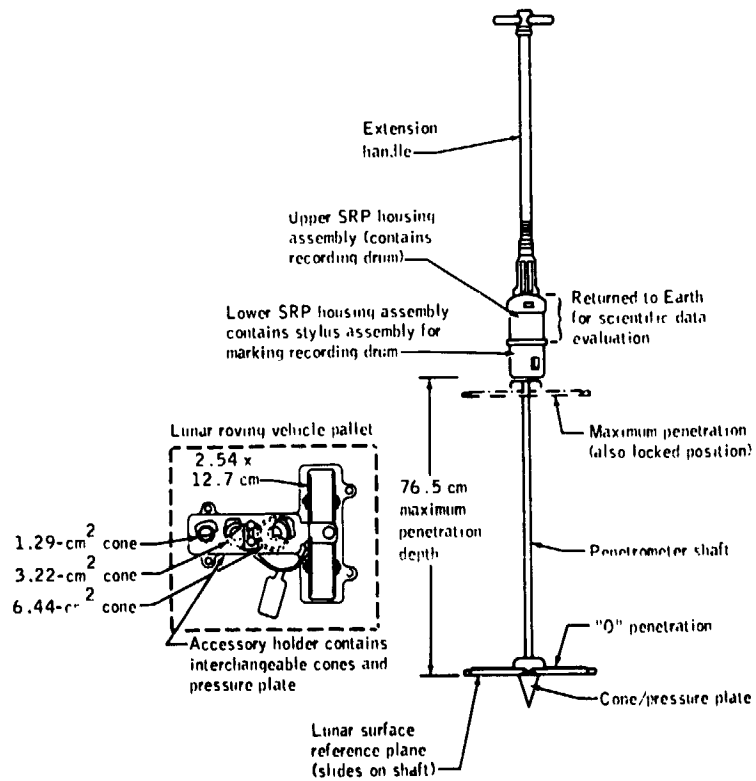
- Bekker, M. G.: Introduction to Terrain-Vehicle Systems. The University of Michigan Press (Ann Arbor, Mich.), 1969.
- Bogard, D. D.; Nyquist, I. E.; Hirsch, W. C.; and Moore, D. R.: Trapped Noble Gas Abundances in Surface and Sub-Surface fines from Apollo 15 and 16. Lunar Science IV (Abs. of papers presented at the Fourth Lunar Science Conference (Houston, Tex.), Mar. 5-8, 1973), pp. 79-81.
- Carrier, W. D., III: Lunar Soil Grain Size Distribution. The Moon, vol. 8, 1973.
- Carrier, W. D., III; Bromwell, L. G.; and Martin, R. T.: Behavior of Returned Lunar Soil in Vacuum. J. Soil Mechanics Foundations Div., ASCE, Nov. 1973.
- Carrier, W. D., III; Mitchell, J. K.; and Mahmood, Arshud: The Relative Density of Lunar Soil. Lunar Science IV (Abs. of papers presented at the Fourth Lunar Science Conference (Houston, Tex.), Mar. 5-8, 1973), pp. 118-120.
- Clanton, U. S.; McKay, D. S.; Taylor, R. M.; and Heiken, G. H.: Relationship of Exposure Age to Size Distribution and Particle Types in the Apollo 15 Drill Core. The Apollo 15 Lunar Samples, Lunar Science Institute (Houston, Tex.), 1972, pp. 54-56.

- Costes, N. C.: Regional Variations in Physical and Mechanical Properties of Lunar Surface Regolith. Lunar Science IV (Abs. of papers presented at the Fourth Lunar Science Conference (Houston, Tex.), Mar. 5-8, 1973), pp. 159-161.
- Costes, N. C.; Farmer, J. F.; and George, E. B.: Mobility Performance of the Lunar Roving Vehicle. Terrestrial Studies: Apollo 15 Results. NASA TR R-401, 1972.
- Eagleston, J. M.; Patterson, A. W.; Throop, J. E.; Arant, W. H.; and Spooner, D. L.: Lunar Rolling Stones. Photogrammetric Eng., vol. 34, no. 3, Mar. 1968, pp. 246-255.
- Filice, A. L.: Lunar Surface Strength Estimate from Orbiter II Photographs. Science, vol. 156, no. 3781, June 16, 1967, pp. 1486-1487.
- Gault, D. E.: Saturation and Equilibrium Conditions for Impact Cratering on the Lunar Surface: Criteria and Implications. Radio Sci., vol. 5, no. 2, Feb. 1970, pp. 273-291.
- Green, A. J.; and Melzer, K. J.: Performance of the Boeing LRV Wheels in a Lunar Soil Simulant: Effect of Wheel Design and Soil. Tech. Rept. M-71-10, Rept. 1, USAF WES, Vicksburg, Miss., 1971.
- Houston, W. N.; Moriwaki, Y.; and Chang, C. S.: Downslope Movement of Lunar Soil and Rock Caused by Meteor Impact. Lunar Science IV (Abs. of papers presented at the Fourth Lunar Science Conference (Houston, Tex.), Mar. 5-8, 1973), pp. 384-385.
- Houston, W. N.; and Namiq, L. I.: Penetration Resistance of Lunar Soils. J. Terramechanics, vol. 8, no. 1, 1971, pp. 59-69.
- Howard, K. A.: Lunar Avalanches. Lunar Science IV (Abs. of papers presented at the Fourth Lunar Science Conference (Houston, Tex.), Mar. 5-8, 1973), pp. 386-388.
- Melzer, K. J.: Performance of the Boeing LRV Wheels in a Lunar Soil Simulant: Effect of Speed, Wheel Load, and Soil. Tech. Rept. M-71-10, Rept. 2, USAF WES, Vicksburg, Miss., 1971.
- Mitchell, J. K.; Bromwell, L. G.; Carrier, W. D., III; Costes, N. C.; et al.: Soil-Mechanics Experiment. Sec. 7 of Apollo 15 Preliminary Science Report. NASA SP-289, 1972.

- Mitchell, J. K.; Bromwell, L. G.; Carrier, W. D., III; Costes, N. C.; and Scott, R. F.: Soil Mechanical Properties at the Apollo 14 Site. J. Geophys. Res., vol. 77, no. 29, Oct. 10, 1972, pp. 5641-5664.
- Mitchell, J. K.; Carrier, W. D., III; Houston, W. N.; Scott, R. F.; et al.: Soil Mechanics. Sec. 8 of Apollo 16 Preliminary Science Report. NASA SP-315, 1972.
- Mitchell, J. K.; Houston, W. N.; Scott, R. F.; Costes, N. C.; et al.: Mechanical Properties of Lunar Soil: Density, Porosity, Cohesion, and Angle of Internal Friction. Proceedings of the Third Lunar Science Conference, vol. 3, MIT Press (Cambridge, Mass.), 1972, pp. 3235-3253.
- Moore, H. J.: Estimates of the Mechanical Properties of Lunar Surface Using Tracks and Secondary Impact Craters Produced by Blocks and Boulders. U.S. Geol. Survey Interagency Rept.: Astrogeology 22, July 1970.
- Moore, H. J.; Vischer, W. A.; and Martin, G. L.: Boulder Tracks on the Moon and Earth. U.S. Geol. Survey Prof. Paper 800-B, 1972, pp. B165-B174.
- Scott, R. F.; and Roberson, F. I.: Soil Mechanics Surface Sampler. Part II: Surveyor Project Final Report, Calif. Inst. Tech. JPL-TR-32-1265, 1968, pp. 195-207.
- Vinogradov, A. P., ed.: Lunokhod-1, Mobile Lunar Laboratory. Nauka Publishers (Moscow), 1971. (Available from National Technical Information Service, Springfield, Virginia.)



(a) Photograph of SRP and components.



(b) Sketch of SRP in upright position.

Figure 17-1.- Self-recording penetrometer (SRP).

18. FAR UV CAMERA/SPECTROGRAPH (NASA EXPERIMENT S-201)

NSSDC IDENTIFICATION NUMBER:

APOLLO 16 72-031C-10



CONTENTS - SECTION 18

	Page
INSTRUMENT DESCRIPTION . . . . .	18-3
INSTRUMENT OPERATION . . . . .	18-4
EXPERIMENT GOALS . . . . .	18-5
DESCRIPTION OF PFOCESSED FLIGHT FILM . . . . .	18-6
DATA AVAILABLE AT NSSDC . . . . .	18-8
BIBLIOGRAPHY . . . . .	18-9

## 18. FAR UV CAMERA/SPECTROGRAPH

Ultraviolet observations from the Moon allow study of the entire atmosphere of the Earth and the geocorona. Photographs taken by the far UV camera show hydrogen and other gases in the solar wind and interplanetary media and provide new data on stars, nebulae, and galaxies much farther away. When used as a spectrograph, the instrument distributes the light it receives according to wavelength, and the resulting spectrum shows bright lines or gaps that are characteristic of various gases. The far UV camera/spectrograph extended stellar research to fainter stars and shorter wavelengths than those studied previously and also obtained quantitative measurements of diffuse background radiation in the far UV wavelengths.

### INSTRUMENT DESCRIPTION

The camera/spectrograph was designed, fabricated, and calibrated at the Naval Research Laboratory in Washington, D.C., to meet the requirements of the experiment goals and the limitations imposed by other crew activities. The basic component was an f/1.0 Schmidt camera of 7.5-cm aperture (fig. 18-1). Incident light passes through the corrector plate and is focused on a potassium bromide (KBr) photocathode, maintained at -25 000 V. Photoelectrons accelerated by this electrostatic field are focused by an axial magnetic field of approximately  $2.39 \times 10^4$  A/m (300 Oe) on film coated with a very thin layer of nuclear-track emulsion (Kodak NTB-3) just behind a 32-mm hole in the primary (concave spherical) mirror. Exposures were initiated by the film transport that automatically turned the takeup reel after a specified exposure time. During each exposure, the NTB-3 film was firmly pressed against the thin (7.7-nm) barrier membrane consisting of a thin plastic, coated with aluminum permeable to the 25 000-V electrons but opaque to light.

In order to select different bands of far UV light, the Schmidt camera was provided with two corrector plates, one of lithium fluoride (LiF) and one of calcium fluoride (CaF<sub>2</sub>), either of which could be accurately seated by a small motor. To photograph spectra, another motor was provided to turn the Schmidt camera 90° to look at a reflection grating behind a photoengraved grid collimator

that admitted light from a 0.25° strip of sky. The motions of film transport, corrector plates, and Schmidt camera were automatically timed by an electronic sequencer, accurate to a fraction of a second.

Operation of the "power on" or "reset" switch initiated an automated sequence of exposures in four modes designated as follows:

<u>Mode</u>	<u>Description</u>
ILi:	Imagery through an LiF filter-corrector with a pass-band of 105 to 160 nm
ICa:	Imagery through a CaF2 filter-corrector with a pass-band of 123 to 160 nm
SLi:	Spectra through an LiF filter-corrector with a 3-nm resolution over the pass-band of 105 to 160 nm
SO:	Spectra with no corrector, with a 4-nm resolution over the pass-band of 50 to 160 nm

This spectral range was limited by the mirror and grating reflectivity at the low end and by the KBr photocathode sensitivity at the long-wave end.

#### INSTRUMENT OPERATION

For proper thermal conditions, the far UV camera had to be in the shadow of the lunar module (LM). Because of the 16-hr delay in touchdown and the higher Sun angle, it was necessary to deploy the camera close to the LM (2 m southwest of the down-Sun footpad) during the first period of extravehicular activity (EVA-1) (fig. 18-2) and even closer during EVA-2 and EVA-3. The LM thus occulted a larger region of the eastern sky (fig. 18-3) and eliminated two of the planned targets (NGC<sup>1</sup> 7317 group of galaxies and Abell Clusters 2634 and 2666).

Pointings of the far UV camera/spectrograph were made by setting two graduated circles on an altitude-azimuth

---

<sup>1</sup>NGC = New General Catalogue of Nebulae and Clusters of Stars by J. L. E. Dreyer, published 1888.

telescope mount. At deployment (approximately 17:40 G.m.t. on April 21), three legs were unfolded and locked to form a tripod under a leveled table. The camera/spectrograph was supported between two vertical stanchions on the table, as shown in figure 18-2, so that it could swing vertically from  $0^\circ$  elevation (pointing at the horizon) to  $90^\circ$  (pointing at the zenith). The desired elevation (EL) angle was set by the astronaut on a sector graduated in degrees. The stanchions could be rotated around a vertical axis centered on the leveled table where the azimuth (AZ) could be read on a circle graduated in degrees. The zero point of this AZ circle was set by the astronaut sighting down-Sun, a few degrees south of west. Hence, the AZ readings for the far UV camera pointings were  $90^\circ$  larger than conventional AZ readings (measured from lunar north) used in other crew activities near the LM.

In the imagery modes (ILi and ICa), the camera viewed the sky directly with a field diameter of more than  $20^\circ$  (fig. 18-3) and a resolution of approximately 2 arc-min. For the spectroscopic modes (SLi and SO), spectra were obtained of everything within a  $20^\circ$  by  $0.25^\circ$  strip parallel to the lunar horizon. The image on the photocathode (fig. 13-1) was transferred to the NTB-3 film behind the primary mirror to give a mirror image of the sky field rotated  $10.5^\circ$  on the film.

To adjust to the EVA time line, pointing times varied from 20 min during crew activities near the LM to 16 or 17 hr during the rest periods between EVA periods. Hence, the targets were designated in advance as S for short pointing times of 20 to 30 min, allowing imagery exposures only; M for medium pointing times of 4 to 5 hr, allowing both imagery and spectroscopic exposures; and L for long pointing times of 16 hr or more, allowing several 200-min spectroscopic exposures. On every target, there is redundancy because of the automatic sequence of repeated exposures. In addition to pure imagery and spectroscopic frames, short combined exposures (designated IS) were obtained during the mode changes when the camera was turned  $90^\circ$  from direct imagery (ILi) to look at the grating and collimator (SLi).

#### EXPERIMENT GOALS

Seven scientific goals were established for this experiment, all of which were at least partly achieved.

1. To determine composition and structure of the Earth upper atmosphere from its spectra

2. To determine the structure of the geocorona from imagery in Lyman-alpha (121.6-nm) light, and to study day and night airglow and polar aurorae in the longer wavelengths (125 to 160 nm)

3. To obtain direct evidence of intergalactic hydrogen in distant clusters of galaxies

4. To obtain spectra and imagery of the solar wind and other gas clouds in the solar system

5. To detect gases in the lunar atmosphere, including volcanic gases, if any

6. To obtain spectra and colors of external galaxies in the far UV regions, adding to knowledge of their composition

7. To obtain spectra and colors of stars and nebulae in the Milky Way

Preliminary results can be reported on four of these goals, most specifically on the first two. Less accurate results are available on goals 4 and 6; definite conclusions on goals 3, 5, and 7 must await further analyses of accurate measurements on the densities of the processed flight film.

Numerous target pointings were considered. Because of the 20° field, each pointing would include several significant objects and would help to meet several experiment goals. It was necessary to verify that each target center would be at least 10° above the lunar horizon and would not be occulted by the LM at the scheduled pointing time. To allow for delays in the time line, the EL and AZ settings were computed for all possible pointing times, and 6 alternate settings were computed in addition to the 11 primary targets. The probable errors in settings were also considered; except for the Earth, which was centered by eye in the sighting tube, these errors were estimated at ±3°. Because the AZ bearing tended to stick, the actual pointing errors were somewhat larger. Table 18-1 shows the requested right ascension (RA) and declination (dec) angles compared with the actual values measured on imagery frames.

#### DESCRIPTION OF PROCESSED FLIGHT FILM

After each of the 11 pointings, the automatic sequence on the camera, timed by film advance, took the following

exposures until the astronaut pressed the "reset" switch for another pointing.

<u>Exposure type</u>	<u>Exposure time, min</u>
ILi	1, 3, 10
ICa	0.5, 3, 10, 30
SLi	3, 10, 30
SO	0.5, 3, 10, 30
SLi	0.5, 200
SO	0.5, 200

There are 209 exposures on 9.727 m (383 in.) of film, plus 0.467 m (18.4 in.) of step-wedge calibration, both preflight and postflight. The background fog, produced principally by Van Allen belt protons during translunar coast, is less than 0.14 net density.

In all, there are 178 usable frames on the exposed film: 85 imagery, 68 spectra, and 25 combined (ILi and SLi) exposures. Of the 85 imagery frames, 13 are heavily overexposed by background Lyman-alpha radiation on the 10-min ILi exposures, and 7 are overlapped by adjacent frames because of inadequate film advance. Four of the combined frames are also overlapped. The distribution among the 10 targets is shown in table 18-II. (The regions covered are each 20° circles in the sky.)

Because of the uneven thickness of the barrier membrane, there are streaks in the instrument sensitivity - approximately ±25 percent in electron flux - inclined 50° to the horizontal, upward to the right in the lunar sky. Also, numerous small blank spots were produced by dust on the barrier membrane, and a lenticular area of lower sensitivity appears at the upper right. All these instrument sensitivity deviations will be removed in the accurate reduction of film density to absolute UV flux. A few scratches on the back of the film, produced by abrasion in the film-transport box (cassette), also affect the photometry and will be removed in the accurate reduction.

The S-201 flight film was originally scanned with a microphotometer at the DICOMED Corp., Minneapolis, Minn.; but the density range was limited to 2.5 D (less than half the film's useful range from 0 to 6 D) and the digitized

tape recordings were very "noisy." During August 1974, 148 frames (omitting 30 frames that were underexposed or overexposed) were scanned with a Photo Data Systems (PDS) microdensitometer at the Boller and Chivens Division of Perkin-Elmer in South Pasadena, Calif. (with a range of 5.2 D). The digitized data, 1024 by 1024 rasters per scan, are on magnetic tape filed at the Lyndon B. Johnson Space Center (JSC), Houston, Texas.

With the JSC Executive II computer system, these tapes have been analyzed in the following steps:

1. Star images on 10 frames were identified with blue stars in the Smithsonian Astrophysical Observatory Catalog.

2. Deviations between the image positions and catalog positions were used to generate a "distortion function" so that images could be corrected for a spirallike distortion introduced in the electrographic camera.

3. An S-201 catalog is being prepared and will contain lists of corrected celestial coordinates (right ascension and declination) of all recorded objects, together with density volumes above background on both ILi and ICa exposures. (These density volumes are proportional to flux in the two pass-bands, 105 to 160 nm and 123 to 160 nm.) The catalog will list several thousand stars in the 10 target areas (table 18-II).

4. Isodensity contour plots were drawn by computer for selected regions with selectable contour interval. (Three of them are shown in figures 18-4 to 18-6.) A catalog of S-201 contour plots is being prepared showing density variations (far-UV intensity variations) across the 10 target areas (table 18-II). These show other identified nebulae and galaxies, as well as variations in the solar wind and interplanetary background. This catalog will contain more than 100 isodensity contour plots.

#### DATA AVAILABLE AT NSSDC

The following experiment data are available at the National Space Science Data Center (NSSDC).

1. A second-generation copy negative of flight film.
2. Nine-track magnetic tape. Tape content is the output of a photo digitation scanning on a 1024 by 1024 matrix of each of the 204 frames obtained from the experiment.

3. A list of 209 frames on the S-201 flight film with time of exposure, central coordinates, mode, duration of exposure, defects, features, and DICOMED tape numbers.

In addition, computer programs used are described in DJSC Abstract D 142.

#### BIBLIOGRAPHY

- Carruthers, George R.: Electronic Imaging Devices in Astronomy. *Astrophys. and Space Sci.*, vol. 14, 1971, pp. 332-377.
- Carruthers, George P.; and Page, Thornton: Apollo 16 Far-Ultraviolet Camera/Spectrograph: Earth Observations. *Science*, vol. 177, no. 4051, Sept. 1, 1972, pp. 788-791.
- Carruthers, George R.; and Page, Thornton: Far Ultraviolet Brightness of Nebulae in Cygnus. *J. Geophys. Res.* (To be published).
- Code, Arthur D.; and Savage, Blair D.: Orbiting Astronomical Observatory: Review of Scientific Results. *Science*, vol. 177, no. 4045, July 21, 1972, pp. 213-221.
- Fric, Robert J.: The Telescope Catalog of Ultraviolet Observations. The Scientific Results From the Orbiting Astronomical Observatory (OAO-2), Arthur D. Code, ed. NASA SP-310, 1972, pp. 321-345.
- De Vaucouleurs, G.: Magellanic Clouds and the Galaxy II. *The Observatory*, vol. 74, 1954, pp. 158-164.
- Gott, J. Richard, III; and Potter, A. E., Jr.: Lunar Atomic Hydrogen and Its Possible Detection by Scattered Lyman-Alpha Radiation. *Icarus*, vol. 13, 1970, pp. 202-206.
- Hanson, W. B.: A Comparison of the Oxygen Ion-Ion Neutralization and Radiative Recombination Mechanisms for Producing the Ultraviolet Nightglow. *J. Geophys. Res.*, vol. 75, no. 22, Aug. 1, 1970, pp. 4343-4346.
- Hanson, W. B.: Radiative Recombination of Atomic Oxygen Ions in the Nighttime F Region. *J. Geophys. Res.*, vol. 74, no. 14, July 1, 1969, pp. 3720-3722.

Henize, Karl G.: Catalogues of H-Alpha Emission Stars and Nebulae in Magellanic Clouds. *Astrophys. J. Supp. No. 22*, vol. II, Sept. 1956, pp. 315-364.

Hicks, G. T.; and Chubb, T. A.: Equatorial Aurora/Airglow in the Far Ultraviolet. *J. Geophys. Res.*, vol. 75, no. 31, Nov. 1, 1970, pp. 6233-6248.

Knudsen, William C.: Tropical Ultraviolet Nightglow From Oxygen Ion-Ion Neutralization. *J. Geophys. Res.*, vol. 75, no. 19, July 1, 1970, pp. 3862-3866.

Olson, Ronald E.; Peterson, James R.; and Moseley, John: Oxygen Ion-Ion Neutralization Reaction as Related to Tropical Ultraviolet Nightglow. *J. Geophys. Res.*, vol. 76, no. 10, Apr. 1, 1971, pp. 2516-2519.

Tinsley, Brian A.; Christensen, Andrew B.; Gouveira, Hermano: Comparison of OI7774 and Ionosonde Data From Brazil and the Excitation of TROPLES. *Trans. Am. Geophys. Union*, vol. 53, no. 7, July 1972, p. 730.

ORIGINAL PAGE IS  
OF POOR QUALITY

TABLE 18-I.- REQUESTED AND ACTUAL ANGLES OF RIGHT ASCENSION AND DECLINATION

Target	Requested RA, deg	Requested dec, deg	Actual RA, deg	Actual dec, deg	Object
1S	313	+37	321	+37	Cygnus Loop Nebula (at edge)
2M	318	-15	318	-15	Earth
3S	037	-05	042	-16	NGC 1068 (missed)
4L	357	-41	355	-41	Grus group of galaxies
5S	321	-53	318	-53	Pavo group
6M	081	-70	089	-74	Large Magellanic Cloud (LMC)
7S	258	-62	261	-59	NGC 6300 group
8L	342	-04	344	-05	Geocorona east of Earth
9S	053	-35	056	-27	Pornax Cluster
10M	275	-23	278	-31	Milky Way center
11S	005	-36	(No film)	(No film)	NGC 134 group (also on target 4L)

TABLE 18-II.- REGIONS COVERED BY THE PAR UV CAMERA/SPECTROGRAPH

Target	Constellation	Duration, hr:min	Frames	Objects
1S	Cygnus (southeast portion)	00:33.5	3 Ili, 4 Ica, 1 IS	North America nebulae, Loop Nebula, 3 planetary nebulae, 60 stars
2M	Aquarius (with Earth)	04:50	7 Ili, <sup>1</sup> 4 Ica, 8 IS, 5 Sli, 4 SO	Earth aurorae-geocorona, 1 planetary nebula, 55 stars
3S	Cetus-Eridanus	00:38	3 Ili, 4 Ica	3 galaxy groups, 20 stars
4L	Grus-Phoenix-Scu.ptor	16:55.5	6 Ili, 8 Ica, 4 IS, 10 Sli, 12 SO	3 galaxy groups, 20 stars
5S	Indus-Pavo	00:20	3 Ili, 3 Ica, 2 IS	1 galaxy group, 15 stars
6M	Mensa-Volans	06:03	3 Ili, 4 Ica, 2 IS, 5 Sli, 6 SO	LMC, 4 galaxies, 70 stars
7S	Ara-Pavo	00:22	3 Ili, 3 Ica, 1 IS	W6300 galaxy group, 6 globular clusters, 100 stars
8L	Aquarius-Pisces-Pegasus	15:52	6 Ili, 8 Ica, 4 IS, 10 Sli, 12 SO	Geocorona up-Sun, Pegasus Cluster and 10 galaxies, 32 stars
9S	Pornax-Eridanus	00:20.5	3 Ili, 3 Ica, 1 IS	Pornax Cluster, Eridanus group of galaxies, 29 stars
10M	Sagittarius	01:04	3 Ili, 4 Ica, 2 IS, 3 Sli, 1 SO	Milky Way center, many nebulae and globular clusters, 150 stars, Jupiter

<sup>1</sup>Three of the Ili frames of the Earth have exposures of 1, 5, and 15 sec, and all seven Ili frames are overlapped.

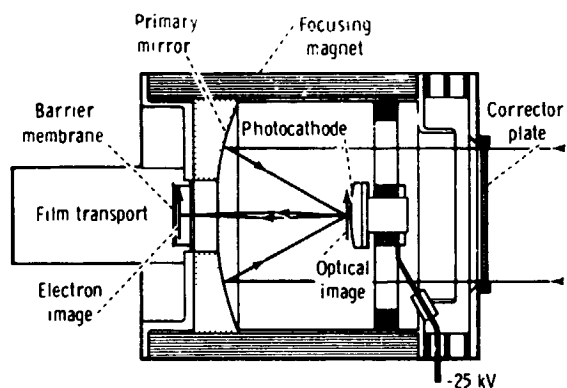


Figure 18-1.- Simplified cross section of the electronographic Schmidt camera.



Figure 18-2.- Far UV camera deployed in the LM shadow on April 22, 1972 (AS16-114-18439).

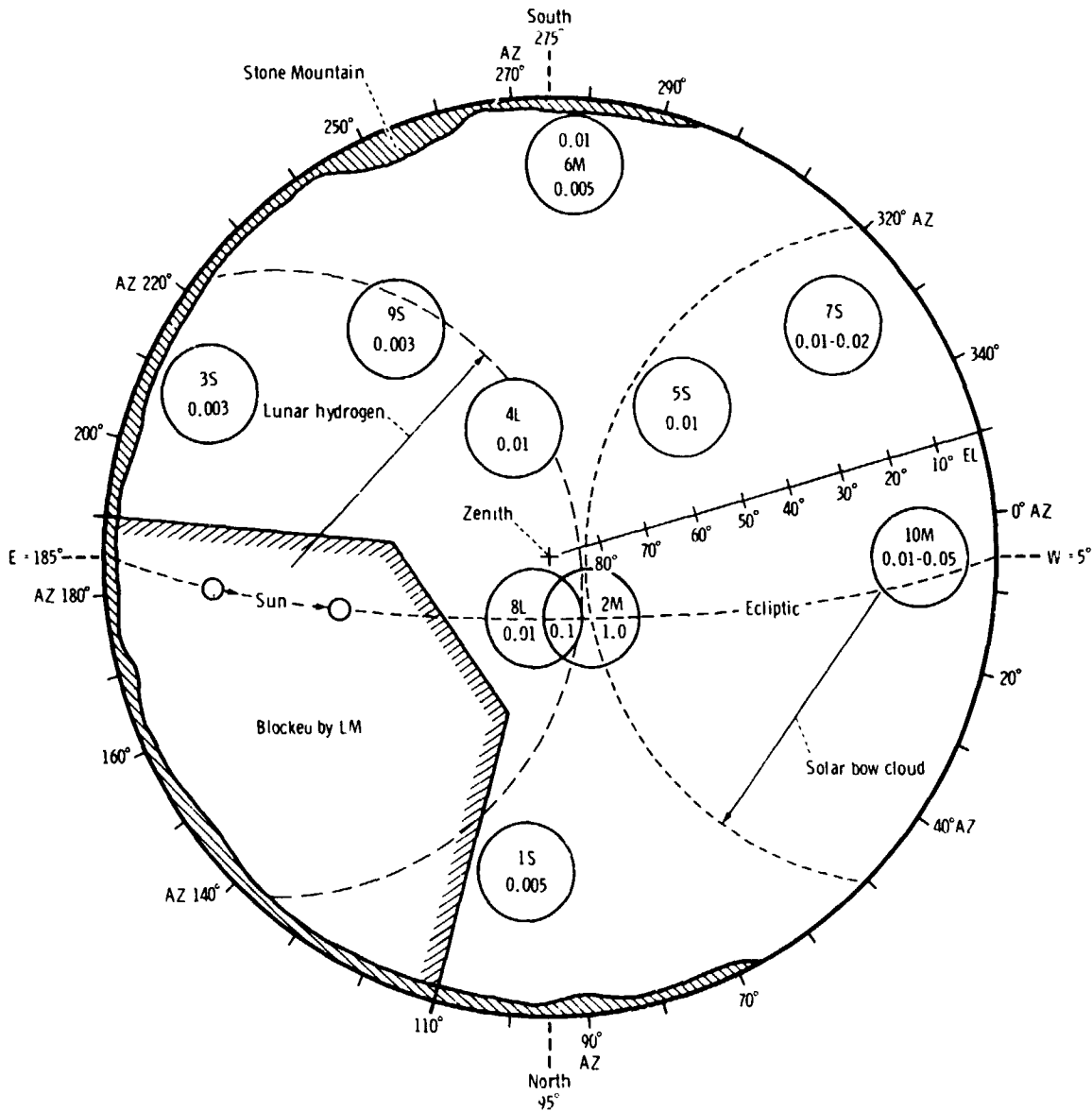


Figure 18-3.- Schematic representation of target pointings in the lunar sky from the Descartes site, an outside view of the celestial sphere of the camera. In each 20° circle are given the target number and a rough estimate of background Lyman-alpha surface brightness relative to the inner geocorona on target 2M. In two cases (targets 7S and 10M), there is a marked change across the field, and two ratios are given. The dashed circles show regions of predicted brightness caused by the lunar hydrogen atmosphere and the solar bow cloud.

SZ01  
UV CAMERA EXPERIMENT  
MISSION FRAME 40  
TARGET: EARTH  
EXPOSURE TIME: 1.00  
EXPOSURE DATE: 04/21/72  
  
SCAN SPEED 30  
DENSITY X 100  
SMOOTHED DATA  
  
MIN/MAX X COORD. 257 , 768  
MIN/MAX Y COORD. 257 , 768  
X/Y INTERVAL 33 , 33  
MINIMUM CONTOUR LEVEL 100  
MAXIMUM CONTOUR LEVEL 500  
CONTOUR INTERVAL 20

CORRECTED FOR DISTORTION

SZ01  
760035

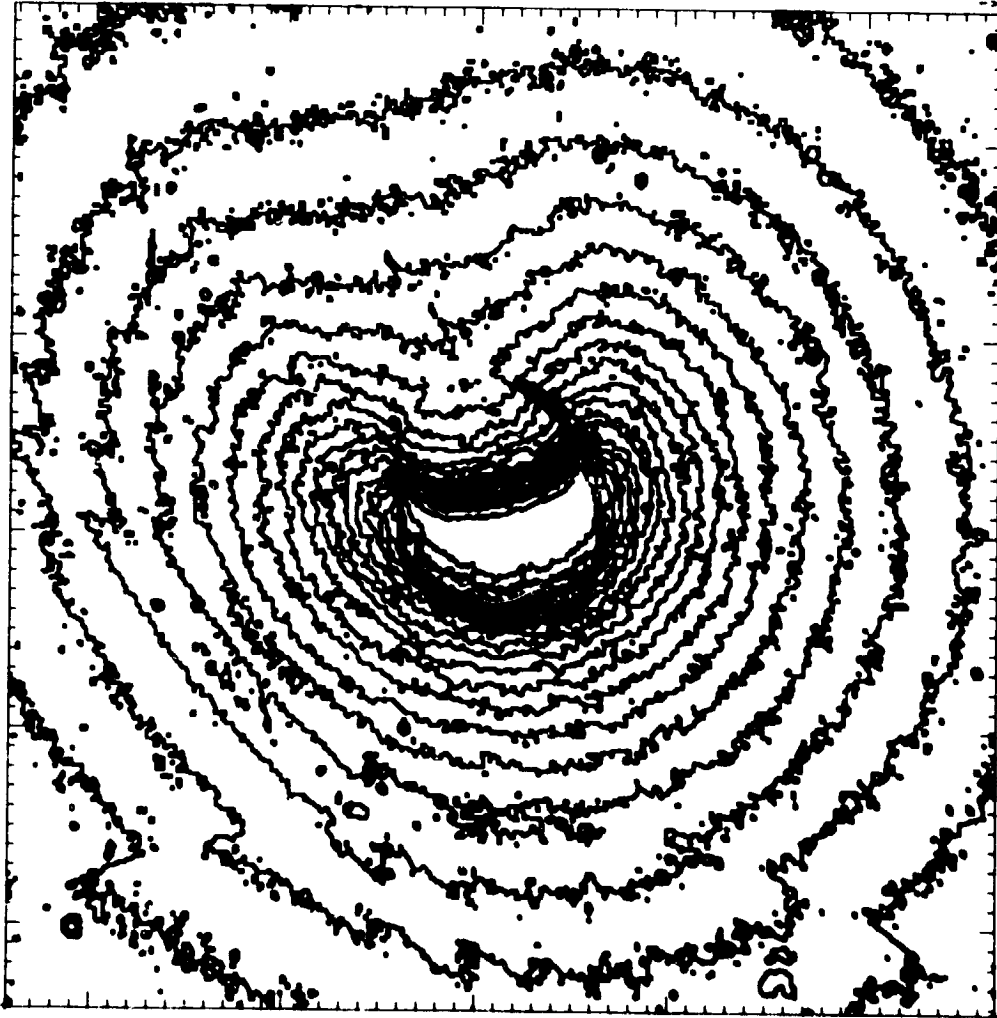


Figure 18.4.- Isodensity contour plot of the center 512 by 512 rasters of frame 40, a 60-sec Ili exposure of the Earth and geocorona (contour interval of 0.2 D). The overexposed Earth image at center is more than 5.0 D; the outer contour is 1.0 D.

5201  
UV CAMERA EXPERIMENT  
MISSION FRAME 45  
TARGET EARTH  
EXPOSURE TIME 10.00  
EXPOSURE DATE 04/21/72

SLAN SPEED 34  
DENSITY 8 100  
SMOOTHED DATA

MIN/MAX I COUNT: 157 1 449  
MIN/MAX V COUNT: 157 1 449  
X/Y INTERVAL: 33 33  
X/Y POSITION: 41 41  
POSITION: 101.0 101.0  
CONTOUR INTERVAL: 10

5201  
749036

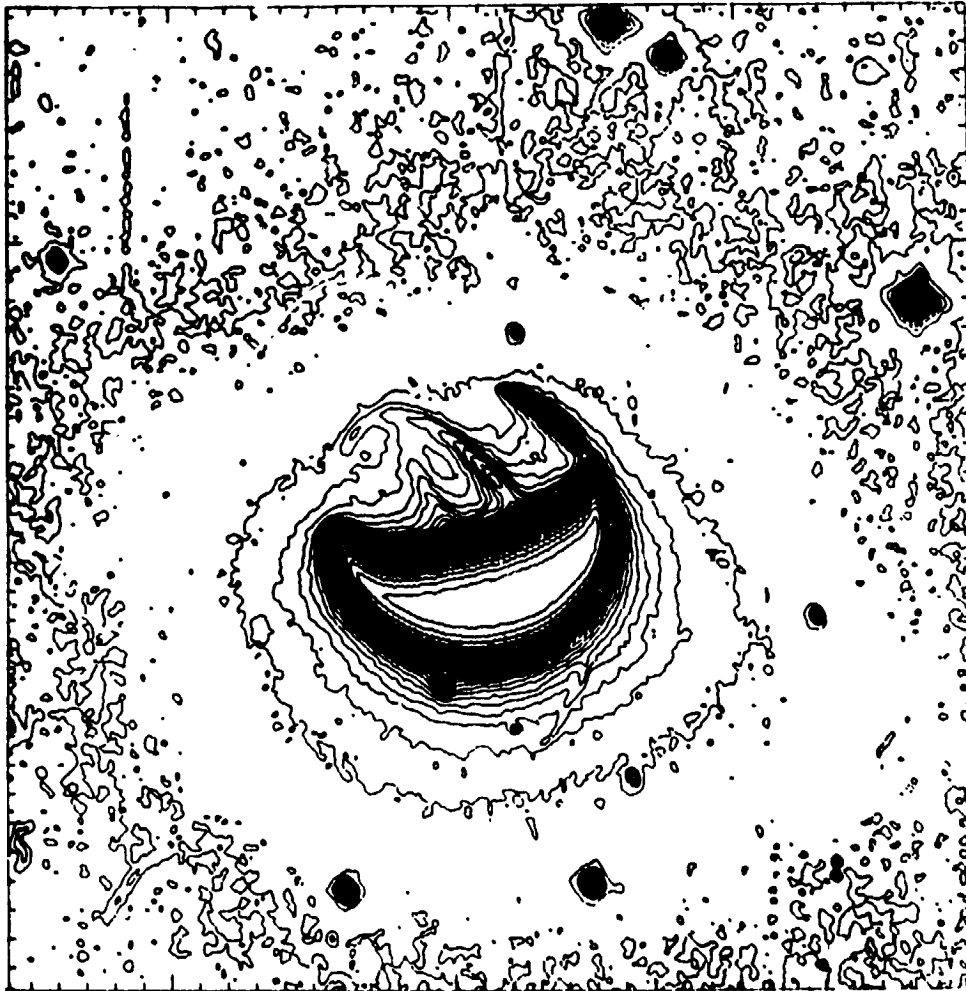
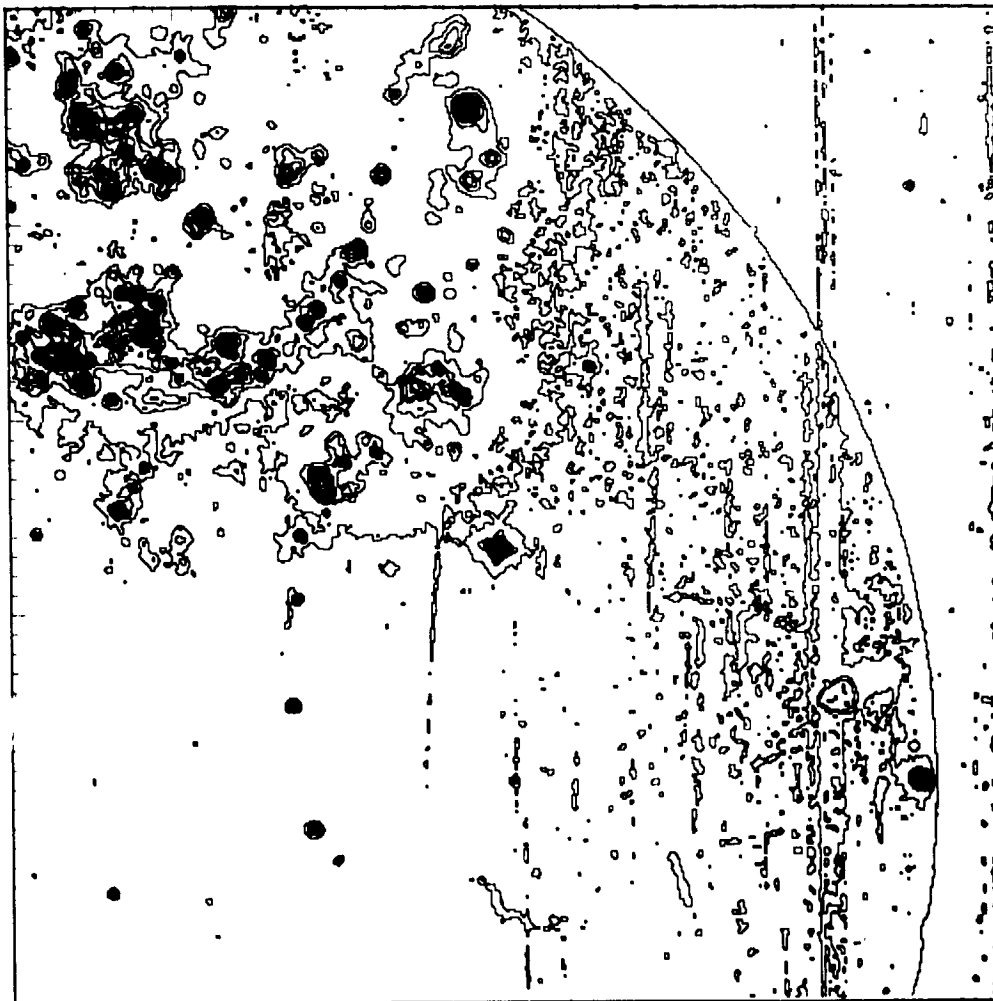


Figure 18-5.- Isodensity contour plot of the center 342 by 342 rasters of frame 45, a 10-min Ica exposure of the Earth and its airglow in 130.4-nm light of oxygen (contour interval of 0.1 D). The overexposed Earth image is more than 5.1 D; the outer contour is 0.2 D. The small, round blobs are blue stars.



5201  
 UV CAMERA EXPERIMENT  
 MISSION FRAME 129

SCAN SPEED 30  
 DENSITY X 100  
 SMOOTHED DATA

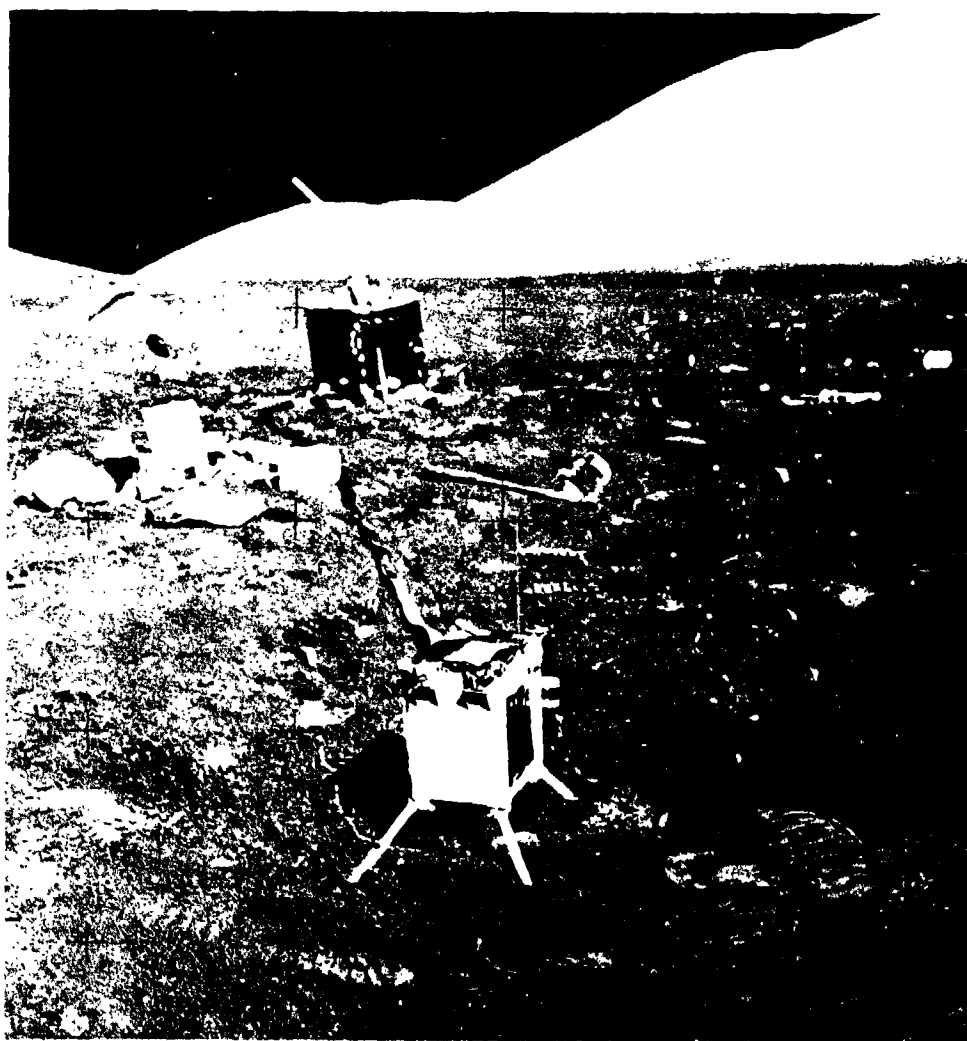
MIN/MAX X COORD 400 . 911  
 MIN/MAX Y COORD 513 . 1024  
 X/Y INTERVAL 33 . 33  
 MINIMUM CONTOUR LEVEL 20  
 MAXIMUM CONTOUR LEVEL 400  
 CONTOUR INTERVAL 20

FR 129  
 TRACE 1

Figure 18-6.- Isodensity contour plot of a quarter (512 by 512 rasters) of frame 129, a 10-min Ica exposure of the Large Magellanic Cloud (nearest galaxy), contour interval of 0.2 D. The large circle is the edge of the 20° field.

19. LUNAR EJECTA AND METEORITES EXPERIMENT  
(NASA EXPERIMENT S-202)

NSSDC IDENTIFICATION NUMBER:  
APOLLO 17 72-096C-05



CONTENTS - SECTION 19

	Page
DESCRIPTION . . . . .	19-3
DATA AND OPERATIONAL HISTORY . . . . .	19-4
DISCUSSION . . . . .	19-6
DATA TO BE ARCHIVED AT NSSDC . . . . .	19-6

## 19. LUNAR EJECTA AND METEORITES EXPERIMENT

The lunar ejecta and meteorites (LEAM) instrument was designed to measure the speed, direction, total energy (kinetic and potential), and momentum of primary cosmic dust particles and lunar ejecta.

### DESCRIPTION

The LEAM experiment consists of three sensor systems: the east sensor, the west sensor, and the up sensor. The basic sensor for each array, shown schematically in figure 19-1, consists of a front "A" film-grid sensor array and a rear "B" film-grid sensor array spaced 5 cm apart (film plane to film plane) and an acoustical impact plate on which the rear film is mounted.

The performance of the sensors depends on two basic measurable phenomena that occur when a hypervelocity particle impacts upon a surface: the formation of an ionized plasma and a transfer of momentum.

In conjunction with the following explanation of the experiment operation, refer to figure 19-1 and consider three probable types of cosmic dust particles:

1. A high-energy hypervelocity particle ( $>10^{-7}$  J ( $>1.0$  erg)).
2. A low-energy hypervelocity particle ( $<10^{-7}$  J ( $<1.0$  erg)).
3. A relatively large high-velocity particle ( $>10^{-10}$  g). This class includes the bulk of lunar ejecta particles.

As a high-energy hypervelocity particle enters the front film sensor, it yields some of its kinetic energy toward the generation of an ionized plasma at the front film. Electrons from the plasma are collected on the positively biased grid (+24 V), producing a negative-going pulse that is amplified as shown. The ions from the plasma are collected on the negatively biased film (-3.5 V), producing a positive-going pulse that is amplified as shown and pulse-height-analyzed as a measure of the kinetic energy

of the particle. As the particle continues on its path, it yields its remaining energy at the rear sensor film (and plate), generating a second set of plasma pulses and an acoustical pulse (if the momentum of the particle is sufficient). A pulse-height analysis is performed on the positive-going plasma pulse, and a peak pulse-height analysis is performed on the acoustical sensor output as a measure of the remaining momentum of the particle. The time lapse between the front film penetration (positive plasma pulse) and the rear film impact (positive plasma pulse) is recorded as the time-of-flight of the particle over a known distance and therefore the particle's speed.

As a low-energy hypervelocity particle enters the front sensor, it yields all its kinetic energy at the front film. A pulse-height analysis is performed on the positive output signal as a measure of the kinetic energy of the particle.

As a relatively large high-velocity particle enters the LEAM experiment, it may pass through the front and rear film sensor arrays without generating a detectable ionized plasma but still impart a measurable impulse to the acoustical sensor. In this event, a peak-pulse-height analysis is performed on the acoustical sensor output pulse.

The time-of-flight sensor, as described, represents one of 256 similar sensor systems that comprise the east and up sensor arrays. The west sensor array was designed specifically to record low-speed ejecta impacts on the microphone plate without retardation by a front film and consequently has no capability to measure particle speed. Figure 19-2 is an exploded schematic view of the overall experiment, showing that 4 vertical film strips are crossed by 4 horizontal grid strips to affect 16 front and 16 rear film sensor arrays (creating 256 possible combinations). Each grid strip and each film strip connects to a separate output amplifier. The output signals from these amplifiers are used to determine the segment in which an impact occurred. Thus, knowing what front film segment was penetrated and what rear film segment was affected by an impact, one can determine the direction of the incoming particle with respect to the sensor axis and eventually with respect to the Sun.

#### DATA AND OPERATIONAL HISTORY

The LEAM was deployed on the lunar surface on December 11, 1972, with the following lunar coordinates: latitude 20.164° N, longitude 30.770° E. The east sensor axis is directed 25° north of east to accommodate interstellar

grains. Accordingly, the west sensor is directed 25° south of west. Pointing accuracy for all sensors is ±2°.

When the LEAM was deployed on the lunar surface, the three sensors and thermal control mirrors were protected by covers to avoid dust contamination. The mirror covers were removed at a Sun angle of 135° during the first lunation. The sensor covers were commanded off at 09:57 G.m.t. on December 28, 1972, but were apparently removed at sunrise of the second lunation, which was 05:58 G.m.t. on January 9, 1973.

Because of the excessive operating temperatures of the LEAM experiments, the instrument was commanded off during the lunar day as follows:

<u>Off/On</u>	<u>Time, G.m.t.</u>	<u>Date</u>
Off	13:38	January 10, 1973
On	13:18	January 22, 1973
Off	05:38	February 8, 1973
On	12:47	February 20, 1973
Off	16:33	March 11, 1973
On	22:20	March 22, 1973
Off	05:10	April 10, 1973
On	16:07	April 22, 1973
Off	00:02	May 10, 1973
On	09:36	May 19, 1973
Off	21:52	June 8, 1973
On	12:38	June 18, 1973
Off	17:37	July 8, 1973
On	13:04	July 17, 1973

From July, 1973, to the date of this publication, the LEAM has been turned on, typically, 52 hr before sunset, and turned off, typically, 71 hr after sunrise.

The instrument is automatically calibrated every 15.4 hr. Two calibration modes are presented and separated by a 3.5-min interval.

#### DISCUSSION

Although the objectives set forth for the LEAM experiment were generally centered around measurements of the impact characteristics of cosmic dust and ejecta, it is now obvious that those measurements represent only a small fraction of the overall data events being registered by the LEAM. Most of the data events represent electrostatic lunar-soil transport. Evidence for this phenomenon was first manifest in a consistent enhancement of the numbers of events associated with the passage of the terminators.

Present conclusions concerning the phenomenon are that (1) it is strictly a lunar surface phenomenon triggered by sunlight, (2) the particles being transported are of the order of 1 micron in diameter; and (3) the particles are relatively slow moving ( $<1$  km/sec) and have a high surface charge ( $>10^{-14}$  C). The extent of the soil transport is such that, if one assumes a mass of  $10^{-12}$  g for the average particle, the churning rate for the east sensor becomes  $4 \times 10^{-18}$  g/cm<sup>2</sup>/sec or in 4.5 billion yr it becomes 0.6 g/cm<sup>2</sup>.

#### DATA TO BE ARCHIVED AT NSSDC

The following data will be available at the National Space Science Data Center (NSSDC):

1. Tapes and microfilm
  - a. Event tapes, disks, or cards
  - b. Microfilm of all changes, based on tabulation from baseline
2. Documentation
  - a. Description of experiment and equipment
  - b. Data history and operational history

---

c. Data processing manual (description of computer program and calibration information)

d. Analytical steps required to obtain event tapes

e. Photograph frame numbers used in analysis

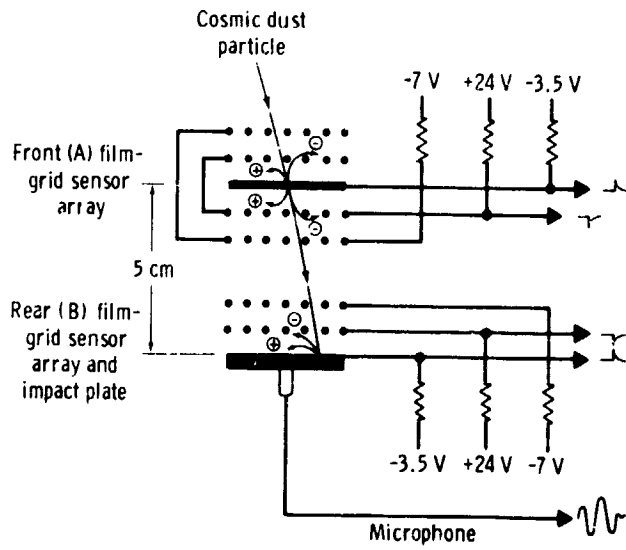
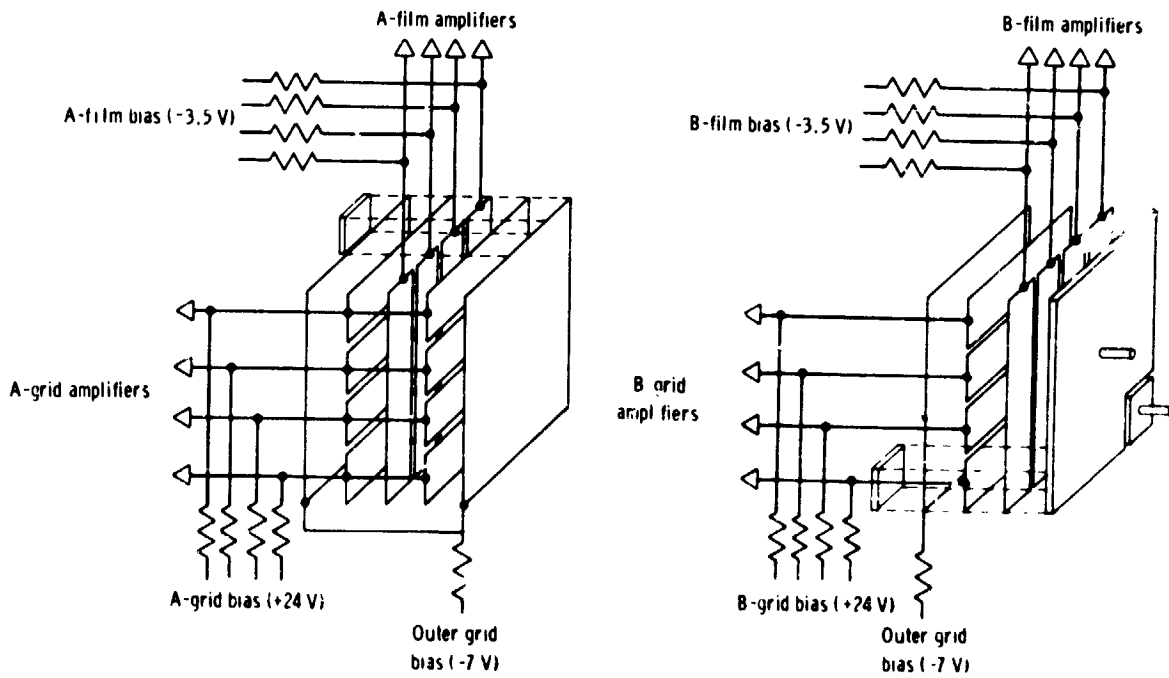


Figure 19-1.- Basic sensor for each array.



(a) Front sensor array.

(b) Rear sensor array.

Figure 19-2.- Exploded schematic of LEAM experiment.

20. SURFACE ELECTRICAL PROPERTIES (NASA EXPERIMENT S-204)

NSSDC IDENTIFICATION NUMBER:

APOLLO 17 72-096C-07



ORIGINAL PAGE IS  
OF POOR QUALITY

---

CONTENTS - SECTION 20

	Page
BACKGROUND . . . . .	20-3
OPERATIONAL HISTORY . . . . .	20-5
DATA AND DISCUSSION . . . . .	20-5
CONCLUSIONS . . . . .	20-8
DATA SUBMITTED TO NSSDC . . . . .	20-9
REFERENCES . . . . .	20-11

## 20. SURFACE ELECTRICAL PROPERTIES

The surface electrical properties (SEP) experiment was flown to the Taurus-Littrow region of the Moon on the Apollo 17 mission. The experiment used megahertz radiofrequencies to determine the following:

1. Electrical layering at the landing site
2. Dielectric properties of the surface material in situ
3. Presence of scattering bodies

To sound into the surface layers, a relatively new technique, radiofrequency interferometry (RFI), was developed for the lunar experiment and was tested extensively on Earth. A transmitter was placed on the lunar surface, and a receiver was carried on the lunar roving vehicle (LRV). As the LRV moved along its traverse, the received magnetic field strength and the position of the LRV with respect to the transmitter were recorded.

At any point on the traverse, several waves reach the receiver, and these waves form interference patterns as shown in figure 20-1. The interference pattern is diagnostic both of the physical properties and of the structure of the upper layers. Field strength data for six frequencies and six combinations of receiving and transmitting antenna orientation (for a total of 36 readings), together with position, calibration, and temperature information, were recorded on a magnetic tape that was returned to Earth. The basis for the interferometry concept and details of the SEP experiment are contained in references 20-1 to 20-5.

### BACKGROUND

Because radio interferometry is a relatively new technique, most of the background experience was acquired explicitly for the lunar experiment. There are three main facets.

1. Theoretical evaluation of the electromagnetic fields surrounding a dipole antenna over a dielectric medium

2. Experimental work by use of an analog scale model
3. Field work on several different glaciers for full-scale experiments

Although the integral expressions for the electromagnetic fields surrounding a dipole antenna over a half-space have been known for some time (e.g., ref. 20-6), their evaluation for layered media with completely general electrical properties is far from insignificant. Straight numerical integration is prohibitively expensive; therefore, three complementary approximate methods were used - a geometric optics approach, the theory of normal modes, and fast Fourier transform (FFT) techniques. The geometric optics formulation (refs. 20-1, 20-4, 20-7, and 20-8) is most accurate for "optically thick" layers and becomes invalid for distances less than about a wavelength. Theoretical curves are most easily calculated with the normal mode formulation for thin layers in which only a few modes propagate. The use of the FFT technique allows the calculation of theoretical interference patterns for models in which the electrical properties vary continuously with depth.

For checking these calculations and for studying cases too complex for theoretical treatment, a scale model was constructed in which microwave frequencies were used. The model consisted of a layer of dielectric oil in which a reflecting plate could be set up in many different orientations. A typical suite of model curves for the layered case of a dielectric over a perfect reflector is shown in figure 20-2, together with the corresponding theoretical curves. The inaccuracy of the geometric optics solution for thin layers is readily apparent.

Field experience with the RFI technique was gained on trips to the Gornier and Athabasca Glaciers (ref. 20-2) and to the Juneau Icefields, using lunar hardware at various stages of development. Because most of the glaciers were known, from independent work, to approximate plane layered media, it was possible to match observed data with curves obtained from the geometric optics formulation for layered media. In the analysis of the glacier field data, trial-and-error suites of theoretical curves were compared with field data. Attempts at formal inversion are currently underway.

A typical set of field profiles for the glacier tests and their corresponding "best fit" theoretical curves are shown in figure 20-3. No single frequency or component was uniquely indicative of the parameters (dielectric constant, loss tangent, and depth to reflector). However, if one

accepts only parameter sets that give consistent, good (but not perfect) fits for all frequencies, and for both of the maximum-coupled components for which there are theoretical solutions, then an "acceptable" interpretation can always be found.

#### OPERATIONAL HISTORY

The SEP experiment was performed at the Apollo 17 Taurus-Littrow landing site. The transmitting dipole antennas were deployed approximately 150 m east of the lunar module (LM) in a north-south and an east-west direction (fig. 20-4). During extravehicular activity (EVA) 2, SEP data were recorded as the LRV moved in a westerly direction away from the SEP transmitter toward station 2. The traverse as reconstructed from the SEP-LRV navigation data is given in figure 20-5.

From the SEP transmitter out to a range of 1.7 km, the receiver operated normally. Between 1.7 and 4.3 km, the receiver operated in an acquisition mode, attempting to acquire a synchronization signal from the transmitter. In the acquisition mode, only partial data were collected. At a range of 4.3 km, because of the low received field strength, the receiver obtained a false resynchronizing pulse that caused an incorrect realignment of receiver and transmitter timing and a subsequent loss of field strength data beyond 4.3 km. At station 2, the receiver was turned off to aid in cooling. The receiver was operating again between stations 4 and 5; however, the signal levels were too low to allow a resynchronization with the transmitter. At the beginning of the station 5 stop, the receiver was turned off. The receiver was turned on again at the end of the station stop; however, because the internal receiver temperature was above a safe limit, a thermal switch prevented receiver operation for the remainder of EVA-2.

Data were to have been recorded during EVA-3 from the SEP transmitter to station 6, but the astronauts failed to turn on the receiver. Therefore, the data used as a basis for this discussion are those taken from the SEP transmitter westward to a range of 4.3 km.

#### DATA AND DISCUSSION

In the RFI technique, electromagnetic waves of six frequencies (1, 2, 4, 8, 16, and 32 MHz) are transmitted sequentially by two orthogonal, horizontal dipole antennas

and received by three orthogonal, selectrically small, loop antennas, resulting in 36 readings of the field strength during each measurement cycle.

Positional information from the LRV navigation system is recorded as increments and decrements of  $1^\circ$  in bearing and 100 m in range and as odometer pulses, each equivalent to a 0.49-m change in position for the right-front and left-rear wheels of the LRV.

The LRV traverse data derived from SEP data are compared in table 20-I with traverse data produced by the United States Geological Survey (USGS) (ref. 20-9) and with the traverse reconstruction created from the NASA Goddard Space Flight Center very long baseline interferometry (VLBI) data.<sup>1</sup> The VLBI data have an absolute accuracy of approximately 40 m. The USGS traverse data are taken from photographic panoramas made at station stops and are accurate to approximately 10 m for explosive package 4 (EP-4), LRV-1, and station 2 and to approximately 50 m for LRV-2 and LRV-3.

The three traverses are plotted in figure 20-6. The maximum differences are approximately 500 m at stops LRV-2 and LRV-3. The differences between USGS and VLBI traverses are larger than expected, and later adjustments of the data may improve the agreement among the three sets. For the first 2 km, all three reconstructions are in good agreement. An example of SEP field strength data is shown in figure 20-7. Each plot contains either the endfire or the broadside components for one frequency, plotted as a function of range, in free-space wavelengths. The data are plotted for a maximum distance of 1.7 km or to 20 free-space wavelengths.

For each frequency, six components are measured. Three components ( $H_\phi$  endfire and  $H_\rho$  and  $H_z$  broadside) are maximum-coupled for a plane, layered geometry, whereas the other three are minimum-coupled to the transmitted signal. For all six frequencies, the maximum-coupled components have an average level from 5 to 15 dB greater than the minimum-coupled components. These results are in direct contrast to glacial observations. For all the glacier runs, the maximum- and minimum-coupled components were approximately equal in level at 6 and 32 MHz. This rough equality of signal level was attributed to the presence of random scatterers (e.g., crevasses) in the ice with dimensions on the order of a wavelength. On this basis, the inference is that few scattering bodies having typical sizes of 10 to 300 m and contrasting dielectric properties are present in the

---

<sup>1</sup>I. Salzberg, personal communication, Jan. 1974.

subsurface near the lunar SEP site. Scattering experiments both in the scale model and on glaciers support this inference.

Further confirmation is obtained by an examination of the  $H_\phi$  endfire component. This component has a near-surface wave so large that it effectively masks any interference. However, if near-surface scattering is important, this component becomes erratic. Data indicate this component is relatively smooth at all SEP frequencies. The residual peaks and nulls correlate well with those in the  $H_\rho$  broadside component. Therefore, it is believed that these two components are slightly mixed because the traverse was not completely east-west (i.e., not directly off the end of the endfire antenna).

The other two maximum-coupled components ( $H_\rho$  and  $H_z$  broadside) have been the most important for interpretation (fig. 20-8). At 16 and 32 MHz, the number of peaks and troughs per free-space wavelength of range is fairly low, indicating a dielectric constant of approximately 2 to 5. However, the lower frequencies show somewhat higher beating rates, indicating a dielectric constant of approximately 6 to 8, and certainly less than 10. These observations imply that the dielectric constant of the near-surface material is lower than that of the deeper material. These results are consistent with the dielectric properties of a soil layer over solid rock, as measured on returned samples (e.g., ref. 20-10).

The loss tangent is estimated from the sharpness of the peaks and nulls in the two major components and from the average decay of the field strength with distance. The analysis indicates that the average loss tangent of the subsurface material to a depth of several hundred meters is less than 0.05 and possibly as low as 0.002. The fact that the higher frequencies have strong signal levels for many tens of wavelengths from the transmitter, whereas the lower frequencies die out relatively quickly, indicates that the loss tangent of the near-surface material is 0.01 or less. These low loss values confirm that no liquid water is present in the outer kilometer of the Moon.

Structure is more difficult to determine unambiguously. By comparing the two major components with suites of theoretical curves for a plane, two-layer geometry (i.e., dielectric layer over a dielectric half-space), no single set of parameters has been found that gives theoretical curves in satisfactory agreement with the data at all frequencies. Several perturbations from the two-layer model have therefore been suggested.

One possible variation is a model that reflects a thinning layer of soil over rock. The layer is 20 m thick near the SEP site, with dielectric constant of 3 to 4, and thins to 15 m a few hundred meters to the west. The lower material has a dielectric constant of 6 to 7. Results from the lunar seismic profiling experiment, conducted over the same region, show good agreement with this model (ref. 20-11). The chief basis for this interpretation is the curve for 2 MHz broadside (fig. 20-8), which shows little interference out to a range of approximately 4 wavelengths but then has several dramatic peaks. This behavior suggests that the layer is just thick enough near the transmitter that little energy is transmitted either through the layer or through the subsurface. However, further from the transmitter, the layer becomes so thin that it is essentially transparent. Although theoretical formulations for sloping interfaces have not been obtained, interference patterns for sloping glacier interfaces and for the microwave model that resemble the lunar pattern have been observed.

Table 20-II contains the parameters of a three-layer model. In this model, the following assumptions are made: (1) that layer 1 is so thin that it is essentially transparent to all frequencies except 16 and 32 MHz and (2) that the boundary between layers 2 and 3 is too deep to have much effect on the 16- and 32-MHz patterns. Typical theoretical curves for this model are shown for comparison with the data in figure 20-8. Although the major features of the data are present also in the theoretical curves, the details are not always in good agreement. This lack of agreement may be due to slight adjustments in loss tangent (i.e., the particular features in most curves are very dependent on the loss tangent), or due to slight dipping of the interfaces (as mentioned previously).

#### CONCLUSIONS

Despite the present inability to match the lunar SEP observations with the theoretical curves calculated for various models, it is believed that the gross electrical properties of the Taurus-Littrow region have been obtained. At the present stage of the analysis of the lunar data, the following conclusions can be made.

1. The loss tangent of the lunar material in situ is less than 0.05 and possibly as low as 0.002, to depths of 2 to 3 km.

2. No liquid water is present at Taurus-Littrow to a depth of 2 to 3 km.

3. Electromagnetic scattering is not important at any of the SEP frequencies.

4. Scattering bodies as large as 10 to 300 m are not present in the vicinity of the traverse from the SEP site to station 2.

5. The relative dielectric constant is approximately 3.5 near the surface and increases with depth to a value of 6 to 8 at approximately 100 m. These values are consistent with the values expected for lunar soil overlying rock.

6. No model consisting of plane layers has been found that fits the observations accurately. Some features of a thinning layer, a three-layer model, and continuously increasing dielectric properties match some of the features of the observed interference patterns.

7. The LRV navigation data recorded on EVA-2 to station 2 agree well with VLBI and USGS traverse reconstructions.

#### DATA SUBMITTED TO NSSDC

The raw SEP data were digitized and demultiplexed at the NASA Lyndon B. Johnson Space Center and submitted to the National Space Science Data Center (NSSDC). The resulting tape contains the following data.

1. Receiver operating mode compared to time
2. Receiver temperature compared to time
3. Received-signal strength during times when the transmitter was turned off (six detection frequencies, three components)
4. Receiver calibration signals - detection of calibrated noise sources (six detection frequencies, three sources (front-end grounded, noise-diode input, and noise-diode input with 20-dB amplification))
5. Data for each experiment frequency: (a) range compared to time array and (b) detected signal strength compared to time for six components (two transmitter antennas and three receiver antennas (2 X 3 = 6))

The navigation data on this tape will be derived from the SEP-LRV navigation data.

A second tape will contain the same science and calibration data, but navigation data will be derived from a combination of VLBI and SEP navigation data. This will be the best estimate (from all sources) of position compared to time.

Microfilm printouts and plots corresponding to each of the data sets will be submitted.

## REFERENCES

- 20-1. Annan, A. P.: Radio Interferometry Depth Sounding: Part I - Theoretical Discussion. Geophysics, vol. 38, no. 3, June 1973, pp. 557-580.
- 20-2. Rossiter, James R.; LaTorraca, Gerald A.; Annan, A. Peter; Strangway, David W.; and Simmons, Gene: Radio Interferometry Depth Sounding: Part II - Experimental Results. Geophysics, vol. 38, no. 3, June 1973, pp. 581-599.
- 20-3. Simmons, G.; Strangway, D. W.; Bannister, L.; Baker, R.; et al.: The Surface Electrical Properties Experiment. Lunar Geophysics: Proceedings of a Conference at the Lunar Science Institute, Houston, Tex., Oct. 18-21, 1971, D. Reidel Pub. Co. (Dordrecht, Holland), 1973, pp. 258-271.
- 20-4. Tsang, L.; Kong, J. A.; and Simmons, Gene: Interference Patterns of a Horizontal Electric Dipole Over Layered Dielectric Media. J. Geophys. Res., vol. 78, no. 17, June 10, 1973, pp. 3287-3300.
- 20-5. Simmons, Gene; Strangway, David; Annan, Peter; Baker, Richard; et al.: Surface Electrical Properties Experiment. Sec. 15 of Apollo 17 Preliminary Science Report, NASA SP-330, 1973.
- 20-6. Baños, Alfredo, Jr.: Dipole Radiation in the Presence of a Conducting Half-Space. Pergamon Press (New York), 1966.
- 20-7. Annan, A. P.: Radio Interferometry Depth Sounding. M.S. Thesis, Univ. of Toronto, 1970.
- 20-8. Kong, J. A.: Electromagnetic Fields Due to Dipole Antennas Over Stratified Anisotropic Media. Geophysics, vol. 37, no. 6, Dec. 1972, pp. 985-996.
- 20-9. Muehlberger, W. R.; Batson, R. M.; Cernan, E. A.; Freeman, V. L.; et al.: Preliminary Geologic Investigation of the Apollo 17 Landing Site. Sec. 6 of Apollo 17 Preliminary Science Report, NASA SP-330, 1973.

- 20-10. Olhoeft, G. R.; Strangway, D. W.; and Frisillo, A. L.: Lunar Sample Electrical Properties. Proceedings of the Fourth Lunar Science Conference, vol. 3, Pergamon Press (New York), 1973, pp. 3133-3149.
- 20-11. Watkins, J. S.; and Kovach, R. L.: Seismic Investigation of the Lunar Regolith. Proceedings of the Fourth Lunar Science Conference, vol. 3, Pergamon Press (New York), 1973, pp. 2561-2574.

TABLE '0-I.- COMPARISON OF EVA-2 TRAVERSE STCPS FROM USGS, VLBI,  
AND SEP-LRV NAVIGATION DATA (See fig. 20-6)

Station	Range, km			Bearing, deg		
	VLBI	USGS	SEP-LRV navigation data	VLBI	USGS	SEP-LRV navigation data
SEP-4	0.500	0.538	0.508	80.4	80	83
LRV-1	2.603	2.603	2.645	80.9	78	82
LRV-2	3.750	3.729	3.811	81.4	86	83
LRV-3	4.248	4.253	4.325	80.2	87	82
Hole in the Wall	5.638	--	5.683	79.5	--	81
Station 2	--	7.46	7.6	--	68	71

Explosive package 4.

TABLE 20-II.- PARAMETERS FOR THREE-LAYER MODEL (See fig. 20-8)

Layer	Depth, m	Dielectric constant	Loss tangent
1	$7 \pm 1$	$3.8 \pm 0.2$	$0.008 \pm 0.004$
2	$100 \pm 10$	$7.5 \pm .5$	$.035 \pm .025$
3	0	9(?)	(?)

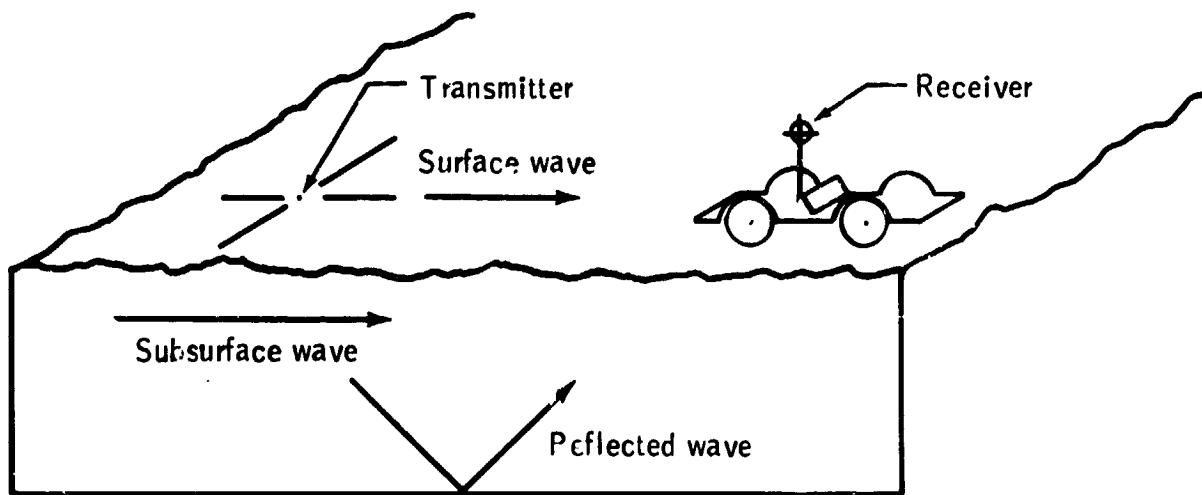


Figure 20-1.- The three main waves used in radio interferometry. The surface wave travels above the surface of the dielectric, and the subsurface wave travels just below the surface. Because the two waves travel at different velocities, their beat frequency is a function of the dielectric constant. Any reflected waves from a subsurface horizon also influence the interference pattern.

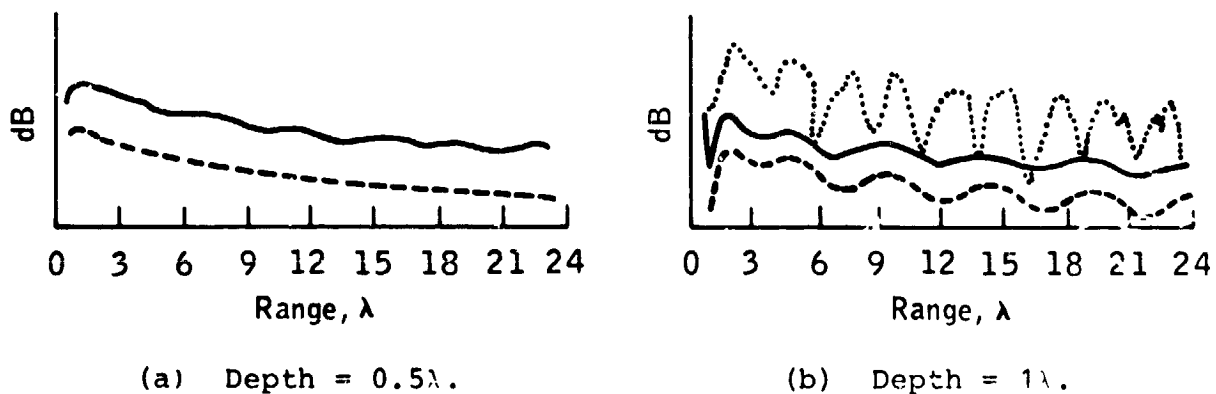
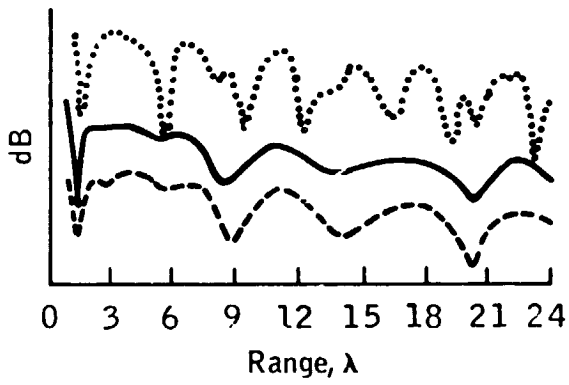
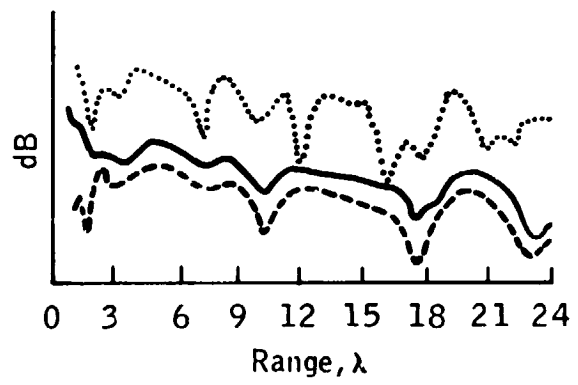


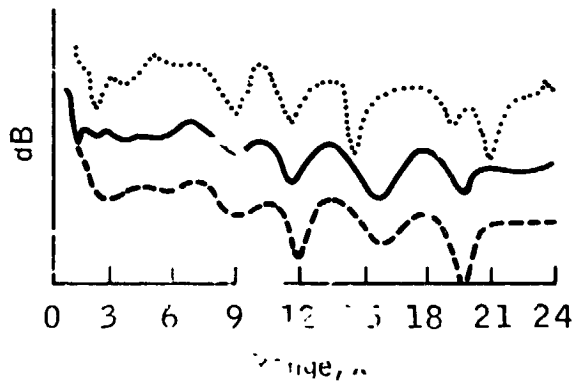
Figure 20-2.- Theoretical solutions and scale-model data for a dielectric over a perfect reflector for various reflector depths. The dielectric constant is 2.16, and the loss tangent is 0.0022. The range is in free-space wavelengths  $\lambda$ . The scale-model data are represented by solid-line curves, the geometric optics solution by dotted lines, and the normal mode solution by dashed lines.



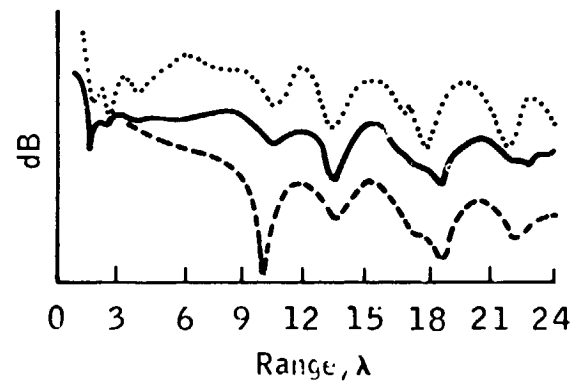
(c) Depth =  $1.5\lambda$ .



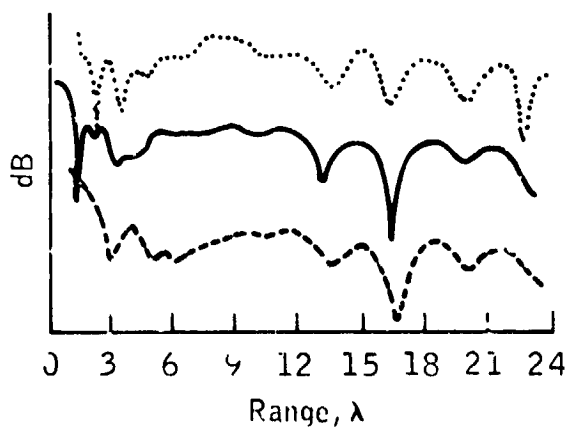
(d) Depth =  $2\lambda$ .



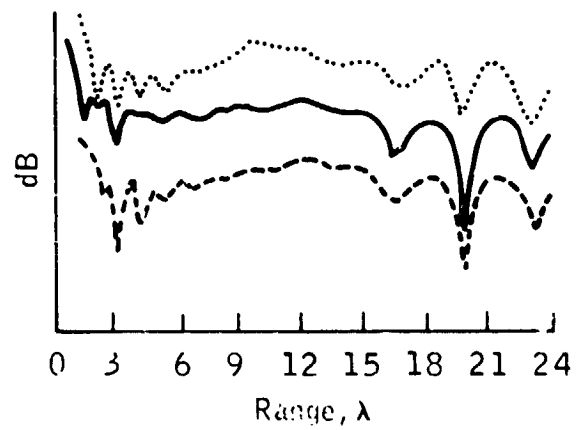
(e) Depth =  $2.5\lambda$ .



(f) Depth =  $3\lambda$ .



(g) Depth =  $4\lambda$ .



(h) Depth =  $5\lambda$ .

Figure 20-2.- Continued.

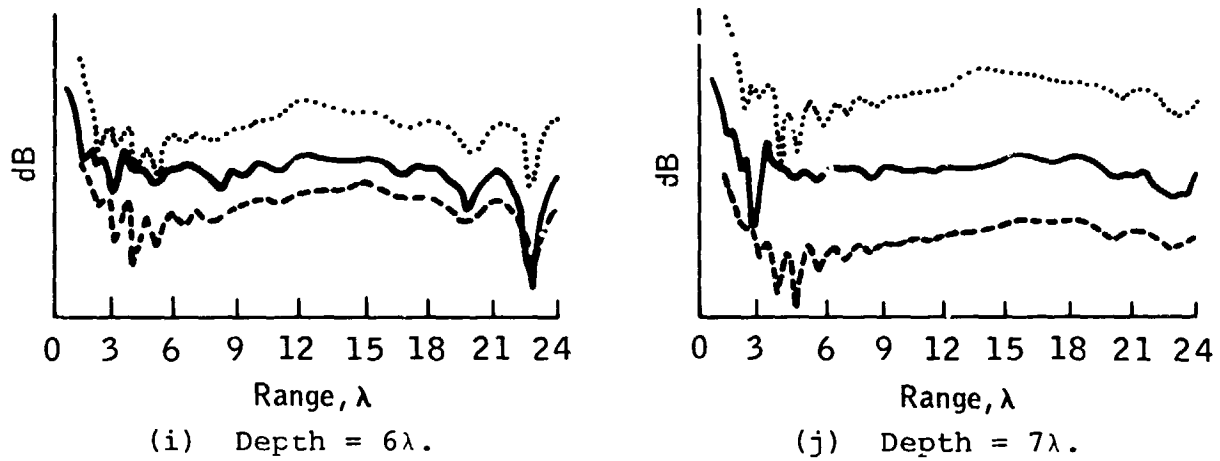


Figure 20-2.- Concluded.

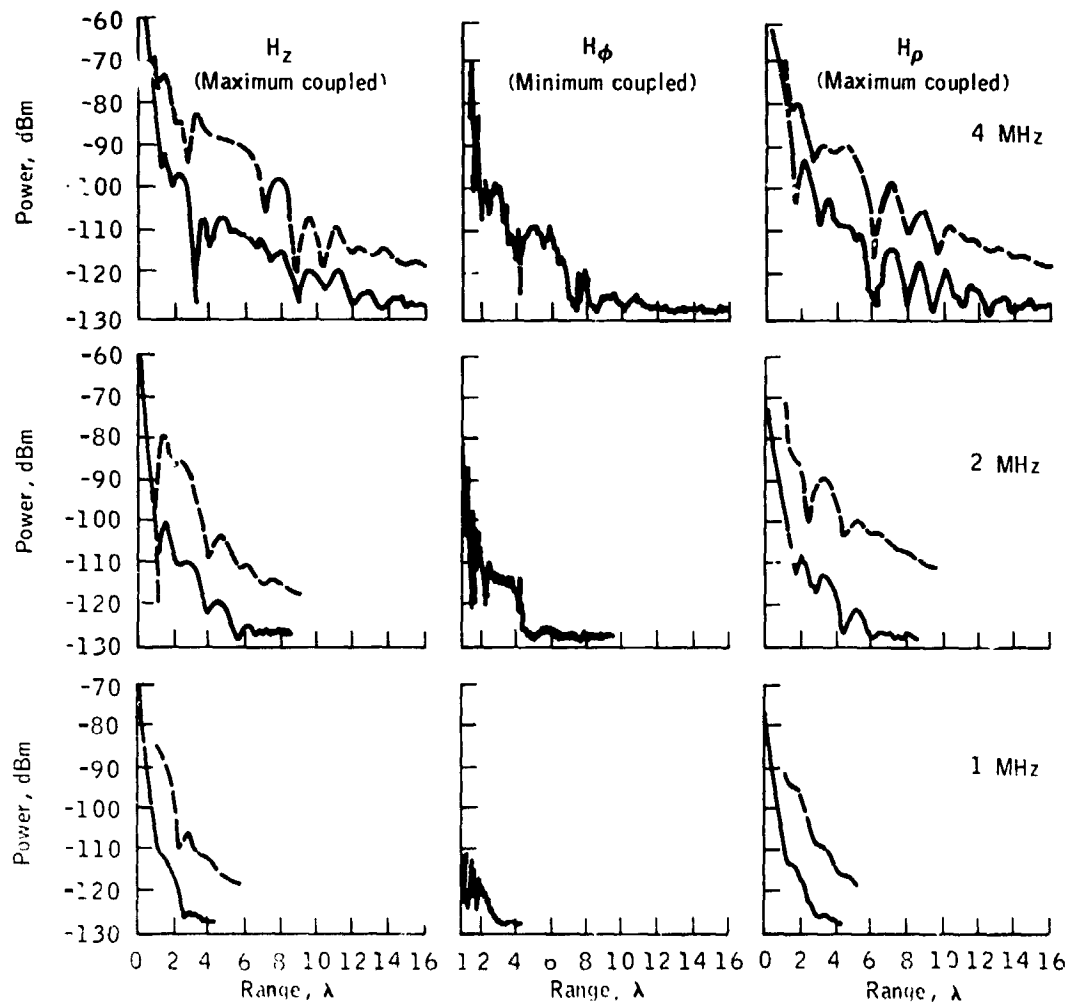


Figure 20-3.- Typical RFI data for the Athabasca Glacier (solid lines) and a set of theoretical curves (dashed lines).

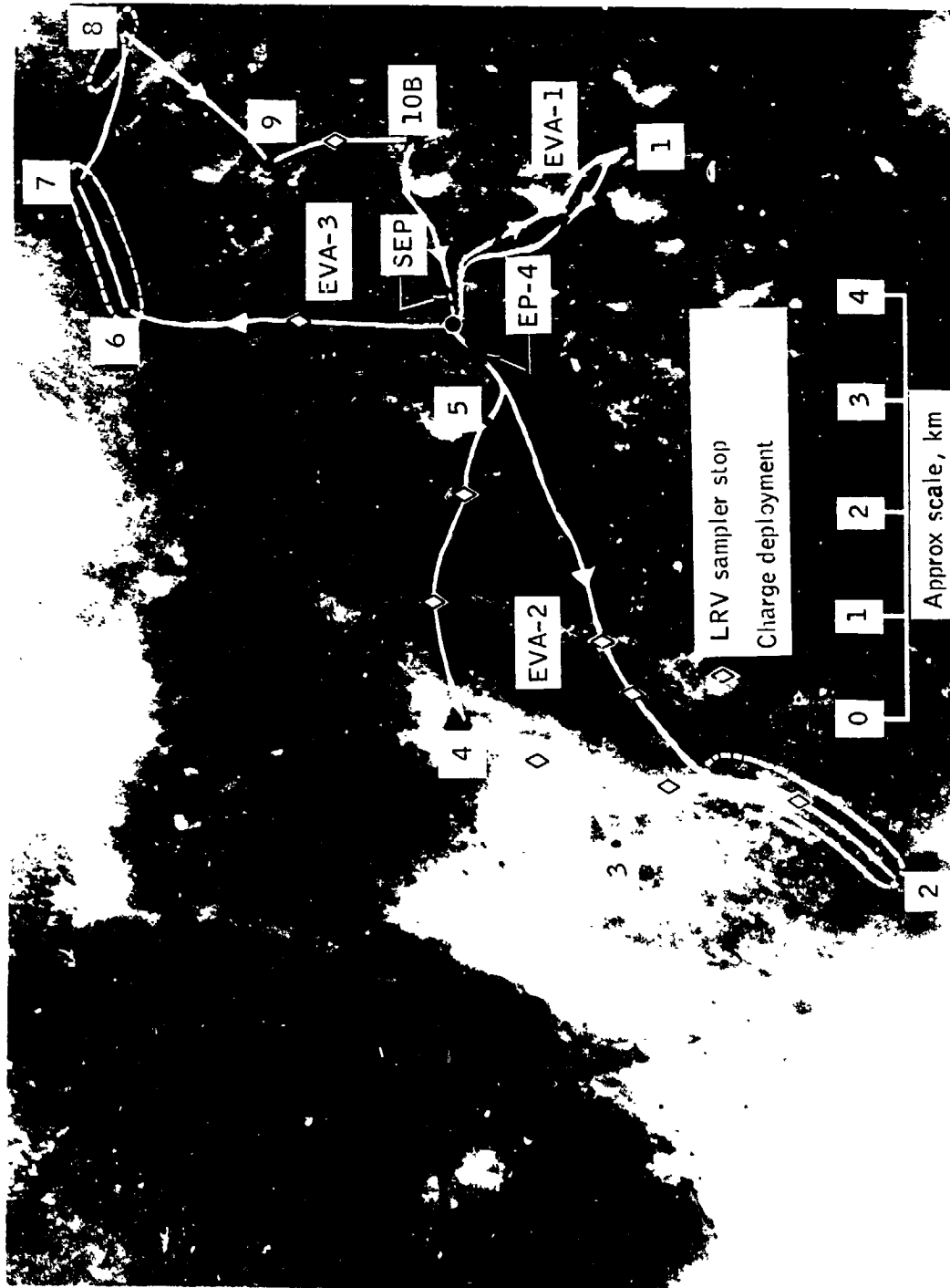


Figure 20-4.- Photograph of the Taurus-Littrow site with superimposed information that shows the locations of traverses, major station stops, SEP transmitter site, and the explosive package (EP-4). The SEP data were collected for a distance of 4 km along the traverse from the SEP site toward station 2.

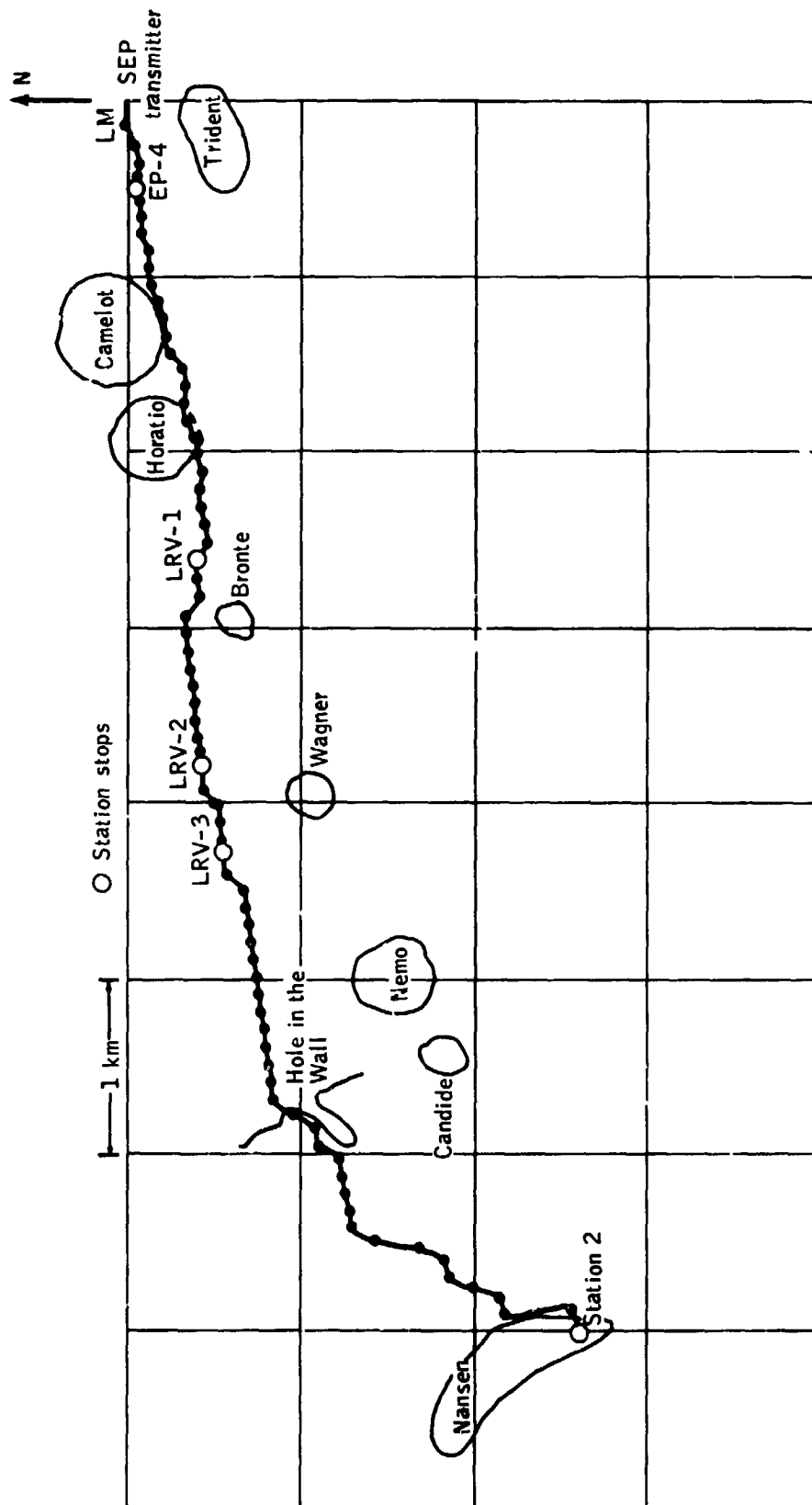


Figure 20-5.- Map of the EVA-2 traverse, based on LRV navigation data, from the SEP site to station 2. The LRV stops are indicated by LRV-1, LRV-2, and LRV-3.

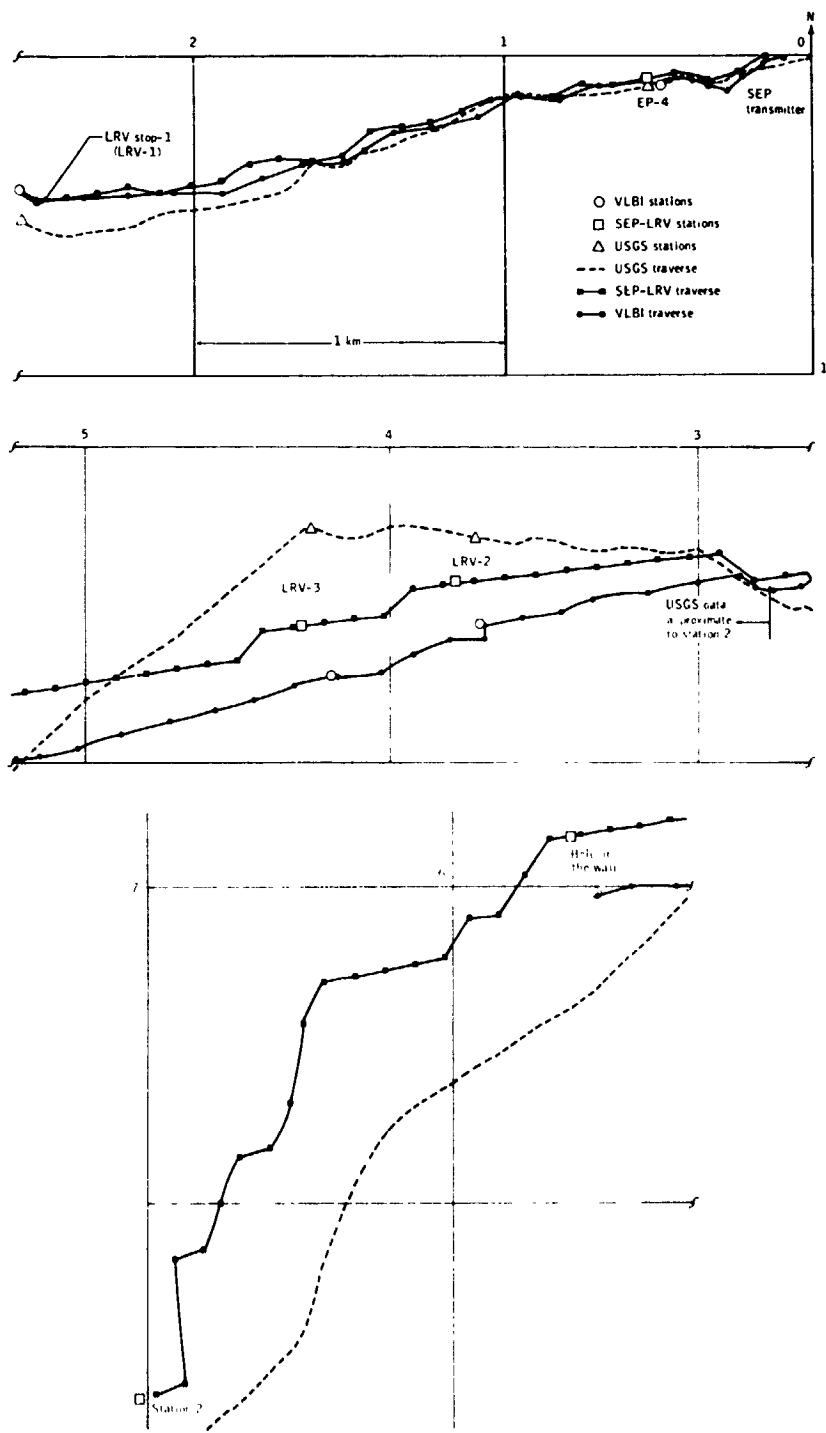


Figure 20-6.- The EVA-2 traverse construction as compiled from LRV navigation data recorded by the SEP experiment, the VLBI data, and the USGS traverse reconstruction from photographic information. The three independent reconstructions compare favorably to a distance of 3 km but disagree more than expected near LRV-2 and LRV-3 at a distance of approximately 4 km.

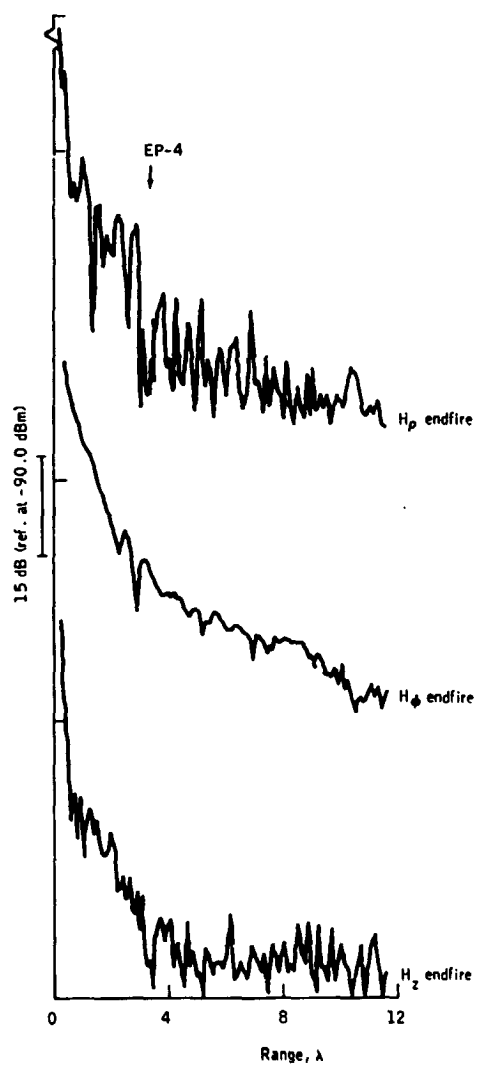


Figure 20-7.- A portion of the SEP experiment data (2.1 MHz) for all 36 "components." Each component has been plotted as a function of free-space wavelength to a maximum of 1.7 km or 20 wavelengths (whichever is smaller). The vertical scale is in decibels, with a reference at -90 dBm as shown. The component is labeled at the end of the curve:  $H_\phi$  endfire is maximum-coupled;  $H_\rho$  endfire and  $H_z$  endfire are minimum-coupled.

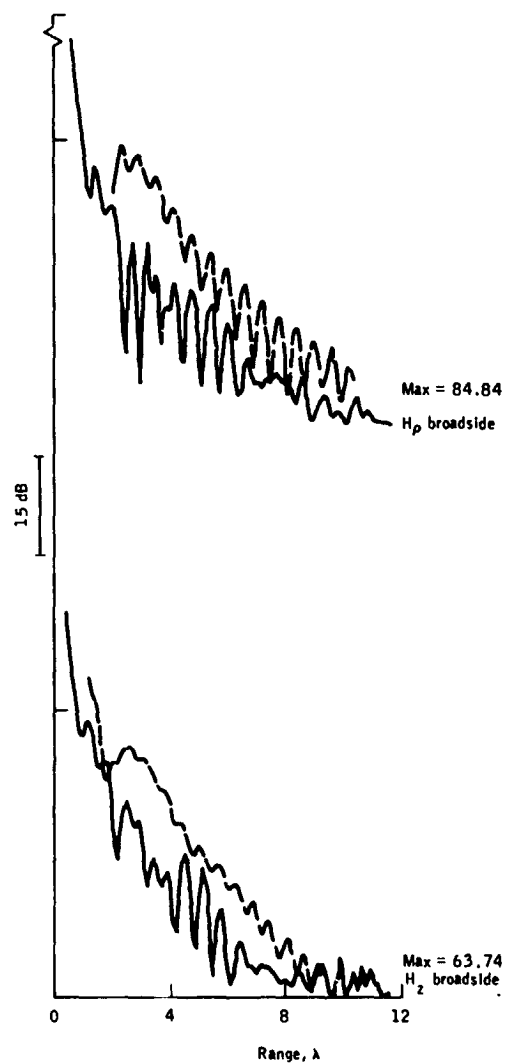


Figure 20-8.- A partial comparison (2 MHz) of the theoretical curves (dashed lines) with observed data (solid lines). The parameters for this model are given in table 20-II.

21. LUNAR ATMOSPHERIC COMPOSITION EXPERIMENT

(NASA EXPERIMENT S-205)

NSSDC IDENTIFICATION NUMBER:

APOLLO 17 72-096C-08



---

CONTENTS - SECTION 21

	Page
INSTRUMENT DESCRIPTION . . . . .	21-3
AVAILABILITY OF DATA . . . . .	21-6
FORMAT OF DATA . . . . .	21-6
BIBLIOGRAPHY . . . . .	21-9

## 21. LUNAR ATMOSPHERIC COMPOSITION EXPERIMENT

On the Apollo 17 mission, a miniature mass spectrometer, called the lunar atmospheric composition experiment (LACE), was carried to the Moon as part of the Apollo lunar surface experiments package (ALSEP) to study the composition of and variation in the lunar atmosphere. The instrument was successfully deployed in the Taurus-Littrow valley with its entrance aperture oriented upward to intercept and measure the downward flux of gases at the lunar surface. Identification of sources, sinks, and transport mechanisms of the lunar gases can lead to a better understanding of the mechanism of gas release from the lunar surface and interior and of the interaction of the solar wind with the Moon.

The existence in the lunar atmosphere of helium, neon, argon, and possibly molecular hydrogen has been confirmed by the Apollo 17 mass spectrometer. The observed helium concentrations and distribution agree closely with model predictions for a noncondensable gas based on a solar-wind source, a thermal escape, and a "Monte Carlo random walk" longitudinal distribution. Heavier gases are lost by photoionization and subsequent sweeping away by the solar-wind electric field. The observed nighttime neon concentration of  $8 \times 10^4$  molecules  $\text{cm}^{-3}$  is consistent with expected amounts. Argon, however, is adsorbed on the lunar surface late at night when the surface temperature is lowest. Argon shows the expected predawn enhancement exhibited by condensable gases released into the atmosphere at the sunrise terminator. Hydrogen appears to exist in the molecular rather than the atomic state, and its observed concentration is less than a factor of 3 higher than that predicted by a model similar to that used for helium. The total nighttime concentration of known species (hydrogen, helium, neon, argon) in the lunar atmosphere is  $2 \times 10^5$  molecules  $\text{cm}^{-3}$ .

### INSTRUMENT DESCRIPTION

Identification of gas molecules in the lunar atmosphere by species and determination of concentrations are accomplished by a miniature magnetic-deflection mass spectrometer. Gas molecules entering the instrument aperture are ionized by an electron bombardment ion source,

collimated into a beam, and sent through a magnetic analyzer to the detector system.

The ion source contains two tungsten (with 1 percent rhenium) filaments, selectable by command, as electron emitters. In the normal mode of operation, called the fixed mode, the electron bombardment energy is fixed at 10 eV, which produces a sensitivity to nitrogen of  $3.8 \times 10^{-7}$  A/N/m<sup>2</sup> ( $5 \times 10^{-5}$  A/torr), sufficient to measure concentrations of gas species in the  $1.3 \times 10^{-13}$  N/m<sup>2</sup> ( $10^{-15}$  torr) range. An alternate mode, the cyclic mode, provides four different electron energies (70, 27, 20, and 18 eV) that are cycled by successive sweeps of the mass spectrum. Identification of gases in a complex mass spectrum is greatly aided when the spectra are taken at several different electron ionization energies, because cracking patterns of complex molecules are a strong function of the bombardment electron energy.

Voltage scan of the mass spectrum is used with a high voltage stepping power supply. The ion-accelerating voltage (sweep voltage) is varied in a stepwise manner through 1330 steps from 320 to 1420 V with a dwell time of 0.6 sec per step. Each step is synchronized to a main frame of the telemetry format; therefore, the telemetry word position serves to identify the atomic mass number. Ten steps of background counts (zero sweep voltage) and 10 steps of an internal calibration frequency are inserted between sweeps, making a total of 1350 steps per spectrum. (Sweep time is 13.5 min.) Because the instrument has three collector assemblies adjusted to collect ion beams, having passed through the magnetic analyzer (fig. 21-1) in the ratio 1:12:27.4, three mass ranges are scanned simultaneously (viz, 1 to 4, 12 to 48, and 27.4 to 110 amu).

In an alternate mode, the sweep voltage may be commanded to lock onto any of the 1350 steps, enabling the instrument to monitor continuously any given mass number peak in the spectrum with a time resolution of 0.6 sec per sample. A one-step advance command is also available. The lock mode permits high time resolution monitoring of mass peaks that may be suspected to be of volcanic origin.

Resolution of the analyzer is set at approximately 100 for the high-mass channel at mass 82. This is defined as less than a 1-percent valley between peaks of equal amplitude at mass 82 and 83. Krypton is used to verify the resolution.

Standard ion-counting techniques using electron multipliers, pulse amplifiers, discriminators, and counters are used; one system for each mass range. The number of

counts accumulated per voltage step (0.6 sec) for each channel is stored in 21-bit accumulators until sampled by the telemetry system. Just before interrogation, the 21-bit word is converted to a floating point number in base 2, reducing the data to a 10-bit word consisting of a 6-bit number and a 4-bit multiplier. This scheme maintains a 7-bit accuracy (1 percent) throughout the 21-bit ( $2 \times 10^6$ ) range of data counts.

Housekeeping circuits monitor 15 functions within the instrument (supply voltages, filament current, emission current, sweep voltage, and several temperatures). One temperature sensor monitors the ion source temperature; this value is used in data reduction. Housekeeping words are subcommutated, one each 90 main-frames, thus requiring a full spectral scan time to read each monitor once.

Calibration of the instrument was performed at the NASA Langley Research Center (LRC) molecular beam facility. A molecular beam apparatus produces a beam of known flux in a liquid helium cryochamber. The instrument entrance aperture intercepts the beam at one end of the chamber. With known beam flux and ion source temperature, instrument calibration coefficients are determined. Variation of gas pressure in the molecular beam source chamber behind a porous silicate glass plug varies the beam flux and provides a test of the linearity of the instrument response. Good linearity was achieved up to  $5 \times 10^5$  counts/sec, where the onset of counter saturation occurs.

Calibrations were done with a number of gases that may be candidates for ambient lunar gases; for example, argon, carbon dioxide, carbon monoxide, krypton, neon, nitrogen, and hydrogen. Because helium is not cryopumped at the wall temperature, no helium beam can be formed in the chamber; therefore, helium calibrations are not possible with this system. Sensitivity to helium was determined in the ultrahigh vacuum chamber at the University of Texas at Dallas using the LRC absolute argon calibration of the instrument as a standard for calibrating an ionization pressure gage. The gage calibration for helium was subsequently inferred from the ratio of ionization cross sections for helium and argon. The resulting helium sensitivity is the ratio of the calibrated gage pressure to the helium counting rate.

Instrument parameters are as follows:

Mass range: 1 to 110 amu

Spectrum scan time: 13.5 min

Mass resolution: 1 percent valley at 82 amu

Sensitivity:  $6.7 \times 10^{-13}$  N/m<sup>2</sup> ( $5 \times 10^{-15}$  torr)

Dynamic range:  $6.7 \times 10^{-13}$  to  $1.3 \times 10^{-7}$  N/m<sup>2</sup>  
( $5 \times 10^{-15}$  to  $1 \times 10^{-9}$  torr)

#### AVAILABILITY OF DATA

The LACE initial turn-on occurred on December 27, 1972, at 18:07 G.m.t. and continued throughout the first lunar night. Operation has been continuous during each lunar night from shortly after sunset to approximately sunrise. During the April and September 1973 sunrise periods, operation continued 4 or 5 hr into the daytime to track the behavior of argon. Daytime operation has been severely curtailed because of the high outgassing rates encountered as the site warms, thus producing a large artifact background that covers most of the ambient gas levels except helium. This relatively high background gas concentration would likely degrade the instrument ion source sensitivity if operated for long periods (hours) in this environment. Likewise, extended daytime operation periods, one in January, one in February, and one in May, have given information on the daytime gas concentrations at the site. Table 21-I lists the periods of instrument operation during its first 9 months on the lunar surface.

In general, the instrument has operated well. All housekeeping data have remained within bounds. A fortuitous occurrence, the slow evaporation of the tungsten filament, which produces doubly charged tungsten peaks in the mass 91 to 93 range of the spectrum, has provided a constant check on the instrument sensitivity, which has remained very stable with time.

#### FORMAT OF DATA

Data processing has resulted in the blocking of data into complete mass spectra on magnetic tape. Brief time gaps in the data are filled with flag words to ensure proper location of the good measurements in the spectra. Reduced data also include the background count level of each analyzer channel and decommutated housekeeping data.

Microfilm records are formatted outputs of the data on magnetic tape. Each mass spectrum produces six pages of data, two each for the low-, mid-, and high-mass ranges.

Examples of the high-mass page are given in Figure 21-2.  
The data format is as follows.

<u>Code</u>	<u>Description</u>
HIGH	Mass range (low, mid, high)
STAT	Tracking station identification
N. ELEV	Elevation of the Sun
AZMUTH	Azimuth of the Sun
ZENITH	Zenith angle of the Sun
T BASE	Temperature of the baseplate, °C
T IONS	Temperature of the ion source, °C
T MOON	Surface temperature of the Moon, K
TCF	Temperature correction factor [ (T IONS + 273.2) / T MOON ] <sup>1/2</sup>
SYNC	Sweep sync code
TAVG	Average time between frames of data, msec
HK SYNC BLK	The block (50 frames) of data in which the internal housekeeping marker was found
EXP I	Instrument current monitor
PMP I	Ion pump current monitor
PMP V	Ion pump voltage monitor
BASE T	Baseplate temperature monitor
IONS T	Ion source temperature monitor
+12V	+12 V temperature monitor
+5V	+5 V temperature monitor
-12V	-12 V temperature monitor
-15V	-15 V temperature monitor
EMIS I	Emission current monitor

<u>Code</u>	<u>Description</u>
FIL1 I	Filament number 1 current monitor
FIL2 1	Filament number 2 current monitor
MHV	Multiplier high-voltage monitor
LVPS T	Low-voltage power supply temperature monitor
SWEEP	Sweep high-voltage monitor
ETEMP	Electronics temperature, °C
MDAPBHF	M = Multiplier high-voltage HI/LO flag D = Disk HI/LO flag A = Sweep high-voltage AUTO/STEP flag P = Ion pump ON/OFF flag B = Bakeout heater ON/OFF flag H = High voltage ON/OFF flag F = Filament ON/OFF flag
73 89 3 25 39	73 = year 89 = Julian day 3 25 39 = hours, minutes, and seconds in G.m.t.
*****	Time gap in data

## BIBLIOGRAPHY

- Hodges, R. R., Jr.: Differential Equation of Exospheric Lateral Transport and Its Application to Terrestrial Hydrogen. J. Geophys. Res., vol. 78, no. 31, Nov. 1, 1973, pp. 7340-7346.
- Hodges, R. R., Jr.: Helium and Hydrogen in the Lunar Atmosphere. J. Geophys. Res., vol. 78, no. 34, Dec. 1, 1973, pp. 8055-8064.
- Hodges, R. R., Jr.; Hoffman, J. H.; Johnson, F. S.; and Evans, D. E.: Composition and Dynamics of Lunar Atmosphere. Proceedings of the Fourth Lunar Science Conference, vol. 3, Pergamon Press (New York), 1973, pp. 2855-2864.
- Hodges, R. R., Jr.; Hoffman, J. H.; and Johnson, Francis S.: The Lunar Atmosphere. Icarus, vol. 21, no. 4, Apr. 1974, pp. 415-426.
- Hoffman, J. H.; Hodges, R. R., Jr.; Johnson, F. S.; and Evans, D. E.: Lunar Atmospheric Composition Experiment. Sec. 17 of Apollo 17 Preliminary Science Report, NASA SP-330, 1973.
- Hoffman, J. H.; Hodges, R. R., Jr.; and Evans, D. E.: Lunar Atmospheric Composition Results From Apollo 17. Proceedings of the Fourth Lunar Science Conference, vol. 3, Pergamon Press (New York), 1973, pp. 2865-2876.
- Hoffman, J. H.; Hodges, R. R.; Johnson, F. S.; and Evans, D. E.: Composition and Physics of the Lunar Atmosphere. COSPAR, Sixteenth Plenary Meeting, Konstanz, Germany, May-June 1973.
- Yeager, P. R.; Smith, A.; Jackson, J. J.; and Hoffman, J. H.: Absolute Calibration of Apollo Lunar Orbital Mass Spectrometer. J. Vac. Sci. Tech., vol. 10, no. 2, Mar./Apr. 1973, pp. 348-354.

TABLE 21-I.- PERIODS OF LACE OPERATION DURING FIRST 9 MONTHS  
ON LUNAR SURFACE

LACE turned on -		LACE turned off -	
Date	Time, G.m.t.	Date	Time, G.m.t.
Dec. 27, 1972	18:07	Jan. 9, 1973	22:36
Jan. 16, 1973	17:19	Jan. 16, 1973	17:46
Jan. 23, 1973	14:39	Feb. 8, 1973	13:29
Feb. 16, 1973	01:00	Feb. 16, 1973	01:26
Feb. 22, 1973	11:02	Mar. 12, 1973	10:55
Mar. 23, 1973	23:20	Apr. 11, 1973	10:14
Apr. 22, 1973	15:33	May 10, 1973	15:13
May 14, 1973	10:33	May 14, 1973	10:49
May 23, 1973	09:12	June 8, 1973	19:09
June 21, 1973	19:21	July 8, 1973	16:09
July 19, 1973	14:53	Aug. 3, 1973	23:45
Aug. 17, 1973	13:17	Sept. 2, 1973	21:33

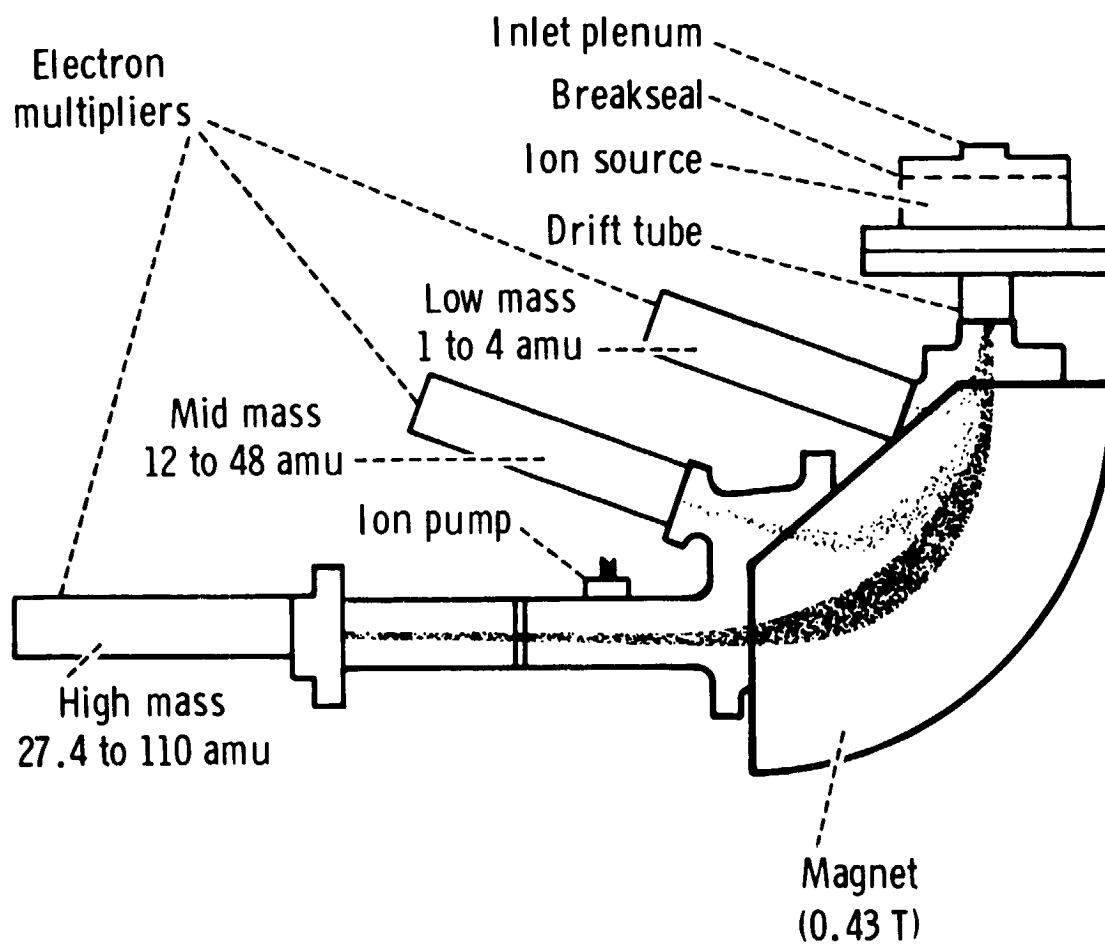


Figure 21-1.- Schematic diagram of mass analyzer, showing three channels.

73 89 3 25 39		APOLLO 17 LMS		SYNC		PRIM		WDABHF	
STAT	3	AMU	N(ME)	1.08	1.20	1.31	1.43	1.53	1.65
M-ELEV	251.86	19.34	2.23E+04	-7.96	-7.96	-7.96	-7.96	-7.96	-7.96
1	0	0	0	0	0	0	0	0	0
2	0	0	0	0	0	0	0	0	0
3	0	0	0	0	0	0	0	0	0
4	0	0	0	0	0	0	0	0	0
5	0	0	0	0	0	0	0	0	0
6	0	0	0	0	0	0	0	0	0
7	0	0	0	0	0	0	0	0	0
8	0	0	0	0	0	0	0	0	0
9	0	0	0	0	0	0	0	0	0
10	0	0	0	0	0	0	0	0	0
11	0	0	0	0	0	0	0	0	0
12	0	0	0	0	0	0	0	0	0
13	0	0	0	0	0	0	0	0	0
14	0	0	0	0	0	0	0	0	0
15	0	0	0	0	0	0	0	0	0
16	0	0	0	0	0	0	0	0	0
17	0	0	0	0	0	0	0	0	0
18	0	0	0	0	0	0	0	0	0
19	0	0	0	0	0	0	0	0	0
20	0	0	0	0	0	0	0	0	0
21	0	0	0	0	0	0	0	0	0
22	0	0	0	0	0	0	0	0	0
23	0	0	0	0	0	0	0	0	0
24	0	0	0	0	0	0	0	0	0
25	0	0	0	0	0	0	0	0	0
26	0	0	0	0	0	0	0	0	0
27	0	0	0	0	0	0	0	0	0
28	0	0	0	0	0	0	0	0	0
29	0	0	0	0	0	0	0	0	0
30	0	0	0	0	0	0	0	0	0
31	0	0	0	0	0	0	0	0	0
32	0	0	0	0	0	0	0	0	0
33	0	0	0	0	0	0	0	0	0
34	0	0	0	0	0	0	0	0	0
35	0	0	0	0	0	0	0	0	0
36	0	0	0	0	0	0	0	0	0
37	0	0	0	0	0	0	0	0	0
38	0	0	0	0	0	0	0	0	0
39	0	0	0	0	0	0	0	0	0
40	0	0	0	0	0	0	0	0	0
41	0	0	0	0	0	0	0	0	0
42	0	0	0	0	0	0	0	0	0
43	0	0	0	0	0	0	0	0	0
44	0	0	0	0	0	0	0	0	0
45	0	0	0	0	0	0	0	0	0

(a) Page 1.  
 Figure 21-2.- Examples of LACE microfilm record representing two pages of high-mass ranges.

ORIGINAL PAGE IS  
 OF POOR QUALITY



22. LUNAR SURFACE GRAVIMETER (NASA EXPERIMENT S-207)

NSSDC IDENTIFICATION NUMBER:

APOLLO 17 72-096C-09



---

CONTENTS - SECTION 22

	Page
INSTRUMENT DESCRIPTION . . . . .	22-3
THERMAL CONTROL . . . . .	22-4
CHRONOLOGY OF LSG OPERATION . . . . .	22-4
DATA AVAILABILITY . . . . .	22-7
BIBLIOGRAPHY . . . . .	22-8

## 22. LUNAR SURFACE GRAVIMETER

The lunar surface gravimeter (LSG) (fig. 22-1) was deployed by the Apollo 17 crew. When the instrument was turned on, the movable beam (fig. 22-2) could not be balanced by sending commands to add or subtract weights. The section entitled "Chronology of LSG Operation" lists operational adjustments to the LSG.

### INSTRUMENT DESCRIPTION

The LSG is a sensitive balance with a mass, spring, and lever system and with electronics for observation of accelerations in the frequency range from 0 to 16 Hz. The LSG has a nominal sensitivity of approximately one part in  $10^{11}$  of lunar gravity.

A schematic diagram of the spring-mass suspension system is shown in figure 22-2. In the instrument, the major fraction of the force supporting the sensor mass (beam) against the local gravitational field is provided by the zero-length spring. A zero-length spring is one in which the restoring force is directly proportional to the spring length; such a spring is very useful in obtaining a long-period sensor. Small changes in force tend to displace the beam up or down. This imbalance is adjusted to the null position by repositioning the spring pivot points by use of micrometer screws. The sensor mass is modified by the addition or removal of small weights, which permits the range of the sensor to be extended from Earth testing to lunar operation. The electronic sensing portion of the instrument consists of a set of capacitor plates. Two plates, which are part of a radio-frequency bridge circuit, are fixed to the frame of the sensor and are geometrically concentric with a third plate of similar size, which is attached to the movable beam of the sensor. The plates are arranged so that the center plate is located exactly between the two outer plates when the beam is exactly horizontal. If the force on the mass changes, it tends to move the beam, and the resulting bridge unbalance creates an ac error voltage. This voltage is amplified and rectified, and the size of the output voltage is determined by the direction of the displacement. A fixed dc bias voltage is applied to the capacitor plates balanced with respect to ground, and these plates are also connected to the rectified error voltage.

If the error voltage is zero, the balanced bias plate voltage produces equal and opposite electrostatic forces on the mass. If a positive error voltage is present, the voltage applied to one plate is increased and the voltage applied to the other plate is decreased. The resulting force tends to restore the mass to its original centered position. This rectified voltage is a measure of the changes in surface acceleration. The mass does not follow fast changes. However, the fast-changing servomechanism error voltage is a measure of the rapidly changing components of the surface acceleration.

#### THERMAL CONTROL

The gravimeter uses a metal spring with a force constant that is, in general, temperature dependent. There are two temperatures at which thermal effects are minimal; for the LSG, one of these occurs near 323 K. To obtain the required performance, it is necessary to control the temperature of the spring to within better than 1 mdeg near the optimum temperature throughout the lunar day/night cycle. Thermal control is accomplished by use of thermal insulation, which limits heat exchange with the lunar surface. A hole in the top of the LSG radiates heat to the cold sky so that an internal heater is required to maintain the 323 K temperature sensed by thermistors. A sunshade prevents the solar heat from directly entering the LSG. The sunshade is tilted at an angle corresponding to the latitude of the emplaced instruments. The thermal control system has controlled the temperature of the spring to within 1 mdeg.

#### CHRONOLOGY OF LSG OPERATION

The following log outlines the endeavors to maximize LSG data return.

<u>Date</u>	<u>Comments</u>
Dec. 12 to 20, 1972	The LSG installed on Moon; trouble-shooting procedures implemented in effort to balance beam. Beam resting on upper stop with post amplifier (PA) gain at 17.
Jan. 4, 1973	Beam centered with PA gain at 86.4; operation for first 45 days showed no seismic signals, but possible

free-mode signal detected with beam centering accomplished by pulling down on the mass-adding/caging mechanism.

Apr. 6, 1973

First major reconfiguration unsaturated the LSG seismic amplifier by using a lower gain setting. Background noise levels higher than those indicated for the Moon by the passive seismic experiment (PSE) and for Taurus-Littrow by the lunar seismic profiling experiment (LSPE). Terminator crossing showed thermoelastic events similar to those recorded by PSE and LSPE. The LSG operated with beam centered, PA gain of 64, and coarse screw at upper limit.

Apr. 19, 1973

The LSG was reconfigured to re-center and lower the resonant frequency of the instrument to approximately 2.2 Hz. Seismic bandpass remained 1 to 16 Hz, but calculated Q of approximately 25 indicated response sharply peaked at resonant frequency. Signal-to-noise improvement of noisy seismic channel was accomplished by filtering of free-mode channel by smoothing the power spectrum through stacking multiday records and averaging out noise. The LSG recordings continued to show high background noise levels. Operation continued with beam centered, PA gain of 64, and coarse screw at the upper limit (operation prior to April 19). Reconfiguration put coarse screw near the bottom of its travel and instrument resonance at approximately 2 Hz. Open-loop configuration was maintained.

Sept. 26, 1973

Data were obtained to determine instrument response characteristics under closed-loop mode of operation. Calculated response of instrument for free-mode output was about 40 dB (100 times) down from design and sharply peaked at approximately 21 min rather than designed broad

band. Began recording lunar solid-body tidal data. Power spectral density analysis of 40 days data from free-mode channel showed no predominant periodicities. The LSG was operated closed loop with integrator mode normal, bias circuit in, seismic gain high, PA gain step 15.

Nov. 30, 1973

Reconfigured to obtain lower resonant frequency by recentring beam using the mass caging mechanism. The natural frequency was lowered from 2.2 to 1.5 Hz, and it improved free-mode response for longer period signals. Tidal output roughly followed calculated lunar tides with overriding higher frequency distortion. Tidal output failed about Nov. 13, 1973.

Dec. 7, 1973

Reconfigured to determine if high-gain amplifier was oscillating and was possible reason for tidal output failure. No conclusions reached on failure cause. Returned to open-loop operation to continue recording seismic and free-mode data. The LSG operating in the integrator shorted mode (bias out, seismic gain high, PA in step 15).

Mar. 15, 1974

The LSG temperature control circuits failed during the 16th lunar night; as a result, the temperature recorder drifted off-scale high. Thermal control by manual operation was unacceptable for reestablishing the collection of science information. Numerous operations to exercise the controls failed to regain automatic control of temperature.

Apr. 10, 1974

Reconfigured to allow useful instrument operation during lunar night by offsetting voltage to compensate for higher heater temperature so that beam would be centered. Attempt to offset voltage to about +5.8 V was unsuccessful because of nonlinearity of voltage

---

increments associated with coarse screw steps used to change instrument attitude. The LSG remained operating in open loop with seismic gain low and post amplifier gain at increment 7 with the slave heater on.

Apr. 20, 1974

The LSG temperature control circuits began automatically controlling at 12:00 G.m.t. on April 20, 1974, during lunar night. Temperature readings are consistently at 322.34 K (49.184° C). Coarse screws were returned to instrument attitude prior to April 10. Seismic high-gain operation will be at step 15 to collect data.

#### DATA AVAILABILITY

No provision has been made to supply data from this experiment to the National Space Science Data Center (NSSDC). When significant and meaningful data formats have been determined, LSG data will be supplied to NSSDC.

## BIBLIOGRAPHY

- Flugge, Siegfried, ed.: Geophysik II. Vol. XLVIII of Handbuch der Physik, Springer-Verlag (Berlin), 1957, p. 803.
- Weber, Joseph: Detection and Generation of Gravitational Waves. Phys. Rev., vol. 117, no. 1, Jan. 1960, pp. 306-313.
- Weber, Joseph: General Relativity and Gravitational Waves. Interscience Pub., Inc. (New York), 1961.
- Weber, Joseph: Evidence for Discovery of Gravitational Radiation. Phys. Rev. Letters, vol. 22, no. 24, June 1962, pp. 1320-1324.
- Weber, Joseph: Gravitational Radiation Experiments. Phys. Rev. Letters, vol. 24, no. 6, Feb. 1970, pp. 276-279.
- Weber, Joseph: Anisotropy and Polarization in the Gravitational-Radiation Experiments. Phys. Rev. Letters, vol. 25, no. 3, July 1970, pp. 180-184.
- Weber, Joseph: The Detection of Gravitational Waves. Sci. Am., vol. 224, no. 5, May 1971, pp. 22-29.
- Weber, Joseph: Computer Analyses of Gravitational Radiation Detector Coincidences. Nature, vol. 240, no. 5375, Nov. 1972, pp. 28-30.
- Weber, Joseph: Pulses of Gravity. Science Year: The World Book Science Annual. Field Enterprises, Inc. (San Francisco), 1972.

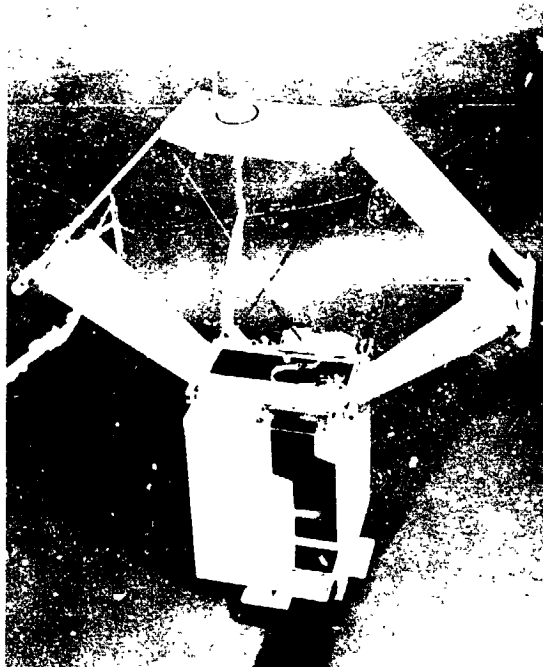


Figure 22-1.- Lunar surface gravimeter.

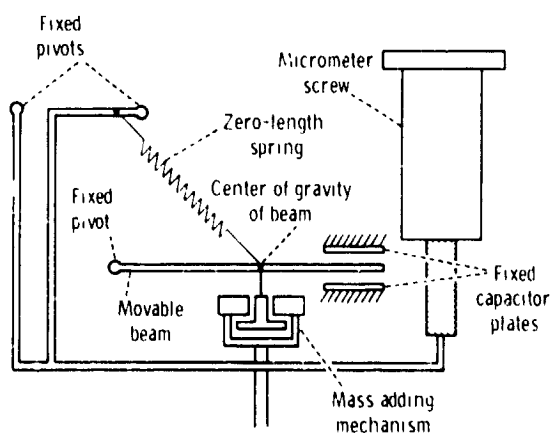


Figure 22-2.- Schematic diagram of the lunar gravity sensor.

ORIGINAL PAGE IS  
OF POOR QUALITY

23. LUNAR SEISMIC PROFILING EXPERIMENT

(NASA EXPERIMENT S-203)

NSSDC IDENTIFICATION NUMBER:

APOLLO 17 72-096C-06



CONTENTS - SECTION 23

	Page
INSTRUMENT DESCRIPTION AND PERFORMANCE . . . . .	23-4
EXPLOSIVE PACKAGE DESCRIPTION AND PERFORMANCE . . . . .	23-5
OPERATION . . . . .	23-6
EXPLOSIVE PACKAGES . . . . .	23-7
DATA FORMAT . . . . .	23-8
RESULTS . . . . .	23-8
CONCLUSIONS . . . . .	23-12
REFERENCES . . . . .	23-14

### 23. LUNAR SEISMIC PROFILING EXPERIMENT

The purpose of the Apollo 17 lunar seismic profiling experiment (LSPE) was to record the vibrations of the lunar surface as induced by explosive charges, by the thrust of the LM ascent engine, and by the crash of the LM ascent stage. Analyses of these seismic data were planned to determine the internal characteristics of the lunar crust to a depth of several kilometers. The traveltimes of seismic waves are inverted to determine the seismic velocity structure with depth and to provide the direct means of probing the lunar interior. A secondary objective of the LSPE was to monitor lunar seismic activity during periodic listening intervals.

Strong seismic signals were recorded from the detonations of eight explosive charges that were armed and placed on the lunar surface by the crewmen at various points along the traverses. Recording of these seismic signals generated traveltime data to a distance of 2.7 km.

One of the more significant events of the Apollo 17 mission was the recording of the seismic signals from the lunar module (LM) ascent stage, which struck the lunar surface 8.7 km southwest of the landing site. The characteristic reverberation from this impact spread outward and was first detected at the Apollo 17 station approximately 6 sec after impact. The seismic signals received from this impact provided a valuable traveltime datum for determining the variation of seismic velocity with depth in approximately the upper 5 km of the Moon.

The most significant discovery resulting from the analysis of the data recorded by the LSPE is that the seismic velocity increases in a marked stepwise manner beneath the Apollo 17 landing site (fig. 23-1). A surface layer with a seismic velocity of 250 m/sec and a thickness of 248 m overlies a layer with a seismic velocity of 1200 m/sec and a thickness of 927 m, with a sharp increase to approximately 4000 m/sec at the base of the lower layer. The seismic velocities for the upper layers are compatible with those for basaltic lava flows, indicating a total thickness of approximately 1200 m for the infilling mare basalts at Taurus-Littrow. Major episodes of deposition or evolution are implied by the observed abrupt changes in seismic velocity.

## INSTRUMENT DESCRIPTION AND PERFORMANCE

The LSPE consists of a geophone array, eight explosive packages, and electronics within the Apollo lunar surface experiments package (ALSEP) central station. Four identical geophones are used in a triangular array; the geophones are miniature seismometers of the moving coil-magnet type. The coil is the inertial mass suspended by springs in the magnetic field. Above the natural resonant frequency of the geophones (7.5 Hz), the output is proportional to ground velocity. The LSPE geophone array was deployed without difficulty in the nominal configuration at the Apollo 17 site approximately 148 m west-northwest of the LM (fig. 23-2). Figure 23-3 is a photographic panorama from geophone 2 to the LM as viewed from geophone 3.

A four-channel amplifier and a logarithmic compressor condition the geophone signals before conversion into a digital format for telemetering to Earth. Because the LSPE signal levels are distributed throughout the dynamic range of the system, logarithmic compression is used. This compression gives signal resolution as some constant fraction of signal amplitude. The logarithmic compressor used in the LSPE has the transfer function

$$V_{out} = \pm M \ln |V_{in}| + b' \quad (23-1)$$

where  $V$  is voltage, the constant  $M$  determines the slope of the transfer function, and  $b'$  is specified by the dc offset of the compressor output and the system noise level. The values of  $M$  and  $b'$  are determined by calibration of the system to provide at least 6-percent accuracy of the data referenced to the level of the input signal. The properties of the LSPE system are listed in tables 23-I and 23-II, and the nominal frequency response is shown in figure 23-4. The output of the logarithmic compressor is referenced to 2.5 V dc.

The analog output of the logarithmic compressor is converted to a 7-bit binary element in the LSPE control electronics by an analog-to-digital converter and transmitted to Earth through the ALSEP communications network. The 7-bit binary encoding provides for an amplitude resolution of 1.277 dB (approximately 16 percent). Each geophone channel is sampled 118 times/sec to provide a minimum of 5 samples/sec at a frequency of 20 Hz.

## EXPLOSIVE PACKAGE DESCRIPTION AND PERFORMANCE

An LS<sup>r</sup> explosive package (EP) is shown in figure 23-5. The eight explosive packages are identical except for the amount of high explosive and the preset runout time of the mechanical timers. An explosive package is activated by removing three pull pins (fig. 23-5). Removal of the first pull pin activates the SAFE/ARM slide timer, which is preset at 89.75, 90.75, 91.75, or 92.75 hr. Removal of the second pull pin releases the SAFE/ARM slide from its constrained SAFE position. Removal of the third pull pin removes a constraint on the firing pin and activates the thermal battery timer.

The LSPE transmitter, which is located within the ALSEP central station, transmits a repetitive pulsed carrier signal. A series of three pulses properly spaced in time is required to elicit a FIRE signal from the signal processor within the explosive package and to detonate the explosives train. The thermal battery, activated by the timer, has a minimum life of 2 min. This 2 min provides a time window long enough to ensure that at least one fire pulse set is received while the explosive package is energized electrically. Because the seismic data subsequently collected must be accurately referenced to the instant of detonation, it is necessary to establish which specific set of pulses is effective. This is done by comparing known times of pulse-set transmission with the time of arrival at the geophones of the initial seismic data. Pulse sets are spaced at 29.55-sec intervals to make such identification possible without ambiguity.

No difficulty was experienced in the deployment of the explosive packages during the periods of extravehicular activity (EVA) (fig. 23-6). The 454-g explosive package (EP-6) was deployed at station 1, and the 227-g explosive package (EP-7) was positioned on the return to the LM from station 1. Explosive packages 4, 1, and 8 were armed and placed on the lunar surface during the second EVA. During the third EVA, explosive packages 3, 5, and 2 were deployed. It was necessary to place the 1361-g explosive package (EP-5) at station 9 when it became apparent that insufficient time remained for a visit to the crater Sherlock. All the explosive packages were successfully detonated (table 23-III), and the detonation of EP-7 was visible from the television camera on the lunar roving vehicle (LRV). Figure 23-7 is a photograph showing EP-8 on the lunar surface approximately 296 m west of the LM.

## OPERATION

The Apollo 17 LSPE was planned to contribute to the understanding of the shallow lunar structure in two major ways: (1) by providing traveltimes of the seismic signals from explosive packages, which were to be detonated on the lunar surface at distances ranging from 100 to 2700 m, to the LSPE geophone array and (2) by impacting the Apollo 17 LM at a nominal distance of 10 km to provide traveltime data for deciphering the variation of seismic velocity with depth in the upper 5 km of the Moon.

The LSPE was commanded on at 22:24:00 G.m.t. on December 14, 1972, to record the impulse produced by the thrust of the LM ascent engine. The effective zero time for the seismic impulse from the LM ascent-engine ignition was determined from NASA postflight analyses, which gave engine buildup pressure data at 5-msec intervals for the LM lift-off. The assigned ignition time of 22:54:38.424 G.m.t. corresponds to the time when the LM ascent engine achieved 20 percent of its maximum propulsion pressure. Clear seismic signals were recorded by the LSPE geophone array at distances of 148, 244, 190, and 187 m (fig. 23-8).

The LSPE was commanded on again at 06:36:00 G.m.t. on December 15 to record the LM ascent-stage impact. The impact occurred at latitude  $19.91^{\circ}$  N, longitude  $30.51^{\circ}$  E, 8.7 km southwest of the Apollo 17 landing site. Other pertinent parameters for the LM impact are given in table 23-IV.

A portion of the seismic signal from the Apollo 17 LM impact is shown in figure 23-9 in a compressed time scale. The impact signal is similar in character to previous impact signals; that is, these signals have an emergent beginning and a long duration. The initial portion of the impact signal on an expanded time scale is shown in figure 23-10. The arrival time of the first compressional wave (P-wave) is marked at 06:50:25.35 G.m.t., giving a traveltime of 5.75 sec.

The amplitude of the impact signal is of interest when compared with the P-wave amplitudes for previous LM and S-IVB impact signals. Comparison of previous LM impact and S-IVB impact signal amplitudes demonstrated that the LM impact data had to be adjusted upward by a factor of 17.4 to allow for the lower kinetic energy and a shallower angle of impact. Extrapolating the earlier LM impact data to a distance of 8.7 km leads to a predicted peak-to-peak amplitude of 26 nm. The Apollo 17 LM impact signal is centered at 4 Hz and has a measured peak-to-peak amplitude

of 400 nm. This amplitude was caused by the Apollo 17 LM ascent stage striking the side of the mountainous South Massif rather than grazing the lunar surface. In other words, if the predicted amplitude of 26 nm is multiplied by the factor 17.4, the resulting figure is 452 nm, which agrees well with the observed amplitude of 400 nm.

Analyses of previous lunar seismic impact signals (ref. 23-1) have demonstrated that many of their characteristics (signal rise time, duration of signal, and lack of coherence between horizontal and vertical components of motion) can be explained by wave scattering. Seismic energy is considered to spread with a diffusivity  $\xi$  proportional to the product of the average seismic velocity and the mean distance between scattering centers; that is, the larger the value of diffusivity, the smaller the amount of scattering. For a surface impact, the theory predicts (ref. 23-1) that the signal rise time (the time from signal onset to its maximum value) is given by  $R^2/\xi$  where  $R$  is the range.

The Apollo 17 LM impact seismic signal rise time of 56 sec leads to a diffusivity of  $1.35 \text{ km}^2/\text{sec}$ , which is significantly larger than the value of  $0.033 \text{ km}^2/\text{sec}$  inferred at the Apollo 16 site (ref. 23-2) from analysis of the seismic signals generated by the LRV at distances of approximately 4 km. The implication is that the Apollo 17 landing area is more homogeneous, for the dimensions of the seismic waves considered (approximately 25 m), than either the Apollo 15 or 16 landing areas. Such a difference in near-surface properties of these landing sites may be attributable to differing ages of the different areas and to the effects of differing amounts of comminution and gardening by meteoroid impacts.

#### EXPLOSIVE PACKAGES

All eight of the explosive packages placed on the lunar surface were successfully detonated. The seismic data recorded for EP-5, which was detonated at station 9, are shown in figure 23-11. The arrows point to the measured onset of the first seismic arrival. Transmissions of the fire pulses at 29.55-sec intervals from the LSPE antenna were observable as crosstalk on the individual geophone data channels and produced convenient, accurate references for selecting the detonation time of the individual explosive packages.

The locations of the explosive packages with respect to the LSPE geophone array were taken from preliminary postmission analyses (refs. 23-3 and 23-4). Adjustments in

the absolute distances of the explosive packages will undoubtedly be necessary when subsequent analyses of the appropriate Apollo 17 lunar surface photographs are completed. However, it is not anticipated that any revisions in the distances will have a major effect on the traveltime data discussed in the results subsection.

#### DATA FORMAT

The data format used is shown in figure 23-12. A data frame consists of three subframes, each consisting of twenty 30-bit words. The first word of each subframe consists of one 10-bit synchronous word and one 5-bit seismic data sample from each of the four seismic data channels. Words 2 to 20 of each subframe are 7-bit samples from each of the four seismic data channels. Engineering data are interleaved and subcommutated, using the remaining 2 bits to form 30-bit words.

In words 2 to 19, geophone samples are sampled on the bit preceding the word on which they are read out; the most significant bit is read out first. In the first word of each subframe, the timing of the data sampling is the same as that in words 2 to 19 except that the samples are stored and read out in the last 20 bits with one 5-bit word/channel.

The time of the RF fire pulses must be accurately known. When the LSPE is commanded to the fire pulses "on" mode, a fire pulse set is transmitted once every 29.55 sec and is flagged in word 3 of subframe 1. This occurs once every 58 frames.

A command system provides for 11 commands associated with the LSPE. Two commands turn the LSPE on and off; two commands control the bit rate; and two commands control downlink formatting. In addition, commands are used to control amplifier gain status, transmission of fire pulses, and calibration of the geophones.

#### RESULTS

The traveltime/distance data obtained from the detonation of the eight explosive packages are shown in figure 23-13. Two sets of seismic wave first arrivals were observed traveling at velocities of 250 and 1200 m/sec. The shortest explosive-charge-to-geophone distance was approximately 100 m. If a seismic velocity of 100 m/sec is

assumed for the regolith at the Apollo 17 site, a regolith as thick as 25 m would not have been detected. The depth of penetration of seismic waves is nominally one-fourth the explosive-charge-to-receiver distance. However, it is probable that the regolith is significantly thinner than 25 m, inasmuch as the 250-m/sec velocity curve extrapolates to a zero intercept time.

The faster seismic arrival with a velocity of 1200 m/sec was observed beginning at a distance of 612 m, indicating that the thickness of the 250-m/sec material was 248 m. Considering uncertainties in the charge distances and in the inferred seismic velocities, the depth estimates are considered accurate to 10 percent. The 1200-m/sec velocity was observed to a distance of approximately 2.5 km. At this distance, the observed traveltimes for EP-1 were offset by approximately 0.5 sec with respect to the 1200-m/sec line.

Examination of the path between EP-1 and the LSPE geophone array revealed that the seismic path was affected by the presence of the 600-m-diameter crater Camelot. The observed time delay on the seismic path can be explained by postulating that low-velocity material extends to a greater depth beneath the crater Camelot than along the remainder of the traveltime path. A simple model approximation for Camelot Crater that explains the observed traveltime delay is shown in fig. 23-14.

The traveltime data from the LSPE explosive charges can be combined with the observed traveltime for the LM impact to provide information about the seismic velocity to a depth of several kilometers. Traveltime data from the seismic signals produced by the LM impact and the explosive charges are shown in figure 23-15. A line with an apparent velocity of 4 km/sec can be fitted through the LM impact data point to intersect close to the corrected traveltime data point for EP-1. Because of obvious uncertainties in allowing for the time delay through the crater Camelot, there is no a priori reason to force a specific apparent-velocity line through the EP-1 data point. The first-order conclusion is that high-velocity material (approximately 4 km/sec) must lie beneath the 1200-m/sec material.

Inasmuch as the LM impacted at an elevation of 1.2 km above the valley floor at the Apollo 17 landing site, the LM impact traveltime can be adjusted to the same reference elevation as the LSPE geophone array. The 1.2-km difference in elevation contributes an additional delay time equal to the ratio of the elevation difference to the seismic velocity of the material traversed multiplied by the cosine of the angle of incidence at which the particular seismic

arrival under consideration departed the source (impact point). Inserting the appropriate values in this case leads to a time correction of 0.18 sec. This correction will shift the position of the 4-km/sec apparent-velocity line downward as shown in figure 23-15 such that its zero distance time intercept is decreased. The end result is a decrease in the derived thickness of the 1200-m/sec material from 1020 to 927 m.

It is possible that a dipping interface exists beneath the 1200-m/sec material that might result in a high apparent velocity, or that the particular seismic ray passed through a high-velocity heterogeneity somewhere along its path. Some of the uncertainty may be resolved by subsequent digital velocity filtering (beam steering) of the LM impact signal on the LSPE array. Before the Apollo 17 mission, the best estimates of the seismic velocity variation in the upper 20 km of the Moon were as depicted by lunar model 1 or 2 in figure 23-16. The seismic velocity was known to increase very rapidly from values of 100 to 300 m/sec in approximately the upper 100 m to a value of approximately 4 km/sec at a depth of 5 km. Even though the seismic velocity variation was depicted as a smooth increase with depth, it was surmised (ref. 23-5) that such a rapid increase of velocity (approximately 2 km/sec/km) could not be explained solely by the pressure effect on dry rocks with macrocracks and microcracks nor by the self-compression of any rock powder.

Laboratory velocity measurements on returned lunar soils (refs. 23-6 to 23-10) and recent measurements under hydrostatic pressure conditions on terrestrial sands and basaltic ash have indicated velocity-depth gradients of 0.4 to 0.8 km/sec/km, but such gradients occur only to pressures of approximately  $50 \times 10^5$  N/m<sup>2</sup> (a lunar depth of approximately 1 km). The measurements on unconsolidated sands and rock powders also have demonstrated that no unique relation exists between seismic velocity and porosity in granular material. An examination of these experimental data led to the inference that compositional or textural changes must be important in the upper 5 km of the Moon (ref. 23-5).

The LSPE results have shown that, at least beneath the Taurus-Littrow site, the seismic velocity increases in a stepwise manner in the upper several kilometers. It is of interest to examine the in situ velocity information with reference to the surface geological investigations at the Apollo 17 site, the laboratory velocity measurements from returned lunar samples, and the seismic velocity measurements on terrestrial lunar analogs.

Pre-mission analyses indicated that much of the Apollo 17 landing site area is covered by a dark mantling material, possibly volcanic ash (ref. 23-11). Crew observations of the lunar surface revealed that there was no readily discernible boundary between the overlying thin regolith and the dark mantling material. The thickness of the dark mantling material was estimated to be between 5 and 10 m (ref. 23-3). As pointed out earlier, whether the dark mantling material/subfloor interface represents a sharp seismic discontinuity or is gradational cannot be determined because the shortest explosive-charge-to-receiver distance was approximately 100 m.

The dominant rock type observed underlying the dark mantling material is a medium-grained vesicular basalt believed to be primarily mare-type basalt. Crew observations of the crater walls revealed textural variations that suggest the involvement of individual flow units. Seismic observations have indicated 248 m of 250-m/sec material overlying 927 m of 1200-m/sec material.

The abrupt change in seismic velocity from 250 to 1200 m/sec and, by inference, in other physical properties suggests a major change in the nature of the evolution or deposition of the Apollo 17 subfloor basalts. However, a similar range of seismic velocities has been observed with refraction surveys on terrestrial lava flows. Some insight can be gained by considering specific lava flows that have been examined in some detail as possible lunar analogs: the Southern Coulee, the SP flow, and the Kana-a flow (refs. 23-12 and 23-13).

The Southern Coulee is a recent lava flow near the Mono Craters in eastern California. Seismic velocities range from 160 m/sec at the surface to 2000 m/sec at depth. The higher velocities are found in more competent, denser lava that underlies higher porosity, lower density surface material. The SP flow is a blocky basalt flow located in the northern part of the San Francisco volcanic field near Flagstaff, Arizona. Vesicularity ranges from 5 to 50 percent, and in situ seismic velocities range from 700 to 1100 m/sec. The Kana-a flow, also located near Flagstaff, is an olivine basalt flow intermingled with ash; seismic velocities range from 700 to 1200 m/sec.

Observed velocities on terrestrial lava flows bracket the velocities measured at the Apollo 17 site and therefore support the presence of lava flows in the Taurus-Littrow valley. Whether the 250-m/sec velocity is representative of a separate flow or is merely the manifestation of shattered near-surface basalts mixed with pyroclastic materials cannot be resolved from the seismic data. Nevertheless, a surface

layer of fractured, loose, blocky material merging into more welded flows is a common occurrence on Earth. Photographs of the walls of Hadley Rille (ref. 23-14) also attest to the blocky nature of the near-surface mare basalts. Because of the similarity in structure and the analogous seismic velocities on the Earth and the Moon, the sum of the 248 m of 250-m/sec material and 927 m of 1200-m/sec material, 1175 m, is designated as representing the full thickness of the subfloor basalts at the Apollo 17 site.

The material underlying the basalts with a seismic velocity of approximately 4 km/sec is difficult to classify by rock type. Based on the geological evidence, it seems likely that the highland massif material that rings the narrow, grabenlike valley at the Apollo 17 site underlies the basalt flow or flows. Several rock types were recognized in the North and South Massifs, but the dominant rock type is apparently a coherent breccia believed to be similar to the breccias sampled at the Apennine Front (Apollo 15) and at Descartes (Apollo 16).

Laboratory velocity measurements have been reported for two Apollo 15 breccias, 15418 and 15015 (ref. 23-15). Sample 15418 is described as a dark-gray breccia of chemical composition similar to that of anorthite-rich gabbro. Sample 15015 is a more friable breccia of unknown composition. The in situ value of approximately 4 km/sec is close to the seismic velocities measured in the laboratory for sample 15015 and shown in figure 23-16.

#### CONCLUSIONS

Before the Apollo 17 mission, the question of how the P-wave velocity increased from 100 to 300 m/sec near the surface (refs. 23-16 to 23-19) to approximately 6 km/sec at a depth of 15 to 20 km (ref. 23-2) was unexplained. The main reason for the uncertainty was the gap in traveltime data between the range of a few hundred meters (previous active seismic experiments) and 67 km (Apollo 14 IM impact as recorded by the Apollo 14 passive seismic experiment). The Apollo 17 lunar seismic profiling results have demonstrated that the seismic velocity increases in a sharp stepwise manner in the upper 2.5 km. A surface layer with a seismic velocity of 250 m/sec overlies a layer with a velocity of 1200 m/sec. Beneath the 1200-m/sec layer, the seismic velocity increases sharply to 4000 m/sec. The velocities of 250 and 1200 m/sec agree with those observed for basaltic lava flows, indicating a total thickness of approximately 1200 m for the infilling mare basalts at Taurus-Littrow. When the Apollo 17 results are combined

with earlier traveltime data for direct and surface-reflected seismic arrivals from LM and S-IV9 impacts (ref. 23-2), it will be possible to construct a velocity model for the upper lunar crust believed to be representative for a mare basin. Such work is now underway.

## REFERENCES

- 23-1. Latham, Gary V.; Ewing, Maurice; Press, Frank; Sutton, George; et al.: Passive Seismic Experiment. Sec. 6 of Apollo 14 Preliminary Science Report. NASA SP-272, 1971.
- 23-2. Latham, Gary V.; Ewing, Maurice; Press, Frank; Sutton, George; et al.: Passive Seismic Experiment. Sec. 9 of Apollo 16 Preliminary Science Report. NASA SP-315, 1972.
- 23-3. Apollo Lunar Geology Investigation Team: Preliminary Report on the Geology and Field Petrology of the Apollo 17 Landing Site. U.S. Geol. Survey, Interagency Rept.: Astrogeology 69, Dec. 17, 1972.
- 23-4. Apollo Lunar Geology Investigation Team: Documentation and Environment of the Apollo 17 Samples: A Preliminary Report. U.S. Geol. Survey, Interagency Rept.: Astrogeology 71, Jan. 21, 1973.
- 23-5. Kevach, R. L.; and Watkins, J. S.: The Velocity Structure of the Lunar Crust. The Moon, vol. 7, Apr. 1973, pp. 63-75.
- 23-6. Kanamori, Hiroo; Nur, Amos; Chung, D.; Wones, D.; and Simmons, G.: Elastic Wave Velocities of Lunar Samples at High Pressures and Their Geophysical Implications. Science, vol. 167, no. 3918, Jan. 30, 1970, pp. 726-728.
- 23-7. Kanamori, H.; Mizutani, H.; and Hamano, Y.: Elastic Wave Velocities of Apollo 12 Rocks at High Pressures. Proceedings of the Second Lunar Science Conference, vol. 3, MIT Press (Cambridge, Mass.), 1971, pp. 2323-2326.
- 23-8. Anderson, Orson L.; Scholz, Christopher; Soga, Naohiro; Warren, Nicholas; et al.: Elastic Properties of a Micro-Breccia, Igneous Rock and Lunar Fines from Apollo 11 Mission. Proceedings of the Apollo 11 Lunar Science Conference, vol. 3, Pergamon Press (New York), 1970, pp. 1959-1973.
- 23-9. Mizutani, H.; Fujii, N.; Hamano, Y.; Osako, M.; et al.: Elastic Wave Velocities and Thermal Diffusivities of Apollo 14 Rocks. Lunar Science-III (Rev. abs. of the Third Lunar Science Conference (Houston, Tex.), Jan. 10-13, 1972), Feb. 18, 1972, pp. 547-549.

- 23-10. Warren, N.; Schreiber, E.; Scholz, C.; Morrison, J. A.; et al.: Elastic and Thermal Properties of Apollo 11 and Apollo 12 Rocks. Proceedings of the Second Lunar Science Conference, vol. 3, MIT Press (Cambridge, Mass.), 1971, pp. 2345-2360.
- 23-11. McGetchin, T. R.; and Head, J. W.: Lunar Cinder Cones. Science, vol. 180, no. 4081, Apr. 6, 1973, pp. 68-71.
- 23-12. Watkins, J. S.: Annual Report, Investigation of In Situ Physical Properties of Surface and Subsurface Site Materials by Engineering Geophysical Techniques. NASA Contract T-25091(G), July 1966.
- 23-13. Watkins, Joel S.; Walters, Lawrence A.; and Godson, Richard H.: Dependence of In Situ Compressional-Wave Velocity on Porosity in Unsaturated Rocks. Geophysics, vol. 37, no. 1, Feb. 1972, pp. 29-35.
- 23-14. Howard, Keith A.; Head, James W.; and Swann, Gordon A.: Geology of Hadley Rille. Proceedings of the Third Lunar Science Conference, vol. 1, MIT Press (Cambridge, Mass.), 1972, pp. 1-14.
- 23-15. Todd, Terrence; Wang, Herbert; Baldrige, W. Scott; and Simmons, Gene: Elastic Properties of Apollo 14 and 15 Rocks. Proceedings of the Third Lunar Science Conference, vol. 3, MIT Press (Cambridge, Mass.), 1972, pp. 2577-2586.
- 23-16. Kovach, Robert L.; Watkins, Joel S.; and Landers, Tom: Active Seismic Experiment. Sec. 7 of Apollo 14 Preliminary Science Report. NASA SP-272, 1971.
- 23-17. Kovach, R. L.; and Watkins, J. S.: The Near-Surface Velocity Structure of the Moon. Lunar Science-III (Rev. abs. of the Third Lunar Science Conference (Houston, Tex.), Jan. 10-13, 1972), Feb. 18, 1972, pp. 461-462.
- 23-18. Watkins, Joel S.; and Kovach, Robert L.: Apollo 14 Active Seismic Experiment. Science, vol. 175, no. 4027, Mar. 17, 1972, pp. 1244-1245.
- 23-19. Kovach, Robert L.; Watkins, Joel S.; and Talwani, Pradeep: Active Seismic Experiment. Sec. 10 of Apollo 16 Preliminary Science Report. NASA SP-315, 1972.

TABLE 23-I.- APOLLO 17 LSPE CHARACTERISTICS

Component characteristics	Channel no.			
	1	2	3	4
<b>Amplifiers:</b>				
Noise level, mv rms at input . . . . .	0.75	0.75	0.83	0.83
Dynamic range, rms signal to rms noise in dB at 10 Hz . . . . .	73.4	76.2	75.6	75.8
<b>Geophones:</b>				
Resistance, ohm . . . . .	5970	5953	6080	6153
Generator constant, V/m/sec at 40 Hz . . . . .	235.6	239.2	237.1	235.3
Natural frequency, Hz . . . . .	7.38	7.31	7.40	7.35
<b>System:</b>				
Signal-to-noise ratio (rms signal to rms noise in dB for a 6-nm rms signal at 10 Hz) . . . . .	24.4	26.9	26.8	26.8
Amplitude sensitivity (measured at input to log compressor), V/ $\mu$ m of peak-to- peak ground displacement at 10 Hz . . . . .	7.33	7.02	7.12	7.13

TABLE 23-II.- LSPE SYSTEM SENSITIVITY

Frequency, Hz	Sensitivity, V/μm			
	Channel 1	Channel 2	Channel 3	Channel 4
1	0.1	0.1	0.1	0.1
2	.7	.8	.8	.8
3	1.7	1.7	1.7	1.7
4	2.4	2.5	2.5	2.5
6	4.3	4.2	4.3	4.3
8	6.0	5.8	5.9	5.8
10	7.3	7.0	7.1	7.1
15	10.9	10.5	10.6	10.6
20	13.2	12.8	12.8	13.0

TABLE 23-III.- DETONATION TIMES OF EXPLOSIVE PACKAGES

Charge no.	Explosive weight, g (lb)	Date, 1972	Time, G.m.t.
EP-6	454 (1)	Dec. 15	23:48:14.56
EP-7	227 (1/2)	Dec. 16	02:17:57.11
EP-4	57 (1/8)	Dec. 16	19:08:34.67
EP-1	2722 (6)	Dec. 17	00:42:36.79
EP-8	113 (1/4)	Dec. 17	03:45:46.08
EP-5	1361 (3)	Dec. 17	23:16:41.06
EP-2	113 (1/4)	Dec. 18	00:44:56.82
EP-3	57 (1/8)	Dec. 18	03:07:22.28

TABLE 23-IV.- PARAMETERS OF APOLLO 17 IM IMPACT

Parameter	Value
Day, G.m.t. . . . . .	Dec. 15, 1972
Range time, <sup>1</sup> G.m.t., hr:min:sec . . . . .	06:50:20.84
Real time, G.m.t., hr:min:sec . . . . .	06:50:19.60
Velocity, km/sec . . . . .	1.67
Mass, kg . . . . .	2260
Kinetic energy, J . . . . .	3.15 X 10 <sup>9</sup>
Heading, deg . . . . .	283

<sup>1</sup>Range time is the time the signal of the event was observed on Earth.

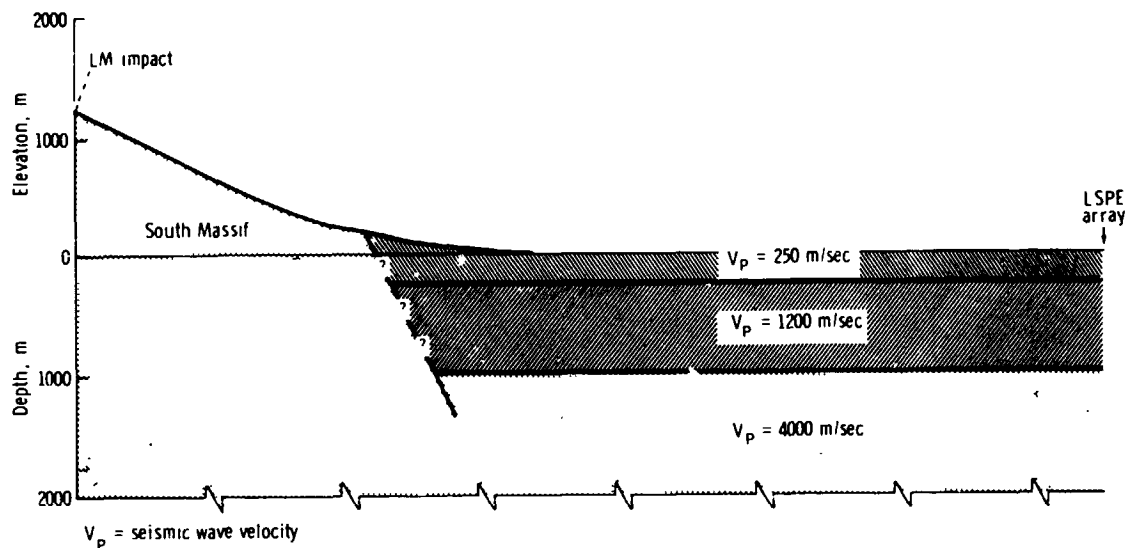
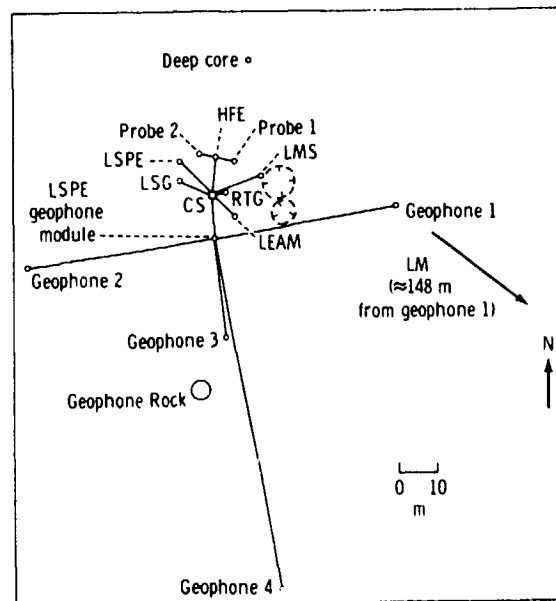


Figure 23-1.- Seismic cross section at the Taurus-Littrow landing site (no vertical exaggeration).



Key: CS - central station  
 HFE - heat flow experiment  
 LEAM - lunar ejecta and meteorites experiment  
 LMS - lunar mass spectrometer  
 LSG - lunar surface gravimeter  
 RTG - radioisotope thermoelectric generator

Figure 23-2.- The LSPE nominal deployment.

ORIGINAL PAGE IS  
 OF POOR QUALITY



Figure 23-3.- Panorama from geophone 2 to the LM as viewed from behind geophone 3 (AS17-147-22546, 22548, 22550, 22552, 22554).

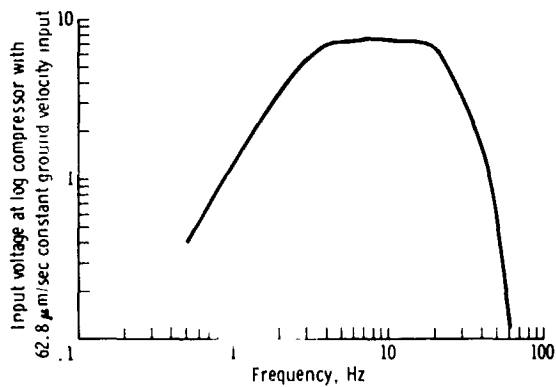
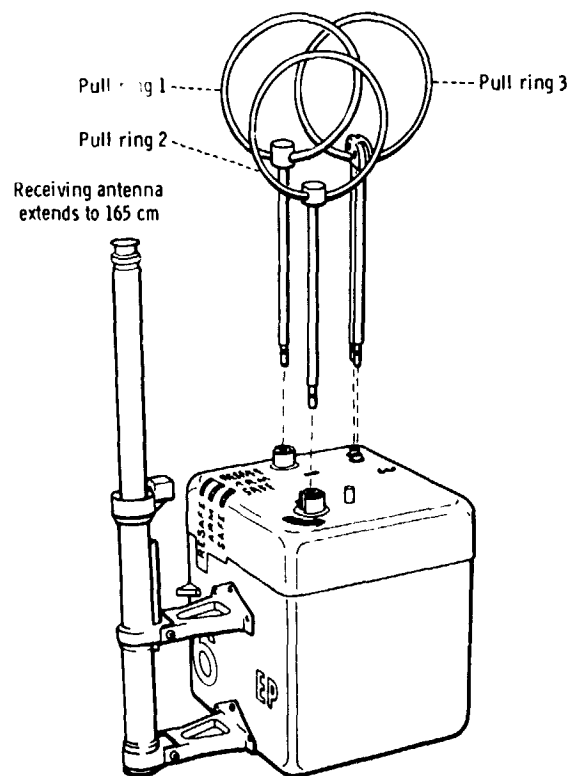


Figure 23-4.- Nominal frequency response of the LSPE.



- Notes: (1) Pull ring 1 - pulls one pin to start SAFE/ARM slide timer  
 (2) Pull ring 2 - swing up ring; rotate 90° counterclockwise; pull pin to release SAFE/ARM plate  
 (3) Pull ring 3 - pulls two pins to free firing pin and start thermal battery timer

Figure 23-5.- Arming sequence for an LSPE explosive package.

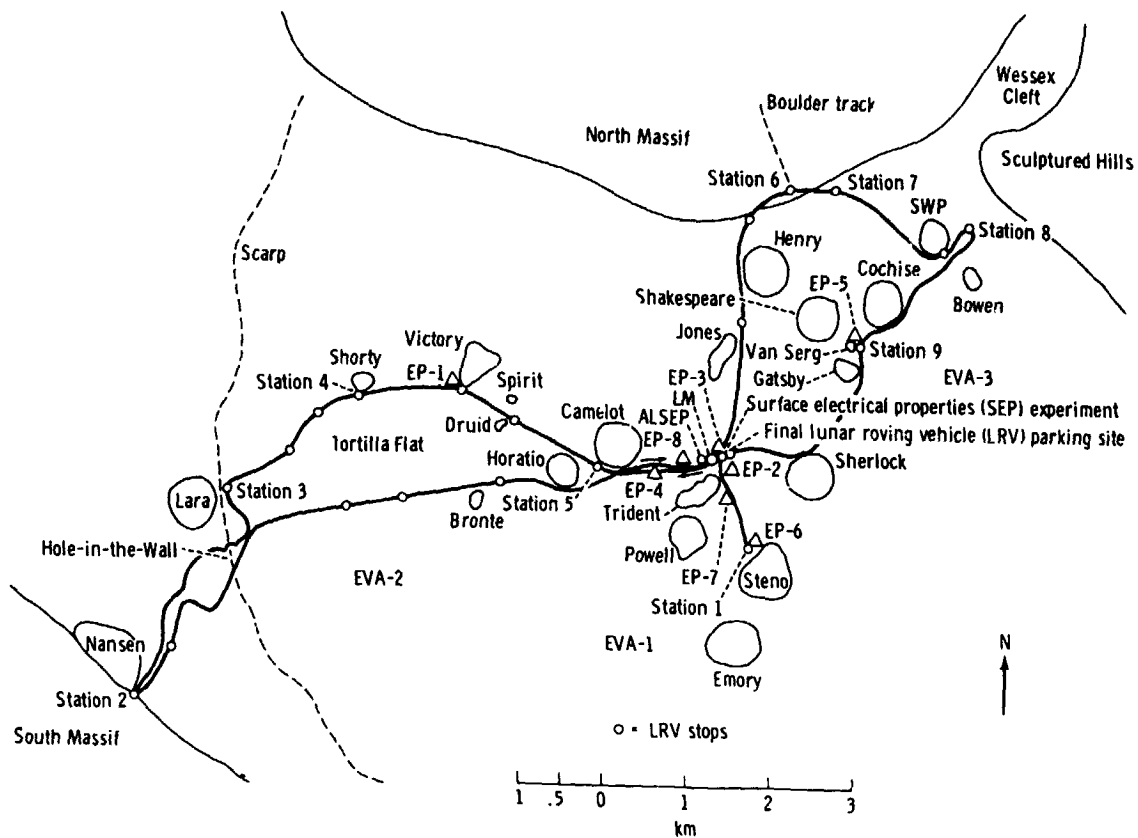


Figure 23-6.- Extravehicular activity traverses showing positions of deployed explosive packages at the Apollo 17 landing site.



Figure 23-7.- Photograph of EP-8 on the lunar surface 296 m west of the LM (AS17-145-22184).

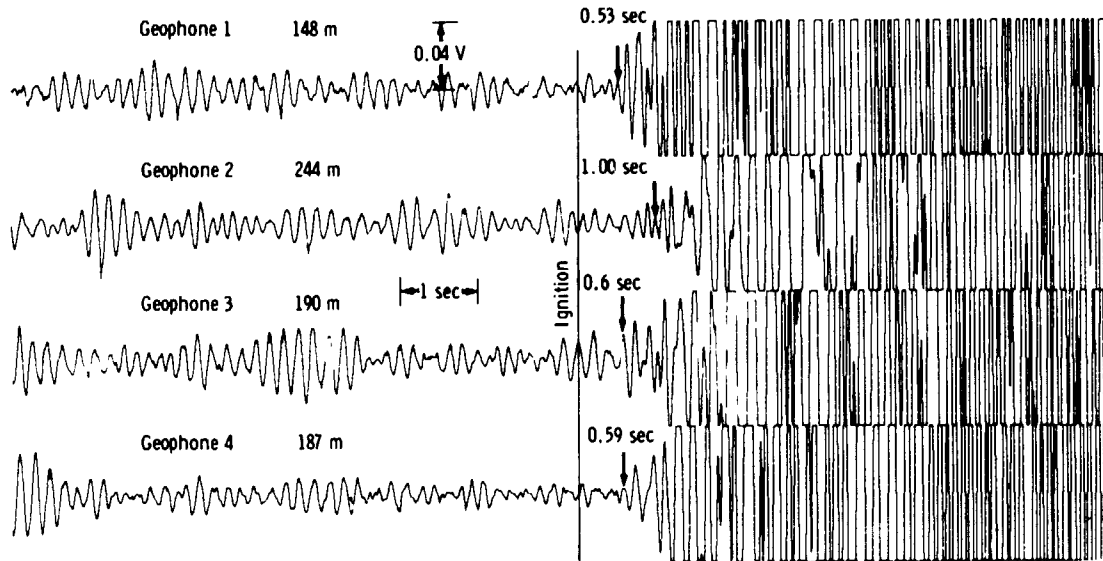


Figure 23-8.- Seismic signals recorded by the LSPE geophones from the lift-off of the Apollo 17 LM ascent stage (Dec. 14). Arrows point to onset of the first seismic arrival.

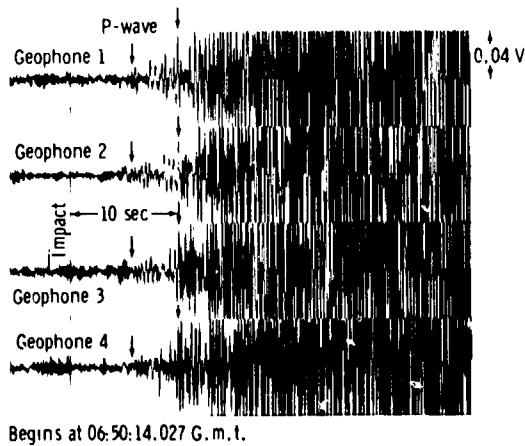


Figure 23-9.- Compressed time-scale record of the seismic signal received from the Apollo 17 LM impact (Dec. 15). Arrows point to measured first and second seismic arrivals.

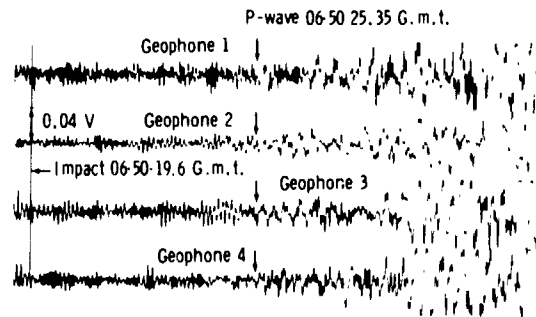


Figure 23-10.- Expanded time-scale record of the seismic signal from the Apollo 17 LM impact.

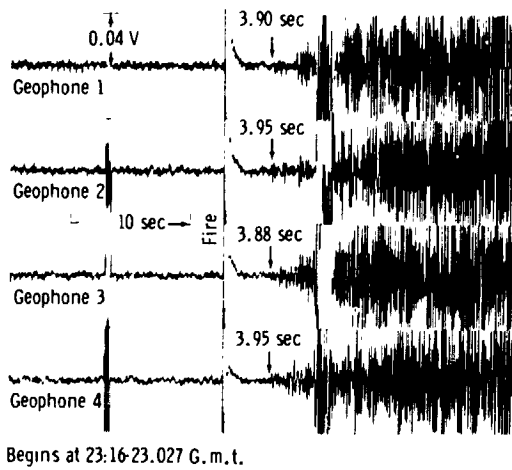


Figure 23-11.- Seismic signals produced by detonation of EP-5 on the lunar surface (Dec. 17). Arrows point to onset of seismic arrival.

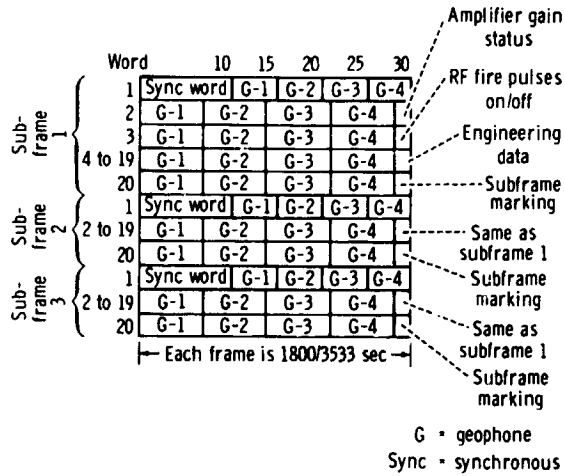


Figure 23-12.- The LSPE data format. Each data frame consists of three subframes of twenty 30-bit words each. Geophone data words are normally 7 bits long except for those in word 1, which are 5-bit samples.

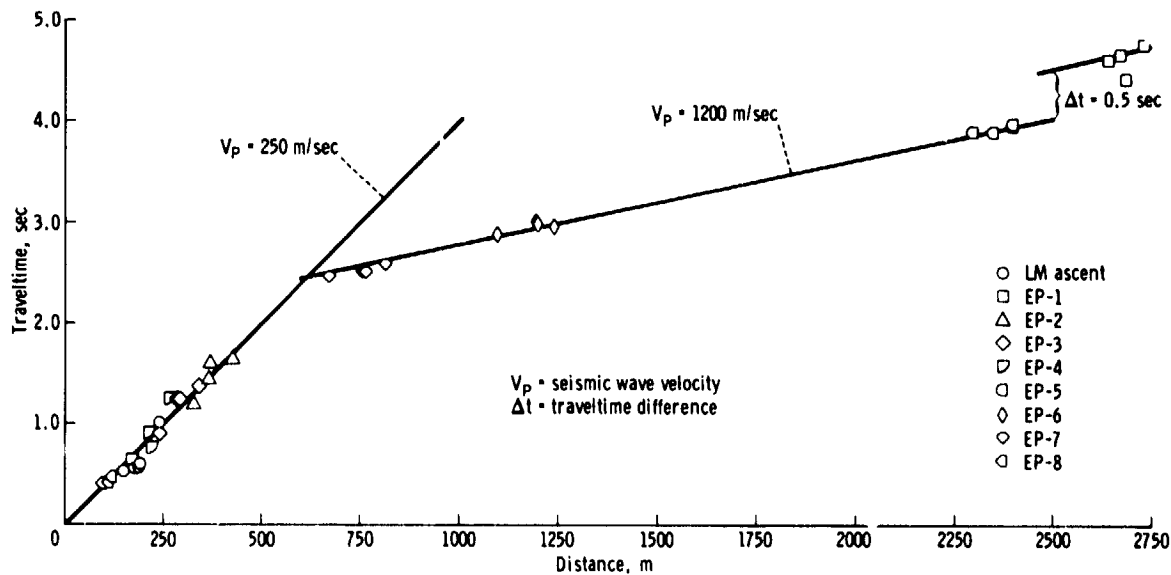


Figure 23-13.- Seismic arrivals from the detonation of the explosive charges plotted on a traveltime/distance graph.

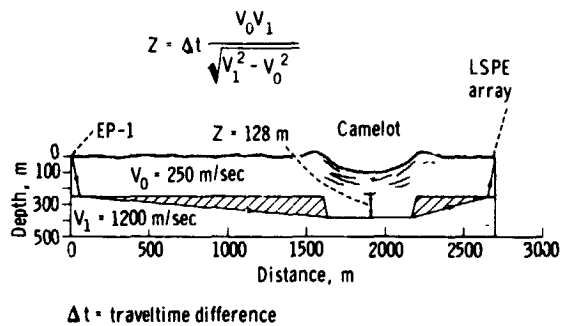


Figure 23-14.- Model approximation for seismic ray path from EP-1 to LSPE array that crosses Camelot Crater. Observed time delay is produced by presence of low-velocity material (of thickness Z) beneath crater.

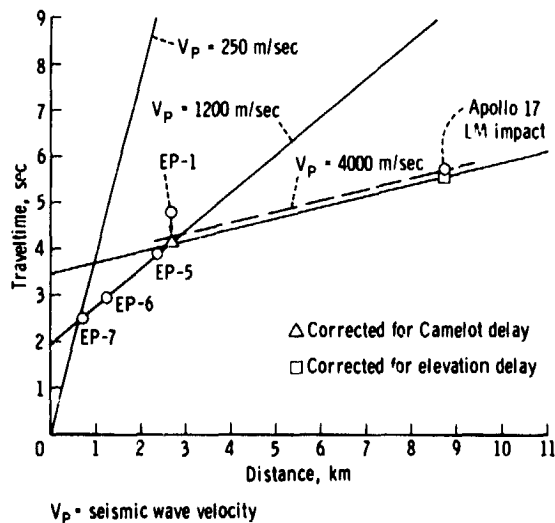


Figure 23-15.- Seismic travel-times from LM impact and LSPE explosive charges. Traveltime for EP-1 has been corrected for Camelot Crater delay, and LM impact traveltime has been corrected for 1.2-km elevation difference between the impact point and the LSPE array. These corrections shift the position of the 4-km/sec apparent velocity slightly downward as shown.

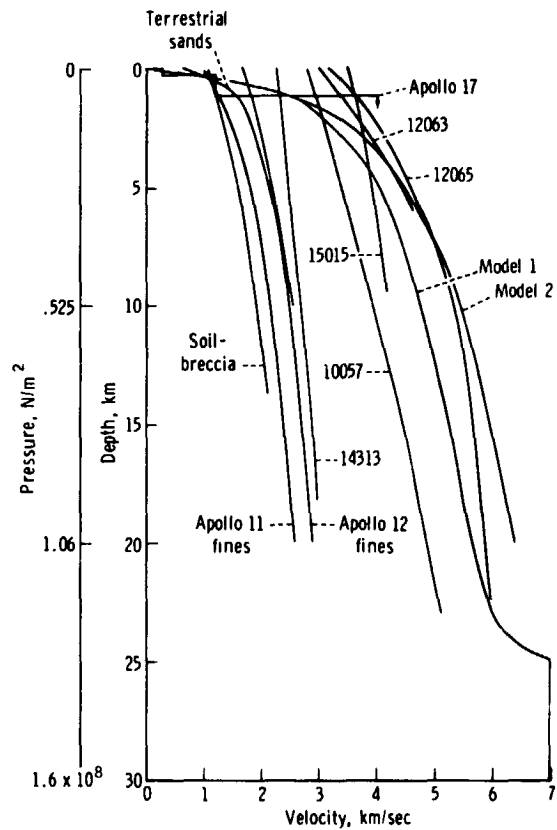


Figure 23-16.- Inferred compressional-wave velocity profiles for the Moon and velocities of lunar and terrestrial rocks measured in the laboratory as a function of pressure. Lunar rocks are identified by sample number. Lunar models 1 and 2 are based on results available through Apollo 16. Apollo 17 results reveal a marked stepwise increase in seismic velocity in the upper 2 km of the Moon.

24. LUNAR NEUTRON PROBE EXPERIMENT (NASA EXPERIMENT S-229)

NSSDC IDENTIFICATION NUMBER:

APOLLO 17 72-096C-13



CONTENTS - SECTION 24

	Page
<u>EXPERIMENT DESCRIPTION</u> . . . . .	24-4
INSTRUMENT DESCRIPTION . . . . .	24-4
TARGETS AND DETECTORS . . . . .	24-7
THE LNPE DEPLOYMENT . . . . .	24-8
<u>ANALYSIS OF MICA DETECTORS</u> . . . . .	24-9
BACKGROUND CORRECTIONS . . . . .	24-10
CALIBRATIONS . . . . .	24-11
ABSOLUTE FISSION RATES . . . . .	24-14
COMPARISON OF EXPERIMENT DATA AND THEORY . . . . .	24-15
COMPARISON WITH NEUTRON CAPTURE RATES MEASURED IN LUNAR SAMPLES . . . . .	24-19
INDUCED FISSION IN LUNAR SAMPLES . . . . .	24-21
FLUENCES IN SURFACE SOIL SAMPLES . . . . .	24-21
<u>ANALYSIS OF PLASTIC DETECTORS</u> . . . . .	24-22
MEASUREMENT ERRORS . . . . .	24-23
BACKGROUND CORRECTIONS . . . . .	24-25
ABSOLUTE NEUTRON CAPTURE RATES AND NEUTRON DENSITIES . . . . .	24-26
COMPARISON WITH THEORETICAL CALCULATIONS . . . . .	24-32
<u>DATA ARCHIVED</u> . . . . .	24-3E
<u>REFERENCES</u> . . . . .	24-39

## 24. LUNAR NEUTRON PROBE EXPERIMENT

Primary cosmic ray protons incident on the lunar surface interact with lunar material by means of nuclear reactions, which produce neutrons as secondary products. The initial investigations of the Apollo 11 samples (ref. 24-1) showed that gadolinium (Gd) in lunar materials contained isotopic variations that could be unambiguously ascribed to neutron capture. Such a record of neutron bombardment had not been observed previously in natural samples, either terrestrial or meteoritic, because, unlike meteorites, lunar samples are materials from a large body that is capable of developing an appreciable secondary flux of low-energy (less than 1 eV) neutrons, and because, unlike the Earth, the Moon has no thick overlaying atmosphere to protect the surface materials from neutron exposure. Since the Apollo 11 mission, neutron capture on samarium-149 ( $^{149}\text{Sm}$ ) (ref. 24-2), europium-151 (ref. 24-3), bromine-79 ( $^{79}\text{Br}$ ) and bromine-81 (ref. 24-4), barium-130 ( $^{130}\text{Ba}$ ) (refs. 24-5 to 24-9), tungsten-186 (ref. 24-10), cobalt-59 ( $^{59}\text{Co}$ ) (ref. 24-11), and calcium-40 ( $^{40}\text{Ca}$ ) (ref. 24-12) also has been observed with fluences (time-integrated fluxes) that range from less than  $1 \times 10^{15}$  to  $1 \times 10^{17}$  neutrons/cm<sup>2</sup>. These data have been used to determine regolith mixing rates and depths, depths of irradiation for lunar rocks, and accumulation rates and deposition times for core samples (refs. 24-1 to 24-7, 24-13, and 24-14). However, all these conclusions depend on knowing the equilibrium neutron energy spectrum, the neutron flux as a function of depth in the regolith, and the absolute rate of neutron production. Until recently, only the theoretical calculations of Lingenfelter et al. (ref. 24-15) and Armstrong and Alsmiller (ref. 24-16) have provided estimates for these quantities. These calculations were of sufficient complexity that it was not possible to be fully confident of the interpretation of the lunar sample data, and, for this reason, the lunar neutron probe experiment (LNPE) was performed. The LNPE was designed to obtain a direct in situ experimental measurement of neutron capture rates as a function of depth in the regolith, as well as to retrieve some information about the energy distribution of the equilibrium neutron flux.

The following sections contain a complete description of the lunar neutron probe and an account of the data. Preliminary results also have appeared in the abstracts for the Fourth Lunar Science Conference (ref. 24-17). All data processing for the LNPE occurred after the return of the instrument to Earth. Excellent agreement was obtained, both for the magnitude and for the depth

dependence of the fission rate, between the experimental (LNPE) and theoretical rates. In this section, the results of the capture rates of Boron-10 ( $^{10}\text{B}$ ) are given, based on the low energy  $^{10}\text{B}(n,\alpha)^7\text{Li}$  neutron capture reaction (where  $n$  refers to neutron capture and  $\alpha$  to alpha particles). This section will focus on the experimental results and the documentation of their accuracy. The implications of the LNPE data for surface mixing processes are discussed in more detail in reference 24-18.

#### EXPERIMENT DESCRIPTION

The LNPE was in the form of a rod that was inserted into the lunar regolith to permit the measurement of neutron capture rates to a depth of 2 m. The LNPE contained two passive particle-track-detector systems: (1) cellulose triacetate plastic (Triafol TN) detectors were used in conjunction with  $^{10}\text{B}$  targets to record the alpha particles emitted by neutron capture on  $^{10}\text{B}$ , and (2) muscovite mica detectors were used to detect the fission fragments resulting from neutron-induced fission in uranium-235 ( $^{235}\text{U}$ ) targets. In addition, 0.46-mm-thick cadmium absorbers were included at two locations to obtain information about the neutron energy spectrum. Cadmium strongly absorbs neutrons that have energies below 0.35 eV; consequently, only the fraction of the neutron population above this energy was measured at these locations. Further spectral information will be available from analyses of krypton-80 and krypton-82 produced by bromine neutron capture in potassium bromide (KBr) contained in three evacuated capsules inserted in the probe. The bromine neutron capture occurs at energies (10 to 100 eV) that are significantly higher than those for  $^{235}\text{U}$  and  $^{10}\text{B}$ . Krypton analyses will be performed by Marti and Osborne of the University of California (San Diego), and results will be published.

#### INSTRUMENT DESCRIPTION

The LNPE was taken to the Moon in a deactivated mode, activated and deployed during the first period of extravehicular activity (EVA-1), then deactivated at the end of EVA-3 and returned to Earth for processing of the track detector materials. Figure 24-1 is a schematic, cross-sectional view of the lunar neutron probe showing the layout of the target-detector systems and illustrating the mechanism of activation and deactivation. The  $^{10}\text{B}$  targets are mounted on one-half of the outer circumference of a central rod (fig. 24-2). The mica detectors are fixed on flats milled on the opposite side of the central rod (fig. 24-3). Concentric with and

surrounding the central rod is an open cylindrical frame structure (rib cage) around which sheets of the plastic detector are wrapped. The  $^{235}\text{U}$  targets are mounted in discrete positions over windows in the rib cage (fig. 24-4). A continuous, black-anodized tube (not shown in fig. 24-1) is used as a casing to enclose and protect the target-detector systems.

The probe is activated and deactivated by a  $180^\circ$  rotation of the central rod with respect to the rib cage (fig. 24-1). In the activated configuration, the uranium-mica and the boron-plastic target-detector pairs are brought into alignment. In the deactivated configuration, the uranium and boron targets are adjacent and the mica and plastic detectors likewise. In the latter configuration, particles emitted from the target surfaces cannot enter the respective detectors; thus, the probe is deactivated. The activation and deactivation mechanism was necessary to prevent the accumulation of background events from neutrons produced by cosmic ray interactions in the spacecraft and by the plutonium-238 ( $^{238}\text{Pu}$ ) power source for the Apollo lunar surface experiments package (ALSEP), the radioisotope thermoelectric generator (RTG), which is a strong neutron source (approximately  $7 \times 10^7$  neutrons/sec).

Figure 24-5 is a schematic, cutaway view of the LNPE showing the manner in which the various detectors were deployed along the length of the probe. For reference, the theoretically predicted depth (in units of grams per square centimeter) profile of the neutron capture rate is plotted. To permit accurate definition of the flux profile, the length of the probe was chosen to be 2 m, a depth that is well below the theoretically predicted peak of the profile (approximately  $150 \text{ g/cm}^2$ ). The boron-plastic detection system was essentially continuous along the full length of the probe. As shown in figure 24-5, 16 uranium targets and mica detectors were mounted at 8 discrete locations along the probe. The uranium-mica target-detector pairs were mounted with uniform separations in the lower half of the probe but were closely spaced and concentrated toward the top in the upper half of the probe. This arrangement was chosen for two reasons. First, the temperature of the probe was expected to be highest near the surface, and the investigators were concerned about thermal annealing of the tracks in the plastic detectors. Fission tracks in mica are not annealed even at peak lunar surface temperatures; thus, if data were lost in the plastic at the top of the probe, the mica data would still provide the near-surface record. Second, from theoretical predictions, the lowest track densities were expected near the surface, and results from the Apollo 16 cosmic ray experiment (ref. 24-19) suggested that these densities might be quite low. At such densities, mica detectors give more reliable results than plastic detectors.

Also displayed in figure 24-5 are the locations of the two cadmium absorbers near the bottom and middle of the probe. A 0.46-mm-thick cadmium sheet was wrapped around the rib cage over the plastic detector at each site (fig. 24-6). The evacuated KBr capsules were inserted at the top, middle, and bottom of the probe, as shown. In addition, three point sources of  $^{238}\text{U}$  were mounted near the bottom, middle, and top of the probe in flats milled on the side of the central rod on which the  $^{10}\text{B}$  targets were mounted (fig. 24-2). The reason for including the point sources was two-fold. The alpha particles emitted by these point (1- to 2-mm) sources registered in the plastic detectors only while the probe was activated and thus provided fiducial marks from which the proper activation of the probe can be verified. Also, from the track densities and the appearance (length, width, etc.) of the  $^{238}\text{U}$  alpha-particle tracks, it will be possible to determine whether the tracks in the plastic detectors have been thermally annealed during and after the activation and the lunar surface exposure.

In wrapping the plastic sheets on the rib cage, an overlapping second layer was placed over the window areas, primarily to secure the plastic to the rib cage. Because the second layer was never exposed to any of the targets, four small portions of plastic in this outer layer were irradiated with a known dose of  $^{238}\text{U}$  alpha particles to provide an additional check on thermal annealing in the plastic. Further, the areas of the plastic detectors in this second layer that were not irradiated provided a continuous record of background events resulting from cosmic rays and tracks produced by nuclear interactions (recoils) of the RTG fast neutrons with the plastic. Based on analyses of small pieces of the Triafol TN plastic carried on the Apollo 15 spacecraft, the background from cosmic ray alpha particles and heavy ions was expected to be negligible. The Apollo 16 cosmic ray experiment results had suggested that the plastic would register tracks from fast-neutron interactions (ref. 24-19). Separate experiments using both californium-252 ( $^{252}\text{Cf}$ ) and plutonium-beryllium (Pu-Be) neutron sources have shown that fast (MeV) neutrons produce tracks with an efficiency of approximately  $2 \times 10^{-6}$ . For this efficiency, an RTG fast-neutron background track density of approximately 150 tracks/cm<sup>2</sup> was expected in the plastic during the flight to the lunar surface. This value is not large compared to predicted  $^{10}\text{B}$  alpha-particle track densities (greater than 1000 tracks/cm<sup>2</sup>).

To provide an actual measurement of the maximum temperature exposure of the LNPE, temperature indicators were fastened to flats in the central rod at four positions along the probe (fig. 24-3). Each temperature indicator contained four separate temperature-sensitive compounds that irreversibly turn black at 333, 344, 355, and 366 K, (140°, 160°, 180°, and 200° F), respectively.

The completely assembled flight unit is shown in figure 24-7. For convenient stowage on the spacecraft, the LNPE was fabricated in two 1-m-long sections that could be activated separately. The upper section (on the right in fig. 24-7) was activated by depressing a bar on the large handle at the upper end and rotating the handle 180°. The lower section was activated by removing the dust cap at its upper end and using it as a tool to rotate the central rod. The center rod was spring loaded to snap into one of two stable configurations differing by a 180° rotation. After activation, the two sections could be coupled for deployment by simply screwing the two sections together.

#### TARGETS AND DETECTORS

The boron targets were prepared with a process especially developed for this experiment. The  $^{10}\text{B}$  was vacuum deposited as metallic boron by the thermal cracking of diborane onto 0.05-mm-thick tantalum half-cylinders. The deposition temperature was approximately 1073 K. The  $^{10}\text{B}$  targets were made "infinitely thick"; that is, they were deposited to an average thickness of  $1.4 \pm 0.2 \text{ mg/cm}^2$ , which is greater than the range of the 1.6-MeV alpha particles emitted with neutron capture on  $^{10}\text{B}$ . Each target was tested individually using a Pu-Be neutron source. The thickness and uniformity of several targets also were checked by alpha backscattering techniques using the California Institute of Technology tandem Van de Graaff accelerator.

The  $^{235}\text{U}$  targets were cut from 0.025-mm-thick foil sheets of 99 percent enriched  $^{235}\text{U}$ , cleaned in nitric acid ( $\text{HNO}_3$ ), and then coated with a 30-nm-thick layer of silver to prevent oxidation and corrosion of the uranium. A film of this thickness produces negligible attenuation of the emitted fission fragments. Alpha-particle counts were determined for each target to verify the relative quality and uniformity of the targets used.

Experimentation with Triafol TN has shown that this plastic is somewhat nonuniform in its track registration properties. Exposure to monoenergetic accelerated alpha particles indicates an energy registration interval from approximately 0.25 to 2.5 MeV, which probably applies to most samples. However, some batches of plastic show considerably reduced sensitivity that is critically dependent on whether the irradiations are performed in air or in vacuum. One batch in particular will not register alpha particles in vacuum but does register the particles in air. These phenomena presumably reflect the critical role played by oxygen in track formation in plastic. This oxygen influence has been studied previously by Monnin (ref. 24-20) and by Crawford et al. (ref. 24-21).

Because of the lack of uniformity, the registration properties of representative samples of the plastic used for the flight unit were determined by using vacuum neutron irradiations of the plastic samples exposed to a  $^{10}\text{B}$  target. The registration of the plastic was uniform to better than  $\pm 10$  percent over an area of approximately  $0.3\text{ m}^2$ . Comparison of air and vacuum registration shows a small vacuum effect, with the vacuum registration efficiency being less by approximately  $12 \pm 3$  percent.

Before incorporation into the probe, the plastic and mica detectors were preannealed to remove any possible background tracks. Preannealing of the mica was particularly important because muscovite, like most natural micas, has a nonnegligible density of fossil fission tracks from the spontaneous fission decay of trace uranium impurities. The mica was annealed at 903 K for 3.5 hr; the plastic, at 389 K for 9 days. In addition to being preannealed, the mica was pre-etched 4 hr in 48 percent hydrofluoric acid (HF) at room temperature and then silver coated (approximately 30 nm thick). Because normal etching time for fission tracks in muscovite mica usually is 20 min to 1 hr, any small, shallow pits left after the preannealing appear as huge, shallow troughs and cannot be confused with the smaller diameter lunar-neutron-induced fission tracks. The silver coating was applied to monitor any possible flaking of the prime detecting surface of the mica. The coating does not affect the registration properties of the mica.

The techniques used for preparing the detectors for data analysis are standard. The mica detectors were first desilvered in a 35-percent solution of  $\text{HNO}_3$  and then etched in 48 percent HF for 25 min or 1 hr. Data reported in this section are from samples etched 25 min and scanned in an optical microscope at 630X magnification. Samples etched 1 hr have larger tracks and were scanned at a lower (500X) magnification. When a sample was etched for 25 min and counted, then etched further to 1 hr and recounted, the results agreed within one standard deviation.

#### THE LNPE DEPLOYMENT

The deployment of the LNPE was nominal. The LNPE was retrieved from the modularized equipment stowage assembly (MESA) and was loaded on the lunar roving vehicle at the beginning of EVA-1. To prevent overheating, the two sections were kept in a thermal bag before actual deployment. Following the ALSEP deployment, the deep drill core-stem sample was acquired at a site approximately 40 m north (ref. 24-22) of the ALSEP central station and the RTC power source. After the recovery of the deep core, the two LNPE sections were removed from the thermal bags, activated, coupled, and emplaced in the deep drill core-stem hole.

The insertion was made after first passing the probe through the hole in the treadle used for recovering the deep core. The treadle was used because, in retrieving the deep core, the top of the hole had been widened; thus, the possibility existed that the probe would drop too far into the hole to be retrieved. Full emplacement of the LNPE was achieved manually. The LNPE was deployed in a shallow depression behind a meter-sized rock to provide additional shielding from the RTG neutrons. To prevent overheating, the top of the probe, which protruded above the surface, was covered with the thermal bag during exposure. The LNPE was recovered, decoupled, deactivated, and returned to the lunar module at the very end of EVA-3, after 49 hr of exposure.

The LNPE was returned to the investigators where it was disassembled. The targets and detectors were in excellent condition; no flaking was observed in the mica detectors or on the boron targets. Furthermore, the temperature indicators showed that the probe temperature did not reach 333 K.

#### ANALYSIS OF MICA DETECTORS

The complete analysis of the mica detectors is presented in this section. The fission track densities in the mica were measured by conventional transmitted-light optical scanning techniques after being etched for usually 1 hr in concentrated HF (48 percent) at room temperature.

Figure 24-8 is a plot of the experimental data in which the measured track densities are plotted against depth in centimeters beneath the lunar surface. Because of the geometrical arrangement of the uranium-mica detectors (fig. 24-1), the fission track density is not uniform over the surface of the mica. The data shown in figure 24-8 represent the average track density of a standard area (approximately  $0.8 \text{ cm}^2$ ) on the mica. The error bars on the experimental data points are  $\pm 1$  standard deviation (typically 3 to 4 percent) based on counting statistics only. All track density measurements were made by the same observer. The reproducibility of the track densities is good, as can be judged by the agreement of the data points, which occur in pairs (fig. 24-8) and correspond to the two mica detectors mounted at essentially the same positions (fig. 24-1). For depths greater than approximately 60 cm, the change in the fission rate is small compared to the separation (4 cm) of the two mica detectors at a given position, and the same track density should be obtained. Figure 24-8 shows that, except for the deepest position at 185 cm, the error bars overlap for all positions even though an interval of 3 months had elapsed between the scanning of the first detector and the scanning of the second detector of each pair. In addition, one of the detectors was rescanned at a later time, and that measurement was in excellent agreement with the previous measurement.

## BACKGROUND CORRECTIONS

Background corrections to the fission track densities, both measured and estimated, are small and none have been applied.

Background from fission in the  $^{235}\text{U}$  targets by neutrons produced by cosmic ray interactions in the spacecraft was not registered in the micas because the probe was only activated when deployed on the lunar surface. Possible fossil fission track background from the spontaneous fission of small amounts of uranium in the mica was eliminated by annealing and pre-etching the mica before exposure. Direct registration of cosmic ray heavy ions was expected to be very small; but, as a check, the back side of one of the mica detectors, which was never exposed to the uranium targets, was scanned and an upper limit of  $10 \text{ tracks/cm}^2$  was obtained. This amount is negligible compared to the track densities measured on the prime detector surfaces. Further, of the  $14\text{-cm}^2$  area scanned, only one anomalously long ( $65 \times 10^{-6} \text{ m}$ , but not fully etched) cosmic ray heavy ion track was observed.

(Fission fragment tracks are, at most, approximately  $10 \times 10^{-6} \text{ m}$ ).

The neutrons produced by the plutonium-oxide ( $\text{PuO}_2$ ) power source (the RTG) during the LNPE deployment were the most important source of background. Because of mission time line restrictions, the LNPE was deployed as close as practicable to the other geophysical experiments. The background effects of the RTG neutrons have been estimated both theoretically and with a field simulation experiment in basaltic terrain using a  $^{252}\text{Cf}$  neutron source. The depth profile of the fission rate produced by the RTG neutrons is quite distinct from the profile due to lunar neutrons in that it peaks closer to the surface, shows less rise from the surface to the maximum, and declines faster at depth. Therefore, the background contributions are highest for the mica detectors nearest the surface and decrease rapidly for the deeper detectors. Based on the theoretically calculated fission rates and profile, the known source strength of the RTG ( $5.8 \times 10^7$  neutrons/sec), the separation of the RTG and the LNPE (36 m), and the variation of the capture rate with distance from the source (as measured in the field simulation), an estimated 2.5 percent background correction for the shallowest mica detector at  $20 \text{ g/cm}^2$  is obtained. Alternatively, taking the measured track density for detectors on the surface during the field simulation and the theoretical fission rate profile, a maximum background correction of 7 percent would be obtained at a depth of  $20 \text{ g/cm}^2$ .

The 7-percent correction is an overestimate because the basaltic material in which the  $^{252}\text{Cf}$  simulation was performed contained 0.6 percent water and had a lower iron and titanium content than the basaltic material on the lunar surface and because the  $^{252}\text{Cf}$  source was placed 50 cm above the surface, whereas the  $\text{PuO}_2$  in the RTG was a distributed source extending from 0 to 45 cm above the lunar surface. Using the theoretical fission rates for lunar material by Lingenfelter, Canfield, and Hess (LCH) (ref. 24-23) and older calculations for basaltic material with approximately 1.5 percent water, the effect of the chemical differences is estimated to be at least a factor of 2.4, which would imply a maximum background correction of 3 percent at  $20 \text{ g/cm}^2$ . This correction is in agreement with that estimated directly from the theoretical calculations. Consequently, the background corrections for fission induced by RTG neutrons are not important and none have been applied to the data.

#### CALIBRATIONS

The relationship between the measured track density  $\rho$  (tracks/cm<sup>2</sup>) in the mica detectors and the fission rate  $n$  (fissions/g( $^{235}\text{U}$ )-sec) in the uranium targets is given by

$$f\rho = nT\frac{R}{2}G \quad (24-1)$$

where  $T$  is the exposure time of the probe,  $R$  is the mean range in grams per square centimeter of a single fission fragment in metallic uranium, and  $G$  is a dimensionless constant defining the geometrical efficiency of the mica detectors compared to  $2\pi$  geometry ( $G \leq 1$ ). The quantity  $R/2$  is the average depth from which fission fragments produced in the uranium will register in a mica detector placed on the surface of the uranium ( $2\pi$  geometry). In the actual experimental configuration, because of the necessity for an on-off mechanism, the targets and detectors were not in contact;  $G$  is the factor that accounts for the decrease in detector efficiency caused by the required separation. A correction for self-absorption  $f$  must be applied because the target materials in the neutron probe are strong neutron absorbers; consequently, the neutron flux and hence the measured track densities in the presence of the probe are somewhat depressed compared to their values in the absence of the probe materials. As defined in equation (24-1),  $f$  is a dimensionless constant and must have a value  $\geq 1$ . The values for  $f$ ,  $R$ , and  $G$  are obtained from laboratory calibration experiments.

The value of  $R$  is expected to be close to the average radiochemically determined fission-fragment range in metallic uranium,  $10 \text{ mg/cm}^2$  (ref. 24-24). However, as indicated by the studies of Reimer et al. (ref. 24-25), the range value appropriate for equation (24-1) may be less than that measured radiochemically because of loss of the very shortest tracks (from barely penetrating fission fragments) in the scanning procedures or from an intrinsic difference between the etchable track length and the actual penetration depth of the fission fragment. Depleted uranium/mica detectors were irradiated in  $2\pi$  geometry in a well-thermalized neutron flux, monitored by gold foil activation.

The determination of the absolute flux was based on scaling the observed gold-198 ( $^{198}\text{Au}$ ) activity to that obtained in an irradiation of the same gold foils in the National Bureau of Standards (NBS) radium-beryllium (Ra-Be) neutron source (ref. 24-26). Fluxes for four different thin gold foils were calculated from the NBS calibration and from independent measurements of the absolute detection efficiency of  $^{198}\text{Au}$  gamma rays. Good agreement was obtained (within  $\pm 1$  percent) between fluxes calculated by the first method and those obtained by the second method. However, the uncertainties in the absolute fluxes measured by both methods are larger. An effective range,  $R = 8.55 \pm 0.32 \text{ mg/cm}^2$ , was obtained for the standardized etching and scanning conditions. The quoted error reflects primarily the uncertainties in the absolute flux determination. Depleted uranium (0.41 percent  $^{235}\text{U}$ ) targets were used to eliminate self-absorption effects.

The value for  $G$  was determined by assembling an instrument fabricated identically to the flight probe but with two mica samples mounted in direct contact with two natural uranium targets on the rib cage and with two mica detectors mounted on the center rod flats in the standard configuration opposite the uranium targets (fig. 24-1). After neutron irradiation,  $G$  was calculated from the ratio of the fission track densities in the mica on the center rod to the densities in the micas irradiated in  $2\pi$  geometry. The agreement between the two measurements of  $G$  was good and yielded a mean value of  $0.58 \pm 0.02$ . This determination was checked by assembling various units of the probe in the same fashion as above but with plastic detectors mounted in place of the micas. The value of  $G$  was calculated from the ratio of the uranium alpha-particle track densities in the center rod plastic to the densities in the plastic in direct contact with the uranium. The results of the second method agree, within the errors, with the first determination. The mica data yield the more reliable results and these have been used. Measurements of the relative efficiency of the 16 mica positions on the flight probe during the calibration irradiations show a spread of  $\pm 3.4$  percent (average deviation); consequently, an additional  $\pm 3.4$  percent error must be added to apply the  $G$  value to the

probe data. Natural uranium and depleted uranium were used in all evaluations of  $R$  and  $G$  to eliminate self-absorption effects.

At present, the principal uncertainty in the absolute fission rate is the value for  $f$ . Unlike the values of the other factors in equation (24-1), the value of  $f$  varies with neutron energy. However, it is possible to estimate  $f$  using only general considerations about the lunar neutron energy distribution without depending on the accuracy of the theoretical energy spectrum. The calibration procedures used have been designed to determine  $f$  by using neutron energy spectra that are harder and softer than the lunar spectrum and thus bracket the lunar self-absorption factor.

Lunar material is a good absorber of low-energy neutrons; thus, the neutron energy spectrum in the region below 1 eV will be significantly shifted to higher energies compared to the Maxwell-Boltzmann distribution that would be expected if the low-energy neutrons were able to come into thermal equilibrium. This shift is shown, for example, by the measured ratio of samarium neutron capture to gadolinium neutron capture in lunar samples, which is much higher than the ratio expected for a thermalized neutron energy distribution (refs. 24-2 and 24-3).

Because the self-absorption is greatest at those energies at which the fission cross sections are large and because the  $^{235}\text{U}$  fission cross section is highest at low neutron energies, the self-absorption factor obtained in an irradiation with a thermal spectrum will be an upper limit for the value of  $f$  that is appropriate for the lunar data.

A calibration irradiation was performed in a uniform, well-thermalized neutron flux, and a value of  $f = 1.42 \pm 0.05$  was determined by comparing track densities from the actual  $^{235}\text{U}$  targets with those from much more dilute  $^{235}\text{U}$  targets, consisting of either natural uranium (0.72 percent  $^{235}\text{U}$ ) or depleted uranium (0.409 percent  $^{235}\text{U}$ ), in which the self-absorption was negligible. The  $^{235}\text{U}/^{238}\text{U}$  ratio in the depleted uranium was measured directly. The  $^{235}\text{U}$  targets were mounted at one end of a test unit of the probe in the actual experimental configuration, including  $^{10}\text{B}$  targets on the center rod. At the other end of the probe, isolated from any  $^{10}\text{B}$  targets, the natural- and depleted-uranium targets were similarly mounted. The measured value of  $f$  thus includes the effect of the  $^{10}\text{B}$  targets on the  $^{235}\text{U}$  fission rate as well as the effect of the  $^{235}\text{U}$  foils.

To estimate  $f$  for a high-energy neutron spectrum, cadmium-covered samples were irradiated in both the actual probe geometry and in  $2\pi$  geometry. In such irradiations, the  $^{235}\text{U}$  fission is produced by the resonance part of the reactor neutron spectrum (i.e., by neutrons of energies greater than 0.52 eV (ref. 24-27), which have a  $1/E$  spectrum, where  $E$  is neutron energy). Unlike the thermal irradiation described in the preceding paragraph, it is not possible to use a comparison with natural uranium targets in the cadmium-covered irradiation to obtain  $f$  because of large (approximately 65-percent) contributions from fast (MeV-neutron) fission of  $^{238}\text{U}$  in the natural uranium foils. The self-shielding for a  $1/E$  spectrum has been estimated two ways: (1) by measuring the absolute resonance flux using  $^{10}\text{B}$ -plastic detectors and comparing the measured track density for a  $^{235}\text{U}$  target to that calculated using the known  $^{235}\text{U}$  fission resonance integral (ref. 24-28) and (2) by measuring the ratio of track densities from pure  $^{235}\text{U}$  and from 5-percent  $^{235}\text{U}$  foils of the same thickness. Corrections ( $\leq 20$  percent) for fast fission in the 5-percent  $^{235}\text{U}$  foils introduce negligible error. Values of  $f$  ranging from 1.0 to 1.3 have been obtained in these experiments. Although the reasons for these variations are not completely understood, the purpose of the experiments was to set a lower bound  $f$  for a lunar spectrum. For this reason and because the more precise experiments gave values of  $f = 1.0$ , the lower boundary on the self-absorption factor for a lunar spectrum must extend as low as 1.0.

This lower limit was combined with the upper boundary of 1.4 from the thermal irradiation, and a self-absorption factor of  $f = 1.2 \pm 0.2$  was adopted for the lunar exposure.

#### ABSOLUTE FISSION RATES

To make an explicit comparison between theory and experiment, the depth of the mica detector pair at 77 cm ( $150 \text{ g/cm}^2$ ) was used as a reference depth. Using the values of  $R$ ,  $G$ , and  $f$  given above, a  $^{235}\text{U}$  fission rate of  $3.4 \pm 0.6 \text{ sec}^{-1} \text{ g} (^{235}\text{U})^{-1}$  is obtained at the reference depth; this rate corresponds to the peak of the fission rate profile. Within these error limits, the  $^{235}\text{U}$  fission rate has been obtained independently of any detailed assumptions about the neutron energy spectrum or reference to the LCH theory.

Capture rates are the most useful quantities for application to lunar sample data, but it is still of interest to estimate the

neutron flux implied by the observed fission rate. To obtain a flux, an energy spectrum must be assumed. Using the LCH spectrum for Apollo 11 material and 200 K, the fission rate of  $3.4 \pm 0.6 \text{ sec}^{-1} \text{ g}({}^{235}\text{U})^{-1}$  corresponds to a flux of  $1.4 \text{ neutrons/cm}^2\text{-sec}$  of neutrons with energies less than 0.2 eV. It should be stressed that, because of the nonthermal spectrum, calculation of accurate capture rates is not possible by simply combining the flux of  $1.4 \text{ neutrons/cm}^2\text{-sec}$  with standard literature thermal cross sections. In addition, if the LCH spectrum is adopted, the flux of neutrons in the resonance energy region (from 0.5 eV to 2.7 keV) can be represented by  $\phi(E) = K/E^{0.9}$  with E in electron volts. A value of  $K = 1.6 \text{ neutrons/cm}^2\text{-sec}$  is obtained from the measured fission rate at  $150 \text{ g/cm}^2$ .

#### COMPARISON OF EXPERIMENT DATA AND THEORY

In this section, a detailed comparison between LNPE results and theory is presented. Primarily, the LCH calculations are used for theoretical comparison, although some reference is made to similar calculations by Armstrong and Alsmiller (ref. 24-16) and by Kornblum et al. (ref. 24-29).

The theoretical  ${}^{235}\text{U}$  fission rate can be calculated

$$n = S \int_0^{\infty} N \sigma_F(E) \phi(E) dE \quad (24-2)$$

where N is the number of atoms per gram  ${}^{235}\text{U}$ ,  $\sigma(E)$  is the fission cross section for  ${}^{235}\text{U}$ ,  $\phi(E)$  is the energy distribution of the neutron flux as calculated by LCH, and S is the ratio of the cosmic ray neutron production rate for the 2 days in which the neutron probe was deployed on the lunar surface to the average rate over the 11-yr solar cycle. The factor S is necessary for the comparison of experiment and theory because the magnitude of the theoretical flux is calculated as the average for the last solar cycle.

The value of  $\phi(E)$  was calculated by LCH for the composition of the Apollo 11 soil sample 16084 at a temperature of 200 K. The correct temperature is 250 K; however, the LCH calculations for temperatures of 0, 200, and 400 K show essentially no variation of the fission rate with temperature. Changes in temperature primarily affect the shape of the low-energy spectrum rather than the neutron density; and, to the extent that the fission cross section at low energies is approximately inversely proportional to velocity, the low-energy ( $\leq 0.5$ -eV) fission rate depends only on the density of low-energy neutrons and is essentially independent of the detailed spectral shape. The high-energy part of the fission rate is expected to be independent of temperature. Changes in the absorption cross section due to chemical variations will change the number of neutrons that are slowed to low energies; thus, the fission rate will be somewhat chemistry dependent (ref. 24-15). However, the average composition of the upper part of the Apollo 17 core (ref. 24-30) corresponds to an effective macroscopic absorption cross section ( $0.00936 \text{ cm}^2/\text{g}$ ) (ref. 24-15) that is virtually identical to that of the Apollo 11 composition of LCH ( $0.00925 \text{ cm}^2/\text{g}$ ). Consequently, negligible error should be introduced by the use of the Apollo 11 calculations.

The solar cycle correction  $S$  can be derived from terrestrial atmospheric fast (2- to 10-MeV) neutron fluxes  $F$  for high altitudes and high geomagnetic latitudes (where the geomagnetic cutoff is negligible). Since  $F$  should be directly proportional to the lunar fast-neutron flux, which is the source of the low-energy neutrons captured by the  $^{235}\text{U}$ ,  $S$  is the ratio of  $F$  (measured during the Apollo 17 mission) to the solar cycle average value. Atmospheric fast-neutron data for the time of the Apollo 17 mission are not available. However, Merker et al. (ref. 24-31) have reported an empirical correlation between  $F$  measured at 50 to  $80 \text{ g/cm}^2$  depth (near the peak of the atmospheric flux profile) and  $F$  measured at high geomagnetic latitudes, with ground-based, high-latitude neutron monitor counting rates. This empirical correlation and the ground-based Deep River neutron monitor (DRNM) data were used to calculate  $S$ . The Merker et al. correlation is well defined between 1965 and 1968. Deviations from this correlation were observed during periods of high solar activity during 1969, but the measurements made between 1970 and 1971 again approximated the earlier correlation. Data are only available through mid-1971; thus, the observed correlation of  $F$  with the DRNM counting rate  $D$  for 1965 to 1968 and 1970 to 1971 is assumed to be valid for December 1972. The average value of  $D$  for the LNPE deployment period, D17, was calculated from hourly DRNM rates. As an approximation of the average value of  $F$  for the solar cycle, the value of  $F$  read from the correlation curve for the solar-cycle-averaged DRNM counting rate,  $\bar{D}$ , is used. Values

for  $\bar{D}$  were calculated both from the curve published by Martinic (ref. 24-32) for the years from 1961 to 1970 and from the yearly DRNM averages for the half-cycle 1965 to 1969 as given by Carmichael and Peterson (ref. 24-33). These values are in good agreement. The corresponding values for  $F$  read from the Merker et al. correlation curve yield the result  $S = F(D17)/F(\bar{D}) = 1.21$ . Based only on the scatter in the correlation curve, the uncertainty in  $S$  is approximately  $\pm 4$  percent. Plots of the DRNM hourly rates and of the daily average rates for a 1-month period before and after the Apollo 17 mission show no indication of anomalies in the cosmic ray intensity for the period of the LNPE deployment.

From equation (24-2), the theoretical fission rate for the reference depth of  $150 \text{ g/cm}^2$  is  $3.9 \text{ fissions/sec-g } ^{235}\text{U}$ , which is in good agreement with the LNPE value of  $3.4 \pm 0.6$ .

The overall comparison of the experiment data and the LCH theory is summarized in figure 24-9, which shows, as data points, the experimental fission rate plotted as a function of depth (in  $\text{g/cm}^2$ ) and, for comparison, the LCH fission rate calculated as described in this section. The gram-per-square-centimeter depth scale has been calculated from the measured density as a function of depth in the Apollo 17 deep core material<sup>1</sup>.

Except for the mica detector pair closest to the lunar surface where the gradient is steep, the data from the two detectors at each target position have been averaged. Before being averaged, the experimental fission rates were corrected for differences in relative efficiencies of the individual detectors (measured in an irradiation of the flight probe in a uniform neutron flux). The total spread in the relative efficiency of all 16 detectors was  $\pm 6$  percent of the mean. The error bars indicate the relative errors of the data points among themselves; they are 1 standard deviation (obtained by combining the statistical errors in the lunar and efficiency measurements). The error bars do not include the overall uncertainty in the absolute fission rate scale ( $\pm 17$  percent). The fission rate scale has been adjusted to the value calculated for the reference depth,  $150 \text{ g/cm}^2$ . Perturbations on the measured profile due to the finite size of the core-stem hole and the topography in the neighborhood of the drill core site were estimated to be unimportant.

---

<sup>1</sup>Lunar Sample Information Catalog, Apollo 17, Document MSC-03211, NASA Lyndon B. Johnson Space Center; also private communication from D. Carrier.

Greenhill et al. (ref. 24-34) report solar cycle variations in the shape of the atmospheric fast-neutron flux profile with changes of approximately 15 percent in the attenuation length of the exponential part of the flux profile at depths greater than approximately  $200 \text{ g/cm}^2$ . This indicates that, strictly speaking, the profile defined by the experimental data is valid only for December 1972 and may differ from the average profile for the 11-yr solar cycle. However, this is not an important effect at present because the shape of the fission profile in the upper  $200 \text{ g/cm}^2$  depends more on the diffusion of the neutrons during moderation than on the shape of the fast-neutron source distribution. At greater depths, an uncertainty of the order of  $\pm 7.5$  percent in the exponential dropoff is not important for any application of the data at present.

A slight increase in the titanium (and to a lesser extent, iron) content is present in the upper parts of the core (ref. 24-30); therefore, because iron and titanium are the principal neutron absorbers, the capture rate is somewhat lower near the surface than that which would be observed in material of uniform composition. However, based on calculations using the LCH energy spectrum, the chemical variations in the fission rate are expected to be small ( $< 5$  percent). Consequently, it is reasonable to compare the experimental points with a theoretical profile calculated for material of uniform composition.

The LCH theoretical fission rate profile, multiplied by a factor of 0.89, is shown in figure 24-9 and matches the trend of the experimental data points well within a 2-standard-deviation error limit on each data point. Thus, both the shape and the magnitude of the experimental and theoretical  $^{235}\text{U}$  capture rates are in good agreement at all depths. This agreement, both for the absolute fission rates and their depth profile, implies that the conclusions made in previous papers (refs. 24-1 to 24-4) by combining the gadolinium-157 ( $^{157}\text{Gd}$ ) capture rate calculated by LCH and gadolinium isotopic data on lunar samples should remain essentially unchanged. The uncertainty in the  $^{157}\text{Gd}$  capture rate (which is more sensitive to the detailed shape of the energy spectrum below 0.5 eV) will be somewhat larger than for the  $^{235}\text{U}$  fission rate, but this difference should not be a serious difficulty. A total evaluation of the reliability of the LCH capture rates is reserved until final data from the  $^{10}\text{B}$  detectors are also available.

The profile of the "thermal neutron flux" (energies less than 0.4 eV) calculated by Armstrong and Alsmiller (ref. 24-16) drops off faster from the peak towards the surface and drops more slowly with depth than does the profile of the experiment data. This

difference is not necessarily inconsistent, because approximately 45 percent of the observed fission events are estimated to occur at energies greater than 0.4 eV, so the fission rate profile should not be exactly identical to the profile of the low-energy neutron flux. Kornblum et al. (ref. 24-29) compared their calculated thermal flux profiles with those of LCH and of Armstrong and Alsmiller and concluded that good agreement exists among the three theoretical calculations. The magnitude of the flux, calculated by Armstrong and Alsmiller, below 0.4 eV (including rare earth absorption) is approximately a factor of 2 lower than that calculated by LCH; consequently, the LNPE data appear to be more in accord with the LCH calculations.

#### COMPARISON WITH NEUTRON CAPTURE RATES MEASURED IN LUNAR SAMPLES

Fireman et al. (ref. 24-35) and Stoenner et al. (ref. 24-36) report data from which the argon-37 ( $^{37}\text{Ar}$ ) profile in the Apollo 16 drill core can be constructed. Although corrections for  $^{37}\text{Ar}$  produced by high-energy nuclear reactions are required and these corrections are not well known, the majority of the  $^{37}\text{Ar}$  appears to have been produced by the  $^{40}\text{Ca}(n,\alpha)^{37}\text{Ar}$  reaction with 1 to 20 MeV neutrons. From the  $^{37}\text{Ar}$  data and using the LCH energy spectrum in the range of 1 to 20 MeV, Kornblum et al. (ref. 24-29) have estimated that  $26.5 \pm 4.5$  neutrons above 1 MeV are produced per square centimeter of lunar surface per second. This quantity is the overall normalization of the LCH fluxes at all energies and was estimated by LCH as  $16 \pm 5$  neutrons/cm<sup>2</sup>-sec. The LNPE data do not apply directly to this energy range; however, the LNPE data as well as those of Finkel et al. (ref. 24-37) rule out the possibility that the overall normalization of the LCH fluxes is low by a factor of 1.6. However, as noted by Kornblum et al., the  $^{37}\text{Ar}$  production rate is very sensitive to the shape of the neutron energy spectrum in the MeV range, whereas the  $^{235}\text{U}$  fission and other low-energy capture rates should be very insensitive. For the purposes of the LCH calculations, accurate definition of the energy spectrum in the MeV range was not important; thus, an error in the MeV spectrum used by LCH could explain the  $^{37}\text{Ar}$  discrepancy but would not affect the low-energy capture rates.

For three depths in the Apollo 15 drill core, Finkel et al. report  $^{60}\text{Co}$  activities, produced by  $^{59}\text{Co}$  neutron capture, which are estimated (for 103 g/cm<sup>2</sup>) to be  $67 \pm 24$  percent of the rate predicted by LCH. The  $^{60}\text{Co}$  capture occurs primarily through one large resonance at 132 eV (ref. 24-14); consequently, the overall

consistency of the  $^{60}\text{Co}$  and the LNPE results indicates that no gross errors (factors of 2) occur in the LCH energy spectrum below a few hundred electron volts.

A small portion of the Apollo 16 lunar surface cosmic ray experiment contained a  $^{10}\text{B}$ -plastic neutron detector, which was conceptually similar to that used in the LNPE but was intended to measure only the neutron leakage flux (ref. 24-38). Although an instrument malfunction resulted in the loss of most data, a small amount of plastic was exposed to the  $^{10}\text{B}$  target. The observed track density was lower (by about a factor of 3) than that calculated by LCH. The low track densities were probably caused by annealing of the plastic at the high temperatures (up to 353 K (80° C)) to which it was exposed.

Fields et al. (ref. 24-39) have reported that a variety of lunar samples have  $^{236}\text{U}/^{238}\text{U}$  ratios (ranging from  $4 \times 10^{-9}$  to  $9 \times 10^{-9}$ ) that are too large to be due to  $^{238}\text{U}$  spallation and are ascribed by Fields et al. to  $^{235}\text{U}$  neutron capture ( $n, \gamma$ ). Three Apollo 12 samples had  $^{236}\text{U}$  contents far too large to be produced by any previously documented natural particle flux and were ascribed to a hundredfold higher solar particle flux in the past  $50 \times 10^6$  yr compared to present-day levels (ref. 24-40).

Assuming that the production and decay of  $^{236}\text{U}$  ( $24 \times 10^6$  yr half-life) are in equilibrium, the  $^{236}\text{U}$  production rates can be directly compared with the  $^{235}\text{U}$  fission rate measured by the LNPE. The comparison is complicated because the  $^{236}\text{U}$  half-life is not negligible compared to estimated lunar surface mixing times; thus, the  $^{236}\text{U}$  contents would represent the average capture rate over the depth of mixing in the last  $25 \times 10^6$  to  $50 \times 10^6$  yr. However, using the ratio of  $^{235}\text{U}$  neutron capture to fission (0.45) calculated for the LCH spectrum, the maximum  $^{236}\text{U}/^{238}\text{U}$  ratio permitted by the LNPE data (corresponding to the peak of the capture rate profile at approximately  $130 \text{ g/cm}^2$ ) would be  $4 \times 10^{-9}$ . In turn, this is at least twice as high as would be expected for a sample that has been irradiated somewhere in the upper  $50 \text{ g/cm}^2$ . Thus, there appears to be at least a factor of 2 to 4 difference between the  $^{236}\text{U}$  contents reported by Fields et al., which were ascribed to  $^{235}\text{U}$  neutron capture, and those calculated from the LNPE data. This report contains detailed documentation of the accuracy of the LNPE data; consequently, the differences represent either

analytical difficulties in the  $^{236}\text{U}$  measurement or significantly higher neutron capture rates in the last  $50 \times 10^6$  yr than those at present. An understanding of the Apollo 12 samples with anomalously high (as large as  $200 \times 10^{-9}$ )  $^{236}\text{U}/^{238}\text{U}$  ratios appears to be the key to resolving the question, particularly because two different aliquots of 12070 give very different results (ref. 24-39).

#### INDUCED FISSION IN LUNAR SAMPLES

The LNPE fission rates can be used to calculate accurately the rates of fission track and fission xenon production due to induced  $^{235}\text{U}$  fission in uranium-rich lunar minerals and to determine the relative importance of these rates compared to fission tracks and xenon production from spontaneous fission of  $^{238}\text{U}$  and  $^{244}\text{Pu}$ . The problem of induced fission is complicated because, in addition to knowledge of the  $^{235}\text{U}$  fission rates, the fission of  $^{238}\text{U}$  and thorium-232 by fast (MeV) neutrons and higher energy particles must be considered and, even more important, the depth and time of the exposure must be known. Based on an analysis of plausible model cases, induced fission may or may not be important, depending on the exposure history of the sample, but it must be taken into account in fission-track dating,  $^{244}\text{Pu}$  fission track, and fission xenon studies. Detailed discussion of special cases does not appear to be warranted at this time; however, the investigators concur with the conclusion of Hutcheon et al. (ref. 24-41) that induced fission tracks cannot account for the excess fission tracks that were found in the whitlockite from lunar sample 14321 and ascribed to  $^{244}\text{Pu}$  spontaneous fission.

#### FLUENCES IN SURFACE SOIL SAMPLES

As has been discussed extensively in previous papers (refs. 24-1 to 24-3), the neutron fluences calculated for lunar surface soil samples from gadolinium isotopic data are low compared to what would be expected for a well-mixed regolith, assuming that regolith depths inferred from field observations or active seismic data are correct (summarized in ref. 24-42). The LNPE results show that this neutron deficit cannot be ascribed to the inaccuracies in the magnitude and depth profile of the theoretical  $^{157}\text{Gd}$  capture rate used in the previous discussions but rather to one of the following factors:

1. The regolith is not uniformly mixed, and progressively more irradiated material is located at the base of the regolith than at the surface.

2. The average cosmic ray flux striking the lunar surface was less in the past  $1 \times 10^9$  yr than at present by a factor of 2 to 3.

3. The regolith depths inferred from the field or seismic data are too low by factors of 2 to 3.

None of these alternatives can be completely ruled out at present. A high ancient solar system magnetic field (ref. 24-43) would provide a mechanism for reducing the cosmic ray flux provided that it persisted at least until approximately  $2 \times 10^9$  yr ago; however, no positive evidence for such a field exists. The first alternative is reasonable if most of the gadolinium found in surface soils is the result of a relatively recent deposition (within the last  $2 \times 10^9$  yr) of previously unirradiated material and has only been mixed through the upper few meters of the regolith. This model is plausible for the Apollo 12 data and possibly for Apollo 15 data because the gadolinium in the soil samples is dominated by potassium, rare earth elements, and phosphorus (KREEP) (ref. 24-44); and evidence exists that the KREEP was deposited 0.8 to  $1.0 \times 10^9$  yr ago (refs. 24-45 to 24-48). The "neutron stratigraphy" implied the first alternative is the inverse of what might be expected for a decreasing impact rate on the lunar surface because the surface layers of the regolith would be less mixed and thus more irradiated than the deeper portions. However, if the impact rate decreased rapidly until approximately  $3 \times 10^9$  yr ago and has been relatively constant since, the inverse stratigraphy is not necessarily a problem.

#### ANALYSIS OF PLASTIC DETECTORS

The plastic detector data have been analyzed to determine the neutron density profile. Strips of plastic about 12 mm in length were cut from various positions along the probe and etched for 4.5 hr in a temperature-controlled bath containing 7 parts 6.25 N sodium hydroxide solution and 5 parts 12 percent sodium hypochlorite solution. The nominal temperature of the bath was 313.35 K (40.2° C); all samples were etched at a temperature within 0.2 K (0.2° C) of this value, and for any given sample the temperature of the bath was maintained constant to within 0.1 K (0.1° C). Track densities in the plastic were measured at approximately 1000X magnification using conventional transmitted light, optical scanning techniques.

The data obtained are shown in figure 24-10, where the track densities are plotted as a function of depth beneath the lunar surface. Because of the geometrical configuration of the targets and detectors (see figure 24-1), the track density is not uniform over the surface of the detector. The data shown in the figure are the background-corrected track densities obtained from a standardized scanning pattern that traversed the relatively uniformly irradiated areas indicated in figure 24-1. The overall track density profile as a function of distance from the midrib, showing the region scanned, is illustrated in figure 24-11. As will be discussed later, duplicate analyses were made in many cases, and it is the average of the two analyses that is plotted in figure 24-10. The error bars on the experimental data points are the best estimate of the overall error to be associated with a single measurement after compounding all measurement errors and errors associated with the background correction of the data. As with all errors quoted here, the error bars in the figure are  $\pm 1$  standard deviation.

In the following paragraphs, the measurement errors are documented, the background corrections are discussed, and the overall error indicated in figure 24-10 is determined.

#### MEASUREMENT ERRORS

Counting statistics errors ranged from 3 to 4 percent. All track density measurements were made by the same observer. However, even for a single observer, the consistency and reproducibility of the scanning over a period of several months is a very real concern, because the particle tracks are small (up to approximately 4- $\mu$ m lengths, uncorrected for index of refraction), and the track densities are relatively low (approximately 5000/cm<sup>2</sup>). An advantage of Triafol TN is that, even after etching, the surface of the plastic is very smooth. Thus, the majority of the etched features in the plastic detectors can be unmistakably classified as either tracks or imperfections. For every 100 unquestionable cone-shaped tracks there were usually about a dozen questionable 'pit' features that required a decision as to whether they were short tracks, tracks at near-vertical incidence, or just surface imperfections of the right geometry and diameter. The scanning criterion used was to decide between these alternatives on the basis of the contrast of the feature and the behavior of the image in focusing down into the plastic. In the scanning of each LNPE detector, separate tallies were made of (1) the unmistakable tracks, (2) the questionable features that were most probably tracks, and (3) the questionable features that were not likely to be tracks. The track densities plotted in figure 24-10 are those calculated from the sum of tallies (1) and (2), where typically tally (2) represents approximately 5 percent of the sum.

Tally (3) was typically approximately 7 percent of the sum (1) plus (2). Similar tallies made for high density (approximately  $100\ 000/\text{cm}^2$ ) samples yielded proportions of the (1) to (2) categories consistent with those observed for the lunar samples. At high track densities, a separate tally of type (3) features is not necessary.

In an effort to maintain and monitor the consistency of the etching and scanning, control samples of the plastic were taken from the bulk roll, one adjacent to each detector used in the probe, and were all neutron-irradiated in contact with a boron target. Each control sample was etched and scanned together with its corresponding detector from the LNPE. The results of the control measurements agree within counting statistics ( $\pm 3$  percent). As will be discussed later, this provides only limited reassurance that consistency in scanning was maintained, because the track densities in the controls were a factor of 50 to 100 greater than the track densities in the LNPE detectors. However, the control sample results show that there is no evidence for significant variations in the registration efficiency of the plastic detectors over the rather large area of bulk plastic from which the LNPE detectors were taken. In addition to the LNPE control samples, two other sets of uniformly irradiated samples showed  $\leq \pm 3$  percent variability for the portion of the roll used for the LNPE. However, other portions of the roll show nonuniformities that could be as large as  $\pm 5$  percent.

Replicate analyses were made of seven of the LNPE detectors to determine the reproducibility of the track density measurements. In most such "rescans" the identity of the sample was unknown to the scanner. From 2- to 9-month intervals separated the initial and subsequent determinations. Taking into account the contribution to the total error from counting statistics, an average reproducibility of  $\pm 5$  percent was obtained with individual values ranging from 0 to 10 percent. No measurements were excluded in the data presented in figure 24-10. It should be emphasized that, in general, different observers will not obtain the same results for these samples. Systematic differences in track densities as great as 10 to 30 percent can be expected. Similarly, unless track counting is continued on a regular basis, a single observer cannot maintain completely consistent scanning criteria at these low densities.

A full evaluation of the errors in measurement also requires consideration of the relative variations in the efficiencies of the boron targets that can result from (1) variations in the thickness and quality of the vapor-deposited boron metal, and (2) small differences in the target-detector geometries. The thickness and uniformity of several of the targets were checked by alpha-backscattering techniques using the California Institute of Technology tandem Van de Graaff accelerator. All targets examined,

although not perfectly uniform, were "infinitely thick"; that is, they were all deposited to thicknesses, at all points on the target, that were greater than the range of the 1.5 MeV alpha particles emitted. In addition, each of the 23 targets used in the instrument was individually tested prior to its incorporation in the probe. A plastic detector was wrapped in direct contact over each target, and the targets were irradiated in a Pu-Be neutron source. The total spread in the relative efficiencies obtained was  $\pm 6.5$  percent of the mean, with a standard deviation of 3.5 percent, which can be ascribed solely to counting statistics. The variation in target efficiencies as a result of variations in target-detector geometries was determined from calibration irradiations, in which the probe was irradiated with fresh detectors in a uniform neutron flux (ref. 24-49). Comparisons between targets (involving half the total number of targets) yielded differences in track densities from 0 to 10 percent with a mean deviation of 4 percent (in excess of that attributable to counting statistics). When applied to specific detector positions, there are no cases where variations observed in the calibration irradiations could be correlated with scatter in the lunar data (fig. 24-10). Thus, it is concluded that the geometry variations are not reproducible when the probe is reassembled and that the previously mentioned error estimate should be applied on a statistical basis rather than to specific detector positions.

Compounding all errors (3.5 percent from counting statistics, 5 percent from scanning reproducibility, and 4 percent from geometry variations) the overall error in measurement is estimated to be  $\pm 7$  percent.

#### BACKGROUND CORRECTIONS

The sources of background include the direct registration of galactic cosmic ray ions (which is more important for the plastic detectors than for the mica because they are more sensitive), the production of interaction tracks in the plastic as a result of high energy cosmic ray protons and alpha particles, and recoil track from the interaction of high energy (MeV) neutrons produced by the RTG during the flight to the Moon. The total contribution from all these sources can be determined experimentally by track density measurements made in areas of the detectors never exposed to the targets, including regions behind the ribs of the rib cage and in an outer second layer of plastic wrapped over the rib cage windows (fig. 24-1). No systematic position dependence of the background was observed; and, in a total of  $0.8 \text{ cm}^2$  scanned, an average track density of  $200 \pm 50 \text{ cm}^{-2}$  was obtained, which is a 3 percent correction for the data at  $140 \text{ g/cm}^2$  and a 6 percent correction for the deepest data point.

Appropriately compounding the error in the correction with the previous 7 percent error, then, one obtains an overall error for a single measurement of from 7 to 9 percent (one standard deviation).

#### ABSOLUTE NEUTRON CAPTURE RATES AND NEUTRON DENSITIES

The measured track density  $\rho$  in the plastic detectors can be related to the  $^{10}\text{B}$  capture rate  $P$  in captures per gram  $^{10}\text{B}$  per second by

$$f\rho = \epsilon PT \quad (24-3)$$

where  $T$  is the exposure time of the probe,  $\epsilon$  is a measure of the detection efficiency, and  $f$  is a self-shielding correction that, as defined, is a dimensionless constant  $\geq 1$ . The self-shielding correction must be applied because the target materials in the neutron probe are strong neutron absorbers, which attenuate the neutron flux, and thus the measured track densities are low compared to the values they would assume in the absence of the probe.

#### Self-Shielding Correction

The self-shielding factor  $f$  was estimated by using the method described in reference 24-49 in which  $f$  for the lunar spectrum is bracketed between measurements of  $f$  for a well-thermalized flux and for a  $1/E$  spectrum ( $E =$  neutron energy). A test unit of the probe was constructed that had targets made from boron of natural isotopic composition (approximately 20 percent  $^{10}\text{B}$ ) in addition to the  $^{10}\text{B}$  targets. Exposure of the test probe to a  $1/E$  spectrum was accomplished by wrapping the unit in 0.45 mm of cadmium. The ratio of the track density per  $^{10}\text{B}$  atom in the natural boron targets to that for the  $^{10}\text{B}$  targets is equal to  $f_{10}/f_n$ , where 10 and  $n$  refer to the  $^{10}\text{B}$  and natural boron targets, respectively. The thermal irradiation gave  $f_{10}/f_n = 1.44 \pm 0.06$ , whereas the exposure in the  $1/E$  spectrum yielded  $1.07 \pm 0.03$ . Unlike the case for uranium, the selfshielding in a natural boron target cannot be neglected (that is,  $f_n$  cannot be assumed to equal unity) for the thermal irradiation. However, the value of the lunar capture rate is comparatively insensitive to  $f_n$  because  $f_n$  enters into the calculation of both

$f$  and  $c$  in equation (24-3) and errors in  $f_n$  tend to cancel. An error of  $x$  percent in  $f_n$  produces an error of approximately  $x/3$  percent in the lunar capture rate. Consequently, it is sufficiently accurate to estimate  $f_n$  theoretically. The investigators have generalized the standard literature calculation of the self-shielding effect on the bulk (volume) activation of a foil (e.g., ref. 24-50) to cover the case of the surface activity of the foil, as measured by a track detector. The actual hemicylindrical probe geometry is rather complicated; thus, they have calculated, as limiting cases, the self-shielding factor for an infinite planar track detector and for a spherical shell detector. The planar case yields  $f_n = 1.12$ , which is a lower limit because all the neutrons in this case will pass through the boron target only once, whereas some neutrons will pass twice in the actual hemicylindrical geometry. The spherical shell case gives  $f_n = 1.19$ , which is an upper limit because essentially all the neutrons will pass through the target twice in this case. The spherical shell calculation yields  $f_{10}/f_n = 1.41$  for a thermal spectrum, in good agreement with the experimental value; consequently, this calculation received double weight and a value of  $f_n = 1.17 \pm 0.02$  for a thermal spectrum was adopted. For the  $1/E$  spectrum,  $f_n$  can be taken as 1. Thus, the  $^{10}\text{B}$  self-shielding for a thermalized spectrum is  $f_{10} = 1.44 \times 1.17 = 1.68$ , whereas for a  $1/E$  spectrum it is 1.07. Following the arguments in reference 24-49, the lunar self-shielding should lie between these values, and the value  $f = 1.37 \pm 0.16$  was adopted. The range of 1.07 to 1.68 is comparatively large and constitutes the largest source of error for the experiment. The  $\pm 0.16$  error estimate was obtained by regarding the total spread between 1.07 and 1.68 as equivalent to  $\pm 2$  standard deviations; consequently  $\pm 0.16$  is the best estimate of the standard deviation and can be compounded with equivalent errors from other sources.

#### Detection Efficiency

For ideal track detectors and targets placed in contact ( $2\pi$  geometry), one obtains

$$\epsilon_{\max} = \frac{1}{4}(R_{\alpha} + R_{\text{Li}}) \quad (24-4)$$

where  $R_{\alpha}$  and  $R_{Li}$  are the ranges in boron metal of the alpha particle and  ${}^7Li$  nucleus from  ${}^{10}B$  neutron capture. In practice, the measured efficiency will be less than that calculated by equation (24-4) because

1. The boron target thickness is larger than the alpha particle range, producing a continuous distribution of alpha particle energies from 0 up to 1.5 MeV. The ionization rate of some of the low energy particles will be insufficient to leave an etchable track (ref. 24-51), and some fraction of the etched tracks near zero length will not be counted. Also, tracks due to particles entering the detector surface at shallow angles will be lost during the etching process (ref. 24-52).

2. There is a gap of 1.9 mm between the targets and detectors.

3. The targets may be porous, contain impurities, or have thin surface films that will lower the efficiency.

Figure 24-11 shows that, in the areas of the detector scanned, the track density profile in the angular direction (i.e., around the probe) is flat to better than  $\pm 4$  percent, indicating that a good approximation to  $2\pi$  geometry is obtained in this region. Similar profiles as a function of length along the probe are also flat (to better than  $\pm 4$  percent) as expected from the target-detector geometry. Thus, losses in efficiency as a result of the 1.9 mm gap appear to be less than 4 percent.

The discussion of intertarget efficiency in the section on measurement errors indicates that intertarget variability is at most  $\pm 4$  percent. However, systematic inefficiencies of the type outlined in item 3 cannot be ruled out. No carbon impurities could be observed in the alpha backscattering measurements, although concentrations  $\geq 5$  percent would have been readily detected. Great care was taken to keep the boron targets clean prior to and during assembly of the probe. A final swabbing with reagent grade acetone was performed after mounting. Residual films from acetone, as judged by hydrogen surface analysis (ref. 24-53), are remarkably small.

An experimental value for the efficiency was obtained by irradiating a calibration unit constructed with natural boron targets. The neutron flux was well-thermalized and uniform (within 2 percent over 1 m). Gold foil activation was used to determine the thermal neutron density. (It was desirable to have the flux monitoring for the calibration irradiations carried out independent of track measurements.) The gold foils were calibrated against the NBS standard neutron source (ref. 24-54). All the

<sup>197</sup>Au measurements were corrected for resonance neutron activation

by cadmium absorption measurements. There are small deviations in the  $^{197}\text{Au}$  capture cross section from  $1/v$  (where  $v$  is neutron velocity) behavior in the neutron energy range below the cadmium cutoff energy, but these introduce negligible error in the neutron density measurement (see, for example, ref. 24-55). The capture rate for the natural boron was calculated from the measured thermal neutron density assuming a cross section for  $^{10}\text{B}(n,\alpha)$  of 3842 b at 2200 m/sec neutron velocity (ref. 24-56). The efficiency for this irradiation was then calculated using the measured track density from the natural boron targets by means of equation (24-3), with  $f_n = 1.17$  as discussed in the previous section, yielding  $\epsilon = 0.137 \pm 0.009 \text{ mg/cm}^2$ . However, there are systematic errors involved in this calibration which require that a correction factor be applied to this value before it is applicable to the LNPE exposure. These are discussed later.

The precision of the data as a result of scanning errors and non-uniformity in the plastic detectors was discussed in the section on measurement errors. However, there are three other sources of error affecting the absolute neutron densities that arise from the (sometimes exasperating) properties of plastic track detectors.

1. As judged by the visual appearance of the tracks, the etching rate of the plastic exposed on the lunar surface was comparatively uniform; however, using the same etching times as for the lunar plastic, the plastic used for the calibration unit (although from the same batch) was distinctly overetched. Consequently, shorter etching times (3 to 4 hr instead of 4.5 hr) were used for the calibration plastic. The etching times were adjusted for each sample until the visual appearance of the tracks matched those observed on the lunar plastic. This procedure is somewhat subjective, but once a calibration sample was accepted for scanning, the resulting track density was accepted without any reevaluation of the suitability of the sample. The quoted efficiency is based on four calibration samples selected in this manner. The standard deviation of the track densities for these four samples was  $\pm 5.7$  percent, which is larger than expected from counting statistics and/or scanning reproducibility and is undoubtedly caused by the variable etching rates observed for the calibration plastic. This is the dominant source of error in the efficiency although not for the experiment as a whole.

2. The registration of low energy alpha tracks in the Triafol TN is different in vacuum than in air, with higher registration efficiency and better formed tracks in air compared to vacuum. This presumably reflects the critical role of oxygen in track registration in plastics as documented in references 24-20 and 24-21. Between atmospheric pressure and approximately  $13 \text{ N/m}^2$

(0.1 torr), there is a  $12 \pm 3$  percent decrease in the registration efficiency. Consequently, all calibrations were done in vacuum.

Exposure of the plastic to high pressure oxygen following  $^{10}\text{B}$  alpha particle irradiation, but prior to etching, did not improve either the appearance of the tracks or the registration efficiency relative to air. Pressures up to  $41 \times 10^6 \text{ N/m}^2$  (6000 psi) for periods up to 10 days were used.

An additional process is that samples exposed at low pressures (approximately  $0.00001 \text{ N/m}^2$  ( $10^{-7}$  torr)) show "aging" or "recovery" effects (ref. 24-57) in that the track density increases with time upon being stored following irradiation. The amount of recovery depends on the ambient pressure during the irradiation. Because the calibration irradiations were performed in relatively bad vacuum (13 to  $133 \text{ N/m}^2$  (0.1 to 1 torr)), whereas the lunar samples were exposed under very good vacuum, comparative measurements were made of control samples of the actual LNPE plastic exposed at 133 and  $0.00001 \text{ N/m}^2$  (1 and  $10^{-7}$  torr) pressure. The  $0.00001 \text{ N/m}^2$  ( $10^{-7}$  torr) samples showed track densities that were approximately 15 percent less than the  $133 \text{ N/m}^2$  (1 torr) samples when etched within 2 days of the irradiations. However, after 3 weeks' storage in the dark in air at room temperature, the track densities in three pairs of 133 and  $0.00001 \text{ N/m}^2$  (1 and  $10^{-7}$  torr) samples were the same to within  $\pm 3$  percent. All lunar plastics were stored at least 6 months prior to use, so errors from recovery effects should not be important.

3. The lunar track densities are approximately 5000 tracks/ $\text{cm}^2$ , whereas the calibration samples have approximately 500 000 tracks/ $\text{cm}^2$ . This factor of 100 was necessary to obtain enough activity in indium foil monitors that were used to determine the relative fluence between the calibration irradiation of the probe and the irradiation of the gold foils. To check whether there was any systematic difference in track counting efficiency over the factor of 100 range in track density, strips of plastic adjacent to those flown were exposed to Pyrex targets in vacuum at two different reactor power levels to produce track densities corresponding to the lunar and calibration samples respectively. The relative fluences for the two irradiations were monitored by indium foil activation.

It was found that the ratio of the scanning efficiency at low track density was  $0.88 \pm 0.07$  of that at high track density. Thus, the appropriate value for  $\epsilon$  to be used with the LNPE track densities in equation (24-3) is  $\epsilon = 0.88 \times 0.137 \times 10^{-3} = (0.120 \pm 0.013) \times 10^{-3} \text{ g/cm}^2$ .

For comparison, the maximum efficiency, calculated from equation (24-4), is  $0.32 \text{ mg/cm}^2$ . If only alpha particle tracks were being counted, the maximum efficiency would be  $0.22 \text{ mg/cm}^2$ . The reasons why the measured efficiency is so much less than either of these values are not completely understood. Recoil  $^7\text{Li}$  ions of 0.86 MeV (the maximum energy of the  $^7\text{Li}$  from  $^{10}\text{B}$  neutron capture) obtained by scattering protons from a lithium fluoride (LiF) target produce recognizable tracks for the etching conditions used for the LNPE plastic. However, to understand the low measured efficiency, one must assume that the overall efficiency for etching and counting  $^7\text{Li}$  ions of this and lower energy must be quite low and also that many of the lower energy alpha tracks must be lost in the etching and scanning. (For example, 0.25 MeV alpha particles do not produce recognizable tracks for the etching and scanning conditions.) Comparative exposures of Triafol TN and good quality cellulose nitrate, placed side by side against a boron target in vacuum, showed that the track density in the Triafol TN was 0.7 of that in the cellulose nitrate. Thus, even if the cellulose nitrate is a perfect track detector, this experiment shows that the relatively low efficiency of the probe can be primarily ascribed to the relatively poorer registration efficiency of Triafol TN for  $^{10}\text{B}$  n-capture products. The Triafol TN was chosen for its greater resistance to annealing, which was a considerable problem for this experiment.

#### Calculation of Capture Rate and Neutron Density

Using the efficiency and self-absorption values discussed earlier, the observed track densities can be used to calculate capture rates by equation (24-3). Adopting, as in reference 24-49, an arbitrary reference depth of  $150 \text{ g/cm}^2$ , a  $^{10}\text{B}$  capture rate of  $467 \pm 74$  captures per second per gram  $^{10}\text{B}$  is obtained. Because  $^{10}\text{B}$  has an absorption cross section that is strictly proportional to  $1/v$  (where  $v$  is neutron velocity), the capture rate can be directly converted to a neutron density of  $(9.2 \pm 1.5) \times 10^{-6}$  neutrons/cm<sup>3</sup>. Either of these values can be used to renormalize the track density profile in figure 24-1. Capture rate and neutron density are equivalent for  $^{10}\text{B}$  and are used interchangeably in the following discussion.

## COMPARISON WITH THEORETICAL CALCULATIONS

### Depth Profiles

In references 24-18 and 24-49, it was shown that the LNPE data were in good accord with the LCH calculations for the case of an Apollo 11 composition (a good approximation for the Apollo 17 deep core) for a temperature of 200 K and for an exponential production profile ( $e^{-x/165}$  where  $x$  is the depth in  $\text{g/cm}^2$ ) of MeV neutrons. The MeV neutrons, following moderation and diffusion, are the source of the low energy neutrons that produce the  $^{10}\text{B}$  and  $^{235}\text{U}$  capture. However, because the various theoretical calculations in the literature do not give identical results, a more detailed comparison is warranted. The neutron density is independent of temperature; consequently, this section focuses on a consideration of alternative MeV neutron source profiles and also discusses calculations published by other groups.

In addition to the exponential case, LCH calculated capture rates for a MeV source neutron depth profile, modeled from the results of Monte Carlo calculations by Armstrong and Alsmiller (ref. 24-16), which was constant to a depth of  $165 \text{ g/cm}^2$  and then decreased exponentially at greater depths. Physically, the MeV neutrons are produced primarily by the evaporation stage of higher energy ( $>20 \text{ MeV}$ ) nuclear reactions; and, because they are secondary particles, they are expected to show a buildup from the surface to a maximum and then to fall off at greater depths. (The effect of surface leakage during moderation converts the MeV neutron profile into the low energy neutron density profile measured by the LNPE.) Thus, the two MeV source profiles used by LCH represent extremes in the sense that the exponential case has too many neutrons close to the surface, whereas the "flat plus exponential" case has the neutron production concentrated at larger depths. Figure 24-12(a) compares the LCH neutron density profiles for the two source profiles. The important point illustrated in figure 24-12 is that, considering the extreme differences in the source profiles, the two curves in figure 24-12(a) are remarkably similar. This is because the shape of the neutron density profile is determined primarily by surface leakage during moderation. Figures 24-12(b) and 24-12(c) show the best fits (visually) of the two profiles to the measured neutron densities. Only the magnitude of the theoretical profiles was varied; the depth scale was held fixed. With the rather large error bars associated with the data, neither of the profiles can be totally eliminated. Nevertheless, the fit for the exponential source function appears better than for the "flat plus exponential," where the data fall consistently above the curve at shallower depths and consistently below at greater depths.

The  $^{37}\text{Ar}$  data for the Apollo 16 and 17 deep core (refs. 24-35 and 24-58) define the MeV source neutron profile better than the neutron density measurements presented here, because the  $^{37}\text{Ar}$  is produced primarily by MeV neutrons reacting with  $^{40}\text{Ca}$ . The  $^{37}\text{Ar}$  production rate peaks at 30 to 50  $\text{g}/\text{cm}^2$ . This implies that the peak in the MeV neutron production rate will be at even shallower depths because surface leakage will shift the peak in the  $^{37}\text{Ar}$  capture rate to larger depths. Independent of any theoretical analysis, this indicates that the LCH exponential MeV neutron source profile is more realistic. Further, Kornblum et al. (ref. 24-29) were able to fit the  $^{37}\text{Ar}$  depth profile for the Apollo 16 deep core with the exponential source profile but not with the "flat plus exponential" case. Thus, it appears that the maximum in the MeV neutron production rate is comparatively close to the surface, probably within the outer 30  $\text{g}/\text{cm}^2$ .

The LNPE neutron density profile can be compared with the "thermal neutron" ( $E < 0.4$  eV) flux profile of Armstrong and Alsmiller (ref. 24-16). Their profiles do not fit the LNPE data nearly as well as that of LCH, most likely because their MeV neutron source function is close to the "flat plus exponential" case in figure 24-12(a). The comparisons have been made with the Armstrong-Alsmiller calculations for both solar minimum and maximum and using the cases that included rare-earth absorption.

The  $^{157}\text{Gd}$  capture rate as a function of depth profile calculated by Kornblum et al. (ref. 24-29) would describe the LNPE neutron density data reasonably well except that this theoretical curve appears to peak somewhat too close to the surface. The neutron density and  $^{157}\text{Gd}$  profiles of LCH are very similar, so the above comparison should be fair.

The investigators conclude that, of the various theoretical calculations, the shape of the LNPE neutron density profile is best reproduced by the LCH calculations for an exponential MeV neutron source profile.

Using the LCH neutron density profile as a basis for extrapolating, one can evaluate the neutron density at the lunar surface as  $(0.72 \pm 0.11) \times 10^{-6}$  neutrons/ $\text{cm}^3$ . The surface neutron density is important because it governs the yield of neutron capture gamma rays that were detected by the Apollo 15 and 16 orbital gamma ray experiment (ref. 24-59). As with  $^{10}\text{B}$ , the neutron capture cross section for elements lighter than iron varies as  $1/v$ ; thus, the LNPE  $^{10}\text{B}$  capture rates per atom can be converted into capture

rates for these elements by multiplying by the ratio of the standard 2200 m/sec neutron capture cross section of that element to that of  $^{10}\text{B}$ . This conversion is independent of any theoretical calculation and involves no additional error other than that in the LNPE data.

#### Comparison of Absolute Capture Rates

The LCH theoretical  $^{10}\text{B}$  capture rate at  $150 \text{ g/cm}^2$ , when adjusted to correspond to the cosmic ray intensity during the Apollo 17 mission according to the methods described in reference 24-49, is 575 captures per second per gram  $^{10}\text{B}$  (using the exponential MeV neutron profile). Although this is higher than the measured capture rate of  $467 \pm 74$ , the agreement is satisfactory, particularly when the  $\pm 30$  percent uncertainty estimated by LCH for the normalization of the theoretical capture rate is considered. Direct comparison of absolute rates for the other theoretical calculations is not possible with results available at present.

In reference 24-18, comparisons were made of the LNPE capture rates and those of  $^{60}\text{Co}$  (ref. 24-60),  $^{37}\text{Ar}$  (ref. 24-35), and  $^{236}\text{U}$  (ref. 24-39) data in lunar samples with the corresponding rates calculated by LCH. Even though the various reactions occur in different neutron energy ranges, all the experimental capture rates except that for  $^{236}\text{U}$  appeared slightly low by about a constant factor (fig. 24-13). Figure 24-13 differs from figure 2 of reference 24-18 in that the final  $^{10}\text{B}$  capture rate is slightly lower and the  $^{37}\text{Ar}$  capture rate has been corrected (using methods described in reference 24-49) for the difference in the galactic cosmic ray intensity between the period just prior to Apollo 16 and that for the average over the last solar cycle. Taking the range of overlap of the one standard deviation error bars of the experimental capture rates excluding  $^{236}\text{U}$  (as discussed in reference 24-18); the investigators conclude that, except at low ( $\leq 0.5$  eV) energies, the best estimate of lunar neutron capture rates is made by taking 0.8 of the rate calculated by LCH. The situation at low energy is discussed in the following paragraphs.

In addition to the factor of 0.8, there are two sets of data that indicate that the calculated LCH rate for  $^{157}\text{Gd}$  neutron capture is high.

1. The measured ratio of the  $^{149}\text{Sm}$  capture rate to that of  $^{157}\text{Gd}$  is about 20 percent higher than that predicted by LCH

(refs. 24-3 and 24-61). The  $^{149}\text{Sm}$  capture occurs primarily through a resonance at 0.1 eV, whereas the equivalent resonance for  $^{157}\text{Gd}$  is at 0.03 eV.

2. The LNPE cadmium absorption measurement (ref. 24-18) indicated that the ratio of the neutron density below 0.5 eV to that above 0.5 eV was  $1.1 \pm 0.2$  at  $180 \text{ g/cm}^2$ , whereas the LCH calculations gave 1.7. At  $370 \text{ g/cm}^2$ , however, the measured ( $1.9 \pm 0.3$ ) and calculated (1.9) ratios were in agreement. Both of these differences (1 and 2) are independent of the 0.8 renormalization discussed earlier. The  $^{157}\text{Gd}$  capture rate for an Apollo 11 composition calculated by Kornblum and Fireman (ref. 24-29) is approximately 13 percent higher than LCH, and their samarium to gadolinium capture rate ratio is lower than LCH. Thus, revisions to the Kornblum-Fireman calculations are also indicated. The following discussion considers only the LCH calculations.

The LNPE  $^{10}\text{B}$  and  $^{235}\text{U}$  data show that the total neutron density, after renormalization, is in accord with LCH; only the distribution in neutron density above and below 0.5 eV is not correct. The sense of the difference is that there are too many neutrons below 0.5 eV in the theoretical spectrum. (The  $^{235}\text{U}$  fission cross section is not exactly  $1/v$ ; however it is close enough that the fission rate is relatively insensitive to variations in the shape of the low energy spectrum provided the total neutron density is held fixed.) Because the  $^{149}\text{Sm}$  resonance is well below 0.5 eV, it follows that, at least in the depth interval near the peak, both the  $^{149}\text{Sm}$  and  $^{157}\text{Gd}$  capture rates calculated by LCH are too high and, from item 1, that the  $^{157}\text{Gd}$  rate deviates more than that for  $^{149}\text{Sm}$ . Thus, an additional correction is required to the  $^{157}\text{Gd}$  capture rate that must be at least as large as the factor of 1.2 difference between the theoretical and measured relative  $^{157}\text{Gd}$  and  $^{149}\text{Sm}$  capture rates (item 1) and relative to the original LCH calculation; the  $^{157}\text{Gd}$  capture rate should be lowered by at least a factor of approximately  $0.8/1.2 = 2/3$ . Strictly speaking, this factor will apply only in the depth range 150 to  $200 \text{ g/cm}^2$ ; but, since the capture rates are highest in this range, it is reasonable, in the absence of more refined calculations, to adopt this factor at all depths.

An actual estimate of the effect of deviations of the low energy spectral shape from that calculated by LCH can be made using the family of spectral shapes that were generated by LCH to explore the effect of variations in the average absorption cross

section on the calculated capture rates (ref. 24-29). Higher absorption gives a harder low energy spectrum and thus gives (1) a higher ratio of the  $^{149}\text{Sm}$  to  $^{157}\text{Gd}$  capture rates,  $P_{149}/P_{157}$ , and (2) a lower ratio of neutron density below to above 0.5 eV. The investigators have used the correlations (fig. 24-14) between the calculated values of the parameters (1) and (2) and the ratio of the  $^{157}\text{Gd}$  to  $^{10}\text{B}$  capture rates for the preceding spectral shapes ( $P_{157}/P_{10}$ ). From these correlations,  $P_{157}/P_{10}$  was interpolated for values of (1) and (2) corresponding to the measured quantities. The interpolated  $P_{157}/P_{10}$  can then be combined with the measured  $^{10}\text{B}$  capture rate to estimate the  $^{157}\text{Gd}$  capture rate.

The correlation curves in figure 24-14 were prepared by using neutron energy spectra obtained by varying the absorption cross section for temperatures of 0 to 400 K. The absorption cross section and temperature have no physical significance in this calculation; they are just parameters that are used to define a systematically varying series of low energy neutron spectra which are used to fit the two experimental parameters defining the low energy spectra. The significant observation from figure 24-14 is that small variations in the neutron density ratio or in the relative samarium to gadolinium capture rate imply relatively large variations in the  $^{157}\text{Gd}$  capture rate. This is reasonable considering the very low energy (0.03 eV) of the  $^{157}\text{Gd}$  capture resonance. Figure 24-14 also shows the experimental LNPE neutron density ratio and the samarium/gadolinium capture rate ratio for soil 10084 (chemically very similar to the Apollo 17 drill core soils) and the associated errors in these quantities. It can be seen from both figures 24-14(a) and 24-14(b) that  $P_{157}/P_{10}$  ratios which are distinctly lower than those calculated by (shown by the cross in the figure) are implied. Table 24-I summarizes the interpolated relative  $^{157}\text{Gd}$  to  $^{10}\text{B}$  capture rates required to fit both the neutron density ratio and the samarium/gadolinium capture rate for the two spectral families. Table 24-I shows that consistent results are obtained for all four interpolations, indicating  $P_{157}/P_{10} = 12 \pm 1.5$ , compared to the LCH ratio of 18.8. Taking the "best" experimental value for the  $^{10}\text{B}$  capture rate as 0.8 times the LCH value, it is estimated that the  $^{157}\text{Gd}$  capture rate is  $12/18.8 \times 0.8 = 0.51$  of that calculated by LCH.

It is important that consistent  $^{157}\text{Gd}$  capture rates are obtained from fitting both the neutron density ratio and the relative samarium to gadolinium capture rates, because there are possible, although less probable, alternative explanations for the differences between theory and experiment. For example, as pointed out by Russ (ref. 24-61), different sets of  $^{149}\text{Sm}$  resonance

parameters than those used by LCH will give calculated relative samarium to gadolinium capture rates more in accord with experiment results. It would probably be worthwhile to have additional measurements of the relative  $^{149}\text{Sm}$  and  $^{157}\text{Gd}$  cross sections in the thermal energy range. Also, it is conceivable that the LNPE cadmium ratios are somewhat too low because of a hardening of the lunar low energy neutron spectrum by the presence of the probe itself. Such an effect is referred to as "flux depression" in the neutron physics literature and is distinct from the "self-shielding" corrections discussed earlier. However, the flux depression effects are less important and usually are not considered in most practical applications (ref. 24-50). In any case, it seems less likely that the LCH low energy spectrum is actually correct and that other effects have independently produced similar discrepancies between theory and experiment for both the samarium/gadolinium capture ratio and the neutron density ratio.

In summary, the preceding discussion indicates that the best estimate at present of the lunar  $^{157}\text{Gd}$  capture rate is, at most, 0.7 and probably 0.5 of the rate calculated by LCH at all depths. However, it should be emphasized that what the investigators have shown is that, if physically reasonable neutron energy spectra are adopted that fit the available experimental data better than the energy spectrum of LCH, then these spectra imply  $^{157}\text{Gd}$  capture rates significantly lower than LCH. The investigators have in no sense uniquely determined the low energy spectrum. Consequently, it would be worthwhile for additional theoretical calculations to be carried out to attempt to reproduce very closely the great variety of experimental data now available on lunar neutron capture. Special emphasis, perhaps even including the effects of crystal binding (ref. 24-62), should be given to calculating the low energy (below 1 eV) spectrum. Except for quantities sensitive to the detailed shape of the low energy spectrum, the LCH calculations reproduce the experimental data admirably well; however, the preceding discussion shows that the most important neutron capture rate ( $^{157}\text{Gd}$ ) is rather sensitive to these differences, thus additional effort on the low energy region is warranted.

Experimentally, the investigators believe that, with additional effort, it would be possible to reduce the errors on the LNPE data by about a factor of 2. They do not feel this effort is warranted at the present time; however, the LNPE materials will be carefully preserved and documented so that additional work will be possible. It should be emphasized that the largest source of error in both the  $^{235}\text{U}$  and  $^{10}\text{B}$  rates is in the self-shielding correction, and this arises because of the belief that it was important to quote experimental results that were completely independent of any theoretical calculation. If a specific form of the neutron energy spectrum is assumed, it should be possible to

calculate the self-shielding factor more closely (or in principle to perform an irradiation in a simulated energy spectrum) and in this sense "reduce" the errors in the LNPE rates.

A lower  $^{157}\text{Gd}$  capture rate will reduce, but probably not completely eliminate, the differences between the measured low energy neutron fluences in lunar soil samples and those calculated from the LCH capture rate, assuming a uniformly mixed regolith. (See reference 24-18 for an extensive discussion of this problem.)

In references 24-18 and 24-49, the relatively good agreement between the LNPE data and the LCH calculations is interpreted as indicating that the conclusions drawn previously from  $^{157}\text{Gd}$  data in lunar samples using the LCH capture rates would not require revision. Although caveats were given about the sensitivity of the  $^{157}\text{Gd}$  production rate to the detailed shape of the low energy spectrum, the investigators did underestimate the sensitivity of the  $^{157}\text{Gd}$  capture rate to relatively small differences in the measured samarium/gadolinium capture rate ratios and the LNPE cadmium ratio with those calculated by LCH. The proposed reduction in the  $^{157}\text{Gd}$  capture rate is regarded to be a significant revision. In particular, it is proposed that the ages and depositional time scales for the Apollo deep core samples (refs. 24-3, 24-14, and 24-61) should be increased by a factor of 1.5 to 2. The revised time scale for the Apollo 15 deep core would not agree with that proposed by Pepin et al. (ref. 24-63) based on spallation  $^{38}\text{Ar}$  data.

The lower  $^{157}\text{Gd}$  capture rate, which is proposed, accentuates a problem pointed out by Russ (ref. 24-61) for rock 12002 in a detailed comparison of different neutron capture effects in lunar samples. For 12002, there exist excellent analytical data for  $^{157}\text{Gd}$  and  $^{131}\text{Xe}$  produced by  $^{130}\text{Ba}$  neutron capture (refs. 24-3, 24-6, 24-61, and 24-64); however the amount of  $^{157}\text{Gd}$  neutron capture was too large compared to that for  $^{130}\text{Ba}$ . A lower  $^{157}\text{Gd}$  capture rate makes the situation still worse and further attention must be given to the 12002 dilemma.

#### DATA ARCHIVED

A copy of the final report will be sent to the National Space Science Data Center (NSSDC). The mica and plastic samples are archived in the Lunar Curatorial Facility at the Lyndon B. Johnson Space Center, Houston, Texas.

## REFERENCES

- 24-1. Eugster, O.; Tera, F.; Burnett, D. S.; and Wasserburg, G. J.: The Isotopic Composition of Gd and the Neutron Capture Effects in Samples from Apollo 11. *Earth Planet. Sci. Lett.*, vol. 8, 1970, pp. 20-30.
- 24-2. Russ, G. P., III; Burnett, D. S.; Lingenfelter, R. E.; and Wasserburg, G. J.: Neutron Capture on  $^{149}\text{Sm}$  in Lunar Samples. *Earth Planet. Sci. Lett.*, vol. 13, Dec. 11, 1971, pp. 53-60.
- 24-3. Russ, G. Price, III: Apollo 16 Neutron Stratigraphy. *Earth Planet. Sci. Lett.*, vol. 19, 1973, pp. 275-289.
- 24-4. Lugmair, G. W.; and Marti, Kurt: Exposure Ages and Neutron Capture Record in Lunar Samples from Fra Mauro. *Proceedings of the Third Lunar Science Conference*, vol. 2, MIT Press (Cambridge, Mass.), 1972, pp. 1891-1897.
- 24-5. Eberhardt, P.; Geiss, J.; Graf, H.; Grogler, N.; et al.: Correlation Between Rock Type and Irradiation History of Apollo 11 Igneous Rocks. *Earth Planet. Sci. Lett.*, vol. 10, 1970, pp. 67-72.
- 24-6. Marti, K.; and Lugmair, G. W.:  $\text{Kr}^{81}$ -Kr and K-Ar $^{40}$  Ages, Cosmic-Ray Spallation Products, and Neutron Capture Effects in Lunar Samples from Oceanus Procellarum. *Proceedings of the Second Lunar Science Conference*, vol. 2, MIT Press (Cambridge, Mass.), 1971, pp. 1591-1605.
- 24-7. Huneke, J. C.; Podosek, F. A.; Burnett, D. S.; and Wasserburg, G. J.: Rare Gas Studies of the Galactic Cosmic Ray Irradiation History of Lunar Rocks. *Geochim. Cosmochim. Acta*, vol. 36, no. 3, Mar. 1972, pp. 269-302.
- 24-8. Kaiser, W. A.; and Berman, B. L.: The Average  $^{130}\text{Ba}$  ( $n, \gamma$ ) Cross Section and the Origin of  $^{131}\text{Xe}$  on the Moon. *Earth Planet. Sci. Lett.*, vol. 15, 1972, pp. 320-324.

- 24-9. Berman, B. L.; and Browne, J. C.: Microscopic  $^{130}\text{Ba}$  ( $n,\gamma$ ) Cross Section and the Origin of  $^{131}\text{Xe}$  on the Moon. *Phys. Rev. C.*, vol. 17, no. 6, 1973.
- 24-10. Michel, R.; Herpens, U.; Kulus, H.; and Herr, W.: Isotopic Anomalies in Lunar Rhenium. *Proceedings of the Third Lunar Science Conference*, vol. 2, MIT Press (Cambridge, Mass.), 1972, pp. 1917-1925.
- 24-11. Finkel, R. C.; Wahlen, M.; Arnold, J. R.; Kohl, C. P.; and Imamura, M.: The Gradient of Cosmogenic Radionuclides to a Depth of  $400\text{ g/cm}^2$  in the Moon. *Lunar Science IV* (Abs. of papers presented at the Fourth Lunar Science Conference (Houston, Tex.), Mar. 5-8, 1973), pp. 242-244.
- 24-12. Kornblum, J. J.; Levine, M.; Aronson, A.; and Fireman, E. L.: Neutrons in the Moon. *Lunar Science IV* (Abs. of papers presented at the Fourth Lunar Science Conference (Houston, Tex.), Mar. 5-8 1973, pp. 441-443.
- 24-13. Burnett, D. S.; Huneke, J. C.; Podosek, F. A.; Russ, G. Price, II; and Wasserburg, G. J.: The Irradiation History of Lunar Samples. *Proceedings of the Second Lunar Science Conference*, vol. 2, MIT Press (Cambridge, Mass.), 1971, pp. 1671-1679.
- 24-14. Russ, G. Price, III; Burnett, D. S.; and Wasserburg, G. J.: Lunar Neutron Stratigraphy. *Earth Planet. Sci. Lett.*, vol. 15, 1972, pp. 172-186.
- 24-15. Lingenfelter, R. E.; Canfield, E. H.; and Hampel, V. E.: The Lunar Neutron Flux Revisited. *Earth Planet. Sci. Lett.*, vol. 16, 1972, pp. 355-369.
- 24-16. Armstrong, T. W.; and Alsmiller, R. G., Jr.: Calculation of Cosmogenic Radionuclides in the Moon and Comparison with Apollo Measurements. *Proceedings of the Second Lunar Science Conference*, vol. 2, MIT Press (Cambridge, Mass.), 1971, pp. 1729-1745.
- 24-17. Woolum, Dorothy S.; Burnett, D. S.; and Bauman, C. A.: The Apollo 17 Lunar Neutron Probe Experiment. *Lunar Science IV* (Abs. of papers presented at the Fourth Lunar Science Conference (Houston, Tex.), Mar. 5-8, 1973), pp. 793-795.

- 24-18. Woolum, Dorothy S.; and Burnett, D. S.: Lunar Neutron Capture as a Tracer for Regolith Dynamics. Proceedings of the Fifth Lunar Science Conference, vol. 2, Pergamon Press, 1974, pp. 2061-2075.
- 24-19. Burnett, D.; Hohenberg, C.; Maurette, M.; Monnin, M.; et al.: Solar Cosmic Ray, Solar Wind, Solar Flare, and Neutron Albedo Measurements. Sec. 15, Part C, of Apollo 16 Preliminary Science Report. NASA SP-315, 1972.
- 24-20. Monnin, Michel: Interaction des Ions Lourds avec des Dielectriques Organiques Macromoleculaires: Contribution a l'Etude des Detecteurs Solides de Traces. Thesis, Universite de Clermont, France, 1969.
- 24-21. Crawford, W. T.; DeSorbo, W.; and Humphrey, J. S., Jr.: Enhancement of Track Etching Rates in Charged Particle-Irradiated Plastics by a Photo-Oxidation Effect. Nature, vol. 220, Dec. 28, 1968, pp. 1313-1314.
- 24-22. Apollo Lunar Geology Investigation Team: Documentation and Environment of the Apollo 17 Samples: A Preliminary Report. U.S. Geol. Survey Interagency Rept., Astrogeol. 71, Jan. 21, 1973.
- 24-23. Lingenfelter, R. E.; Canfield, E. H.; and Hess, W. N.: The Lunar Neutron Flux. J. Geophys. Res., vol. 66, no. 9, Sept. 1961, pp. 2665-2671.
- 24-24. Alexander, John M.; Gazdik, M. F.; Trips, A. R.; and Wasif, Saad: Kinetic Energy Release in 23-MeV Deuteron Fission of  $U^{238}$ . Phys. Rev., vol. 129, no. 6, Mar. 15, 1963, pp. 2659-2663.
- 24-25. Reimer, G. M.; Storer, D.; and Wagner, G. A.: Geometry Factor in Fission Track Counting. Earth Planet. Sci. Lett., vol. 9, 1970, pp. 401-404.
- 24-26. Mosburg, E. R., Jr.; and Murphey, W. M.: A Recalibration of the NBS Standard Thermal Neutron Flux. J. Nuclear Energy, vol. 14, Apr. 1961, pp. 25-30.
- 24-27. Zijp, W. J.: Contributor to Neutron Fluence Measurements. International Atomic Energy Agency Tech. Rept. 107 (Vienna, Austria), 1970, pp. 99-100.

- 24-28. Eiland, H. M.; Esch, L. J.; Feiner, F.; and Mewherter, J. T.: Epithermal Measurements of Capture and Fission Resonance Integrals in  $^{235}\text{U}$ ,  $^{233}\text{U}$ ,  $^{239}\text{Pu}$ , and  $^{241}\text{Pu}$ . Nuclear Sci. and Eng., vol. 44, no. 2, May 1971, pp. 180-189.
- 24-29. Kornblum, J. J.; Fireman, E. L.; Levine, M.; and Aronson, A.: Neutrons in the Moon. Proceedings of the Fourth Lunar Science Conference, vol. 2, Pergamon Press (New York), 1973, pp. 2171-2182.
- 24-30. Helmke, P. A.; Blanchard, D. P.; Jacobs, J. W.; Telander, K. M.; and Haskin, L. A.: Major and Trace Elements in Materials from the Apollo 17 Deep Drill Core. EOS, Trans. Am. Geophys. Union, vol. 54, 1973, p. 595.
- 24-31. Merker, M.; Light, E. S.; Verschell, H. J.; Mendell, R. B.; and Korff, S. A.: Time Dependent Worldwide Distribution of Atmospheric Neutrons and of Their Products. Paper no. 1: Fast Neutron Observations. J. Geophys. Res., vol. 78, no. 16, June 1, 1973, pp. 2727-2741.
- 24-32. Martinic, N. J.: Cosmic Ray Intensity Large Period Modulation During 1961-70. Cosmic Ray Conference Papers of 12th International Conference on Cosmic Rays (Hobart, Tasmania, Australia), Aug. 16-25, 1971, vol. 2, pp. 745-749.
- 24-33. Carmichael, H.; and Peterson, R. W.: Dependence of the Neutron Monitor Attenuation on Atmospheric Depth and Geomagnetic Cutoff. Cosmic Ray Conference Papers of 12th International Conference on Cosmic Rays (Hobart, Tasmania, Australia), Aug. 16-25, 1971, vol. 3, pp. 887-893.
- 24-34. Greenhill, J. G.; Fenton, A. G.; and Fenton, K. B.: Solar Cycle Variations in the Polar Atmospheric Neutron Flux at Balloon Altitudes. Cosmic Ray Conference Papers of 12th International Conference on Cosmic Rays (Hobart, Tasmania, Australia), Aug. 16-25, 1971, vol. 2, pp. 758-764.
- 24-35. Fireman, E. L.; D'Amico, J.; and De Felice, J.: Depth Variation of  $\text{Ar}^{37}$ ,  $\text{Ar}^{39}$ , and  $\text{H}^3$  in Apollo 16 Material. Abs. of papers presented at the Fourth Lunar Science Conference (Houston, Tex.), Mar. 5-8, 1973, pp. 248-250.

- 24-36. Stoenner, R. W.; Davis, R., Jr.; and Bauer, M.: The Fast Neutron Production Rate at Great Depths in the Lunar Soil. Abs. of papers presented at the Fourth Lunar Science Conference (Houston, Tex.), Mar. 5-8, 1973, pp. 692-693.
- 24-37. Finkel, R. C.; Wahlen, M.; Arnold, J. R.; Kohl, C. P.; and Imamura, M.: The Gradient of Cosmogenic Radionuclides to a Depth of 400 g/cm<sup>2</sup> in the Moon. Abs. of papers presented at the Fourth Lunar Science Conference (Houston, Tex.), Mar. 5-8, 1973, pp. 242-244.
- 24-38. Burnett, D.; Hohenberg, C.; Maurette, M.; Walker, R.; et al.: Solar Cosmic Ray, Solar Wind, Solar Flare, and Neutron Albedo Measurements. Sec. 15, Part C, of Apollo 16 Preliminary Science Report. NASA SP-315, 1972.
- 24-39. Fields, P. R.; Diamond, H.; Metta, D. N.; and Rokop, D. J.: The Reaction Products of Lunar Uranium and Cosmic Rays. Abs. of papers presented at the Fourth Lunar Science Conference (Houston, Tex.), Mar. 5-8, 1973, pp. 239-241.
- 24-40. Fields, P. R.; Diamond, H.; Metta, D. N.; Rokop, D. J.; and Stevens, C. M.: <sup>237</sup>Np, <sup>236</sup>U, and Other Actinides on the Moon. Proceedings of the Third Lunar Science Conference, vol. 2, MIT Press (Cambridge, Mass.), 1972, pp. 1637-1644.
- 24-41. Hutcheon, I. D.; Phakey, P. P.; and Price, P. B.: Studies Bearing on the History of Lunar Breccias. Proceedings of the Third Lunar Science Conference, vol. 3, MIT Press (Cambridge, Mass.), 1972, pp. 2845-2866.
- 24-42. Watkins, J. S.; and Kovach, R. L.: Seismic Investigation of the Lunar Regolith. Proceedings of the Fourth Lunar Science Conference, vol. 3, Pergamon Press (New York), 1973, pp. 2561-2574.
- 24-43. Pearce, G. W.; Strangway, D. W.; and Gose, W. A.: Remanent Magnetization of the Lunar Surface. Proceedings of the Third Lunar Science Conference, vol. 3, MIT Press (Cambridge, Mass.), 1972, pp. 2449-2464.

- 24-44. Hubbard, Norman J.; Meyer, Charles, Jr.; Gast, Paul W.; and Wiesmann, Henry: The Composition and Derivation of Apollo 12 Soils. Earth Planet. Sci. Lett., vol. 10, 1971, pp. 341-350.
- 24-45. Eberhardt, P.; Eugster, O.; Geiss, J.; Grogger, N.; et al.: When Was the Apollo 12 KREEP Ejected? Lunar Science III (Rev. abs. of papers presented at the Third Lunar Science Conference (Houston, Tex.), Jan. 10-13, 1972), pp. 206-208.
- 24-46. Pepin, R. O.; Bradley, J. G.; Dragon, J. C.; and Nyquist, L. E.: K-Ar Dating of Lunar Fines. Proceedings of the Third Lunar Science Conference, vol. 2, MIT Press (Cambridge, Mass.), 1972, pp. 1569-1588.
- 24-47. Silver, Leon T.: U-Th-Pb Isotopic Systems in Apollo 11 and 12 Regolithic Materials and a Possible Age for Copernicus Impact Event. (Abs. of papers presented at the AGU Fifty-Second Annual Meeting), EOS, Trans. Am. Geophys. Union, vol. 52, no. 7, July 1971, p. 533.
- 24-48. Tatsumoto, M.; Knight, R. J.; and Doe, B. R.: U-Th-Pb Systematics of Apollo 12 Lunar Samples. Proceedings of the Second Lunar Science Conference, vol. 2, A. A. Levinson, ed., MIT Press (Cambridge, Mass.), 1971, pp. 1521-1546.
- 24-49. Woolum, Dorothy S.; and Burnett, D. S.: In-Situ Measurement of the Rate of  $^{235}\text{U}$  Fission Induced by Lunar Neutrons. Earth Planet. Sci. Lett., vol. 21, 1974, pp. 153-163.
- 24-50. Droulers, Yves: Neutron Fluence Measurement. Internat. Atomic Energy Agency (Vienna) Tech. Rept. Series no. 107, 1970, pp. 52-58.
- 24-51. Fleischer, R. L.; Price, P. B.; Walker, R. M.; and Hubbard, E. L.: Criterion for Registration in Dielectric Track Detectors. Phys. Rev., vol. 156, no. 2, Apr. 10, 1967, pp. 353-355.
- 24-52. Fleischer, R. L.; and Price, P. B.: Glass Dating by Fission Fragment Tracks. J. Geophys. Res., vol. 69, no. 2, Jan. 15, 1964, pp. 331-339.
- 24-53. Leich, D. L.; Tombrello, T. A.; and Burnett, D. S.: The Depth Distribution of Hydrogen in Lunar Materials. Earth Planet. Sci. Lett., vol. 19, 1973, pp. 305-314.

- 24-54. Murphey, J. M.; and Caswell, R. S.: Analysis of Results of the Bureau International des Poids et Mesures Thermal Neutron Flux Density Intercomparison. *Metrologia*, vol. 6, Oct. 1970, pp. 111-115.
- 24-55. Axton, E. J.: Results of the Intercomparisons of the Thermal Flux Density Unit (1966-1968). *Metrologia*, vol. 6, no. 1, Jan. 1970, pp. 25-32.
- 24-56. Meadows, J. W.: Thermal Capture Cross Sections of  ${}^6\text{Li}$   ${}^{10}\text{B}$  by Pulsed Neutron Method. Neutron Standards and Flux Normalization, U.S. Atomic Energy Commission Symposium Series no. 23, 1971, pp. 129-135.
- 24-57. Blanford, G. E., Jr.; Walker, R. M.; and Wefel, J. P.: Track Etching Parameters for Plastics Radiation Effects, vol. 3, no. 3-4, June 1970, pp. 267-270.
- 24-58. Stoenner, R. W.; Davis, Raymond, Jr.; Norton, Elinor; and Bauer, Micheal: Radioactive Rare Gases, Tritium, Hydrogen, and Helium in the Sample Return Container, and in the Apollo 16 and 17 Drill Stems. Proceedings of the Fifth Lunar Science Conference, vol. 2, Pergamon Press, 1974, pp. 2211-2229.
- 24-59. Reedy, R. C.; Arnold, J. R.; and Trombka, J. I.: Expected Gamma Ray Emission Spectra From the Lunar Surface as a Function of Chemical Composition. *J. Geophys. Res.*, vol. 78, no. 26, Sept. 10, 1973, pp. 5847-5866.
- 24-60. Wallen, M.; Finkel, R. C.; Imamura, M.; Kohl, C. P.; and Arnold, J. R.:  ${}^{60}\text{Co}$  in Lunar Samples. *Earth Planet. Sci. Lett.*, vol. 19, 1973, pp. 315-320.
- 24-61. Russ, G. P., III: Chemistry, Nuclear: Neutron Stratigraphy in the Lunar Regolith. Ph. D. Thesis, Calif. Inst. Tech., 1973.
- 24-62. Williams, M. M.: The Slowing Down and Thermalization of Neutrons. American Elsevier, 1966, ch. 3.
- 24-63. Pepin, R. O.; Basford, J. R.; Drogon, J. C.; Coscio, M. R.; and Murthy, V. R.: Rare Gases and Trace Elements in Apollo 15 Drill Core Fines: Depositional Chronologies and K-Ar Ages, and Production Rates of Spallation-Produced  ${}^3\text{He}$ ,  ${}^{21}\text{Ne}$ , and  ${}^{38}\text{Ar}$  Versus Depth. Proceedings of the Fifth Lunar Science Conference, vol. 2, Pergamon Press, 1974, pp. 2149-2184.

- 
- 24-64. Alexander, E. C.: Spallogenic Ne, Kr, and Xe From a Depth Study of 12002. Proceedings of the Second Lunar Science Conference, vol. 2, MIT Press (Cambridge, Mass.), 1971, pp. 1643-1650.

TABLE 24-I.- RELATIVE PRODUCTION RATES<sup>a</sup> OF <sup>157</sup>Gd AND <sup>10</sup>B

Ratio	Spectral family (fig. 24-14)	
	T = 0 K	T = 400 K
Experimental		
P <sub>149</sub> /P <sub>157</sub>	10.8 ± 1.3	13.0 ± 1.6
Ratio of neutron density below 0.5 eV to neutron density above 0.5 eV	13.5 ± 2.3	11.4 ± 2.1
Theoretical		
LCH <sup>b</sup>	18.8	--

<sup>a</sup>Production rates per target atom.

<sup>b</sup>Calculation for Apollo 11 composition, 200 K, and depth averaged energy spectrum.

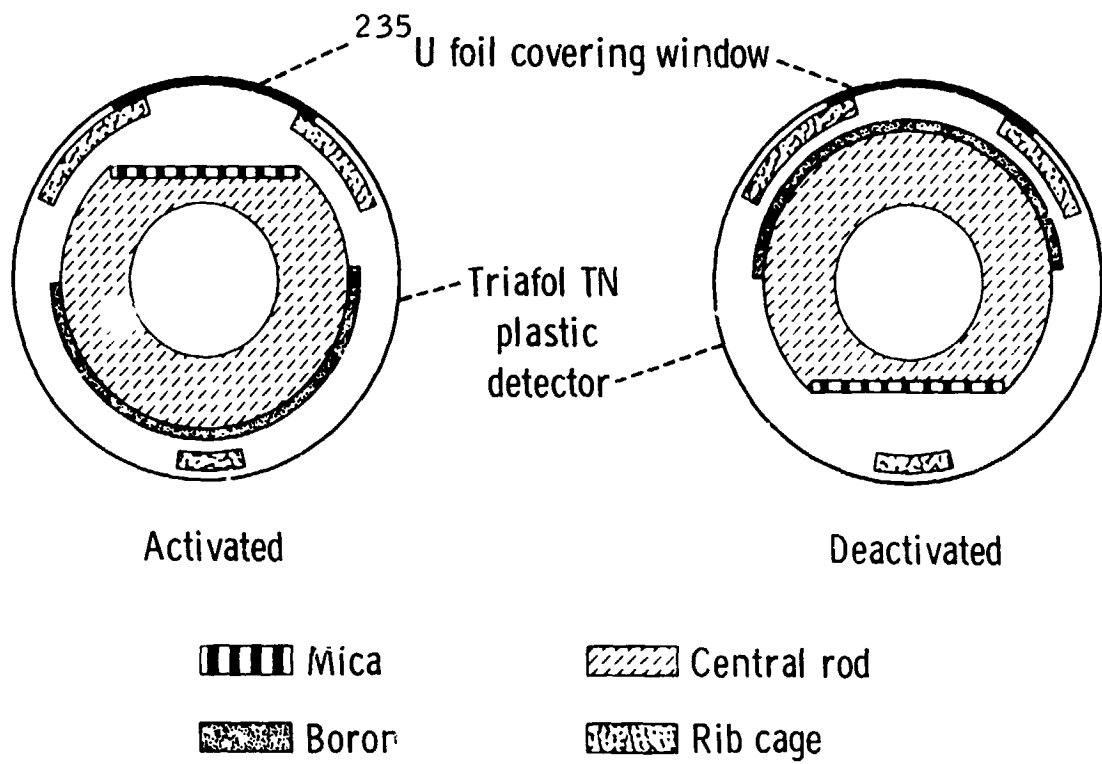


Figure 24-1.- A schematic, cross-sectional view of the lunar neutron probe, illustrating the disposition of the targets and detectors in the activated (on) and deactivated (off) modes. The boron targets and mica detectors are mounted on the central rod; the plastic detectors and uranium targets are mounted on the rib cage. When activated, the targets face their respective detectors; when deactivated, the target and detector systems are 180° out of alignment.

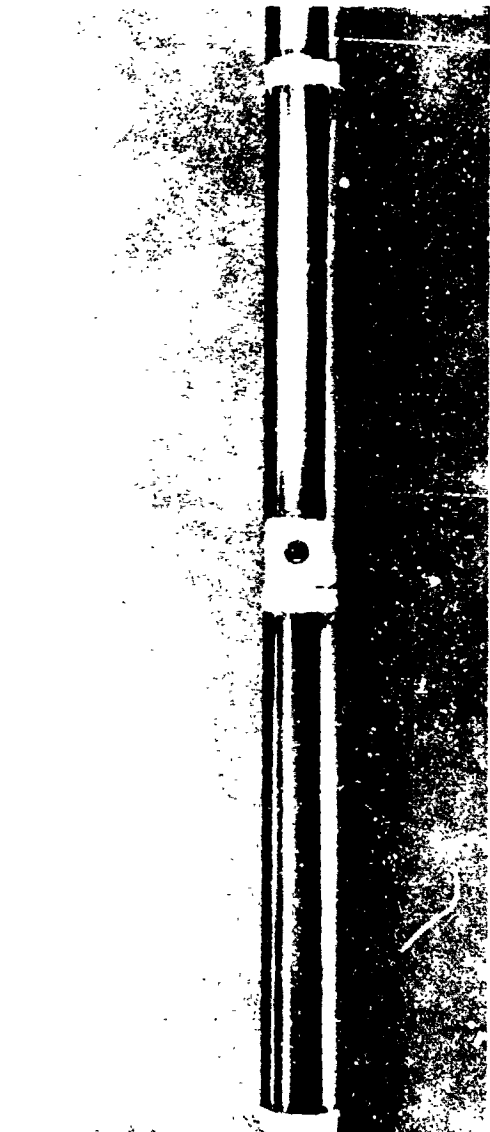


Figure 24-2.- A portion of the central rod, showing the boron target half cylinders mounted on it. The dark, circular area contains one of the uranium-238 ( $^{238}\text{U}$ ) metal disks masked to a diameter of approximately 1 mm. The  $^{238}\text{U}$  was used to provide fiducial marks in the plastic detectors for verifying activation and deactivation. The boron targets are 7.5 cm long.

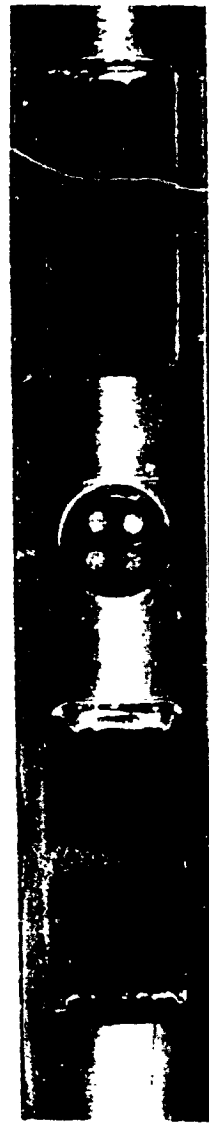


Figure 24-3.- A photograph of two rectangular mica detectors mounted on flats in the central rod. The mica detectors are 1.8 cm long. Also included at this location is one of the circular temperature sensors. None of the four circular indicators had turned black, indicating that the temperature never exceeded 333 K. The photograph was taken during the photodocumentation of the LNPE after the Apollo 17 mission.

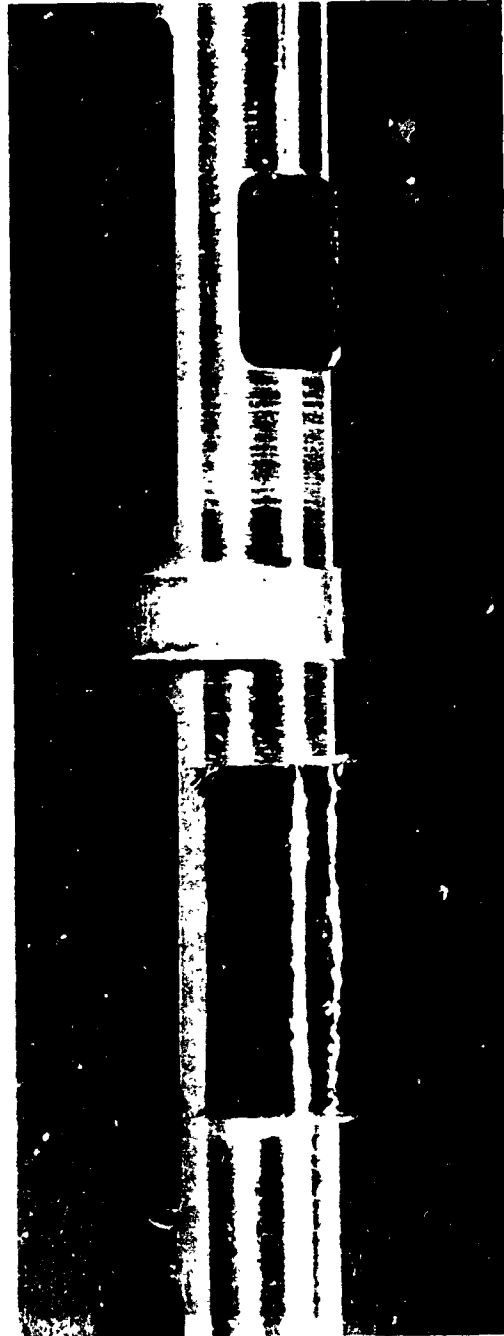


Figure 24-4.- A portion of the rib cage during the early stages of the assembly of the probe, before the mounting of the plastic detectors. Visible are one of the open windows and a window covered with a  $^{235}\text{U}$  metal target that has, in turn, been completely covered with aluminum foil to prevent the registration of alpha particles in the plastic detectors when they are wrapped onto the rib cage. The windows are 1.2 cm long.

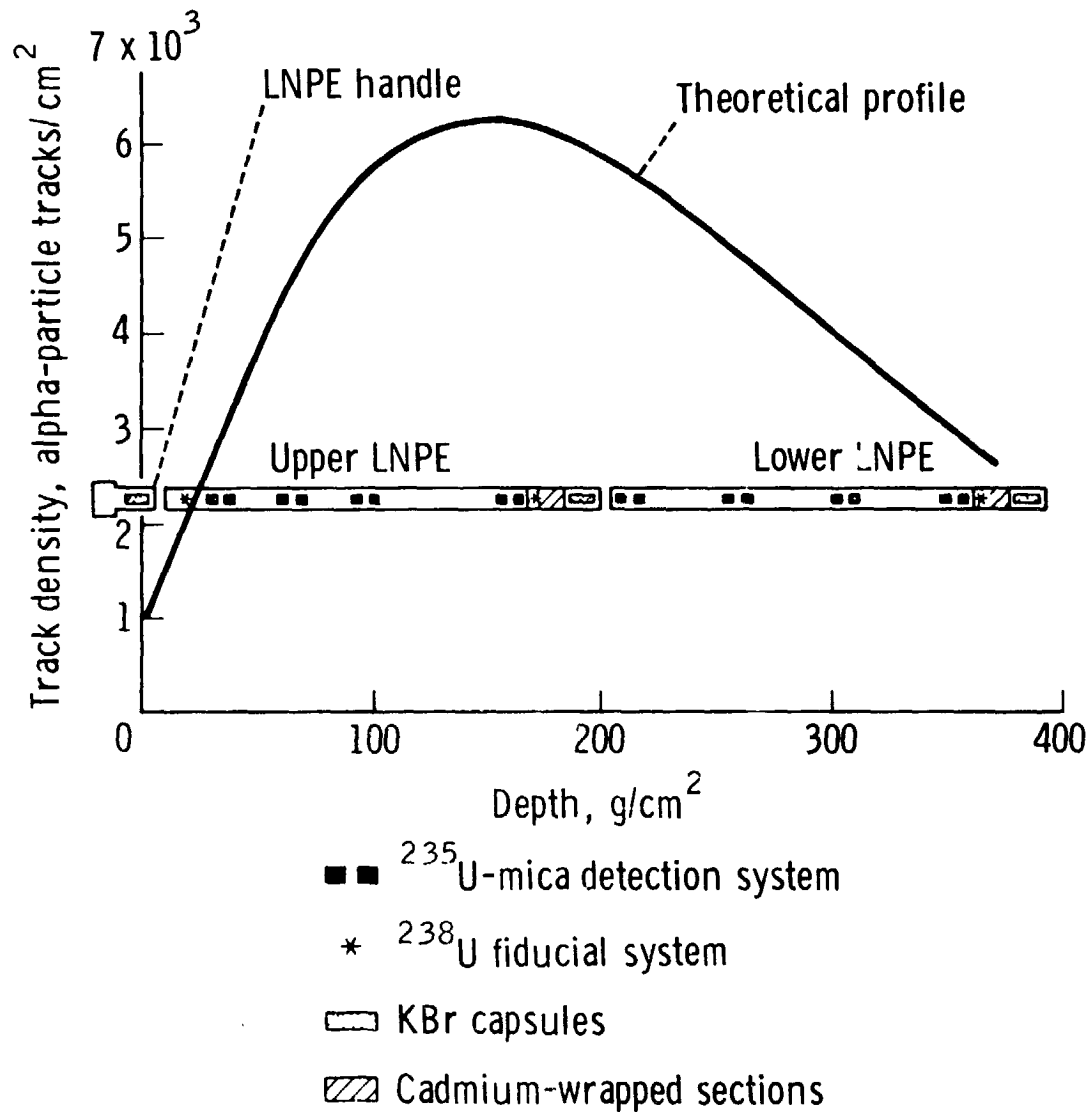


Figure 24-5.- A schematic view of the lunar neutron probe showing how the various targets and detectors are distributed with depth and including the theoretically predicted track density versus depth curve. The <sup>10</sup>B targets and plastic detectors (not shown) are essentially continuous along the entire length of the probe.

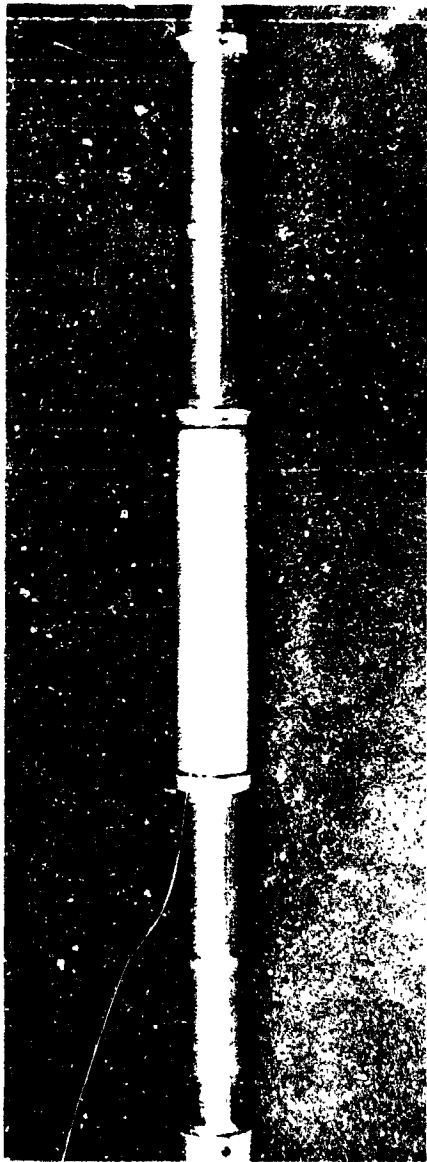


Figure 24-6.- A portion of one of the fully assembled rib cages. Two plastic detectors and one of the cadmium-wrapped areas are shown. The cadmium cylinder is 7.5 cm long.



Figure 24-7.- The assembled flight unit of the lunar neutron probe. The upper section, with the probe handle at the top, is on the right. The lower section with its removable dust cap is on the left. Coupling of the two sections is accomplished by screwing the lower and upper units together after removing the dust cap. Each section is approximately 1 m long.

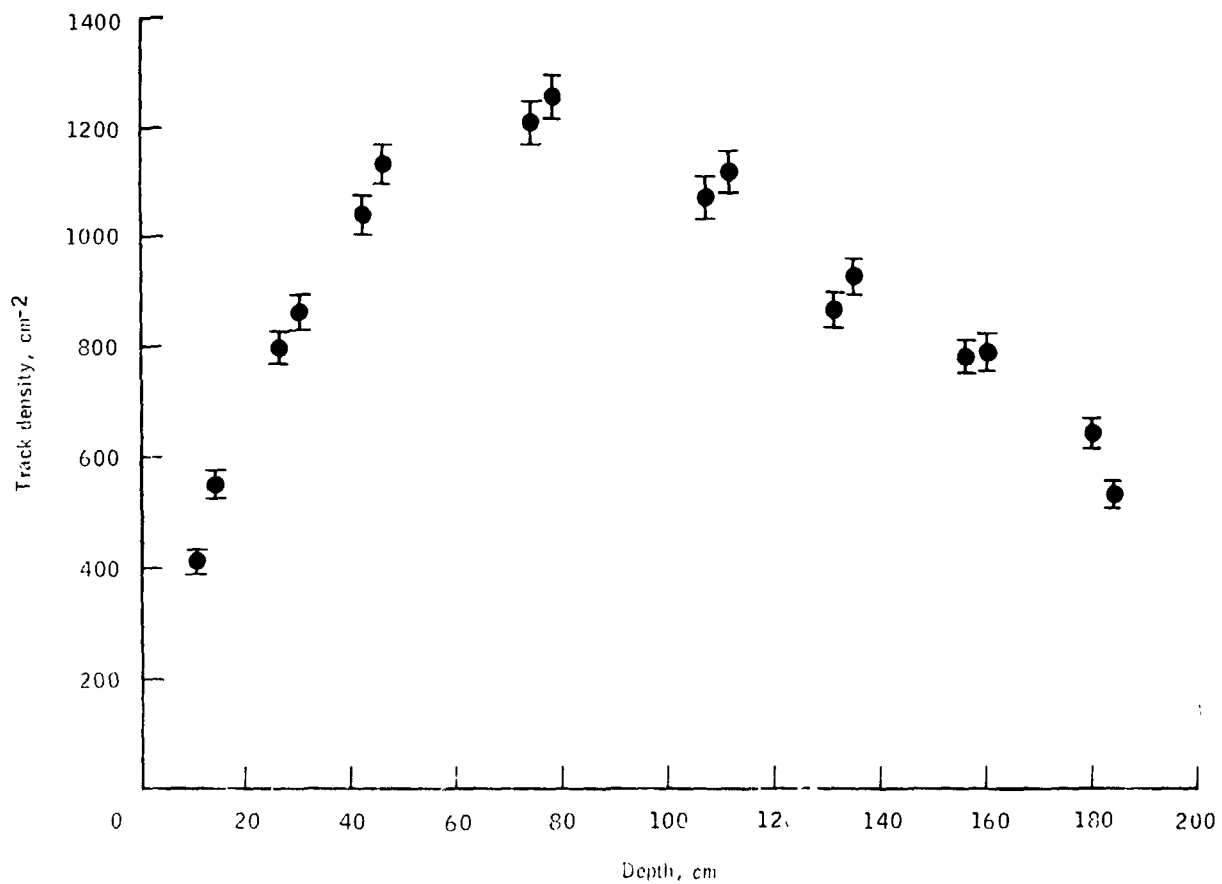


Figure 24-8.- The measured  $^{235}\text{U}$  fission track density in the mica detectors plotted against depth in centimeters beneath the lunar surface. Error bars are  $\pm 1$  standard deviation based solely on counting statistics.

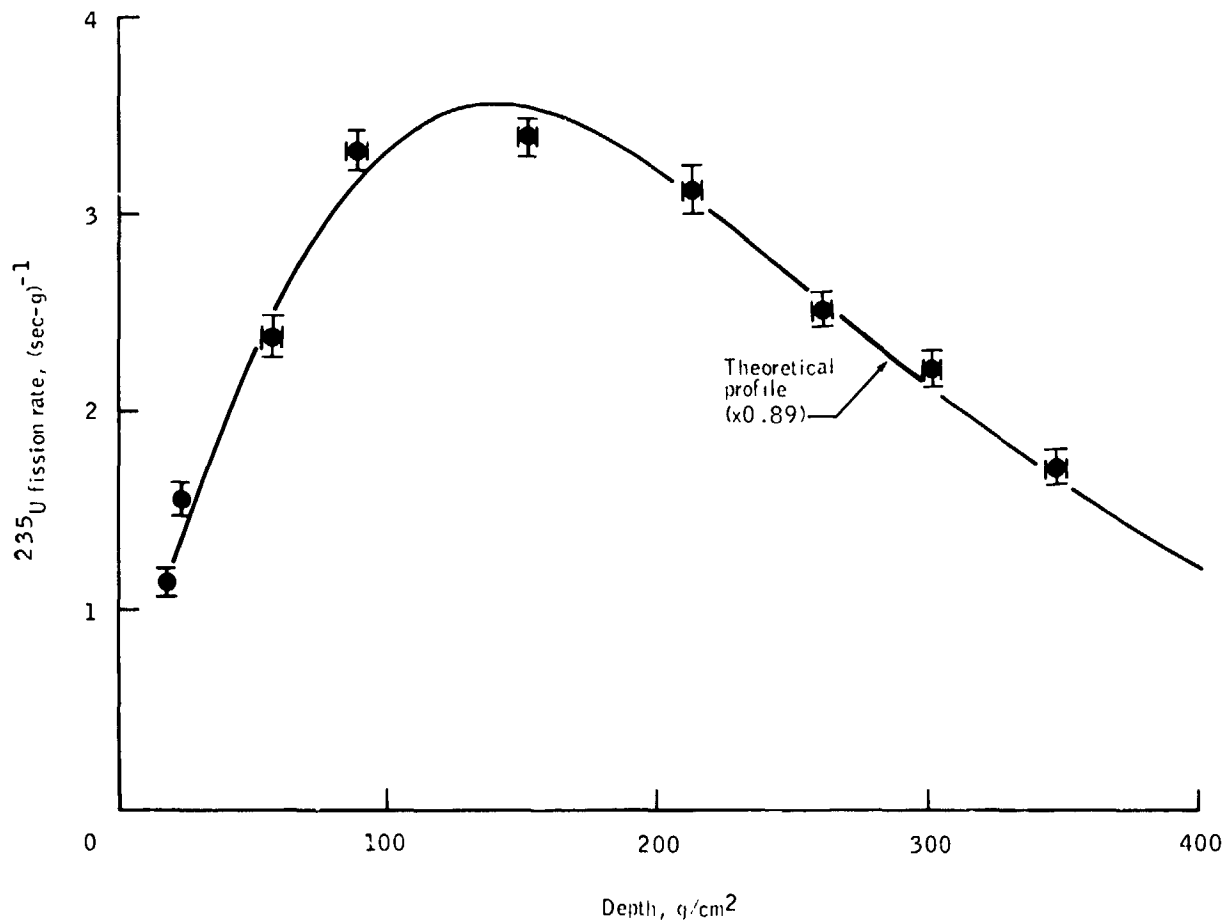


Figure 24-9.- The experimental  $^{235}\text{U}$  fission rate (points), with all corrections applied, plotted against depth and compared with the theoretical profile (solid curve) from LCH. The fission rate (ordinates) scale has been calculated based on the data point at  $150\text{ g/cm}^2$ . As an approximate best fit to the data, the theoretical curve has been multiplied by a factor of 0.89 at all depths for the purpose of comparison; no other adjustment has been made. The theoretical curve describes the trend of the data points very well.

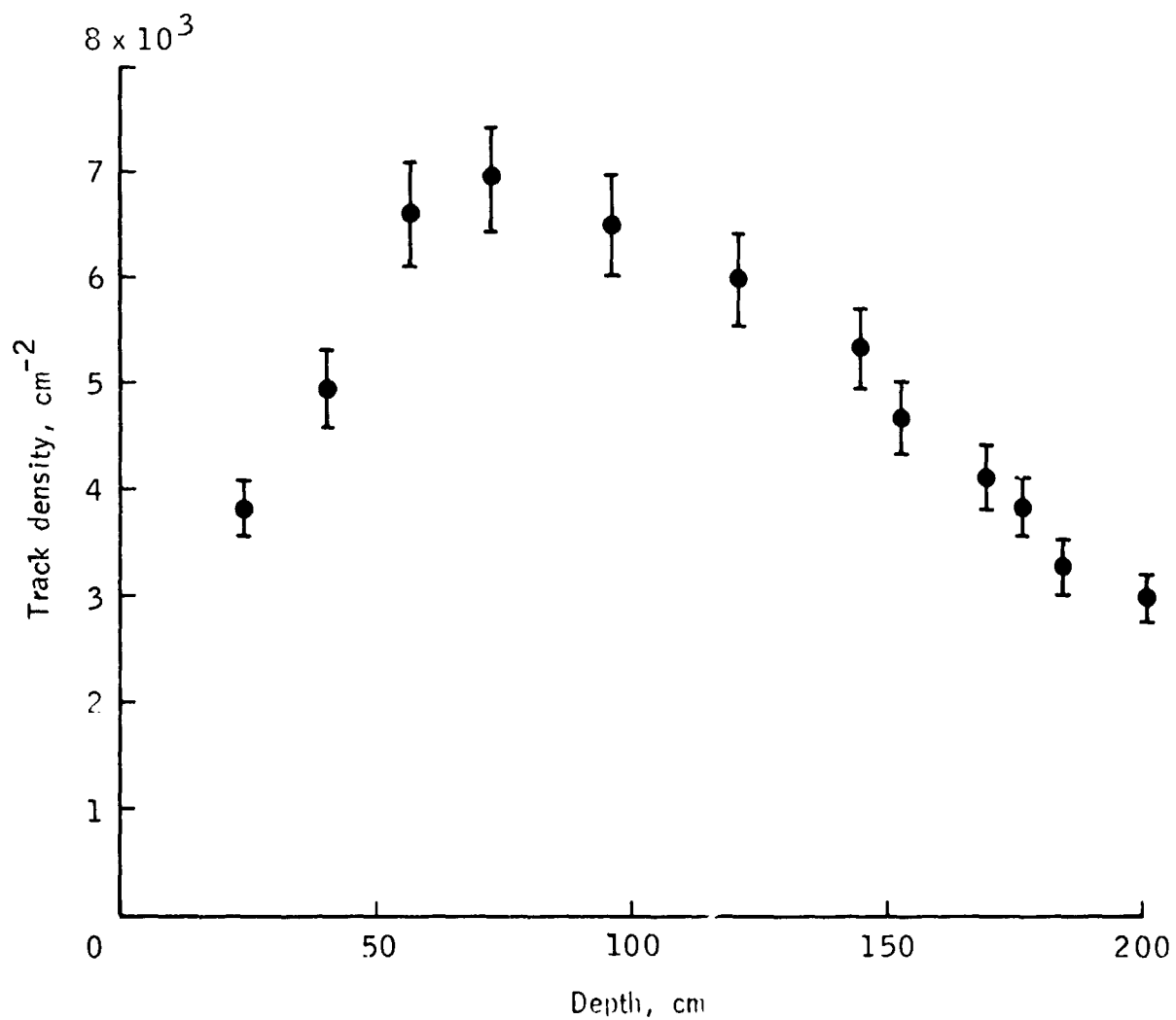


Figure 24-10.- Measured track densities from <sup>10</sup>B neutron capture as a function of depth beneath the lunar surface. The error bars include all sources of measurement error that affect the precision of a single measurement.

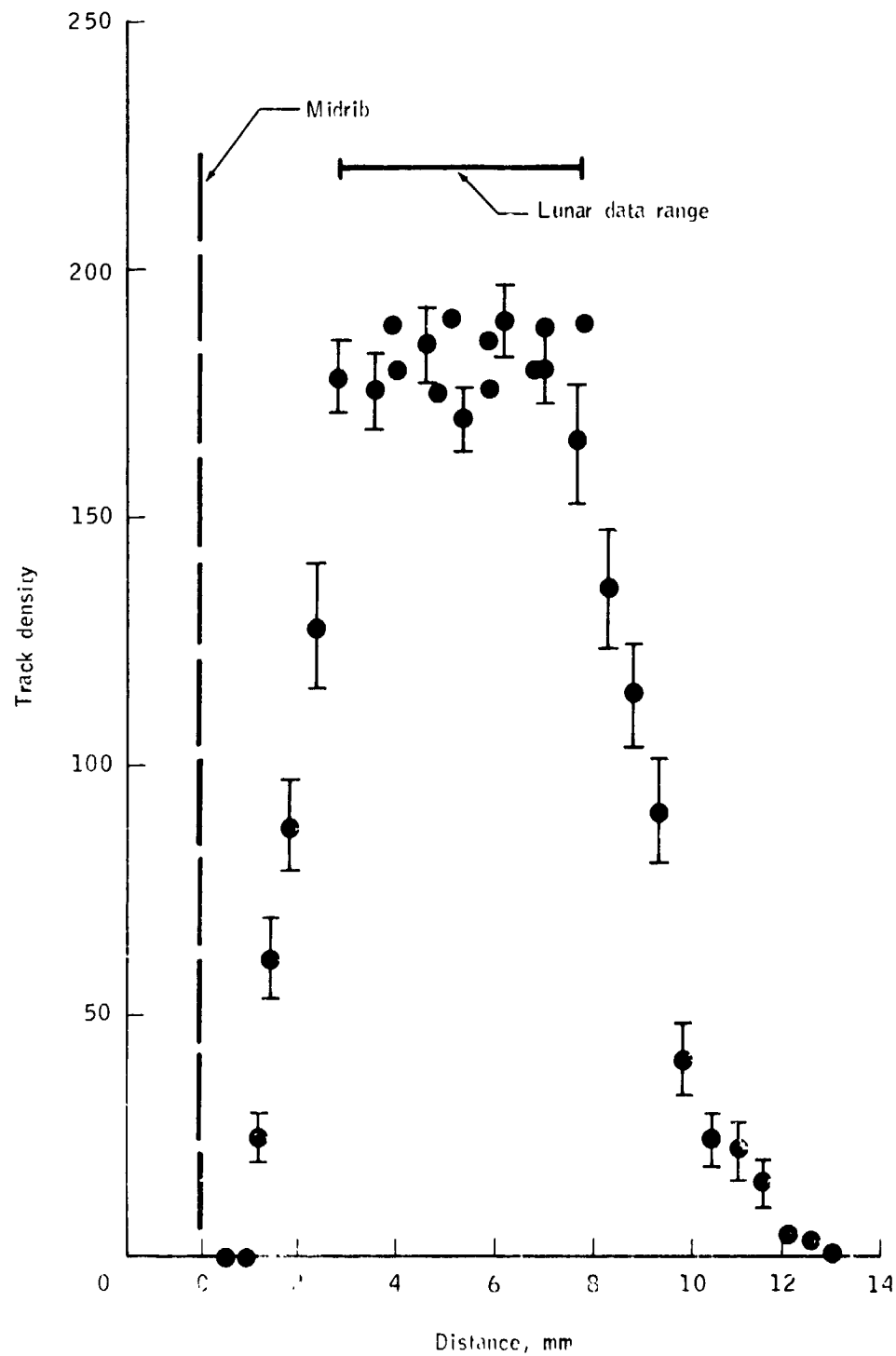
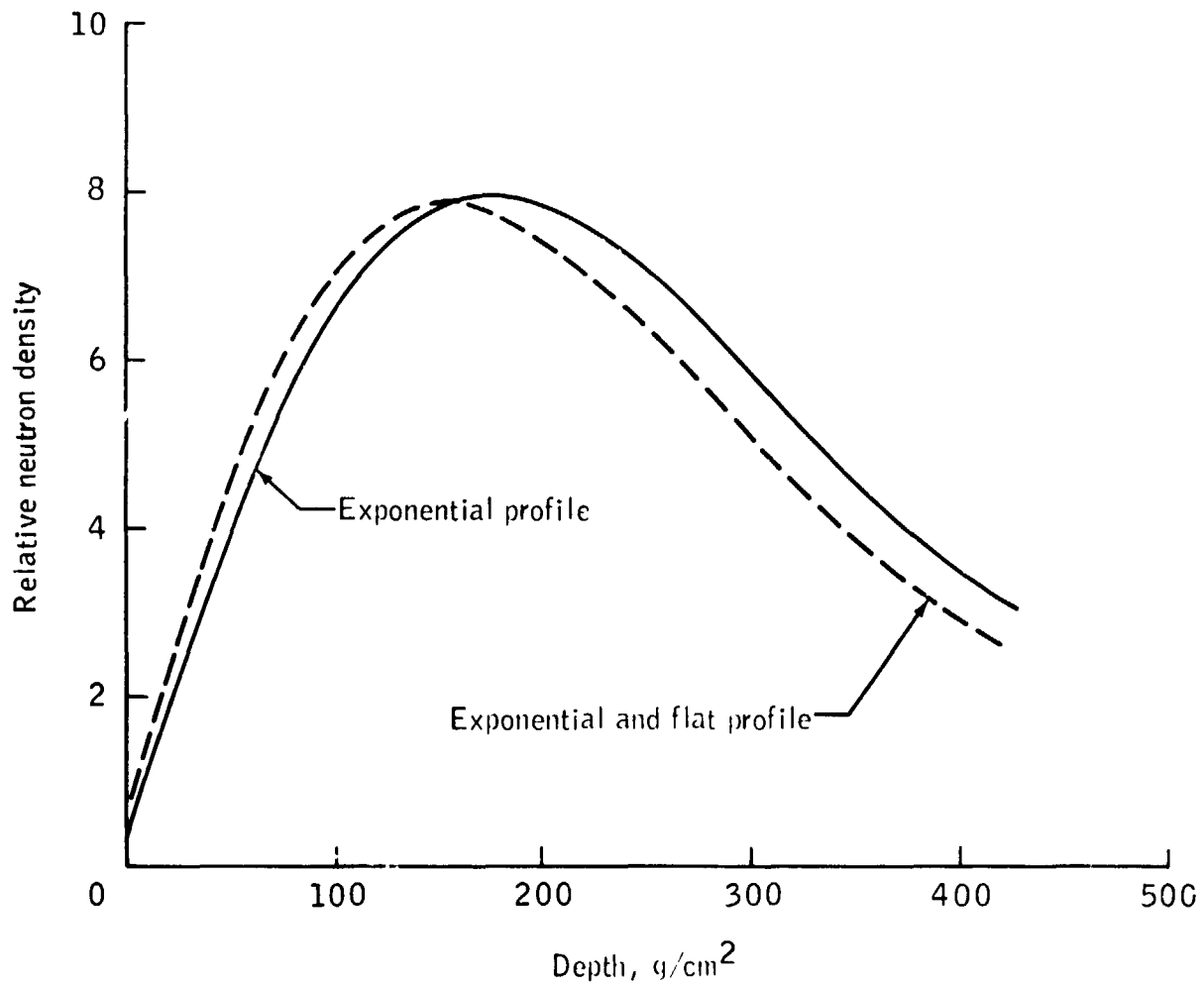
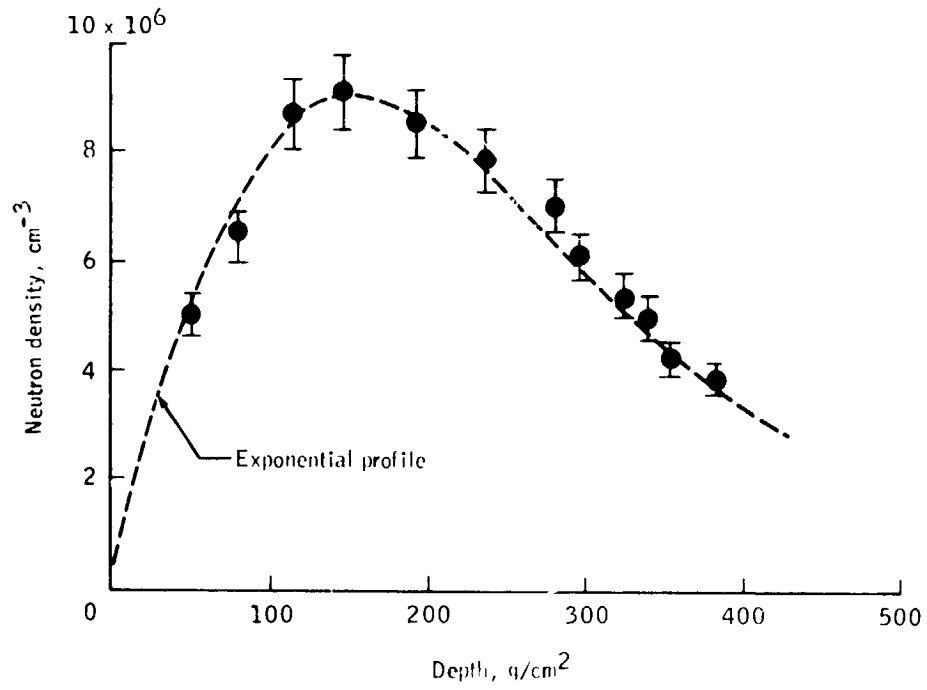


Figure 24-11.- Sample track density (arbitrary units) profile in angular direction around probe (fig. 24-1) showing that track density is flat in the actual range scanned for lunar data. Data obtained from calibration irradiation of flight unit. For clarity, only representative error bars are shown.

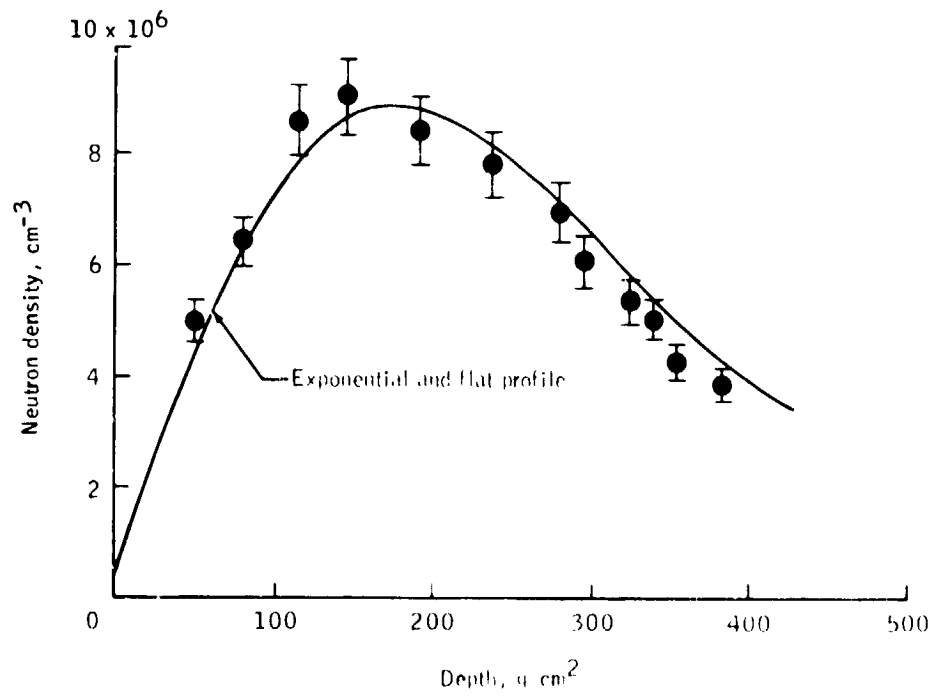


(a) Comparison of neutron density profiles calculated by LCH for two different MeV neutron source profiles.

Figure 24-12.- Comparison of LCH neutron density profiles with LNPE data. Note that the exponential profile (fig. 24-12(b)) describes the LNPE somewhat better. Only the vertical scale of the LCH profiles have been normalized to obtain a best fit in each case. No adjustment of the depth scales of the theoretical profiles was made.



(b) Exponential profile compared to LNPE data.



(c) Exponential and flat profile compared to LNPE data.

Figure 24-12.- Concluded.

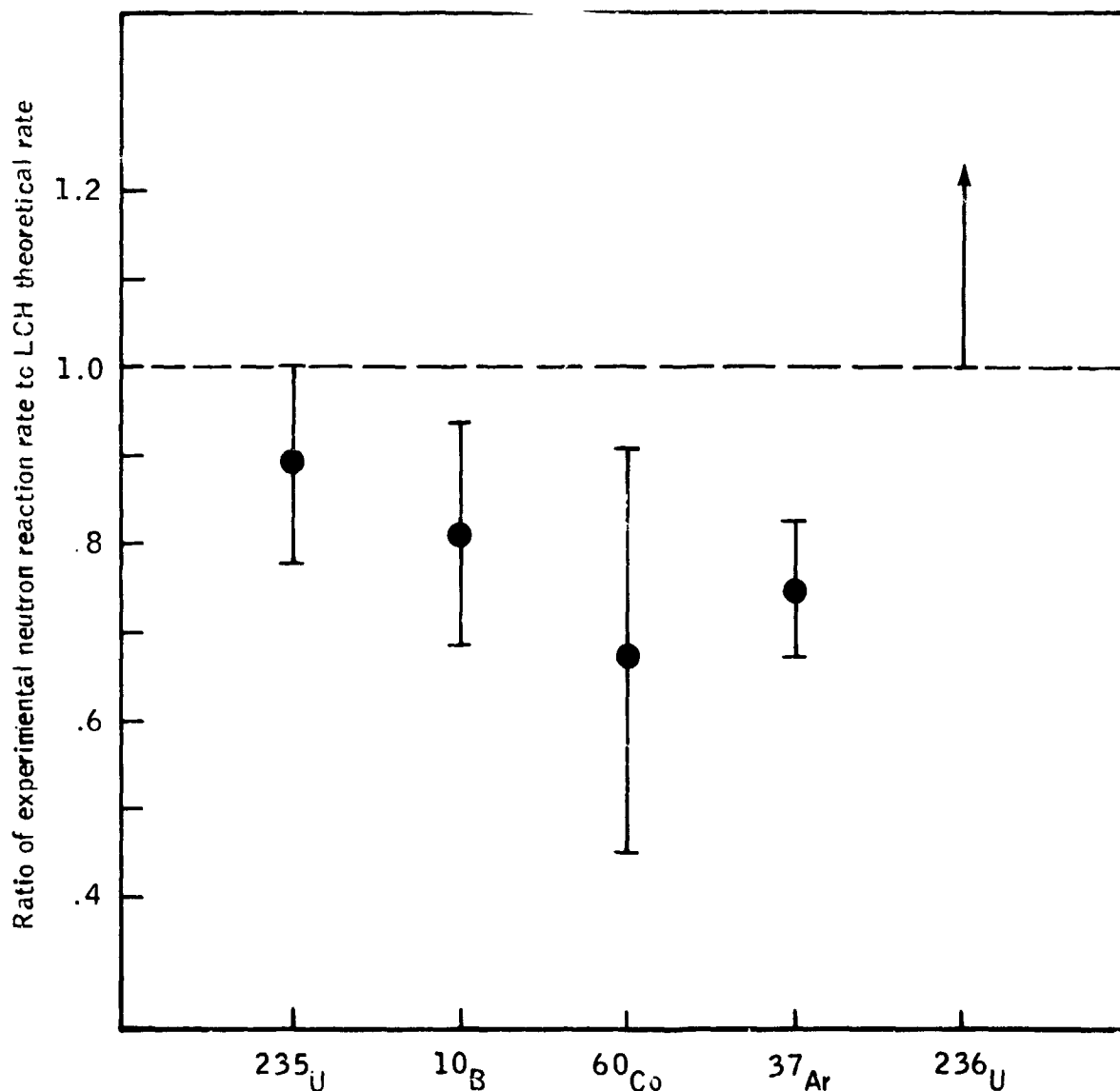
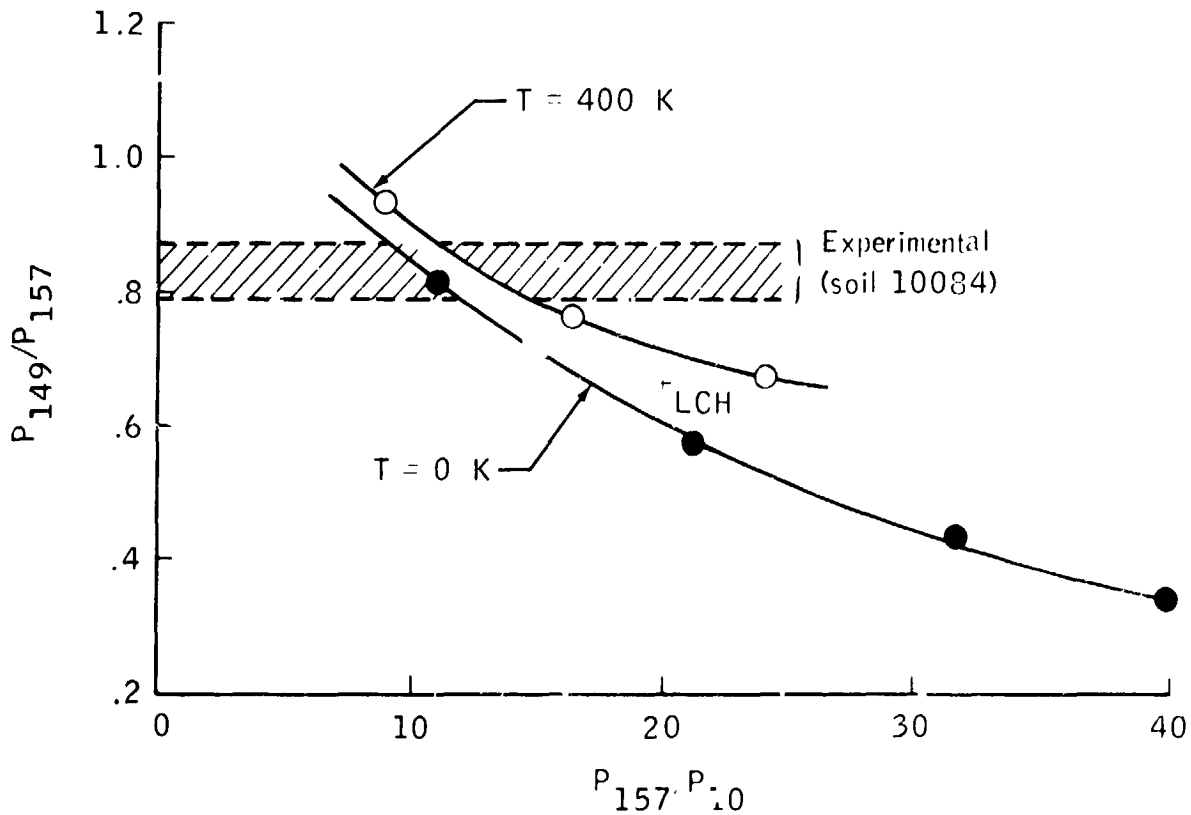
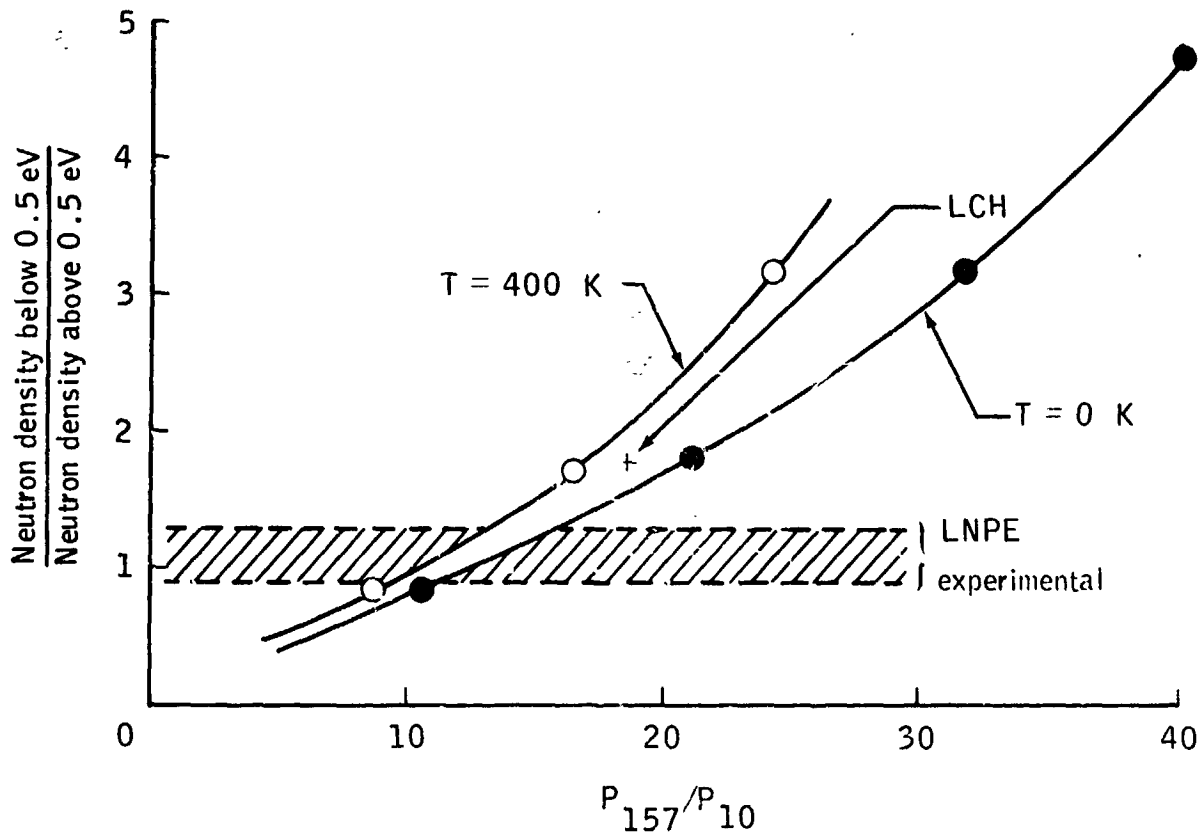


Figure 24-13.- Sketch displays the ratio of the experimental neutron reaction rate to that calculated theoretically (LCH). For the LNPE data ( $^{235}\text{U}$  fission and  $^{10}\text{B}$ ), the symbols denote the targets for the reaction; whereas, for lunar sample data, the induced radioactivity is denoted by the symbol  $^{60}\text{Co}$  (ref. 24-60),  $^{37}\text{Ar}$  (ref. 24-29),  $^{236}\text{U}$  (ref. 24-39). The arrow in the  $^{236}\text{U}$  position indicates that the measured  $^{236}\text{U}$  decay rate is at least twice that calculated theoretically. The agreement between theory and experiment is good overall.



(a) Correlation curve of  $P_{149}/P_{157}$  to  $P_{157}/P_{10}$ .

Figure 24-14.- Correlation curves for the calculated ratio of the  $^{149}\text{Sm}$  to  $^{157}\text{Gd}$  capture rates ( $P_{149}/P_{157}$ ) and the ratio of neutron density below and above 0.5 eV compared to the ratio of the  $^{157}\text{Gd}$  to the  $^{10}\text{B}$  capture rate ( $P_{157}/P_{10}$ ) for various theoretical low energy neutron spectra taken from LCH. Two families of spectra were used, parameterized by  $T = 0\text{ K}$  and  $T = 400\text{ K}$ . For each family, the spectrum was systematically varied to give the observed correlation lines. The hatched regions show the experimental values for the quantities on the ordinates. The intersections of the curves and the experimental values correspond to neutron energy spectra that fit the experimental data. These intersections correspond to  $P_{157}/P_{10}$  values that are distinctly lower than those calculated by LCH (indicated by crosses in the figure).



(b) Correlation curve of  $P_{157}/P_{10}$  to the ratio of neutron density below 0.5 eV to that above 0.5 eV.

Figure 24-14.- Concluded.

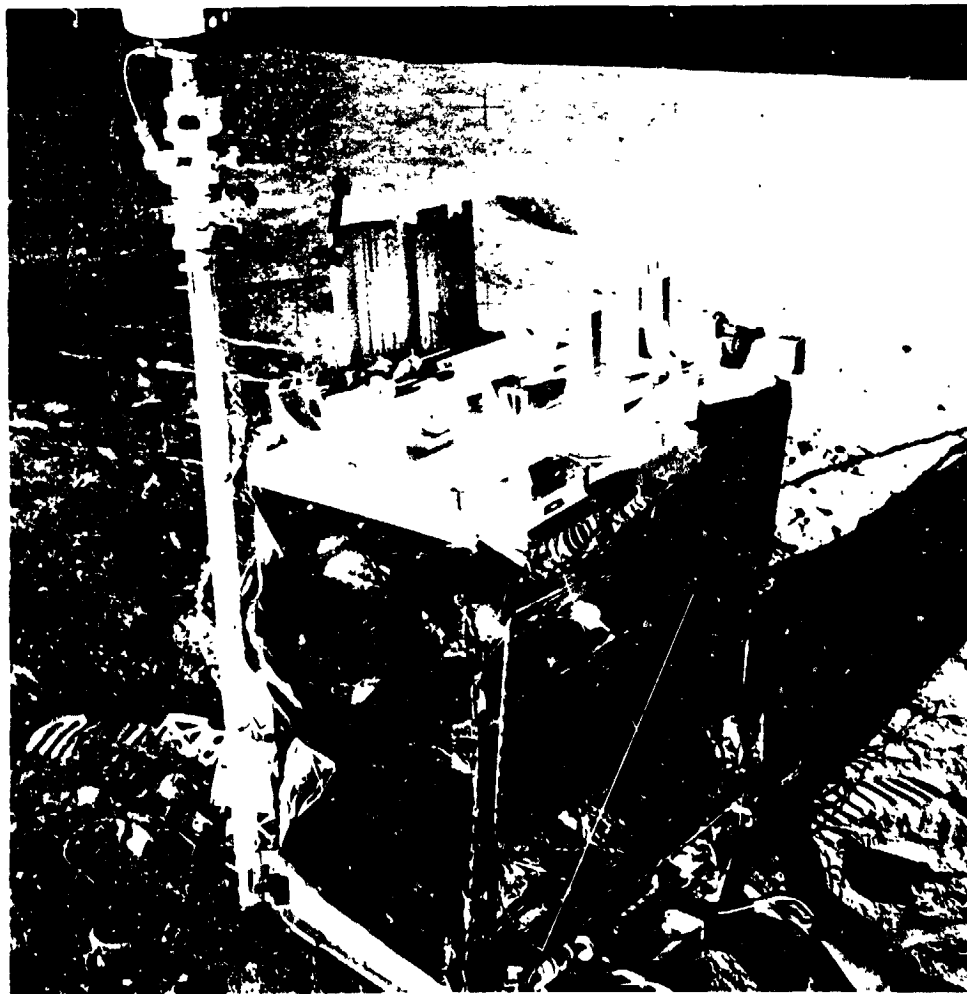
G-7

25. DUST THERMAL RADIATION ENGINEERING MEASUREMENT

(NASA EXPERIMENT M-515)

NSSDC IDENTIFICATION NUMBERS:

APOLLO 11 69-059C-05  
APOLLO 14 71-008C-12  
APOLLO 15 71-063C-09



CONTENTS - SECTION 25

	Page
BACKGROUND . . . . .	25-3
EXPERIMENT SIGNIFICANCE . . . . .	25-3
CONCEPT . . . . .	25-4
PROCEDURES . . . . .	25-4
MEASUREMENTS . . . . .	25-5
DATA ANALYSIS . . . . .	25-5
CONSTRAINTS ON RESULTS . . . . .	25-6
BASELINE OR CONTROL DATA . . . . .	25-6
EQUIPMENT DESCRIPTION . . . . .	25-7
RESULTS . . . . .	25-7
DATA ARCHIVED AT NSSDC . . . . .	25-8

## 25. DUST THERMAL RADIATION ENGINEERING MEASUREMENT

The purpose of the dust thermal radiation engineering measurement (DTREM) was to measure the long-term effects of the lunar environment on solar cells. When the lunar dust detector was reconfigured for solar-cell degradation measurements, plans were being made for manned lunar bases using large arrays of solar cells for power. The lunar surface, with its severe temperature extremes every month and deep-space environment, is an ideal test area for such measurements. By operating for long periods in the lunar environment, the DTREM will add measurably to solar-cell test data in the optimization of solar-cell power supplies for lunar bases.

### BACKGROUND

The DTREM flown on the Apollo 11, 14, and 15 missions is a reconfiguration of the originally designed lunar dust detector (flown on the Apollo 12 and 13 missions). This original configuration was designed to measure the "then anticipated" heavy dust accumulations on lunar experiment packages. However, subsequent engine firings of the Surveyor spacecraft on the lunar surface showed the dust layer and resultant blowing of dust to be much less than expected; therefore, it appeared that the dust detector would be measuring very little dust accumulations. About 6 months before the Apollo 11 mission, it was decided to modify and possibly expand the capability of the lunar dust detector (part of the Apollo 11 passive seismic experiments package/early Apollo scientific experiments package (PSEP/EASEP)); thus, the DTREM was developed. By using the basic sensor substructure and electronics, it was possible to expand from a device measuring dust only to one measuring radiation effects and lunar reflectance temperatures in addition to the dust accretion.

### EXPERIMENT SIGNIFICANCE

High-energy particles from solar particle events can provide very noticeable degradation of the cell outputs. If the long-term (1 yr or greater) solar radiation effects can be measured at the lunar surface, these data can provide

information useful in optimizing solar-cell radiation shields for lunar use and can provide long-term shielding information for use in construction of lunar bases.

The reflected infrared "brightness" temperature together with the internal DTREM-package temperature can be used in computing the lunar surface temperatures, thereby aiding in the design of extravehicular activity space suits and in the thermal control of lunar hardware.

### CONCEPT

The DTREM uses a sensor package modified from the original lunar dust detector flown on the Apollo 12 and 13 missions (fig. 25-1). To satisfy the objectives, the one large solar cell at the top was replaced by three smaller (1 by 2 cm) cells (also, the two solar cells on the sides were removed); one cell is bare and each of the other two has a glass cover 0.15 mm (6 mil) thick (fig. 25-2). The temperature of the cell mounting plate is also provided.

The concept of the experiment is fairly straightforward. Radiation degrades the voltage output of the cell in a predictable manner. If a cover glass shield is attached to the surface of a cell, then, theoretically, only those particles above a certain energy (determined by the shield thickness and density) can reach the solar cell surface and release energy (table 25-I).

One of the 0.15-mm (6 mil) covered cells was heavily damaged by radiation (intentionally) before launch. This cell would then be damaged much less than an unirradiated cell when exposed to the same amount of added lunar radiation. Therefore, the irradiated cell served as a quasi-standard cell.

### PROCEDURES

The DTREM was mounted atop the central station sunshade of the Apollo lunar surface experiments package (ALSEP). No special deployment procedures by crewmen were required; the DTREM "deployed" when the central station was deployed. Earth-based control could command "on" the preamplifiers (located in the central station) as required for cell output voltages. Thermistors on the DTREM sensor package were continuously powered by 12 V dc from the central station. All the solar cells generated their own voltages and

required no external electromagnetic force except for signal amplification in the preamplifiers.

To support baseline "brightness" temperature data, photographs were taken of the deployed ALSEP central station. (These photographs were taken of the lunar surface area in the direction the infrared sensor was "looking".) After deployment, the DTREM should provide data to Earth as long as the ALSEP data transmission systems continued to operate. Baseline data were gathered from the initial telemetry after deployment and during the first lunation.

#### MEASUREMENTS

Voltages from each cell and temperature from the three thermistors constitute the entire telemetry output of the DTREM. The following list gives DTREM outputs in terms of telemetry output designations (e.g., AX01) and telemetry channel (e.g., CH83).

- AX01 - (CH83) - Internal temperature
- AX02 - (CH30) - Cell temperature
- AX03 - (CH56) - External infrared temperature
- AX04 - (CH84) - Bare-cell output
- AX05 - (CH26) - 0.15-mm (6 mil) irradiated-cell output
- AX06 - (CH41) - 0.15-mm (6 mil) cell output

Voltages from the cells prior to amplification should range from 0 to 70 mV during the lunar day, depending on the Sun angle and the individual cell characteristics. Temperature readouts of the cells should range from 298 to 398 K (25° to 125° C). Note that the temperatures are provided even with the preamplifiers commanded "off".

#### DATA ANALYSIS

The cell voltages are corrected for the temperature variables (fig. 25-3). Analog data recordings, plots, and computer printouts of the voltages and temperatures are all the data required. The data, however, must be as continuous as possible, considering ground monitoring constraints.

Baseline data were obtained during the first few hours or days after deployment when there was no appreciable radiation degradation, which is caused primarily by particles from major solar flares. The degradation of the DTREM solar-cell voltages can be compared with laboratory

results of simulated solar wind effects on similar cells (fig. 25-4).

If a large solar particle event registered in the Earth/Moon region during DTREM operation, particle data from satellites could be used to confirm the degradation caused by the event. Supporting degradation effects could be determined by simulating the solar event in an accelerator, using the test unit. A comparison of the degradation caused by a known laboratory event to the measured (DTREM) solar-cell degradation could provide an indirect measurement of the actual solar particle environment of the Moon. The lunar surface "brightness" temperature is determined from the detector energy-rate balance; that is, the net rate of energy flow out of the detector is equal to the net rate of energy into the detector.

$$\epsilon_D \sigma T_D^4 = \sigma F_{SD} \epsilon_D \epsilon_S T_S^4 + \dot{q} \quad (25-1)$$

where D denotes the detector, S the lunar surface,  $\dot{q}$  the net algebraic sum of all heat leaks to the detector,  $\epsilon$  the hemispherical emissivity,  $\sigma$  the Boltzmann constant, T the absolute temperature, and F the configuration factor. The internal DTREM temperature measurement (AX01) is used to compute  $\dot{q}$ .

#### CONSTRAINTS ON RESULTS

Because this experiment relies on a comparison of the results obtained from a ground-based experiment to the results of an unretrievable, lunar-based experiment, uncertainties in the following areas are expected.

1. Degradation of cells due to dust accumulation or ultraviolet darkening of cover glass and bonding material
2. Accuracy of ground-based calibrations

#### BASELINE OR CONTROL DATA

Some tests have been conducted on individual DTREM solar cells in the solar wind simulator, the Van de Graaff accelerator, and the lunar environment simulator facilities at the NASA Lyndon B. Johnson Space Center (JSC). Numerous

radiation degradation studies of solar cells have been performed and are well documented. Data from these tests will supplement the JSC-derived baseline data.

#### EQUIPMENT DESCRIPTION

The DTPEM has two components, a sensor package (fig. 25-1) and a printed circuit board. The sensor package, located on the ALSEP central station sunshade, has three solar cells (1 by 2 cm each) mounted on the top horizontal surface. The three cells are NPN 10 ohm-cm silicon cells. One solar cell has no cover glass; the second cell has been significantly damaged intentionally by radiation before flight (irradiated by  $1 \times 10^{15}$  electrons of 1 MeV.) The radiation environment can be measured by a reduction in the voltages of cells due to radiation degradation.

A temperature sensor is placed on the bottom of the Kovar cell mounting plate. Two other temperature sensors are mounted, internally and externally, on a vertical side of the DTREM and can be used to measure the lunar surface "brightness" temperature. The sensors are high-precision nickel resistance thermometers of wide dynamic range (84 to 408 K). The sensor package is connected through an H-film cable to the printed circuit board that is located in the power distribution unit of the data subsystem. The circuit board has electronics subassemblies for signal conditioning of cell outputs, for switching power "on" and "off" for the preamplifiers, and for routing power to the thermistors.

#### RESULTS

The following is a synopsis of results received to date from the Apollo 14 and 15 DTREM's. Results of the Apollo 14 DTREM are shown in figure 25-5 and are summarized as follows:

1. The irradiated cell with 0.15-mm (6 mil) cover glass (AX05) shows an average power drop of 2.5 percent per year.
2. The nonirradiated cell with 0.15-mm (6 mil) cover glass (AX06) shows a power drop of approximately 4.3 percent per year.
3. The bare cell (AX04) has shown a total power drop of 33 percent since deployment. The reason for the large

decrease from the initial lunation to the fourth lunar noon point has not yet been determined.

The August 1972 major solar flare caused a power drop of approximately 9.5 percent, which is in the range expected from a total dose of  $10^9$  to  $10^{10}$  protons of  $E > 60$  keV.

Results of the Apollo 15 DTREM are shown in figure 25-6 and are summarized as follows:

1. The irradiated cell with 0.15-mm (6 mil) cover glass (AX05) shows only an average of 1-percent decrease in power per year.

2. The nonirradiated cell with 0.15-mm (6 mil) cover glass (AX06) shows an average power drop of approximately 3.5 percent in output per year.

3. The bare cell (AX04) has shown a total power drop of approximately 16 percent since deployment.

The August 1972 major solar particle event caused a total drop of approximately 7 percent, which is in the range of expected damage from a total dose of  $10^9$  to  $10^{10}$  protons of  $E > 60$  keV.

#### DATA ARCHIVED AT NSSDC

Microfilm data at the National Space Science Data Center (NSSDC) will cover only the data up to February 22, 1976. Figure 25-7 shows the data format, which includes the following terms.

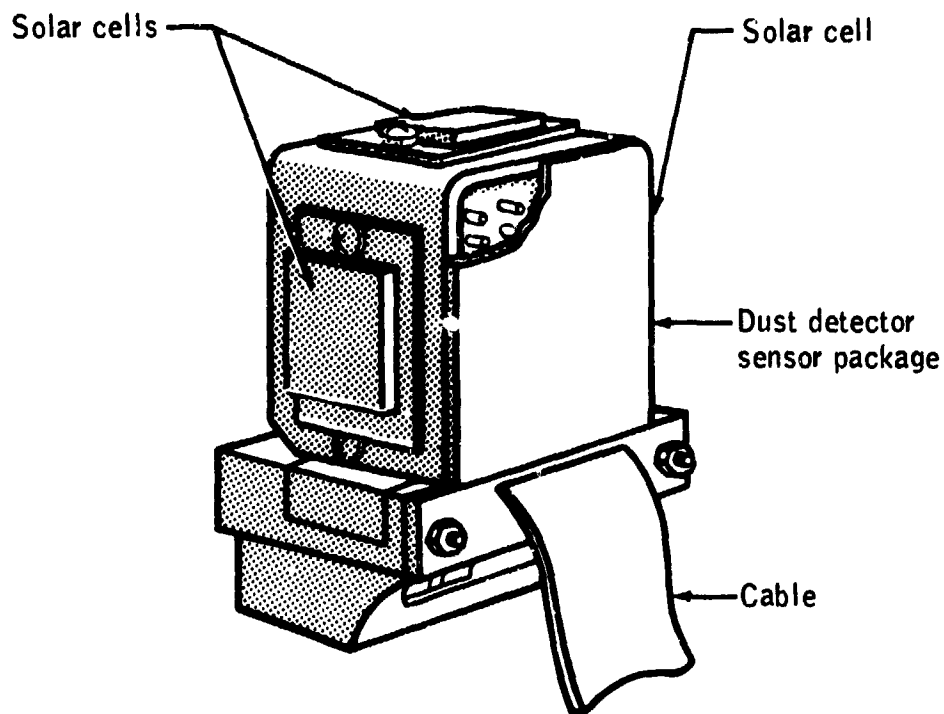
<u>Term</u>	<u>Description</u>
Days	Day of the year, numbered consecutively from January 1st as day 1.
Hr Min Sec	Greenwich mean time (universal time).
Sun elevation angle	Angle from spherical lunar surface to center of Sun at ALSEP location.

<u>Term</u>	<u>Description</u>
AX01	Internal sensor temperature which correlates with cell temperature AX02 so that the two sets of data are interchangeable
AX03	External radiated (brightness) temperature.
AX04, AX05, AX06 uncorrected	Raw outputs of solar cells.
AX04, AX05, AX06 corrected	Solar cell outputs that are temperature corrected by multiplying the raw outputs by a correction factor. The correction factor is derived from curves of temperature compared to cell output (at constant illumination).

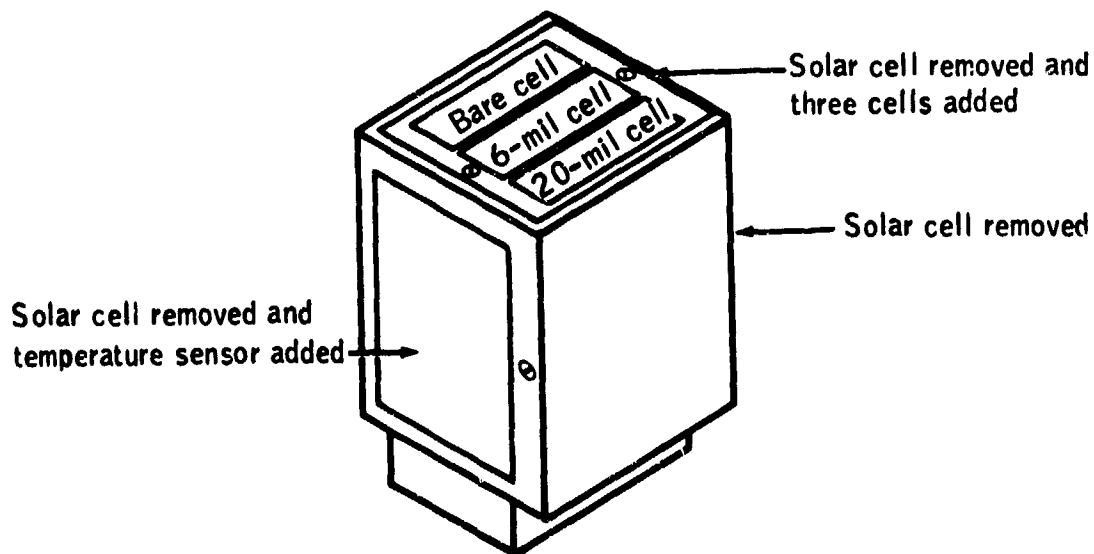
TABLE 25-I.- ENERGY THRESHOLDS OF DTREM (APOLLO 11  
EASEP AND APOLLO 14 AND 15 ALSEP)

Type of cell	Energy threshold <sup>1</sup>
Bare cell	e <sup>-</sup> > 173 keV p <sup>+</sup> > 60 keV
0.15-mm (6 mil) cell	e <sup>-</sup> > 175 keV p <sup>+</sup> > 4.25 MeV
0.51-mm (20-mil) cell (Apollo 11 EASEP only)	e <sup>-</sup> > 380 keV p <sup>+</sup> > 8.5 MeV

<sup>1</sup>Symbol e<sup>-</sup> = electrons and p<sup>+</sup> = protons.

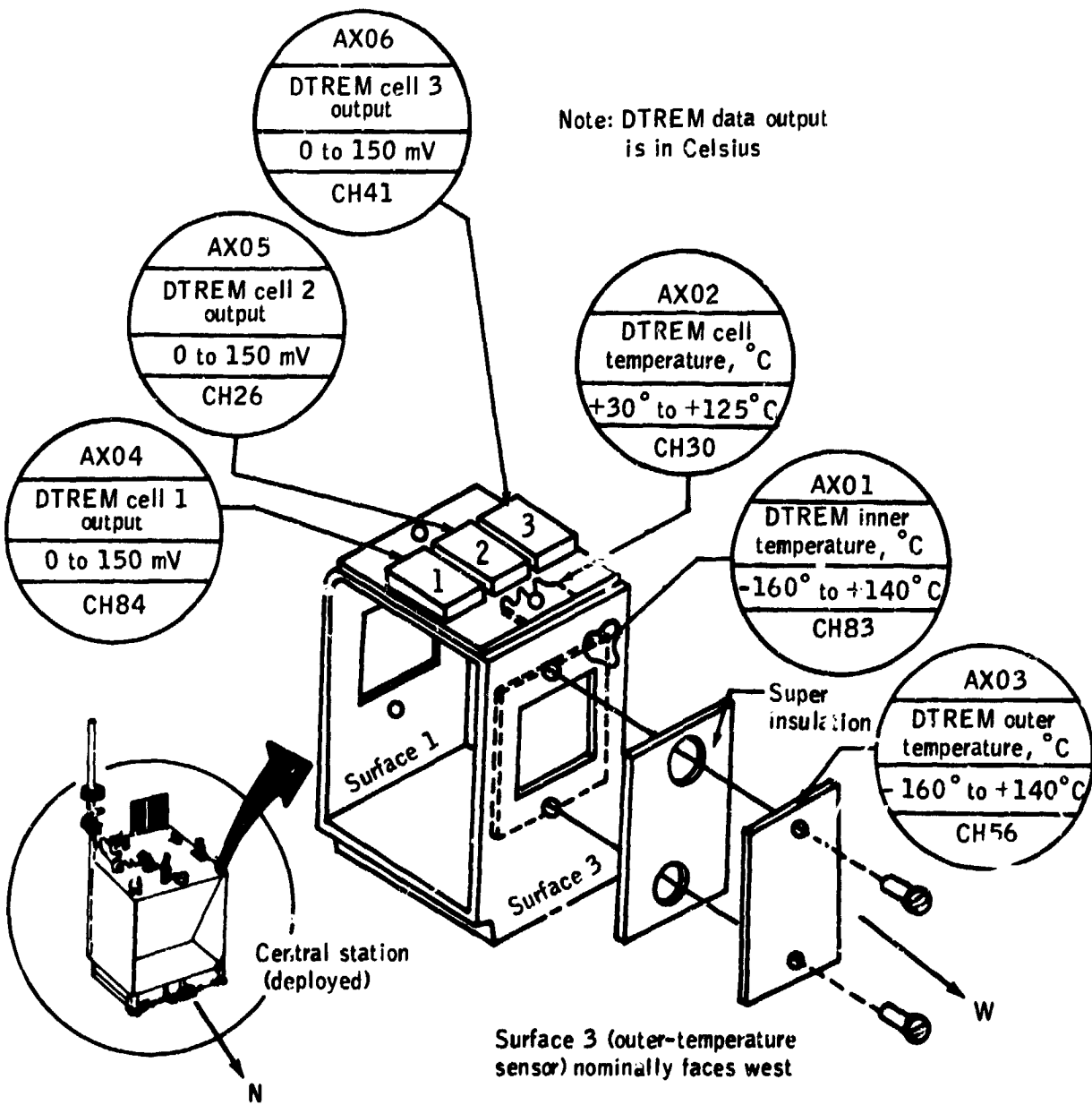


(a) Original dust detector sensor (Apollo 12 and 13).



(b) Modified dust detector (DTREM) sensor (Apollo 11, 14, and 15).

Figure 25-1.- Original dust detector and the DTREM.



Cell 1 - no filter  
 Cell 2 - irradiated cell, 0.15-mm (6 mil) blue filter  
 Cell 3 - 0.15-mm (6 mil) blue filter

Figure 25-2.- Dust thermal radiation engineering measurement.

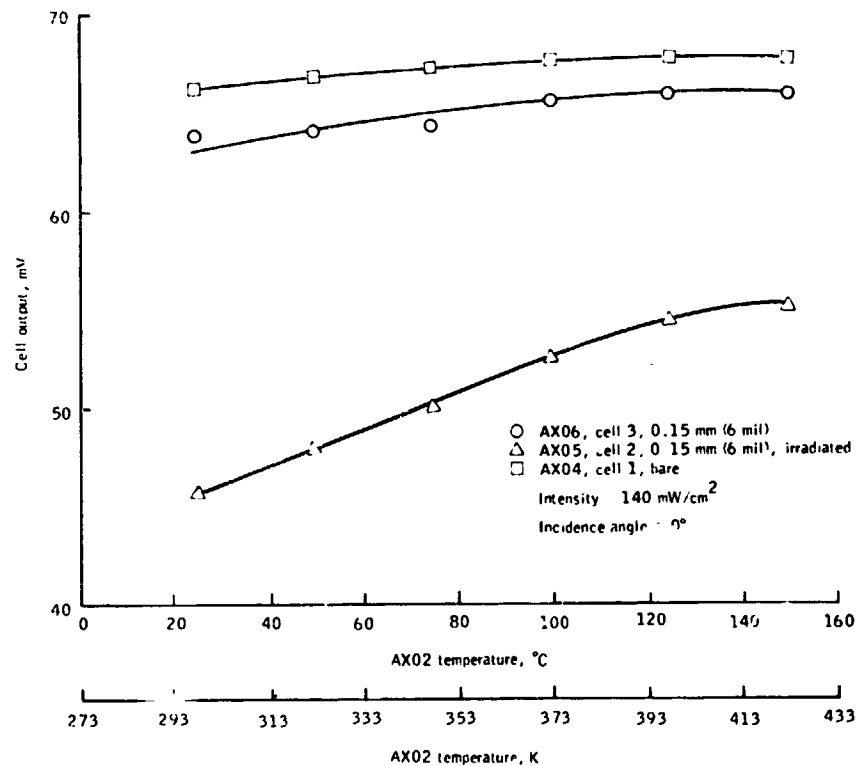


Figure 25-3.- Typical DTREM temperature response curves (Apollo 14).

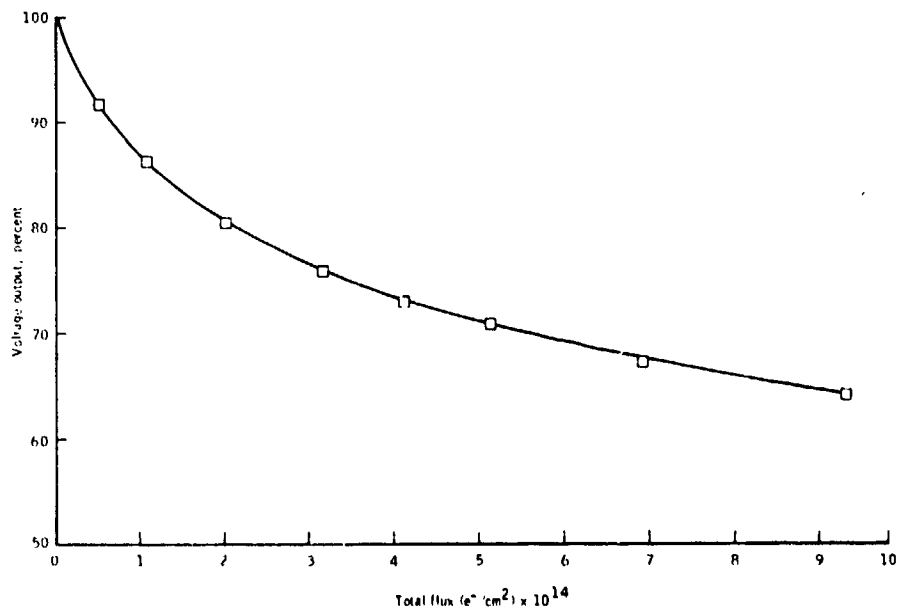


Figure 25-4.- Solar cell damage caused by laboratory radiation. Flight-type solar cell irradiated with 10<sup>15</sup> 1 MeV electrons in Van de Graaff accelerator at the NASA Lyndon B. Johnson Space Center.

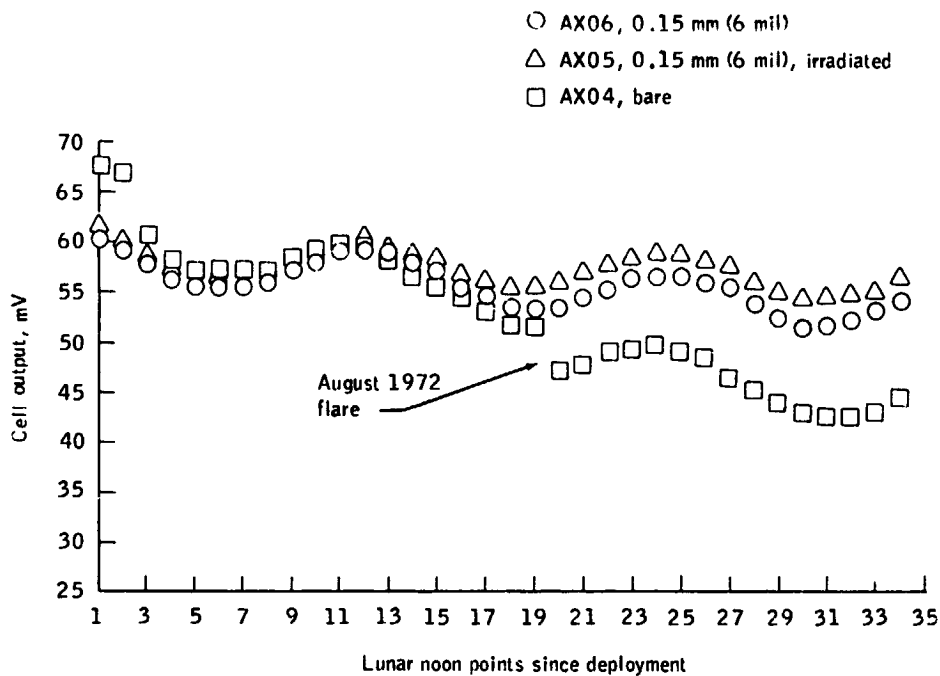


Figure 25-5.- Apollo 14 DTREM cell output as a function of time.

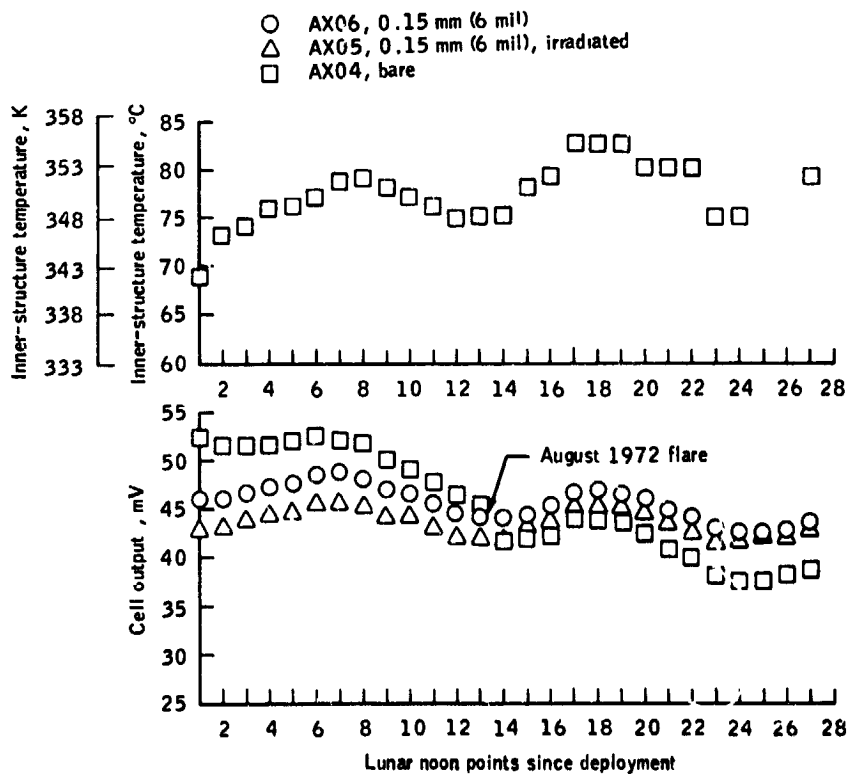


Figure 25-6.- Apollo 15 DTREM cell output and temperature as a function of time.

ALSEP LUNAR DUST DETECTOR												
DAYS	HR	MIN	SECS	SUN ELEVATION ANGLE DEC	AX01 DEC. C	AX03 DEC. C	AX04 UN- CORRECTED MV	AX05 UN- CORRECTED MV	AX06 UN- CORRECTED MV	AX04 CORRECTED MV	AX05 CORRECTED MV	AX06 CORRECTED MV
30	8	11	8.239	66.03	69.63	52.95	54.70	52.83	53.91	55.02	56.02	64.54
30	8	12	2.575	66.04	68.13	52.95	54.70	52.83	53.91	55.05	56.17	64.59
30	8	12	56.912	66.05	69.63	54.42	54.70	52.83	53.91	55.02	56.02	64.54
30	8	13	51.288	66.06	69.63	52.95	54.70	52.83	53.91	55.05	56.17	64.59
30	8	14	45.585	66.07	68.13	52.95	54.70	52.83	53.91	55.05	56.17	64.59
30	8	15	39.920	66.07	68.13	54.42	54.70	52.83	53.91	55.02	56.02	64.54
30	8	16	34.257	66.08	69.63	54.42	54.70	52.83	53.91	55.05	56.17	64.59
30	8	17	28.594	66.09	69.63	54.42	54.70	52.83	53.91	55.02	56.02	64.54
30	8	18	22.930	66.10	68.13	52.95	54.70	52.83	53.91	55.05	56.17	64.59
30	8	19	17.267	66.10	68.13	52.95	54.70	52.83	53.91	55.05	56.17	64.59
30	8	20	11.603	66.11	68.13	52.95	54.70	52.83	53.91	55.05	56.17	64.59
30	8	21	5.939	66.12	68.13	54.42	54.70	52.83	53.91	55.05	56.17	64.59
30	8	22	-2.76	66.13	68.13	54.42	54.70	52.83	53.91	55.05	56.17	64.59
30	8	23	48.989	66.14	68.13	52.95	54.70	52.83	53.91	55.05	56.17	64.59
30	8	24	43.285	66.15	69.63	52.95	54.70	52.83	53.91	55.05	56.17	64.59
30	8	25	37.621	66.16	68.13	52.95	54.70	52.83	53.91	55.05	56.17	64.59
30	8	26	31.958	66.16	68.13	52.95	54.70	52.83	53.91	55.05	56.17	64.59
30	8	27	26.294	66.17	68.13	52.95	54.70	52.83	53.91	55.05	56.17	64.59
30	8	28	20.630	66.18	68.13	52.95	54.70	52.83	53.91	55.05	56.17	64.59
30	8	29	14.967	66.19	68.13	52.95	54.70	52.83	53.91	55.05	56.17	64.59
30	8	30	9.303	66.19	68.13	52.95	54.70	52.83	53.91	55.05	56.17	64.59
30	8	31	3.640	66.20	68.13	52.95	54.70	52.83	53.91	55.05	56.17	64.59
30	8	32	57.976	66.21	68.13	51.49	51.44	50.27	50.64	51.77	53.45	51.29
30	8	33	52.313	66.22	68.13	51.49	50.79	49.63	50.64	51.11	52.77	51.29
30	8	34	46.649	66.22	68.13	51.49	49.49	48.99	49.35	50.46	52.09	49.27
30	8	35	40.985	66.23	68.13	50.03	49.49	48.99	48.06	49.81	52.09	48.67
30	8	36	35.322	66.24	66.64	50.03	48.85	47.72	48.06	49.18	50.87	48.71
30	8	37	29.658	66.25	66.64	48.56	47.56	47.72	46.78	47.88	50.87	47.41
30	8	38	23.995	66.25	66.64	48.56	46.91	46.44	46.14	47.23	49.51	47.41
30	8	39	18.330	66.26	66.64	48.56	46.27	46.44	46.14	46.58	49.51	46.76
30	8	40	12.667	66.27	66.64	47.10	45.63	45.16	44.87	45.94	48.15	45.47
30	8	41	7.004	66.28	65.15	47.10	44.98	44.52	43.80	45.31	47.59	44.23
30	8	42	1.340	66.29	65.15	45.64	44.34	43.88	42.97	44.67	46.91	43.59
30	8	43	55.677	66.29	65.15	45.64	43.07	42.61	42.97	43.38	45.54	43.59
30	8	44	50.013	66.30	63.66	44.19	42.43	41.97	41.72	42.76	44.98	42.35
30	8	45	44.349	66.31	63.66	44.19	41.16	40.69	41.09	41.48	43.30	41.72
30	8	46	38.686	66.31	63.66	42.73	40.53	40.69	39.23	40.84	43.61	39.83
30	8	47	33.022	66.32	63.66	41.27	39.26	39.41	39.23	39.57	42.24	39.83
30	8	48	27.359	66.33	62.17	41.27	38.64	38.77	37.99	38.95	41.67	38.61
30	8	49	21.695	66.34	60.68	39.82	37.38	38.14	37.38	37.70	41.09	38.02
30	8	50	16.031	66.34	60.68	38.36	36.13	36.86	36.16	36.44	39.71	36.78
30	8	51	10.368	66.35	59.20	36.91	34.88	36.22	34.35	36.46	39.13	34.96
30	8	52	4.704	66.36	59.20	35.49	34.88	34.94	34.35	35.20	37.75	34.26
30	8	53	59.049	66.37	57.71	35.46	34.28	34.30	33.15	34.59	37.16	33.77
30	8	54	53.377	66.37	57.71	34.01	33.03	33.03	31.95	33.34	35.77	32.56
30	8	55	47.713	66.38	56.23	32.56	31.79	32.39	31.36	32.11	35.17	31.98
30	8	56	42.050	66.39	56.23	31.12	31.18	31.75	30.77	31.49	34.48	31.38
30	8	57	36.386	66.40	54.75	29.67	29.96	30.47	29.01	30.27	33.18	29.61
30	8	58	30.723	66.40	53.27	28.67	28.74	29.83	28.43	29.05	32.57	29.04

Figure 25-7.- Eclipse data for January 30, 1972. The underscored values indicate the change in data magnitude as a result of the eclipse.

ALSEP LUNAR DUST DETECTOR												
DAYS	HR	MIN	SECS	SUN ELEVATION ANGLE DEG	AK01 DEG. C	AK03 DEG. C	AK04 UN- CORRECTED MV	AK05 UN- CORRECTED MV	AK06 UN- CORRECTED MV	AK09 CORRECTED MV	AK05 CORRECTED MV	AK06 CORRECTED MV
30	8	57	19.395	66.42	51.79	26.78	26.92	27.28	26.71	27.23	29.86	27.30
30	8	58	13.732	66.43	50.31	25.34	26.32	26.64	25.57	26.64	29.23	26.16
30	8	59	8.068	66.43	48.83	23.90	25.12	26.00	24.43	25.83	28.60	25.03
30	9	0	2.405	66.44	48.83	22.46	23.93	24.72	23.87	24.23	27.20	24.45
30	9	0	56.741	66.45	47.36	21.58	23.34	24.08	22.20	23.64	26.56	22.76
30	9	1	51.077	66.46	45.88	18.15	22.15	22.81	21.65	22.85	25.21	22.22
30	9	2	45.414	66.46	44.41	15.29	20.56	22.17	21.10	21.87	24.57	21.08
30	9	3	39.750	66.47	42.94	15.29	20.39	20.89	20.02	20.69	23.21	20.58
30	9	4	34.087	66.48	42.94	13.84	19.23	20.25	18.94	19.50	22.50	19.47
30	9	5	28.423	66.49	41.47	12.41	18.07	18.98	17.87	18.34	21.13	18.39
30	9	6	22.759	66.49	40.00	10.98	17.49	18.34	17.34	17.76	20.47	17.86
30	9	7	17.096	66.50	38.54	9.55	16.91	17.06	16.29	17.19	19.09	16.79
30	9	8	11.432	66.51	37.07	8.13	15.77	16.42	15.77	16.03	18.42	16.27
30	9	9	5.769	66.52	35.61	5.27	15.20	15.78	14.74	15.46	17.75	15.22
30	9	10	0.105	66.52	34.14	3.85	14.07	14.50	14.22	14.32	16.35	14.71
30	9	10	54.441	66.53	32.68	2.43	12.94	13.87	13.21	13.18	15.67	13.67
30	9	11	48.778	66.54	31.22	-0.41	12.88	13.23	12.21	12.61	14.98	12.64
30	9	12	43.114	66.55	29.76	-1.83	11.82	11.95	11.22	12.05	13.57	11.63
30	9	13	37.450	66.55	28.31	-3.25	10.71	11.31	10.73	10.93	12.87	11.13
30	9	14	31.787	66.56	26.85	-4.67	10.16	10.67	9.75	10.37	12.17	10.13
30	9	15	26.123	66.57	25.39	-6.10	9.61	10.03	9.27	9.81	11.47	9.64
30	9	16	20.460	66.58	23.94	-7.50	8.52	8.76	7.85	8.70	10.03	8.16
30	9	17	14.796	66.58	22.48	-8.91	7.98	8.12	7.85	8.15	9.35	8.16
30	9	18	9.132	66.59	19.59	-13.14	7.43	7.48	7.38	7.60	8.62	7.70
30	9	19	3.469	66.60	18.14	-14.55	6.89	6.84	6.91	7.05	7.89	7.21
30	9	19	57.805	66.61	16.70	-15.96	5.82	6.20	6.45	5.95	7.15	6.73
30	9	20	52.142	66.61	15.25	-18.77	5.82	5.56	5.54	5.95	6.41	5.78
30	9	21	46.478	66.62	13.81	-20.17	4.76	4.92	5.09	4.87	5.68	5.31
30	9	22	40.814	66.63	12.36	-22.97	4.23	4.28	4.19	4.32	4.94	4.37
30	9	23	35.150	66.64	9.43	-24.37	3.70	3.65	4.19	3.79	4.20	4.37
30	9	24	29.487	66.64	8.05	-25.77	3.01	3.01	3.75	3.25	3.47	3.91
30	9	25	23.824	66.65	6.61	-27.17	3.18	2.37	3.32	3.25	2.73	3.46
30	9	26	18.160	66.66	5.17	-29.96	2.66	1.73	2.88	2.72	2.00	3.01
30	9	27	12.496	66.67	3.74	-31.35	2.14	1.73	2.45	2.00	2.00	2.56
30	9	28	6.833	66.67	2.30	-34.14	1.62	-77777.00	2.02	1.65	-77777.00	2.11
30	9	29	1.169	66.68	-0.56	-35.53	1.10	-77777.00	1.60	1.13	-77777.00	1.67
30	9	29	55.505	66.69	-1.98	-38.30	1.10	-77777.00	1.60	1.13	-77777.00	1.67
30	9	30	49.842	66.70	-4.84	-39.69	0.59	-77777.00	1.60	1.13	-77777.00	1.67
30	9	31	44.178	66.70	-6.26	-41.07	0.59	-77777.00	1.60	1.13	-77777.00	1.67
30	9	32	38.514	66.71	-7.69	-43.84	-77777.00	-77777.00	-77777.00	-77777.00	-77777.00	-77777.00
30	9	33	32.850	66.72	-9.11	-45.22	-77777.00	-77777.00	-77777.00	-77777.00	-77777.00	-77777.00
30	9	34	27.186	66.73	-11.54	-46.60	-77777.00	-77777.00	-77777.00	-77777.00	-77777.00	-77777.00
30	9	35	21.522	66.74	-13.97	-47.98	-77777.00	-77777.00	-77777.00	-77777.00	-77777.00	-77777.00
30	9	36	15.858	66.75	-16.40	-49.36	-77777.00	-77777.00	-77777.00	-77777.00	-77777.00	-77777.00
30	9	37	10.194	66.76	-18.83	-50.74	-77777.00	-77777.00	-77777.00	-77777.00	-77777.00	-77777.00
30	9	38	4.530	66.77	-21.26	-52.12	-77777.00	-77777.00	-77777.00	-77777.00	-77777.00	-77777.00
30	9	39	0.866	66.78	-23.69	-53.50	-77777.00	-77777.00	-77777.00	-77777.00	-77777.00	-77777.00
30	9	40	0.202	66.79	-26.12	-54.88	-77777.00	-77777.00	-77777.00	-77777.00	-77777.00	-77777.00
30	9	41	0.538	66.80	-28.55	-56.26	-77777.00	-77777.00	-77777.00	-77777.00	-77777.00	-77777.00
30	9	42	0.874	66.81	-30.98	-57.64	-77777.00	-77777.00	-77777.00	-77777.00	-77777.00	-77777.00
30	9	43	0.210	66.82	-33.41	-59.02	-77777.00	-77777.00	-77777.00	-77777.00	-77777.00	-77777.00
30	9	44	0.546	66.83	-35.84	-60.40	-77777.00	-77777.00	-77777.00	-77777.00	-77777.00	-77777.00
30	9	45	0.882	66.84	-38.27	-61.78	-77777.00	-77777.00	-77777.00	-77777.00	-77777.00	-77777.00
30	9	46	0.218	66.85	-40.70	-63.16	-77777.00	-77777.00	-77777.00	-77777.00	-77777.00	-77777.00

Figure 25-7.- Concluded.

## PART B: LUNAR ORBITAL EXPERIMENTS

Most of the lunar orbital experiments were added to the Apollo Program during missions 15, 16, and 17. The objectives of these experiments were to determine and understand regional variations in the chemical composition of the lunar surface, to study the gravitational field of the Moon, to determine the induced and permanent magnetic fields of the Moon, and to obtain a detailed study of the morphology and albedo of the lunar surface. These experiments and the respective missions during which they were performed are listed in the following table. Groundtracks of the lunar missions are shown in appendix B.

Number	Experiment	Apollo mission				
		12	14	15	16	17
S-160	Gamma-Ray Spectrometer			X	X	
S-161	X-Ray Fluorescence			X	X	
S-162	Alpha-Particle Spectrometer			X	X	
S-164	S-Band Transponder (subsattellite)			X	X	
S-164	S-Band Transponder (CSM/LM)	X	X	X	X	X
S-165	Mass Spectrometer			X	X	
S-169	Far UV Spectrometer					X
S-170	Bistatic Radar		X	X	X	
S-171	Infrared Scanning Radiometer					X
S-173	Particle Shadow/Boundary Layer (subsattellite)			X	X	
S-174	Magnetometer (subsattellite)			X	X	
S-175	Laser Altimeter			X	X	X
S-209	Lunar Sounder					X

26. GAMMA-RAY SPECTROMETER (EXPERIMENT S-160)

NSSDC IDENTIFICATION NUMBERS:

APOLLO 15 71-063A-08  
APOLLO 16 72-031A-07



ORIGINAL PAGE IS  
OF POOR QUALITY

CONTENTS - SECTION 26

	Page
BASIC THEORY . . . . .	26-3
INSTRUMENT DESCRIPTION . . . . .	26-4
OPERATIONAL HISTORY . . . . .	26-6
RESULTS . . . . .	26-8
CONCLUSIONS . . . . .	26-12
GAMMA-RAY ASTRONOMY . . . . .	26-12
APOLLO GRS MERGED-TAPE FORMAT . . . . .	26-13
Mixed-Type Data . . . . .	26-14
Record 1 . . . . .	26-15
Record 2 . . . . .	26-15
Record 3 . . . . .	26-15
Record 4 . . . . .	26-15
REFERENCES . . . . .	26-17

## 26. GAMMA-RAY SPECTROMETER

The Apollo gamma-ray spectrometer (GRS) experiment was one of a group of three orbital geochemistry experiments. All three experiments had in common the broad objective of geochemical mapping of the lunar surface. One task of the orbital geochemical experiments was to verify for mapping purposes the regions of the Moon in which each distinct material is the dominant constituent. A knowledge of the distribution of these materials is essential to an understanding of the nature and the origin of the materials. The transearth coast period of the missions provided an opportunity for a detailed study of the astronomical sources of gamma radiation by using the spacecraft to occult possible source regions.

### BASIC THEORY

Gamma rays are absorbed or scattered by passing through lunar soil or rock tens of centimeters thick; therefore, the gamma-ray experiment could sample the composition of the Moon to that depth. This layer of soil and rock is generally well within the regolith and can be assumed to be well mixed.

The chemical information in a gamma-ray spectrum is carried by discrete lines having energies that are characteristic of individual elements. Two broad classes of such lines exist. The first class, which traditionally is called natural radioactivity, results from the decay of potassium-40 and the radioactive daughters of thorium and uranium. The second class is composed of the lines that result from the bombardment of the lunar surface by high-energy-charged particles, the cosmic rays. These particles interact with the lunar surface to produce secondary particles and excited nuclei.

The galactic cosmic rays are responsible for nearly all the emitted gamma rays of this type. A typical galactic-cosmic-ray (GCR) particle is a proton having a kinetic energy comparable to the rest mass, approximately  $1 \times 10^9$  eV. The GCR particle interacts near the lunar surface to produce a cascade of lower energy particles, of which the most important are neutrons. These neutrons in turn give rise to excited nuclei that are capable of emitting line

radiation in three ways. First, the neutrons may scatter inelastically and leave the target nucleus in an excited state. This process is important for neutron energies of a few million electron volts. Each major element produces such lines. An example is the 0.84-MeV line of iron. The second major process is neutron capture. Neutrons lose energy by successive collisions until they either escape from the surface or are captured. The binding energy of the added neutron, typically approximately 8 MeV, is emitted from the product nucleus in a complex decay scheme, which sometimes contains a few dominant lines. The line emitted by iron at 7.64 MeV is an important case. Finally, gamma rays are emitted by radioactive nuclides produced by nuclear reactions, such as aluminum-26 from aluminum and silicon. These reactions are generally less important but not negligible.

During major solar flares, the Sun emits high-energy particles, the solar cosmic rays. The important energy region for these particles is in the range of 10 to 100 MeV. The particles lose energy mainly by ionization, but sometimes nuclear reactions occur. Except during the occurrence of a solar flare, the rapid processes of capture and scattering discussed previously cannot be observed. Radioactivity induced by solar cosmic rays is a small component in the Apollo data.

The expected intensities of the spectral lines as functions of chemical composition can be calculated from a knowledge of the physical processes involved. In the case of the natural radioactivities, this calculation is simple and unambiguous. For the lines induced by high-energy bombardment, the required particle fluxes and cross sections are known only approximately. The availability of "ground truth" for areas such as Mare Fecunditatis and the Descartes landing site, overflowed by the Apollo 16 command and service module, is of great value.

The GRS is omnidirectional and, therefore, has some response to all areas within the field of view. However, counts come mainly from the areas relatively near the detector; these areas subtend the largest solid angle. Resolution on a scale of approximately  $2^\circ$  to  $3^\circ$  on the Moon, or approximately 70 km, has been inferred from theory and verified in the Apollo data.

#### INSTRUMENT DESCRIPTION

Within the GRS cylindrical thermal shield were the detection, amplification, encoding, and data-processing

systems that identified and characterized the incident gamma rays as functions of time and energy. The sensing element of the detector was a 6.99- by 6.99-cm cylindrical scintillation crystal of sodium iodide (NaI) that was thallium (Tl) activated. The energy lost by gamma rays in traversing the crystals was converted, by means of ionization processes, into light that was sensed and transformed into a proportionate charge output by a 7.62-cm-diameter photomultiplier tube (PMT), which was optically coupled to the NaI(Tl) crystal. After amplification and shaping, the output signal passed to an analog-to-digital converter (ADC), which was controlled by a crystal-clock pulse generator that transformed the detector signal into an accurately measured pulse train. This pulse train was counted in an accumulator and resulted in a number proportional to the charge output of the detector for that particular event. The data were sent on an event by event basis either to the spacecraft telemetry system for direct transmission or to a tape recorder for intermediate storage when the spacecraft was behind the Moon.

The NaI(Tl) scintillator responded to charged particles as well as to gamma rays. To eliminate charged-particle events, a plastic-scintillator shield surrounded the NaI(Tl) crystal. The plastic scintillator detected all charged particles above a minimum energy but had a low probability of interacting with gamma rays. Events in the plastic scintillator produced a signal in a second 3.81-cm PMT that was transmitted to a gate ahead of the ADC to inhibit (veto) the acceptance of a coincident pulse from the NaI(Tl) PMT.

In addition to the accumulators that processed the primary-data pulse train, separate accumulators were provided for counting the number of events in the plastic-scintillator shield, the number of events coincident in both the NaI(Tl) and plastic scintillators, and a live-time pulse train. The live-time pulse train provided the factor to derive the rate at which gamma rays were entering the NaI(Tl) crystal from the number that were analyzed. The command capability of the GRS allowed enabling and disabling of the veto function, varying of the high-voltage bias on the 7.62-cm-diameter PMT in steps amounting to a total range in gain of a factor of approximately 3, and activating and deactivating of power.

Besides the passive thermal control provided by a striped-paint pattern on the thermal shield, a thermal-control circuit supplied power to a heating blanket around the central detector when a control sensor indicated that the temperature in the immediate vicinity of the central detector had dropped to less than 288 K. The purpose of this capability was to minimize thermally induced variations

in gain that, if rapid and continuous, would have degraded the energy resolution of the instrument.

In normal operation, the GRS was deployed on a 7.6-m-long boom that extended normal to the surface of the scientific instrument module (SIM) bay. The purpose of the boom was to decrease the response of the GRS to cosmic-ray interactions and radioactive sources in the spacecraft. The importance of these effects can be seen from the observation that the count rates observed when the boom was retracted during transearth coast were close to those in lunar orbit with the boom extended; that is, the GRS response to the spacecraft was approximately the same as that to the Moon. In the extended position, the GRS response to the spacecraft was reduced to a few percent of the total count rate.

#### OPERATIONAL HISTORY

When the Apollo 15 gamma-ray spectrometer was first turned on shortly before injection into lunar orbit, its gain was within 2 percent of the final prelaunch checkout value. The gain immediately began to decline at a rate of 1 percent/hr. This rate slowly decreased until the GRS was essentially stable by the end of the lunar orbiting phase of the mission. The overall drop in gain amounted to 40 percent. The gain-step command capability was used successfully to offset this trend. In the task of data reduction, the recognizable features in the spectrum, including the prominent 0.51-MeV peak, along with a calibration source of mercury-203 at 0.279 MeV can be used to normalize any part of the data. The hypothesis that the effect was the result of aging on the part of the 7.62-cm-diameter PMT in the high-energy cosmic-ray-flux environment of space was confirmed by ground testing.

Based on experience from the Apollo 15 mission, the Apollo 16 GRS was subjected to several days of high-current conditioning before flight to minimize the drop in gain during the mission. The observed gain decrease during the mission was 20 percent beginning at a rate of 0.2 percent/hr for the first 20 hr, declining to less than half this rate for the following 100 hr, then rising to approximately 0.15 percent/hr for the last half of transearth coast, possibly resulting from temperature excursions accompanying the gamma-ray sky-survey sequences.

The presence of a radioisotope thermoelectric generator (RTG) on the lunar module (LM), although interfering almost totally with lunar observations before undocking, provided several prominent high-energy features that indicated

nominal energy resolution and zero offset (the intercept of channel number and energy). Immediately after the first extension of the gamma-ray boom for the Apollo 15 transearth coast, the zero offset shifted. The shift disappeared when the instrument was repowered after extravehicular activity (EVA). Subsequent operation was normal for approximately 30 hr; then, the offset shift reappeared and remained until mission completion. The shift was due to the loss of a timing signal in the ADC; this loss resulted in an eight-channel offset in the spectrum as well as in the recording of the first eight channels of information in channel 1. The latter effect was also noted in the data when the zero-offset shift was present. The flight data have been corrected for this shift without difficulty. The Apollo 16 mission was free of this problem.

The pilot B scintillator shield rate and the pilot B/NaI scintillator coincidence count rate above noise in the instrument-deployed position are essentially the values expected for the cosmic-ray flux. The effectiveness of the charged-particle veto system is shown by a comparison of the veto-enabled spectrum with the veto-disabled spectrum. The proportion of incident events rejected increases with increasing energy. The threshold of the veto system is near 0.6 MeV. All scaler functions operated properly during the Apollo 15 mission. The Apollo 16 GRS developed a noisy shield during preflight testing, but the defect was waived because of the exceptionally good energy resolution of the unit. On the Apollo 15 mission, the count rate was much lower. Spectra, coincidence rates and live times were unaffected. A comparison between the ratio of coincidence rates for the Apollo 15 and 16 missions and the ratio of spectral intensities for areas overflowed during both missions shows close agreement. The increase in Apollo 16, which is approximately 4, evidently thus reflects a small change in the cosmic-ray-flux modulation between the two missions.

Temperature measurements agreed well with predictions, during both lunar orbit and transearth coast. The thermal-control system maintained the detector temperature within  $\pm 2$  K ( $\pm 2^\circ$  C) of the nominal value as intended except for periods immediately following boom extension, when slightly lower temperatures occurred at times, and also during prolonged pointing periods in transearth coast. The gamma-ray boom was operated through its many cycles of extension and retraction without mechanical difficulty on the Apollo 15 mission, although the variations in measured times placed the estimated locations of the intermediate portions at  $1.8 \pm 0.2$ ,  $2.4 \pm 0.2$ , and  $4.6 \pm 0.2$  m ( $6 \pm 0.6$ ,  $8 \pm 0.6$ , and  $15 \pm 0.6$  ft). On the Apollo 16 mission, the boom did not retract completely at 168:32 ground elapsed time and before

the EVA, but came within the 0.3-m (1 ft) recognition range of a proximity switch system. Because of a mechanical problem, the thoriated mapping camera lens was not covered during the Apollo 15 transearth-coast period. The effect on the data collected at the 7.6-m (25 ft) boom position has thus far not been significant.

Lunar operational profiles were generally similar for the Apollo 15 and 16 missions. On the Apollo 16 mission, the instrument was put in the lowest gain state for much of the time before LM separation to emphasize data from energies above the RTG-contributed background. Some 15 hr of prime data were lost by the earlier-than-planned departure from lunar orbit, but the regional statistical significance of Apollo 16 data compared favorably to that of Apollo 15 because of the smaller inclination of the Apollo 16 trajectory.

The transearth-coast operations were dissimilar for the two missions. The Apollo 15 mission concentrated on obtaining spectra at the fully extended 7.6-m (25 ft) and intermediate boom positions, for the purpose of separating the cosmic-gamma-ray and spacecraft-induced spectra from each other and from the spectra obtained in lunar orbit. The gain was reduced to a minimum for 6 hr to obtain the diffuse cosmic-gamma-ray flux to as high an energy as possible (27.5 MeV). On the Apollo 16 mission, following a period at 7.6 m (25 ft) in the nominal gain to obtain a background spectrum for lunar analysis, the remaining time was devoted to a sequence of scanning and pointing operations at an extended distance of 2 m (6 ft) to make use of the spacecraft as an occulting body. During this time, the gain was maximized because sensitivity increases with decreasing energy.

The spacecraft spin axis was positioned to sweep out four scan planes for periods noted in parentheses: ecliptic (8 hr), ecliptic complementary (2 hr), supergalactic (8.5 hr), and supergalactic complementary (3 hr). Because the spacecraft spin axis was inadvertently pointed 180° out of the planned direction during the supergalactic scan, the survey was incomplete.

## RESULTS

The Apollo 15 experiment operated successfully in lunar orbit and during transearth coast. The total time during which data were taken in lunar orbit was close to nominal. Because the mapping camera door was open during transearth coast, corrections for the thorium contained in the camera

lens as well as in the structural material of the guidance and navigation system must be made. Two instrument problems were encountered during the mission: a shift in gain that gradually stabilized and a discontinuous zero offset that occurred for a period during transearth coast. The causes of both problems now seem to be understood; and the data analysis will not be affected.

The energy region above the 0.51-MeV positron peak, including the 2.62-MeV thorium line, contains a major contribution from the radioactivity of thorium, uranium, and potassium. A high counting rate of approximately 60 counts/sec occurred in this broad energy band; therefore, good statistical precision can be achieved. Thus, the accumulations over 5 min, or approximately 15° of longitude, can be compared directly.

The highest activity regions are in the western maria, Oceanus Procellarum and Mare Imbrium. Mare Tranquillitatis and Mare Serenitatis have a much lower activity, and the highlands are even lower. The lowest activity seen is in the eastern far-side highlands. The highest levels of radioactivity seen are well below those seen in the Apollo 14 soil samples and are in the general range of the radioactivity observed in the Apollo 12 soil samples. This analysis also has been conducted for the earlier revolutions (39 to 41); data are not as comprehensive but are broadly similar. A sampling of data from other revolutions shows the same tendencies. In other energy bands, and especially for individual lines, data for single passes have less statistical significance.

The measured gamma-ray spectra can be considered to be made up of two components -- a featureless continuum and a discrete spectrum that contains the information from which inferences about surface composition can be made. Positions of significant discrete gamma-ray lines are noted. By determining and removing the continuum component, the discrete line spectrum becomes more obvious. By knowing the characteristic energies and intensities of the various lines in the discrete spectrum, elemental abundances for the lunar surface can be determined.

Preliminary examination of transearth-coast data permits a number of interesting conclusions to be made. Spectra obtained with the boom extended provide the first measurements of the total cosmic-gamma-ray background of energies as high as 27 MeV. This spectrum confirms previous measurements of energies as high as approximately 1 MeV, but falls below the singular ERS-18 (military satellite) data points in the 2- to 6-MeV energy range. The spectrum obtained from the Apollo 15 mission is a steep continuum

having very little structure and some indication of a change in slope for energies greater than 20 MeV. Further analysis is required to determine whether this effect is instrumental, involves the detector response, or represents a real feature of cosmic gamma rays. The most extreme models of cosmic-ray acceleration during early epochs of the expansion of the universe seem to be ruled out by the present results.

The line at 0.51 MeV, which apparently results from positron annihilation, is more clearly visible in the data obtained during transearth coast. Whether the line is of cosmic origin or is associated with materials near the detector may be difficult to determine. Comparison with results obtained from Ranger III suggests the latter. Most components of the spectrum measured in interplanetary space are factors of 3 to 7 below the components measured for the Moon and for the spacecraft with the boom retracted. Therefore, spacecraft production is not a dominant background effect for the lunar measurements. Based on the rather small intensity change with the boom extensions at 2.4, 4.6, and 7.6 m, the tentative conclusion can be made that spacecraft production makes about a 10-percent contribution to the transearth-coast flux at 7.6 m.

The Apollo 16 experiment was an advance over that performed on the Apollo 15 mission in the following manner.

1. The energy resolution of the spectrometer was improved from approximately 8.5 to 7.5 percent. This improvement resulted in a clearer resolution of lines and a greater precision of analysis.
2. The data made available during the mission included preliminary data-stream tapes. These tapes enabled the making of a more rapid and thorough analysis of the data during the mission.
3. The mission plan included a substantial increase in the amount of prime data obtained in lunar orbit. The decision to return 1 day early reduced the amount of data, but the gain was still significant.
4. The results of the Apollo 15 experiment in the transearth-coast phase indicated that the correction of the lunar data for sky background was largely understood and also gave indications of further possibilities in gamma-ray astronomy. The Apollo 16 spacecraft was maneuvered in an extended series of special rotations and was pointed to exploit these possibilities.

5. The Apollo 15 experiment encountered two instrument problems: a drift in gain stabilizing throughout the mission and discontinuous zero offset that occurred during a large part of the transearth-coast phase. On the Apollo 16 mission, as predicted, the gain drift was much smaller and the zero offset did not occur. A noisy auxiliary channel seen before and during the mission caused no serious problems, and overall performance was excellent.

The improved resolution of the instrument shows plainly in the spectrum after continuum subtraction. (See ref. 26-1 for comparison.)

The first analysis for the Apollo 16 mission emphasized the energy region from 0.55 to 2.75 MeV, which contains the main radioactive lines of thorium, uranium, and potassium. In this energy band, the regional differences in count rate result from varying intensities in the lines of the radioactive elements thorium, uranium, and potassium. For this reason, fortunately the statistical precision of the total count rate in the region (fixed in practice at 0.55 to 2.75 MeV) is excellent and the best possible areal resolution can be obtained. At a nominal altitude of 100 km above the lunar surface, the theoretical distance resolution of the system is approximately 70 km, or 2.5°.

The flux of particle radiation as observed during veto-disable periods was 5 percent greater on the Apollo 16 mission than on the Apollo 15 mission. When the gamma-ray results are normalized to the Apollo 15 results using this factor (the procedure used here), the results in the trajectory crossover regions are in good agreement. The data from both missions have been corrected to an altitude of 100 km; the solid angle subtended by the Moon at the detector is a reasonably accurate normalization over the narrow range of altitudes at which data were taken. The data were also corrected for instrument live time; no other corrections have been applied.

The range of the corrected counting rates is from 73 to 93 counts/sec, or approximately 25 percent. The most striking observation of the mission was the high count rates in the western mare regions; the highest count rate was observed south of the crater Fra Mauro. This region is at the southern end of the Fra Mauro formation; the Apollo 14 landing site was near the northern edge of this north-south trending feature.

The data are represented more thoroughly by a map of the count rate summed in 5° by 5° areas of the overflown surface (ref. 26-2). Such a map has previously been prepared from the Apollo 15 prime data. The standard

deviation for a typical counting time of 300 sec/5° square is approximately 0.5 count/sec based on counting statistics alone; it is approximately 1 count/sec for the shortest counting times used. The reproducibility of successive passes, and in regions overflown on both missions, is good.

### CONCLUSIONS

1. The Apollo 16 results extend and confirm the Apollo 15 finding that all 5° regions within the boundaries of the western maria are higher in radioactivity than any 5° region outside this area. These results strongly suggest that the western mare regions not scanned are also highly radioactive and that other regions of the Moon are generally less so.

2. Detailed structure exists within the high-radioactivity region. The high observed in the Fra Mauro area is at about the same level as those seen around Aristarchus and south of Archimedes during the Apollo 15 mission. These levels are comparable to that observed in the soil at the Apollo 14 landing site.

3. The eastern maria show evidence of lower (and variable) radioactivity. Structure is visible in Mare Fecunditatis (more apparent on a 2° scale) and elsewhere.

4. The highland regions are characterized by low radioactivity, except near the western maria where some lateral mixing has occurred. The maximum seen near Van de Graaff during the Apollo 15 mission has no counterpart on this track. A visible low near longitude 120° E may reflect slightly higher values in the large basins on either side.

### GAMMA-RAY ASTRONOMY

The transearth-coast period of the Apollo 16 mission presented an opportunity to continue measurements of the cosmic-gamma-ray spectrum started on the Apollo 15 mission. This period on the Apollo 15 mission was devoted primarily to operating the instrument and the spacecraft in a mode designed to provide measurements of the total spectrum in space and various background effects that may confuse this spectrum. Based on the results, it was concluded that some knowledge of the directionality or anisotropy of the cosmic-gamma-ray fluxes was obtainable and would provide badly needed astrophysical information. Positioning the detector boom at approximately 2 m during transearth coast causes occulting of an appreciable region of the sky by the

spacecraft. As the spacecraft rotates at approximately 3 revolutions/hr for thermal control, various regions of the sky become occulted. Changing the spacecraft spin axis causes various planes to become occulted. Preflight analysis indicated that a "map" of the sky could be obtained in 1-MeV gamma rays containing 40 resolution elements at approximately the 2-percent-difference level.

The uncorrected counting-rate spectrum obtained during the Apollo 15 and 16 missions is compared with previous results on the energy-loss spectrum measured in cislunar space on the Ranger III and ERS-18 satellites (refs. 26-3 and 26-4). The near agreement of Apollo 15 and 16 data, which also agree with other data to within approximately 2 MeV, gives considerable confidence in the new results. At energies higher than 2 MeV, these results are less than a previous measurement. The Apollo data still contain a small contribution caused by gamma-ray lines from spacecraft natural and induced radioactivity and caused by continuum processes as a result of high-energy cosmic rays. Furthermore, an appreciable but uncertain contribution is caused by cosmic-ray-produced spallation (ref. 26-5) in the scintillation crystal. The total cosmic-gamma-ray flux higher than approximately 2 MeV is considerably less than that implied by the ERS-18 satellite; therefore, some cosmological models that had been proposed to explain the high flux in the 2- to 6-MeV have been rejected (ref. 26-6).

The spin-axis positions and scan planes and the resultant occulted regions permit occultation of possible strong, compact, gamma-ray sources such as the Crab Nebula, Sagittarius, and perhaps others that may be in the galactic plane. In addition, scan planes were selected that would provide information on anisotropies associated with the local cluster of galaxies and with the supercluster, which contains the Virgo cluster. It may also be possible to detect global anisotropies associated with the initial formation of the universe, to which these gamma rays are thought to be couples, at least on a "big bang" model of the universe.

#### APOLLO GRS MERGED-TAPE FORMAT

The Apollo GRS merged tapes contain four record types. Each record type is separated from other types by an interrecord gap. The tapes have the following characteristics: 800 bpi, 36-bit words, unblocked records, and mixed-type data within a record.

<u>Record</u>	<u>Words</u>	<u>Time_word</u>	<u>Data_type</u>
1	32	1	Floating point
2	13	1	Mixed
3	13	1	Mixed
4	513	1	Integer
5	32	1	Floating point
6	13	1	Mixed
7	13	1	Mixed
.			
.			
.			
N	32	None	Integer (Ø111111111111) (Integer (Ø222222222222) last reel)

Records 1 to 4 and 5 to 8 of the following table form groups of related data. The records within a selected group (four records each) are as follows.

<u>Record</u>	<u>Data Description</u>
1	NASA Apollo trajectory (NAT) data
2	Apollo gamma-ray spectrometer (AGRS) and Apollo X-ray spectrometer (AXRS) common parameter
3	Service module housekeeping data
4	Apollo gamma-ray spectrometer data

#### Mixed-Type Data

The entire contents of record 2 are single-precision, 36-bit integers except for word 2 (SIM-bay temperature) and words 3 and 13 (28-Vdc power), which are floating point, single-precision words. Six of the 13 words in record 3 are floating point words. These are words 2, 3, and 4 (temperature data) and words 8, 9, and 10 (shield,

coincidence events data, and live time, respectively). The remaining seven words are 36-bit integers. The last record on each reel contains 32 words of 011111111111 followed by two end-of-file marks.

#### Record 1

The NAT data are located in record 1. Table 26-I includes the parameters contained in each word at the two mission phases. The column "Data type" defines the type of data item as it is written on tape (e.g., floating point (F) or integer (I)). A linear interpolation is performed on the NAT data to find values (record 1) at each AGRS tape time. Time words (word 1 of each record) in each record type (1 to 4) are identical in magnitude (not in type).

#### Record 2

The AGRS/AXRS common data appear in record 2. Parameters stored are described in Table 26-II. The "Data type" column of table 26-II shows that the data are mixed-type data. A linear interpolation is performed on the SIM-bay temperature and the 28-Vdc power to find values at each AGRS tape time. These two parameters appear as degrees Fahrenheit and volts direct current, respectively. The remainder of the words in record 2 are integer flags denoting mission events.

#### Record 3

The service module housekeeping data are found in record 3 (table 26-III). These data, like record 2 data, are mixed type. Six of the 13 words are floating point values. The temperatures, words 2, 3, and 4, are derived by the same method employed with the SIM-bay temperature in record 2. The remaining three floating point words are the shield, live-time, and coincidence-events register averaged over 10 pulse code modulation (PCM) frames. Shield- and coincidence-events values are expressed in counts per second. The live-time word is an average (percent) over 10 PCM frames. The remaining seven integer words are time, event flags, and high-voltage (HV) gain.

#### Record 4

The AGRS data are contained in record 4 (table 26-IV). Word 1 is the time word, which has a 1:1 correspondence with the AGRS binary tape time (AGRS binary tape time is

milliseconds, whereas AGRS merged binary tape time is truncated to seconds). The remaining 512 integer words are the total accumulated counts (over 10 PCM frames, 3.2768 sec) in each of the 512 (0 to 511) channels.

#### REFERENCES

- 26-1. Arnold, J. R.; Peterson, L. E.; Metzger, A. F.; and Trombka, J. I.: Gamma Ray Spectrometer Experiment. Sec. 16 of Apollo 15 Preliminary Science Report. NASA SP-289, 1972.
- 26-2. Metzger, A. E.; Trombka, J. I.; Peterson, L. E.; Reedy, R. C.; and Arnold, J. R.: Lunar Surface Radioactivity: Preliminary Results of the Apollo 15 and Apollo 16 Gamma-Ray Spectrometer Experiments. *Science*, vol. 179, no. 4075, Feb. 23, 1973, pp. 800-803.
- 26-3. Metzger, A. E.; Anderson, E. C.; Van Dilla, M. A.; and Arnold, J. R.: Detection of an Interstellar Flux of Gamma Rays. *Nature*, vol. 204, no. 4960, 1964, pp. 766-767.
- 26-4. Vette, J. I.; Gruber, D.; Matteson, J. L.; and Peterson, L. E.: A New Component of Cosmic Gamma Rays Near 1 MeV Observed by the ERS-18 Satellite. NASA TM X-63912, 1970.
- 26-5. Fishman, G. J.: Cosmic-Ray Effects on Diffuse Gamma-Ray Measurements. *Astrophys. J.*, vol. 171, Jan. 1972, pp. 163-167.
- 26-6. Stecker, F. W.: Primordial Cosmic-Ray Sources. *Nature*, vol. 224, no. 5222, 1969, p. 870.

TABLE 26-I.- APOLLO 16 TRAJECTORY PARAMETERS

Word	Lunar orbit	Changes in transearth coast	Changes in requested attitude data	Data type
1	G.m.t., sec	G.m.t., sec	--	F
2	Ho, n. mi.	Ro, n. mi. (geocentric)	--	F
3	$\phi_s$ , deg	$X_i$ , ft	(a)	F
4	$\lambda_s$ , deg	$Y_i$ , ft	(a)	F
5	$R_s$ , ft	$Z_i$ , ft	(a)	F
6	Vis, fps	CDUX, deg	(a)	F
7	$\beta$ , deg	CDUY, deg	--	F
8	$\theta$ , deg	CDUZ, deg	--	F
9	Revolution no.	Interpolation time for angle data	--	F
10	$\lambda_{as}$ , ft	$\delta v$ , deg (geocentric)	(a)	F
11	$\lambda_{ps}$ , ft	$\alpha_s$ , deg	(a)	F
12	$h_{as}$ , n. mi.	$\beta_s$ , deg	(a)	F
13	$h_{ps}$ , n. mi.	$\alpha_E$ , deg	(a)	F
14	$X_{is}$ , ft	$\beta_E$ , deg	(a)	F
15	$Y_{is}$ , ft	$\alpha_m$ , deg	(a)	F
16	$Z_{is}$ , ft	$\beta_m$ , deg	(a)	F

<sup>a</sup>Parameter to be obtained from either the lunar orbit or the translunar/transearth column as applicable.

TABLE 26-I.- APOLLO 16 TRAJECTORY PARAMETERS - Concluded

Word	Lunar orbit	Changes in transearth coast	Changes in requested attitude data	Data type	
17	$\dot{X}_{is}$ , fps	Roll	(a)	F	
18	$\dot{Y}_{is}$ , fps		(b)	F	
19	$\dot{Z}_{is}$ , fps		(b)	F	
20	$\ddot{X}_{is}$ , ft/sec <sup>2</sup>	Pitch	(b)	F	
21	$\ddot{Y}_{is}$ , ft/sec <sup>2</sup>		9 elements of the 3 unit vectors (MCDUxRa)	(b)	F
22	$\ddot{Z}_{is}$ , ft/sec <sup>2</sup>			(b)	F
23	$\ddot{X}_p$ , ft/sec <sup>2</sup>	Yaw		(b)	F
24	$\ddot{Y}_p$ , ft/sec <sup>2</sup>		(b)	F	
25	$\ddot{Z}_p$ , ft/sec <sup>2</sup>		(b)	F	
26	$\dot{X}_p$ , fps	RA, deg	(b)	F	
27	$\dot{Y}_p$ , fps	$\delta$ , deg	(b)	F	
28	$\dot{Z}_p$ , fps	RA, deg	(b)	F	
29	H s, ft	$\delta$ , deg	(b)	F	
30	$\dot{H}$ s, fps	RA, deg	(b)	F	
31	$\alpha_m$ , deg	$\delta$ , deg	(b)	F	
32	$\beta_m$ , deg	Time period between trajectory records, sec			

<sup>a</sup>Parameter to be obtained from either the lunar orbit or the translunar/transearth column as applicable.

<sup>b</sup>These items are calculated and are not available from trajectory tape.

TABLE 26-II.- AGRS/AXRS COLUMN DATA

Word output	Data type	Description
1	I	G.M.t. of ground receipt, sec (year to date)
2	F	SIN-bay temperature, °F
3	F	28-V power A, Vdc
4	I	Power on-off flag (1 = on, 0 = off)
5	I	Playback/real-time (RT) flag (1 = real time, 0 = playback)
6	I	LM docking and separation (1 = docked, 0 = separated)
7	I	Waste dump (1 = yes, 0 = no)
8	I	Reaction control system firing (1 = yes, 0 = no)
9	I	Service propulsion system firing (1 = yes, 0 = no)
10	I	Loss of telemetry (1 = yes, 0 = no)
11	I	Loss of frame synchronization (1 = yes, 0 = no)
12	I	Word parity error count (Apollo 16 RT; 0 = valid, 1 = invalid)
13	F	28-V power B, Vdc

TABLE 26-III.- APOLLO 16 HOUSEKEEPING DATA

Word output	Data type	Content of word
1	I	G.m.t. of ground receipt, sec (year to date)
2	F	Electronics temperature, °F
3	F	Detector temperature, °F
4	F	Boom temperature, °F
5	I	Boom-position flag (3-bit flag)  Retracted = 0 Partly extended 1 = 1 1.2 m (4 ft) Partly extended 2 = 2 2.4 m (8 ft) Partly extended 3 = 3 4.6 m (15 ft) Fully extended = 4 7.6 m (25 ft) Boom transition 5 = 5 -- Partly extended 6 = 6 0.6 m (2 ft) Partly extended 7 = 7 1.8 m (6 ft) Partly extended 8 = 8 2.7 m (9 ft)
6	I	Veto (0 = disabled, 1 = normal)
7	I	Mapping camera lens covered (1 = yes, 0 = no)
8	F	Shield-events counter (averaged over 10 PCM frames), count/sec
9	F	Coincident-events counter (averaged over 10 PCM frames), count/sec
10	F	Live-time counter (averaged over 10 PCM frames), percent of 3.2768 sec
11	I	Gain (high voltage), Vdc
12	I	Shield-events overflow, number of overflows/record
13	I	Coincident-events overflow, number of overflows/record

ORIGINAL PAGE IS  
OF POOR QUALITY

TABLE 26-IV.- GAMMA-RAY SPECTRUM (3.2768-SEC INTERVAL)

Word output	Data type	Content of word
1	I	G.m.t. of ground receipt, sec (year to date)
2	I	Channel 0, events in 10 PCM frames
3	I	Channel 1, events in 10 PCM frames
4	I	Channel 2, events in 10 PCM frames
.	.	.
.	.	.
.	.	.
513	I	Channel 511, events in 10 PCM frames

27. X-RAY FLUORESCENCE SPECTROMETER (NASA EXPERIMENT S-161)

NSSDC IDENTIFICATION NUMBERS:

APOLLO 15 71-063A-09  
APOLLO 16 72-031A-C8



ORIGINAL PAGE IS  
OF POOR QUALITY

CONTENTS - SECTION 27

	Page
INSTRUMENT DESCRIPTION . . . . .	27-3
EXPERIMENT OPERATION . . . . .	27-4
DATA SETS AND FORMATS . . . . .	27-5
SUMMARY OF KEY RESULTS . . . . .	27-5
BIBLIOGRAPHY . . . . .	27-7

## 27. X-RAY FLUORESCENCE SPECTROMETER

An X-ray fluorescence spectrometer carried in the scientific instrument module (SIM) bay of the command and service module (CSM) was used for orbital mapping of the lunar-surface composition and for X-ray galactic observations during transearth coast. The lunar-surface measurements involved observations of the intensity and characteristic energy distribution of the secondary or fluorescent X-rays produced by the interaction of solar X-rays with the lunar surface. The astronomical observations consisted of relatively long periods of X-ray measurements of preselected galactic sources such as Cygnus (Cyg X-1) and Scorpius (Sco X-1). The basis for the X-ray fluorescence experiment is that characteristic secondary X-rays are produced on the lunar surface by interactions with the primary X-ray flux from the Sun. A typical quiet solar X-ray spectrum is energetically capable of producing measurable amounts of characteristic X-rays from all abundant elements with atomic numbers of approximately 14 (silicon) or less. During brief periods of more intense solar activity, observation of radiation from elements of higher atomic number should also be possible.

### INSTRUMENT DESCRIPTION

The X-ray fluorescence spectrometer was part of a total assembly containing the alpha-particle experiment. The spectrometer consisted of three main subsystems:

1. Three large-area proportional counters that have state-of-the-art energy resolution and 0.0025-cm-thick beryllium windows
2. A set of large-area filters for energy discrimination among the characteristic X-rays of aluminum, silicon, and magnesium
3. A data-handling system for count accumulation, for sorting into eight pulse-height channels, and for relaying the data to the spacecraft telemetry

The X-ray detector assembly consists of three proportional-counter detectors, two X-ray filters, mechanical collimators, an in-flight calibration device,

temperature monitors, and associated electronics. The detector assembly senses X-rays emitted from the lunar surface and converts the X-rays to voltage pulses that are processed in the X-ray processor assembly. Provisions for in-flight calibration are made by means of programmed calibration sources, which, upon internal command, assume a position in front of the three detectors for calibration of gain, resolution, and efficiency. Thermistors located at strategic points sense the temperature of the detector assembly for telemetry monitoring and temperature control of the detectors by means of heaters located near the proportional-counter windows.

The behavior of the X-ray output of the Sun was simultaneously monitored with the lunar surface measurements by means of the solar monitor, a small proportional detector mounted on the opposite side of the spacecraft from the surface detectors. On the Apollo 16 spacecraft, a thin beryllium foil filter was added in front of the detector window to enable the spectrometer to view high-Sun X-ray fluxes without experiencing the detector gainshifts that were observed during the Apollo 15 flight.

#### EXPERIMENT OPERATION

The X-ray experiment began to function on April 20, 1972, at approximately 02:00 G.m.t. and was operated for approximately 12 hr in an elliptical orbit (approximately 18 by 111 km (10 by 60 n. mi.)). At approximately 04:00 G.m.t. on April 21, the experiment was again activated; the spacecraft was in a circular lunar orbit of approximately 111 km (60 n. mi.). The estimated field of view for each data point used in this report is approximately 111 by 148 km (60 by 80 n. mi.).

The overlap of orbital coverage between the Apollo 15 and 16 groundtracks (mainly from 50° to 100° E) makes it possible to compare the reproducibility of the measurements for both missions. The total coverage for the two missions is greater than 20 percent of the surface of the Moon. It is encouraging that, for these areas, the aluminum/silicon and magnesium/silicon chemical ratios for both flights agreed to better than 10 percent. This agreement makes it possible to draw comparisons between the two flights. It also demonstrates that the X-ray spectral distribution of the Sun, which produces lunar fluorescent X-rays, was about the same on both missions. In fact, this conclusion has

been confirmed by examination of the SOLRAD data<sup>1</sup> available for those periods. Another point of considerable interest is that the spectrometer obtained a large number of data points over the Descartes landing site. Hopefully, the results will show how representative the data are of the Descartes area.

#### DATA SETS AND FORMATS

The data set consists of two IBM industry-compatible 9-track magnetic tapes. These tapes were obtained by merging 47 X-ray data tapes with 5 trajectory tapes. Tape 1 contains 83 hr of recovered lunar data between 85 hr 10 min ground elapsed time (GET) and 220 hr 17 min GET. Tape 2 contains 6 hr of X-ray astronomy data recorded during the transearth coast period from 224 hr 46 min to 236 hr 20 min GET.

For both tapes, a total of 46 500 X-ray data sets were recovered consisting of three X-ray detectors and one solar monitor of eight channels each, status flags, and housekeeping parameters merged with trajectory data. Of this data, approximately 12 percent of the spectra are not usable because the spectrometer was turned off or because telemetry synchronization was lost, resulting in partial rather than full data sets. Both tapes are recorded at 1800 bpi, variable block size with record lengths of 900 and block size 20 C04. The tapes are not standard label tapes.

The format consists of 39 trajectory values followed by the number of X-ray data sets in this time period. Then, the X-ray data sets of 220 values are recorded until all data sets have been read and the next 39 trajectory values will again appear.

#### SUMMARY OF KEY RESULTS

The X-ray experiment performed nominally and provided a great deal of data as described in the preceding sections. The following is a summary of the key results.

1. Maps showing the variation of aluminum/silicon and magnesium/silicon ratios along the projected groundtracks

---

<sup>1</sup>The SOLRAD data are obtained by satellite monitoring solar radiation and are reported by the National Oceanic and Atmospheric Administration, Rockville, Maryland.

were made, thus permitting a direct comparison between mare areas and highlands and verifying that the highlands are indeed feldspathic.

2. The aluminum/silicon values for the various areas correspond closely to published results for analyzed lunar rocks and soils for selected areas.

3. Because of greater background corrections, the magnesium/silicon values are less reliable than the aluminum/silicon values, but generally there is an inverse relationship.

4. Except for anomalous values around Copernican-type craters, there is an excellent correspondence between optical albedo values and aluminum/silicon values. They vary in the same direction.

5. Good contrast is evident in observed aluminum/silicon values between dark mare areas and the surrounding highlands, which establishes some limits on the transport of highland materials into the mare basins as a fill.

## BIBLIOGRAPHY

- Adler, I.; Gerard, J.; Trombka, J.; Schmadebeck, R.; et al.:  
The Apollo 15 X-Ray Fluorescence Experiment. Proceedings  
of the Third Lunar Science Conference, vol. 3, David R.  
Criswell, ed., MIT Press (Cambridge, Mass.), 1972.
- Adler, I.; Trombka, J.; Gerard, J.; Lowman, P.; et al.:  
Apollo 15 Geochemical X-Ray Fluorescence Experiment:  
Preliminary Report. Science, vol. 175, no. 4020, Jan. 28,  
1972, pp. 436-440.
- Adler, I.; Trombka, J.; Gerard, J.; Schmadebeck, R.; et al.:  
X-Ray Fluorescence Experiment. Sec. 17 of Apollo 15  
Preliminary Science Report. NASA SP-289, 1972.
- Apollo 15 Preliminary Examination Team: The Apollo 15 Lunar  
Samples: A Preliminary Description. Science, vol. 175,  
no. 4020, Jan. 28, 1972, pp. 363-375.
- Bolton, C. T.: Identification of Cygnus X-1 with HDE  
226868. Nature, vol. 235, no. 5336, Feb. 4, 1972, pp.  
271-273.
- Gault, D. E.; Adams, J. B.; Collins, R. J.; Kuiper, G. F.;  
et al.: Lunar Theory and Processes. Sec. 9 of Surveyor  
VII, A Preliminary Report. NASA SP-173, 1968.
- Head, James W., III; and Goetz, Alexander F. H.: Descartes  
Region: Evidence for Copernican-Age Volcanism. J.  
Geophys. Res., vol. 77, no. 8, Mar. 10, 1972, pp. 1368-  
1374.
- Levinson, A. A., ed.: Proceedings of the Apollo 11 Lunar  
Science Conference. Pergamon Press (New York), 1970.
- Levinson, A. A., ed.: Proceedings of the Second Lunar  
Science Conference. MIT Press (Cambridge, Mass.), 1971.
- Lunar Sample Preliminary Examination Team: Preliminary  
Examination of Lunar Samples From Apollo 14. Science,  
vol. 173, no. 3998, Aug. 20, 1971, pp. 681-693.
- Marvin, U. B.; Wood, J. A.; Taylor, G. J.; Reid, J. B.;  
et al.: Relative Proportions and Probable Sources of Rock  
Fragments in the Apollo 12 Soil Samples. Proceedings of  
the Second Lunar Science Conference, vol. 1, A. A.  
Levinson, ed., MIT Press (Cambridge, Mass.), 1971, pp.  
679-700.

- Mason, Brian; and Melson, William G.: The Lunar Rocks. John Wiley & Sons, Inc., 1970, p. 11.
- McKay, D. S.; Morrison, D. A.; Clanton, U. S.; Ladle G. E.; and Lindsay, J. F.: Apollo 12 Soil and Breccia. Proceedings of the Second Lunar Science Conference, vol. 1, A. A. Levinson, ed., MIT Press (Cambridge, Mass.), 1971, pp. 755-774.
- Meyer, C.; Brett, R.; Hubbard, N. J.; Morrison, D. A.; et al.: Mineralogy, Chemistry, and Origin of the KREEP Component in Soil Samples From the Ocean of Storms. Proceedings of the Second Lunar Science Conference, vol. 1, A. A. Levinson, ed., MIT Press (Cambridge, Mass.), 1971, pp. 393-412.
- Milton, Daniel J.; and Hodges, Carroll Ann: Geologic Map of the Descartes Region of the Moon. Geol. Atlas of the Moon, Apollo 16 Pre-Mission Map, Sheet 1. U.S. Geol. Survey Misc. Geol. Inv. Map I-748, 1972.
- Oda, M.; Gorenstein, P.; Gursky, H.; Kellogg, E.; et al.: X-Ray Pulsations From Cygnus X-1 Observed From OHURU. Astrophys. J. (Letters), vol. 166, no. 1, pt. 2, May 15, 1971, pp. 11-17.
- Pohn, H. A.; and Wildey, R. L.: A Photoelectric-Photographic Study of the Normal Albedo of the Moon, Accompanied by an Albedo Map of the Moon by H. A. Pohn, R. L. Wildey, and G. E. Sutton (Contributions to Astrogeology). U.S. Geological Survey Professional Paper 599-F, 1970.
- Schreier, E.; Levinson, R.; Gursky, H.; Kellogg, E.; et al.: Evidence for the Binary Nature of Centaurus X-3 From OHURU X-Ray Observations. Astrophys. J. (Letters), vol. 172, no. 3, pt. 2, Mar. 15, 1972, pp. 179-189.
- Turkevich, Anthony L.; Franzgrote, Ernest J.; and Patterson, James H.: Chemical Analysis of the Moon at the Surveyor V Landing Site: Preliminary Results. Science, vol. 158, no. 3801, Nov. 3, 1967, pp. 635-637.
- Turkevich, Anthony L.; Patterson, James H.; and Franzgrote, Ernest J.: Chemical Analysis of the Moon at the Surveyor VI Landing Site: Preliminary Results. Science, vol. 160, no. 3832, Jan. 7, 1968, pp. 1108-1110.
- Turkevich, Anthony L.; Franzgrote, Ernest J.; and Patterson, James H.: Chemical Analysis of the Moon at the Surveyor VII Landing Site: Preliminary Results. Science, vol. 162, no. 3849, Oct. 4, 1968, pp. 117-118.

Vinogradov, A. P.: Preliminary Data on Lunar Ground Brought to Earth by Automatic Probe Luna-16. Proceedings of the Second Lunar Science Conference, A. A. Levinson, ed., MIT Press (Cambridge, Mass.), 1971, pp. 1-16.

Webster, B. Louise; and Murdin, Paul: Cygnus X-1 - A Spectroscopic Binary With a Heavy Companion? Nature, vol. 235, no. 5332, Jan. 7, 1972, pp. 37-38.

Whitaker, P. A.: The Surface of the Moon. Sec. 3 of The Nature of the Lunar Surface; Proceedings of the 1965 IAU-NASA Symposium, Wilnot N. Hess, Donald H. Menzel, and John A. O'Keefe, eds., Johns Hopkins Press (Baltimore), 1966, pp. 79-98.

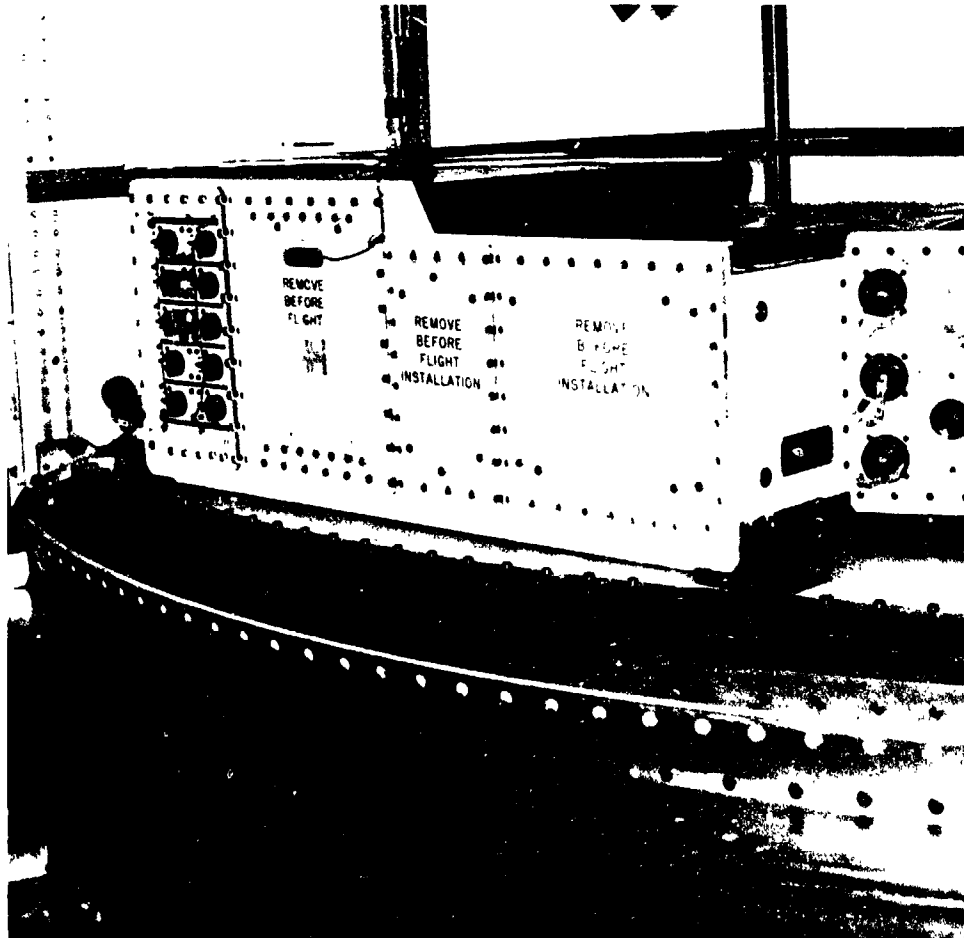
Wood, J. A.; Marvin, U. B.; Powell, E. N.; and Dickey, J. S., Jr.: Mineralogy and Petrology of Apollo 11 Samples. Smithsonian Astrophysical Observatory Special Rept. 307, Jan. 1970. (Also available as NASA CR-107932, Jan. 1970.)

28. ALPHA-PARTICLE SPECTROMETER AND X-RAY FLUORESCENCE  
SPECTROMETER (TRANSEARTH)

(NASA EXPERIMENT S-162)

NSSDC IDENTIFICATION NUMBERS:

APOLLO 15 71-063A-10  
APOLLO 16 72-031A-09



CONTENTS - SECTION 28

	Page
PART A: ALPHA-PARTICLE SPECTROMETER . . . . .	28-3
EQUIPMENT DESCRIPTION . . . . .	28-4
INSTRUMENT PERFORMANCE . . . . .	28-5
OPERATIONAL HISTORY . . . . .	28-5
DATA REDUCTION . . . . .	28-8
TEMPERATURE CORRECTIONS . . . . .	28-8
PROCESSED TELEMETRY FILE . . . . .	28-9
DATA ARCHIVED AT NSSDC . . . . .	28-11
REFERENCE . . . . .	28-13
BIBLIOGRAPHY . . . . .	28-13
PART B: X-RAY FLUORESCENCE SPECTROMETER (TRANSEARTH) . . . . .	28-17
INSTRUMENT DESCRIPTION . . . . .	28-18
TRANSEARTH COAST OBSERVING PROGRAM . . . . .	28-19
RESULTS . . . . .	28-21
CONCLUSIONS . . . . .	28-22
REFERENCES . . . . .	28-24

## 28. ALPHA-PARTICLE SPECTROMETER AND X-RAY FLUORESCENCE SPECTROMETER (TRANSEARTH)

### PART A: ALPHA-PARTICLE SPECTROMETER

The scientific objectives of the alpha-particle spectrometer experiment were to measure the rate of emanation of radioactive radon gas from the Moon and to locate and identify lunar regions with unusual activity. Any lunar region that is characterized by a locally higher rate of radon emanation is probably active internally. Orbital investigations from the Apollo 15 and 16 command and service module have shown that areas on the Moon with detectable rates of radon emanation do exist and that certain lunar regions are characterized by transient or nonequilibrium radon emanation. Identification of radon isotopes and their daughter products is based on the detection of their characteristic alpha particles in an array of detectors with good energy resolution.

Natural concentrations of uranium and thorium are the source of radon gas. A qualitative description of the processes that lead from natural uranium and thorium concentrations to the existence of a thin radon atmosphere above the lunar surface is given in reference 28-1. Two decaying radon isotopes are of interest: radon-222 ( $^{222}\text{Rn}$ ) with a 3.7-day half life (an intermediate product of the uranium series) and  $^{220}\text{Rn}$  with a 56-sec half life (a member of the thorium series). Decay of these isotopes results in the production of monoenergetic alpha particles that escape from the Moon. Their heavy decay products are deposited directly upon the uppermost layer of the lunar surface and are themselves unstable against radioactive decay.

A third decaying species is very significant, lead-210 ( $^{210}\text{Pb}$ ), a descendant of  $^{222}\text{Rn}$  with a half life of 21 yr. The lifetime of  $^{210}\text{Pb}$  is long, compared to all other intermediate members of the series. The  $^{210}\text{Pb}$  atom, which does not produce alpha particles, is detected indirectly through its alpha-emitting granddaughter, polonium-210 ( $^{210}\text{Po}$ ). The significance of  $^{210}\text{Po}$  is that the existence of a transient or non-steady-state radon emanation within a 21-yr period will cause its activity to be higher than predicted from observations of  $^{222}\text{Rn}$ . Thus, at locations

where the  $^{210}\text{Po}/^{222}\text{Rn}$  ratio departs from radioactive equilibrium, there is evidence for transient emanation.

The alpha-particle spectrometer, mounted in the Apollo scientific instrument module (SIM), detects individual alpha particles and measures their energy. The presence of radon and its daughter products appears as a distinct set of peaks in an energy spectrum. The background is caused primarily by cosmic-ray effects. Spatial resolution is achieved by restricting the field of view of the spectrometer to  $45^\circ$  by  $45^\circ$  (full width at half maximum).

#### EQUIPMENT DESCRIPTION

The sensing elements of the lunar alpha-particle spectrometer were 10 totally depleted silicon surface-barrier detectors, each approximately  $100\ \mu\text{m}$  thick, having  $3\ \text{cm}^2$  of active area and a  $90^\circ$  field of view, and operating at a  $-50\ \text{V}$  bias. Additional gold, aluminum, and nickel layers were used at the contacts to ensure that exposure to visible light would not degrade the experiment performance. The thickness of the detectors was chosen so that any background protons (deuterons or tritons) would produce an output signal whose amplitude would be below that of the lowest energy alpha particle of interest. The response of the detectors to alpha particles up to  $12\ \text{MeV}$  would be linearly proportional to energy. This design precluded the necessity for discriminating against other particles in any other way.

The 10 detector preamplifier outputs were merged in a single summing amplifier and processed by a single analog to digital converter (ADC). Although the use of one ADC minimized the complexity of the hardware, summing the noise from all 10 preamplifiers resulted in degrading the resolution by a factor of approximately 3. To circumvent the degradation problem, each preamplifier had a bias offset corresponding to  $350\ \text{keV}$ . The bias offset effectively removed the noise, except from the pre-amplifiers giving a signal pulse, and allowed the use of a single ADC without significant degradation in resolution.

The ADC converted the energy pulse into a 9-bit digital signal. If the most significant bit was a 1, the ADC was disabled and the digital signal was held until the next telemetry readout (every  $100\ \text{msec}$ ). If the most significant bit was a 0, the ADC was reset, and the next pulse was processed. This design enabled the instrument to digitize to a 9-bit accuracy and transmit only 8 bits. Therefore, only the upper half of the digitized energy range was telemetered. This process was reasonable physically because

the alpha-particle energies of interest ranged from 5.3 to 8.8 MeV; also, the usage of telemetry time by any low-energy background particles was prevented. The actual telemetered energy range of the instrument was 4.7 to 9.1 MeV. Parallel circuitry generated an analog signal of 0.25 to 4.75 V in steps of 0.5 V; this signal identified the detector that originated any given pulse.

Because the digital telemetry was limited to 80 bits/sec (10 counts/sec), an additional circuit was used to generate an analog signal proportional to the time from the end of one telemetry read cycle to the sensing of the first pulse having energy greater than 4.7 MeV. The analog signal allowed the dead-time correction of the data for count rates exceeding approximately 20 counts/sec. Exclusive of housekeeping, the output consisted of an 8-bit energy word, an analog voltage identifying the detector, and an analog voltage exponentially proportional to the count rate.

#### INSTRUMENT PERFORMANCE

The Apollo 15 alpha-particle spectrometer was turned on at 15:47 G.m.t. July 29, 1971, and remained on until 12:43 G.m.t. August 7, 1971, except for short periods during major burns and fluid dumps. The spectrometer functioned normally except for short noise bursts in two detectors resulting in an approximately 10-percent reduction in sensitivity in approximately 20 percent of the data. Because the loss of sensitivity was minimal and confined to a small amount of data, the overall capability of the experiment was only slightly affected.

The Apollo 16 spectrometer was activated at approximately 02:00 G.m.t. April 20, 1972, and remained on during the remainder of the mission except for periods during major burns or fluid dumps and periods during which the mission significantly deviated from the nominal time line. The spectrometer functioned normally throughout the mission.

#### OPERATIONAL HISTORY

A brief summary of the operational history of the Apollo 15 and 16 alpha-particle spectrometers follows.

Apollo 15

<u>Ground elapsed time, hr:min</u>	<u>Remarks</u>
74:00	SIM door jettisoned.
74:05	Alpha switch positioned to ON; alpha door closed.
77:28	Alpha, OFF.
79:02	Alpha, ON; door closed.
82:18	Alpha, OFF.
84:08	Alpha, ON; door open; SIM attitude (SA).
94:47	Maneuver out of SA.
95:12	Alpha, ON; door closed.
101:25	Alpha, OFF.
101:50	Alpha, ON; door closed.
106:51	Alpha, ON; door open.
109:09	Alpha, ON; close door.
111:40	Alpha, ON; open door.
121:40	Alpha, ON; door open; maneuver to camera pass.
122:35	Alpha, ON; door open; maneuver to deep space.
123:00	Alpha, ON; close door.
125:50	Alpha, ON; open door.
130:45	Alpha, ON; close door.
133:08	Alpha, ON; open door.
143:11	Alpha, ON; open door; maneuver to camera pass.
144:30	Alpha, ON; open door; maneuver to SA.
145:06	Alpha, ON; open door; maneuver to camera pass.
146:17	Alpha, ON; open door; maneuver to deep space.
146:52	Alpha, ON; close door.
147:26	Alpha, ON; open door; in SA.
164:01	Alpha, OFF; close door (plane change).
165:20	Alpha, ON; door closed.
166:24	Alpha, ON; door open; SA.
168:11	Alpha, ON; door closed.
171:20	Alpha, OFF.
174:25	Alpha, ON; door open; SA; post- lunar module (LM) rendezvous.
176:00	Door closed; LM jettison.
182:20	Alpha, ON; door closed.
193:20	Alpha, ON; door closed.
193:51	Alpha, OFF.
194:51	Alpha, ON; door closed.
194:54	Alpha, ON; door open.

Ground elapsed  
time, hr:min

Remarks

195:40	Maneuver to deep space; alpha, ON; door open.
201:30	Maneuver to SA.
215:23	Maneuver to deep space.
215:53	Maneuver to camera pass.
217:17	Maneuver to SA.
220:57	Alpha, OFF; door closed.
221:46	Alpha, ON; door closed.
223:07	Alpha, OFF; end surface data.

Apollo 16

Ground elapsed  
time, hr:min

Remarks

70:00	SIM door jettison; alpha, ON; door closed; out of SA.
73:25	Alpha, OFF; lunar orbit insertion.
75:20	Alpha, ON; door closed.
79:00	Alpha, OFF.
80:00	Alpha, ON; door open.
92:10	Alpha, ON; door closed.
94:23	System off.
106:08	Alpha, ON; door open.
119:10	Alpha, ON; door closed.
120:10	Alpha, ON; door open.
121:10	Alpha, ON; door open; out of SA.
122:10	Resume SA.
130:30	Alpha, ON; door closed.
131:30	Alpha, ON; door open.
142:00	Maneuver out of SA (Gegenschein).
144:30	Maneuver to deep space; alpha, ON; door open.
146:30	Resume SA; alpha, ON; door open.
150:20	Alpha, ON; door closed.
151:10	Alpha, ON; door open; out of SA.
168:10	Alpha, ON; door closed.
170:10	Alpha, ON; maneuver to deep space.
176:00	Alpha, OFF.
178:00	Alpha, ON; door open; out of SA.
179:00	Alpha, ON; door open; in SA.
192:00	Alpha, ON; door closed.
193:00	Alpha, OFF.
193:40	Alpha, ON; door closed.
200:33	Transearth injection; end sur- face data.

## DATA REDUCTION

The telemetered data were sent directly from the NASA Lyndon B. Johnson Space Center (JSC) to American Science and Engineering, Inc., for processing. Three types of tapes were used: (1) digital alpha-particle spectrometer data, (2) trajectory data (derived from tracking information by JSC), and (3) standard SIM support tapes.

The SIM support tapes were required for engineering purposes in case of abnormal performance of the instruments. The ephemeris tapes are normally used in routine processing. Selected ephemeris data words were chosen from the tapes and rewritten on a time-merged working tape. Each spectrometer data tape had to be individually read, bad telemetry data removed, time backups and overlaps corrected, data skew detected and corrected, and housekeeping data verified and flagged if cut of specification. After preprocessing, the data tapes were time merged to produce two time-continuous tapes with only good, corrected data. The data then were scanned to detect systematic drifts due to temperature variations. A set of empirical temperature corrections of the gain were generated. The data could then be searched for the alpha decay products of radon. The following computer programs were generated during this phase.

1. A preprocessing program for verifying validity of data and making any required formatting corrections
2. A summary program for reading data tapes and summarizing the data and the experiment configuration in 5-min intervals
3. A summary program for the ephemeris tapes and printing hard copies
4. A general-purpose tape-merging routine for creating a single time-sequential tape from several tapes
5. An overlay program for combining data from specified time and/or longitude intervals
6. An overlay program for combining data in  $10^\circ$  by  $10^\circ$  bins

## TEMPERATURE CORRECTIONS

To overlay data from different detectors and temperatures, it is necessary to compensate for gain and

bias differences. An alpha particle of energy  $E$  stopping in the  $i$ th detector produces a count in channel number  $N$  according to the formula

$$N = [E - B(i,T)]/[G(i,T) - 256] \quad (28-1)$$

where the gain of the  $i$ th detector at temperature  $T$  is fitted to the quadratic form

$$G(i,T) = G_0(i) + G_1(i)T + G_2(i)T^2 \quad (28-2)$$

and the bias is

$$B(i,T) = B_0(i) + B_1(i)T + B_2(i)T^2 \quad (28-3)$$

The coefficients  $G_0$ ,  $G_1$ , ..., were calculated from data obtained in laboratory tests using americium-241 ( $E = 5.486$  MeV) and curium-242 ( $E = 6.115$  MeV) test sources. The values obtained are given in tables 28-I and 28-II. The temperature, measured in degrees centigrade, was monitored by averaging the readings of two sensors attached to the cases of detectors 5 and 6. A temperature measurement at the low-voltage power supply (LVPS) is also available.

#### PROCESSED TELEMETRY FILE

The processed telemetry file is a sequential file with fixed-length records. The record length is 48 words and the block length is 960 words. Each record corresponds to 1 sec of telemetry; that is, to one of the "good" records in the raw telemetry tape. A "good" raw telemetry record is one that has time in reasonable sequence and that has no more than 19 bad data flags set. Any skew that was detected in the raw tape has been corrected. Each record can be represented by a PI/1 structure as follows:

<u>Code</u>	<u>Description</u>
01	RECORD ALINED
02	TIME FIXED BINARY (31,0)
02	TEMPERS (3) FIXED BINARY (15,5)

02	IBADCT
02	ICOUNT (10) BIT (8)
02	ICHANNEL (10) BIT (8)
02	CTRATE (10) BIT (8)
02	HSKP (5) BIT (3)
02	STATUS BIT (8)

where the following definitions apply.

TIME is ground elapsed time in milliseconds, given as a full-word (4 byte) binary integer.

TEMPERS are the three temperatures, in degrees centigrade, given as half-word (2 byte) binary fractions with 5 bits after the binary point. The three temperatures are #1, #2, and LVPS, respectively.

IBADCT is the number of bad data flags set in the original raw telemetry record. All 47 meaningful (nonspare) data flags are counted.

ICOUNT is an array of ten 8-bit bytes, giving data derived from the 10 counter readouts in the raw telemetry record. Each byte is arranged as follows.

1. The first 3 bits indicate whether the 3 data items (counter identification channel, and count rate) were flagged (or if flagged) in the raw telemetry record.
2. The remaining 5 bits contain a binary integer giving counter identification (0 to 10, of which 0 indicates no valid data).

ICHANNEL is an array of ten 8-bit bytes maintained parallel to ICOUNT; (that is, ICOUNT (1) corresponds to ICHANNEL (1) and so forth). Each byte contains an unsigned binary integer giving channel number (0 to 255) for the data readout for which the counter identification was given in the corresponding ICOUNT.

CTRATE is an array of ten 8-bit bytes (not used currently) parallel to ICOUNT and ICHANNEL. Each byte contains the count-rate raw telemetry value from the raw telemetry tape.

HSKP is an array of five 3-bit fields. Each field gives the status of one of the five housekeeping values. Only one of the 3 bits in each field is set depending on the following conditions.

1. Bit 1 is set if bad data flag was on for the housekeeping data readout.
2. Bit 2 is set if housekeeping data are out of expected range.
3. Bit 3 is set if housekeeping data are acceptable.

STATUS is an 8-bit byte that gives the following information about the telemetry frame.

1. Bit 1 is on if an interval of good data is started after a synchronizer failure.
2. Bit 2 is on if the last frame of good data is started before a synchronizer failure. (A synchronizer failure is occurrence of 1 or more raw telemetry frames with 20 or more flagged data words, but a synchronizer failure is also considered to occur at the beginning and end of the raw telemetry tape.)
3. Bit 3 is on if an interval of good data is started after the raw telemetry tape-processing program skipped frames in accordance with a user-inserted SKIPTO command.
4. Bit 4 is on if a good interval of data is started after a time discrepancy.
5. Bits 5 to 7 were not used during the Apollo 15 mission. For the Apollo 16 mission, bit 5 was always on.
6. Bit 8 is always on.

#### DATA ARCHIVED AT NSSDC

The submittal of the alpha-particle spectrometer data to the National Space Science Data Center (NSSDC) is complete. Included in the submittal were the following.

1. Instrument description
2. Processed telemetry data from the Apollo 15 mission

- 
3. Processed telemetry data from the Apollo 16 mission
  4. Format description of data files
  5. Instructions for temperature correction of data
  6. Empirical temperature-correction coefficients for the Apollo 15 instruments
  7. Empirical temperature-correction coefficients for the Apollo 16 instruments
  8. Mission profile of instrument status for the Apollo 15 mission
  9. Mission profile of instrument status for the Apollo 16 mission
  10. Documentation of data records for the Apollo 15 mission
  11. Documentation of data records for the Apollo 16 mission

## REFERENCE

- 28-1. Gorenstein, P.; and Bjorkholm, P.: Alpha-Particle Spectrometer Experiment. Sec. 18 of Apollo 15 Preliminary Science Report, NASA SP-289, 1972.

## BIBLIOGRAPHY

- Bjorkholm, P.; Golub, L.; and Gorenstein, P.: Detection of a Nonuniform Distribution of Polonium-210 on the Moon with the Apollo 16 Alpha Particle Spectrometer. *Science*, vol. 180, no. 4081, Apr. 1973, pp. 957-959.
- Bjorkholm, P.; Golub, L.; and Gorenstein, P.: Distribution of  $^{222}\text{Rn}$  and  $^{210}\text{Po}$  on the Lunar Surface as Observed by the Alpha Particle Spectrometer. *Proceedings of the Fourth Lunar Science Conference*, vol. 3, Pergamon Press (New York), 1973, pp. 2793-2802.
- Gorenstein, P.; and Bjorkholm, P.: Observation of Lunar Radon Emanation with the Apollo 15 Alpha-Particle Spectrometer. *Proceedings of the Third Lunar Science Conference*, vol. 3, D. R. Criswell, ed., MIT Press (Cambridge, Mass.), 1972, pp. 2179-2188.
- Gorenstein, P.; and Bjorkholm, P.: Alpha-Particle Spectrometer Experiment. Sec. 20 of Apollo 16 Preliminary Science Report, NASA SP-315, 1973.
- Gorenstein, P.; and Bjorkholm, P.: Detection of Radon Emission from the Crater Aristarchus by the Apollo 15 Alpha Particle Spectrometer. *Science*, vol. 179, no. 4068, Jan.-Mar. 1973, pp. 792-794.
- Gorenstein, P.; Golub, L.; and Bjorkholm, P.: Radon Emission from the Moon, Spatial and Temporal Variability. *The Moon*, vol. 9, Jan.-Feb. 1974, pp. 129-140.
- Gorenstein, Paul; Golub, Leon; and Bjorkholm, Paul: Detection of Radon Emission at the Edges of Lunar Maria with the Apollo Alpha-Particle Spectrometer. *Science*, vol. 183, no. 4123, Feb. 1, 1974, pp. 411-413.
- Gorenstein, P.; Golub, L.; and Bjorkholm, P.: Radon Emission from the Moon - Spatial and Temporal Variability. Paper presented at COSPAR Plenary Meeting, 16, Konstanz, West Germany, May 23 to June 5, 1973.

Gorenstein, P.; Golub, I.; and Bjorkholm, P.: Spatial Features and Temporal Variability in the Emission of Radon from the Moon: An Interpretation of Results from the Alpha Particle Spectrometer. Proceedings of the Fourth Lunar Science Conference, vol. 3, Pergamon Press (New York), 1973, pp. 2803-2810.

ORIGINAL PAGE IS  
OF POOR QUALITY

TABLE 28-I.- APOLLO 15 TEMPERATURE-CORRECTION COEFFICIENTS

Detector	Temperature-correction coefficient					
	G <sub>0</sub>	G <sub>1</sub>	G <sub>2</sub>	B <sub>0</sub>	B <sub>1</sub>	B <sub>2</sub>
1	0.016511	1.11682 x 10 <sup>-5</sup>	1.27294 x 10 <sup>-6</sup>	0.454456	-2.41821 x 10 <sup>-3</sup>	9.97633 x 10 <sup>-5</sup>
2	1.63657 x 10 <sup>-2</sup>	3.6229 x 10 <sup>-6</sup>	8.69821 x 10 <sup>-7</sup>	.490183	-6.31298 x 10 <sup>-4</sup>	-1.51433 x 10 <sup>-4</sup>
3	1.62476 x 10 <sup>-2</sup>	1.52751 x 10 <sup>-5</sup>	-1.94532 x 10 <sup>-7</sup>	.366534	-3.30811 x 10 <sup>-3</sup>	1.44618 x 10 <sup>-4</sup>
4	.0162368	6.8522 x 10 <sup>-6</sup>	8.04508 x 10 <sup>-7</sup>	.52963	-6.33949 x 10 <sup>-4</sup>	-1.45574 x 10 <sup>-4</sup>
5	1.65264 x 10 <sup>-2</sup>	8.1722 x 10 <sup>-6</sup>	4.30857 x 10 <sup>-7</sup>	.449883	-1.89982 x 10 <sup>-3</sup>	-5.371 x 10 <sup>-5</sup>
6	1.67874 x 10 <sup>-2</sup>	1.65262 x 10 <sup>-5</sup>	-9.95569 x 10 <sup>-6</sup>	.405481	-1.70306 x 10 <sup>-3</sup>	8.27454 x 10 <sup>-5</sup>
7	1.66394 x 10 <sup>-2</sup>	8.92561 x 10 <sup>-6</sup>	5.14425 x 10 <sup>-7</sup>	.422976	-1.63199 x 10 <sup>-3</sup>	-3.81668 x 10 <sup>-5</sup>
8	1.69597 x 10 <sup>-2</sup>	1.1724 x 10 <sup>-5</sup>	1.29059 x 10 <sup>-6</sup>	.344155	-3.29596 x 10 <sup>-3</sup>	8.34875 x 10 <sup>-5</sup>
9	.0161482	6.30958 x 10 <sup>-6</sup>	1.3558 x 10 <sup>-6</sup>	.593791	-9.17572 x 10 <sup>-4</sup>	-2.99962 x 10 <sup>-4</sup>
10	.0161449	5.07239 x 10 <sup>-6</sup>	1.4812 x 10 <sup>-6</sup>	.579663	-1.23281 x 10 <sup>-3</sup>	-3.34881 x 10 <sup>-4</sup>

TABLE 28-II.- APOLO 16 TEMPERATURE-CORRECTION COEFFICIENTS

Detector	Temperature-correction coefficient					
	G <sub>0</sub>	G <sub>1</sub>	G <sub>2</sub>	B <sub>0</sub>	B <sub>1</sub>	B <sub>2</sub>
1	1.67799 x 10 <sup>-2</sup>	-1.42899 x 10 <sup>-3</sup>	0.00000	3.23599 x 10 <sup>-1</sup>	8.89399 x 10 <sup>-3</sup>	0.00000
2	1.63499	-5.79999 x 10 <sup>-4</sup>	1.17399 x 10 <sup>-6</sup>	4.84999 x 10 <sup>-1</sup>	2.13199 x 10 <sup>-3</sup>	-2.71499 x 10 <sup>-4</sup>
3	1.66299	6.61199 x 10 <sup>-6</sup>	3.47299 x 10 <sup>-7</sup>	4.02099 x 10 <sup>-1</sup>	-9.74499 x 10 <sup>-4</sup>	-1.53099 x 10 <sup>-6</sup>
4	1.69599	1.30999 x 10 <sup>-5</sup>	-2.51299 x 10 <sup>-7</sup>	2.97099 x 10 <sup>-1</sup>	-2.27099 x 10 <sup>-3</sup>	1.48999 x 10 <sup>-4</sup>
5	1.68099	9.64799 x 10 <sup>-6</sup>	2.53399 x 10 <sup>-7</sup>	3.47999 x 10 <sup>-1</sup>	-1.53999 x 10 <sup>-3</sup>	-2.94999 x 10 <sup>-6</sup>
6	1.78699	3.17799 x 10 <sup>-5</sup>	-1.63799 x 10 <sup>-6</sup>	2.09999 x 10 <sup>-3</sup>	-8.87499 x 10 <sup>-3</sup>	5.86799 x 10 <sup>-4</sup>
7	1.70899	-1.86499 x 10 <sup>-5</sup>	.00000	3.20999 x 10 <sup>-1</sup>	8.69499 x 10 <sup>-3</sup>	.00000
8	1.66499	5.49499 x 10 <sup>-6</sup>	4.97799 x 10 <sup>-7</sup>	3.89899 x 10 <sup>-1</sup>	-2.26199 x 10 <sup>-3</sup>	-6.74499 x 10 <sup>-5</sup>
9	1.66499	4.61899 x 10 <sup>-6</sup>	3.23799 x 10 <sup>-7</sup>	4.10599 x 10 <sup>-1</sup>	-4.85999 x 10 <sup>-4</sup>	-1.44499 x 10 <sup>-5</sup>
10	1.70099	1.28899 x 10 <sup>-5</sup>	7.73999 x 10 <sup>-8</sup>	2.98599 x 10 <sup>-1</sup>	-3.21599 x 10 <sup>-3</sup>	6.36599 x 10 <sup>-5</sup>

## PART B: X-RAY FLUORESCENCE SPECTROMETER (TRANSEARTH)

During the transearth coast portions of the Apollo 15 and 16 missions, the X-ray fluorescence spectrometer was used to study the temporal behavior of pulsating X-ray sources. About a hundred sources of X-ray emission have been discovered beyond the solar system. The sources include a large variety of unusual objects such as supernova remnants, energetic external galaxies, and quasars and a large number in our galaxy that cannot be associated with any previously known class of objects. Several of these are detectable as emitters of radio waves or can be seen as faint stars, but their emission occurs predominantly at X-ray frequencies. Understanding the nature of these X-ray sources is one of the prime objectives of astrophysics. The first NASA X-ray astronomy satellite, Explorer 42 (UHURU), has recently discovered fast time variability or pulsations in the output from several sources (refs. 28-2 to 28-4). Occurrence of the fast time variability on a time scale of minutes, seconds, or less implies that the emitting regions are very small, much smaller than the Sun, although they are emitting about a thousand times more power. Because it is such an unusual phenomenon, the fast time variability may provide the clue needed to understand the mechanisms that drive these sources.

The objective of the Apollo observations was to record the emission from several objects continuously for a period of approximately 1 hr. The capability for observing time variations was unique because the Apollo spacecraft could be pointed at the source for the entire time. On the other hand, UHURU can observe only for approximately 1 or 2 min per sighting. Consequently, the Apollo instrument had the capability for determining whether periodicities exist in the range  $1 \times 10^1$  to  $1 \times 10^3$  sec.

A secondary objective was to study the cislunar space environment as a site for pointed X-ray astronomy observations. Specifically, the objective was to determine how the soft particle background in the X-ray detectors (from trapped electrons or protons in cislunar space) compared to the near-Earth and lunar environments. Analysis of the data from the standpoint of this secondary objective may be useful in the planning of future observations from other spacecraft.

Counterparts to two powerful X-ray sources observed during Apollo missions, Scorpius (Sco) X-1 and Cygnus (Cyg) X-1, can be seen on the Earth in other regions of the electromagnetic spectrum. Sco X-1 is detectable in both visible light and radio emission; Cyg X-1 is detectable only in radio emission. That the visible light and radio emissions are also variable is known, but not how the light or radio variability correlates with the X-ray variability. Particular models for these X-ray objects make rather specific predictions concerning the relation of X-ray and other variability ranging from no correlation to complete correlation. Consequently, to broaden the scope of the investigation, arrangements were made for ground-based observatories to monitor the visible light and radio emissions simultaneously with the Apollo experiment. Because of difficulties in coordinating the observing schedules, only a small amount of overlap was actually achieved between ground-based optical observations and the Apollo X-ray observations.

#### INSTRUMENT DESCRIPTION

The same instrumentation is used for Apollo X-ray astronomy observations as for X-ray fluorescence studies of the lunar surface chemical composition. There are three gas-filled proportional counters and an entrance window of 0.0025-cm-thick beryllium (Be). The effective Be area is approximately 25 cm<sup>2</sup>. The window is segmented into a number of separate units by a strong framework. Individual X-ray photons are counted for successive 8-sec intervals. The proportional counters are filled to a pressure of 101 325 N/m<sup>2</sup> (1 atm) with a mixture of 90 percent argon, 9.5 percent carbon dioxide, and 0.5 percent helium. To change the wavelength response, filters are mounted across the Be window aperture on two of the proportional counters. The filters (a magnesium foil and an aluminum foil) are  $5.08 \times 10^{-4}$  to  $1.27 \times 10^{-3}$  cm thick. The third counter does not have a filter. A single collimator assembly is used to define the field of view (FOV) of the three proportional counters as a single unit. The collimator consists of multicellular baffles that combine a large sensitive area and high resolution but are restricted in FOV. The FOV determines the total flux recorded from the lunar surface and the spatial resolution. The FOV of the collimator has a full width, half maximum (FWHM) of 30° in two perpendicular directions. The FWHM is the total angular width at which the collimator drops to one-half of its peak response. The net FOV of the entire instrument is actually considerably less than 30° and quite complicated because of the peculiar geometry of the Be window and collimator combination.

The proportional counters provide a degree of energy resolution. A count results in a pulsed signal the amplitude of which is proportional to the photon energy. Typically, the resolution is approximately 30 to 40 percent at 2 keV. Pulse amplitude analysis is used to sort the signals among seven bins of energy between 0.7 and 3 keV; an eighth channel is used for higher energies. The instrument also has an "attenuate mode" in which amplifier gains are cut in half. This mode changes the energy range from 0.7 to 3 keV to 1.4 to 6 keV. The instrument is programmed to be in the attenuate mode for the first 10 min of operation following turnon. It then enters the normal gain mode for 6 hr followed by 2 hr in the attenuate mode. This cycle of 6 hr in the normal mode followed by 2 hr in the attenuate mode is repeated until the instrument is turned off. Calibration sources automatically irradiate the counters every 15 min as a check of instrument operation. The instrument, hard-mounted in the SIM bay of the service module, is used for galactic X-ray astronomy observations during transearth coast. The instrument is pointed at a cosmic X-ray source for a sustained period of continuous counting. The spacecraft is required to hold the pointing position accurately to within approximately  $1^\circ$  for the entire time of observation, which is approximately 1 hr.

#### Time Resolution

The instrument operates by accumulating an eight-channel spectrum every 8 sec in each of the three lunar X-ray detectors (and the solar monitor). Thus, the minimum time resolution of the instrument is 8 sec, and it is essentially insensitive to change on a smaller time scale.

#### Field of View

Corrections for instrument field of view are available from the NSSDC.

#### TRANSEARTH COAST OBSERVING PROGRAM

The Apollo 15 and 16 spacecraft pointed at a number of fixed locations in the sky for intervals of time that varied from 0.5 to 3 hr. The pointing position was not the actual position of the source. In the case of Cyg X-1 and Sco X-1, the position was approximately  $7^\circ$  off to avoid counts from neighboring sources. During the long X-ray pointing observations of Cyg X-1, it was necessary for thermal reasons to roll the spacecraft about the pointing position

after approximately 0.5 hr of observation. The purpose of the closed-door observations was to measure the penetrating component of the background during a time interval near the actual observation period. Because the position of the spacecraft in cislunar space changes considerably, the background may not be constant.

Tables containing the Apollo 15 and Apollo 16 X-ray pointing positions are available from the NSSDC. In addition to the pointing positions, the instrument was on and the covers open during the final passive-thermal-control roll maneuvers of both missions. Instrument performance apparently did not deteriorate during subjection to the very high flux levels of the Sun.

#### Background Measurements

For background measurements, the instrument was pointed at regions of the sky from which no significant contributions from discrete sources were expected. These pointing positions were chosen as a control for the analysis of data from variable sources. Another reason for observing source-free regions was to measure the diffuse X-ray background outside the Earth magnetosphere and to look for gross anisotropies among several regions of galactic latitude. However, there is reason to believe that scattered X-rays from the Sun could have been contributing to the observed number of counts in several of the positions, although the Sun itself was not in the field of view.

#### Coordinated Optical and Radio Observations

In conjunction with the Apollo pointed X-ray observations, an attempt was made to obtain simultaneous optical and radio observations on Sco X-1 and Cyg X-1. The optical and radio data are available at the respective observatories, and the principal investigator also has copies.

#### Instrument Performance

During the Apollo 15 and Apollo 16 transearth coasts, the X-ray fluorescence spectrometer continued to function well, even during periods of prolonged deep-space X-ray-pointing holds in which the instrument became quite cold.

## Data Records

The permanent data records for the X-ray fluorescence spectrometer contain most of the data for the Apollo 15 observations. The Apollo 16 permanent, final data records appear to be incomplete. Two observations appear to be missing entirely from the permanent records, and only a portion of a third is present. Some of these data are contained in the format 16 decomposition into experimental data that took place during the Apollo 16 mission.

## RESULTS

### Cyg X-1

All the results described are from the analysis of data from the unfiltered counter only. No data from the other two detectors have been analyzed.

Two observations of Cyg X-1 were made during the Apollo 16 mission. During the second observation, there were two large increases in count rate. However, neither of these appears to be intrinsic to Cyg X-1. The rise time or pulse shape discriminator (PSD) channel is conditioned primarily by the strength of the particle background. It is also affected by X-rays with energy  $E > 7$  keV. The fact that the PSD channel exhibits a stronger counting rate change than the two energy ranges is probably an indication of a sudden increase in the particle background. The spacecraft encountered two pulses of electrons or protons (or both) of durations of approximately 2 to 5 min in cislunar space. It may be possible that hard X-ray flares have occurred in Cyg X-1, but the particle interpretation is more likely.

In addition to the effect described previously, there is a significant change in the mean intensity of Cyg X-1 between the two Apollo 16 observations. The near equality between the PSD count rates of the two observations (before the particle events) indicates that the particle background is the same. Cyg X-1 is twice as intense in the second observation. The slight excess of PSD events, 3100 as compared to 2900, can be explained as a doubling of the number of events in the energy range above 7 keV.

### Sco X-1

Results from a preliminary analysis of the Apollo 16 data show the temporal behavior of Sco X-1 during the first two observation periods. Significant changes in count rate

originate partly from Sco X-1 and partly from motion of the spacecraft. Although spacecraft steadiness was well within the nominal Apollo capability, spacecraft motion does appear to be reflected in the variation of count rate. However, there are important changes in the count rate of Sco X-1 that cannot be explained by spacecraft motion. Very little overlapping data were obtained because of the rescheduling of observations during the Apollo 16 mission.

In the Apollo 15 observation, there are three sets of data and, therefore, three pairs of correlations to be checked. There is a significant correlation only between two sets of X-ray data. The same is true for the Apollo 16 observation, which includes four sets of data and six pairs of correlations. The optical B vs. V data do not show a significant correlation; however, sky conditions were very poor during the observation because of passing clouds and a full Moon.<sup>1</sup>

During the Apollo 16 observation of April 26, 1972 (Apollo elapsed time 224:23 to 226:48), Sco X-1 exhibited an active phase during the first half of the observation and a passive phase during the second half. The active phase shows amplitude variations of 20 to 30 percent and a quasi-periodic behavior with period of approximately 20 min. The passive phase shows variations smaller than 10 percent and no readily discernible periodicity. No other evidence of periodicity between 20 min and 16 sec was observed during either phase.

#### CONCLUSIONS

The following conclusions can be made from the pointed observations of Sco X-1 and Cyg X-1.

1. Sco X-1 is characterized by quiet periods and by periods in which intensity changes of approximately 10 to 30 percent occur in a few minutes. The active periods can last for at least a day.

2. When Sco X-1 shows changes in X-ray intensity, concurrent but not necessarily simultaneous changes are observed in its optical and radio intensity.

3. There is no evidence for any stable period in Sco X-1 in the time regime of  $1 \times 10^{-1}$  to  $1 \times 10^3$  sec.

---

<sup>1</sup>A. M. Van Genderen, personal communication.

---

4. Cyg X-1 can double in intensity within a day or so, an increase that is larger than the observed changes in Sco X-1. The increase occurs in all three energy ranges: 1 to 3 keV, greater than 3 keV, and greater than 7 keV. The average intensity of Cyg X-1 over a time of several minutes can remain relatively stable for at least 1 hr.

5. The time variability of Sco X-1 and Cyg X-1 does not appear to be similar in the time regime of several seconds to 2 hr. Although Cyg X-1 exhibits subsecond pulsations during active periods, Sco X-1 has greater variability on a time scale of a few minutes than has Cyg X-1 as seen during the Apollo 16 mission.

6. Transient particle effects lasting several minutes exist in cislunar space. The strength of the two events observed during the Apollo 16 mission is approximately 100 particles/cm<sup>2</sup>-sec. These events can lead to background problems in instruments having broad fields of view and can simulate flares in X-ray stars. (An event, not as large as the two mentioned here, was subsequently identified as a cosmic gamma-ray burst because it was coincident in time to one seen from the Vela 6-A satellite. The event occurred during Apollo 16 on April 27, 1972, at 10:58 universal time.)

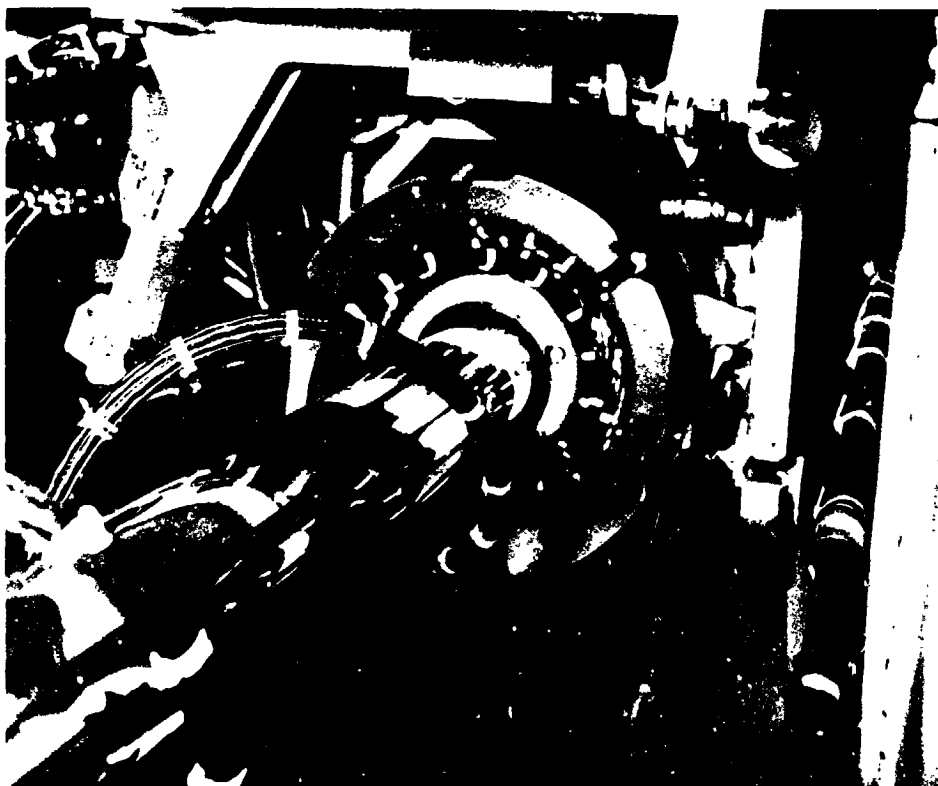
#### REFERENCES

- 28-2. Oda, M.; Gorenstein, P.; Gursky, H.; Kellogg, E.; et al.: X-Ray Pulsations From Cygnus X-1 Observed From UHURU. *Astrophys. J. (Letters)*, vol. 166, no. 1, pt. 2, May 15, 1971, pp. L1-L7.
- 28-3. Schreier, E.; Levinson, R.; Gursky, H.; Kellogg, E.; et al.: Evidence for the Binary Nature of Centaurus X-3 From UHURU X-Ray Observations. *Astrophys. J. (Letters)*, vol. 172, no. 3, pt. 2, Mar. 15, 1972, pp. L79-L89.
- 28-4. Tananbaum, H.; Gursky, H.; Kellogg, E.; Levinson, R.; et al.: Discovery of a Periodic Pulsating Binary X-Ray Source in Hercules from UHURU. *Astrophys. J. (Letters)*, vol. 174, no. 3, pt. 1, June 15, 1972, pp. L143-L149.

29. LUNAR ORBITAL MASS SPECTROMETER (NASA EXPERIMENT S-165)

NSSDC IDENTIFICATION NUMBERS:

APOLLO 15 71-063A-13  
APOLLO 16 72-031A-11



CONTENTS - SECTION 29

	Page
INSTRUMENT DESCRIPTION . . . . .	29-3
OPERATIONAL HISTORY . . . . .	29-5
FORMAT OF DATA . . . . .	29-6
SAMPLES OF DATA . . . . .	29-7
Low Mass . . . . .	29-7
High Mass . . . . .	29-8
Apollo 16 Peak Summary . . . . .	29-9
Apollo 16 Trajectory Summary . . . . .	29-9
Apollo 16 Housekeeping Summary . . . . .	29-10
BIBLIOGRAPHY . . . . .	29-12

## 29. LUNAR ORBITAL MASS SPECTROMETER

The lunar orbital mass spectrometer, flown on the Apollo 15 and 16 missions as part of the orbital science payload, measured the concentration of gas molecules it encountered both in lunar orbit and during transearth coast (TEC) for the purpose of studying the sources, sinks, and transport mechanisms of the lunar atmosphere. Nearly 80 hr of operation in lunar orbit and 50 hr in TEC produced some 8000 spectra of gases in the vicinity of the instrument entrance aperture.

### INSTRUMENT DESCRIPTION

The instrument, a sector-field, dual-collector mass spectrometer, was mounted on a boom stowed in the scientific instrument module bay of the service module, which was capable of extending the instrument to a distance of 7.3 m from the spacecraft. The purpose of the boom mount was to extend the instrument a reasonable distance from the spacecraft so that it would be beyond the interacting cloud of outgassing molecules from the spacecraft and in a collisionless, outwardly, free-streaming region. The instrument is shown in figure 29-1. The instrument package was a rectangular box, 30 by 32 by 23 cm, weighing 11 kg, and bisected by a baseplate; the electronics portion was on one side, the mass analyzer on the other. A plenum, in the form of a scoop, was mounted on the outboard side of the package and directed along the -X axis of the spacecraft (i.e., opposite the command module end). When the flight-path was oriented so that the velocity vector was in the -X direction, the gas inlet was in the ram direction with respect to native gases in the lunar atmosphere, whereas the reverse direction of flight (+X) produced a wake condition at the inlet.

The plenum contains the mass spectrometer ion source with redundant tungsten (with 1 percent rhenium) filaments mounted on either side of the ionization chamber. Ions formed by electron bombardment are collimated into a beam and accelerated into the mass analyzer, a single focusing permanent magnet, giving a mass resolution of more than a 1-percent valley between peaks at 40 and 41 amu. Two collector systems permit simultaneous scanning of two mass ranges, 12 to 28 amu and 28 to 66 amu.

Voltage scan is employed by using a stepping high-voltage power supply. The ion accelerating voltage sweep is generated by varying the sweep high voltage in a series of 590 steps from 620 V to 1560 V with a dwell time of 0.1 sec/step. Between each sweep, 30 additional steps at zero V are used to determine the background-counting rate and to apply an internal calibration frequency. Therefore, the entire spectrum is obtained every 62 sec, giving a spatial resolution of each mass peak of approximately 100 km. A sweep-start flag indicates data or background and serves as a marker for the start of each sweep. The mass number of the ion being detected is determined by the voltage step number at which the peak is detected. This step number is advanced by an enable pulse from the data-handling system. The minimum number of steps between adjacent mass peaks below mass 54 is 12.

Electron multipliers, preamplifiers, and discriminators, which count the number of ions that pass through each collector slit on each of the sweep voltage steps, are used in the detector systems. The ion-count numbers are stored in 21-bit accumulators (one for each channel) until sampled by the data-handling system. Just before sampling, each data word is converted to a floating-point number in base 2, reducing the data to a 10-bit word consisting of a 6-bit number and a 4-bit multiplier. The data-handling system maintains 7-bit accuracy throughout the 21-bit range of data counts.

Instrument parameters, such as certain internal voltages, electron emission in the ion source, filament currents (to determine which filament is operating), multiplier voltages, sweep voltages, temperatures, multiplier and discriminator settings, and instrument current, are monitored by a housekeeping circuit. The instrument parameters are as follows:

Mass range:	12 to 66 amu
Spectrum scan time:	62 sec
Spatial resolution:	100 km
Mass resolution:	1 percent valley at 40 amu
Sensitivity:	$10^{-11}$ N/m <sup>2</sup> ( $10^{-13}$ torr)
Dynamic range:	$10^{-11}$ to $10^{-6}$ N/m <sup>2</sup> ( $10^{-13}$ to $10^{-8}$ torr)

Initial calibration of the mass spectrometers, performed in a high-vacuum chamber at the University of

Texas at Dallas, verified that the proper mass ranges were scanned and tested the resolution, linearity, mass discrimination, and dynamic range of the analyzer. Neon was introduced into the vacuum chamber by using isotopic partial pressures ranging from  $10^{-9}$  to  $10^{-5}$  N/m<sup>2</sup> ( $10^{-11}$  to  $10^{-7}$  torr). The instrument response was linear up to  $10^{-6}$  N/m<sup>2</sup> ( $10^{-8}$  torr) where the onset of saturation of the data-counting system occurred. The sensitivity of the instrument was verified to be greater than  $2 \times 10^{-7}$  A/N/m<sup>2</sup> ( $3 \times 10^{-5}$  A/torr), enabling the instrument to measure partial pressures down to  $10^{-11}$  N/m<sup>2</sup> ( $10^{-13}$  torr). The final absolute calibration was made at the NASA Langley Research Center Molecular Beam Facility in the same manner as for the lunar atmospheric composition experiment (S-205) also described in this handbook.

#### OPERATIONAL HISTORY

The operational history of the Apollo 15 lunar orbital mass spectrometer is given in the following tabulation. Time is in terms of ground elapsed time (GET) and is measured in hours from lift-off at 13:34:00.79 G.m.t. on July 26, 1971.

<u>Time, hr:min</u>	<u>Spacecraft attitude</u>
85:05 to 95:15	-X
108:55 to 119:20	-X
130:30 to 141:00	-X
195:50 to 200:25	+X
202:00 to 211:40	-X
211:40 to 214:15	+X
224:30 to 238:00	TEC
245:50 to 288:05	TEC

A similar tabulation of the operation of the Apollo 16 experiment follows. The GET is measured from lift-off at 17:54:00.57 G.m.t. on April 16, 1972.

<u>Time, hr:min</u>	<u>Spacecraft attitude</u>
81:10 to 92:03	-X
108:00 to 121:20	-X
121:20 to 124:40	+X (oblique photographs)
124:40 to 131:10	+X
131:10 to 142:10	-X
142:10 to 143:15	antisolar hold
143:15 to 144:15	-X
144:15 to 146:20	+X (oblique photographs)
146:20 to 151:20	+X
151:20 to 152:50	+X (oblique photographs)
152:50 to 164:20	+X
164:20 to 167:00	+X
167:00 to 168:10	+X (oblique photographs)
180:05 to 193:45	-X

#### FORMAT OF DATA

Data processing has resulted in the blocking of data into complete mass spectra on magnetic tape. Brief time gaps in the data, caused by telemetry dropouts, are filled with flag words to ensure proper location of the good measurements in the spectra. Reduced data also include the background-count level of each analyzer channel, the amplitude of each mass peak, the decommutated housekeeping data, and the pertinent spacecraft-trajectory information.

Microfilm records are formatted outputs of the data on magnetic tape. The format gives sequential pairs of mass spectra (high- and low-mass channels) together with background, peak amplitude, housekeeping, and trajectory data. Periodic tabulated summaries of the peak amplitudes, housekeeping, and trajectory data are also given. Each summary covers several hours of experiment operation.

## SAMPLES OF DATA

Computer printouts showing examples of each type of data are given in figures 29-2 to 29-6. The codes and definitions are as follows:

	Low Mass
GET TIME	GET from lift-off
APOLLO 16	Apollo mission number
A0, A1, B0, B1	Peak-location coefficients for high-mass channel
RFV	Orbit number
SUN HR	Longitude - subsolar longitude
LONG	Subsatellite longitude
LAT	Subsatellite latitude
SUN A	Angle from command and service module (CSM) X axis to Sun
SUN B	Azimuth of Sun from -Z axis
TEMP	Ion-source temperature monitor
ALT	CSM altitude (kilometers)
VEL ALPHA	Angle of attack from X axis
VEL	CSM velocity (km/sec)
BACKGROUND	Background data
CALIBRATE	Interval calibrate data
HOUSEKEEPING	
+12	+12 V monitor
+5	+5 V monitor
-12	-12 V monitor
-15	-15 V monitor

EM	Emission current monitor
F1	Filament 1 current monitor
F2	Filament 2 current monitor
LM	Low-mass multiplier, high-voltage monitor
HM	High-mass multiplier, high-voltage monitor
SW	Sweep high-voltage monitor
T1	Electronics temperature monitor
T2	Ion-source temperature monitor
MF	Multiplier high-voltage HI/LO flag
DF	Discriminator HI/LO flag
IC	Instrument current
PEAK AMPLITUDES	Mass number and peak amplitude
PRE BKG	Background counts at start of sweep
CUR BKG	Background counts at end of sweep
NUM	Number data points used in calculating BKG
	High Mass
GET TIME	GET from lift-off
APOLLO 16	Apollo mission number
24 October 1972	Date data tapes were processed
A0, A1, B0, B1	Peak-location coefficients for high mass channel
STEP NO	A0 + A1/mass step <400 B0 + B1/mass step >400

SYNC START	Data count at start of sweep
SYNC END	Data count at end of sweep
PBKG	Background count at start of sweep
BKG	Background count at end of sweep
N	Number data points used in calculating BKG
BACKGROUND	Background data
CALIBRATE	Internal calibrate data
PEAK AMPLITUDES	Mass number and peak amplitude
STAR	Incorrect peak shape

#### Apollo 16 Peak Summary

GET TIME	GET from lift-off
SUN HR	Longitude - subsolar longitude
C	Peak-error code. If code greater than zero, previous peak-location coefficients are used
27 → 39	Mass number
L	Low-mass BKG
H	High-mass BKG
GAP	Time gap in data
STAR	Incorrect peak shape
CSM DIRECTION	Minus (-) denotes -X orientation

#### Apollo 16 Trajectory Summary

GET TIME	GET from lift-off
----------	-------------------

REV	Orbit number
SUN HR	Longitude - subsolar longitude
LONG	Subsatellite longitude
LAT	Subsatellite latitude
RADIUS	Orbit radius (kilometers)
VELOCITY	CSM velocity (km/sec)
ALTITUDE	CSM altitude (kilometers)
SS LONG	Subsolar longitude
SS LAT	Subsolar latitude
SUN A	Angle from CSM X axis to Sun
SUN B	Azimuth of Sun from -Z axis
VEL ALPHA	Angle of attack from X axis
VEL BETA	Azimuth of Vel vector from -Z axis

Apollo 16 Housekeeping Summary

GET TIME	GET from lift-off
+12	+12 V monitor
+5	+5 V monitor
-12	-12 V monitor
-15	-15 V monitor
EMISSION	Emission current monitor
FIL 1	Filament 1 current monitor
FIL 2	Filament 2 current monitor
LM HV	Low-mass multiplier, high-voltage monitor
HM HV	High-mass multiplier, high-voltage monitor

---

S HV	Sweep high-voltage monitor
ETEMP	Electronics temperature monitor
STEMP	Ion source temperature monitor
M LO/HI	Multiplier high-voltage LO/HI flag
D HI/LO	Discriminator HI/LO flag
I	Instrument current (total)

## BIBLIOGRAPHY

- Hodges, R. R., Jr.: Response of Lunar Atmosphere to Volcanic Gas Release. Planet. Space Sci., vol. 20, no. 11, Nov. 1972, pp. 1849-1864.
- Hodges, R. R., Jr.; Hoffman, J. H.; and Evans, D. E.: Lunar Orbital Mass Spectrometer Experiment. Sec. 21 of Apollo 16 Preliminary Science Report, NASA SP-315, 1972.
- Hodges, R. R., Jr.; Hoffman, J. H.; Yeh, T. T. J.; and Chang, G. K.: Orbital Search for Lunar Volcanism. J. Geophys. Res., vol. 78, no. 22, Aug. 1, 1972, p. 4079.
- Hoffman, J. H.; Hodges, R. R., Jr.; and Evans, D. E.: Lunar Orbital Mass Spectrometer Experiment. Sec. 19 of Apollo 15 Preliminary Science Report, NASA SP-315, 1972.
- Hoffman, J. H.; Hodges, R. R., Jr.; and Evans, D. E.: Lunar Orbital Mass Spectrometer Experiment. Proceedings of the Third Lunar Science Conference, vol. 3, D. R. Criswell, ed., MIT Press (Cambridge, Mass.), 1972, pp. 2205-2216.

C.7

ORIGINAL PAGE IS  
OF POOR QUALITY

29-13



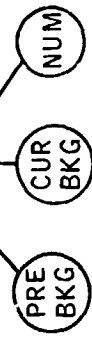
Figure 29-1.- Apollo 16 mass spectrometer.

GET TIME	APOLLO 16	AU	A1	80	BI	REV	SUN	MR	LOGC	LAT	SUN A	CUM A	VEL
187 26 50	LOJ	MACS	-505.32	34644.32	-55.41	17427.50	-0.46	-40.89	7.28	-7.23	40.11	215.33	177.71
1	1423	291	55	53	116	201	63807	44503	9471	53	911	3232	
2	1503	307	45	64	187	195	63999	44513	9577	55	1037	520	
3	1471	343	52	113	109	219	64311	44543	9471	46	1103	120	
4	1455	331	54	113	109	219	64311	44543	9471	46	1103	120	
5	1407	339	57	114	125	303	65223	44531	9343	55	1170	0	
6	1167	319	48	107	229	503	65223	44531	9343	55	1170	0	
7	071	323	59	152	231	599	65223	44531	9343	43	1119	0	
8	551	327	49	112	235	591	65223	44531	9343	47	1132	0	
9	535	307	46	103	239	631	64211	44519	7331	42	1135	0	
10	1301	335	46	103	259	631	64211	44519	7331	45	1071	1	
11	4095	343	43	111	233	637	63999	44515	7907	45	1103	1	
12	6143	321	40	112	249	623	63999	44515	7907	45	1103	1	
13	6555	351	37	121	249	655	63999	44503	1557	112	1037	2	
14	6703	294	37	115	249	623	62975	41903	543	119	1037	2	
15	6555	247	24	115	259	607	62975	41903	543	119	1037	2	
16	6581	207	30	117	307	631	62463	40447	135	229	903	0	
17	6443	115	22	131	599	631	62463	40447	135	503	823	1616	
18	6527	03	25	99	711	639	60927	27697	105	503	823	1616	
19	6359	64	26	71	735	615	55295	19199	103	339	567	1616	
20	6335	67	23	76	687	615	49543	12031	69	111	203	1616	
21	6335	63	20	53	607	599	30719	6703	94	62	131	1616	
22	6143	97	24	41	695	591	10431	1615	105	60	60	1616	
23	5695	99	10	47	679	503	19343	1775	91	38	65	1616	
24	4223	110	10	40	679	503	4079	967	92	29	70	1616	
25	2207	105	17	51	671	403	2227	631	81	31	62	1616	
26	871	119	19	44	655	371	1711	403	81	37	62	1616	
27	347	104	26	47	630	339	1167	351	111	37	79	1616	
28	233	99	26	45	500	207	911	255	167	37	79	1616	
29	591	110	23	45	623	267	719	271	157	37	79	1616	
30	751	107	20	51	567	279	567	243	1055	50	67	1616	
31	759	103	20	49	623	203	535	263	1055	50	67	1616	
32	727	113	20	47	587	299	463	225	1913	50	77	1616	
33	711	94	18	45	501	323	463	225	1913	50	77	1616	
34	759	91	27	49	607	323	423	225	1913	50	77	1616	
35	711	91	27	54	593	303	379	219	1951	69	69	1616	
36	759	104	27	47	427	359	355	219	1951	69	69	1616	
37	735	104	25	51	423	423	367	231	1951	69	69	1616	
38	719	63	25	51	413	503	463	203	1951	69	69	1616	
39	695	57	25	51	413	503	463	203	1951	69	69	1616	
40	695	57	25	51	413	503	463	203	1951	69	69	1616	
41	695	57	25	51	413	503	463	203	1951	69	69	1616	
42	679	50	20	44	44	623	1119	431	1775	63	70	1616	
43	639	45	19	44	44	623	1119	431	1775	63	70	1616	
44	535	45	19	44	44	623	1119	431	1775	63	70	1616	
45	299	50	24	60	117	1819	25290	1055	435	49	67	1616	
46	173	46	24	60	117	1819	25290	1055	435	49	67	1616	
47	104	49	24	60	117	1819	25290	1055	435	49	67	1616	
48	86	53	29	60	117	1819	25290	1055	435	49	67	1616	
49	105	58	29	60	117	1819	25290	1055	435	49	67	1616	
50	205	52	36	81	307	6399	45025	5503	55	233	233	1616	
51	647	75	0	112	237	6399	45025	5503	55	233	233	1616	
52	701	27	0	112	237	6399	45025	5503	55	233	233	1616	
53	303	27	0	112	237	6399	45025	5503	55	233	233	1616	

Background

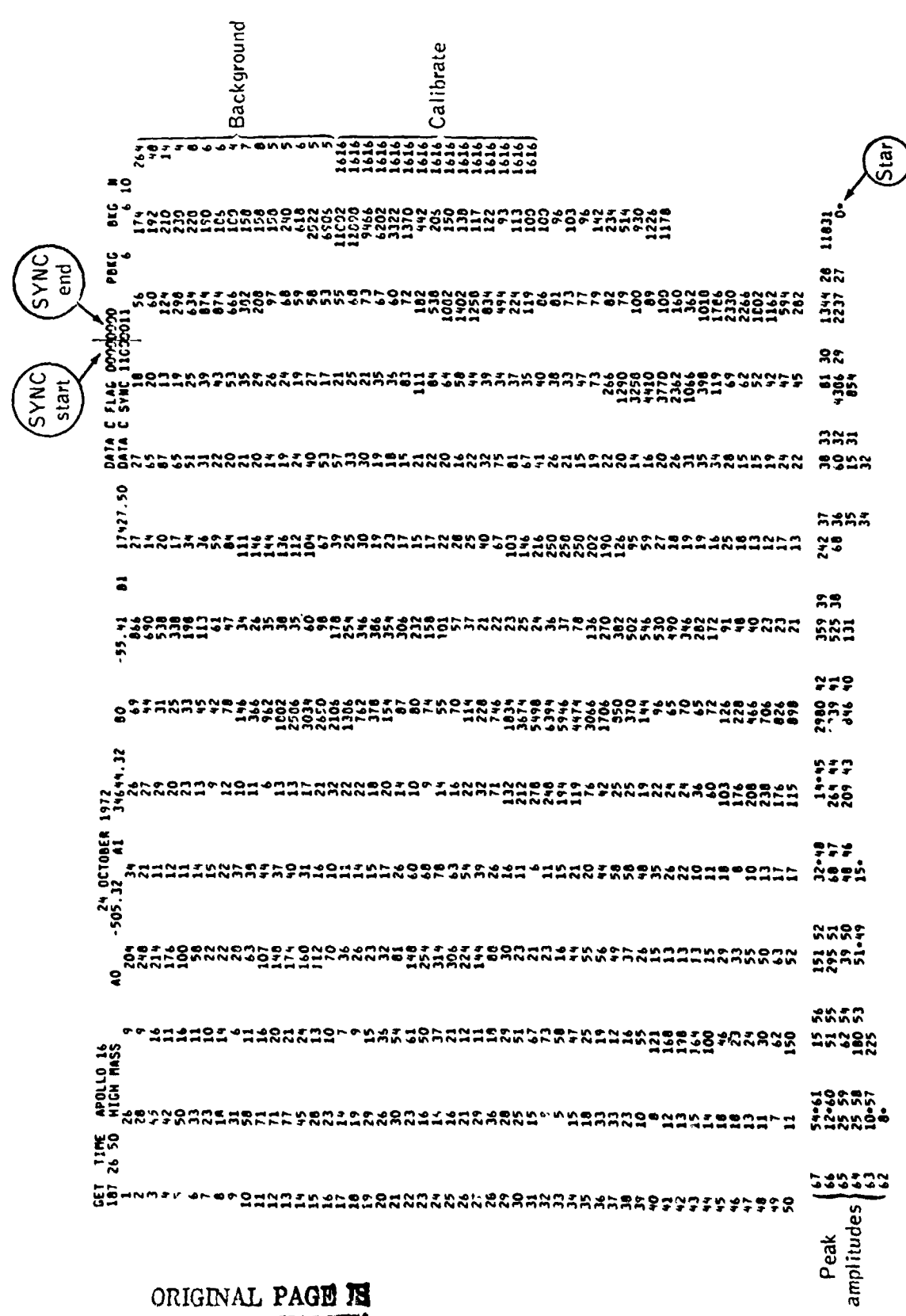
Calibrate

Housekeeping



ORIGINAL PAGE IS  
OF POOR QUALITY

Figure 29-2.- Low-mass data format.



ORIGINAL PAGE IS  
OF POOR QUALITY

Figure 29-3.- High-mass data format.

GET	TIME	SUM	MR	C	CSM direction	Low mass	High mass	APOLLO 16 PEAK SUMMARY	70	71	72	21	24	25	26	M
-187 2 3	53.1	0	1	0	0	0	0	0	0	0	0	0	0	0	0	10 209
-187 3 5	30.0	1	0	0	0	0	0	0	0	0	0	0	0	0	0	7 232
-187 4 7	26.9	1	0	0	0	0	0	0	0	0	0	0	0	0	0	7 233
-187 5 9	23.9	1	0	0	0	0	0	0	0	0	0	0	0	0	0	5 170
-187 6 11	20.8	0	629	0	0	0	0	0	214	0	0	0	0	0	0	5 172
-187 7 13	17.7	1	605	0	0	0	0	0	282	0	0	0	0	0	0	4 135
-187 8 15	14.6	0	547	0	0	0	0	0	300	0	0	0	0	0	0	2 225
-187 9 17	11.5	0	522	0	0	0	0	0	326	0	0	0	0	0	0	2 34
-187 10 19	8.5	0	645	0	0	0	0	0	304	0	0	0	0	0	0	2 148
-187 11 21	5.4	0	646	0	0	0	0	0	170	0	0	0	0	0	0	2 166
-187 12 22	2.4	0	830	0	0	0	0	0	488	0	0	0	0	0	0	2 249
-187 13 24	-0.7	0	810	0	0	0	0	0	474	0	0	0	0	0	0	2 249
-187 14 26	-3.8	0	753	0	0	0	0	0	920	0	0	0	0	0	0	2 249
-187 15 28	-6.8	0	985	0	0	0	0	0	597	0	0	0	0	0	0	1 114
-187 16 30	-9.9	0	1034	0	0	0	0	0	631	0	0	0	0	0	0	1 64
-187 17 32	-13.0	1	1056	0	0	0	0	0	600	0	0	0	0	0	0	2 24
-187 18 34	-16.1	1	1207	0	0	0	0	0	610	0	0	0	0	0	0	2 35
-187 19 36	-19.2	1	964	0	0	0	0	0	423	0	0	0	0	0	0	1 10
-187 20 38	-22.3	0	1075	0	0	0	0	0	403	0	0	0	0	0	0	1 6
-187 21 40	-25.4	0	1275	0	0	0	0	0	444	0	0	0	0	0	0	1 6
-187 22 42	-28.5	0	1041	0	0	0	0	0	499	0	0	0	0	0	0	1 6
-187 23 44	-31.6	0	1149	0	0	0	0	0	540	0	0	0	0	0	0	1 6
-187 24 46	-34.7	1	891	0	0	0	0	0	551	0	0	0	0	0	0	1 6
-187 25 48	-37.8	0	970	0	0	0	0	0	599	0	0	0	0	0	0	1 6
-187 26 50	-40.9	0	1059	0	0	0	0	0	644	0	0	0	0	0	0	1 6
-187 27 52	-44.0	0	1006	0	0	0	0	0	687	0	0	0	0	0	0	1 6
-187 28 54	-47.1	0	825	0	0	0	0	0	742	0	0	0	0	0	0	1 6
-187 29 56	-50.2	0	1005	0	0	0	0	0	797	0	0	0	0	0	0	1 6
-187 30 58	-53.3	0	921	0	0	0	0	0	852	0	0	0	0	0	0	1 6
-187 31 0	-56.4	0	921	0	0	0	0	0	907	0	0	0	0	0	0	1 6
-187 32 0	-59.5	0	971	0	0	0	0	0	962	0	0	0	0	0	0	1 6
-187 33 1	-62.6	0	923	0	0	0	0	0	1017	0	0	0	0	0	0	1 6
-187 34 3	-65.7	0	770	0	0	0	0	0	1072	0	0	0	0	0	0	1 6
-187 35 5	-68.8	0	817	0	0	0	0	0	1127	0	0	0	0	0	0	1 6
-187 36 7	-71.9	0	818	0	0	0	0	0	1182	0	0	0	0	0	0	1 6
-187 37 9	-75.0	0	763	0	0	0	0	0	1237	0	0	0	0	0	0	1 6
-187 38 11	-78.1	0	618	0	0	0	0	0	1292	0	0	0	0	0	0	1 6
-187 39 13	-81.2	0	662	0	0	0	0	0	1347	0	0	0	0	0	0	1 6
-187 40 15	-84.3	0	716	0	0	0	0	0	1402	0	0	0	0	0	0	1 6
-187 41 17	-87.4	0	640	0	0	0	0	0	1457	0	0	0	0	0	0	1 6
-187 42 19	-90.5	0	646	0	0	0	0	0	1512	0	0	0	0	0	0	1 6
-187 43 21	-93.6	0	769	0	0	0	0	0	1567	0	0	0	0	0	0	1 6
-187 44 23	-96.7	0	676	0	0	0	0	0	1622	0	0	0	0	0	0	1 6
-187 45 25	-99.8	0	867	0	0	0	0	0	1677	0	0	0	0	0	0	1 6
-187 46 27	-102.9	0	667	0	0	0	0	0	1732	0	0	0	0	0	0	1 6
-187 47 29	-106.0	0	665	0	0	0	0	0	1787	0	0	0	0	0	0	1 6
-187 48 31	-109.1	0	815	0	0	0	0	0	1842	0	0	0	0	0	0	1 6
-187 49 33	-112.2	0	677	0	0	0	0	0	1897	0	0	0	0	0	0	1 6
-187 50 35	-115.3	0	740	0	0	0	0	0	1952	0	0	0	0	0	0	1 6
-187 51 37	-118.4	0	740	0	0	0	0	0	2007	0	0	0	0	0	0	1 6
-187 52 39	-121.5	0	744	0	0	0	0	0	2062	0	0	0	0	0	0	1 6
-187 53 41	-124.6	0	761	0	0	0	0	0	2117	0	0	0	0	0	0	1 6

Figure 29-4.- Peak summary format.

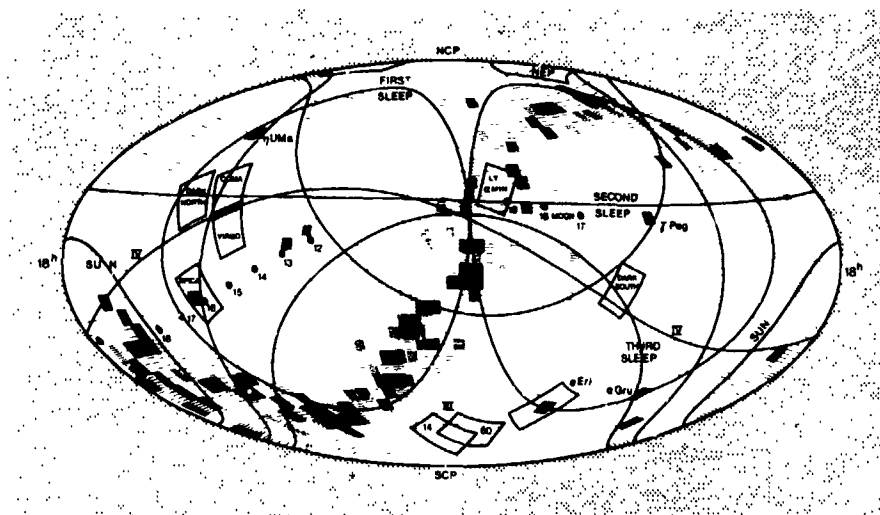
GET	TIME	REV	SUN HR	LONG	LAT	RADIUS	VELOCITY	ALTITUDE	SS	LONG	SS	LAT	SUN A	SUN B	VEL ALPHA	VEL BETA
187	2	3	58.27	81.48	2.41	1097.55	1.4301	109.72	40.39	40.39	1.57	120.42	219.18	177.48	219.06	
187	3	5	58.28	78.39	1.85	1090.14	1.4295	110.33	40.38	40.38	1.57	116.91	214.83	177.09	217.87	
187	4	7	58.29	75.31	1.28	1090.78	1.4290	110.95	40.37	40.37	1.57	113.71	214.52	176.65	215.58	
187	5	9	58.30	72.22	.71	1099.40	1.4284	111.57	40.36	40.36	1.57	110.42	214.22	176.22	215.17	
187	6	11	58.31	69.14	.14	1050.03	1.4279	112.20	40.35	40.35	1.57	107.14	213.91	175.79	214.76	
187	7	13	58.32	66.06	-.43	1050.65	1.4273	112.82	40.34	40.34	1.57	103.86	213.60	175.36	214.35	
187	8	15	58.33	62.98	-1.00	1051.27	1.4268	113.44	40.33	40.33	1.57	100.58	213.29	174.93	213.94	
187	9	17	58.34	59.91	-1.56	1051.89	1.4263	114.06	40.32	40.32	1.57	97.30	212.98	174.50	213.53	
187	10	19	58.35	56.83	-2.12	1052.51	1.4257	114.68	40.31	40.31	1.57	94.02	212.67	174.07	213.12	
187	11	21	58.36	53.75	-2.68	1053.13	1.4252	115.30	40.30	40.30	1.57	90.74	212.36	173.64	212.71	
187	12	22	58.37	50.68	-3.24	1053.75	1.4247	115.92	40.29	40.29	1.57	87.46	212.05	173.21	212.30	
187	13	24	58.38	47.60	-3.79	1054.37	1.4242	116.54	40.28	40.28	1.57	84.18	211.74	172.78	211.89	
187	14	26	58.39	44.52	-4.35	1054.99	1.4237	117.16	40.27	40.27	1.57	80.90	211.43	172.35	211.48	
187	15	28	58.40	41.44	-4.90	1055.61	1.4233	117.78	40.26	40.26	1.57	77.62	211.12	171.92	211.07	
187	16	30	58.41	38.36	-5.46	1056.23	1.4228	118.40	40.25	40.25	1.57	74.34	210.81	171.49	210.66	
187	17	32	58.42	35.28	-6.01	1056.85	1.4224	119.02	40.24	40.24	1.57	71.06	210.50	171.06	210.25	
187	18	34	58.43	32.20	-6.57	1057.47	1.4219	119.64	40.23	40.23	1.57	67.78	210.19	170.63	209.84	
187	19	36	58.44	29.12	-7.12	1058.09	1.4215	120.26	40.22	40.22	1.57	64.50	209.88	170.20	209.43	
187	20	38	58.45	26.04	-7.68	1058.71	1.4211	120.88	40.21	40.21	1.57	61.22	209.57	169.77	209.02	
187	21	40	58.46	22.96	-8.24	1059.33	1.4207	121.50	40.20	40.20	1.57	57.94	209.26	169.34	208.61	
187	22	42	58.47	19.88	-8.79	1059.95	1.4203	122.12	40.19	40.19	1.57	54.66	208.95	168.91	208.20	
187	23	44	58.48	16.80	-9.35	1060.57	1.4200	122.74	40.18	40.18	1.57	51.38	208.64	168.48	207.79	
187	24	46	58.49	13.72	-9.91	1061.19	1.4196	123.36	40.17	40.17	1.57	48.10	208.33	168.05	207.38	
187	25	48	58.50	10.64	-10.47	1061.81	1.4192	123.98	40.16	40.16	1.57	44.82	208.02	167.62	206.97	
187	26	50	58.51	7.56	-11.03	1062.43	1.4188	124.60	40.15	40.15	1.57	41.54	207.71	167.19	206.56	
187	27	52	58.52	4.48	-11.59	1063.05	1.4185	125.22	40.14	40.14	1.57	38.26	207.40	166.76	206.15	
187	28	54	58.53	1.40	-12.15	1063.67	1.4181	125.84	40.13	40.13	1.57	34.98	207.09	166.33	205.74	
187	29	56	58.54	-.68	-12.71	1064.29	1.4177	126.46	40.12	40.12	1.57	31.70	206.78	165.90	205.33	
187	30	58	58.55	-3.76	-13.27	1064.91	1.4173	127.08	40.11	40.11	1.57	28.42	206.47	165.47	204.92	
187	31	58	58.56	-6.84	-13.83	1065.53	1.4170	127.70	40.10	40.10	1.57	25.14	206.16	165.04	204.51	
187	32	58	58.57	-9.92	-14.39	1066.15	1.4166	128.32	40.09	40.09	1.57	21.86	205.85	164.61	204.10	
187	33	58	58.58	-13.00	-14.95	1066.77	1.4162	128.94	40.08	40.08	1.57	18.58	205.54	164.18	203.69	
187	34	58	58.59	-16.08	-15.51	1067.39	1.4158	129.56	40.07	40.07	1.57	15.30	205.23	163.75	203.28	
187	35	58	58.60	-19.16	-16.07	1068.01	1.4155	130.18	40.06	40.06	1.57	12.02	204.92	163.32	202.87	
187	36	58	58.61	-22.24	-16.63	1068.63	1.4151	130.80	40.05	40.05	1.57	8.74	204.61	162.89	202.46	
187	37	58	58.62	-25.32	-17.19	1069.25	1.4147	131.42	40.04	40.04	1.57	5.46	204.30	162.46	202.05	
187	38	58	58.63	-28.40	-17.75	1069.87	1.4143	132.04	40.03	40.03	1.57	2.18	204.00	162.03	201.64	
187	39	58	58.64	-31.48	-18.31	1070.49	1.4140	132.66	40.02	40.02	1.57	0.90	203.69	161.60	201.23	
187	40	58	58.65	-34.56	-18.87	1071.11	1.4136	133.28	40.01	40.01	1.57	0.00	203.38	161.17	200.82	
187	41	58	58.66	-37.64	-19.43	1071.73	1.4132	133.90	40.00	40.00	1.57	0.00	203.07	160.74	200.41	
187	42	58	58.67	-40.72	-19.99	1072.35	1.4128	134.52	40.00	40.00	1.57	0.00	202.76	160.31	200.00	
187	43	58	58.68	-43.80	-20.55	1072.97	1.4125	135.14	40.00	40.00	1.57	0.00	202.45	159.88	199.59	
187	44	58	58.69	-46.88	-21.11	1073.59	1.4121	135.76	40.00	40.00	1.57	0.00	202.14	159.45	199.18	
187	45	58	58.70	-49.96	-21.67	1074.21	1.4117	136.38	40.00	40.00	1.57	0.00	201.83	159.02	198.77	
187	46	58	58.71	-53.04	-22.23	1074.83	1.4113	137.00	40.00	40.00	1.57	0.00	201.52	158.59	198.36	
187	47	58	58.72	-56.12	-22.79	1075.45	1.4110	137.62	40.00	40.00	1.57	0.00	201.21	158.16	197.95	
187	48	58	58.73	-59.20	-23.35	1076.07	1.4106	138.24	40.00	40.00	1.57	0.00	200.90	157.73	197.54	
187	49	58	58.74	-62.28	-23.91	1076.69	1.4102	138.86	40.00	40.00	1.57	0.00	200.59	157.30	197.13	
187	50	58	58.75	-65.36	-24.47	1077.31	1.4098	139.48	40.00	40.00	1.57	0.00	200.28	156.87	196.72	
187	51	58	58.76	-68.44	-25.03	1077.93	1.4094	140.10	40.00	40.00	1.57	0.00	199.97	156.44	196.31	
187	52	58	58.77	-71.52	-25.59	1078.55	1.4090	140.72	40.00	40.00	1.57	0.00	199.66	156.01	195.90	
187	53	58	58.78	-74.60	-26.15	1079.17	1.4086	141.34	40.00	40.00	1.57	0.00	199.35	155.58	195.49	
187	54	58	58.79	-77.68	-26.71	1079.79	1.4082	141.96	40.00	40.00	1.57	0.00	199.04	155.15	195.08	
187	55	58	58.80	-80.76	-27.27	1080.41	1.4078	142.58	40.00	40.00	1.57	0.00	198.73	154.72	194.67	
187	56	58	58.81	-83.84	-27.83	1081.03	1.4074	143.20	40.00	40.00	1.57	0.00	198.42	154.29	194.26	
187	57	58	58.82	-86.92	-28.39	1081.65	1.4070	143.82	40.00	40.00	1.57	0.00	198.11	153.86	193.85	
187	58	58	58.83	-90.00	-28.95	1082.27	1.4066	144.44	40.00	40.00	1.57	0.00	197.80	153.43	193.44	
187	59	58	58.84	-93.08	-29.51	1082.89	1.4062	145.06	40.00	40.00	1.57	0.00	197.49	153.00	193.03	
187	60	58	58.85	-96.16	-30.07	1083.51	1.4058	145.68	40.00	40.00	1.57	0.00	197.18	152.57	192.62	
187	61	58	58.86	-99.24	-30.63	1084.13	1.4054	146.30	40.00	40.00	1.57	0.00	196.87	152.14	192.21	
187	62	58	58.87	-102.32	-31.19	1084.75	1.4050	146.92	40.00	40.00	1.57	0.00	196.56	151.71	191.80	
187	63	58	58.88	-105.40	-31.75	1085.37	1.4046	147.54	40.00	40.00	1.57	0.00	196.25	151.28	191.39	
187	64	58	58.89	-108.48	-32.31	1085.99	1.4042	148.16	40.00	40.00	1.57	0.00	195.94	150.85	190.98	
187	65	58	58.90	-111.56	-32.87	1086.61	1.4038	148.78	40.00	40.00	1.57	0.00	195.63	150.42	190.57	
187	66	58	58.91	-114.64	-33.43	1087.23	1.4034	149.40	40.00	40.00	1.57	0.00	195.32	150.00	190.16	
187	67	58	58.92	-117.72	-33.99	1087.85	1.4030	150.02	40.00	40.00	1.57	0.00	195.01	149.57	189.75	
187	68	58	58.93	-120.80	-34.55	1088.47	1.4026	150.64	40.00	40.00	1.57	0.00	194.70	149.14	189.34	
187	69	58	58.94	-123.88	-35.11	1089.09	1.4022	151.26	40.00	40.00	1.57	0.00	194.39	148.71	188.93	
187	70	58	58.95	-126.96	-35.67	1089.71	1.4018	151.88	40.00	40.00	1.57	0.00	194.08	148.28	188.52	
187	71	58	58.96	-130.04	-36.23	1090.33	1.4014	152.50	40.00	40.00	1.57	0.00	193.77	147.85	188.11	
187	72	58	58.97	-133.12	-36.79	1090.95	1.4010	153.12	40.00	40.00	1.57	0.00	193.46	147.42	187.70	
187	73	58	58.98	-136.20	-37.35	1091.57	1.4006	153.74	40.00	40.00	1.57	0.00	193.15	146.99	187.29	
187	74	58	58.99	-139.28	-37.91	1092.19	1.4002	154.36	40.00	40.00	1.57	0.00	192.84	146.56	186.88	
187	75	58	59.00	-142.36	-38.47	1092.81	1.4000	154.98	40.00	40.00	1.57	0.00	192.53	146.13	186.47	
187	76	58	59.01	-145.44	-39.03	1093.43	1.3996	155.60	40.00	40.00	1.57	0.00	192.22	145.70	186.06	
187	77	58	59.02	-148.52												



30. ULTRAVIOLET SPECTROMETER (NASA EXPERIMENT S-169)

NSSDC IDENTIFICATION NUMBER:

APOLLO 17 72-096A-02



CONTENTS — SECTION 30

	Page
INSTRUMENT DESCRIPTION AND CALIBRATION . . . . .	30-3
LUNAR ATMOSPHERE OBSERVATIONS . . . . .	30-5
LUNAR ALBEDO MEASUREMENTS . . . . .	30-11
OTHER OBSERVATIONS . . . . .	30-12
DATA FORMAT . . . . .	30-14
REFERENCES . . . . .	30-16

### 30. ULTRAVIOLET SPECTROMETER

An ultraviolet spectrometer (UVS) on board the Apollo 17 orbiting spacecraft was used in an attempt to measure ultraviolet emissions from the lunar atmosphere. The only emissions observed in the lunar atmosphere were from a transient atmosphere introduced by the lunar module descent engine; 4 hr after the lunar module landed, these emissions were no longer detectable by the spectrometer. The absence of atomic hydrogen (H) expected to be present from the solar wind source leads to the conclusion that solar wind protons are neutralized and converted to molecular hydrogen ( $H_2$ ) at the lunar surface.

During crossings of the solar-illuminated surface, the spectrometer measured significant variations in surface albedo. These variations are ascribed to variations in the refractive index of the lunar surface material.

The spectrometer made a number of nonlunar observations in lunar orbit and during transearth coast (TEC), including a search for the ultraviolet zodiacal light, solar atmosphere emissions, Earth emissions (including those from the geomagnetic tail), stellar emissions, and galactic emissions. During TEC, the fluorescence spectrum of  $H_2$  was observed during a purge of the Apollo 17 fuel cells.

#### INSTRUMENT DESCRIPTION AND CALIBRATION

The Apollo 17 UVS has been described in great detail elsewhere (ref. 30-1). In summary, it is of the Ebert type, which has been broadly used for space research, but employed new optical and electronic techniques that provided about an order of magnitude improvement in sensitivity. These improvements included exit slit mirrors that provided a 2.5 increase in the signal to the detector pulse-counting electronics (which permitted detection of single photoelectrons) and a precision wavelength scan system that permitted the summation of a large number of spectra without loss of spectral resolution. The slits were 2 mm in width, providing a resolution of approximately 1 nm.

The spectrometer is shown in figure 30-1. The triangular stand on which the instrument was mounted (fig. 30-1(a)) was attached to a spacecraft bulkhead that was perpendicular to the spacecraft longitudinal axis. The large baffle over the entrance slit excluded stray light and was designed with multiple angles in

several sections to provide a very large capability for rejection of unwanted radiation. There were no external optical components.

As seen in figure 30-1(b), light rays passing through the spectrometer entrance slit are rendered parallel by an area on one side of the spherical Ebert mirror, which directs the rays to the grating. Diffracted rays from the grating go to the area on the other side of the Ebert mirror that focuses the rays through the entrance slit to the face of a solar-blind photomultiplier tube, which transforms each photoelectron produced by a photon into several million electrons. An accumulator circuit counts and stores these pulses for 0.1 sec, and the accumulated pulse count is transmitted to the spacecraft data system as a 16-bit word.

The wavelength scan system consisted of a synchronous, motor-driven, cyclical cam, which encapsulated the pin on a follower arm. The follower arm was attached to the grating shaft. The 3600-lines/mm grating was rotated approximately 5° by the cam drive system to scan the spectral region 118 to 168 nm once every 12 sec. The cam was programmed to scan linearly in wavelength at the rate of approximately 7.5 nm/sec except for two 5-nm regions centered at 121.6 and 147.0 nm, where the scan rate was approximately 1.7 nm/sec to give temporal preference to Lyman-alpha radiation (121.6 nm) and to the resonance line of the heaviest atmospheric gas xenon (Xe) at 147.0 nm. The 144.5- to 149.5-nm region also included a fluorescent line of molecular hydrogen and one of carbon monoxide (CO).

The sensitivity  $S$  of the spectrometer to a gas column that is emitting  $1 \times 10^6$  photons/sec-cm<sup>2</sup>

$$S \text{ (counts/sec)} = \frac{1 \times 10^6}{4\pi} \frac{A_s A_g}{F^2} QT \quad (30-1)$$

where  $A_s$  = slit area  $\approx 1.14$  cm<sup>2</sup>

$A_g$  = grating area  $\approx 1 \times 10^2$  cm<sup>2</sup>

$F$  = spectrometer focal length = 50 cm

$Q$  = quantum efficiency of the detector  $\approx 10$  percent

$T$  = transmission of the optical system  $\approx 30$  percent

or

$$S \text{ (count/sec)} \approx 100 \text{ photoelectrons/sec/R} \quad 30-2)$$

To provide precision measurements with the spectrometer, it is necessary to measure the value of  $Q$  over the exposed area of the photomultiplier tube and to measure the transmission of the optical system over the entire field of view of the spectrometer. No standard source exists for the far ultraviolet region, and a spatially uniform reference source to fill the wide aperture of the spectrometer is beyond the state of the art. A high-precision calibration was accomplished in a specially built vacuum facility, which provided an intense, high f-number, monochromatic beam that could be focused into a very small spot on any point of the entrance slit. The flight spectrometer was mounted in the vacuum chamber on a tilting platform so that the calibrating beam could be directed through the entrance slit to each area of the diffraction grating. A calibrated photomultiplier tube could be inserted in the monochromatic beam to measure the number of photons passing through the entrance slit. A National Bureau of Standards calibrated photodiode was used to calibrate the reference photomultiplier tube before and after each calibration of the spectrometer.

The calibration was performed at a total of 10 wavelengths in the spectral region that the instrument scanned. Successive calibrations provided very reproducible sensitivity values at all wavelengths. A cross-check of the system was provided by calibration of a spare instrument in the vacuum optical bench at the NASA Goddard Space Flight Center, which confirmed the absolute value of the calibration. It is believed that these careful techniques ensure that the signals observed in flight were measured to an accuracy of  $\pm 10$  percent.

#### LUNAR ATMOSPHERE OBSERVATIONS

The Apollo 17 UVS experiment has as its primary objective the measurement of the density and composition of the lunar atmosphere by observing resonance scattering and fluorescence of solar far ultraviolet radiation. This technique can provide density measurements in the range  $1 \times 10^1$  to  $1 \times 10^4$  atoms/cm<sup>3</sup> for H, H<sub>2</sub>, atomic oxygen (O), carbon (C), atomic nitrogen (N), CO, carbon dioxide, and Xe but, because of spectral range limitations, could not measure helium, neon, or argon-36, all of which may be present as major constituents of the lunar atmosphere, if the solar wind is the major source for the atmosphere. In addition, radiogenic argon-40 (<sup>40</sup>Ar) from potassium-40 decay should be present. The present results indicate that the surface concentration of atomic hydrogen is less than 10 atoms/cm<sup>3</sup>, almost three orders of magnitude less than predicted (ref. 30-2), whereas the concentration of H<sub>2</sub>, if present, is less than  $6.0 \times 10^3$  atoms/cm<sup>3</sup>.

This is consistent with the hypothesis that the solar wind protons are completely converted into hydrogen molecules at the lunar surface. None of the other observable constituents were detected. A transient atmosphere was observed shortly after lunar module touchdown but disappeared in a matter of hours. No evidence of outgassing was detected in the vicinity of the crater Aristarchus, where many transient optical phenomena have been reported.

Previous measurements of the lunar atmosphere based on an in situ pressure gage (ref. 30-3) indicated that the total surface density at the subsolar point may be as small as  $1 \times 10^7$  atoms/cm<sup>3</sup>. More recent, mass spectrometer measurements from lunar orbit (ref. 30-4) and from the lunar surface (ref. 30-5) have resulted in detection of neon, argon, and helium. Lunar outgassing, the only possible source of a substantial atmosphere, occurs at a rate several orders of magnitude less than the corresponding rate on Earth (ref. 30-6). Apart from <sup>40</sup>Ar and radiogenic helium (ref. 30-7), the lunar atmosphere may consist only of neutralized solar wind ions. Thus, the lunar atmosphere would be expected to be composed primarily of neon, argon, hydrogen, and helium, the subsolar surface concentrations of which would lie in the range  $2 \times 10^3$  to  $7 \times 10^3$  atoms/cm<sup>3</sup> (ref. 30-7).

The Apollo 17 UVS was mounted in the scientific instrument module (SIM) with the optic axis pointed 23° forward and 18° right of the SIM center line (when looking toward the spacecraft nose). The SIM center line nominally pointed through the center of the Moon when the spacecraft was constrained to local horizontal attitude. Atmospheric observations were made in various spacecraft attitudes as shown in figure 30-2. The principal mode of operation was the observation through the illuminated atmosphere above the terminator against the dark side of the Moon (mode A in fig. 30-2). This was done automatically once per revolution if the spacecraft was maintained in the local horizontal attitude (twice if the spacecraft axis reversal was performed between terminator crossings). A total of 1200 of these terminator spectra was obtained.

To allow for the possibility that the atmospheric emissions might be too weak for detection in the principal mode, two special modes were provided to enhance the sensitivity. These modes resulted in most of the upper limits quoted in this report. In the first mode, the spectrometer was pointed at a fixed point in space and, as the spacecraft moved in its orbit, the line of sight extended through a tangential slice of illuminated atmosphere (mode B in fig. 30-2). The enhancement provided by this mode is  $\approx 20$  for H and H<sub>2</sub> and  $\approx 10$  for O, based on Chamberlain's model of an evaporating corona with the lunar surface as the critical level (ref. 30-8). The second mode (mode C in fig. 30-2) was used immediately after trans-earth injection (TEI) and is similar to mode A except for the much greater optical path length.

For all atmospheric constituents other than hydrogen (Lyman alpha, 121.6 nm), the sensitivity limit was set by the background count rate ( $\approx 25$  counts/sec), which was caused by solar cosmic ray protons. At 121.6 nm, solar radiation resonantly scattered from hydrogen atoms in the interplanetary medium produces a background of between 200 and 400 R (depending on the viewing direction), in good agreement with previous measurements (ref. 30-9). Emission rates of 6 to 12 R (450 to 900 counts/sec) are obtained when the scattered radiation is observed after reflection from the surface of the dark side of the Moon. Solar Lyman alpha scattered from the Earth hydrogen geocorona and then reflected from the Moon beyond the lunar terminator adds a 1-R contribution to the background for crossings of the terminator facing Earth. During TEC, the fixed areas of space observed in the tangential mode (mode B in fig. 30-2) were again observed to provide a sky background correction for the tangential mode.

Define

$$N_i(z_1, z_2) = \int_{z_1}^{z_2} n_i(z') dz' \quad (30-3)$$

where  $z_1$  and  $z_2$  are two altitudes above the lunar surface, and  $n_i(z')$  is the density in atoms per cubic centimeter of atomic species  $i$  at altitude  $z'$ , so that  $N_i(0, z)$  is the vertical column density of that atomic species between the surface and altitude  $z$ . For observations at an angle  $\theta$  to the local vertical the emission rate  $4\pi I_i$ , in rayleighs, for resonance scattering of solar flux in the  $i$ th line is given by

$$4\pi I_i = 1 \times 10^{-6} g_i [N(0, z)] [CH(\theta)] \quad (30-4)$$

where  $g_i$  is the resonance g-factor and  $CH(\theta)$  is the Chapman function (ref. 30-10). For molecular species, it is necessary to specify  $g_{v', v''}$ , where  $v'$  and  $v''$  are vibrational quantum numbers of the excited and ground states, respectively. Table 30-I lists the transitions of interest, the resonance g-factors, the instrument sensitivity, and the minimum detectable concentration for the particular mode of observation.

68

Figure 30-3 shows the difference between the average of the sum of 70 spectra observed in mode B in lunar orbit and the average of 210 spectra obtained during TEC (mode C) when the spectrometer axis was pointed at the same point in space. The spacecraft altitude varied from 70 to 46 km, and the spacecraft was near the subsolar point throughout the observation. Wavelengths corresponding to the resonance transitions of O, C, Xe, and N, to the Lyman bands of H<sub>2</sub>, and to the fourth-positive bands of CO are indicated. No emission features are apparent in the spectrum. Figure 30-4(a) shows a sum of 25 spectra obtained at the near-side terminator 2 hr after the lunar module had landed and indicates a slight enhancement at 130.4 nm (atomic oxygen) and at least one band of the CO fourth-positive system. None of these enhancements appear in figure 30-4(b), which shows the sum of 25 spectra obtained on the following orbit, 4 hr after landing.

In figure 30-5, the Lyman-alpha signal (121.6 nm) observed below the spacecraft between the terminator and a point 15° beyond the terminator (270° to 255°) (fig. 30-5(a)) is compared to the signal observed when the spacecraft was in full shadow (255° to 240°) (fig. 30-5(b)). The signal in figure 30-5(b) originated from solar radiation that was resonantly scattered from the solar system hydrogen atmosphere. The difference between the signals shown in figures 30-5(a) and 30-5(b) was initially misinterpreted as being of lunar atmospheric origin (ref. 30-1). More detailed data analysis, particularly of data from mode C (fig. 30-2), shows no signal that can be ascribed to an atomic hydrogen atmosphere to a limit of 10 atoms/cm<sup>3</sup> at the lunar surface. In mode C, the spacecraft altitude was increased by a factor of 5 with no increase in the Lyman-alpha (121.6 nm) signal. The signal difference (figs. 30-5(a) and 30-5(b)) is ascribed to an asymmetry in Lyman-alpha emission in the solar atmosphere. The existence of the asymmetry was confirmed by observations during TEC.

A number of conclusions emerge from the preceding results. The fact that xenon must be at best a minor component of the lunar atmosphere, despite its large mass (131.3), indicates that the mechanism of photoionization loss followed by acceleration in the solar wind electric field dominates over Jean's evaporative escape, at least for the heavy gases. The small concentrations of H, C, N, O, and CO, which are photodissociation products of many gases of volcanic origin, also place severe restrictions on present levels of lunar volcanism. (The limits on the outgassing rates are being described in detail by G. E. Thomas et al.) The most surprising result is the absence of atomic hydrogen to an upper limit almost three orders of magnitude below the predicted value (ref. 30-2). The effect of the terrestrial magnetic field in shielding the lunar surface from the incident solar wind proton

flux would be important only late in the mission.<sup>1</sup> Other possible ways of accounting for the absence of hydrogen atoms are as follows.

1. Adsorption of solar wind protons in the lunar soil
2. Direct reflection of solar wind protons from the lunar surface
3. Neutralization and rapid escape from the lunar surface as suprathermal hydrogen atoms
4. Recombination to form molecular hydrogen

In current models of the interaction of the solar wind with the lunar soil (ref. 30-13), protons of  $\approx 1$ -keV energy penetrate to a depth of  $\approx 1 \times 10^{-6}$  cm. They will neutralize to form hydrogen atoms and may combine with other H atoms to form hydrogen molecules. Diffusion to the surface or into the dust grains to a depth of  $\approx 1 \times 10^{-5}$  cm may occur. For adsorption within the soil to occur, the diffusion must be retarded, either by the formation of stable hydrides or by trapping in a lattice site. In either case, after sufficient exposure, the soil becomes saturated and diffusion from the surface will occur. Saturation occurs only for the outer surfaces of soil grains, which are exposed to the solar wind for periods ranging from  $0.1 \times 10^6$  to  $20 \times 10^6$  yr (ref. 30-14). Even for an exposure period of 1 million years (during which the solar wind is assumed constant), complete adsorption of the solar protons would give a density of  $4 \text{ mg/cm}^2$  of hydrogen over the entire lunar surface. This value exceeds the measured composition of lunar soil by a factor of  $\approx 1 \times 10^5$  (ref. 30-13).

The reflection of solar wind particles has been measured by several solar wind composition experiments on the lunar surface. The albedo for alpha particles is 10 percent (ref. 30-15), and the albedo for protons should not be significantly higher. In addition, significant reflection of solar wind ions would produce measurable perturbations of the solar wind magnetic field that have not been observed from lunar orbit (ref. 30-16).

---

<sup>1</sup>According to the empirical geomagnetic-tail model of Fairfield (ref. 30-11), the Moon should have entered the Earth bow shock 13 hr before the TEI maneuver. However, according to measurements of the solar wind at the surface of the Moon (ref. 30-12), the proton flux is not appreciably disturbed until the Moon enters the geomagnetic tail. The cut-off of solar wind flux should have occurred at approximately 18:00 G.m.t. on December 18, which was 44 hr after TEI.

A "sputtering" atmosphere of atomic hydrogen has been advocated (ref. 30-17), in which hydrogen atoms with average velocities of 15 km/sec are ejected from the lunar surface as a result of energetic ion impact. However, because hydrogen is a minor constituent of the lunar surface, the dominant composition of the sputtered material would probably be that of the lunar soil itself. Even if all the sputtered atoms were hydrogen with the previously mentioned average velocity, the maximum Doppler shift (0.006 nm) of the absorption line would not be sufficient to remove it from the wide solar Lyman-alpha line. The predicted value at the subsolar point of  $340 \text{ atoms/cm}^3$  for the previously mentioned sputtering model (ref. 30-17) is far above the detection limit shown in table 30-I.

Thus, efficient surface recombination of solar protons to molecular hydrogen appears to be the most probable explanation for the low atomic hydrogen density. It is reasonable to expect an efficient trapping of kilovolt protons on the lunar surface (ref. 30-18), followed by an upward diffusion of hydrogen atoms. This upward diffusion would promote recombination either within or at the surface of the soil grains. The molecular hydrogen would then be released by the surface as thermal energy. A theoretical model of Hodges (ref. 30-19) predicts  $\text{H}_2$  concentrations of  $3.6 \times 10^3 \text{ atoms/cm}^3$  at the subsolar point and  $2.3 \times 10^4 \text{ atoms/cm}^3$  at the antisolar point.

As shown in table 30-I, the fluorescence in the  $\text{H}_2$  Lyman bands from expected density would have escaped detection in the UVS experiment. The expected nighttime density, however, may ultimately be detected by the Apollo 17 neutral mass spectrometer surface experiment (ref. 30-20).

In conclusion, the Apollo 17 UVS experiment has revealed that atomic hydrogen is almost totally absent in the lunar atmosphere. To explain this observation, it is believed that almost 100-percent conversion of solar wind protons to molecular hydrogen probably occurs at the lunar surface. The expected  $\text{H}_2$  density would have so far escaped detection. It is also expected that  $\text{H}_2$  will predominate over H for the case of Mercury if its atmosphere is thin enough to allow direct solar wind impact on the surface. A related problem on which this result may bear is the formation of interstellar  $\text{H}_2$  on dust particles (refs. 30-21 and 30-22).

## LUNAR ALBEDO MEASUREMENTS

During the orbital mission, approximately 50 hr of data were obtained with the UVS observing the sunlit side of the Moon and approximately 50 hr of data were obtained on the dark side. Also during the mission, a rocket experiment conducted by the University of Colorado from the White Sands Missile Range measured the absolute spectral brightness of the Sun in the ultraviolet while the UVS was measuring the sunlit spectrum of the Moon. Thus, it was possible to make an absolute measurement of the spectral albedo of the lunar surface.

Before the mission, laboratory measurements had been made of the spectral albedo of lunar dust samples obtained on the Apollo 11, 12, and 14 missions. The laboratory measurements showed that all three lunar samples had an ultraviolet albedo of approximately  $2.2 \pm 0.2$  percent at all wavelengths in the range of 121.6 to 165.7 nm (ref. 30-23). Because almost all minerals are opaque in the spectral region to which the UVS is sensitive, body color plays a small role in the spectral properties of minerals, and refractive index effects probably dominate. Alternatively, metallic sputtering produced by solar wind impact (ref. 30-24) may coat the surface and create the observed grayness in the lunar samples. However, the laboratory-measured albedo is not inconsistent with the assumption that the refractive index, and therefore the mineralogical character of the lunar material, is the factor that controls the far ultraviolet albedo.

Figure 30-6 shows a spectrum obtained from the lunar surface near the subsolar point. The very substantial signals shown, combined with the rocket measurements described previously, permit an accurate measurement of the lunar albedo in the spectral range 118 to 168 nm. This in situ albedo measurement agrees very well with the 2.2-percent value observed in the laboratory.

Figure 30-7 shows the signal at 147 nm and its variation with lunar longitude during one albedo pass (revolution 28). This curve agrees closely with the behavior of the lunar albedo in the visible region as analyzed by Hapke (ref. 30-25). Figure 30-8 is a plot of the data shown in figure 30-7 divided by the Hapke function for the visible region. Large variations near the terminator are caused by shadowing effects. If the visible Hapke function were the same as the far ultraviolet function, the curve in figure 30-8 would be independent of lunar longitude. In figure 30-9, the residual longitude effect shown in figure 30-8 has been removed by an arbitrary modification of the part of the visible Hapke function that might reasonably be expected to change in the far ultraviolet. Also plotted in figure 30-9 are the normalized data from the next passage across the illuminated surface (revolution 29).

Figure 30-9 demonstrates that the small variations in albedo with longitude are reproducible from one orbit to the next. The most spectacular demonstration is in the crater Neper, which shows an albedo peak in the center of the crater and minimums at the crater edges. However, many other variations are clearly identifiable and are shown to be reproducible in figure 30-9. As might be expected, the variations from point to point on the maria are less pronounced than in other areas. This effect can most clearly be seen in figure 30-7.

Analysis of other bright-side passes demonstrates that the maria show little albedo variation, but there are exceptions (e.g., the southern portion of Mare Crisium). Perhaps the most important observations at this stage of data reduction are that Neper Crater is an exception, that most craters are not distinguishable in the ultraviolet, and that most of the variations in the ultraviolet albedo seem to occur in regions that show little visible variations. Because the albedo observations may have important geological or mineralogical significance, data reduction and analysis is continuing, and a program of intercomparison with other lunar observations is planned.

During the passage of the unilluminated portion of the Moon, a reflected Lyman-alpha signal from solar system hydrogen was observed. Albedo variations were also observed in this signal and may be of particular importance because the signal includes areas that have not been studied in great detail. However, because the signal is so much weaker than the bright-side signal, little analysis of these data has been performed to date.

#### OTHER OBSERVATIONS

Twice during lunar orbit, when the spacecraft had just entered the shadow behind the terminator, the spacecraft was oriented so that ultraviolet zodiacal light emissions from the inner solar atmosphere could be observed. These data have only been preliminarily analyzed but generally support the ultraviolet zodiacal light observations by Orbiting Astronomical Observatory 2 (OAO-2) (ref. 30-26).

Several times during TEC, the UVS observed the Earth. Preliminary analysis (ref. 30-27) indicates that the data support the Orbiting Geophysical Observatory IV (OGO IV) orbital observations of the ultraviolet Earth airglow and provide an overall view of the Earth for comparison with other planets.

During TEC, the UVS was operated almost continuously to provide a detailed ultraviolet survey of our galaxy and to observe selected stellar spectra. A massive amount of data was obtained, but its analysis awaits viewing direction information in galactic

coordinates. Preliminary analysis of the spectra of isolated bright stars demonstrates that significant data were obtained. The observed ultraviolet spectral distributions agree with previous observations and provide the most precise measurement of absolute ultraviolet brightness obtained to date (ref. 30-28).

The full sky survey described previously also provided a measure of the distribution of solar system Lyman-alpha (121.6 nm) emission that is produced by resonance re-radiation of solar radiation by atomic hydrogen in the solar system. The survey also provided an opportunity to search for a geomagnetic tail of atomic hydrogen downwind from the Sun.

Once during TEC, the UVS was operating during a molecular hydrogen purge of the fuel cells that produced the ultraviolet spectrum shown in figure 30-10. This spectrum arises from absorption by molecular hydrogen of Lyman-beta and Lyman-gamma solar radiation and fluorescent re-radiation of this energy at longer wavelengths. From knowledge of the brightness of these solar emission features and of the Franck-Condon factors for molecular hydrogen, the expected fluorescence spectrum of molecular hydrogen has been calculated. This theoretical spectrum is shown in figure 30-11 where the intensity of one of the bands has been normalized to the experimental data of figure 30-10. The observed and calculated distributions agree very well. According to calculations, the observed spectral brightness gives a column density of approximately  $1 \times 10^{14}$  molecules/cm<sup>2</sup>, in close agreement with the calculated column density based on a nominal H<sub>2</sub> purge rate and the spacecraft geometry.

The H<sub>2</sub> spectrum provides an internal calibration of the UVS as a molecular hydrogen sensor and gives high reliability to the upper limit on H<sub>2</sub> at the subsolar point discussed in the section entitled "Lunar Atmosphere Observations" and shown in table 30-I. The H<sub>2</sub> observation is also important as an unambiguous means of identifying molecular hydrogen in the atmospheres of planets and comets (ref. 30-29).

## DATA FORMAT

The UVS data are contained on five magnetic tapes covering the following time periods:

<u>Tape number</u>	<u>Time period, computer time elapsed (CTE)</u>
1	81:37:30 to 95:27:21
2	110:51:58 to 188:55:06
3	188:55:18 to 234:54:00
4	235:04:08 to 273:08:39
5	273:09:19 to 299:31:22

Each 12-sec spectrometer scan is represented by one physical record containing 125 36-bit integer words. The record format is as follows:

<u>Word</u>	<u>Function</u>
0	Johns Hopkins "green" word (ignore)
1	Sync word = 65514
2	Sync word = 21
3	Motor step count (typically 4800)
4	Sync word = 21
5	Sync word = 65514
6 to 120	Data words
121	Original tape number
122	Record and word location on original
123	tape of first sync word
124	Time (CTE) in integer milliseconds of word 1

The data words represent the number of photoelectrons per 0.1 sec, and the wavelengths corresponding to each data word are given in table 30-II. Note that at large counting rates, the data words must be corrected for counter deadtime according to the following expression:

$$C_{\text{actual}} = \frac{C_{\text{obs}}}{1 - (C_{\text{obs}} \tau)} \quad (30-5)$$

where  $C_{\text{actual}}$  is the real count rate per 0.1 sec,  $C_{\text{obs}}$  is the observed count rate per 0.1 sec, and  $\tau = 1.83 \times 10^{-5}$ . Data records that have flagged data dropouts or do not match the sync words have been eliminated from the final tape.

To convert the actual count rate to brightness, use the expression

$$S = B \left( \frac{1 \times 10^{-6}}{4\pi} \right) \left[ \frac{A_s A_g (QT)}{F^2} \right] \quad (30-6)$$

where  $S$  is the signal in counts per second;  $B$  is the brightness in rayleighs;  $A_s$  is the slit area,  $1.14 \text{ cm}^2$ ;  $A_g$  is the grating area,  $104 \text{ cm}^2$ ; and  $F$  is the focal length, 50 cm. The product of quantum efficiency and transmission  $QT$  is given in table 30-III at 11 wavelengths, together with the instrument sensitivity in photoelectrons per second per rayleigh.

During the mission, the sensitivity of the instrument deteriorated because of continuous exposure to solar Lyman-alpha radiation reflected by the Moon. During TEC, the sensitivity was reduced to 83 percent of the value given in the calibration table.

#### REFERENCES

- 30-1. Fastie, William G.: The Apollo 17 Far Ultraviolet Spectrometer Experiment. *The Moon*, vol. 7, nos. 1/2, Mar./Apr. 1973, pp. 49-62.
- 30-2. Johnson, F. S.: Lunar Atmosphere. *Rev. Geophys. Space Phys.*, vol. 9, no. 3, Aug. 1971, pp. 813-823.
- 30-3. Johnson, Francis S.; Carroll, James M.; and Evans, Dallas E.: Lunar Atmosphere Measurements. *Proceedings of the Third Lunar Science Conference*, vol. 3, MIT Press (Cambridge, Mass.), 1972, pp. 2231-2242.
- 30-4. Hodges, R. R.; Hoffman, J. H.; and Evans, D. E.: Lunar Orbital Mass Spectrometer Experiment. Sec. 21 of the Apollo 16 Preliminary Science Report. NASA SP-315, 1972.
- 30-5. Hoffman, J. H.; Hodges, R. R., Jr.; and Evans, D. E.: Lunar Atmospheric Composition Results from Apollo 17. *Lunar Science IV* (Abs. of papers presented at the Fourth Lunar Science Conference (Houston, Tex.), Mar. 5-8, 1973), pp. 376-377.
- 30-6. Hodges, R. R.; Hoffman, J. H.; Yeh, T. T. J.; and Chang, G. K.: Orbital Search for Lunar Volcanism. *J. Geophys. Res.*, vol. 77, no. 22, Aug. 1, 1972, pp. 4079-4085.
- 30-7. Hodges, R. R.; Hoffman, J. H.; Johnson, F. S.; and Evans, D. E.: Composition and Dynamics of Lunar Atmosphere. *Proceedings of the Fourth Lunar Science Conference*, Pergamon Press (New York), Dec. 1973.
- 30-8. Chamberlain, J. W.: Planetary Coronae and Atmospheric Evaporation. *Planet. Space Sci.*, vol. 11, no. 8, Aug. 1963, pp. 901-960.
- 30-9. Thomas, G. E.; and Krassa, R. F.: OGO 5 Measurements of the Lyman Alpha Sky Background. *Astron. Astrophys.*, vol. 11, no. 2, Apr. 1971, pp. 218-233.
- 30-10. Barth, Charles A.: Planetary Ultraviolet Spectroscopy. *Appl. Optics*, vol. 8, no. 7, July 1969, pp. 1295-1304.
- 30-11. Fairfield, D. H.: Average and Unusual Locations of the Earth's Magnetopause and Bow Shock. *J. Geophys. Res.*, vol. 76, no. 28, Oct. 1, 1971, pp. 6700-6717.

- 30-12. Neugebauer, M.; Snyder, C. W.; Clay, D. R.; and Goldstein, B. E.: Solar Wind Observations on the Lunar Surface with the Apollo-12 ALSEP. Planet. Space Sci., vol. 20, no. 2, Oct. 1972, pp. 1577-1591.
- 30-13. Leich, D. A.; Tombrello, T. A.; and Burnett, D. G.: The Depth Distribution of Hydrogen in Lunar Materials. Lunar Science IV (Abs. of papers presented at the Fourth Lunar Science Conference (Houston, Tex.) March 5-8, 1973), pp. 463-465.
- 30-14. Fleischer, Robert L.; and Hart, Howard R., Jr.: Surface History of Lunar Soil and Soil Columns. Lunar Science IV (Abs. of papers presented at the Fourth Lunar Science Conference (Houston, Tex.), Mar. 5-8, 1973), pp. 251-253.
- 30-15. Geiss, J.; Buehler, F.; Cerutti, H.; Eberhardt, P.; and Filleux, Ch.: Solar Wind Composition Experiment. Sec. 14 of the Apollo 16 Preliminary Science Report. NASA SP-315, 1972.
- 30-16. Siscoe, G. L.; and Mukherjee, N. R.: Upper Limits on the Lunar Atmosphere Determined from Solar-Wind Measurements. J. Geophys. Res., vol. 77, no. 31, Nov. 1, 1972, pp. 6042-6051.
- 30-17. Gott, J. Richard, III; and Potter, A. E., Jr.: Lunar Atomic Hydrogen and Its Possible Detection by Scattered Lyman- $\alpha$  Radiation. Icarus, vol. 13, 1970, pp. 202-206.
- 30-18. Manka, R. H.; and Michel, F. C.: Lunar Atmosphere as a Source of Lunar Surface Elements. Proceedings of the Second Lunar Science Conference, vol. 2, MIT Press (Cambridge, Mass.), 1971, pp. 1717-1728.
- 30-19. Hodges, R. R.: Helium and Hydrogen in the Lunar Atmosphere. J. Geophys. Res., vol. 78, 1973.
- 30-20. Hoffman, J. A.; Hodges, R. R., Jr.; and Evans, D. E.: Lunar Atmosphere Composition Results from Apollo 17. Proceedings of the Fourth Lunar Science Conference, Pergamon Press (New York), Dec. 1973.
- 30-21. Spitzer, L.; Drake, J. F.; Jenkins, E. B.; Morton, D. C.; et al.: Spectrophotometric Results from the Copernicus Satellite. IV, Molecular Hydrogen in Interstellar Space. Astrophys. J. Letters, vol. 181, May 1, 1973, pp. L116-L121.

- 30-22. Hollenbach, D.; and Salpeter, E. E.: Surface Recombination of Hydrogen Molecules. *Astrophys. J.*, vol. 163, no. 1, Jan. 1971, pp. 155-164.
- 30-23. Lucke, R. L.; Henry, R. C.; and Fastie, W. G.: Far Ultraviolet Reflectivity of Lunar Dust Samples: Apollo 11, 12, and 14. *Astron. J.*, vol. 78, no. 3, Apr. 1973, pp. 263-266.
- 30-24. Hapke, B. W.; Cohen, A. J.; Cassidy, W. A.; and Wells, E. N.: Solar Radiation Effects on the Optical Properties of Apollo 11 Samples. *Proceedings of the Apollo 11 Lunar Science Conference*, vol. 3, Pergamon Press (New York), 1970, pp. 2199-2212.
- 30-25. Hapke, Bruce W.: A Theoretical Photometric Function for the Lunar Surface. *J. Geophys. Res.*, vol. 68, no. 15, Aug. 1, 1963, pp. 4571-4586.
- 30-26. Lillie, C. F.: OAO-2 Observations of the Zodiacal Light. *The Scientific Results from the Orbiting Astronomical Observatory (OAO-2)*. NASA SP-310, 1972, pp. 95-108.
- 30-27. Feldman, P. D.; Fastie, W. G.; Henry, R. C.; Moos, H. W.; et al.: Far Ultraviolet Observations of the Earth's Airglow from Apollo 17. Paper presented at 54th Annual Meeting, Am. Geophys. Union (Washington, D.C.), Apr. 1972.
- 30-28. Henry, R. C.; Moos, H. W.; Fastie, W. G.; and Weinstein, A.: Low-Resolution Ultraviolet Spectroscopy of Several Stars. Paper presented at 16th Plenary Meeting, COSPAR (Konstanz, W. Germany), June 1973.
- 30-29. Feldman, P. D.; and Fastie, W. G.: Fluorescence of Molecular Hydrogen Excited by Solar Extreme Ultraviolet Radiation. *Astrophys. J. (Letters)*, vol. 185, Oct. 15, 1973, pp. L101-L104.
- 30-30. Fastie, William G; Feldman, Paul D.; Henry, Richard C.; Moos, H. Warren; et al.: Ultraviolet Spectrometer Experiment. Sec. 23 of the Apollo 17 Preliminary Science Report. NASA SF-330, 1973.

ORIGINAL PAGE IS  
OF POOR QUALITY

TABLE 30-1.- ULTRAVIOLET SPECTROMETER OBSERVATIONS

Species	Energy-state transition	Wavelength, nm	Resonance g-factor, photon/sec/molecule	Mode of observation <sup>a</sup>	Sensitivity, photoelectrons/sec/R	Observed surface density, atoms/cm <sup>3</sup>
Atomic						
H	2s - 2p	C 121.6	2.2 x 10 <sup>-3</sup>	C	75	<10
O	3p - 3s	130.4	d <sub>8</sub> x 10 <sup>-6</sup>	B	99	d <sub>8</sub> <100
N	4s - 4p	120.0	d <sub>9</sub> x 10 <sup>-7</sup>	B	70	d <sub>9</sub> <1200
C	3p - 3po	165.7	d <sub>2,0</sub> x 10 <sup>-5</sup>	B	25	d <sub>2,0</sub> <120
Kr	1s - 3p	123.6	1.6 x 10 <sup>-7</sup>	A	85	<16 000
Xe	1s - 3p	147.0	1.5 x 10 <sup>-6</sup>	A	75	<1 000
Molecular						
H <sub>2</sub>	1 <sub>u</sub> <sup>+</sup> - X 2 <sub>g</sub> <sup>+</sup> (6,9)	146.2	4.0 x 10 <sup>-8</sup>	B	75	<6 000
CO	A 1 <sub>u</sub> <sup>+</sup> - X 1 <sub>g</sub> <sup>+</sup> (1,0)	151.0	7.5 x 10 <sup>-8</sup>	B	60	<20 000

<sup>a</sup>See figure 30-2.

<sup>b</sup>At the subsolar point, except for H, krypton (Kr), and Xe, which are terminator values. The entries in this column are based on the spectral feature not exceeding 1 standard deviation in the counting rate.

<sup>c</sup>Lyman alpha.

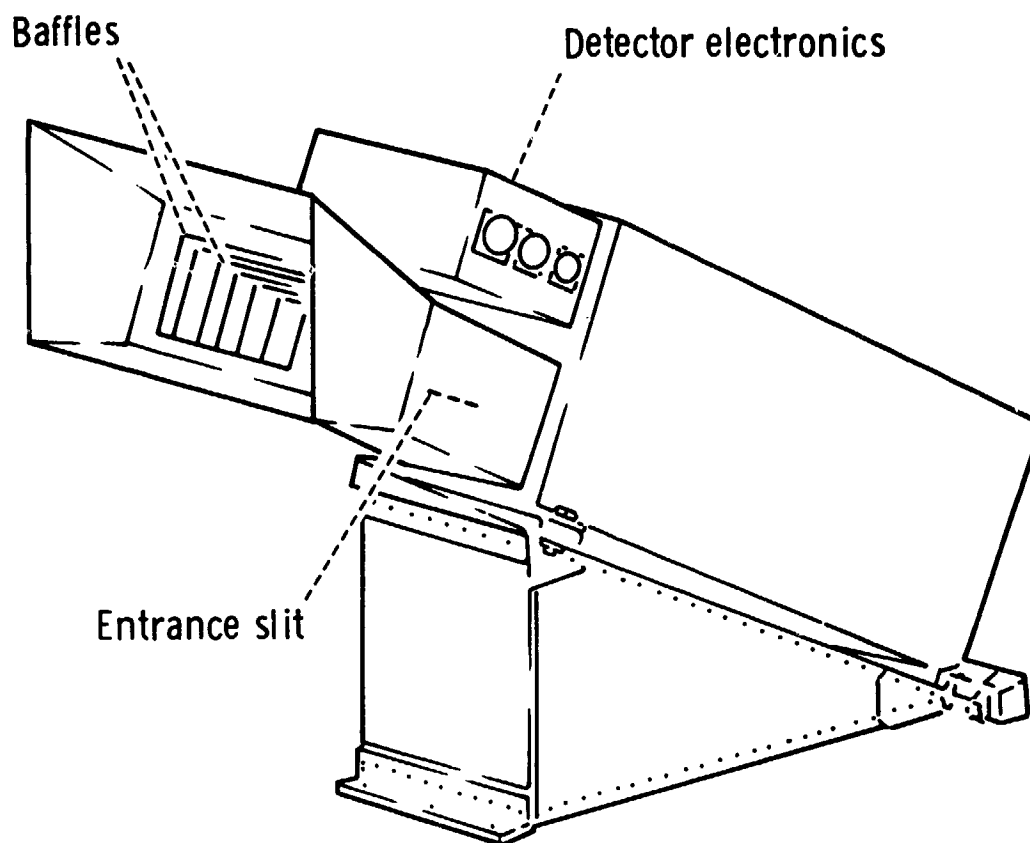
<sup>d</sup>Values in the Apollo 17 Preliminary Science Report (ref. 30-30) and in reference 30-1 have been reevaluated using more recent solar flux data.

TABLE 30-II.- WAVELENGTHS CORRESPONDING TO EACH 0.1-SEC WORD

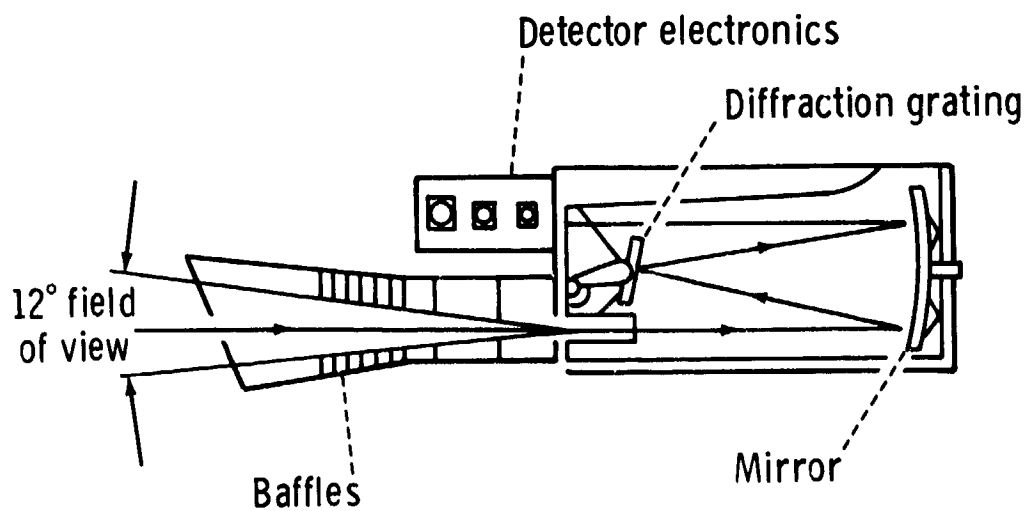
Word no.	Wavelength interval, nm		Word no.	Wavelength interval, nm	
	From -	To -		From -	To -
6	118.400	118.409	66	143.997	144.357
7	118.409	118.905	67	144.357	144.595
8	118.905	119.450	68	144.595	144.908
9	119.450	119.767	69	144.808	144.557
10	119.767	119.946	70	144.967	145.144
11	119.946	120.133	71	145.144	145.316
12	120.133	120.299	72	145.316	145.454
13	120.299	120.522	73	145.454	145.634
14	120.522	120.738	74	145.634	145.808
15	120.738	120.935	75	145.808	145.959
16	120.935	121.114	76	145.959	146.141
17	121.114	121.285	77	146.141	146.318
18	121.285	121.461	78	146.318	146.464
19	121.461	121.627	79	146.464	146.603
20	121.627	121.788	80	146.603	146.744
21	121.788	121.972	81	146.744	146.913
22	121.972	122.148	82	146.913	147.054
23	122.148	122.312	83	147.054	147.251
24	122.312	122.480	84	147.251	147.387
25	122.480	122.638	85	147.387	147.535
26	122.638	122.776	86	147.535	147.694
27	122.776	122.916	87	147.694	147.853
28	122.916	123.040	88	147.853	148.022
29	123.040	123.211	89	148.022	148.196
30	123.211	123.403	90	148.196	148.378
31	123.403	123.571	91	148.378	148.567
32	123.571	123.711	92	148.567	148.742
33	123.711	123.867	93	148.742	148.887
34	123.867	124.017	94	148.887	149.015
35	124.017	124.131	95	149.015	149.289
36	124.131	124.224	96	149.289	149.883
37	124.224	124.315	97	149.883	150.648
38	124.315	124.683	98	150.648	151.446
39	124.683	125.410	99	151.448	152.222
40	125.410	126.182	100	152.222	152.978
41	126.182	126.987	101	152.978	153.681
42	126.987	127.711	102	153.681	154.402
43	127.711	128.399	103	154.402	155.092
44	128.399	129.164	104	155.092	155.821
45	129.164	129.870	105	155.821	156.591
46	129.870	130.616	106	156.591	157.371
47	130.616	131.383	107	157.371	158.071
48	131.383	132.109	108	158.071	158.784
49	132.109	132.826	109	158.784	159.589
50	132.826	133.543	110	159.589	160.334
51	133.543	134.209	111	160.334	161.074
52	134.209	134.998	112	161.074	161.778
53	134.998	135.722	113	161.778	162.505
54	135.722	136.376	114	162.505	163.287
55	136.376	137.059	115	163.287	163.987
56	137.059	137.790	116	163.987	164.764
57	137.790	138.513	117	164.764	165.535
58	138.513	139.216	118	165.535	166.247
59	139.216	139.908	119	166.247	166.972
60	139.908	140.643	120	166.972	167.157
61	140.643	141.363			
62	141.363	142.087			
63	142.087	142.793			
64	142.793	143.484			
65	143.484	143.997			

TABLE 30-III.- CALIBRATION DATA

Wavelength, <sup>a</sup> nm	QT	Photoelectrons/sec/R
119.2	0.0163	61.5
121.6	.0196	74
128.0	.0263	99
133.6	.0251	95
139.5	.0233	88
146.3	.0200	75.5
151.8	.0156	59
158.2	.0093	35
160.8	.0079	29.8
163.9	.0070	26.4
165.5	.0078	29.4



(a) Isometric view of the instrument mounted on stand.



(b) Optical ray diagram.

Figure 30-1.- Ultraviolet spectrometer.

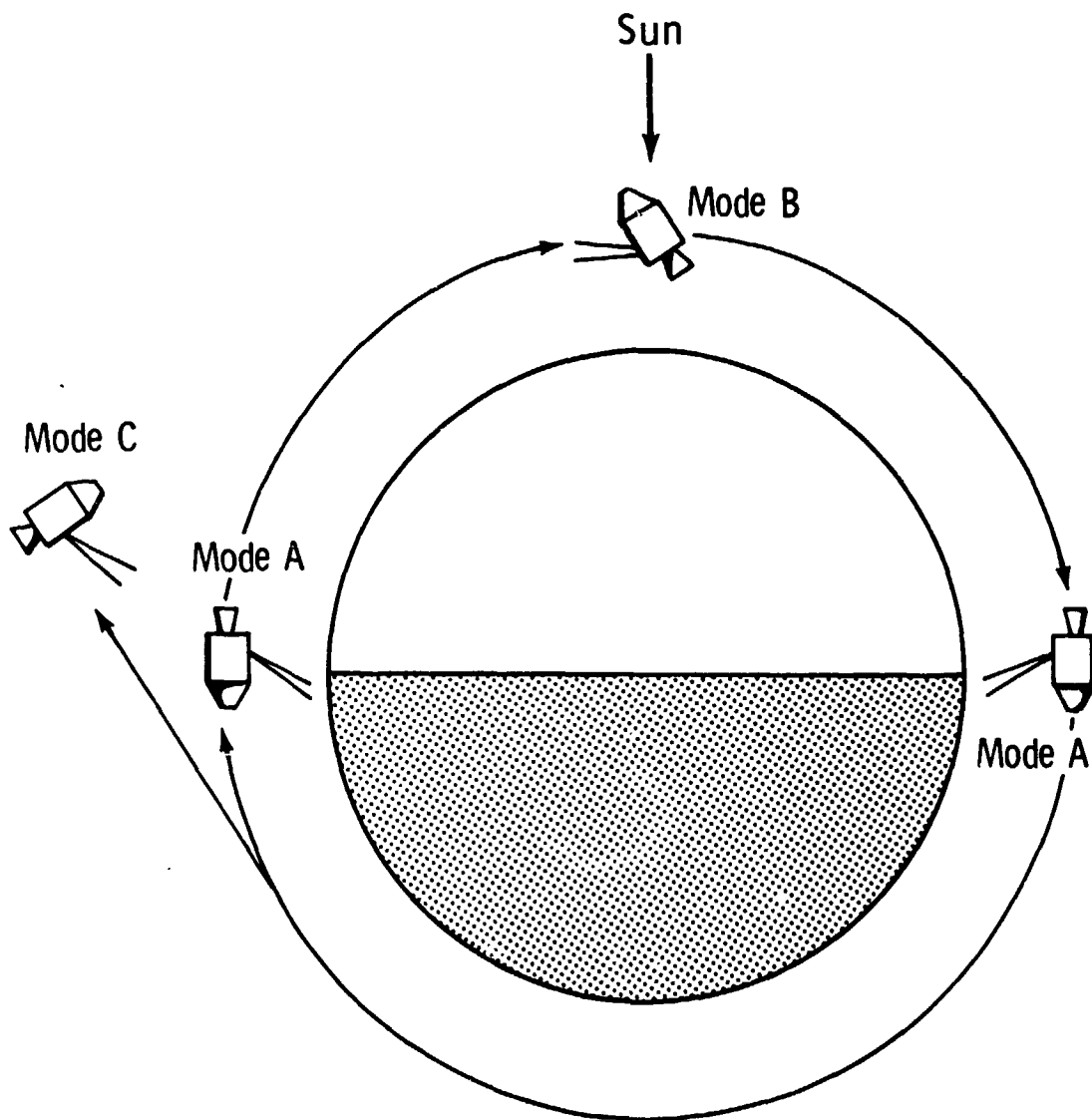


Figure 30-2.- Schematic representation of the modes of observation of the lunar atmosphere. Mode A, the principal orbital mode, consists of observation through the illuminated atmosphere above the terminator against the dark side of the Moon. In mode B, a contingency orbital mode, the spectrometer is pointed at a fixed point in space, and the line of sight extends through a tangential slice of illuminated atmosphere. Mode C was used immediately after transearth injection. The Apollo 17 UVS has a field of view of  $12^\circ$  by  $12^\circ$  and looks forward  $23^\circ$  relative to the normal to the spacecraft longitudinal axis.

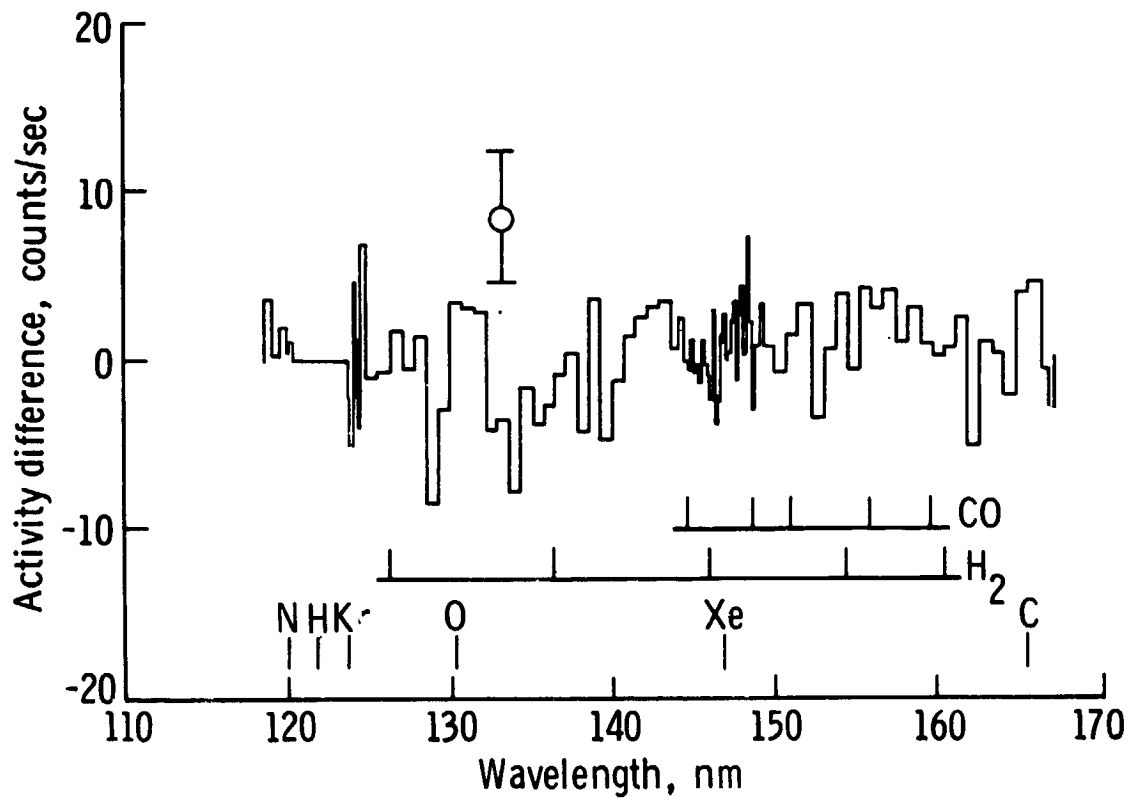
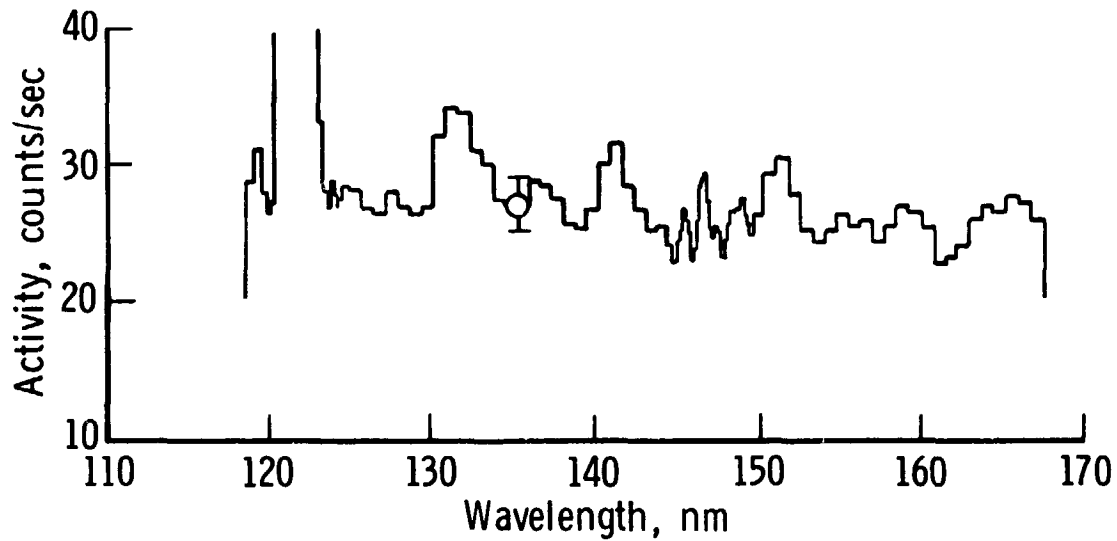
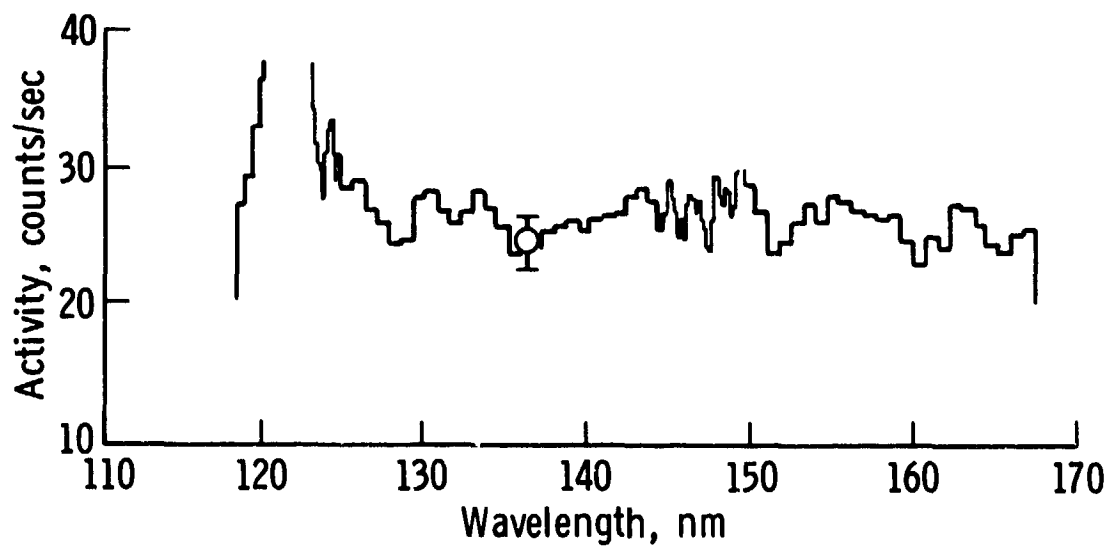


Figure 30-3.- The average of 70 spectra obtained during a tangential mode (mode B in fig. 30-2) observation with the sky background (observed during TEC) subtracted. The wavelengths of the principal emission features expected are indicated. The error bar represents 1 standard deviation in the observed counting rate.

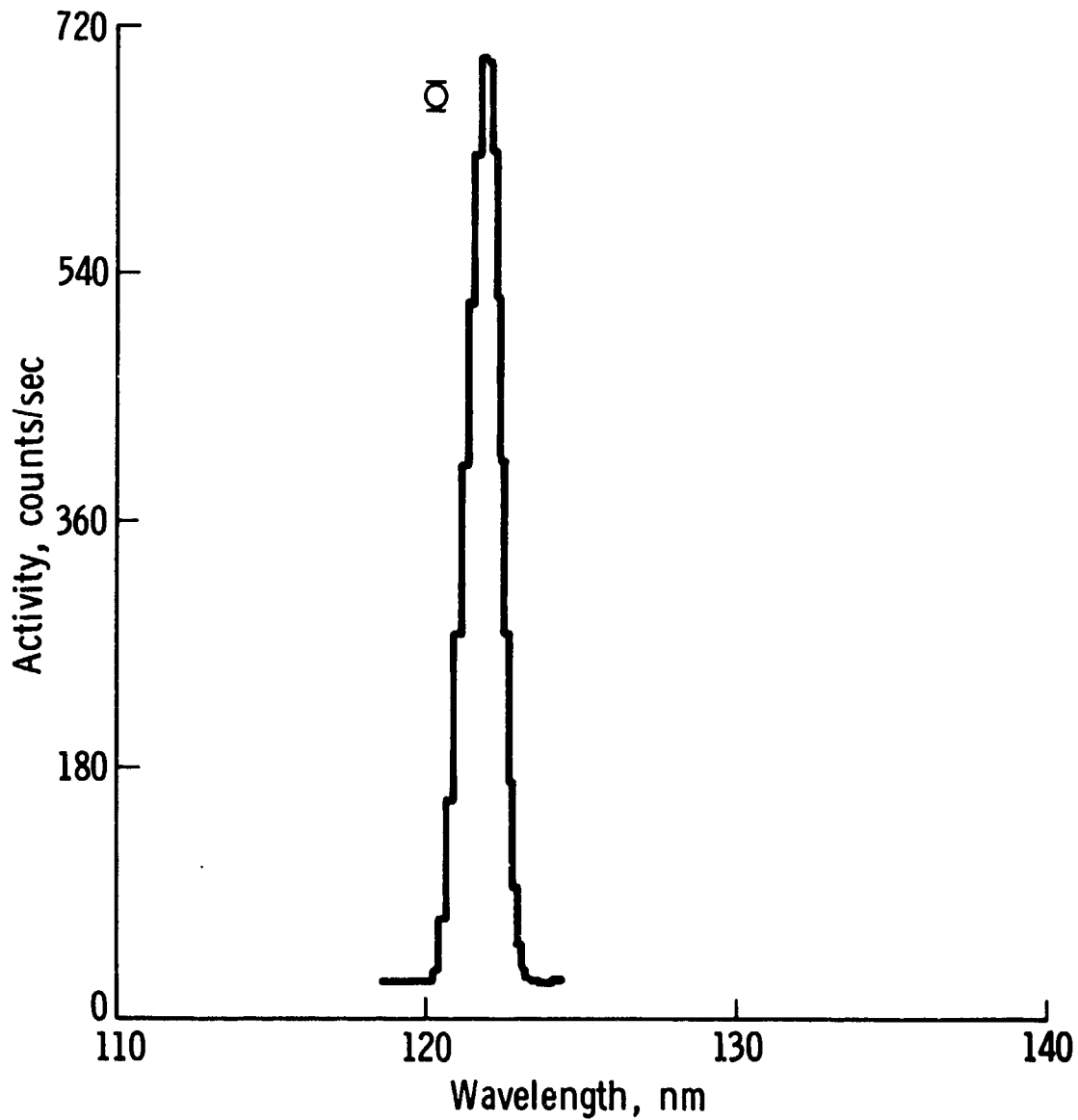


(a) Spectrum obtained 2 hr after lunar module landing, showing mild indication of emission features at 130.4 nm (O) and 151 nm (□).



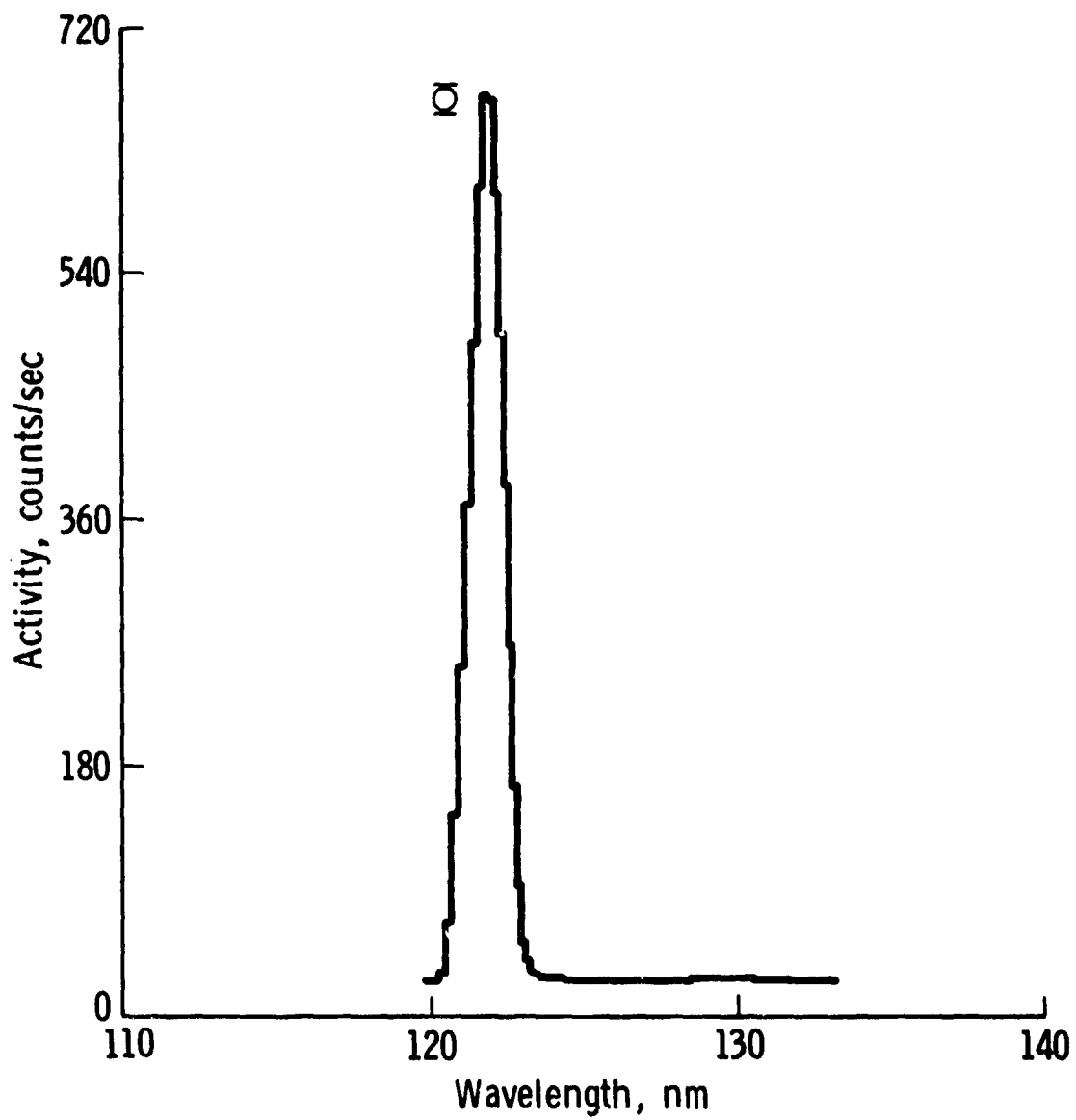
(b) Spectrum obtained 4 hr after lunar module landing, showing no emission features.

Figure 30-4.- Comparison of UVS spectra. The error bars represent 1 standard deviation in the observed counting rate.



(a) Signal observed just beyond the near-side terminator; coverage extends from  $270^\circ$  to  $255^\circ$ .

Figure 30-5.- Comparison of Lyman-alpha signals obtained on revolution 38. The signals are caused by reflected solar atmosphere radiation; the difference between the signals is due to asymmetry in the reflected solar radiation, not to a lunar H atmosphere. The error bars represent 1 standard deviation in the observed counting rate.



(b) Signal observed when spacecraft was in full shadow;  
coverage extends from 255° to 240°.

Figure 30-5.- Concluded.

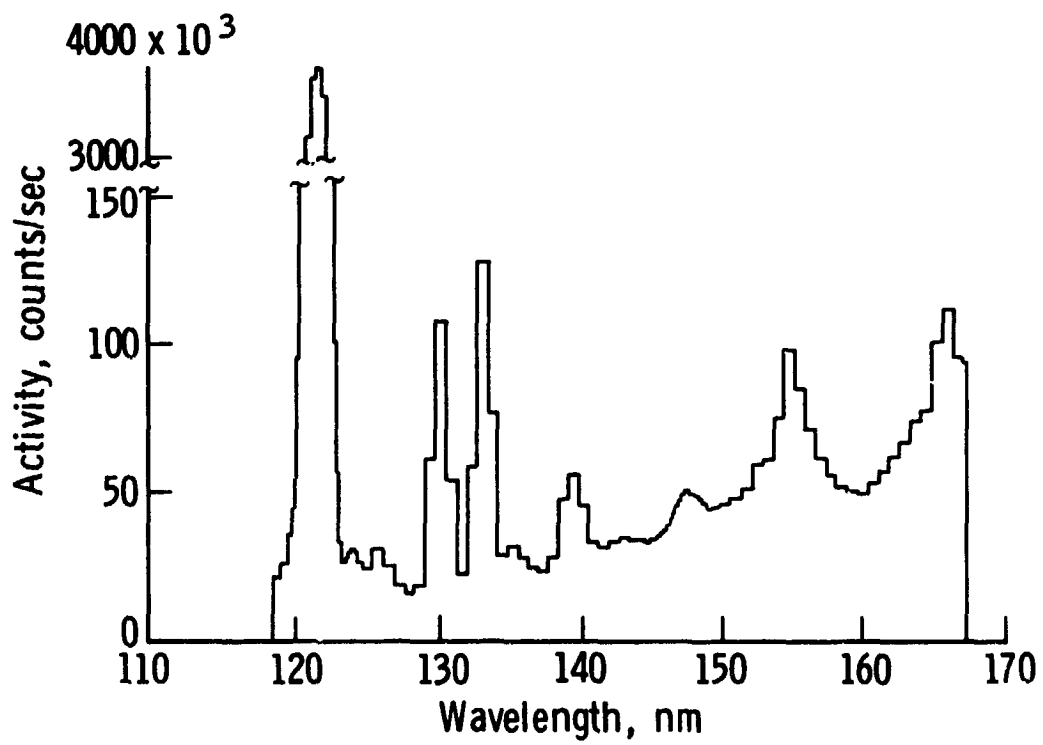


Figure 30-6.- Spectrum obtained from UVS observation of the lunar surface near the subsolar point.

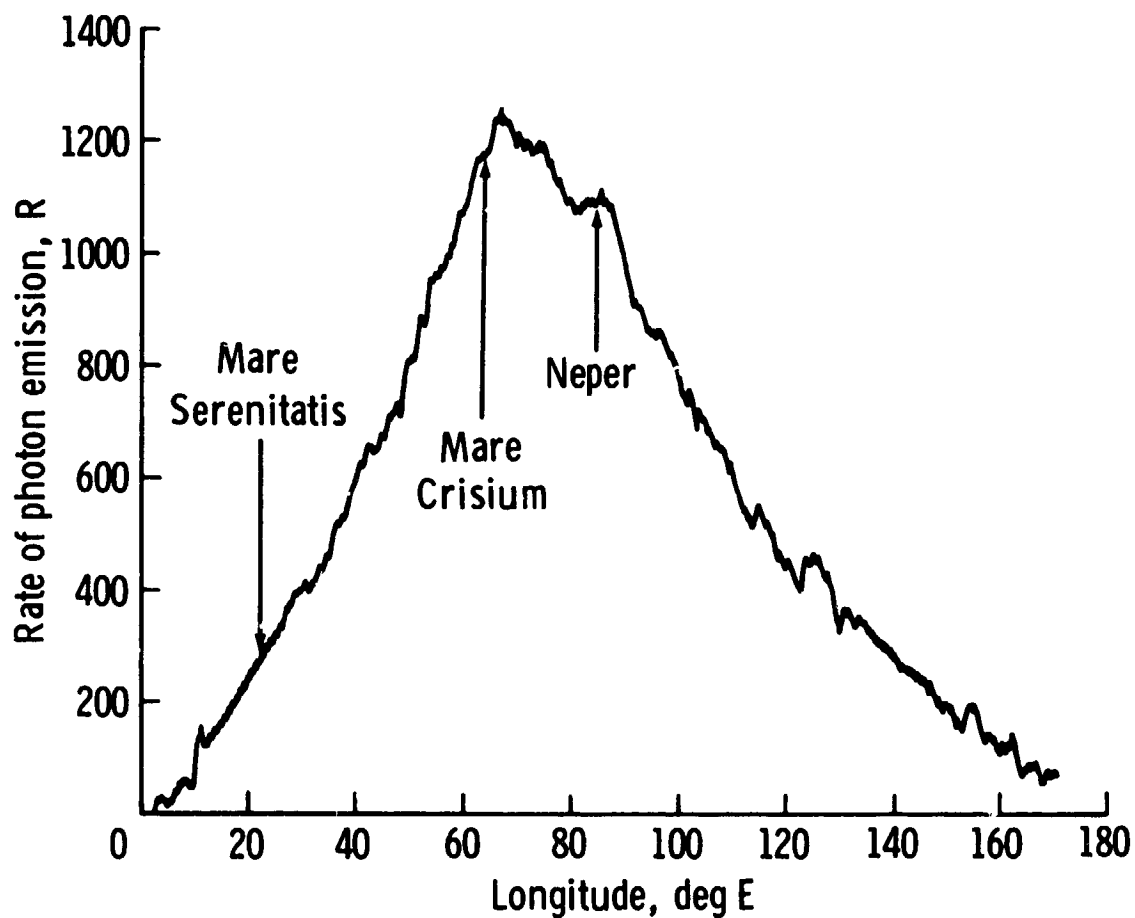


Figure 30-7.- Variation of brightness with lunar longitude for the signal observed at 147 nm (fig. 30-6) as the spacecraft traversed the illuminated lunar surface on revolution 28.

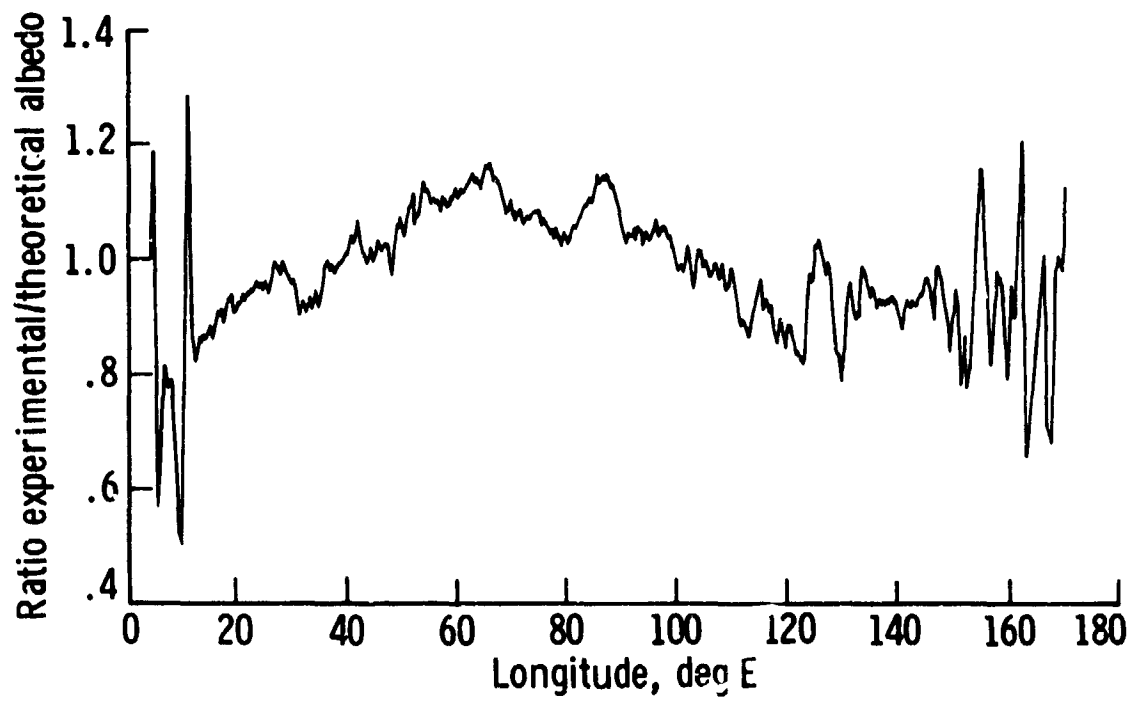
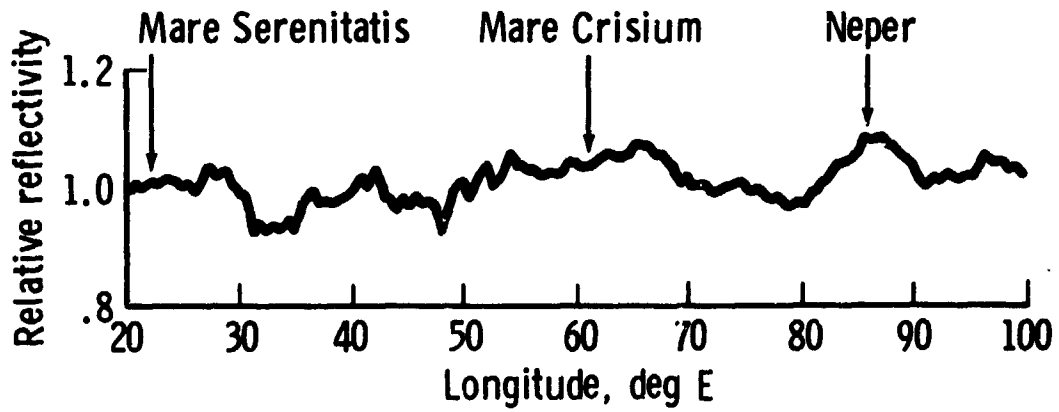
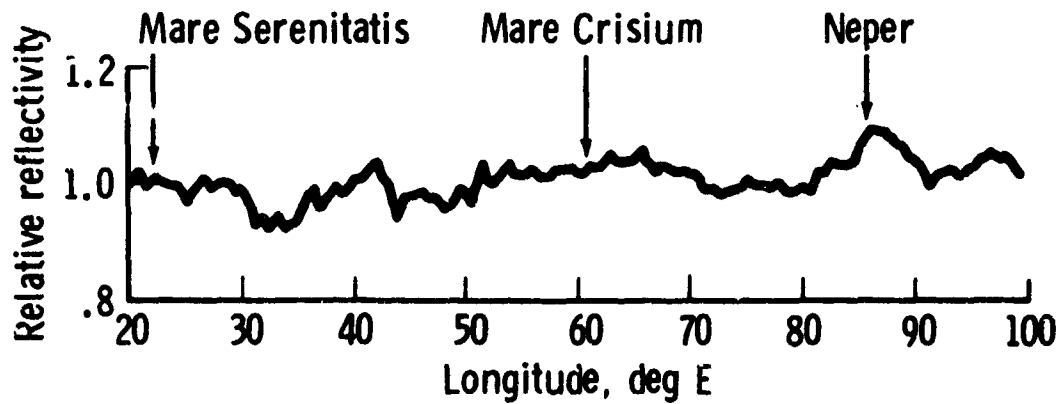


Figure 30-8.- Transit data of figure 30-7 divided by visible Hapke function.



(a) Revolution 28.



(b) Revolution 29.

Figure 30-9.- Lunar transit data divided by far ultraviolet Hapke function.

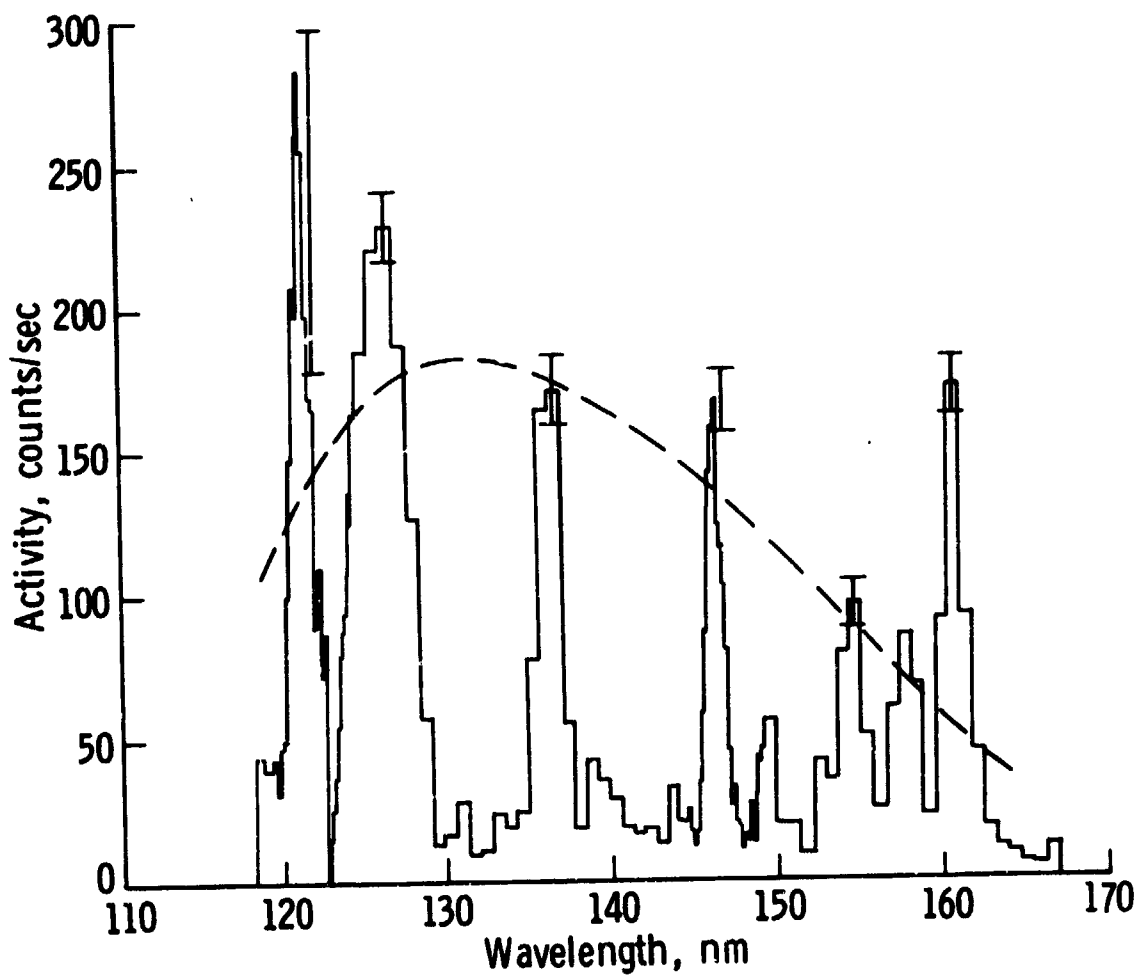


Figure 30-10.- Spectrum obtained in TEC during molecular hydrogen purge of fuel cells. The dashed curve represents a brightness of 2 R. The error bars represent 1 standard deviation in the observed counting rate.

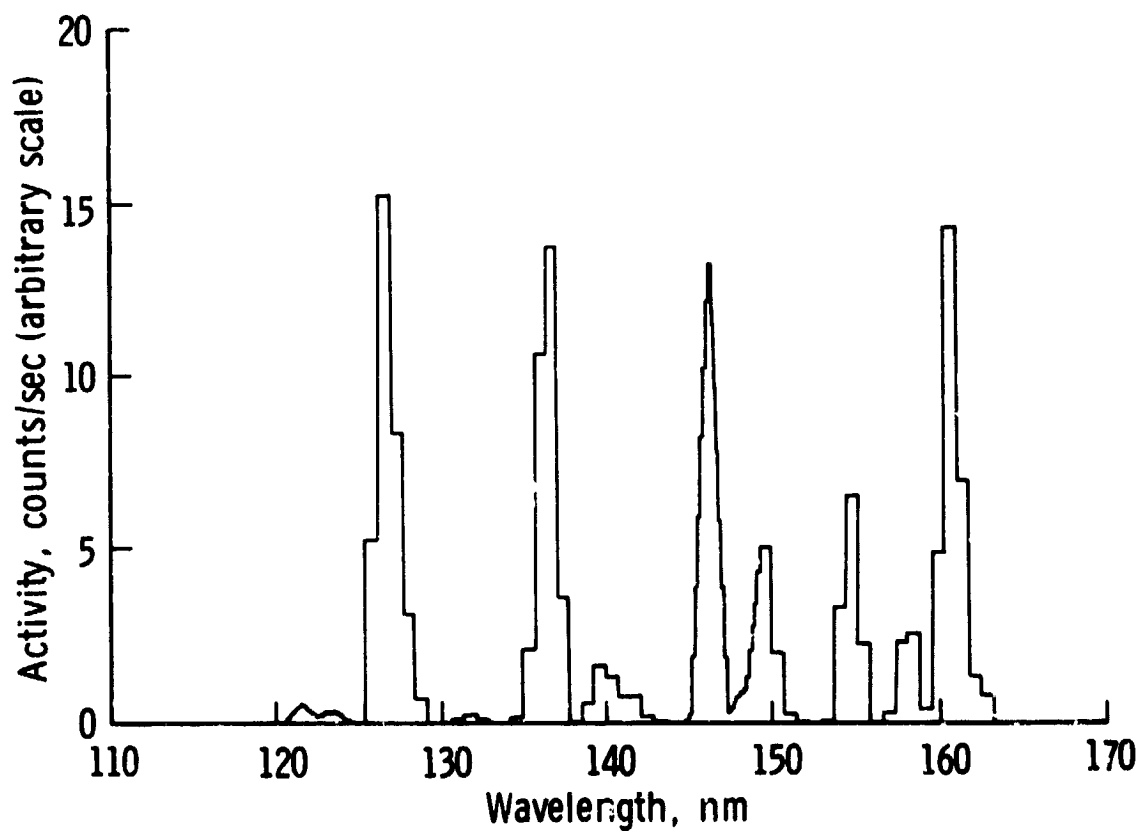


Figure 30-11.- Calculated fluorescence spectrum of molecular hydrogen excited by far ultraviolet solar radiation. (Intensity of one band normalized to experimental data (fig. 30-10).)

31. BISTATIC-RADAR EXPERIMENT (NASA EXPERIMENT S-170)

NSSDC IDENTIFICATION NUMBERS:

APOLLO 14	71-008A-04
APOLLO 15	71-063A-14
APOLLO 16	72-031A-12



ORIGINAL PAGE IS  
OF POOR QUALITY

31-1

REPRODUCIBILITY OF THE  
ORIGINAL PAGE IS POOR

CONTENTS - SECTION 31

	Page
SYNOPSIS OF OBSERVATIONS . . . . .	31-4
DATA COLLECTION, PROCESSING, AND REDUCTION . . . . .	31-5
APPENDIX 31-A — CARRIER SUPPRESSION ALGORITHM . . . . .	31-31
APPENDIX 31-B — RELATIONSHIP BETWEEN THE COHERENCY MATRIX AND OTHER SPECIFICATIONS OF POLARIZATION . . . . .	31-36
APPENDIX 31-C — JM DOPTRACK TAPE FORMATS . . . . .	31-40
APPENDIX 31-D — MATRIX CORRECTION FACTORS . . . . .	31-46
APPENDIX 31-E — INTEGRAL TAPE FORMAT . . . . .	31-48
APPENDIX 31-F — XDS SIGMA 5 MACHINE IMAGES . . . . .	31-67
APPENDIX 31-G — CROSS-REFERENCE TABLE FOR JM DOPTRACK/ INTEGRAL TAPE TRAJECTORY PARAMETERS . . . . .	31-69
APPENDIX 31-H — COORDINATE TRANSFORMATIONS . . . . .	31-71
REFERENCES . . . . .	31-79

### 31. BISTATIC-RADAR EXPERIMENT

The Apollo bistatic-radar experiment was performed during the lunar orbit phase of the Apollo 14, 15, and 16 flights. The experiment had two unique aspects: no special equipment was placed on board the Apollo vehicles and carried to the Moon, and principal observations were performed on the ground. Radiofrequency transmissions from the orbiting command and service module (CSM) were directed toward the Moon and received on the Earth after reflection from the lunar surface. Two wavelengths 13 cm (2287.5 MHz, S-band) and 116 cm (259.7 MHz, VHF), were used. The best data were obtained during periods when the spacecraft was maneuvered to maintain a predetermined, although changing, attitude with respect to the Earth and the Moon. During these periods, data were obtained at the two wavelengths simultaneously. Data were also obtained at the 116-cm wavelength during periods of inertial hold and scientific instrument module (SIM) bay attitude maneuvers. Data were received at two sites on the Earth: the NASA Deep Space Network (DSN) 64-m antenna facility located near Barstow, California, and the Stanford Research Institute (SRI)/Stanford University 46-m antenna facility located on the campus of Stanford University, Stanford, California. The NASA facility was used for reception of the 13-cm data; the Stanford facility, for the 116-cm data. In both cases, the elements of the receiving system critical to the experimental objectives were under direct control of the experimenters. At the DSN, a signal conditioning unit designed and constructed at Stanford was inserted as a critical series element in the data receiving system and used to set system bandwidths, levels, and timing information for the analog recording system. Input signal levels, bandwidths, and frequencies to the signal conditioning unit from the DSN were specified and monitored in real time during data collection by the experimenters. Data were reduced at the Stanford Sigma 5 Real-Time Computation Facility. With two exceptions (note 4d of fig. 31-1 and appendix 31-A), identical programs and procedures were used for 13- and 116-cm data. Also, with one exception, the same programs were used for all three flights. (See the section entitled "Subtask 2 - Sampling.") However, certain parameters, defined elsewhere in the report, were varied for data at the two wavelengths.

Good data were obtained from the three flights. The data sets include the simultaneous 13- and 116-cm observations, but not the 116-cm data obtained in the inertial hold and SIM-bay attitudes. Data are given in two forms.

1. A complete set of observations reduced to short-time averages of the electromagnetic wave spectra for the 13- and 116-cm observations is provided. These observations have been corrected for instrumental effects and are unedited. Tapes containing these data are referred to as JM doptrack tapes. The observations have been merged with trajectory data obtained from the NASA Lyndon B. Johnson Space Center (JSC) in Houston, and with certain ancillary data computed from the trajectory.

2. A complete set of reduced data records, called integral tapes, obtained from the JM doptrack tapes are provided. The integral tapes describe certain properties of the JM doptrack data, such as moments of the echo spectra, and inferred properties of the lunar surface, such as rms slopes.

A one-to-one correspondence exists between the integral data and the JM doptrack data; an interested investigator either may use the reduced data records given on the integral tapes or may use the JM doptrack tapes to verify the reduction procedure and perform additional reductions.

Data collection and reduction systems are described in detail. Cautions to the data user and descriptions of tape contents and formats for JM doptrack and integral tapes are given. However, no particular attempt to explain the motivation for the overall data reduction procedures is made, except as it affects individual steps not described elsewhere. A more general understanding of the experiment and of its goals, limitations, and preliminary results may be obtained from references 31-1 to 31-5.

#### SYNOPSIS OF OBSERVATIONS

A synopsis of the observations is given in table 31-I. Parameters given include the Apollo mission number and the lunar revolution, counted from lunar orbit insertion, during which the experiment was performed. The wavelengths of electromagnetic radiation from the CSM of 13 and 116 cm correspond to frequencies of 2287.5 and 259.7 MHz, respectively. The CSM antenna used and the mode chosen are given. The Apollo 14 experiment required compromise in spacecraft attitude to accommodate patterns from two fixed antennas. Also included in table 31-I are one-half power antenna beam widths (3-dB beam width), polarization and gain of the CSM antenna, CSM transmitted power, and system temperature. The last parameter is the equivalent temperature of the receiving system on Earth when looking at cosmic background radiation perpendicular to the galactic plane.

## DATA COLLECTION, PROCESSING, AND REDUCTION

In figure 31-1, the flow of data through collection, processing, and reduction is shown. Annotations and notes (circled numbers) are brief comments or descriptive titles as guides for reference. The overall data flow is divided into 11 subtasks, indicated by horizontal brackets. General familiarity with analog-to-digital and digital techniques for data reduction and analysis is assumed. Critical data reduction parameters are given in table 31-II, and antenna parameters are given in table 31-III.

Each subtask description provides a general explanation of that subtask function. An attempt has been made to maintain independent description, with minimum reference to other functions. Highly technical details, such as magnetic tape formats and coordinate descriptions, are reserved for the appendixes. Thus, a careful reading of the subtask descriptions, in connection with figure 31-1, should provide a good overview of the data reduction process. The appendixes may be read later or consulted for details. Figure 31-1 should be studied carefully before repository data are used.

### Subtask 1 — Data Collection

Subtask 1 consists of data collection. Information on the 116- and 13-cm receivers and on critical bandwidths is given in the following paragraphs.

The 116-cm receiver.— The 116-cm receiver (fig. 31-2(a)) is a standard superheterodyne receiver. An unusual feature of this system is the summed second local oscillator signal used to produce offset 9.0- and 10.003-MHz intermediate-frequency signals. In operation, the 10.003-MHz channel was tuned to the downlink signal carrier and its accompanying echo, whereas the 9.0-MHz channel was tuned to the subcarrier signal displaced  $\pm 31.6$  kHz from the 259.7-MHz carrier. This procedure was adopted to provide frequency dispersive redundancy against locally generated interference at the main carrier frequency. The receiver passband characteristics are given in figure 31-3(a). However, all data given here were obtained through the main 10-MHz channel. Receiver outputs were multiplexed with standard frequency references and clock signals and recorded on analog tape. Parameters of the Stanford Research Institute 46-m dish are given in table 31-III.

The 13-cm receiver.— Standard superheterodyne techniques also are employed for the 13-cm receiver (fig. 31-2(b)). All 13-cm data were obtained from a phase-lock-loop signal tracking

system using manual tracking when the direct signal dropped below threshold of the phase-lock loop. The receiver passband characteristics are given in figure 31-3(b). Again, analog signals from the receiver output multiplexed with clock and reference frequencies were recorded. Parameters of the DSN 64-m dish are given in table 31-III.

Critical bandwidths.- The power spectral densities obtained at the receiver outputs for the three Apollo experiments with uniform power spectrum (white) noise input are given in figures 31-3(a) and 31-3(b). These curves were obtained in subtask 4 and were used in the data normalization. For the 116-cm system, additional checks made with coherent signals within  $\pm 5$  MHz either side of the 10-MHz intermediate frequency and within  $\pm 20$  MHz of the first intermediate frequency verified the absence of spurious responses that would not be detected by the noise calibration technique. Similar tests have been performed by the DSN and the experimenters at the 64-m facility. Thus, the curves (figs. 31-3(a) and 31-3(b)) accurately represent the receiver response to signals near the frequency to which the receivers were tuned. Image rejection in the 116-cm system was greater than 100 dB.

#### Subtask 2 — Sampling

In subtask 2, data were sampled by using standard techniques on the Stanford Sigma 5 Real-Time Computation Facility. Right circular and left circular polarization signal channels were sampled simultaneously in synchronism with the multiplexed time reference signals. Sampling was initiated at the start of an even 10-sec interval (UT2) by a start pulse derived from the recorded time code. The sampling programs were improved between the Apollo 15 and 16 experiments to obtain higher playback rates for the 13-cm data. (See fig. 31-1, note 4d.) With this exception, the same computer programs were used for reducing data from the three sets of observations. A small overlap was provided between subsequent sample data tapes. These overlaps were carried through the remainder of the data processing. Tape recorder playback levels were adjusted for equality between left circular and right circular polarization, using the controlled reference signal levels for calibration. The playback recorder electronics were equalized for the particular tape source (FR-1400A, FR-1400B, HP-3955B) before data from that source were sampled. Output from the data sampling process was stored on magnetic tape. The quantization level was 8 bits. The  $i$ th data sample generally will be denoted  $d_i$ ; data from the left circularly polarized antenna,  ${}_1d_i$ , and data from the right circularly polarized antenna,  ${}_2d_i$ .

### Subtask 3 — Conversion to Frequency Domain

In subtask 3, all data have been rendered in the frequency domain in the form of modified complex Fourier coefficients (ref. 31-6). A sequence of data samples was multiplicatively weighted with a sine-squared (Hanning) data window and then Fourier analyzed using fast Fourier transform techniques. Analytically, the data samples were grouped, separately for each polarization, according to

$$d_j^n = \hat{d}_i \quad (31-1)$$

where  $i = nN + j$ ,  $j \leq N$ ;  $n, N, j$  positive integers or zero. The modified complex Fourier coefficients are

$$f_k^n = \sum_{j=0}^{N-1} \sin^2\left(\frac{2\pi}{N}j + \frac{\pi}{N}\right) d_j^n e^{-i\frac{2\pi}{N}jk} \quad (31-2)$$

where  $i = \sqrt{-1}$ ,  $0 \leq k \leq (N - 1)$ . In the Apollo data reduction programs, the number of analysis bins  $N$  was either 1024 or 2048. (See table 31-II.) Each set of coefficients corresponds to a time interval  $T = N \cdot (\text{sampling interval})$ . (See table 31-II for values.) The outputs of the transformation are the values of  $f_k^n$  (eq. (31-2)).

### Subtask 4 — Generation of Coherency Matrix

The coherency matrix (ref. 31-7) was determined directly from the function  $f_k^n$  by forming the summed products

$$\begin{bmatrix} \sum_{n=1}^L |1f_k^n|^2 & \sum_{n=1}^L 1f_k^n 2f_k^{n*} \\ \sum_{n=1}^L 1f_k^{n*} 2f_k^n & \sum_{n=1}^L |2f_k^n|^2 \end{bmatrix} \quad (31-3)$$

where \* denotes a complex conjugate. Each sum is a function of the frequency index k. To compensate for the nonuniform effects of the receiving system filters, the following is formed.

$$\left. \begin{aligned} \hat{q}_k^2 &= \langle q_k^2 \rangle = \sum_{n=1}^M |q_k^n|^2 \\ \hat{q}_k^2 &= \langle q_k^2 \rangle = \sum_{n=1}^M |q_k^n|^2 \end{aligned} \right\} \quad (31-4)$$

where  $q_k^n = f_k^n$  for periods with signal absent. The functions  $\hat{q}_k^2$  and  $\hat{q}_k^2$  are the receiving system output power spectra for a noise input. The upper bound M was chosen to reduce the fluctuations in  $\hat{q}_k^2$  to a small value. Typically,  $M \approx 10^4$ , for which  $\hat{q}_k^2$  is determined to approximately 1 percent. The coherency matrix, corrected for receiver power transfer characteristics, is

$$J_k = \begin{bmatrix} J_{11} & J_{12} \\ J_{21} & J_{22} \end{bmatrix} \quad (31-5)$$

where

$$\left. \begin{aligned}
 J_{11} &= \frac{1}{1\hat{q}_k^2} \sum_{n=1}^L |1f_k^n|^2 \\
 J_{22} &= \frac{1}{2\hat{q}_k^2} \sum_{n=1}^L |2f_k^n|^2 \\
 J_{12} &= \frac{1}{1\hat{q}_k 2\hat{q}_k} \sum_{n=1}^L 1f_k^n 2f_k^{n*} \\
 J_{21} &= J_{12}^*
 \end{aligned} \right\} \quad (31-6)$$

The fractional polarization of the received signal may be computed directly from the value of  $\underline{J}_k$  as

$$\gamma_k = \left( 1 - \frac{4 \text{Det } \underline{J}_k}{\text{Trace}^2 \underline{J}_k} \right)^{\frac{1}{2}} \quad (31-7)$$

Again,  $\gamma_k$  is a function of the frequency index  $k$ . The output of subtask 4 consists of the spectra  $\underline{J}_k$  and  $\gamma_k$ . The parameters  $L$ , the number of transforms averaged per JM record, and  $N$  used in the reduction of the several sets of observations are included in table 31-II. Calculating the value of  $\underline{J}_k$  (subtasks 2 to 4) represented the greatest portion of the computational expense for this experiment. Additional results may be obtained directly from  $\underline{J}_k$  and  $\gamma_k$ . For example, the power in the polarized and unpolarized parts of the echo is

$$\left. \begin{aligned}
 \text{Polarized power } P_p(k) &= \gamma_k \cdot \text{Trace } \underline{J}_k \\
 \text{Unpolarized power } P_u(k) &= (1 - \gamma_k) \cdot \text{Trace } \underline{J}_k
 \end{aligned} \right\} \quad (31-8)$$

Other parameters of the echo spectra may be obtained similarly (ref. 31-7 and appendix 31-B).

#### Subtask 5 — Correction for System Polarization Parameters

The quantities  $\underline{J}_k$  and  $\gamma_k$  discussed in the previous section were derived directly from the sample data as they came from the analog tapes. As mentioned in the discussion of subtask 4, certain corrections have been made for the receiver filter characteristics. However, the data were treated as though they were derived from perfect antennas. That is, the antennas were assumed to consist of a pair of right and left circularly polarized elements. It was further assumed that, with the exception of the filter corrections already applied, the gains in the two receiver channels were equal. In the case of the 13-cm data, this assumption was very good. The isolation of the DSN 64-m antenna has been measured as >26 dB with an axial ratio of  $\lesssim 0.8$  dB.<sup>1</sup> At 116 cm, the properties of the SRI 46-m antenna are not nearly so well known. Polarization of the 46-m antenna was controlled principally through the constraints applied to the construction of the feed system, which consisted of a crossed dipole array of linear elements connected through a standard hybrid to obtain circular polarization. The array elements were mechanically and electrically identical. The hybrid combiner and associated phase-shift elements were adjusted to within 1° and 1 dB of the ideal transfer function for such a device. Coupling between the orthogonal linear array elements was less than 40 dB with the feed removed from the dish. Cross-coupling between the two circular polarizations, observed at the hybrid output with the feed in place at the focus of the dish, was 16 dB. The axial ratio of the overall system with the feed in place in the dish could not be measured. The axial ratio of the 116-cm system is estimated to be approximately 1 dB for either polarization. For certain received polarizations, axial ratios of this magnitude can introduce significant errors in the calculation of fractional polarization. Consequently, a correction for this uncertainty was applied in subtask 5. This correction was applied to the 116-cm Apollo 14 and 16 data only. The output tapes from subtask 5 preserve the original value of  $\underline{J}_k$  computed earlier.

The corrections were determined as follows (ref. 31-8). Consider the signals arriving at the antenna terminals in terms of their right and left circularly polarized components, which are denoted  $E_r$  and  $E_l$ , respectively. The relationship between the

---

<sup>1</sup>Private communication, D. Bathker, NASA Jet Propulsion Laboratory, 1973.

arriving signals and the signals at the antenna terminals may be expressed as a matrix multiplication

$$\begin{bmatrix} E_r' \\ E_1' \end{bmatrix} = \begin{bmatrix} c_{11} & c_{12} \\ c_{21} & c_{22} \end{bmatrix} \begin{bmatrix} E_r \\ E_1 \end{bmatrix} \quad (31-9)$$

where the variables denoted  $c$  are complex and arbitrary. The matrix elements may be considered the transmission coefficients of the four-part network consisting of pairs of antenna elements and terminals. Physically, the  $c$  variables may represent attenuation, gain, and cross-coupling. In an ideal system,  $c_{11} = 1$ ,  $c_{12} = c_{21} = 0$ , and  $c_{22} = 1$ .

The effect of such a transformation on the coherency matrix  $\underline{J}$  is easily shown to be

$$\begin{bmatrix} J_{11}' \\ J_{12}' \\ J_{21}' \\ J_{22}' \end{bmatrix} = \begin{bmatrix} |c_{11}|^2 & c_{11}c_{12}^* & c_{11}^*c_{12} & |c_{12}|^2 \\ c_{11}c_{21}^* & c_{11}c_{22}^* & c_{12}c_{21}^* & c_{22}^*c_{12} \\ c_{11}^*c_{21} & c_{21}c_{12}^* & c_{22}c_{11}^* & c_{22}c_{12}^* \\ |c_{21}|^2 & c_{22}^*c_{21} & c_{22}c_{21}^* & |c_{22}|^2 \end{bmatrix} \begin{bmatrix} J_{11} \\ J_{12} \\ J_{21} \\ J_{22} \end{bmatrix} \quad (31-10)$$

where  $J'$  is the coherency matrix of the wave associated with  $\underline{J}$  observed at the antenna terminals. The  $k$  subscripts have been suppressed for convenience. However, it is assumed that the  $c$  values are independent of frequency over the spectrum of interest. Given  $J'$  and the  $c$  values, the original  $\underline{J}$  may be recovered through an inverse matrix manipulation. In the present case, the matrix  $\underline{J}'$  is observed, but the  $c$  values are unknown.

The  $c$  values may be estimated from an observation of an unpolarized signal (ref. 31-8). System noise inputs to the 116-cm receiver system were used to estimate the  $c$  values and to perform a correction. The method was based on an experimenter

selection of those portions of the receiver output spectrum that contained only receiver noise. If the noise input is assumed to be unpolarized, then

$$\left. \begin{aligned} J'_{11} &= (|c_{11}|^2 + |c_{12}|^2)J_0 \\ J'_{12} &= (c_{11}c_{21}^* + c_{22}^*c_{12})J_0 \\ J'_{21} &= J'_{12}^* \\ J'_{22} &= (|c_{21}|^2 + |c_{22}|^2)J_0 \end{aligned} \right\} \quad (31-11)$$

where  $J_0 = kT_{\text{sys}}/2$ ,  $k = 1.38 \times 10^{-23}$  J/K, and  $T_{\text{sys}}$  = system temperature. The signal will appear unpolarized if

$$\left. \begin{aligned} J'_{12} &= 0 \\ J_{11} &= J_{22} \end{aligned} \right\} \quad (31-12)$$

or if

$$\left. \begin{aligned} c_{11}c_{21}^* &= -c_{22}^*c_{12} \\ |c_{11}|^2 + |c_{12}|^2 &= |c_{21}|^2 + |c_{22}|^2 \end{aligned} \right\} \quad (31-13)$$

from which the required inverse transformation can be obtained. In practice, a numerical estimate of the correction matrix was obtained as described previously. This estimate was then used as a starting point in a search to find the values of  $c$  that minimized the apparent polarization of the corrected  $J'_k$  in the noise portions of the spectrum. The corrections in the form just described were then used to compute the corrected  $J'_k$  for the entire spectrum. A corrected fractional polarization  $\gamma'_k$  based on  $J'_k$  was then obtained.

The output tapes from subtask 5 contain values of the original  $\underline{J}_k$  and the new, corrected  $\gamma_k'$ . A data user may easily recompute the original  $\gamma_k$  from the  $\underline{J}_k$  values that have been preserved and that are available on the tapes supplied. (See the section entitled "Subtask 6 — Merging Observations With Trajectory" and appendix 31-C.) The correction factors employed in the generation of  $\gamma_k'$  are given in appendix 31-D.

In summary, steps in this subtask are

1. Read  $\underline{J}_k$  source tapes from subtask 4.
2. Determine elements of the correction matrix based on minimization of the polarized part of the noise.
3. Compute  $\gamma_k'$ .
4. Generate new tape containing the original  $\underline{J}_k$  and the new  $\gamma_k'$ .

This process was applied to the Apollo 14 and 16 116-cm data; 13-cm data are uncorrected (i.e., for 13-cm data,  $\gamma_k' = \gamma_k$ ). In subsequent steps, the  $\gamma_k'$  values were used in all computations of the polarized and unpolarized parts of the 116-cm echo spectrum.

#### Subtask 6 — Merging Observations With Trajectory

The output of subtask 5, the  $\underline{J}_k, \gamma_k'$  tapes, represents the experimenter's best estimate of the received spectra, averaged over the time intervals previously defined; that is, a complete second-order description of the received echo signal. In subtask 6, these data (which were previously processed without regard to lunar coordinates or other geophysical considerations) were combined with the Apollo CSM ephemeris. The ephemeris first was interpolated to the midpoint of the averaging period used in the computation of the matrix  $\underline{J}_k$ , then certain ancillary quantities were computed. The interpolated ephemeris and the derived quantities were then merged with the experimental data to form a basic set of source tapes designated JM doptrack. After further processing in subtask 10, these tapes became the primary source tapes supplied to the National Space Science Data Center (NSSDC).

The ephemeris-based quantities added to the observational data were the following.

1. Time corresponding to midpoint of averaging period
2. Predicted difference between reflected and direct Doppler shifts
3. Predicted echo bandwidth for a Moon with rms slope of 0.1
4. Angle of incidence on mean spherical Moon
5. Spacecraft altitude above mean spherical surface
6. Spacecraft speed
7. Bistatic-radar cross section of a smooth, perfectly conducting, spherical Moon for the current spacecraft-Moon-Earth geometry
8. Normalized signal strength for a conducting Moon and instantaneous geometry
9. Spacecraft position in selenographic coordinates
10. Specular point position on a mean spherical lunar surface in selenographic coordinates
11. Selenographic latitude and longitude of spacecraft position
12. Doppler shift due to Earth rotation
13. Total Doppler shift of the reflected signal
14. Selenographic latitude and longitude of specular point on the mean spherical lunar surface
15. Speed of the specular point on the mean lunar surface
16. Look angles to Earth in spacecraft coordinates
17. Euler angles of spacecraft attitude in local horizon system
18. Selenographic unit velocity vector of spacecraft
19. Selenographic unit vector location of Earth

These tapes are organized in groups of six data records, referred to as a data frame, corresponding to each time interval. The JM doptrack tape formats and contents are described in appendix 31-C.

#### Subtask 7 — Computation of Polarized and Unpolarized Parts, Carrier Suppression

The JM doptrack tapes contain spectrally analyzed 13- and 116-cm receiver outputs. No provision was made within the receivers or in subtasks 2 to 6 for removal of the directly propagating telemetry carrier from the echo data. In terms of the polarization parameters, this signal cannot be removed completely. However, much of the data analysis is based only on the low-order moments of the polarized part of the echo. In subtask 7, polarized and unpolarized spectra were computed from equation (31-8), then an empirically derived algorithm was used to remove the carrier signal from the polarized spectra; these data, together with the ephemeris data described in subtask 6, constitute the intermediate data set generated in subtask 7. The algorithm for carrier suppression is described in appendix 31-A. Carrier suppression was also applied to unpolarized data. However, the carrier was largely suppressed in those data by coherency matrix processing because the signal was polarized. The output of this subtask, the P tapes, contain the experimenter's best estimate of the power spectra of the polarized and unpolarized components of the echo signal.

#### Subtask 8 — Computation of Total Received Power, Echo Moments

Inputs to subtask 8 were the polarized and unpolarized power spectra derived from the JM doptrack source tapes in subtasks 6 and 7. The purpose of subtask 8 was to derive numerical measures of the echo spectra. Selected measures of the echo spectra were corrected for predictable trajectory effects and converted into scientific units. In all cases, the designation of the echo signal location in a spectrum was made by the experimenter's visually scanning plots of the polarized and unpolarized power spectra. The values of the  $k$  indices bounding the echo were input to a computer program that actually reduced the data. An average noise level, determined from a region of the spectra not containing echo, was also input to the computer program. The data were monitored at approximately 30-sec intervals and the echo limits reset to account for motion of the echo in the receiver passband. It was also necessary to occasionally reset the noise level since it also varied during the experiment, principally because of the

receiving antenna scan across the lunar terminator. The derived quantities are defined as follows.

1. Polarized echo power is the integral of the polarized power spectra between the frequency limits set by the experimenter and above the system noise level. This quantity is the best measure of the polarized echo power received.

2. Normalized polarized echo power is the polarized echo power divided by the polarized system noise level.

3. Unpolarized echo power is the integral of the unpolarized power spectra between the frequency limits set by the experimenter and above the system noise level. This quantity is the best measure of the unpolarized echo power received.

4. Normalized unpolarized echo power is the unpolarized echo power divided by the unpolarized system noise level.

5. Equivalent area bandwidth is the bandwidth of the polarized echo signal between the frequency limits set by the experimenter and above the polarized system noise level as determined by the ratio of the total polarized echo power to the peak polarized echo power.

6. Normalized absolute-moment bandwidth is the bandwidth of the polarized power echo (item 5) computed from a Gaussian equivalent absolute moment divided by the equivalent area bandwidth.

7. Normalized second-moment bandwidth is the bandwidth of the polarized power echo (item 5) computed from a Gaussian equivalent second moment divided by the equivalent area bandwidth.

8. Centroid of echo spectrum is the centroid of the polarized power echo (item 5).

9. The rms slope is the rms slope of the lunar surface inferred from the equivalent area bandwidth and the predicted bandwidth for an rms surface slope of 0.1, using linear interpolation.

Formulas for the computation of the preceding quantities and a brief explanation of their use may be found in appendix 31-E. The trajectory data added in subtask 6 were retained throughout subtask 8. A simple correspondence between the output of subtask 8 and the JM doptrack tapes was maintained through inclusion of ephemeris data in both data sets.

### Subtask 9 — Final Editing of Data

Final editing of the output from subtask 8 resulted in a set of reduced data records designated integral tapes. These tapes constitute the second form of data supplied to the NSSDC. Final editing of data (subtask 9) included the following steps.

1. Addition of hand-scaled bandwidths as a partial independent check on subtask 8 (See the section entitled "Subtask 10 — Displaying, Scaling, and Copying Data.")
2. Addition of spacecraft antenna gain in the direction of specular reflection
3. Notation of operational or data processing changes
  - a. Polarized band bad
  - b. Unpolarized data bad
  - c. Change in polarized noise level
  - d. Change in polarized  $k$  indices for echo limits
  - e. Change in unpolarized noise level
  - f. Change in unpolarized  $k$  indices for echo limits
  - g. Change in system gain

As a precaution, it should be noted that some integral data, primarily at the beginning or end of a transmission, have been deleted. Large overlaps in the 13-cm data caused by the use of two analog tape recorders have also been deleted. In all other cases (e.g., when interference is present), bad data are flagged on the edited integral tapes as described in item 3 of the preceding paragraph. (See appendix 31-E, item E47.) The data contained on the integral tapes are still the experimenter's best estimates of the values. However, in the case of flagged data, that estimate may be very poor. No flagged data should be used without examining the spectra on the corresponding JM doptrack tapes. For example, in the 116-cm data, occasional interference produced marked increases in the apparent polarized echo power but evidently left the unpolarized power unaffected. A flag for polarized power thus may also cast suspicion on the unpolarized power. The experimenters have evaluated these cases and indicated their opinions in the data accordingly. Other individuals may arrive at different conclusions. It is primarily for this reason that the JM doptrack/integral tape frame-to-record correspondence (through ephemeris data) has been maintained; reduced data records

on the integral tapes may, if questioned, be reevaluated from the JM doptrack source tapes. A complete description of the integral tape formats and the flags is given in appendix 31-E.

#### Subtask 10 — Displaying, Scaling, and Copying Data

Output from subtask 6, the JM doptrack tapes, is used in miscellaneous programs in preparation for data analysis and distribution. An important step in producing the final integral tapes (subtask 9) was performed in subtask 10. Polarized power spectra obtained from JM doptrack tapes are computer plotted and visually examined to determine specifically the proper receiver operation, proper receiver tuning, and presence of interference. Such plots are also used to determine the one-half power, hand-scaled bandwidths added to the data set in subtask 9. This bandwidth is determined by measuring the width of the polarized echo spectrum at a point one-half the distance from the apparent system noise level to the mean echo peak. The measured distance is scaled by the appropriate factor to determine the width in hertz. Such measures can be related to the rms slope of the lunar surface from the quasi-specular scattering theory (appendix 31-E). The hand-scaled values are used to verify the machine algorithms used in computing lunar rms slopes and as a simple means of quickly estimating the slope. Finally, subtask 10 included copying the JM doptrack tapes for shipment to the NSSDC. These tapes were not edited.

#### Subtask 11 — Utility Routines

Integral tapes have been organized as a sequence of records describing the data and experimental geometry at successive instances of time. It is then a simple matter, in subtask 11, to determine any set of variables from this tape with time as a parameter. Data users should consider these data as a set of dependent functions parameterized in time. It is hoped that such a presentation is found useful.

TABLE 31-1.- APOLLO BISTATIC-RADAR EXPERIMENT PARAMETERS

Wavelength, cm	Antenna (a)	3-dB beam width, deg	Polarization	Gain, dB (b)	Power, W (c)	System temperature, K (d)
Apollo 14 revolution 25						
13	Cavity backed helix (OMNI, C)	≈60	Right elliptical, axial ratio ≈7 dB	-1.5	≈4	27 ± 3
116	Scimitar (VHF, left)	(e)	Linear, maintained in plane of incidence	≈0	≈2.5	≈1000 ± 50
Apollo 15 revolution 28						
13	Steerable crossed dipoles (high gain, wide)	≈40	Right circular, axial ratio <math>\leq 1.0</math> dB	-1.5	≈4	27 ± 3
116	Scimitar (VHF, right)	(e)	Linear, varies with respect to plane of incidence	≈0	≈2.5	≈1000 ± 50
Apollo 16 revolution 40						
13	Steerable crossed dipoles (high gain, wide)	≈40	Right circular, axial ratio <math>\leq 1.0</math> dB	-1.5	≈4	27 ± 3
116	Scimitar (VHF, left)	(e)	Linear, maintained in plane of incidence	≈0	≈2.5	≈1000 ± 50

<sup>a</sup>Designations in parentheses are spacecraft antenna and mode.

<sup>b</sup>Includes circuit losses, nominal values ± 3 dB.

<sup>c</sup>In carrier signal nominal values, actual values not measured in flight.

<sup>d</sup>Varies with orbital position of spacecraft; cold sky values given.

<sup>e</sup>Beam width of scimitar antenna not defined.

ORIGINAL PAGE IS  
OF POOR QUALITY

TABLE 31-II.- APOLLO DUAL-FREQUENCY BISTATIC-RADAR DATA SUMMARY

Parameter	Apollo 14		Apollo 15		Apollo 16	
	110 cm (VHF)	13 cm (S-band)	116 cm (VHF)	13 cm (S-band)	116 cm (VHF)	13 cm (S-band)
Julian ephemeris day (00:00 UT2 preceding data)	2440988.5	2440988.5	2441164.5	2441164.5	2441430.5	2441430.5
Reference epoch for coordinate systems	2440952.509 Feb. 6, 1971	2440952.509 Feb. 6, 1971	2441317.752 Aug. 1, 1971	2441317.752 Aug. 1, 1971	2441317.752 Apr. 23, 1972	2441317.752 Apr. 23, 1972
Calendar date	Feb. 6, 1971	Feb. 6, 1971	Aug. 1, 1971	Aug. 1, 1971	Apr. 23, 1972	Apr. 23, 1972
Revolution number (for Lunar orbit insertion)	25	25	28	28	40	40
Transmitter frequency, MHz	259.7	2287.5	259.7	2287.5	259.7	2287.5
UT2 start/stop time, hr:min:sec	06:37:17/07:30:34	06:38:30/07:32:28	01:23:00/02:23:58	01:16:30/02:29:00	01:16:30/02:16:26	01:17:00/02:27:05
Spacecraft antenna and mode (JSC designation)	VHF, left	OMNI, C	VHF, right	High gain, wide	VHF, left	High gain, wide
High-gain antenna pointing angles, deg	--	--	--	144 122	--	145 302
Data source	SRI 10.003-MHz i.f. rcvr	DSN/SRI closed loop rcvr	SRI 10.003-MHz i.f. rcvr	DSN/SRI closed loop rcvr	SRI 10.003-MHz i.f. rcvr	DSN/SRI closed loop rcvr
Receiver bandwidth, kHz	≈3.5	≈20.0	≈3.5	≈20.0	≈3.5	≈20.0
Data sampling frequency, kHz	10.0	43.0	10.0	43.0	10.0	43.0
Total analysis bandwidth, kHz	5.0	21.5	5.0	21.5	5.0	21.5
Number of analysis bins, N	1024	1024	2048	1024	2048	1024
Analysis resolution, Hz	9.8	42.0	4.9	42.0	4.9	42.0
Length of data window/transform, sec	0.1024	0.02381395	0.2048	0.02381395	0.2048	0.02381395
Number of transforms averaged per JM record, L	26	100	23	99	23	99
Frame length, sec	2.6624	2.381395	4.7104	2.357581	4.7104	2.357581

<sup>a</sup>See the section entitled "Subtask 4 — Generation of Coherency Matrix."

TABLE 31-III.- ANTENNA PERFORMANCE

Aperture diam, m	Efficiency, percent	Feed system	Mount	Pointing loss, dB
SRI 46-m antenna (116-cm wavelength)				
46	$\approx 35 \pm 5$	Crossed dipole array: axial ratio $a \approx 1 \pm 0.5$ dB, isolation $\approx 16 \pm 1.0$ dB	Elevation/ azimuth	$< 0.1$
DSN 64-m antenna (13-cm wavelength)				
64	$58 \pm 4$	Waveguide horn: axial ratio $b^a < 0.8$ dB, isolation $b^b > 26$ dB	Elevation/ azimuth	$< 0.03$

<sup>a</sup>Estimated value.

<sup>b</sup>Private communication, D. Bathker, NASA Jet Propulsion Laboratory, 1973.

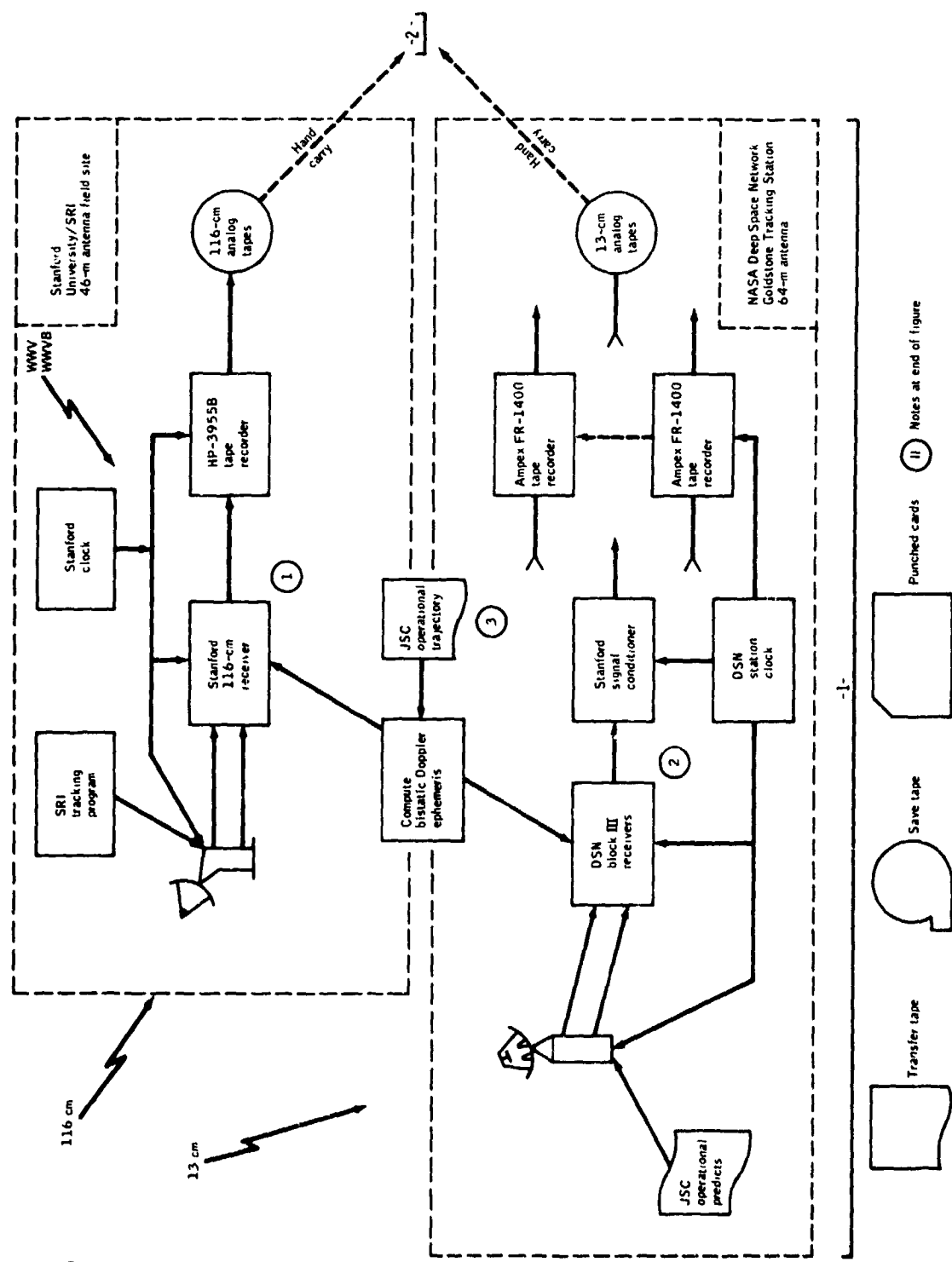


Figure 31-1.- Simplified block diagram, Apollo bistatic-radar data processing and reduction.

ORIGINAL PAGE IS  
OF POOR QUALITY

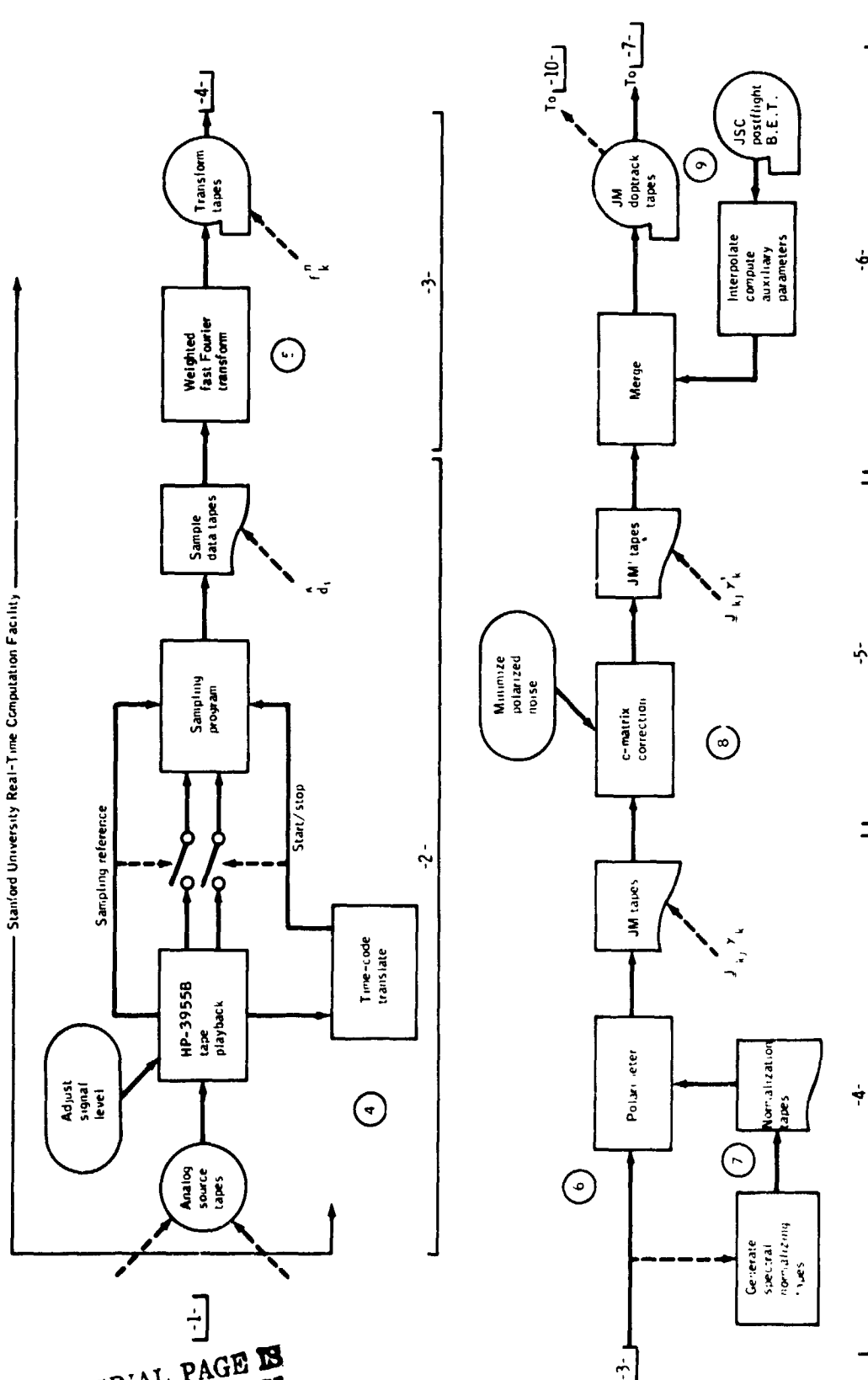


Figure 31-1.- Continued.

ORIGINAL PAGE IS  
OF POOR QUALITY

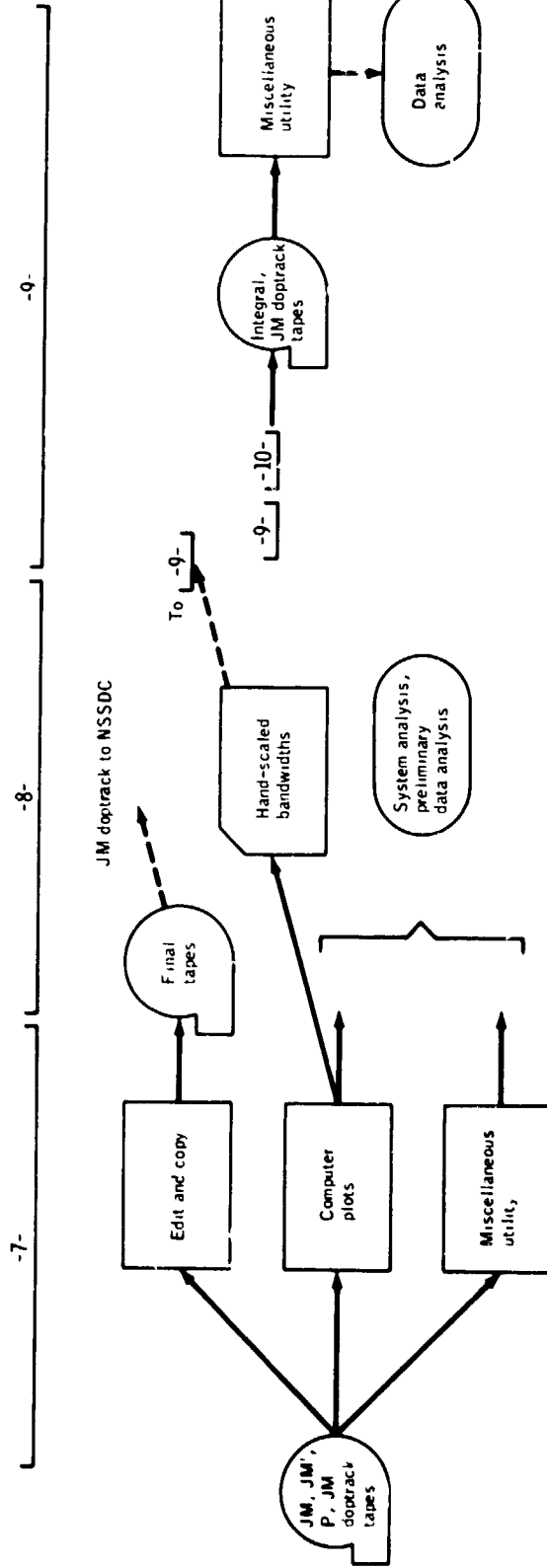
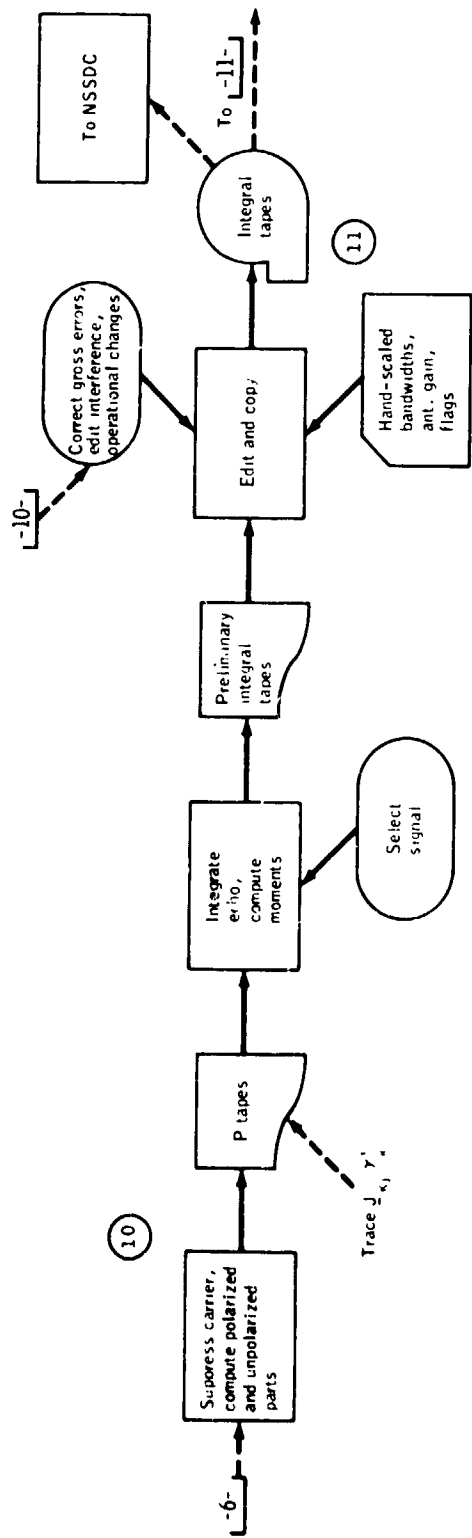


Figure 31-1.- Concluded.

NOTES FOR FIGURE 31-1

- ①
  - a. The receiving systems are shown in figures 31-2(a) and 31-2(b).
  - b. Critical filter responses are given in figures 31-3(a) and 31-3(b).
  - c. Right circular polarization (RCP) and left circular polarization (LCP) coherency was maintained throughout entire system.
  - d. Antenna pointing was maintained toward center of Moon using Stanford Research Institute (SRI) lunar ephemeris.
  - e. Absolute phase in LCP, RCP channels not controlled; relative phase maintained.
  - f. Spectral purity of downlink signals was measured for Apollo equipment.
  
- ②
  - a. Deep Space Network (DSN) station is under NASA control; standardized procedures were used except as noted.
  - b. Apollo operational system used for 64-m dish pointing, closed loop receiver acquisition.
  - c. Absolute phase in RCP, LCP not controlled, relative phase maintained.
  
- ③
  - a. Stanford signal conditioning unit provided critical control over system frequency response. Filter characteristics are given in figures 31-3(a) and 31-3(b).
  - b. Tape recorders FR-1400A and FR-1400B were used to provide continuous data across tape changes.
  
- ④
  - a. Frequency response of tape recorder HP-3955B was adjusted for a maximally flat frequency response on playback using calibration tapes from data source machine (HP-3955B for 116-cm data; FR-1400A and FR-1400B for 13-cm data).
  - b. Coherent sampling was maintained. Reference signal from tape was used to synchronize samples.

- c. Actual time was recovered by use of time-code-translator clock output to establish start times. Time from start was maintained by counting sampling pulses.
- d. Actual sampling rates were as follows.

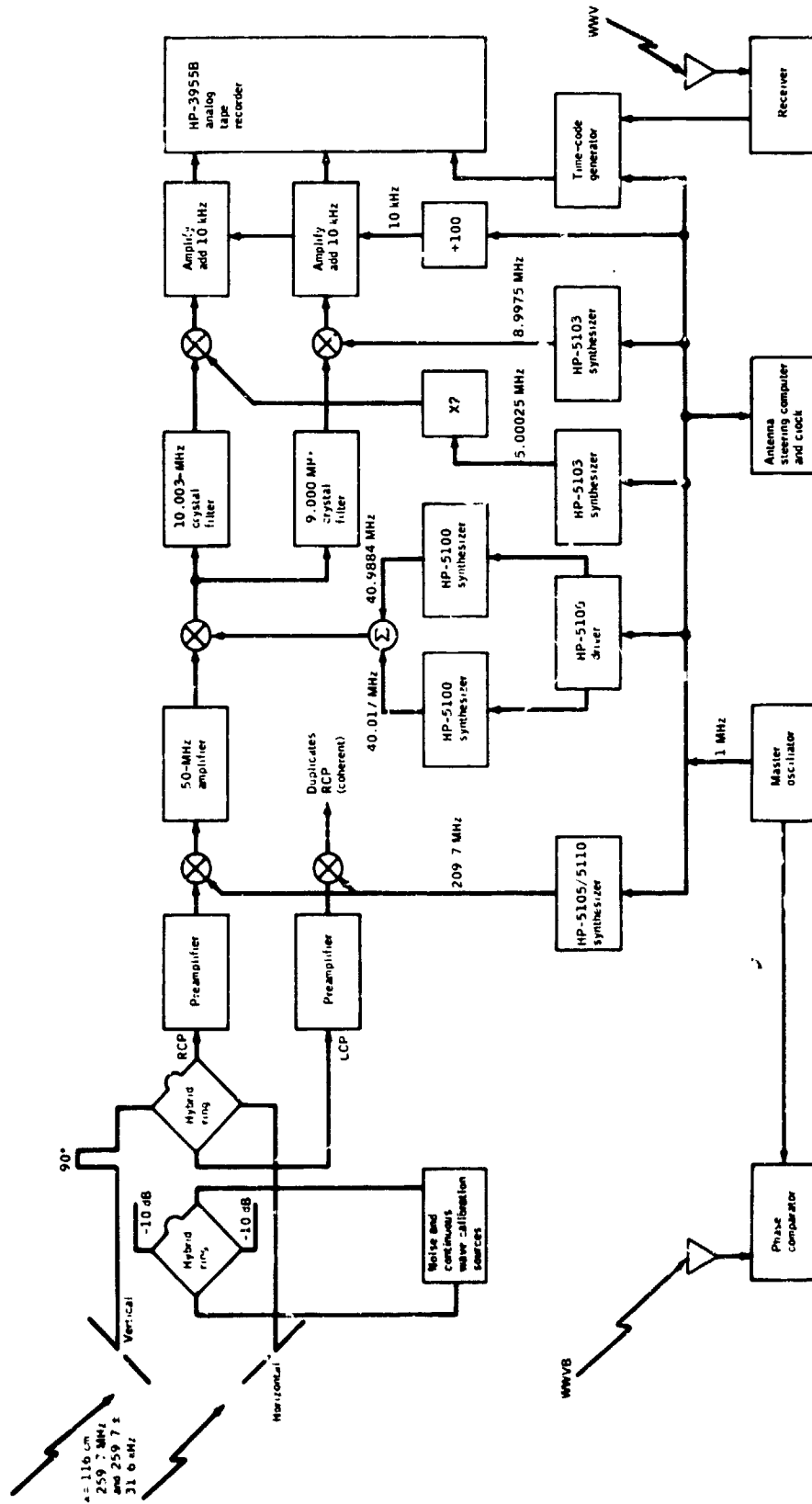
<u>Flight</u>	<u>Wavelength, cm</u>	<u>Sampling rate, kHz</u>	<u>Ratio of effective sampling rate to actual sampling rate</u>
Apollo 14	13	10.75	4
Apollo 14	116	10.00	1
Apollo 15	13	10.75	4
Apollo 15	116	10.00	1
Apollo 16	13	21.5	2
Apollo 16	116	10.00	1

- ⑤ a. Fourier coefficients were computed from successive groups of weighted data: data group length is either 1024 or 2048 samples; weighting function is  $\sin^2(\pi t/T)^T$ , where  $t$  is time and  $T$  is duration of sample group length.
- b. Data analysis lengths were as follows.

<u>Data source</u>	<u>Sample Length</u>	<u>Analysis bandwidth, Hz</u>
Apollo 14 S-band	1024	42.0
Apollo 14 VHF	1024	9.8
Apollo 15 S-band	1024	42.0
Apollo 15 VHF	2048	4.9
Apollo 16 S-band	1024	42.0
Apollo 16 VHF	2048	4.9

- ⑥ Polarimeter computed elements of signal covariance matrix (subtask 5).

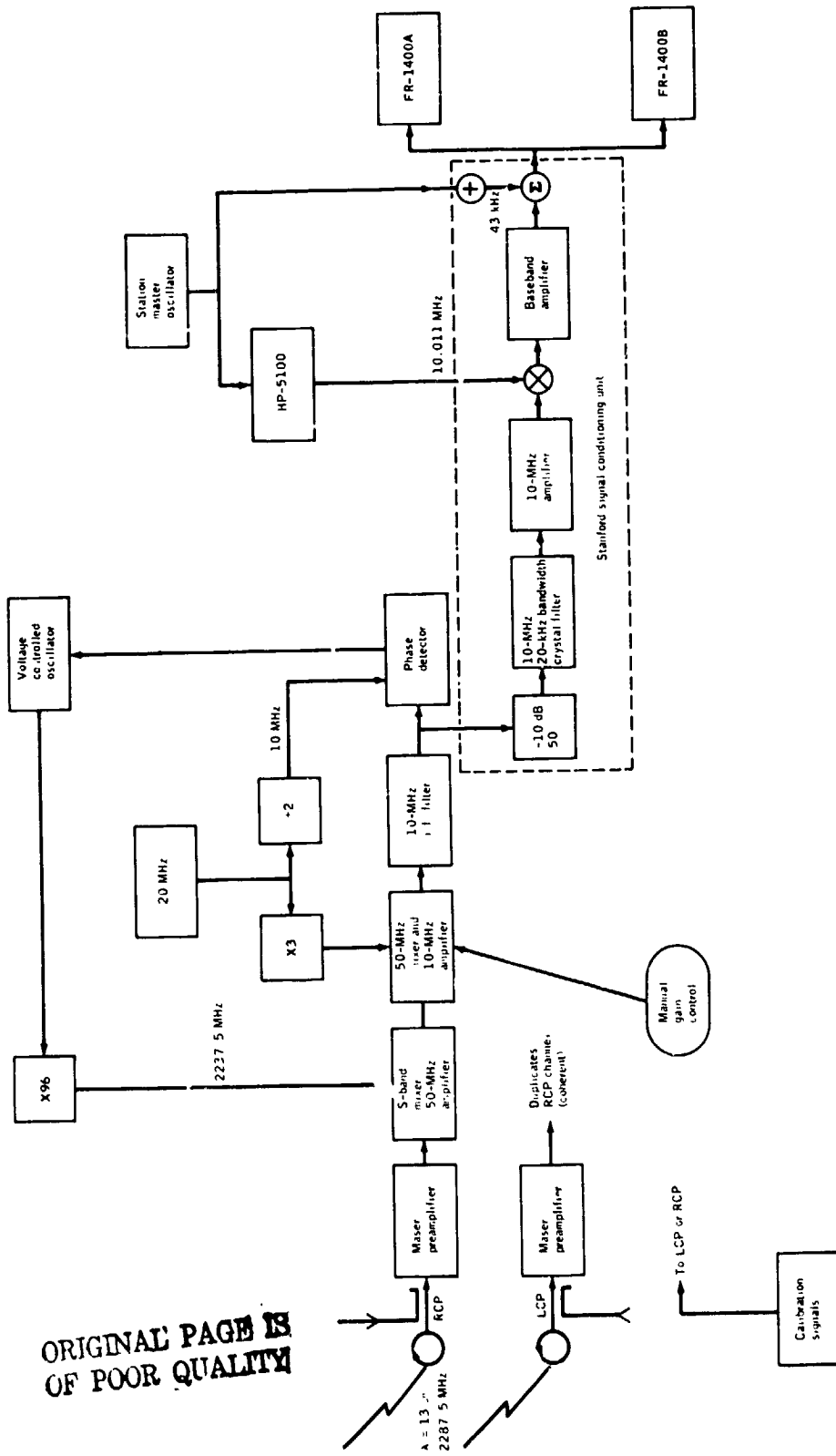
- ⑦
  - a. Normalizing data were obtained from data runs employing noise input. The purpose was to compensate for variations in receiver passband.
  - b. Normalizing tapes contain smoothed power spectra from noise source data.
  
- ⑧
  - a. The c-matrix correction was a polarization coordinate transformation to correct for errors in receiver antenna system. Applied to 116-cm data only.
  - b. Criterion for choosing c-matrix was to minimize polarized part of system noise.
  
- ⑨
  - a. Merge combined data tapes with geometrical parameters obtained from NASA Lyndon B. Johnson Space Center (JSC) (best-estimate trajectory (B.E.T.) postflight tapes.
  - b. The JSC data are interpolated to center of data averaging window.
  - c. The JM doptrack tapes constitute primary data source for analysis.
  
- ⑩  
Carrier suppression deleted direct signal from the data by means of an empirical algorithm (subtask 7 and appendix A).
  
- ⑪
  - a. Tapes were edited for changes indicated in operational logs and for interference.
  - b. Hand-scaled data were added to tape from card source.
  - c. Edited integral tapes constitute reduced data records.



(a) 116-cm wavelength (VHF).

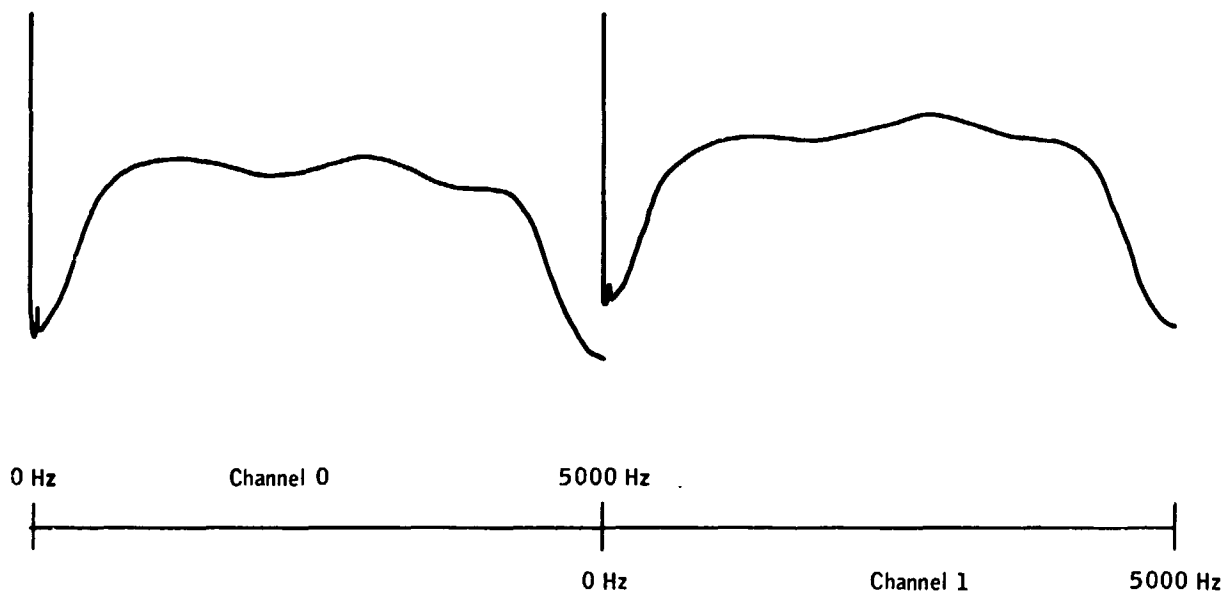
Figure 31-2.- Block diagram of Apollo bistatic-radar receiving system.

ORIGINAL PAGE IS  
OF POOR QUALITY

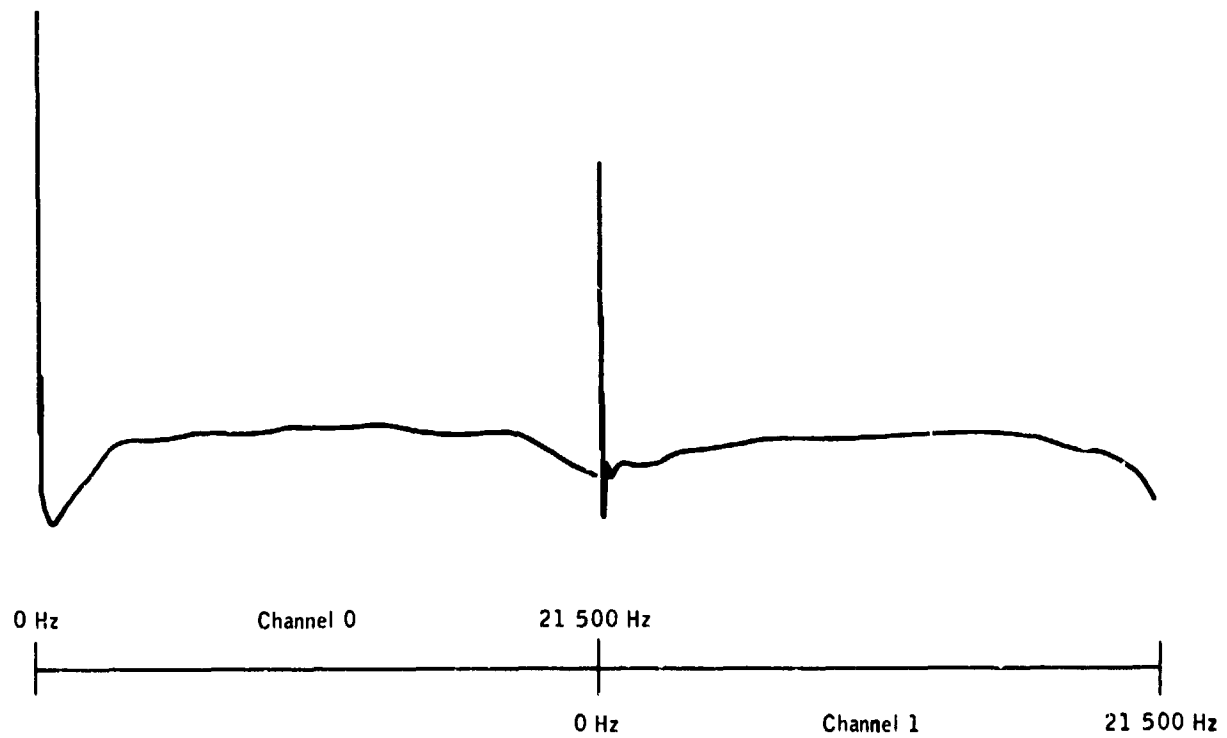


(b) 13-cm wavelength (S-band).

Figure 31-2.- Concluded.



(a) 116-cm wavelength.



(b) 13-cm wavelength.

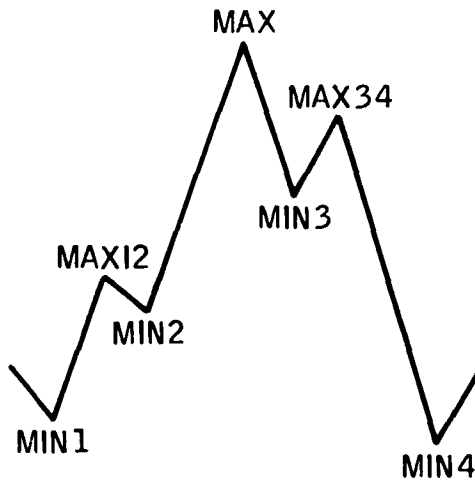
Figure 31-3.- Apollo bistatic-radar receiving system uncorrected frequency response.

## APPENDIX 31-A — CARRIER SUPPRESSION ALGORITHM

This appendix describes the algorithm used to remove the direct signal from the polarized and unpolarized parts of the bistatic-radar echo spectrum (subtask 7). This algorithm was used on each frame of polarized and unpolarized data yielded by the JM doptrack tapes according to equation (31-8). Two slightly different procedures were used for the 116- and 13-cm data. These differences constituted the only difference in procedure between the 116- and 13-cm data. Both data sets were processed by the same computer program, using different program branches for the two cores. The direct signal observed at 13 cm was free of spurious sidebands to the level of the experimenters' observations. At 116 cm, the direct signal contained two weak sidebands symmetrically displaced approximately 20 dB below the direct signal. Consequently, during periods of strong direct signal at the 116-cm wavelength, it was also necessary to correct for the presence of these sidebands. The procedures described in the following paragraphs were developed empirically but were found to give good results. The approach was to find the maximum of the power spectrum and to assume that this maximum represented the direct signal. This assumption was tested by determining the height of the maximum with respect to the fluctuations in the spectrum in the immediate vicinity of the maximum. If the maximum exceeded the fluctuation criteria, an interpolation procedure was used to provide a smoothed estimate of the spectrum. For the 116-cm data, sideband suppression was achieved by reducing the local maximum on either side of the direct signal by an amount proportional to the strength of the direct signal. A detailed summary of this procedure follows.

INITIAL TEST

1. Find the absolute maximum of all the data MAX. (See diagram.)



2. Find the adjacent local maximums MAX12 and MAX34.

3. Test MAX to determine whether or not it represents the direct signal.

a. 
$$\text{SUM} = \frac{\text{MIN1} + \text{MIN2}}{8} + \frac{\text{MAX12}}{4} + \frac{\text{MIN3} + \text{MIN4}}{8} + \frac{\text{MAX34}}{4} \quad (31-A1)$$

b. 
$$\text{CRIT} = 1.2 \cdot \text{SUM} \quad (31-A2)$$

c. (MAX.LT.CRIT) → no direct signal present, terminate procedure; go to next frame, initial test 1 (LT = less than)

d. (MAX.GE.CRIT) → direct signal present, continue (GE = greater than or equal to)

4. Check data type. If data are 116 cm, go to step 8; otherwise, continue with step 5.

#### SUPPLEMENTAL TESTS

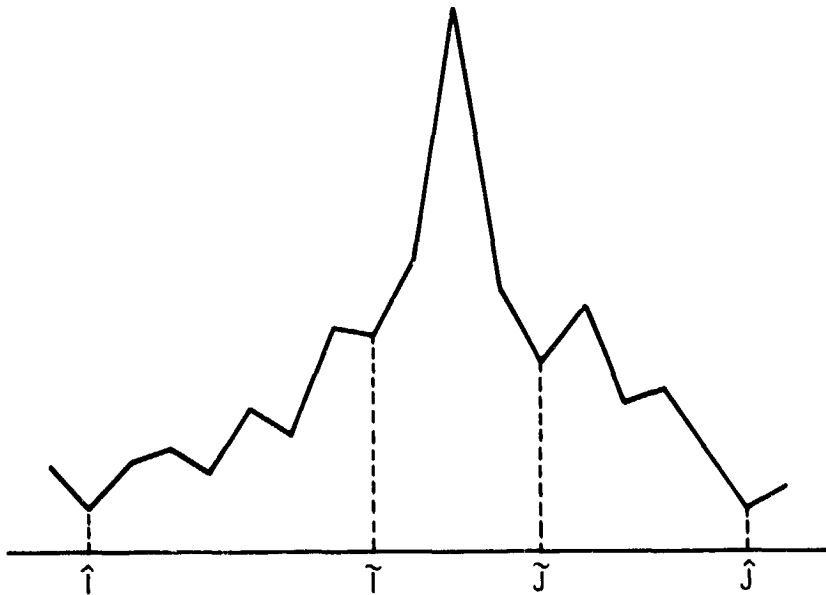
##### Procedure for 13-cm Data

5. Test for a smooth direct signal:

IF  $(2.0 \cdot \text{MIN}1 \cdot \text{GE} \cdot \text{MIN}2)$  and  
 $(2.0 \cdot \text{MIN}4 \cdot \text{GE} \cdot \text{MIN}3) \rightarrow$  smooth direct signal

If the direct signal is smooth, all values between MIN2 and MIN3 greater than CRITC are set equal to CRITC and the procedure is terminated; initial test 1 is then begun on the next frame. If the test for smoothness is failed, continue with step 6.

6. This procedure is applied only if the direct signal is spread through several frequency analysis bins. Determine the first minimum on either side of the direct signal that satisfies the condition  $(\text{MIN}(I) \cdot \text{LT} \cdot \text{MIN}(I - 1) \cdot 2.0)$  and  $(\text{MIN}(J) \cdot \text{LT} \cdot \text{MIN}(J + 1) \cdot 2.0)$ , where I indexes the left side of the direct signal and J indexes the right side of the direct signal. (See following diagram.)



If the conditions are not satisfied in 15 minimums, choose the 15th minimum. Denote the extreme minimums  $\hat{I}$  and  $\hat{J}$ . The factors  $\text{MIN}(\hat{I})$  and  $\text{MIN}(\hat{J})$  locate the extent of the spread direct signal. Denote the minimums adjacent to the direct signal  $\tilde{I}$  and  $\tilde{J}$ , then replace the data  $D(\ )$  with  $D'(\ )$  calculated as follows.

$$\left. \begin{aligned} D'(L) &= D(L) - \frac{D(\tilde{I}) - D(\hat{I})}{\tilde{I} - \hat{I}} \cdot (L - \hat{I}); \hat{I} + 1 \leq L \leq \tilde{I} - 1 \\ D'(L) &= D(L) - \frac{D(\hat{J}) - D(\tilde{J})}{\hat{J} - \tilde{J}} \cdot (L - \hat{J}); \tilde{J} + 1 \leq L \leq \hat{J} - 1 \\ D'(L) &= D(\tilde{I}) + \frac{D(\tilde{J}) - D(\tilde{I})}{\tilde{J} - \tilde{I}} \cdot (L - \tilde{I}); \tilde{I} \leq L \leq \tilde{J} \end{aligned} \right\} (31-A3)$$

7. Terminate procedure; go to next frame, initial test 1.

#### Procedure for 116-cm Data

8. Find the largest local maximum within 60 Hz of the direct signal on first the left side and then the right side of the direct signal. Designate these maximums  $\text{MAXL}$  and  $\text{MAXR}$ , respectively.

9. Determine relative magnitude of the direct signal.

$$\text{CRITSB} = 200.0 \cdot \text{SUM} \quad (31-A4)$$

If  $(\text{MAX.GE.CRITSB})$ , the direct signal is sufficiently large to require compensation for the sidebands. Replace  $\text{MAXL}$  and  $\text{MAXR}$  by the average value of their respective adjacent minimums.

10. If  $(\text{MAX.LT.CRITSB})$ , the direct signal is small. Subtract a constant from the maximums  $\text{MAXL}$  and  $\text{MAXR}$  defined previously. The constant is

$$\text{ESUB} = (\text{MAX} - \text{SUM})/500.0 \quad (31-A5)$$

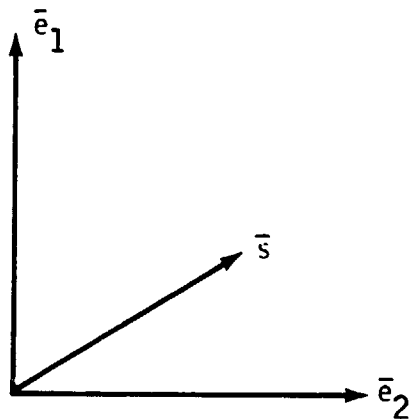
The subtraction is performed only if the data value is greater than  $\text{ESUB}$ .

- 
11. Replace MAX by the average of MIN2 and MIN3.
  12. Terminate procedure and go to next frame, initial test 1.

APPENDIX 31-B — RELATIONSHIP BETWEEN THE COHERENCY MATRIX  
AND OTHER SPECIFICATIONS OF POLARIZATION

The methods used to estimate the polarization state of Apollo bistatic-radar data are those described in reference 31-9. This appendix describes the relationship of the coherency matrix to the more common descriptors intensity, axial ratio, and orientation of the polarization ellipse. The coherency matrix is from reference 31-7.

$$\left. \begin{aligned} \bar{e}_1(t) &= \text{Re} \left\{ E_1 e^{j\omega t} \right\} \bar{e}_1 \\ \bar{e}_2(t) &= \text{Re} \left\{ E_2 e^{j\omega t} \right\} \bar{e}_2 \end{aligned} \right\} \quad (31-B1)$$



$$\left. \begin{aligned} \underline{J} &= \begin{bmatrix} \langle E_1 E_1^* \rangle & \langle E_1 E_2^* \rangle \\ \langle E_1^* E_2 \rangle & \langle E_2 E_2^* \rangle \end{bmatrix} \\ \underline{J} &= \begin{bmatrix} J_{11} & J_{12} \\ J_{21} & J_{22} \end{bmatrix} \\ J_{ij} &= \langle E_i E_j^* \rangle \end{aligned} \right\} \quad (31-B2)$$

where  $E_1$  and  $E_2$  are complex magnitudes associated with any pair of orthogonal linear polarizations.

$$\left. \begin{aligned} \underline{\rho} &= \text{Tr}(\underline{J}) \begin{bmatrix} \rho_{11} & \rho_{12} \\ \rho_{21} & \rho_{22} \end{bmatrix} \\ \text{Tr}(\underline{J}) &= J_{11} + J_{22} = \text{total received power} \end{aligned} \right\} \quad (31-B3)$$

Born and Wolf (ref. 31-7) show that the percentage polarization  $\gamma$  (i.e., the fraction of  $\text{Tr}(\underline{J})$  that may be described by a deterministic polarization ellipse) is

$$\gamma = \sqrt{1 - 4(\rho_{11}\rho_{22} - \rho_{12}\rho_{21})} \quad (31-B4)$$

Then any  $\underline{J}$  may be written as

$$\underline{J} = \underbrace{\frac{1}{2}(1 - \gamma)\text{Tr}(\underline{J}) \begin{bmatrix} 1 & 0 \\ 0 & 1 \end{bmatrix}}_{\text{unpolarized part}} + \underbrace{\gamma \text{Tr}(\underline{J}) \begin{bmatrix} q_{11} & q_{12} \\ q_{21} & q_{22} \end{bmatrix}}_{\text{polarized part}} \quad (31-B5)$$

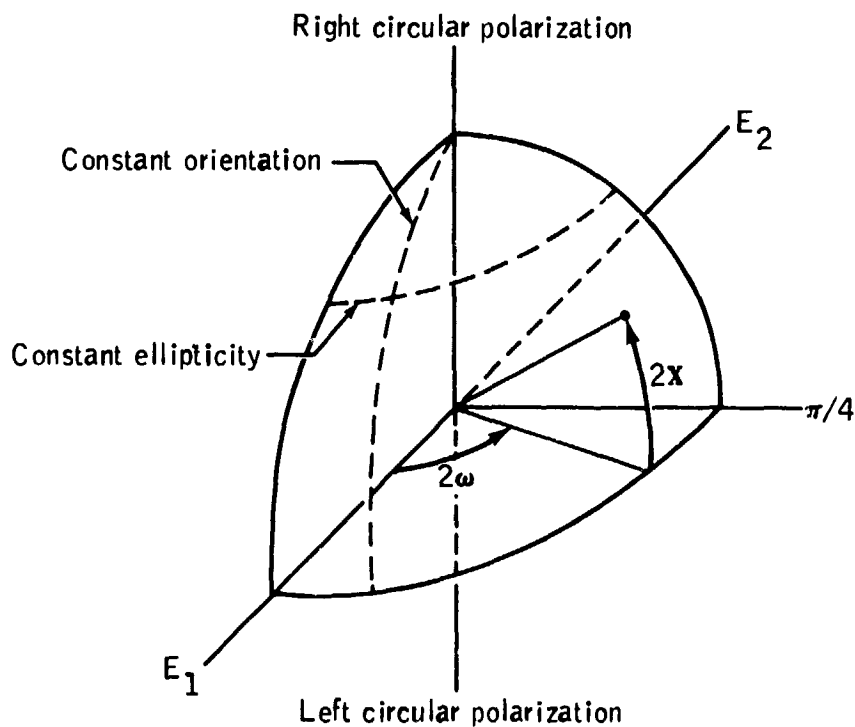
where

$$\left. \begin{aligned} q_{ii} &= \frac{1}{\gamma} \left[ \rho_{ii} - \frac{1}{2}(1 - \gamma) \right] \\ q_{ij} &= \frac{1}{\gamma} \rho_{ij} \end{aligned} \right\} \quad (31-B6)$$

Ko (ref. 31-10) gives the relationship between the matrix  $\underline{q}$  and the Poincaré sphere (ref. 31-11) as

$$\left. \begin{aligned} q_{11} &= \cos 2\omega, \quad 0 \leq \omega \leq \pi \\ q_{12} &= \sin \omega \cos \omega e^{j2\chi} \rightarrow \tan 2\chi = \frac{\text{Im}(q_{12})}{\text{Re}(q_{12})}, \quad -\frac{\pi}{2} < 2\chi < \frac{\pi}{2} \end{aligned} \right\} (31-B7)$$

The relationship is shown schematically in the following diagram.



Also note

$$\tan \omega = \sqrt{\frac{q_{22}}{q_{11}}}, \quad \tan \chi = \frac{M}{N},$$

$$\tan \chi > 0 \rightarrow \text{right elliptical polarization} \quad (31-B8)$$

For Apollo data, a similar matrix  $\underline{J}_c$ , where the subscript  $c$  designates decomposition of the incident wave into circular components, is used.

$$\underline{J}_c = \begin{bmatrix} \langle E_l E_l^* \rangle & \langle E_l E_r^* \rangle \\ \langle E_l^* E_r \rangle & \langle E_r E_r^* \rangle \end{bmatrix} \begin{bmatrix} J_{c11} & J_{c12} \\ J_{c21} & J_{c22} \end{bmatrix} \quad (31-B9)$$

where  $E_l$  and  $E_r$  denote left and right circular waves, respectively. Defining  $\rho_c$  and  $q_c$  in an analogous manner

$$\underline{J}_c = \begin{bmatrix} \rho_{c11} & \rho_{c12} \\ \rho_{c21} & \rho_{c22} \end{bmatrix} \left. \begin{array}{l} \\ \\ \\ \end{array} \right\} (31-E10)$$

$$= \frac{1}{2}(1 - \gamma) \text{Tr}(\underline{J}_c) \begin{bmatrix} 1 & 0 \\ 0 & 1 \end{bmatrix} + \gamma \text{Tr}(\underline{J}_c) \begin{bmatrix} q_{c11} & q_{c12} \\ q_{c21} & q_{c22} \end{bmatrix}$$

where as before

$$\gamma = \sqrt{1 - 4(\rho_{c11} \rho_{c22} - \rho_{c12} \rho_{c21})} \quad (31-B11)$$

However, the interpretation of the matrix  $q_c$  is modified in accordance with the new definition

$$\left. \begin{array}{l} \tan \chi = \frac{M}{N} = \frac{-\sqrt{q_{c11}} + \sqrt{q_{c22}}}{\sqrt{q_{c11}} + \sqrt{q_{c22}}} \\ \omega = \frac{1}{2} \arg(q_{12}) \end{array} \right\} (31-B12)$$

where  $\omega$  is referenced to the instantaneous  $E_l$  position at time  $t = 0$ . The invariance of  $\text{Tr}(\cdot)$ ,  $\text{Det}(\cdot)$ , and  $\gamma$  under transformations to circular coordinates can be verified by direct computation.

## APPENDIX 31-C — JM DOPTRACK TAPE FORMATS

This appendix describes the tape formats for the JM doptrack tapes generated in subtask 6 of the text. Tapes are nine track, binary in XDS Sigma 5 machine images. (See appendix 31-F for description of Sigma 5 machine images.) These tapes contain the output of the polarimeter in subtask 4, the corrected fractional polarization obtained from subtask 5, NASA Lyndon B. Johnson Space Center trajectory data, and certain ancillary quantities computed at Stanford University. All records within the given file are the same length. There may be more than one tape per file. Files are identified by a header record which contains a brief description of the file contents. The tape organization, the file organization, and the record formats for the JM doptrack tapes are described in this appendix. Definitions of the tape contents are either given herein or described by reference.

### A. File organization

<u>File</u>	<u>No. tapes</u>	<u>Contents</u>	<u>Record length</u>
1	1	Apollo 14, 116 cm	514 words
2	1	Apollo 14, 13 cm	514 words
3	1	Apollo 15, 116 cm	1026 words
4	2	Apollo 15, 13 cm	514 words
5	1	Apollo 16, 116 cm	1026 words
6	2	Apollo 16, 13 cm	514 words

### B. File organization

#### 1. Header record

2. Data record	1	}	Observational data	}	Data frame
Data record	2				
Data record	3				
Data record	4				
Data record	5				
Data record	6	} Ephemeris data			

.  
.  
.

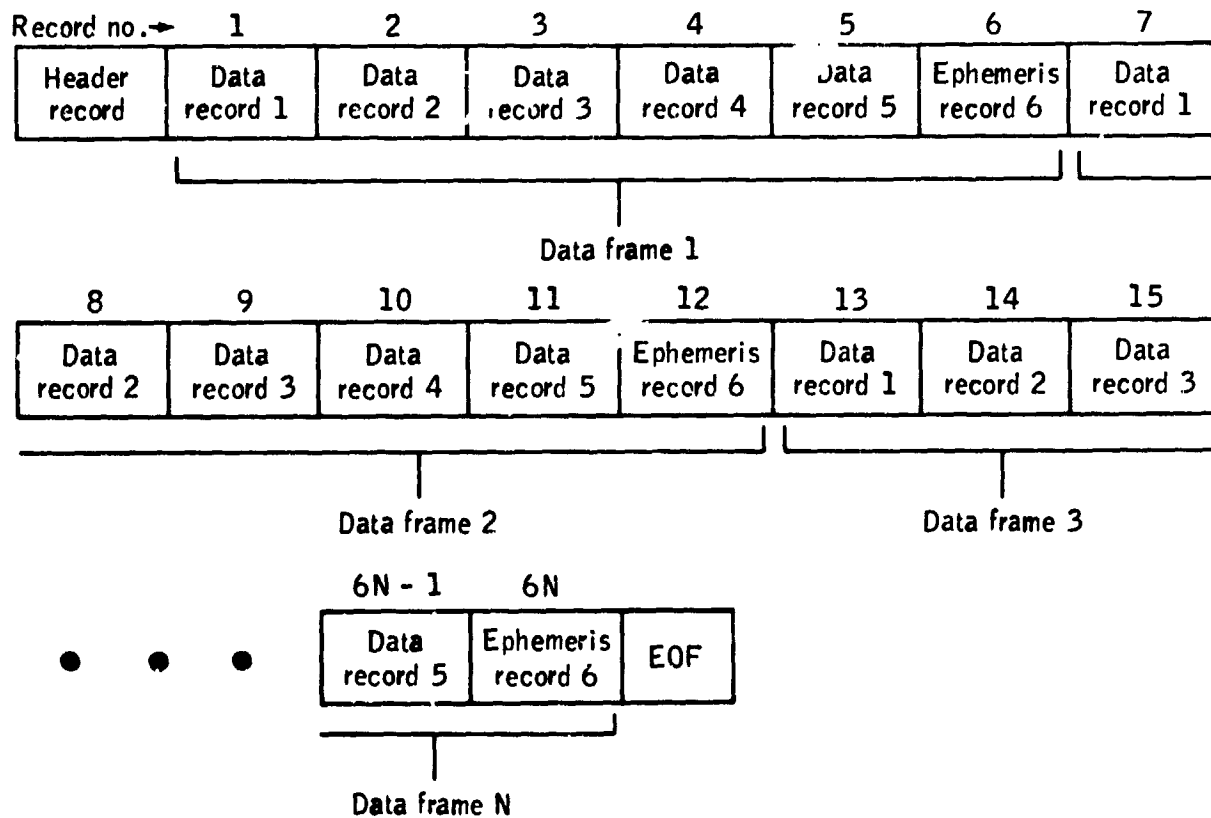
<Many data frames>

•  
•  
•

3. End of file (EOF) mark

If more than one tape was needed to contain the JM doptrack file, the file was continued across the end of the tape to the next tape without interruption; there is only one header record per file, at the beginning of the first tape of the file. Once again, even though the files are physically nothing more than a continuous string of records, all of equal length, it is helpful to think of them as being composed of a header record followed by groups (frames) of six data records. The ephemeris data record concludes the frame and, since each JM data frame is a short-time average, the ephemeris data have been calculated using the midpoint of the frame as the instantaneous time reference point. The following diagram is an illustration of the JM doptrack file.

JM Doptrack File Containing N Data Frames



C. Header record formats

<u>Word no.</u>	<u>Contents</u>	<u>Units</u>	<u>Machine type</u> <sup>2</sup>
1 to 42	Alphanumeric file identifier	--	A
43	Day of year on which data were collected (January 1 = 1)	days	I
44	Year data were taken (Gregorian)	year	I
45 and 46	Julian ephemeris day at 00:00 UT2 on the day the data were taken	days	DPR
47 and 48	Julian ephemeris day of reference epoch	days	DPR
49	Time increment between center point of data averaging frame	sec	R
50	Number of data records following this header record (Number of data frames = number of data records divided by 6.)	--	I
51 to 514/ 1026	Not used	--	--

D. Data frame formats

1. Data record organization

<u>Record no.</u>	<u>Contents</u>	<u>Notes:</u>
1	$J_{11}(k)$	116-cm data
2	$J_{22}(k)$	$J_{11}(k)$ - Left circular polarization

<sup>2</sup>A = alphanumeric; I = integer; R = real; DPR = double precision real.

1. Data record organization - concluded

<u>Record no.</u>	<u>Contents</u>	<u>Notes:</u>
3	Real part of $J_{12}(k)$	$J_{22}(k)$ - Right circular polarization
4	Imaginary part of $J_{12}(k)$	13-cm data
5	$\gamma(k)$	$J_{11}(k)$ - Right circular polarization
6	Spacecraft ephemeris and ancillary data	$J_{22}(k)$ - Left circular polarization

2. Format records 1 to 5 (all machine type real)<sup>3</sup>

<u>Record no.</u>	<u>Contents</u>
1 to 513/1025	Data described under item D1
514/1026	Meaningless

3. Format record 6 (all machine type real)

<u>Word no.</u>	<u>Contents</u>	<u>Units</u>
1	Meaningless	
2	UT2 at midpoint of frame	sec
3	Reflected Doppler minus direct Doppler	Hz
4	Predicted bandwidth for rms surface slope of 0.1	Hz
5	Angle of incidence	deg

<sup>3</sup>Because of a hardware problem in the data processing, words 1 to 15 are zero in the Apollo 14, 116- and 13-cm files and the Apollo 15, 13-cm file.

3. Format record 6 (all machine type real) - continued

<u>Word no.</u>	<u>Contents</u>	<u>Units</u>	
6	Spacecraft altitude (mean lunar radius assumed 1736 km)	km	
7	Spacecraft speed	m/sec	
8	Radar cross section predicted for smooth conducting Moon	dimension (dim)	
9	(Radar cross section) / (received power)	$m^2/W$	
10	X } Components of selenographic unit position vector of spacecraft location	dim	
11			Y }
12			Z }
13	X } Components of selenographic unit position vector of specular point location	dim	
14			Y }
15			Z }
16	Selenographic latitude of subspacecraft position	deg	
17	Selenographic longitude of subspacecraft position	deg	
18	Component of Doppler shift due to Earth rotation	Hz	
19	Total Doppler shift of reflected signal	Hz	
20	Selenographic latitude of specular point	deg	
21	Selenographic longitude of specular point	deg	
22	Speed of specular point on the lunar surface	m/sec	
23	$\alpha_e$ } Vehicle look angles to Earth	deg	
24			$\beta_e$ }

3. Format record 6 (all machine type real) - concluded

<u>Word no.</u>		<u>Contents</u>	<u>Units</u>
25	$\theta$	Euler angles of local horizon coordinates	deg
26	$\psi$		
27	$\phi$		
28	X	Spacecraft selenographic unit velocity vector	dim
29	Y		
30	Z		
31	X	Selenographic unit vector from center of Moon to center of Earth	dim
32	Y		
33	Z		
34 to 514/1026		Not used	

Note: Data do not always progress uniformly in time. Occasionally, data frames will reverse in time for one frame, then continue forward. This effect is caused by the sampling procedure in which deliberate overlap was inserted. Time on data is correct.

E. Definition of Contents

1. Data are defined under subtasks 4 and 5 of the text.
2. Ephemeris and ancillary data are described in greater detail in appendix 31-E.

APPENDIX 31-D — MATRIX CORRECTION FACTORS

The following tables contain the matrix correction factors (c-matrix) that were applied to the 116-cm data in subtask 5 of text. No corrections were applied to the 13-cm data. In all cases, the following values were used for  $C_{12}$  and  $C_{22}$ .

$$\left. \begin{aligned} C_{12} &= 0.0 + j 0.0 \\ C_{22} &= 1.0 + j 0.0 \end{aligned} \right\} \quad (31-D1)$$

Only  $C_{11}$  and  $C_{21}$  were varied. Start times shown in the following table refer to the time on the first frame to which the particular c-matrix was applied; the same c-matrix was used on all succeeding frames with times less than the next entry in the table.

Apollo 14

<u>Time UT2, sec</u>	<u>c-matrix</u>	
Start	$C_{11}$	$C_{21}$
23 838.35	1.100 + j 0.0	0.0 + j 0.0
25 155.63	1.960 + j .0	.050 + j .200
25 166.28	1.230 + j .0	.070 + j .150
25 168.94	1.100 + j .0	.0 + j .0
25 190.24	1.200 + j .0	.0 + j .07
25 192.91	1.960 + j .0	.050 + j .200
25 198.23	1.200 + j .0	.0 + j .070
25 206.22	1.100 + j .0	.0 + j .0
26 348.41	.929 + j .0	.189 + j .0

Apollo 15

<u>Time UT2, sec</u>	<u>c-matrix</u>	
Start	$C_{11}$	$C_{21}$
All data	1.000 + j 0.0	0.0 + j 0.0

Apollo 16

<u>Time UT2, sec</u>	<u>c-matrix</u>	
Start	$C_{11}$	$C_{21}$
4592.35	0.913 + j 0.0	-0.134 - j 0.045
4780.77	.958 + j .0	-.040 - j .010
<sup>4</sup> 5432.35	.944 + j .0	-.055 - j .032
5587.79	1.000 + j .0	-.060 + j .020
5983.46	.900 + j .0	-.100 - j .050
<sup>4</sup> 6272.35	.830 + j .0	-.100 - j .040
6484.32	.870 + j .0	-.090 + j .0
7030.72	.860 + j .0	-.060 - j .050
<sup>4</sup> 7112.35	.871 + j .0	-.072 - j .490
7333.74	.815 + j .0	-.066 + j .010
7701.15	.778 + j .0	-.060 - j .040
<sup>4</sup> 7952.35	.740 + j .0	-.100 - j .040

---

<sup>4</sup>These changes are located in overlap areas described in appendix 31-C, item D3. The change takes effect on the frame with the time (word 2, record 6; appendix 31-C) closest to that shown here.

## APPENDIX 31-E — INTEGRAL TAPE FORMAT

The integral tape contains reduced data records generated in subtasks 7 to 9. (See fig. 31-1.) This appendix contains the detailed formatting of that tape and describes all ancillary computations.

- A. Tape Organization — The following table contains the file contents and the data record length for the integral tape.

<u>File no.</u>	<u>Contents</u>	<u>Record length</u>
1	Apollo 14, 116 cm	50 words
2	Apollo 14, 13 cm	50 words
3	Apollo 15, 116 cm	50 words
4	Apollo 15, 13 cm	50 words
5	Apollo 16, 116 cm	50 words
6	Apollo 16, 13 cm	50 words

The tape is nine track, 800 bpi, binary in XDS Sigma 5 machine images. See appendix 31-F for a description of Sigma 5 machine images.

### B. File Organization

1. Header record
2. Data record
  - .
  - .
  - .
  - <many data records>
  - .
  - .
  - .
3. End of file
4. Header record
5.
  - .
  - .
  - .

C. Header record format

<u>Word no.</u>	<u>Contents</u>	<u>Units</u>	<u>Machine type</u> <sup>5</sup>
1 to 42	Alphanumeric file identifier	--	A
43	Day of year on which data were collected (January 1 = 1)	days	I
44	Year data were taken	year	I
45 and 46	Julian ephemeris day at 00:00 UT2 on the day the data were taken	days	DPR
47 and 48	Julian ephemeris day of reference epoch	days	DPR
49	Time increment between center point of data averaging frame	sec	R
50	Number of data records following this header record	--	I

D. Data Record Format (all machine type real)

<u>Word no.</u>	<u>Contents</u>	<u>Units</u>
1	Meaningless	--
2	UT2 at midpoint of frame	sec
3	X } Components of selenographic Y } unit position vector of Z } spacecraft location	dimension (dim)
4		
5		
6	X } Components of selenographic Y } velocity unit Z } vector	dim
7		
8		

<sup>5</sup>A = alphanumeric; I = integer; R = real; DPR = double precision real.

D. Data Record Format (all machine type real) - continued

<u>Word no.</u>	<u>Contents</u>	<u>Units</u>
9	Speed: magnitude of spacecraft velocity vector	m/sec
10	X } Components of selenographic unit vector Y } from center of the Moon Z } to center of the Earth	dim
11		
12		
13	X } Components of selenographic unit position Y } vector of specular Z } point location	dim
14		
15		
16	θ } Euler angles of spacecraft attitude and ψ } local horizon frame φ }	deg
17		
18		

$$\bar{A}_{veh} = \begin{bmatrix} \phi \\ (X) \end{bmatrix} \begin{bmatrix} \psi \\ (Z) \end{bmatrix} \begin{bmatrix} \theta \\ (Y) \end{bmatrix} \begin{bmatrix} \bar{A}_1 \end{bmatrix}$$

(clockwise rotation looking in plus-axis direction)

19	α <sub>s</sub> } Vehicle look angles to specular β <sub>s</sub> } point	deg
20		
21	δ } Angle between plane of incidence and plane containing both the vehicle X-axis and the direction vector to specular point	deg
22	α <sub>e</sub> } Vehicle look angles to Earth β <sub>e</sub> }	deg
23		
24	Selenographic latitude of spacecraft position	deg
25	Selenographic longitude of spacecraft position	deg
26	Selenographic latitude of specular point	deg

D. Data Record Format (all machine type real) - continued

<u>Word no.</u>	<u>Contents</u>	<u>Units</u>
27	Selenographic longitude of specular point	deg
28	Angle of incidence	deg
29	Instantaneous speed of specular point on lunar surface	m/sec
30	Predicted bandwidth for rms surface slope of 0.1	Hz
31	Reflected Doppler minus direct Doppler	Hz
32	Total Doppler shift of reflected signal	Hz
33	Component of Doppler shift due to Earth rotation	Hz
34	Altitude of spacecraft above lunar surface; radius of the Moon assumed to be 1736 km	km
35	Radar cross section predicted for smooth conducting Moon	dim
36	(Radar cross section)/(received power)	m <sup>2</sup> /W
37	Polarized power	arb
38	Normalized polarized power	K
39	Unpolarized power	arb
40	Normalized unpolarized power	K
41	Equivalent area bandwidth	Hz
42	Normalized absolute-moment bandwidth	dim
43	Normalized second-moment bandwidth	dim
44	Centroid of the echo spectrum	Hz

D. Data Record Format (all machine type real) - concluded

<u>Word no.</u>	<u>Contents</u>	<u>Units</u>
45	rms slope inferred from equivalent area bandwidth	deg
46	Spare if value equals zero; otherwise, hand-scaled one-half power echo bandwidth	Hz
47	Data validity flag	--
48	Spare if value equals zero; otherwise, value of spacecraft antenna gain in $\alpha_s$ and $\beta_s$ direction (See words 19 and 20.)	dim
49	Not used	--
50	Data record sequence number	--

Note: Data do not always progress uniformly in time. Occasionally, data records will reverse in time for one record, then continue forward. This effect is caused by the sampling procedure in which a small deliberate overlap was inserted. Time tags on data are correct. Overlapping data correspond to the same time interval but different sampling passes. Slight differences arise from variation in exact times averaged.

E. Data Parameter Definitions — The remainder of this section is used to define the contents of the data records described in the preceding table. The individual subsection numbers correspond to the word numbers in item D (data record format). If a particular quantity has been described at length elsewhere, a reference will be given. Otherwise, the quantity is defined herein. The cross-reference table for JM doptrack/integral tape trajectory parameters is contained in appendix 31-G.

1. Meaningless.
2. Time is the UT2 in seconds at which the data were taken. This time corresponds to the midpoint of the averaging interval, as described under subtask 4. All trajectory parameters have been interpolated to this time so that geometrical quantities correspond to the location of the

specular point on the mean lunar surface at the middle of the averaging interval.

- 3, 4, 5. Selenographic Unit Position Vector is defined with respect to the lunar surface. This vector is a unit vector directed from the center of the Moon for the instantaneous location of the spacecraft. The X, Y, and Z directions are defined as follows: X = mean Earth direction, Y = mean direction of the following limb, and Z = north polar direction. The selenographic coordinates were obtained by rotation from the selenocentric geoequatorial units of the epoch given in the header record. Procedures are described in reference 31-12.
- 6, 7, 8. Selenographic Unit Velocity Vector is a unit vector in the direction of the spacecraft velocity. The coordinate system is the same as that given in item 3, 4, 5.
9. Speed is the magnitude of the spacecraft velocity vector.
- 10, 11, 12. Selenographic Unit Vector to Earth is a unit vector giving the direction from the lunar center of mass to the terrestrial center of mass in the selenographic coordinate system described in item 3, 4, 5.
- 13, 14, 15. Selenographic Unit Position Vector of Specular Point is a unit vector from the center of mass of the Moon to the location of the specular point on the mean spherical lunar surface. For this computation, the lunar radius was taken as 1736 km. The specular point is the location on the mean lunar surface at which the angles of incidence and reflection are equal (ref. 31-12).
- 16, 17, 18. Euler Angles of Spacecraft Attitude connect the spacecraft attitude with a local horizon reference frame. Both the local horizon system and the Euler angles are defined in appendix 31-H.
- 19, 20. Look Angles to Specular Point are in vehicle polar coordinates. These quantities are defined in appendix 31-H.
21. Plane of the Vehicle, the orientation with respect to the plane of incidence, is given by the angle  $\delta$ . This quantity is necessary to define the vehicle attitude with respect to the plane of incidence. The angle  $\delta$  is defined in appendix 31-H.
- 22, 23. Look Angles to Earth are the vehicle polar coordinates of a unit vector in the Earth direction.

direction. These quantities were computed in the same manner as in item 19, 20 using the unit vector to Earth.

24. Selenographic Latitude of Spacecraft Position is the selenographic latitude of the subspacecraft point computed from the Z component of the unit vector given in item 3, 4, 5.
25. Selenographic Longitude of Spacecraft Position is the selenographic longitude of the subspacecraft position computed from item 3, 4, 5 according to astrometric convention, western limb of the Moon leading.
26. Selenographic Latitude of Specular Point is the selenographic latitude of the specular point on a mean spherical lunar surface computed from item 15.
27. Selenographic Longitude of Specular Point is the selenographic longitude of the specular point on the mean spherical lunar surface computed from item 13, 14, 15.
28. Angle of Incidence is the angle of incidence on mean spherical lunar surface at the specular point (ref. 31-12).
29. Speed of the Specular Point is the speed with which the instantaneous specular point moves across the mean lunar surface (ref. 31-12).
30. Predicted Bandwidth is the one-half power spectral width predicted for an rms surface slope of 0.1, based on the instantaneous angle of incidence and specular point velocity. Computation is after reference 31-13 and is also described in reference 31-12. Fjeldbo (ref. 31-13) gives a theoretical expression for one-half power echo bandwidth:

$$\Delta f = 4(2 \ln 2)^{\frac{1}{2}} \frac{v_s}{\lambda} \frac{h_0}{d_0} \cos \phi \quad (31-E1)$$

where  $v_s$  = velocity of the specular point on the mean lunar surface,  $\lambda$  = wavelength of the radiation (either 116 or 13 cm),  $\phi$  = angle of incidence at the specular point, and the quantity  $h_0/d_0$  = the mean lunar rms slope.

The quantity  $\Delta f$  is the one-half power bandwidth predicted for a Gaussian spectrum. Such a spectrum would

result from a gently undulating surface with Gaussian autocorrelation function.

31. Difference Between Reflected and Direct Doppler Shifts is the predicted frequency difference between a wave reflected from the specular point and the signal traveling directly from the spacecraft to Earth. Sign convention is such that the difference is positive for a reflected Doppler shift greater than the direct Doppler shift.
32. Doppler Shift is the total Doppler shift expected from the reflected signal. Computation of this Doppler shift included spacecraft motion and the Earth rotation, but did not include the rate of change of distance between the Earth and the Moon.
33. Doppler Due to Earth Rotation is the component of the observed Doppler shift due to Earth rotation for a signal arriving from the direction of the Moon.
34. Altitude of the spacecraft above the lunar surface has been computed assuming a lunar radius equal to 1736 km. The magnitude of the spacecraft radius vector from the lunar center of mass is obtained by adding the contents of word 34 to 1736 km.
35. Normalized Bistatic-Radar Cross Section is the bistatic-radar cross section of a smooth conducting sphere of the same radius and relative geometry as the Moon. Following reference 31-13, this cross section is given by

$$\sigma_B = \frac{4\pi R_1^2 \cos \phi}{\left(\cos \phi + \frac{2d_{0r}}{R}\right) \left(1 + \frac{2d_{0r} \cos \phi}{R}\right)} \quad (31-E2)$$

where  $R_1$  = distance from transmitter to the center of the Moon

$R$  = lunar radius ( $1.736 \times 10^6$  m)

$\phi$  = angle of incidence (item 28)

$d_{0r}$  = distance from the transmitter to the specular point on the mean lunar surface

36. (Radar Cross Section)/(Received Power) is a multiplicative constant relating instantaneous geometry and received power to surface reflectivity.

$$\frac{\text{radar cross section}}{\text{received power}} = \frac{(4\pi)^2 R_1^2 R_2^2}{A P_T G_T \sigma_B} \quad (31-E3)$$

where  $R_1$  = distance from transmitter to center of the Moon

$R_2$  = distance from receiving site to center of the Moon

A = effective aperture of receiving antenna

$P_T$  = transmitted power

$G_T$  = transmitting antenna gain in specular point direction

$\sigma_B$  = bistatic-radar cross section for a perfectly conducting Moon

For convenience, this expression was evaluated with the following numerical values for the preceding quantities.

$R_1$  = instantaneous value from NASA Lyndon B. Johnson Space Center trajectory data

$\sigma_B$  = instantaneous value from item 35

$R_2 = 4 \times 10^8$  m

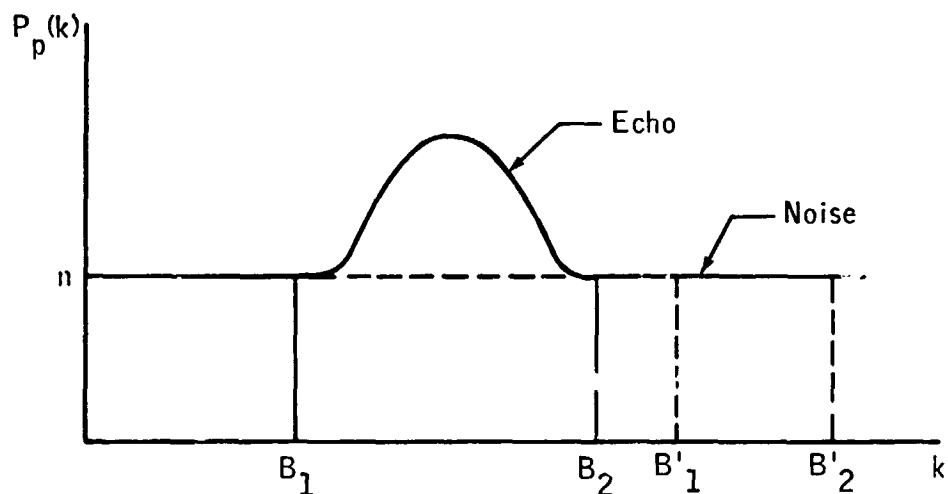
A =  $0.5(22.5)^2 \pi$

$G_T = 1$

$P_T = 2.5$  W

These values give only order of magnitude results for this experiment.

37. Polarized Power is the experimenter's best estimate of the polarized component of the received echo total power. Extraction of the polarized power is discussed under subtask 8. Denote the polarized power spectrum  $P_p(k)$ . Consider the following diagram.



Polarized power is determined from

$$P = \sum_{k=B_1}^{B_2} [P_p(k) - n] \quad (31-E4)$$

The  $P_p(k)$  is a polarized power spectrum. In the determination of  $P$ , the signal limits  $B_1$ ,  $B_2$ , and  $n$  were selected by the experimenter. The quantity  $n$  was chosen on the basis of

$$\sum_{B_1}^{B_2} [P_p(k) - \hat{n}] \approx 0 \quad (31-E5)$$

where  $B'_1$  and  $B'_2$  represent spectral limits containing no echo signal, and  $\hat{n}$  represents a sequence of trials

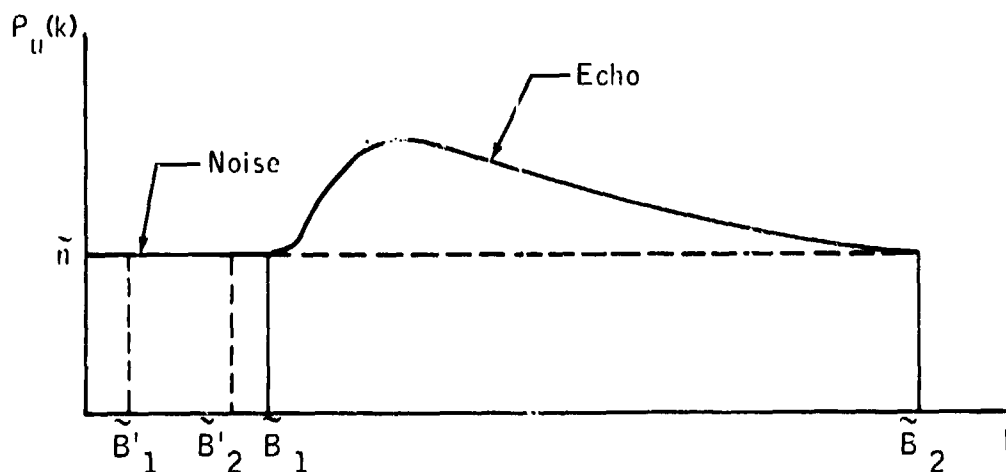
of  $n$ . The limits  $B_1$ ,  $B_2$ ,  $B_1'$ , and  $B_2'$  were varied as necessary to follow the changing echo signal.

38. Normalized Polarized Power is the quantity contained in item 37 divided by the average power spectral density of the system noise level. This quantity was discussed in detail under subtask 8. Using the notation introduced under item 37, normalized polarized power =  $P/n$ , where  $P$  and  $n$  have the same meaning as before.

Note: The ratio  $P/n$  is extremely sensitive to the choice of  $n$ . Thus, polarized power is considered the best overall measure of received polarized echo power. However,  $P/n$  provides the only method, through the measure of system temperature, of obtaining an absolute power calibration. Similarly, the value of  $n$  may be determined from the ratio of polarized power to  $P/n$ , so that the variations in system temperature or gain (or both) may be estimated.

39. Unpolarized Power is the analogous quantity to item 37 for the unpolarized power spectrum. The unpolarized power was obtained in a manner similar to that used to compute polarized power. Letting  $P_u(k)$  represent the unpolarized power spectra, and referring to the diagram below, the unpolarized power is given by

$$U = \sum_{\tilde{B}_1}^{\tilde{B}_2} [P_u(k) - \tilde{n}] \quad (31-E6)$$



C. 8

where the tildes refer to the values of  $B$  and  $n$  used in the unpolarized power spectrum. In general, the limits for the polarized and unpolarized echoes were different, as was the value of the system noise level. The difference in frequency limits arose from the difference in the spectral distribution of the unpolarized power; the difference in system noise temperature arose from the signal processing used to separate these quantities (subtasks 4 and 5). The value of  $\tilde{n}$  was chosen in a manner similar to that of  $n$  in item 37. In some cases, it was not clear that all the unpolarized power is contained in the receiver passband. In this event,  $\tilde{B}_1$  or  $\tilde{B}_2$  was set equal to the upper or lower frequency limit as appropriate.

40. Normalized Unpolarized Power is the analogous quantity to item 38, for the unpolarized power spectrum. By definition, normalized unpolarized power =  $U/\tilde{n}$ , where the symbols have the same meaning as in item 39. Comments given under item 38 are also germane to normalized unpolarized power.
41. Equivalent Area Bandwidth<sup>6</sup> — The spectrum of a bistatic-radar echo from a well-behaved surface may be written as follows (ref. 31-13).

---

<sup>6</sup>The three machine-calculated bandwidths (i.e., the equivalent area bandwidth, the absolute-moment bandwidth, and the second-moment bandwidth) provide three quasi-independent methods of determining the spectral width of the received echoes. The equivalent area bandwidth provides a standard result that is not particularly sensitive to the Gaussian or the non-Gaussian nature of the echo spectrum. The absolute-moment bandwidth and the second-moment bandwidth thus emphasize departures from Gaussian because of the increasing importance given to the wings of the spectrum.

Equivalent area bandwidths have been used to determine lunar rms slopes. The absolute-moment bandwidths and the second-moment bandwidths, when normalized by the equivalent area bandwidth, give a sensitive measure of the departures of the echo spectra from the Gaussian conditions. The rms slopes derived from these measures are termed "Gaussian equivalent slopes" in that they would correspond to true surface conditions for a surface with Gaussian statistics and a Gaussian autocorrelation function with the same equivalent widths. A more complete description of the lunar slopes requires additional analysis (e.g., ref. 31-14).

$$S(f) = e^{-\frac{\pi^2 f^2}{2}} \left[ 4v_s (\pi/\lambda) \cos \phi \left( \frac{h_0}{d_0} \right) \right]^{-2} = e^{-\frac{f^2}{2\sigma^2}} \quad (31-E7)$$

where  $f$  = frequency measured from the centroid of the echo spectrum

$v_s$  = speed of the specular point across the mean lunar surface

$\lambda$  = wavelength

$\theta$  = angle of incidence

$h_0/d_0$  = unidirectional rms slope

Solving for rms slope in terms of measured values of standard deviation  $\hat{\sigma}$  of an experimental spectrum yields

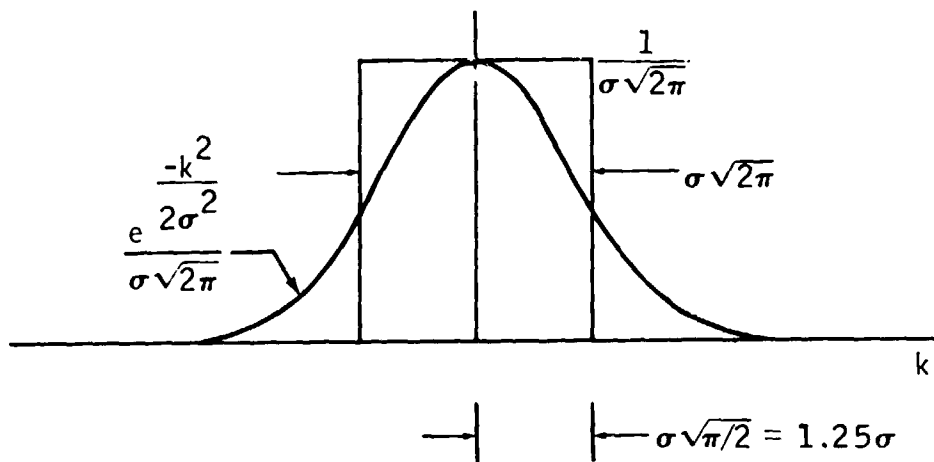
$$\frac{h_0}{d_0} = \frac{\hat{\sigma}}{2(v_s/\lambda) \cos \phi} \quad (31-E8)$$

Thus, the rms slope may be readily determined from an experimental curve in terms of the  $e^{-1}$  width of that curve. The equivalent area bandwidth is a measure of  $\hat{\sigma}$  based on an equivalent rectangular spectrum of the same area as the experimental spectrum. This width is computed as

$$\hat{\sigma}_{ea} = \frac{\sum_{C_1}^{C_2} P_p(k)}{\max P_p(k)} \cdot (2\pi)^{-\frac{1}{2}}; \quad C_1 < k < C_2 \quad (31-E9)$$

In the following diagram, the quantity  $\hat{\sigma}_{ea} = \sigma$  if the observed curve is Gaussian and noiseless. For non-Gaussian data,  $\hat{\sigma}_{ea}$  is still a measure of the bandwidth, although the interpretation must be modified. The rms

slopes determined from  $\hat{\sigma}_{ea}$  and from equation (31-E8) will be referred to as equivalent area slopes. The quantity  $\hat{\sigma}_{ea}$  is the equivalent area bandwidth.



42. Normalized Absolute-Moment Bandwidths are based on an equivalent value of  $\hat{\sigma}$  computed from the absolute moment of the data. That is,

$$\hat{\sigma}_{am} = \frac{\sum_{k=C_1}^{C_2} P_p(k) |k - \bar{k}|}{\sum_{k=C_1}^{C_2} P_p(k)} \cdot \sqrt{\frac{\pi}{2}} ; \bar{k} = \frac{\sum_{k=C_1}^{C_2} P_p(k) k}{\sum_{k=C_1}^{C_2} P_p(k)} \quad (31-E10)$$

For a Gaussian spectrum, the equivalent area moments and the absolute moments will be equal.

$$\hat{\sigma}_{am} = \hat{\sigma}_{ea} = \sigma \quad (31-E11)$$

where the symbols have the same meaning as in item 41. The normalized absolute-moment bandwidth is  $\hat{\sigma}_{am}/\hat{\sigma}_{ea}$ . For a Gaussian echo spectrum, this ratio will be unity.

43. Normalized Second-Moment Bandwidth is also based on Gaussian equivalence. This bandwidth is defined as

$$\hat{\sigma}_{sm}^2 = \frac{\sum_{k=C_1}^{C_2} P_p(k) (k - \bar{k})^2}{\sum_{k=C_1}^{C_2} P_p(k)}; \quad \bar{k} = \frac{\sum_{k=C_1}^{C_2} P_p(k) \cdot k}{\sum_{k=C_1}^{C_2} P_p(k)} \quad (31-E12)$$

For a Gaussian echo spectrum

$$\hat{\sigma}_{sm} = \hat{\sigma}_{am} = \hat{\sigma}_{ea} = \sigma \quad (31-E13)$$

where the symbols have the same meaning as under items 41 and 42. The normalized second-moment bandwidth is given by  $\hat{\sigma}_{sm}/\hat{\sigma}_{ea}$ . Again, departures of this ratio from unity are indicative of a non-Gaussian received echo spectrum.

44. Centroid of the Echo Spectrum is defined in the standard way.

$$\bar{k} = \frac{\sum_{k=C_1}^{C_2} P_p(k) \cdot k}{\sum_{k=C_1}^{C_2} P_p(k)} \quad (31-E14)$$

where the symbols have the same meaning as in items 41 to 43. The values of  $C_1$  and  $C_2$  are held constant throughout items 41 to 44. The echo spectrum centroid is used in the computations of the absolute-moment bandwidths and the second-moment bandwidths. It is also useful for estimation of the observed Doppler difference (item 31). However, the centroid has no direct meaning in an absolute sense because the transmitter frequencies from the spacecraft are not known precisely.

45. The rms Slopes are obtained from the equivalent area bandwidths according to

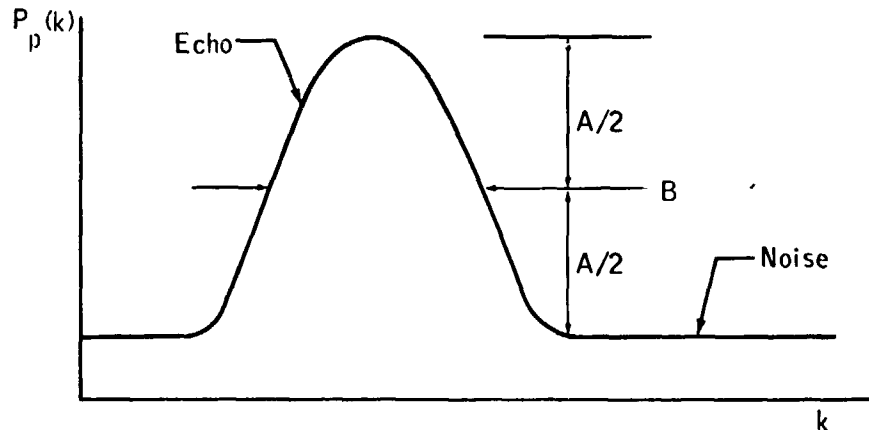
$$\frac{h_0}{d_0} = \frac{\hat{\sigma}_{ea}}{2(v_s/\lambda) \cos \phi} \quad (31-E15)$$

and

$$\text{unidirectional rms slope (deg)} = \tan^{-1} (h_0/d_0) \quad (31-E16)$$

where the results are expressed in degrees for convenience. The quantities  $v_s$ ,  $\lambda$ ,  $\phi$ , and  $\hat{\sigma}_{ea}$  have been defined in item 41.

46. Hand-Scaled One-Half Power Echo Bandwidths have been discussed previously under subtask 10. A one-half power echo bandwidth is defined as the quantity B in the following diagram. In practice, this value was obtained by hand scaling  $\tau$  from plots.



The hand-scaled bandwidths provide a rapid, simple technique for the evaluation of lunar rms surface slopes. The hand-scaled bandwidths were also used as a controlling parameter in development of automated techniques for obtaining echo bandwidths. The rms slopes may be obtained from the hand-scaled bandwidths by

$$\text{rms slope} = 5.7^\circ \times \frac{B}{\text{(predicted one-half power bandwidth for rms slope of 0.1)}} \quad (31-E17)$$

where the result is given in degrees for convenience. Predicted one-half power bandwidths for 0.1 rms slopes are given in word 30 of the integral tape data records. Hand measurements were made only for selected segments of the data.

47. Flag — The flag word contains a seven-level binary code that indicates data quality. A bit in the "1" condition indicates the existence of a special condition in the data. A bit position in the "0" state indicates only that the data are normal. The interpretation of the bit positions is as follows.

<u>Bit in "1" condition</u>	<u>Implication</u>
1	Polarized power data questionable or no good
2	Unpolarized power data questionable or no good

<u>Bit in "1" condition</u>	<u>Implication</u>
3	Polarized noise level $n$ (item 37) changed this data record
4	Polarized integration bounds $B_1$ and $B_2$ (item 37) changed this data record
5	Unpolarized noise level $\tilde{n}$ (item 39) changed this data record
6	Unpolarized integration bounds $\tilde{B}_1$ and $\tilde{B}_2$ (item 39) changed this data record
7	System gain changed this data record

#### Explanation

Bit Position "1" — Polarized data may be flagged for any of several reasons. The presence of interference, an error in setting the integration bounds, or a tape drive error in the data processing are examples of difficulties that would result in such a flag. In case of gross errors, the flag represents an objectively known bad data point. In the case of a more subtle phenomenon such as interference, the flag represents an experimenter's subjective opinion. For the 116-cm data, interference is the predominant cause of a data bad flag. Data users who wish to examine this question for themselves may do so by reprocessing the data from the JM doptrack tapes. It is very strongly recommended that no flagged data be used without taking this precaution.

Bit Position "2" — Unpolarized data may be flagged for the same reasons as those given for the polarized data under bit position "1." However, because gross errors for polarized and unpolarized data may be independent, and because the unpolarized data possess a certain immunity to interference, which tends to be polarized, the flags in bit positions "1" and "2" are not necessarily coincident. As before, in the case of interference, the investigator's judgment is involved.

Bit Position "3" — This flag is set when the noise level (i.e.,  $\bar{n}$  in item 37) is changed during the data reduction process. This flag serves to alert the user that such a change has been made. Any discontinuity that occurs when this bit is set is likely to result from this cause. In the polarized power case, such discontinuities are generally quite small, on the order of 1 percent. However, in the normalized polarized power case, such discontinuities may be large, on the order of two. Obviously, no physical significance should be attached to such discontinuities.

Bit Position "4" — Changes in the integration bounds are flagged for reasons similar to those given under bit position "3." The bounds  $B_1$  and  $B_2$  vary with the changing width and location of the polarized echo. Usually, such changes are very small and do not affect the data noticeably.

Bit Position "5" — Changes in the unpolarized noise level  $\bar{n}$  are made for the same reasons as those described under bit position "3." As before, changes in the unpolarized power, and especially the normalized unpolarized power, that occur with these changes in the value of  $\bar{n}$  are nonphysical.

Bit Position "6" — The comments that apply to the polarized integration bounds given under bit position "4" also apply here.

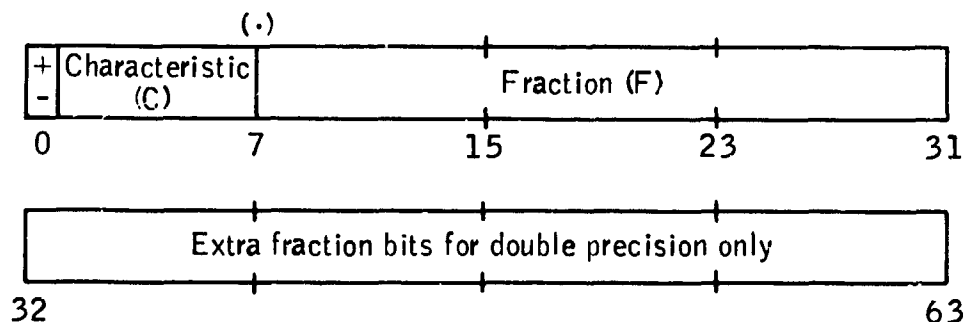
Bit Position "7" — System gain changes may occur during data reception in the receiving systems or during data playback in the record reproduction system. Such changes are flagged since they will appear as a change in the polarized and unpolarized signal levels. Gain changes do not affect measures of echo bandwidths.

48. Antenna Gain is the gain of the spacecraft antenna in the  $\alpha_s, \beta_s$  direction determined from antenna patterns.
49. Not used.
50. Sequence Number, where the first data record = 1.

APPENDIX 31-F — XDS SIGMA 5 MACHINE IMAGES

All data on the JM doptrack and integral tapes are in the form of XDS Sigma 5 machine images. One word is 32 bits; one byte, 8 bits. The data are real (floating point), integer, or alphanumeric. The machine images are as follows.

- A. Real — A single precision real number consists of a sign bit (bit 0), a biased,<sup>7</sup> base 16 exponent called a characteristic (bits 1 to 7), and a 24-bit fraction. A double precision number consists of a single precision number followed by an additional 32 bits of fractional significance, as indicated in the following diagram. Unless otherwise noted, all numbers referred to in this report as "real" are single precision.



A real number N is defined as follows.

$$N = F \times 16^{C-64}$$

where  $F \neq 0$

or  $2^{-24} \leq |F| < 1$  (single precision)

or  $2^{-56} \leq |F| < 1$  (double precision)

and  $0 \leq C \leq 127$

---

<sup>7</sup>The bias value of  $64_{10}$  is added to the exponent to make possible comparison of the absolute magnitude of two numbers without reference to a sign bit.

In contrast with the IBM 360 system, a negative real number is the two's complement of its positive representation.

- B. Integer — Integers are written in full-word, two's complement representation.
- C. Alphanumeric — Alphanumeric data (strings of characters) are represented in extended binary-coded-decimal interchange code. Each character occupies one byte (8 bits); therefore, each word of alphanumeric data contains four characters.

APPENDIX 31-G — CR SS-REFERENCE TABLE FOR JM DOPTRACK/INTEGRAL  
TAPE TRAJECTORY PARAMETERS

The following table provides a cross-reference between the JM doptrack trajectory parameter records and the integral tape data records. The JM doptrack tapes are described in appendix 31-C, which contains the detailed format for those tapes but does not define all of the trajectory parameters. Integral tapes are described in detail in appendix 31-E, which does include a detailed description of the various trajectory parameters. All trajectory parameters given on the JM doptrack tapes are also found on the integral tapes. This appendix provides a convenient means for determining the location of a given JM doptrack tape trajectory parameter in the integral tape format. For reference, the trajectory parameters are found in the sixth record of a data frame on the JM doptrack tape (i.e., in record number N·6, N = 1, 2, 3, ..., where the first data record = 1).

<u>JM doptrack</u> <u>word no.</u>	is found in	<u>Integral tape</u> <u>word no.</u>
1		1
2		2
3		21
4		30
5		28
6		34
7		9
8		35
9		36
10		3
11		4
12		5
13		13
14		14

---

<u>JM doptrack</u> <u>word no.</u>	is found in	<u>Integral tape</u> <u>word no.</u>
15		15
16		24
17		25
18		33
19		32
20		26
21		27
22		29
23		22
24		23
25		16
26		17
27		18
28		6
29		7
30		8
31		10
32		11
33		12

Units and scale factors are identical on JM doptrack and integral tapes.

APPENDIX 31-H — COORDINATE TRANSFORMATIONS

This appendix contains the necessary coordinate transformations for Apollo bistatic-radar data. Terms and the local horizontal coordinate system are defined; specification of spacecraft attitude, conversion of reference coordinate to local horizontal system, conversion of reference coordinates for vehicle coordinates, and computation of spacecraft-to-specular-point look angles are discussed; and data sources are given.

A. General definitions

$\bar{a}_{\Delta H}$  = vector in local horizon system

$\bar{a}_{\Delta P}$  = vector in primary or principal reference system

$\bar{a}_{\Delta V}$  = vector in vehicle reference frame

$\bar{p}$  = spacecraft position vector

$\bar{r}$  = specular point position vector

$\bar{v}$  = spacecraft velocity vector

$\left. \begin{matrix} \alpha \\ \beta \end{matrix} \right\}$  look angles to specular point in vehicle system

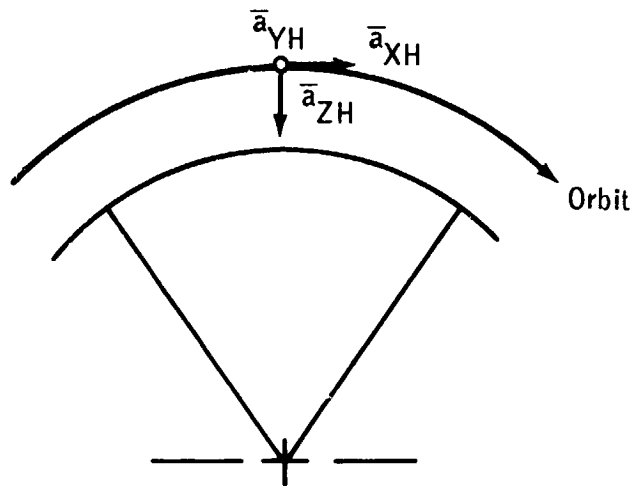
$\delta$  } orientation of vehicle along  $\alpha, \beta$  direction (defined in item G)

$\left. \begin{matrix} \phi \\ \psi \\ \theta \end{matrix} \right\}$  Euler angles between local horizon and vehicle systems (defined in item C)

B. Data supplied by the NASA Lyndon B. Johnson Space Center (JSC) contain spacecraft attitude in a "local horizontal" coordinate system, which is defined as follows.

$$\left. \begin{aligned} \bar{a}_{ZH} &= \frac{-\bar{p}}{|\bar{p}|} \\ \bar{a}_{YH} &= \frac{\bar{v} \times \bar{p}}{|\bar{v} \times \bar{p}|} \\ \bar{a}_{XH} &= \bar{a}_{YH} \times \bar{a}_{ZH} \end{aligned} \right\} \quad (31-H1)$$

69



where  $\bar{a}_{ZH}$  is directed toward the nadir,  $\bar{a}_{YH}$  is directed along the angular momentum vector, and  $\bar{a}_{XH}$  is in the plane of the orbit roughly along  $\bar{v}$ .

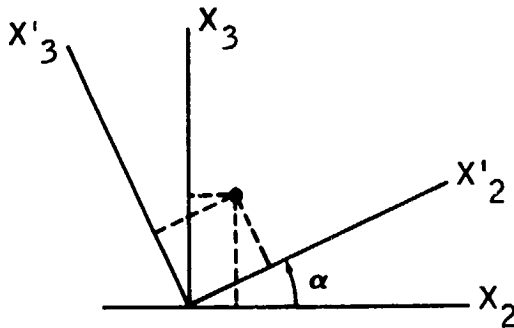
- C. Specification of spacecraft attitude — The Euler angles  $\phi, \psi, \theta$  specify the sequence of rotations required to transform local horizontal coordinates to vehicle coordinates as follows.

$$\begin{bmatrix} X_V \\ Y_V \\ Z_V \end{bmatrix} = \begin{bmatrix} \phi \\ (X) \end{bmatrix} \begin{bmatrix} \psi \\ (Z) \end{bmatrix} \begin{bmatrix} \theta \\ (Y) \end{bmatrix} \begin{bmatrix} X_H \\ Y_H \\ Z_H \end{bmatrix} \quad (31-H2)$$

where the matrix  $\begin{bmatrix} (\text{ang}) \\ (\text{axis}) \end{bmatrix}$  denotes a rotation of (ang)

about the current (axis). Rotations are in the sequence (Y,Z,X). The sense of rotation is clockwise when looking in the + (axis) direction. For instance, consider the following.

$$\left. \begin{aligned}
 \begin{bmatrix} x_1' \\ x_2' \\ x_3' \end{bmatrix} &= \begin{bmatrix} \alpha \\ (X_1) \end{bmatrix} \begin{bmatrix} x_1 \\ x_2 \\ x_3 \end{bmatrix} \\
 x_1' &= x_1 \\
 x_2' &= x_2 \cos \alpha + x_3 \sin \alpha \\
 x_3' &= -x_2 \sin \alpha + x_3 \cos \alpha
 \end{aligned} \right\} (31-H3)$$



Then, the transformation is

$$\begin{bmatrix} x_1' \\ x_2' \\ x_3' \end{bmatrix} = \begin{bmatrix} 1 & 0 & 0 \\ 0 & \cos \alpha & \sin \alpha \\ 0 & -\sin \alpha & \cos \alpha \end{bmatrix} \begin{bmatrix} x_1 \\ x_2 \\ x_3 \end{bmatrix} \quad (31-H4)$$

Thus

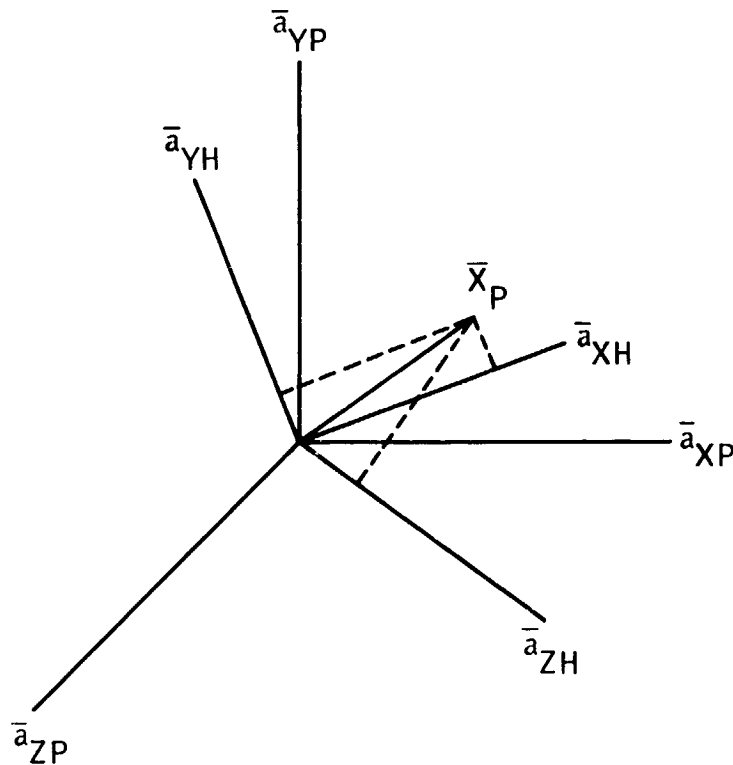
$$\begin{bmatrix} \phi \\ (X) \end{bmatrix} \begin{bmatrix} \psi \\ (Z) \end{bmatrix} \begin{bmatrix} \theta \\ (Y) \end{bmatrix} = \begin{bmatrix} R \end{bmatrix} \quad (31-H5)$$

$$\begin{aligned}
 [R] = & \begin{bmatrix}
 \cos \psi \cos \theta & \sin \psi \\
 \sin \phi \sin \theta - \cos \phi \sin \psi \cos \theta & \cos \phi \cos \psi \\
 \sin \phi \sin \psi \cos \theta + \cos \phi \sin \theta & -\sin \phi \cos \psi \\
 -\cos \psi \sin \theta \\
 \cos \phi \sin \psi \sin \theta + \sin \phi \cos \theta \\
 \cos \phi \cos \theta - \sin \phi \sin \psi \sin \theta
 \end{bmatrix} \quad (31-H6)
 \end{aligned}$$

- D. Conversion of reference coordinate to local horizontal system — Quantities that are known in the principal reference system may be converted to the local horizon system through the directional cosines connecting the two. These are given by the vector components of  $\bar{a}_{\Delta H}$ , expressed in the primary system. The  $\bar{a}_{\Delta H}$  functions form the rows of the transformation (rotation only) matrix. Thus

$$\begin{bmatrix} \bar{x}_H \end{bmatrix} = \begin{bmatrix} a_{XH_1} & a_{XH_2} & a_{XH_3} \\ a_{YH_1} & a_{YH_2} & a_{YH_3} \\ a_{ZH_1} & a_{ZH_2} & a_{ZH_3} \end{bmatrix} \begin{bmatrix} \bar{x}_P \end{bmatrix} \quad (31-H7)$$

as indicated in the diagram on the following page.



Components in the subscript H system are projections onto reference axes of that system.

- E. Conversion of reference coordinates for vehicle coordinates — Conversion from principal coordinates to vehicle coordinates may be made by two successive rotations: principal coordinates → local horizontal coordinates; local horizontal coordinates → vehicle coordinates. Or

$$\bar{x}_V = [R_{VH}] [x_H = [R_{VH}] [R_{HP}] [\bar{x}_P \quad (31-H8)$$

where  $R_{ij}$  implies a rotation from the  $j$  to  $i$  system.

Thus

$$[R_{VP}] = [R_{VH}] [R_{HP}] \quad (31-H9)$$

F. Computation of spacecraft-to-specular-point look angles  $\alpha_s, \beta_s$  — The direction to the specular point from the spacecraft is

$$\frac{\bar{r} - \bar{p}}{|\bar{r} - \bar{p}|} = \bar{\gamma} \quad (31-H10)$$

In vehicle coordinates

$$\bar{\gamma}_V = [R_{VP}] \bar{\gamma}_P \quad (31-H11)$$

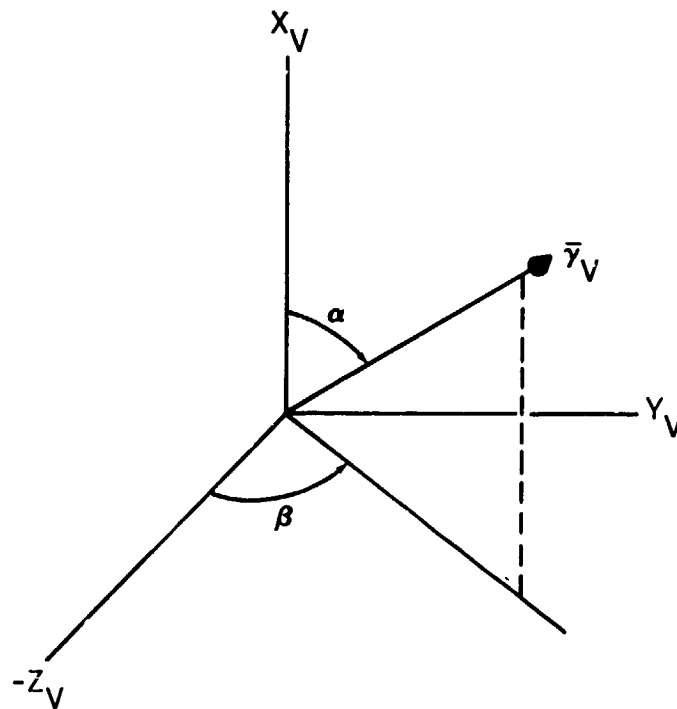
The quantity  $\alpha$  is measured from the +X direction,

$$\alpha_s = \arccos(\gamma_{XV}); \quad 0 \leq \alpha \leq \pi \quad (31-H12)$$

The quantity  $\beta_s$  is the azimuthal angle (minimum angle to  $\bar{\gamma}, X_V$  plane) measured from the  $-Z_V$  axis, positive toward  $+Y_V$ :

$$\beta_s = \text{signum}(\gamma_{YV}) \cdot \arccos(-\gamma_{ZV}); \quad -\pi \leq \beta \leq \pi \quad (31-H13)$$

where  $\text{signum}(X) = X/|X|$ . These quantities are depicted in the following diagram.

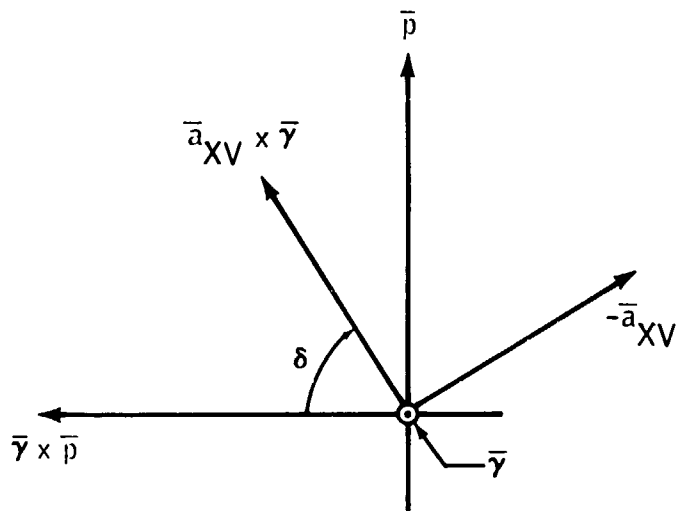


- G. Definition and computation of  $\delta$  — The angle  $\delta$  is the included angle between the  $\bar{\gamma}, \bar{a}_{XV}$  plane and the plane of incidence, the  $\bar{\gamma}, \bar{p}$  plane. (See diagram.)

$$\delta = \text{signum}(\bar{p} \cdot \bar{a}_{XV} \otimes \bar{\gamma}) \cdot \arccos \left( \frac{\bar{\gamma} \otimes \bar{p} \cdot \bar{a}_{XV} \otimes \bar{\gamma}}{\bar{\gamma} \otimes \bar{p} \cdot \bar{a}_{XV} \otimes \bar{\gamma}} \right);$$

$$-\pi \leq \delta \leq \pi$$

(31-H14)



- H. Sources — Additional information regarding the definitions of local horizon and vehicle coordinates may be found in JSC publications describing trajectory tapes. Input for  $\alpha_s, \beta_s, \delta$  computations are JSC-supplied experimenter trajectory tapes. The principle reference frame is selenographic.

#### REFERENCES

- 31-1. Howard, H. T.; and Tyler, G. L.: Bistatic-Radar Investigation. Sec. 17 of Apollo 14 Preliminary Science Report, NASA SP-272, 1971.
- 31-2. Howard, H. T.; and Tyler, G. L.: Bistatic-Radar Investigation. Sec. 23 of Apollo 15 Preliminary Science Report, NASA SP-289, 1972.
- 31-3. Howard, H. T.; and Tyler, G. L.: Bistatic-Radar Investigation. Sec. 25 of Apollo 16 Preliminary Science Report, NASA SP-315, 1972.
- 31-4. Howard, H. T.; and Tyler, G. L.: Bistatic-Radar Observations of the Lunar Surface with Apollos 14 and 15. Lunar Science III (Abs. of papers presented at the Third Lunar Science Conference (Houston, Tex.), Jan. 10-13, 1972), p. 398.
- 31-5. Tyler, G. Leonard; and Ingalls, Daniel H. H.: Functional Dependences of Bistatic-Radar Frequency Spectra and Cross Sections on Surface Scattering Laws. J. Geophys. Res., vol. 76, no. 20, July 1971, pp. 4775-4785.
- 31-6. Blackman, R. B.; and Tukey, J. W.: The Measurement of Power Spectra. Dover Publications, Inc. (New York), 1958.
- 31-7. Born, Max; and Wolf, Emil: Principles of Optics. Pergamon Press (New York), 1959.
- 31-8. Tyler, G. Leonard: Estimation of Polarization with Arbitrary Antennas. NASA CR-116449, 1970.
- 31-9. Tyler, G. Leonard; and Simpson, Richard A.: Bistatic-Radar Studies of the Moon with Explorer 35. Part 2: Methods of Data Reduction and Reduced Observations, Final Report. NASA CR-119032, 1970.
- 31-10. Ko, H. C.: On the Reception of Quasi-Monochromatic, Partially Polarized Radio Waves. Proc. IRE, vol. 50, no. 9, Sept. 1962, pp. 1950-1956.
- 31-11. Beckmann, P.: The Depolarization of Electromagnetic Waves. The Golem Press (Boulder, Colo.), 1968.

- 31-12. Tyler, G. L.: Oblique-Scattering Radar Reflectivity of the Lunar Surface: Preliminary Results from Explorer 35. J. Geophys. Res., vol. 73, no. 24, Dec. 1968, pp. 7609-7620.
- 31-13. Fjeldbo, G.: Bistatic Radar Methods for Studying Planetary Ionospheres and Surfaces. Ph. D. Dissertation, Stanford Univ., 1964.
- 31-14. Parker, M. N.; and Tyler, G. L.: Bistatic Radar Estimation of Surface-Slope Probability Distributions with Applications to the Moon. Radio Science, vol. 8, no. 3, Mar. 1973, pp. 177-184.

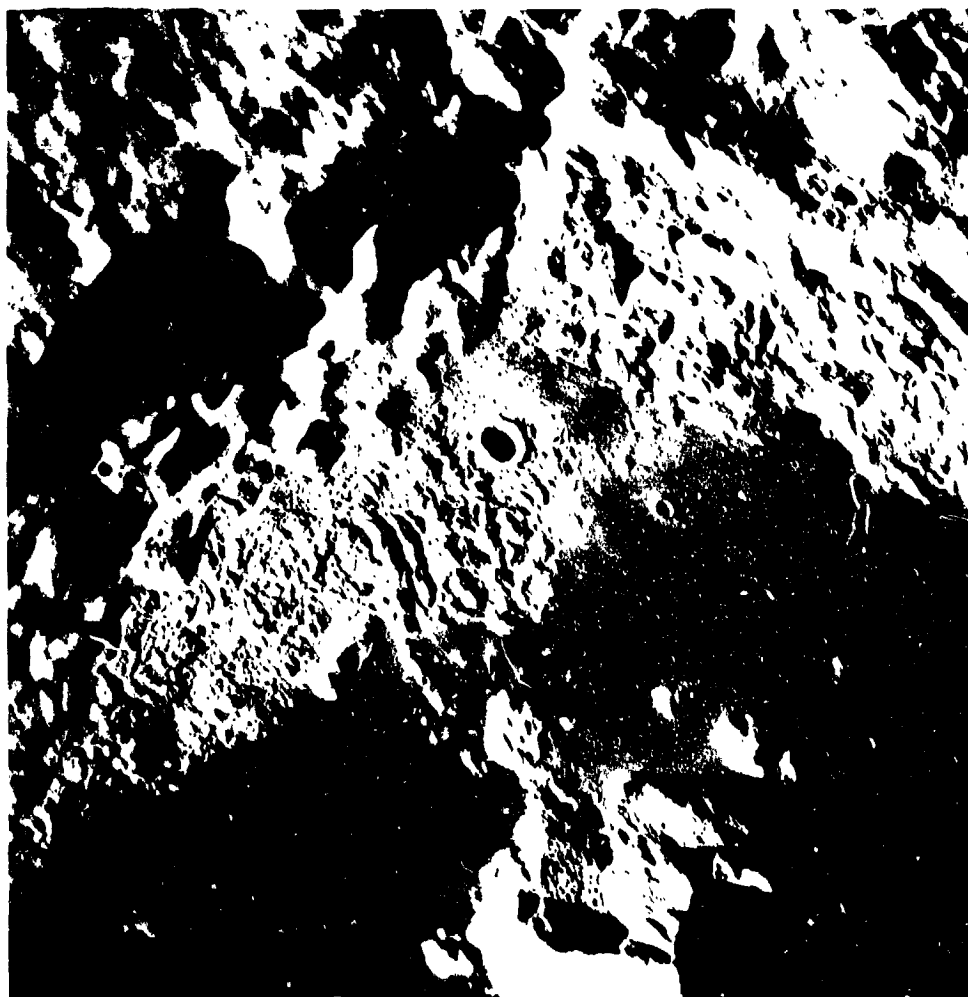
#### BIBLIOGRAPHY

- Moore, H. J.; and Tyler, G. L.: Comparison Between Photogrammetric and Bistatic-Radar Slope-Frequency Distributions. Sec. 33, Part C, of Apollo 17 Preliminary Science Report, NASA SP-330, 1973.
- Thompson, T. W.; Howard, K. A.; Shorthill, R. W.; Tyler, G. L.; et al.: Remote Sensing of Mare Serenitatis. Sec. 33, Part A, of Apollo 17 Preliminary Science Report, NASA SP-330, 1973.
- Thompson, T. W.; Masursky, H.; Shorthill, R. W.; Tyler, G. L.; and Zisk, S. H.: A Comparison of Infrared, Radar, and Geologic Mapping of Lunar Craters. The Moon, vol. 10, no. 1, 1974, pp. 87-117.
- Tyler, G. L.; and Howard H.: Dual-Frequency Bistatic-Radar Investigations of the Moon with Apollos 14 and 15. J. Geophys. Res., vol. 78, no. 23, Aug. 10, 1973, pp. 4852-4874.

32. INFRARED SCANNING RADIOMETER (NASA EXPERIMENT S-171)

NSSDC IDENTIFICATION NUMBER:

APOLLO 17 72-096A-03



ORIGINAL PAGE IS  
OF POOR QUALITY

CONTENTS - SECTION 32

	Page
INSTRUMENT DESCRIPTION . . . . .	32-4
LUNAR SURFACE COVERAGE . . . . .	32-5
DATA QUALITY . . . . .	32-5
CONCLUSIONS . . . . .	32-8
DATA ARCHIVED AT NSSDC . . . . .	32-9
REFERENCES . . . . .	32-10

## 32. INFRARED SCANNING RADIOMETER

The infrared scanning radiometer (ISR) is a thermal imaging device capable of mapping lunar surface thermal emission from lunar orbit. The principal experimental objective of the ISR is the measurement of lunar nighttime temperatures and cooling rates for that portion of the Moon overflown by the orbiting command and service module. Such data are related to the physical parameters (density and thermal conductivity) of the local surface layer.

The thermal emission at the surface of the Moon serves to balance the solar radiation absorbed at the surface and the heat flow into or out of the subsurface. Heat conduction through the surface is generally small because the lunar soil is an excellent thermal insulator. Therefore, the daytime temperature regime is dominated by such factors as albedo, Sun angle, and local slope. Conversely, the nighttime emission represents the reradiation of heat stored during the lunar day and is largely dependent on the physical properties of the surface layer.

A simple, one-dimensional model of the soil layer (ref. 32-1) can be used to demonstrate the general behavior of surface temperature. In such a model, families of temperature curves (faired curves in fig. 32-1) can be generated in terms of a single thermal parameter  $\gamma = (k\rho c)^{-1/2}$ , where  $k$  is the thermal conductivity,  $\rho$  is the bulk density, and  $c$  is the specific heat. This simplified model disregards radiative transfer in the surface layer, but it is still useful to characterize the thermal response in terms of  $\gamma$ . Earth-based measurements of the lunar midnight temperature (ref. 32-2) place  $\gamma \approx 850 \text{ cal}^{-1} \text{ cm}^2 \text{ K sec}^{1/2}$ .

Shorthill and Saari's (ref. 32-3) thermal mapping of the eclipsed Moon from a telescope in Egypt demonstrated a wide variety of thermal behavior on the visible hemisphere. At a spatial resolution of approximately 20 km at the center of the disk, the Moon possessed hundreds of features that remained warm relative to their environs during the eclipse. Studies of these "thermal anomalies" indicated surface rock exposures associated with fresh impact features as an explanation. More recent correlations of the eclipse data with Earth-based radar measurements (ref. 32-4) show that a one-to-one correspondence does not exist between boulder fields and infrared anomalies.

In contrast to the eclipse cooling, which lasts for only a few hours, the lunar nighttime cooling regime lasts for 14 days. The nighttime thermal gradients extend deeper into the subsurface, and the surface temperature distributions are influenced by structure to a depth of a few tens of centimeters. Many observers (refs. 32-5 to 32-9) have attempted to map the nighttime Moon from Earth to take advantage of the improved subsurface resolution. However, the observational difficulties (ref. 32-8) associated with the low level of thermal emission and with the terrestrial atmosphere have precluded substantial success. The ISR provides a solution to the observational problem with an absolute radiometric measurement of lunar nighttime temperatures that represents an order-of-magnitude improvement in spatial and radiometric resolution over Earth-based work.

#### INSTRUMENT DESCRIPTION

The ISR is a thermal imaging line scanner (ref. 32-10). A schematic diagram of the optical system is shown in figure 32-2. The spherical-spherical Cassegrain optical system has a 17.78-cm (7 in.) aperture. The instantaneous field of view is 20 mrad, which translates to a circular lunar surface resolution element ranging from 2.0 to 2.6 km in diameter during accumulation of data from the spacecraft circularized orbit. This spatial resolution is an order-of-magnitude improvement over Earth-based observations.

The secondary mirror is mounted concentric with the 45° plane scanning mirror, and the entire assembly rotates continuously at 41.7 rpm during ISR operation. An aperture in the casting allows the beam to sweep from horizon to horizon perpendicular to the spacecraft groundtrack. The orbital motion of the command and service module spaces the scans along the groundtrack. The angular velocity of mirror rotation was chosen such that consecutive scans would be contiguous on the lunar surface when the spacecraft altitude was 111 km (60 n. mi.).

The detector assembly, consisting of a thermistor bolometer bonded to a hyperhemispheric silicon immersion lens, is mounted at the Cassegrain focus of the optical system. The spectral response of the radiometer is determined primarily by the lens, the only transmitting element in the optical path. The effective spectral pass band detectable by the ISR ranges from 1.2 to approximately 70  $\mu\text{m}$ . The long-wavelength cut-off is apparently caused by transparency of the detector flake. No filter was found that was capable of filtering out the reflected solar radiation at short wavelengths without compromising the long-wavelength (low temperature) sensitivity.

---

The ISR measured the full range of lunar temperatures from 80 to 400 K. The instrument output was simultaneously transmitted on three different channels at different gains. In this manner, the low-temperature sensitivity was maintained while the large dynamic range of signal was covered.

A special feature of the ISR radiometric calibration is the space clamping circuit. Once each scan, as the radiometer views deep space before crossing the lunar limb, the detector output is sampled and saved. This stored voltage is electronically subtracted from the detector output for the remainder of the scan. Therefore, each lunar scan is referenced to the radiometric "zero" of deep space. The clamping circuit enhances the absolute accuracy of the measurement while suppressing low-frequency detector noise.

#### LUNAR SURFACE COVERAGE

The sunrise terminator was located at longitude 28° E, in the eastern part of Mare Serenitatis, at the time of the first ISR scans of the Moon. By the time of transearth injection, the terminator had moved to longitude 46° W, just east of the crater Aristarchus. On the near side of the Moon, the orbit constrained nighttime coverage to the southern portions of Mare Serenitatis and Mare Imbrium, to Oceanus Procellarum, and to the equatorial region at the western limb. On the far side, the nighttime groundtracks passed south of the craters Hertzsprung and Korolev over to the craters Aitken and Van de Graaff.

A horizon-to-horizon scan from an altitude of 111 km includes an arc of 40° on the lunar sphere. Foreshortening seriously degrades surface resolution at the horizon. Good spatial resolution is achieved over a lunar spherical arc of 20° centered on the groundtrack. Somewhat more than 35 percent of the lunar surface was mapped during the course of the Apollo 17 mission.

#### DATA QUALITY

During the Apollo 17 mission, the ISR transmitted approximately 97 hr of lunar data containing approximately  $1 \times 10^8$  independent temperature measurements. Data were received at range stations by way of telemetry from the spacecraft and were recorded on magnetic tape. Samples of the data were available in real time at the Mission Control Center so that instrument performance could be assessed continuously. The available sampling

was equivalent to a scan of the lunar surface once every 6° of longitude. The overall impressions and tentative conclusions presented in this section are based on this sparse sampling plus additional, more comprehensive, quick-look displays of full data sets.

The scans in figures 32-3 and 32-4 have not been processed, and the amplitudes are proportional to radiance (instrument output voltage) rather than temperature. The figure legends indicate the approximate temperatures of various features.

In principle, each scan of the lunar surface should be preceded and followed by a short zero signal representing the sweep of the ISR beam through deep space on either side of the Moon. However, examination of the scans showed that the signal from space just past the trailing limb of the Moon (right side of figs. 32-3 and 32-4) was not zero. Scans of deep space during transearth coast were studied for clues to the problem. It was found that each scan contained a small ramp feature, commencing approximately at midscan and increasing linearly until the beam entered the ISR housing. The cause of the feature is not clear, but further work has shown that it can be removed from the data with only a modest increase in noise.

The ISR low-gain channel (channel 3) consistently saturated at the subsolar point. The phenomenon is attributed to the accumulation of error in the estimation of various instrument parameters such as the detector response to reflected sunlight and the wings of the field of view. An underestimation of the relevant quantities on the order of 5 to 15 percent can explain the effect. No scientific objective of the experiment was compromised by this occurrence.

In figure 32-3, two daytime scans received during the mission are compared. The scan centers are separated by only 6° of longitude, but the contrasting effects of topography in the maria and the highlands are quite clear. In figure 32-3(a), the thermal spike to the right of the mare and the dip to the left correspond to the northern and southern rims, respectively, of Mare Crisium. The difference in the thermal signatures of the two scarps demonstrates the dominance of local slope (i.e., local Sun angle) in the daytime thermal regime.

In figure 32-4, three lunar nighttime scans are shown. The scan in figure 32-4(a) comes from Oceanus Procellarum. The center of the scan is dominated by the crater Kepler A. The altitude of the spacecraft was 39.7 km at the time of the scan, making the ISR resolution element 0.8 km wide on the surface. The width of the broad base of the enhancement is 10 km, coinciding with the crater diameter. The thermal peak in the center is approximately 2 km across. The measured radiance in the central region

increases linearly from both sides to the center, implying that the actual temperature at the center has not been fully resolved. The dramatic change of material properties within the crater probably reflects exposure of bedrock. The radial gradient may be caused by a corresponding radial distribution of slump material from the crater walls. Unfortunately, no lunar photographs that contain a good view of the crater bottom have been found.

The scan shown in figure 32-4(b) contains predawn temperatures, the coldest for any given surface region. The scan center is located just north of Mare Vaporum and south of the Apollo 15 landing site. On the right portion of the scan is a negative anomaly, a region having depressed temperatures relative to its environs. In this case, the temperature difference is  $>8$  K. A lower limit is given because the width of the deflection, only one resolution element, implies that the anomaly may not be fully resolved. The anomalous region lies south of the crater Conon in Montes Apenninus. The magnitude of the temperature contrasts implies that the thermal conductivity of the soil in that region is approximately one-half that of the surrounding material. These underdense regions cannot be impact features. The preservation of the density contrast also implies that the regions are relatively young on a geologic scale. Cold nighttime anomalies are particularly difficult to detect from Earth-based observations. Although such features have been reported previously (refs. 32-8 and 32-11), the ISR results provide the first opportunity to study them in detail.

The scan in figure 32-4(c) includes far-side anomalies. Our abbreviated data survey shows that such features are not common in the nighttime data on the lunar far side (fig. 32-5). A low frequency of occurrence was anticipated because near-side anomalies occur preferentially in the maria (regions which are generally absent in the other hemisphere). The two prominent anomalies on the left side of the scan (fig. 32-4(c)) are located between the large craters Aitken and Van de Graaff. The large peak at the right limb corresponds to the crater Birkeland; the smaller structure to its left is in the crater Van de Graaff.

In figure 32-6, the scan in figure 32-4(a) is shown in its full data context. In this sequence of scans, north is to the left and west is upward. The extended feature just past the middle of the sequence is the crater Kepler. An interesting aspect of this set is the general lack of features except for the two major craters. As part of the Kepler ejecta blanket, this region might have been expected to be littered with debris and, consequently, to show considerable thermal structure.

Farther to the west, near the equator south of the crater Reiner, an area in Oceanus Procellarum that is devoid of craters displays many thermal anomalies (fig. 32-7). This structure

cannot be attributed to residual, postsunset, topographic cooling differences. Figure 32-5 shows that such structure is entirely absent in a highland region northeast of Mare Orientale and nearer the sunset terminator. It is probable that the amount of thermal structure is associated with the age of the region; older regions have a featureless, soil-like response.

In figure 32-1, lunar temperatures as measured by the ISR are plotted as a function of brightness longitude. The values were taken from scans made by the Apollo 17 spacecraft during revolution 20. An attempt was made to choose a point from each scan on the lunar equator. The spacecraft orbital motion causes the actual sequence of the points to go from right to left on the figure. The first data point of the sequence lies 5.3 days after lunar sunset (abscissa of 0.43 in fig. 32-1) and was measured at 08:26 G.m.t. on December 12, 1972. The final point (at approximately the same lunation coordinate) was measured at 10:25 G.m.t. on the same day. A data gap exists near the subsolar point for this orbit.

The plotted temperatures will change as the ISR values are refined. The error estimate is 3 K for the nighttime measurements; the values probably are systematically low. No correction for albedo or topography has been made.

Theoretical curves for various values of  $\gamma$  are also plotted in figure 32-1. The theoretical calculations represent the cooling behavior at a single point, whereas the measured data are taken over many different types of material. The cooling curve apparently falls below  $\gamma \approx 850 \text{ cal}^{-1} \text{ cm}^2 \text{ K sec}^{1/2}$ , even if the error estimate is taken into account. The elevated temperatures near lunar midnight fall in Oceanus Procellarum, where general thermal enhancement has been noted in eclipse measurements (ref. 32-12).

The data for lunar afternoon temperatures come from the highlands on the far side, and the morning points fall in Mare Fecunditatis and Mare Tranquillitatis. The combined effects of albedo and directionality of emissivity account for the apparent systematic deviations to either side of the theoretical curve.

## CONCLUSIONS

This brief survey of the ISR data has confirmed that a variety of thermal behavior exists on the lunar surface. Further work on the measurements will establish the cooling behavior of the major types of lunar regions and the most significant exceptions within each category.

DATA ARCHIVED AT NSSDC

The following ISR data are planned for archiving at the National Space Science Data Center (NSSDC).

1. Merged data tape: The merged data tape will contain data points expressed as temperatures; the data points will be time sequenced and merged with spacecraft ephemeris data.

2. Image tape: The image tape will contain reconstructed lunar surface radiance expressed as a rectilinear array of values from an oblique Mercator projection centered on the spacecraft groundtrack.

3. Thermal properties tape: The thermal properties tape will contain a thermal properties map of the Moon samples and will be uniformly distributed on a map projection that is not yet defined.

The tape formats have not been determined and will be stored with the tapes at NSSDC.

## REFERENCES

- 32-1. Krotikov, V. D.; and Shchuko, O. B.: The Heat Balance of the Lunar Surface Layer During a Lunation. Soviet Astron.-AJ, vol. 7, no. 2, Sept.-Oct. 1963, pp. 228-232.
- 32-2. MenJell, W. W.; and Low, F. J.: Low-Resolution Differential Drift Scans of the Moon at 22 Microns. J. Geophys. Res., vol. 75, no. 17, June 10, 1970, pp. 3319-3324.
- 32-3. Shorthill, R. W.; and Saari, J. M.: Infrared Observation of the Eclipsed Moon. Boeing Sci. Res. Lab. Dcmt. AD-689076, DL-82-0778, Jan. 1969.
- 32-4. Thompson, T. W.; Masursky, H.; Shorthill, R. W.; Zisk, S. H.; and Tyler, G. L.: A Comparison of Infrared, Radar, and Geologic Mapping of Lunar Craters. Contribution 16, Lunar Sci. Inst., Symposium on the Geophysical Interpretation of the Moon (Houston, Tex.), June 1970.
- 32-5. Wildey, Robert L.; Murray, Bruce C.; and Westphal, James A.: Reconnaissance of Infrared Emission From the Lunar Nighttime Surface. J. Geophys. Res., vol. 72, no. 14, July 15, 1967, pp. 3743-3749.
- 32-6. Shorthill, Richard W.; and Saari, John M.: Radiometric and Photometric Mapping of the Moon Through a Lunation. Ann. N.Y. Acad. Sci., vol. 123, July 15, 1965, pp. 722-739.
- 32-7. Allen, David A.: Infrared Studies of the Lunar Terrain. I: The Background Moon. The Moon, vol. 2, no. 3, 1971, pp. 320-337.
- 32-8. Mendell, Wendell W.; and Low, Frank J.: Lunar Differential Flux Scans at 22 Microns, Final Report. NASA CR-121457, 1971.
- 32-9. Raine, W. L.: Thermal Mapping of the Lunar Surface. Final Rept. SE-SSL-1649, Contract NAS8-26343, Teledyne Brown Engineering (Huntsville, Ala.), Sept. 1972.
- 32-10. McIntosh, R. B., Jr.; and Mendell, W. W.: Infrared Scanning Radiometer for Temperature Mapping of the Lunar Surface on the Apollo 17 Flight. Proceedings of the Technical Program, Fourth Annual Electro-Optical Systems Design Conference, Industrial and Scientific Conference Management, Inc. (Chicago), 1972, pp. 356-361.

- 
- | 32-11. Low, Frank J.: Lunar Nighttime Temperatures Measured  
at 20 Microns. *Astrophys. J.*, vol. 142, no. 2, Aug. 15,  
1965, pp. 806-808.
- 32-12. Saari, J. M.; and Shorthill, R. W.: Thermal Anomalies on  
the Totally Eclipsed Moon of December 19, 1964. *Nature*,  
vol. 205, no. 4975, Mar. 6, 1965, pp. 964-965.

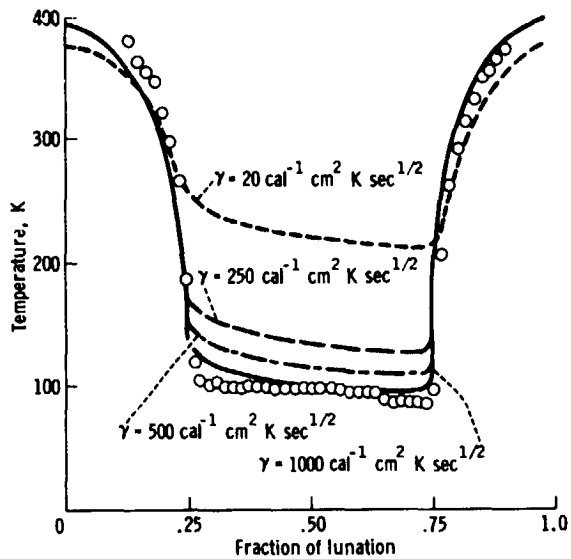


Figure 32-1.- Lunar equatorial temperatures (data points) plotted as a function of the lunation coordinate. Theoretical curves for various values of  $\gamma$  are from reference 32-1.

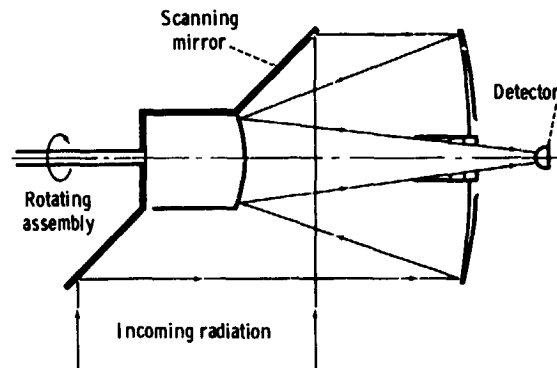
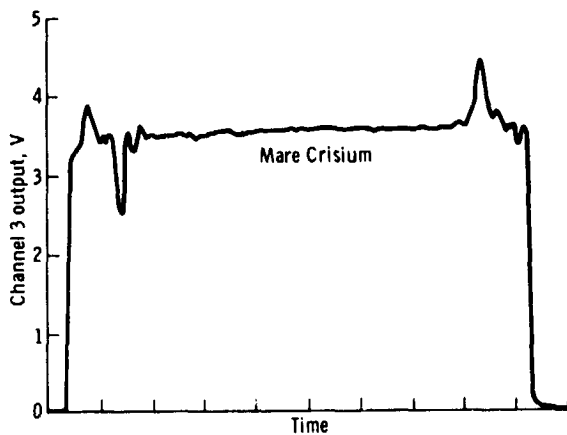
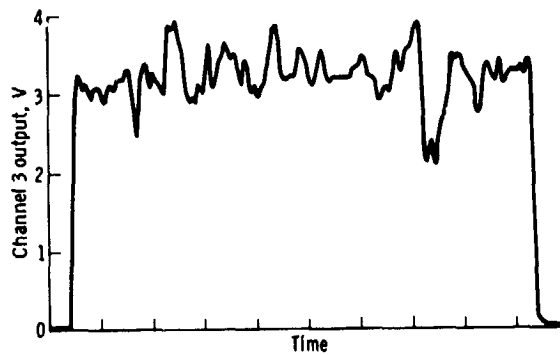


Figure 32-2.- Schematic diagram of the optical system for the Apollo 17 infrared scanning radiometer.

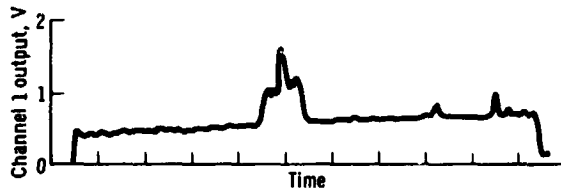


(a) Mare terrain at a scan center of latitude  $17.2^\circ$  N, longitude  $53.0^\circ$  E, a phase angle of  $315.7^\circ$ , and an altitude of 121.2 km. The temperature in Mare Crisium is approximately 368 K.

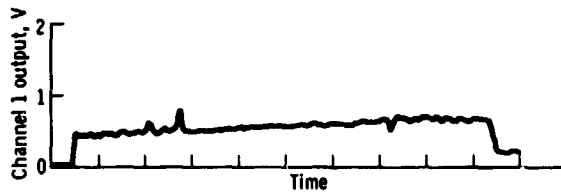


(b) Highland terrain at a scan center of latitude  $18.2^\circ$  N, longitude  $47.7^\circ$  E, a phase angle of  $310.4^\circ$ , and an altitude of 119.7 km.

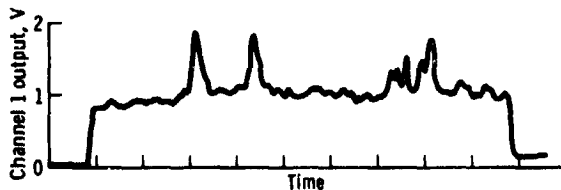
Figure 32-3.- Daytime scans of the lunar surface, demonstrating the extreme contrast in the amount of thermal structure in near-by mare and highland terrain. Each division on the ordinates represents 62.5 msec.



- (a) Scan at a scan center of latitude  $7.0^{\circ}$  N, longitude  $35.9^{\circ}$  W, a phase angle of  $14.1^{\circ}$ , and an altitude of 39.7 km. The crater Kepler A is thermally enhanced relative to the 92 K background in Oceanus Procellarum. The temperature in the crater ranges from 112 K on the wall to a maximum of 126 K in the center.

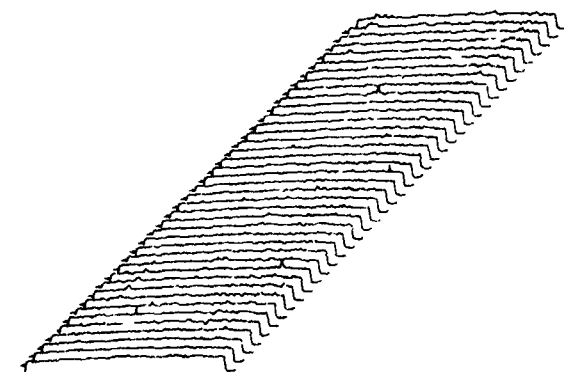


- (b) Scan at a scan center of latitude  $18.9^{\circ}$  N, longitude  $2.0^{\circ}$  E, a phase angle of  $264.8^{\circ}$ , and an altitude of 109.3 km. A predawn cold spot shows an 8 K contrast to the 90 K background in Montes Apenninus.



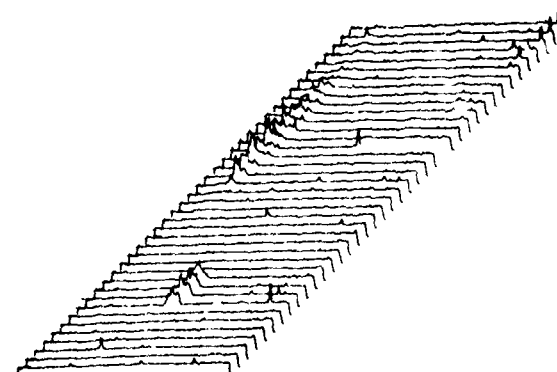
- (c) Scan at a scan center of latitude  $22.5^{\circ}$  S, longitude  $178.4^{\circ}$  E, a phase angle of  $120.8^{\circ}$ , and an altitude of 118.0 km. These large far-side anomalies are enhanced approximately 22 K relative to a 108 K background 2.5 days after lunar sunset.

Figure 32-4.- Nighttime scans of the lunar surface. Each division on the ordinates represents 62.5 msec.



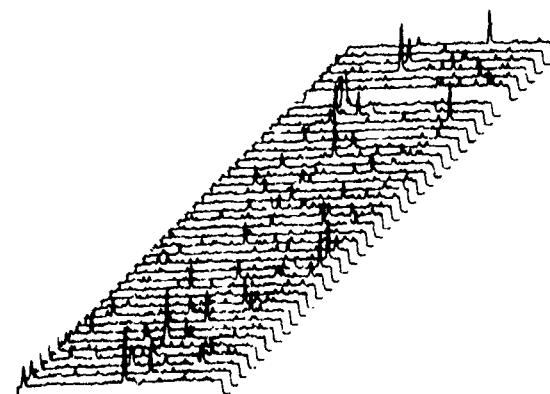
Dec. 11, 1972, 12:45:29.209 G.m.t.

Figure 32-5.- Scan sequence of a featureless region north-east of Mare Orientale and South of the crater Hartwig. North is to the left; west is at the top.



Dec. 11, 1972, 12:31:17.993 G.m.t.

Figure 32-6.- This sequence of nighttime scans runs westward approximately between  $35^{\circ}$  and  $38^{\circ}$  W longitude at latitude  $7^{\circ}$  N. The crater in the foreground is Kepler A, and the extended feature in the background is the crater Kepler. North is to the left; west is at the top.



Dec. 11, 1972, 12:36:59.643 G.m.t.

Figure 32-7.- This sequence of scans runs from  $53^{\circ}$  to  $56^{\circ}$  W longitude just north of the lunar equator. North is to the left; west is at the top.

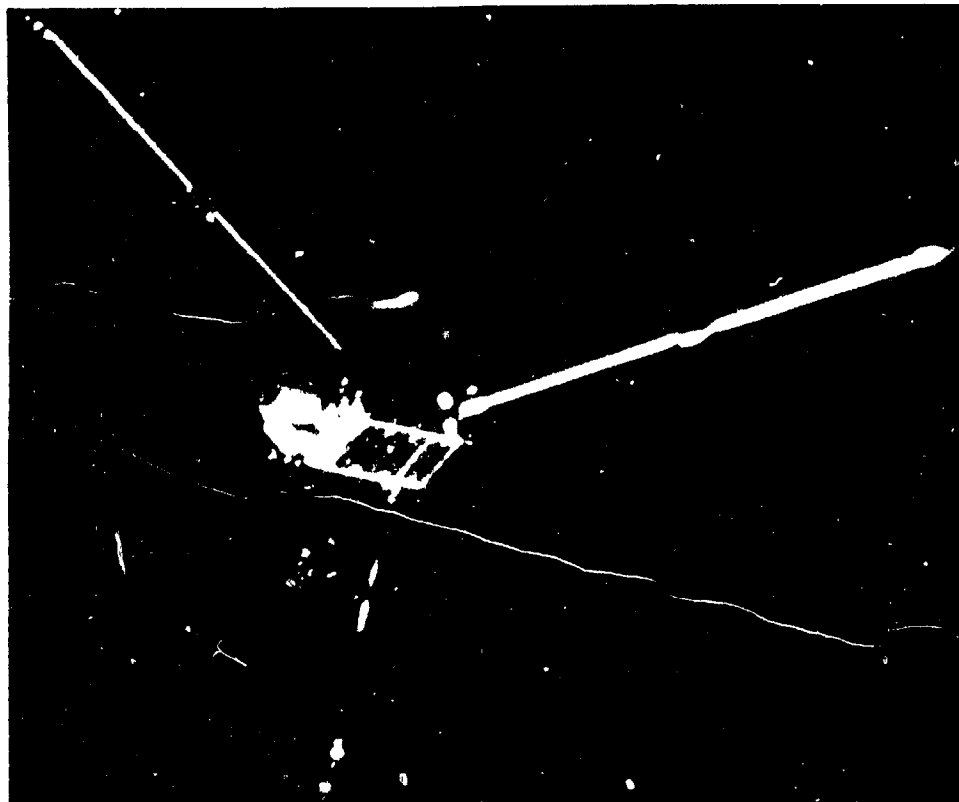
### 33. SUBSATELLITE EXPERIMENTS

PART A: PARTICLES AND FIELDS SUBSATELLITE PARTICLES  
(NASA EXPERIMENT S-173)

PART B: PARTICLES AND FIELDS SUBSATELLITE MAGNETOMETER  
(NASA EXPERIMENT S-174)

PART C: S-BAND TRANSPONDER (NASA EXPERIMENT S-164)

(FOR NSSDC NUMBERS, SEE PAGE 33-3)



CONTENTS - SECTION 33

	Page
INTRODUCTION . . . . .	33-3
SUBSATELLITE DESCRIPTION . . . . .	33-4
PART A: PARTICLES AND FIELDS SUBSATELLITE	
PARTICLES . . . . .	33-9
DETAILED DESCRIPTION OF PARTICLE DETECTORS . . . . .	33-9
DESCRIPTION OF MATERIALS SENT TO NSSDC . . . . .	33-14
DESCRIPTION OF DATA PLOTS . . . . .	33-15
OUTLINE OF PFS-1 EXPERIMENT HISTORY . . . . .	33-17
OUTLINE OF PFS-2 EXPERIMENT HISTORY . . . . .	33-17
DETAILED PROCEDURES FOR CORRECTING THE ACCUMU- LATOR OR TELEMETRY CONVERSION ERROR . . . . .	33-18
TIME CORRECTION PROCEDURE . . . . .	33-21
PART B: PARTICLES AND FIELDS SUBSATELLITE	
MAGNETOMETER . . . . .	33-37
OPERATING HISTORY . . . . .	33-38
THE DATA . . . . .	33-38
SUMMARY OF RESULTS . . . . .	33-44
TRANSFER FUNCTION OF THE MOON . . . . .	33-47
PART C: S-BAND TRANSPONDER . . . . .	33-61
DATA HISTORY AND OPERATIONS . . . . .	33-62
DATA SETS . . . . .	33-63
EXPLANATION OF ACCELERATION DATA LISTING . . . . .	33-63
EXPLANATION OF ACCELERATIONS ON MAGNETIC TAPES . . . . .	33-71
SUMMARY OF KEY EVENTS . . . . .	33-71

### 33. SUBSATELLITE EXPERIMENTS

For the subsatellite experiments, the National Space Science Data Center (NSSDC) identification numbers are as follows:

<u>EXPERIMENT</u>	<u>NSSDC IDENTIFICATION NUMBER</u>
Particles and Fields	Apollo 15 71-063D-01
Subsatellite Particles (S-173)	Apollo 16 72-031D-01
Particles and Fields	Apollo 15 71-063D-02
Subsatellite Magnetometer (S-174)	Apollo 16 72-031D-02
S-Band Transponder (S-164)	Apollo 12 - CSM - 69-099A-12 LM - 69-099C-09
	Apollo 14 - CSM - 71-008A-03 LM - 71-008C-11
	Apollo 15 - CSM - 71-063A-11 LM - 71-063C-12 P&FS - 71-063D-03
	Apollo 16 - CSM - 72-031A-10 LM - 72-031C-11 P&FS - 72-031D-03
	Apollo 17 - CSM - 72-096A-01 LM - 72-096C-14

#### INTRODUCTION

On August 4, 1971, the Apollo 15 astronauts launched a small scientific spacecraft into lunar orbit. The Apollo 15 particles and fields subsatellite (PFS-1) provided approximately 6 months of data coverage before two successive electronic failures in February 1972 caused the loss of most of the data channels. The surviving data channels were monitored intermittently until June 1972 and more or less continuously afterward to January 1973, when ground support was terminated. A second satellite (PFS-2)

launched by the Apollo 16 astronauts on April 24, 1972, provided good data until May 29, 1972, when it impacted on the far side of the Moon.

The particles and fields subsatellites were instrumented to make the following measurements (principal investigators in parentheses): (1) plasma and energetic-particle intensities (K. A. Anderson, University of California at Berkeley), (2) vector magnetic fields (P. J. Coleman, Jr., University of California at Los Angeles (UCLA)), and (3) velocity of the particles and fields subsatellite to high precision for determining gravitational anomalies (W. Sjogren, NASA Jet Propulsion Laboratory, Pasadena, California).

#### SUBSATELLITE DESCRIPTION

This small scientific spacecraft had a mass of approximately 38 kg and a length of 78 cm. The cross section was hexagonal, and the distance between opposite corners was approximately 36 cm. The satellite had three deployable booms hinged from one of the end platforms. One of the booms carried the two-axis fluxgate magnetometer sensor, whereas the other two carried tip masses to provide balance and a proper moment of inertia ratio to avoid precession. The satellite had a short, cylindrical section attached to one of the end platforms. This cylinder was placed inside a barrel attached to the scientific instrument module of the Apollo command and service module (CSM). A compression spring pushed the satellite away and at the same time imparted a spin. Precessional and nutational motions imparted by the launch and boom deployment were removed by a wobble damper. The spin axis of the satellite was initially pointed normal to the ecliptic plane. Very precise pointing of the CSM by the astronauts resulted in an error of less than  $1^\circ$ . The spin period was 5 sec. Each of the six sides of the satellite formed a solar panel. The power output of the array was approximately 24 W. Averaged over an orbit about the Moon, the power was 14 W. The power subsystem also included a battery pack of 11 silver cadmium cells.

The particle detectors included several electrostatic analyzers and two solid-state telescopes. These instruments covered the electron kinetic energy range of 530 to 300 000 eV in nine intervals and 40 keV to 6 MeV for protons in six intervals. One of the analyzers (13.5- to 15-keV electrons) was sectored by using as a reference the zero crossings of the transverse magnetic field component from the UCLA magnetometer. The telescopes pointed along the spin axis. The counting rates of the C1 to C4 analyzers, described in

table 33-1, were accumulated for an integral number of spin periods. Therefore, they provided spatially averaged intensity data over a rather large pitch angle interval. The C5 analyzer provided unidirectional intensities averaged over  $45^\circ$  pitch angle intervals.

A basic scientific requirement placed on the subsatellite was that it must collect particle and field data everywhere in the orbit about the Moon. This requirement demanded a data storage capability. The magnetic-core memory unit used provided a capacity of 49 152 bits. Data could be read into the memory at a rate of 8 bits/sec, which allowed coverage of nearly the entire orbit (2-hr period). Data also could be read in at a rate of 16 bits/sec if a better time resolution in the measurements, at the expense of covering only about one-half the orbit, was desired. Real-time data at the rate of 128 bits/sec could also be acquired from the experiments, but the tradeoff here was that battery power as well as solar-cell power was being used beyond a certain point. In normal operation, the transmitter was commanded on after the subsatellite appeared from behind the Moon. Real-time housekeeping and scientific data were transmitted for a short time to ensure that the receiving stations were locked onto the signal. Then, the data in the memory unit were dumped in 512 sec at a rate of 128 bits/sec. The transmitter was then turned off, and accumulation of data in the storage units began again. A system block diagram of the fields and particles subsatellite is given in figure 33-1.

The orbital periods of both subsatellites were 120 min to within a few seconds. The orbital inclination of PFS-1 with respect to the lunar equator, was approximately  $28^\circ$ , that of PFS-2 was approximately  $10^\circ$ . The sense of revolution about the Moon was clockwise viewed from the north. Perturbations of the orbit affected the periselene.

TABLE 33-1.- SUMMARY OF DETECTOR CHARACTERISTICS

Designation	Type	Energy range		Geometric factor, cm <sup>2</sup> sr	Angular aperture, deg	Angle to spin axis, deg	Minimum detectable flux, cm <sup>-2</sup> sec <sup>-1</sup> sr <sup>-1</sup>
		Protons, Mev	Electrons, kev				
SA1-f	Open solid-state detector with anticoincidence detector in back (six-channel pulse-height analyzer)	0.04 to 2.0	20 to 300	0.045	40 (cone)	0	≈0.01
SB1-6	Same type as SA1-6 except with 375-μg/cm <sup>2</sup> thick foil over detector	.34 to 2.0	20 to 300	.045	40 (cone)	0	≈0.01
(1)	Channel electron multiplier in hemispherical plate analyzer	(1)	.52 to .58	±5.6 X 10 <sup>-3</sup>	20 by 60 (PWH) <sup>3</sup>	90	≈1 X 10 <sup>4</sup>
(1)	Channel electron multiplier in hemispherical plate electrostatic analyzer	(1)	1.87 to 2.08	±1.9 X 10 <sup>-4</sup>	20 by 60	90	≈1 X 10 <sup>4</sup>
(1)	Channel electron multiplier in hemispherical plate electrostatic analyzer	(1)	5.9 to 6.3	±2.4 X 10 <sup>-4</sup>	15 by 60	90	≈1 X 10 <sup>4</sup>
(1)	Funnel-mouthed channel electron multiplier hemispherical plate electrostatic analyzer	(1)	5.8 to 6.5	±0.046	18 by 60	90	≈1
(1)	Funnel-mouthed channel electron multiplier hemispherical plate electrostatic analyzer	(1)	13.6 to 14.8	±0.071	13 by 60	90	≈1

<sup>1</sup>NO response.  
<sup>2</sup>Includes channeltron efficiency; values expressed in square centimeter-steradian-kiloelectron volts.  
<sup>3</sup>Full width, half maximum.

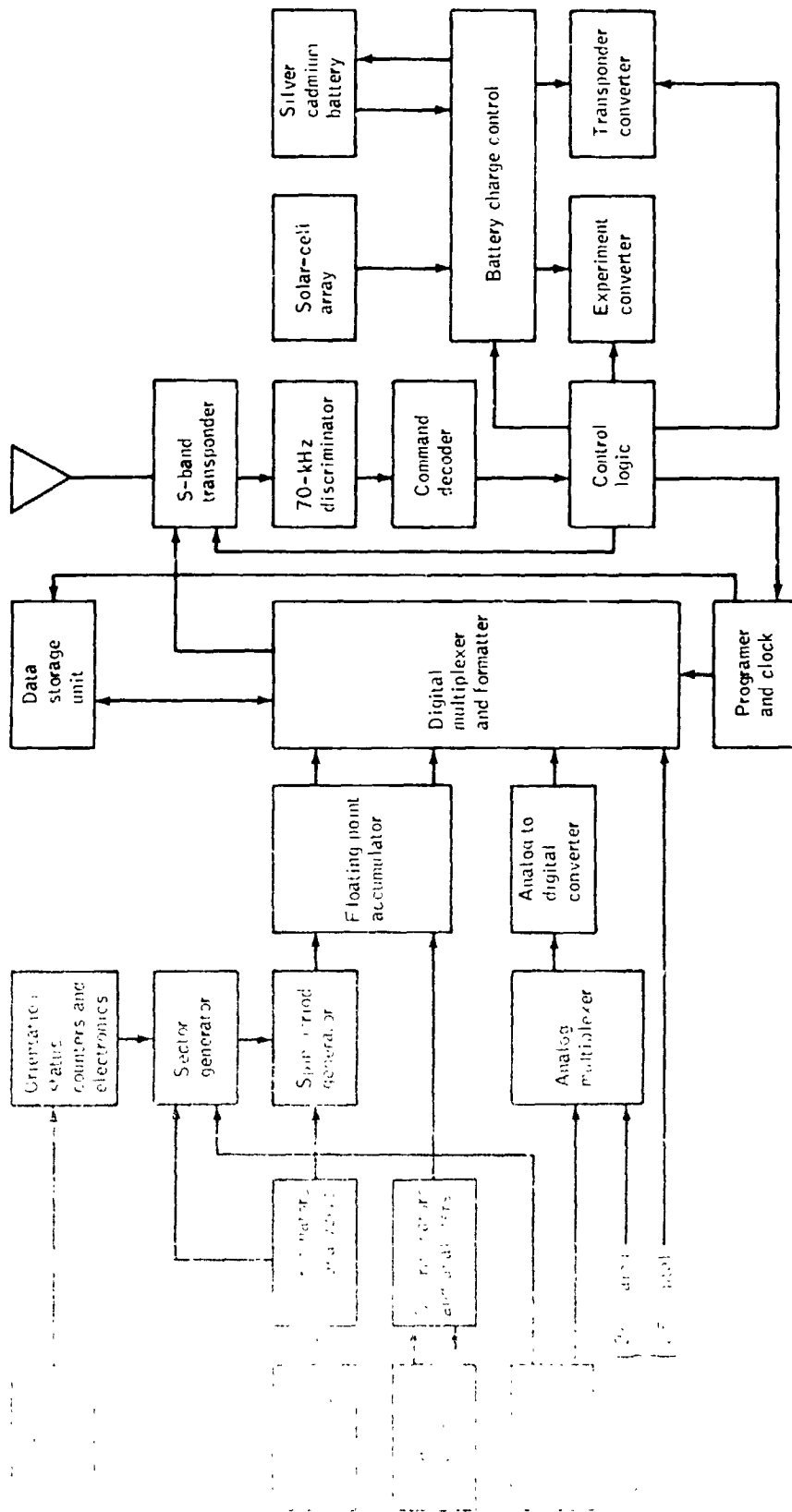


Figure 33-1.- Functional block diagram of the subsatellite.

## PART A

### PARTICLES AND FIELDS SUBSATELLITE PARTICLES

The main objectives of the subsatellite plasma and energetic-particle experiment were to describe the various plasma regimes in which the Moon moves, to determine how the Moon interacts with the plasmas and the magnetic fields of its environment, and to determine certain features of the Earth magnetospheric structure and dynamics.

#### DETAILED DESCRIPTION OF PARTICLE DETECTORS

##### Energetic-Particle Telescopes

Absolute intensities and energy spectra of electrons and protons in the range from 20 to approximately 2000 keV were obtained from two telescopes using solid-state particle detectors (fig. 33-2). Each telescope contained a 25-mm<sup>2</sup> silicon surface barrier detector. In terms of particle kinetic energies, this detector had a thickness that stopped electrons having energies below 320 keV and protons of energies below 6 MeV. Behind this detector was a second one of a 50-mm<sup>2</sup> area. The output of the back detector was placed in anticoincidence with the front detector.

The front detector was a fully depleted surface barrier detector mounted with the active surface barrier side away from the collimator. Thus, the aluminum-coated surface was the particle entrance surface. This orientation minimized radiation damage effects and light sensitivity while it provided a thin (40  $\mu\text{g}/\text{cm}^2$ ) entrance window. The opposite surface of the front detector was the surface barrier covered by 40- $\mu\text{g}/\text{cm}^2$ -thick evaporated gold. The rear detector was oriented oppositely so that the surface barriers of the two detectors directly faced one another.

One of the telescopes (the B telescope) had a 375- $\mu\text{g}/\text{cm}^2$ -thick organic foil ahead of the front solid-state detector. This foil, uniform in thickness to within 10 percent, stopped incident protons with energy up to 310 keV but reduced the energy of a 26-keV electron by only 5 keV. Thus, except for a

small energy shift, a flux of electrons having energies in the 20- to 320-keV range would cause both telescopes to count at the same rate.

However, when protons were incident on the telescopes, the counting rates would show large differences. In addition to this means of particle discrimination, the fact that protons and electrons of the same energy are shadowed by the Moon quite differently was used.

Detector pulses were analyzed into eight energy channels, the nominal thresholds of which are given in table 33-II. The upper two channels were transmitted in calibration mode only, when they were substituted for low-energy proton channels 5 and 6. The electron thresholds were switched when the analyzer was switched from one telescope to the other; thus, the channel edges corresponded to the same incident electron energy to compensate for the loss in the foil (approximately 5 keV at the lowest threshold). The foil and the 320- and 520-keV thresholds were adjusted so that 40- to 340-keV protons detected by the open telescope (the A telescope) were degraded below the lowest threshold of the shielded telescope and 340- to 520-keV protons detected by the open telescope deposited 20 to 320 keV energy in the shielded telescope. When the 340- to 520-keV proton fluxes detected by the telescope covered by the foil were low, these constraints allowed a subtraction of the proton and electron spectra.

A weak radioactive source (plutonium 239) was placed near the front detector in each telescope. The alpha particles from these sources provided well-defined and known energy losses as a check on detector and electronic stability.

The low-energy thresholds of the telescopes could be varied by ground command. This feature was included to enable operation of the telescope as near the thermal noise levels as possible. Because the temperatures were somewhat higher than anticipated, the threshold was raised during the third week of PFS-1 orbital operation.

#### Telescope Gain Shift

Analysis of data during the PFS-1 lifetime indicates that the B or shielded telescope often was counting at rates significantly in excess of the A or open telescope. The malfunctions that might explain this behavior include the following.

1. Incomplete depletion of the A solid-state detector
2. Failure or partial failure of the B telescope anticoincidence

3. Mismatching of one or more of the energy thresholds on either the A or the B telescope

4. Mismatching of the telescope geometry factors

5. Occurrence of an upward gain shift in the B telescope or a downward gain shift in the A telescope

Analysis of electron spectra indicates that the malfunction preserves spectral slope for a power-law spectrum. Item 4 is considered an unlikely possibility; therefore, item 5 is the probable cause. Noise considerations suggest that the shift in gain was downward in the A telescope. From the mismatch of the spectra, a tentative value for the shift is 0.72; that is, a 100-keV electron in the A telescope would be treated by the pulse-height analyzer as a 72-keV electron. Existing examples, however, indicate that the telescopes were not gain-shifted when PFS-1 was cold. Although the analysis is not complete, a tentative model has been adopted having a step function in the gain between 1.0 and 0.72 dependent irregularly on temperature. The 0.72 gain shift probably existed during most of the PFS-1 mission. Table 33-III contains the corrected energy thresholds used for PFS-2 under this assumption. After October 5, 1971, the A telescope in PFS-1 malfunctioned intermittently because of subjection to high temperatures. Count rates for these periods in channels 1 to 4 are high and unreliable. The telescope apparently recovered in large measure by December 1971. In addition to the A telescope breakdown, short periods of high noise were occasionally seen in the B telescope. Because of temperature redesign of the spacecraft, the telescopes on board PFS-2 remained cool and performed well throughout their short lifetime.

#### Telescope Background Considerations

Electrons above 300 keV were stopped with the same efficiency by both the A and B telescopes (electron straggle). Using data from reference 33-1 for 300- $\mu$ m silicon (Si) detectors, the estimated efficiency of the telescopes as a function of energy is plotted in figure 33-3.

Because of the geometrical arrangement of the detectors, the telescopes were not in complete anticoincidence against high energy cosmic rays and spacecraft secondary particles produced by them. A small background count rate produced by the calibration sources also was present in the low-energy channels of the telescopes. Analysis of the actual fluxes seen under quiet conditions in both solar wind and magnetotail electron shadows yields upper limits to this combined background in the low-energy channels under quiet conditions. Calculation and ground calibration yield estimated background contributions from primary cosmic rays

and calibration sources in all channels. Because the effect of spacecraft secondary particles cannot be included, the calculations are essentially lower limits to the background. The background fluxes are summarized in table 33-IV.

### Electrostatic Analyzers

The electrostatic analyzer assembly consisted of four electrostatic analyzers, analog electronics, high-voltage power supplies, and logic circuits in the programming and data handling subassembly. Each electrostatic analyzer consisted of two concentric sections of spherical copper plates. The outer plate in each pair was grounded, whereas the inner plate was raised to a positive potential. The plates were shaped to provide a  $180^\circ$  by  $90^\circ$  volume between them for the electron trajectories. One of the analyzers (C5) is shown in figure 33-4.

Analyzers C1 and C2 were geometrically identical and employed a one-channel multiplier (without funnel) to detect intense fluxes of low-energy electrons. Analyzers C1 and C2 differed only in the plate voltage and hence in the mean detected energy. Analyzers C3 and C4 used the same set of plates, but the output of analyzer C4 was derived from two funnel-mouthed multipliers in parallel. The output of analyzer C3 was derived from one small-aperture multiplier. This arrangement permitted a wider dynamic range. The funnel multipliers were surrounded by a plastic scintillator viewed by a photomultiplier, which was connected in anticoincidence to eliminate charged-particle counts induced by cosmic rays.

The electrostatic analyzers were oriented perpendicular to the spin axis. To avoid spin biasing of the data due to directional anisotropy of particle flux, data were accumulated for integral spin periods only. In addition, the output of the C5 detector was time division multiplexed such that particle intensities from various sectors of satellite rotation could be obtained. The sectoring was made with respect to the magnetic field line as sensed by the transverse magnetometer. Sector 4 constituted  $-45^\circ$  to  $+45^\circ$  of the B field vector (i.e., sector 4 observed particles traveling in a direction opposite that of the magnetic field), sector 3 consisted of  $+45^\circ$  to  $+90^\circ$  and  $+270^\circ$  to  $+315^\circ$ , sector 2 consisted of  $+90^\circ$  to  $+135^\circ$  and  $+225^\circ$  to  $+270^\circ$ , and sector 1 constituted  $+135^\circ$  to  $+225^\circ$  of the B field vector. The precision to which each sector edge was determined was  $\pm 5^\circ$ . This technique of sectoring off the magnetometer output enabled the obtaining of a particle pitch angle distribution directly and thus the avoiding of costly and time-consuming merging of magnetometer and particle data at a much later date. The absolute direction of the magnetic field in space was determined from a Sun pulse. When the spacecraft was in the shadow of the Moon, the Sun pulse was not available, and absolute direction of the magnetic field depended on a precise knowledge of the spin period. However, at all times, the

particle data from C5 were being organized by the onboard magnetometer. Therefore, the pitch angle distribution could always be obtained, even when the absolute direction of the field was unknown.

In the high-bit-rate or real-time mode, the automatic C5 sectoring was disabled and data were stored at 0.5-sec intervals. Plots of the separate sectors in the real-time mode are not meaningful.

The C3 channeltron on PFS-1 malfunctioned shortly after launch and was not usable. Electronic noise from C3 probably contaminated the C4 output at low count rates with some time and temperature dependence on the resulting background levels. The PFS-1 C5 channeltron probably was contaminated by solar ultraviolet rays when the subsatellite was in sunlight at a flux level on the order of  $5(\text{cm}^2 \text{ sr sec keV})^{-1}$ .

#### Accumulator or Telemetry Conversion Error

The small size and limited power capabilities of the subsatellite forced the adoption of a compressed 8-bit format in storage and transmission of the 19-bit count accumulators for the analyzers and telescopes. An engineering oversight in the conversion logic design from a 19- to an 8-bit format caused readings of 16 to 31 counts per accumulator period to be transmitted as 0 to 15 counts per accumulation period. That is, for any single data point representing a true number of counts  $N_T$  in a given data channel during its accumulation period, a data point  $N_A$  was received on the ground according to the function  $f_1(N_T)$ .

$$N_A = f_1(N_T) = \begin{cases} N_T & \text{for } 0 \leq N_T \leq 15 \\ N_T - 16 & 16 \leq N_T \leq 31 \\ N_T & 32 \leq N_T \end{cases} \quad (33-1)$$

The function  $f_1$  is graphed in figure 33-5. Each data point that lies in the range 0 to 15 is thus ambiguous by an additive factor of 16. The design problem was corrected for the PFS-2 spacecraft. Computer procedures were constructed in an attempt to correct this error by statistical analysis of the count rate distribution. A detailed description of these procedures is given in the section entitled "Detailed Procedures for Correcting the Accumulator or Telemetry Conversion Error."

Examination of test data simulating the telemetry conversion error (TCE) and of actual data indicates as expected that the correction procedures were not entirely effective. Problems were primarily created by periods of time variations. Data points that were increased by the correction procedure are indicated on the plots by tick marks above the graphs. The plot format is discussed in more detail in a later section.

#### Time Correction Procedure

Memory store data taken after the second PFS-1 telemetry logic failure (data after March 1, 1972) contain no direct timing information. The only time information available is the time of ground receipt of the data and the known time properties of auto-cycle mode operations. As discussed in the section entitled "Time Correction Procedure," it is possible to correct the timing to a high degree of accuracy with this information, however, and the data have been corrected in that manner.

#### DESCRIPTION OF MATERIALS SENT TO NSSDC

##### Orbit Average Tapes

Three tapes are sent to NSSDC. Each tape consists of one file and has one record/orbit assigned as follows.

1st tape	PFS-1	Revolutions 1 to 2195
2nd tape	PFS-1	Revolutions 2194 to 6459
3rd tape	PFS-2	Revolutions 1 to 424

Each record is 276 60-bit words long, and each word is a CDC 6600 binary word. The format of the records is as follows.

<u>Word</u>	<u>Parameter</u>	<u>Mode</u>
1	Orbit no.	Integer
2	Orbit date	CDC display code
3	Fractional day of start	Real
4	Active time of C1 for entire orbit	Real

<u>Word</u>	<u>Parameter</u>	<u>Mode</u>
5 to 16	Active time of C1 for 12 successive 10-min averages from orbit start	Real
17 to 276	13 by 20 array stored by columns	Real

The first row of the array consists of orbit averages for each detector channel; each of the next 12 rows is a 10-min average. Columns are in the following order: SA1-4, SB1-4, SA2, SB2...SA6, SB6, SECT1, SECT2, SECT4, SECT3, SUMC5, C4, C1, and C2.

1. The revolution number is defined for missing orbits, but the fractional day = -0 (all 60 bits on).
2. The orbit date is in the form MM/DD/YY.
3. Missing averages or active times are represented by a -0.

#### DESCRIPTION OF DATA PLOTS

##### Orbital Summaries

The processing program produces 10 plots on microfilm for each revolution of the subsatellite about the Moon, covering 20 data channels. A sample plot is shown in figure 33-6. Particle flux expressed as counts per square centimeter-second-steradian-kiloelectronvolt is plotted vertically as a logarithmic scale of 6 decades from  $10^{-1}$  to  $10^5$ . Time is plotted horizontally starting at the closest approach of the subsatellite to the subsolar point on the Moon. Tick marks are indicated every 2 min; universal time in the form "hours.minutes.seconds" is labeled every 30 min. Primary tick marks occur at 10-min intervals. The date is marked at the bottom of each plot in the form month/day/year, and the day number of the year is indicated in the upper right corner (day 1 = January 1). The orbit number is given in the upper left corner and the subsatellite number in the lower left corner. Two traces are plotted within each grid, and one of the traces is marked with periodic asterisks (\*). The traces are labeled at the top of each grid along with a scale factor required to convert from fluxes as plotted to true flux (i.e., true flux equals plotted flux divided by scale factor). Table 33-V contains a list of the traces in plotted order and the scale factors. Two asterisk symbols are plotted along the top of each grid indicating, from left to right, respectively, sunset and sunrise. The

plot symbols (- and \*) also appear at the upper right corner. Small, vertical bars appearing horizontally across from these symbols indicate the times (if any) at which TCE corrections have been made in each of the two traces. The plot symbols also appear further down along the right margin of the grid to indicate the flux level of the orbit averages of the given traces. It should be noted that although an editing procedure has been used to delete points having bit errors, not all such points have been deleted; these points may cause spuriously high fluxes to appear in 10-min or 2-hr averages.

The data accumulation periods for the various channels (real time (RT), telemetry-store fast (TSF), and telemetry-store normal (TSN)) in the three data modes are summarized in table 33-VI. The points plotted are either approximately 10.1-sec averages or single data points; the averages are used for data point intervals smaller than 10 sec. Because the telemetry switches between the A and B telescopes (e.g., in the TSN mode, the output is 48 sec from the A telescope, then 48 sec from the B telescope, then 48 sec from the A telescope, etc.), the telescope data are not continuous. Data gaps are plotted as straight lines between adjacent data points. No explicit indication of the data mode exists on the plots. The RT data can generally be distinguished on the plots, however, by the much finer appearance of the time resolution in the upper channels of the telescopes. The point is significant because the automatic C5 sectoring is disabled in the RT mode and the separate sectors as plotted are not significant.

#### Daily and 10-Day Plots

The daily and 10-day plots are generally similar in format to the orbital summary plots; 10-min averages are plotted on the daily plots, orbit averages on the 10-day plots. A sample of each is shown in figures 33-7 and 33-8, respectively. Horizontal tick marks are spaced at 30-min intervals and labels at 4-hr intervals; the time labels are in the same format used for the orbital summary plots. Associated with each plot in addition to the regular plot symbols are diamonds and squares that indicate the start time of each orbit and the average flux in the given detector over the orbit. On the 10-day plots, horizontal tick marks are spaced at 4-hr intervals with primary tick marks at 1-day intervals and labels at 2-day intervals. The time labels are in the format "day.hour." The lunation number appears at the right of the grid. Plots with lunation numbers ending in 0.00 start at the subsolar point of the Moon on its orbit about the Earth; plots with numbers ending in 0.33 or 0.67 start one-third and two-thirds around the orbit, respectively. Lunation numbers ending with 0.33 generally contain the tail pass data. The 10-day plots are interspersed

with daily plots on the film. The daily and 10-day plots on the film are in a different order than that of the orbital summary plots (i.e., SA1-4 to SB6 and SECT1 to C2 for the daily and 10-day plots compared to SECT1 to C2 and SA1-4 to SB6 for the orbital summary plots). In figure 33-8, note that the labels SA1 and SB1 are intended to be SA1-4 and SB1-4.

#### OUTLINE OF PFS-1 EXPERIMENT HISTORY

The following is a summary of the PFS-1 experiment history.

<u>Event</u>	<u>Date and time</u>
Launch	August 4, 1971, 20:30 u.t.
Analyzers turned on	August 5, 1971, 20:00 u.t.
Pulse-height analyzer threshold raised from low to high	August 19, 1971, 20:50 u.t.
Breakdown of A telescope	Approximately October 6, 1971
First telemetry failure	February 4, 1972
Second telemetry failure	February 26, 1972
Termination of ground support	January 22, 1973
Performance of calibrations longer than 1 min	November 10, 1971, 15:20 to 15:25 u.t. January 20, 1972, 14:20 to 14:50 u.t. January 31, 1972, 17:31 to 17:33 u.t.

#### OUTLINE OF PFS-2 EXPERIMENT HISTORY

Significant events in the history of the PFS-2 experiment were as follows:

<u>Event</u>	<u>Date and time</u>
Launch	April 24, 1972
Telescopes turned on	April 25, 1972, 18:25 u.t.

## OUTLINE OF PFS-2 EXPERIMENT HISTORY

<u>Event</u>	<u>Date and time</u>
Analyzers turned on	April 27, 1972, 00:20 u.t.
Impact on far side of Moon	May 29, 1972, 22:00 u.t.
Performance of calibrations longer than 1 min	April 30, 1972, 06:08 to 06:11 u.t. May 10, 1972, 18:57 to 18:59 u.t. May 12, 1972, 15:25 to 19:50 u.t. May 23, 1972, 04:22 to 04:56 u.t.

### DETAILED PROCEDURES FOR CORRECTING THE ACCUMULATOR OR TELEMETRY CONVERSION ERROR

To "correct" the data for the TCE, a determination of whether each data point  $N_A$  in the range 0 to 15 corresponds to an  $N_T = N_A$  or to an  $N_T = N_A + 16$  must be made. Since every data point in this range is ambiguous individually, the only manner by which the additional information needed to make the choice of  $N_T$  can be derived is by examination of the data points that surround the point in question, either in time (sequential points from the data channel at the same bit rate) or in some other fashion (e.g., simultaneous points from data channels covering adjacent energy ranges). The latter approach is difficult to develop as an automated procedure without making a priori assumptions about the relation between count rates in the various channels and even then is difficult to implement. The former approach is more tractable, if the necessary but drastic assumption is made that the true particle count rates change only slowly as a function of time.

If the count rates are sufficiently stable, the distribution of the values of  $N_T$  would be expected to be a Poisson distribution, with probability  $g(N_T)$  of obtaining  $N_T$  counts in an accumulation period given by

$$g(N_T) = \frac{\bar{N}_T^{N_T}}{N_T!} e^{-\bar{N}_T} \quad (33-2)$$

The function  $\bar{N}_T$  is the average of the  $N_T$  values. Figure 33-9(a) contains some sample calculated Poisson distributions for relevant  $\bar{N}_T$ ; figure 33-9(b) includes the distributions of apparent counts  $N_A$  produced by the TCE. Note that for a given  $\bar{N}_T$ , where  $g(N_T)$  is appreciable,  $g(N_T \pm 16)$  is typically small. Therefore, given the value of  $\bar{N}_T$ , the mapping relationship  $N_A \rightarrow N_T$  can be constructed with substantial certainty and, thereby, individual points in the sequence can be corrected. The distributions of  $N_A$  defined by  $\bar{N}_T$  yield an apparent average  $\bar{N}_A$  according to a function

$$\bar{N}_A = f_2(\bar{N}_T) \quad (33-3)$$

The function  $f_2$  is graphed in figure 33-10. Note that for  $\bar{N}_A \leq 6.5$  or  $\bar{N}_A \geq 9.5$ , the function  $f_2^{-1}(\bar{N}_A) = \bar{N}_T$  can be uniquely defined and thus the critical mapping of  $N_A$  back to  $N_T$  can be defined. For values of  $\bar{N}_T$  between 6.5 and 24.0 ( $\bar{N}_A$  between 6.5 and 9.5), the relation  $f_2^{-1}$  is triple-valued and the distribution of the  $N_A$  values must be examined to determine the branch of  $f_2^{-1}$  involved (i.e.,  $\bar{N}_T \in (6.5, 11.5)$ ,  $(11.5, 19.0)$ , or  $(19.0, 24.0)$ ).

In broad terms, the recognition tests to distinguish the branches will consist of noting the presence or absence in the distribution of  $N_A \geq 32$  and determining the presence or absence of points in ranges of  $N_A$  in which any one of the branches has a maximum or a minimum. The specific structure and the interpretation of the tests depend on the value of  $\bar{N}_A$  and on the number of data points used to determine the distribution. If many points are taken and  $\bar{N}_T$  is in fact constant, recognitions can be made highly reliable and the problem solved. However, the more points taken to form distributions from the actual data, the more likely that  $\bar{N}_T$  will vary with time and that the entire process will break down. The correction procedures were therefore constructed to use a minimum number of points consistent with a reasonably high probability of success in identifying branches of  $f_2^{-1}$ .

Calculations and a series of tests on sequences of points simulating Poisson distributions indicated that a total of seven points, three points on either side of a given point in question, is optimal in determining the value of  $\bar{N}_A$  and the distributions.

Using a seven-point procedure,  $\bar{N}_A$  is determined for  $\bar{N}_T \leq 27$  to an accuracy  $\pm \sigma$  of better than 2.0, where  $\sigma$  is standard deviation. This kind of accuracy is consistent with defining  $\bar{N}_A < 5.1$  and  $\bar{N}_A > 12.5$  as the regimes of a well-defined  $f_2^{-1}$ , and with dividing the range of  $\bar{N}_A$  values for which distributions must be tested in the following three test ranges.

1.  $\bar{N}_A \in (5.7, 7.3)$  or  $\bar{N}_T \in (5.1, 7.3), (16.1, 21.7)$
2.  $\bar{N}_A \in (7.3, 8.9)$  or  $\bar{N}_T \in (7.3, 9.3), (14.7, 16.1), (21.7, 23.5)$
3.  $\bar{N}_A \in (9.3, 12.5)$  or  $\bar{N}_T \in (9.3, 14.7), (23.5, 26.0)$

The process of recognition in the final form adopted is summarized in a flow diagram shown in figure 33-11. The specific tests applied are included in this diagram.

Two problems have not been dealt with in the TCE correction scheme as outlined to this point: isolated, statistically unlikely points will confuse the correction logic for adjacent points; and fast time variations will confuse the correction logic. To minimize to at least some extent the effects of these two problems, certain additional tests have been built into the correction logic. Values of  $N_A \geq 64$  will inhibit corrections on adjacent points since  $N_T < 32$  will occur next to  $N_T \geq 64$  statistically only if a time variation in  $\bar{N}_T$  has occurred. If  $\bar{N}_T$  has varied substantially, too little information is available to attempt a correction. Also, differences between adjacent points on either side of the point in question may be combined to form a coefficient

$$(\sigma')^2 = \min. \left\{ \frac{\sum_{I=1}^3 [N_A(I+1) - N_A(I)]^2}{2}, \frac{\sum_{I=5}^7 [N_A(I) - N_A(I-1)]^2}{2} \right\} \quad (33-4)$$

which may then be compared to a theoretical standard deviation  $\sigma = \bar{N}_A$ . If  $\sigma' \leq 1.39\sigma$  and the distribution recognition indicates that an upward correction should be made on the point in question, the upward correction is inhibited on the rationale that  $\sigma'$  is compatible with a low branch distribution of points on at least one side of the point in question. Thus, sharp changes in count rate from the low to the high branch of  $f_2^{-1}$  or the reverse should not confuse the logic. Assuming a constant  $\bar{N}_T$  and assuming that the previous steps in the correction have accomplished at least an approximately correct mapping of  $\bar{N}_A$  into  $\bar{N}_T$ , a second pass is also made through the array of data points recorrecting individual points on the basis of their seven-point averages. This logic is summarized in table 33-VII under the subroutine name of PHASE 2. All the previous logic is contained in the subroutine titled PHASE 1. The entire correction logic is summarized in figure 33-12, with reference to both figure 33-11 and table 33-VII.

Several additional notes should be made on the application of the correction routines to actual satellite data. Three points at the beginning and three points at the end of any given sequence of data points were not corrected. Data gaps of longer than 14 data points in the sum channel of the solid-state telescopes or 10 data points in all other data channels caused the correction procedure to stop and restart on the next stretch of data longer than 7 data points. Changes of data mode obviously were defined as a restart condition. For sectorized data, data points from each sector were corrected separately as were the data points alternating between two accumulation times in the real-time sum-channel telescope data. The low count rates in the sectorized C5 data in TSF and TSN data modes and the variability of these count rates forced use of a modified minimum correction procedure on these data (only PHASE 1 through the test average  $\text{Avg} > 12.5$  in fig. 33-11).

#### TIME CORRECTION PROCEDURE

One cycle of automode data has timing of 256 sec of standby (SB), 192 sec of RT data at 2 sec/frame, 512 sec of memory readout (MRO) at 2 sec/frame, and 6144 sec of telemetry-store operation at 24 sec/frame. Timing of the RT data can be directly derived from ground time to within 1 sec. In principle, the MRO data can also be timed from ground time if any of the following times are known: (1) the precise time at which the autocycle was

initiated, (2) the precise start of the RT data stream, (3) the precise start of the MRO, or (4) the precise end of the MRO. Time (1) is available fairly accurately from the command history log, but placement of great reliance on the precise times of the log entries has been avoided. Also, any small departure in the autocycle period from the nominal 7104 sec will cause large cumulative errors in MRO timing for orbits sufficiently long after the autocycle initiation. Time (2) cannot be obtained unless a ground station is locked up on the subsatellite at the very beginning of its transmission, which is not generally the case. Time (3) can be determined only from examination of the particle data to determine the increase in particle counts per accumulation period at the change from RT to TSN data and is probably not derivable dependably. Time (4), however, is likely to be a fairly accurate time because it follows approximately 11.5 min of subsatellite transmission in which good ground station lockup should have been obtained. This transmission can be easily identified because it generally precedes an apparent 1.8-hr gap in the data stream. For each autocycle, then, given the MRO end time  $t_L$  (i.e., the time of the end of transmission from the subsatellite), any transmission time  $t$  can be easily converted to a subsatellite store time  $t^1$  by using the equation

$$t^1 = (t - t_s)(t_e - t_b) / (t_L - t_s) + t_b \quad (33-5)$$

where  $t_s = t_L - 512$  sec,  $t_b = t_L - 7104$  sec, and  $t_e = t_L - 960$  sec. The process is schematically illustrated in figure 33-13. The initial MRO after the autocycle command cannot be timed in this manner and tends to duplicate data already transmitted in the current pattern of subsatellite operation. Therefore, these data have been discarded unless clearly required.

The preceding procedure will be degraded if even a few of the last frames of any MRO are lost from the autocycle. A solution is consideration of the measured MRO end times from a series of cycles during which no commands were sent to the subsatellite. When graphed, the times appear as in figure 33-14. Assuming that the real MRO end time for each orbit is greater than or equal to the measured MRO end time, a line is drawn through certain of the measured end times such that all measured end times fall essentially on the line or below it. In figure 33-14, four measured end times fall on a line that meets the criteria. The line can then be numerically determined by a least-squares procedure applied to the points that graphically lie on it. Generally, over the period between commands, at least three measured MRO end times will be real end times (i.e., with no frames at the end of the MRO lost at the ground station). The least-squares line will enable

very precise determination of both the exact length of the autocycle and the true MRO end times for each orbit. Equation (33-5) can then be used to assign store times to the individual data frames. As an example, for the data of figure 33-14, the four points on the line fit within 1 sec of the least-squares fit; thus, the length of the autocycle was determined to be  $7104.7 \pm 0.1$  sec.

#### REFERENCE

- 33-1. Berger, M. J.; Seltzer, S. M.; Chappell, S. E.; Humphreys, J. C.; and Motz, J. W.: Response of Silicon Detectors to Mono-Energetic Electrons with Energies Between 0.15 and 5.0 MeV. Nuclear Instru. Meth., vol. 67, Apr. 1969, p. 181.

#### BIBLIOGRAPHY

- Anderson, K. A.: Intensity and Energy Spectrum of Electrons Accelerated in the Earth's Bow Shock. J. Geophys., vol. 40, 1974, pp. 701-712.
- Anderson, K. A.; Chase, L. M.; Lin, R. P.; McGuire, R. E.; and McCoy, J. E.: Particles and Plasmas in the Earth's Magnetotail at  $60R_E$ . Correlated Interplanetary and Magnetospheric Observations, D. E. Page, ed., D. Reidel Publishing Co., 1974, pp. 297-316.
- Anderson, K. A.; Lin, R. P.; McCoy, J. E.; and McGuire, R. E.: Measurement of Lunar Magnetic Fields by Reflection of Low Energy Electrons. Space Sciences Lab., Univ. of California (Berkeley, Calif.).
- Anderson, K. A.; Lin, R. P.; McCoy, J. E.; and McGuire, R. E.: Measurement of Lunar and Planetary Magnetic Fields by Reflection of Low Energy Electrons. Space Sciences Lab., Univ. of California (Berkeley, Calif.), July 1975.
- Chase, L. M.; McGuire, R. E.; McCoy, J. E.; Lin, R. P.; et al.: Plasma and Energetic Particles in the Magnetotail at  $60R_E$ . J. Geophys. Res., vol. 79, no. 31, Nov. 1, 1974, pp. 4779-4785.
- Howe, Herbert C.; Lin, R. P.; McGuire, R. E.; and Anderson, K. A.: Energetic Electron Scattering From the Lunar Remanent Magnetic Field. Geophys. Res. Lett., vol. 1, no. 3, July 1974, pp. 101-104.

Lin, R. P.: Suprathermal Particles. Space Sciences Lab., Univ. of California (Berkeley, Calif.).

Lin, R. P.; McGuire, R. E.; and Anderson, K. A.: Acceleration, Containment, and Emission of Very Low Energy Solar Flare Particles. Coronal Disturbances, Gordon Newkirk, Jr., ed., D. Reidel Publishing Co., 1974, pp. 461-469.

Lin, R. P.; McGuire, R. E.; Howe, H. C.; Anderson, K. A.; and McCoy, J. E.: Mapping of Lunar Surface Remanent Magnetic Fields by Electron Scattering. Proceedings of the Sixth Lunar Science Conference, vol. 3, Pergamon Press, 1975, pp. 2971-2973.

McCoy, J. E.; Lin, R. P.; McGuire, R. E.; Chase, L. M.; and Anderson, K. A.: Magnetotail Electric Fields Observed From Lunar Orbit. J. Geophys. Res., vol. 80, no. 22, Aug. 1, 1975, pp. 3217-3224.

McCoy, J. E.; Lin, R. P.; Mozer, F. S.; McGuire, R. E.; et al.: Comparison of Simultaneous Magnetotail and Polar Ionospheric Electric Fields and Energetic Particles. Space Sciences Lab., Univ. of California (Berkeley, Calif.), May 1975.

TABLE 33-II.- NOMINAL TELESCOPE ENERGY CHANNELS

Channel	A telescope		B telescope	
	Electrons, keV	Protons, keV	Electrons, keV	Protons, keV
Apollo 15 subsatellite (PFS-1)				
1 to 4 low	18.4 to 331.5	32 to 343	18.4 to 331.5	342 to 538
1 to 4 high	21.4 to 331.5	36 to 343	21.4 to 331.5	345 to 538
2	40.2 to 83.3	56 to 99	40.2 to 83.3	356 to 377
3	83.3 to 153.4	99 to 167	83.3 to 153.4	377 to 416
4	153.4 to 331.5	167 to 343	153.4 to 331.5	416 to 538
5	331.5 to 528	343 to 537	331.5 to 528	538 to 696
6	528 to 2000	537 to 2000	528 to 2000	696 to 2000
17	--	2000 to 4000	--	2000 to 4000
18	--	>4000	--	>4000
Apollo 16 subsatellite (PFS-2)				
1 to 4 low	22.5 to 322	39 to 334	22.5 to 322	333 to 519
1 to 4 high	25.7 to 322	42 to 334	25.7 to 322	335 to 519
2	43.6 to 86.5	62 to 105	43.6 to 86.5	344 to 367
3	86.5 to 157	105 to 171	86.5 to 157	367 to 406
4	157 to 322	171 to 334	157 to 322	406 to 519
5	322 to 508	334 to 518	322 to 508	519 to 670
6	508 to 2000	518 to 2000	508 to 2000	670 to 2000
17	--	2000 to 4000	--	2000 to 4000
18	--	>4000	--	>4000

<sup>1</sup>Channels 7 and 8 were transmitted only in calibration mode, when their output was substituted for channels 5 and 6 in the data format.

TABLE 33-III.- TELESCOPE ENERGY CHANNELS FOR PFS-1 WITH A TELESCOPE GAIN SHIFT OF 0.72

Channel	A telescope		B telescope	
	Electrons, keV	Protons, keV	Electrons, keV	Protons, keV
1 to 4 low	25.6 to 460	39 to 472	18.4 to 331.5	342 to 538
1 to 4 high	29.7 to 460	42 to 472	21.4 to 331.5	345 to 538
2	56 to 116	72 to 132	40.2 to 83.3	356 to 377
3	116 to 213	132 to 227	83.3 to 153.4	377 to 416
4	213 to 460	227 to 472	153.4 to 331.5	416 to 538
5	460 to 735	472 to 744	331.5 to 528	538 to 696
6	735 to 2800	744 to 2800	528 to 2000	696 to 2000

TABLE 33-IV.- TELESCOPE BACKGROUND FLUXES

[Normalized to channel widths in electron energy]

Channel	Calculated telescope background flux due to penetrating cosmic rays, (cm <sup>2</sup> sr sec kev) <sup>-1</sup>		Calibration source background flux, (cm <sup>2</sup> sr sec kev) <sup>-1</sup>		Upper limits to quiet-time background flux, (cm <sup>2</sup> sr sec kev) <sup>-1</sup>	
	PPS-1		PPS-1	PPS-2	PPS-1	PPS-2
	With nominal energy thresholds	With an A telescope gain of 0.72				
SA1-4	1.7 X 10 <sup>-3</sup>	2.3 X 10 <sup>-3</sup>	3 X 10 <sup>-4</sup>	2 X 10 <sup>-4</sup>	--	--
SA2	0.0	0.0	3	2	--	--
SA3	0.0	0.0	3	2	--	--
SA4	3.1 X 10 <sup>-3</sup>	3.5 X 10 <sup>-3</sup>	3	2	--	--
SA5	2.8 X 10 <sup>-3</sup>	1.3 X 10 <sup>-3</sup>	3	2	--	--
SA6	3.4 X 10 <sup>-4</sup>	1.7 X 10 <sup>-4</sup>	3	2	--	--
SB1-4	2.1 X 10 <sup>-3</sup>	2.1 X 10 <sup>-3</sup>	3	2	1.7 X 10 <sup>-2</sup>	3.6 X 10 <sup>-2</sup>
SB2	0.0	0.0	3	2	2.0	5.2
SB3	0.0	0.0	3	2	1.7	3.1
SB4	3.8 X 10 <sup>-3</sup>	3.8 X 10 <sup>-3</sup>	3	2	1.0	1.8
SB5	2.6 X 10 <sup>-3</sup>	2.7 X 10 <sup>-3</sup>	3	2	--	--
SB6	3.0 X 10 <sup>-4</sup>	3.0 X 10 <sup>-4</sup>	3	2	--	--

TABLE 33-V.- TRACES AND SCALE FACTORS BY PLOT NUMBER

Plot no.	Symbol	Detector	Scale factor
1	-	SECT1	10 <sup>-1</sup>
	*	SECT2	10 <sup>1</sup>
2	-	SECT4	10 <sup>-1</sup>
	*	SECT3	10 <sup>1</sup>
3	-	SUMC5	10 <sup>-1</sup>
	*	C4	10 <sup>-1</sup>
4	-	C1	10 <sup>-4</sup>
	*	C2	10 <sup>-3</sup>
5	-	SA1-4	10 <sup>2</sup>
	*	SB1-4	10 <sup>1</sup>
6	-	SA2	10 <sup>2</sup>
	*	SB2	10 <sup>1</sup>
7	-	SA3	10 <sup>3</sup>
	*	SB3	10 <sup>2</sup>
8	-	SA4	10 <sup>3</sup>
	*	SB4	10 <sup>2</sup>
9	-	SA5	10 <sup>3</sup>
	*	SB5	10 <sup>2</sup>
10	-	SA6	10 <sup>4</sup>
	*	SB6	10 <sup>3</sup>

TABLE 33-VI.- ACCUMULATION PERIODS

Detector	Time difference, sec		
	TSN	TSP	RT
C1	2 spins <sup>1</sup>	1 spin <sup>1</sup>	1.0
C2	4 spins <sup>1</sup>	2 spins <sup>1</sup>	2.0
C4	4 spins <sup>1</sup>	2 spins <sup>1</sup>	2.0
C5-SECT1,2,3,4	.5 spin <sup>1</sup>	.25 spin <sup>1</sup>	.5
SA1-4, SB1-4	4.0	2.0	<sup>2</sup> .5, .25
SA2, SB2	24.0	12.0	2.0
SA3, SB3	48.0	24.0	4.0
SA4, SB4	48.0	24.0	4.0
SA5, SB5	48.0	24.0	4.0
SA6, SB6	48.0	24.0	4.0

<sup>1</sup>Spin period = 5.06 sec for PFS-1; spin period = 5.12 sec for PFS-2.

<sup>2</sup>Data readouts for SA1-4 and SB1-4 in RT mode alternate between 0.25- and 0.5-sec accumulation periods.



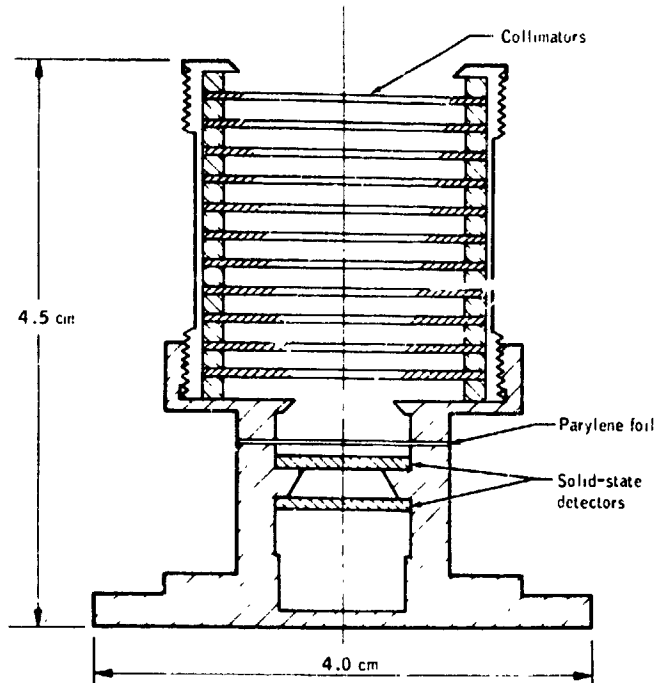


Figure 33-2.- One of the solid-state telescopes used on the sub-satellite to detect electrons and protons in the energy range 20 to 4000 keV. The other telescope was identical except that it had no foil. The foil had a very large effect on protons in the range of interest and thus made particle identification possible.

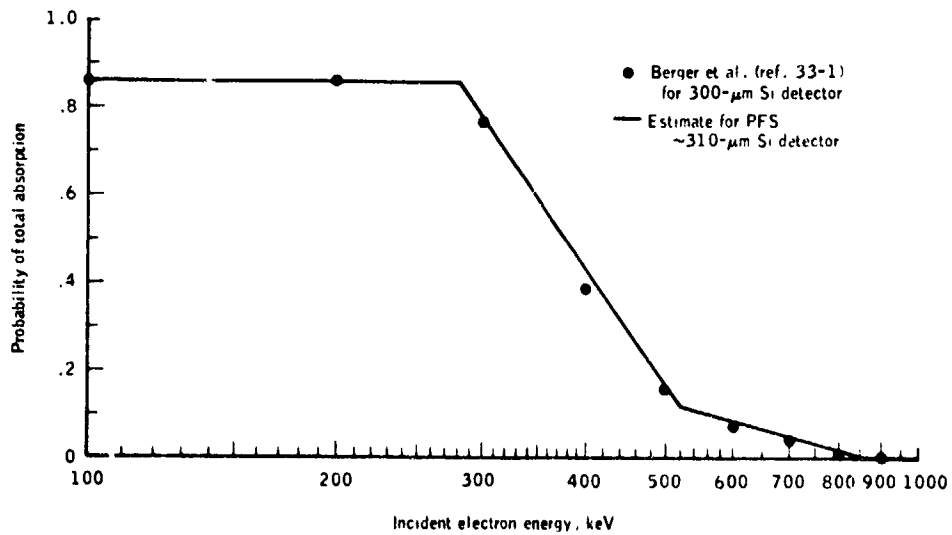


Figure 33-3.- Silicon detector response to electrons as a function of energy.

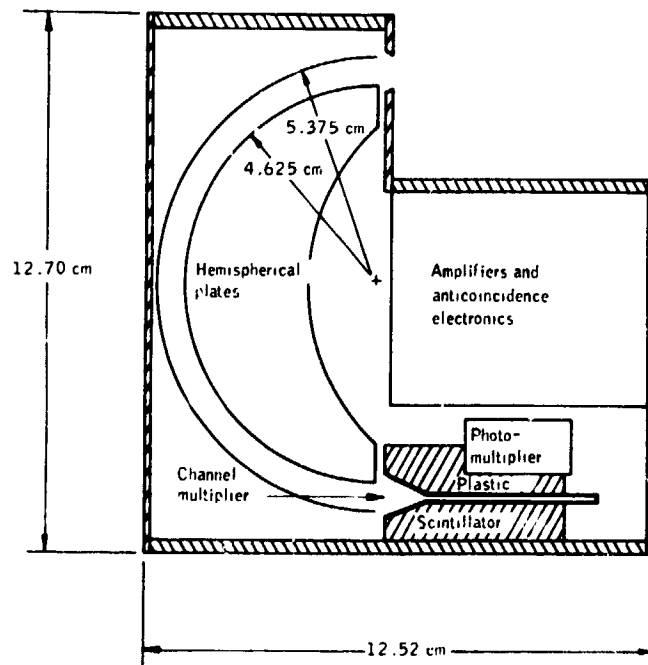


Figure 33-4.- The largest electrostatic analyzer (C5) flown on the subsatellite. The C5 analyzer measured electrons in the energy interval 13.5 to 15 keV with high sensitivity and was sectorized by using the magnetometer output as reference. The other analyzers were similar, but they measured electrons at lower energies.

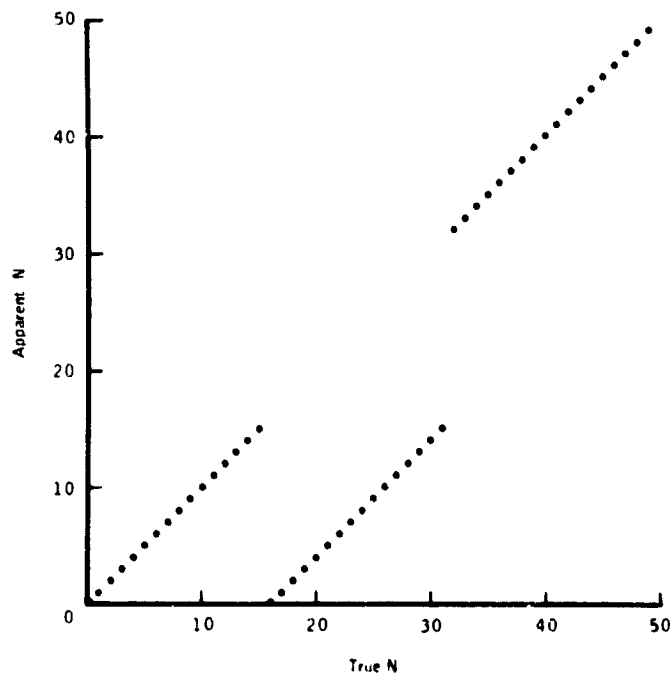


Figure 33-5.- True counts  $N_T$  as a function of measured counts  $N_A$  with telemetry conversion error.

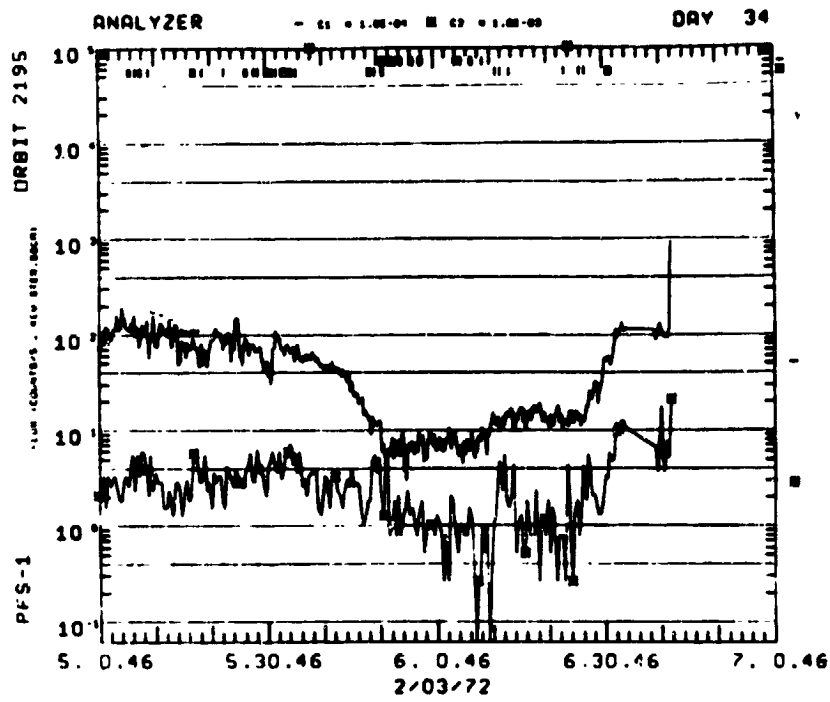


Figure 33-6.- Sample 2-hr plot.

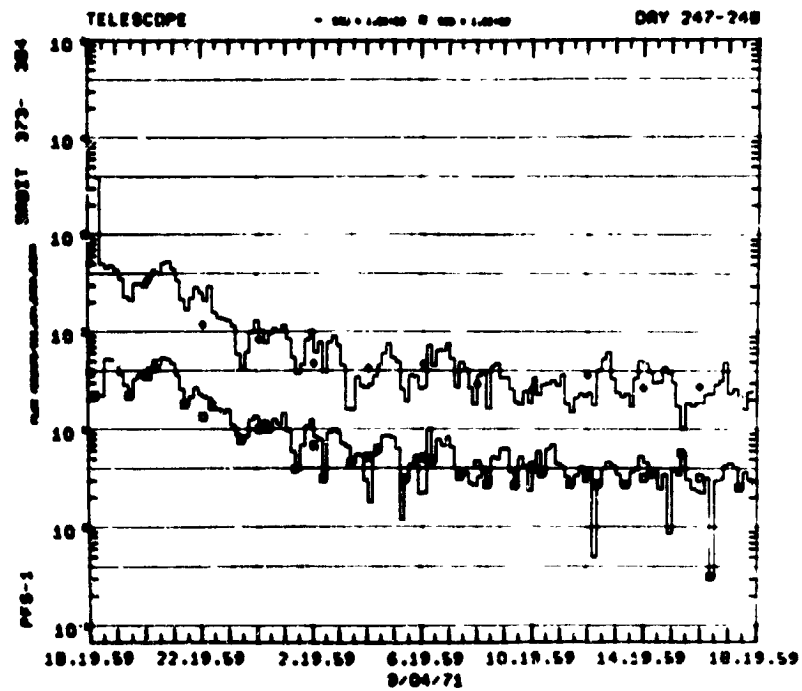


Figure 33-7.- Sample 1-day plot.

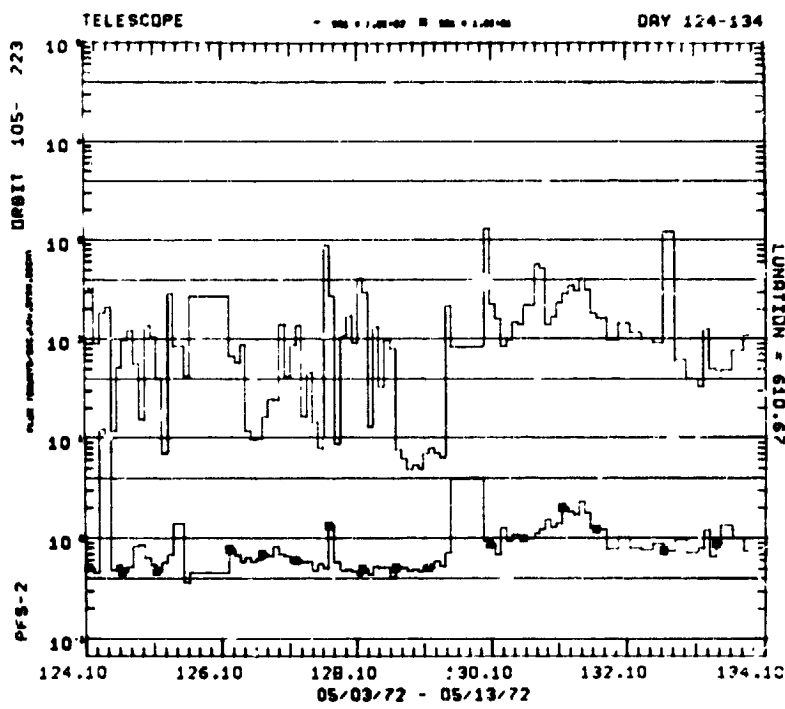
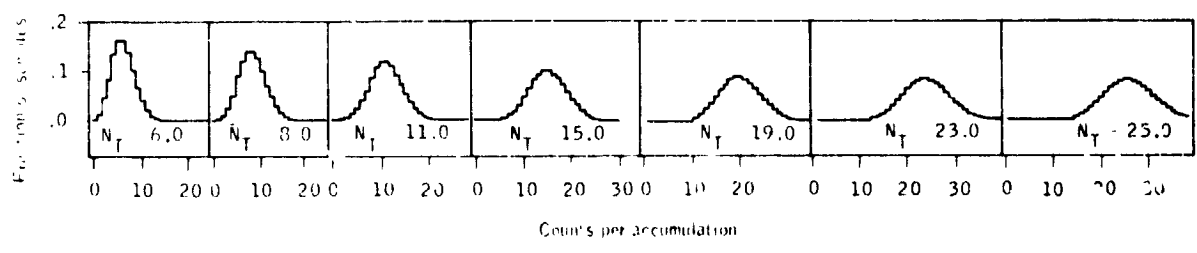
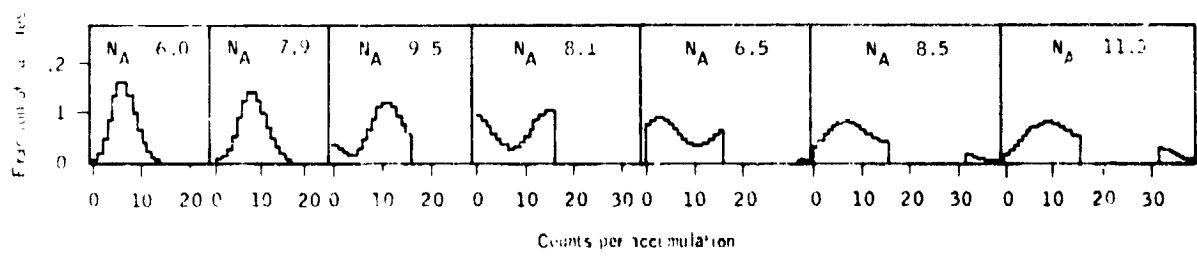


Figure 33-8.- Sample 10-day plot



(a) Without TCE.



(b) With TCE.

Figure 33-9.- Sample distributions for various true average count rates  $\bar{N}_T$ .

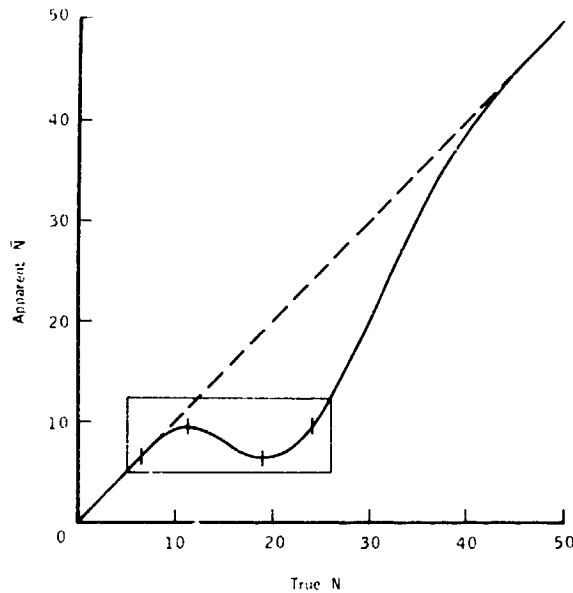


Figure 33-10.- The function  $\bar{N}_A = f_2(\bar{N}_T)$ .

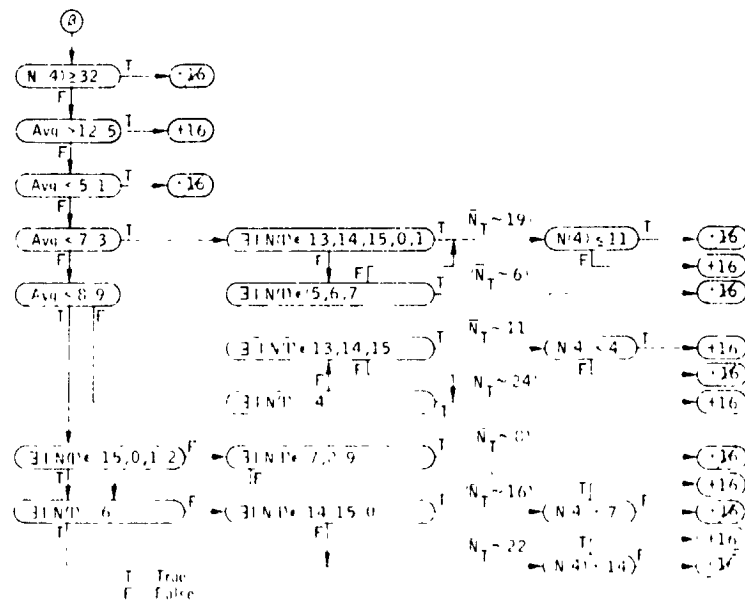
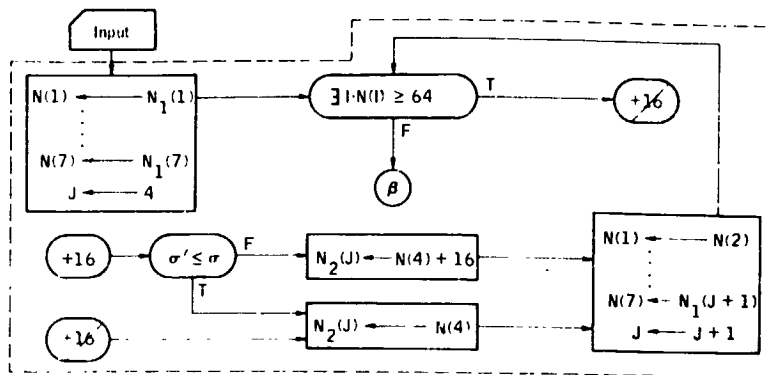
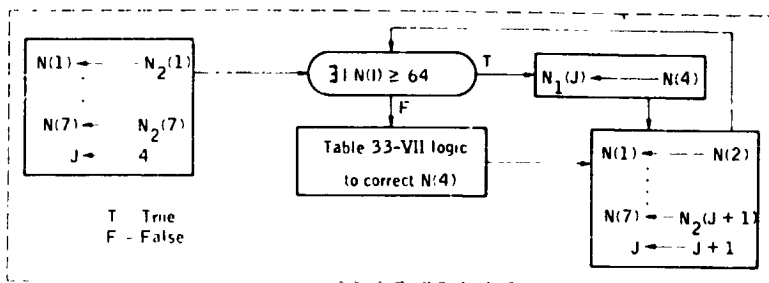


Figure 33-11.- Flow diagram of the distribution recognition procedure. Entry point to the routine is  $\beta$ ; the function  $I$  is a variable. Seven data points are supplied,  $N(1)$  to  $N(7)$ , with  $N(4)$  the point to be corrected. The quantity  $Avg$  is the average of points  $N(1)$  to  $N(7)$ . The exit symbol  $+16$  indicates that  $N(4)$  should be  $N(4) + 16$ , whereas the symbol  $-16$  indicates that  $N(4)$  is correct as is.



(a) PHASE 1 subroutine.



(b) PHASE 2 subroutine.

Figure 33-12.- Flow diagram of the correction logic. Input consists of an array in a matrix  $N_2$ ; the function  $J$  is a variable. The entry points  $\beta$ ,  $+16$ , and  $+16$  are defined with respect to figure 33-11. The quantity  $Avg$  is the average in either of the routines of the seven points at a given time.

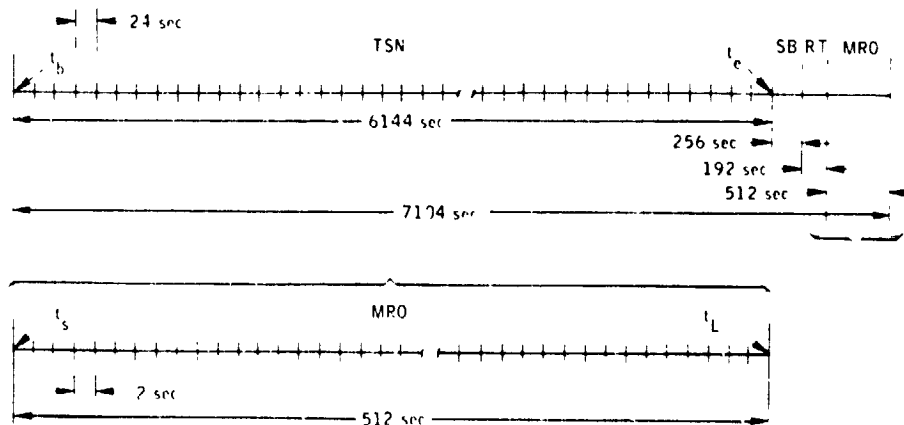


Figure 33-13.- Accumulator time scales compared to readout time scales in TSN mode.

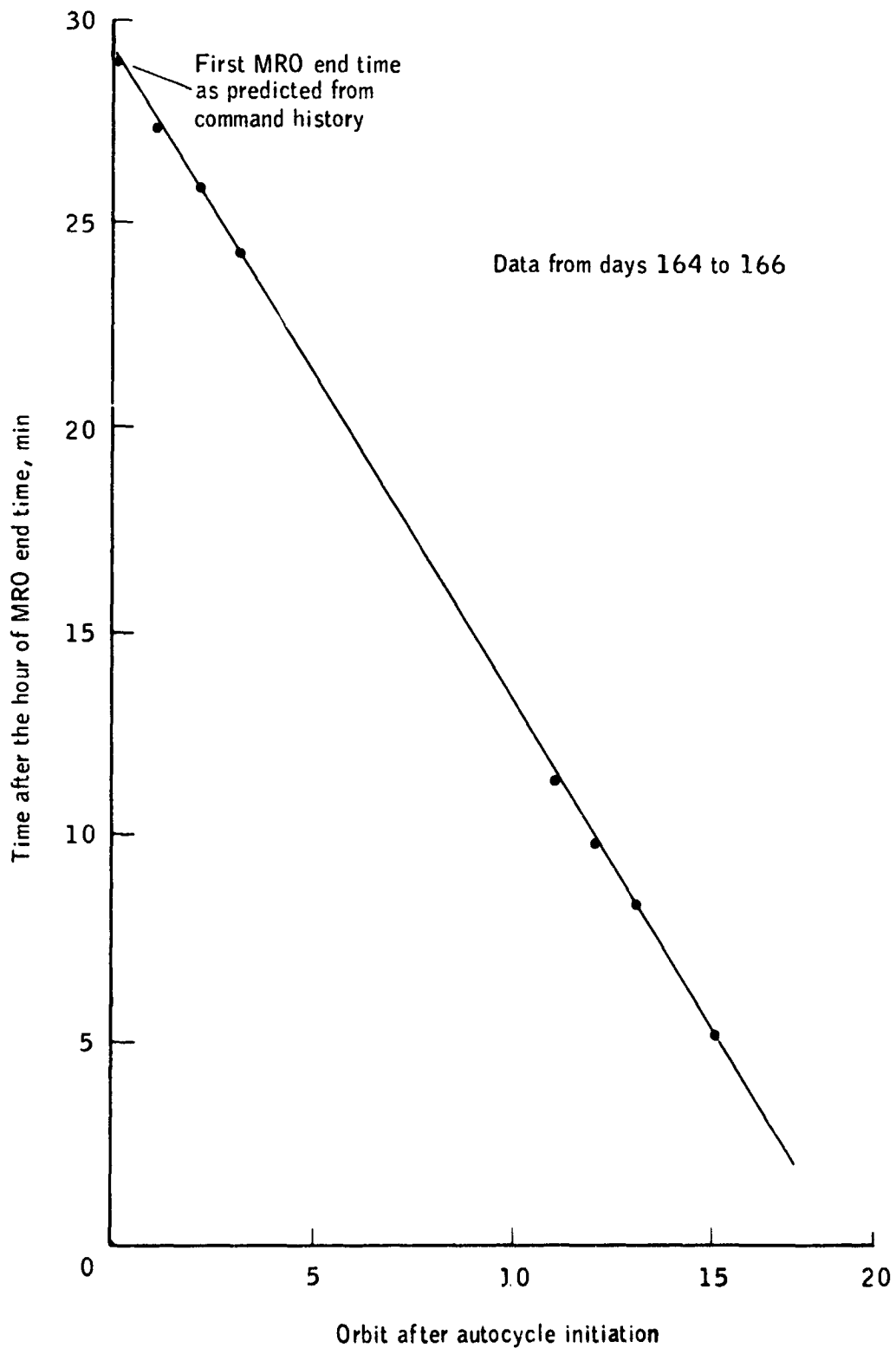


Figure 33-14.- Sample plot of MRO end times compared to orbit number from start of autocycle.

## PART B

### PARTICLES AND FIELDS SUBSATELLITE MAGNETOMETER

The subsatellite magnetometer consisted of two fluxgate sensors mounted orthogonally at the end of a 1.83-m-long boom and an electronics unit housed in the main body of the spacecraft. One sensor is mounted parallel to the spin axis, and the other, perpendicular. On the Apollo 15 subsatellite, there were two automatically selected dynamic ranges, 0 to  $\pm 50$  nT (0 $\gamma$  to  $\pm 50\gamma$ ) and 0 to  $\pm 200$  nT (0 $\gamma$  to  $\pm 200\gamma$ ). These were called the high and low sensitivity ranges, respectively. The resolution of each measurement was 0.4 to 1.6 nT (0.4 $\gamma$  to 1.6 $\gamma$ ) depending on range. There were three sampling rates referred to as telemetry-store normal (TSN), telemetry-store fast (TSF), and real time (PT). In the first two modes, the magnetometer measured the magnetic field magnitude and phase in the spin plane and the vector component along the spin axis. The sample rates were one vector every 24 sec and every 12 sec, respectively. The magnitude in the spin plane was measured by filtering the transverse magnetometer output about the spin frequency, then rectifying and filtering this output. The phase was obtained by measuring both the time of the positive-going-zero crossing of the magnetometer output and the time of the Sun crossing. In eclipse, the Sun-crossing time was computed from a model of the eclipse spin up and from a knowledge of the spin frequency and phase during the sunlit portion of the orbit.

During real-time operations, one sample of the spin plane output was returned every 1 sec and one sample of the spin axis output every 2 sec. Thus, approximately five samples of the spin plane signal were taken per revolution. This signal was Fourier analyzed to obtain a magnitude and phase and referenced to the Sun-crossing time. Real-time data were, of course, only obtained across the near side of the Moon, whereas the recorded TSF and TSN data were available from both near and far sides. The subsatellite did not store data while transmitting. Thus, gaps occurred in the records each orbit when data were telemetered to Earth. A summary of the magnetometer characteristics is given in table 33-VIII. The only significant difference between the Apollo 15 and Apollo 16 magnetometers was an increase by a factor of 2 in the sensitivity of the Apollo 16 magnetometer that increased the resolution to 0.2 and 0.8 nT (0.2 $\gamma$  and 0.8 $\gamma$ ) and decreased the range to  $\pm 25$  and  $\pm 100$

nT ( $\pm 25\gamma$  and  $\pm 100\gamma$ ) for high and low sensitivity ranges, respectively.

#### OPERATING HISTORY

The Apollo 15 subsatellite was launched on August 4, 1971. A failure in the telemetry system after 7 months of operation prevented further transmission of data from most of the magnetometer outputs, although the magnetometer continued to operate normally. The Apollo 16 subsatellite was launched on April 24, 1972, into an approximately circular orbit at an altitude of 100 km, having an orbital period of approximately 2 hr. Because of the decision not to perform a shaping burn before jettisoning the subsatellite, the Apollo 16 subsatellite crashed into the Moon after 34 days in lunar orbit. During this period, the magnetometers operated normally. The minimum correlation technique of Hedgecock was used to measure sensor drift of the parallel axis on the Apollo 15 subsatellite. The drift rate was well within the range expected. Table 33-IX contains the offsets for each lunation. These numbers should be added to the values appearing on the plots and tapes obtained from the preliminary calibration.

The orientation of the subsatellite spin axis was determined from the variation of the Sun elevation angle with time during the first 30 days after launch. On the Apollo 15 subsatellite, the predicted variation and the measured variation of this angle followed each other almost exactly until December 1971. Thereafter, measurable deviation occurred that amounted to  $1^\circ$  in February 1972.

#### THE DATA

##### Orbit Data

Three different displays of orbit data were made plus one tape. These were all created at the NASA Lyndon B. Johnson Space Center (JSC). The three orbit plots are altitude as a function of time, selenographic longitude as a function of latitude, and the ecliptic projection of the Earth-Moon system.

Altitude as a function of time.- This plot shows altitude as a function of time for one orbit, but information on as many as six consecutive orbits is included. At the top of the plot are the orbit number, the orbit start time (hours and minutes, day/month/year), the

perilune time and altitude in kilometers, the apolune time and altitude, and the time of sunrise and sunset. The plot includes two vertical shaded bars marking sunset and sunrise at the subsatellite. Time grids below the plot permit the use of this graph for as many as six consecutive orbits. However, these grids may be up to 4 minutes off. Figure 33-15 is a sample plot.

Latitude as a function of longitude.- The plot of latitude as a function of longitude shows the track of the satellite across the lunar surface in selenographic coordinates. The vertical and horizontal scales are different by a factor of 2. The points of sunrise and sunset at the subsatellite are indicated by shaded vertical bars. Perilune and apolune are marked on the orbit track with an X and labeled with P and A, respectively. The subsolar point is similarly marked with an X and labeled with an S. The location of the Apollo 15 Apollo lunar surface experiments package (ALSEP) is similarly shown and encircled by an ellipse showing the area within 15° of the ALSEP site. Underneath the plot are given orbit numbers and perilune and apolune times. Figure 33-16 is a sample plot.

Earth-Moon system plots.- The Earth-Moon system plot contains the ecliptic plane projection of the Earth-Moon system and includes the expected position of the magnetopause and bow shock. One point is given per orbit. Distances are labeled in Earth radii. Figure 33-17 is a sample plot.

Magnetic tape.- The orbit tape contains position and orientation information that changed slowly in a header record once per orbit and contains rapidly changing positional data every minute in a data record (1 record/min). The format of this tape is given in table 33-X.

#### Magnetometer Data

Two microfilm reels of data and one magnetic tape were produced in preliminary processing of the data. The first reel contains two plots. Magnetometer measurements appear on the A plot and engineering data on the B plot. The second reel contains a computer listing of 192-sec averages of the data. The magnetic tape contains 24-sec averages of the data. Apollo 16 data submitted by JSC to the National Space Science Data Center (NSSDC) were processed with Apollo 15 calibration constants. Therefore, field scales on Apollo 16 plots are a factor of 2 too large. (For more details, see the section entitled "Converting Apollo 16 Data to Proper Units.")

The A plot.- The A plot shows the  $B_x, B_y, B_z$  components and  $B$  (total field) in spacecraft coordinates compared to time for one orbit. The orbit start time is defined here and in the orbit data to be the time of the crossing of the lunar noon meridian. Spacecraft coordinates have X and Y in the spin plane with X along the projection of the Earth-Sun line in the spin plane and Y roughly antiparallel to the direction of planetary motion. The Z direction is chosen to be parallel to the spin axis and points northward relative to the ecliptic plane. At launch, the spin axes of both the Apollo 15 and 16 subsatellites were close to perpendicular to the ecliptic. Thus, the data were initially returned in essentially solar ecliptic coordinates. Time on the horizontal scale is given in terms of day of year (January 1 = 1), hour, and minute. No sensor drift corrections have been applied to these data. Note that the scale of this plot varies to keep the data on scale. Figure 33-18 is a sample plot.

The B plot.- The B plot contains relevant engineering and processing data and some data from the Berkeley particle experiment. The top line indicates the telemetry mode (TSN, TSF, or RT). The second line includes the array current in amperes; the third line, the spin period in seconds, is measured in sunlight and predicted in eclipse. Finally, on the bottom, plotted on the same scale, are Berkeley particle counts per accumulation period for the shielded and unshielded detectors. Figure 33-19 is a sample plot.

The printout.- The microfilm reel containing the printout of the data first contains data and tables generated during the processing of the data. The printouts that follow are 192-sec averages of the data. (The basic repetition cycle of the data system is 192 sec.) The following data are given.

1. Day of year (January 1 = 1)
2. Month/day
3. Elapsed time on spacecraft clock (1 tick = 16 sec)
4.  $B_x, B_y, B_z, B_T$  (spacecraft coordinates, in gammas)
5. Open counts (Berkeley data)
6. Shielded counts (Berkeley data)
7. Sun elevation angle (degrees)
8. Spin period (seconds)

9. Spin count (from Sun pulse or magnetometer pulse)
10. Magnetometer temperature (degrees Fahrenheit)
11. Battery temperature (degrees Fahrenheit)
12. Battery voltage (volts)
13. Battery current (amperes)
14. Array current (amperes)
15. Reference voltage of magnetometer (volts)
16. Flag 1
  - a. I - satellite identity (1 = Apollo 15)
  - b. F - data format (0 = store mode, 1 = real time)
  - c. M - automatic/manual (0 = manual mode)
  - d. C - calibration (1 = on)
  - e. T - transverse range (1 = low sensitivity)
  - f. P - parallel range (1 = low sensitivity)
17. Flag 2 not used (repeats elapsed time, fine)

Figure 33-20 is a sample plot.

Magnetic tape. - The magnetic tape contains magnetic field data every 24 sec and associated engineering data every 192 sec. The magnetic tape format is given in table 33-XI.

#### Data Cycle Description

One data cycle consists of 80 words (an array dimensioned 8 by 10). Then, for DATCYC(8,10) or DATCYC(I,J), the symbols I and J have the following functions.

1. I implies  $A_I$  for  $I = 1$  to  $I = 8$ .
2. J implies frame of  $A_1$  for  $J = 1$  to  $J = 8$ .
3. J is meaningless for  $A_I$  for  $J = 9$  to  $J = 10$ , but the  $B_K$  data are contained in these cells.

- a. K takes on values 1 to 16.
- b.  $K = I + (J - 9) * 8$  for  $I = 1$  to  $I = 8$ ,  
 $J = 9$  and  $J = 10$ .

Graphically, DATCYC(8,10) is shown in figure 33-21.  
 From figure 33-21, the following information is evident.

1. ((A(I,J), I=1,3), J=1,8) are integer numbers.
2. ((A(I,J), I=4,8), J=1,8) are floating point numbers.
3. (B(K), K=1,3) and B(7) are integer numbers.
4. (B(K), K=4,6) and (B(K), K=8,13) are floating point numbers.
5. (B(K), K=14,16) are unused cells.

<u>Quantity</u>	<u>Description</u>
A(1,J)	Time (days)
A(2,J)	Time (milliseconds of day)
A(3,J)	Flag
A(4,J)	Transverse field (gammas)
A(5,J)	Parallel field (gammas)
A(6,J)	Sun pulse delay (seconds)
A(7,J)	Field longitude (radians)
A(8,J)	Particle counts

<u>Quantity</u>	<u>Description</u>
B(1)	Elapsed time, coarse
B(2)	Elapsed time, fine
B(3)	Flag
B(4)	Sun elevation angle (degrees)
B(5)	Spin period

B (6)	Sector period
B (7)	Spin count
B (8)	Magnetometer temperature (degrees Fahrenheit)
B (9)	Battery temperature (degrees Fahrenheit)
B (10)	Battery current (amperes)
B (11)	Battery voltage (volts)
B (12)	Array current (amperes)
B (13)	Reference voltage (volts)

#### Converting Apollo 16 Data to Proper Units

When the Apollo 16 subsatellite is in sunlight, the following formulas may be used to obtain proper values for data given on the magnetic tape. For the magnetic field transverse to the spin axis (stored mode), use

$$B_T = B_T (0.512 - 0.1013)$$

For the magnetic field transverse to the spin axis (real time), use

$$B_T = B_T \times 0.503$$

For the magnetic field parallel to the spin axis, use

$$B_P = 0.4981 [ (B_P + 51.95) - (0.0279 \times B8) ] - 24.72$$

where  $B_T$  = transverse field, word A(4,J) in data cycle

$B_P$  = parallel field, word A(5,J) in data cycle

B8 = magnetometer temperature, word B(8) in data cycle

Note: In real time, flag A3 = X0XXXX; in memory store, flag A3 = X1XXXX.

## SUMMARY OF RESULTS

### Lunar Magnetic Field Maps

The first attempt to map the lunar surface field consisted of simply superposing measurements on successive orbit tracks when the Moon was in the geomagnetic tail. Because the data were not available in machine-readable format until many months after launch and because the orientation of the spin axis of the subsatellite was not known until well after that, the early maps were constructed from data on "quick look" computer listings of the raw data obtained in real time from the JSC Mission Control Center computer. The raw data consisted of the field component parallel to the spin axis, the magnitude in the spin plane, and the time that the magnetic field in the spin plane crossed the zero field reading going positive. This latter measurement has meaning only when referenced to the Sun pulse. Therefore, it was not used in the early mapping studies. Such superposed epoch plots were presented by Coleman et al. (refs. 33-2 to 33-5) and Russell et al. (ref. 33-6) for Apollo 15 data and by Coleman et al. (ref. 33-7) for Apollo 16 data.

While these plots clearly demonstrated that the field variations observed by the subsatellite were correlated with selenographic position, it was highly desirable to attempt to derive information about the lateral extent of these surface fields. Thus, surface contour maps of the raw data were constructed. The first such map, using the magnitude of the field in the spin plane, was made by subtracting the minimum field strength observed on each orbit near the crater Van de Graaff from each of the readings on that orbit, and then scaling the resulting residuals by the altitude raised to the 2.5 power (refs. 33-4 and 33-5).

The next field map covered only the Van de Graaff-Aitken region (refs. 33-6 to 33-8) and was produced from 10 successive orbits of data at an altitude of approximately 70 km. This map used the vector information reduced from the raw data listings. First, the three field components in spacecraft coordinates were computed from the transverse magnitude, the zero crossing delay, the Sun pulse delay, and the component parallel to the spin axis. Next, the average field for each orbit was subtracted and the residuals contoured. No altitude-dependent corrections were applied, nor were the data rotated into local lunar coordinates.

When digital tapes became available, more data could be incorporated into the maps, and a greater portion of the lunar surface could be covered. The first such map for only

the radial component was published by Sharp et al. (ref. 33-9). Again, the average field in inertial space was removed for each orbit and the altitude dependence empirically removed with an altitude to the 1.5 power correction. Superposed epoch plots of each of the field components were also shown (together with a map of the Van de Graaff region at 130-km altitude) in addition to the 70-km map.

When all the data from the Apollo 15 mission became available, the next generation field map was attempted. For these maps, the average and linear slopes were removed from each of the components in inertial space (solar ecliptic coordinates); and then the residuals were rotated into radial, east, and north selenographic components. These residuals were not altitude corrected. The data were then sorted and averaged in  $1^\circ$  by  $1^\circ$  boxes, and the resulting averages smoothed with a two-dimensional filter (full-width, half-maximum  $2^\circ$  by  $2^\circ$ ). These maps were not completed in time for presentation at the Fourth Lunar Science Conference, but the radial component map was completed in time for inclusion in the frontispiece of the conference proceedings. A map of all three components, produced in this manner but covering only the Van de Graaff-Aitken region, was published by Russell et al. (ref. 33-10) and Schubert and Lichtenstein (ref. 33-11). These maps portray the lunar field (at the altitude of the subsatellites) over all scales from global to approximately  $1^\circ$ , with some attenuation of the quadrupole field and nearby harmonics (ref. 33-10).

One of the most serious limitations of these mapping studies is the assumption that the magnetic field of the geomagnetic tail, in which the Moon is immersed during the mapping passes, remains constant (in the cases for which the average is removed) or varies linearly with time (in the cases for which the average and trend are removed). In short, the natural power spectrum of fluctuations in the tail from periods of roughly 1 hr to 24 sec is converted to surface correlated features with wavelengths of from  $180^\circ$  to  $1^\circ$ . Over some of the mapped tracks, there is sufficient redundant coverage so that such noise fluctuations are attenuated in the averaging process. In other regions, the lunar field itself is so large that it clearly dominates over the background noise. However, there are several regions on these maps that display the signature of contamination by the natural fluctuations (i.e., elongated contours parallel to the orbit track). Thus, when the Apollo 16 data became available for addition to these maps, the mapping procedure was refined once more.

The most striking features of all the maps was the small scale size of even the largest anomalies

(approximately  $10^\circ$  maximum). Therefore, the bandwidth of the data being used in the mapping studies was restricted, thereby reducing the power in the natural fluctuations affecting the accuracy of the map. To effect this bandwidth limitation, the raw data were passed through a high-pass filter with a corner frequency corresponding to wavelengths of  $20^\circ$ . Then, they were rotated into the local lunar coordinate system of radial, east, and north components; and they were sorted into  $1^\circ$  by  $1^\circ$  bins, averaged, and then further filtered by a two-dimensional Gaussian filter, as in past studies. These maps were then printed in the frontispieces of the Fifth and Sixth Lunar Science Conference Proceedings (refs. 33-12 and 33-13). These maps are discussed in more detail by Russell et al. (ref. 33-14) together with the altitude dependence of the fine scale field.

#### Permanent and Induced Lunar Magnetic Moment

There apparently is no global magnetic field. Fourier analysis of the tangential and radial components of the Apollo subsatellite magnetic field observations in the relatively steady field and near vacuum conditions of the geomagnetic tail provides a precise measurement of the projection of the lunar magnetic moment in the subsatellite orbit plane. Analysis of the 7-month sample of Apollo 15 results in an upper limit of  $130 \text{ MT-m}^3$  ( $1.3 \times 10^{18} \text{ G-cm}^3$ ) in the Apollo 15 subsatellite orbit plane (refs. 33-15 and 33-16). If one assumes the moment is parallel to the lunar rotation axis, this limits the total moment to less than  $300 \text{ MT-m}^3$  ( $3 \times 10^{18} \text{ G-cm}^3$ ). Analysis of the smaller 2-month sample of Apollo 16 data gives a moment of  $650 \pm 540 \text{ MT-m}^3$  ( $6.5 \pm 5.4 \text{ G-cm}^3$ ) in the Apollo 16 orbit plane (ref. 33-17). Combining the two results gives a moment of  $(200, -600, -900) \text{ MT-m}^3$  ( $(2, -6, -9) \times 10^{18} \text{ G-cm}^3$ ) along the three selenographic axes. However, because both the Apollo 15 and 16 measurements do not differ significantly from zero, the combined result is also consistent with zero.

A significant induced lunar dipole moment was measured with the Apollo 15 data (refs. 33-15 and 33-16). Combining the results from both spacecraft, one obtains an induced moment of  $(-4.9 \pm 1.9) \times 10^{16} \text{ T-m}^3$  per tesla ( $(-4.9 \pm 1.9) \times 10^{22} \text{ G-cm}^3$  per gauss) of applied external field (ref. 33-17). While the induced moment was originally postulated to result from a lunar icosphere, Goldstein and Russell have more recently suggested that this is due instead to the presence of an iron core (ref. 33-18).

## Solar Wind Interaction With the Moon

The previously known enhancement in the field strength on the antisolar side of the Moon, when the Moon is in the solar wind, known as the diamagnetic cavity was also seen at the 100-km altitude of the subsatellite (refs. 33-2 and 33-8). Also observed were the dips in field strength adjacent to the cavity, which are presumed to occur because of the expansion of the solar wind flow into the cavity. This interaction produced frequent increases in field strength just in front of the terminator. Although these features were previously reported on Explorer 35, they were much larger at the low altitude of the subsatellite. These features were previously termed limb shocks or penumbral increases. The more conservative term is limb compression. They were definitely correlated with the appearance of certain regions at the limbs (refs. 33-4, 33-6, and 33-19). The property of the lunar surface that appears to be responsible for the deflection of the solar wind leading to a limb compression is the lunar remanent magnetic field (refs. 33-8 and 33-9). On the other hand, the occurrence rate also depends on the orientation of the interplanetary magnetic field in a manner similar to the dependence of the Earth bow shock structure on the interplanetary field orientation (ref. 33-20).

## TRANSFER FUNCTION OF THE MOON

The region of the lunar limbs was usually disturbed even when limb compressions were absent (refs. 33-2 and 33-3). However, comparisons with Explorer 35 magnetometer measurements showed that the field was often undisturbed by the presence of the Moon over much of the subsolar hemisphere (refs. 33-10 and 33-21). Thus, the subsatellite magnetometer at times could be used as a measure of the input wave spectrum to the Moon. On the other hand, when the subsatellite was in the diamagnetic cavity, it was responsive to both the solar wind input and the scattered spectrum.

---

#### REFERENCES

- 33-2. Coleman, Paul J., Jr.; Schubert, G.; Russell, C. T.; and Sharp, L. R.: The Particle and Fields Subsatellite Magnetometer Experiment. Sec. 22 of Apollo 15 Preliminary Science Report, NASA SP-289, 1972.
- 33-3. Coleman, P. J., Jr.; Schubert, G.; Russell, C. T.; and Sharp, L. R.: Satellite Measurements of the Moon's Magnetic Field. *The Moon*, vol. 4, nos. 3/4, May-June 1972, pp. 419-429.
- 33-4. Coleman, Paul J., Jr.; Lichtenstein, B. R.; Russell, C. T.; and Sharp, L. R.: Magnetic Fields Near the Moon. Proceedings of the Third Lunar Science Conference, vol. 3, David R. Criswell, ed., MIT Press (Cambridge, Mass.), 1972, pp. 2271-2286.
- 33-5. Coleman, P. J., Jr.; Russell, C. T.; Sharp, L. R.; and Schubert, G.: Preliminary Mapping of the Lunar Magnetic Field. *Physics of Earth and Planetary Interiors*, vol. 6, no. 1-3, Dec. 1972, pp. 167-174.
- 33-6. Russell, C. T.; Coleman, P. J., Jr.; Lichtenstein, B. R.; Schubert, G.; and Sharp, L. R.: Surface and Orbital Results from Apollo 15. Vol. 2 of Space Research XIII, M. J. Rycroft and S. K. Runkorn, eds., Akademie-Verlag (Berlin), 1973, pp. 951-960.
- 33-7. Coleman, P. J., Jr.; Lichtenstein, B. R.; Russell, C. T.; Schubert, G.; and Sharp, L. R.: The Particles and Fields Subsatellite Magnetometer Experiment. Sec. 23 of Apollo 16 Preliminary Science Report, NASA SP-315, 1972.
- 33-8. Russell, C. T.; Coleman, P. J., Jr.; Lichtenstein, B. R.; Schubert, G.; and Sharp, L. R.: Subsatellite Measurements of the Lunar Magnetic Field. Proceedings of the Fourth Lunar Science Conference, vol. 3, Pergamon Press (New York), 1973, pp. 2833-2845.
- 33-9. Sharp, L. R.; Coleman, P. J., Jr.; Lichtenstein, B. R.; Russell, C. T.; and Schubert, G.: Orbital Mapping of the Lunar Magnetic Field. *The Moon*, vol. 7, nos. 3/4, May-June 1973, pp. 322-341.

- 33-10. Russell, C. T.; Coleman, P. J., Jr.; Lichtenstein, B. R.; Schubert, G.; and Sharp, L. R.: Apollo 15 and 16 Subsatellite Magnetometer Measurements of the Lunar Magnetic Field, Space Research XIV, 1974, pp. 629-634.
- 33-11. Schubert, Gerald; and Lichtenstein, Bernard R.: Observations of Moon-Plasma Interactions by Orbital and Surface Experiments. Rev. Geophys. Space Phys., vol. 12, no. 4, 1974, pp. 592-626.
- 33-12. Russell, C. T.; Coleman, P. J., Jr.; and Schubert, G.: Contour Maps of the Fine Scale Lunar Magnetic Field. Frontispiece in Proceedings of the Fifth Lunar Science Conference, vol. 1, Pergamon Press (New York), 1974.
- 33-13. Russell, C. T.; Coleman, P. J., Jr.; and Schubert, G.: Contour Maps of the Fine Scale Lunar Magnetic Field. Frontispiece in Proceedings of the Sixth Lunar Science Conference, vol. 3, Pergamon Press (New York), 1975.
- 33-14. Russell, C. T.; Coleman, P. J., Jr.; Fleming, B. K.; Hilburn, L.; et al.: The Fine-Scale Lunar Magnetic Field. Proceedings of the Sixth Lunar Science Conference, vol. 3, Pergamon Press (New York), 1975, pp. 2955-2969.
- 33-15. Russell, C. T.; Coleman, P. J., Jr.; Lichtenstein, B. R.; and Schubert, G.: The Permanent and Induced Magnetic Dipole Moment of the Moon. Proceedings of the Fifth Lunar Science Conference, vol. 3, Pergamon Press, (New York), 1974, pp. 2747-2760.
- 33-16. Russell, C. T.; Coleman, P. J., Jr.; and Schubert, G.: Lunar Magnetic Field: Permanent and Induced Dipole Moments. Science, vol. 186, no. 4166, 1974, pp. 825-826.
- 33-17. Russell, C. T.; Coleman, P. J., Jr.; and Schubert, G.: The Lunar Magnetic Field, Space Research XV, (To be published).
- 33-18. Goldstein, B. E.; and Russell, C. T.: On the Apparent Diamagnetism of the Lunar Environment in the Geomagnetic Tail Lobes. Proceedings of the Sixth Lunar Science Conference, vol. 3, Pergamon Press (New York), 1975, pp. 2999-3012.

- 33-19. Lichtenstein, B. R.; Russell, C. T.; and Coleman, P. J., Jr.: Magnetic Measurements of the Solar Wind Interaction with the Moon. Paper presented at the Symposium on Photon and Particle Interactions with Surfaces in Space, ESLAB (Noordwijk, Netherlands), Sept. 1972.
- 33-20. Lichtenstein, B. R.; Russell, C. T.; and Coleman, P. J., Jr.: On the Nature of Lunar Limb Compressions (abs.). EOS, vol. 54, no. 4, April 1973, p. 443.
- 33-21. Schubert, G.; Lichtenstein, B. R.; Coleman, P. J., Jr.; and Russell, C. T.: Simultaneous Explorer 35 and Apollo 15 Orbital Magnetometer Observations: Implications for Lunar Electrical Conductivity Inversions. J. Geophys. Res., vol. 79, no. 14, 1974, pp. 2007-2013.

#### BIBLIOGRAPHY

- Anderson, K. A.; Chase, L. M.; Lin, R. P.; McCoy, J. E.; and McGuire, R. E.: Measurements of the Solar Wind Cavity Behind the Moon from the Apollo 15 Subsatellite (abs.). EOS, vol. 52, no. 11, Nov. 1971, p. 910.
- Anderson, K. A.; Chase, L. M.; Lin, R. P.; McCoy, J. E.; and McGuire, R. E.: Solar Wind and Interplanetary Electron Measurements on the Apollo 15 Subsatellite. J. Geophys. Res., vol. 77, no. 25, Sept. 1972, pp. 4611-4626.
- Anderson, K. A.; Chase, L. M.; Lin, R. P.; McCoy, J. E.; and McGuire, R. E.: Subsatellite Measurements of Plasma and Energetic Particles. Sec. 22 of Apollo 16 Preliminary Science Report, NASA SP-315, 1972.
- Anderson, K. A.; Chase, L. M.; Lin, R. P.; McCoy, J. E.; and McGuire, R. E.: Subsatellite Measurements of Plasmas and Solar Particles. Sec. 21 of Apollo 15 Preliminary Science Report, NASA SP-289, 1972.
- Anderson, K. A.; Howe, H. C.; Lin, R. P.; McGuire, R. E.; et al.: Observation of Energetic Electron Mirroring from Lunar Remanent Magnetic Field. Proceedings of the 5th Lunar Science Conference (abstracts volume), part 1, 1974, pp. 18-20.

- Anderson, K. A.; Lin, R. P.; and McGuire, R. E.: Observation of 38-344 keV Interplanetary Protons During Quiet Times. International Cosmic Ray Conference, 13th, Proceedings, vol. 2. University of Denver (Denver, Colo.), 1973, pp. 1624-1629.
- Chase, L. M.: Particle Characteristics in the Earth's Magnetotail at 60 Re (abs.). EOS, vol. 53, no. 11, Nov. 1972, p. 1101.
- Chase, L. M.: The Geometrical Factor of Large Aperture Hemispherical Electrostatic Analyzers. Rev. Sci. Instr., vol. 44, no. 8, Aug. 1973, pp. 998-1002.
- Coleman, P. J., Jr.; Russell, C. T.; and Sharp, L. R.: Magnetic Field Measurements with the Apollo 15 Subsatellite. Paper presented at 41st Annual International Meeting of the Society of Exploration Geophysicists (Houston, Texas), Nov. 1971.
- Coleman, P. J., Jr.; Schubert, G.; Russell, C. T.; and Sharp, L. R.: Satellite Measurements of the Moon's Magnetic Field: A Preliminary Report. Conference on Lunar Geophysics, Zdenek Kopal and David Strangway, eds., D. Reidel (Dordrecht, Holland), 1973, pp. 122-132.
- Coleman, P. J., Jr.; Sharp, L. R.; Russell, C. T.; and Schubert, G.: Lunar Limb Effects in the Solar Wind (abs.). EOS, vol. 52, no. 11, Nov. 1971, p. 855.
- Fenner, Martha A.; Freeman, J. W., Jr.; Hills, H. K.; and Lindeman, R. A.: Magnetosheath Structure Observed by 3 ALSEP/SIDE Plasma Detectors (abs.). EOS, vol. 53, no. 4, April, 1972, p. 486.
- Lichtenstein, B. R.; Russell, C. T.; and Coleman, P. J., Jr.: Measurements of the Solar Wind-Moon Interaction with the Apollo 15 and 16 Subsatellite Magnetometers (abs.). EOS, vol. 53, no. 11, Nov. 1972, p. 1033.
- Lichtenstein, B. R.; Russell, C. T.; and Coleman, P. J., Jr.: On the Nature of Lunar Limb Compressions (abs.). EOS, vol. 54, no. 4, April 1973, p. 443.
- Lin, R. P.; Evans, L. G.; and Fainberg, J.: Simultaneous Observation of Fast Solar Electrons and Type III Radio Burst Emission Near 1 AU. Astrophys. Lett., vol. 14, no. 4, April 1973, pp. 191-198.
- Lin, R. P.; McGuire, R. E.; and Anderson, K. A.: Observations of 38-344 keV Interplanetary Protons During Solar Quiet Times. Phys. Rev. Lett., vol. 31, no. 20, Nov. 1973, pp. 1268-1271.

- Lin, R. P.; McGuire, R. E.; and Anderson, K. A.: Observations of 38-344 keV Protons and 2 to 100 keV Electrons in Solar Events. International Cosmic Ray Conference, 13th, Proceedings, vol. 2. University of Denver (Denver, Colo.), 1973, pp. 1624-1629.
- Lin, F. P.; Meng, C.-I.; and Anderson, K. A.: 30-100 keV Protons Upstream from the Earth's Bow Shock. J. Geophys. Res., vol. 79, no. 4, Feb. 1, 1974, pp. 489-498.
- McGuire, R. E.; Anderson, K. A.; Chase, L. M.; Lin, R. P.; and McCoy, J. E.: Particle Observations During the Passage of the Interplanetary Shock of May 15, 1972 (abs.). EOS, vol. 53, no. 11, Nov. 1972, p. 1086.
- Russell, C. T.; Coleman, P. J., Jr.; Lichtenstein, B. R.; Schubert, G.; and Sharp, L. R.: Apollo 15 and 16 Subsatellite Measurements of the Lunar Magnetic Field. Lunar Science IV (abs. of papers presented at the Fourth Lunar Science Conference (Houston, Texas), Mar. 5-8, 1973), pp. 645-646.
- Russell, C. T.; Coleman, P. J.; Lichtenstein, B. R.; Schubert, G.; and Sharp, L. R.: Lunar Magnetic Fields (abs.). The Moon, vol. 9, nos. 1/2, Jan.-Feb. 1974, pp. 234-235.
- Russell, C. T.; Coleman, P. J., Jr.; Lichtenstein, B. R.; Schubert, G.; and Sharp, L. R.: Subsatellite Measurements of the Lunar Magnetic Field. Proceedings of the Fourth Lunar Science Conference, vol. 3, Pergamon Press (New York), 1973, pp. 2833-2845.
- Sharp, L. R.; Coleman, P. J., Jr.; and Russell, C. T.: Lunar Surface Remanent Magnetization as Measured by the Apollo 15 and 16 Subsatellite Magnetometers (abs.). EOS, vol. 54, no. 11, Nov. 1972, p. 1033.
- Sharp, L. R.; Coleman, P. J., Jr.; Russell, C. T.; and Schubert, G.: Lunar Magcons (abs.). EOS, vol. 52, no. 11, Nov. 1971, p. 857.
- Sharp, L. R.; Coleman, P. J.; Russell, C. T.; and Schubert, G.: The Magnetic Field of the Moon (abs.). EOS, vol. 53, no. 4, April 1972, p. 441.
- Sharp, L. R.; Russell, C. T.; and Coleman, P. J., Jr.: The Dipole Field of the Moon (abs.). EOS, vol. 54, no. 4, April, 1973, p. 358.

TABLE 33-VIII.- APOLLO SUBSATELLITE MAGNETOMETER SPECIFICATIONS

Characteristic	Specification
Type . . . . .	Second-harmonic, saturable-core fluxgate
Sensor configuration . . . . .	Two sensors, one sensor parallel B <sub>p</sub> and one perpendicular $\hat{a}_T$ to the satellite spin axis
Mounting . . . . .	Sensor unit at end of 1.83-m-long boom; electronics unit in spacecraft body
Automatically selected dynamic ranges, nT . . . . .	0 to $\pm 50$ at higher sensitivity, 0 to $\pm 200$ at lower sensitivity
Resolutions, nT . . . . .	.4 and 1.6, depending on range
Sampling rates:	
Real time . . . . .	B <sub>p</sub> every 2 seconds, B <sub>T</sub> every 1 sec
High-rate storage . . . . .	B <sub>p</sub> and B <sub>T</sub> magnitude and B <sub>T</sub> phase once every 12 sec
Low-rate storage . . . . .	B <sub>p</sub> and B <sub>T</sub> magnitude and B <sub>T</sub> phase once every 24 sec
Power, W . . . . .	.70
Weight:	
Electronics unit, kg . . . . .	approximately .8
Sensor unit, kg . . . . .	approximately .2
Size:	
Electronics unit, cm . . . . .	27.9 by 15.9 by 3.8
Sensor unit, cm . . . . .	1.5 (diameter) by 7.6
Operating temperature range, K . . . . .	344 to 172

TABLE 33-IX.- MAGNETOMETER OFFSETS

Lunation	Orbit numbers	Offset, nT
1	1 to 378	0.27
2	379 to 732	.05
3	733 to 1086	-.17
4	1087 to 1440	-.38
5	1441 to 1784	-.60
6	1785 to end	-.81

TABLE 33-X. - ORBIT TAPE CONTENTS

Word or code	Definition
Reader record - record 1 <sup>1</sup>	
1	Number of orbits on tape
2	Orbit number
3/4	Date calculated/processed
5/6	Altitude of perilune/apolune
7/8	Day of year of orbit start/year mod. 1900
9	Start time (seconds)
10	Number of points (records) in orbit
11/12	Time of perilune/apolune
13/14	Sunset time (start/stop)
15/16	Sunrise time (start/stop)
17/18	Earthrise/earthset times
19	End time of orbit
*20 to 28	GEI to GSE
*29 to 37	GEI to GSM
*38 to 46	GEI to GSFQ
*47 to 55	GSM to GSE
*56 to 64	GSM to GSEQ
*65 to 73	GSE to GSEQ
*74 to 82	GEI to SSP
*83 to 91	GEI to SSEQ
*92 to 100	SSE to SSEQ
*101 to 109	GEI to SG
*110 to 118	SG to SSE
*119 to 127	SG to SSEQ
*128 to 136	SG to GSM
*137 to 145	S/C to SSE
*146 to 154	S/C to SSEQ
*155 to 163	S/C to GSM
*164 to 172	S/C to GSE
*173 to 181	S/C to SG
GEI	Geocentric equatorial inertial coordinates
GSE	Geocentric solar ecliptic
GSM	Geocentric solar magnetospheric
GSEQ	Geocentric solar equatorial
SSE	Selenocentric solar ecliptic
SSEQ	Selenocentric solar equatorial
SG	Selenographic
S/C	Spacecraft coordinate
Data record <sup>2</sup>	
1/2	Day of year/year mod. 1900
3	Seconds of day
4/5	Earth-Sun/Earth-Moon distances
6/7	Sun-Moon/subsatellite-Moon distances
8 to 10	Unit vector to Sun GEI
11 to 13	Unit vector to Moon GEI
14 to 16	Unit vector parallel to PPS spin axis GEI
17 to 19	Unit vector parallel to Earth dipole GEI
20 to 22	Unit vector to Earth SSE
23 to 25	Unit vector to subsatellite SSE
26 to 28	Unit vector parallel to PPS spin axis SSE
29 to 31	Unit vector to subsatellite SG
32 to 34	Unit vector to Earth SG
35 to 37	Unit vector to Sun SG
38 to 40	Unit vector parallel to PPS spin axis SG
41	Altitude of PFS

<sup>1</sup>Words 1 to 4 integer, words 5 on real.

<sup>2</sup>Transformation matrices of form A11 A12 A13, A21 A22 A23, A31 A32 A33.

<sup>3</sup>Repeated N times - all real.

TABLE 33-11. - LUNAR SUBSATELLITE MAGNETOMETER DATA REDUCTION PROGRAM (SSMAGE)  
 PHASE 3 DATA TAPE FORMAT<sup>1</sup>

Record number	Number of words	Mode	Array	Description
1	5	MIXED	--	Processing date and routine version Word Mode Description 1 PIPIDATA Date processed "DDMMYY" 2 PIELDATA Time of day processed "HHMMSS" 3 INTEGER Routine version number 4 PIELDATA Routine version generation date "DDMMYY" 5 PIELDATA Routine version generation time of day "HHMMSS"
2	100	INTEGER	ORBIT(100)	Lunar orbit numbers for data contained on this tape
3	100	INTEGER	MOON(100)	Lunar noon meridians associated with the beginning of each of the previously mentioned orbits
4	100	INTEGER	ECLIPSF(100)	Lunar eclipse time associated with the previously mentioned orbits
5	100	INTEGER	SUNPIS(100)	Lunar sunrise time associated with the previously mentioned orbits
6	200	INTEGER	ECL(100,2)	Lunar eclipse intervals (start and stop times) determined from the data (last subscript denotes start or stop)
7	200	INTEGER	SUN(100,2)	Lunar sunlight intervals determined from the data
8	200	INTEGER	ASUN(100,2)	Lunar sunlight intervals before lunar eclipse determined from the data associated with the previously mentioned orbits
9	200	INTEGER	NITE(100,2)	Lunar eclipse intervals determined from the data associated with the previously mentioned orbits
10	200	INTEGER	MSUN(100,2)	Lunar sunlight intervals after lunar eclipse determined from the data associated with the previously mentioned orbits
11	200	INTEGER	BN(100,2)	TSM data intervals determined from the data
12	200	INTEGER	TSP(100,2)	TSP data intervals determined from the data
13	200	INTEGER	RT(100,2)	Real-time data intervals determined from the data (All times are integer milliseconds: 1 day = 86 400 000 msec, 1 hr = 3 600 000 msec, 1 min = 60 000 msec.)
14-WZ	560	MIXED	BUF(560)	24-sec average data (The BUF array is described in terms of 8 words per frame, 8 frames per data cycle, 16 extra words per data cycle, 80 total words per data cycle, 7 data cycles per record, and 192 sec per data cycle.)

<sup>1</sup>Parity - odd; density - 800 bpi; word length - 36 bits; word codes used - INTEGER, FLOATING POINT, and PIELDATA.  
<sup>2</sup>W is the total number of records on the tape and is followed by two 1108 software end-of-file marks (i.e., one-word records containing an octal 17 in the 6 most significant bits and the remaining 30 least significant bits are zero).  
<sup>3</sup>See the section entitled "Data Cycle Description."

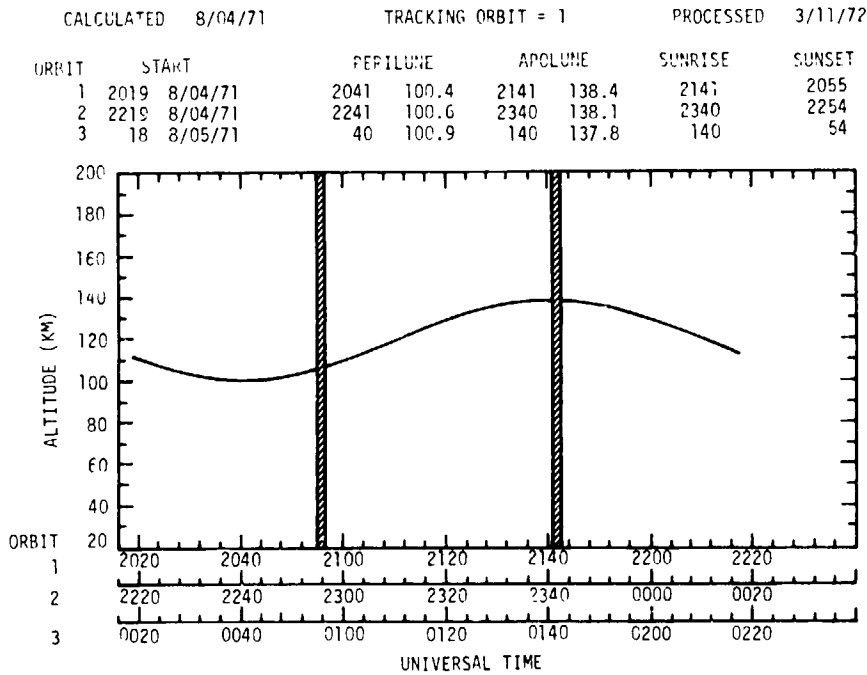


Figure 33-15.- Apollo 15 subsatellite tracking for one orbit.

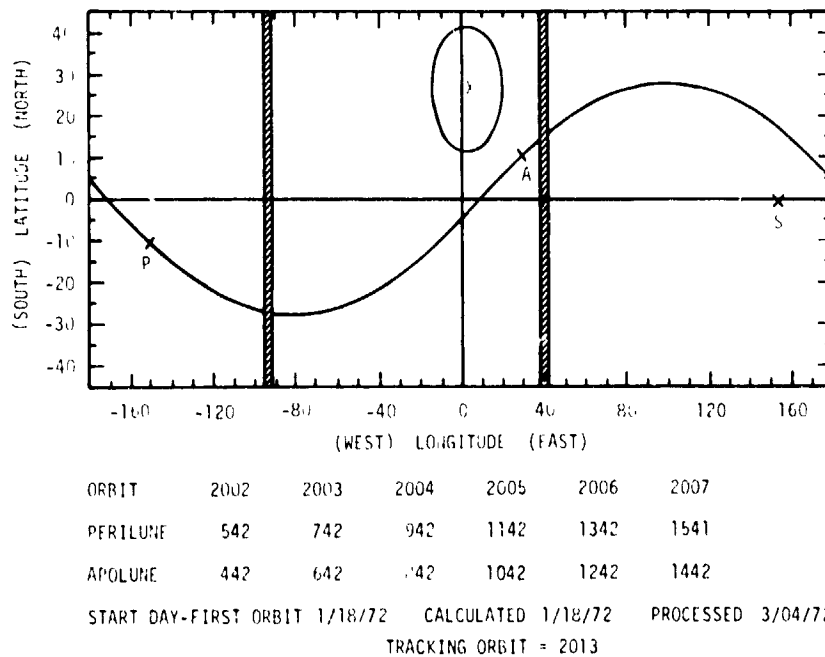


Figure 33-16.- Apollo 15 subsatellite selenographic coordinates.

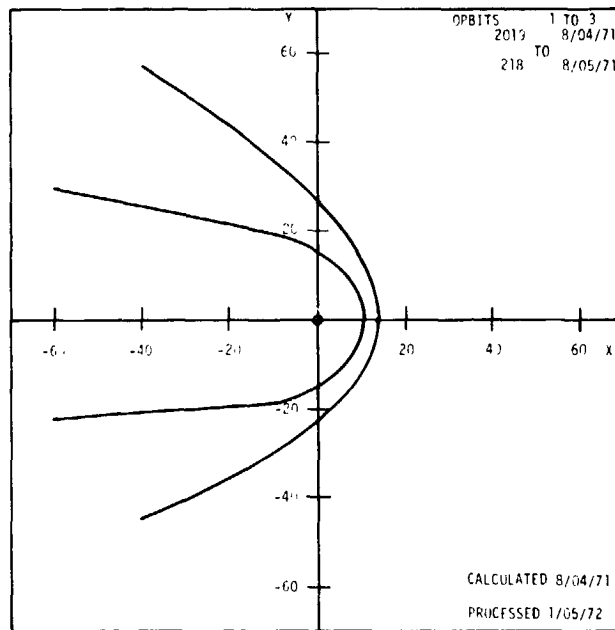


Figure 33-17.- Solar ecliptic position Earth-Moon system.

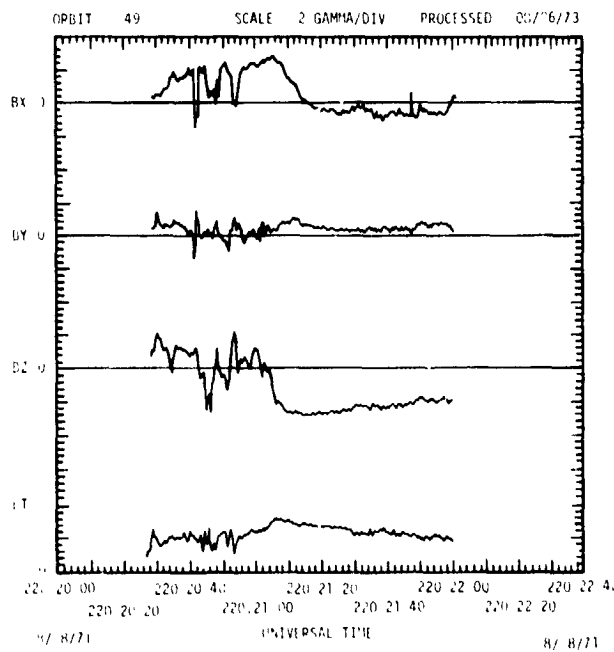


Figure 33-18.- Apollo 15 particles and fields subsatellite UCLA fluxgate magnetometer data for orbit 49. Spacecraft coordinates, plot A.

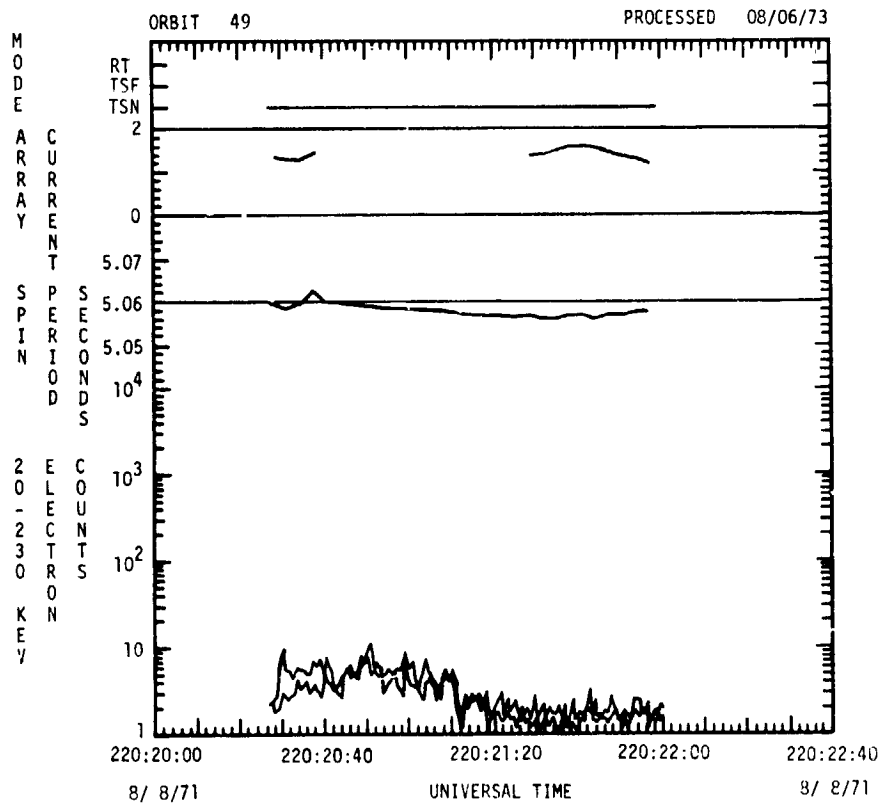


Figure 33-19.- Apollo 15 particles and fields subsatellite LA fluxgate magnetometer data for orbit 49. Spacecraft coordinates, plot B.

APOLLO 15 PARTICLES AND FIELDS MAGNETOMETER DATA ORBIT 49 PROCESSED 08/06/73

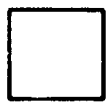
DAY	HR	MIN	SEC	UT	RT	TSN	CURRENT	SPIN PERIOD	ELECTRON COUNTS	MAGNETIC FIELD (GAMMA) AT	FIELD (GAMMA) BY	PARTICLE COUNTS (OPEN SHIELDED)	SUN ANG	SPIN PER	SPIN COUNT	MAG TEMP	BATT TEMP	BATT VOLT	BATT CHRG	ARRAY CURR	REP VOLT	FRAG1	FRAG2
220	22	20	00	220:20:00	2	11	3.75	7.30	8.58	2	-2	-3	5	959	170	67.8	70.2	14.8	57	1.31	2.50	111000	192
220	22	20	10	220:20:10	2	11	3.75	7.30	8.58	2	-2	-3	5	959	170	67.8	70.2	14.8	57	1.31	2.50	111000	192
220	22	20	20	220:20:20	2	11	3.75	7.30	8.58	2	-2	-3	5	959	170	67.8	70.2	14.8	57	1.31	2.50	111000	192
220	22	20	30	220:20:30	2	11	3.75	7.30	8.58	2	-2	-3	5	959	170	67.8	70.2	14.8	57	1.31	2.50	111000	192
220	22	20	40	220:20:40	2	11	3.75	7.30	8.58	2	-2	-3	5	959	170	67.8	70.2	14.8	57	1.31	2.50	111000	192
220	22	20	50	220:20:50	2	11	3.75	7.30	8.58	2	-2	-3	5	959	170	67.8	70.2	14.8	57	1.31	2.50	111000	192
220	22	21	00	220:21:00	2	11	3.75	7.30	8.58	2	-2	-3	5	959	170	67.8	70.2	14.8	57	1.31	2.50	111000	192
220	22	21	10	220:21:10	2	11	3.75	7.30	8.58	2	-2	-3	5	959	170	67.8	70.2	14.8	57	1.31	2.50	111000	192
220	22	21	20	220:21:20	2	11	3.75	7.30	8.58	2	-2	-3	5	959	170	67.8	70.2	14.8	57	1.31	2.50	111000	192
220	22	21	30	220:21:30	2	11	3.75	7.30	8.58	2	-2	-3	5	959	170	67.8	70.2	14.8	57	1.31	2.50	111000	192
220	22	21	40	220:21:40	2	11	3.75	7.30	8.58	2	-2	-3	5	959	170	67.8	70.2	14.8	57	1.31	2.50	111000	192
220	22	21	50	220:21:50	2	11	3.75	7.30	8.58	2	-2	-3	5	959	170	67.8	70.2	14.8	57	1.31	2.50	111000	192
220	22	22	00	220:22:00	2	11	3.75	7.30	8.58	2	-2	-3	5	959	170	67.8	70.2	14.8	57	1.31	2.50	111000	192
220	22	22	10	220:22:10	2	11	3.75	7.30	8.58	2	-2	-3	5	959	170	67.8	70.2	14.8	57	1.31	2.50	111000	192
220	22	22	20	220:22:20	2	11	3.75	7.30	8.58	2	-2	-3	5	959	170	67.8	70.2	14.8	57	1.31	2.50	111000	192
220	22	22	30	220:22:30	2	11	3.75	7.30	8.58	2	-2	-3	5	959	170	67.8	70.2	14.8	57	1.31	2.50	111000	192
220	22	22	40	220:22:40	2	11	3.75	7.30	8.58	2	-2	-3	5	959	170	67.8	70.2	14.8	57	1.31	2.50	111000	192

Figure 33-20.- Printout of Apollo 15 particles and fields magnetometer data, orbit 49.

	1	9	17	25	33	41	49	57	65	73
	A <sub>1,1</sub>	A <sub>1,2</sub>	A <sub>1,3</sub>	A <sub>1,4</sub>	A <sub>1,5</sub>	A <sub>1,6</sub>	A <sub>1,7</sub>	A <sub>1,8</sub>	B <sub>1</sub>	B <sub>9</sub>
	2	10	18	26	34	42	50	58	66	74
	A <sub>2,1</sub>	A <sub>2,2</sub>	A <sub>2,3</sub>	A <sub>2,4</sub>	A <sub>2,5</sub>	A <sub>2,6</sub>	A <sub>2,7</sub>	A <sub>2,8</sub>	B <sub>2</sub>	B <sub>10</sub>
	3	11	19	27	35	43	51	59	67	75
	A <sub>3,1</sub>	A <sub>3,2</sub>	A <sub>3,3</sub>	A <sub>3,4</sub>	A <sub>3,5</sub>	A <sub>3,6</sub>	A <sub>3,7</sub>	A <sub>3,8</sub>	B <sub>3</sub>	B <sub>11</sub>
	4	12	20	28	36	44	52	60	68	76
	A <sub>4,1</sub>	A <sub>4,2</sub>	A <sub>4,3</sub>	A <sub>4,4</sub>	A <sub>4,5</sub>	A <sub>4,6</sub>	A <sub>4,7</sub>	A <sub>4,8</sub>	B <sub>4</sub>	B <sub>12</sub>
A <sub>1</sub>	5	13	21	29	37	45	53	61	69	77
	A <sub>5,1</sub>	A <sub>5,2</sub>	A <sub>5,3</sub>	A <sub>5,4</sub>	A <sub>5,5</sub>	A <sub>5,6</sub>	A <sub>5,7</sub>	A <sub>5,8</sub>	B <sub>5</sub>	B <sub>13</sub>
	6	14	22	30	38	46	54	62	70	<del>78</del>
	A <sub>6,1</sub>	A <sub>6,2</sub>	A <sub>6,3</sub>	A <sub>6,4</sub>	A <sub>6,5</sub>	A <sub>6,6</sub>	A <sub>6,7</sub>	A <sub>6,8</sub>	B <sub>6</sub>	<del>B<sub>14</sub></del>
	7	15	23	31	39	47	55	63	71	<del>79</del>
	A <sub>7,1</sub>	A <sub>7,2</sub>	A <sub>7,3</sub>	A <sub>7,4</sub>	A <sub>7,5</sub>	A <sub>7,6</sub>	A <sub>7,7</sub>	A <sub>7,8</sub>	B <sub>7</sub>	<del>B<sub>15</sub></del>
	8	16	24	32	40	48	56	64	72	<del>80</del>
	A <sub>8,1</sub>	A <sub>8,2</sub>	A <sub>8,3</sub>	A <sub>8,4</sub>	A <sub>8,5</sub>	A <sub>8,6</sub>	A <sub>8,7</sub>	A <sub>8,8</sub>	B <sub>8</sub>	<del>B<sub>16</sub></del>



Integer cells



Floating point cells



Unused cells

Figure 33-21.- An 8 by 10 data cycle array (DATCYC(8,10)).

## PART C: S-BAND TRANSPONDER

The purpose of the S-band transponder experiment was to measure the lunar gravitational field, which in turn provided information on the distribution of lunar mass and its correlation with surface features such as craters, mountains, and maria. Lack of correlation would imply subsurface structures. The lunar gravitational field is measured by observing the dynamical motion of spacecraft in free-fall orbits. Effective detection of mass variations is greatly enhanced by low-altitude trajectories, such as the eccentric orbits during revolutions 3 to 16 of the Apollo 16 spacecraft and the 11-km periapsis of the Apollo 16 subsatellite during May 1972. The observational data are the precise Earth-based radio tracking measurements initially used for real-time navigation. However, these line-of-sight velocity measurements can be obtained only while the spacecraft is in view of the Earth. As a result, no direct far-side measurements are available. The only information about the far-side gravity field is indirectly inferred from the spacecraft conditions immediately after occultation over many revolutions.

A very stable frequency of 2115 MHz obtained from a cesium reference was transmitted to the orbiting spacecraft. The transponder in the spacecraft multiplied the received frequency by the constant 240/221 (to avoid self-lockup) and transmitted the signal to Earth. (The transmitted and received frequencies were within the S-band region.) At the Earth-based receiver, the initial transmitted frequency (multiplied by the same constant) was subtracted, and the resulting cycle-count differences were accumulated in a counter along with the precise time at which differencing occurred. These cycle-count differences were the Doppler shift in frequency  $f_d$  caused by the line-of-sight (radial) component  $V_r$  of the spacecraft velocity, or  $2V_r/c \times 2300$  MHz, where  $c$  is the speed of light. At times of high resolution, the counter was read every second; at low resolution, it was read once a minute. Not only was the cycle-count difference recorded, the fractional part of the cycle was measured. This capability allowed a resolution of approximately 0.01 Hz or 0.65 mm/sec in the measurements.

The approach for reducing these data is the same as that applied to the Lunar Orbiter data for the mascon analysis (i.e., not spherical harmonics or brute-force dynamic estimation). The raw data contain many components

of motion that must be removed before gravity analysis can proceed. Factors to be accounted for include the tracking station rotation about the Earth spin axis; the spacecraft motion perturbed by point-mass accelerations from the Sun, the Earth, the Moon, and the planets; and atmospheric effects and signal transit times. All these quantities are known a priori and are determined to accuracies well beyond those required to evaluate local gravitational effects.

#### DATA HISTORY AND OPERATIONS

The following is a summary of S-band transponder data collected.

1. Apollo 12 - one arc of descent November 19, 1969
2. Apollo 14 - 10 CSM orbits at low altitude February 4, 1971
3. Apollo 15 - 10 CSM orbits at low altitude July 30, 1971
4. Apollo 16 - 10 CSM orbits at low altitude April 20, 1972
5. Apollo 17 - 10 CSM orbits at low altitude December 11, 1972

The Apollo 15 subsatellite (PFS-1) was active from August 9, 1971, to September 1973, when the battery failed. The spacecraft was tracked usually 2 to 3 times per week except during mission operations. There are four regions of dense tracking in which the spacecraft was tracked every second or third orbit for 2 to 3 weeks. These times are (1) September 27 to October 3, 1971, (2) November 30 to December 19, 1971, (3) October 31 to November 18, 1972, and (4) January 23 to February 23, 1973. The Apollo 16 subsatellite (PFS-2) was active from April 24 to May 29, 1972, when it crashed. Tracking was similar to that for the Apollo 15 subsatellite; a dense tracking period was started May 7 and was ended May 19, 1972.

High quality data (noise less than 1 mm/sec) were obtained during all missions with no failures at any time of the S-band transponder. Data were corrupted over small time intervals during spacecraft maneuvers. Also, periodic equipment failures at Earth-based receiving stations when tracking the subsatellite caused minor data loss.

## DATA SETS

The data sets are available at three different levels of data reduction. The first level consists of the raw Doppler counts, which contains all relative effects between the receiving ground antenna and the spacecraft. These data are on magnetic tapes and require major editing and orbit determination programs for proper handling. To obtain documents on accessing the many parameters involved for processing raw Doppler data, contact W. Wollenhaupt ((713) 483-4366) at JSC. The second level of reduction consists of the Doppler residuals from the orbit determination fit. These data are located on microfilm at NSSDC at the NASA Goddard Space Flight Center (GSFC). (The last two dense data coverages from the Apollo 15 subsatellite were not at GSFC at the time of publication of this report.) The format is described in the section entitled "Explanation of Acceleration Data Listing."

The third level of reduction consists of the line-of-sight accelerations obtained from the Doppler residuals. These data are contained on the microfilm with the Doppler residuals, but they are also on magnetic tape as described in the section entitled "Explanation of Acceleration Data Listing."

Two sets of orbital element histories covering 2 years for the Apollo 15 subsatellite and 35 days for the Apollo 16 subsatellite are in preparation. These histories will be available on microfilm and magnetic tape when analysis has been completed.

## EXPLANATION OF ACCELERATION DATA LISTING

The acceleration data explained in this section are available on microfilm at NSSDC. The first four pages of each orbit printout contain program parameter inputs. Some of the older listings may not contain all the parameters contained in the newest program version (July 1974). There are three basic blocks of information: (1) trajectory controls, (2) spline fit controls, and (3) plotting controls. The parameters in the microfilm listing are interspersed from each block, but the members of each block listed here are in the sequential order of the microfilm.

## Trajectory Controls

1. Input label = any label of user information.
2. LONEP = selenographic longitude of probe at EPOCH.
3. LATPER = latitude of periapsis (not required input).
4. LONPER = longitude of periapsis (not required input).
5. ECC = eccentricity (not required input).
6. PER = period of orbit in minutes (not required input).
- 7 to 12. X,Y,Z,DX,DY,DZ = unused position and velocity components.
- 13 to 18. XS,YS,ZS,DXS,DYS,DZS = Cartesian position and velocity components of the probe at EPOCH, referenced to the true lunar equator, space fixed coordinates with X defined by the prime meridian at 0° longitude.
19. LON = selenographic longitude of probe.
20. INC - nominal = 0 inclination of orbit, if intersection of orbit plane with the lunar equator is desired to be at plot center; see PMIN for explanation. If INC = 0, pericenter passage time is used for fixed-mode plot center of 90-min frame.
21. N = dummy variable, nominal = 0.
22. LUN = 4-digit orbit identifier.
23. EPOCH = YMMODDHH,MMSSXXX; where YY = year of 1900, MM = month of year, 0 = fixed zero, DD = day of month, HH = G.m.t. hours, MM = minutes beyond hour, SS = seconds beyond minutes, and XXX = milliseconds beyond seconds.
24. EPOK = YMMODDHH,MMSSXXX; where YY = year of 1900, MM = month of year, 0 = fixed zero, DD = day of month, HH = G.m.t. hours, MM = minutes beyond hour, SS = seconds beyond minutes, and XXX = milliseconds beyond seconds.
25. LTE = latitude of Earth in degrees in body fixed coordinates.
26. LNE = longitude of Earth in degrees in body fixed coordinates.

27. NORM - nominal = 0; (0,1) for (NO,YES) to normalize accelerations to 100-km altitude by the factor  $(H + 50)^2/150^2$  where H is spacecraft altitude.

28. NAVE - nominal = 1. This factor causes NAVE consecutive points to be averaged. This process effectively reduces the number of points to be fitted from number input to  $1/NAVE$  as many. The factor is used for data compression where the deck of input points is larger than approximately 300 cards.

29. REVSIN - nominal = +1; optional = -1, which reverses the sign on Doppler residuals. This factor is just a convention, because accelerations away from the observer on Earth are considered positive.

30. RADIUS is the radius of central body; nominal = 1738 km.

31. GM is the gravitational constant of the central body in cubic kilometers per second squared; nominal =  $4902.78 \text{ km}^3/\text{sec}^2$ .

32. TARGET - nominal value = 0 for lunar orbit; TARGET = 1 for Martian orbit; governs body rotation rate.

33. REFER = reference EPOCH for Mars light time corrections, 0 for lunar case.

34. DUTSEC = difference in seconds between universal and ephemeris time.

35. TRANSA = the constant term in the light time correction equation for Mars.

36. TRANSB = the coefficient for the linear term in the light time correction equation for Mars.

37. EP2 = Mars EPOCH needed in light time corrections.

38. NEWFP = new EPOCH due to light time corrections for Mars.

39. IPR = 5, debug print for Martian data times.

40. EP3 = Martian EPOCH for light time correction.

### Spline Fit Controls

Note the formula computed internally for NPUTIN:  
$$\text{NPUTIN} = \text{integer part } ((\text{ALTITUDE} - \text{BKSUB}) * \text{EKFAC} * .01 + 1.0).$$
This determines how many points are to be put in each interval as a factor function of spacecraft mean altitude since last point. The following terms are used as spline fit controls.

1. BKTIMS - array input optional. If breaktimes are manually input, in minutes, see BKTYPE. The factor BKTIMS = 93., 95., 99., 108., ..., 0. An ending zero is required.

2. TFIT - nominal = 90. This factor is an upper limit in minutes added to TSTART, which equals EPOCH plus TADD, over which data will be fitted. Less will be fitted if there is less data.

3. DFIT - nominal = 2.0. This factor is minutes per breakpoint in case DOBKS is negative; see DOBKS for explanation.

4. DOBKS - nominal = 0; (NEG, 0, POS) for breaks; (NEG) at equal intervals of DFIT minutes, (ZERO) automatic selection by following parameters, and (POS) use input BKTIMS previously computed or punched out. See BKTYPE.

5. TADD - nominal = 0. This value is the time in minutes to be added to EPOCH at which data fitting is to begin. This factor can ignore data, but must be used to EPOCH forward to within approximately 1 min of first data.

6. BFAC - nominal = 1. This factor changes NPUTIN. For example, if BFAC = 2, NPUTIN = 2 down to 50 km instead of 100 km. If BFAC = 0.5, NPUTIN = 1 up to 200-km spacecraft altitude.

7. PDEBUG - nominal = 0; (0, 1) for (NO, YES) to print debug output blocks.

8. PUNOUT - nominal = 1; (0, 1) for (NO, YES) to punch out breaktimes.

9. BKTYPE - nominal = 0; (-1, 0, 1). If (0), use BKTIMS as input. (See DOBKS.) If (-1), truncate set for shorter fit interval than input. If (1), takes time in minutes past  $\text{plc} + \text{EPOCH}$  as the value of input BKTIMS instead of the nominal punched-out value.

10. MAXBKS - nominal = 12. This factor is the maximum number of points in any interval (except TFAC overrides all above and MAXBKS and may require more). For high-rate low-

altitude data, set MAXBKS and TFAC to admit the desired number of points and to control the minimum length of interval. If MAXBKS = N and TFAC = 0, then no more than N points will be in any interval. If TFAC is not zero after N points are in, even though altitude indicates more should be in, TFAC is tested to see if interval is longer; if it is, a breakpoint is placed there. If not, processing continues.

11. MINBKS = minimum number of breakpoints over data span.

12. INLAST - nominal = 7. This factor is like NFIRST except that it requires a minimum number of points in last interval. The value must be  $\geq 2$  but, in practice, for low-altitude trajectories with clean data, should be set at expected NPUTIN or slightly greater.

13. TFAC - nominal = 0.95. The nominal value admits intervals no shorter than 1 min, which is acceptable providing spacecraft altitude is over 50 km since the spacecraft travels at 100 km/min. For lower altitudes, a smaller value may be desired. Unless single points are admissible, TFAC should not be less than the data rate or the altitude NPUTIN calculation will require a larger number. The factor TFAC is in minutes, and when NPUTIN equation or MAXBKS are satisfied, TFAC is tested, last of all, to make sure the interval is at least of this length in minutes. For low-altitude trajectories of less than approximately 50 km, it is desirable to reduce TFAC if the data rate is high.

14. BKSUB - nominal = 0. Subtracts constant from spacecraft altitude in equation for NPUTIN. (Input negative number to increase effective spacecraft altitude.) Useful to emphasize the few points that occur below a specified altitude or, from another standpoint, can change the origin from which NPUTIN is calculated from 100 km to  $100 - \text{BKSUB}$ . To change the single-point threshold from 100 to 120 km, input BKSUB = 20. To increase it from 40 to 400 km, input BKSUB = -60.

15. REJECT - nominal = 5.00, set for largest residual desired in fit; if larger, it will be deleted from data set.

16. BFAC = BKFAC.

17. DTACC - nominal = 0.25 min. This factor is time between acceleration points computed after the fitting; that is, resolution of acceleration data. Each interval contains 500 points maximum; (total time)/DTACC must be less than 500.

18. TAPE = T; writes an output tape with acceleration data.
19. DATYPE = 1; reads JSC data files, MODE must be 0.
20. MODE - nominal = 0; if (1), reads other than JSC files.
21. SPSN - nominal = F; if (T), does spline fit to JSC accelerations from SPSN.

#### Plotting Controls

1. DOSTOP - nominal = 0. If this factor is 1, the data name-list input block will be interpreted as a dummy, and this dummy last input block is required if a data tape is being written on unit 2. The factor gives an end-of-file code to unit 2.
2. RESINT is an array of length 4 containing thresholds for blank, O, R, and X labels above plotted point in case residuals after the fitting are greater than corresponding threshold. In the program, RESINT(1) = 0, and nominals are 0.,.005,.01,.02 Hz. To change, simply input RESINT = 0.,W.,X.,Y.,Z.; where W,X,Y,Z are the desired thresholds.
3. PMIN - nominal = 0. If input is nonzero, it is of the form MMM.FFF (minutes from 0 hr G.m.t.) desired for plot center if the plot is manual-fixed mode. Both PPASS and PMIN cannot be nonzero.
4. PPASS - nominal = 0. If input is nonzero, it is of the form HHMMSS.FFF and is the time desired at center of the plot in fixed-manual mode.
5. PDIV = total plot time divided into PDIV plot frames.
6. PLTYPE - nominal = 0, (0, 1). If (0), plots according to preceding parameters on fixed 90-min base. This process is desirable for most Lunar Orbiter data because it permits overlay of adjacent orbits for comparison in selenographic coordinates transformed into time. If (1), plot time scale is set to best fit the whole fit interval from the first data point in the fit to the last on a single frame. Use for either very short or very long intervals only. This process abandons automatic overlay capability, since EPOCH will be taken arbitrarily by the data and not in selenographic time. Useful for short fitting with high data rate. Minimum time of plot is 10 min, maximum is 1000 min.

Minimum ordinate is 0.2 Hz, maximum is 7 Hz. For high-amplitude residual, the parameter reject should be reset.

7. DIPLT - nominal = 0. This factor consists of minutes to add to or subtract from first data point (which is determining plot EPOCH as the even minute of the first observation) to readjust plot EPOCH if desired. This factor can be used to normalize time to selenographic coordinates manually, if desired.

8. ORDIN fixes the ordinate on plots.

9. AUTOX - nominal = 1; automatic X-axis scaling for Cal Comp plots.

10. AUTOY - nominal = 2; automatic Y-axis scaling for Cal Comp plots.

11. IDOX > 1, then AUTOX control is canceled and fixed value XINC input.

12. IDOY > 1, then AUTOY control is canceled and fixed value YSCA input.

13. XINC = fixed Cal Comp plot X-axis length in minutes per inch.

14. OPDNIN = maximum ordinate for Stromberg Carlson plots.

15. YSCA = fixed Cal Comp plot (axis length in hertz per inch).

16 and 17. SCALEX, SCALEY - nominal = 0. For automatic mode, this factor sets minimum allowable X- and Y-axis limits and overrides automatic scaling. This factor cannot result in plot that truncates data. To do this, set SCALEY equal to negative value of desired absolute scale.

#### Numerical Listing

Numerical data are plotted usually in 13 columns. In some cases, 12 columns are used; however, the 13th column is irrelevant to this work and is usually zero. The following quantities are represented in the columns.

1. Column 1 is Greenwich mean time in hours, minutes, and seconds on the day of the reference orbit for the received Doppler observations. (See EPOCH in program parameters.)

2. Column 2 is column 1 time converted to minutes.
  3. Column 3 is time in minutes past the reference EPOCH.
  4. Column 4 is the time in minutes on the associated plot for this particular point.
  5. Column 5 is the Doppler residual in hertz (1 Hz = 65 mm/sec) from a least-squares reduction in which a rather complete theoretical model (having planetary perturbations, Earth rotation, precise station locations, tropospheric model, and precise signal station transit times) has removed the primary Doppler signal. The lunar gravity field was  $GM = 4902.78 \text{ km}^3/\text{sec}^2$ ,  $J_2 = 2.07108E^{-4}$ ,  $J_3 = -0.21E^{-4}$ ,  $C_{22} = 0.20716E^{-4}$ ,  $C_{31} = 0.34E^{-4}$ , and  $C_{32} = 0.02583E^{-4}$  (L1 model). In the reduction of the raw Doppler observation, only 65 min of data were fitted (signal acquisition to loss of signal) and only the six state parameters (position and velocity at EPOCH) were estimated. Usually, two or three tracking stations were viewing, but the residual is that of the transmitting station rather than of the receiving-only stations.
  6. Column 6 is the spacecraft altitude in kilometers above a 1738-km sphere.
  7. Column 7 is the spacecraft selenographic latitude in degrees.
  8. Column 8 is the spacecraft selenographic longitude in degrees.
- Note: A correction should be applied to longitude for dates prior to January 1972 (Apollo 12, 14, and 15 command-service module and Apollo 15 subsatellite). The correction factor  $\Delta\lambda$  should be subtracted from the tabulated value:  $\Delta\lambda = 0.0178\Delta T$ , where the answer is in degrees. The value for  $\Delta T$  is printed in the third column (i.e., minutes from the EPOCH).
9. Column 9 is the theoretical value in hertz calculated by the SPLINE program used in the least-squares fit to the Doppler residuals. The splines are cubics with second derivatives continuous at the patch points.
  10. Column 10 is the acceleration in millimeters per second squared by analytic differentiation of the spline at the reference time. This parameter is one component of the acceleration vector perturbing the spacecraft and is measured along the tracking station/spacecraft line. The initial least-squares filtering of the Doppler data has

reduced the true acceleration amplitude by approximately 0.3 (ref. 33-22).

11. Column 11 is a normalized acceleration in millimeters per second squared. However, because no normalization has been applied in any case, column 11 is the same as column 10.

12. Column 12 is the residual in hertz after the spline has been fitted to the Doppler residuals. For good data and a good spline fit, these numbers should appear almost random (+,-) with an amplitude not exceeding 0.01 Hz (usual rms = 0.005 Hz).

13. Column 13 has no relevance to this work.

#### EXPLANATION OF ACCELERATIONS ON MAGNETIC TAPES

Magnetic tape acceleration data consist of one observation per data record written in binary coded decimal card image. Each observation has the following four quantities: (1) latitude of spacecraft in degrees, (2) longitude of spacecraft in degrees, (3) line-of-sight acceleration at spacecraft altitude in millimeters per second squared, and (4) altitude of spacecraft in kilometers.

#### SUMMARY OF KEY EVENTS

The following summary includes conclusions derived from analysis of S-band transponder data.

1. Mascons are near-surface, disk-type objects producing excess loads of 800 to 1000 kg/cm<sup>2</sup> (refs. 33-23 to 33-25).

2. All 100-km-diameter size craters have negative anomalies consistent with an impactor ejecting mass that has never been isostatically adjusted (refs. 33-25 to 33-27).

3. The Montes Apenninus have undergone considerable isostatic adjustment (ref. 33-25).

4. The Marius Hills have not undergone isostatic adjustment (ref. 33-25).

5. Grimaldi is the smallest mascon detected and has the largest loading of 1240 kg/cm<sup>2</sup>.

6. Density calculations of mass ejected from craters like Langrenus and Copernicus indicate almost mean density material  $3.3 \text{ g/cm}^3$  to depths of 2 km.

7. The mascons are complex features requiring irregular mass distributions beyond the first-order disk model (refs. 33-24 and 33-25).

8. The orbital gravity estimate for the Apollo 17 Taurus-Littrow landing site agrees well with the surface measurement. A  $-200 \times 10^{-5} \text{ m/sec}^2$  ( $-200 \text{ mgal}$ ) anomaly is present (ref. 33-28).

9. Features that do not correlate well with visible topography, such as the positive anomaly southeast of Copernicus Crater (PFS-2) and the positive anomaly north of Theophilus Crater, are present.

10. Detailed gravity is obtained in a band from latitude  $0^\circ$  to  $10^\circ \text{ N}$  in width and from  $-70^\circ$  to  $70^\circ$  in longitude at 20- to 40-km altitudes (PFS-2). Also, over the same longitudes but from latitude  $20^\circ$  to  $30^\circ \text{ S}$ , detailed gravity is obtained at approximately 40 to 60 km (ref. 33-26).

11. Mare Orientale has a definite ring structure in its gravity contours and an anomaly that is 50 percent more negative than positive (ref. 33-26).

12. Gravity highs are found over the Rima Triesnecker system and over Lamont Crater in Mare Tranquillitatis (ref. 33-26).

13. Broad gravity highs of  $40 \times 10^{-5}$  to  $50 \times 10^{-5} \text{ m/sec}^2$  (40 to 50 mgal) are found in Mare Procellarum, Mare Tranquillitatis, and Mare Fecunditatis (refs. 33-26 to 33-28).

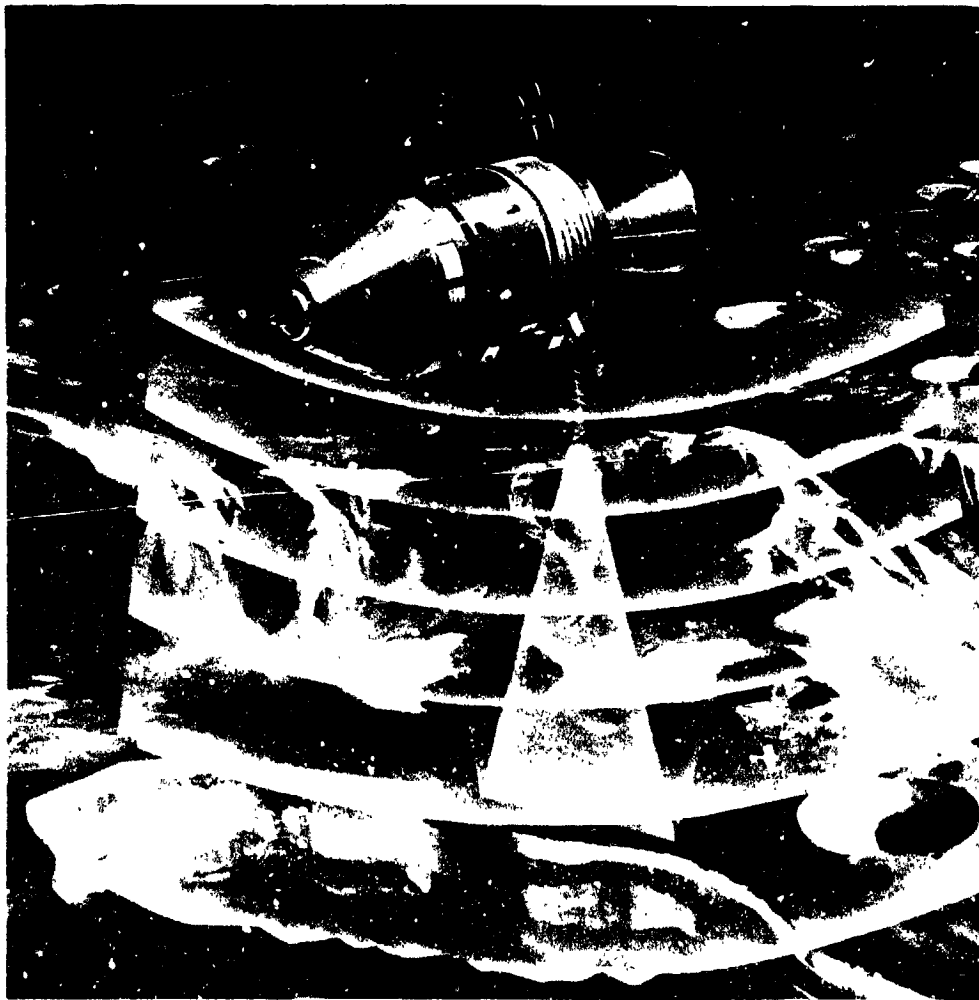
#### REFERENCES

- 33-22. Gottlieb, Peter: Estimation of Lunar Gravity Features. Radio Science, vol. 5, no. 2, Feb. 1970, pp. 301-312.
- 33-23. Phillips, R. J.; Conel, J. E.; Abbott, E. A.; Sjogren, W. L.; and Morton, J. B.: Mascons: Progress Toward a Unique Solution for Mass Distribution. J. Geophys. Res., vol. 77, no. 35, Dec. 10, 1972, pp. 7106-7114.
- 33-24. Sjogren, W. L.; and Wollenhaupt, W. R.: Gravity - Mare Humorum. The Moon, vol. 8, nos. 1/2, July-Aug. 1973, pp. 25-32.
- 33-25. Sjogren, W. L.; Gottlieb, P.; and Muller, P. M.: Lunar Gravity via Apollo 14 Doppler Radio Tracking. Science, vol. 175, no. 4018, Jan. 14, 1972, pp. 165-168.
- 33-26. Sjogren, W. L.; Wollenhaupt, W. R.; and Wimberly, R. N.: Lunar Gravity via the Apollo 15 and 16 Subsatellites. The Moon, vol. 9, nos. 1/2, Jan.-Feb. 1974, pp. 115-128.
- 33-27. Gottlieb, P.; Muller, P. M.; and Sjogren, W. L.: Lunar Gravity over Large Craters from Apollo 12 Tracking Data. Science, vol. 168, no. 3930, Apr. 24, 1970, pp. 477-479.
- 33-28. Sjogren, W. L.; Wollenhaupt, W. R.; and Wimberly, R. N.: S-Band Transponder Experiment. Sec. 14 of Apollo 17 Preliminary Science Report, NASA SP-330, 1973.

34. APOLLO LUNAR SOUNDER EXPERIMENT (NASA EXPERIMENT S-209)

NSSDC IDENTIFICATION NUMBER:

APOLLO 17 72-096A-04



ORIGINAL PAGE IS  
OF POOR QUALITY

CONTENTS - SECTION 34

	Page
THE ALSE SYSTEM . . . . .	34-4
The HF Antennas . . . . .	34-4
The VHF Antenna . . . . .	34-5
The Radar (CSAR) System . . . . .	34-5
The Optical Recorder . . . . .	34-5
DATA PRODUCTS . . . . .	34-6
PRELIMINARY RESULTS . . . . .	34-7
Sounding . . . . .	34-7
Profiling and Imaging . . . . .	34-10
GALACTIC NOISE DATA . . . . .	34-16
DATA TO BE ARCHIVED AT NSSDC . . . . .	34-17
REFERENCES . . . . .	34-19

#### 34. APOLLO LUNAR SOUNDER EXPERIMENT

The scientific objectives of the Apollo lunar sounder experiment (ALSE) are (1) mapping of subsurface electrical conductivity structure to infer geological structure, (2) surface profiling to determine lunar topographic variations, (3) surface imaging, and (4) measuring galactic electromagnetic radiation in the lunar environment. The ALSE was a three-frequency, wide-band, coherent radar system operated from lunar orbit during the Apollo 17 mission.

The concept of radar sounding is quite analogous to active seismic profiling; that is, a continuous series of short pulses of (electromagnetic) energy are propagated toward the Moon and are reflected from the lunar surface and from subsurface geologic interfaces. The energy reflected from the Moon is continuously recorded as the command and service module (CSM) moves in lunar orbit, and thus a profile of surface and subsurface structure is assembled. The capability to map the lunar interior is dependent on a low-electrical-loss subsurface; that is, the attenuation of the signal must not preclude a significant depth of exploration. Pre-mission estimates of path loss, based on measurements from returned lunar samples, indicated a maximum depth of exploration of approximately 1 km. Further, for the reflection of energy at a geologic boundary, an electrical-property contrast must exist across an interface. The electrical property controlling the amount of reflected energy is the dielectric constant  $\epsilon$ . The pre-mission estimate of the typical dielectric-constant ratio across an interface was 1.25.

Profiling is accomplished by maintaining an absolute timing reference between the firing of the radar transmitter and the reception of the energy returned from the lunar surface. The rate of transmitter firing is sufficiently high to make the profiling essentially continuous. In addition to acquiring the global profile for selenodesy studies, detailed profiles were acquired that may be used to address local selenomorphological problems.

In the active sounding mode, the quality of imagery is dependent, for a given frequency, on the diffuse backscattering properties of the lunar surface. One record of the surface backscattered energy is compiled from each transmitted pulse reflected from the Moon. A sequence of records then comprises a two-dimensional data array necessary to create an image. The

image is typically bounded on one side by the spacecraft-nadir topographic profile, and the combination of profile and image is very useful for surface geologic interpretation.

The ALSE system was operated in three frequency ranges: 5 MHz (HF-1), 15 MHz (HF-2), and 150 MHz (VHF). The HF-1 system is capable of the deepest exploration. The HF-2 system was operated simultaneously with the HF-1 system to provide partial overlap in depth of exploration, trading off depth of exploration for improved resolution. The VHF system was designed for shallow sounding and for surface imaging. All three frequencies are capable of surface profiling.

The ALSE had four major hardware components (fig. 34-1). At the heart of the system is the coherent synthetic aperture radar (CSAR) containing the transmitting and receiving elements. Separate transmit/receive antenna systems were provided for the HF and VHF ranges. The received signal is fed to an optical recorder. The voltage into the recorder modulates the light-intensity output of a cathode ray tube (CRT). The CRT output was recorded on a continuously moving strip of photographic film. The film, representing the prime data storage medium, was recovered during the transearth-coast extravehicular activity.

The CSAR receiver also monitored the average reflected electromagnetic power and transmitted these data, together with other engineering data, by way of the CSM 51.2-kbps telemetry channel. The average reflected power data are used for calibration purposes as well as for aid in data interpretation. A representative example of these data is shown in figure 34-2.

The CSAR also had a receive-only (nonsounding) capability to measure the noise background in the HF ranges. These data were also transmitted by way of the 51.2-kbps telemetry channel.

## THE ALSE SYSTEM

### The HF Antennas

The HF-1 and HF-2 systems used a dipole antenna of 0.4 and 1.2 wavelengths, respectively. To achieve an antenna tip-to-tip length of 24 m, two extendable/retractable elements were required. A retracted element was spooled as two flat metallic ribbons, which, upon extension, curled together into a circular rod (fig. 34-1). To match the complex antenna impedance to the radar, an electrical network was constructed and mounted in the antenna housing. A hybrid unit mounted in the scientific instrument module provided the power division and the appropriate electrical phase to feed the antenna elements as a dipole. To

maintain low side lobes, the antennas were designed with extreme amplitude and phase linearity across the bandwidth. This was done at the expense of antenna efficiency; the minimum efficiency across the band was 65 percent for the HF-1 system and 43 percent for the HF-2 system.

#### The VHF Antenna

The VHF antenna was designed to satisfy a linear amplitude and phase response as well as a directionality requirement. The antenna was a yagi of five directors and one reflector (fig. 34-1). The yagi, mounted at the rear of the service module, was erected by a spring mechanism when the CSM separated from the Saturn launch adapter. The antenna had a beamwidth of 70° in the plane containing the antenna elements and a beamwidth of 50° in the orthogonal plane. To suppress ambiguity between terrain returns on the left and right sides of the spacecraft in the imaging mode, the antenna axis was pointed 20° off nadir.

#### The Radar (CSAR) System

The central element of the radar system (figs. 34-3 and 34-4) was the frequency reference, which provided a stable reference for all system timing and sweep generation. The FM sweep was obtained by driving a voltage-controlled oscillator (VCO) with a ramp voltage. Each frequency was swept approximately 10 percent as follows: HF-1, 5 to 5.53 MHz; HF-2, 15 to 16.6 MHz; and VHF, 150 to 166 MHz. The VCO was phase locked to a stable local oscillator to retain pulse-to-pulse coherency. The signal was transmitted after a slight shaping of the risetime and faltime of the pulses; the reflected signal was received in a broadband phase-locked receiver to preserve phase and amplitude response and then converted to a video signal for storage in the optical recorder. The receiver used stepwise automatic gain control to stay within the dynamic range constraints of the film. Additionally, the VHF receiver had a sensitivity time control wherein a gain of 20 dB was added 13  $\mu$ sec after detection of the specular return to enhance the imaging capability. The CSAR parameters are summarized in table 34-I.

#### The Optical Recorder

The primary function of the optical recorder (figs. 34-5 and 34-6) was to process the CSAR output, record the output of the CSAR on film, and time reference the received signals for later data reduction and analysis studies. The video signal from the CSAR was used to modulate the intensity of the CRT beam while the beam was deflected rapidly across the range direction of the

film. Simultaneously, the film was slowly moved across the face of the CRT in the azimuth direction.

The CRT was swept at one of two basic rates depending on the operation mode of the CSAR. The sweep frequencies for the HF and VHF modes were approximately 396.8 and 1984.1 sweeps/sec, respectively. The VHF mode used an echo tracker function that enhanced the resolution of the recorded data. Instead of monitoring the entire 275  $\mu$ sec that the receiver gate was open, a 70- $\mu$ sec section, or "window," of the data was recorded. The tracker circuit had the capability to shift the 70- $\mu$ sec window in 25- $\mu$ sec increments until the window contained the return signal. The 275- $\mu$ sec gate is required to take into account variations in spacecraft orbit and lunar topography. For short periods of time, however, 70  $\mu$ sec were sufficient to record the returned signal. Because the time-bandwidth product of the CRT could not exceed 1300, echo tracking allowed a larger bandwidth and, hence, finer resolution.

Five auxiliary data tracks were included on the film exposed by the optical recorder, recording an IRIG-B time code as well as engineering information. Additionally, an optical recorder frequency response calibration signal was recorded at the start of every CRT sweep to maintain recorder calibration.

#### DATA PRODUCTS

Before considering the preliminary results, it is worthwhile to discuss the data products of the ALSE. The prime data storage medium is the signal film recovered from the optical recorder during the transearth-coast extravehicular activity. The signal film may be processed by optical techniques, by digital techniques, or by an optical-digital combination.

Optical processing techniques allow the use of optical setups for batch processing of the data. The linear FM property of both the signal and the Doppler signature of point targets may be viewed as a linearly varying diffraction grating. Such a grating will collapse or focus incident coherent collimated light, accomplishing the desired compression step (fig. 34-7). Additionally, spherical lenses are used for a Fourier transform of the data and to place the signal frequency plane in the optical path. Here, the range spectrum is shaped to reduce side-lobe levels, and, in general, two-dimensional range-Doppler filtering is performed. The focused output appears in the image plane; additional lenses (cylindrical telescopes, not shown in fig. 34-7) are used to ensure that both the range and azimuth axes focus in the same plane. The full dynamic range of the experiment (approximately 55 dB) is available in the image plane. Viewing in the image plane is limited, however, by the dynamic range of the human eye,

perhaps 45 dB. If image film is exposed in the image plane, then this product has a dynamic range of only 25 dB. This dynamic range is adequate for imaging, but generally not for sounding, as will be discussed subsequently.

If the light output is exposed out of focus, then the dynamic range of the image may be dispersed to within the film limitations. In this optical setup, a reference beam is used to create a phase reference in the output. This hologram, generated with the precision optical processor at the Environmental Research Institute of Michigan (ERIM), may then be used with very simple optical setups at the Jet Propulsion Laboratory (JPL) and the University of Utah to recreate the full dynamic range of the image.

The hologram is used to scan all ALSE sounding data for subsurface events. Promising regions are digitized for more detailed analysis. The digitizer consists of a scanning photodetector placed in the image plane, along with appropriate analog-to-digital circuitry; the dynamic range of the digitizer is approximately 55 dB. A preferred mode is to use the precision optical processor for azimuth processing only and to digitize the signals uncompressed in range. General two-dimensional digital processing requires prohibitively large computer storage. One-dimensional digital range processing is amenable to sophisticated amplitude and phase filters not available optically. Additionally, frequency-dependent calibration corrections can be made.

## PRELIMINARY RESULTS

### Sounding

Imagery.- The data products in relation to sounding are summarized in figure 34-8. The signal shown is representative of a compressed surface pulse. The hypothetical, dashed side lobes indicate side-lobe reduction due to system correction or deconvolution. In this case, a simple two-layer model has been adopted; the subsurface return will fall along the line shown as a function of depth  $d$ . Note that when a depth is achieved that will resolve the subsurface return from the surface return, the subsurface return is below the dynamic range available on the image film if the surface return is not overexposed. This problem may be somewhat circumvented by overexposing the main lobe or by not shaping or weighting the range-frequency amplitude spectrum. This latter step narrows the main lobe by a factor of approximately 2.5 at the expense of raising the side lobes; however, the image film may then be scanned for shallow subsurface events. A section of unweighted HF-2 image film from western Mare Serenitatis is shown in figure 34-9. The broad line is the main lobe of

the specular surface return. Faint lines parallel to and above the surface main lobe are negative time side lobes of the surface pulse. The positive time region is dominated by scattering from random reflectors; this is termed "clutter" or "clutter noise." Also, a faint event, occasionally broken up, may be seen approximately parallel to the surface. The event seems to be too broad to be a side lobe (side-lobe width one-half of main-lobe width); that is, it appears to be a real feature associated with the lunar surface or subsurface. If it is a surface feature, it must be approximately linear and trending parallel to the CSM ground-track. The most likely explanation for the event is a subsurface interface at a depth of approximately 100 m.

Digital data.- Forty seconds of HF-1 signal film data were digitized to test the large dynamic range capabilities of digital data reduction as well as to search for subsurface events. The digitized data are from a region at the eastern edge of Mare Serenitatis, extending westward for approximately 60 km and defined by the groundtrack of revolution 16 (fig. 34-10). There were 1200 traces or range records digitized, each representing a ground spacing of 50 m. Each digitized record contains 2048 words, yielding a total data set in excess of 2 million words. The data were low-pass filtered in the azimuth or Doppler direction; the capability for more sophisticated azimuth processing was constrained by large computer storage requirements as discussed in the preceding section. Each record was Fourier transformed, and its amplitude and phase (complex) spectrum was stored on magnetic tape. The complex spectra showed a large, apparently random variability from record to record. The spectra were coherently added or "stacked." After stacking approximately 1000 records, the addition of further records failed to change the characteristics of the stack; that is, the process had converged and remained constant for further stacking. This stacked spectrum was taken as the ALSE system transfer function for setting up a deconvolution filter. The spectrum of the stacked records was filtered and inverse Fourier transformed to yield the compressed time-domain system response shown in figure 34-11. This response agrees very well with premission measurements and indicates that no surface or subsurface events persisted in the 1200-record stack. Persistence of a lunar subsurface event or of surface clutter would require a nearly constant phase contribution (relative to the phase of the specular surface return) from trace to trace over the 1200 records. The maximum distance for which the spectra of an event will constructively add is called the "coherence length" for the event.

The randomness of the spectra is primarily attributable to the random clutter noise from the surface (and perhaps subsurface). The compressed pulse from a single weighted, deconvolved spectrum is shown in figure 34-12. The return signal is completely dominated by clutter noise, an indication that detectable

subsurface events must have a long coherence length compared to the coherence length of the clutter. A 15-km stack is shown in figure 34-13, in which four events in addition to the surface return may be identified. Except perhaps for the third event, comparison with figure 34-11 shows that the events are probably not side lobes but are likely subsurface or surface returns that are coherent for at least 15 km. It is possible that a time-varying systematic phase error could cause a similar response, but, to date, results obtained primarily from prelaunch testing have indicated that this is probably not the case. This possibility will be further investigated by comparing results from multiple orbits over similar lunar regions.

The general approach was to take nonoverlapping sets of records and to process 5-, 10-, and 15-km stacks. Events were plotted in cross sections, and those events that appeared to be aligned for at least three separate stacks were connected by straight lines (fig. 34-14). In addition, single events are shown for the 15-km stacks.

It is important to note that the coherence length of a geologic structure may be much less than the actual physical length of the structure. It may be possible to map out the structure by a series of short stacks, but the structure may be noncoherent for a length equivalent to the physical length. An example of this is the second event shown on the right side of the cross sections in figure 34-14. The event persists in five 5-km stacks and three 10-km stacks, indicating a geologic length of 25 to 30 km. The event appears only in the most easterly 15-km stack and is noncoherent for the 15-km stack to the west. The most likely cause of the noncoherence is the (apparent or real) dip of the feature. The stacking process, as described previously, is only coherent for events approximately parallel to the actual lunar surface. (The topographic profile has been mapped into the horizontal line indicating zero apparent depth in fig. 34-14(c).) Later digital processing capabilities will include directional stacking. Events with a low signal-to-clutter-noise ratio may only show up for longer stacking lengths. An example of this case is the event that occurs on each of the 15-km stacks with an apparent depth of approximately 700 m.

As discussed previously, a surface location for these events requires the fortuitous occurrence of linear features that are parallel to the flightpath and that also present surface normals pointing to the spacecraft. Preliminary photogeologic examination of Apollo 15 and Apollo 17 photographs reveals no such features.

The event strengths relative to the surface specular strength are also shown in figure 34-14. If these are subsurface features, then they indicate a lunar loss tangent and a relative dielectric

constant slightly lower than had been anticipated. Furthermore, a complex stratigraphy is indicated for the eastern margin of Mare Serenitatis.

### Profiling and Imaging

Characteristics of imagery.- Data processing techniques to produce surface profile imagery and side-looking surface imagery in spacecraft flight-time/echo-delay-time coordinates are well developed and were available for quick-look images to yield preliminary results from the ALSE. The ALSE radar image is a composite of a surface profile along the groundtrack of the spacecraft and two side-looking images (fig. 34-15). The profile appears at the top of the image, and the two side-looking surface images stretch below the profile and are superposed on each other. The side-looking imagery to the right and left of the spacecraft groundtrack for HF imaging have equal intensity. For VHF imaging, the 20° off-vertical positioning of the antenna beam greatly reduced the superposition, or left-right ambiguity problem. However, stereoscopic viewing of overlapping images from adjacent revolutions permits separation of the two images. (See the discussion under "Stereoscopic ALSE imagery.")

The side-looking HF imagery (fig. 34-16, top and center) is dominated by the discontinuous scattering of near-specular reflections from surface elements. There is little continuous imaging in the scene because, in preliminary processing, only a small part of the Doppler history of a feature, centered around zero Doppler shift, was retained. Thus, the near-specular returns from slopes with contours oblique to the spacecraft groundtrack, seen only with positive or negative Doppler shifts while approaching or departing from oblique slopes, are filtered out during conversion from signal film to image film. Only very weak signal returns near zero Doppler are passed to the image film for the oblique slopes.

The VHF imagery (fig. 34-16, bottom) has much more pictorial content than the longer wavelength imagery. This detail results primarily from the finer ground resolution of the 2-m-wavelength radar and the greater abundance of small-scale features discernible at the 2-m wavelength. The slopes of these features with contours parallel to the spacecraft groundtrack densely populate the radar image with near-zero Doppler, near-specular, small images. This effect is conspicuous in the bottom imagery of figure 34-16, to the left of center.

Utility of images.- The profiles, when closely correlated with orbital camera photographs, yield abundant quantities of important metric data on the vertical relief and slopes of a host of lunar geologic features. Preliminary imagery, the first data

produced, also contains "qualitative" profile information. Although the ellipticity of the CSM orbit has not yet been removed from the data, the profiles are immediately useful for addressing local selenomorphological problems. A later step in the ALSE data processing will include digitizing of the signal film and recovery of the "quantitative" profile, as discussed previously.

The global profiling capability of the ALSE is suggested by the top and center parts of figure 34-16 showing an HF-1 image for one revolution of the Moon. The profile is superimposed on the sinusoid resulting from the elliptical orbit. As a point of reference, the crater Aitken, approximately 80 km wide under the orbital track and approximately 5 to 6 km deep from rim to floor, appears at the extreme left of the center imagery in figure 34-16. The spacecraft track may be followed, right to left and top to bottom, progressing from far-side highlands across Mare Crisium and Mare Serenitatis (all in fig. 34-16 (top)) on to Mare Imbrium, Oceanus Procellarum, and far-side highlands (all in fig. 34-16 (center)). The local profiling-imaging capability of the ALSE is illustrated in the bottom imagery of figure 34-16, a north-looking VHF image recorded during revolution 73.

An important aspect of the ALSE imagery is that it provides a source of improved positional information across a substantial area of the eastern lunar far side. Unlike all Apollo orbital camera imagery, ALSE imagery does not depend on solar illumination. As a result, the ALSE side-looking surface imagery is the only Apollo imagery obtained between longitudes 68° and 152° W (other than very limited, 1-km-resolution earthshine photography, ref. 34-1). For determination of lunar positions in terms of a coordinate measured along the length of the orbit, this ALSE imagery is free from the troublesome mosaicking and rectification problems that beset the determination of lunar positions in this region from the melange of variously scaled and tilted Lunar Orbiter images covering the area.

One other significant aspect of the side-looking surface imagery is that, in some places, where slope effects are negligible or predictable, local differences in relative radar albedo can be read directly from the side-looking imagery.

Stereoscopic ALSE imagery.- A major aid to the use of the geometrically complex ALSE imagery derives from the observation format in which much of the data was obtained. Of the approximately six revolutions of data that were collected, a little more than two revolutions each were gathered during adjoining revolutions by using the HF systems (20-m- and 60-m-wavelength imagery) on the one hand and by using the VHF system (2-m-wavelength imagery) on the other. Essentially all the 60-m-wavelength

imagery from adjacent revolutions and much of the 2-m-wavelength imagery from adjoining revolutions can be viewed stereoscopically with the result that the side-looking images from the two sides of the pair of adjoining orbital tracks become segregated in space in the stereoscopic image. Otherwise, the two side-looking images to the north and south of the track in a single composite radar image are superposed on each other in some monoscopic image space. The effect of stereoscopic viewing is as though a radar range of a strip of the lunar surface were wrapped around a hyperbolic cylindrical surface tangent to the radar profile (fig. 34-17). Stereoscopically, the lunar relief is seen superposed on the general cylindrical form of the image. The format of the radar data permits close correlation of the side-looking radar imagery with the orbital camera imagery. Thus, very exact location of the radar profile among and within lunar features, as recognized in the camera imagery, is possible.

Stereoscopic HF imagery.- A sample of stereoscopic HF imagery was studied and measured to evaluate the feasibility and the achievable precision of measuring the relative positions of individual features in the stereoscopic images. The locations numbered in figure 34-18 were identified in the three-dimensional image formed by viewing stereoscopically the radar images obtained on revolution 16-17 and revolution 17-18. For the time being, the map projection of the cylindrically distorted image has been measured. Ultimately, measurements rectified to conventional lunar coordinates will be sought. The coordinates of the points in the stereoscopic model were measured by using a computerized analytical stereoplotter and are plotted in figure 34-19. An interim arbitrary orthogonal coordinate system was used (fig. 34-17(a)). The system was oriented with the Y-axis approximately along the profile (plus-Y eastward) and the X-axis in the plane of the monoscopic images (plus-X upward in the profile). The Z-axis was oriented perpendicular to the plane of the monoscopic images in the direction of stereoscopic depth (plus-Z northward). The coordinates were read in millimeters at the scale of the original 70-mm image film. In a set of 51 measured points, readings of the coordinates in the plane of the film were repeatable to within 5 or 10  $\mu\text{m}$  and depth measurements of the stereoscopic image perpendicular to the plane of the film were repeatable to within approximately 50  $\mu\text{m}$  in a range that varies from more than 3.5 mm near longitude 170° W to more than 9.5 mm near longitude 130° E. The range is attributable in part to the variation in the spacing of the spacecraft groundtracks. The stereoscopic image in figure 34-20 shows the details of the area at the eastern end of figures 34-18 and 34-19 and includes all the points in that area the positions of which were measured. The measured coordinates of this subset of points are plotted in figure 34-21.

VHF imagery.- The VHF imagery from the area around the Apollo 17 landing site, shown in figure 34-22, was used to investigate the feasibility of using an analytical stereoplotter to measure and plot profiles from the generally continuous scene in the stereoscopic 2-m-wavelength imagery. An interim orthogonal coordinate system in the stereoscopic image was again used, but the Y-axis was made approximately coincident with the foreground (northern) edge of the image. Otherwise, the coordinate system is oriented as in the stereoscopic model for the 60-m-wavelength images. A profile trending perpendicular to the spacecraft groundtracks in the stereoscopic radar image then lies in an X-Z plane (fig. 34-17(b)). Coordinates in the stereoscopic image were again measured in millimeters at the scale of the original 70-mm image film.

An example of such a profile runs through the numbered points in figure 34-23 and is plotted in figure 34-24. The features in the radar image have been correlated with geologic units and terrain features using the nomenclature of Scott and Carr (ref. 34-2) and of the Apollo Lunar Geology Investigation Team (ref. 34-3). The profile in figure 34-24 illustrates the general distribution of scenery in the stereoscopic image with the scene south of the spacecraft groundtracks lying behind or below (more negative values on the X-axis) the scene north of the groundtracks. The effect of high relief near the spacecraft groundtrack is also illustrated; for example, by the profile of the North Massif, which lies north of the groundtracks. The image of the crest of its south-facing slope (point 6) is recorded at earlier echo delay time (more negative values on the X-axis) than the radar image (point 104) of the edge of the plain to the south, which is, of course, closer to the groundtrack in map view.

Results from surface profile and side-looking surface imagery.- The unadjusted HF-1 surface profile in figure 34-18 includes several features that are noteworthy. The profile from longitude 114° to 147° E is relatively flat compared to the remainder of the profile farther east. The relatively flat part of the profile is deeply notched by two large depressions. One is the 75-km-diameter crater Marconi, which was profiled off center toward the southern rim. Part of the crater floor shows in the profile, and the southern rim appears in the side-looking imagery. The other depression has been recognized by El-Baz (ref. 34-4) in Apollo 16 orbital photographs. This depression is approximately 180 km in diameter, and the profile in figure 34-18 is a nearly central section of it. The crater is very old; approximately 50 percent of its interior is overlapped by superposed craters larger than 20 km in diameter. The crater was in an overexposed part of Lunar Orbiter I frame M-136 and is difficult to recognize there but is decipherable in enhanced copies. Apparently, the feature was overlooked in the preparation of Aeronautical Chart and Information Center lunar charts at

scales of 1:5,000,000 and 1:2,750,000, as it is essentially unrecognizable in printed copy, although traces of the appropriate shading are present. In addition to the Apollo 16 coverage, Apollo 14 Hasselblad frames AS14-75-10298 to 10300 show much of the crater near the terminator at approximately 1-km resolution; subsequent frames 10303, 10308, 10313, 10315, 10317, and 10318 show the entire crater at lower resolutions. Several useful stereoscopic images can be formed from this set of photographs. The moderately rough plain between Marconi Crater and the crater in question appears to be very primitive in the sense of being a dissected remnant of an old plane situated between many 25- to 100-km-diameter craters.

High points along the profile in figure 34-15 near longitudes  $160^{\circ}$  E,  $177.5^{\circ}$  W, and  $170^{\circ}$  W may represent the high parts of very ancient multi-ringed basins tentatively recognized during the preparation of geologic maps for planning ALSE observations. In this preliminary mapping, the two basins in question can best be fitted by a 630-km-diameter circle centered north of the groundtrack of revolution 16-17 near latitude  $9^{\circ}$  S, longitude  $164^{\circ}$  E, and circles of 690, 930, and 1140 km centered south of the groundtrack near latitude  $32^{\circ}$  S, longitude  $159^{\circ}$  E.

Other noteworthy aspects of the present quick-look 60-m side-looking imagery of craters are illustrated by the images of two craters with central peaks that lie south of the groundtrack in figure 34-18. One crater, De Vries (fig. 34-20), is 60 km in diameter, and the other, lying near longitude  $134^{\circ}$  E between points 45 and 41 (fig. 34-18), measures 58 km in diameter. The central peak of De Vries Crater is close enough to the spacecraft groundtrack, like the southern walls of Aitken Crater and its western neighbor, to reflect a fairly strong signal. The return from the more distant southern wall of De Vries Crater is barely discernible, and the still more distant northern walls of Aitken Crater and its neighbor are not detected. Further data reduction will be performed to minimize this systematic variation in image brightness. The near-circular image at longitude  $134^{\circ}$  E actually consists of the images of the central peak and part of the southern wall of the 58-km-diameter crater, the northern rim of which is essentially at the profile. This example illustrates that a geometric rectification of the imagery to eliminate the cross-track scale variation will substantially aid interpretation of the side-looking surface imagery.

The utility of the ALSE data for studying the tectonics of lunar basins may be seen in samples of VHF imagery in figures 34-16 (bottom) and 34-25. In figure 34-16 (bottom), the crater Dawes and the flat floor of Mare Tranquillitatis are on the left. An arched and fractured (rilles) boundary separates Mare Serenitatis and Mare Tranquillitatis, the outer basin of the

former lying approximately 900 m lower than the latter. The wrinkle ridge (right) separates the outer and inner basins; the inner basin is 200 m lower. Phillips et al. (ref. 34-5) showed that the wrinkle ridge bounds the Serenitatis mascon. The same wrinkle ridge system may also be seen in figure 34-25. Here, in western Mare Serenitatis, the inner basin is also downdropped approximately 200 m. The profile in figure 34-25 suggests that the ridge represented a zone of elastic bending followed by mechanical failure.

The ALSE data shown here support the idea that the Serenitatis basin structure is consistent with a model of progressive tectonic failure as a consequence of a superisostatic load placed by the mascon. Such sagging at the lunar surface, with local faulting, could also be caused by a withdrawal of mare magmas from depth.

Differences in radar albedo.- Two types of variations in radar albedo have been noted in the 2-m-wavelength imagery. One is a bright horizontal band around a crater wall, and the other consists of highly reflective halos around certain small craters. Recognition of the quantitative albedo differences depends on the removal of variations in scene brightness due to topographic effects. In the following examples, topographic effects are assumed to be of second order.

The 2-m-wavelength imagery of the 6-km-diameter crater Eratosthenes B in southern Mare Imbrium shows a bright horizontal ring from approximately one-fourth to one-half of the distance from the rim crest to the floor (figs. 34-26 and 34-27). It can be seen in the stereoscopic image that the crater shape is that of a truncated cone. Thus, the bright ring is not due to a difference in slope. It is probably due to layering in the materials intersected by the crater, to the character of erosional debris covering part or all of the wall, or to a combination of these.

Two examples of small craters with surrounding radar-bright halos, Bessel G and Bessel F, 1.2 and 0.7 km in diameter, respectively, lie in southwestern Mare Serenitatis (fig. 34-25). The similarity of the images in both revolutions 25 and 26 is noteworthy. The bright halos extend from the crater rim crest outward approximately one crater diameter (fig. 34-28). The dark interior of the image of a crater slightly smaller than Bessel G interrupts the bright halo of Bessel G on the eastern side. Bessel G and Bessel F are very young craters with well-preserved rim and ray deposits. (See, for example, Apollo 17 metric camera frame AS17-1512 and Apollo 16 panoramic camera frames AS16-9910, 9912, 9915, and 9917.) The bright, blocky rim deposits form a continuous blanket from the rim crest outward for approximately one crater diameter. Bright filamentous rays extend at least seven crater diameters beyond the continuous rim deposits of Bessel G

and 12 crater diameters in the case of Bessel F. The radar brightness of the rim deposit is probably a result of rock fragments in the continuous rim deposit. In fact, it appears that it may be possible to correlate individual bright reflections in the radar image with the larger fragments in the field of blocks surrounding the crater. The radar brightness of young lunar crater rim deposits is known from Earth-based radar mapping (ref. 34-6). Apollo lunar sounder images like those of Bessel G Crater may explain the low-resolution brightness in terms of the energy component reflected from the individual blocks in the deposits. In this way, the ALSE imagery can substantially aid in geologically calibrating detailed Earth-based lunar radar images, which have been obtained for the whole Earth-side hemisphere of the Moon at 70- and 3.8-cm wavelengths (ref. 34-6). The ejecta deposits and the ray materials of Bessel G and Bessel F Craters make bright radar anomalies extending approximately five and six crater diameters, respectively, beyond their rim crests in the depolarized return (effectively the relative radar albedo) of the Earth-based 3.8-cm radar imagery. At least the ejecta deposit of Bessel G Crater is a bright anomaly in the depolarized return in 70-cm Earth-based radar imagery.

#### GALACTIC NOISE DATA

The receive-only data showed a very high terrestrial component in both channels on the lunar near side, as can be seen in the comparison of the near-side and far-side noise measurements in figure 34-29. This result was particularly surprising at the HF-1 range, in which it would be expected that the ionosphere of the Earth would block most signals of surface origin.

The nighttime portion of the lunar far side provided, however, an opportunity to measure the galactic noise. The power measured by the antenna-receiver system, subjected to an isotropic noise of temperature  $T$ , is

$$P_n = KT\beta\eta\frac{\Omega}{4\pi} \quad (34-1)$$

where  $K$  is the Boltzmann constant,  $\beta$  is the bandwidth of the system,  $\eta$  is the efficiency of the system, and  $\Omega$  is the effective solid angle of the source observed. For the case of the CSM in a 110-km lunar orbit, the ratio  $\Omega/4\pi$  is equal to 0.67. The

average radio brightness  $B$  can then be determined from the temperature through

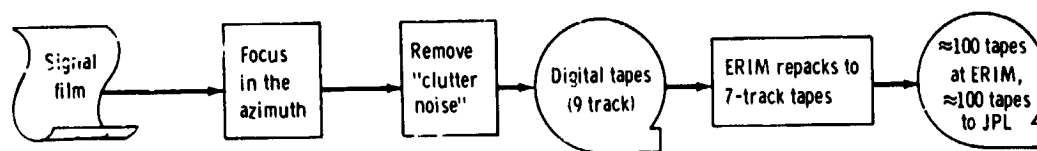
$$B = \frac{2Kf^2}{c^2} \quad (34-2)$$

The results for the noise brightness intensity measured on the nighttime lunar far side are shown in figure 34-30 along with a summary of measurements by other workers (ref. 34-7). The ALSE results are in generally good agreement with these other measurements, but they must be taken as preliminary because the CSM guidance and navigation system is a source of interference in the HF range, the contribution of which is being investigated.

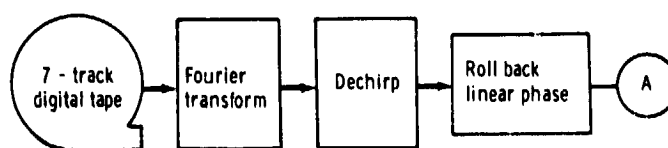
The near-side brightness intensities corresponding to the levels in figure 34-29 are, for both HF frequencies, approximately  $2.3 \times 10^{-19} \text{ W/m}^2\text{-Hz-sr}$ .

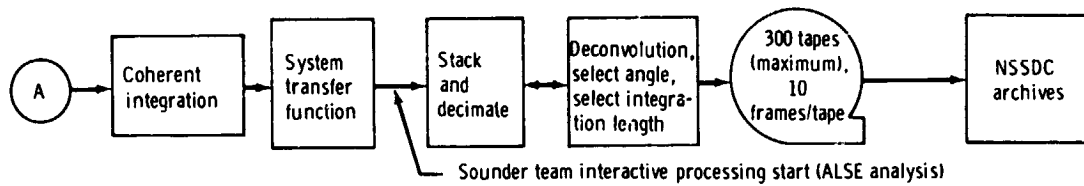
#### DATA TO BE ARCHIVED AT NSSDC

The following flow diagram shows the ALSE data processing flow from receipt of the signal film by the Environmental Research Institute of Michigan (ERIM), through ERIM processing, to JPL, through JPL processing, and to the archives of the National Space Science Data Center (NSSDC).



The Jet Propulsion Laboratory makes a repack on digital tape for each of its 100 tapes from ERIM (for a total of 600 digitized tapes of data). Approximately 300 (maximum) of these JPL tapes then flow through the following process.





As shown in the preceding flow diagram and based on present plans, only 50 percent (maximum of 300) of the digitized ALSE tapes will be submitted to NSSDC together with the following data.

1. All imagery film and prints, approximately 30 m (100 ft) (10 reels of microfilm)
2. Profile tapes and plots (4 tapes)
3. Subsurface mapping, microfilm, and prints (1 tape of logs)

All tapes and film sent to NSSDC will be accompanied by documentation giving detailed descriptions. (Note: Signal film will be stored at the photographic laboratory at the Lyndon B. Johnson Space Center, Houston, Texas.)

The ALSE data can be used to study geological features; radar imagery shows changes undetectable by photographic imagery. The geometry of lunar features generally gives higher decibel variation than does the composition (40 dB for geometry, 10 dB for composition).

## REFERENCES

- 34-1. Lloyd, D. D.; and Head, J. W.: Orientale Basin Deposits (Riccioli Area) in Apollo 16 Earthshine Photography. Sec. 29, Part E, of Apollo 16 Preliminary Science Report, NASA SP-315, 1972.
- 34-2. Scott, D. H.; and Carr, M. H.: Geologic Map of the Taurus-Littrow Region of the Moon. Apollo 17 Pre-Mission Map. U.S. Geol. Survey Misc. Geol. Inv. Map I-800, sheet 1, 1972.
- 34-3. Apollo Lunar Geology Investigation Team: Preliminary Report on the Geology and Field Petrology at the Apollo 17 Landing Site. U.S. Geol. Survey Open-File Report, 1972. (Available from Center of Astrogeology, Flagstaff, Ariz.)
- 34-4. El-Baz, Farouk: Discovery of Two Lunar Features. Sec. 29, Part H, of Apollo 16 Preliminary Science Report, NASA SP-315, 1972.
- 34-5. Phillips, R. J.; Conel, J. E.; Abbott, E. A.; Sjogren, W. L.; and Morton, J. B.: Mascons: Progress Toward a Unique Solution for Mass Distribution. J. Geophys. Res., vol. 77, no. 35, Dec. 10, 1972, pp. 7106-7114.
- 34-6. Thompson, Thomas W.; and Zisk, Sidney [Stanley] H.: Radar Mapping of Lunar Surface Roughness. Thermal Characteristics of the Moon, vol. 28 of Progress in Astronautics and Aeronautics, MIT Press (Cambridge, Mass.), 1972, pp. 83-117.
- 34-7. Alexander, J. K.; Brown, L. W.; Clark, T. A.; Stone, R. G.; and Weber, R. R.: The Spectrum of the Cosmic Radio Background Between 0.4 and 6.5 MHz. Astrophys. J., vol. 157, no. 3, Sept. 1969, pp. L163-L165.

TABLE 34-I.- ALSE RADAR SYSTEM PARAMETERS

Parameter	Operating mode		
	HF-1	HF-2	VHF
Nominal wavelength, m . . . . .	60	20	2
Initial frequency, MHz . . . . .	5	15	150
Frequency rate, kHz/ $\mu$ sec . . . . .	2.222	20.0	2000
Frequency sweep, MHz . . . . .	.533	1.6	16
Pulse duration, $\mu$ sec . . . . .	240	80	8
Pulse risetime, percent . . . . .	3.6 $\pm$ 0.4	3.6 $\pm$ 0.4	10 $\pm$ 0.5
Pulse-repetition period, $\mu$ sec . . . . .	2520	2520	504
Pulse energy, J . . . . .	.02 to .026	.007 to .009	.0007 to .0009
Time-bandwidth product . . . . .	128	128	128
Receiver output frequency range, MHz . . . . .	.233 to .766	.9 to 2.5	3.0 to 19.0

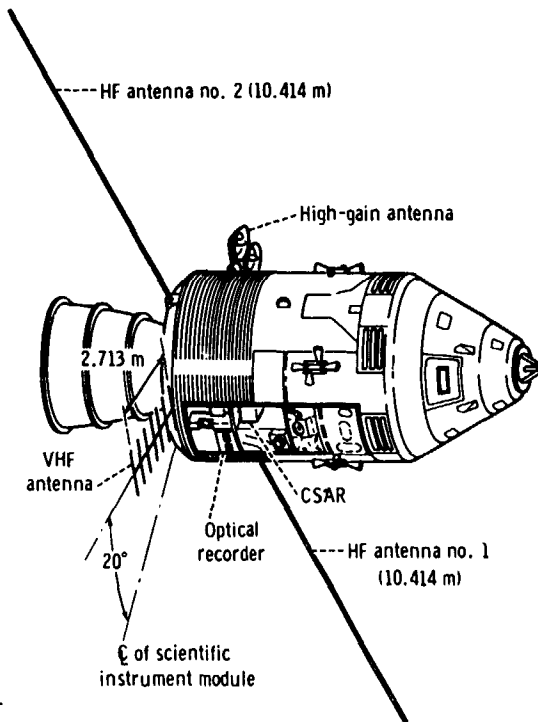


Figure 34-1.- The CSM, showing the ALSE configuration.

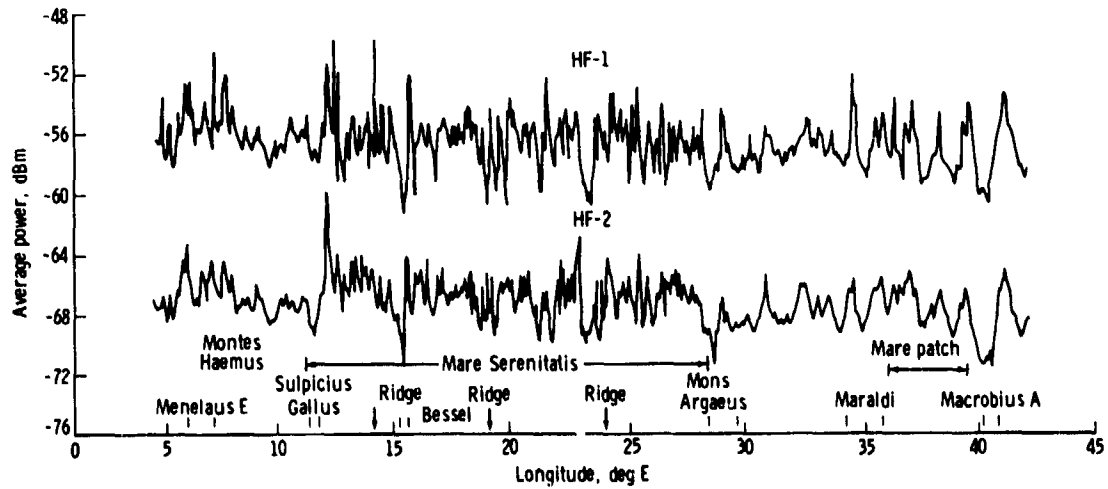


Figure 34-2.- Typical output of the specular power monitor on lunar revolution 17.

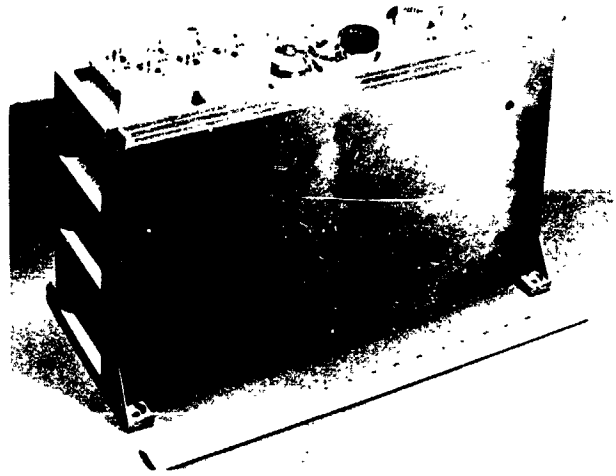


Figure 34-3.- Photograph of the CSAR.

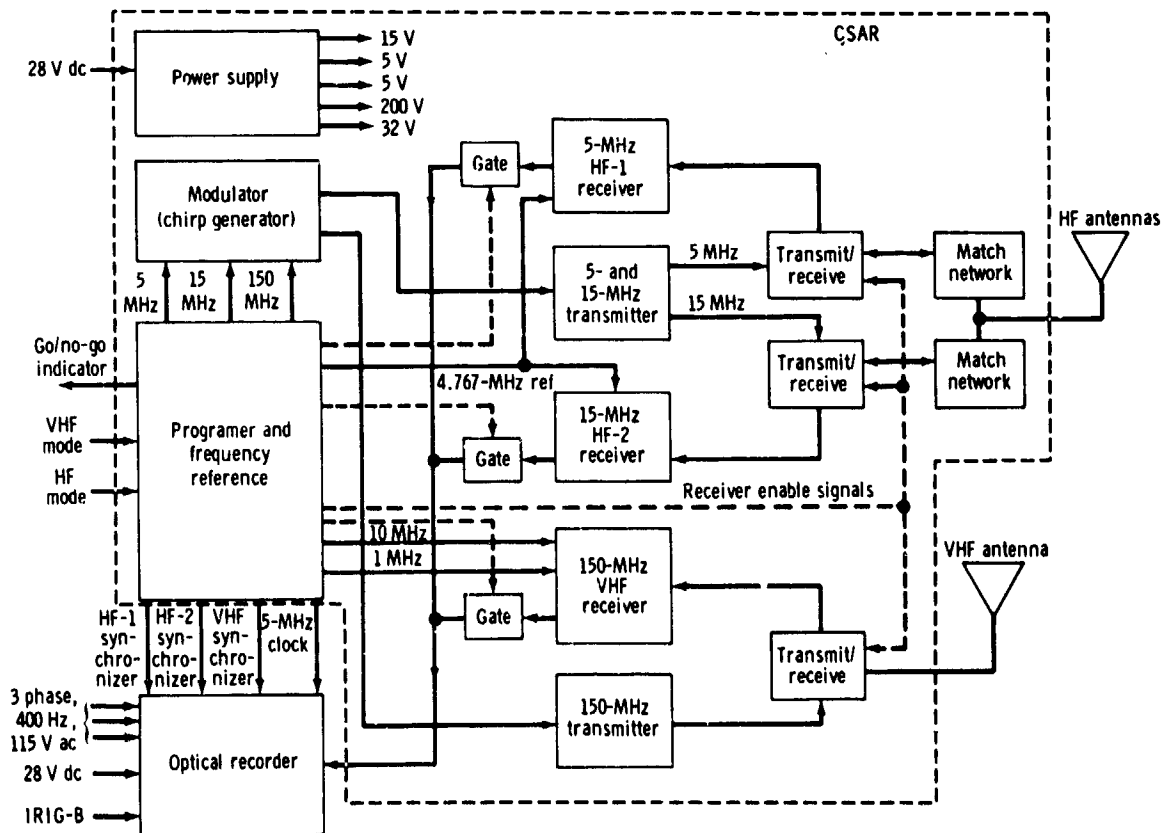


Figure 34-4.- Block diagram of the CSAR.

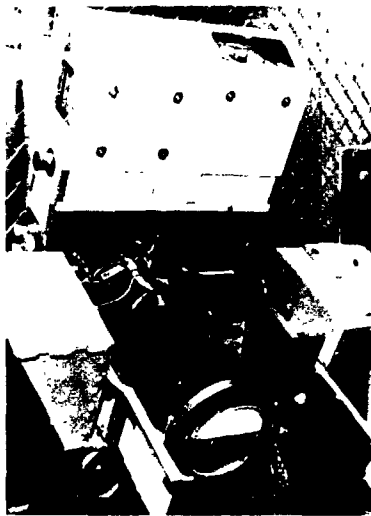


Figure 34-5.- Photograph of the optical recorder.

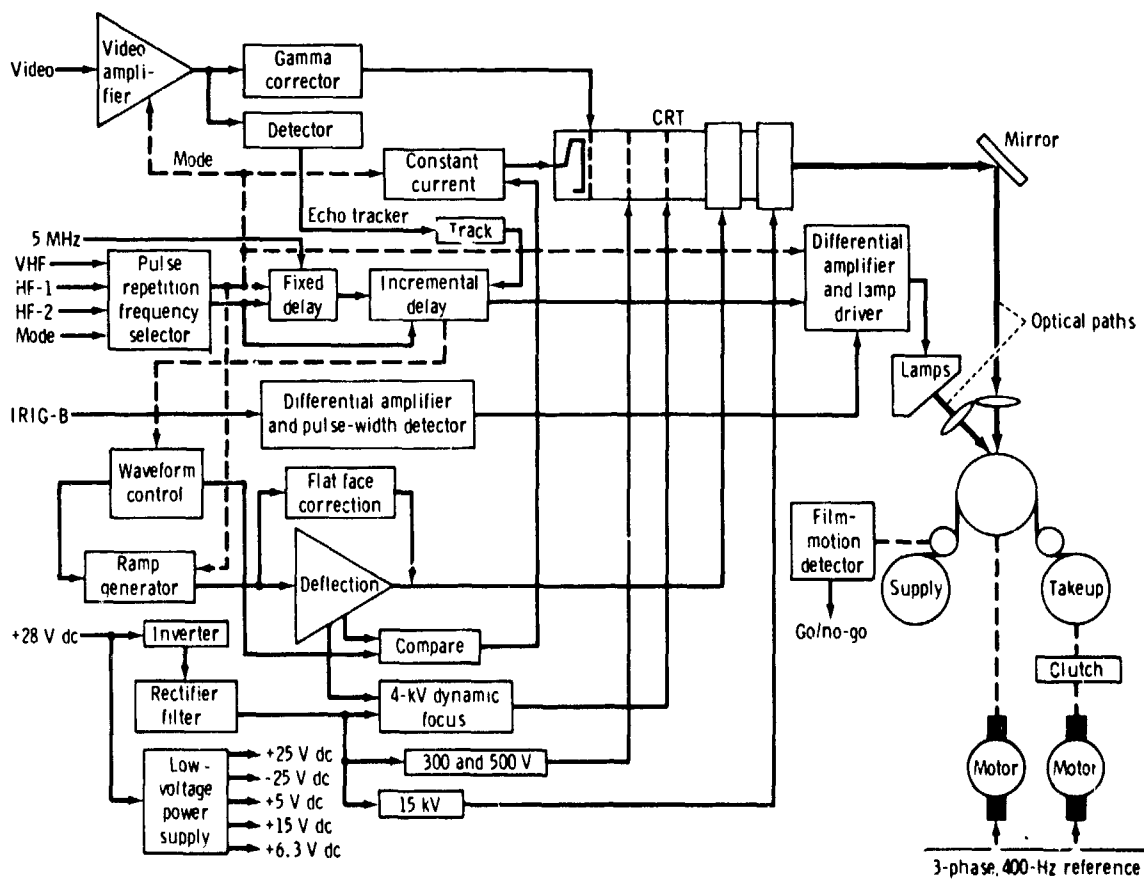


Figure 34-6.- Block diagram of the optical recorder.

ORIGINAL PAGE IS  
OF POOR QUALITY

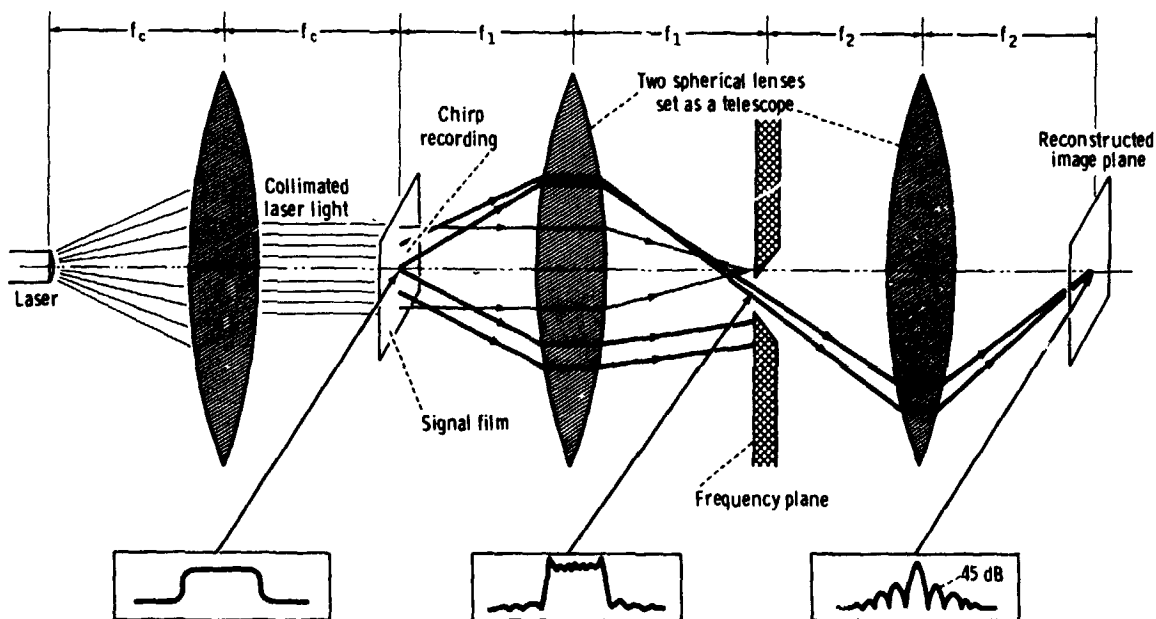


Figure 34-7.- Schematic illustration of optical setup. Focal distances are designated  $f_1$ ,  $f_2$ , and  $f_c$ .

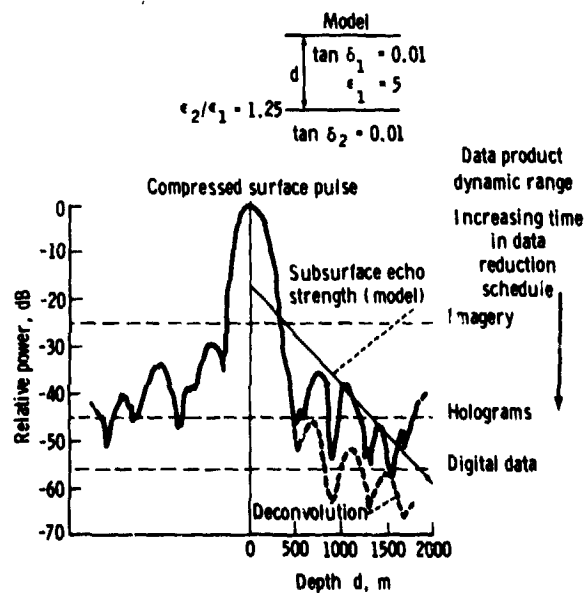


Figure 34-8.- Dynamic range of various ALSE data products in relation to a subsurface event at depth  $d$ .

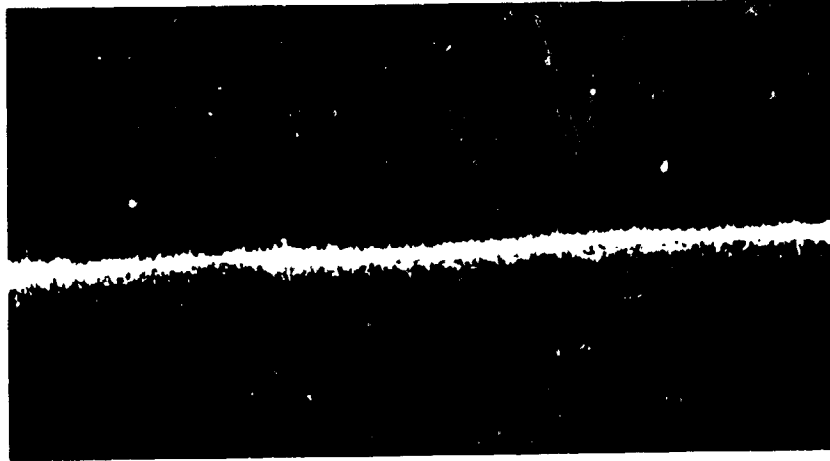


Figure 34-9.- Candidate subsurface feature at a depth of approximately 100 m, as seen in HF-2 imagery. Region shown is approximately 150 km along the groundtrack in western Mare Serenitatis.

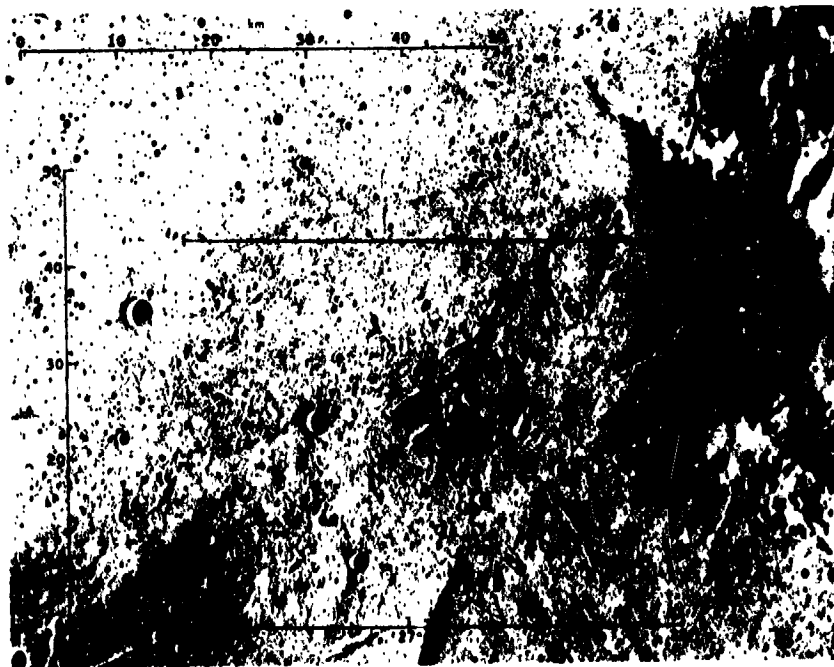


Figure 34-10.- Groundtrack for digital data reduction test area shown on Apollo 17 metric camera frame AS17-0598. Area is located at eastern boundary of Mare Serenitatis. Scale at bottom is longitude, degrees east.

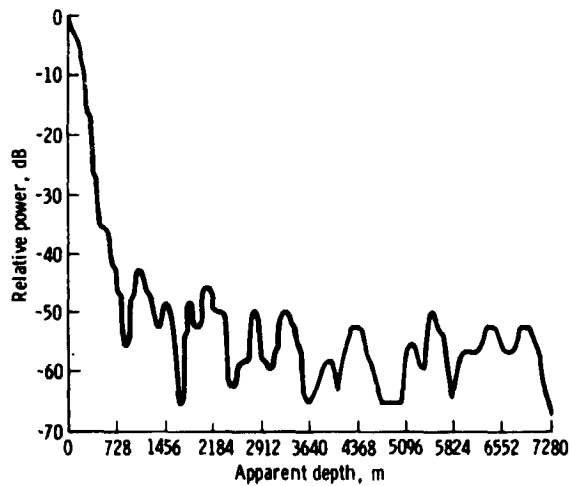


Figure 34-11.- Side-lobe response of the ALSE determined from 1200-record stack. Depth is derived by converting time to distance, using a relative dielectric constant of 4 to obtain velocity.

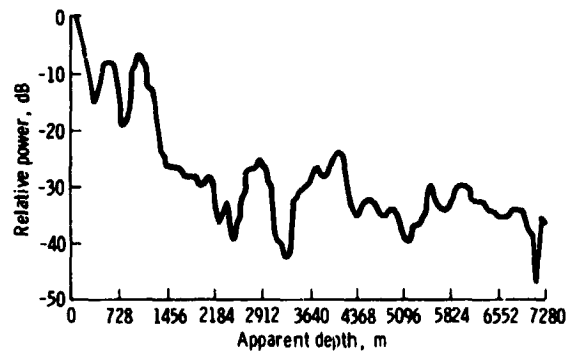


Figure 34-12.- Lunar return for one record, showing high clutter level. Depth is derived by converting time to distance, using a relative dielectric constant of 4 to obtain velocity.

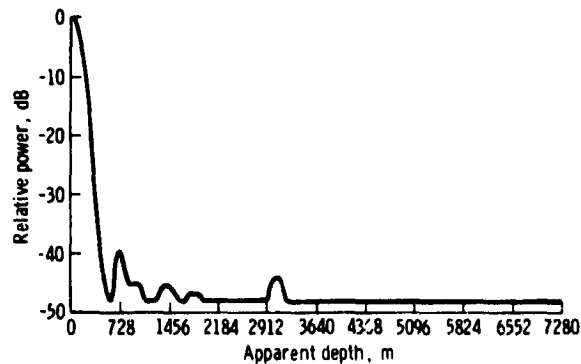
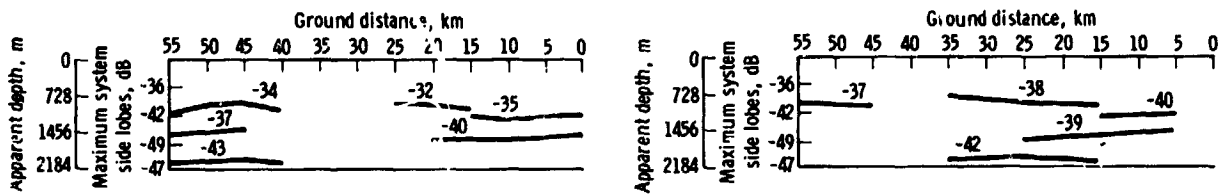
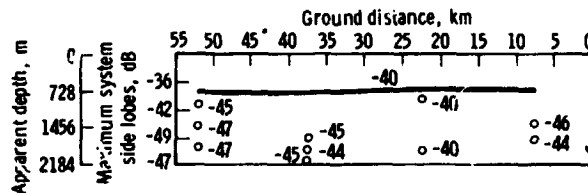


Figure 34-13.- Lunar return for 300-record (15 km) stack. Depth is derived by converting time to distance, using a relative dielectric constant of 4 to obtain velocity.

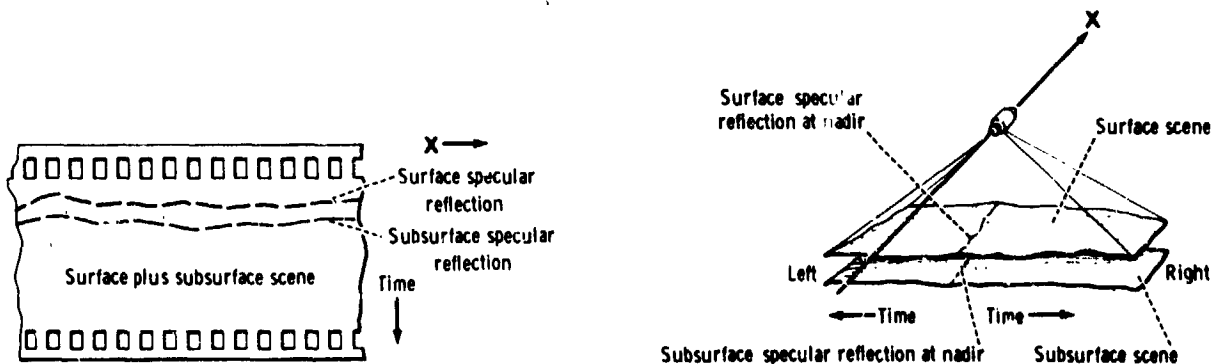


(a) 100 stacked spectra (5 km). (b) 200 stacked spectra (10 km).



(c) 300 stacked spectra (15 km).

Figure 34-14.- Apparent cross section for eastern Mare Serenitatis region for 5-, 10-, and 15-km stacks. Depth is derived by converting time to distance, using a relative dielectric constant of 4 to obtain velocity. The data begin at approximately latitude  $20^{\circ}$  N, longitude  $28.5^{\circ}$  E, on lunar revolution 16. The inner ordinate scale indicates the position and maximum strength (relative to the specular surface return main lobe) of the surface return side lobes. Events are labeled with their relative energies. East is to the right; west, to the left.



(a) Radar image of scene.

(b) Actual scene.

Figure 34-15.- Relationship between actual scene and radar image of scene. The earliest return is the surface specular reflection followed by backscatter creating the surface scene. At some later time, the much weaker subsurface specular reflection and scene, both generally not seen in imagery, superimpose upon the surface scene. Additionally, "left" and "right" scenes are superimposed. However, the VHS antenna was oriented  $20^{\circ}$  off nadir to suppress the left scene.

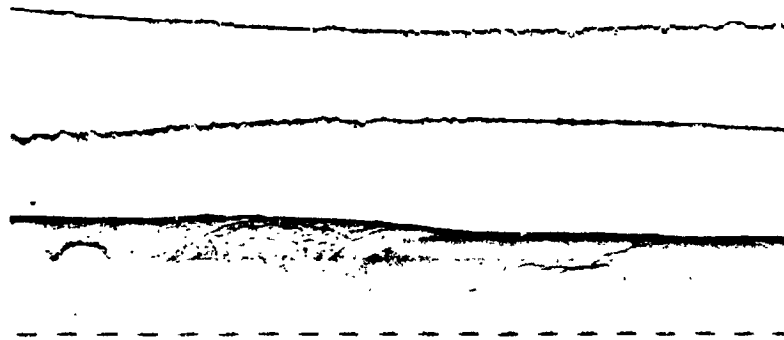


Figure 34-16.- Typical ALSE imagery. Top: HF-1 profile of one-half lunar revolution including (right to left) far-side highlands, Mare Crisium, and Mare Serenitatis. Center: HF-1 profile of one-half lunar revolution including (right to left) Mare Imbrium, Oceanus Procellarum, and far-side highlands. Bottom: VHF image of the Tranquillitatis-Serenitatis boundary region. Time marks (broken line) represent ground spacing of approximately 15 km.

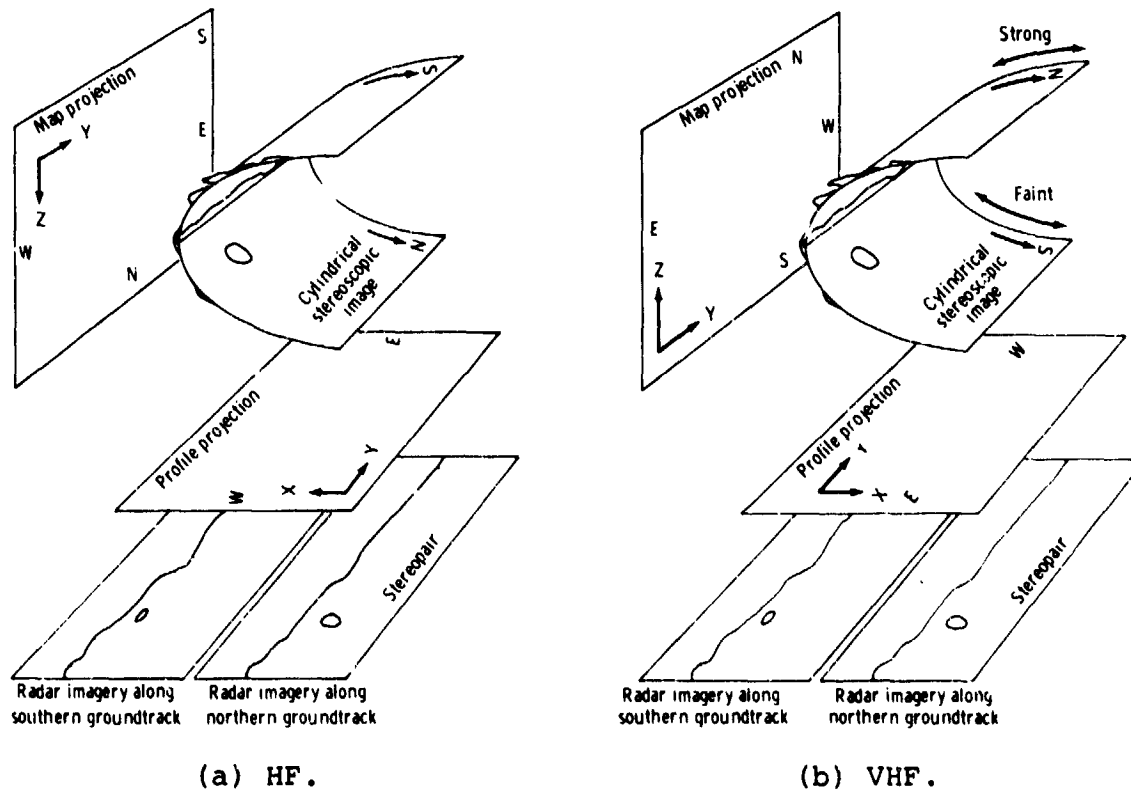


Figure 34-17.- Stereoscopic viewing geometry showing "map" and "profile" projections, as well as cylindrical cross-section profile.

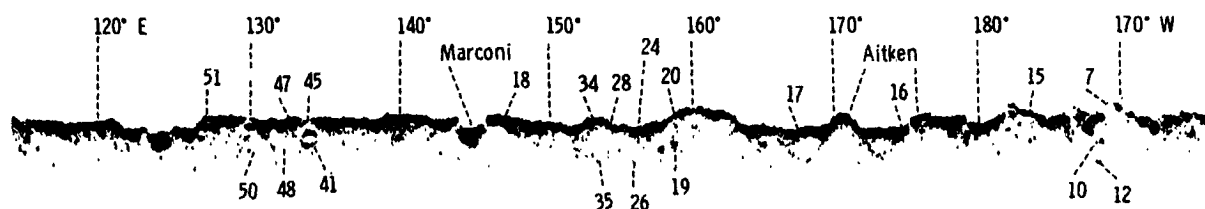
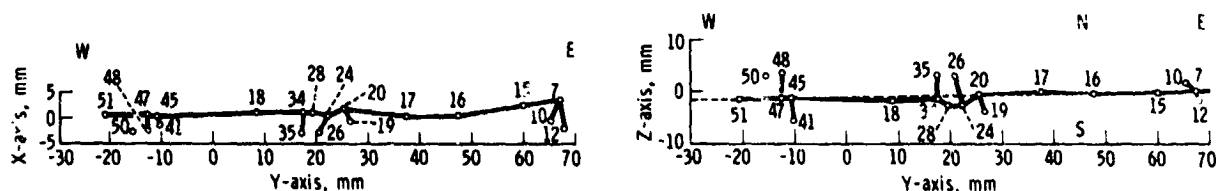


Figure 34-18.- A segment of 60-m-wavelength ALSE imagery in the western half and central part of the lunar far side obtained on revolution 16-17. The numbered points correspond to those in figure 34-19 and are explained in the text. The longitudes in this figure and in figure 34-20 are preliminary and are probably correct within approximately  $0.5^\circ$ .



(a) Profile.

(b) Map.

Figure 34-19.- Plots of the stereoscopic image coordinates of points numbered in figure 34-18 as seen by stereoscopic viewing of the 60-m-wavelength ALSE images along revolutions 16-17 and 17-18. Coordinates are measured at the scale of the original 70-mm image film.

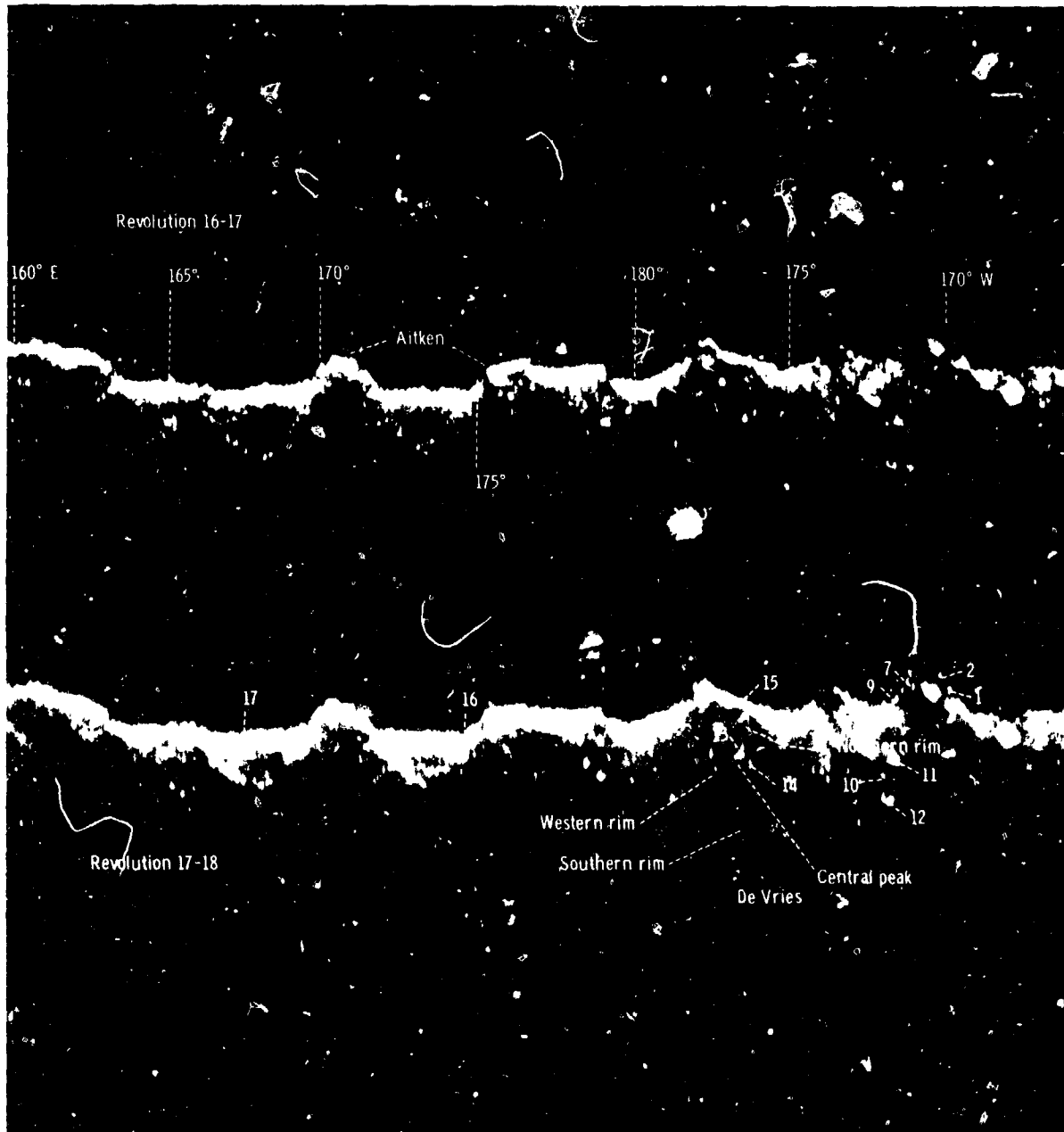
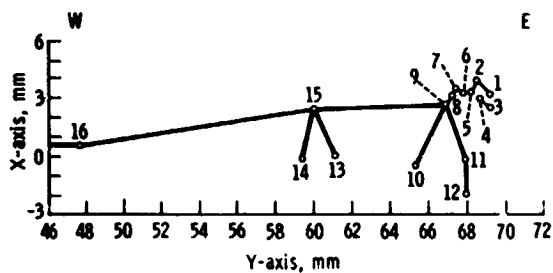
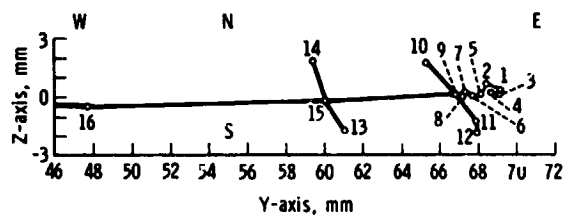


Figure 34-20.- Stereoscopic radar image in the central region of the lunar far side composed of 60-m-wavelength ALSE imagery obtained on revolutions 16-17 and 17-18. The numbered points correspond to those in figure 34-21 and are explained in the text.

ORIGINAL PAGE IS  
OF POOR QUALITY



(a) Profile.



(b) Map.

Figure 34-21.- Plots of the stereoscopic image coordinates of points numbered in figure 34-20 as seen by stereoscopic viewing of the 60-m-wavelength ALSE images along revolutions 16-17 and 17-18. Coordinates are measured at the scale of the original 70-mm image film.

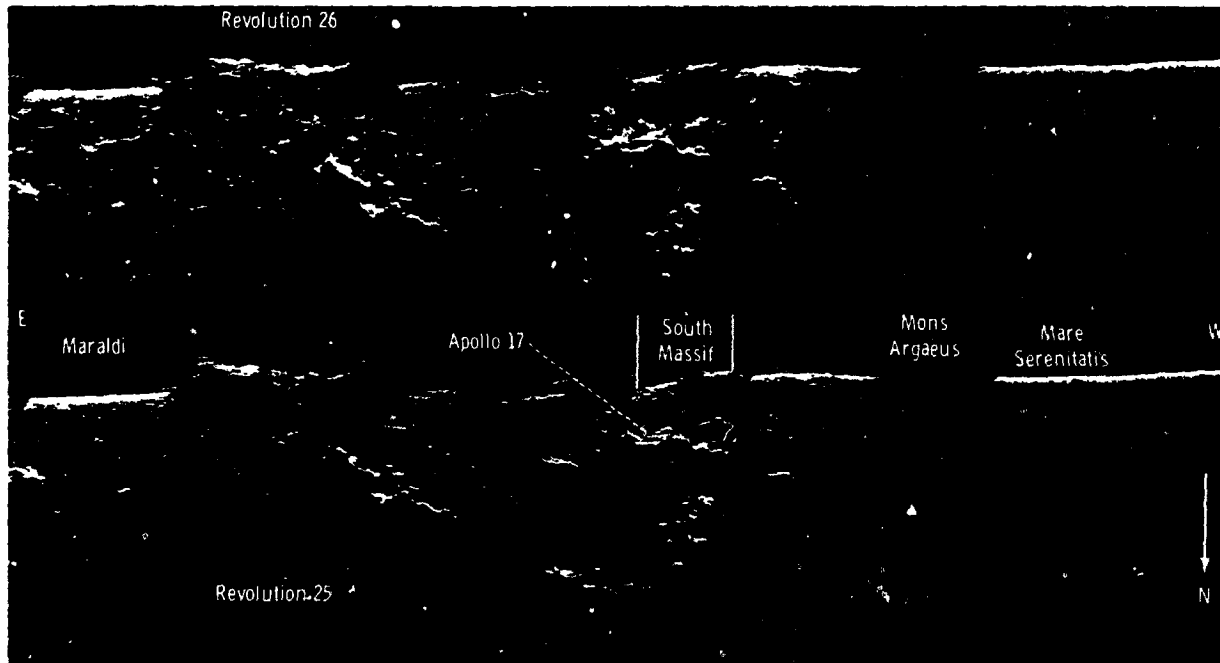


Figure 34-22.- Stereoscopic 2-m-wavelength ALSE radar image composed of imagery obtained on revolutions 25 and 26. The image covers a large region extending from southeastern Mare Serenitatis eastward across the mountains forming the southeastern border of the Serenitatis basin. The Apollo 17 landing site is near the center of the figure. The brightness change located approximately one-fourth of the distance from the profile to the opposite edge of the image is introduced by the sensitivity time control. The dark vertical band, approximately 30 km wide, through Mons Argæus is due to the automatic gain control. The imagery north of the groundtracks is systematically brighter than that south of the groundtracks because of the nature of the radar antenna pattern. Thus, most of the scenery lies north of the groundtracks. Hence, in order to orient the profiles right side up, north is downward in the side-looking imagery, and, in order to place the features in the northward side-looking imagery in a distribution like that on a map, these images are printed with east on the left.

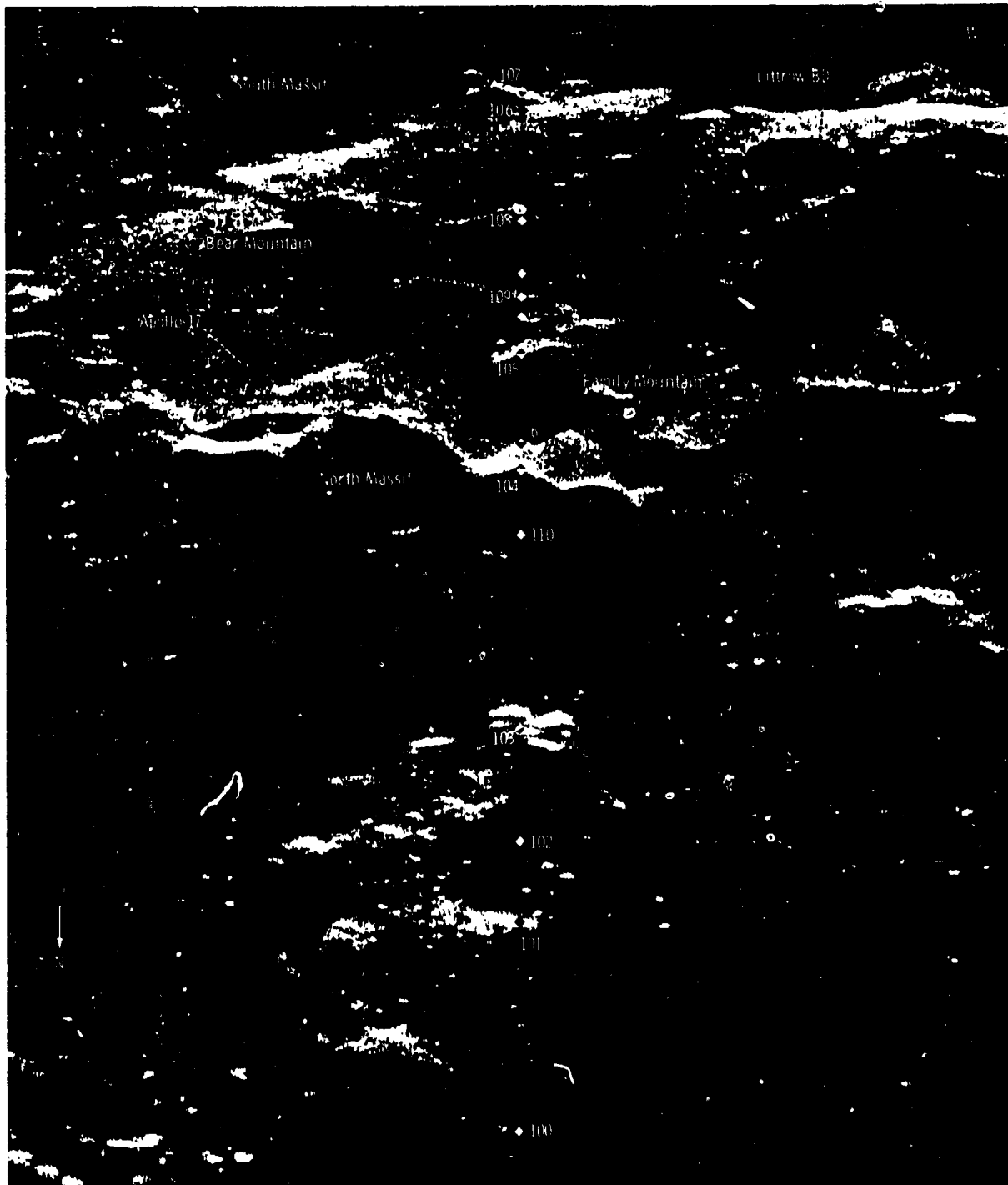


Figure 34-23.- ALSE 2-m-wavelength image of the area around the Apollo 17 landing site obtained during revolution 25. See figure 34-22 for the appearance of the scene in a stereoscopic view. The numbered points correspond to those in figure 34-24. The crater Littrow BD is 4 km in diameter.

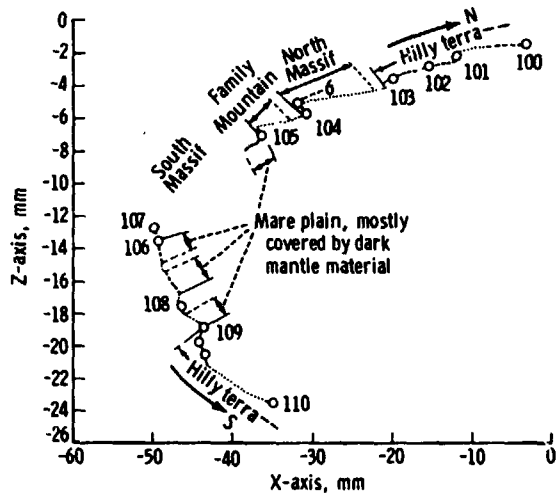


Figure 34-24.- Profile through the stereoscopic image in figure 34-22. The profile is in a plane oriented perpendicular to both the surface profile and the plane of the page in figure 34-22. The profile runs through the numbered points in figure 34-23.

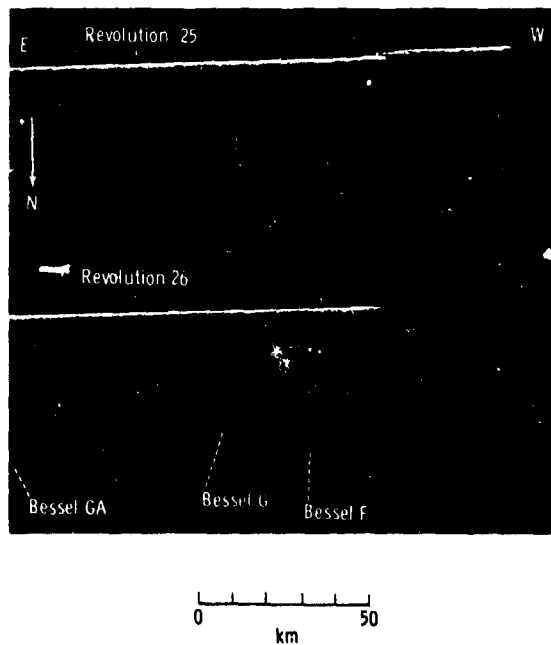


Figure 34-25.- Stereoscopic 2-m-wavelength ALSE radar image in southwestern Mare Serenitatis obtained on revolutions 25 and 26. The image shows two kilometer-size craters with radar-bright halos, Bessel G and Bessel F. A mare ridge trends from the lower right corner of the figure up across the surface profile image and thence eastward along the southern limb of the stereoscopic image. Where the ridge crosses the profile, it may be seen to mark a substantial step in the mare surface with the peripheral part of the mare standing higher.

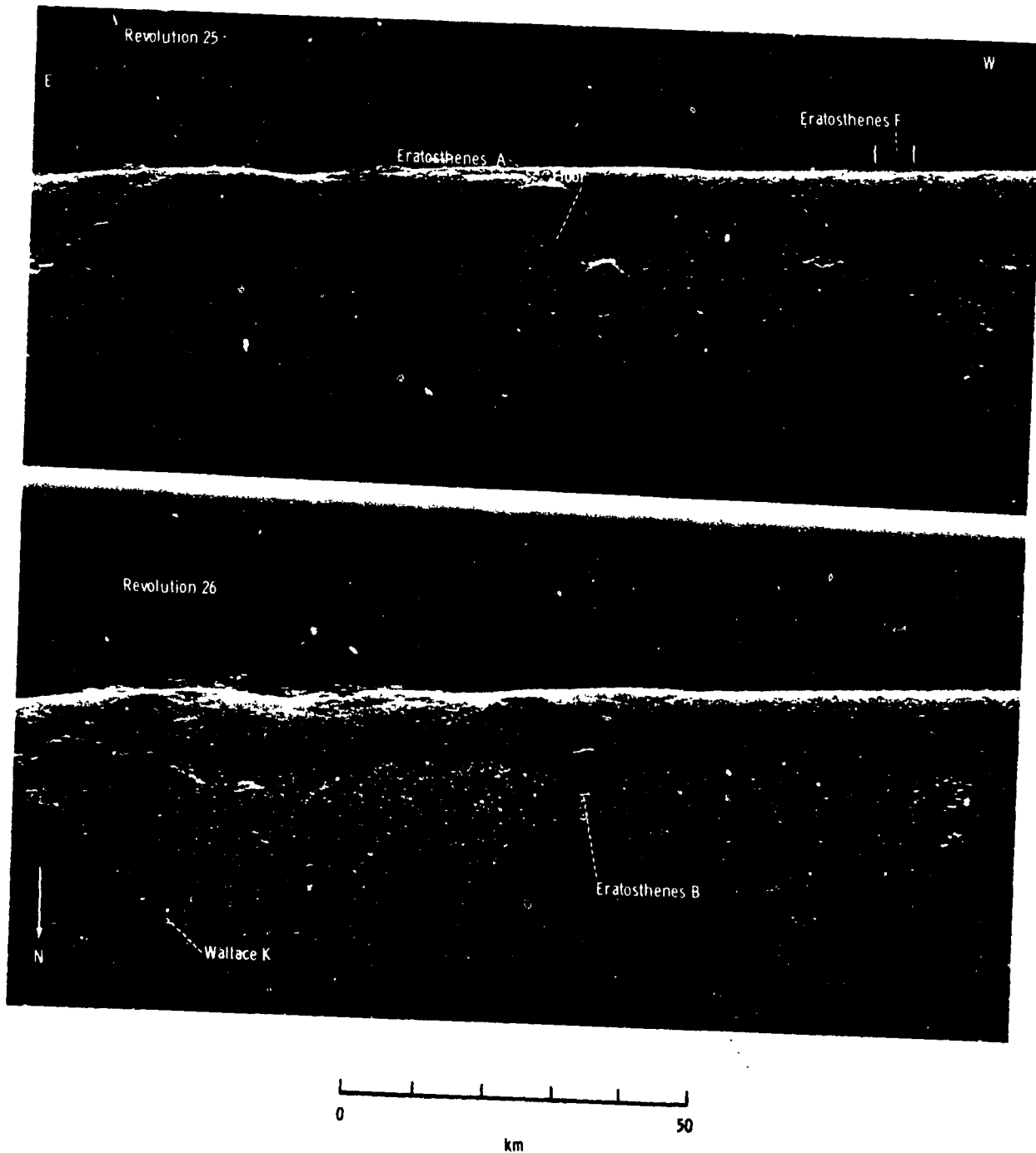


Figure 34-26.- Stereoscopic 2-m-wavelength ALSE radar image of southeastern Mare Imbrium composed of imagery obtained on revolutions 25 and 26. The stereoscopic image includes a variety of typical craters a few kilometers in diameter.

ORIGINAL PAGE IS  
OF POOR QUALITY

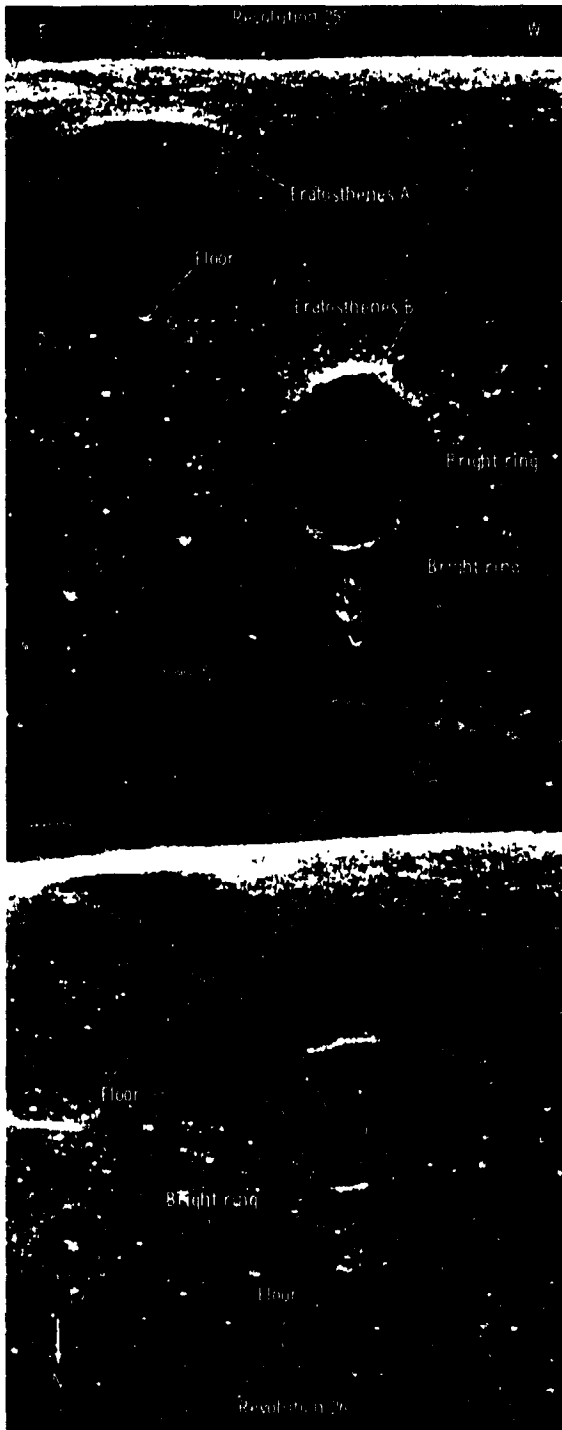


Figure 34-27.- Stereoscopic radar image of the 6-km-diameter crater Eratosthenes B with Eratosthenes A and other smaller nearby craters. Enlarged from figure 34-26.

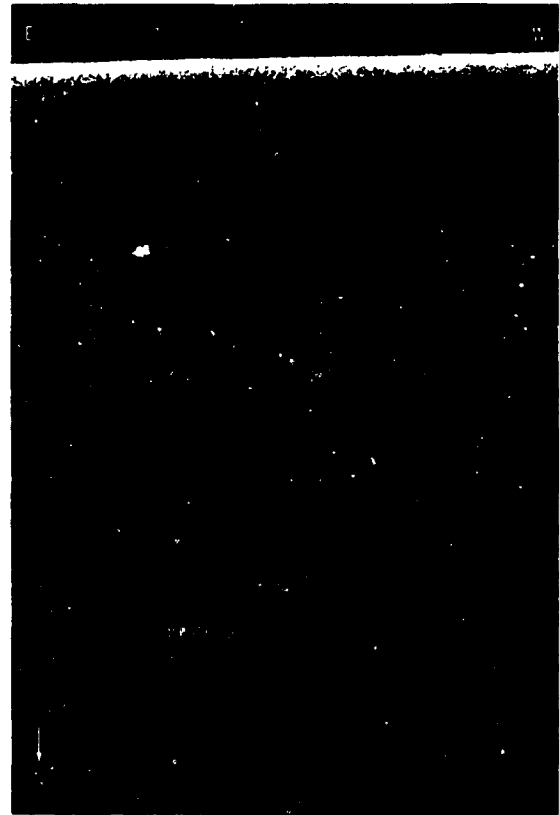


Figure 34-28.- Enlarged 2-m-wavelength ALSE image of the 1.2-km-diameter crater Bessel G and its surrounding radar-bright halo, obtained during revolution 26.

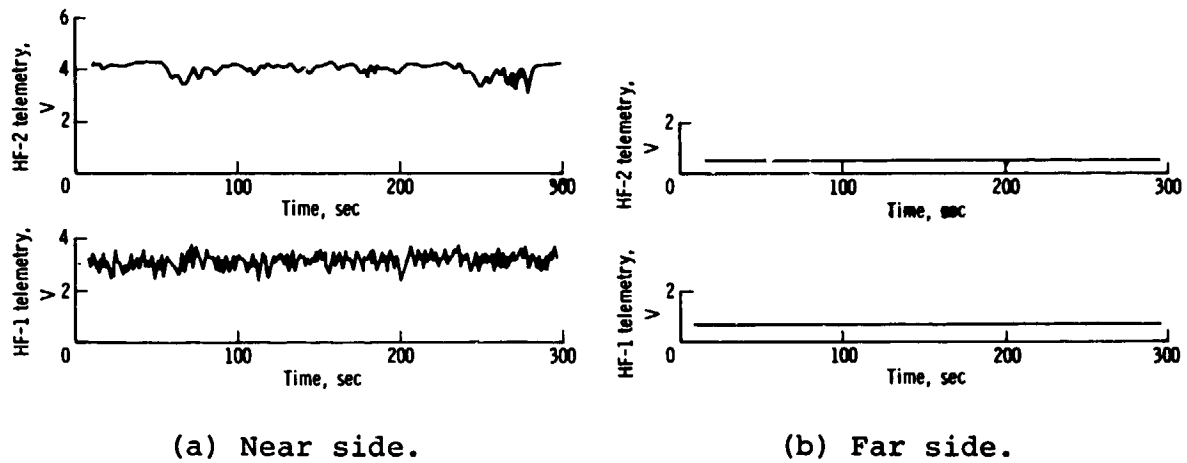


Figure 34-29.- Telemetry recordings of the receive-only noise levels observed on the lunar near side and far side.

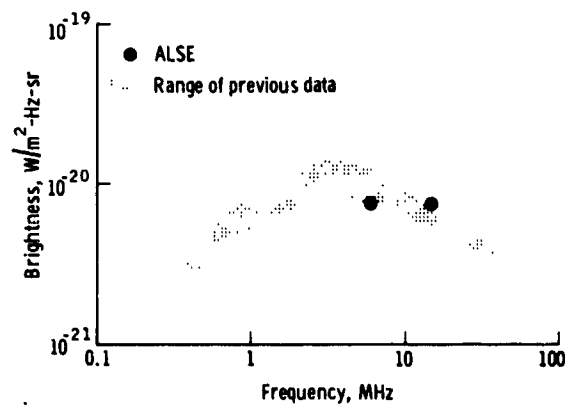
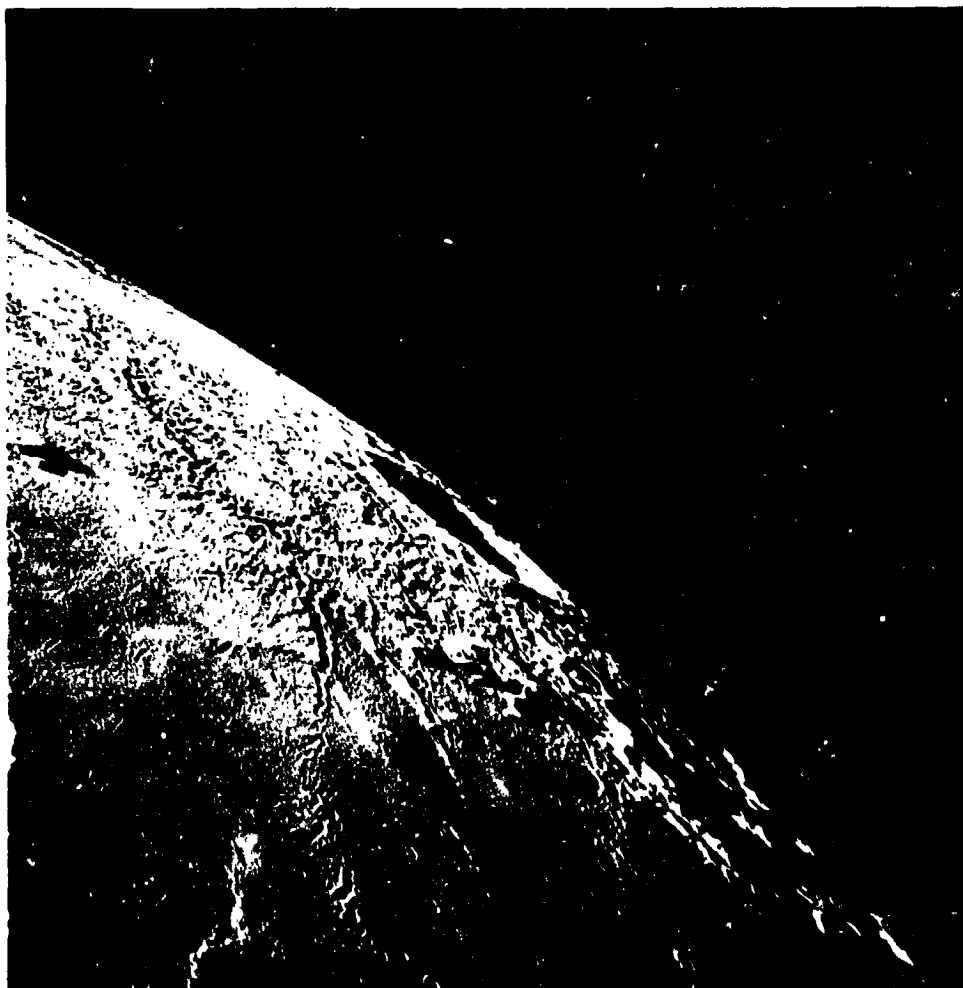


Figure 34-30.- Preliminary determination of noise brightness from the ALSE HF-1 and HF-2 channels. Range of results from other investigators (ref. 34-7) is also shown.

35. LASER ALTIMETER (NASA EXPERIMENT S-175)

NSSDC IDENTIFICATION NUMBERS:

APOLLO 15	71-063A-05
APOLLO 16	72-031A-05
APOLLO 17	72-096A-09



ORIGINAL PAGE IS  
OF POOR QUALITY

CONTENTS - SECTION 35

	Page
INSTRUMENT DESCRIPTION . . . . .	35-3
MISSION OPERATIONS . . . . .	35-4
Apollo 15 Mission . . . . .	35-4
Apollo 16 Mission . . . . .	35-4
Apollo 17 Mission . . . . .	35-5
ANALYTICAL TECHNIQUES . . . . .	35-5
PRELIMINARY RESULTS . . . . .	35-6
CONCLUSIONS . . . . .	35-8
ALTIMETRY DATA ARCHIVED AT NSSDC . . . . .	35-8
REFERENCES . . . . .	35-9
BIBLIOGRAPHY . . . . .	35-10

### 35. LASER ALTIMETER

The laser altimeter and cameras carried in the scientific instrument module bay of the Apollo 15, 16, and 17 spacecraft represent an integrated system capable of yielding high-quality quantitative data on the Moon. Laser altimetry, used in conjunction with known spacecraft positions, can yield data on the shape and size of the Moon, on the large-scale topography of the Moon, and on the center-of-mass displacement in the Moon with respect to the geometric center thereof. The altimeter used on the missions is a ruby-laser type that can function successfully in an altitude range of approximately 74 to 178 km, either with the metric (mapping) camera or independently. In the camera mode, the laser altimeter ranges at the time of each exposure, which varies between 20 and 28 sec (i.e., 30 to 43 km along the lunar surface). In the independent mode, the laser altimeter ranges every 20 sec.

These altitude data and the spacecraft attitudes derived from simultaneous stellar photography are used in the photogrammetric reduction of corresponding lunar surface photographs to ensure accurate results when cartographic products are generated. In addition, the altimeter measurements alone can be used to determine broad-scale topographic relief around the entire circumference of the Moon. These data are useful in investigating the selenodetic figure of the Moon and may provide information regarding gravitational anomalies on the lunar far side.

#### INSTRUMENT DESCRIPTION

The laser altimeter weighs approximately 22.5 kg (50 lb) and consists of a ruby laser, transmitting and receiving optics and telescopes, and a range counter. When a signal is received from the control circuit (ref. 35-1), the pulse-forming network discharges through flashlamps and produces a light pulse that primes the ruby rod such that light amplification occurs. A Q-switch is then used to transfer the light pulse to the output resonant reflector. At this point, the output beam of the laser has a diameter of 0.635 cm (0.25 in.) and a width of 4.8 mrad. A 16-power telescope then expands the beam dimensions to a 10.16-cm (4 in.) diameter and a 0.3-mrad width. The expanded beam would cover a 30-m-diameter spot on the lunar surface from a

spacecraft altitude of 100 km. A portion of the output is applied to a photodiode to generate a start pulse, which is sent to the range counter through a delay line. The delay line is calibrated to compensate for the delay through the receiver photomultiplier and the video amplifier. The range counter counts increments of 6.67 nsec (supplied by a 149.8962-MHz crystal oscillator) and thereby provides a 1-m resolution. The return pulse, which is reflected from the lunar surface, is applied to the photomultiplier tube through the receiver telescope. The electrical output of the photomultiplier, amplified by the video amplifier, stops the range counter.

#### MISSION OPERATIONS

The mission operations relative to the laser altimeter are discussed in the following paragraphs.

##### Apollo 15 Mission

During the Apollo 15 mission, test data were obtained during partial passes of lunar revolutions 3 to 9 and primarily on the lunar far side, when the command and service module (CSM) altitude above the lunar surface exceeded 75 km. Test data were obtained for two complete 360° passes during revolutions 15-16 and 21-22. During revolutions 22 and 23, telemetry indications of anomalous altimeter performance began to appear. The altimeter performance gradually degraded during revolutions 26, 27, and 33; during revolution 38, the altimeter stopped recording valid altitude data. Altimeter data were reduced only for the two full passes; namely, 15-16 and 21-22.

##### Apollo 16 Mission

During the Apollo 16 mission, laser altimeter measurements were obtained during data periods corresponding to lunar revolutions 3 and 4, 17 and 18, 28 and 29, 37 to 39, 47 and 48, 60, and 63. Most of the time, the altimeter was operated under mapping camera control. At least four of the data periods contained measurements made during an entire revolution plus some overlap. A fifth period, revolutions 37 to 39, contained measurements made during almost two full consecutive revolutions. Although a system modification had been incorporated to avoid the short lifetime of the instrument experienced during the Apollo 15 mission, the instrument performance was somewhat degraded during the second operating period and continued to degrade

during subsequent operating periods. The laser altimeter stopped recording valid data during revolution 63. A total of 2372 laser firings was made during the mission.

#### Apollo 17 Mission

Several changes were made in the Apollo 17 laser altimeter in an attempt to avoid the degraded performance experienced during the Apollo 15 and 16 missions. The major modifications were (1) a change to an oil-impregnated type of bearing in the Q-switch rotor to eliminate contamination of the optical surfaces and (2) a change to high-quality quartz (Suprasil) envelopes on flashlamps to maintain a higher flashlamp light output level. The laser altimeter operated excellently throughout the mission; so well that it was turned on for six consecutive revolutions toward the end of the mission. Laser firings totaling 4026 were made on lunar revolutions 1 and 2, 13 and 14, 15, 23 and 24, 27 to 29, 38 and 39, 49, 62 and 63, 65 and 66, 67 to 72, and 73 and 74 and resulted in approximately 9 complete sets of data containing measurements for the entire circumference of the Moon in the orbital plane.

#### ANALYTICAL TECHNIQUES

An accurate estimate of spacecraft position with respect to the Moon is required for the interpretation of altimeter measurements to be used for selenodetic investigations. This estimate was made by reducing the Earth-based Doppler radio-tracking data for the orbiting CSM. These data are essentially line-of-sight velocity measurements taken every 10 sec by at least two tracking stations of the Spaceflight Tracking and Data Network. The Doppler data are processed by using a weighted least-squares technique to determine a unique orbit for the CSM. A theoretical model of the Earth-Moon system is included in the computations. The accuracy of the determined orbit limits the accuracy of the laser altimeter results. The dominant error source in the orbit determination and trajectory prediction process is the mathematical model used to describe the lunar gravitational effects. No known mathematical model accurately describes the observed gravitational effects, at least in a global sense. (The far side has never been measured.) The absolute radial position uncertainty is approximately 400 m; however, the relative-radial-position uncertainty for successive altimetry points along an orbital track is estimated to be less than 10 m. Furthermore, the relative position uncertainty for two nearly parallel tracks will be appreciably less than 400 m,

because the two orbits will be affected similarly by the principal error source, the inadequacy of the gravitational model.

After the spacecraft orbit has been determined, the laser altimeter measurements are subtracted from the corresponding selenocentric radius vectors of the CSM orbit to obtain complete lunar topographic profiles. Because the CSM orbit is a dynamic solution about the center of gravity (c.g.) of the Moon, the profile is referenced to the c.g. rather than to the geometric center. The c.g. is also the more important center, of course, in analyzing the structural significance of the topographic elevations. Corrections are applied for timing and laser pointing to adjust the slant range measurements to altitudes above the local vertical. The data required to make these corrections are available. These corrections, however, should not significantly change the preliminary results discussed in the following paragraphs.

#### PRELIMINARY RESULTS

The general lunar surface coverage for the three Apollo missions is shown in figures 35-1 and 35-2. In these figures, the groundtrack for one selected data period (corresponding to specific revolutions) from each mission was used. The following results and comments were extracted from references 35-2 to 35-4.

The topographic profile that resulted from the processing of Apollo 15 altimeter measurements (obtained during revolution 15-16), as outlined previously, is presented in figure 35-3.<sup>1</sup> Many interesting details, the most noticeable of which are the extreme altitude variations on the lunar far side, can be seen in this profile. The altitude profile also illustrates that the lunar far side is considerably rougher than the near side, at least in this plane of measurement. The most intriguing far-side feature is what appears to be, in the gross shape, a very large depression the deepest point of which is located at approximately 180° longitude (near Van de Graaff). The depression extends approximately 47° in a longitudinal direction, a distance corresponding to approximately 1400 km

---

<sup>1</sup>This profile and the Apollo 16 and 17 profiles are shown as elevations with respect to a sphere having a radius of 1738 km (centered at the lunar center of mass). The value of 1738 km was used because it is the mean radius of the lunar limb (ref. 35-5).

on the lunar surface. The extent of this feature in a latitudinal direction cannot be ascertained. On the lunar near side, the maria are shown to be depressed with respect to the surrounding terrae. The deepest depression was measured in Mare Smythii. The ringed maria, Smythii, Crisium, and Serenitatis, are essentially flat. Mare Imbrium appears to slope upward slightly in the direction of Oceanus Procellarum, which, in turn, is relatively flat.

The topographic profile that resulted from the processing of Apollo 16 altimeter measurements (obtained during revolutions 17 and 18) is presented in figure 35-4. There is very good agreement between the Apollo 15 and Apollo 16 altitude measurements where the two trajectories crossed, particularly in the flat region of Mare Smythii. The central highlands near the Apollo 16 landing site are a definite high region, having a radius very close to the presently accepted mean radius of 1738 km. The profiles of the large near-side basins with their flat floors are very evident in the figure. The large far-side depression observed in Apollo 15 data is not evident in the Apollo 16 data. At a point near the longitudinal center of the depression, the groundtracks were widely separated. That is, at a longitude of approximately  $180^\circ$ , the Apollo 16 groundtrack was approximately  $35^\circ$  north of the Apollo 15 groundtrack. The large far-side basins of Hertzsprung and Mare Mendeleev can be seen in the Apollo 16 profile.

The topographic profile resulting from processing the Apollo 17 altimeter measurements, obtained during revolutions 27 to 29, is presented in figure 35-5. For most of the large near-side features, the altitudes are remarkably close to those measured during the Apollo 15 experiment; the groundtrack of the Apollo 15 experiment is usually within approximately 200 km of that of the Apollo 17 experiment. The elevations of the adjacent maria, Serenitatis and Crisium, are virtually the same in both the Apollo 15 and 17 data. The pronounced near-side feature unique to the Apollo 17 data is the deep crater Neper. On the far side, the Apollo 17 altitude profile resembles the Apollo 15 altitude profile; but, because the far-side terrain is extremely rough, only a qualitative comparison can be made. The Apollo 17 data show a depression near  $180^\circ$  longitude, but the depression is not quite as broad or as deep as observed in the Apollo 15 data; the greatest depth is approximately 4 km below a 1738-km-radius sphere. There appears to be reasonable agreement where the Apollo 17 and Apollo 16 groundtracks intersect.

## CONCLUSIONS

The Apollo 15, 16, and 17 topographic profiles show that the lunar far side may be considerably rougher than previously anticipated and indicate the presence of very extensive mountainous and highland regions. The large far-side depression may possibly be correlated with the Russian feature observed in Zond 6 photography (ref. 35-6). The large near-side basins, particularly the ringed maria, appear to be depressed with respect to surrounding terrae. This observation agrees with previous independent knowledge. Least-squares regressions have been performed, using the laser altimeter measurements, to estimate the lunar-shape parameters relative to the optical center. Results from this processing indicate that the center of gravity of the Moon is some 2 km closer to the Earth than the optical center and is displaced approximately 1 km eastward. These data apparently are insufficient to enable estimating the displacement along the lunar polar axis.

## ALTIMETRY DATA ARCHIVED AT NSSDC

The measurements obtained during the Apollo 15, 16, and 17 laser altimeter experiments will be placed in permanent archives at the National Space Science Data Center (NSSDC). Also, the corresponding spacecraft ephemeris and attitude data and the Earth-based radio-tracking observations required to generate independent ephemerides will be archived. These data will be documented in NASA Technical Notes to enable wide dissemination. The specific data that will be archived are as follows.

1. Raw laser altimeter slant range measurements
2. Laser altimeter measurements adjusted to height above local vertical surface
3. Spacecraft attitude data required to calculate altimeter-pointing direction
4. Spacecraft positions at laser altimeter measurement times
5. Earth-based Doppler frequency shift measurements required to compute independent spacecraft positions

## REFERENCES

- 35-1. Anon.: Operating and Instruction Manual for Laser Altimeter. RCA (Burlington, Mass.), CR70-588-14J1, 1970.
- 35-2. Wollenhaupt, W. R.; and Sjogren, W. L.: Comments on the Figure of the Moon Based on Preliminary Results from Laser Altimetry. *The Moon*, vol. 4, nos. 3/4, June/July 1972, pp. 337-347.
- 35-3. Sjogren, W. L.; and Wollenhaupt, W. R.: Lunar Shape Via the Apollo Laser Altimeter. *Science*, vol. 179, no. 4070, Jan. 19, 1973, pp. 275-278.
- 35-4. Wollenhaupt, W. R.; Sjogren, W. L.; Lingenfelter, R. E.; Schubert, G.; and Kaula, W. M.: Apollo 17 Laser Altimeter. Sec. 33, Part E, of Apollo 17 Preliminary Science Report, NASA SP-330, 1973.
- 35-5. Van Flandern, Thomas C.: Some Notes on the Use of the Watts Limb-Correction Charts. *Astron. J.*, vol. 75, no. 6, Aug. 1970, pp. 744-746.
- 35-6. Rodionov, B. N.; Isavnina, I. V.; Avdeev, Yu.F.; Blagov, V. D.; et al.: New Data on the Configuration and Relief of the Moon from the Results of Processing Photographs Furnished by Zond-6. *Kosmicheskie Issledovaniya*, vol. 9, May-June 1971, pp. 450-458.

## BIBLIOGRAPHY

- Adler, I.; Trombka, J.; Gerard, J.; Lowman, P.; et al.:  
Apollo 15 Geochemical X-Ray Fluorescence Experiment:  
Preliminary Report. *Science*, vol. 175, no. 4020, Jan. 28,  
1972, pp. 436-440.
- Baldwin, Ralph B.: Ancient Giant Craters and the Age of the  
Lunar Surface. *Astron. J.*, vol. 74, no. 4, May 1969,  
pp. 570-571.
- Campbell, Malcolm J.; and Ulrichs, Juris: Electrical Prop-  
erties of Rocks and Their Significance for Lunar Radar  
Observations. *J. Geophys. Res.*, vol. 74, no. 25, Nov. 15,  
1969, pp. 5867-5881.
- Carr, M. H.: Geologic Map of the Mare Serenitatis Region  
of the Moon. U.S. Geol. Survey Misc. Geol. Inv. Map  
I-489, 1966.
- Carr, M. H.; Howard, K. A.; and El-Baz, Farouk: Geologic  
Maps of the Apennine-Hadley Region of the Moon: Apollo 15  
Pre-Mission Maps. U.S. Geol. Survey Misc. Geol. Inv. Map  
I-723, 1971.
- Gault, Donald E.: Saturation and Equilibrium Conditions for  
Impact Cratering on the Lunar Surface: Criteria and  
Implications. *Radio Sci.*, vol. 5, no. 2, Feb. 1970,  
pp. 273-291.
- Gold, T.; Bilson, E.; and Yerbury, M.: Grain Size Analysis  
and High Frequency Electrical Properties of Apollo 15 and  
16 Samples. Lunar Science IV (Abs. of papers presented  
at the Fourth Lunar Science Conference (Houston, Tex.),  
Mar. 5-8, 1973), pp. 293-294.
- Hagfors, T.: Relationship of Geometric Optics and Auto-  
correlation Approaches to the Analysis of Lunar and  
Planetary Radar. *J. Geophys. Res.*, vol. 71, no. 2,  
Jan. 15, 1966, pp. 379-383.
- Head, James W.: Distribution and Interpretatio. of Crater-  
Related Facies: The Lunar Crater Aristarchus. *Trans. Am.  
Geophys. Union*, vol. 50, no. 11, Nov. 1969, p. 637.
- Howard, H. T.; and Tyler, G. L.: Bistatic-Radar Investi-  
gation. Sec. 17 of Apollo 14 Preliminary Science Report.  
NASA SP-272, 1971.

Howard, H. T.; and Tyler, G. L.: Bistatic-Radar Investigation. Sec. 23 of Apollo 15 Preliminary Science Report. NASA SP-289, 1972.

Howard, H. T.; and Tyler, G. L.: Bistatic-Radar Investigation. Sec. 25 of Apollo 16 Preliminary Science Report. NASA SP-315, 1972.

Kuiper, Gerard P.; Whitaker, E. A.; Strom, R. G.; Fountain, J. W.; and Larson, S. M.: Consolidated Lunar Atlas. U.S.A.F. Photographic Lunar Atlas, Supp. nos. 3 and 4, Lunar and Planetary Lab., Univ. of Arizona, 1967.

Lucchitta, B. K.: Evaluation of Photometric Slope Deviation. Analysis of Apollo 10 Photography and Visual Observations. NASA SP-232, 1971, pp. 31-35.

McCord, T. B.; Charette, M. P.; Johnson, T. V.; Lebofsky, L. A.; and Pieters, C.: Spectrophotometry (0.3 to 1.1 micron) of Visited and Proposed Apollo Lunar Landing Sites. The Moon, vol. 5, Sept. 1972, pp. 52-89.

McCord, Thomas B.; and Johnson, Torrence V.: Relative Spectral Reflectivity (0.4-1 $\mu$ ) of Selected Areas of the Lunar Surface. J. Geophys. Res., vol. 74, no. 17, Aug. 15, 1969, pp. 4395-4401.

McCord, Thomas B.: Color Differences on the Lunar Surface. J. Geophys. Res., vol. 74, no. 12, June 15, 1969, pp. 3131-3142.

Milton, D. J.: Geologic Map of the Theophilus Quadrangle of the Moon. U.S. Geol. Survey Misc. Geol. Inv. Map I-546, 1968.

Moore, H. J.: Geological Map of the Aristarchus Region of the Moon. U.S. Geol. Survey Misc. Geol. Inv. Map I-465, 1965.

Moore, H. J.: Geological Map of the Seleucus Quadrangle of the Moon. U.S. Geol. Survey Misc. Geol. Inv. Map I-527, 1965.

Muller, P. M.; and Sjoqren, W. L.: Mascons: Lunar Mass Concentrations. Science, vol. 161, no. 3843, Aug. 16, 1968, pp. 680-684.

Parker, M. N.; and Tyler, G. L.: Bistatic-Radar Estimation of Surface-Slope Probability Distributions with Applications to the Moon. Radio Science, vol. 8, no. 3, Mar. 1973, pp. 177-184.

- Pieters, C.; McCord, T. B.; Zisk, S. H.; and Adams, J. B.: Lunar Black Spots and the Nature of the Apollo 17 Landing Area. *J. Geophys. Res.*, vol. 78, no. 26, Sept. 10, 1973.
- Pike, Richard J.: Preliminary Quantitative Terrain-Analysis Results from Three Apollo 10 Photographs. Analysis of Apollo 10 Photography and Visual Observations. NASA SP-232, 1971, pp. 5-14.
- Riley, L. A.; and Hall, J. S.: High Resolution Measures of Polarization and Color of Selected Lunar Areas. *Lowell Observatory Bull. No. 159*, vol. VII, no. 22.
- Roberson, F. I.; and Kaula, W. M.: Apollo 15 Laser Altimeter. Sec. 25, Part D, of Apollo 15 Preliminary Science Report. NASA SP-289, 1972.
- Shorthill, Richard W.: Infrared Atlas Charts of the Eclipsed Moon. *The Moon*, vol. 7, nos. 1/2, Mar./Apr. 1973, pp. 22-45.
- Shorthill, R. W.; and Saari, J. M.: Nonuniform Cooling of the Eclipsed Moon: A Listing of Thirty Prominent Anomalies. *Science*, vol. 150, no. 3693, Oct. 8, 1965, pp. 210-212.
- Stuart-Alexander, Desiree E.; and Howard, Keith A.: Lunar Maria and Circular Basins - A Review. *Icarus*, vol. 12, no. 3, May 1970, pp. 440-456.
- Thompson, Thomas W.; and Zisk, Sidney [Stanley] H.: Radar Mapping of Lunar Surface Roughness. In *Thermal Characteristics of the Moon*, MIT Press (Cambridge, Mass.), 1972, pp. 83-117.
- Thompson, T. W.; Masursky, H.; Shorthill, R. W.; Zisk, S. H.; and Tyler, G. L.: A Comparison of Infrared Radar and Geologic Mapping of Lunar Craters. Lunar Science Institute, Symposium on the Geophysical Interpretation of the Moon (Houston, Tex.), June 1970.
- Thompson, T. W.; Shorthill, R. W.; Whitaker, F. A.; and Zisk, S. H.: Mare Serenitatis: A Preliminary Definition of Surface Units by Remote Observations. Lunar Science Institute, Symposium on the Geophysical and Geochemical Exploration of the Moon and Planets (Houston, Tex.), Jan. 1973.
- Tyler, G. L.; and Howard, H. T.: Dual-Frequency Bistatic-Radar Investigations of the Moon with Apollos 14 and 15. *J. Geophys. Res.*, vol. 78, no. 23, Aug. 10, 1973, pp. 4852-4874.

- Tyler, G. L.; and Ingalls, D. H. H.: Functional Dependence of Bistatic-Radar Frequency Spectra on Lunar Scattering Laws. J. Geophys. Res., vol. 76, no. 20, July 1971, pp. 4775-4785.
- Tyler, G. L.; and Simpson, R. A.: Bistatic Radar Measurements of Topographic Variations in Lunar Surface Slopes with Explorer 35. Radio Science, vol. 5, no. 2, Feb. 1970, pp. 263-271.
- Tyler, G. L.; Simpson, R. A.; and Moore, H. J.: Lunar Slope Distributions: A Comparison of Bistatic Radar and Photographic Results. J. Geophys. Res., vol. 76, no. 11, Apr. 1971, pp. 2790-2795.
- Whitaker, Ewen A.: Lunar Color Boundaries and Their Relationship to Topographic Features: A Preliminary Survey. The Moon, vol. 4, nos. 3/4, June/July 1972, pp. 348-355.
- Wilhelms, D. E.; and McCauley, J. F.: Geologic Map of the Near Side of the Moon. U.S. Geol. Survey Misc. Geol. Inv. Map I-703, 1971.
- Wise, D. U.: Pseudo-Radar Topographic Shadowing for Detection of Sub-continental Sized Fracture Systems. Proceedings of the Sixth International Symposium on Remote Sensing of Environment, vol. 1, Univ. of Mich. Press (Ann Arbor, Mich.), 1969, pp. 603-615.
- Wu, Sherman S. C.; and Moore, H. J.: Frequency Distributions of Lunar Slopes. Sec. 30, Part C, of the Apollo 16 Preliminary Science Report. NASA SP-315, 1972.
- Zisk, S. H.; and Hagfors, T.: Radar Atlas of the Moon, Final Report: Vols. 2 and 3. MIT Lincoln Lab. (Cambridge, Mass.), 1970.
- Zisk, S. H.; and Moore, H. J.: Calibration of Radar Data from Apollo 16 Results. Sec. 29, Part X, of the Apollo 16 Preliminary Science Report. NASA SP-315, 1972.

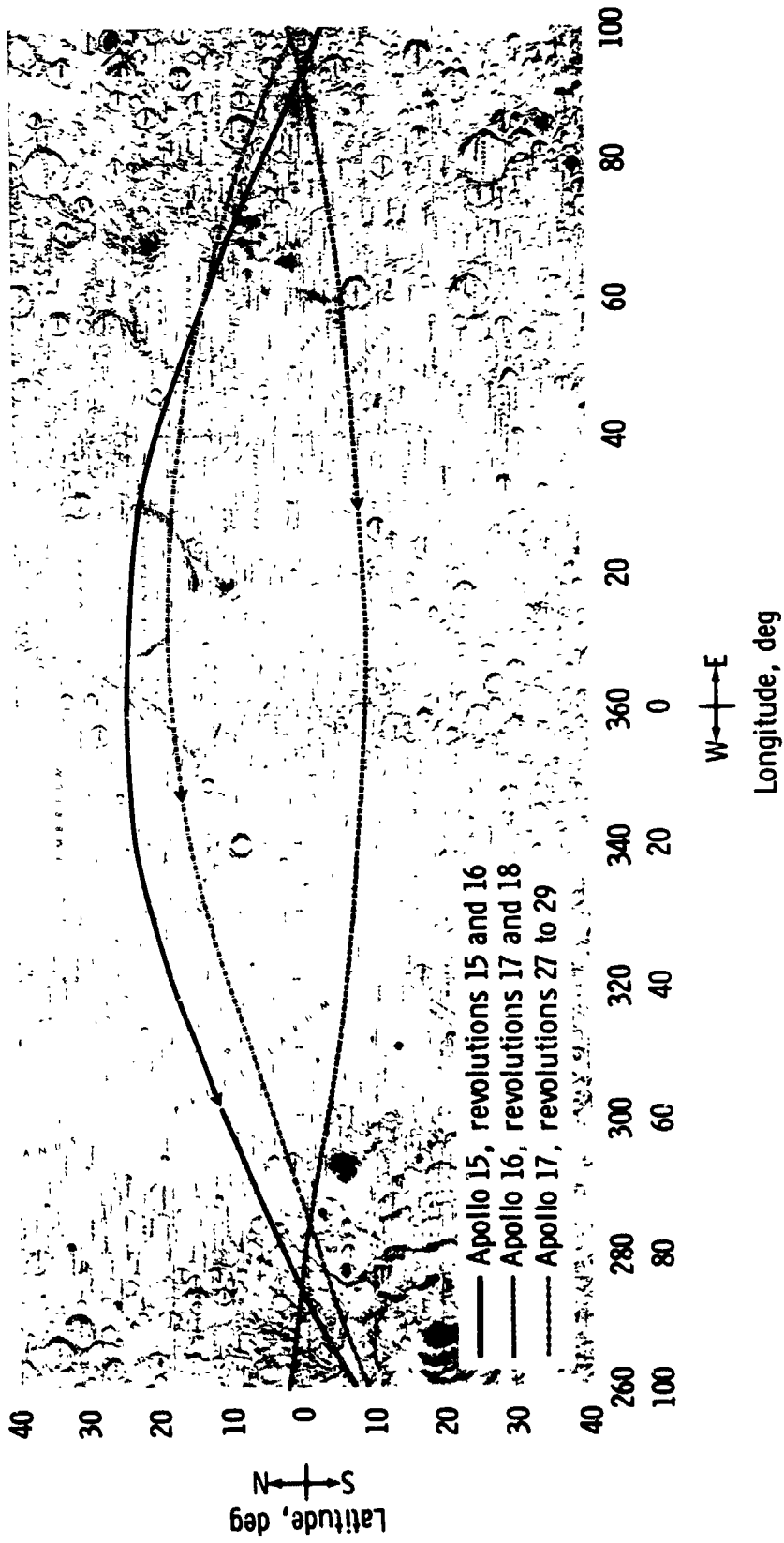


Figure 35-1.- Altimeter measurement trace (lunar near side).

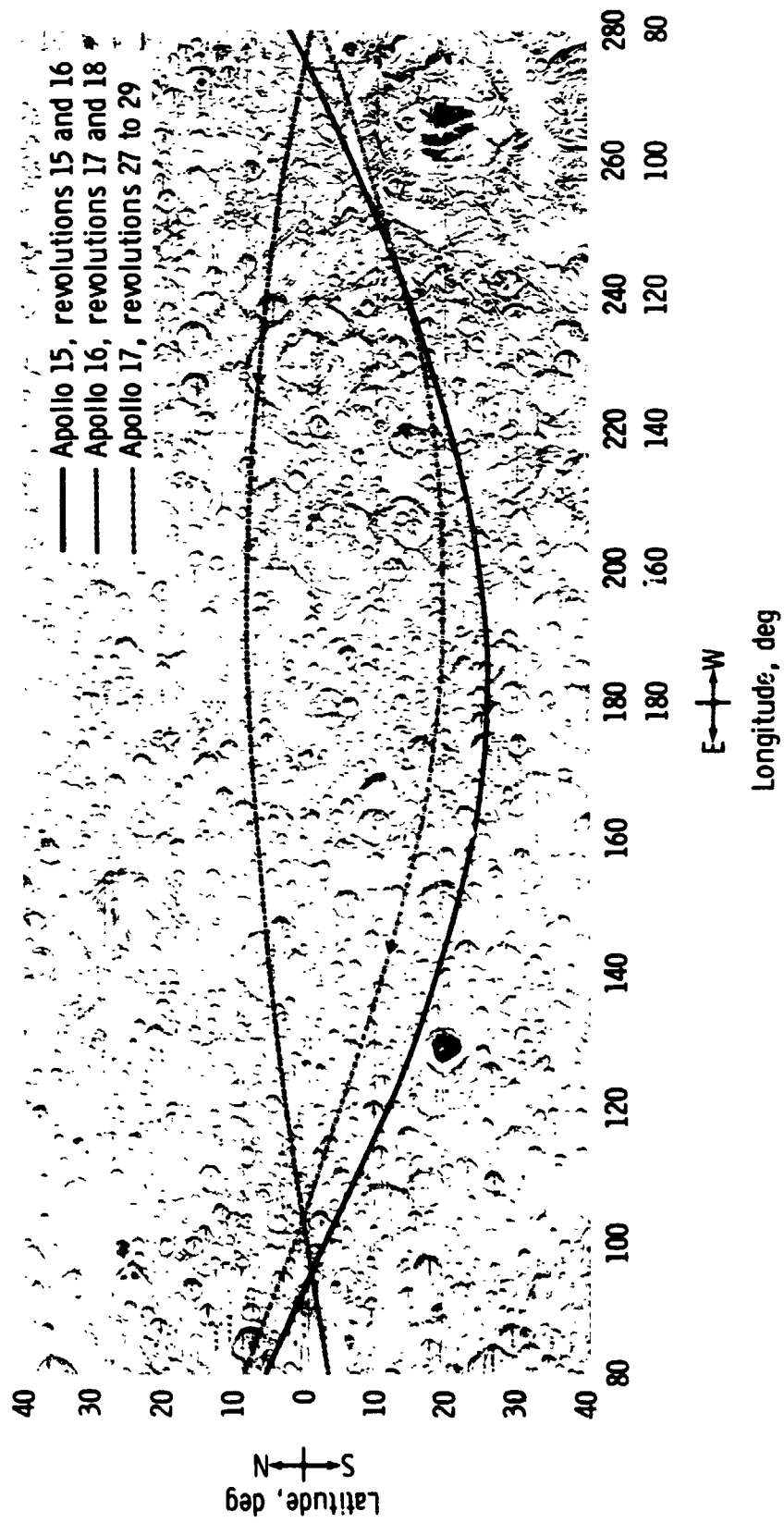


Figure 35-2.- Altimeter measurement trace (lunar far side).

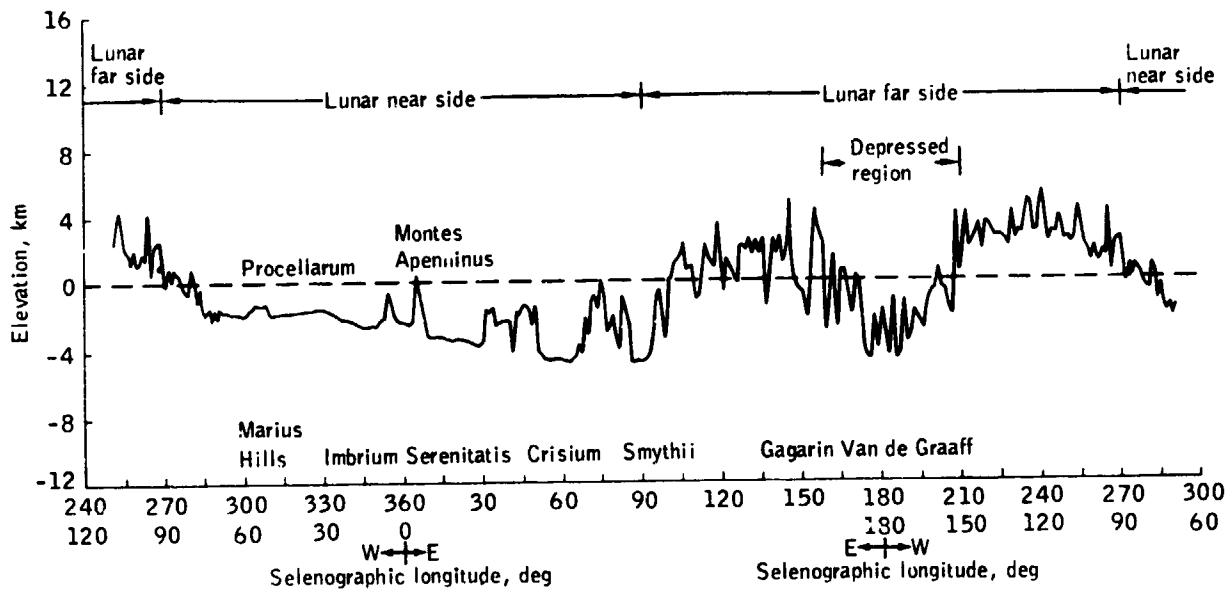


Figure 35-3.- Apollo 15 altitude profile.

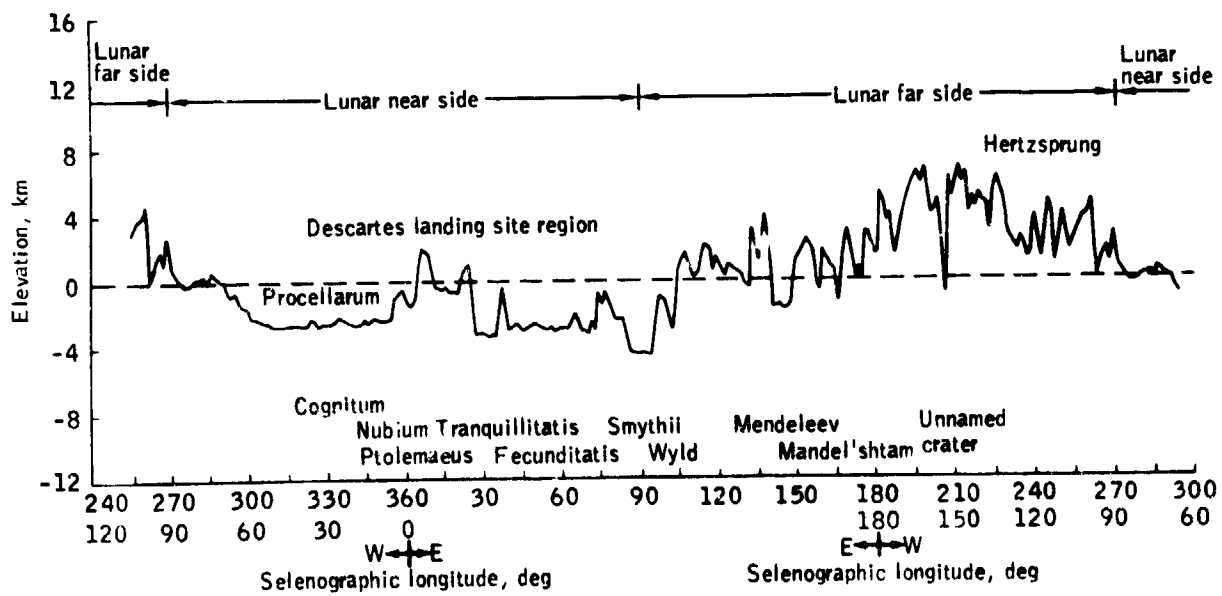


Figure 35-4.- Apollo 16 altitude profile.

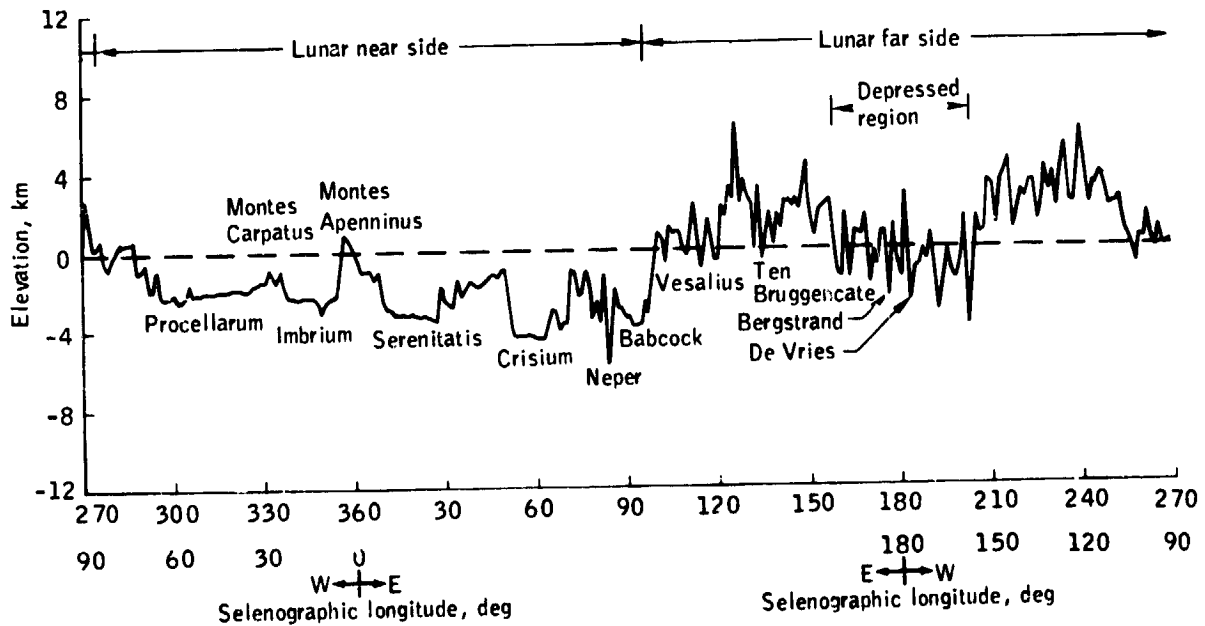
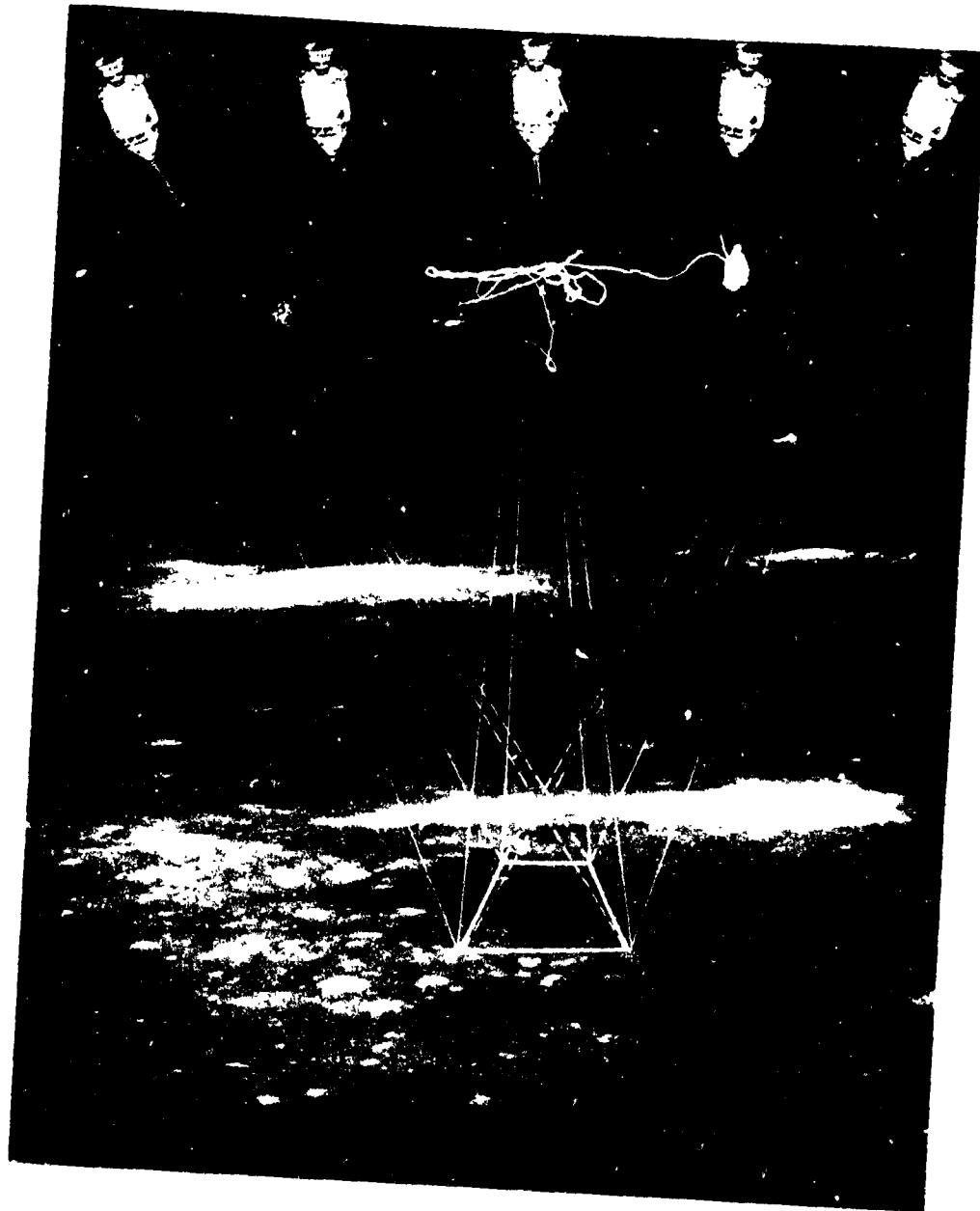


Figure 35-5.- Apollo 17 altitude profile.

36. LUNAR PHOTOGRAPHIC AND CARTOGRAPHIC PRODUCTS



CONTENTS - SECTION 36

	Page
ORBITAL PHOTOGRAPHY INDEXES . . . . .	36-3
LUNAR SURFACE PHOTOGRAPHY . . . . .	36-4
LUNAR SURFACE PHOTOGRAPHY INDEXES . . . . .	36-5
NEW LUNAR CARTOGRAPHIC PRODUCTS . . . . .	36-5
General . . . . .	36-5
1:250,000-Scale Map Products . . . . .	36-6
Special Scale Maps . . . . .	36-7
Special Purpose Maps . . . . .	36-8
LUNAR NOMENCLATURE . . . . .	36-8

## 36. LUNAR PHOTOGRAPHIC AND CARTOGRAPHIC PRODUCTS

This section discusses the availability of lunar orbital photographs and lunar surface photographs together with the indexes that are useful in locating photographs of interest. Tables 36-I and 36-II also contain limited tabulations of lunar and planetary cartographic products and their sources of availability. Current information may be obtained from the National Space Science Data Center (NSSDC).

### ORBITAL PHOTOGRAPHY INDEXES

Indexes to orbital photography are produced by the Mapping Sciences Branch of the NASA Lyndon B. Johnson Space Center and by the Department of Defense Mapping Agency (DMA) and its predecessors. The indexes are in two parts. The first part consists of lunar maps having color-printed overlays of the orbit paths, photographic center points, and outlines of the field of view of selected frames. All lunar orbital photographs taken using the Hasselblad camera (Apollo 8 to 17 missions), the Hycon camera (Apollo 14 mission), the panoramic camera (Apollo 15 to 17 missions), and the mapping camera (Apollo 15 to 17 missions) are indexed in this manner. The second part of the index is a tabular list containing the orbit revolution number, the camera lens focal length, the altitude of the spacecraft, the longitude and latitude of the photographic center point, the camera tilt and azimuth (i.e., departure from vertical), the Sun elevation, and the name of the geographic feature of primary interest in the photograph. Both the graphic and tabular indexes are extremely useful in enabling a person to select the specific photographs as long as he knows the location of the selenographic feature of interest. Several views of the same location under different lighting conditions can also be obtained by selecting photographs made at different Sun elevations and having approximately the same center point. Of special interest are photographs of the landing sites.

The Lunar Science Institute (LSI) photomap library has copies of all Apollo and Lunar Orbiter photography in the

form of both transparencies and prints. The LSI library also has copies of all relevant indexes. This collection of more than 50 000 pictures is arranged in numerical sequence. Rolls of transparencies are available for interlibrary loan. Interested individuals should have their librarian contact

Photo/Map Library Interlibrary Loan  
The Lunar Science Institute  
3303 NASA Road 1  
Houston, Texas 77058

In addition, LSI personnel will assist any person in ordering pictures from NSSDC, the distribution center for Lunar Orbiter and Apollo photographs.

#### LUNAR SURFACE PHOTOGRAPHY

Photographs were taken of the lunar surface using a 70-mm Hasselblad camera (with both a 70-mm and a 500-mm lens), a 16-mm movie camera, a television camera (with a zoom lens), and a special stereographic closeup camera. Photographs were taken to document the collection of samples and to show the general physiography of each sampling station and the distant scenery (especially with the 500-mm telephotographic lens). Beginning with the Apollo 12 mission, both astronauts on the lunar surface had cameras; therefore, different views of the same feature taken by both astronauts have different film magazine numbers. In general, the Hasselblad photograph number is referenced as follows. For NASA photograph AS15-89-11768, the prefix is the mission designation (Apollo-Saturn 15), the first two digits (89) are the magazine number, and the last five digits (11768) are the frame number.

On the Apollo 14 to 17 missions, a standard photographic sequence was established for each document sample. The sequence included the following photographs.

1. A 45.8-dm (15 ft) locator shot
2. A 33.6-dm (11 ft) down-Sun shot
3. Two 21.4-dm (7 ft) precollection shots making up a stereopair
4. A 21.4-dm (7 ft) postcollection shot

This scheme was not rigidly followed, but it does constitute the most that can be expected for sample documentation. In addition to lunar surface photography, astrogeology reports

contain the orientation of a sample and the number of the curatorial photograph, appropriately angled, showing that sample with simulated lunar surface lighting.

#### LUNAR SURFACE PHOTOGRAPHY INDEXES

Indexes to photographs taken on the lunar surface are prepared by both the U.S. Geological Survey (USGS) Astrogeology Branch and the NSSDC. Both documents have a tabular format similar to that of the orbital photography indexes except that a rough description of the subject is added. When looking for photographs of a particular sample, one can begin with the sample location and documentation document prepared by the Astrogeology Branch. This document or article has well-selected examples of the photography for each sample as well as a tabulated index of the photographs by sample number. In addition, the volume for later missions contains excerpts from air-to-ground transcripts pertaining to the collection of each sample.

Most of the astrogeology reports are no longer available, except on loan from the LSI library or the USGS library in Flagstaff, Arizona. The LSI has copies of all lunar surface, still-camera photography (Hasselblad) in both transparency and print form. The photograph indexes are available from NSSDC.

#### NEW LUNAR CARTOGRAPHIC PRODUCTS

##### General

In 1972, the NASA Lunar Programs Office initiated the Apollo Photographic Data Analysis Program. The principal objective of this program was a detailed scientific analysis of the orbital and surface experiments data derived from Apollo missions 15, 16, and 17. Another goal of the program was to produce detailed photo base maps at scales that could be used by principal investigators who were working with orbital photography and who were doing surface investigations (table 36-III). The NASA in conjunction with DMA commenced a mapping program in early 1973. This section of the handbook gives the necessary background information for users to become familiar with the cartographic products resulting from the mapping programs.

Inquiries concerning the availability of these maps should be sent to

Lunar Programs Office  
NASA Headquarters  
Washington, D.C. 20546

#### 1:250,000-Scale Map Products

Each 1:250,000-scale map sheet covers an area 4° north/south by 5° east/west. The base is compiled from vertical metric photography from Apollo missions 15, 16, and 17. In isolated instances, the Apollo oblique metric photography, the Apollo panoramic photography, and the Lunar Orbiter photography were used to fill small gaps or to extend imagery to include features within the sheet. Figures 36-1(a) and 36-1(b) illustrate the area covered by the vertical metric photography.

Each 1:250,000-scale map sheet is available in two forms:

1. Lunar topographic orthophotomap (LTO)
2. Lunar orthophotomap (LO)

The basic photographic coverage for the LTO and LO maps is the orthophotomosaic. The LTO contains the grid, names data, and relief represented by contours, elevations, and other relief symbolization as required. The LO contains only the orthophotomosaic base with the exterior grid ticks and values.

Map sheets published after May 1, 1974, have lines of longitude numbered 0° to 360° E. Latitude will still be measured in degrees north or south of the equator. A "conversion table" (table 36-IV) is included to illustrate the new procedure. For instance, 1° W is now 359°, and 2° W is now 358°, etc.

The medium scale (1:250,000) LO and LTO maps contain two grids: (1) the geographic coordinate system and (2) the lunar transverse Mercator (LTM) grid system.

Geographic coordinate system. - The origin of the system is referenced to the center of crater Mosting A (latitude 3°10'47" S, longitude 355°09'50"). Mosting A is the fundamental crater for selenographic measures. It is a small bright crater located closest to the center of the disk. Lines of longitude are numbered 0° to 360° E as referenced to the origin of longitude (NASA adopted this

procedure for maps published after May 1, 1974); lines of latitude are numbered 0° to 90° progressively north and south from the lunar equator. On the face of the map, each 1° interval is shown as a black line extending across the map, and labeled in the margin with its value. The southwest corner of each sheet is labeled with cardinal directions.

Lunar transverse Mercator grid system.- The LTM system consists of equally spaced parallel lines intersecting at right angles to form 10 000-meter squares. The north-south grid lines are designated as "easting" (E) lines, and the east-west grid lines as "northing" (N) lines. The primary value of the LTM system is that it enables a user to reference a discrete point on a map without plotting degrees, minutes, and seconds as with the geographic coordinate system.

The LTM grid system was developed by dividing the Moon longitudinally into 5° zones, which are numbered consecutively 1 to 72, starting with zone 1, located at 180° to 185°, zone 2 at 185° to 190°, etc. (fig. 36-2). The central meridian for each zone is assigned the coordinate value of 100 000 meters easting. For instance, the central meridian for zone 1 is located midway between 180° and 185° (182°30') and has a coordinate value of 100 000 meters easting. The equator is assigned the coordinate value of 2 500 000 meters. The northing lines increase in value going north from the equator and decrease in value going south from the equator.

The LTM grid is shown at 10 000-meter intervals by red tick lines emanating from the edge of the map (neatline). Each 10 000-meter tick is labeled with the full 10-kilometer value only (i.e., the central meridian for each zone is labeled 100, rather than 100 000). The first LTM-grid tick in the southwest corner of each map sheet is shown with full meter values. Instructions for computing LTM grid coordinates are printed in red on each LO and LTO published.

#### Special Scale Maps

In some instances it was desirable to produce photomaps at special scales for detailed analysis of geologically interesting areas. The maps are compiled at three scales: 1:50,000, 1:25,000 and 1:10,000 (table 36-III). Because the maps cover very limited areas of the lunar surface, the higher resolution Apollo panoramic photography obtained on missions 15, 16, and 17 was rectified and mosaicked for the base. The special scale maps are similar in format to the 1:250,000-scale products; however, the numbering system was

slightly expanded. Whereas the 1:250,000-scale maps are systematically arranged (nested) within an LAC region, the special scale products are not. Each special scale photomap carries the number of the corresponding 1:250,000-scale map followed by an "S number," and a scale code. For instance, 38B-2S1(50) is a 1:50,000-scale map located within the 1:250,000-scale map numbered 38B-2 (where 38B-2 is the 1:250,000-scale map sheet number, S1 indicates the map is the first special scale map located within the 38B-2 area, and the (50) indicates the scale (i.e., 1:50,000)).

All special scale map products are designed to fit the area of interest. The sheet size varies, as well as the orientation.

The numbering system for the series is based on the existing 1:1,000,000-scale lunar astronomical charts (LAC). Each LAC region is divided into four provinces lettered A, B, C, and D. Each province is then divided into quarters numbered 1, 2, 3, and 4. The sheet number for each 1:250,000-scale map consists of the LAC number, a province letter, and the number of the quarter. The "sheet numbering guide" (fig. 36-3) illustrates LAC 58 subdivided into its corresponding 1:250,000-scale map sheets.

Figure 36-4 shows the location of the 1:250,000-scale maps published through January 1975. Table 36-V(a) lists the map numbers and names in numerical order, and table 36-V(b) gives an alphabetical listing. Table 36-III lists the available special scale maps by number, name, and corner coordinates. Table 36-V(c) lists the 17 lunar maps at a scale of 1:250,000 that were in production in January 1976.

#### Special Purpose Maps

In early 1975, NASA prepared and published photomaps of the Apollo 15, 16, and 17 landing sites. These maps were prepared from rectified Apollo panoramic photography and published at a scale of 1:25,000. The maps show the postmission traverses as derived from surface photography and selected landmark feature names.

#### LUNAR NOMENCLATURE

Maps are one of the basic tools that man uses to pass on information. In the case of Earth maps, there are navigation aids like roads, railroads, rivers, towns, etc. On the Moon, there are holes, hills, cracks, rocks, etc. It would be very difficult to write about "the 102.5-mile wide,

black-floored crater, with the W-shaped central peak on the backside of the Moon" and have everyone understand which crater was being discussed. Langrenus is credited as the first to assign names to lunar features (1645). By the year 1900, lunar nomenclature differed so greatly that no one understood it. In 1921, the newly formed International Astronomical Union (IAU) appointed a small committee to clarify the existing situation and to standardize the nomenclature.

When NASA started the 1:250,000-scale map program, it was obvious that something would have to be done to increase the number of names. There were many instances of new maps falling between named features. In August 1973, the IAU met in Sydney, Australia. The delegates were shown examples of the new maps, and the problem of additional names was discussed. Several new policies were adopted, and these policies are outlined here.

1. If a lunar feature is important enough to talk about, it should have a name.

2. In the past, lunar names were derived from deceased astronomers or scientists in related fields. The newly adopted policy permits the assignment of names of deceased writers, painters, composers, and other contributors to culture and knowledge. Excluded are political, military, and religious figures, as well as modern philosophers. Table 36-VI lists the new lunar names assigned by the Working Group for Lunar Nomenclature and approved by the IAU. These names appear on the 1:250,000-scale LTO's published up to January 1976.

3. The system of lunar names also includes, to some extent, a means of classifying broad types of features. Persons using lunar maps or charts are already familiar with terms like

Mare - sea	Mons - peak
Oceanus - ocean	Promontoria - cape
Sinus - bay	Rupes - scarp
Lacus - lake	Vallis - valley
Palus - marsh	Rima (rimae) - rilles
Montes - mountains	

Newly adopted classifications are

Catena (catenae)

Latin for chain;  
will be used to  
designate crater  
chains.

Dorsum (dorsa)

Latin for backbone;  
will be used to  
designate sinuous  
ridges.

TABLE 36-I.- LUNAR AND PLANETARY CHARTS<sup>1</sup>

Chart no.	Name	Scale	Date	Sheet size, cm (in.)	Price, \$
Lunar astronomical charts (LAC)					
LAC 11	J. Herschel	1:1,000,000	1967	56 by 74 (22 by 29)	0.35
LAC 12	Plato	1:1,000,000	1967	56 by 74 (22 by 29)	.35
LAC 13	Aristoteles	1:1,000,000	1967	56 by 74 (22 by 29)	.35
LAC 23	Rumker	1:1,000,000	1967	56 by 74 (22 by 29)	.35
LAC 24	Sinus Iridum	1:1,000,000	1966	56 by 74 (22 by 29)	.35
LAC 25	Cassini	1:1,000,000	1966	56 by 74 (22 by 29)	.35
LAC 26	Eudoxus	1:1,000,000	1967	56 by 74 (22 by 29)	.35
LAC 27	Geminus	1:1,000,000	1967	56 by 74 (22 by 29)	.35
LAC 38	Seleucus	1:1,000,000	1965	56 by 74 (22 by 29)	.35
LAC 39	Aristarchus	1:1,000,000	1963	56 by 74 (22 by 29)	.35
LAC 40	Timocharis	1:1,000,000	1963	56 by 74 (22 by 29)	.35
LAC 41	Montes Apenninus	1:1,000,000	1963	56 by 74 (22 by 29)	.35
LAC 42	Mare Serenitatis	1:1,000,000	1965	56 by 74 (22 by 29)	.35
LAC 43	Macrobius	1:1,000,000	1965	56 by 74 (22 by 29)	.35
LAC 44	Cleomedes	1:1,000,000	1966	56 by 74 (22 by 29)	.35
LAC 56	Hevelius	1:1,000,000	1966	56 by 74 (22 by 29)	.35
LAC 57	Kepler	1:1,000,000	1963	56 by 74 (22 by 29)	.35
LAC 58	Copernicus	1:1,000,000	1964	56 by 74 (22 by 29)	.35
LAC 59	Mare Vaporum	1:1,000,000	1963	56 by 74 (22 by 29)	.35
LAC 60	Julius Caesar	1:1,000,000	1965	56 by 74 (22 by 29)	.35
LAC 61	Taruntius	1:1,000,000	1963	56 by 74 (22 by 29)	.35
LAC 62	Mare Undarum	1:1,000,000	1964	56 by 74 (22 by 29)	.35
LAC 74	Grimaldi	1:1,000,000	1964	56 by 74 (22 by 29)	.35
LAC 75	Letronne	1:1,000,000	1963	56 by 74 (22 by 29)	.35
LAC 76	Montes Rhiphaeus	1:1,000,000	1964	56 by 74 (22 by 29)	.35
LAC 77	Ptolemaeus	1:1,000,000	1965	56 by 74 (22 by 29)	.35
LAC 78	Theophilus	1:1,000,000	1963	56 by 74 (22 by 29)	.35
LAC 79	Colombo	1:1,000,000	1963	56 by 74 (22 by 29)	.35
LAC 80	Langrenus	1:1,000,000	1964	56 by 74 (22 by 29)	.35
LAC 92	Pyrgius	1:1,000,000	1966	56 by 74 (22 by 29)	.35
LAC 93	Mare Humorum	1:1,000,000	1962	56 by 74 (22 by 29)	.35
LAC 94	Pitatus	1:1,000,000	1964	56 by 74 (22 by 29)	.35
LAC 95	Purbach	1:1,000,000	1965	56 by 74 (22 by 29)	.35
LAC 96	Rupes Altai	1:1,000,000	1965	56 by 74 (22 by 29)	.35
LAC 97	Pracastorius	1:1,000,000	1965	56 by 74 (22 by 29)	.35
LAC 98	Petavius	1:1,000,000	1966	56 by 74 (22 by 29)	.35
LAC 110	Schickard	1:1,000,000	1967	56 by 74 (22 by 29)	.35
LAC 111	Wilhelm	1:1,000,000	1967	56 by 74 (22 by 29)	.35
LAC 112	Tycho	1:1,000,000	1967	56 by 74 (22 by 29)	.35

<sup>1</sup>Available from Superintendent of Documents, U.S. Government Printing Office, Washington, D.C. 20402 U.S.A. All orders must be prepaid by check, money order, or Superintendent of Documents coupons.

TABLE 36-I.- LUNAR AND PLANETARY CHARTS<sup>1</sup> - Continued

Chart no.	Name	Scale	Date	Sheet size, cm (in.)	Price, \$
Lunar astronomical charts - Concluded					
LAC 113	Maurolycus	1:1,000,000	1967	56 by 74 (22 by 29)	0.35
LAC 114	Pheita	1:1,000,000	1966	56 by 74 (22 by 29)	.35
LAC 125	Schiller	1:1,000,000	1967	56 by 74 (22 by 29)	.35
LAC 126	Clavius	1:1,000,000	1967	56 by 74 (22 by 29)	.35
LAC 127	Hommel	1:1,000,000	1967	56 by 74 (22 by 29)	.35
Apollo intermediate charts (AIC)					
AIC 57C	Encke	1:500,000	1966	56 by 74 (22 by 29)	0.35
AIC 57D	Maestlin	1:500,000	1966	56 by 74 (22 by 29)	.35
AIC 58C	Gambart	1:500,000	1965	56 by 74 (22 by 29)	.35
AIC 58D	Reinhold	1:500,000	1965	56 by 74 (22 by 29)	.35
AIC 59C	Triesnecker	1:500,000	1966	56 by 74 (22 by 29)	.35
AIC 59D	Pallas	1:500,000	1966	56 by 74 (22 by 29)	.35
AIC 60C	Arago	1:500,000	1966	56 by 74 (22 by 29)	.35
AIC 60D	Agrippa	1:500,000	1965	56 by 74 (22 by 29)	.35
AIC 61C	Secchi	1:500,000	1967	56 by 74 (22 by 29)	.35
AIC 61D	Maskelyne D	1:500,000	1966	56 by 74 (22 by 29)	.35
AIC 75A	Plamsted	1:500,000	1966	56 by 74 (22 by 29)	.35
AIC 75B	Wichmann	1:500,000	1966	56 by 74 (22 by 29)	.35
AIC 76A	Euclides P	1:500,000	1966	56 by 74 (22 by 29)	.35
AIC 76B	Fra Mauro	1:500,000	1966	56 by 74 (22 by 29)	.35
AIC 77A	Plannarion	1:500,000	1965	56 by 74 (22 by 29)	.35
AIC 77B	Hipparchus	1:500,000	1966	56 by 74 (22 by 29)	.35
AIC 78A	Delambre	1:500,000	1966	56 by 74 (22 by 29)	.35
AIC 78B	Torricelli	1:500,000	1966	56 by 74 (22 by 29)	.35
AIC 79A	Capella	1:500,000	1966	56 by 74 (22 by 29)	.35
AIC 79B	Messier	1:500,000	1967	56 by 74 (22 by 29)	.35
Ranger VII lunar charts (RLC)					
RLC 1	Mare Cognitum	1:1,000,000	1964	56 by 74 (22 by 29)	1.75 for set of 5
RLC 2	Guericke	1:500,000	1964	56 by 79 (22 by 31)	
RLC 3	Bonpland H	1:100,000	1964	56 by 79 (22 by 31)	
RLC 4	Bonpland PQC	1:10,000	1964	56 by 74 (22 by 29)	
RLC 5	Unnamed	1:1,000	1964	56 by 74 (22 by 29)	

<sup>1</sup>Available from Superintendent of Documents, U.S. Government Printing Office, Washington, D.C. 20402 U.S.A. All orders must be prepaid by check, money order, or Superintendent of Documents coupons.

TABLE 36-I.- LUNAR AND PLANETARY CHARTS<sup>1</sup> - Concluded

Chart no.	Name	Scale	Date	Sheet size, cm (in.)	Price, \$
Ranger VIII lunar charts					
RLC 6	Hypatia	1:1,000,000	1966	56 by 74 (22 by 29)	2.50 for set of 7
RLC 7	Sabine	1:250,000	1966	56 by 74 (22 by 29)	
RLC 8	Sabine D	1:100,000	1966	56 by 74 (22 by 29)	
RLC 9	Sabine DM	1:50,000	1966	56 by 74 (22 by 29)	
RLC 10	Sabine EF	1:15,000	1966	56 by 74 (22 by 29)	
RLC 11	Sabine FB	1:5,000	1966	56 by 74 (22 by 29)	
RLC 12	Sabine EBF	1:2,000	1966	56 by 74 (22 by 29)	
Ranger IX lunar charts					
RLC 13	Ptolemaeus	1:1,000,000	1966	56 by 74 (22 by 29)	1.75 for set of 5
RLC 14	Alphonsus	1:250,000	1966	56 by 74 (22 by 29)	
RLC 15	Alphonsus GA	1:50,000	1966	56 by 74 (22 by 29)	
RLC 16	Alphonsus GP	1:10,000	1966	56 by 74 (22 by 29)	
RLC 17	Alphonsus GLH	1:2,000	1966	56 by 74 (22 by 29)	
Small-scale lunar charts					
LMP 1	Lunar Earth-side	1:5,000,000	1970	74 by 104 (29 by 41)	0.50
LMP 2	Lunar far-side	1:5,000,000	1970	74 by 104 (29 by 41)	.50
LMP 3	Lunar polar chart	1:5,000,000	1970	74 by 119 (29 by 47)	.50
LPC 1	Lunar chart	1:10,000,000	1970	66 by 97 (26 by 38)	.50
Lunar mosaics					
LEM 1A	Lunar reference	1:10,000,000	1962	43 by 46 (17 by 18)	0.35
LEM 1	Lunar reference	1:5,000,000	1962	86 by 89 (34 by 35)	1.00
LEM 1B	Lunar wall mosaic (2 sheets)	1:2,500,000	1962	147 by 178 (58 by 70)	2.00
Chart of Mars					
MEC 1	Chart of the planet Mars	1:35,000,000	1962	56 by 74 (22 by 29)	0.35
MEC 2	Mariner 69 Mars chart	1:25,000,000	1968	76 by 89 (30 by 35)	.35

<sup>1</sup>Available from Superintendent of Documents, U.S. Government Printing Office, Washington, D.C. 20402 U.S.A. All orders must be prepaid by check, money order, or Superintendent of Documents coupons.

TABLE 36-II.- GEOLOGIC ATLAS OF THE MOON<sup>1</sup>

Map no.	Name	Scale
Regional reconnaissance maps (telescopic and Lunar Orbiter bases)		
I-355	Kepler	1:1,000,000
I-385	Letronne	1:1,000,000
I-458	Riphaeus Mountains	1:1,000,000
I-462	Timocharis	1:1,000,000
I-463	Montes Apenninus	1:1,000,000
I-465	Aristarchus	1:1,000,000
I-485	Pitatus	1:1,000,000
I-489	Mare Serenitatis	1:1,000,000
I-491	Hevelius	1:1,000,000
I-495	Mare Humorum	1:1,000,000
I-510	Julius Caesar	1:1,000,000
I-515	Copernicus	1:1,000,000
I-527	Seleucus	1:1,000,000
I-546	Theophilus	1:1,000,000
I-548	Mare Vaporum	1:1,000,000
I-566	Ptolemaeus	1:1,000,000
I-602	Sinus Iridum	1:1,000,000
I-604	J. Herschel	1:1,000,000
I-666	Cassini	1:1,000,000
I-690	Rupes Altai	1:1,000,000
I-694	Rheita	1:1,000,000
I-691	Schiller	1:1,000,000
I-799	Macrobius	1:1,000,000
I-701	Plato	1:1,000,000
Apollo site maps (Lunar Orbiter bases)		
I-616	Maskelyne DA (includes Apollo landing site 1)	1:100,000
I-618	Sabine D (Apollo 11) (includes Apollo landing site 2)	1:100,000
I-620	Oppolzer A (includes Apollo landing sites 3 and 3R)	1:100,000
I-622	Maestlin G (includes Apollo landing site 5)	1:100,000
I-624	Wichmann CA (includes Apollo landing sites 4 and 4R)	1:100,000
I-626	Flamsteed K (includes Surveyor site 1)	1:100,000

<sup>1</sup>Available from USGS at Washington Distribution Section, 1200 South Eads Street, Arlington, Virginia 22202, or at Denver Federal Center, Branch of Distribution, Bldg. 41, Denver, Colorado 80225. The price for each item is \$1.00. (If two maps are indicated, the price is \$1.00 for the set.) All orders must be prepaid by check or money order.

TABLE 36-II.- GEOLOGIC ATLAS OF THE MOON<sup>1</sup> - Concluded

Map no.	Name	Scale
Apollo site maps (Lunar Orbiter bases) - Concluded		
I-627	Lansberg P	1:100,000
I-617	Apollo landing site 1 (part of Maskelyne DA region)	1:25,000
I-619	Apollo landing site 2 (Apollo 11) (part of Sabine E region)	1:25,000
I-621	Apollo landing sites 3 and 3R	1:25,000
I-623	Apollo landing site 5 (part of Maestlin G region)	1:25,000
I-625	Apollo landing sites 4 and 4R (part of Wichmann CA region)	1:25,000
Ranger maps		
I-599	Alphonsus (RLC 14)	1:250,000
I-693	Bonpland H (RLC 3)	1:100,000
I-586	Alphonsus GA (RLC 15)	1:50,000
I-594	Sabine DM (RLC 9)	1:50,000
I-678	Bonpland PQC (RLC 4)	1:10,000
I-679	Sabine EB (RLC 11)	1:5,000
Apollo premission maps		
I-708	Fra Mauro (Apollo 14), 2 maps	1:250,000 and 1:25,000
I-723	Apennine-Hadley (Apollo 15), 2 maps	1:250,000 and 1:50,000
I-748	Descartes (Apollo 16), 2 maps	1:250,000 and 1:50,000
I-800	Taurus-Littrow (Apollo 17), 2 maps	1:250,000 and 1:50,000
Hemisphere chart		
I-703	Geologic map of near side of the Moon	1:5,000,000

<sup>1</sup>Available from USGS at Washington Distribution Section, 1200 South Eads Street, Arlington, Virginia 22202, or at Denver Federal Center, Branch of Distribution, Bldg. 41, Denver, Colorado 80225. The price for each item is \$1.00. (If two maps are indicated, the price is \$1.00 for the set.) All orders must be prepaid by check or money order.

TABLE 36-III.- DETAILED MAPS FOR SPECIALIZATION

Map number	Sheet name	Corner coordinates			
		Upper left	Upper right	Lower left	Lower right
Scale of 1:50,000					
38B-2S1 (50)	Montes Agricola	30°12' N 305°57'	30°12' N 307°23'	29°12' N 305°57'	29°12' N 307°23'
39A-1S1 (50)	Van Biesbroeck	29°29' N 313°49'	29°29' N 315°15'	28°29' N 313°49'	28°29' N 315°15'
39A-3S1 (50)	Rima Prinz	27°11' N 315°21'	29°11' N 316°53'	26°11' N 315°21'	26°11' N 316°53'
39B-3S1 (50)	Zahia	25°20' N 328°19'	25°20' N 329°42'	24°20' N 328°19'	24°20' N 329°42'
39C-2S1 (50)	Rima Paier	20°58' N 327°37'	20°58' N 328°41'	19°43' N 327°37'	19°43' N 328°41'
40A-1S1 (50)	Dorsum Zirkel	30°21' N 333°36'	30°21' N 335°03'	29°21' N 333°36'	29°21' N 335°03'
41A-3S1 (50)	Rima Mozart	25°52' N 359°03'	25°52' N 0°26'	24°52' N 359°03'	24°52' N 0°26'
41B-4S1 (50)	A-15 landing area	26°45' N 2°47'	26°45' N 4°11'	25°45' N 2°47'	25°45' N 4°11'
41B-4S2 (50)	Rima Hadley Central	25°45' N 2°00'	25°45' N 3°23'	24°45' N 2°00'	24°45' N 3°23'
41B-4S3 (50)	Rima Hadley South	25°00' N 2°00'	25°00' N 3°23'	24°00' N 2°00'	24°00' N 3°23'
42C-2S1 (50)	Possae Littrow	22°19' N 28°	22°19' N 29°35'	21°04' N 28°30'	21°04' N 29°35'
42C-3S3 (50)	Nons Argseus	20°19' N 28°43'	20°19' N 30°03'	19°19' N 28°43'	19°19' N 30°03'
42C-4S1 (50)	Dorsum Nicol	18°17' N 22°31'	18°17' N 23°50'	17°17' N 22°31'	17°17' N 23°50'
43D-1S1 (50)	A-17 landing area	20° N 30°03'	20°41' N 31°23'	19°41' N 30°03'	19°41' N 31°23'
61A-2S1 (50)	King Central Peaks (1)	5°38' N 120°00'	5°38' N 121°10'	4°15' N 120°00'	4°15' N 121°10'
65C-1S1 (50)	King North Peaks (1)	6°49' N 119°10'	6°49' N 120°16'	5°30' N 119°10'	5°38' N 120°16'
65D-2S1 (50)	Plank Possae	12°19' S 357°29'	12°19' S 358°46'	13°19' S 357°29'	13°19' S 358°46'
77D-3S1 (50)	Alphonsus A-16 landing area	8°21' S 15°00'	8°21' S 16°01'	9°36' S 15°00'	9°36' S 16°01'
100C-1S1 (50)	Siegfried	25°09' S 102°10'	25°09' S 103°17'	26°24' S 102°10'	26°24' S 103°17'
102A-1S1 (50)	Kira	17°15' S 132°09'	17°15' S 133°12'	18°30' S 132°09'	18°30' S 133°12'

\*These special scale maps have recently been assigned for production. Sheet limits (i.e., boundaries) and sheet names are usually determined and assigned late in the production cycle. These maps are not available.

TABLE 36-III.- DETAILED MAPS FOR SPECIALIZATION - Concluded

Map number	Sheet name	Corner coordinates			
		Upper left	Upper right	Lower left	Lower right
398-251 (25) 398-252 (25)	(1) (1)	-- --	-- --	-- --	-- --
Scale of 1:25,000					
40A-451 (10) 41C-351 (10) 42A-451 (10) 42A-452 (10) 42C-351 (10) 42C-352 (10) 77D-151 (10)	Artemis Ina Lorca West Lorca East Isis Osiris Davy Catena	25°08'20" N 18°45' 509' 24°41' 10°57'50" 24°41' 11°11' 19°04'40" N 27°21'30" 18°42' 27°30' 10°50'40" S 353°42'30"	25°08'20" N 334°43'20" 18°45' 5025' 24°41' 11°11' 24°41' 11°24'10" 19°04'40" N 27°21'30" 18°42' 27°30' 10°50'40" S 353°57'50"	24°53'20" N 334°30' 18°33' 509' 24°26' 10°57'50" 24°26' 11°11' 18°49'50" N 27°21'30" 18°30' 27°30' 11°02'40" S 353°42'30"	24°53'20" N 334°43'20" 18°33' 5025' 24°26' 11°11' 24°26' 11°24'10" 18°49'50" N 27°21'30" 18°30' 27°30' 11°02'40" S 353°57'50"
Scale of 1:10,000					

These special scale maps have recently been assigned for production. Sheet limits (i.e., boundaries) and sheet names are usually determined and assigned late in the production cycle. These maps are not available.

TABLE 36-IV.- LONGITUDE CONVERSION

From - longitude, deg W	To - longitude, deg on a 360° basis	From - longitude, deg W	To - longitude, deg on a 360° basis	From - longitude, deg W	To - longitude, deg on a 360° basis
1	359	37	323	73	287
2	358	38	322	74	286
3	357	39	321	75	285
4	356	40	320	76	284
5	355	41	319	77	283
6	354	42	318	78	282
7	353	43	317	79	281
8	352	44	316	80	280
9	351	45	315	81	279
10	350	46	314	82	278
11	349	47	313	83	277
12	348	48	312	84	276
13	347	49	311	85	275
14	346	50	310	86	274
15	345	51	309	87	273
16	344	52	308	88	272
17	343	53	307	89	271
18	342	54	306	90	270
19	341	55	305	91	269
20	340	56	304	92	268
21	339	57	303	93	267
22	338	58	302	94	266
23	337	59	301	95	265
24	336	60	300	96	264
25	335	61	299	97	263
26	334	62	298	98	262
27	333	63	297	99	261
28	332	64	296	100	260
29	331	65	295	101	259
30	330	66	294	102	258
31	329	67	293	103	257
32	328	68	292	104	256
33	327	69	291	105	255
34	326	70	290	106	254
35	325	71	289	107	253
36	324	72	288	108	252

TABLE 36-IV.- LONGITUDE CONVERSION - Concluded

From - longitude, deg W	To - longitude, deg on a 360° basis	From - longitude, deg W	To - longitude, deg on a 360° basis
109	251	145	215
110	250	146	214
111	249	147	213
112	248	148	212
113	247	149	211
114	246	150	210
115	245	151	209
116	244	152	208
117	243	153	207
118	242	154	206
119	241	155	205
120	240	156	204
121	239	157	203
122	238	158	202
123	237	159	201
124	236	160	200
125	235	161	199
126	234	162	198
127	233	163	197
128	232	164	196
129	231	165	195
130	230	166	194
131	229	167	193
132	228	168	192
133	227	169	191
134	226	170	190
135	225	171	189
136	224	172	188
137	223	173	187
138	222	174	186
139	221	175	185
140	220	176	184
141	219	177	183
142	218	178	182
143	217	179	181
144	216	180	180

TABLE 36-V.- TOPOGRAPHIC ORTHOPHOTOGRAPHS

[1:250,000 scale]

(a) Numerical listing

Number	Name	Number	Name	Number	Name
38B-1	Humason	42C-1	Deseilligny	62A-2	Curtis
38B-2	Nielsen	42C-2	Clerke	62A-3	Shapley
38B-3	Freud	42C-3	Daves	62A-4	Tebbutt
38B-4	Zinner	42C-4	Brackett		
				62B-1	Fahrenheit
39A-1	Krieger	42D-1	Rusby	62B-2	Condorcet
39A-2	Angström	42D-2	Bessel	62B-3	Krogh
39A-3	Prinz	42D-3	Menelaus	62B-4	Auzout
39A-4	Väisälä	42D-4	Sulpicius Gallus	62C-1	Firmicus
				62C-2	Dubyago
39B-1	Pedorov	43A-4	le Monnier	62C-3	Pomortsev
39B-2	Delisle			62C-4	Condon
39B-3	Diophantus	43C-1	Hill		
39B-4	Artsimovich	43C-3	Proclus	62D-1	Abbot
		43C-4	Carmichael	62D-2	Daly
40A-1	Caventou			62D-3	Ameghino
40A-2	McDonald	43D-1	Littrow	62D-4	Smithson
40A-3	Lambert	43D-2	Franch		
40A-4	La Hire	43D-3	Theophrastus	63B-3	Jansky
		43D-4	Vitruvius		
40B-1	Sampson			63C-1	Knorr-Shaw
40B-2	Landsteiner	44D-3	Eckert	63C-2	Tachinni
40B-3	Kovalevskij	44D-4	Peirce	63C-3	Peek
40B-4	Heinrich			63C-4	Schubert
		60A-1	Daubrée		
40C-2	Pupin	60A-2	Auvers	63D-1	Boethius
				63D-3	Nobili
41A-3	Spurr	60B-1	Plinius	63D-4	Respighi
41A-4	Beer	60B-2	Jansen		
				64D-1	Nunn
41B-3	Joy	61A-1	Cajal	64D-2	Erro
41B-4	Hadley	61A-2	Lucian	64D-3	Fox
		61A-3	Cauchy	64D-4	McAdie
41C-1	Conon			65A-3	Guyot
41C-2	Galen	61B-1	Lyell		
41C-3	Bowen	61B-2	Glaisher	65B-4	Recht
41C-4	Yangel'	61B-3	Watts		
		61B-4	da Vinci	65C-1	King
41D-1	Wallace			65C-4	Zanstra
41D-2	Huxley	61C-1	Lawrence		
		61C-2	Cameron	65D-2	Katchalsky
42A-3	Banting	61C-3	Anville	65D-3	Abul Wafa
42A-4	Linne	61C-4	Secchi		
				66A-3	Rutherford
42B-3	Very	62A-1	Yerkes		
42B-4	Sarabhai			66B-4	Glauber

TABLE 36-V.-TOPOGRAPHIC ORTHOPHOTOGRAPHS - Continued

[1:250,000 scale]

(a) Numerical listing - Concluded

Number	Name	Number	Name	Number	Name
66C-1	Fischer	80B-1	Morley	102A-1	Patsaev
66D-2	Bergman	80B-2	MacLaurin	102A-4	Fesenkov
75C-1	Scheele	80B-4	Acosta	102B-2	Isaev
75C-2	Norman	80C-1	Somerville	102B-3	Andronov
75D-2	Winthrop	80D-2	Al-Marrakushi	102D-1	Stark
76C-1	Bonpland	81A-1	Rankine	103A-1	Grave
76C-2	Guericke	81A-2	Gilbert	103A-4	Raspletin
76D-1	Eppinger	81A-3	Kästner		
76D-2	Kuiper	81A-4	Von Behring		
77C-1	Albategnius	81B-1	Haldane		
77C-2	Halley	81B-2	Runge		
77D-1	Davy	81B-3	Widmannstätten		
77D-2	Ammonius	81B-4	Kiess		
78A-3	Alfraganus	81C-1	Kreiken		
78B-3	Torricelli	81C-2	Houtermans		
78B-4	Hypatia	82A-1	Purkyně		
78C-1	Kant	82A-2	Wylđ		
78C-2	Mädler	82A-3	Ludwig		
78D-1	Anděl	82A-4	Hirayama		
78D-2	Descartes	82D-1	Brunner		
79A-2	Leakey	82D-2	Ganskij		
79A-3	Capella	83C-1	Danjon		
79A-4	Isidorus	83C-3	Dobrovolskij		
79B-1	Lubbock	83C-4	Delporte		
79B-2	Messier	83D-2	Sherrington		
79B-3	Amontons	84D-4	Volkov		
79B-4	Gutenberg	100C-1	Titius		
79D-1	Daguerre	101B-1	Litke		
79D-2	Gaudibert	101B-2	Tsiolkovskij		
80A-1	Geikie		Borealis		
80A-2	Webb	101B-3	Tsiolkovskij		
80A-3	Bilharz		Australis		
80A-4	Linberg	101B-4	Babakin		
		101C-1	Neujmin		
		101C-2	Waterman		

TABLE 36-V.- TOPOGRAPHIC ORTHOPHOTOMAPS - Continued

[1:250,000 scale]

(b) Alphabetical listing

Name	Number	Name	Number
Abbot	62D-1	Davy	77D-1
Abul Wafa	65D-3	Dawes	42C-3
Acosta	80B-4	Delisle	59B-2
Albategnius	77C-1	Delporte	83C-4
Alfranganus	78A-3	Descartes	78D-2
Al-Marrakushi	80D-2	Deseilligny	42C-1
Ameghino	62D-3	Diophantus	39B-3
Ammonius	77D-2	Dobrovolskij	83C-3
Amontons	79B-3	Dubyago	62C-2
Anděl	78D-1		
Andronov	102B-3	Eckert	44D-3
Angström	39A-2	Eppinger	76D-1
Anville	61C-3	Erro	64D-2
Artsimovich	39B-4		
Auvers	60A-2	Fahrenheit	62B-1
Auzout	62B-4	Fedorov	39B-1
		Fesenkov	102A-4
Babakin	101B-4	Firmicus	62C-1
Banting	42A-3	Fischer	66C-1
Beer	41A-4	Fox	64D-3
Bergman	66D-2	Franck	43D-2
Bessel	42D-2	Freud	38B-3
Bilharz	80A-3		
Boethius	63D-1	Galen	41C-2
Bonpland	76C-1	Ganskij	82D-2
Bowen	41C-3	Gaudibert	79D-2
Brackett	42C-4	Geikie	80A-1
Brunner	82D-1	Gilbert	81A-2
		Glaisher	61B-2
Cajal	61A-1	Glauber	66B-4
Cameron	61C-2	Grave	103A-1
Capella	79A-3	Guericke	76C-2
Carmichael	43C-4	Gutenberg	79B-4
Cauchy	61A-3	Guyot	65A-3
Caventou	40A-1		
Clerke	42C-2	Hadley	41B-4
Condé	62C-4	Haldane	81B-1
Condorcet	62B-2	Halley	77C-2
Conon	41C-1	Heinrich	40B-4
Curtis	62A-2	Hill	43C-1
		Hirayama	82A-4
Daguerre	79D-1	Hornsby	47D-1
Daly	62D-2	Houtermans	81C-2
Danjon	83C-1	Humason	38B-1
Daubrée	60A-1	Huxley	41D-2
da Vinci	61B-4	Hypatia	78B-4

TABLE 36-V.- TOPOGRAPHIC ORTHOPHOTOGRAPHS - Continued

[1:250,000 scale]

(b) Alphabetical listing - Concluded

Name	Number	Name	Number
Isaev	102B-2	Prinz	39A-3
Isidorus	79A-4	Proclus	43C-3
		Pupin	40C-2
Jansen	60B-2	Purkyně	82A-1
Jansky	63B-3		
Joy	41B-3	Rankine	81A-1
		Raspletin	103A-4
Kant	78C-1	Recht	65B-4
Kästner	81A-3	Respighi	63D-4
Katchalsky	65D-2	Runge	81B-2
Kiess	81B-4	Rutherford	66A-3
King	65C-1		
Knox-Shaw	63C-1	Sampson	40B-1
Kovalevskij	40B-3	Sarabhai	42B-4
Kreiken	81C-1	Scheele	75C-1
Krieger	39A-1	Schubert	63C-4
Krogh	62B-3	Secchi	61C-4
Kuiper	76D-2	Shapley	62A-3
		Sherrington	83D-2
La Hire	40A-4	Smithson	62D-4
Lambert	40A-3	Somerville	80C-1
Landsteiner	40B-2	Spurr	41A-3
Lawrence	61C-1	Stark	102D-1
Leakey	79A-2	Sulpicius Gallus	42D-4
le Monnier	43A-4		
Lindbergh	80A-4	Tachinni	63C-2
Linne	42A-4	Tebbutt	62A-4
Litké	101B-1	Theophrastus	43D-3
Littrow	43D-1	Titius	100C-1
Lubbock	79B-1	Torricelli	78B-3
Lucian	61A-2	Tsiolkovskij	
Ludwig	82A-3	Australis	101B-3
Lyell	61B-1	Borealis	101F-2
Maclaurin	80B-2	Väisälä	39A-4
Mädler	78C-2	Very	42B-3
McAdie	64D-4	Vitruvius	43D-4
McDonald	40A-2	Volkov	84D-4
Menelaus	42D-3	Von Behring	81A-4
Messier	79B-2		
Morley	80B-1	Wallace	41D-1
		Waterman	101C-2
Neujmin	101C-1	Watts	61B-3
Nielsen	38B-2	Webb	80A-2
Nobili	63D-3	Widmannstätten	81F-3
Norman	75C-2	Winthrop	75D-2
Nunn	64D-1	Wylde	82A-2
Patsaev	102A-1	Yangel'	41C-4
Peck	63C-3	Yerkes	62A-1
Peirce	44D-4		
Plinius	60B-1	Zanstra	65C-4
Pomortsev	62C-3	Zinner	38B-4

**TABLE 36-V.- TOPOGRAPHIC ORTHOPHOTOGRAPHS - Concluded**

[1:250,000 scale]

(c) Lunar maps assigned for production<sup>1</sup>

Map number	Map number
39C-1 <sup>2</sup>	84B-3
61D-4	85A-4
63B-4 <sup>2</sup>	85C-1
77A-3	85C-2
77B-3	85C-3
77B-4	86D-4
78A-4	103B-2
80B-3 <sup>2</sup>	104A-1
83B-4 <sup>2</sup>	

<sup>1</sup>For locations, see figures 36-3 and 36-4.

<sup>2</sup>Became available at time handbook was printed.  
Sheet names are as follows: 39C-1, Brayley;  
63B-4, Virchow; 80B-3, Born; and 83B-4, Mecho.

TABLE 36-VI.- NEW LUNAR NAMES

New name	Old name	Location		Comments
		Longitude	Latitude	
Abbot	Apollonius K	54.7°	5.5°N	
Artsimovich	Diophantus A	323.4°	27.6°N	
Avery	Gilbert U	81.4°	1.3°S	
Babakin	- -	123.3°	20.8°S	
Banting	Linné E	16.4°	26.6°N	
Black	Kästner F	80.4°	9.2°S	
Borel	le Monnier C	26.4°	22.4°N	
Bowen	Manilius A	9.1°	17.6°N	
Brackett	- -	23.5°	17.9°N	
Cajal	Jansen F	31.1°	12.6°N	
Cameron	Taruntius C	45.9°	6.2°N	
Carmichael	Macrobius A	40.4°	19.5°N	
Caventou	La Hire D	330.6°	29.7°N	
Clerke	Littrow B	29.8°	21.7°N	
Curtis	Picard Z	56.8°	14.5°N	
Daly	Apollonius P	59.5°	5.7°N	
Daubrée	Menelaus S	14.8°	15.7°N	
Dobrovolskij	- -	129.7°	12.7°S	
Dubyago	Dubiago	70.0°	4.0°N	Corrected spelling
Eckert	- -	58.4°	17.3°N	
Esclançon	Macrobius L	42.1°	21.5°N	
Fedorov	- -	322.9°	28.2°N	
Feuillet	Feuilleé	350.5°	27.4°N	Old name, corrected spelling
Fox	- -	98.2°	.5°N	

TABLE 36-VI.- NEW LUNAR NAMES - Continued

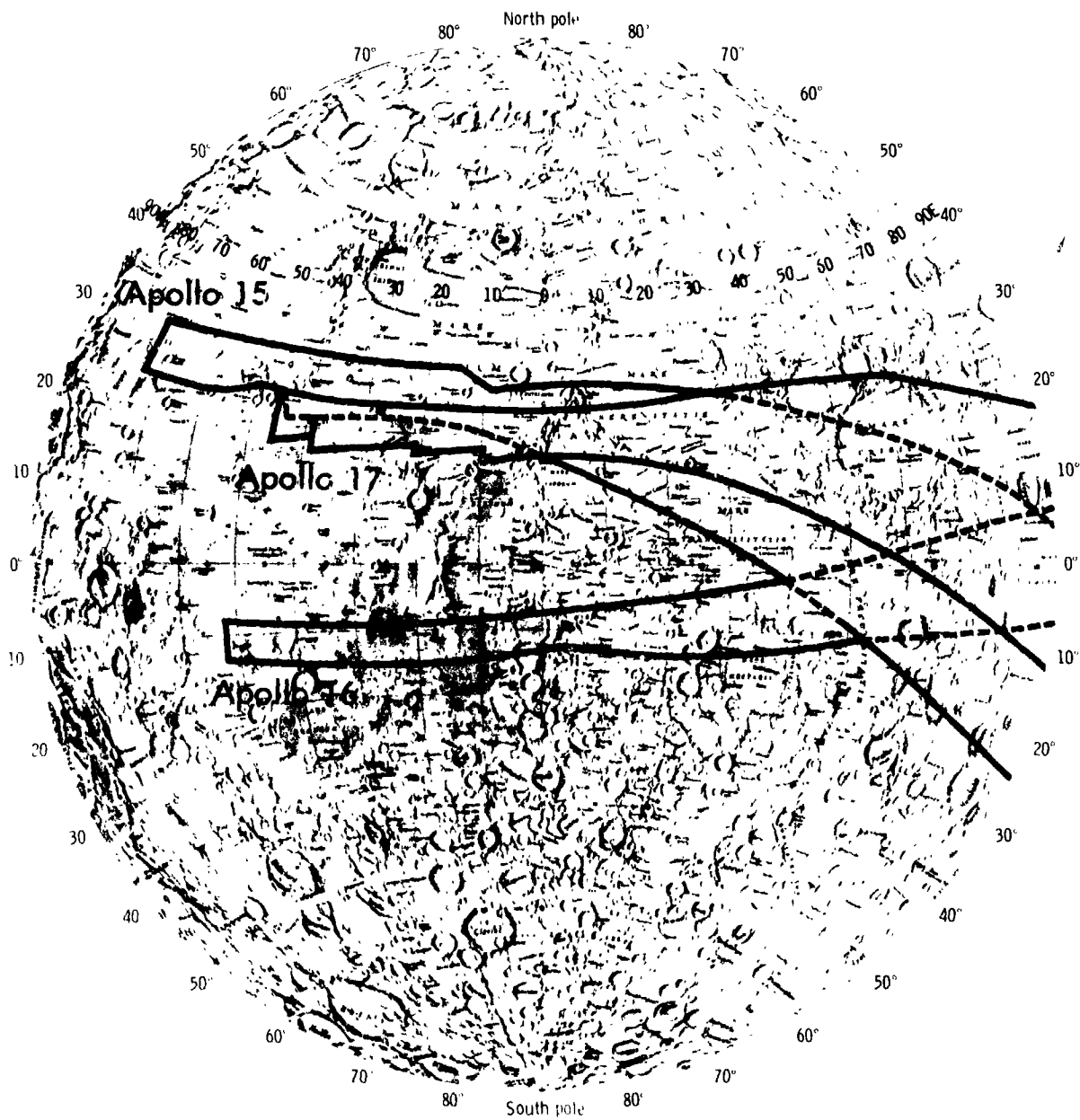
New name	Old name	Location		Comments
		Longitude	Latitude	
Franck	Römer K	35.6°	22.6°N	
Franz	Proclus D	41.0°	17.4°N	Old name; relocated to more definite feature
Fredholm	Macrobius D	46.5°	18.3°N	
Freud	- -	307.6°	25.8°N	
Galen	Aratus A	4.9°	21.9°N	
Ganskij	Gansky	97.0°	9.6°S	Corrected spelling
Gardner	Vitruvius A	33.8°	17.8°N	
Golgi	Schiaparelli D	300.1°	27.7°N	
Greaves	Lick D	52.8°	13.2°N	
Hadley	Hadley C	2.8°	25.5°N	
Haldane	- -	84.0°	1.7°S	
Hargreaves	Maclaurin S	64.1°	2.1°S	
Heinrich	Timocharis A	344.6°	24.8°N	
Hill	Macrobius B	40.8°	20.9°N	
Hornsby	Aratus CB	12.5°	23.8°N	
Houtermans	- -	87.4°	9.4°S	
Humason	Lichtenberg G	303.3°	30.7°N	
Huxley	Wallace B	355.5°	20.2°N	
Isaev	- -	147.5°	17.5°S	
Jenkins	Schubert Z	78.1°	.4°N	
Joy	Hadley A	6.6°	25.0°N	
Katchalsky	- -	116.1°	5.9°N	
Kiess	- -	84.1°	6.3°S	
Knox-Shaw	- -	80.1°	5.4°N	
Kovalevskij	Timocharis B	347.8°	27.9°N	
Kreiken	- -	84.6°	9.0°S	
Krogh	Auzout B	65.7°	9.4°N	
Landsteiner	Timocharis F	345.2°	31.2°N	

TABLE 36-VI.- NEW LUNAR NAMES - Continued

New name	Old name	Location		Comments
		Longitude	Latitude	
Lawrence	Taruntius M	43.3°	7.5°N	
Liouville	Dubiago S	73.6°	2.7°N	
Litke	Lütke	123.1°	16.7°S	Corrected spelling
Lucian	Maraldi B	36.8°	14.3°N	
Lyell	Proclus A	42.2°	13.3°N	Old name; relocated to more definite feature
McAdie	- -	92.1°	2.1°N	
McDonald	Carlini B	339.1°	30.4°N	
Morley	Maclaurin R	64.6°	2.8°S	
Nielsen	Wollaston C	308.2°	31.6°N	
Noether	Cauchy D	40.3°	10.0°N	
Peek	- -	86.9°	2.6°N	
Pomortsev	Dubiago P	66.9°	.8°N	
Pupin	Timocharis K	349.0°	23.9°N	
Raman	Herodotus D	304.8°	27.0°N	
Recht	- -	124.0°	9.8°N	
Respighi	Dubiago C	71.9°	2.8°N	
Runge	- -	86.8°	2.5°S	
Sampson	- -	343.5°	29.6°N	
Santos-Dumont	Hadley B	4.7°	27.8°N	
Sarabhai	Bessel A	21.0°	24.7°N	
Scheele	letronne D	322.1°	9.4°S	
Shapley	Picard H	56.8°	9.4°N	
Sherrington	- -	118.1°	11.1°S	
Spurr	Archimedes K	358.7°	27.9°N	
Stewart	Dubiago Q	67.0°	2.2°N	
Swift	Peirce R	53.4°	19.3°N	
Tachinni	Neper K	85.9°	5.0°N	
Tebbutt	Picard G	53.5°	9.5°N	

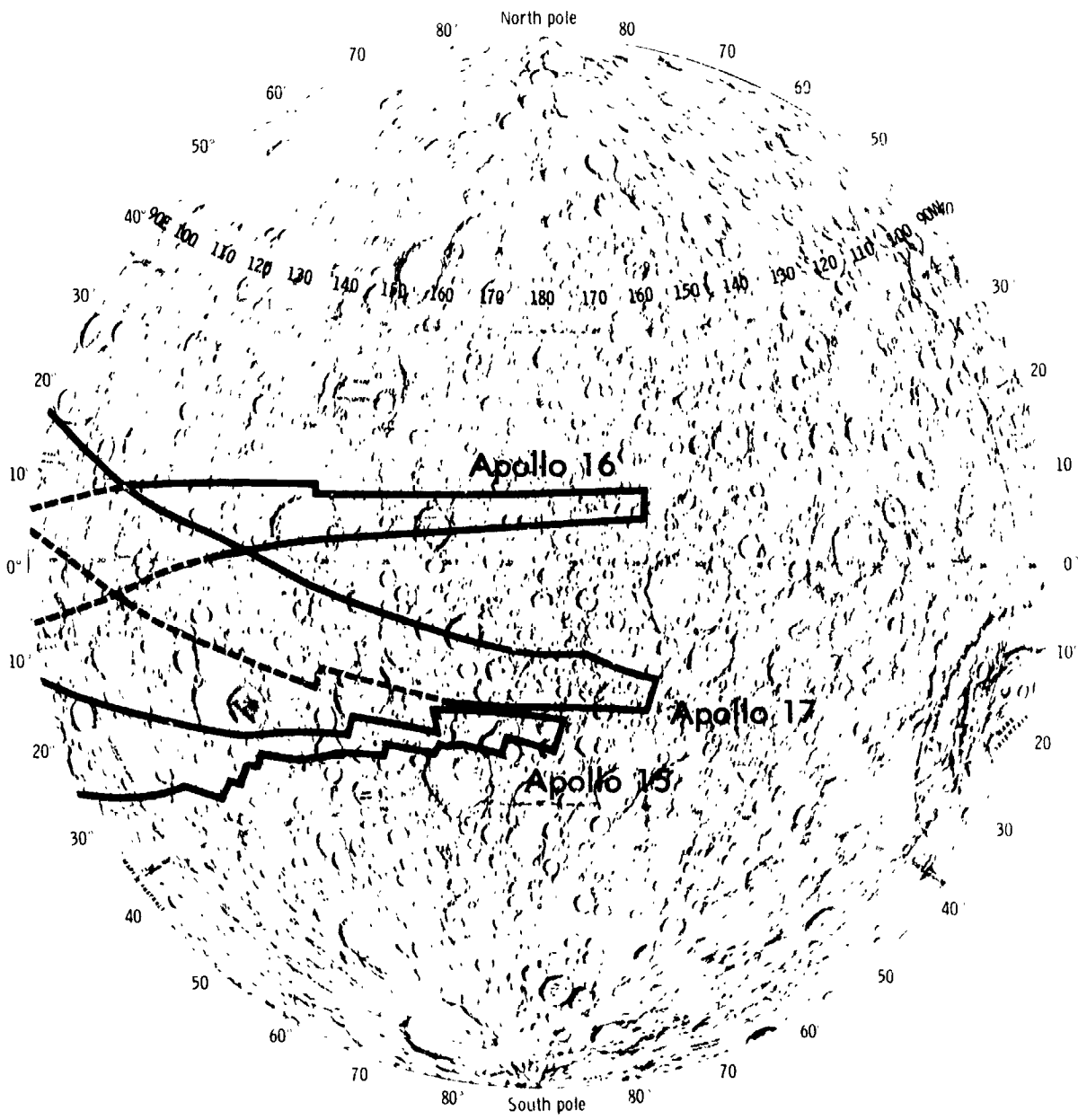
TABLE 36-VI.- NEW LUNAR NAMES - Concluded

New name	Old name	Location		Comments
		Longitude	Latitude	
Theophrastus	Haraldi M	39.1°	17.5°N	Corrected spelling
Townley	Apollonius G	63.2°	3.4°N	
Toscanelli	Aristarchus C	312.4°	27.9°N	
Tsiolkovskij	Tsiolkovsky	129.0°	20.0°S	
Väisälä	Aristarchus A	312.1°	25.9°N	
Van Albada	Auzout A	64.4°	9.4°N	
Van Vleck	Gilbert M	78.2°	1.8°S	
Very	le Monnier B	25.4°	25.6°N	
Volkov	- -	131.7°	13.6°S	
Watts	Taruntius D	46.3°	8.8°N	
Weierstrass	Gilbert M	77.2°	1.3°S	
Widmannstätten	- -	85.5°	6.0°S	
Yangel'	Manilius F	4.7°	17.0°N	
Zanstra	- -	124.8°	2.9°N	
Zasyadko	- -	94.2°	3.9°N	
Zinner	Schiaparelli B	301.1°	26.6°N	



(a) Near side.

Figure 36-1.- Areas covered by the vertical metric photography.



(b) Far side.

Figure 36-1. Concluded.



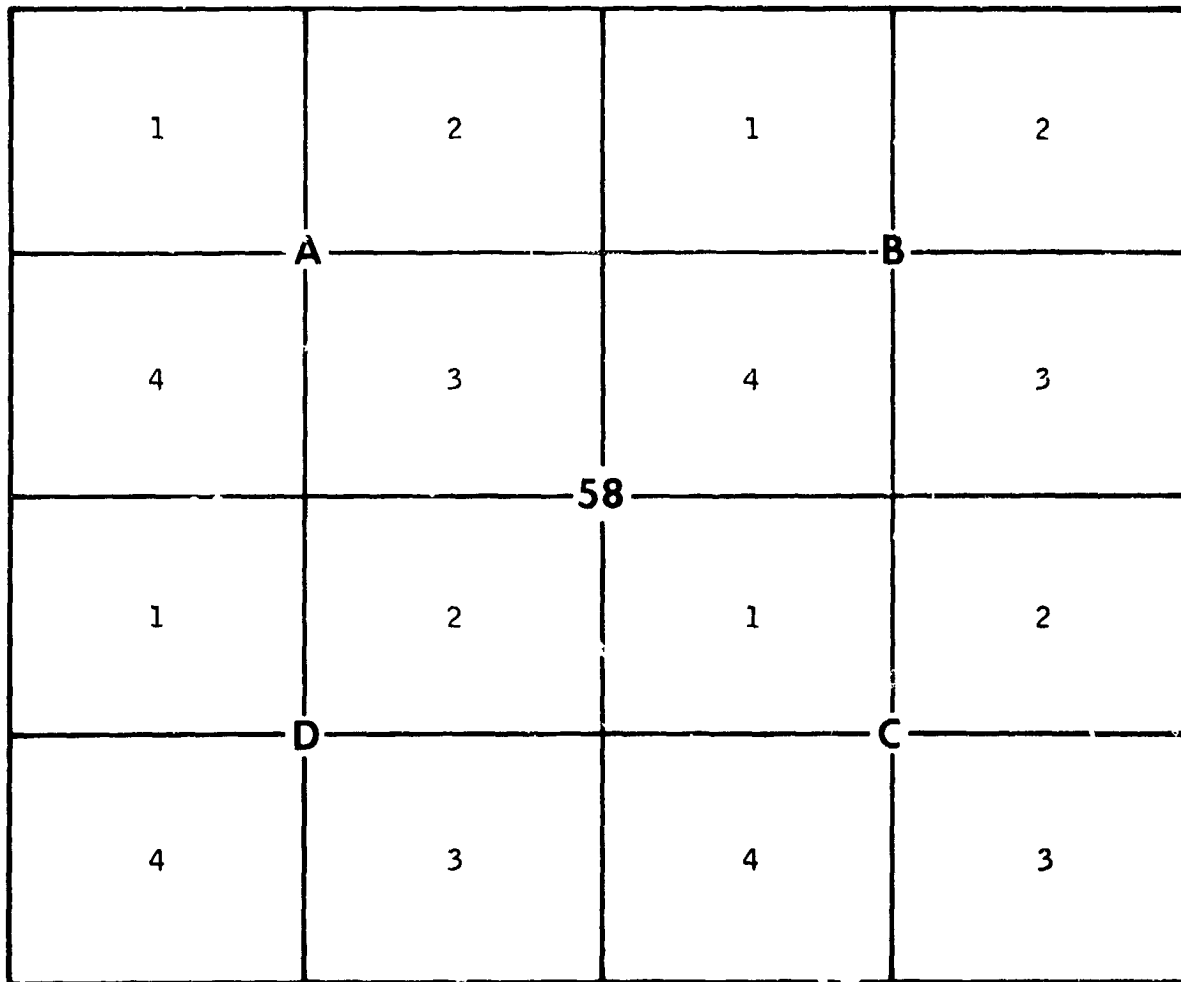
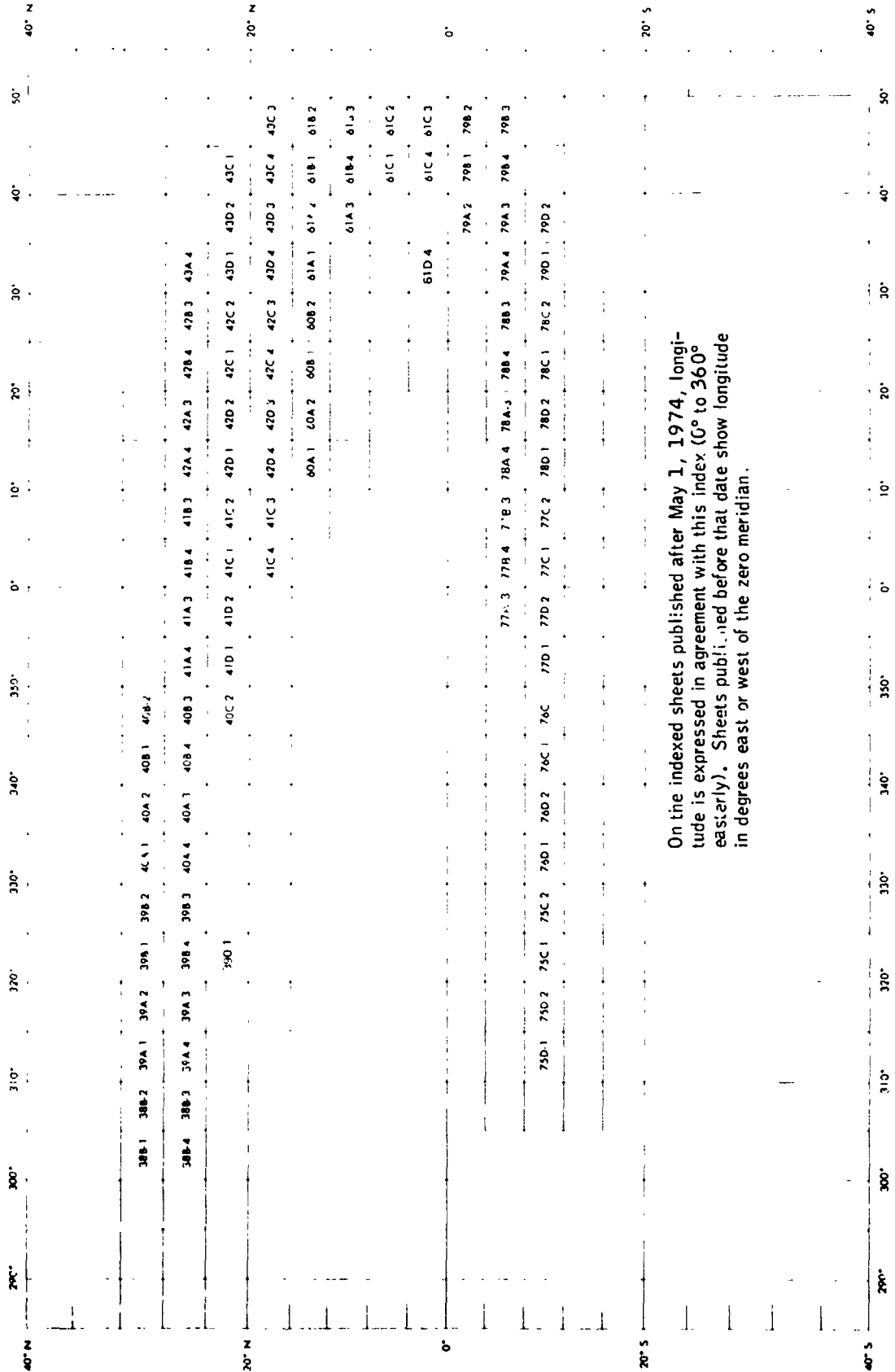


Figure 36-3.- Sheet numbering guide.



On the indexed sheets published after May 1, 1974, longitude is expressed in agreement with this index (0° to 360° easterly). Sheets published before that date show longitude in degrees east or west of the zero meridian.

Figure 36-4.- Key for quadrant locations of lunar topophotomaps/orthophotomaps, 1:250,000 scale (January 1976).

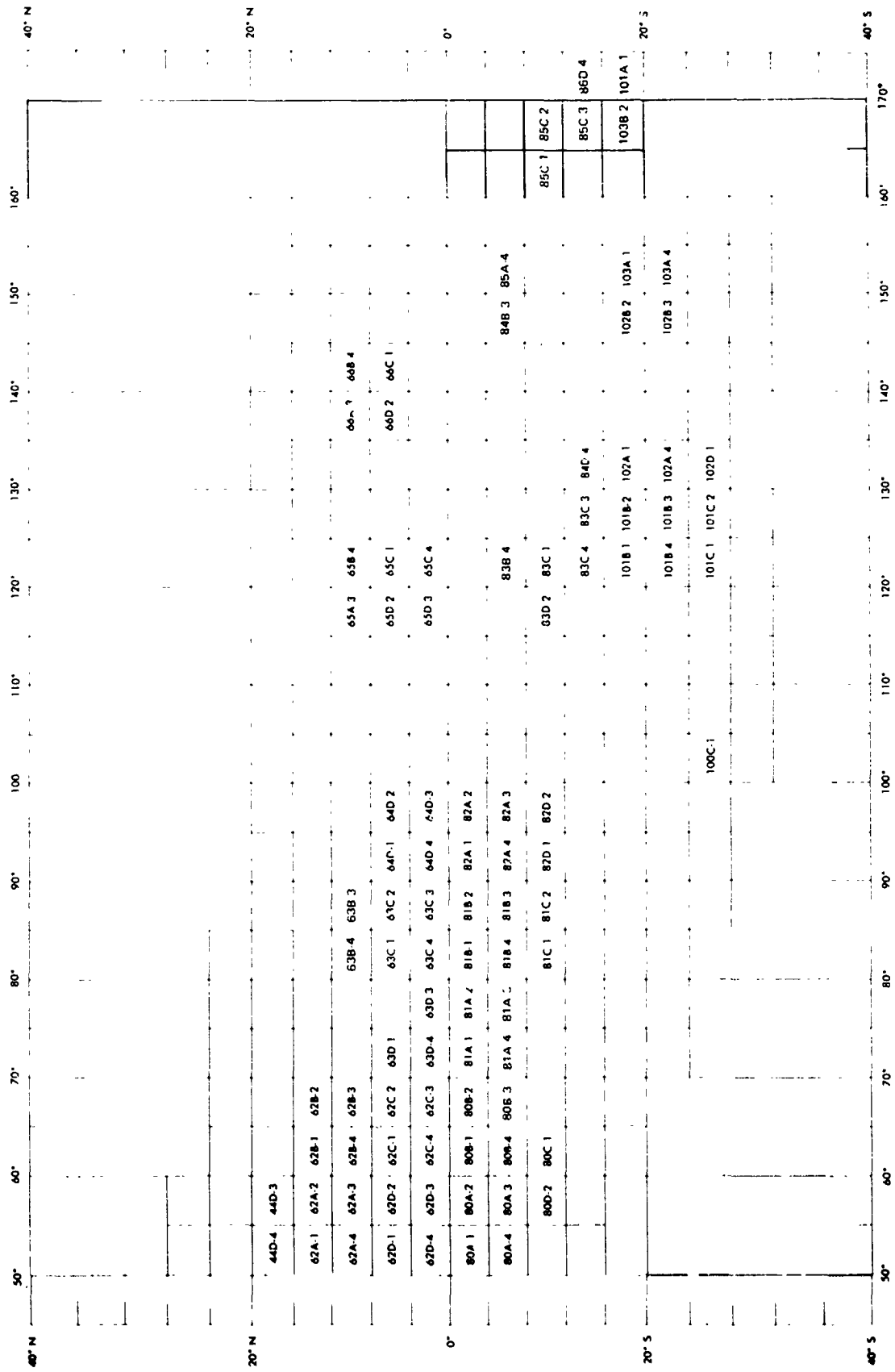


Figure 36-4.- Concluded.

37. LUNAR SAMPLE RESEARCH PROGRAM



CONTENTS - SECTION 37

	Page
LUNAR SAMPLE SECURITY AND ACCOUNTABILITY PROCEDURES . . . . .	37-3
PROCEDURE FOR APPLYING FOR LUNAR SAMPLE PROGRAM . . . . .	37-3
Proposal Submission . . . . .	37-4
Sample Allocations . . . . .	37-4
Sample Requests . . . . .	37-4
SAMPLE PROCESSING, DISSECTION AND DESCRIPTION . . .	37-5
SOURCES OF LUNAR SURFACE INFORMATION . . . . .	37-6
SOURCES OF LUNAR SAMPLE INFORMATION . . . . .	37-8
SOURCES OF LUNAR SAMPLE PHOTOGRAPHS . . . . .	37-9
CHEMISTRY AND PETROGRAPHIC-MODE DATA BASE FOR LUNAR SAMPLES . . . . .	37-9
ADDITIONAL PROGRAM INFORMATION . . . . .	37-10

### 37. LUNAR SAMPLE RESEARCH PROGRAM

The Lunar Sample Research Program is concerned with the scientific study of materials returned from the Moon. The materials generally encompassed are surface rocks and fines and core samples consisting of fines.

#### LUNAR SAMPLE SECURITY AND ACCOUNTABILITY PROCEDURES

The lunar samples are the property of the U.S. Government, and the NASA policy is that lunar sample materials are to be used only for authorized purposes; therefore, rigorous security and accountability procedures must be followed by all persons who have access to lunar materials. The elements of these procedures are (1) adherence to lunar sample security plans, (2) continuous accountability for the samples, and (3) periodic inventory of the samples.

The investigator is responsible for the control and safeguarding of all lunar samples consigned to his custody. To ensure that appropriate procedures and safeguards are carried out at the laboratory used by the investigator and at the laboratories used by co-investigators, if different, a detailed sample security plan must be approved by the NASA Lyndon B. Johnson Space Center (JSC) Security Branch. This plan should be submitted to the TL/Lunar Sample Curator. A historical record of the names of all persons who have had access to lunar samples and the corresponding time periods of access must be maintained by the principal investigator and made available to NASA on request. This record must be submitted to the curator at the termination of the investigator's participation in the Lunar Sample Research Program. It is recognized that the plans will be unique for each institution.

#### PROCEDURE FOR APPLYING FOR LUNAR SAMPLE PROGRAM

"The Handbook for the Lunar Sample Program" (JSC-06090) describes the application procedure for admission to the lunar sample program and provides detailed information about the proper methods for handling, storing, and transferring

lunar samples. The handbook is distributed by the lunar sample curator (TL/JSC, Houston, Texas 77058).

#### Proposal Submission

Information pertaining to the appropriate format for new proposals can be obtained from

Chief, Planetary Programs  
National Aeronautics and Space Administration  
Washington, D.C. 20546

Only duly approved principal investigators are given access to samples for study. Prospective investigators who reside in the United States must submit proposals to

PY/Office of University Affairs  
National Aeronautics and Space Administration  
Washington, D.C. 20546

Prospective investigators who reside outside the United States must submit proposals to

I/Office of International Affairs  
National Aeronautics and Space Administration  
Washington, D.C. 20546

Opportunities for participation in the Lunar Sample Research Program are announced periodically by NASA; proposals, however, may be submitted at any time.

#### Sample Allocations

Samples are allocated to investigators on the recommendation of the Lunar Sample Analysis Planning Team (LSAPT), which may respond to investigator requests or which may initiate allocations they believe will provide important new data. An investigator is not obligated to accept an allocation made by the LSAPT but should make his position clear so that the curator will not be required to expend effort to produce unwanted allocations. Allocation plans are reviewed and approved by the associate administrator for space science before implementation.

#### Sample Requests

In the post-Apollo allocation mode, priority in sample allocation will be given to requests oriented toward the

solution of specific, important, lunar science problems. Consequently, it will be necessary to have each sample request accompanied by a scientific discussion of the specific problems the investigator is interested in addressing and how the samples he proposes to study relate to those problems.

Post-Apollo-Program sample allocation is anticipated to be an ongoing process. Investigators will be asked to revise and update sample requests and requirements at approximately 4- to 6-month intervals, and major allocation plans will be drawn up at these times. As in the past, however, requests for specific interim allocations may be submitted at any time.

There are a variety of ways in which sample requests can be filled. Table 37-I categorizes these according to their impact on curatorial staff and on sample integrity. The samples that have never been investigated and those requiring sawing or chipping of the main rock are the least accessible. Work on these samples is not ruled out, but investigators are urged to attempt to fulfill their scientific needs with more accessible samples. Samples for major allocation will be selected by NASA; the selection will be based on an evaluation of the relative scientific merits of proposed studies and on the number of proposed investigations. When a suite has been selected, all investigators will be notified and given the opportunity to revise their sample requests.

#### SAMPLE PROCESSING, DISSECTION, AND DESCRIPTION

An extensive and detailed history of each lunar sample is maintained both in computerized and hard-copy formats by the lunar sample curator. These systems include the following.

1. The samples (including a library of petrographic thin sections). The thin sections, most of which are polished, may be examined in the curator's facilities by approved sample investigators and by others after special prearrangements with the curator. The special prearrangements involve the submission of a brief proposal justifying the study, which will receive a prompt review.
2. Allocation plans. The allocation plans give the distribution of samples to scientific investigators. Copies may be obtained from the curator, and copies are kept on file in the Lunar Science Institute (LSI) sample-information library.

3. Data packs. These items are hard-copy records of each step in the curatorial handling of each sample. Information derived from these sources can be obtained from the curator; approved investigators may examine the actual data packs.

4. Cutting plans. These plans show the geometry of dissection. Specific plans may be obtained from the curator. A set is kept on file in the LSI sample-information library.

5. PACRAT (a computerized inventory). Information derived from this computerized inventory may be obtained from the curator.

6. History of the degradation of lunar samples returned to the curator after scientific investigations. Information on this aspect may be obtained from the curator.

7. Three-dimensional plastic models. The models are available on a loan basis from the curator.

8. Orthogonal photographs of rocks (known as "mug shots"). The National Space Science Data Center (NSSDC) is the general distributor. Approved investigators may obtain sets from the curator. A set is kept on file in the LSI sample-information library.

9. Photomicrographs of preliminary evaluation team (PET) thin sections. Copies may be obtained from the curator. A representative set is kept on file in the LSI sample-information library.

#### SOURCES OF LUNAR SURFACE INFORMATION

The principal sources of information describing the local features of each Apollo landing site are contained in the reports published by the U.S. Geological Survey and obtainable from the U.S. Geological Survey, Branch of Astrogeologic Studies, Flagstaff, Arizona.

Apollo Field Geology Investigation Team: Apollo 16 Exploration of Descartes: A Geologic Summary. Science, vol. 179, no. 4068, Jan. 1973, pp. 62-69.

Apollo Lunar Geology Investigation Team: Documentation and Environment of the Apollo 16 Samples: A Preliminary Report. U.S. Geol. Survey Interagency Rept., Astrogeol. 51, May 26, 1972.

Apollo Lunar Geology Investigation Team: Documentation and Environment of the Apollo 17 Samples: A Preliminary Report. U.S. Geol. Survey Interagency Rept., Astrogeol. 71, Jan. 21, 1973.

Muehlberger, W. R.; Batson, R. M.; Boudette, E. I.; Duke, C. M.; et al.: Preliminary Geologic Investigation of the Apollo 16 Landing Site. Sec. 6 of Apollo 16 Preliminary Science Report, NASA SP-315, 1972.

Muehlberger, W. R.; Batson, R. M.; Cernan, E. A.; Freeman, V. L.; et al.: Preliminary Geologic Investigation of the Apollo 17 Landing Site. Sec. 6 of Apollo 17 Preliminary Science Report, NASA SP-330, 1973.

Shoemaker, E. M.; Bailey, N. G.; Batson, R. M.; Dahlem, D. H.; et al.: Geologic Setting of the Lunar Samples Returned by the Apollo 11 Mission. Sec. 3 of Apollo 11 Preliminary Science Report, NASA SP-214, 1969.

Shoemaker, E. M.; Batson, R. M.; Bean, A. L.; Conrad, C., Jr.; et al.: Geology of the Apollo 12 Landing Site. Sec. 10, Part A, of Apollo 12 Preliminary Science Report, NASA SP-235, 1970.

Shoemaker, E. M.; Hait, M. H.; Swann, G. A.; Schleicher, D. L.; et al.: Lunar Regolith at Tranquility Base. Science, vol. 167, no. 3948, Jan. 1970, pp. 452-455.

Sutton, R. L.; Batson, R. M.; Larson, K. B.; Schafer, J. P.; et al.: Documentation of the Apollo 14 Samples. U.S. Geol. Survey Interagency Rept. 28, May 1971.

Sutton, R. L.; Hait, M. H.; Larson, K. B.; Swann, G. A.; et al.: Documentation of Apollo 15 Samples. U.S. Geol. Survey Interagency Rept., Astrogeol. 47, Apr. 1972.

Swann, G. A.; Bailey, N. G.; Batson, R. M.; Eggleton, F. E.; et al.: Preliminary Geologic Investigations of the Apollo 14 Landing Site. Sec. 3 of Apollo 14 Preliminary Science Report, NASA SP-272, 1971.

Swann, G. A.; Trask, N. J.; Hait, M. H.; and Sutton, R. L.: Geologic Setting of the Apollo 14 Samples. Science, vol. 173, no. 3998, Aug. 1971, pp. 716-719.

Swann, G. A.; Hait, M. H.; Schaber, G. G.; Freeman, V. I.; et al.: Preliminary Description of Apollo 15 Sample Environments. U.S. Geol. Survey Interagency Rept. 36, Sept. 1971.

Swann, G. A.; Bailey, N. G.; Batson, R. M.; Freeman, V. L.; et al.: Preliminary Geologic Investigation of the Apollo 15 Landing Site. Sec. 5 of Apollo 15 Preliminary Science Report, NASA SP-289, 1972.

Swann, G. A.; Bailey, N. G.; Batson, R. M.; Freeman, V. L.; et al.: Geologic Setting of the Apollo 15 Samples. Science, vol. 175, no. 4020, Jan. 1972. pp. 407-415.

#### SOURCES OF LUNAR SAMPLE INFORMATION

**Descriptive Catalog** - A lunar sample catalog containing sample descriptions was published after each Apollo mission. The catalogs for the Apollo 11, 12, and 15 missions are out of print, but the catalogs for the Apollo 14, 16, and 17 missions are available at the office of the curator.

**Orientation of Lunar Samples** - Determination of the lunar surface orientation of lunar rocks is one of the prime responsibilities of the Field Geology Experiment Team. This information is transmitted to the investigators, usually in the form of U.S. Geological Survey interagency reports, on receipt by the curator. Extra copies are generally not available; inquiries concerning these reports should be sent to the U.S. Geological Survey, Astrogeology Branch, Flagstaff, Arizona.

**Special Sample Publications** - Publications of special-sample reports are provided to investigators by the curator. Such publications include descriptions of 4- to 10-mr. coarse fines (from the Apollo 15, 16, and 17 missions), rake fragments (from the Apollo 16 and 17 missions), and dissected cores. The following publications are available from the curator:

Burlingame, A. L.: University of California, Berkeley, Space Science Laboratory Organic Clean Room and Lunar Material Transfer Facility. The Transfer of Pristine Lunar Material from Apollo 15 SESC 15012 and SESC 15013. NASA Lyndon B. Johnson Space Center (JSC), 1972.

Horz, F.; Carrier, W. D., III; Young, J. W.; Duke, C. M.; et al.: Apollo 16 Special Samples. Sec. 7, Part B, of Apollo 16 Preliminary Science Report, NASA SP-315, 1972.

Keil, K.; Dowty, E.; Prinz, M.; and Bunch, T. E.: Description, Classification, and Inventory of 151 Apollo 16 Rake Samples from the LM Area and Station 5. NASA JSC, 1972.

Marvin, U. B.: Apollo 16 Coarse Fines (4-10 MM): Sample Classification, Description and Inventory. NASA JSC, 1972.

Meyer, C., Jr.: Apollo 17 Coarse Fines (4-10 MM): Sample Location, Classification, and Photo Index. NASA JSC, 1973.

Phinney, W.; and Lofgren, G.: Description, Classification, and Inventory of Apollo 16 Rake Samples from Stations 1, 4, and 13. NASA JSC, 1973.

Powell, B. N.: Apollo 15 Coarse Fines (4-10 MM): Sample Classification, Description and Inventory. NASA JSC, 1972.

Smith, J. V.; and Steele, I. M.: Apollo 16 Rake Samples 67515 to 68537: Sample Classification, Description and Inventory. NASA JSC, 1972.

#### SOURCES OF LUNAR SAMPLE PHOTOGRAPHS

A large collection of rock and thin-section photographs is available for inspection in the office of the curator. Comprehensive photographic indexes for distribution to principal investigators are being prepared. Photographs can be ordered from

National Space Science Data Center  
Code 601.4  
Goddard Space Flight Center  
Greenbelt, Maryland 20771

Phone: (301) 982-6695

#### CHEMISTRY AND PETROGRAPHIC-MODE DATA BASE FOR LUNAR SAMPLES

Curatorial personnel with the aid of Dr. J. L. Warner continuously scan the published literature for tabulated elemental and isotopic chemistry data, petrographic mode data, and age determination data on lunar samples. The data are stored in a computerized system. This data base does not contain lead isotope or rare-gas data, which are published in a wide variety of formats, because much of that data is based on fractions extracted at a series of temperatures or by the use of a series of chemical leaches and is not easily presented in the computer format now in use.

The data output may be in either of two formats. The first format is an organization by sample number under which is a listing of all determinations relative to a particular elemental, isotope concentration or isotopic ratio or mineral percentage. For example, all of the determinations of iron in sample 10084 are listed in a line. The second format is also an organization by sample number; then, however, all elements or compounds (or both), reported from an analysis, are grouped. For example, a single analysis of sample 10084 might include silicon dioxide, aluminum oxide, ferrous oxide, magnesium oxide, calcium oxide, manganous oxide, titanium oxide, potassium oxide, and sodium oxide. Outputs of this continuously updated data base are available from

Dr. J. L. Warner  
Code TN6  
NASA Lyndon B. Johnson Space Center  
Houston, Texas 77058

Recently updated copies of the data base are archived at the NSSDC and are kept on file at the LSI.

Interlibrary Loan  
The Lunar Science Institute  
3303 NASA Road 1  
Houston, Texas 77058

#### ADDITIONAL PROGRAM INFORMATION

Lists of principal investigators currently active in the program are distributed periodically by the curator and are available from the curator. This enables an investigator to contact others who may have results useful to him.

Newsletters also are issued (at irregular intervals) to the principal investigators by the curator. The purpose of this procedure is to keep the investigators apprised of latest developments in the program.

TABLE 37-I.- CATEGORIZATION OF LUNAR SAMPLES RELATIVE TO  
FULFILLMENT OF SAMPLE REQUESTS

Sample types <sup>1</sup>	Fulfillment of sample request
<p>Thin-section collection</p> <p>Transfers between principal investigators</p> <p>Samples returned by principal investigators</p> <p>Prepackaged samples of fines</p> <p>Packaged rock chips</p> <p>Additional samples of fines, including open cores</p> <p>Samples from rocks that previously have been distributed and that do not require additional sawing</p> <p>Samples from rocks that previously have been distributed but that require additional sawing</p> <p>Samples never before distributed, including unopened cores</p>	<p>Immediate if sections are not in use</p> <p>Requires cooperation of other principal investigators</p> <p>Readily accomplished</p> <p>Readily accomplished</p> <p>Readily accomplished</p> <p>Possible in most cases</p> <p>Possible in many cases</p> <p>Requires special justification and availability of data summary for basic description</p> <p>Will be considered (New samples will be scheduled as time permits.)</p>

<sup>1</sup>Sample types are listed in order of decreasing accessibility.

---

A PENDING A  
APOLLO EXPERIMENT PRINCIPAL INVESTIGATORS

CONTENTS - APPENDIX A

	Page
LUNAR SURFACE EXPERIMENTS INVESTIGATORS . . . . .	A-3
LUNAR OPBITAL EXPERIMENTS INVESTIGATORS . . . . .	A-6

C-11

APPENDIX A

APOLLO EXPERIMENT PRINCIPAL INVESTIGATORS

The principal investigators for the lunar surface and lunar orbital experiments are listed by experiment numbers. The lunar surface group is listed first.

LUNAR SURFACE EXPERIMENTS INVESTIGATORS

<u>Number</u>	<u>Experiment</u>	<u>Principal Investigator</u>
S-031	Passive Seismic	Dr. G. V. Latham Marine Biomedical Institute 200 University Blvd. Galveston, Tex. 77550
S-033	Active Seismic	Dr. Robert L. Kovach
S-203	Lunar Seismic Profiling	Dept. of Geophysics Stanford University Stanford, Calif. 94305
S-034	Lunar Surface Magnetometer	Dr. Palmer Dyal, SSE NASA Ames Research Center Moffett Field, Calif. 94035
		Dr. C. Sonnet Lunar and Planetary Laboratory University of Arizona Tucson, Ariz. 85721
S-035	Solar-Wind Spectrometer	Dr. Conway W. Snyder, 169-236 Jet Propulsion Laboratory 4800 Oak Grove Dr. Pasadena, Calif. 91103
S-036	Suprathermal Ion Detector	Dr. John W. Freeman Dept. of Space Science Rice University Houston, Tex. 77001

<u>Number</u>	<u>Experiment</u>	<u>Principal investigator</u>
S-037	Heat Flow	Dr. Marcus E. Langseth Lamont-Doherty Geological Observatory Columbia University Palisades, N.Y. 10964
S-038	Charged-Particle Lunar Environ- ment Experiment	Dr. D. L. Reasoner Dept. of Space Sciences Rice University Houston, Tex. 77001
S-058	Cold Cathode Gage	Dr. Francis S. Johnson Institute for Physical Sciences University of Texas at Dallas P.O. Box 688 Richardson, Tex. 75080
S-059	Lunar Geology	Dr. Gordon A. Swann Center of Astrogeology U.S. Geological Survey 601 East Cedar Ave. Flagstaff, Ariz. 86001  Dr. William R. Muehlberger Geology Department University of Texas Austin, Tex. 78712
S-078	Laser Ranging Retroreflector	Dr. James E. Faller Scott Laboratory Wesleyan University Middletown, Conn. 06457
S-080	Solar-Wind Composition	Dr. Johannes Geiss University of Berne Physikalisches Institut Sidlerstrasse 5 Berne Switzerland
S-152	Cosmic Ray Detector	Dr. R. L. Fleischer General Physics Laboratory General Electric Research and Development Laboratory Schenectady, N.Y. 12301

<u>Number</u>	<u>Experiment</u>	<u>Principal investigator</u>
		Dr. Buford Price Dept. of Physics University of California at Berkeley Berkeley, Calif. 94726
		Dr. Robert M. Walker Physics Dept. Washington University St. Louis, Mo. 63130
S-198	Lunar Portable Magnetometer	Dr. Palmer Dyal, SSE NASA Ames Research Center Moffett Field, Calif. 94035
S-199	Traverse Gravimeter	Dr. Manik Talwani Lamont-Doherty Geological Observatory Columbia University Palisades, N.Y. 10964
S-200	Soil Mechanics	Dr. J. Mitchell University of California at Berkeley Berkeley, Calif. 94726
S-201	Far UV Camera/ Spectograph	Dr. G. R. Carruthers, 7124.3 E. O. Hurlburt Center for Space Research Naval Research Laboratory Washington, D.C. 20390
		Dr. Thornton Page, TN NASA Lyndon B. Johnson Space Center Houston, Tex. 77058
S-202	Lunar Ejecta and Meteorites	Otto E. Berg, 641 Theoretical Studies Branch NASA Goddard Space Flight Center Greenbelt, Md. 20771
S-204	Surface Electrical Properties	Dr. M. Gene Simmons, MIT 54-314 Massachusetts Institute of Technology 77 Massachusetts Ave. Cambridge, Mass. 02139

<u>Number</u>	<u>Experiment</u>	<u>Principal investigator</u>
		Dr. David W. Strangway University of Toronto Toronto, Ontario Canada
S-205	Lunar Atmospheric Composition	Dr. J. H. Hoffman Institute for Physical Sciences University of Texas at Dallas P.O. Box 688 Richardson, Tex. 75080
S-207	Lunar Surface Gravimeter	Dr. Joseph Weber Dept. of Physics and Astronomy University of Maryland at College Park College Park, Md. 20740
S-229	Lunar Neutron Probe	Dr. D. S. Burnett California Institute of Technology Dept. of Geology and Geophysics Pasadena, Calif. 91109
M-515	Dust Thermal Radiation Engineering Measurement	James R. Bates, TN-3 Lyndon B. Johnson Space Center Houston, Tex. 77058

LUNAR ORBITAL EXPERIMENTS INVESTIGATORS

<u>Number</u>	<u>Experiment</u>	<u>Principal investigator</u>
S-160	Gamma-Ray Spectrometer	Dr. James R. Arnold Dept. of Chemistry University of California at San Diego La Jolla, Calif. 92037
S-161	X-Ray Fluorescence	Dr. Isidore Adler Dept. of Chemistry University of Maryland at College Park College Park, Md. 20740

<u>Number</u>	<u>Experiment</u>	<u>Principal investigator</u>
S-162	Alpha-Particle Spectrometer	Dr. Paul Gorenstein Center for Astrophysics Smithsonian Astrophysical Observatory 60 Garden Street Cambridge, Mass. 02138
S-164	S-Band Transponder	William L. Sjogren, CPB 208 Jet Propulsion Laboratory 4800 Oak Grove Dr. Pasadena, Calif. 91103
S-165	Lunar Orbital Mass Spectrometer	Dr. J. H. Hoffman Institute for Physical Sciences University of Texas at Dallas P.O. Box 688 Richardson, Tex. 75080
S-169	Ultraviolet Spectrometer	Prof. William E. Fastie Johns Hopkins University Baltimore, Md. 21218
S-170	Bistatic Radar	H. Taylor Howard Stanford Electronics Laboratory Stanford University Stanford, Calif. 94305
S-171	Infrared Scanning Radiometer	Dr. Frank J. Low Lunar and Planetary Laboratory University of Arizona Tucson, Ariz. 85721  W. W. Mendell, TN2 NASA Lyndon B. Johnson Space Center Houston, Tex. 77058
S-173	Subsatellite Particles and Shadows	Dr. Kinsey A. Anderson Space Science Laboratory University of California at Berkeley Berkeley, Calif. 94726
S-174	Particles and Fields Subsatellite Magnetometer	Dr. P. J. Coleman Dept. of Planetary and Space Science University of California at Los Angeles Los Angeles, Calif. 90024

<u>Number</u>	<u>Experiment</u>	<u>Principal investigator</u>
S-175	Laser Altimeter	<p>Dr. William M. Kaula  Institute of Geophysics and  Planetary Physics  University of California at  Los Angeles  Los Angeles, Calif. 90024</p> <p>William L. Sjogren, CPB 208  Jet Propulsion Laboratory  4800 Oak Grove Dr.  Pasadena, Calif. 91103</p>
S-209	Lunar Sounder	<p>Dr. Roger J. Phillips  Jet Propulsion Laboratory  4800 Oak Grove Dr.  Pasadena, Calif. 91103</p> <p>Dr. Stanley Ward  Dept. of Geological and  Geophysical Sciences  University of Utah  Salt Lake City, Utah 84112</p> <p>Walter E. Brown, Jr.  Jet Propulsion Laboratory  4800 Oak Grove Dr.  Pasadena, Calif. 91103</p>

The section entitled "Lunar Photographic and Cartographic Products" was prepared by Danny C. Kinsler, Administrative Assistant to the Lunar Photography and Cartography Committee. His address is

Lunar Science Institute  
3303 NASA Road 1  
Houston, Tex. 77058

---

APPENDIX B  
APOLLO ALSEP DEPLOYMENT CONFIGURATIONS  
AND LUNAR GROUNDTRACKS

APPENDIX B

APOLLO ALSEP DEPLOYMENT CONFIGURATIONS  
AND LUNAR GROUNDTRACKS

This appendix contains the following background information for users of the experiments handbook.

1. Deployment configurations of Apollo lunar surface experiments package (ALSEP) systems for the Apollo 12, 14, 15, 16, and 17 missions (figs. B-1 to B-5).

2. Groundtrack maps relative to lunar orbital experiments during the Apollo 15, 16, and 17 missions (figs. B-6 to B-8).

**PRECEDING PAGE BLANK NOT FILMED**

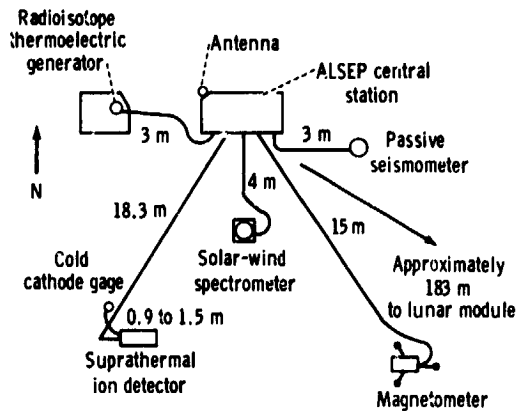


Figure B-1.- Deployment configuration for Apollo 12 ALSEP.

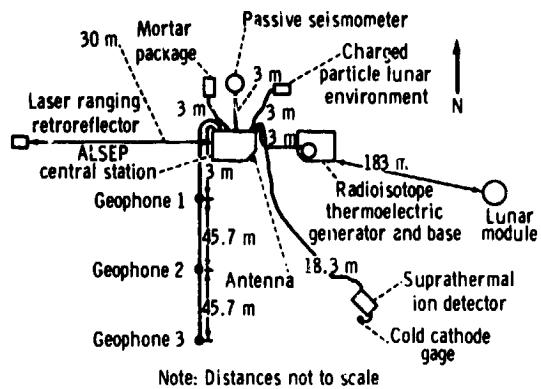


Figure B-2.- Deployment configuration for Apollo 14 ALSEP.

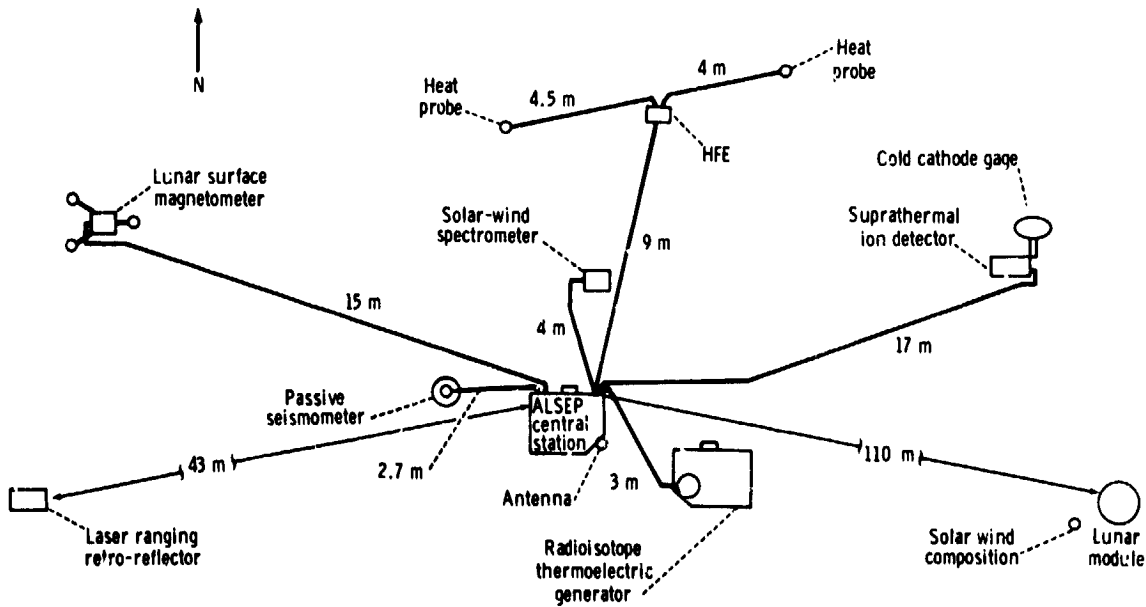


Figure B-3.- Deployment configuration for Apollo 15 ALSEP.

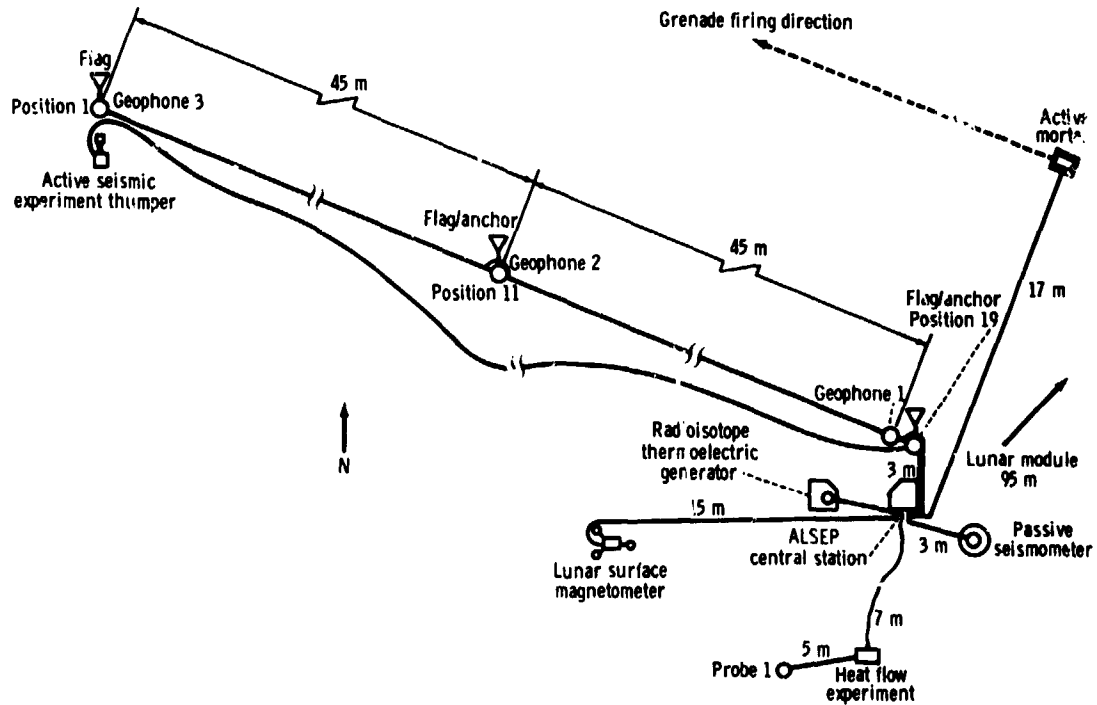


Figure B-4.- Deployment configuration for Apollo 16 ALSEP.

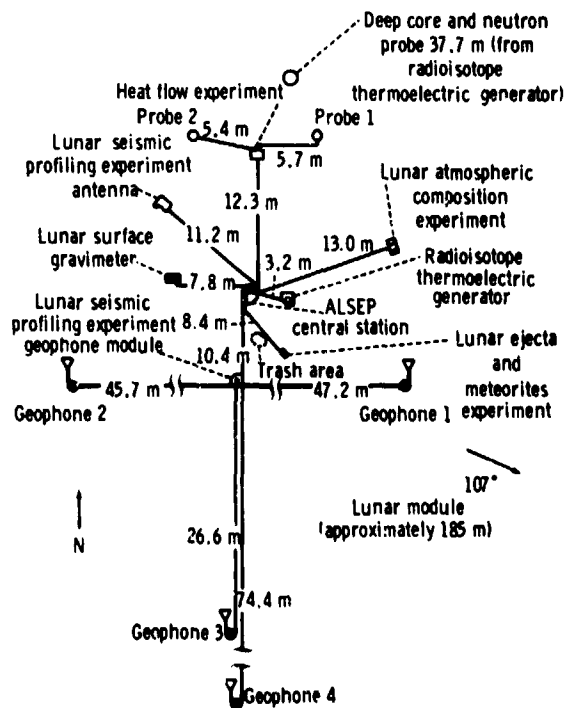
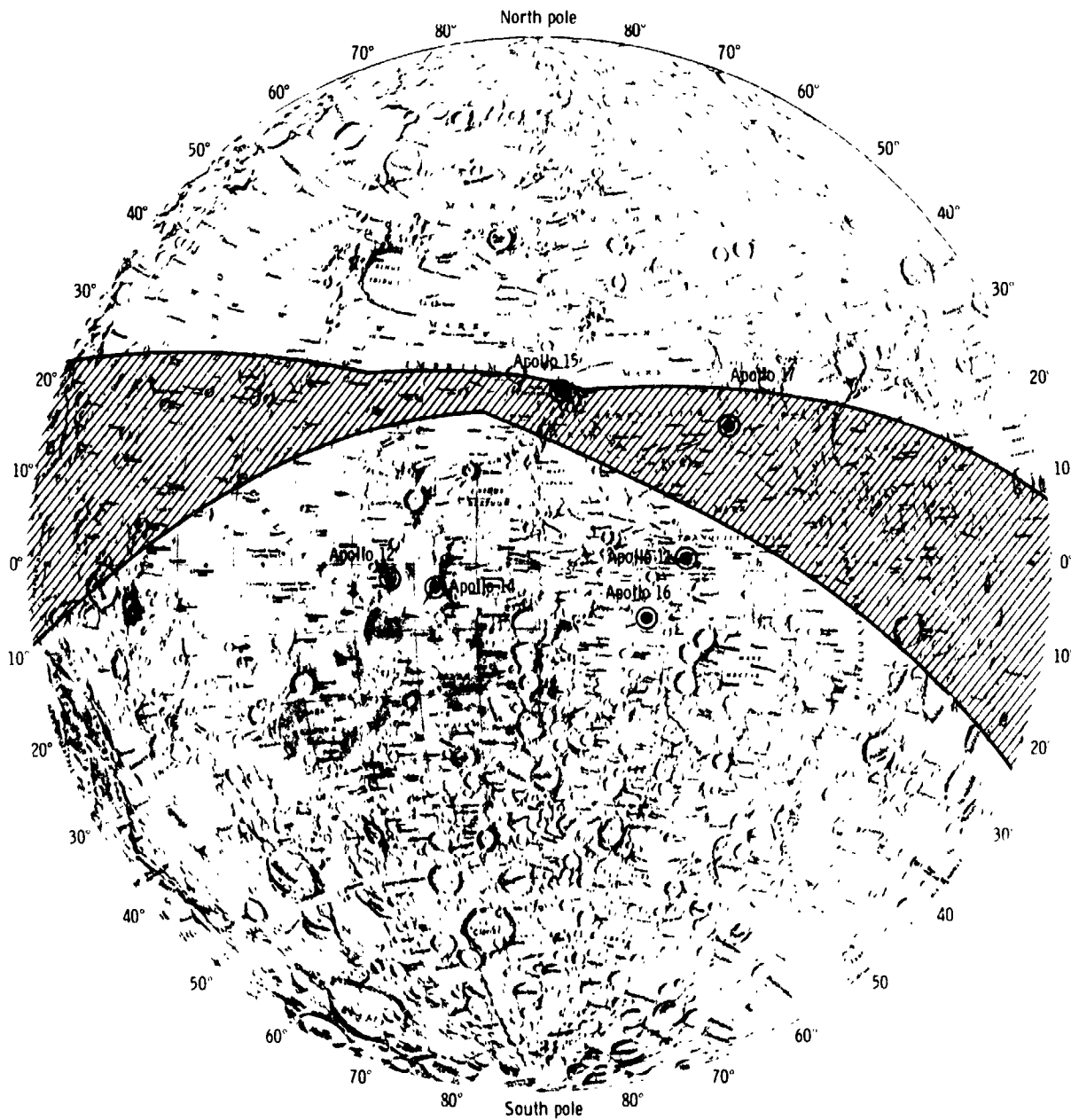


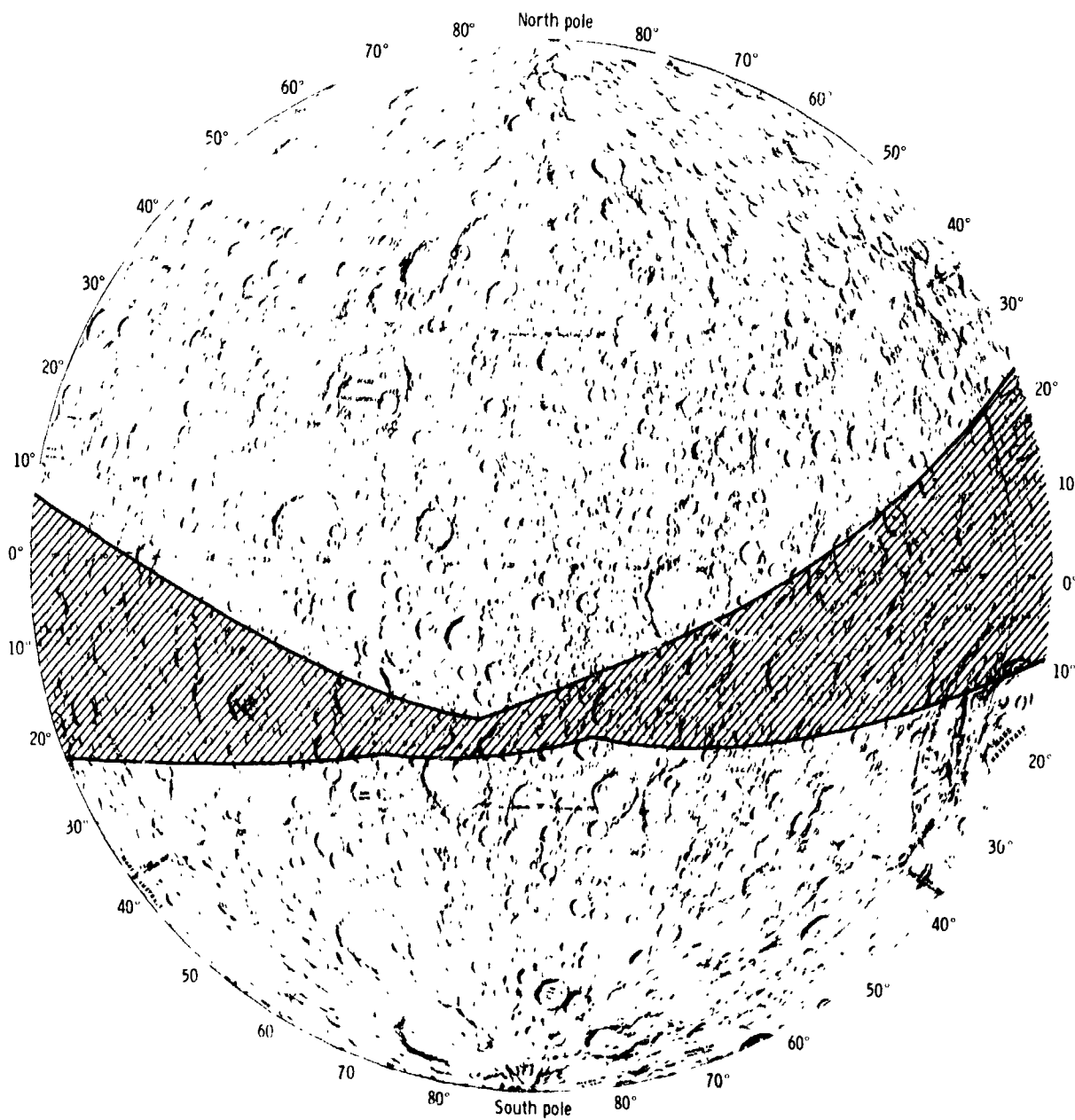
Figure B-5.- Deployment configuration for Apollo 17 ALSEP.

ORIGINAL PAGE IS  
OF POOR QUALITY



(a) Near side.

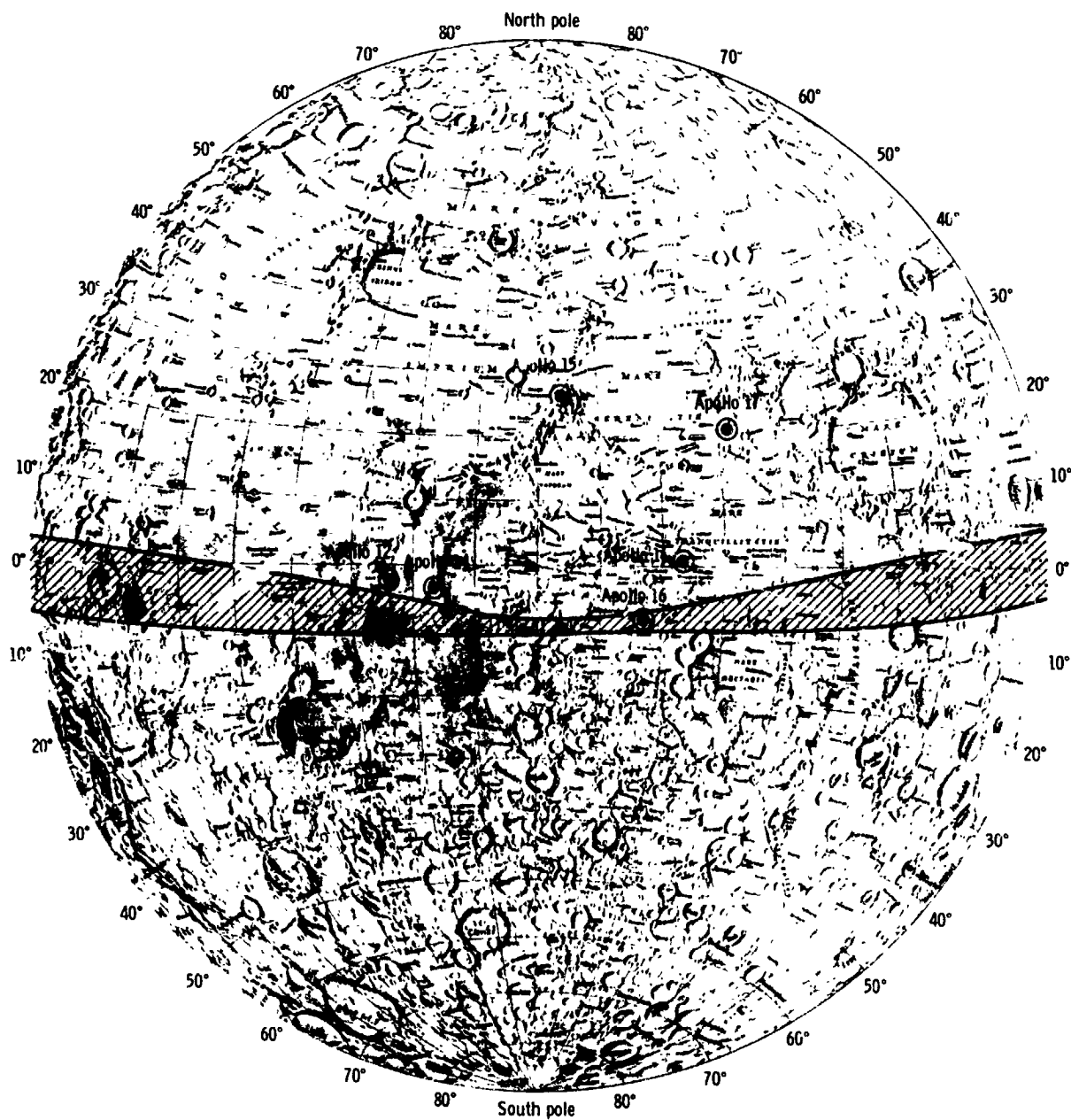
Figure B-6.- Lunar surface groundtrack envelope of the Apollo 15 orbiting spacecraft for revolutions 1 to 74. Areas of additional data coverage outside the envelope are determined by the fields of view of experiment instruments and photographic cameras.



(b) Far side.

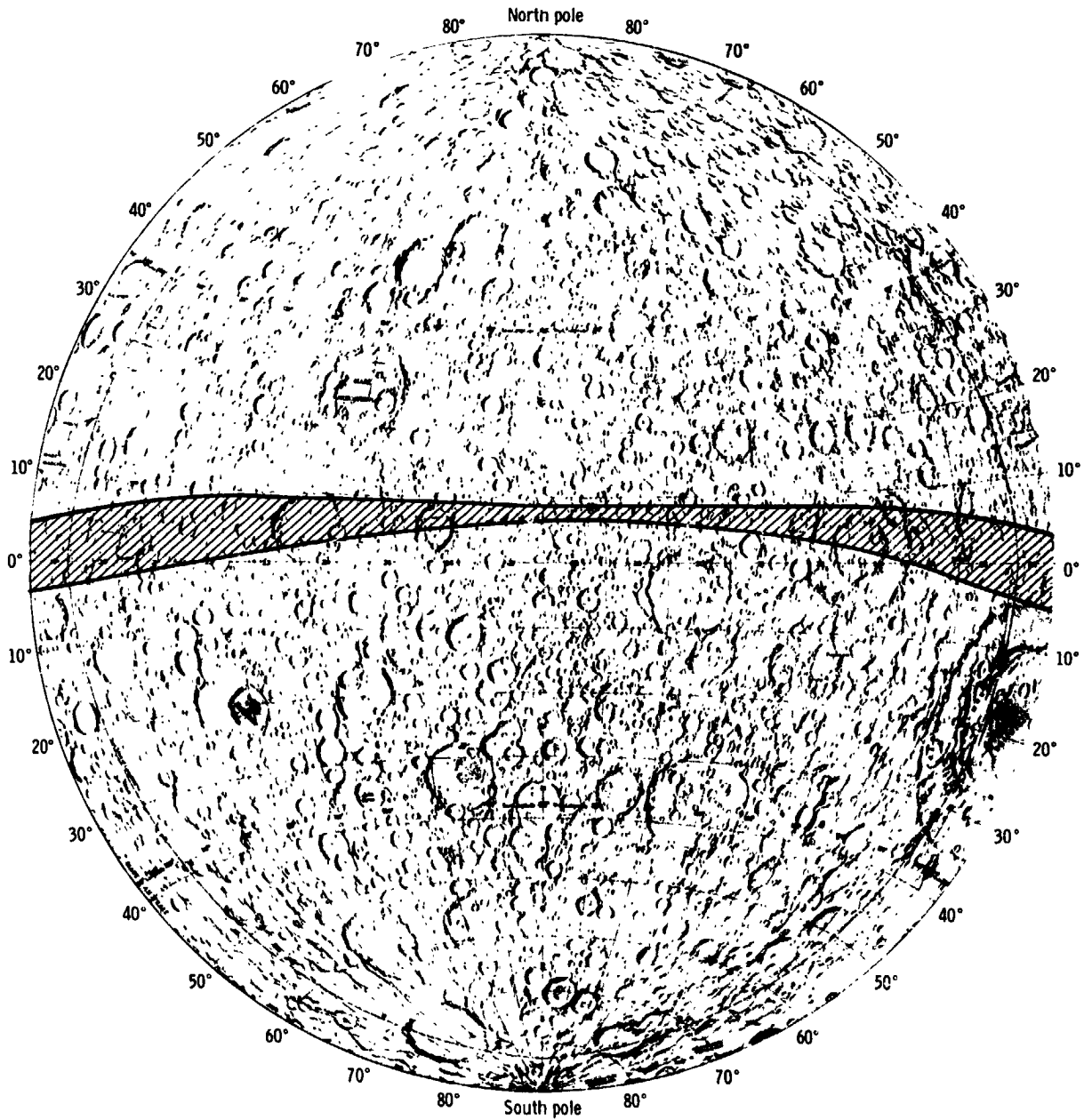
Figure B-6.- Concluded.

ORIGINAL PAGE IS  
OF POOR QUALITY



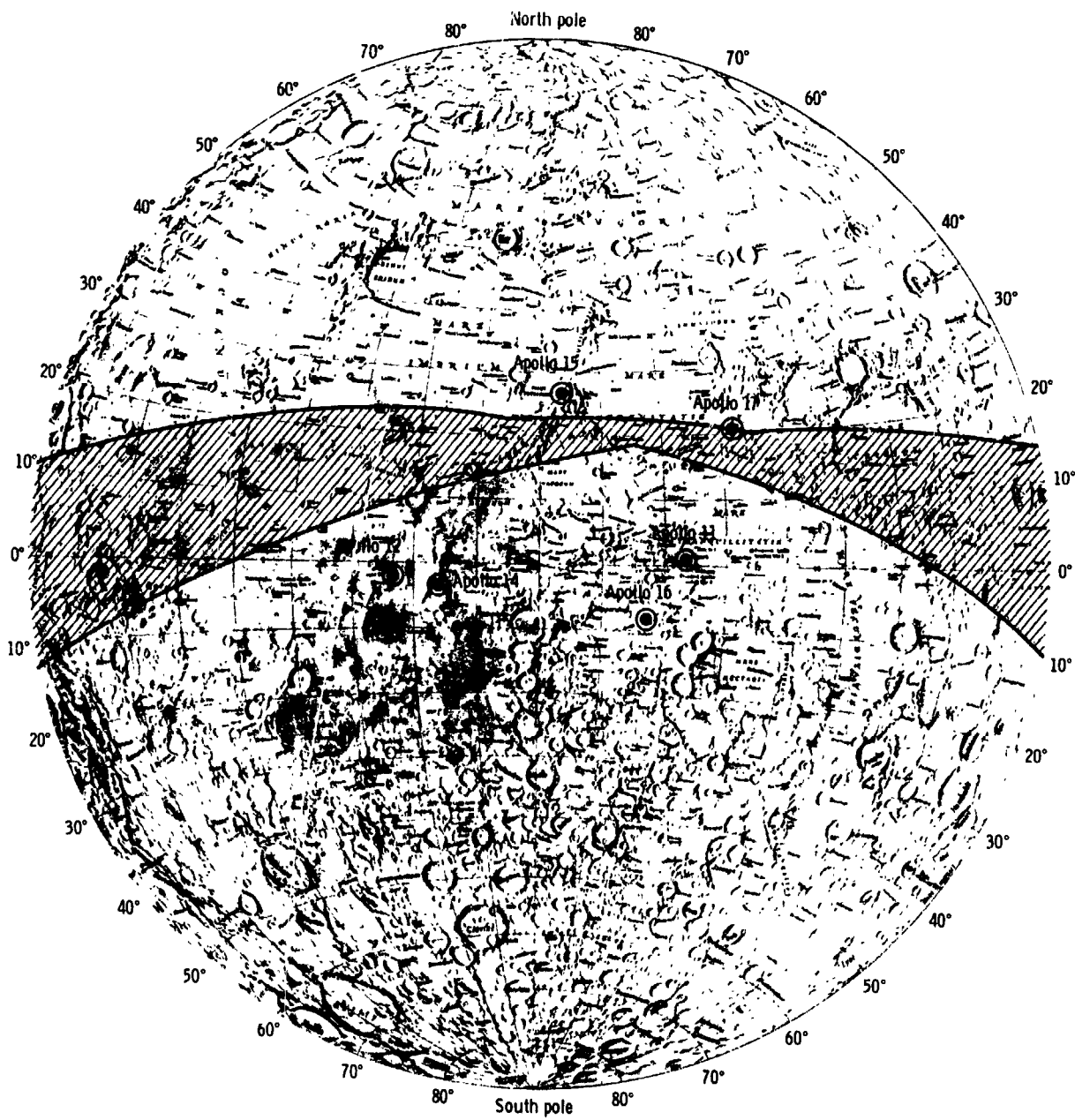
(a) Near side.

Figure B-7.- Lunar surface groundtrack envelope of the Apollo 16 orbiting spacecraft for revolutions 1 to 65. Areas of additional data coverage outside the envelope are determined by the fields of view of experiment instruments and photographic cameras.



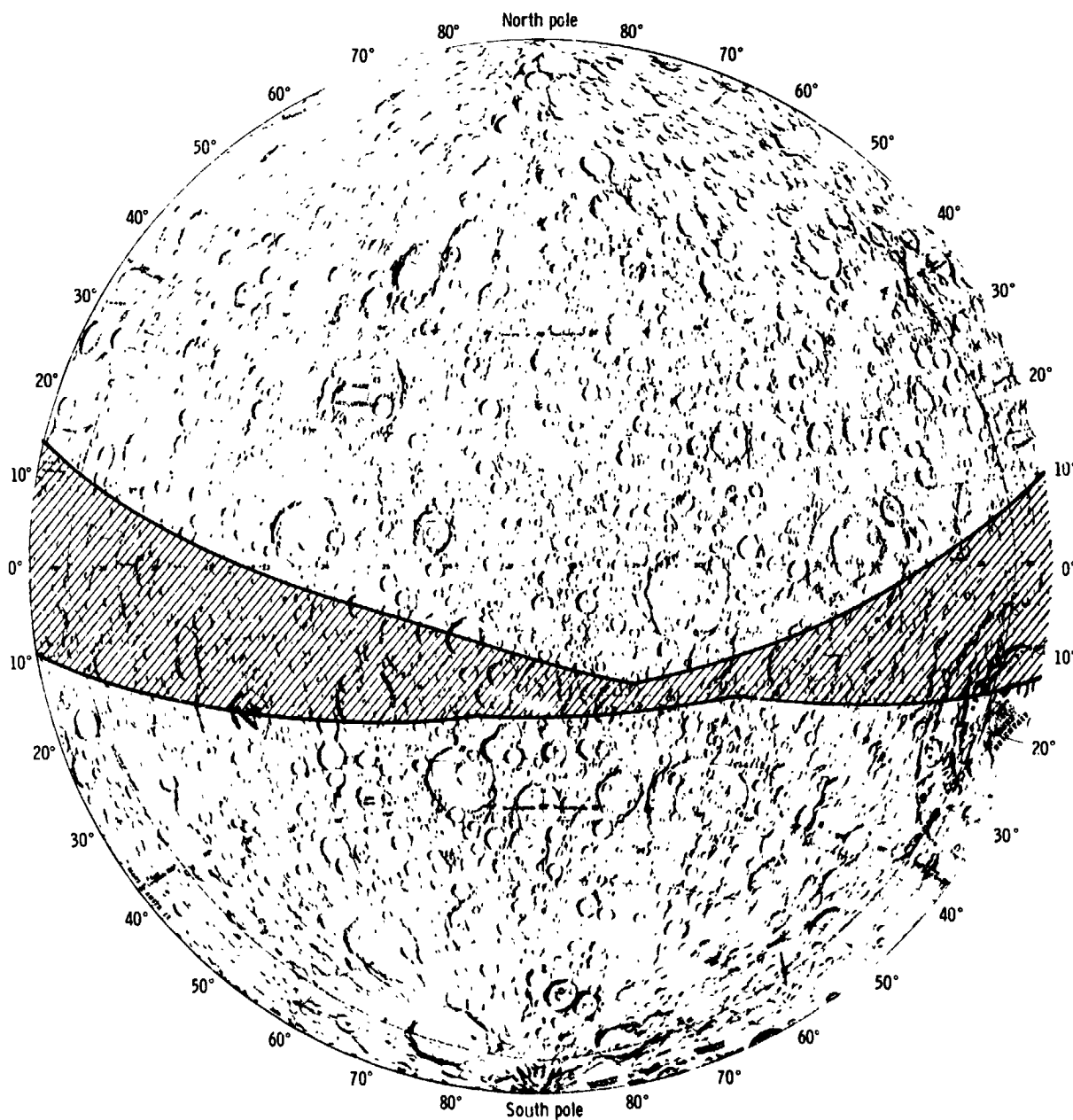
(b) Far side.

Figure B-7.- Concluded.



(a) Near side.

Figure B-8.- Lunar surface groundtrack envelope of the Apollo 17 orbiting spacecraft for revolutions 1 to 75. Areas of additional data coverage outside the envelope are determined by the fields of view of experiment instruments and photographic cameras.



(b) Far side.

Figure B-8.- Concluded.

ORIGINAL PAGE IS  
OF POOR QUALITY

---

APPENDIX C  
LIST OF ACRONYMS

APPENDIX C

LIST OF ACRONYMS

ADC	analog-to-digital converter
AET	Apollo elapsed time
AGRS	Apollo gamma-ray spectrometer
AIC	Apollo intermediate charts
ALSE	Apollo lunar sounder experiment
ALSEP	Apollo lunar surface experiments package
ASE	active seismic experiment
ATS	Applied Technology Satellite
AXRS	Apollo X-ray spectrometer
AZ	azimuth
BCD	binary coded decimal
CCGE	cold cathode gage experiment
CCIG	cold cathode ion gage
CDC	Control Data Corporation
CDR	commander
c. g.	center of gravity
CPLEE	charged-particle lunar environment experiment
CRT	cathode ray tube
CSAR	coherent synthetic aperture radar
CSM	command and service module
CTE	computer time elapsed
Cyg	Cygnus
dec	declination
DRNM	Deep River Neutron Monitor
DSN	Deep Space Network
DTREM	dust thermal radiation engineering measurement
EASEP	early Apollo scientific experiments package
E-frame	electronic frame
EL	elevation
EMI	electromagnetic interference
EOP	end of file
EOT	end of tape
EP	explosive package
ERIM	Environmental Research Institute of Michigan
EVA	extravehicular activity
FET	field effect transistor
FFT	fast Fourier transform
FM	frequency modulation
FOV	field of view
FWHM	full width, half maximum
GCR	galactic cosmic ray
GE	General Electric
GET	ground elapsed time

PRECEDING PAGE BLANK NOT FILMED

G.m.t.	Greenwich mean time
GRS	gamma-ray spectrometer
GSFC	Goddard Space Flight Center
HF	high frequency
HFE	heat flow experiment
HV	high voltage
IMP	Interplanetary Monitoring Platform
IR	infrared
ISR	infrared scanning radiometer
JPL	Jet Propulsion Laboratory
JSC	Lyndon B. Johnson Space Center
LAC	lunar astronomical charts
LACE	lunar atmospheric composition experiment
L-DGO	Lamont-Doherty Geological Observatory
LEAM	lunar ejecta and meteorites
LIT	local lunar time
LM	lunar module
LMC	large Magellanic Cloud
LNPE	lunar neutron probe experiment
LP	long period
LP#	lunar portable magnetometer
LPX	long period horizontal (X-axis) or long-period horizontal seismometer
LPY	long period horizontal (Y-axis) or long-period horizontal seismometer
LPZ	long period vertical (Z-axis) or long-period vertical seismometer
LRC	Langley Research Center
LRV	lunar roving vehicle
LSAPT	Lunar Sample Analysis Planning Team
LSG	lunar surface gravimeter
ISI	Lunar Science Institute
LSM	lunar surface magnetometer
LSPE	lunar seismic profiling experiment
LURE	Lunar Laser Ranging Experiment
LVPS	low-voltage power supply
MA	mass analyzer
MESA	modularized equipment stowage assembly
MET	modularized equipment transporter
MPA	mortar package assembly
MRO	memory readout
NAT	NASA Apollo trajectory
NBS	National Bureau of Standards
NSSDC	National Space Science Data Center
OAO-2	Orbiting Astronomical Observatory 2
OGO IV	Orbiting Geophysical Observatory IV
PA	post amplifier
PCM	pulse code modulation
PFS	particles and fields subsatellite
PMT	photomultiplier tube
PSD	pulse shape discriminator
PSE	passive seismic experiment

**ORIGINAL PAGE IS  
OF POOR QUALITY**

PSEP	passive seismic experiments package
RA	right ascension
rev	revolution
RFI	radiofrequency interferometry
RLC	Ranger VII lunar charts
rms	root mean square
RT	real time
RTG	radioisotope thermoelectric generator
SA	SIM attitude
SAO	Smithsonian Astrophysical Observatory
SB	standby
Scor	Scorpius
SE	solar ecliptic
SEM	scanning electron microscope
SEP	surface electrical properties
SIDE	suprathermal ion detector experiment
SIM	scientific instrument module
SIVB	Saturn IVB
SM	solar magnetospheric
SP	short period
SRI	Stanford Research Institute
SRP	self-recording penetrometer
SWS	solar-wind spectrometer
TCE	telemetry conversion error
TEC	transearth coast
TEI	transearth injection
TGE	traverse gravimeter experiment
TID	total ion detector
TSP	telemetry-store fast
TSN	telemetry-store normal
UCLA	University of California at Los Angeles
USGS	U.S. Geological Survey
UTD	University of Texas at Dallas
UV	ultraviolet
UVS	ultraviolet spectrometer
VCO	voltage-controlled oscillator
VHF	very high frequency
VLBI	very long baseline interferometry
VSA	vibrating string accelerometer
WDC-A-R&S	World Data Center A for Pockets and Satellites

ORIGINAL PAGE IS  
OF POOR QUALITY

---

APPENDIX D  
SOLAR-WIND-COMPOSITION EXPERIMENT  
(NASA EXPERIMENT S-080)

CONTENTS - APPENDIX D

	Page
EQUIPMENT DESCRIPTION AND LUNAR SURFACE OPERATION . . . .	D-4
EXPERIMENT HANDLING PROCEDURES (APOLLO 11 TO APOLLO 16) . . . . .	D-5
RESULTS OF FOIL ANALYSES . . . . .	D-6
AIMS OF FURTHER FOIL ANALYSES . . . . .	D-7
DISCUSSION . . . . .	D-7
CONCLUDING REMARKS . . . . .	D-9
AVAILABILITY OF FOIL MATERIAL . . . . .	D-10
REFERENCES . . . . .	D-10
BIBLIOGRAPHY . . . . .	D-12

## APPENDIX D

### SOLAR-WIND-COMPOSITION EXPERIMENT

The solar-wind-composition experiment was conducted during the Apollo 11, 12, 14, 15, and 16 missions. The major objective was to measure the abundances and isotopic compositions of noble gases in the solar wind.

For several years, the fact has been established that  ${}^4\text{He}^{2+}$  ions are present in the solar wind and that the relative abundance of the ions is highly variable. Helium-to-hydrogen values from 0.01 to 0.25 have been observed by instruments flown on unmanned spacecraft, but the average helium-to-hydrogen ratio in the solar wind is approximately 0.04 to 0.05. At least during stationary conditions, the bulk velocities of hydrogen and helium are normally the same to within a few percent. The presence of  ${}^3\text{He}$  and oxygen in the solar wind has also been reported. However, because these ion species were observed only under very favorable conditions, no values can be given for the averages and variations of their abundance.

Plasma and magnetic field measurements of Explorer 35 have established that, to a good approximation, the Moon behaves like a passive obstacle to the solar wind, and no evidence for a bow shock has been observed. Thus, during the normal lunar day, the solar-wind particles can be expected to reach the surface of the Moon with essentially unchanged energies. The grains of the fine lunar surface material contain great amounts of these particles. Consequently, it should be possible to extract valuable information on the composition of the solar wind from analyses of lunar surface material. However, the dust on the lunar surface is a solar-wind collector of uncertain properties, integrating the flux over an unknown period of time during which relative element abundances are probably changing significantly by both diffusion losses and saturation effects. No information on short-time variations can be derived from solar-wind particles implanted in lunar surface material; thus, the possibility that hydro-magnetic processes influence the solar-wind composition cannot be assessed from data obtained only from analysis of lunar surface material.

For the foregoing reasons, it appeared worthwhile to conduct an experiment in which the solar wind would be sampled over a definite period of time by collecting solar-wind particles in a foil with well-defined trapping properties. The Apollo solar-wind-

composition experiment was the first attempt at collecting the solar wind by this method.

#### EQUIPMENT DESCRIPTION AND LUNAR SURFACE OPERATION

The experiment hardware consisted of a metallic telescopic pole approximately 4 cm in diameter and approximately 40 cm in length when collapsed. In the stowed position, the foil was enclosed in the tubing and rolled up on a spring-driven roller. The instrument weighed 430 g. When extended at the lunar surface, the pole was approximately 1.5 m long and a 30- by 140-cm foil area was exposed. Only the foil assembly was recovered at the end of the lunar exposure period; it was rolled on the spring-driven roller and returned to Earth.

The aluminum foil, with an area of approximately  $4000 \text{ cm}^2$ , was exposed to the solar wind at the lunar surface approximately perpendicular to the sunrays. Data concerning the lunar surface exposure are given in table D-I, and details of the exposed foil assembly are shown in figure D-1. The main part of the assembly is a 15- $\mu\text{m}$ -thick aluminum foil. The backside of the foil was anodically covered with approximately 1  $\mu\text{m}$  of  $\text{Al}_2\text{O}_3$ , to keep the foil temperature below 373 K (100° C) during exposure on the Moon. For reinforcement, the foil was rimmed with Teflon tape.

Test pieces 1, 3, and 5 are foils that were bombarded in the laboratory before the mission with a known flux of neon ions with an energy of 15 keV. The amounts of neon used were large by comparison with the expected solar-wind neon fluxes. Determination of the amount of neon implanted in these test pieces would have indicated if solar-wind noble-gas losses had occurred during the mission because of some unexpected diffusion or surface erosion processes. Test piece 5 was mounted in a closed pocket and remained shielded during the exposure on the lunar surface; test pieces 1 and 3 were exposed to the solar wind. Test piece 4 was a piece of foil taped to the backside of the main foil. A solar-wind flux coming from a direction opposite to the Sun could be distinguished by means of test piece 4. Test piece 2 was mounted in a position that remained shielded from the solar wind.

The foil assembly was modified for Apollo 16, this configuration is shown in figure D-1(b). Platinum sections were mounted on this aluminum foil by adhesive Teflon tape. Lunar dust that cannot be removed from these sections by ultrasonic cleaning will be attacked by hydrofluoric acid. Previous tests have shown that gases trapped in platinum foils are not affected by this treatment, but that a high percentage of the noble gases implanted in dust are removed by the treatment.

One section on the backside of the Apollo 16 foil consisted of platinum covered by a 1- $\mu$ m deposit of aluminum. After removal of the aluminum layer in a hydrofluoric acid bath, analysis of the rare gas atoms that are trapped in the platinum will show which part of the particles coming from the direction opposite to the Sun have sufficient energy (above approximately 40 keV/nucleon) to go through a 1- $\mu$ m layer of aluminum.

Before flight, the trapping properties of the foil material for kiloelectron-volt ions were extensively investigated in the laboratory. Trapping probabilities for helium, neon, and argon were determined in a wide energy range. For average solar-wind energies, the probabilities are 89 percent for helium (3 keV), 100 percent for neon (15 keV), and 99 percent for argon (3 keV). (These values are approximate for normal incidence.) Because these figures are only slightly energy dependent, they can be used even if, during exposure, the solar-wind velocity was quite different from the average. The trapping probabilities were found to be independent of foil temperature (293 to 393 K (20° to 120° C)), and they were not affected by simultaneous bombardment with kiloelectron-volt hydrogen ions ( $H_2^+$ ).

#### EXPERIMENT HANDLING PROCEDURES (APOLLO 11 TO APOLLO 16)

All materials used in the construction of the reel and foil assemblies were analyzed for 13 geochemically important trace elements (lithium, beryllium, boron, magnesium, potassium, rubidium, strontium, yttrium, lanthanum, ytterbium, lead, thorium, and uranium). All concentrations were low enough to be geochemically acceptable.

To avoid organic contamination of the lunar surface material in the container, the instrument was subjected to several heating cycles, and the degree of decontamination was controlled by mass spectrometric analysis. Prior to shipment to the NASA Lyndon B. Johnson Space Center (JSC) and the NASA Kennedy Space Center for installation into the lunar module, the instrument was double bagged in Teflon and heat sterilized. For the Apollo 11, 12, and 14 missions, the returned assemblies were kept behind the primary biological barrier in the Lunar Receiving Laboratory (LRL) and released after the quarantine periods. The Apollo 15 and 16 assemblies were sent to the University of Berne immediately after their return from the mission. For the Apollo 11 mission, a 0.09 m<sup>2</sup> (1 ft<sup>2</sup>) portion was cut from the midsection of the foil during quarantine and heat sterilized for 39 hr at 398 K (125° C) for a first investigation in Berne. To restrict foil handling and to avoid additional contamination with lunar dust in the LRL quarantine cabinets, no early release was attempted with the other foils.

---

For analysis, small pieces were cut from the foil, cleaned of lunar dust contamination, and melted in a vacuum. The noble gases were then measured in mass spectrometers. Helium, neon, and argon were found in significant quantities. In the Apollo 11 foil, argon of solar wind origin could not be detected because the exposure period had been too short.

#### RESULTS OF FOIL ANALYSES

For the five solar-wind-composition experiments, a large number of clean foil pieces of different sizes have been analyzed for their helium and neon isotope contents (refs. D-1 to D-6); the number of argon analyses is somewhat smaller. The data from different pieces of one foil always agree very well. As an example, the results of five Apollo 16 foil pieces are given in table D-II.

The average solar-wind abundance ratios determined for the five Apollo solar-wind-composition exposure times are listed in table D-III. They were obtained from the measured ratios by correcting for the differences in trapping probabilities. This correction is typically 14 percent for the  $^4\text{He}/^{20}\text{Ne}$  ratio and 2 percent for the  $^4\text{He}/^3\text{He}$  ratio. The isotopic ratios of Ne were not corrected. The results of the argon measurements are summarized in table D-IV. The  $^{20}\text{Ne}/^{36}\text{Ar}$  ratios given in this table correspond to the ratios of the trapped gases. They cannot be directly considered as solar-wind abundance ratios because there is a definite contribution of  $^{36}\text{Ar}$  from the lunar atmosphere. This atmospheric argon is ionized by solar ultraviolet and then accelerated by the electric field that is induced by the magnetic field moving with the solar wind (refs. D-7 and D-8). This contribution is strongest in the case of Apollo 15.

In addition to the published data, a large number of foil pieces have been analyzed. The results are presented in two theses of the University of Berne (refs. D-9 and D-10). These new data do not change the abundance ratios of the helium and neon isotopes published so far. However, they contain much new information on the arrival directions of solar-wind ions. They also give an improved estimate of the  $^{20}\text{Ne}/^{36}\text{Ar}$  ratio in the solar wind.

## AIMS OF FURTHER FOIL ANALYSES

The remaining clean parts of the foils will be used to make further analyses with the following aims:

1. The  $^{22}\text{Ne}/^{21}\text{Ne}$  ratio can be obtained with higher precision by analyzing a larger foil area and by using a somewhat modified method of analysis.
2. Some foil pieces will be analyzed with the specific aim of obtaining precise  $^{36}\text{Ar}/^{38}\text{Ar}$  ratios.
3. Certain parts (including those of the Apollo 16 foil that consist of platinum) of the foil that were not looking into the solar wind will be used to improve the estimate of solar-wind particle albedo.
4. A part of the Apollo 16 foil consists of several layers. It will be used to obtain an upper limit of the flux of particles that have energies much higher than those in the solar wind.

## DISCUSSION

The relative elemental and isotopic abundances of helium and neon in the solar wind measured for the Apollo 12, 14, 15, and 16 exposure times are quite similar, in spite of large (factor of 4) variations in the  $^4\text{He}$  flux. However, the abundances obtained for Apollo 11 are different. In figure D-2,  $^3\text{He}/^4\text{He}$  is plotted against  $^4\text{He}/^{20}\text{Ne}$ . It has been shown (ref. D-1) and verified (ref. D-6) that these abundance ratios are correlated, with high  $^3\text{He}/^4\text{He}$  ratios corresponding to low  $^4\text{He}/^{20}\text{Ne}$  ratios. Just the opposite correlation would be expected if electromagnetic separation effects were operating in the corona (ref. D-11) or near the Moon (ref. D-4). Conversely, theoretical considerations (refs. D-11 and D-12) on the acceleration of ions in the corona predict larger fluctuations in the  $^4\text{He}$  abundance than in the  $^3\text{He}$  and  $^{20}\text{Ne}$  abundances, and, in fact, the  $^3\text{He}/^{20}\text{Ne}$  ratio is the same for the five solar-wind-composition experiments within the limits of error.

Particularly noteworthy is the absence of any indication of electromagnetic separation effects at the Apollo 16 landing site vicinity where local magnetic fields exist with strengths up to

313 nT (313  $\gamma$ ) and with an average field of the order of 200 nT (200  $\gamma$ ) (ref. D-13). The gyroradii of  $^3\text{He}^{2+}$ ,  $^4\text{He}^{2+}$ , and  $^{20}\text{Ne}^{8+}$  with energies of 750 eV/nucleon in a field of 200 nT (200  $\gamma$ ) are 29, 38, and 48 km, respectively. The facts that solar-wind ions reach the lunar surface at the Apollo 16 landing site and that there does not appear to be any mass discrimination limit the spatial extent of an organized magnetic field of 200 nT (200  $\gamma$ ). The measurement of the arrival directions conducted on section 3 of the foil allows a quantitative estimate of the extent and regularity of the magnetic field in the area east of the Apollo 16 landing site.

Data obtained with the Vela 3A and 3B satellites suggest a dependence of the He/H ratio on solar activity (ref. D-14). Explorer 34 results have shown an association of high He/H ratios with geomagnetic storms (ref. D-15). Also, it has been observed that interplanetary shocks are followed by a helium-rich plasma interpreted as the driver gas that produces the shock (refs. D-16 and D-17). To gain a better understanding of the dynamic processes underlying these observations, it is important to study the behavior of other ion species. In figure D-3, the  $^4\text{He}/^3\text{He}$  abundance ratio is plotted as a function of the geomagnetic index  $K_p$ . Included in figure D-3 is the  $^4\text{He}/^3\text{He}$  ratio obtained from a Surveyor III aluminum tube returned from the Moon by the Apollo 12 crewmen. A correlation clearly seems to exist.

The correlation rests very strongly on the low  $^4\text{He}/^3\text{He}$  ratio measured during the time of the Apollo 11 extravehicular activity, a period of low  $K_p$ . The other exposure periods include times of lower and higher  $K_p$ ; therefore, it can be assumed that the  $^4\text{He}/^3\text{He}$  variability would be higher if shorter periods were sampled. For example, in the case of the Apollo 16 exposure period,  $K_p$  was  $0^\circ$  and  $0^+$  during the first 12 hr, rising afterwards to reach a maximum value of  $4^\circ$  that lasted 6 hr. On the basis of figure D-3, it must be assumed that these  $K_p$  changes were accompanied by composition changes and that the variability during this exposure period may have been larger than the entire range of measured values given in figure D-3.

Weighted averages of ion abundances in the solar wind for the period during which solar-wind-composition foils were exposed are given in table D-V. Judging from the  $K_p$  values during these exposures, the averages should be fairly representative for the period from the Apollo 11 landing to the Apollo 16 landing (summer 1969 and spring 1972). The errors given are an attempt to estimate the uncertainty of the averages for the indicated period. The errors are based on the variability of the observed

abundances obtained from the four long-exposure times. The question is to what extent the averages given in table D-V would have to be corrected to obtain values representative for the average solar wind. These corrections should be largest for  $^{20}\text{Ne}/^{36}\text{Ar}$  and  $^4\text{He}/^{20}\text{Ne}$ , smaller for  $^4\text{He}/^3\text{He}$ , and virtually negligible for the neon isotopic abundances. The  $^{20}\text{Ne}/^{36}\text{Ar}$  value for the solar wind ( $45 \pm 10$ ) is higher than the ratios of the trapped gases (table D-IV) because of the presence of a lunar atmospheric  $^{36}\text{Ar}$  component.

The average solar-wind composition is not necessarily identical with the abundances in the outer convective zone of the Sun. The latter can only be derived accurately after the fractionation processes in the solar-wind source region have been sufficiently studied by investigating solar-wind abundance variations.

The gases concentrated on the surfaces of the grains of lunar material and in the solar wind differ in their composition (table D-V). This difference is probably a result of diffusive losses of gases from the lunar material and perhaps a result of other secondary effects such as saturation or retrapping. The mineral ilmenite ( $\text{FeTiO}_3$ ) appears to have preserved the original abundances better than the other constituents in the lunar fines material. However, even in ilmenite, the isotopic ratios of helium and neon are significantly different from the solar-wind values. The relative differences for the  $^4\text{He}/^3\text{He}$  and  $^{20}\text{Ne}/^{22}\text{Ne}$  ratios are of the order of  $(\Delta M/M)^{1/2}$  where  $M$  is the mass of the element and  $\Delta M$  is the difference in mass of the isotopes. The  $^4\text{He}/^3\text{He}$  ratio in the breccia ilmenite is significantly higher than in the ilmenite separated from the fines material. This observation is an indication of a secular variation in the  $^4\text{He}/^3\text{He}$  ratio (ref. D-20).

#### CONCLUDING REMARKS

The isotopic abundance of neon contained in the atmosphere of the Earth is highly fractionated with respect to solar neon. An even stronger fractionation was anticipated long ago (refs. D-21 and D-22) on the basis of the apparent element fractionation of noble gases in the atmosphere. On Venus, these fractionations might very well be smaller, and, judging from elemental abundances, even less fractionation can be expected for the major planets. If noble-gas elemental and isotopic abundances in the different planetary reservoirs are measured in the future, they

will have to be discussed in relation to the corresponding solar abundances, which, in turn, have to be derived from precise measurements of abundance averages and variations in the solar wind.

#### AVAILABILITY OF FOIL MATERIAL

The solar-wind-composition experiment foils are stored at the University of Berne. Most of the remaining foil material (approximately two-thirds of each foil) is slightly contaminated by lunar dust, and the methods used by the investigators have not been sufficient to remove this dust completely. However, valuable experiments can be conducted with moderately contaminated foils. Thus, an upper limit was obtained for the radioactive isotope  $^{56}\text{Co}$  (H. H. Loosli, personal communication). Also the radon emanation from the Moon was measured by using these foil pieces (R. L. Brodzinski, unpublished data). Investigators interested in obtaining foil pieces should direct their requests to the principal investigator, Dr. J. Geiss (appendix A), with a description of the experiment to be conducted. The decision to supply foil material will then be made in consultation with the JSC Lunar Sample Curator.

#### REFERENCES

- D-1. Geiss, J.; Bühler, F.; Cerutti, H.; and Eberhardt, P.: Solar-Wind Composition Experiment. Sec. 15 of Apollo 15 Preliminary Science Report. NASA SP-289, 1972.
- D-2. Bühler, F.; Eberhardt, P.; Geiss, J.; Meister, J.; and Signer, P.: Apollo 11 Solar Wind Composition Experiment: First Results. *Science*, vol. 166, no. 3912, Dec. 19, 1969, pp. 1502-1503.
- D-3. Geiss, J.; Eberhardt, P.; Signer, P.; Bühler, F.; and Meister, J.: The Solar-Wind Composition Experiment. Sec. 8 of Apollo 12 Preliminary Science Report. NASA SP-235, 1970.
- D-4. Geiss, J.; Eberhardt, P.; Bühler, F.; Meister, J.; and Signer, P.: Apollo 11 and 12 Solar Wind Composition Experiments: Fluxes of He and Ne Isotopes. *J. Geophys. Res.*, vol. 75, no. 31, Nov. 1970, pp. 5972-5979.
- D-5. Geiss, J.; Bühler, F.; Cerutti, H.; Eberhardt, P.; and Meister, J.: The Solar-Wind Composition Experiment. Sec. 12 of Apollo 14 Preliminary Science Report. NASA SP-272, 1971.

- D-6. Geiss, J.; Buehler, F.; Cerutti, H.; Eberhardt, P.; and Filleux, Ch.: Solar Wind Composition Experiment. Sec. 14 of Apollo 16 Preliminary Science Report. NASA SP-315, 1972.
- D-7. Michel, F. C.: Interaction Between the Solar Wind and the Lunar Atmosphere. Planet. Space Sci., vol. 12, no. 11, Nov. 1964, pp. 1075-1091.
- D-8. Manka, R. H.; and Michel, F. C.: Lunar Atmosphere as a Source of Argon-40 and Other Lunar Surface Elements. Science, vol. 169, no. 3942, July 17, 1970, pp. 278-280.
- D-9. Filleux, Ch.: Häufigkeiten der Helium- und Neonisotope im Sonnenwind aus Messungen an den Apollo-SWC-Folien. Ph. D. Dissertation, Univ. of Berne, 1975.
- D-10. Cerutti, H.: Die Bestimmung des Argons im Sonnenwind aus Messungen an den SWC-Folien. Ph. D. Dissertation, Univ. of Berne, 1974.
- D-11. Geiss, J.: On Elemental and Isotopic Composition of the Solar Wind. Paper presented at the Asilomar Conference on Solar Wind, Mar. 1971.
- D-12. Geiss, J.; Hirt, P.; and Leutwyler, H.: On Acceleration and Motion of Ions in Corona and Solar Wind. Solar Phys., vol. 12, 1970, pp. 458-483.
- D-13. Dyal, P.; Parkin, C. W.; Sonett, C. P.; DuBois, R. L.; and Simmons, G.: Lunar Portable Magnetometer Experiment. Sec. 12 of Apollo 16 Preliminary Science Report. NASA SP-315, 1972.
- D-14. Robbins, D. E.; Hundhausen, A. J.; and Bame, S. J.: Helium in the Solar Wind. J. Geophys. Res., vol. 75, no. 7, Mar. 1970, pp. 1178-1187.
- D-15. Ogilvie, K. W.; and Wilkerson, T. D.: Helium Abundance in the Solar Wind. Solar Phys., vol. 8, 1969, p. 435.
- D-16. Hirshberg, J. A.; Alksne, A.; Colburn, D. S.; Bame, S. J.; and Hundhausen, A. J.: Observation of a Solar Flare Induced Interplanetary Shock and Helium-Enriched Driver Gas. J. Geophys. Res., vol. 75, Jan. 1970, pp. 1-15.
- D-17. Hirshberg, J. A.: Solar Wind Helium Enhancements Following Major Solar Flares. Paper presented at the Asilomar Conference on Solar Wind, Mar. 1971.

- D-18. Bühler, F.; Eberhardt, P.; Geiss, J.; and Schwarzmüller, J.: Trapped Solar Wind Helium and Neon in Surveyor 3 Material. *Earth Planet. Sci. Lett.*, vol. 10, no. 3, Feb. 1971, pp. 297-306.
- D-19. Eberhardt, P.; Geiss, J.; Graf, H.; Grögler, N.; et al.: Trapped Solar Wind Noble Gases, Exposure Age and K/Ar Age in Apollo 11 Lunar Fine Material. *Proceedings of the Apollo 11 Lunar Science Conference, Supp. 1, vol. 2*, A. A. Levinson, ed., Pergamon Press (New York), 1970, pp. 1037-1070.
- D-20. Eberhardt, P.; Geiss, J.; Graf, H.; Grögler, N.; et al.: Trapped Solar Wind Noble Gases in Apollo 12 Lunar Fines 12001 and Apollo 11 Breccia 10046. *Proceedings of the Third Lunar Science Conference, vol. II*, Dieter Heymann, ed., MIT Press (Cambridge), 1972, pp. 1821-1856.
- D-21. Suess, H. E.: Die Häufigkeit der Edelgase auf der Erde und im Kosmos. *J. Geol.*, vol. 57, 1949, p. 600.
- D-22. Geiss, J.: Ueber die Geschichte der Meteorite aus Isotopenmessungen. *Chimia (Switzerland)*, vol. 11, 1957, pp. 349-363.

#### BIBLIOGRAPHY

- Bame, S. J.; Asbridge, J. R.; Hundhausen, A. J.; and Strong, I. B.: Solar Wind and Magnetosheath Observations During the Jan. 13-14, 1967, Geomagnetic Storm. *J. Geophys. Res.*, vol. 73, no. 17, Sept. 1, 1968, pp. 5761-5767.
- Black, D. C.: On the Origins of Trapped Helium, Neon and Argon Isotopic Variations in Meteorites - I. Gas-Rich Meteorites, Lunar Soil and Breccia. *Geochim. Cosmochim. Acta*, vol. 36, no. 3, Mar. 1972, pp. 347-375.
- Bühler, F.; Geiss, J.; Meister, J.; Eberhardt, P.; et al.: Trapping of the Solar Wind in Solids. *Earth Planet. Sci. Lett.*, vol. 1, 1966, pp. 249-255.
- Cerutti, H.: Einfang von niederenergetischen Edelgasen durch Silikate. M.S. Thesis, Univ. of Berne, 1970.
- Danziger, I. J.: The Cosmic Abundance of Helium. *Ann. Rev. Astron. Astrophys.*, vol. 8, Leo Goldberg, ed., Annual Reviews Inc. (Palo-Alto), 1970, pp. 161-178.

- Davies, J. A.; Brown, F.; and McCargo, M.: Range of Xe<sup>133</sup> and Ar<sup>41</sup> Ions of Kiloelectron Volt Energies in Aluminum. *Can. J. Phys.*, vol. 41, no. 6, June 1963, pp. 829-843.
- Eberhardt, P.; Geiss, J.; and Grögler, N.: Further Evidence on the Origin of Trapped Gases in the Meteorite Khor Temiki. *J. Geophys. Res.*, vol. 70, no. 17, Sept. 1, 1965, pp. 4375-4378.
- Eberhardt, P.; Geiss, J.; Graf, H.; Grögler, N.; et al.: Trapped Solar Wind Noble Gases, Exposure Age and K/Ar Age in Apollo 11 Lunar Fine Material. *Proceedings of the Apollo 11 Lunar Science Conference, Supp. 1, vol. 2, A. A. Levinson, ed., Pergamon Press (New York), 1970, pp. 1037-1070.*
- Eberhardt, P.; and Hofmann, A.: Diffusion Behavior of Low-Energy Helium Ions Implanted in Aluminum. *Earth Planet. Sci. Lett.*, vol. 23, 1974, pp. 304-307.
- Ezer, D.; and Cameron, A. G. W.: A Study of Solar Evolution. *Can. J. Phys.*, vol. 43, Aug. 1965, pp. 1497-1517.
- Filleux, Ch.: Einfangverhalten von Al<sub>2</sub>O<sub>3</sub> für niederenergetische Edelgasionen, M. S. Thesis, Univ. of Berne, 1971.
- Geiss, J.; Eberhardt, P.; Signer, P.; Bühler, F.; and Meister, J.: The Solar-Wind Composition Experiment. Sec. 8 of Apollo 11 Preliminary Science Report. NASA SP-214, 1969.
- Geiss, J.; and Reeves, H.: Cosmic and Solar System Abundances of Deuterium and Helium-3. *Astron. Astrophys.*, vol. 18, no. 1, Apr. 1972, pp. 126-132.
- Hundhausen, A. J.: Composition and Dynamics of the Solar Wind Plasma. *Rev. Geophys. Space Phys.*, vol. 8, no. 4, Nov. 1970, pp. 729-811.
- Hundhausen, A. J.; Asbridge, J. R.; Bane, S. J.; Gilbert, H. E.; and Strong, I. B.: Vela 3 Satellite Observations of Solar Wind Ions: A Preliminary Report. *J. Geophys. Res.*, vol. 72, no. 1, Jan. 1967, pp. 87-100.
- Meister, J.: Ein Experiment zur Bestimmung der Zusammensetzung und der Isotopenverhältnisse des Sonnenwindes: Einfangverhalten von Aluminium für niederenergetische Edelgasionen. Ph. D. Dissertation, Univ. of Berne, 1969.
- Signer, P.; Eberhardt, P.; and Geiss, J.: Possible Determination of the Solar Wind Composition. *J. Geophys. Res.*, vol. 70, no. 9, May 1965, pp. 2243-2244.

Snyder, Conway W.; and Neugebauer, Marcia: Interplanetary Solar-Wind Measurements by Mariner II. Space Res., vol. 4, 1964, pp. 89-113.

Stettler, W.: Einfangverhalten von Platin für Edelgasen mit Sonnenwindenergien. M. S. Thesis, Univ. of Berne, 1972.

Wolfe, J. H.; Silva, R. W.; McKibbin, D. D.; and Mason, R. H.: The Compositional, Anisotropic, and Nonradial Flow Characteristics of the Solar Wind. J. Geophys. Res., vol. 71, no. 13, July 1966, pp. 3329-3335.

TABLE D-I.- DATA ON LUNAR SURFACE EXPOSURE FOR  
SOLAR-WIND COMPOSITION EXPERIMENTS

Mission	Exposure initiation		Exposure duration, hr:min
	Date	G.m.t., hr:min	
Apollo 11	July 21, 1969	03:35	01:17
Apollo 12	Nov. 19, 1969	12:35	18:42
Apollo 14	Feb. 5, 1971	15:15	21:00
Apollo 15	July 31, 1971	19:36	41:08
Apollo 16	Apr. 21, 1972	23:01	45:05

TABLE D-II.- FIRST RESULTS FROM THE ANALYSES OF THE ALUMINUM FOIL  
FROM THE APOLLO 16 SOLAR-WIND-COMPOSITION EXPERIMENT

Apollo 16 sample no.	Area, cm <sup>2</sup>	<sup>4</sup> He concentration, 10 <sup>10</sup> atoms/cm <sup>2</sup>	<sup>4</sup> He/ <sup>3</sup> He	<sup>4</sup> He/ <sup>20</sup> Ne	<sup>20</sup> Ne/ <sup>22</sup> Ne	<sup>22</sup> Ne/ <sup>21</sup> Ne	<sup>20</sup> Ne/ <sup>36</sup> Ar
<sup>a</sup> 2-1	5.02	108	2290	510	14.0	32	29
2-2	4.98	107	2300	490	13.9	27	30
<sup>a</sup> 2-3	5.04	101	2280	500	13.5	31	27
2-4	5.17	108	2280	490	13.7	27	31
<sup>a</sup> 2-5	10.35	100	2310	490	13.9	35	28

<sup>a</sup>Oxide layer on back side of aluminum foil mechanically removed.

TABLE D-III.- SOLAR-WIND ABUNDANCE RATIOS DETERMINED FROM  
THE FOIL EXPOSURE PERIODS OF THE APOLLO MISSIONS

Mission	${}^4\text{He}/{}^3\text{He}$	${}^4\text{He}/{}^{20}\text{Ne}$	${}^{20}\text{Ne}/{}^{22}\text{Ne}$	${}^{22}\text{Ne}/{}^{21}\text{Ne}$
Apollo 11	1860 ± 140	430 ± 90	13.5 ± 1.0	-
Apollo 12	2450 ± 100	620 ± 70	13.1 ± 0.6	26 ± 12
Apollo 14	2230 ± 140	550 ± 70	13.65 ± 0.50	-
Apollo 15	2310 ± 120	550 ± 50	13.65 ± 0.30	31 ± 4
Apollo 16	2260 ± 100	570 ± 50	13.80 ± 0.40	31 ± 4

TABLE D-IV.- PRELIMINARY RESULTS ON ARGON  
TRAPPED IN SOLAR-WIND-COMPOSITION FOILS

Mission	${}^{20}\text{Ne}/{}^{36}\text{AR}$
Apollo 14	37 + 10 - 5
Apollo 15	20 + 8 - 5
Apollo 16	29 ± 6

TABLE D-V.- COMPARISON OF WEIGHTED AVERAGES OF SOLAR-WIND ION ABUNDANCES OBTAINED FROM  
THE SOLAR-WIND-COMPOSITION EXPERIMENTS WITH ABUNDANCES IN SURFACE-CORRELATED  
GASES<sup>a</sup> OF LUNAR FINES MATERIALS AND A BRECCIA AND IN

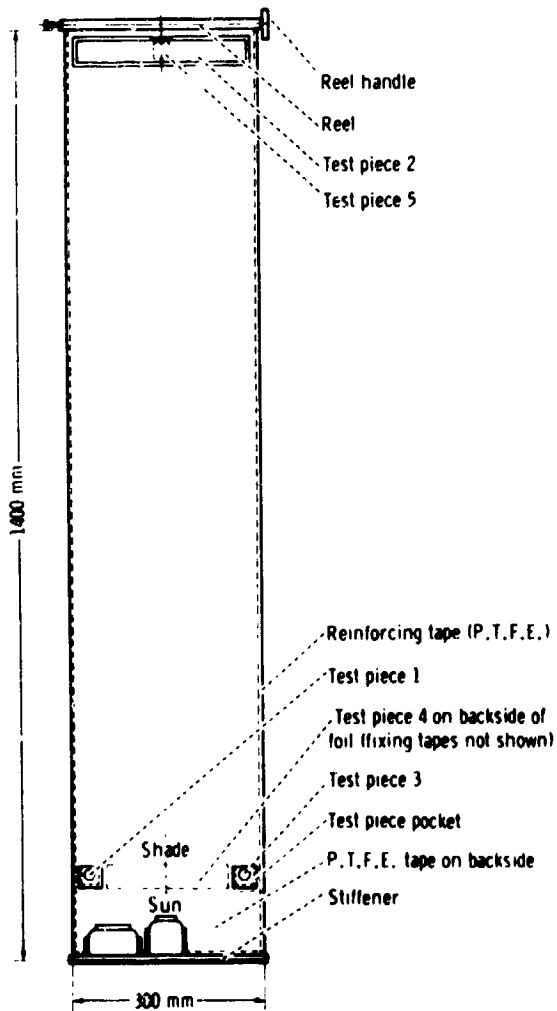
THE ATMOSPHERE OF THE EARTH

Source	$^4\text{He}/^3\text{He}$	$^4\text{He}/^{20}\text{Ne}$	$^{20}\text{Ne}/^{22}\text{Ne}$	$^{22}\text{Ne}/^{21}\text{Ne}$	$^{20}\text{Ne}/^{36}\text{Ar}$
Solar wind (average from solar- wind-composition experiments)	2350 ± 120	570 ± 70	13.7 ± 0.3	30 ± 4	<sup>b</sup> 45 ± 10
Lunar fines 10084	2550 ± 250	96 ± 18	12.65 ± 0.2	31.0 ± 1.2	7 ± 2
Ilmenite from 10084	2720 ± 100	218 ± 8	12.85 ± 0.1	31.1 ± 0.8	27 ± 4
Ilmenite from 12001	2700 ± 80	253 ± 10	12.9 ± 0.1	32.0 ± 0.4	27 ± 5
Ilmenite from breccia 10046	3060 ± 150	231 ± 13	12.65 ± 0.15	31.4 ± 0.4	(c)
Terrestrial atmosphere	7 × 10 <sup>5</sup>	.3	9.80 ± 0.08	34.5 ± 1.0	.5

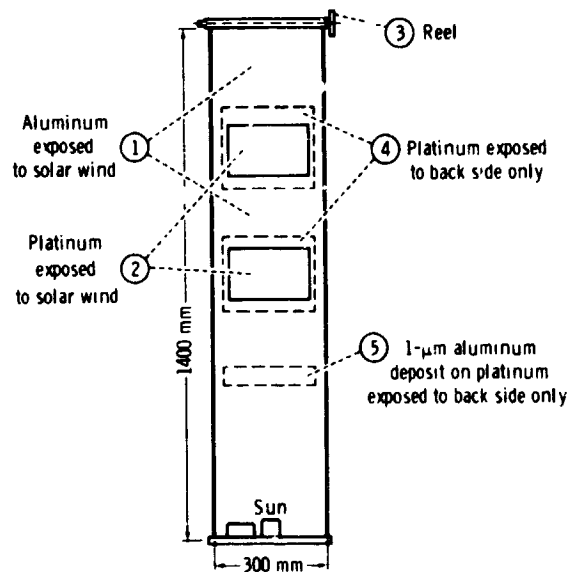
<sup>a</sup>Data for surface-correlated gases in lunar materials are from references D-19 and D-20.

<sup>b</sup>Based on new results obtained after publication of reference D-6.

<sup>c</sup>Variable.



(a) Configuration for Apollo missions 11, 12, 14, and 15.



Numbers in circles refer to sections.

1. Section composed of 15- $\mu\text{m}$  aluminum with an oxide layer of 0.7  $\mu\text{m}$  on the back side.
2. Section of 5- $\mu\text{m}$  platinum foil exposed to the Sun and shade.
3. Section remaining wound around the reel.
4. Platinum foils exposed to the antisolar direction.
5. Platinum foil covered by an aluminum deposit 0.98 + 0.02  $\mu\text{m}$  thick; exposed to the antisolar direction.

(b) Configuration for Apollo mission 16.

Figure D-1.- Details of exposed foil assembly.

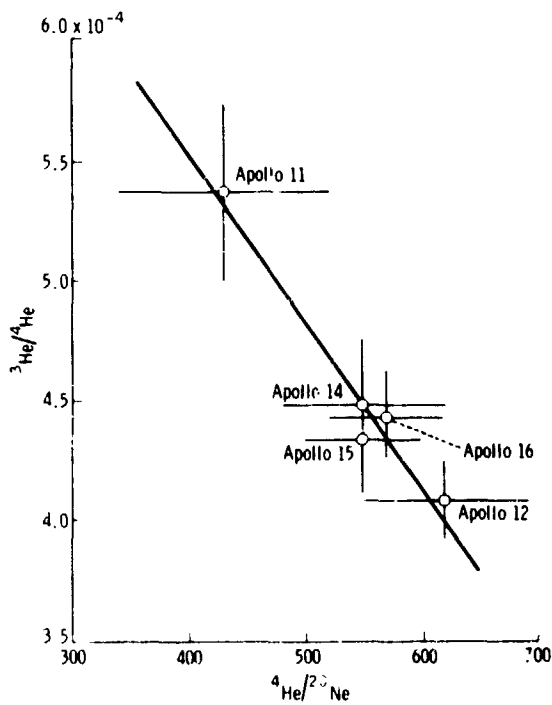


Figure D-2.- Correlation between the  $^3\text{He}/^4\text{He}$  and  $^4\text{He}/^{20}\text{Ne}$  solar wind abundance ratios as determined from the five Apollo foil exposures.

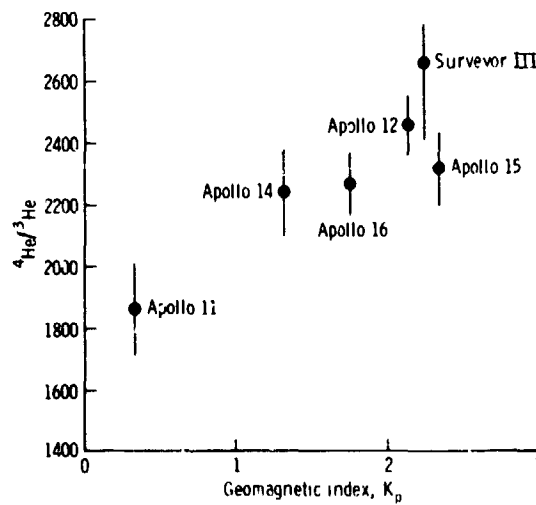


Figure D-3.- Correlation between the solar wind  $^4\text{He}/^3\text{He}$  abundance ratio and the level of disturbance in the solar wind as indicated by the geomagnetic index  $K_p$ . The data obtained from the analysis of Surveyor III material are described in reference D-18.